

**Bio-orthogonal conjugation for “wiring”  
redox-active proteins/enzymes to any  
conductive surface**

**Nicholas David James Yates**

**Doctor of Philosophy**

**University of York**

**Chemistry**

**March 2021**

## Abstract

This thesis first illustrates the utility and limitations of protein film electrochemistry of adsorbed species via the analysis of a fungal Lytic Polysaccharide Monooxygenase enzyme. While a useful enzyme assay of H<sub>2</sub>O<sub>2</sub> reduction is developed, detailed analysis of the underpinning reversible enzyme electron transfer processes is limited by background redox contributions from the carbon nanotubes which are required to stabilise the enzyme in an electroactive configuration. The rest of this thesis describes the development of methodologies for achieving electroactive immobilisation of redox proteins/enzymes onto electrode surfaces. Electroactive immobilisation of redox proteins/enzymes via covalent bonds has applications in the fabrication of biosensors and the development of green technologies/biochemical synthetic approaches, yet most published methodologies for achieving covalent immobilisation of proteins have relied on performing ligations between amine-reactive motifs on electrode surfaces and protein lysine residues. This results in many redox proteins/enzymes becoming immobilised in non-electroactive orientations or in orientations that otherwise hinder the redox enzyme's ability to perform catalysis. In an effort to address this, methodologies for the incorporation of bio-orthogonal aldehyde motifs into proteins were investigated, and a protein immobilisation approach was developed in which hydroxylamine-functionalised electrode surfaces undergo bio-orthogonal ligation to aldehyde-functionalised proteins. As characterising and controlling surface chemistries is notoriously difficult, a new method is also under development that aims to enable covalent orientation-selective electroactive redox protein/enzyme immobilisation via the direct electro-grafting of redox proteins/enzymes that have been site-specifically labelled with aryl diazonium cations. I report the first ever usage of triazabutadienes as photocaged sources of aryl diazonium cations for use as electrode derivatisation agents in aqueous solutions at near-neutral pH, and, to the best of my knowledge, the first site-specific installations of triazabutadienes/diazonium cations onto the surfaces of proteins. I hope that further development of this method will enable the orientation-selective electroactive immobilisation of redox proteins/enzymes.

---

## Table of Contents

<b>Abstract .....</b>	<b>2</b>
<b>Table of Contents .....</b>	<b>3</b>
<b>List of Abbreviations.....</b>	<b>10</b>
<b>List of Tables .....</b>	<b>12</b>
<b>List of Figures/Schemes .....</b>	<b>15</b>
<b>Acknowledgements .....</b>	<b>31</b>
<b>Authors Declaration .....</b>	<b>33</b>
<b>Chapter 1. Introduction .....</b>	<b>35</b>
<b>1.1 Redox proteins.....</b>	<b>35</b>
<b>1.2 Why immobilise redox proteins onto electrode surfaces?.....</b>	<b>36</b>
<b>1.3 Existing strategies for redox protein/enzyme immobilisation .....</b>	<b>39</b>
<b>1.3.1 Electroactive protein adsorption onto unmodified conducting surfaces .....</b>	<b>39</b>
1.3.1.1 Carbon bulk materials.....	40
1.3.1.2 Carbon nanomaterials.....	44
1.3.1.3 Metal oxide semiconductors.....	45
<b>1.3.2 Common electrode functionalisation strategies to promote electroactive surface adsorption .</b>	<b>46</b>
1.3.2.1 Thiol self-assembled monolayers on gold.....	47
1.3.2.2 Single component SAMs on gold .....	48
1.3.2.3 Multicomponent SAMs on gold .....	49
1.3.2.4 Long length conducting SAMs.....	50
1.3.2.5 Aryl diazonium salt reduction .....	51
<b>1.3.3 Covalent coupling of electrodes to native proteins.....</b>	<b>54</b>
1.3.3.1 Peptide bond formation.....	54
1.3.3.2 Imine tethering .....	56
<b>1.3.4 Crosslinking strategies for site-specifically connecting proteins to electrodes .....</b>	<b>57</b>
1.3.4.1 Redox-centre targeted binding .....	57
1.3.4.2 Cysteine-based surface ligations.....	59
1.3.4.3 Crosslinking to unnatural amino acids .....	61
<b>1.3.5 Reflection upon the existing strategies for redox protein/enzyme immobilisation .....</b>	<b>63</b>

---

<b>1.4</b>	<b>The techniques commonly used in protein film electrochemistry</b> .....	<b>63</b>
<b>1.4.1</b>	<b>Direct current cyclic voltammetry</b> .....	<b>63</b>
1.4.1.1	The measurement of the number of electrons involved in a redox couple and the determination of the Gibbs free energy change associated with electron transfer .....	65
1.4.1.2	The measurement of electron-transfer kinetics. ....	68
1.4.1.3	Other uses of cyclic voltammetry .....	70
<b>1.4.2</b>	<b>Linear sweep voltammetry</b> .....	<b>70</b>
<b>1.4.3</b>	<b>Square wave voltammetry</b> .....	<b>71</b>
<b>1.4.4</b>	<b>Chronoamperometry/amperometry</b> .....	<b>73</b>
<b>1.4.5</b>	<b>Fourier-transform alternating current voltammetry</b> .....	<b>75</b>
<b>1.5</b>	<b>Summary and concluding remarks</b> .....	<b>78</b>
<b>1.6</b>	<b>Aims of the project and thesis overview</b> .....	<b>79</b>
<b>Chapter 2. Electrochemical interrogation of an AA9 LPMO</b> .....		<b>82</b>
<b>2.1</b>	<b>Introduction</b> .....	<b>82</b>
<b>2.1.1</b>	<b>LPMO overview</b> .....	<b>82</b>
<b>2.1.2</b>	<b>The possible reaction mechanisms of LPMOs</b> .....	<b>86</b>
<b>2.1.3</b>	<b>The need for electrochemical assay of LPMOs</b> .....	<b>92</b>
<b>2.1.4</b>	<b>Aims</b> .....	<b>94</b>
<b>2.2</b>	<b>Results and Discussion</b> .....	<b>95</b>
<b>2.2.1</b>	<b>Preliminary analysis of an AA9 from <i>Aspergillus nidulans</i>: An6428-AA9</b> .....	<b>95</b>
2.2.1.1	Copper-loading and purification .....	95
2.2.1.2	Structural analysis .....	96
2.2.1.3	Redox titration with <i>N,N,N',N'</i> -tetramethyl-p-phenylenediamine .....	98
<b>2.2.2</b>	<b>Electroactive immobilisation of An6428-AA9</b> .....	<b>99</b>
<b>2.2.3</b>	<b>The nature of the background signals</b> .....	<b>103</b>
<b>2.2.4</b>	<b>Electrochemical analysis of the putative An6428-AA9 redox couple</b> .....	<b>110</b>
2.2.4.1	Isolation and analysis .....	110
<b>2.2.5</b>	<b>Amperometric responses to H<sub>2</sub>O<sub>2</sub> and oxygen</b> .....	<b>113</b>
<b>2.3</b>	<b>Summary and conclusions</b> .....	<b>117</b>
<b>Chapter 3. The functionalisation of electrode surfaces with amine moieties</b> .....		<b>120</b>
<b>3.1</b>	<b>Introduction</b> .....	<b>120</b>



## Table of Contents

---

3.1.1	The utility of amine-functionalised surfaces .....	120
3.1.2	Common approaches for amine-functionalisation of electrode surfaces .....	121
3.1.3	Monolayer amine-functionalisation of electrode surfaces using diazonium chemistry .....	123
3.1.4	Aims .....	131
<b>3.2</b>	<b>Results and Discussion.....</b>	<b>132</b>
3.2.1	Screening diazonium electro-reduction-based approaches relevant to the introduction of amine functionalities onto electrode surfaces .....	132
3.2.2	Development of a method for the introduction of reactive aliphatic amine functionalities onto electrode surfaces as near-monolayers .....	138
3.2.2.1	The functionalisation of electrode surfaces with aliphatic amine near-monolayers.....	138
3.2.2.2	Derivatisation of aliphatic amine-functionalised electrode surfaces via amide bond formation .....	142
3.2.3	Further applications of the near-monolayer amine-functionalisation system .....	145
3.2.3.1	A model system for the development of Pure Sinusoidal Voltammetry.....	145
<b>3.3</b>	<b>Summary and conclusions .....</b>	<b>146</b>
<b>Chapter 4. Introduction of aldehydes into proteins and solution-phase ligation .....</b>		<b>149</b>
<b>4.1</b>	<b>Introduction.....</b>	<b>149</b>
4.1.1	Aims .....	151
<b>4.2</b>	<b>Results and Discussion.....</b>	<b>152</b>
4.2.1	Performing oxidative cleavage of <i>N</i> -terminal threonine/serine residues .....	152
4.2.1.1	One-pot oxidation and derivatisation of the CTB <i>N</i> -terminus .....	152
4.2.1.2	Oxidation of the <i>N</i> -terminus of thioredoxin 1 .....	156
4.2.2	Performing oxidative cleavage on glycan 1,2-cis diols.....	159
4.2.2.1	Aldehyde-functionalisation and fluorescent labelling of the glycans on an AA9 LPMO .....	162
4.2.3	Pyridoxal 5'-phosphate (PLP) mediated transamination of the <i>N</i> -terminal glycine residue of a <i>c</i> -type cytochrome.....	168
4.2.3.1	Initial work with CjX183-D.....	168
4.2.3.2	Wild-type CjX183-D.....	170
4.2.3.3	A lysine mutant of CjX183-D .....	177
4.2.4	Introduction of formylglycine residues into peptides and proteins.....	183
4.2.4.1	Introduction of fGly into peptides .....	186
4.2.4.2	Introduction of fGly into a redox protein.....	194
<b>4.3</b>	<b>Summary and conclusions. ....</b>	<b>201</b>

---

4.3.1	Critical assessment of aldehyde incorporation strategies .....	201
4.3.2	Critical assessment of aldehyde ligation strategies .....	203
<b>Chapter 5. Aldehyde-mediated protein-to-surface tethering via controlled diazonium electrode functionalisation using protected hydroxylamines..... 205</b>		
5.1	Introduction.....	205
5.1.1	Aims .....	206
5.2	Results and Discussion.....	206
5.2.1	Development of a method for the introduction of hydroxylamine functionalities onto electrode surfaces as a near-monolayer .....	206
5.2.1.1	The design and synthesis of a suitable aryl diazonium precursor.....	206
5.2.1.2	The functionalisation of electrode surfaces with hydroxylamines .....	208
5.2.1.3	Characterising derivatised electrode surfaces .....	210
5.2.1.4	Ligating hydroxylamine-functionalised electrode surfaces to aldehyde-functionalised redox-active molecules.....	217
5.2.2	Immobilisation of horseradish peroxidase onto a hydroxylamine-functionalised electrode surface .....	222
5.2.2.1	Electrochemical assay .....	222
5.2.2.2	Quartz crystal microbalance with dissipation monitoring .....	225
5.3	Summary and conclusions. ....	227
<b>Chapter 6. Usage of triazabutadienes as a photocaged source of diazonium cations in diazonium electro-grafting ..... 229</b>		
6.1	Introduction.....	229
6.1.1	Aryl-diazonium cation functionalisation of proteins could be used in a “protein- down” approach to redox protein immobilisation .....	231
6.1.2	Considerations regarding the design and synthesis of triazabutadiene probes .....	235
6.1.3	Aims .....	238
6.2	Results and Discussion.....	239
6.2.1	The synthesis of different classes of triazabutadiene probes .....	239
6.2.1.1	“Classic” triazabutadiene probes .....	239
6.2.1.2	3-(1-mesityl-1 <i>H</i> -imidazol-3-ium-3-yl)propane-1-sulfonate based triazabutadiene probes.	242
6.2.1.3	Phthalimide-type triazabutadiene probes .....	243
6.2.2	UV-initiated diazonium release from different classes of triazabutadiene .....	243

## Table of Contents

---

6.2.2.1	UV-initiated diazonium release from 3-(1-mesityl-1 <i>H</i> -imidazol-3-ium-3-yl)propane-1 - sulfonate derived triazabutadiene probes.....	243
6.2.2.2	UV-initiated diazonium release from “Classic” triazabutadiene probes.....	245
6.2.2.3	UV-initiated diazonium release from phthalimide-type triazabutadiene probes.....	254
<b>6.2.3</b>	<b>Reviewing the suitability of triazabutadiene scaffolds for usage in the diazonium electro-grafting of proteins.....</b>	<b>256</b>
<b>6.2.4</b>	<b>Bioconjugation of triazabutadiene probes to redox proteins.....</b>	<b>257</b>
6.2.4.1	The usage of <b>T8</b> in maleimide ligation to DsbA mutants .....	257
6.2.4.2	The usage of <b>T14</b> for amide bond formation to CjX183-D .....	267
<b>6.2.5</b>	<b>Preliminary attempts at diazonium electro-grafting using triazabutadiene-labelled proteins... ..</b>	<b>275</b>
6.2.5.1	Attempted usage of DsbA <sub>middle</sub> + <b>T8</b> in direct electro-grafting to electrode surfaces .....	275
6.2.5.2	Attempted usage of triazabutadiene-labelled CjX183-D R51K in direct electro-grafting to electrode surfaces.....	279
<b>6.3</b>	<b>Summary and conclusions .....</b>	<b>282</b>
<b>Chapter 7. Conclusion and future perspectives.....</b>		<b>285</b>
<b>Chapter 8. Experimental procedures and characterisation .....</b>		<b>293</b>
<b>8.1</b>	<b>Non-chapter specific experimental procedures/information.....</b>	<b>293</b>
<b>8.1.1</b>	<b>Spectroscopic and spectrometric instruments and standard practices.....</b>	<b>293</b>
8.1.1.1	ESI-LC/MS of peptides and proteins.....	293
<b>8.1.2</b>	<b>Sodium dodecyl sulfate polyacrylamide gel electrophoresis (SDS-PAGE) analysis of proteins... ..</b>	<b>294</b>
<b>8.1.3</b>	<b>Bradford Assay and protein extinction coefficients.....</b>	<b>296</b>
<b>8.1.4</b>	<b>Protein preparations.....</b>	<b>297</b>
8.1.4.1	Preparation of DsbA mutants .....	297
8.1.4.2	Preparation of CjX183-D variants.....	299
<b>8.1.5</b>	<b>Electrochemical apparatus and standard electrochemical practice .....</b>	<b>302</b>
8.1.5.1	Electrochemical cells and electrode setup.....	302
8.1.5.2	Working Electrodes .....	303
8.1.5.3	Potentiostats.....	303
8.1.5.4	Standard electrochemical practice .....	304
<b>8.2</b>	<b>Experimental procedures for Chapter 2.....</b>	<b>305</b>
<b>8.2.1</b>	<b>Materials .....</b>	<b>305</b>
<b>8.2.2</b>	<b>Chemical oxidation of MWCNT A.....</b>	<b>305</b>

## Table of Contents

---

<b>8.2.3</b>	<b>Copper-loading and purification of An6428-AA9.....</b>	<b>305</b>
<b>8.2.4</b>	<b>Electrochemical experiments/procedures/electrode modification .....</b>	<b>306</b>
<b>8.3</b>	<b>Experimental procedures for Chapter 3.....</b>	<b>310</b>
<b>8.3.1</b>	<b>Materials .....</b>	<b>310</b>
<b>8.3.2</b>	<b>Synthetic procedures/molecular characterisations.....</b>	<b>310</b>
8.3.2.1	Protected aliphatic amine functionalised aryl diazonium precursors.....	310
8.3.2.2	Ferrocene derivatives.....	315
<b>8.3.3</b>	<b>Electrochemical experiments/procedures/electrode modification .....</b>	<b>317</b>
8.3.3.1	Functionalisation of glassy carbon electrode surfaces with amines.....	319
8.3.3.2	Functionalisation of glassy carbon electrode surfaces with ferrocene moieties .....	320
<b>8.4</b>	<b>Experimental procedures for Chapter 4.....</b>	<b>321</b>
<b>8.4.1</b>	<b>Oxidative cleavage of <i>N</i>-terminal threonine/serine residues .....</b>	<b>321</b>
	CTB oxidation and labelling: .....	321
	Thioredoxin 1 oxidation:.....	321
	Solution phase oxime ligation to thioredoxin 1:.....	321
<b>8.4.2</b>	<b>Oxidative cleavage of glycan cis-diols .....</b>	<b>321</b>
	Aldehyde installation via oxidative cleavage of An6428-AA9 glycan 1,2-cis diols.....	321
	Labelling of An6428-AA9 glycan aldehydes.....	322
	De-glycosylation of An6428-AA9 .....	322
<b>8.4.3</b>	<b>Pyridoxal 5'-phosphate mediated transamination of <i>N</i>-terminal glycine residues .....</b>	<b>323</b>
	Transamination of the <i>N</i> -terminal glycine residue of CjX183-D.....	323
	Organocatalyst-mediated protein aldol ligation to aldehyde-functionalised CjX183-D.....	323
<b>8.4.4</b>	<b>Formylglycine installation .....</b>	<b>324</b>
<b>8.4.5</b>	<b>Synthesis of aldehyde-ligating probes.....</b>	<b>328</b>
8.4.5.1	Synthesis of <b>Dan6</b> .....	328
8.4.5.2	Synthesis of <b>Pyr3</b> .....	339
8.4.5.3	Synthesis of <b>IP8</b> .....	343
<b>8.5</b>	<b>Experimental procedures for Chapter 5.....</b>	<b>349</b>
<b>8.5.1</b>	<b>Synthesis of protected hydroxylamine-functionalised aryl diazonium precursors .....</b>	<b>349</b>
<b>8.5.2</b>	<b>Solution analogues of the electrode-surface reactions .....</b>	<b>354</b>
<b>8.5.3</b>	<b>Functionalisation of electrode surfaces with hydroxyl amines via diazonium electro-grafting..</b> .....	<b>362</b>
<b>8.6</b>	<b>Experimental procedures for Chapter 6.....</b>	<b>368</b>

## Table of Contents

---

<b>8.6.1</b>	<b>Synthetic procedures/molecular characterisations</b> .....	<b>368</b>
8.6.1.1	Synthesis of triazabutadienes .....	368
8.6.1.2	Synthesis of resorcinol probes .....	415
<b>8.6.2</b>	<b>UV-initiated diazonium release from different classes of triazabutadiene</b> .....	<b>424</b>
8.6.2.1	Tracking triazabutadiene degradation/diazonium cation reactivity via UV-vis spectrometry .. .....	424
8.6.2.2	Tracking triazabutadiene degradation/diazonium cation reactivity using <sup>1</sup> H-NMR .....	424
<b>8.6.3</b>	<b>Bio-conjugation of triazabutadienes to redox proteins</b> .....	<b>426</b>
8.6.3.1	The usage of <b>T8</b> in maleimide ligation to DsbA mutants and subsequent ligation to resorcinol probes .....	426
8.6.3.2	The usage of <b>T14</b> in amide bond formation ligation to CjX183-D .....	427
<b>8.6.4</b>	<b>Electrochemical experiments/procedures/electrode modification</b> .....	<b>428</b>
8.6.4.1	Specialised electrochemical experiment methods .....	430
<b>Appendix 1. The connection of electrochemistry to thermodynamics</b> .....		<b>432</b>
<b>Appendix 2. Specially written code package</b> .....		<b>437</b>
Using the code package .....		437
Common problems.....		449
Advanced usage .....		450
<b>Appendix 3. Supplementary Figures and Tables</b> .....		<b>452</b>
<b>Appendix 4. Experimentation with creating a CjX183-D-TEV-HIS<sub>6</sub>_pET construct</b> .....		<b>458</b>
Commercially available PET vector.....		458
The CjX183D_pCW construct .....		461
Making the CjX183-D-TEV-HIS <sub>6</sub> _pET construct .....		463
<b>Appendix 5. Preparation of the CjX183D-R51K_pCW construct</b> .....		<b>465</b>
<b>Appendix 6. Gene/amino acid sequences, theoretical isoelectric points and molecular weights of proteins</b> .....		<b>467</b>
<b>References</b> .....		<b>469</b>

---

## List of Abbreviations

AA	Auxiliary-activity
ac	Alternating current
AFM	Atomic force microscopy
Ald-TrxA	Thioredoxin 1 from <i>E. coli</i> functionalised with an N-terminal aldehyde
AMP	Ampicillin
anSME	Anaerobic sulfatase maturing enzyme
ATR	Attenuated Total Reflection
BDD	Boron-doped diamond
CD	Circular dichroism
CDI	1,1' Carbonyldiimidazole
C <sub>DL</sub>	Double layer capacitance
CMC	<i>N</i> -cyclohexyl- <i>N'</i> -(2-morpholinoethyl)carbodiimide-methyl- <i>p</i> -toluenesulfonate
CoEMS	The University York Centre of Excellence in Mass Spectrometry
CT	Cholera toxin
CTA	Cholera toxin subunit A
CTB	Cholera toxin subunit B
CV	Cyclic voltammogram
DCC	<i>N,N'</i> -Dicyclohexylcarbodiimide
DCM	Dichloromethane
dCV	Direct current cyclic voltammetry
DIAD	Diisopropyl azodicarboxylate
DMF	Dimethylformamide
DMP	2,6-Dimethoxyphenol
DMSO	Dimethylsulfoxide
DPPH	2,2-Diphenyl-1-picrylhydrazyl
<i>E. Coli</i>	<i>Escherichia Coli</i>
E <sup>0</sup>	Standard reduction potential
EDC	1-Ethyl-3-(3-dimethylaminopropyl)carbodiimide
E <sup>f</sup>	Formal reduction potential
EIS	Electrochemical impedance spectroscopy
Endo H	Endoglycosidase H
ESI	Electrospray ionisation
FGE	Formylglycine generating enzyme
fGly	Formylglycine
FT	Fourier-transform
FTacV	Fourier-transform alternating current voltammetry
GC	Glassy carbon
HBTU	Benzotriazol-1-yloxy(dimethylamino)methylidene]-dimethylazanium hexafluorophosphate

## List of Abbreviations

---

HCTU	2-(6-Chloro-1-H-benzotriazole-1-yl)-1,1,3,3-tetramethylamminium hexafluorophosphate
HOBt	Hydroxybenzotriazole
HPLC	High-performance liquid chromatography
HRMS	High-resolution mass spectrometry
HRP	Horseradish peroxidase
IR	Infrared
LB	Lysogeny broth
LC	Liquid chromatography
LPMO	Lytic polysaccharide monoxygenase
MBTH	3-Methyl-2-benzothiazolinone hydrazone
MS	Mass spectrometry
MWCNT	Multi-walled carbon nanotube
NHS	N-Hydroxysuccinimide
NMR	Nuclear magnetic resonance
PFE	Protein film electrochemistry
PFV	Protein film voltammetry
PGE	Pyrolytic graphite edge
Phos	Phosphate
PLP	Pyridoxal 5'-phosphate
PNGase F	Peptide <i>N</i> Glycosidase F
PSV	Pure Sinusoidal Voltammetry
QCM-D	Quartz Crystal Microbalance with Dissipation monitoring
$R_{ct}$	Resistance to charge transfer
$R_t$	Room temperature
SAM	Self-assembled monolayer, typically of alkanethiols
SCE	Saturated calomel electrode
SDS	Sodium dodecyl sulfate
SDS-PAGE	Sodium dodecyl sulfate polyacrylamide gel electrophoresis
SE	Standard error
SECM	Scanning electrochemical microscopy
SHE	Standard hydrogen electrode
Sulfo-NHS	<i>N</i> -Hydroxysulfosuccinimide sodium salt
SWCNT	Single-walled carbon nanotube
THF	Tetrahydrofuran
TMP	<i>N,N,N',N'</i> -Tetramethyl- <i>p</i> -phenylenediamine
TrxA	Thioredoxin 1 from <i>E. coli</i>
UV	Ultraviolet
UV-vis	Ultraviolet-visible
$v$	Scan rate
XPS	X-ray photoelectron spectroscopy

---

## List of Tables

### Chapter 1

**Table 1.1.** A selection of strategies for the functionalisation of electrode surfaces via diazonium cation electro-grafting, and subsequent chemical/electrochemical treatments that further modify the electrode surface polarity or provide chemical derivatives that can be exploited in covalent coupling strategies. (Page 53)

### Chapter 2

**Table 2.1.** The origin and substrate specificities of the six LPMO families currently recognised in the CAZY database. (Page 83)

**Table 2.2.** Reduction potentials reported for LPMOs. Values marked with an \* were recorded at 50 °C. Those without were recorded at temperatures close to 25 °C (i.e.  $25 \pm 2$  °C). Note that, with the exception of reference [298], it would seem that those using redox titration as the method for determination of reduction potential use a literature value for the reduction potential of the redox dye *N,N,N',N'*-tetramethyl-*p*-phenylenediamine (TMP) at pH 8 of 273 mV vs SHE, whereas reference [298] reports the reduction potential of TMP to be 330 mV vs SHE. This means that the reduction potentials of the LPMOs reported in this table could actually be up to 57 mV higher than they have been reported to be. (Page 93)

**Table 2.3.** MWCNT samples sourced from several suppliers, and the information available regarding them. (Page 99)

**Table 2.4.** Parameters fitted to the baseline-subtracted signals in **Figure 2.10**, using **Equation 7 (Section 1.4.1)**, showing that the suspected *An6428-AA9* redox signal is characteristic of a 1 electron process. The exact surface area of the electrode cannot be easily determined due to the nature of the drop-cast MWCNT deposit. The surface area parameter of **Equation 7**, *A*, has thus been set to unity and rendered dimensionless. As such the coverages, *Γ*, in this table are indicative of the total molar quantity of electroactive species present, not the molar quantity present per unit area. (Page 111)

**Table 2.5.** Values of  $K_m^{app}$ ,  $i_{max}$  and  $k_{cat}$  yielded from the non-linear regression in **Figure 2.22c**.  $k_{cat}$  was calculated using **Equation 13**. The moles of *An6428-AA9* enzyme present on the electrode surface ( $\Gamma \times A$  in **Equation 13**) was determined to be 12→18 pmol using baseline subtraction and simulation of the extracted signals (**Figure S5, Table S2**). (Page 115)

### Chapter 3

**Table 3.1.** A brief guide to the different electrode functionalisation strategies investigated for the introduction of amine functionalities onto electrode surfaces. (Page 133)

**Table 3.2.** Conditions trialled in the attempted immobilisation of ferrocene carboxylic acid onto aniline functionalised electrode surfaces. Carbonyldiimidazole (CDI) and 2-(6-Chloro-1-H-benzotriazole-1-yl)-1,1,3,3-tetramethylammonium hexafluorophosphate (HCTU) are common carboxylic activating agents, and hydroxybenzotriazole (HOBt) is sometimes used as an additive in amide bond coupling reactions. (Page 134)

### Chapter 4

**Table 4.1.** The treatments the samples of *An6428-AA9* in **Figure 4.17** were subjected to. (Page 165)

**Table 4.2.** The treatments the samples of *An6428-AA9* in **Figure 4.18** were subjected to. (Page 1683)

**Table 4.3:** Parameters fitted to the baseline-subtracted signals in **Figure 4.22**, using **Equation 7**, showing that the CjX183-D redox signal is characteristic of a 1-electron process. (Page 171)

**Table 4.4:** Parameters fitted to the baseline-subtracted signals in **Figure 4.29 A and B**, using **Equation 7**, showing that the CjX183-D redox signals are characteristic of a 1 electron process. (Page 178)



**Table 4.5.** The  $m/z$  values expected for the ALCTPSRGSFLTGRG substrate peptide in a series of derivatisation states. (Page 187)

## Chapter 5

**Table 5.1.** Electrochemical impedance spectroscopy analysis (kindly performed by Dr Mark Dowsett) of different electrodes at different stages in the modification process. Experiments were conducted in an aqueous solution of 1 mM ferricyanide and 0.1 M NaCl. (Page 212)

## Chapter 6

**Table 6.1.** The experimental conditions of the UV-vis interrogation of the UV-responsive behaviour of a 500  $\mu\text{M}$  solution of T-PEG in pH 7.55 buffer (20 mM phosphate, 200 mM NaCl + 10% DMSO). Samples were UV-irradiated at 0 °C using a 7 W 365 nm UV light bulb. Room temperature is denoted as rt. (Page 250)

**Table 6.2.** The identities of the samples ran in the 15% polyacrylamide SDS-PAGE gel presented in **Figure 6.19**. All samples were exposed to UV light for 5 min at 0 °C using a 7 W 365 nm UV light bulb. (Page 258)

**Table 6.3.** The results of the digestion experiments conducted on the DsbAc-term samples in the 15% polyacrylamide SDS-PAGE gel in **Figure 6.19**. The sequence covered by detected peptide fragments is coloured black, whereas sequences that were undetected are coloured red. Mutant cysteine residues are highlighted yellow. (Page 260)

**Table 6.4.** The results of the digestion experiments conducted on the DsbAmiddle samples in the 15% polyacrylamide SDS-PAGE gel in **Figure 6.19**. The sequence covered by detected peptide fragments is coloured black, whereas sequences that were undetected are coloured red. Mutant cysteine residues are highlighted yellow. (Page 261)

**Table 6.5.** The identities of the DsbAmiddle (*no TCEP*) samples ran in the 15% polyacrylamide SDS-PAGE gel shown in **Figure 6.21**. UV treated samples were exposed to UV light for 5 min at 0 °C using a 7 W 365 nm UV light bulb. (Page 263)

**Table 6.6.** The identities of the DsbAmiddle (TCEP-removed) samples ran in the 15% polyacrylamide SDS-PAGE gel shown in **Figure 6.22**. UV treated samples were exposed to UV light for 5 min at 0 °C using a 7 W 365 nm UV light bulb. (Page 264)

**Table 6.7.** The reaction conditions trialled to find optimal conditions for the coupling of **T14** to PLP-treated CjX183-D R51K. Reactions were performed in pH 7.5 (25 mM sodium phosphate buffer + 10% DMSO), or pH 8 (25 mM sodium phosphate buffer, titrated from pH 7.5 to pH 8 using saturated  $\text{NaHCO}_3$ , + 10% DMSO) buffer. Reactions were incubated in darkness. (Page 272)

**Table 6.8.** The treatments the samples of CjX183-D R51K used in electrode-immobilisation experiments were subjected to. All CjX183-D R51K samples (including the R51K control) were treated with PLP to convert the *N-terminal* glycine residue to a glyoxylamide, ensuring that triazabutadiene labels were site-selectively introduced onto the mutant lysine residue. Samples treated with UV were exposed to UV light for 3 min at 0 °C using a 7 W 365 nm UV light bulb. Protein samples were in pH 7.5 buffer (25 mM sodium phosphate + 150 mM NaCl). Electro-grafting was performed using a solution of triazabutadiene-labelled protein (25  $\mu\text{M}$ ) in pH 7.5 buffer (25 mM sodium phosphate + 150 mM NaCl) by recording 12 CVs at 50 mV s<sup>-1</sup> at 22 °C, using a PGE working electrode cycling between +0.5 and -0.5 V vs SHE under an N<sub>2</sub> atmosphere using a leak free Ag/AgCl reference electrode (see **Appendix 3, Figure S6**). (Page 279)

## Supplementary / Appendix Tables

**Table S1.** Parameters fitted to the baseline-subtracted signals in **Figure S2**, using **Equation 7**, showing that the suspected An6428-AA9 redox signal is characteristic of a 1 electron process. The exact surface area of the electrode cannot be easily determined due to the nature of the drop-cast MWCNT deposit. The surface area,  $A$ , has thus been set to unity, and the coverages,  $\Gamma$ , are therefore indicative of the total molar quantity of species present, not the molar quantity present per unit area. (Page 453)

## List of Tables

---

**Table S2.** Parameters fitted to the baseline-subtracted signals in **Figure S5**, using **Equation 7**, showing that the suspected *An6428-AA9* redox signal is characteristic of a 1 electron process. The exact surface area of the electrode cannot be easily determined due to the nature of the drop-cast MWCNT deposit. The surface area, *A*, has thus been set to unity, and the coverages, *Γ*, are therefore indicative of the total molar quantity of species present, not the molar quantity present per unit area. (**Page 456**)

**Table S3.** The primers used to linearise Addgene plasmid #48285. (**Page 459**)

**Table S4.** The setup of the PCR experiment used to linearise Addgene plasmid #48285. dNTP stands for deoxynucleoside triphosphate. (**Page 460**)

**Table S5.** The conditions used in the linearisation of Addgene plasmid #48285 by PCR. (**Page 460**)

**Table S6.** The primers used to clone-out the pelB-CjX183-D fragment from CjX183D\_pCW. (**Page 462**)

**Table S7.** The setup of the PCR experiment used to linearise Addgene plasmid #48285. CloneAmp is a premix that contains a DNA polymerase, dNTPs and buffer, all at 2 × working concentration. (**Page 463**)

**Table S8.** The PCR conditions used for amplification and isolation of the pelB-CjX183-D fragment. (**Page 463**)

**Table S9.** In-Fusion® reaction setup. (**Page 463**)

**Table S10.** The primers used for QuickChange Site-Directed Mutagenesis. (**Page 464**)

**Table S11.** QuickChange Site-Directed Mutagenesis reaction setup. (**Page 465**)

**Table S12.** The PCR conditions used for QuickChange Site-Directed Mutagenesis. (**Page 466**)

**Table S13.** The primers used to sequence the CjX183-D R51K\_pCW construct. (**Page 466**)

## List of Figures/Schemes

### Chapter 1

**Figure 1.1.** Examples of the diverse range of redox centres utilized in redox proteins and enzymes. (Page 35)

**Figure 1.2.** The voltage range spanned by biological redox centres. Figure adapted with permission from reference [1], <http://pubs.acs.org/doi/abs/10.1021/cr400479b>. Readers should note that further permissions regarding this figure should be directed to the ACS. (Page 36)

**Figure 1.3.** The mode of action of the blood glucose sensor. When glucose oxidase enzyme oxidises glucose, it passes the electrons to redox mediators which themselves pass the electrons to an electrode. The oxidative current flowing through the electrode is therefore reflective of the rate at which the glucose oxidase is encountering glucose, and by extension the concentration of glucose in the blood.<sup>11,43</sup> (Page 38)

**Figure 1.4.** Non-specific protein adsorption outcomes. **a)** Electrostatic attraction of oppositely charged protein residues and electrode surface facilitates the immobilisation of the protein in an electroactive orientation, facilitating direct electron transfer between a redox centre and the electrode. **b)** Protein becomes immobilised in an orientation that does not facilitate direct electron transfer. **c)** Protein does not adsorb to the electrode surface. (Page 39)

**Figure 1.5. a)** The edge and basal planes of highly ordered pyrolytic graphite (HOPG). **b)** The different potential configurations of HOPG in disk electrodes, either **(i)** with the basal plane exposed, or **(ii)** the edge plane (often denoted pyrolytic graphite edge or "PGE" electrodes). (Page 41)

**Figure 1.6. a)** SEM images of the rough surface topology of PGE adapted with permission from N. Patel, S. Y. Tan, T. S. Miller, J. V. MacPherson and P. R. Unwin, *Anal. Chem.*, 2013, 85, 11755–11764. Copyright © 2013, American Chemical Society.<sup>[64]</sup> **b)** The chemical groups presented at the edge plane of HOPG. **c)** The facilitation of electroactive adsorption of redox proteins onto PGE by the rough topology of the surface. (Page 42)

**Figure 1.7. (Left)** The interaction of polycationic species such as polylysine with negatively charged PGE surfaces. **(Right)** The formation of ternary salt bridges between negatively charged protein surfaces and negatively charged electrode surfaces using polycationic species can facilitate the adsorption of negatively charged proteins. (Page 43)

**Figure 1.8.** The water-splitting photoelectrochemical cell developed by Erwin Reisner and co-workers, utilizing photosystem II and hydrogenase enzymes immobilised on hierarchically structured ITO electrodes.<sup>98</sup> (Page 46)

**Figure 1.9. (Left)** Depiction of an alkanethiol SAM on a gold surface, and **(Right)** the generic structure of alkanethiols used in SAM construction. (Page 47)

**Figure 1.10.** Tethered bilayer lipid membrane on gold electrode for the immobilisation of membrane-bound redox proteins. **a)** The structures of the components used in tethered bilayer lipid membrane assembly: lipid tethers, spacer units and quinone-type molecules. **b)** The structure of a tethered bilayer lipid membrane on a gold electrode, including embedded transmembrane proteins. **c)** The mediation of electron transfer by quinone type molecules.<sup>147-149</sup> (Page 50)

**Figure 1.11.** Characteristic cyclic voltammograms for the reduction of an aryl diazonium salt generated in situ from 2-(4-aminobenzyl)isoindoline-1,3-dione. Potential vs Ag/AgCl (3 M KCl), scan rate 20 mV s<sup>-1</sup>. GC working electrode. Solvent system 1:5 water:acetonitrile + 0.1 M Bu4NPF6 + 0.5% v/v 6.6 M HCl. Ambient temperature. (Page 52)

**Figure 1.12.** Amide bond formation between surfaces and protein residues, catalysed via EDC/NHS activation. **a)** Activation of electrode-surface carboxylic acid groups and reaction with protein lysine residues. **b)** Activation of carboxylic acid groups on the protein surface and reaction with electrode surface amine groups. **c)** Due to the presence of many amine/carboxylic acid moieties on protein surfaces, immobilisation via EDC/NHS activation often leads to a dispersion in immobilised protein orientation. (Page 54)

**Figure 1.13.** Generic strategy for site selectively crosslinking a redox protein to an electrode. (Page 57)

**Figure 1.14.** Membrane free H<sub>2</sub>/O<sub>2</sub> fuels cells can be fabricated by coupling the redox activity of hydrogenases to oxidases.<sup>206,207,209</sup> The orientation of the multicopper oxidase *Trametes versicolor* laccase III (PDB code: 1KYA) onto an electrode surface for O<sub>2</sub> reduction catalysis can be achieved via the modification of the electrode surface with an anthracene substrate mimics, thereby anchoring the enzyme via its binding pocket and allowing for facile direct electron transfer.<sup>206,207</sup> (Page 59)

**Figure 1.15.** Azide-alkyne cycloaddition click reactions between surfaces and proteins. **a) (Top)** Copper-free uncatalysed azide-alkyne cycloaddition click reaction, promoted by a ring strained alkyne. **(Bottom)** Copper-catalysed azide-alkyne cycloaddition reaction. **b)** Due to the precedence for unnatural amino acids bearing both alkyne and azide functionalities, it

is possible to functionalise a protein with either azides or alkynes. **c)** The site-selective electroactive immobilisation of a laccase onto a MWCNT via the use of a copper-free uncatalysed azide-alkyne cycloaddition click reaction between an azide-functionalised UAA and a surface-confined cyclooctyne, as described in ref [235]. Residues from only one monomer are depicted (pdb code: 3CG8240). (Page 62)

**Figure 1.16.** The covalent crosslinking of myoglobin to a gold electrode as a homogeneous monolayer, via the incorporation and Diels-Alder reaction of a 3-amino-L-tyrosine residue.<sup>237</sup> (Page 63)

**Figure 1.17.** The potential waveform that is applied to the working electrode in a cyclic voltammetry experiment. (Page 64)

**Figure 1.18.** (Black) CV of the redox protein YedY immobilised onto a PGE electrode, showing two Faradaic signals. The CV was recorded in 50 mM Mes buffer at pH 7 at a scan rate of 100 mV s<sup>-1</sup>. The baseline fitted to the background capacitive current is shown by the red dashed line; the baseline-subtracted signals (scaled by a multiplication factor of 20) are depicted by the grey solid lines. Figure reproduced with permission from reference [242], <https://www.pnas.org/content/112/47/14506>. Readers should note that further permissions regarding this figure should be directed to the PNAS. (Page 64)

**Figure 1.19.** A trumpet plot, depicting how the position of the oxidative and reductive peaks (Ep) of a surface-confined redox couple deviate as a function of  $\ln(v)$ . (Page 69)

**Figure 1.19.** A trumpet plot, depicting how the position of the oxidative and reductive peaks (Ep) of a surface-confined redox couple deviate as a function of  $\ln(v)$ . (Page 71)

**Figure 1.21.** The potential waveform that is applied across the working electrode during square wave voltammetry. (Page 71)

**Figure 1.22.** Simulated square wave voltammograms showing the effect of the dimensionless electrode kinetic parameter  $K$  (where  $K = k_0/f$ , where  $f$  is the SW frequency) on the features of square-wave voltammograms of surface-confined redox couples. The simulation parameters were SW frequency  $f = 10$  Hz,  $\Delta EP$  amplitude = 50 mV, potential step  $\Delta E_s = 4$  mV, temperature  $T = 298$  K. In all simulations, the value of electron transfer coefficient was  $\alpha = 0.5$ , while the number of electrons exchanged was  $n = 2$ . The values of  $K$  are given in the charts. In both simulated voltammograms the forward current (I1) is assigned with a blue line, the backward current (I2) is assigned with red line, while the black line represents  $\Delta I$ . Figure reproduced with permission from reference [261], <https://link.springer.com/article/10.1007%2Fs10008-019-04320-7>, under license from Springer Nature. License number 4800821185943 (valid for electronic and printed copies with an expected circulation of 1-29 readers). (Page 72)

**Figure 1.23.** Amperometric responses of glucose oxidase enzyme electroactively immobilised onto a glassy carbon electrode derivatised with carbon nanochips and chitosan exposed to successive additions of 0.1 M glucose in PBS (0.1 M, pH 7.2) while holding the applied potential at  $-400$  mV. Inset (a): plot of catalytic current vs. glucose concentration. Inset (b): Lineweaver–Burk plot for  $K_m^{app}$  determination. This figure was reproduced from reference [256], <https://pubs.rsc.org/ko/content/articlehtml/2017/ra/c6ra26636c>, under a Creative Commons Attribution 3.0 Unported Licence.<sup>263</sup> (Page 74)

**Figure 1.24.** The product of a classical cyclic voltammetry waveform (A) and a high frequency sinusoidal waveform (B) yields an FTacV waveform (C). (Page 75)

**Figure 1.25.** The processing of an FTacV experiment to yield FTacV voltammograms. This figure was reproduced from reference [264], <https://pubs.rsc.org/en/content/articlehtml/2017/cc/c7cc03870d>, under a Creative Commons Attribution 3.0 Unported Licence.<sup>263</sup> (Page 77)

**Figure 1.26.** FTacV measurements of the YedY two-electron redox transition. Gray solid lines show, in descending order, the 7th, 8th, 9th, and 10th ac harmonic signals measured for YedY using FTacV with a frequency of 9 Hz. The response from a bare (YedY-free) graphite electrode under the same conditions is shown by light red dotted lines. Simulated signals are shown by dashed black lines. Experimental conditions were as follows: PGE electrode scan rate = 15.83 mV s<sup>-1</sup>; amplitude, 150 mV; buffer solution of 50 mM Mes and 2 M NaCl, pH 7, 25 °C. Figure reproduced with permission from reference [242], <https://www.pnas.org/content/112/47/14506>. Readers should note that further permissions regarding this figure should be directed to the PNAS. (Page 78)

**Scheme 1.1.** The electrochemical reduction of aryl diazonium salts resulting in the formation of a pacifying multilayer film. (Page 51)

**Scheme 1.2.** The use of an imine functionalised electrode to immobilize horseradish peroxidase, as detailed in reference [177]. (Page 56)

**Scheme 1.3.** Maleimide-thiol Michael addition reactions between maleimide groups introduced onto an electrode surface and cytochrome c surface cysteine residues.<sup>186</sup> (Page 61)

## Chapter 2

**Figure 2.1.** Crystal structure of an AA9 LPMO from *Lentinus similis* (PDB: 5N05)<sup>300</sup> showcasing the general features of LPMOs, including the  $\beta$ -sandwich core, and the surface-exposed histidine-brace ligated copper active site residing in the centre of a flattened substrate binding face. (Page 85)

**Figure 2.2.** The conserved active sites of different LPMO families.<sup>292</sup> Examples of cellulose-active AA10 LPMOs have been demonstrated which bare a tyrosine in the axial position instead of a phenylalanine,<sup>301</sup> and chitin-specific AA15s are suspected to bare phenylalanine residues in the axial position rather than tyrosine residues.<sup>292</sup> \*Note that the AA14 crystal structure currently available is for a protein originating from a white-rot fungus but produced in yeast.<sup>302</sup> As such this AA14 crystal structure does not show a  $\tau$ -methylation on the *N-terminal* histidine residue as yeast lack the required methyl transferase.<sup>291</sup> (Page 85)

**Figure 2.3. Top)** Proposed mechanisms for the LPMO-catalysed cleavage of polysaccharide chains using molecular oxygen as the co-substrate. Different proposed mechanistic pathways are denoted with different colours, whereas paths shared between numerous proposed mechanisms are denoted in black. All proposed mechanistic pathways start from (and most finish with) the resting Cu(II) state of the LPMO, which has been marked with a chequered flag. **Bottom)** Cellulose structures are used to depict how the identity of species R-H, R<sup>\*</sup> and R-OH depend on the site of hydrogen atom abstraction, which is itself dependent on the particular LPMO under study. (Page 88)

**Figure 2.4.** Proposed mechanisms for the LPMO-catalysed cleavage of cellulose chains using hydrogen peroxide as a co-substrate. Different proposed mechanistic pathways are denoted with different colours, whereas paths shared between several proposed mechanisms are denoted in black. Evidence for the green pathway is detailed in references [320-323], and while the red pathway is listed as a possibility in ref [323], it is not deemed likely. Note that the Cu(II)-oxyl species is also found in the monooxygenase mechanisms proposed in **Figure 2.3**, which is why H<sub>2</sub>O<sub>2</sub> is sometimes described as being a “shunt” for the LPMO monooxygenase mechanism.<sup>293</sup> Note that the Cu(II)-oxyl produced in this way could also be hypothesized to be able to follow the Cu(III)-OH pathway (**Figure 2.3**, green dashed path), but this path has been omitted from the above scheme for simplicity. (Page 90)

**Figure 2.5.** 15% SDS-PAGE gel illustrating the presence of purified *An6428-AA9*. (Page 95)

**Figure 2.6.** UV vis spectrum of *An6428-AA9* at a concentration of 208  $\mu$ M, based on an  $\epsilon_{280}$  of 47180 M<sup>-1</sup>cm<sup>-1</sup>. (Page 95)

**Figure 2.7.** BLAST and Needle sequence alignment analyses of *An6428-AA9* against *LsAA9*. Aligned residues from Range 1 of the BLAST analysis and those residues are highlighted in green, whereas those from Range 2 of the BLAST analysis are highlighted in yellow. BLAST analysis did not consider the first 32 residues of *An6428-AA9* to have significant similarities with the first 31 residues of *LsAA9*, but Needle analysis did find a similarity of 41.2%. Residues suggested to be aligned by Needle analysis are highlighted in orange. Residues Trp5, Trp64 and Tyr65 in *LsAA9* have been highlighted in red and appear to have no counterparts in *An6428-AA9*. (Page 97)

**Figure 2.8. Left)** The mapping of the aligned residues from *An6428-AA9* and *LsAA9* (identified using the sequence alignments in **Figure 2.7**) onto the crystal structure of *LsAA9* (PDB: 5N05).<sup>300</sup> Aligned residues from *An6428-AA9* **Figure 2.7** Range 1 are coloured green on the crystal structure of *LsAA9*, as is the *N-terminal* histidine residue. Residues aligned using Needle are coloured orange and locations corresponding to *An6428-AA9* sites predicted to be *N-glycosylated* are coloured purple. The sites coloured yellow are those that have been identified using **Figure 2.7** Range 2, and are likely not relevant, as the residues in question (*An6428-AA9* residues 194-205) are already accounted for by **Figure 2.7**, Range 1. **Right)** Predicted fold of *An6428-AA9* generated using Phyre2.<sup>342</sup> Residues identified as aligned with *LsAA9* by BLAST or Needle analysis are once again coloured green or orange, and predicted *N-glycosylation* sites are coloured purple. (Page 98)

**Figure 2.9.** UV vis spectra of 35  $\mu$ M solutions of *An6428-AA9* + 300  $\mu$ M (black) or +200  $\mu$ M (blue) TMP. The concentration of oxidised TMP was determined based on an  $\epsilon_{610}$  of 14000 M<sup>-1</sup>cm<sup>-1</sup>.<sup>343</sup> (Page 99)

**Figure 2.10.** Cyclic voltammograms illustrating the absence of redox signals for unfunctionalised glassy carbon surfaces and GC surfaces functionalised with drop-cast nanotubes, and the presence of several redox signals upon that adsorption of *An6428-AA9* onto the nanotube functionalised electrodes. Scans recorded at 33 mV s<sup>-1</sup> at 298 K under N<sub>2</sub> atmosphere in pH 7 buffer (20 mM sodium phosphate, 20 mM sodium acetate, 500 mM Na<sub>2</sub>SO<sub>4</sub>), using a glassy carbon working electrode, a platinum wire counter electrode and a saturated calomel reference electrode (saturated KCl). All scans commence at the most negative potential. Redox signals were isolated and simulated using the specialised code package described in **Appendix 2**, and the isolated signals are here replotted at 2  $\times$  their intensity. (Page 100)

**Figure 2.11.** Cyclic voltammograms illustrating the appearance an oxidative feature that onsets at  $\sim$ 0.8 V vs SHE for GC electrodes functionalised with **MWCNT A** and then treated with protein. This oxidation feature decays in subsequent scans, whereas other redox signals become more intense with increasing scan number, before reaching a stable intensity. The pair of Faradaic signals centred at  $\sim$ 0.28 V vs SHE only become visible for samples of MWCNTs treated with *An6428-AA9*. Scans

recorded at 113 mV s<sup>-1</sup> at 298 K under N<sub>2</sub> atmosphere in pH 7 buffer (20 mM sodium phosphate, 20 mM sodium acetate, 500 mM Na<sub>2</sub>SO<sub>4</sub>). (Page 101)

**Figure 2.12.** Cyclic voltammograms illustrating that a redox couple centred at ~0.28 V vs SHE is only present for samples of nanotubes treated with *An6428-AA9*, whereas the redox couples centred at ~0.41 V vs SHE and ~0.09 V vs SHE becomes present when any protein adsorbs to the nanotubes and is subjected to the oxidation process at ~0.8 V vs SHE, even non-redox-active proteins such as BSA. Scans recorded at 33 mV s<sup>-1</sup> at 298 K under N<sub>2</sub> atmosphere in pH 7 buffer (20 mM sodium phosphate, 20 mM sodium acetate, 500 mM Na<sub>2</sub>SO<sub>4</sub>), using a glassy carbon working electrode, a platinum wire counter electrode and a calomel reference electrode (saturated KCl). Prior to recording these scans, the working electrode was held at 0.94 V vs SHE for 60 seconds, to allow the oxidative process to occur. All scans commence at the most negative potential. (Page 102)

**Figure 2.13.** Reproduced from Ref. [345] with permission from The Royal Society of Chemistry (license number: 1096409-1). (A) Recorded CVs with scan rate of 0.1 V s<sup>-1</sup> from the amino-CNTs-Gr-based electrode in 1:1 acetonitrile/DMF solution containing 1 mM PBA and 0.05 M tetraethylammonium hexafluorophosphate as supporting electrolyte, in the absence (a) and presence (b) of PBA. (B) Recorded cyclic voltammograms of GC/Gr/NH<sub>2</sub>-CNTs modified electrode in acetonitrile/DMF solution containing 1 mM PBA and 0.05 M tetraethylammonium hexafluorophosphate during 6 successive cycles. (Page 103)

**Figure 2.14. a)** Proposed oxidative reaction pathway between 1-pyrenebutyric acid and a primary amine. Note that many regioisomeric products are possible, but only one is presented. **b)** Proposed redox behaviour of a pyrene compound substituted with an amino bridge, based on the redox behaviour of anilines.<sup>348</sup> (Page 104)

**Figure 2.15. A)** The midpoint potential of the dominant background redox couple is constant for scan rates < 200 mV s<sup>-1</sup>, and thus reflects the formal potential of the redox couple for these scan rates. B) The relationship between formal potential and pH for the dominant background signal. Scans recorded at a range of scan rates at 298 K under N<sub>2</sub> atmosphere in buffer (20 mM sodium phosphate, 20 mM sodium acetate, 500 mM Na<sub>2</sub>SO<sub>4</sub>) at the appropriate pHs, using samples of **MWCNT A** treated with *An6428-AA9*. (Page 105)

**Figure 2.16.** IR (ATR) spectrum of as-received **MWCNT A** (blue) and a sample of **MWCNT A** that had been subjected to chemical oxidation using a H<sub>2</sub>SO<sub>4</sub>/HNO<sub>3</sub> mixture (red). (Page 107)

**Figure 2.17. a)** Cyclic voltammograms illustrating the absence of an oxidative feature that onsets at ~0.8 V vs SHE for samples of chemically oxidised **MWCNT A** not treated with *An6428-AA9*. **b)** Cyclic voltammograms illustrating the presence of a small oxidative feature that onsets at ~0.8 V vs SHE for samples of chemically oxidised **MWCNT A** treated with *An6428-AA9*. This oxidation feature decays in subsequent scans, while the feature at ~0.41 V vs SHE becomes more intense with increasing scan number, before reaching a stable intensity. **c)** The feature at ~0.41 V vs SHE is still dependent on the presence of adsorbed protein, while it is still visible and when using chemically oxidised **MWCNT A**, the signal at ~0.28 V vs SHE, specific to *An6428-AA9*, is not. **d)** When samples of as-received **MWCNT A** are used, the signal at ~0.41 V vs SHE is more intense and the signal at ~0.28 V vs SHE, specific to *An6428-AA9*, is clearly visible. The cyclic voltammograms shown in **a)** and **b)** were recorded at 113 mV s<sup>-1</sup>, while those shown in **c)** and **d)** were recorded at 18 mV s<sup>-1</sup>. All cyclic voltammograms were recorded at 298 K under N<sub>2</sub> atmosphere in pH 7 buffer (20 mM sodium phosphate, 20 mM sodium acetate, 500 mM Na<sub>2</sub>SO<sub>4</sub>), using a glassy carbon working electrode, a platinum wire counter electrode and a calomel reference electrode (saturated KCl). All scans commence at the most negative potential. (Page 108)

**Figure 2.18.** Trumpet plot showcasing the relationship between the natural logarithm of scan rate and the displacement of anodic (blue) and cathodic (red) peaks from the formal potential of the dominant background redox couple for **MWCNT A-functionalised** electrodes treated with *An6428-AA9*. Scans recorded at a range of scan rates at 298 K under N<sub>2</sub> atmosphere in pH 7 buffer (20 mM sodium phosphate, 20 mM sodium acetate, 500 mM Na<sub>2</sub>SO<sub>4</sub>). (Page 109)

**Figure 2.19. A)** The midpoint potential of the putative *An6428-AA9* redox couple is constant for scan rates < 200 mV s<sup>-1</sup>, and thus reflects the formal potential of the redox couple for these scan rates. **B)** The relationship between formal potential and pH for the putative *An6428-AA9* redox couple. Scans recorded at a range of scan rates at 298 K under N<sub>2</sub> atmosphere in buffer (20 mM sodium phosphate, 20 mM sodium acetate, 500 mM Na<sub>2</sub>SO<sub>4</sub>) at the appropriate pHs, using GC electrodes drop-cast with **MWCNT A** and subsequently treated with *An6428-AA9*. (Page 111)

**Figure 2.20.** The mapping of the aligned residues from *An6428-AA9* and *LsAA9* (identified using the sequence alignments in **Figure 2.7**) onto the crystal structure of *LsAA9* (PDB: 5N05).<sup>300</sup> Aligned residues from *An6428-AA9* **Figure 2.7** are coloured green on the crystal structure of *LsAA9*. (Page 112)

**Figure 2.21.** Trumpet plot showcasing the relationship between the natural logarithm of scan rate and the estimated displacement of anodic (blue) and cathodic (red) peaks from the formal potential of the putative *An6428-AA9* redox couple. Scans recorded at a range of scan rates at 298 K under N<sub>2</sub> atmosphere in pH 7 buffer (20 mM sodium phosphate, 20 mM sodium acetate, 500 mM Na<sub>2</sub>SO<sub>4</sub>). (Page 113)

**Figure 2.22. a)** Amperometric experiments show that electrocatalytic H<sub>2</sub>O<sub>2</sub> reduction only occurs for samples of nanotubes (**MWCNT A**) drop cast onto a GC electrode and subsequently treated with *An6428-AA9*, and not for “plain” nanotubes or

nanotubes treated with BSA. Amperometric traces were recorded by holding at a potential of 50 mV vs SHE, at 298 K under N<sub>2</sub> atmosphere in pH 7 buffer (20 mM sodium phosphate, 20 mM sodium acetate, 500 mM Na<sub>2</sub>SO<sub>4</sub>). Prior to recording these traces, 10 cyclic voltammograms (akin to those shown in Figure 2.11) were recorded, sweeping from -0.05 → 0.95 V vs SHE at 113 mV s<sup>-1</sup>, thereby allowing the oxidative process that facilitates direct electron-transfer to An6428-AA9 to occur. **b) Fitting** of the cathodic currents to a Lineweaver–Burk equation (Section 1.4.5, Equation 12) gave two plausible linear fits, each yielding different values of  $K_m^{app}$  and  $i_{max}$ , which are tabulated in Table 2.5. **c)** The accuracy of these parameters was evaluated by using Equation 11 (Section 1.4.5) to simulate values of  $i_c$  and comparing the simulated dataset to the experimental dataset. Non-linear fitting of the experimental data to Equation 11 was also used to yield values for  $K_m^{app}$  and  $i_{max}$ . (Page 114)

**Figure 2.23.** Amperometric experiments showing electrocatalytic O<sub>2</sub> reduction by samples of nanotubes drop-cast onto a GC electrode. It can be seen that treatment of the drop-casted nanotubes (**MWCNT A**) with An6428-AA9 does not improve their ability to function as an O<sub>2</sub> electroreduction catalyst. **a)** Amperometric traces recorded by holding at a potential of 150 mV vs SHE, at 298 K under N<sub>2</sub> atmosphere in pH 7 buffer (20 mM sodium phosphate, 20 mM sodium acetate, 500 mM Na<sub>2</sub>SO<sub>4</sub>). **b)** Amperometric traces recorded by holding at a potential of 50 mV vs SHE, at 335 K under N<sub>2</sub> atmosphere in pH 7 buffer (20 mM sodium phosphate, 20 mM sodium acetate, 500 mM Na<sub>2</sub>SO<sub>4</sub>). Prior to recording these traces, 10 cyclic voltammograms (akin to those shown in Figure 2.11) were recorded, sweeping from -0.05 → 0.95 V vs SHE at 113 mV s<sup>-1</sup>, thereby allowing the oxidative process that facilitates direct electron-transfer to An6428-AA9 to occur. (Page 116)

**Figure 2.24.** Cyclic voltammograms illustrating electrocatalytic O<sub>2</sub> reduction by samples of nanotubes drop-cast onto a GC electrode. It can be seen that treatment of the drop-cast nanotubes (**MWCNT A**) with An6428-AA9 does not improve their ability to function as an O<sub>2</sub> electroreduction catalyst. Scans recorded at 18 mV s<sup>-1</sup> at 335 K under either N<sub>2</sub> or N<sub>2</sub> + 20% O<sub>2</sub> atmosphere in pH 7 buffer (20 mM sodium phosphate, 20 mM sodium acetate, 500 mM Na<sub>2</sub>SO<sub>4</sub>), commencing at the most negative potential. Prior to recording these traces, 10 cyclic voltammograms (akin to those shown in Figure 2.11) were recorded, sweeping from -0.05 → 0.95 V vs SHE at 113 mV s<sup>-1</sup>, thereby allowing the oxidative process that facilitates direct electron-transfer to An6428-AA9 to OCCUR. (Page 117)

**Scheme 2.1.** The overall reaction of an LPMO on a cellulosic polysaccharide chain. (Page 82)

## Chapter 3

**Figure 3.1.** The usage of surface-confined amines for subsequent electrode derivatisation. (Page 120)

**Figure 3.2.** The electrochemical oxidation of diamines to yield amine functionalised electrode surfaces. Protecting groups are denoted as “PG.” (Page 122)

**Figure 3.3.** The potential usage of electrochemical oxidation of carboxylic acids to yield amine functionalised electrode surfaces. Protecting groups are denoted as “PG.” (Page 123)

**Figure 3.4.** The electrochemical reduction of nitro groups to yield amine functionalities. (Page 123)

**Figure 3.5.** The diazotisation of an aniline via reaction with the nitrosonium cation. Bases are denoted “B”. (Page 124)

**Figure 3.6.** The reactions of **a)** aliphatic primary amines and **b)** secondary amines with the nitrosonium cation (NO<sup>+</sup>). (Page 124)

**Figure 3.7. a)** The structures of 4-nitrobenzene diazonium tetrafluoroborate, 4-nitroaniline, p-phenylenediamine, DPPH, and the reported radical scavenging product isolated during electro-grafting of 4-nitrobenzenediazonium in the presence of DPPH: 2-[4-(4-nitro)phenyl]-2-phenyl-1-picrylhydrazine. **b)** Hypothetical mechanism to yield 1-(4'-nitro-[1,1'-biphenyl]-3-yl)-1-phenyl-2-(2,4,6-trinitrophenyl)hydrazine as the radical scavenging product produced during electro-grafting of 4-nitrobenzenediazonium in the presence of DPPH. **c)** Postulated mechanism via which redox cross-reactions between the DPPH anion and aryl diazonium cations limit multilayer electro-grafting, as described in ref [173]. (Page 126)

**Figure 3.8.** The methods of **a)** Hauquier et al<sup>171</sup> and **b)** Downard and co-workers<sup>197</sup> for introducing aliphatic amines onto electrode surfaces in near-monolayer or monolayer coverage, courtesy of the usage of protecting groups with aromatic systems which, while grafted to, can be cleaved using deprotective chemistry. (Page 130)

**Figure 3.9.** The electrochemical reduction of NP groups grafted onto a GC electrode as a multilayer or monolayer film. Solvent system: 1:5 water:acetonitrile + 1% 6.6 M HCl. Scans recorded at 50 mV s<sup>-1</sup> under an ambient atmosphere at room

temperature. Potentials are reported against the Ag/AgCl (3 M NaCl) reference electrode. Scans commence at the most positive potential. (Page 132)

**Figure 3.10.** Carboxylic acid (or activated derivatives thereof) functionalised ferrocene compounds. (Page 135)

**Figure 3.11.** The methods of Hauquier et al,<sup>171</sup> and Downard and co-workers,<sup>197</sup> detailing the usage of a specially prepared and isolated diazonium cations bearing protected aliphatic amine groups for the introduction of aliphatic amine groups onto electrode surfaces, and the coupling of the aliphatic amines to a redox-active species via amide bond formation. (Page 137)

**Figure 3.12.** Nitro-grafting of species **A1 (A)**, and **A2 (B)**. Cyclic voltammograms were recorded using a 4 mM solution of the relevant nitro-phenyl compound in 1:5 water:acetonitrile + 0.1 M Bu4NPF6 + 29 mM NaNO2 + 4% 6.6 M HCl at 0 °C, using a GC working electrode, a platinum wire counter electrode and a Ag/AgCl (3 M NaCl) reference electrode under an ambient atmosphere. Scan rate = 500 mV s<sup>-1</sup> in (A) and 50 mV s<sup>-1</sup> in (B). Scans commence at the most positive potential. (Page 139)

**Figure 3.13.** In-situ generation diazonium grafting of species **A3 (A)**, and **A4 (B)**. Cyclic voltammograms were recorded using a 1 mM solution of the in-situ generated diazonium salt in 1:5 water:acetonitrile + 0.1 M Bu4NPF6 at 0 °C, using a GC working electrode, a platinum wire counter electrode and a Ag/AgCl (3 M NaCl) reference electrode under an ambient atmosphere. Scan rate = 20 mV s<sup>-1</sup>. Scans commence at the most positive potential. (Page 139)

**Figure 3.14.** The functionalisation of GC electrode surfaces with, **a**) Benzylamine, **b**) 2-phenylethan-1-amine, functionalities using diazonium precursors, via either "nitro-grafting" or "in-situ generation" methods. (Page 140)

**Figure 3.15.** CVs of a 1 mM K3Fe(CN)<sub>6</sub> + 0.1 M KCl solution recorded using clean GC electrodes (black), and electrodes functionalised with **A1-A4**, both before (blue) and after treatment with hydrazine (red). Scan rate = 50 mV s<sup>-1</sup> for electrodes functionalised with **A1** and **A2**. Scan rate = 500 mV s<sup>-1</sup> for electrodes functionalised with **A3** and **A4**. Potentials are reported vs an Ag/AgCl (3 M NaCl) reference electrode. Scans recorded at room temperature under an ambient atmosphere, and commence at the most negative potential. (Page 141)

**Figure 3.16.** The Fe<sup>3+</sup>/Fe<sup>2+</sup> redox couple of ferricyanide is reversible on GC electrode surface, yet becomes hindered when electrode surfaces are functionalised with the phthalimide protected amine multilayers, presumably due to an interplay between physical obstruction by the contracted non-polar film and the lack of permeation of the charged ferricyanide anion through the non-polar film. Upon treatment of these functionalised electrode surfaces with hydrazine, the phthalimide protecting groups are cleaved, removing the pacifying multilayer, and leaving a near-monolayer coverage of amine functionalities. Once this has been conducted, the Fe<sup>3+</sup>/Fe<sup>2+</sup> redox couple of ferricyanide is once again reversible. (Page 141)

**Figure 3.17.** Coupling of ferrocene functionalities to surfaces functionalised with **a**) 2-phenylethan-1-amine functionalities **b**) benzylamine functionalities to yield **FSA** and **FSB** respectively. (Page 143)

**Figure 3.18.** Top, CVs recorded at a scan rates of 300 mV s<sup>-1</sup> in pH 7.5 buffer (10 mM sodium phosphate, 140 mM NaCl) at 25 °C using GC working electrodes functionalised with **FSA** (left) and **FSB** (right), a platinum wire counter electrode and a SCE reference electrode under an N<sub>2</sub> atmosphere. Potentials are reported vs SHE, and scans commence at the most negative potential. Middle, extraction of the redox signals. Bottom, the peak intensity of the redox signals is directly proportional to scan rate, which is characteristic of the signals being from a surface-confined regime.<sup>171,386</sup> Note that the fitting of polynomials to fit the background capacitive current in the CVs presented was difficult due to the size of and broadness of the Faradaic signals, which occupying most of voltage window spanned by the CV. As such the size of the Faradaic signals have likely been underestimated in this figure. (Page 144)

**Figure 3.19.** The waveform of a "pure sinusoidal voltammetry" (PSV) experiment. (Page 145)

**Figure 3.20.** The assay of a glassy carbon electrode functionalised with **FSB** by cyclic voltammetry (top), FTacV (second from top), cyclic voltammetry (middle), PSV (second from bottom), and cyclic voltammetry (bottom). The applied potentials throughout the voltammetric experiments are shown on the left, whereas the resultant voltammograms (current plotted against applied potential) are shown on the right. The harmonic responses from the FTacV experiment are shown to the right of the FTacV voltammogram. Experiments performed in pH 7.4 buffer (100 mM sodium phosphate, 100 mM NaCl) at 25 °C under an N<sub>2</sub> atmosphere, using a platinum wire counter electrode and a Ag/AgCl (3 M KCl) reference electrode. Cyclic voltammetry and FTacV experiments commenced from the most negative potential. (Page 147)

**Scheme 3.1.** Synthesis of species **A1-A4**. (Page 138)

**Scheme 3.2.** The synthesis of 3-(ferrocenyl) propanoic acid *N*-hydroxyphthalimide hydroxyphthalimide ester, **F4**. (Page 142)



## Chapter 4

**Figure 4.1.** Summary of the variety of methods via which aldehyde motifs can be introduced into protein scaffolds. **(A)** The oxidation of a glycan presenting a cis-1,2 diol with sodium metaperiodate. **(B)** The oxidation of a 1,2-amino alcohol, such as *N-terminal* serine or threonine residues, with sodium metaperiodate. **(C)** Pyridoxal 5'-phosphate (PLP) mediated transamination of *N-terminal* glycine residues. **(D)** Post-translational modification of a pre-installed recognition sequence by formyl glycine generating enzyme (FGE), or an anaerobic sulfatase maturation enzyme (anSME). **(E)** Unnatural amino acid installation and manipulation using pyrrolysyl-tRNA synthetase (pyIRS) in conjunction with transfer RNA bearing the CUA anticodon (tRNACUA). **(Page 149)**

**Figure 4.2.** Selected methods of bio-orthogonal aldehyde ligation. **(A)** Oxime ligation.<sup>395</sup> **(B)** Hydrazone ligation.<sup>396</sup> **(C)** Iso-Pictet-Spengler-type ligations.<sup>397,398</sup> **(D)** Organocatalyst-mediated protein aldol ligation (OPAL).<sup>399</sup> **(Page 150)**

**Figure 4.3.** Oxidation of the *N-terminal* threonine residue of CTB using sodium metaperiodate to yield an exploitable aldehyde functionality. CTB structure from PDB: 1PZJ.424 **(Page 153)**

**Figure 4.4.** Deconvoluted mass spectrometric trace of CTB before (black) and after (blue) treatment with NaIO<sub>4</sub>. The oxidised CTB can exist in two forms, both as the free aldehyde ("glyoxyl-CTB", calculated mass 11599 Da) or as the hydrate of the aldehyde, a geminal diol ("hydrated glyoxyl-CTB", calculated mass 11617 Da). **(Page 153)**

**Figure 4.5.** The reaction of MBTH with aldehydes to form azines (top), and the resonance of an azine formed via the reaction of an *N-terminal* glyoxylamide with MBTH (bottom). Note that the MBTH-glyoxylamide azine would likely be present as several stereoisomers. **(Page 154)**

**Figure 4.6.** Formation of azine-derivatised CTB via the reaction of MBTH with the aldehyde functionality introduced at the *N-terminus* of CTB, at pH 7 in the presence of an aniline catalyst. CTB structure from PDB: 1PZJ.424 **(Page 155)**

**Figure 4.7.** HPLC-coupled-UV-vis-spectroscopy-chromatogram stack-plot of student-acquired data, showing a consistent peak for the CTB-MBTH azine derivative. **(Page 155)**

**Figure 4.8.** Preparation and detection of a CTB-MBTH adduct. The CTB-MBTH adduct can be distinguished from "untagged" proteins using a UV-vis-spectroscopy band with a maximum at 345 nm. A wavy bond line indicates the stereochemistry is unknown. **(Page 156)**

**Figure 4.9.** The structure of thioredoxin 1 from *E. coli*. Crystal structure PDB: 2TRX.428 The 15.2 Å distance is taken between the sulfur atom of residue Cys35 and the backbone carbon atom of the *N-terminal* serine residue. **(Page 157)**

**Figure 4.10.** Protein mass spectrometry of unmodified TrxA. **Top)** Raw spectrometric data showing the TrxA charge-state ladder. **Bottom)** Deconvolution of the raw spectrometric data yields a single peak at *m/z* 11675.58, which is in excellent agreement with the theoretical mass of unmodified TrxA (11675.43 Da). **(Page 157)**

**Figure 4.11.** Mass spectrometric evidence of successful aldehyde introduction into TrxA after treatment with NaIO<sub>4</sub>. **Top)** Raw spectrometric data showing Ald-TrxA charge-state ladders. **Bottom)** Deconvolution of the raw spectrometric data yields a strong peak in which is in excellent agreement with the theoretical mass of the hydrated form of Ald-TrxA (11662.39 Da) at an *m/z* of 11663.03, and three smaller peaks, one of which is in excellent agreement with the theoretical mass of Ald-TrxA in the free-aldehyde form (11644.37 Da), at an *m/z* of 11644.08. **(Page 158)**

**Figure 4.12.** Mass spectrometry of a solution of Ald-TrxA treated with 10 equiv *O*-benzylhydroxylamine for 4 hours in a pH 4.5 buffer (100 mM sodium acetate + 100 mM aniline). **Top)** Raw spectrometric data showing charge-state ladders. **Bottom)** Deconvolution of the raw spectrometric data yields a pair strong peaks at *m/z* 11717.88 and 11747.62, which are in excellent agreement with the theoretical masses of the aniline Schiff base of Ald-TrxA (11719.49 Da) and the *O*-benzyl oxime adduct with Ald-TrxA (11749.51 Da). **(Page 159)**

**Figure 4.13.** The structures of 2-keto-3-deoxyonic acid and *N-acetylneuraminic* acid, which are examples of a sialic acids, and the structures of mannose and galactose. The cis-1,2-diol units in these sugars are marked, as are the susceptibility of these units to oxidation with NaIO<sub>4</sub>. **(Page 160)**

**Figure 4.14.** Example structures of oligomannose, complex and hybrid type *N-glycans*, and the sites at which the deglycosylating enzymes Endo H and PNGase F can cleave on each type of *N-glycan*.<sup>435,436</sup> Cis 1,2-diols susceptible to oxidative cleavage with 1 mM NaIO<sub>4</sub> are shown in red, whereas those susceptible to oxidative cleavage with 10 mM NaIO<sub>4</sub> are shown in dark green. **(Page 161)**

**Figure 4.15.** Output of the NetNGlyc server, identifying putative sites of *N-glycosylation* in An6428-AA9. **(Page 162)**

**Figure 4.16.** Continuous wave (cw) X-band EPR spectra collected for frozen solutions of An6428-AA9 (ca. 0.1 mM) at pH 6.0 (20 mM sodium MES buffer) at 150 K. A sample of An6428-AA9 was analysed at three different stages of derivatisation, firstly the underderivatised protein was analysed (before treatment with NaIO<sub>4</sub>, black), secondly the protein was analysed after

treatment with NaIO<sub>4</sub> (blue) and finally after treatment with NaIO<sub>4</sub> and 100 equiv **Dan6**. Data collection was performed using a Bruker micro EMX spectrometer using a frequency of ca. 9.30 GHz, with modulation amplitude of 4 G, modulation frequency of 100 kHz and a microwave power of 10.02 mV. The data was intensity averaged over 3 scans. (Page 163)

**Figure 4.17.** SDS-PAGE gel of samples of *An6428-AA9* glycoprotein (referred to here simply as “AA9”) subjected to a series of reaction conditions detailed in **Table 4.1**, including aldehyde introduction via cis-1,2-diol oxidative cleavage with NaIO<sub>4</sub>, labelling of aldehydes with fluorescent hydroxylamine-functionalised probe **Dan6** and enzymatic deglycosylation. (Page 165)

**Figure 4.18.** SDS-PAGE gel of samples of *An6428-AA9* glycoprotein subjected to aldehyde introduction via cis-1,2-diol oxidative cleavage with NaIO<sub>4</sub> and the labelling of these aldehydes with either dansylated or pyrene-functionalised fluorescent hydroxylamine probes, **Dan6** or **Pyr3**. (Page 167)

**Figure 4.19.** The structure of CjX183-D. Crystal structure yet to be published. (Page 169)

**Figure 4.20. (Left)** Cyclic voltammogram illustrating the mediation of CjX183-D electrochemical reduction by methyl viologen, showing a large catalytic reductive current in the presence of 0.01 equiv methyl viologen. **(Right)** UV-vis spectra illustrating the successful reduction of CjX183-D, due to the appearance of the two-pronged feature at ~540 nm. CjX183-D solution was at a concentration of 235 μM in pH 7 buffer (150 mM NaCl, and 50 mM each of Tris, acetate, phosphate and MES). The electrochemical experiment was conducted at 0 °C at a scan rate of 20 mV s<sup>-1</sup> under ambient atmosphere, using a Pt counter electrode, a Ag/AgCl (3 M NaCl) reference electrode and a carbon felt working electrode. All scans commenced from the most positive potential. (Page 169)

**Figure 4.21.** 15% SDS-PAGE gels illustrating the presence of WT **CjX183-D**. **Top)** 15% SDS-PAGE gel showing the purification of WT CjX183-D using Ni affinity chromatography. **Bottom)** 15% SDS-PAGE gel showing further purification of WT CjX183-D via size exclusion chromatography. CjX183-D has a theoretical molecular weight of 11.2 kDa, including the covalently attached c-type heme unit. (Page 171)

**Figure 4.22.** Cyclic voltammogram illustrating protein film voltammetry of WT CjX183-D in pH 7 buffer (50 mM phosphate, 150 mM NaCl). The electrochemical experiment was conducted at 5 °C at a scan rate of 30 mV s<sup>-1</sup> under a nitrogen atmosphere, using a Pt counter electrode, a calomel (sat KCl) reference electrode and a pyrolytic graphite edge working electrode. Scans commenced from the most negative potential. (Page 172)

**Figure 4.23.** Positive ion mode ESI-LC/MS analysis of samples of WT CjX183-D. **Top)** The raw MS data showing the protein charge ladders. **Bottom)** Deconvoluted mass spectrum, showing a peak at m/z 11236.73, which is +10.59 greater than the theoretical m/z of CjX183-D holo protein: 11226.14. (Page 173)

**Figure 4.24.** OPAL conjugation of phenylacetaldehyde to aldehyde-functionalised CjX183-D, using 20 equiv of phenylacetaldehyde and 25 mM (S)-5-(pyrrolidin-2-yl)-1H-tetrazole, at pH 7.5 for 1 hour at 37 °C.

**Figure 4.25.** Positive ion mode ESI-LC/MS analysis of samples of WT CjX183-D that has been subjected to PLP-mediated transamination and OPAL to phenylacetaldehyde. **Top)** The raw MS data showing the protein charge ladders. **Bottom)** Deconvoluted mass spectrum, showing a peak at m/z 11238.16, which is +12.02 greater than the theoretical m/z of CjX183-D holo protein: 11226.14. The OPAL product of glyoxylamide-functionalised CjX183-D to phenylacetaldehyde would be expected to give a peak with an m/z 119.12 greater than that of WT CjX183-D, and the peak at m/z 11357.42 is 119.26 greater than that at m/z 11238.16. (Page 175)

**Figure 4.26.** Positive ion mode ESI-LC/MS analysis of a sample of WT CjX183-D that has been subjected to OPAL conditions with phenylacetaldehyde, not to PLP-mediated transamination. **Top)** The raw MS data showing the protein charge ladders. **Bottom)** Deconvoluted mass spectrum, showing a peak at m/z 11238.34, which is +12.2 greater than the theoretical m/z of CjX183-D holo protein: 11226.14. The OPAL product of glyoxylamide-functionalised CjX183-D to phenylacetaldehyde would be expected to give a peak with an m/z 119.12 greater than that of WT CjX183-D, and no such peak is in evidence. (Page 176)

**Figure 4.27.** Circular dichroism of CjX183-D (green) and PLP-treated CjX183-D (blue), illustrating that the protein remains folded during PLP-mediated transamination. Dr Andrew Leech (from the Bioscience Technology Facility, University of York) is thanked for performing these Circular Dichroism experiments. (Page 176)

**Figure 4.28.** Depiction of the structure of CjX183-D R51K, based on the unpublished crystal structure of WT CjX183-D. The mutant lysine residue is highlighted in yellow. (Page 177)

**Figure 4.29.** Protein film electrochemistry experiments of CjX183-D variants. **A)** Cyclic voltammogram illustrating protein film voltammetry of WT CjX183-D **B)** Cyclic voltammogram illustrating protein film voltammetry of R51K CjX183-D. **C)** Harmonic 6 of FTacV of R51K and WT CjX183-D. All experiments were performed in pH 7 buffer (50 mM phosphate, 150 mM NaCl) at 5 °C under a nitrogen atmosphere, using the same Pt counter electrode, calomel (sat KCl) reference electrode and pyrolytic graphite edge working electrode. Cyclic voltammograms were recorded at a scan rate of 30 mV s<sup>-1</sup>, FTacV experiments were recorded using a scan rate of 22.35 mV s<sup>-1</sup> at a frequency of 8.85 Hz. All scans commence from their most negative potential.

**Figure 4.30.** Positive ion mode ESI-LC/MS analysis of samples of CjX183-D R51K. **Top)** The raw MS data showing the protein charge ladders. **Bottom)** Deconvoluted mass spectrum, showing a peak at  $m/z$  11210.13, which is +12.00 greater than the theoretical  $m/z$  of CjX183-D R51K holo protein: 11198.13. **(Page 179)**

**Figure 4.31.** Positive ion mode ESI-LC/MS analysis of samples of CjX183-D R51K that has been subjected to PLP-mediated transamination and OPAL to phenylacetaldehyde. **Top)** The raw MS data showing the protein charge ladders. **Bottom)** Deconvoluted mass spectrum, showing a peak at  $m/z$  11210.15, which is +12.02 greater than the theoretical  $m/z$  of CjX183-D R51K holo protein: 11226.14. The OPAL product of glyoxylamide-functionalised CjX183-D R51K to phenylacetaldehyde would be expected to give a peak with an  $m/z$  119.12 greater than that of CjX183-D R51K, and the peak at  $m/z$  11329.36 is 119.21 greater than that at  $m/z$  11210.15. **(Page 180)**

**Figure 4.32.** Positive ion mode ESI-LC/MS analysis of a sample of CjX183-D R51K that has been subjected to OPAL conditions with phenylacetaldehyde, not to PLP-mediated transamination. **Top)** The raw MS data showing the protein charge ladders. **Bottom)** Deconvoluted mass spectrum, showing a peak at  $m/z$  11210.26, which is +12.13 greater than the theoretical  $m/z$  of CjX183-D R51K holo protein: 11198.13. The OPAL product of glyoxylamide-functionalised CjX183-D R51K to phenylacetaldehyde would be expected to give a peak with an  $m/z$  119.12 greater than that of WT CjX183-D, and no such peak is in evidence. **(Page 181)**

**Figure 4.33.** Circular dichroism of CjX813-D R51K (green) and PLP-treated CjX183-D R51K (blue), illustrating that the protein remains folded during PLP-mediated transamination. Dr Andrew Leech (from the Bioscience Technology Facility, University of York) is thanked for performing these Circular Dichroism experiments. **(Page 181)**

**Figure 4.34.** Circular dichroism overlays showing that the fold of the WT CjX813-D is essentially identical to that of CjX813-D R51K, both before and after PLP-mediated transamination. WT CjX813-D (dark green), CjX183\_D R51K (brown), PLP-treated WT CjX183-D (blue), PLP-treated CjX183-D R51K (light green). Dr Andrew Leech (from the Bioscience Technology Facility, University of York) is thanked for performing these Circular Dichroism experiments. **(Page 182)**

**Figure 4.35. Left)** Crystal structure of FGE from *Streptomyces coelicolor* (PDB code 6MUJ).<sup>450</sup> **Right)** Crystal structure of an anSME from *Clostridium perfringens* (PDB code 4K36).<sup>453</sup> **(Page 184)**

**Figure 4.36.** A proposed mechanism for fGly incorporation by FGE.<sup>450</sup> **(Page 184)**

**Figure 4.37.** A proposed mechanism for fGly incorporation by anSME using a cysteine residue substrate. Note that it is thought that the same mechanism applies for anSME acting on a serine residue substrate.<sup>454</sup> **(Page 185)**

**Figure 4.38.** The structure of substrate peptide ALCTPSRGSFLTGRG. **(Page 186)**

**Figure 4.39.** Positive ion mode ESI-LC/MS elution trace of substrate peptide ALCTPSRGSFLTGRG, monitoring the absorbance at 280 nm. **(Page 186)**

**Figure 4.40.** Mass spectrum of substrate peptide ALCTPSRGSFLTGRG from positive ion mode ESI-LC/MS elution trace. **(Page 182)**

**Figure 4.41.** Tandem MS of fGly labelled peptide product ion peak at  $m/z$  502. The site of the fGly modification is highlighted in red. Peptide fragments are assigned according to standard peptide fragmentation nomenclature.<sup>458</sup> **(a)** The  $[M+3H]^{3+}$  product ion at  $m/z$  502.4 in the positive ion mode ESI-LC/MS trace of *Mt-FGE-treated* substrate peptide (shown in the black box) is fragmented and peaks assigned. Highlighted in the blue box is the most abundant fragment ion at  $m/z$  661.0, which is attributable to the  $[M+2H]^{2+}$  ion of the  $\gamma$ 13 peptide fragment, the structure of which is shown. **(b)** The  $[M+2H]^{2+}$  ion of the  $\gamma$ 13 peptide fragment was subjected to further fragmentation, and all peptide fragments identified were successfully assigned to the fGly-labelled peptide product. Figure adapted from the Advanced Research Project Dissertation of Owen Jarman. **(Page 188)**

**Figure 4.42.** The mass differences between the different peptide/protein derivatisation states encountered in this Chapter. **(Page 189)**

**Figure 4.43.** The mass spectroscopy peak attributed to fGly *O*-benzyl oxime functionalised peptide. **(Page 190)**

**Figure 4.44. (Left)** Mass spectroscopy of samples of *Mt-FGE-treated* peptide after exposure to IP8. **(Right)** Mass spectroscopy of samples of *Mt-FGE-treated* peptide that have been treated with IP8 and *O*-benzyl hydroxylamine sequentially. **(Page 192)**

**Figure 4.45. (Left)** The structure of the ferrocene-labelled CTPSRG-containing peptide "Ferropeptide", and **(Right)** the structure of "fGly-ferropeptide." **(Page 193)**

**Figure 4.46.** Positive ion mode ESI-LC/MS-spectra of samples of ferropeptide **(top)**, FGE-treated ferropeptide **(middle)** and *Mt-FGE-treated* ferropeptide treated with *O*-benzylhydroxylamine **(bottom)**. **(Page 193)**

**Figure 4.47.** Positive ion mode ESI-LC/MS of samples of DsbAC-term (**top**), and DsbAmiddle (**bottom**). Raw MS data showing the protein charge ladders are shown on the left whereas deconvoluted spectra are shown on the right. (**Page 195**)

**Figure 4.48.** Positive ion mode ESI-LC/MS analysis of samples of *Mt-FGE* treated DsbAC-term. The raw MS data showing the protein charge ladders is shown on the left whereas the deconvoluted spectrum is shown on the right. (**Page 196**)

**Figure 4.49.** Positive ion mode ESI-LC/MS analysis of samples of fGly-labelled DsbAC-term treated with *O*-benzylhydroxylamine. The raw MS data showing the protein charge ladders is shown on the left whereas the deconvoluted spectrum is shown on the right. (**Page 197**)

**Figure 4.50.** Positive ion mode ESI-LC/MS analysis of samples of DsbAmiddle treated with **Alk1**. The raw MS data showing the protein charge ladders is shown on the left whereas the deconvoluted spectrum is shown on the right. (**Page 198**)

**Figure 4.51.** Positive ion mode ESI-LC/MS analysis of samples of DsbAmiddle treated with **Alk1** and then subjected to 365 nm UV-irradiation for 1 hour. **Top**) The raw MS data showing the protein charge ladders. **Bottom**) Deconvoluted mass spectrum. (**Page 200**)

**Scheme 4.1.** The synthesis of a dansylated hydroxylamine-functionalised probe (**Dan6**). (**Page 164**)

**Scheme 4.2.** The synthesis of a pyrene-functionalised aldehyde-reactive hydroxylamine probe **Pyr3**. (**Page 167**)

**Scheme 4.3.** The oxidation of cysteine or serine residues by either FGE or anSME enzymes to yield formylglycine residues. (**Page 183**)

**Scheme 4.4.** The *iso-Pictet* Spengler ligation of an aldehyde or ketone with **IP8** to yield a product ligated by a stable C-C bond. The alpha-effect from the oxygen increases the nucleophilicity of the amine group, making nucleophilic attack of the amine group on the carbonyl carbon more favoured. The methylation on the amine nitrogen means the Schiff base formed between the amine group and the carbonyl compound carries a positive charge, increasing the electrophilicity of the Schiff base carbon, increasing the rate of C-C bond formation step. (**Page 190**)

**Scheme 4.5.** The synthesis of *iso-Pictet* Spengler ligating probe **IP8**. (**Page 191**)

**Scheme 4.6.** The gluconoylation of protein *N-termini*. (**Page 194**)

**Scheme 4.7.** The structure of alkylating agent **Alk1** and the mechanism of its reaction with cysteine residues. (**Page 197**)

**Scheme 4.8.** Photofragmentation of **Cys-Alk1** via a Norrish Type II reaction to yield thioaldehyde, thiol-ene and fGly. (**Page 199**)

## Chapter 5

**Figure 5.1.** The generation of aryl diazonium cations from an aryl triazene precursor using a Brønsted-Lowry acid. (**Page 207**)

**Figure 5.2.** (ESI)HRMS spectrum of **HA-2**, illustrating its propensity to yield diazonium cations upon protonation. (**Page 208**)

**Figure 5.3.** Cyclic voltammograms of a glassy carbon electrode during 20 mV s<sup>-1</sup> electro-reductive modification scans with the aryl diazonium salt generated in situ from a 1 mM solution of **HA-2** in 1:5 v:v water:acetonitrile and 0.1 M Bu4NPF6, 0 °C. The scans commence at the most positive potential, then the voltage is lowered before being increased again. (**Page 209**)

**Figure 5.4.** Cyclic voltammograms of a **(A)** BDD electrode and a **(B)** gold electrode during 20 mV s<sup>-1</sup> electro-reductive modification scans with aryl diazonium salt generated in situ from a 1 mM solution of **HA-2** in 1:5 v:v water:acetonitrile and 0.1 M Bu4NPF6, 0 °C. The scans commence at the most positive potential. (**Page 210**)

**Figure 5.5. (Main)** Cyclic voltammograms of GC electrodes from various stages in the modification process and after a “quench” reaction with propanal. All scans were measured at 500 mV s<sup>-1</sup> in an aqueous solution of 1 mM potassium ferricyanide and 0.1 M NaCl. Scans commenced from the most negative potential. **(Inset)** The change in the resistance to charge transfer (RCT) determined from EIS experiments measured on the same electrodes and under the same experimental conditions. (**Page 211**)

**Figure 5.6.** Graphical summary of the resistance to charge transfer (RCT) and capacitance of the double layer (CDL) data from **Table 5.1**. (**Page 212**)

**Figure 5.7.** Cyclic voltammograms of ferricyanide in solution measured using a BDD electrode at various stages of surface modification. Scans measured at 500 mV s<sup>-1</sup> in an aqueous solution of 1 mM ferricyanide and 0.1 M NaCl. Scans commenced from the most negative potential. (Page 213)

**Figure 5.8.** Cyclic voltammograms of 8 mm × 8 mm gold coated silicon wafer during 20 mV s<sup>-1</sup> electroreductive modification scans with aryl diazonium salt generated *in situ* from a 1 mM solution of HA-2 in 1:5 v:v water:acetonitrile and 0.1 M Bu4NPF6, 0 °C. The scans commence at the most positive potential, then the voltage is lowered to the most reductive potential before being increased again. Note that the irregular shape of the cyclic voltammogram is due to the square shape leading to irregular mass-transfer. (Page 214)

**Figure 5.9.** AFM analysis of (Top) an underivatized gold-coated silicon wafer and (Bottom) a gold-coated silicon wafer derivatised with a near-monolayer of propionaldehyde-O-benzyl oxime functionality. AFM was performed with the assistance of Dr. S. P. Tear and Dr M. Dowsett. (Page 215)

**Figure 5.10.** XPS of the surface of a gold-coated silicon wafer at different states of functionalisation. (A) Survey scans, each with the intensity normalized to the average count between 600 and 700 eV. (B) Detailed scans, for (i) and (iii) the relative intensities were scaled using the survey scan data while for (ii) data is scaled to the noise level. XPS data was recorded by Dr Andrew Pratt and Dr Phillip Bentley. (Page 216)

**Figure 5.11.** (A) Cyclic voltammograms of glassy carbon electrodes from various stages in the modification process and after a “quench” reaction with propanal that have been subsequently reacted with 2,5-dihydroxybenzaldehyde (DHBA). All scans were measured at 500 mV s<sup>-1</sup>, nitrogen, in aqueous pH 4.0 buffer solution (100 mM sodium acetate + 150 mM sodium sulfate). (B) Cyclic voltammograms of glassy carbon electrodes functionalised with DHBA via oxime ligation recorded at a variety of scan rates under nitrogen in aqueous pH 4.0 buffer solution (100 mM sodium acetate + 150 mM sodium sulfate). (B, inset) Analysis of the quinone-derived baseline-subtracted anodic (red) and cathodic (blue) peak currents shows a linear relationship to scan rate (v). (Page 217)

**Figure 5.12.** Solution phase cyclic voltammetry of 1 mM 2,5-dihydroxybenzaldehyde in a pH 4.0 buffer solution (100 mM sodium acetate, 150 mM NaCl) at a GC electrode under an N<sub>2</sub> atmosphere at 21 °C. (Page 218)

**Figure 5.13.** Cyclic voltammograms illustrating that signals from surface-confined quinone/hydroquinone redox chemistry do not appear when a hydroxylamine-modified electrode is incubated in hydroquinone. Scans recorded in pH 4.0 buffer (100 mM sodium acetate, 150 mM NaCl) at a modified glassy carbon electrode under a N<sub>2</sub> atmosphere at room temperature (21 °C). Scan rate = 1000 mV s<sup>-1</sup>. (Page 220)

**Figure 5.14.** Cyclic voltammetry of a (A) BDD electrode and (B) gold electrode which have been electro-grafted with compound HA-2, and then (black line) hydrazine-treated prior to reaction with 2,5-dihydroxybenzaldehyde (DHBA), or (blue line) treated with DHBA while still in the electro-grafted state. (Red dashed line) Data from a control experiment where the hydrazine-treatment is not followed by DHBA reaction. The voltammograms shown were recorded at 500 mV s<sup>-1</sup> at 25 °C under N<sub>2</sub> in an aqueous pH 4.0 buffer solution (100 mM sodium acetate + 150 mM Na<sub>2</sub>SO<sub>4</sub>). (Page 221)

**Figure 5.15.** Cyclic voltammetry of a (A) BDD electrode and (B) gold electrode which have been electro-grafted with compound HA-2, and then hydrazine-treated prior to reaction with 2,5-dihydroxybenzaldehyde. (Insets) The magnitude of the baseline-subtracted (red) anodic and (blue) cathodic peak currents (i<sub>p</sub>) vs scan rate (v). All voltammograms were recorded at the scan rates indicated in the legends in a pH 4 buffer solution (100 mM sodium acetate + 150 mM Na<sub>2</sub>SO<sub>4</sub>) under N<sub>2</sub> at 25 °C. (Page 221)

**Figure 5.16.** 30 mV s<sup>-1</sup> cyclic voltammograms showing that significant faradaic current attributable to horseradish peroxidase (HRP) is detected when the oxidised, aldehyde-containing enzyme is reacted with a hydrazine-treated gold electrode (black line), while far smaller redox peaks are observed when hydrazine-treated electrode surfaces are reacted with native (aldehyde-free) horseradish peroxidase (grey line). All experiments were conducted under nitrogen at 25 °C in (pH 7.4 100 mM sodium phosphate buffer solution). (Page 223)

**Figure 5.17.** Cyclic voltammograms summarising the resultant responses of combining different electrode-surface derivatisation states with different HRP enzyme samples. All experiments were conducted under N<sub>2</sub> at 25 °C in pH 7.4 0.1 M sodium phosphate buffer solution at a scan rate of 30 mV s<sup>-1</sup>. Scans commence at the most positive potential. (Page 224)

**Figure 5.18.** (Left) Amperometric plots showing that both clean gold and hydrazine-treated gold electrodes are highly effective at the electroreduction of H<sub>2</sub>O<sub>2</sub> in the absence of horseradish peroxidase. (Right) The current response of the derivatised electrode surfaces as a function of H<sub>2</sub>O<sub>2</sub> concentration. All experiments were conducted under N<sub>2</sub> at 25 °C in pH 7.4 0.1 M phosphate buffer solution. Micromolar concentrations of H<sub>2</sub>O<sub>2</sub> were incrementally increased in the following series: 10, 20, 70, 120, 170, 270, 370, 470, 620, 780, 930. (Page 224)

**Figure 5.19.** Cyclic voltammograms of QX301 quartz crystal microbalance during 20 mV s<sup>-1</sup> electroreductive modification scans with the aryl diazonium salt generated *in situ* from HA-2 in 1:5 v:v water:acetonitrile and 0.1 M Bu<sub>4</sub>NPF<sub>6</sub>, 0 °C. The scans commence at the most positive potential. (Page 225)

**Figure 5.20.** QCM-D results of frequency change ( $\Delta f$ ) and dissipation change ( $\Delta d$ ) against time for a gold-coated quartz crystal microbalance sensor electro-grafted with **HA-2** prior to the start of the experiment. Subsequent treatments are as indicated above the plot. The experiment was conducted at 50 °C. Values for  $\Delta f$  are divided by the harmonic number (Q-sense convention). (Page 226)

**Scheme 5.1.** The ligation of a hydroxylamine to an aldehyde or ketone to form an oxime. (Page 205)

**Scheme 5.2.** The incompatibility of the benzyl ether unit with palladium on carbon catalysed hydrogenation. (Page 207)

**Scheme 5.3:** The synthesis of aryl triazene **HA-2**. (Page 208)

**Scheme 5.4.** The use of aryl triazene **HA-2** in the diazonium electro-grafting based functionalisation of electrode surfaces with near-monolayers of hydroxylamines. (Page 209)

**Scheme 5.5.** The reaction of hydroxylamine ether functionalities on hydrazine-treated electrode surfaces with the aldehyde-functionalised redox-active probe 2,5-dihydroxybenzaldehyde yields surface-confined redox-active moieties. (Page 218)

**Scheme 5.6.** The decoration of conducting surfaces with a near-monolayer of hydroxylamines via the in-situ generation and electroreduction of phthalimide-protected hydroxylamine-functionalised diazonium cations and subsequent hydrazine treatment, and the immobilisation of selected aldehyde species onto the hydroxylamine-functionalised surface via oxime ligation. (Page 219)

**Scheme 5.7.** Solution-phase analogue experiments to prove the phthalimide protecting group is cleaved from **HA-2** via hydrazine treatment (panel **A**), and that oxime bond formation is possible between 2,5-dihydroxybenzaldehyde and the revealed hydroxylamine functionalities (panels **A** and **B**). (Page 220)

## Chapter 6

**Figure 6.1.** The steps involved in the covalent immobilisation of protein onto electrode surfaces via either **i**) “*electrode-up*” or **ii**) “*protein-down*” approaches. (Page 230)

**Figure 6.2. (Top)** Amide bond formation between a *N*-hydroxysuccinimide-type activated ester and an amine. **(Bottom)** Maleimide ligation between a maleimide and a thiol. (Page 239)

**Figure 6.3.** Candidate probes **T5** and **T8** for use in bioconjugation to lysine and cysteine tagged proteins respectively. (Page 240)

**Figure 6.4. a)** UV-vis spectra illustrating the degradation of a 50  $\mu$ M solution of **T18** in pH 7.4 buffer (sodium phosphate 100 mM) at 0 °C under exposure to UV irradiation from a 7 W 365 nm bulb. **b)** UV-initiated diazonium electro-grafting using a 1 mM solution of **T18** in pH 7.4 buffer at 0 °C. **c)** UV-vis spectra illustrating the degradation of a 50  $\mu$ M solution of **T18** in pH 7.4 buffer (100 mM sodium phosphate) at 4 °C in darkness. **d)** UV-initiated diazonium electro-grafting from a 1 mM solution of **T18** that has been incubated in pH 7.4 buffer (100 mM sodium phosphate) for 2 hours in darkness at 4 °C. Cyclic voltammograms were recorded at 0 °C in pH 7.4 buffer (100 mM sodium phosphate) under an ambient atmosphere at a scan rate of 20 mV s<sup>-1</sup> using a GC working electrode, a Ag/AgCl (3 M NaCl) reference electrode and a platinum wire counter electrode. The cyclic voltammograms commence at the most positive potential, then the voltage is lowered before being increased again. UV-vis spectra were recorded by undergraduate student Samuel Aron. (Page 244)

**Figure 6.5.** UV-vis spectra illustrating the degradation of a 50  $\mu$ M solution of **T18** in pH 7.4 buffer (100 mM sodium phosphate) at 4 °C in darkness overnight. (Page 244)

**Figure 6.6.** The decolourisation of a 500  $\mu$ M solution of **T-PEG** in pH 7.55 buffer (20 mM sodium phosphate, 200 mM NaCl + 10% DMSO) after irradiation from a 7 W 365 nm UV light bulb at 0 °C for 4 min. (Page 246)

**Figure 6.7.** CVs illustrating UV-initiated diazonium electro-grafting of a 500  $\mu$ M solution of **T-PEG**, recorded at 20 mV s<sup>-1</sup> in pH 7.55 buffer (20 mM sodium phosphate, 200 mM NaCl + 10% DMSO) buffer at 0 °C on a BDD electrode. Left) Comparison of the CVs for a 500  $\mu$ M solution of **T-PEG** that has been exposed to 365 nm UV irradiation (After UV, 1) with a 1 mM solution of **T-PEG** that has been kept in darkness (Before UV, 1), and a blank solution of the pH 7.55 buffer (Blank 1), shows that diazonium electro-grafting is only observed **after** **T-PEG** has been exposed to UV irradiation. Right) The Diazonium electro-grafting observed for **UV-irradiated** **T-PEG** follows the typical trend of being a broad reductive wave that decays over subsequent SCANS. (Page 247)

**Figure 6.8.** CVs recorded using either a clean BDD electrode (Clean) or a BDD electrode that has been subjected to UV-initiated diazonium electro-grafting with **T-PEG** (UV-grafted). Scans were recorded at 500 mV s<sup>-1</sup> using a Ag/AgCl (3 M NaCl) reference electrode and a platinum-wire counter electrode in an aqueous solution of 1 mM potassium ferricyanide and 0.1 M NaCl at room temperature. Scans commenced from the most negative potential. (Page 247)

**Figure 6.9.** CVs illustrating UV-initiated diazonium electro-grafting of a saturated solution of **T8**, recorded at 20 mV s<sup>-1</sup> in pH 7.2 (20 mM phosphate, 200 mM NaCl + 10% DMSO) buffer at 0 °C on a GC working electrode. **Left**) Comparison of the CVs for a saturated solution of **T8** that has been exposed to 365 nm UV irradiation (UV, scan 1) with a saturated solution of **T8** that has been kept in darkness (No UV, scan 1), and a blank solution of the pH 7.2 buffer (Blank, scan 1), shows that strong diazonium electro-grafting is only observed after **T8** has been exposed to UV irradiation. **Right**) The Diazonium electro-grafting observed for UV-irradiated **T8** follows the typical trend of being a broad reductive wave that decays over subsequent scans.

**Figure 6.10. A)** The reaction of diazonium cations with a variety of phenolic species to form azo-dyes. **B)** The general structure of an azo-dye. **C)** The mechanism of reaction of resorcinol with a diazonium cation. (Page 248)

**Figure 6.11. A)** UV-vis spectra showing the UV-initiated degradation of a 500 µM solution of **T-PEG** in pH 7.55 buffer (20 mM phosphate, 200 mM NaCl + 10% DMSO) in response to being subjected to UV-irradiation. **B)** UV vis spectra showing that when **T-PEG** is subjected to UV-irradiation in the presence of resorcinol, a new UV-peak will appear, attributable to the formation of an azo-dye. **C)** UV-vis spectra recorded before and after UV-initiated degradation of a 500 µM solution of **T-PEG** in the presence of **Res1**. Experiments were conducted in pH 7.55 aqueous buffer using the conditions tabulated in Table 6.1; entries 1 and 2 correspond to plot **A**, conditions 3 and 4 correspond to plot **B** and entries 5 and 6 correspond to plot **C**. (Page 250)

**Figure 6.12.** The UV-initiated reaction of **T-PEG** with **Res1** in the presence of formic acid, as evidenced by <sup>1</sup>H-NMR. (Page 251)

**Figure 6.13.** UV-initiated release of diazonium cations from **T-PEG** in the presence of formic acid, as evidenced by <sup>1</sup>H-NMR. (Page 252)

**Figure 6.14.** The reaction of **T8** with L-CYSTEINE to form **T8-cys**. (Page 253)

**Figure 6.15.** UV-vis spectra showing the UV-initiated degradation of a 1 mM solution of **T8-cys** in pH 7.2 aqueous buffer (20 mM sodium phosphate, 200 mM NaCl + 10% DMSO) over time. (Page 253)

**Figure 6.16.** The UV-initiated reaction of **T8** with **Res1** in the presence of formic acid, as evidenced by <sup>1</sup>H-NMR. (Page 254)

**Figure 6.17.** The reaction of **T23** with potassium thioacetate to form **T23-acetate**. (Page 255)

**Figure 6.18.** UV-vis spectra showing the UV-initiated degradation of a 500 µM solution/dispersion of **T23-acetate** in pH 7.4 aqueous buffer (pH 7.2, 20 mM sodium phosphate, 200 mM NaCl + 20% DMSO) over time. (Page 255)

**Figure 6.19.** 15% polyacrylamide SDS-PAGE gel of showing DsbA cysteine mutants labelled with **T8** or **T8-Res1** azo-dye photographed under visible light (**top**), mid wave fluorescence (**middle**), and visible light after staining with Coomassie dye (**bottom**). (Page 259)

**Figure 6.20.** Models of DsbAc-term and DsbAmiddle based on the crystal structure of WT DsbA (PDB ID: 4K6X). The active site disulfide is circled, and the distances between the mutant cysteine residues and the active site disulfide are marked. (Page 261)

**Figure 6.21.** 15% polyacrylamide SDS-PAGE gel of DsbAmiddle (no TCEP) samples subjected to the various treatments without using TCEP under mid wave fluorescence (**bottom**), and visible light after staining with Coomassie dye (**top**). No staining from azo-dyes was observed under visible light. (Page 263)

**Figure 6.22.** 15% polyacrylamide SDS-PAGE gel of DsbAmiddle (TCEP-removed) samples subjected to the various treatments without using TCEP under mid wave fluorescence (**bottom**), and visible light after staining with Coomassie dye (**top**). No staining from azo-dyes was observed under visible light. (Page 264)

**Figure 6.23. (Left)** UV-vis experiments showing the presence of **T8** on the surface of DsbAmiddle and the breakdown of the triazabutadiene motif under UV irradiation. **(Right)** When a sample of DsbAmiddle labelled with **T8** is subjected to UV-irradiation in the presence of resorcinol, a new absorption band attributable to an azo-dye is observed. UV-treated samples were exposed to UV light for 2 min at 0 °C using a 7 W 365 nm UV light bulb. (Page 266)

**Figure 6.24. (Top)** Deconvoluted protein ESI mass spectrum obtained on a Bruker Solarix XR 9.4 T instrument for a sample of TCEP-treated DsbAmiddle ligated to **T8**, exposed to UV irradiation for 5 min at 0 °C using a 7 W 365 nm UV light bulb in the presence of resorcinol, then incubated at rt for 30 min. **(Bottom)** The raw protein ESI mass spectrum. (Page 267)

**Figure 6.25.** A depiction of the structure of CjX183-D R51K, based on the unpublished crystal structure of WT CjX183-D. The distance between the  $\epsilon$ -amine of the mutant lysine residue and the Fe centre is shown in black. (Page 268)

**Figure 6.26.** The structure of activated ester functionalised triazabutadiene probes **T5**, **T13**, **T14** and **T15**, and their ability to react with CjX183-D variants. (Page 269)

**Figure 6.27.** The functionalisation of CjX183-D variants with **T14** and further derivatisation with **Res6**. WT CjX183-D is only expected to become conjugated to a single **Res6** azo-dye motif as the only amine present is the *N-terminal* glycine residue, whereas CjX183-D R51K is expected to become conjugated to two **Res6** azo-dye motifs as it contains a mutant lysine residue. (Page 269)

**Figure 6.28.** Positive ion mode ESI-LC/MS analysis of a sample of WT CjX183-D treated with **T14**, **Res6** and 365 nm UV irradiation sequentially. **Top**) The raw MS data showing the protein charge ladders. **Bottom**) Deconvoluted mass spectrum, showing a peak at  $m/z$  11798.60. This is 561.87 greater than the  $m/z$  observed for unmodified WT CjX183-D, which was 11236.73 (Section 4.2.3, Figure 4.23). The theoretical additional mass for the addition of the **Res6** azo-dye motif is 560.63 Da. (Page 270)

**Figure 6.29.** Positive ion mode ESI-LC/MS analysis of a sample of CjX183-D R51K treated with **T14**, **Res6** and 365 nm UV irradiation sequentially. **Top**) The raw MS data showing the protein charge ladders. **Bottom**) Deconvoluted mass spectrum, showing a peak at  $m/z$  12331.98. This is 1121.85 greater than the  $m/z$  observed for unmodified CjX183-D R51K, which was 11210.13 (Section 4.2.3, Figure 4.30). The theoretical additional mass for the addition of two **Res6** azo-dye motifs is 1121.25 Da. (Page 271)

**Figure 6.30.** Positive ion mode ESI-LC/MS analysis of a sample of PLP-treated CjX183-D R51K reacted with **T14** using the conditions described in Table 6.7 Entry 2 and purified using a His SpinTrapTM. **Bottom**) Deconvoluted mass spectrum. A peak would be expected at +467.56  $m/z$  relative to CjX183-D R51K for protein labelled with the intact triazabutadiene probe and with an *N-terminal* glyoxylamide in a hydrated form (at  $m/z$  11677.71 if accounting for the +12 Da systematic error) and at +149.11  $m/z$  for the free diazonium (at  $m/z$  11359.26 if accounting for the +12 Da systematic error, and at  $m/z$  11347.26 if using the theoretical mass of the protein). (Page 272)

**Figure 6.31.** Purification of a PLP-treated CjX183-D R51K-triazabutadiene conjugate using a His SpinTrapTM. As can be seen, excess **T14** can be removed by washing with a low-imidazole buffer (25 mM sodium phosphate, titrated from pH 7.5 to pH 8 with saturated NaHCO<sub>3</sub>, + 30 mM imidazole) while the CjX183-D conjugate is retained on the Ni-affinity resin, and the CjX183-D can later be eluted using a high-imidazole buffer (25 mM sodium phosphate, titrated from pH 7.5 to pH 8 with saturated NaHCO<sub>3</sub>, + 800 mM imidazole). (Page 273)

**Figure 6.32.** Positive ion mode ESI-LC/MS analysis of a sample of PLP-treated CjX183-D R51K reacted with **T14** using the conditions described in Table 6.7 Entry 2, purified using a His SpinTrapTM, and then treated with 365 nm UV irradiation from a 7 W 365 nm UV light bulb at 0 °C for 3 min. **Bottom**) Deconvoluted mass spectrum. A peak would be expected at +149.11  $m/z$  for protein labelled with the free diazonium and with an *N-terminal* glyoxylamide in a hydrated form (at  $m/z$  11359.26 if accounting for the +12 Da systematic error, and at  $m/z$  11347.26 if using the theoretical mass of the protein). A peak would be expected at +103.10  $m/z$  relative to CjX183-D R51K for a carbocation probe at ( $m/z$  11331.25 when accounting for the +12 Da systematic error). (Page 274)

**Figure 6.33. a)** UV-vis experiments showing that the UV-vis spectrum of CjX183-D R51K does not change after exposure to UV-radiation for a short period of time. **b)** UV-vis experiments showing that the UV-vis spectrum of triazabutadiene-labelled CjX183-D R51K changes after exposure to UV-radiation for a short period of time, with the visible absorption peak at 410 nm becoming slimmer in profile due to the loss of the underlying broad triazabutadiene absorbance band. UV-treated samples exposed to UV light for the specified time 0 °C using a 7 W 365 nm UV light bulb. (Page 275)

**Figure 6.34. (Top)** Cyclic voltammograms recorded at 25 mV s<sup>-1</sup> in a pH 7.2 (20 mM phosphate, 200 mM NaCl) buffer solution at 25 °C using a GC electrode (Left) and a BDD electrode (Right) both before and after performing an amperometric experiment holding at -0.56 V vs SHE for 10 min. **(Bottom)** Cyclic voltammograms recorded at 25 mV s<sup>-1</sup> in a 700  $\mu$ M solution of **T8-labelled** DsbAmiddle (exposed to UV light for 3 min at 0 °C using a 7 W 365 nm UV light bulb) in pH 7.2 (20 mM phosphate, 200 mM NaCl) buffer solution at 25 °C using a GC electrode (Left) and a BDD electrode (Right), both before and after performing an amperometric experiment holding at -0.56 V vs SHE for 10 min. (Page 277)

**Figure 6.35.** The third harmonic for the FTacV experiments recorded at 16.76 mV s<sup>-1</sup> with an applied sinusoidal waveform with a frequency of 8.9 Hz and an amplitude of 150 mV in a pH 7.2 (20 mM sodium phosphate, 200 mM NaCl) buffer solution at 25 °C using a GC electrode (left) and a BDD electrode (right) both before and after performing an amperometric experiment holding at -0.56 V vs SHE for 10 min for both control and DsbAmiddle + **T8** experiments. (Page 277)

**Figure 6.36.** The third harmonic of an FTacV experiment recorded at 16.76 mV s<sup>-1</sup> with an applied sinusoidal waveform with a frequency of 8.9 Hz and an amplitude of 150 mV in a pH 7.2 (20 mM phosphate, 200 mM NaCl) buffer solution at 25 °C using PGE electrode both before and after applying a film of DsbAmiddle (as a 10  $\mu$ L droplet of a 120  $\mu$ M solution, which was allowed to adsorb for 5 min). (Page 278)



**Figure 6.37.** Representative CVs recorded for the samples of CjX183-D R51K described in **Table 6.8** after 23.7 min on the electrode. CVs were recorded in pH 7 buffer (50 mM phosphate, 150 mM NaCl). The electrochemical experiment was conducted at 5 °C at a scan rate of 30 mV s<sup>-1</sup> under a nitrogen atmosphere, using a Pt counter electrode, a calomel (sat KCl) reference electrode and a PGE working electrode. Scans commenced from the most negative potential. (**Page 280**)

**Figure 6.38.** For each of the electrode-immobilisation experiments described in **Table 6.8**, **a)** The fitted cathodic signals derived from CjX183-D R51K after desorption of protein has been allowed to occur for 3 min. **b)** The fitted cathodic signals derived from CjX183-D R51K after desorption of protein has been allowed to occur for 31 min. **c)** Plots of electrode coverage of CjX183-D R51K against time after electrode tip immersion. The CVs from which these data were extracted were recorded on triplicate every 5 min, under a nitrogen atmosphere in pH 7 buffer (50 mM phosphate, 150 mM NaCl) at 5 °C at a scan rate of 30 mV s<sup>-1</sup> using a Pt counter electrode, a calomel (sat KCl) reference electrode and a PGE working electrode. Scans commenced from the most negative potential. (**Page 281**)

**Scheme 6.1:** The functionalisation of an electrode surface via the electrochemical reduction of an aryl diazonium salt. (**Page 231**)

**Scheme 6.2.** The generation of diazonium salts under mild conditions via the irradiation of a light-activated triazabutadiene. (**Page 234**)

**Scheme 6.3.** Possible mechanism of reaction between N-heterocyclic carbenes and aryl azides to form triazabutadienes. (**Page 235**)

**Scheme 6.4.** The cross-reactivities and reaction condition incompatibilities that might be expected of triazabutadienes or triazabutadiene precursors with reference to common deprotection strategies and popular bio-orthogonally ligating motifs.<sup>535</sup> (**Page 237**)

**Scheme 6.5.** The synthesis of **T1**. (**Page 239**)

**Scheme 6.6.** The synthesis of initial candidate triazabutadiene probes **T5** and **T8**. The literature route for synthesising **T5** is shown in blue,<sup>529</sup> whereas the shortened synthesis is shown in green. (**Page 240**)

**Scheme 6.7.** The synthesis of the heterobifunctional maleimide and amine functionalised PEG-1 linker **T7**. (**Page 240**)

**Scheme 6.8.** The synthesis of a triazabutadiene probe **T13**, which bears a more reactive NHS ester than probe **T5**. (**Page 241**)

**Scheme 6.9.** The synthesis of water-soluble candidate triazabutadiene probes **T14** and **T15**. (**Page 241**)

**Scheme 6.10.** The synthesis of **T17-derived** triazabutadiene probes **T18** and **T19**. (**Page 242**)

**Scheme 6.11.** The synthesis of **T1-derived** phthalimide-type triazabutadiene probes. (**Page 243**)

**Scheme 6.12.** The synthesis of **T-PEG** from **T5**. (**Page 246**)

**Scheme 6.13.** The synthesis of **Res1**. (**Page 249**)

**Scheme 6.14.** The functionalisation of DsbA cysteine mutants with **T8** and further derivatisation with **Res1**. (**Page 258**)

**Scheme 6.15.** The reduction of a **Res1** azo-dye into anilines, via a hydrazine. (**Page 260**)

**Scheme 6.16.** The synthesis of **Res6** via intermediate species **Res2-5**. (**Page 262**)

## Chapter 7

**Figure 7.1.** A potential method for the orientation-specific covalent immobilisation of LPMOs via the targeting of a solvent-exposed tyrosine residue commonly found on the LPMO binding face in the vicinity of the active site. Once a 3-amino-L-tyrosine residue has been installed, crosslinking to the residue could be achieved via **a)** a Diels-Alder reaction or **b)** oxidative coupling to an aminophenol. The LPMO depicted in this figure is *LsAA9* (PDB: 5N05),<sup>300</sup> and is coloured as described in the caption of **Figure 2.8**. (**Page 286**)

**Figure 7.2.** A potential method for the preparation of a fused construct of CjX183-D and an AA9, via forming a covalent linkage between the mutant lysine residue of CjX183-D R51K and the solvent exposed tyrosine residue located on the binding face of many AA9 LPMOs. The fused CjX183-D-AA9 construct proposed in this figure was made by fusing the crystal structures

of CjX183-D (unpublished) and LsAA9 (PDB: 5N05),<sup>300</sup> and is only intended to be an illustration. LsAA9 is coloured as described in the caption of **Figure 2.8. (Page 287)**

**Figure 7.3.** Potential approaches whereby of oxidative amine-pyrene<sup>345</sup> or pyrene-pyrene<sup>555</sup> coupling reactions could be used to facilitate the immobilisation of proteins in specific orientations via covalent bond formation. **i)** Usage of a pyrene-functionalised electrode to direct the orientation in which a pyrene-functionalised protein adsorbs to an electrode via  $\pi$ - $\pi$  stacking, and subsequent electro-oxidative coupling of the electrode-confined pyrene motif to a proximal protein amine residue. **ii)** Usage of a pyrene-functionalised electrode to direct the orientation in which a pyrene-functionalised protein adsorbs to an electrode via  $\pi$ - $\pi$  stacking, and subsequent electro-oxidative coupling of the pyrene motifs. **iii)** Electro-oxidative coupling of a pyrene-functionalised protein to an amine-functionalised electrode surface. (**Page 289**)

## Supplementary / Appendix Figures

**Figure S1.** Cyclic voltammetry of *N,N,N',N'*-tetramethyl-*p*-phenylenediamine (TMP) at a concentration of 1 mM in pH 6 buffer (30 mM Na MES, 100 mM NaCl) at 293 K using a glassy carbon working electrode, a platinum wire counter electrode and a calomel reference electrode (saturated KCl). Scans recorded under a nitrogen atmosphere at a scan rate of 50 mV s<sup>-1</sup>. (**Page 452**)

**Figure S2.** Cyclic voltammograms illustrating the absence of redox signals for unfunctionalized glassy carbon surfaces and GC surfaces functionalised with drop-cast nanotubes, and the presence of several redox signals upon that adsorption of *An6428-AA9* onto the nanotube functionalised electrodes. Scans recorded at 33 mV s<sup>-1</sup> at 298 K under N<sub>2</sub> atmosphere in pH 6 buffer (20 mM sodium phosphate, 20 mM sodium acetate, 500 mM Na<sub>2</sub>SO<sub>4</sub>), using a glassy carbon working electrode, a platinum wire counter electrode and a saturated calomel reference electrode (saturated KCl). Redox signals were isolated and simulated using the specialised code package described in **Appendix 2**. Extracted signals are shown at twice their intensity. (**Page 452**)

**Figure S3.** Cyclic voltammograms showing two redox couples are present for samples of **MWCNT B** and **MWCNT C** (see table **Table 2.3**) treated with BSA, even though BSA is not redox-active. This illustrates that the phenomenon of background redox signals, dependent on the presence of a protein-film (but independent of the identity of that protein) is not restricted to **MWCNT A**. **MWCNT C** does seem to show some background redox activity even in the absence of a protein film, perhaps due to a carboxylic acid or quinone-type redox couple. Scans recorded at 33 mV s<sup>-1</sup> at 298 K under N<sub>2</sub> atmosphere in pH 7 buffer (20 mM sodium phosphate, 20 mM sodium acetate, 500 mM Na<sub>2</sub>SO<sub>4</sub>), using a glassy carbon working electrode, a platinum wire counter electrode and a calomel reference electrode (saturated KCl). (**Page 454**)

**Figure S4.** Trumpet plot showcasing the relationship between the natural logarithm of scan rate and the displacement of anodic peaks ( $E_p - E_f > 0$ ) and cathodic peaks ( $E_p - E_f < 0$ ) from the formal potential of the dominant background redox couple for **MWCNT A-functionalised** electrodes treated with *An6428-AA9*. Scans recorded at a range of scan rates at 298 K under N<sub>2</sub> atmosphere at a range of pHs. Buffer conditions: pH 5-8, 20 mM sodium phosphate, 20 mM sodium acetate, 500 mM Na<sub>2</sub>SO<sub>4</sub>). (**Page 455**)

**Figure S5.** The fitting of simulated signals to cyclic voltammograms recorded for the electrode surface (GC working electrode, functionalised with drop-cast **MWCNT A** and subsequently treated with *An6428-AA9*) used for amperometry experiments with H<sub>2</sub>O<sub>2</sub>. Scans recorded at 33 mV s<sup>-1</sup> at 298 K under N<sub>2</sub> atmosphere in pH 7 buffer (20 mM sodium phosphate, 20 mM sodium acetate, 500 mM Na<sub>2</sub>SO<sub>4</sub>), using a platinum wire counter electrode and a saturated calomel reference electrode (saturated KCl). Redox signals were isolated and simulated using the specialised code packaged described in **Appendix 2**. (**Page 455**)

**Figure S6. a)** CVs showing the electro-grafting of a 25  $\mu$ M solution of diazonium-labelled CjX183-D R51K (CjX183-D R51K labelled with **T14** and treated with irradiation from a 7 W 365 nm UV light bulb for 5 minutes at 0 °C prior to electro-grafting) in pH 7.5 buffer (25 mM sodium phosphate + 150 mM NaCl). **b)** CVs showing comparable scans recorded using a blank solution of pH 7.5 buffer (25 mM sodium phosphate + 150 mM NaCl). **c)** Overlays of scans recorded in both the blank and diazonium-labelled CjX183-D R51K solutions. Scans were recorded at 50 mV s<sup>-1</sup> at 22 °C under an N<sub>2</sub> atmosphere using a leak free Ag/AgCl reference electrode, a platinum wire counter electrode and a PGE working electrode. (**Page 457**)

**Figure S7.** Plasmid map of Addgene plasmid #48285. (**Page 458**)

**Figure S8.** The location within Addgene plasmid #48285 that the primers in **Table S3** served to linearise. (**Page 459**)

**Figure S9.** Plasmid map of CjX183D\_pCW. (**Page 461**)

**Figure S10.** The location within CjX183D\_pCW that the primers in **Table S6** anneal. (**Page 462**)

**Figure S11.** The site of mutation in the CjX183-D gene targeted by the primers in **Table S10**. (**Page 465**)

## Acknowledgements

I would like to thank all the amazing people it has been my pleasure to meet over the course of my PhD. Firstly, I'd like to thank my wonderful supervisors, Dr Alison Parkin and Dr Martin Fascione (both of whom are from the University of York), who have consistently nurtured my enthusiasm and indulged my curiosity; I cannot stress how important this has been to me and how grateful I am for the guidance you both have given me. Secondly, the SUPER Julia Walton has been invaluable in keeping our lab running and has also done a fantastic job in imbuing me with molecular biology skills. Prof. Gideon Davies (University of York) is also gratefully acknowledged for being so supportive in his role of Independent Panel Member. I would also like to apologise to Prof. Gideon Davies for the length of this thesis, as he hoped it would only be about 200 pages long. I kindly ask him to direct his ire onto Dr Alison Parkin and Dr Martin Fascione.

I'd like to thank all the diligent undergraduate students who have worked with me (and worked so hard) over the years: Owen Jarman, Ben Jancso, Jack Dickenson-Fogg, Suzanne Van Wier, Jake Smith, Barnaby Woods, Alice Hewson, Jack Firth and Samuel Aron. I have also had the privilege of working with many wonderful collaborators. Dr César Terrasan (University of Campinas), the king of filamentous fungus, who prepared *An6428-AA9* for me. Dr Glyn Hemsworth, Dr Jessie Branch and Dr Badri Rajagopa (all from the University of Leeds), who generously gifted me with the plasmid for the protein that would become the co-star of my final results Chapter. Dr Eddie Myers and Dr Lee-Ann Keane of the National University of Ireland, Galway, with whom I collaborated in my investigation of formyl glycine incorporation into proteins. Peter Lindley (University of York), who, when I was working with *An6428-AA9* was an invaluable source of knowledge, and of course, recorded all the lovely EPR for me! Dr Christopher Blanford (University of Manchester), the QCM-D extraordinaire. Dr Andrew Pratt and Dr Phillip Bentley (both from the University of York), who conducted insightful XPS experiments. Dr Adam A. Dowle and Dr Chris J. Taylor (both from the Bioscience Technology Facility, Metabolomics and Proteomics lab, University of York), who conducted Trypsin and endoproteinase AspN digestion experiments. Dr Andrew Leech (from the Bioscience Technology Facility, University of York) is thanked for performing Circular Dichroism experiments. Dr. S. P. Tear (University of York) is thanked for help in obtaining AFM measurements. I would also like to point out that without Dr Ed Bergström (University of York) my ability to collect decent LC-MS data would have taken a steep nose-dive, and Karl Heaton has similarly been tireless in his running of the University of York Department of Chemistry's MS service. Abigail Mortimer (University of York) deserves commendation for her skilful construction (and all-too-often repair!) of the electrochemical glassware I used throughout my PhD.

## Acknowledgments

---

I also owe my thanks to all the wonderful PhD students and Postdoctoral researchers within my own research group. However, I'd like to specifically mention that Dr Tessa Keenan, Dr Emily Flack, Dr Harriet Chidwick, and Tom Ward have been of great help in ushering an indelicate chemist like me into the biological disciplines. Dr Lewis Gooch, Katie Huxley and Jenny Hayes, you were all a hoot to share an office with. Finally, Dr Mark Dowsett, who won the game of hide the plasticine poop; it took me ages to find it. I'd also like to thank Dr Mark Dowsett for expertly performing electrochemical impedance spectroscopy for me. What a wizard. A poop-hiding wizard.

Lastly of course I would like to thank Natasha Hatton, who has had to sit next to me for the past 3.5 years, and has had the misfortune of becoming my partner and supporting me every day ever after.

These works were supported by the Biotechnology and Biological Sciences Research Council (BBSRC, studentship BB/M011151/1).

## Authors Declaration

I, Nicholas David James Yates, declare that this thesis is a presentation of original work and I am the sole author. This work has not previously been presented for an award at this, or any other, University. All sources are acknowledged as References. Contributions to this work by other researchers are indicated either when relevant figures are discussed, in the relevant experimental section.

**Chapter 1** contains content from the publication:

Yates, N. D. J., Fascione, M. A. & Parkin, A. Methodologies for “Wiring” Redox Proteins/Enzymes to Electrode Surfaces. *Chemistry – A European Journal* **24**, 12164-12182, doi:10.1002/chem.201800750 (2018).

I, Nicholas David James Yates, am the first author of this above publication, and prepared the majority of the manuscript. A list of acknowledgements is available for this article.

**Chapter 4** contains content from the publication:

Yates, N. D. J. *et al.* Chemical Bioconjugation of Proteins in an Undergraduate Lab: One-Pot Oxidation and Derivatization of the N-Terminus. *Journal of Chemical Education* **96**, 1245-1249, doi:10.1021/acs.jchemed.8b00787 (2019).

I, Nicholas David James Yates, am the first author of this above publication, and prepared the majority of the manuscript. A list of acknowledgements is available for this article.

**Chapter 5** contains content from the publication:

Yates, N. D. *et al.* Aldehyde-Mediated Protein-to-Surface Tethering via Controlled Diazonium Electrode Functionalization Using Protected Hydroxylamines. *Langmuir* **36**, 5654-5664, doi:10.1021/acs.langmuir.9b01254 (2020).

I, Nicholas David James Yates, am the first author of this above publication, and prepared the majority of the manuscript. A list of acknowledgements is available for this article.

# Chapter 1

## Introduction

## Chapter 1. Introduction

### 1.1 Redox proteins

Redox proteins are the proteins that facilitate biological electron transfer processes. Without such proteins many biological processes, including photosynthesis, respiration, nitrogen fixation, bioluminescence, nucleic acid biosynthesis and apoptosis, would cease to function<sup>1,2</sup> The thermodynamics and kinetics of the biological electron transfer reactions are determined by the nature of the redox centres within the participating proteins. These redox-active centres can be either organic cofactors (e.g. quinones and flavins),<sup>3</sup> metal centres (e.g. iron sulfur clusters and Cu sites),<sup>1</sup> disulfide bridges or selenosulfide bridges,<sup>4</sup> as exemplified in **Figure 1.1**. The coordination sphere and the local environment afforded by the surrounding protein structure exquisitely and uniquely tunes the ligand field surrounding the redox centre. This enhances the ability of the redox centre to catalyse the desired electron transfer processes, by both optimising the reduction potential of the redox centre and by improving the rate at which electrons can be exchanged with the redox centre by minimizing structural rearrangement, as is required by Marcus theory.<sup>5,6</sup> The dependence of the reduction potential of biological redox centres on both the redox centre architecture and the surrounding protein structure has been elegantly demonstrated during recent studies of azurin, a single-copper electron-transfer protein.<sup>7,8</sup>

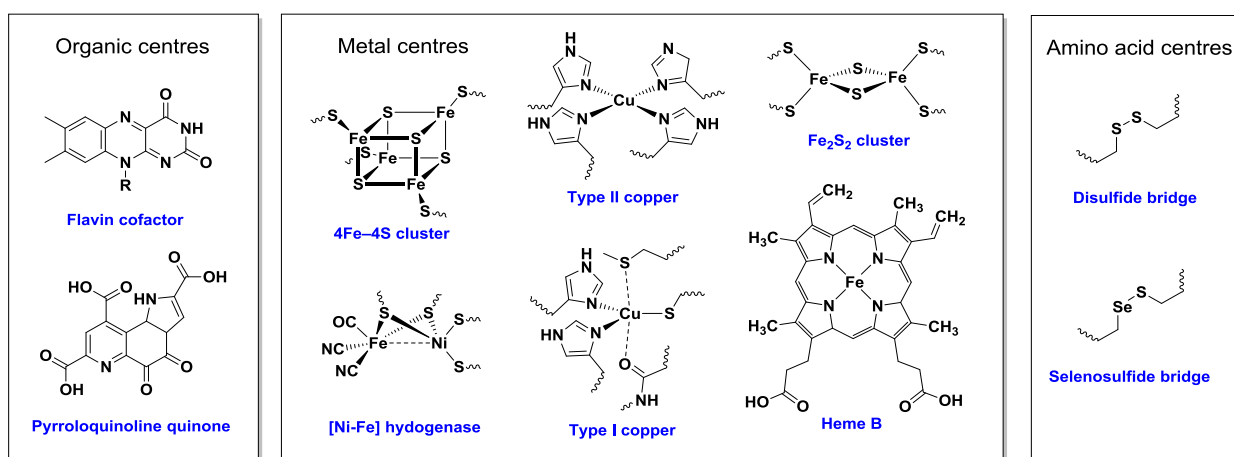


**Figure 1.1.** Examples of the diverse range of redox centres utilized in redox proteins and enzymes.

*Redox enzymes* are a subset of redox-active proteins which catalyse the oxidation or reduction of substrate molecules at a redox-active centre. The approximately 1.5 V potential window which such biological redox centres span (see **Figure 1.2**) is wider than the thermodynamic stability window of

water, since proton reduction to hydrogen ( $E(2\text{H}^+/\text{H}_2) = -0.41 \text{ V}$  at pH 7) and water oxidation to oxygen ( $E(\text{O}_2/\text{H}_2\text{O}) = +0.82 \text{ V}$  at pH 7) are both processes which have been occurring in biology for millennia.<sup>9</sup>

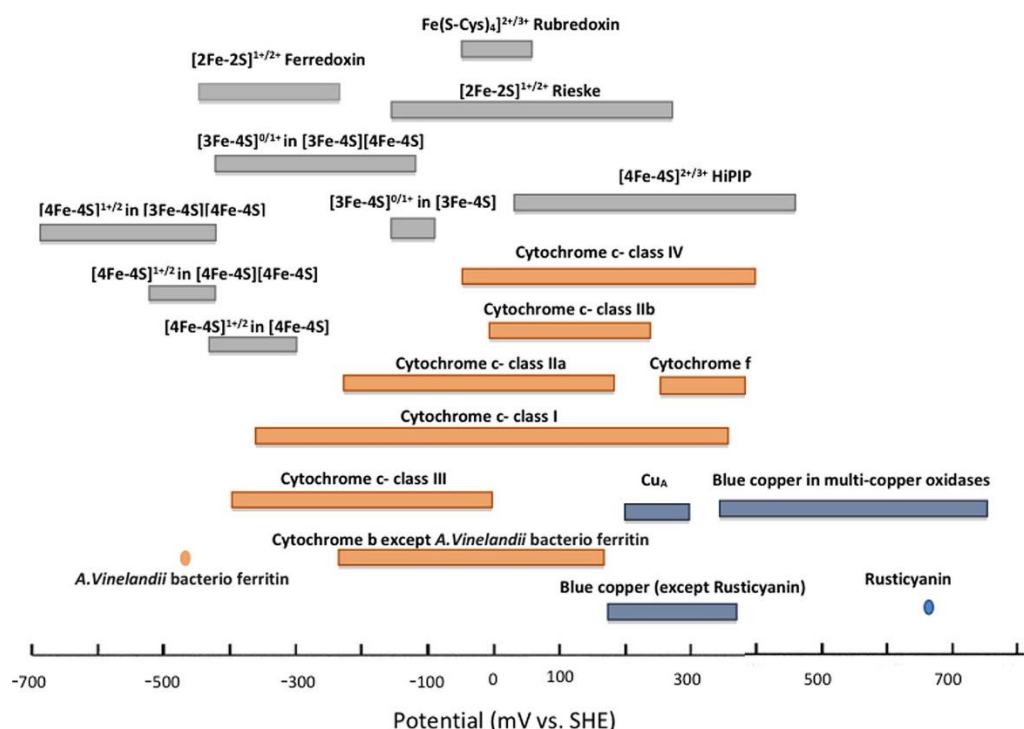


**Figure 1.2.** The voltage range spanned by biological redox centres. Figure adapted with permission from reference [1], <http://pubs.acs.org/doi/abs/10.1021/cr400479b>. Readers should note that further permissions regarding this figure should be directed to the ACS.

## 1.2 Why immobilise redox proteins onto electrode surfaces?

Direct electron transfer between an electrode and the redox-active site of a redox protein/enzyme allows the electrode to act as the electron donor/acceptor to the redox protein. The thermodynamic driving force available for electron transfer(s) and any associated catalysis can be controlled directly (by varying the voltage applied across the electrode surface).<sup>10</sup> When a sufficient thermodynamic driving force for electron transfer is provided (i.e. the reduction potential associated with the electron-accepting reaction is more positive than the reduction potential associated with the electron-donating reaction,  $E_{\text{cathode}} > E_{\text{anode}}$ ), an electrical current will flow as electrons move between the protein molecules and the electrode. Detecting the onset voltage of current flow therefore allows the thermodynamic driving forces required for biological electron transfers to be directly measured through the use of techniques such as cyclic voltammetry (**Section 1.4.1**).



Analysis of redox proteins via voltammetry is generally carried out using a “film” of protein electroactively immobilised on the electrode surface (i.e. immobilised in an orientation that facilitates direct electron transfer between the redox-active site and electrode). Such an approach is useful as it removes mass transport considerations which must be accounted for if a small protein is in solution and diffusing to the electrode surface. For larger proteins, the rate of diffusion is so slow that it will not support electron transfer rates fast enough to generate a detectable current. In this latter case, redox-mediators must be used to support solution protein voltammetry, and this removes the ability to directly determine the limiting factors controlling the protein redox chemistry. Overall, protein film techniques have therefore become the standard method to interrogate redox proteins and enzymes.

For an electroactively immobilised redox enzyme, film electrochemistry can be a powerful activity assay technique. In spectroscopic solution assays, the rate of electron transfer between a redox enzyme and its redox partner (i.e. oxidising or reducing agent) is often the limiting factor. Conversely, in film electrochemistry, the current flow between electrode and enzyme provides a direct measure of the rate of electron movement. Stirring the solutions in the electrochemical experiment provides fast mass transport of substrate and products by convection (i.e. constantly supplying the immobilised redox enzyme with substrate from the bulk solution and constantly removing product) to ensure that the rate at which the electroactively immobilised redox enzyme can turn over substrate is not limited by mass transfer, allowing the intrinsic kinetics of the redox enzyme’s mode of action to be directly assessed by recording the catalytic current. As such, an electrochemical assay of electroactively immobilised redox proteins/enzymes allows both the thermodynamics and kinetics of their mechanisms of action to be elucidated. Additionally, since catalytic currents will only flow if the redox enzyme can turn-over the supplied substrate, electrochemical assay of electroactively immobilised redox enzymes can also be used for substrate screening.

Collectively, the electrochemical interrogation of redox proteins and enzymes electroactively immobilised onto to an electrode surface is often referred to as “protein film electrochemistry” (PFE).<sup>10-15</sup> Besides PFE, other biophysical analysis techniques that are also dependent on the surface immobilisation of a biomolecule include surface plasmon resonance (SPR) detection of drug molecule binding,<sup>16-19</sup> which is inherently reliant on the attachment of proteins or enzymes onto sensor chips<sup>20</sup> or nanoparticles,<sup>16</sup> and quartz crystal microbalance with dissipation monitoring (QCM-D), a surface sensitive, label-free technology that measures mass and conformation changes in proteins immobilised on a surface.<sup>21-23</sup> 3D cell culture scaffolds are also under development in the attempt to harness stem cells for *in vitro* organ growth and the immobilisation of growth factor proteins also an important consideration in this work.<sup>24-28</sup>

Beyond academic circles, several of the processes that redox proteins/enzymes facilitate are of potential commercial interest, including the production of biofuels, hydrogen generation,<sup>29-31</sup> methane production,<sup>32</sup> and cellulose degradation.<sup>33</sup> Redox enzymes can also be used as novel biocatalysts in chemical synthesis,<sup>34,35</sup> and in the sequestering of atmospheric CO<sub>2</sub>.<sup>36,37</sup> In industrial catalysis, the localisation of enzymes to the surface of a solid support can help overcome high operation costs, improving the ease of separation of enzyme from product, the lifetime and reusability of the enzyme and potentially enhancing the thermostability.<sup>38</sup> Additionally, electroactive immobilisation of redox enzymes allows for the development of electrodes with electro-biotechnological applications, such as solar fuel production<sup>39,40</sup> or cofactor regeneration.<sup>41</sup> As befitting of their role in biological systems, redox proteins and enzymes can also be used to elicit an electronic response from a biological stimulus, and as such redox proteins find a wealth of applications in medical bio-sensing.<sup>10,42</sup> Perhaps the most famous example of a biosensor that uses redox proteins is the blood glucose sensor (see **Figure 1.3**), a device that allows millions of diabetics worldwide to monitor the concentration of glucose in their bloodstream through the electrochemical response of glucose oxidase (a redox enzyme that oxidises glucose).<sup>11,43</sup>

Existing methods for the immobilisation of redox proteins onto electrode surfaces are discussed in **Section 1.3**, whereas the various electrochemical techniques that are used collectively in PFE are introduced in **Section 1.4**.

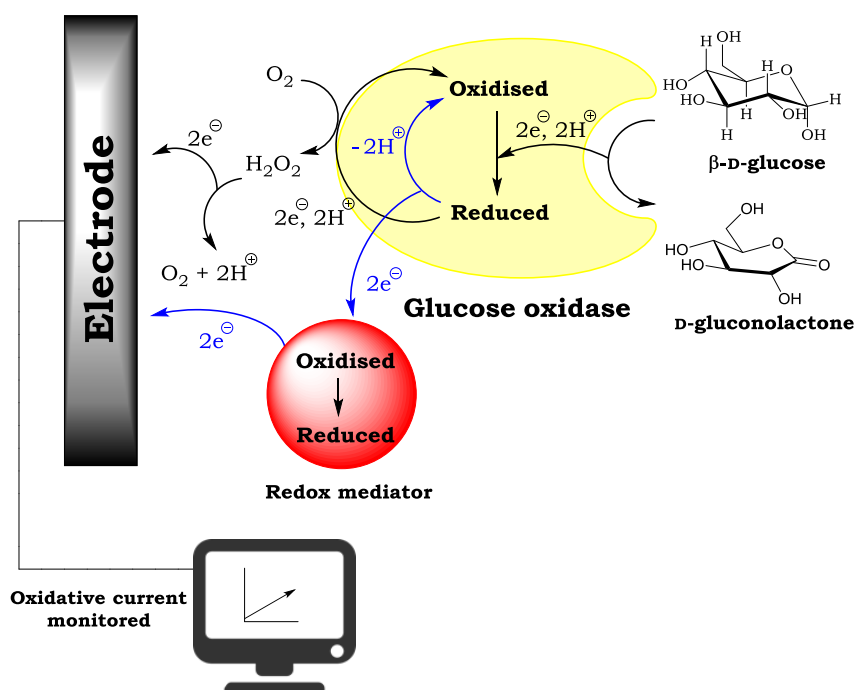


**Figure 1.3.** The mode of action of the blood glucose sensor. When glucose oxidase enzyme oxidises glucose, it passes the electrons to redox mediators which themselves pass the electrons to an electrode. The oxidative current flowing through the electrode is therefore reflective of the rate at which the glucose oxidase is encountering glucose, and by extension the concentration of glucose in the blood.<sup>11,43</sup>

### 1.3 Existing strategies for redox protein/enzyme immobilisation

Due to the great interest in the immobilisation of proteins in both academic and non-academic circles, many methods have been developed to affect protein immobilisation. Existing methods for redox protein/enzyme immobilisation onto conductive surfaces are discussed below.

#### 1.3.1 Electroactive protein adsorption onto unmodified conducting surfaces

Adsorption of proteins onto unmodified electrode surfaces via non-covalent interactions is by far the most common and the simplest approach for achieving an electroactive film of redox protein or enzyme. The wealth of detailed mechanistic PFE studies, conducted using a wide range of different redox proteins/enzymes directly adsorbed onto electrodes, clearly demonstrates the feasibility of this immobilisation methodology,<sup>10-15</sup> but it should be noted that for this methodology to prove successful appropriate non-covalent interactions between the redox protein/enzyme and the electrode surface are required.

The exchange of electrons between soluble redox proteins *in vivo* is dependent on the two proteins “docking” so that the electron-donor and electron-acceptor redox centres are brought into close enough approach to facilitate rapid, direct electron transfer.<sup>44</sup> These interactions are often mediated by areas of complementary polarity on the donor and acceptor proteins.<sup>44</sup> Thus, a simple model for understanding successful direct electroactive protein adsorption onto electrode surfaces is to envisage the electrode surface polarity complementing a region of oppositely charged residues on the protein surface that is proximal to the electron entry/exit redox centre (**Figure 1.4**).<sup>45</sup> This means that direct electron transfer between redox proteins and electrode surfaces is most easily achieved when the electron entry/exit redox centre is close to the protein surface.<sup>46</sup> The adsorption of proteins onto surfaces (and the orientation of the adsorbed proteins) can be influenced by the solution electrolyte conditions; ionic strength and pH are also both important variables. Adsorption of proteins, being an entropically disfavoured process, is also more favoured at lower temperatures.<sup>15</sup>

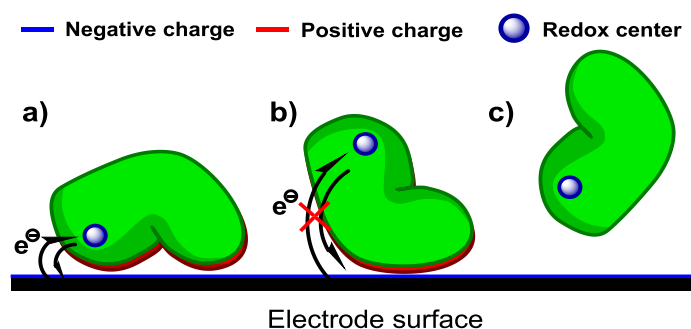


**Figure 1.4.** Non-specific protein adsorption outcomes. **a)** Electrostatic attraction of oppositely charged protein residues and electrode surface facilitates the immobilisation of the protein in an electroactive orientation, facilitating direct electron transfer between a redox centre and the electrode. **b)** Protein becomes immobilised in an orientation that does not facilitate direct electron transfer. **c)** Protein does not adsorb to the electrode surface.

Detailed work by Harry Gray and co-workers has demonstrated that electrons quantum-tunnel through the protein structure which separates electron donor and acceptor partner redox-active centres, and that distance therefore plays a crucial role in determining the rate of electron transfer.<sup>47,48</sup> A helpful rule of thumb provided by Dutton and co-workers is that within metalloenzyme structures a tunnelling distance of less than 14 Å between redox-active sites appears to enable electron transfer rates that are sufficiently fast to avoid limiting the rate of redox catalysis.<sup>45</sup> Ideally, within a single “film” all protein or enzyme molecules would therefore orient themselves onto the electrode with the same sub-14 Å distance between the redox-active centre and the conducting surface. However, in some cases the electrochemical response of otherwise identical protein molecules differs, and this has been attributed to a “dispersion” in protein/enzyme orientation.<sup>15,29,49</sup>

Redox proteins/enzymes can also become adsorbed onto surfaces in configurations which do not facilitate direct electron transfer at all, as illustrated in **Figure 1.4**. Alternatively, the biomolecules may remain in solution, with the slow rate of diffusion of these macromolecules impeding solution electrochemistry, and electron transfer to the electrode instead relying on the introduction of redox mediators. Such mediated bioelectrochemistry is extremely useful in sensor development,<sup>50-52</sup> and careful design of electron-transfer polymer gels can even permit simultaneous entrapment of enzymes on the electrode and modification of the reactivity, with a H<sub>2</sub>-enzyme recently made functional in O<sub>2</sub> through use of a viologen-polymer net.<sup>53</sup> However, as noted above, the focus herein is on protein/enzyme to electrode immobilisation strategies that permit direct, unmediated, electron transfer.

No tools are currently available to predict the likelihood that a redox protein or enzyme of interest will become adsorbed in an electroactive configuration on a solid support, and screening for a successful protein-surface combination remains an empirical process.<sup>15</sup> The electrode surfaces most commonly used for electroactive protein/enzyme electrode immobilisation are briefly reviewed below.

### 1.3.1.1 Carbon bulk materials

Carbon is an extremely popular material for constructing electrodes for the electrochemical interrogation of small molecules.<sup>54</sup> As a highly conductive allotrope of carbon, graphite electrodes are common.<sup>54</sup> Either pyrolytic graphite edge (PGE) or basal plane graphite (BPG) electrodes can be fabricated from cutting highly ordered pyrolytic graphite (HOPG) substrate in perpendicular directions, across or parallel to the graphite sheets, respectively (**Figure 1.5**).<sup>55</sup>

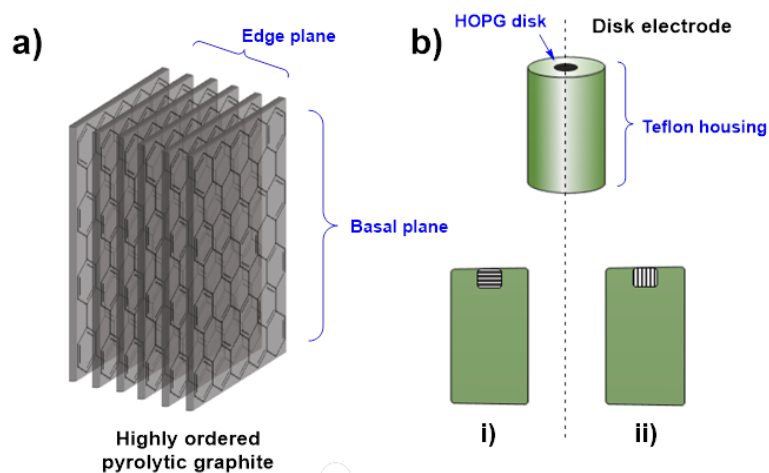


**Figure 1.5.** **a)** The edge and basal planes of highly ordered pyrolytic graphite (HOPG). **b)** The different potential configurations of HOPG in disk electrodes, either **(i)** with the basal plane exposed, or **(ii)** the edge plane (often denoted pyrolytic graphite edge or “PGE” electrodes).

For PFE, PGE has proved to be the most successful carbon electrode material for the electroactive adsorption of redox proteins and enzymes.<sup>10-15,56,57</sup> This has been attributed to the PGE surface’s diverse range of aromatic, hydrophilic (i.e. phenolic) and carboxylate functionalities that are present as defects on the edge plane (**Figure 1.5**), yielding a generally negatively-charged surface which will electrostatically attract regions of complementary positive polarity on the protein surface.<sup>58,59</sup> Electrode surface polishing/abrasion processes using emery paper or pastes of diamond or alumina are often used to actively increase the surface roughness and thus increase the number of defect sites.<sup>15</sup> Alumina and diamond polishing materials have been found to remain on the electrode surface even after rinsing and sonicating the electrodes, so it is also possible that the presence of polishing materials contributes to the performance of PGE electrodes.<sup>57</sup>

The combination of the chemical heterogeneity and the topological roughness of the PGE surface has also been credited with making it particularly suitable for electroactive protein/enzyme immobilisation.<sup>56</sup> The chemical heterogeneity allows multiple and varied favourable contacts to be made between the protein and the electrode surface.<sup>15</sup> The roughness of the surface can ensure that a range of immobilised protein orientations are electroactive,<sup>60</sup> as even if the face through which the protein is adsorbed to the electrode surface is distant from an electron entry/exit site, rapid electron transfer may still be feasible because this site is close to another part of the electrode surface (**Figure 1.6**).<sup>15</sup> Such orientational flexibility may also explain a statistical variation in the electrochemical reaction parameters. For example, in H<sub>2</sub>-enzyme voltammetry modelling studies, the need to include a range of different interfacial electron transfer kinetic rate constants in the calculations is attributed to dispersion in the distance between the electrode surface and the electron entry/exit site in the

protein.<sup>10,49,61</sup> In studies on azurin, variations in the apparent midpoint potential of the biological electron transfer were attributed to different protein-surface orientations/environments.<sup>62,63</sup>

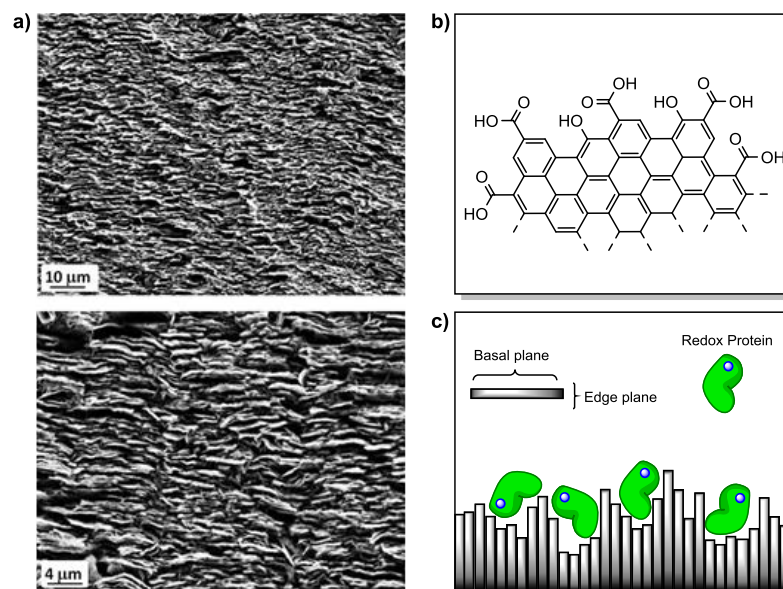


**Figure 1.6.** a) SEM images of the rough surface topology of PGE adapted with permission from N. Patel, S. Y. Tan, T. S. Miller, J. V. MacPherson and P. R. Unwin, *Anal. Chem.*, 2013, 85, 11755–11764. Copyright © 2013, American Chemical Society.<sup>[64]</sup> b) The chemical groups presented at the edge plane of HOPG. c) The facilitation of electroactive adsorption of redox proteins onto PGE by the rough topology of the surface.

In cases where the electron entry/exit site of the protein or enzyme is located within a region of negative charge, the polarity of the PGE surface may not help facilitate electroactive adsorption, and may instead promote the desorption of adsorbed proteins.<sup>59,65</sup> Alleviating the electrostatic repulsion between protein and electrode can be achieved via mild acidification, or via the co-adsorption of protein with polycationic hydrophilic compounds such as aminocyclitols,<sup>46</sup> polylysine,<sup>46</sup> polymyxin<sup>10,15,65</sup> or polyethyleneimine.<sup>59,65</sup> Polycationic species have an affinity for the PGE surface, and are thought to mediate protein adsorption via the formation of ternary salt bridges between areas of negative charge on the protein and electrode surface (**Figure 1.7**).<sup>15,46</sup>

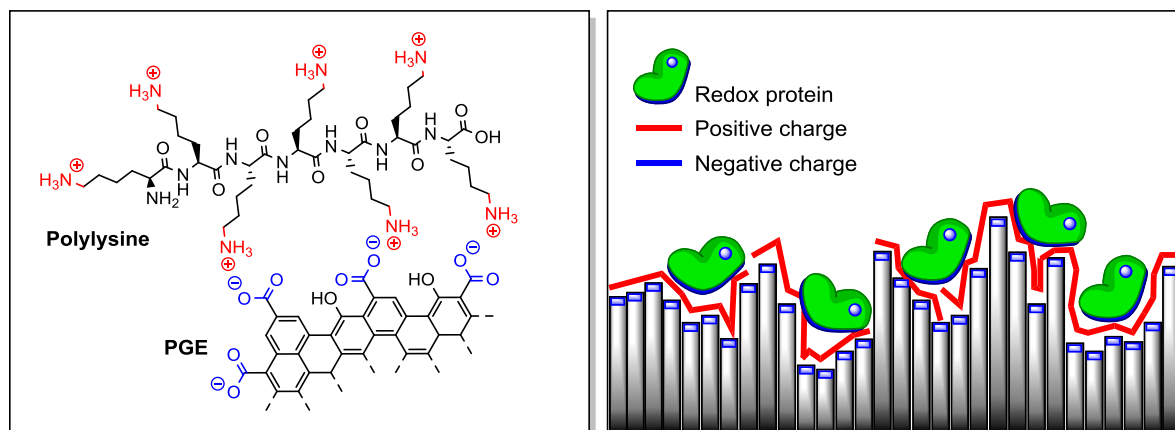


**Figure 1.7. (Left)** The interaction of polycationic species such as polylysine with negatively charged PGE surfaces. **(Right)** The formation of ternary salt bridges between negatively charged protein surfaces and negatively charged electrode surfaces using polycationic species can facilitate the adsorption of negatively charged proteins.

Aside from PGE, other carbon surfaces have also proved successful for producing electroactive films of redox proteins or enzymes. Carbon felt is comprised of an amorphous tangle of smooth carbon fibres.<sup>66</sup> The high surface area, high conductivity, large void spaces and low cost of this material make it suitable for application in redox-enzyme biofuel devices.<sup>66</sup> Carbon felt electrodes of small geometric surface area can accommodate and directly exchange electrons with large quantities of enzymes, which has been exemplified by the usage of a di-iron hydrogenase in a bio-H<sub>2</sub> device.<sup>67</sup> Such porous materials can be less useful in mechanistic studies of redox enzymes since the rate of substrate-, product- or inhibitor-diffusion through the material may limit the rate of reactivity. This would mean that electrochemical current cannot be used to monitor the inherent maximum turnover rate of the enzyme. However, in enzyme fuel cell developments, where the focus is to maximize the enzyme current per unit surface area, such porous materials are very useful, and have enabled order-of-magnitude power increases.<sup>68</sup>

In solution electrochemical studies of small redox-active molecules, common carbon-based electrode substrates include boron-doped diamond (BDD) and glassy carbon (GC).<sup>69</sup> BDD consists of diamond in which approximately one atom in a thousand has been replaced by boron, giving the material p-type semi conductivity and yielding the hardest carbon material used for electrodes.<sup>55</sup> The very low capacitance of BDD minimizes background current, effectively enhancing the sensitivity of the electrochemical measurement.<sup>55</sup> However, BDD is not widely utilized in PFE, presumably indicating that the surface electrostatics do not facilitate protein adsorption. The structure of GC consists of interwoven graphite ribbons, reminiscent of a 3-dimensional chainmail.<sup>55</sup> GC is much harder than HOPG, and contains hydrophobic basal-like and hydrophilic edge-like regions within the same plane.

This complex surface can facilitate the adsorption of some proteins onto the bare GC surface,<sup>10,70</sup> but much of the recent literature using GC electrodes for direct immobilisation of redox proteins describes the functionalisation of the GC surface with nanomaterials, such as carbon nanotubes (CNTs),<sup>71-74</sup> carbon black,<sup>75</sup> and even silicon dioxide nanoparticles.<sup>76</sup>

### 1.3.1.2 Carbon nanomaterials

There are two classes of CNT: single-wall carbon-nanotubes (SWCNTs) and multi-wall carbon nanotubes (MWCNTs).<sup>77,78</sup> SWCNTs have a cylindrical nanostructure, and can be thought of as a single graphite sheet rolled up into a tube,<sup>77</sup> whereas MWCNTs comprise of several layers of SWCNTs concentrically arranged like rings in a tree trunk.<sup>77</sup> The ability of CNTs to mediate direct ET is attributed to the combination of their high surface area, high conductivity, and the polarities of the surfaces they present - the side walls of CNT likely have properties similar to those of the basal plane of HOPG, while the ends of the tubes likely have properties akin to PGE.<sup>77,79</sup> The walls of these nanotubes are capable of forming strong  $\pi$ - $\pi$  interactions to small molecule species, such as pyrene.<sup>78</sup>

There are a variety of methods for structuring CNT/redox protein assemblies on electrode surfaces, and these methods have been comprehensively reviewed.<sup>77,80,81</sup> Simple approaches include the evaporation of a droplet of redox protein/CNT dispersion onto a GC electrode surface, followed by the addition of a small amount of Nafion® membrane to act a binding agent,<sup>74</sup> or the filling of micro cavities in the bulk electrode surface with CNTs.<sup>82</sup> Such methods have resulted in facile direct ET being established between the electrode surface and a range of proteins, including hemoglobin,<sup>74</sup> horseradish peroxidase<sup>74</sup> and, remarkably, glucose oxidase,<sup>74,82</sup> a protein for which the establishment of direct ET is infamously difficult due to the coenzyme flavin adenine dinucleotide (FAD) unit of GOx being deeply embedded within the protein structure.<sup>83</sup> More advanced techniques, such as the construction of "CNT forests" - short SWCNTs arranged orthogonally to an electrode surface by self-assembly<sup>84</sup> - provide high surface area assemblies into which redox proteins can be spontaneously incorporated,<sup>79</sup> or atop which redox enzymes can be covalently wired.<sup>85</sup>

Graphene can also be formulated as a highly conductive carbon nanomaterial, that can also be used to make electrode surfaces amenable for PFE. Application of graphene to a supporting electrode can be achieved via simple electrode treatments, such as the application of graphene suspensions to GC, which promotes the formation of a stable thin film due to  $\pi$ - $\pi$  stacking interactions.<sup>86</sup> Alternatively, composite mixtures of chitosan and graphene can be applied to carbon electrode surfaces as thin films which promote the physisorption of redox proteins.<sup>87-90</sup> A review of the uses of graphene in electrochemical sensors and biosensors has been compiled by Shao et al.<sup>91</sup>



The functionalisation of electrode surfaces with high conductivity carbon black (CB) nanomaterials, such as Ketjen Black powder,<sup>92</sup> can also promote direct ET to redox proteins or enzymes.<sup>92,93</sup> The affinity between CB and protein surfaces has been attributed to hydrophobic-hydrophobic interactions, high porosity and high surface area-to-volume ratio.<sup>94</sup> The electroactive immobilisation procedure is often performed via the evaporation of suspension/slurries of CB particles onto carbon electrodes.<sup>75,92,93,95</sup> More complex hybrid bio-synthetic catalytic systems can be generated by combining CB particles with redox enzymes and other nanoparticles. For example, Matteo Duca and coworkers showed that a nitrate reductase from *E. coli* could be immobilised onto carbon black, and the co-deposition onto a PGE of these bio-modified particles along with Pt or Rh nanoparticles yielded a system capable of the electrocatalysis of nitrate to ammonia at neutral pH.<sup>96</sup> In the absence of enzyme, the slow reduction of nitrate by the noble metal catalysts alone significantly limited the rate of denitrification, whereas the enzyme containing system may be applicable for wastewater treatment.<sup>96</sup>

### 1.3.1.3 Metal oxide semiconductors

Electrodes constructed of metal oxide semiconductors have become increasingly important in both PFE studies and metalloenzyme biotechnological device development. In particular, n-type metal oxide semiconductors such as TiO<sub>2</sub>,<sup>97</sup> indium tin oxide (ITO)<sup>98</sup> and CdS<sup>99</sup> have been used for solar fuel applications<sup>40</sup> and NADH recycling.<sup>41</sup> TiO<sub>2</sub> electrode surfaces are rough, porous structures consisting of aggregated nanoparticles.<sup>40</sup> The CdS surface topology is similar, being comprised of a highly porous 3-dimensional network of CdS sheets.<sup>40,60</sup> ITO electrodes with porous architectures suitable for redox protein immobilisation can also be constructed,<sup>98,100</sup> and along with PGE<sup>40,59</sup> and TiO<sub>2</sub>,<sup>101,102</sup> present negatively charged oxide functionalities to adsorbing protein or enzyme molecules at neutral pH.<sup>103</sup> The rough/porous nature of these electrode materials is thought to aid in electroactive enzyme immobilisation, as described for PGE.<sup>60,100</sup> Indeed, PFE of a H<sub>2</sub>-producing [FeFe]-hydrogenase from *Clostridium acetobutylicum* has been recently achieved using a TiO<sub>2</sub> electrode,<sup>104,105</sup> whereas previously immobilisation of [FeFe]-hydrogenases on native electrode surfaces had only been achieved using rough carbon electrode substrates, such as PGE<sup>106,107</sup> or carbon felt.<sup>67</sup>

Unlike PGE, ITO is transparent, and the porosity of such metal oxide electrode surfaces is also readily tunable.<sup>98,100</sup> An especially high surface area hierarchically-structured ITO electrode with a microporous inverse opal architecture and a mesoporous skeleton has recently been developed by Reisner and co-workers.<sup>98</sup> Immobilisation of high quantities of the enzymes photosystem II and hydrogenase onto a photoanode and a cathode respectively yielded a photoelectrochemical solar-water splitting enzyme cell (Figure 1.8).<sup>98</sup> This device is capable of yielding a light-to-hydrogen

conversion efficiency of as much as 5.4%.<sup>98</sup> Alternatively, using photosystem I, cytochrome c and human sulfite oxidase, Lisdat and co-workers have demonstrated the possibility of using ITO as a support for light-driven bio-sensing redox enzyme devices.<sup>108</sup>

As with PGE, non-specific adsorption of protein to a semiconductor can be facilitated by considering the effect of pH. For example, the isoelectric point of a TiO<sub>2</sub> surface was found to be 6.2<sup>109</sup> while those of two different enzymes, a carbon monoxide dehydrogenase<sup>110</sup> and a [NiFeSe]-hydrogenase,<sup>97</sup> were found to be 5.5 and 5.4, respectively. Both enzymes could be successfully adsorbed to TiO<sub>2</sub> nanoparticles at pH 6,<sup>97,111,112</sup> and this has been rationalized by considering that under these conditions the net surface charge of the enzymes is negative whereas that of the TiO<sub>2</sub> is positive. Similarly, the work of Emmanuel Topoglidis and co-workers<sup>109</sup> has shown that the adsorption to TiO<sub>2</sub> of cytochrome c and hemoglobin was greater at pH 7 than at pH 6.<sup>109</sup> Likewise, this was explained by considering that at pH < 7.5, the proteins would be positively charged whereas the TiO<sub>2</sub> surface is negatively charged at pH 7 but not at pH 6.<sup>109</sup>

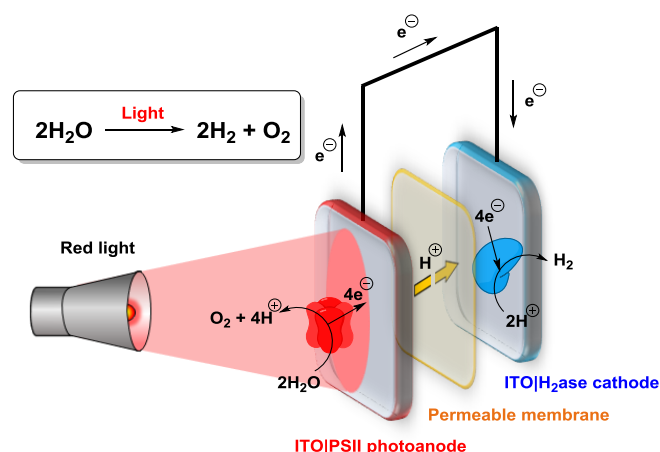


**Figure 1.8.** The water-splitting photoelectrochemical cell developed by Erwin Reisner and co-workers, utilizing photosystem II and hydrogenase enzymes immobilised on hierarchically structured ITO electrodes.<sup>98</sup>

### 1.3.2 Common electrode functionalisation strategies to promote electroactive surface adsorption

In this section we outline surface functionalisation strategies that make electrode surfaces amenable to electroactive redox protein/enzyme adsorption. The general merit of all such electrode modification strategies is that they do not require changes to be made to the protein structure. Instead, the surface-protein interactions should ideally mimic those which underpin electron exchange between the biological molecule and its redox partner(s) *in vivo*. Covalent bonding strategies that aim to make single, site-specific linkages between electrodes and proteins or enzymes will be discussed in **Section 1.3.4**.

### 1.3.2.1 Thiol self-assembled monolayers on gold

A significant amount of literature describes the immobilisation of redox proteins onto surface-modified gold nanoparticles and surface-modified macroscopic gold surfaces.<sup>57</sup> The requirement for surface modification does not arise because proteins cannot bind to gold surfaces; computational evidence suggests the alcohol moieties of serine and threonine amino acid residues can bind to crystalline Au (111) surfaces.<sup>113</sup> The problem is that such interactions can induce protein unfolding.<sup>57</sup> The functionalisation of gold surfaces with alkanethiol-based self-assembled monolayers (SAMs) is thus common practice as it offers the dual opportunity to both mask the gold atoms<sup>114</sup> and present a suitable headgroup to the solution which may facilitate the adsorption of the protein in an electroactive configuration (**Figure 1.9**).<sup>115-123</sup>

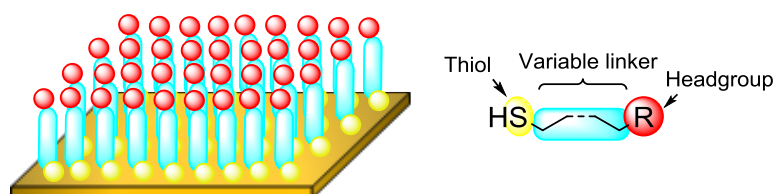


**Figure 1.9.** (Left) Depiction of an alkanethiol SAM on a gold surface, and (Right) the generic structure of alkanethiols used in SAM construction.

SAM formation is generally achieved by immersing a clean gold substrate into a dilute solution of the desired thiol in ethanol, whereupon the thiol functionalities chemisorb to the gold, spontaneously forming S-Au bonds.<sup>124</sup> The “self-assembled” nature of the monolayer arises due to the hydrophobic effect which drives the spontaneous vertical alignment of the alkane chains, yielding a uniform monolayer of densely packed alkanethiols (**Figure 1.9**).<sup>125</sup> The gold cleaning process is necessary to remove any oxide coating and/or adsorbed organic moieties on the gold surface.<sup>126</sup>

Metals other than gold also form strong bonds to thiols, enabling alkanethiol SAM formation. This is relatively trivial for palladium and mercury which, like gold, do not form stable oxide layers.<sup>127-130</sup> However, it is more challenging to form high-quality SAMs on silver (the surface of which oxidises when exposed to ambient atmosphere)<sup>129</sup> and significantly more challenging to form high-quality SAMs on copper (the surface of which oxidises rapidly and extensively when exposed to ambient atmosphere),<sup>127,129</sup> and accordingly such surface modifications are more poorly understood than those constructed on other coinage metals.<sup>125</sup>

The biggest limitation for using gold-thiol based SAM systems in redox protein/enzyme electrochemical applications, is that they have a limited electrode potential window over which they are stable. This window has been reported as between -0.9 and +1.0 V vs SHE at ambient

temperature,<sup>126,131</sup> but a more conservative estimate further limits this range to between -0.4 and +0.6 V vs SHE.<sup>57</sup> At a sufficiently negative potential, reduction of the gold–thiol bond causes the SAM to detach from the surface, whereas over-oxidisation leads to SAM detachment due to the generation of sulfur oxides.<sup>57</sup> This inherent SAM redox activity prevents their use in some bioelectrochemical applications,<sup>57</sup> e.g. the construction of enzymatic CO<sub>2</sub> reduction or H<sub>2</sub>O oxidation systems. SAMs also often have poor long-term storage stability, due to air-induced oxidation of the metal-thiolate bond.<sup>126</sup> As exemplified below, this has not prevented the use of Au-SAMs in a significant number of analytical bioelectrochemical studies, but potentially introduces the requirement for more stable electrode modification routes for the development of commercial technological devices.

### 1.3.2.2 Single component SAMs on gold

Alkanethiol SAMs are frequently used to tailor the polarity of a metal electrode to complement that of the target protein, mediating immobilisation via non-specific interactions, as described in **Section 1.3.1**.<sup>116-123,128</sup> Azurin, a blue type-I copper protein, has been successfully immobilised as monolayers or submonolayers using simple SAMs of different length, such as pentanethiol<sup>117</sup> and decanethiol.<sup>116</sup> Such non-functionalised (i.e. alkane headgroup) alkanethiols are thought to facilitate direct electron transfer between a gold electrode and azurin because the protein has a patch of hydrophobic surface residues proximal to the redox-active copper centre.<sup>132,133</sup> The stability of azurin on such alkanethiol SAMs has been put to particularly good use in the quantification of kinetic and thermodynamic dispersion, via the coupling of fluorescence monitoring of the copper redox state with electrochemical control of the redox potential.<sup>134,135</sup>

The immobilisation of proteins which interact well with negatively-charged PGE electrodes has been achieved via the use of carboxylic acid terminated SAMs.<sup>119-123,136</sup> This has been probed in detail using cytochrome *c*, a protein thought to transfer electrons via interaction with redox partners that are attracted to the positively charged surface lysine moieties close to the redox-active haem group.<sup>15,51,137</sup> When a SAM with SO<sub>3</sub>H headgroups was used instead of a COOH-terminated SAM, successful electroactive electrode immobilisation was still achieved.<sup>138</sup> Cytochrome *c* has also been used in experiments to probe the impact of alkane chain length on the rate of electron transfer,  $k_{ET}$ , between a gold electrode and a protein sitting atop a SAM. When shorter alkanethiols ( $\leq 6$  carbons) are used,  $k_{ET}$  is independent of the alkane-chain length, indicating that the electrochemistry is reporting on the inherent maximum rate of the  $\text{Fe}^{3+} + 1e^- \rightleftharpoons \text{Fe}^{2+}$  biological redox process of interest.<sup>121,139,140</sup> However,  $k_{ET}$  decreases exponentially with the length of the alkanethiol when molecules of more than nine carbons are used.<sup>121,139,140</sup> This indicates that the tunnelling of the electron through the SAM has become the rate limiting step in electron transfer.<sup>121,139,140</sup>

For redox proteins bearing negative surface charges close to the electron entry/exit site, such as plastocyanin or ferredoxins,<sup>46</sup> amino-terminated SAMs can support direct electron transfer in a similar way.<sup>51</sup> Alternatively, as with PGE (**Figure 1.7**), the treatment of acid-terminated alkanethiol SAMs with poly-L-lysine allows for electroactive immobilisation of negatively charged proteins such as cytochrome b5,<sup>141</sup> avidin,<sup>142</sup> and glucose oxidase,<sup>143</sup> with the cationic poly-amine again acting as an electrostatic “glue” between the negative protein and SAM surfaces.<sup>141</sup>

Alkanethiols are not the only molecules which can be used for the formation of SAMs that support electron transfer to an immobilised redox protein or enzyme. Short peptides have been used to form SAMs that permit the electrochemical assay of cytochrome b562 from *E. coli*<sup>144</sup> and a methane monooxygenase from *Methylococcus capsulatus*.<sup>145</sup>

### 1.3.2.3 Multicomponent SAMs on gold

Mixing two or more different alkanethiol molecules together enables the formation of multicomponent SAMs. For example, myoglobin has been stabilized by forming a multicomponent SAM using alkanethiols with OH headgroups and alkanethiols with COOH headgroups.<sup>118</sup> In certain cases, mixed SAM systems may prove superior for electroanalytical applications. The standard rate constant for electron transfer,  $k_{ET}$ , to cytochrome c immobilised on a multicomponent SAM of composition 8:2 mercaptoundecanoic acid (MUA) to decanethiol was about 5 times greater than that on a single-component SAM of MUA at pH 7.<sup>138,146</sup> This was attributed to the notion that deprotonation of the headgroups of a SAM formed from just COOH-terminated alkanethiols introduces such a high concentration of negative charge on the surface of the electrode that it causes the immobilised protein to adopt an orientation that is not optimized for rapid electron transfer.<sup>138</sup>

In a particularly elegant example of biological mimicry, the incorporation of further self-assembling layers on top of multicomponent SAMs can be used to fabricate structures that mimic biological membranes (**Figure 1.10**).<sup>147,148</sup> Such electrode confined tethered bilayer lipid membranes are constructed by first creating a multicomponent SAM using a mixture of specially designed lipid tethers and small alkanethiol molecules, such as 6-mercaptohexanol (**Figure 1.10**).<sup>147,148</sup> Due to the mismatches in chain length and polarity between these two species, they form nanoscale phase-separated domains on the gold surface. The lipid tethers bind to the electrode surface via an Au-S bond, while their headgroups (often cholesterol lipids) induce the self-assembly of phospholipid layers on top of them. Phospholipid bilayers are formed to span across the alkanethiol spacer domains that sit between the lipid tether domains and transmembrane proteins can be embedded into these bilayer regions and electrochemically interrogated, often via the mediation of electron transfer by quinone

molecules that are incorporated into the bilayer, such as ubiquinone (**Figure 1.10**).<sup>147,148</sup> This technique has been applied to study proteins ranging from the relatively small cytochrome bo3 from *Escherichia coli*<sup>147</sup> (*E. coli*) to the very large [NiFe]-hydrogenase of *Ralstonia eutropha*.<sup>148,149</sup>

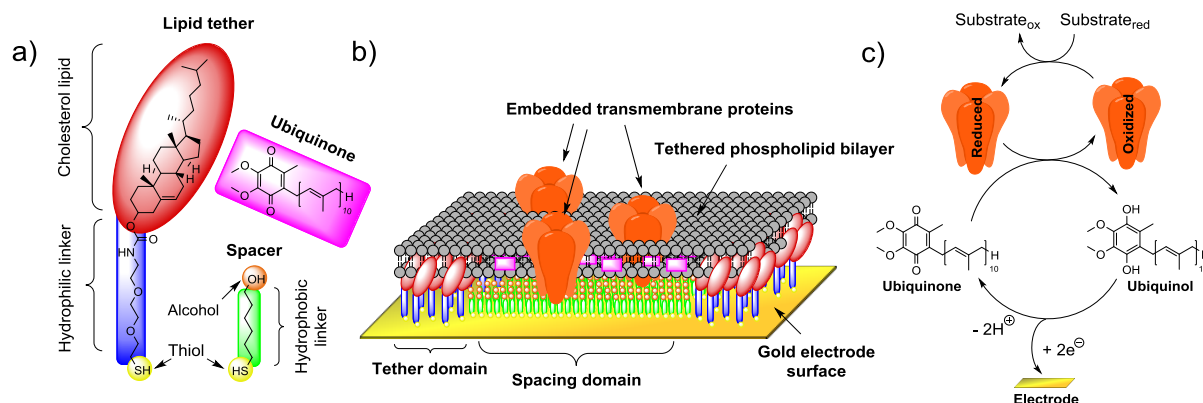


**Figure 1.10.** Tethered bilayer lipid membrane on gold electrode for the immobilisation of membrane-bound redox proteins. **a)** The structures of the components used in tethered bilayer lipid membrane assembly: lipid tethers, spacer units and quinone-type molecules. **b)** The structure of a tethered bilayer lipid membrane on a gold electrode, including embedded transmembrane proteins. **c)** The mediation of electron transfer by quinone type molecules.<sup>147-149</sup>

It should be noted however that the SAM layers are actually dynamic due to the mobility of thiols on gold,<sup>150,151</sup> making SAMs potentially unsuitable for constructing nanostructured arrays intended to have a long lifetime. Thiol exchange can also occur when trying to apply mixed SAM monolayers, with the fraction of longer chains anchored to the surface increasing upon prolonged exposure to the mixed alkanethiol deposition solution.<sup>150,151</sup> As such the composition of a mixed SAM on an electrode surface may be different to the composition of the deposition solution, especially after long periods of incubation.<sup>150,151</sup>

#### 1.3.2.4 Long length conducting SAMs

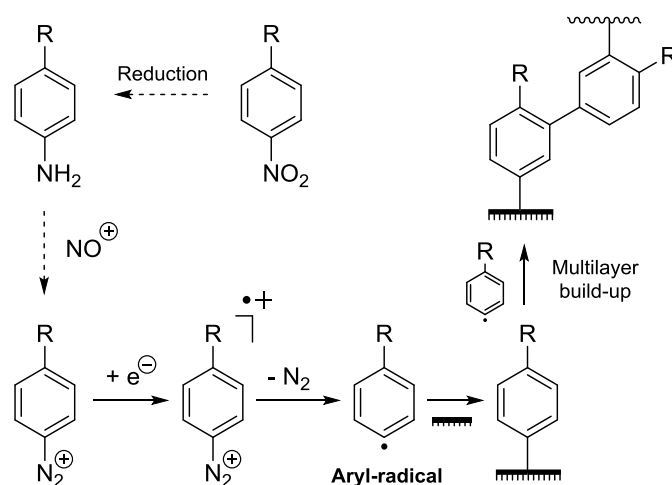
As described in **Section 1.3.2.2**, slow electron transfer through long-length alkanethiols (> 9 carbons) can introduce an artefact into biological electrochemistry experiments, with the limiting rate of the redox process reflecting the interfacial electrode-to-protein electron transfer rate instead of the speed of the biological reaction.<sup>121,139,140</sup> This can be overcome using better conducting SAMs.<sup>152</sup> For example, the use of a SAM containing a highly conjugated diarylethene moiety for modification of a gold electrode enabled fast electron transfer to the small blue copper protein azurin.<sup>152</sup> The redox chemistry rate constant was higher (3-27 times faster) than obtained when using SAMs formed from alkanethiols of a similar length.<sup>152</sup>

Alternatively, redox-active so-called electron transfer “mediator” units can be built into SAMs. An example of such a conducting SAM precursor molecule is 1-(10-mercaptodecyl)-1'-benzyl-4,4'-

bipyridinium dibromide, which was synthesized for immobilisation of a H<sub>2</sub>-producing [FeFe] hydrogenase.<sup>153</sup> Unfortunately the enzymatic activity was only approximately 2.5% of that expected based on solution based experiments, illustrating the complexity in optimizing such a SAM-enzyme system.<sup>153</sup>

### 1.3.2.5 Aryl diazonium salt reduction

The reduction of aryl diazonium salts for the functionalisation of electrodes has been demonstrated on a variety of different materials including all conducting allotropes of carbon,<sup>154-156</sup> silicon,<sup>157</sup> ITO,<sup>158</sup> and a range of metals including gold, platinum and copper.<sup>159</sup> A surface-to-carbon bond is formed via the one-electron reductive formation of an aryl radical, which subsequently attacks the electrode surface, as illustrated in **Scheme 1.1**.<sup>154,160,161</sup> Electrode functionalisation using aryl diazonium salts is therefore electrochemically controllable (**Figure 1.11**) fast, and can often be performed in aqueous or organic electrolyte.<sup>154,160,161</sup> Either isolated aryl diazonium salts can be utilized, or they can be generated *in situ* using an aniline or nitrophenyl derivative and a source of the NO<sup>+</sup> cation, such as NaNO<sub>2</sub>/HCl or NOBH<sub>4</sub> (**Scheme 1.1**).<sup>162,163</sup>



**Scheme 1.1.** The electrochemical reduction of aryl diazonium salts resulting in the formation of a pacifying multilayer film.

Given the range of commercially available aniline and nitrophenyl derivatives, the scope of chemical functionalities that can be introduced onto the surface using diazonium chemistry is comparable to that which can be accessed using commercial alkanethiol derivatives for SAM formation. Unlike SAM formation, this methodology is theoretically applicable to the covalent functionalisation of any conducting surface, not just those which form a stable bond to sulfur. The redox stability of the electrode-carbon bond does not restrict the electrochemical window of biological experiments, and

such surface modifications are also more amenable to long-term storage than SAM modified gold surfaces.<sup>161,164-167</sup>

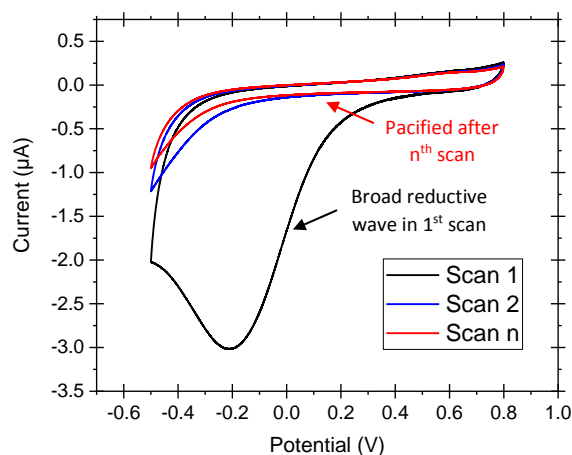


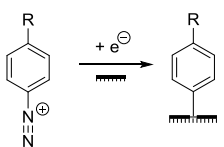
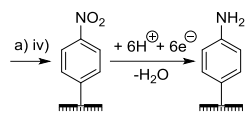
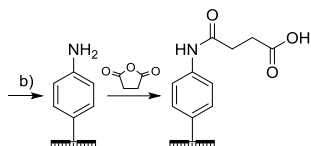
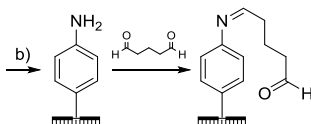
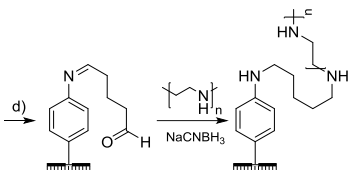
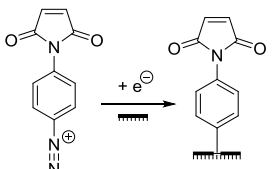
**Figure 1.11.** Characteristic cyclic voltammograms for the reduction of an aryl diazonium salt generated in situ from 2-(4-aminobenzyl)isoindoline-1,3-dione. Potential vs Ag/AgCl (3 M KCl), scan rate 20 mV s<sup>-1</sup>. GC working electrode. Solvent system 1:5 water:acetonitrile + 0.1 M Bu<sub>4</sub>NPF<sub>6</sub> + 0.5% v/v 6.6 M HCl. Ambient temperature.

Diazonium electrode modification is not entirely without its challenges. Multilayer formation can occur when further aryl radicals attack the unsaturated bonds of the aromatic  $\pi$  systems of the original monolayer, resulting in carbon-carbon bonds.<sup>161,168-170</sup> Alternatively, multilayers can arise from diazonium cations coupling to surface phenyl groups via azo bond formation.<sup>161,168-170</sup> Both modes of multilayer formation can contribute to the build-up of an amorphous, organic, insulating layer on the surface of the electrode.<sup>161,168-170</sup> Methodologies to prevent or minimize multilayer formation have been reported, such as the use and subsequent cleavage of bulky protecting groups (see **Section 3.1.3**),<sup>171</sup> sterically hindering the 3,5-positions of the aryl diazonium salt,<sup>172</sup> and the addition of species capable of suppressing multilayer formation via redox cross-reactions, such as 2,2-diphenyl-1-picrylhydrazyl (DPPH).<sup>169,170,173</sup>

In the context of bioelectrochemistry, diazonium electrode modifications can be used to induce protein adsorption via non-covalent interactions in a similar manner to that achieved using unmodified PGE or SAMs on gold. **Table 1.1** summarizes some of the literature examples that have utilized different diazonium electrode functionalisation methods. The flexibility of the method is illustrated by the literature precedence of the use of the same diazonium-protein immobilisation strategy on a range of different electrode surfaces to immobilize a range of redox proteins. The coupling of dialdehydes to aryl amine groups, introduced via diazonium cation electro-grafting (**Table 1.1**, entry d) has been used to immobilize several redox enzymes on both carbon<sup>174,175</sup> and gold electrodes.<sup>176,177</sup>



**Table 1.1.** A selection of strategies for the functionalisation of electrode surfaces via diazonium cation electro-grafting, and subsequent chemical/electrochemical treatments that further modify the electrode surface polarity or provide chemical derivatives that can be exploited in covalent coupling strategies.

Surface functionalisation strategy <sup>[a]</sup>	References
<p>a)</p>  <p>The diagram shows a diazonium cation with an R group on a benzene ring. It reacts with an electrode surface (represented by a horizontal line with vertical bars) and an electron (<math>e^-</math>) to form a phenyl ring with the R group attached to the electrode surface.</p>	<p>i) R = COOH [178]                      ii) R = CH<sub>2</sub>COOH [179]                      iii) R = CH=CHCOOH [180]                      iv) R = NO<sub>2</sub> [83, 181-184]                      v) R = NH<sub>2</sub> [185]</p>
<p>b)</p>  <p>The diagram shows a nitro group (NO<sub>2</sub>) on a benzene ring attached to an electrode surface. It reacts with 6 protons (<math>6H^+</math>) and 6 electrons (<math>6e^-</math>) to form an amino group (NH<sub>2</sub>) on the electrode surface, with the loss of water (<math>-H_2O</math>).</p>	[83, 181-184]
<p>c)</p>  <p>The diagram shows an amino group (NH<sub>2</sub>) on a benzene ring attached to an electrode surface. It reacts with a cyclic anhydride (succinic anhydride) to form an amide linkage to a succinic acid chain.</p>	[83]
<p>d)</p>  <p>The diagram shows an amino group (NH<sub>2</sub>) on a benzene ring attached to an electrode surface. It reacts with a dialdehyde (glyoxal) to form an imine linkage to a chain ending in an aldehyde group.</p>	[174-177]
<p>e)</p>  <p>The diagram shows an imine on a benzene ring attached to an electrode surface. It reacts with a polyamine (represented by a chain of nitrogen atoms) and sodium cyanoborohydride (NaCNBH<sub>3</sub>) to form a secondary amine linkage to a polyamine chain.</p>	[174]
<p>f)</p>  <p>The diagram shows a diazonium cation with a succinimide group on a benzene ring. It reacts with an electrode surface and an electron (<math>e^-</math>) to form a phenyl ring with the succinimide group attached to the electrode surface.</p>	[186]

### 1.3.3 Covalent coupling of electrodes to native proteins

Attempts to physically adsorb proteins onto surfaces in an electroactive configuration are not always successful and, as described above, even when they do work, the adsorption strategies may be strongly dependent on the pH of the electrolyte solution. Alternatively, the film of molecules may only be transiently stabilized, with either misfolding<sup>187</sup> or possible desorption processes leading to a steady drop in redox activity. To avoid such problems, the covalent attachment of proteins to electrode surfaces is therefore desirable, particularly in biotechnological device development. Such a covalent coupling approach often requires a complementary surface functionalisation strategy so either thiol self-assembly or diazonium modification is often used to introduce surface groups that will react with protein moieties.<sup>171,172,174,188-191</sup>

#### 1.3.3.1 Peptide bond formation

The most common covalent protein immobilisation strategy is to mimic nature and generate peptide bonds, either through coupling carboxylic acid functionalised surfaces to protein surface lysine residues,<sup>82,171,172,174,178-181,192,193</sup> or crosslinking glutamate and aspartate residues that adorn protein surfaces to amine functionalised surfaces.<sup>175,181-183,194</sup> The use of 1-ethyl-3-(3-dimethylaminopropyl)carbodiimide and *N*-hydroxysuccinimide (EDC/NHS) coupling is one way to form these peptide bonds (**Figure 1.12**).<sup>181,193</sup> Carbodiimide-based activating reagents find popular usage, with alternatives to EDC/NHS including EDC/sulfo-NHS<sup>195</sup> or *N*-cyclohexyl-*N'*-(2-morpholinoethyl)carbodiimide-methyl-*p*-toluenesulfonate (CMC).<sup>192</sup> Alternatively, long-chain carboxylic acid terminated alkanethiols can be activated towards nucleophilic attack by an amine using trifluoroacetic acid anhydride, via the formation of interchain acid anhydrides.<sup>190</sup>

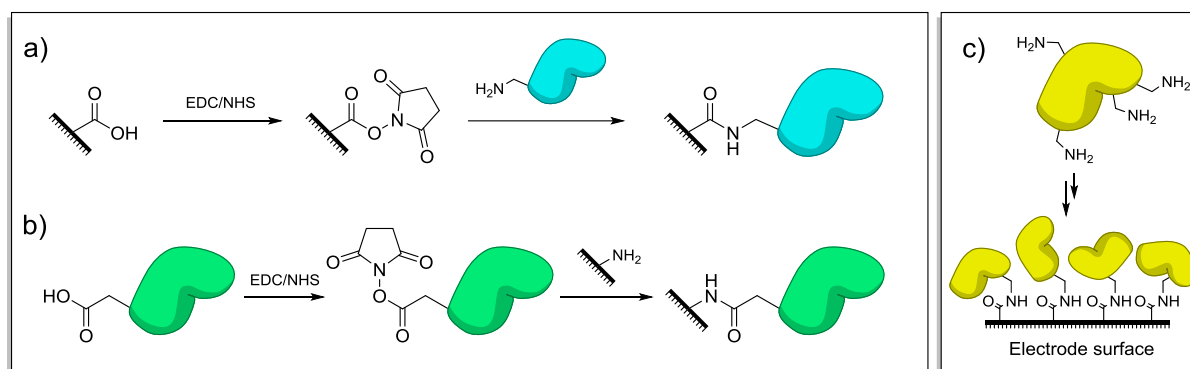


**Figure 1.12.** Amide bond formation between surfaces and protein residues, catalysed via EDC/NHS activation. **a)** Activation of electrode-surface carboxylic acid groups and reaction with protein lysine residues. **b)** Activation of carboxylic acid groups on the protein surface and reaction with electrode surface amine groups. **c)** Due to the presence of many amine/carboxylic acid moieties on protein surfaces, immobilisation via EDC/NHS activation often leads to a dispersion in immobilised protein orientation.

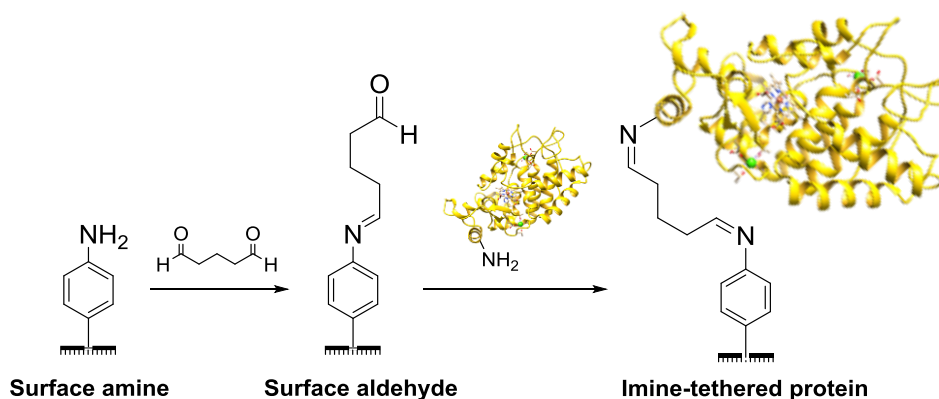
As described in **Section 1.3.2.2**, carboxylic acid or amine headgroups can be readily introduced onto gold electrodes through the selection of appropriate alkanethiols, and there are numerous examples of such a strategy being harnessed to form amide bonds to redox proteins.<sup>189,192,193</sup> Likewise, carboxylic acid groups can be readily introduced onto electrode surfaces via the reduction of suitable diazonium precursors.<sup>167,178,179</sup> Using isolated diazonium salts, the introduction of an amine functionality can be achieved via the reduction of the p-aminodiazonium cation.<sup>185</sup> Alternatively, the same surface modification can be achieved using the commercially available 4-nitrobenzenediazonium tetrafluoroborate salt, with electrochemical reduction being used to reduce the nitro “headgroups” to the desired amine functionalities in a post-diazonium crosslinking step.<sup>168,176,177</sup> The introduction of more reactive aliphatic amine groups to electrode surfaces via diazonium modification can be achieved via the use of the 4-aminoethylbenzenediazonium cation,<sup>196</sup> phthalimide-protected aliphatic amine functionalities.<sup>171</sup> or Fmoc-protected aliphatic amine functionalities.<sup>197</sup>

Amide-bond formation strategies have been used in the fabrication of many mediator-free biosensors; EDC/NHS activated tyrosinase has been crosslinked to aminophenyl groups on BDD electrodes and used to detect phenolic compounds.<sup>181</sup> The EDC/NHS activation and crosslinking of horseradish peroxidase or cytochrome P450 enzymes to amine moieties on carbon electrodes has been used in the fabrication of biosensors for the detection of a series of pharmaceutically relevant drugs.<sup>175,182,183</sup> While horseradish peroxidase could be used to sense levetiracetam,<sup>182</sup> specific cytochrome P450's could be used to detect phenobarbital<sup>175</sup> and codeine.<sup>183</sup> The immobilisation of an oxygen-tolerant hydrogenase onto pyrene-modified multiwalled carbon nanotubes coated onto PGE electrodes has also been achieved via EDC/NHS coupling.<sup>195</sup> The resultant derivatised PGE electrode was utilized as the anode in the fabrication of an enzyme H<sub>2</sub>/O<sub>2</sub> fuel cell; this resulted in significantly improved current density and stability when compared to a fuel cell containing a hydrogenase-electrode fabricated using simple adsorption procedures.<sup>195</sup>

The most significant limitation of such approaches is that regardless of whether carboxylic acid residues or lysine groups are targeted, because there are often multiple occurrences of such amino acid side chains on the surface of the redox protein or enzyme of interest, significant dispersion in the orientation of the immobilised biomolecule commonly results (**Figure 1.12**). Careful genetic engineering of the target protein can be used to overcome this problem. A recent publication by Lalaoui *et al*<sup>198</sup> reports the site specific immobilisation of a laccase onto CNTs via the generation of a variant enzyme that only contains a single surface accessible lysine residue that is located proximal to the electron entry/exit type 1 copper centre.<sup>198</sup>

### 1.3.3.2 Imine tethering

Redox proteins or enzymes can also be covalently crosslinked to surfaces via imine bond formation between electrode surface aldehyde moieties and protein surface lysine residues (**Scheme 1.2**). For example, diazonium electro-grafting methods have been used to introduce aldehyde functionality onto electrodes (**Table 1.1**, entry d) that have subsequently been modified with enzymes, including acetylcholinesterase<sup>174,199</sup> horseradish peroxidase,<sup>177</sup> and tyrosinase.<sup>176</sup> Analogously, the reaction of glutaraldehyde with amine terminated SAMs yields an aldehyde functionalised surface that can be used to attach proteins via their surface lysine residues.<sup>191,200,201</sup> To generate more stable covalent linkages, the imine bonds can be reduced to amine linkages using reagents such as sodium cyanoborohydride.<sup>202</sup>



**Scheme 1.2.** The use of an imine functionalised electrode to immobilize horseradish peroxidase, as detailed in reference [177].

As with amide bond formation between an electrode and surface lysine residues on a protein or enzyme, the same limitation remains; crosslinking electrodes to lysine residues that are not within close approach of the electron entry/exit site in a protein or enzyme will not yield electroactively bound biomolecules. Additionally, the presence of multiple surface lysine residues could result in dispersion in the orientation of the protein or enzyme on the electrode surface, as illustrated in **Figure 1.12**.

### 1.3.4 Crosslinking strategies for site-specifically connecting proteins to electrodes

In theory, an excellent way to generate a uniform configuration of proteins or enzymes on a surface, with each biomolecule attached via the same single point, is to develop site-selective covalent crosslinking strategies, as illustrated in **Figure 1.13**. This is often a complex process which usually requires a combination of genetic manipulation and surface chemistry to ensure that there is a single amino acid residue suitable for selective reaction with a complementary surface moiety. The advantage of modifying electrodes rather than non-conductive solid substrates is that redox-activated reactions such as diazonium salt electroreduction can be utilized in the surface chemistry (**Section 1.3.2.5**). However, this is tempered by the disadvantage that for direct electron transfer between the electrode surface and a redox protein or enzyme to be feasible the target amino acid reaction site must be sufficiently close to the electron entry/exit site (**Section 1.3.1**).

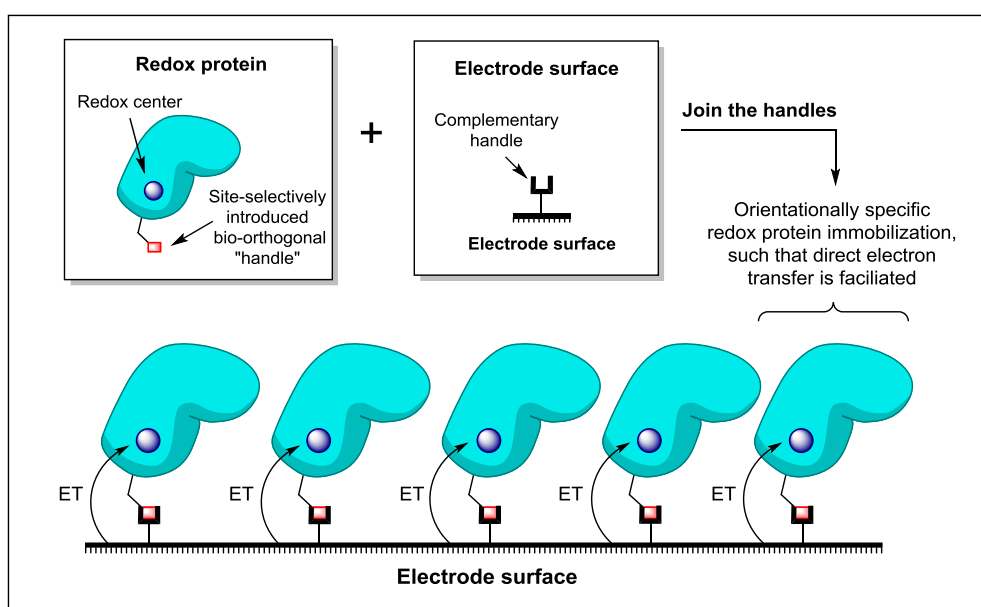


**Figure 1.13.** Generic strategy for site selectively crosslinking a redox protein to an electrode.

#### 1.3.4.1 Redox-centre targeted binding

The easiest way to avoid the need for genetic manipulation of the target redox protein or enzyme is to devise an electrode binding strategy which anchors the biomolecule to the conducting surface via a non-amino acid functionality. An obvious choice of centre for such linking strategies is the electron entry/exit redox-active cofactor of the protein/enzyme, since anchoring to the electrode surface via such a group will ensure that the biomolecule is crosslinked to the electrode in an electroactive configuration. A number of approaches that have used this understanding of biological structure and function to rationally design bespoke wiring strategies for attaching proteins or enzymes to electrodes are described below. The most obvious limitation of such cofactor-targeted surface binding strategies

is that biology utilizes a wide range of different redox-active cofactors, as illustrated by **Figure 1.1**. Anchoring different classes of redox proteins or enzymes via a redox centre targeted binding strategy therefore requires the design and optimisation of many different chemical strategies, a non-trivial synthetic task. In the case of enzymes such as lytic polysaccharide monooxygenases,<sup>11</sup> the fact they contain a single redox site where the substrate must bind also introduces the challenge of whether linkers can be designed that do not hinder substrate binding and catalysis.

#### **1.3.4.1.1 Cofactor ligation**

In some instances, redox-active cofactors can be synthesized and incorporated into so-called cofactor-free “apo-proteins”. This offers a route to generating redox proteins containing modified redox cofactors which have chemical functionalities that are complementary to those which can be added to the electrode surface. For example, the incorporation of an azide-functionalised heme group into cytochrome b562 enabled copper(I)-catalysed azide–alkyne cycloaddition to an alkyne functionalised CNT that was immobilised onto a GC electrode.<sup>203</sup> Alternatively, for proteins containing metal electron entry/exit sites that have multiple ligands, genetic removal of an amino acid ligand residue offers the opportunity for structural reconstitution of the redox protein with an external ligand that is tethered to the electrode surface. This strategy has been demonstrated for an azurin variant.<sup>204</sup> The copper-coordinating histidine residue (His117) was replaced with a glycine residue via genetic manipulation.<sup>204</sup> This opened the coordination sphere around the redox-active metal and allowed a pyridine headgroup tethered to an electrode surface to coordinate directly to the copper centre, immobilizing the azurin in an orientation suitable for facile direct electron transfer and mimicking the native copper ligation that is afforded by His117.<sup>204</sup> The surface attachment of the pyridine group was enabled by the synthesis of a thiol-terminated linker that covalently bound to gold surfaces.<sup>204</sup>

#### **1.3.4.1.2 Substrate electrode tethers**

With redox enzymes that internally transfer electrons from the oxidation of a substrate in one binding pocket to reduce a second substrate in a second binding site, surface attachment can be achieved based on the “lock and key” model<sup>205</sup> of site selective enzyme-substrate binding. For example, multicopper oxidases (which have evolved to couple organic-substrate oxidation at one copper site to oxygen reduction at another copper site) can be immobilised for use as Pt-free, low overpotential O<sub>2</sub>-reduction electrocatalysts via the use of surface attached organic-substrate mimics (Figure 1.14).<sup>206,207</sup> The highly conjugated nature of an anthracene electrode linker, immobilised onto graphite via diazonium chemistry, was shown to ensure rapid electron transfer from the electrode surface to laccase.<sup>206,207</sup> Via a similar strategy, surface naphthoic acid moieties were effective in the

immobilisation of bilirubin oxidase from *Myrothecium verrucaria*.<sup>208</sup> O<sub>2</sub>-reduction by this enzyme was externally wired to a hydrogenase-coated electrode so that an all-enzyme, membrane-free H<sub>2</sub>/O<sub>2</sub> fuel cell could be constructed where H<sub>2</sub>-oxidation is used as the source of electrons for O<sub>2</sub> reduction (Figure 1.14).<sup>209</sup>

In a similar vein, the surface binding of DNA can be used to immobilise redox proteins for the electrochemical interrogation of the redox reactions which may underpin DNA translation and repair *in vivo*.<sup>210</sup>

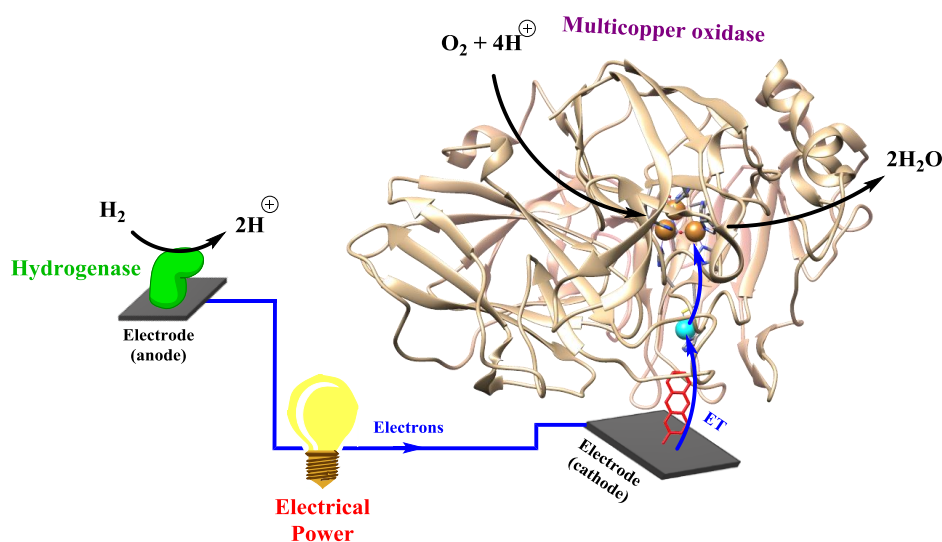


**Figure 1.14.** Membrane free H<sub>2</sub>/O<sub>2</sub> fuels cells can be fabricated by coupling the redox activity of hydrogenases to oxidases.<sup>206,207,209</sup> The orientation of the multicopper oxidase *Trametes versicolor* laccase III (PDB code: 1KYA) onto an electrode surface for O<sub>2</sub> reduction catalysis can be achieved via the modification of the electrode surface with an anthracene substrate mimics, thereby anchoring the enzyme via its binding pocket and allowing for facile direct electron transfer.<sup>206,207</sup>

#### 1.3.4.2 Cysteine-based surface ligations

As the sole thiol-containing canonical amino acid, cysteine presents a unique chemical functionality that can be harnessed in the design of biochemical ligation methodologies that selectively target only cysteine residues.<sup>211-214</sup> This chemical selectivity is complemented by the fact that relative to other amino acids, cysteines rarely occur on protein surfaces.<sup>215</sup> Thus, it can be relatively trivial to use site directed mutagenesis and chemical biology conjugation methods to engineer proteins and enzymes with single, covalently modified surface cysteine residues<sup>211-214</sup> Such strategies are of enormous value in the development of new biopharmaceutical therapies.<sup>211,214</sup> Surface-attachment strategies have been developed along similar lines, with the added consideration that for direct electron transfer between a conducting surface and a redox protein or enzyme, the cysteine residue must serve as a tethering site that holds the redox protein/enzyme in an electroactive orientation.<sup>103,216,217</sup>

The most significant limitations to the use of cysteine residues for enzyme electrode “wiring” applications arise from the potential for these residues to form intermolecular disulfide bonds,<sup>218</sup> or to cause misfolding via the formation of non-native disulfide bond formation,<sup>219</sup> or through the accidental introduction of an extra metal-ligand residue to a metalloprotein or enzyme. For example, iron-sulfur cluster incorporation into a protein structure is dependent on metal cluster binding to a highly conserved sequence of cysteines,<sup>1</sup> and addition of extra residues can be used to convert a [Fe<sub>3</sub>S<sub>4</sub>] centre into a [Fe<sub>4</sub>S<sub>4</sub>].<sup>220</sup> To avoid the issue of unwanted disulfide bond formation, proteins displaying free surface cysteine residues can be kept under reducing conditions via addition of dithiothreitol (DTT). However, because DTT contains thiol groups, this reducing agent must be removed before surface bioconjugation is attempted, to avoid unwanted reactions between DTT and the electrode surface.<sup>221</sup>

#### **1.3.4.2.1 Direct immobilisation onto gold**

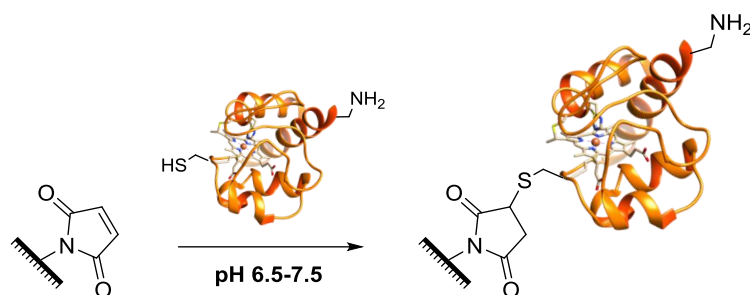
As described in **Section 1.3.2**, the formation of SAMs onto gold electrodes is facilitated by the generation of gold-sulfur bonds. An analogous approach is to therefore graft surface-cysteine containing proteins or enzymes directly onto gold surfaces.<sup>222,223</sup> The ability of this approach to immobilize redox proteins in chosen orientations has been definitively demonstrated using a cytochrome b 562 engineered to present cysteine residues on either its long axis or short axis.<sup>222</sup> The resultant orthogonal orientations of these different protein variants on atomically flat gold was then observed via STM imaging.<sup>222</sup> As with SAMs on gold, a significant limitation of this method is the redox instability of such covalent electrode-protein modifications (**Section 1.3.2.1**). The fact that electroreduction can be used to break Au-S bonds at relatively high reducing potentials impedes the use of this methodology for studying important biofuel reactions such as hydrogen production.

#### **1.3.4.2.2 Thiol-Michael addition click reactions**

In recent years, the reaction between cysteine residues and unsaturated  $\pi$ -systems via Michael addition has been used as a general tool for the chemical modification of many proteins, extending well beyond electrode-protein surface ligation strategies.<sup>224-227</sup> Numerous different methodologies using different  $\pi$ -systems have been optimized for different applications.<sup>224</sup> In the field of electrode-ligation, surfaces have been functionalised with maleimide groups, the most reactive of the commonly available vinyl Michael acceptors.<sup>224</sup> Between pH 6.5 and 7.5, maleimide groups react selectively with thiols, as within this pH range amines remain protonated and are thus not of a high enough nucleophilicity to partake in competing side reactions (Scheme 3).<sup>217</sup>



Maleimide groups can be introduced onto electrode surfaces via a variety of techniques, including the use of specially designed alkanethiol SAMs,<sup>225,228</sup> diazonium cation electro-grafting (**Table 1**, entry f),<sup>186</sup> and a sequential electrochemical and solid-phase preparation.<sup>217</sup> The reaction between surface maleimide groups and one of the two thiol groups that naturally occur near the heme cofactor of cytochrome c results in the immobilisation of this protein in a near site-specific orientation that is suitable for direct electron transfer (**Scheme 1.3**).<sup>186</sup>



**Scheme 1.3.** Maleimide-thiol Michael addition reactions between maleimide groups introduced onto an electrode surface and cytochrome c surface cysteine residues.<sup>186</sup>

#### 1.3.4.3 Crosslinking to unnatural amino acids

Unnatural amino acid (UAA) mutagenesis is a technique which utilizes codon reassignment to expand the amino acids available for the synthesis of a target protein of interest.<sup>223-225,229-234</sup> This allows amino acids with novel functionalities to be introduced at specific locations within proteins, and such residues can be subsequently targeted in bio-orthogonal chemical ligations (i.e. covalent bond forming reactions that target functionalities which are orthogonal to those which occur in nature).<sup>213,230,231</sup> This is a rapidly expanding field of research.<sup>223-225,229-234</sup> and there are now a few examples of such methodologies being adapted for covalent crosslinking of redox proteins and enzymes to electrode surfaces.<sup>235-237</sup> A practical consideration that makes the use of UAA mutagenesis potentially unsuitable for “wiring” redox metalloenzymes onto electrodes, is that highly complex biosynthetic pathways can make protein overexpression challenging; in such scenarios substantial quantities of synthetic UAA may be required to generate useable quantities of UAA containing protein.

For UAA mutagenesis to serve as an immobilisation methodology, functionalities complementary to those of the UAA must also be introduced to the electrode surface. Azide-alkyne cycloaddition click reactions therefore represent an attractive approach since methods for the introduction of these moieties onto electrode surfaces have been developed for other applications such as DNA sensor development.<sup>238</sup> Should the use of a copper catalyst for activation of the cycloaddition reaction be undesirable, copper-free reactions can be performed via the use of ring-

strained alkynes (**Figure 1.15**).<sup>239</sup> Surprisingly, based on the robust nature of this chemical ligation strategy,<sup>240</sup> the only example we can find of the use of azide-alkyne UAA reactions for the site specific linkage of a redox protein or enzyme to an electrode is the immobilisation of the 4-azido-L-phenylalanine (**1**, **Figure 1.15**) containing laccase from *Streptomyces coelicolor* onto a MWCNT-coated electrode functionalised with complementary cyclooctyne containing linkers (**Figure 1.15**).<sup>235</sup> Interestingly, the most effective orientation for direct electron transfer was found to be one that tethered the laccase at a site distal from any redox centres but adjacent to a water channel; the structured water molecules within which are thought to substantially enhance the electron transfer rate between the electrode and the laccase.<sup>235</sup> A similar strategy has also been used to wire whole bacteria to electrodes.<sup>236</sup> Via the incorporation of UAA **1** into an alcohol dehydrogenase that is displayed on the surface of *E. coli*,<sup>236</sup> copper(I)-catalysed cycloaddition to an alkyne functionalised SAM linker was used to bond bacterial cells to a gold surface.<sup>236</sup>

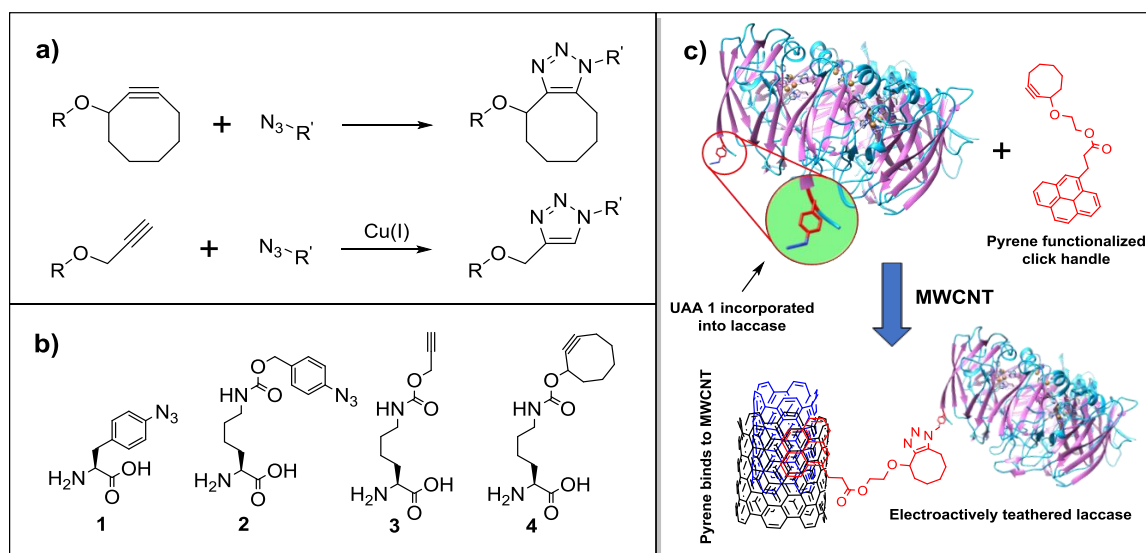


**Figure 1.15.** Azide-alkyne cycloaddition click reactions between surfaces and proteins. **a) (Top)** Copper-free uncatalysed azide-alkyne cycloaddition click reaction, promoted by a ring strained alkyne. **(Bottom)** Copper-catalysed azide-alkyne cycloaddition reaction. **b)** Due to the precedence for unnatural amino acids bearing both alkyne and azide functionalities, it is possible to functionalise a protein with either azides or alkynes. **c)** The site-selective electroactive immobilisation of a laccase onto a MWCNT via the use of a copper-free uncatalysed azide-alkyne cycloaddition click reaction between an azide-functionalised UAA and a surface-confined cyclooctyne, as described in ref [235]. Residues from only one monomer are depicted (pdb code: 3CG8<sup>240</sup>).

Other, non azide-alkyne, chemical ligation strategies can be realized via the use of different UAA residues. The incorporation of 3-amino-L-tyrosine ( $\text{NH}_2\text{Tyr}$ ) into myoglobin has been used to covalently attach the protein a gold surface derivatised with acryloyl moieties, courtesy of a Diels-Alder reaction specific to  $\text{NH}_2\text{Tyr}$  (**Figure 1.16**).<sup>237</sup> The rate of electron transfer between the electrode and myoglobin was slow, which was attributed to the length of the anchoring tether (26.7 Å).<sup>237</sup>

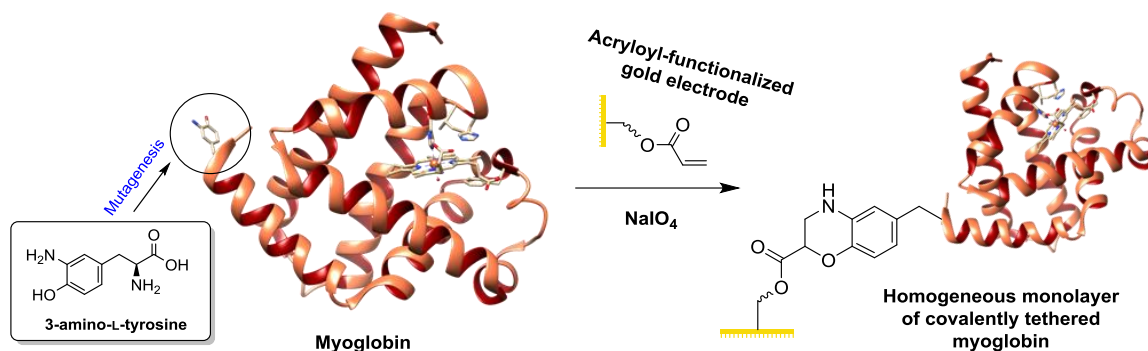


**Figure 1.16.** The covalent crosslinking of myoglobin to a gold electrode as a homogeneous monolayer, via the incorporation and Diels-Alder reaction of a 3-amino-L-tyrosine residue.<sup>237</sup>

### 1.3.5 Reflection upon the existing strategies for redox protein/enzyme immobilisation

**Section 1.3** demonstrates that although many different approaches can be used to immobilise redox-proteins or enzymes in electroactive configurations, there is still no single reliable method that delivers site-selective, stable bond formation to facilitate covalent immobilisation that is broadly applicable to many biological systems. Excitingly, the continually expanding toolbox of chemical biology techniques can be applied in solving this problem, and in the latter Results chapters I will describe new approaches that I have developed and tested during my PhD.

## 1.4 The techniques commonly used in protein film electrochemistry

Having established the advancements and complexities that need to be considered in obtaining the protein “film” required for protein film electrochemistry in the preceding Sections, the remainder of this Introduction serves to acquaint the reader with some of the electrochemistry techniques commonly used in PFE. Specifically, the aim is to ensure that the experimental data presented in the Results chapters is placed into a theoretical context. For the very interested readers, a detailed explanation of how measured electrode potentials directly report on the thermodynamics of a system is available in **Appendix 1**.

### 1.4.1 Direct current cyclic voltammetry

Direct current cyclic voltammetry (dCV), often referred to simply as cyclic voltammetry, involves applying a potential to the working electrode that changes linearly with time, sweeping between two

potentials, E1 and E2 (**Figure 1.17**). The rate of change of the applied potential is known as the scan rate ( $\nu$ ).

The current that flows through the working electrode is plotted as a function of the potential applied to the working electrode, yielding a plot known as a cyclic voltammogram (CV). This plot will contain capacitive current, which flows due to ions in the electrolyte solution moving in response to the changes in the applied electrode potential, and Faradaic signals arising from species directly transferring electrons with the working electrode, i.e. undergoing a formal redox reaction.<sup>241</sup> The capacitive current usually appears as a typical hysteresis (a parallelogram-like signal), whereas the Faradaic signals appear as bumps (**Figure 1.18**). The applied potential of the working electrode may be held at E1 for a given time period before the CV is recorded, to allow conditions to reach equilibrium before measurements are taken.

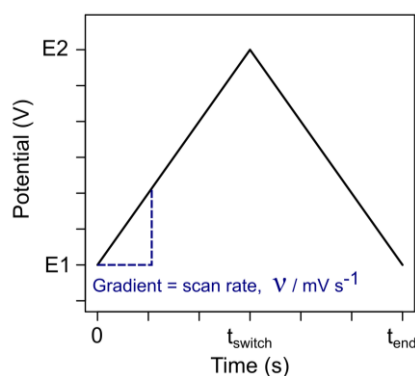


**Figure 1.17.** The potential waveform that is applied to the working electrode in a cyclic voltammetry experiment.

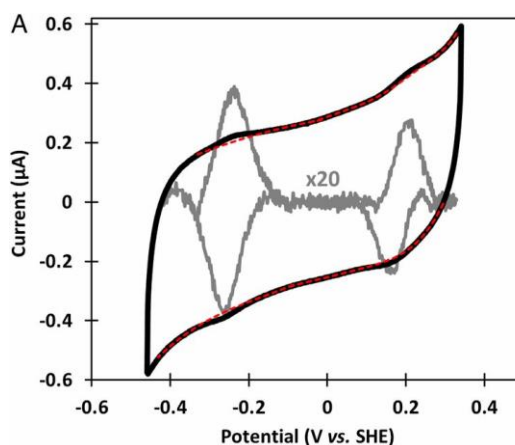
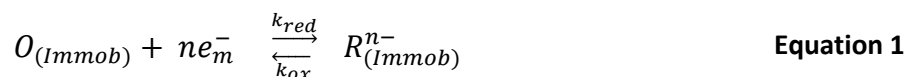


**Figure 1.18.** (Black) CV of the redox protein YedY immobilised onto a PGE electrode, showing two Faradaic signals. The CV was recorded in 50 mM Mes buffer at pH 7 at a scan rate of 100 mV s<sup>-1</sup>. The baseline fitted to the background capacitive current is shown by the red dashed line; the baseline-subtracted signals (scaled by a multiplication factor of 20) are depicted by the grey solid lines. Figure reproduced with permission from reference [242], <https://www.pnas.org/content/112/47/14506>. Readers should note that further permissions regarding this figure should be directed to the PNAS.

Consider the redox couple defined in **Equation 1** for redox proteins/enzymes electroactively immobilised as a film on an electrode surface in the absence of enzyme substrate. A CV recorded using this film-covered electrode would show Faradaic signals arising from the reduction and oxidation of the redox sites within the protein. If two redox-active sites were present in the protein, and both were able to partake in direct electron transfer with the electrode, two sets of Faradaic signals would be observed, as is the case in **Figure 1.18**.



$O_{(Immobilized)}$  = oxidised species of the immobilised redox couple

$n$  = number of electrons transferred in redox couple.

$e_m^-$  = an electron. The (m) denotes that the electron comes from the electrode.

$R_{(Immobilized)}^{n-}$  = reduced species of the immobilised redox couple.

$k_{red}$  = rate constant for the reduction of  $O_{(Immobilized)}$ .

$k_{ox}$  = rate constant for the oxidation of  $R_{(Immobilized)}^{n-}$ .

The value for  $v$  can be varied across a large range (i.e. between  $1 \text{ mV s}^{-1}$  and  $10 \text{ V s}^{-1}$ ) and this dynamic range provides access to both thermodynamic and kinetic descriptions of redox chemistry, as described in **Sections 1.4.1.1** and **1.4.1.2** respectively.<sup>243</sup> Cyclic voltammetry is thus a highly versatile technique, and the interpretation of CVs is relatively easy relative to the plots yielded by other voltammetric techniques (such as the harmonic signals of Fourier transform alternating current voltammetry, which is discussed in **Section 1.4.5**). The main drawback to cyclic voltammetry is that the capacitive contributions to the current can be significantly larger than the current arising from Faradaic processes; this low ratio of signal to background lowers the sensitivity of cyclic voltammetry. Faradaic signals also have to be isolated from the background capacitive current before the signals can be analysed, which is often accomplished by fitting a polynomial to the background current either side of a Faradaic signal and subtracting it (**Figure 1.18**).

#### 1.4.1.1 The measurement of the number of electrons involved in a redox couple and the determination of the Gibbs free energy change associated with electron transfer

The parameter  $k_0$  is the heterogeneous electron transfer rate constant, the rate at which electrons can be exchanged between the electrode and the redox couple.<sup>244</sup> When  $v < k_0 RT/F$  the rate of electron transfer is fast enough to allow equilibrium (the thermodynamically favoured state) to be established between the redox couple and the applied electrode potential at a rate fast enough to keep up with the changes in the applied potential.<sup>245</sup>

The point midway between the peaks of these Faradaic current signals gives the formal potential ( $E_f$ ) of the redox couple (which is fully defined in **Appendix 1, Equation 28**),<sup>246,247</sup> and assuming there are no interactions between the immobilised redox proteins/enzymes and all the proteins are immobilised identically (i.e. the ideal conditions of a Langmuir isotherm), this formal potential is equivalent to the standard reduction potential ( $E^0$ ).<sup>245</sup> As such the midway point between the Faradaic peaks directly reports on the standard Gibbs free energy change associated with the electron transfer, as described by the relationship  $\Delta G^0 = -nFE^0$ .<sup>248</sup> To be able to use this relationship, and otherwise learn more about the redox protein/enzyme system under assay, the number of electrons transferred in the redox couple ( $n$ ) still has to be discerned.

The current flowing through the electrode from the immobilised redox protein/enzymes is proportional to the change in the surface coverage of immobilised oxidised species per unit time. The change in the coverage of oxidative species will be the negative of the change in coverage of reduced species per unit time, as the movement of electrons from the electrode to the immobilised sample of proteins will be causing oxidised redox proteins to become reduced. This relationship is described by **Equation 2**.<sup>249</sup>

$$i = nFA \frac{d\Gamma_{O(Immobilized)}}{dt} = -nFA \frac{d\Gamma_{R(Immobilized)}^{n-}}{dt} = -nFA \left( \frac{dE}{dt} \right) \left( \frac{d\Gamma_{R(Immobilized)}^{n-}}{dE} \right) \quad \text{Equation 2}$$

$i$  = the current flowing into the electrode / A.

$\Gamma_{O(Immobilized)}$  = the surface concentration of the oxidised species of the immobilised redox couple.

$\Gamma_{R(Immobilized)}^{n-}$  = the surface concentration of the reduced species of the immobilised redox couple.

$n$  = number of electrons transferred in redox couple.

$A$  = the surface area of the electrode.

$F$  = the Faraday constant / C mol<sup>-1</sup>.

$t$  = time / s

$E$  = electrode potential / J C<sup>-1</sup>.

Assuming ideal conditions for the immobilised redox protein, the Nernst for the redox couple can be written as **Equation 3**.<sup>248,250-252</sup>

$$E = E_{(O/R)}^0 - \left( \frac{RT}{nF} \right) \ln \left( \frac{\Gamma_{R(Immobilized)}^{n-}}{\Gamma_{O(Immobilized)}} \right) \quad \text{Equation 3}$$

$E$  = electrode potential / J C<sup>-1</sup>.

$E_{(O/R)}^0$  = standard potential of the redox couple / J C<sup>-1</sup>.

$R$  = gas constant / J mol<sup>-1</sup> K<sup>-1</sup>.

$T$  = temperature / K.

$n$  = the number of electrons transferred in the redox couple.

$F$  = the Faraday constant / C mol<sup>-1</sup>.

$\Gamma_{O(Immobilized)}$  = the surface concentration of the oxidised species of the immobilised redox couple.

$\Gamma_{R(Immobilized)}^{n-}$  = the surface concentration of the reduced species of the immobilised redox couple.

The surface concentration ( $\Gamma$ ) of the redox protein/enzyme on the electrode surface can be determined via the integration of a Faradaic signal with respect to applied voltage, as described by **Equation 4**.<sup>46</sup>

$$\Gamma_{Total(Immobilized)} = \frac{\int I_{Faradic} dE}{nvFA} \quad \text{Equation 4}$$

$\Gamma_{Total(Immobilized)}$  = the surface concentration of the immobilised redox species.

$\int I_{Faradic} dE$  = the area enclosed by the Faradaic signal / J s<sup>-1</sup>.

$n$  = the number of electrons transferred in the redox couple.

$F$  = the Faraday constant / C s<sup>-1</sup> mol<sup>-1</sup>.

$A$  = the surface area of the electrode.

$v$  = scan rate / J C<sup>-1</sup> s<sup>-1</sup>.

Using **Equation 3** and the fact that  $\Gamma_{Total(Immobilized)} = \Gamma_{R^{n-}} + \Gamma_{O(Immobilized)}$ , **Equation 5**, can be derived and substituted into **Equation 2** to yield **Equation 6**.<sup>249</sup> This describes the current found in a peak at any potential relative to the standard potential of the redox couple under equilibrium conditions.

$$\Gamma_{R^{n-}} = \frac{\Gamma_{Total(Immobilized)}}{1 + e^{(nF(E - E_{(O/R)}^0)/RT)}} \quad \text{Equation 5}$$

$$i = v \left( \frac{n^2 F^2 A \Gamma}{RT} \right) \left( \frac{e^{(nF(E - E_{(O/R)}^0)/RT)}}{[1 + e^{(nF(E - E_{(O/R)}^0)/RT)}]^2} \right) \quad \text{Equation 6}$$

Experimentally derived signals from a redox protein can thus be fitted using **Equation 6**,<sup>249</sup> solving for parameters such as  $n$  and  $\Gamma$  to reveal how many electrons take part in the electron transfer to the protein redox site – an important parameter to learn when trying to discern the mechanism via which a redox protein operates.

The peak in current occurs when  $E = E_{(O/R)}^0$ , and is thus given by  $i = v \left( \frac{n^2 F^2 A \Gamma}{4RT} \right)$ .<sup>46</sup> As can be seen, the peak height scales linearly with scan rate ( $v$ ), and as such a plot of peak height vs  $v$  for surface-confined redox processes yields a straight line. By contrast, the peak height for a solution-phase redox couple scales linearly with  $\sqrt{v}$ , and thus it is easy to distinguish signals coming from a surface-confined redox couple from those from a solution-phase redox couple.<sup>241</sup>

An ideal Faradaic signal from a surface-confined reversible redox signal would be perfectly simulated by **Equation 6**. In practice however, a redox couple is unlikely to behave entirely ideally. As

such, a popular variation of **Equation 6** is **Equation 7**,<sup>10,249</sup> which introduces  $n_{app}$  and  $n_s$ . Here  $n_s$  is an integer and is equivalent to  $n$  in **Equation 6**, but  $n_{app}$  does not have to be an integer;  $n_{app}$  can thus account for a degree of non-ideality in the extracted signal, such as thermodynamic dispersion causing the signal to be slightly broader than expected ( $n_{app} < n_s$ ), or a non-perfect baseline subtraction causing the extracted signal to be sharper than the true signal ( $n_{app} > n_s$ ). For an ideal Faradaic signal,  $n_{app}$  would be equal to  $n_s$ , and so the agreement between these constants gives an indication of the quality of the simulated extracted signal.

$$i = v \left( \frac{n_s n_{app} F^2 A \Gamma}{RT} \right) \left( \frac{e^{(n_{app} F (E - E_{(O/R)}^0) / RT)}}{[1 + e^{(n_{app} F (E - E_{(O/R)}^0) / RT)}]^2} \right) \quad \text{Equation 7}$$

#### 1.4.1.2 The measurement of electron-transfer kinetics.

As previously mentioned,  $k_0$ , is a measurement of the rate with which electroactive species exchange electrons with the electrode surface.<sup>244</sup> When  $v > k_0 RT / F$  the rate of electron transfer between the electrode and the redox-active site is not fast enough to maintain equilibrium between the redox couple and the sweeping applied potential, and as such kinetic control starts to take effect in place of thermodynamic control.<sup>245</sup> When this happens the shape of the redox peaks in the cyclic voltammogram become distorted and move further apart. Under kinetic control, the rate of the electrochemical reaction is dictated by how much energy is available to overcome the activation energy of the process, which for electron transfer processes is dictated by the overpotential ( $E - E_0$ ).<sup>253</sup> For a simple, unimolecular redox reaction in which both the cathodic and anodic reactions occur on the same electrode, the current response of a system under kinetic control is described by the Butler–Volmer equation (**Equation 8**).<sup>246,254</sup>

$$i = nFk_0 \left[ -c_O^s e^{\left\{ \frac{-\alpha n F}{RT} (E - E^0) \right\}} + c_R^s e^{\left\{ \frac{(1-\alpha) n F}{RT} (E - E^0) \right\}} \right] \quad \text{Equation 8}$$

$n$  = the number of electrons transferred in the redox couple.

$F$  = the Faraday constant / C mol<sup>-1</sup>.

$k_0$  = rate constant for heterogeneous electron transfer / s<sup>-1</sup>.

$c_R^s$  = concentration of reduced species at the electrode surface / mol cm<sup>-2</sup>.

$c_O^s$  = concentration of oxidised species at the electrode surface / mol cm<sup>-2</sup>.

$E$  = electrode potential of cathodic peak / J C<sup>-1</sup>.

$E^0$  = the standard/formal electrode potential of the redox couple / J C<sup>-1</sup>.

$R$  = gas constant / J mol<sup>-1</sup> K<sup>-1</sup>.

$T$  = temperature / K.

$\alpha$  = the charge transfer coefficient (dimensionless).



A “trumpet plot” can be constructed by plotting the displacement of positions ( $E_p - E^0$ ) against the natural logarithm of  $\nu$  (**Figure 1.19**), and such plots can be used to obtain some of the parameters defined in **Equation 8**.

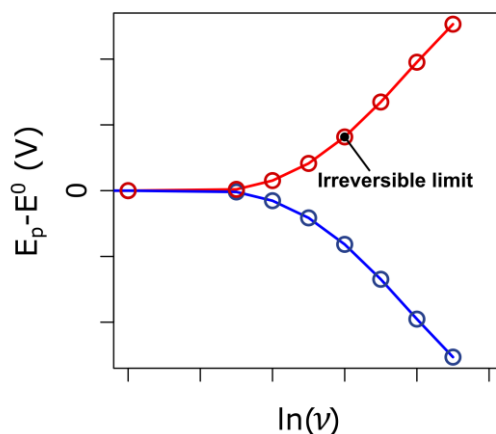


**Figure 1.19.** A trumpet plot, depicting how the position of the oxidative and reductive peaks ( $E_p$ ) of a surface-confined redox couple deviate as a function of  $\ln(\nu)$ .

Past the irreversible limit the trumpet plot becomes linear (**Figure 1.19**), and anodic (oxidative) peak positions obey **Equation 9** and cathodic (reductive) peak positions obey **Equation 10**.<sup>255-258</sup> A number of brilliant formulations by Laviron<sup>255</sup> can be used to obtain parameters for both the charge transfer coefficient ( $\alpha$ ) and the rate constant for heterogenous electron transfer ( $k_0$ ) from this data, but the simplest approach is to fit linear regressions to the linear data and use the gradients of the lines to determine  $\alpha$ . The linear regression can then be used to find the values for  $\nu$  for which  $E_p - E^0 = 0$ , and with  $\alpha$  being determined, **Equation 9** and **Equation 10** can be solved for  $k_0$ .  $\alpha$  reflects the symmetry of the activation barrier in the reaction coordinate for the electron transfer (which can be thought of as how reactant or product-like the transition state is), and values for  $\alpha$  are typically around 0.5.<sup>247</sup> The lack of accuracy in the value of  $k_0$  determined via this method is due to the peak positions only being sensitive to the logarithm of  $\nu/k_0$ . As an experimental note, when recording the data for a trumpet plot it is essential to use high concentrations of electrolyte as otherwise the measurements at fast scan rates will be affected by uncompensated resistance.<sup>242</sup>

For a more accurate determination of  $k_0$  using cyclic voltammetry, voltammograms recorded at high scan rates are fitted to voltammograms generated by computational simulations.<sup>259</sup>

$$E_{pa} - E^0 = + \frac{RT}{(1 - \alpha)nF} \ln \left( \frac{nF\nu(1 - \alpha)}{RTk_0} \right) \quad \text{Equation 9}$$

$$E_{pc} - E^0 = -\frac{RT}{\alpha nF} \ln \left( \frac{nFv\alpha}{RTk_0} \right) \quad \text{Equation 10}$$

$E_{pa}$  = electrode potential of anodic peak / J C<sup>-1</sup>.

$E_{pc}$  = electrode potential of cathodic peak / J C<sup>-1</sup>.

$E^0$  = the standard/formal electrode potential of the redox couple / J C<sup>-1</sup>.

$R$  = gas constant / J mol<sup>-1</sup> K<sup>-1</sup>.

$T$  = temperature / K.

$n$  = the number of electrons transferred in the redox couple.

$F$  = the Faraday constant / C mol<sup>-1</sup>.

$k_0$  = rate constant for heterogeneous electron transfer / s<sup>-1</sup>.

$\alpha$  = the charge transfer coefficient (dimensionless).

$v$  = scan rate / J C<sup>-1</sup> s<sup>-1</sup>.

### 1.4.1.3 Other uses of cyclic voltammetry

Cyclic voltammetry has many other uses that will not be discussed here. It can be used to determine whether protonation is involved in a redox protein/enzymes mode of action by screening the dependence of the standard potential of the redox protein/enzyme on pH.<sup>46,243</sup> It can also be used to screen which substrates a redox enzyme can turn-over by detecting the presence of a catalytic current response. Note however, if the kinetics associated with a redox enzymes action on a substrate are desired, chronoamperometry/ampereometry should be used. Chronoamperometry/ampereometry is also more sensitive to the presence of catalytic currents.

## 1.4.2 Linear sweep voltammetry

Essentially representing half of a cyclic voltammetry experiment, a linear sweep voltammetry experiment involves applying a potential to the working electrode that changes linearly with time, sweeping between potentials  $E_1$  and  $E_2$ , as shown in **Figure 1.20**. The current that flows through the working electrode is plotted as a function of the potential applied to the working electrode. The potential applied to the working electrode may be held at  $E_1$  for a given time period ( $t_{\text{equil}}$ ) before the voltammogram is recorded, to allow conditions to reach equilibrium before measurements are taken.

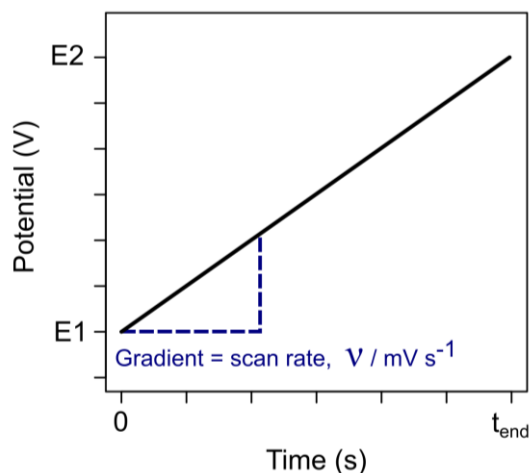


**Figure 1.20.** The potential waveform that is applied to the working electrode during a linear-sweep voltammetry experiment.

### 1.4.3 Square wave voltammetry

Square wave voltammetry (SWV) is considered to be a special case of differential pulse voltammetry (DPV). Square wave voltammetry is far more popular than conventional DPV, which will not be discussed here. SWV applies a square wave over a staircase waveform to yield a new “square wave” waveform (**Figure 1.21**).<sup>247</sup> The underlying staircase increases by  $\Delta E_s$  after each cycle period ( $t_s$ ). The length of the cycle period ( $t_s$ ) and  $\Delta E_s$  thus define the scan rate of SWV experiments. The square wave has an amplitude of  $\Delta E_p$ , and a pulse time ( $t_p$ ) equal to half of  $t_s$  (and thus a frequency of  $\frac{1}{2t_p}$ ) (**Figure 1.21**). A constant voltage may be applied for a period of time before the experiment truly begins ( $t_{eq}$ ) to allow equilibrium to be reached (**Figure 1.21**). Note that while  $\Delta E_p$  is far greater than  $\Delta E_s$ , it is still of a small amplitude.<sup>247</sup>

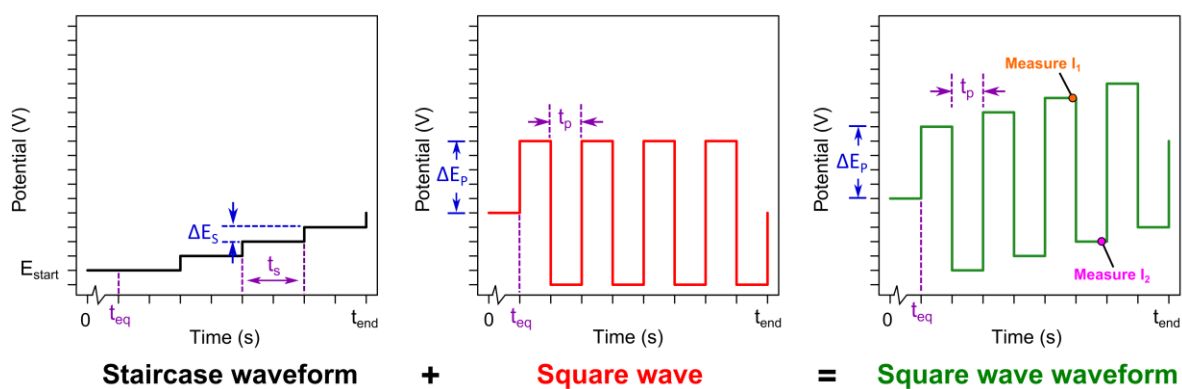


**Figure 1.21.** The potential waveform that is applied across the working electrode during square wave voltammetry.

During the voltammetric experiment, the current response to the applied square wave waveform is sampled at two points per cycle, giving a value of  $I_1$  and  $I_2$  for each cycle period.<sup>247</sup> A plot is typically constructed that consists of plots of  $I_1$ ,  $I_2$  and  $\Delta I$  (where  $\Delta I = I_1 - I_2$ ) as functions of the potential of the staircase waveform (**Figure 1.22**). As such, a single SWV experiment generates three voltammograms simultaneously, although the plot of  $\Delta I$  vs staircase potential is typically the most useful.<sup>247</sup> This is because over the small potential range defined by  $2\Delta E_p$  the difference between the capacitive currents contributing to  $I_1$  and  $I_2$  is typically small, meaning that  $\Delta I$  contains a relatively small contribution from capacitive current.<sup>247</sup>

Due to the ability to filter out much of the capacitive current, SWV is far more sensitive to Faradaic current than conventional cyclic voltammetry, and is an order of magnitude more sensitive than conventional differential pulse voltammetry.<sup>247</sup> SWV experiments can also be run at faster scan rates than conventional differential pulse voltammetry, and as such it is an increasingly popular option for experimental electrochemists as data can be collected more quickly. Variations of square wave voltammetry can be used to measure values for heterogeneous electron transfer constants ( $k_0$ ).<sup>260</sup> A paper that excellently showcases the mathematics and power of SWV being applied to PFE has been written by Gulaboski et al.<sup>261</sup> One of figures from this paper has been reproduced (with permission) in **Figure 1.22**.<sup>261</sup>

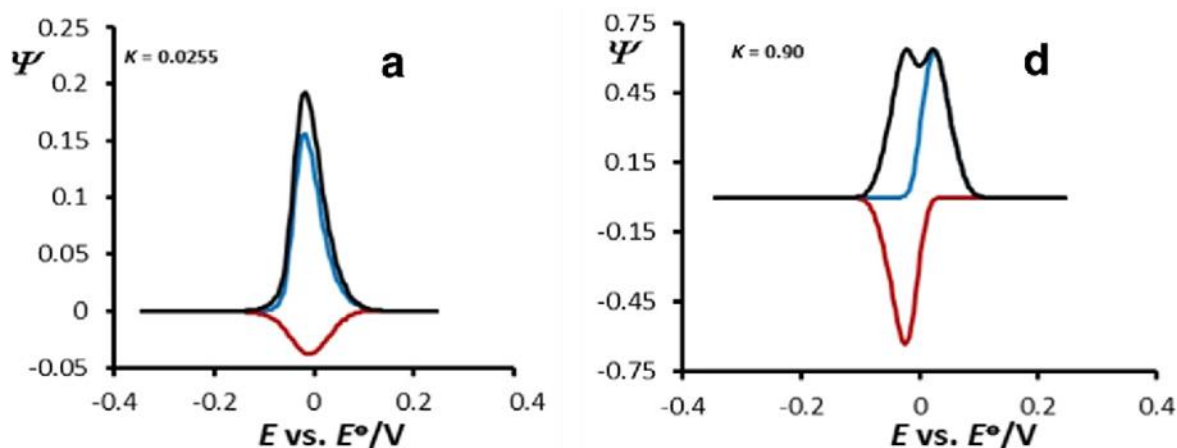


**Figure 1.22.** Simulated square wave voltammograms showing the effect of the dimensionless electrode kinetic parameter  $K$  (where  $K = k_0/f$ , where  $f$  is the SW frequency) on the features of square-wave voltammograms of surface-confined redox couples. The simulation parameters were SW frequency  $f = 10$  Hz,  $\Delta E_p$  amplitude = 50 mV, potential step  $\Delta E_s = 4$  mV, temperature  $T = 298$  K. In all simulations, the value of electron transfer coefficient was  $\alpha = 0.5$ , while the number of electrons exchanged was  $n = 2$ . The values of  $K$  are given in the charts. In both simulated voltammograms the forward current ( $I_1$ ) is assigned with a blue line, the backward current ( $I_2$ ) is assigned with red line, while the black line represents  $\Delta I$ . Figure reproduced with permission from reference [261], <https://link.springer.com/article/10.1007%2Fs10008-019-04320-7>, under license from Springer Nature. License number 4800821185943 (valid for electronic and printed copies with an expected circulation of 1-29 readers).

Square wave voltammetry has found uses in the analysis of some very high-profile redox enzymes, such as NADH-dependent ferredoxin NADP<sup>+</sup> oxidoreductase I.<sup>262</sup> However, while SWV voltammetry may provide a better separation of Faradaic and capacitive currents, cyclic voltammetry is generally preferred in PFE since the resulting voltammogram is simpler and is generally more readily interpreted.<sup>243,261</sup> A particular complication associated with the interpretation of SWV can be encountered when irreversible electrode kinetics are in effect; under these circumstances the square wave voltammogram for  $\Delta I$  could show two peaks, which could be mistakenly interpreted as being from two different redox couples, even though only a single redox couple is present.<sup>247</sup> This can be seen in the right hand plot of **Figure 1.22**.

#### 1.4.4 Chronoamperometry/amperometry

The chronoamperometric method involves holding the applied potential of the working electrode at  $E_{\text{applied}}$  for a time period  $t_{\text{run}}$ , while plotting the current that flows through the working electrode as a function of time. Several values for  $E_{\text{applied}}$  may be switched between during a single chronoamperometry experiment, although many experiments only use one value of  $E_{\text{applied}}$  (and when only one  $E_{\text{applied}}$  value is used the technique is more correctly referred to as “amperometry” rather than chronoamperometry). If any pre-conditioning required (e.g. redox activation of an enzyme), a potential,  $E_{\text{deposit}}$ , may be applied for a time period  $t_{\text{deposit}}$ , as a means of pre-treatment before the chronoamperometric/amperometric plot is recorded.

If an immobilised redox enzyme is capable of turning over a substrate, the addition of that substrate will cause the current flowing into or out of the electrode/solution interface to increase. The current response at different substrate concentrations can be used to construct a plot such as that shown in **Figure 1.23**. In accordance with Michaelis-Menten enzyme kinetics,<sup>205</sup> below a certain substrate concentration, the rate at which the immobilised enzyme encounters substrate restricts how quickly it can turn the substrate over, and within this concentration range the current response can be expected to increase linearly with the concentration of substrate (**Figure 1.23**, inset **a**). However, at sufficiently high concentrations the availability of substrate ceases to be the rate-determining factor in the rate at which the enzyme can turn over the substrate; the current response ceases to be linear with respect to substrate concentration and reaches a plateau at  $i_{\text{max}}$  (**Figure 1.23**, inset **a**). Provided that the rate of electron-transfer between the redox enzyme and the electrode is sufficiently fast, and thus is not the rate-determining step in the enzymes reaction mechanism, the current passing through the electrode will reflect the innate kinetics of the enzymes mechanism of action. The apparent Michaelis–Menten constant ( $K_m^{\text{app}}$ ), an important parameter in the evaluation

of enzyme–substrate reaction kinetics, can be calculated via non-linear fitting of experimental data to **Equation 11**, or by using a version of the Lineweaver–Burk equation adapted for electrochemistry (**Equation 12**) (**Figure 1.23**, inset b).<sup>256</sup> Once  $K_m^{app}$  and  $i_{max}$  have been determined, the turn-over rates of the redox enzyme can be calculated using **Equation 13**.

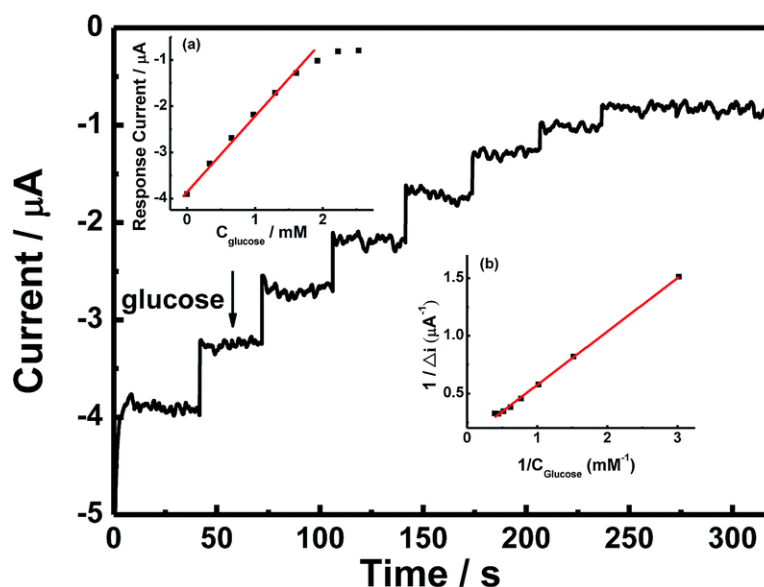


**Figure 1.23.** Amperometric responses of glucose oxidase enzyme electroactively immobilised onto a glassy carbon electrode derivatised with carbon nanochips and chitosan exposed to successive additions of 0.1 M glucose in PBS (0.1 M, pH 7.2) while holding the applied potential at  $-400$  mV. Inset (a): plot of catalytic current vs. glucose concentration. Inset (b): Lineweaver–Burk plot for  $K_m^{app}$  determination. This figure was reproduced from reference [256], <https://pubs.rsc.org/ko/content/articlehtml/2017/ra/c6ra26636c>, under a Creative Commons Attribution 3.0 Unported Licence.<sup>263</sup>

$$i = i_{max} \frac{c}{K_m^{app} + c} \quad \text{Equation 11}$$

$i$  = steady state current after the addition of substrate / A.

$c$  = bulk concentration of substrate / mol dm<sup>-3</sup>.

$i_{max}$  = the maximum current measured under once substrate saturation has been reached / A.

$K_m^{app}$  = the apparent Michaelis–Menten constant / mol dm<sup>-3</sup>.

$$\frac{1}{i} = + \frac{K_m^{app}}{i_{max}} \left( \frac{1}{c} \right) + \frac{1}{i_{max}} \quad \text{Equation 12}$$

$i$  = steady state current after the addition of substrate / A.

$c$  = bulk concentration of substrate / mol dm<sup>-3</sup>.

$i_{max}$  = the maximum current measured under once substrate saturation has been reached / A.

$K_m^{app}$  = the apparent Michaelis–Menten constant / mol dm<sup>-3</sup>.

$$k_{cat} = \frac{i_{max}}{nF\Gamma A} \quad \text{Equation 13}$$

$k_{cat}$  = enzyme turnover number /  $s^{-1}$ .

$i_{max}$  = the maximum current measured under once substrate saturation has been reached / A.

$n$  = the number of electrons transferred in the redox couple.

$F$  = the Faraday constant /  $C s^{-1} mol^{-1}$ .

$\Gamma$  = enzyme coverage /  $mol cm^{-2}$ .

$A$  = the surface area of the electrode /  $cm^2$ .

### 1.4.5 Fourier-transform alternating current voltammetry

Fourier-transform alternating current voltammetry (FTacV) is a relatively new voltammetric technique which allows the experimentalist to probe both the thermodynamics and kinetics associated with an electron transfer. Whereas the waveform used in classic cyclic voltammetry consists of a linear potential ramp applied from  $E_1$  to  $E_2$  over time  $t_{switch}$  and then from  $E_2$  to  $E_1$  from time  $t_{switch}$  to  $t_{end}$  (**Figure 1.24**), in FTacV a high frequency sinusoidal waveform is superimposed over an underlying potential ramp (**Figure 1.24**). As a consequence of this, the total current response recorded in an FTacV experiment (**Figure 1.25**) contains kinetic information about the electron transfer, due to the relationship between the frequency and time domains. Put simply, a really slow electron transfer process will only “feel” the underlying linear potential ramps, as it would be unable to give a current response rapid enough to be in resonance with the sinusoid, whereas fast electron transfer processes will “feel” every part of the FTacV waveform as they respond to the rapid changes brought about by the action of the sinusoid, and as such will give high frequency responses. Capacitive (background) current responds slowly to changes in applied potential, and as such higher harmonics (typically harmonic 3 or higher) are essentially free of capacitive current. This makes FTacV far more sensitive than direct current cyclic voltammetry, as is exemplified by the comparison of the direct current cyclic voltammetry of YedY (**Figure 1.18**) with the FTacV of YedY (**Figure 1.26**).

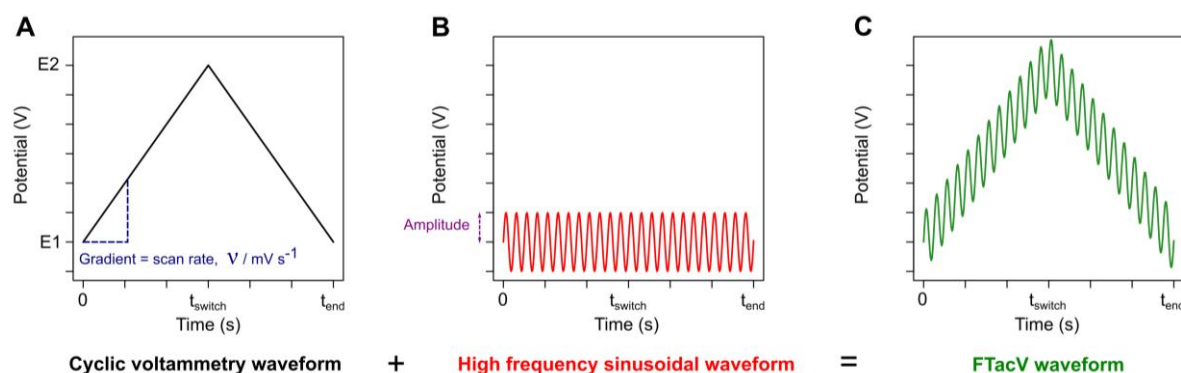


**Figure 1.24.** The product of a classical cyclic voltammetry waveform (A) and a high frequency sinusoidal waveform (B) yields an FTacV waveform (C).

By Fourier transforming the current response in an FTacV experiment, information in the time domain is converted into information in the frequency domain, yielding a power spectrum of resonances in a similar manner to an NMR experiment (**Figure 1.25**). Each resonance in the power spectrum is a harmonic of the frequency of the applied sinusoid (i.e. is of a frequency that is a multiple of the frequency of the applied sinusoid). Reverse Fourier transforming one of these resonance peaks back into the time domain (which is coupled to the voltage domain due to the relationship between time and applied potential) yields a FTacV voltammogram (**Figure 1.25**). If a Faradaic electron transfer process has taken place during the FTacV experiment, the voltammograms yielded as described will contain signals that are symmetric about the potential at which the Faradaic electron-transfer process took place, yielding thermodynamic information about the Faradaic electron transfer.

Kinetic information can be delved from the relationship between the interplay between the intensity of the Faradaic signals in an FTacV voltammogram and the harmonic that voltammogram is derived from, as the higher the harmonic number the higher the frequency of the current response. As such, slow Faradaic electron transfer processes would be expected to give signals in FTacV voltammograms that decrease in intensity rapidly with respect to increasing harmonic number, whereas the signals from fast Faradaic electron transfer processes will decrease more slowly with respect to increasing harmonic number. Such approaches can even be used to distinguish between fast reversible electron transfers between electrodes and the redox centres of redox enzymes and the slow electron transfers associated with coupled redox catalysis.



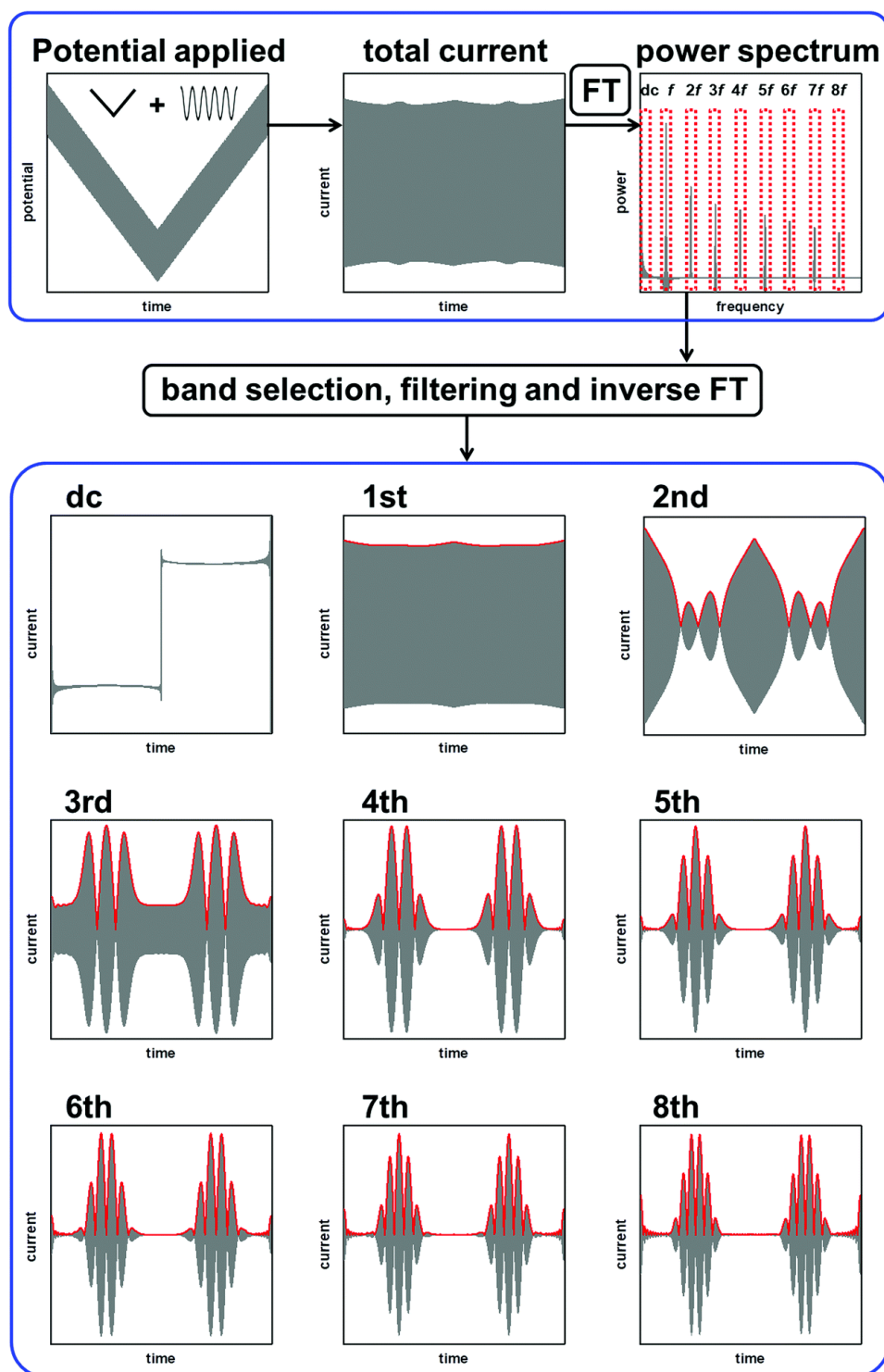


**Figure 1.25.** The processing of an FTacV experiment to yield FTacV voltammograms. This figure was reproduced from reference [264], <https://pubs.rsc.org/en/content/articlehtml/2017/cc/c7cc03870d>, under a Creative Commons Attribution 3.0 Unported Licence.<sup>263</sup>

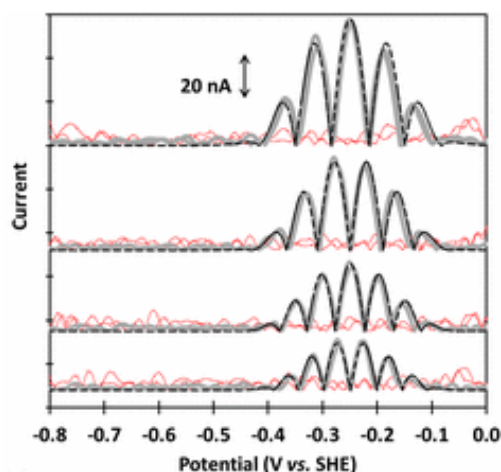


**Figure 1.26.** FTacV measurements of the YedY two-electron redox transition. Gray solid lines show, in descending order, the 7<sup>th</sup>, 8<sup>th</sup>, 9<sup>th</sup>, and 10<sup>th</sup> ac harmonic signals measured for YedY using FTacV with a frequency of 9 Hz. The response from a bare (YedY-free) graphite electrode under the same conditions is shown by light red dotted lines. Simulated signals are shown by dashed black lines. Experimental conditions were as follows: PGE electrode, scan rate = 15.83 mV s<sup>-1</sup>; amplitude, 150 mV; buffer solution of 50 mM Mes and 2 M NaCl, pH 7, 25 °C. Figure reproduced with permission from reference [242], <https://www.pnas.org/content/112/47/14506>. Readers should note that further permissions regarding this figure should be directed to the PNAS.

Although the scope and power of FTacV is vast, its usage is currently in its infancy. This is partly because extracting parameters from an FTacV experiment currently requires a heuristic approach whereby an experimentalist manually enters parameters to try and optimise the goodness of fit of a simulated spectrum. This is a lengthy process due to the multidimensional nature of the parameter space that has to be explored. Computational methods are currently being developed to optimise the fitting of parameters to an FTacV experiment, but at present these methods are computationally very expensive, often taking several days to complete.<sup>265</sup> Efforts to address this are currently underway, and one such approach is described in **Section 3.2.3.1**.

## 1.5 Summary and concluding remarks

Although a wealth of primary literature and highly informative reviews exist regarding the powerful bio-analysis technique of PFE, the fundamental step of protein film formation is often overlooked. This is understandable, as to establish the technique of PFE it has been necessary to provide substantial insight into electrochemical method design and data analysis approaches, as well as showcase the powerful insight which can be gained from conducting such experiments on biologically and biotechnologically important systems. Similarly, while the literature regarding bio-orthogonal ligation stratagems is well developed with respect to performing bio-orthogonal ligations in solution, very few strategies have been successfully implemented in the coupling of proteins to surfaces. Performing bio-

orthogonal ligations between proteins and surfaces is clearly far more difficult than performing analogous ligations in solution – e.g. Strain-Promoted Azide-Alkyne Cycloaddition (SPAAC) reactions have respectable rate constants ( $0.0012 \text{ M}^{-1} \text{ s}^{-1} \rightarrow 4 \text{ M}^{-1} \text{ s}^{-1}$ ),<sup>266,267</sup> and while such ligations can be performed in a matter of hours in solution,<sup>267</sup> performing a SPAAC ligation between a surface-confined strained cyclooctyne and an azide-functionalised laccase protein is reported as an overnight reaction.<sup>235</sup> This is likely due to the extreme steric/kinetic demands associated with the collision between a macromolecule and a surface; this collision having to occur not only in suitable orientation, but also with enough kinetic energy to enable a successful chemical reaction, all at temperatures lower than 37 °C. Additionally, control over the equivalents of reagents is far more difficult when performing ligation to a surface, as the functionality on the surface will almost always be the limiting reagent.

Due to the diversity of redox proteins and the wide range of possible usages, there are currently no universal surface-confinement approaches. There is however a clear need to address the lack of bio-orthogonal ligation methodologies applicable to the electroactive immobilisation of redox proteins. This thesis showcases the development of chemistries that marry well-developed bio-orthogonal ligation methods with surface functionalisation techniques. Additionally, whereas the functionalisation of surfaces with moieties capable of reacting with proteins is a reasonably well documented tool for redox protein immobilisation, the functionalisation of proteins with moieties that are capable of reacting with surfaces is scarcely documented.<sup>198</sup>

### 1.6 Aims of the project and thesis overview

The overall aim of this project is to develop and critically assess surface modification methodologies that facilitate the immobilisation of redox-active proteins/enzymes, preferably via covalent bonds. It is hoped that this will help future readers select an appropriate electroactive surface immobilisation technique for use in studying/harnessing new redox proteins and enzymes. For gifted bioconjugation chemists, it is hoped this thesis will inspire further method development, as the scientific community is still largely lacking robust methodologies via which robust, site-selective bonds can be made between any protein/enzyme and any electrode surface.

**Chapter 2** sets the scene in showcasing the power of enzyme electrochemical measurements by reporting the electrochemical interrogation of an AA9 LPMO immobilised onto a MWCNT-functionalised electrode surface via adsorption, and the limitations that arise when simple adsorption is used.

**Chapter 3** explores and critically assesses the usage of various diazonium electro-grafting techniques for the introduction of amine functionalities onto electrode surfaces. The ability to further derivatise amine-functionalised electrode surfaces is then demonstrated via amide bond formation to small molecule probes.

While amine-functionalised electrode surfaces can further be derivatised with motifs capable of bioconjugation via amide bond formation, performing and characterising a multi-step reaction on an electrode surface can prove challenging.

**Chapter 4** explores the functionalisation of proteins with aldehyde functionalities, for usage in either site-selective or site-specific bioconjugation whereas **Chapter 5** describes the development and application of a methodology whereby hydroxylamine functionalities are introduced in near-monolayer coverage to electrode surfaces via diazonium electro-grafting, offering a direct route to electrode surfaces functionalised with motifs capable of bio-orthogonal ligation to aldehyde-functionalised proteins

**Chapter 6** details the first ever usage of triazabutadienes, a photocaged source of aryl diazonium salts, in the derivatisation of electrode surfaces via diazonium electro-grafting under physiologically relevant conditions. The site-selective functionalisation of proteins with triazabutadienes could allow proteins to be directly electro-grafted to electrode surfaces under mild conditions, potentially circumventing the challenges typically associated with electroactive immobilisation of redox proteins via covalent bonds.

**Chapter 7** concludes the current research and suggests some directions that further research may follow. The appendices contain supplementary information and figures for interested readers.

**Chapter 8** is the Experimental Chapter, and details general practice/procedures applied across several Chapters, and is further split into subsections containing the Experimental procedures specific to each individual Results Chapter.

# Chapter 2

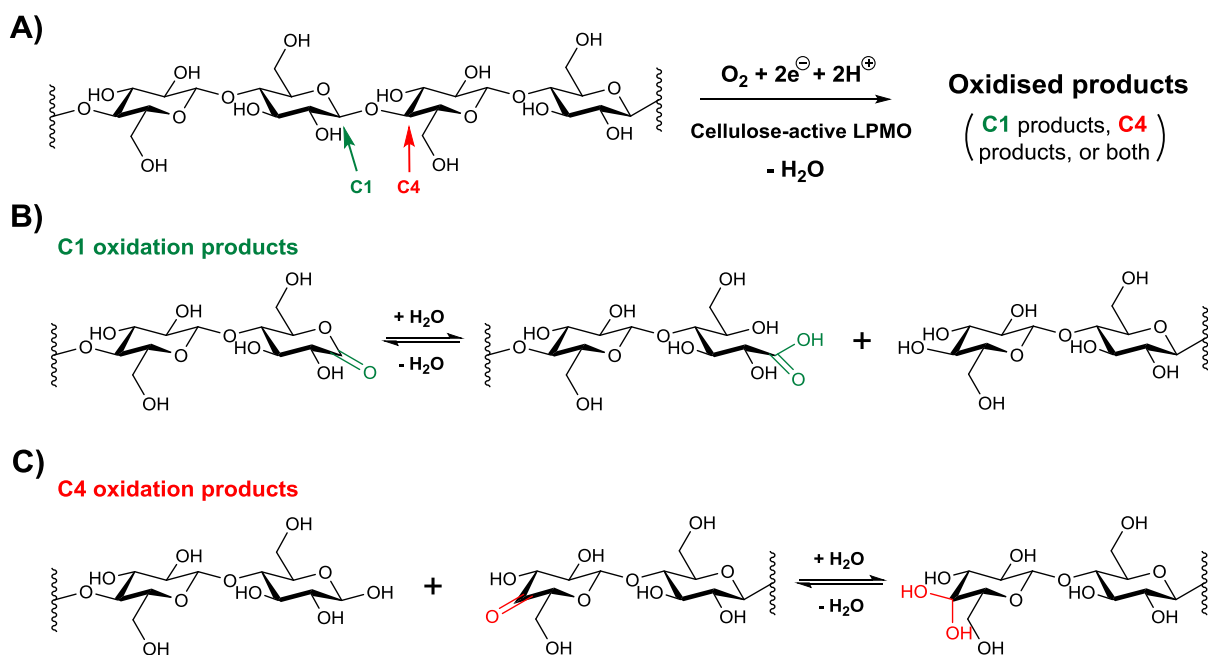
Electrochemical interrogation of an  
AA9 LPMO

## Chapter 2. Electrochemical interrogation of an AA9 LPMO

### 2.1 Introduction

#### 2.1.1 LPMO overview

Lytic polysaccharide monoxygenases (LPMOs) are enzymes that cleave bonds within polysaccharide chains via an oxidative mode of action.<sup>268</sup> The polysaccharide substrates targeted by different LPMOs include, but are not limited to, cellulose, xylan, chitin and retrograded starch.<sup>268</sup> While so-called “canonical” LPMOs are type 2 copper metallo-enzymes, a subclass of LPMO discovered in 2019<sup>269</sup> and named “Arg-AA9s” are not copper metallo-enzymes, and have different, as yet unknown, roles in polysaccharide degradation.<sup>269</sup> Henceforth, only type 2 copper-containing LPMOs are discussed in this Chapter and the overall reaction that can be catalysed by a canonical cellulose-active LPMO acting on a substrate polysaccharide chain is depicted in **Scheme 2.1**. Note that this scheme illustrates both C1 and C4 oxidation products, and different LPMO enzymes show different selectivities for these oxidation products.<sup>270,271</sup>



**Scheme 2.1.** The overall reaction of an LPMO on a cellulosic polysaccharide chain.

The first LPMOs were reported in a pair of landmark papers in 2010<sup>272,273</sup> which described two subclasses of fungal and bacterial copper metallo-enzymes that were subsequently reclassified as the AA9 and AA10 families.<sup>274</sup> Since then, research into LPMOs has proceeded rapidly, and 6 different

families of LPMO are currently recognised. The generally preferred substrates and organisms of origin of the LPMO families are tabulated in **Table 2.1**, but more comprehensive lists of characterised LPMOs and their known substrates are reported in refs [268] and [270]. In general, the catalytic action of an LPMO introduces amorphous regions and chain termini within their polysaccharide substrates upon which other carbohydrate-active enzymes (e.g. glycoside hydrolases) can act. It has also been postulated that LPMOs may help prevent the aggregation of oligosaccharide substrates via the introduction of negatively-charged carboxylate groups onto the substrate surface,<sup>275,276</sup> thus increasing the surface area exposed to other carbohydrate-active enzymes. It is their assistive role in increasing the rate at which glycoside hydrolases can act which has led to the “AA” classification of LPMOs, since this abbreviation denotes an “auxiliary activity” according to the principles of the database of Carbohydrate-Active enZYmes (www.cazy.org). Because of their functionality in boosting the rate of carbohydrate degradation, LPMOs are usually understood to play a physiological role in the metabolism of their parent organism,<sup>277</sup> although LPMO activity has also been linked to virulence in bacteria,<sup>277-280</sup> the breaching of cellular defences by plant pathogens,<sup>270,281</sup> and the restructuring of the chitinous exoskeletons of arthropods during development and metamorphosis.<sup>282</sup> From a chemical viewpoint however, it is the structure-function relationship of LPMOs and their ability to utilise a cheap, readily-available transition metal to selectively enact bond cleavage within highly recalcitrant substrates that is of interest.

**Table 2.1.** The origin and substrate specificities of the six LPMO families currently recognised in the CAZY database.

LPMO family	Substrate specificity	Organism of origin
AA9	All known members act on Cellulose, some have been shown to also act on hemicelluloses. <sup>268</sup>	Fungal
AA10	Predominantly chitin, although some members act on cellulose <sup>283</sup>	Bacteria, eukaryota, viruses, archaea <sup>270</sup>
AA11	Chitin <sup>284</sup>	Fungal
AA13	Retrograded starch <sup>285</sup>	Fungal
AA14	Xylan <sup>286</sup>	Fungal
AA15	Some members act on chitin, other members act on cellulose <sup>270,282</sup>	Eukaryota, viruses <sup>270,287</sup>
AA16	Chitin <sup>288</sup>	Fungal

As indicated by **Table 2.1**, despite being a relatively new enzyme class, a substantial number of LPMOs have now been characterised. Different LPMOs have low sequence identities (even within the same LPMO family), but all share a highly conserved fold, featuring a core immunoglobulin-like  $\beta$ -sandwich structure and a flat face, shown at the top of **Figure 2.1**, which interacts with the crystalline surface of polysaccharide substrates.<sup>268</sup> Centrally located within the flat face is a copper active site with a highly conserved coordination geometry (**Figure 2.1**). This geometry is afforded by a T-shaped arrangement

of three nitrogen ligands called a “histidine brace”; a motif comprised of the *N*-terminal histidine residue bidentately coordinating through both the *N*-terminal amine group and the imidazole group, and the imidazole group of a second histidine residue (**Figure 2.2**).<sup>268,289,290</sup> The histidine brace is conserved across all canonical LPMO families (see **Figure 2.2**), and the unique ligation it affords to the Cu centre is therefore assumed to be critical to LPMO reactivity. In fungal LPMOs the *N*-terminal histidine imidazole group often bears a  $\tau$ -methylation (**Figure 2.2**).<sup>285,291</sup> It has been previously postulated that this methylation could affect the pKa of the *N*-terminal histidine, but a recent study on AA9 LPMOs has found that this methylation has little effect on pKa, and instead serves to protect the LPMO from oxidative inactivation by reactive oxygen species, such as H<sub>2</sub>O<sub>2</sub>.<sup>291</sup>

Another feature shared across all LPMO families is the presence of an aromatic side chain occupying an axial position relative to the copper (**Figure 2.2**).<sup>268,292</sup> In most LPMO families a tyrosine residue is the predominant occupant of this axial site, but in chitin-active AA10s and chitin-active AA15s this site is instead occupied by a phenylaniline (**Figure 2.2**).<sup>292</sup> Due to being relatively distant ( $\sim 2.7$  Å)<sup>33,290</sup> from the copper centre, it is not thought that the axial tyrosine residues directly bond to the copper,<sup>293</sup> and axial phenylaniline residues would lack the ability to coordinate strongly to the copper centre even if they were more proximally located. Point mutation of the axial phenylaniline in a cellulose-active AA10 to a tyrosine or aniline was shown to adversely affect the activity and alter the EPR traces of the LPMO under assay;<sup>294</sup> such results indicate that the “choice” between a tyrosine or phenylaniline residue is not arbitrary, and show that the identity of the axial secondary coordination-sphere residue greatly impacts the electronic structure of the copper active site.<sup>290</sup> Several recent papers have also proposed that axial tyrosine residues may protect the LPMO active sites from sustaining oxidative damage in the absence of the substrate.<sup>293,295,296</sup>

Some LPMO families (AA10s and AA15s) also have a conserved alanine residue facing the axial coordination site of the copper centre (opposite the conserved aromatic residue) (**Figure 2.2**),<sup>297,298</sup> although an example of an AA10 is known in which an isoleucine residue is present instead of an alanine residue.<sup>280</sup> This alanine residue sterically congests the axial coordination site, thereby disfavours axial coordination of exogenous ligands.<sup>290,298</sup> This has the effect of restricting coordination of exogenous ligands to the equatorial site, thereby directing the mechanism of action of these enzymes.<sup>290,298</sup> It has also been suggested that the steric restrictions imposed by this alanine residue could increase the stability of mechanistically-important equatorially coordinated species, such as Cu(II)-superoxide (discussed later in **Section 2.1.2**), by disfavours associative displacement reactions initiated by the axial coordination of exogenous ligands.<sup>299</sup>



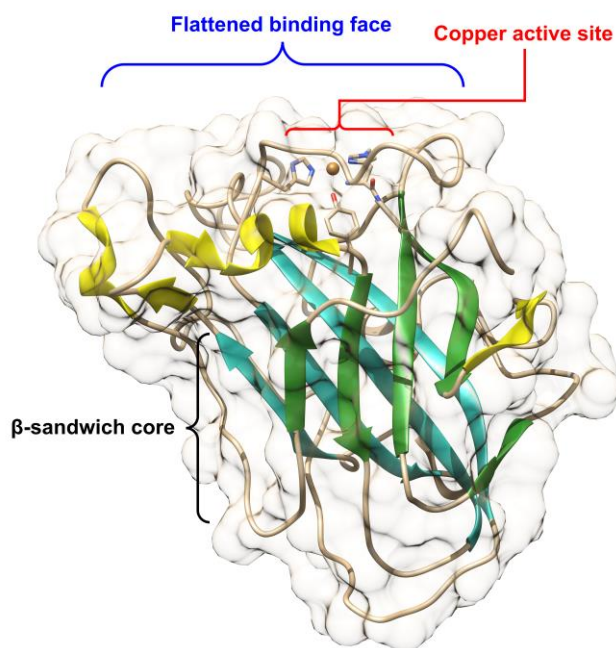


**Figure 2.1.** Crystal structure of an AA9 LPMO from *Lentinus similis* (PDB: 5N05)<sup>300</sup> showcasing the general features of LPMOs, including the  $\beta$ -sandwich core, and the surface-exposed histidine-brace ligated copper active site residing in the centre of a flattened substrate binding face.

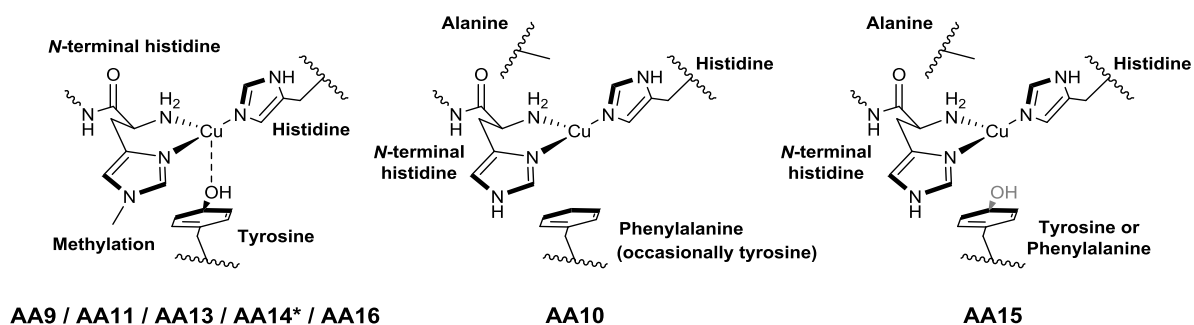


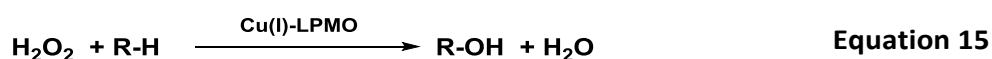
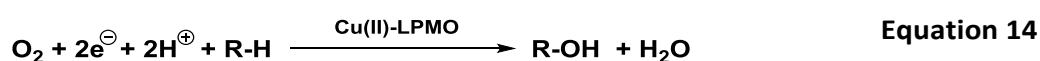
**Figure 2.2.** The conserved active sites of different LPMO families.<sup>292</sup> Examples of cellulose-active AA10 LPMOs have been demonstrated which bare a tyrosine in the axial position instead of a phenylalanine,<sup>301</sup> and chitin-specific AA15s are suspected to bare phenylalanine residues in the axial position rather than tyrosine residues.<sup>292</sup> \*Note that the AA14 crystal structure currently available is for a protein originating from a white-rot fungus but produced in yeast.<sup>302</sup> As such this AA14 crystal structure does not show a  $\tau$ -methylation on the *N*-terminal histidine residue as yeast lack the required methyltransferase.<sup>291</sup>

The mechanism(s) of action of LPMOs remain largely unknown but allude to powerful and novel copper-oxygen chemistries capable of performing energetically challenging hydrogen atom abstractions;<sup>290,303</sup> an academically intriguing prospect. In addition, the ability of LPMOs to significantly boost the rate of recalcitrant biopolymer degradation while working in synergism with commercially available glycoside hydrolases means they have the potential to make enzymatic production of bioethanol biofuel from lignocellulosic feeds more economically viable, making them of interest industrially.<sup>268,270,291,304,305</sup> Cellulose-active LPMOs are the most appealing LPMOs from this industrial

viewpoint. The remainder of this introduction aims to contextualise the electrochemistry experiments which have been conducted by describing the questions that surround the catalytic reaction mechanisms of LPMOs and explaining what an electrochemical assay could contribute to the study of this class of enzymes.

### 2.1.2 The possible reaction mechanisms of LPMOs

It is notable that while most other copper monooxygenases have two or three copper atoms within their active site centres,<sup>306-309</sup> LPMOs are mono-copper monooxygenases and can therefore be expected to function via a different reaction pathway. Many mechanistic pathways have been postulated for the action of AA9 LPMOs, but all the proposed mechanisms start with the one-electron reduction of the Cu(II) centre to Cu(I).<sup>299</sup> After this point, the variety of different literature proposals can be split into two major groups: i) those that postulate that molecular oxygen is the optimal co-substrate of AA9s (**Figure 2.3**) and the reaction is thus a true monooxygenase process (**Equation 14**); and ii) those that postulate that H<sub>2</sub>O<sub>2</sub> is the true physiological co-substrate (**Figure 2.4**), and the reaction is a peroxygenase process (**Equation 15**).<sup>290</sup> Determining the true physiological co-substrate of LPMOs has proven challenging for the scientific community and requires careful consideration of rates, lifetimes and *in vivo* versus *in vitro* reaction conditions.



Early studies on LPMO reactivity concluded that molecular oxygen was the co-substrate of LPMOs, with most studies suggesting that a Cu(II)-superoxide species was responsible for hydrogen atom abstraction (HAA), as indicated by the black reaction stages in **Figure 2.3** (note that the LPMO is shown as a cellulose-active enzyme although the same theories can be applied to different substrates).<sup>290</sup> The superoxide is thought to bind the LPMO in an end-on ( $\eta_1$ ) fashion, and the Cu(II)-superoxide is proposed to have a triplet ground state;<sup>290</sup> it has been shown in computational studies that such end-on Cu-superoxide complexes have a lower energy barrier towards hydrogen atom abstraction.<sup>310</sup> One of the conundrums facing many of the proposed oxygen co-substrate mechanisms is that, as shown in

the blue and yellow pathways of **Figure 2.3**, additional electrons must be delivered to the Cu centre after hydrogen abstraction (i.e. after the LPMO has bound to its substrate) before the hydroxylated product (R-OH) is released.<sup>290</sup> However, once the LPMO is bound to crystalline substrates the Cu centre will be inaccessible to many of the redox partners that have been shown to reduce LPMOs. For example, cellobiose dehydrogenase (CDH) is known to provide reducing equivalents to LPMOs,<sup>311</sup> and early crystal structures postulated that some LPMOs bear a CDH binding site on their flank, and that long range electron transfer of electrons from CDH through the LPMO via conserved aromatic residues could deliver the electrons required to complete the monooxygenase catalytic cycle to the copper centre even when substrate is bound.<sup>293,312</sup> However, other papers have presented evidence that CDH instead interfaces with the copper centre directly, with docking studies suggesting that surface residues close to the copper active site interact with the cytochrome domain of CDH during electron transfer, and that substrate binding prevents this interaction from occurring.<sup>313,314</sup>

The red pathway in **Figure 2.3** would seem to circumvent the problem of supplying the Cu centre with additional electrons while substrate is bound. This putative LPMO reaction pathway, proposed by Solomon and co-workers,<sup>310</sup> is based on a study of the noncoupled binuclear copper enzyme peptidylglycine.<sup>290,315</sup> However, subsequent work by the same authors<sup>310</sup> showed that the proposed interaction of the substrate radical (R<sup>\*</sup>) with Cu(II)-OOH<sup>-</sup> to liberate R-OH would have to overcome a significant energy barrier, and it was ultimately suggested that the blue pathway is more feasible.<sup>290,310</sup>

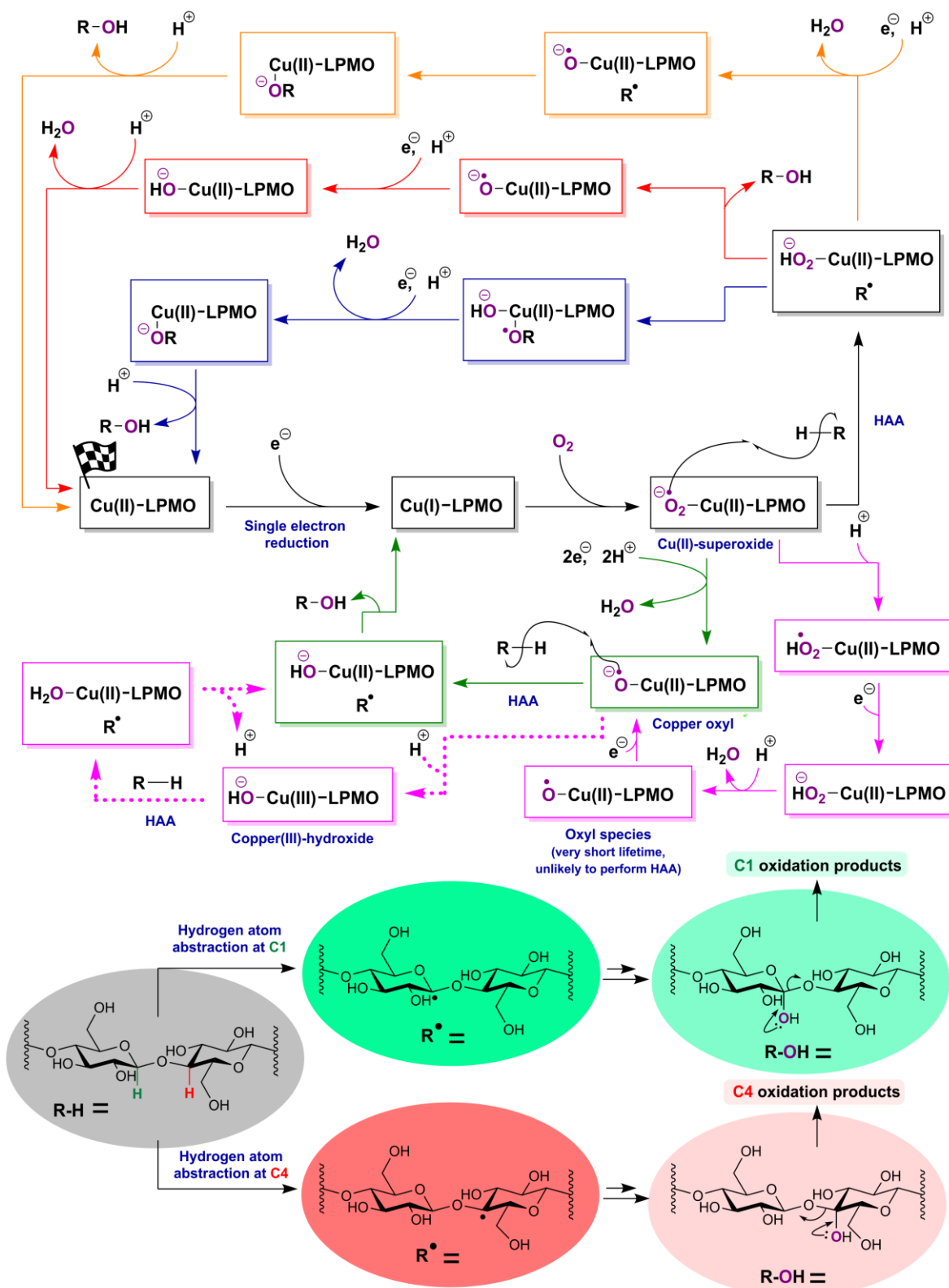


**Figure 2.3. Top)** Proposed mechanisms for the LPMO-catalysed cleavage of polysaccharide chains using molecular oxygen as the co-substrate. Different proposed mechanistic pathways are denoted with different colours, whereas paths shared between numerous proposed mechanisms are denoted in black. All proposed mechanistic pathways start from (and most finish with) the resting Cu(II) state of the LPMO, which has been marked with a chequered flag. **Bottom)** Cellulose structures are used to depict how the identity of species R-H,  $\text{R}^\bullet$  and R-OH depend on the site of hydrogen atom abstraction, which is itself dependent on the particular LPMO under study.

Interestingly, the mechanistic pathway shown in green in **Figure 2.3** circumvents the problem of supplying electrons to the substrate-bound state of the active site by proposing that two electrons and two protons are transferred to the Cu(II)-superoxide (by a donor such as ascorbic acid) to generate a Cu(II)-oxyl species, which subsequently performs hydrogen atom abstraction on the carbohydrate substrate, regenerating Cu(I)-LPMO at the end of the catalytic cycle.<sup>316</sup> The Cu(II)-oxyl species, calculated to be present in a triplet ground state, has a substantially lower energy barrier for hydrogen atom abstraction than the Cu(II)-superoxide species, and further evidence in support of hydrogen atom abstraction occurring after O-O bond cleavage comes from the works of Tolman and co-workers,<sup>317,318</sup> who reported the one-electron oxidation of a tetragonal Cu(II) species to form a Cu(III)-OH species which is capable of abstracting hydrogen from hydrocarbon substrates.<sup>317,318</sup> A Cu(III)-OH species is formally a protonated form of a Cu(II)-oxyl species (the pKa of Cu(III)-OH is approximately 11.7),<sup>317</sup> but it should be noted that a Cu(III)-OH species has a singlet ground state whereas a Cu(II)-oxyl species has a triplet ground state. The mechanism, as described in ref [316] came under scrutiny as the DFT model proposes axial O<sub>2</sub> coordination, which is not consistent with other published computational and crystallographic works, which show that equatorial coordination of dioxygen to the copper centre would be favoured over axial coordination,<sup>319</sup> and that substrate binding constrains the coordination sphere of the copper centre such that exogenous ligand coordination could only occur at the equatorial position.<sup>290,299,316</sup> The largely conserved active site alanine residue in AA10s also likely restricts access to the axial position of the Cu centre (**Figure 2.2**).<sup>290</sup> However, while supporting equatorial O<sub>2</sub> coordination over axial coordination, more recent computational results are in agreement with elements of this pathway, showing that Cu(II)-oxyl species can be accessed via successive one-electron one-proton reductions of the Cu-superoxide species (**Figure 2.3**, pink pathway), and that the Cu(III)-OH species (generated via the protonation of the Cu(II)-oxyl species) is capable of performing hydrogen atom abstraction on the saccharide substrate before subsequently deprotonating and completing the mechanistic pathway (**Figure 2.3**, pink dotted pathway).<sup>320</sup>

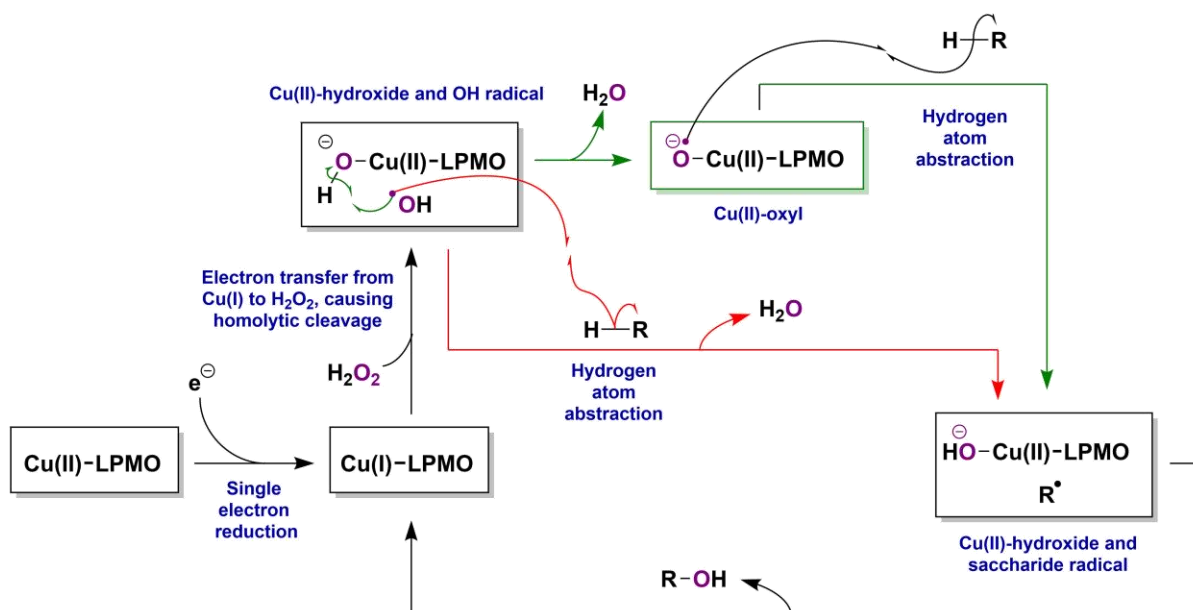


**Figure 2.4.** Proposed mechanisms for the LPMO-catalysed cleavage of cellulose chains using hydrogen peroxide as a co-substrate. Different proposed mechanistic pathways are denoted with different colours, whereas paths shared between several proposed mechanisms are denoted in black. Evidence for the green pathway is detailed in references [320-323], and while the red pathway is listed as a possibility in ref [323], it is not deemed likely. Note that the Cu(II)-oxyl species is also found in the monooxygenase mechanisms proposed in **Figure 2.3**, which is why H<sub>2</sub>O<sub>2</sub> is sometimes described as being a “shunt” for the LPMO monooxygenase mechanism.<sup>293</sup> Note that the Cu(II)-oxyl produced in this way could also be hypothesized to be able to follow the Cu(III)-OH pathway (**Figure 2.3**, green dashed path), but this path has been omitted from the above scheme for simplicity.

In conflict with the mechanisms depicted in **Figure 2.3**, recent pieces of literature have presented evidence in favour of the preferred mechanism of action of LPMOs being a peroxygenase reaction (**Equation 15**), as summarised in **Figure 2.4**.<sup>290,320-324</sup> It has been argued that under the conditions of the early LPMO studies (O<sub>2</sub> atmosphere in the presence of excess reducing agent) H<sub>2</sub>O<sub>2</sub> would have been generated via ambient direct two-electron, two-proton chemical reduction of O<sub>2</sub>, and that this H<sub>2</sub>O<sub>2</sub> could then have functioned as the LPMO co-substrate.<sup>321</sup> Additionally, it has also been shown that LPMOs can catalyse the generation of H<sub>2</sub>O<sub>2</sub> from oxygen and reducing agent.<sup>322,325</sup> The rate at which LPMOs utilise H<sub>2</sub>O<sub>2</sub> as a co-substrate has been found to be far faster than the rate at which LPMOs utilise O<sub>2</sub>,<sup>326</sup> and as such there is conjecture as to whether the slow rate constants of O<sub>2</sub>-dependant substrate turnover by LPMOs are in fact merely reflective of the rate-limiting speed at which LPMO-catalysis and ambient O<sub>2</sub> reduction are generating H<sub>2</sub>O<sub>2</sub>.<sup>290,321</sup> Such proposals remain controversial however, as there are many copper enzymes for which O<sub>2</sub> is known to be the true co-substrate.<sup>306-309</sup>

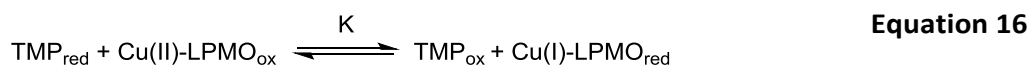
As of the time of writing, the most recent publication to argue that H<sub>2</sub>O<sub>2</sub> is the favoured substrate of LPMOs was submitted for review in March 2019.<sup>321</sup> It argues that with low-affinity

substrates and high concentrations of H<sub>2</sub>O<sub>2</sub> LPMOs would likely only be able to perform a low over of turnovers before becoming oxidatively damaged, but under optimal conditions (i.e. in the presence of saturating amounts of high-affinity substrate) H<sub>2</sub>O<sub>2</sub> could end up being delivered to the LPMO in a timely fashion such that the LPMO is always likely to be polysaccharide-bound rather than substrate-free, and will thus be less likely to ensue oxidative damage and instead be capable of many turnovers.<sup>321</sup> Conversely, a paper submitted for review in January 2018 argued that LPMOs may have evolved to use both O<sub>2</sub> and H<sub>2</sub>O<sub>2</sub> as co-substrates, catalysing both monooxygenase and peroxygenase reactions.<sup>326</sup> The paper points out that while the rate of the peroxygenase reaction far outstrips that of the monooxygenase reaction, the concentration of H<sub>2</sub>O<sub>2</sub> in an extracellular environment would likely be far lower than that of O<sub>2</sub>. Additionally, the authors show that the monooxygenase reaction is more regioselective and results in minimal oxidative damage to the LPMO, even if the carbohydrate substrate is not present.<sup>326</sup>

Consistently, the possibility of oxidative damage by H<sub>2</sub>O<sub>2</sub> is the most controversial aspect of the suggestion that LPMOs have evolved to function via a peroxygenase, rather than a monooxygenase, pathway. The LPMO degradation that can be induced by H<sub>2</sub>O<sub>2</sub> is particularly well explored in a paper published in November 2019 where the treatment of AA9 LPMOs with excess H<sub>2</sub>O<sub>2</sub> in the absence of carbohydrate substrate was shown to lead to the formation of a stable active site copper(II)-tyrosyl complex, and result in the oxidative modification of several non-surface exposed conserved aromatic amino acids that have been theorised to be part of a long-range electron transfer pathway.<sup>293</sup> Oxidative modification of non-surface exposed amino acids by H<sub>2</sub>O<sub>2</sub> does indicate that electron transfer from the LPMO surface – most likely the Cu-centre – to these buried sites is possible. This paper also makes the argument that comparing the rates of product formation between LPMOs using O<sub>2</sub>/excess reducing agent as co-substrate vs LPMOs using H<sub>2</sub>O<sub>2</sub> may not truly be reflective of the rates of the relative O<sub>2</sub>/H<sub>2</sub>O<sub>2</sub> pathways, as reducing equivalents travelling through the long-range electron transfer pathway could quench the highly oxidising species present at the Cu active site, lowering the rate of product formation in O<sub>2</sub>/excess reducing agent regimes.<sup>293</sup> This study described the usage of H<sub>2</sub>O<sub>2</sub> as a “shunt” in the reaction pathway of LPMOs with O<sub>2</sub>+reducing agent, which would imply that the authors believe O<sub>2</sub> and H<sub>2</sub>O<sub>2</sub> reaction mechanisms use the same species to perform hydrogen atom abstraction – i.e. an Cu(II)-oxyl / Cu(III)-OH species.<sup>293</sup> However, it is unclear as to why performing a mechanistic “shunt” would result in diminished regioselectivity in the reaction products, as reported by other authors.<sup>326</sup>

### 2.1.3 The need for electrochemical assay of LPMOs

As can be seen in **Section 2.1.2** the debate regarding the mechanism of action of LPMOs is by no means resolved. Much of the recent work has centred on spectroscopic measurements of the copper centre and associated calculations, but there is a notable dearth of electrochemical measurements. Redox titration experiments have been used to calculate the Cu<sup>(II/I)</sup> reduction potentials of several LPMOs,<sup>298,327-330</sup> but only Karantonis and co-workers have reported the usage of voltammetry to interrogate LPMOs (**Table 2.2**).<sup>331,332</sup> The redox titration method for the calculation of the Cu<sup>(II/I)</sup> reduction potentials was first used by Achmannan.<sup>329</sup> This method works by mixing a solution of reduced *N,N,N',N'*-tetramethyl-*p*-phenylenediamine (TMP<sub>red</sub>) with Cu(II)-LPMO and monitoring the extent of reaction by measuring the absorbance at  $\lambda = 610$  nm from the TMP radical cation (TMP<sub>ox</sub>), which is formed upon Cu(II)-LPMO reduction to Cu(I)-LPMO by TMP<sub>red</sub> (**Equation 16**). As such, [TMP<sub>ox</sub>] = [Cu(I)-LPMO] and [TMP<sub>red</sub>] = [TMP<sub>total</sub>] - [TMP<sub>ox</sub>] = [Cu(II)-LPMO], and with these concentrations known, the equilibrium constant of the TMP+LPMO redox reaction can be calculated using **Equation 16**, and thus so can  $\Delta_r G^\theta$ , and by extension, the standard cell potential of the redox reaction,  $E^\theta$ , (using **Equation 17**). Addition of the standard reduction potential of TMP ( $E_{TMP}^\theta$ ) to the standard cell potential of the TMP+LPMO redox reaction,  $E_{TMP+LPMO}^\theta$ , gives the LPMO-Cu<sup>(II/I)</sup> reduction potential,  $E_{LPMO-Cu}^\theta$  (as is shown in **Equation 18**).



$$K = \frac{[\text{TMP}_{\text{ox}}][\text{Cu(I)-LPMO}_{\text{red}}]}{[\text{TMP}_{\text{red}}][\text{Cu(II)-LPMO}_{\text{ox}}]}$$

$$\Delta_r G^\theta = -RT \ln K = -nFE^\theta \quad \text{Equation 17}$$

$\Delta_r G^\theta$  = standard Gibbs free energy change of reaction / J mol<sup>-1</sup>.

$R$  = gas constant / J mol<sup>-1</sup> K<sup>-1</sup>.

$T$  = temperature / K.

$K$  = equilibrium constant.

$n$  = the number of electrons transferred in the redox couple.

$F$  = the Faraday constant / C mol<sup>-1</sup>.

$E^\theta$  = standard reduction potential / J C<sup>-1</sup>.

$$E_{TMP+LPMO}^\theta = E_{LPMO-Cu}^\theta - E_{TMP}^\theta \quad \text{Equation 18}$$

$E_{TMP+LPMO}^\theta$  = standard reduction potential of the TMP+LPMO reaction / J C<sup>-1</sup>.

$E_{LPMO-Cu}^\theta$  = standard reduction potential of the LPMO Cu<sup>(II/I)</sup> redox couple / J C<sup>-1</sup>.

$E_{TMP}^\theta$  = standard reduction potential of the TMP / J C<sup>-1</sup>.



It is likely that many of the literature values for LPMO reduction potential determined via the redox titration method of Aachmannan<sup>329</sup> carry error due to the literature value of TMP reduction potential used, which is for TMP reduction at pH 8,<sup>333</sup> whereas most of the redox titration assays are in fact conducted at pH's between 6 and 5 (see **Table 2.2**). In addition, while redox titrations can be used to determine the Cu<sup>(II/I)</sup> reduction potential of LPMOs, they are more limited in their scope than a PFE assay would be, as redox titrations cannot be used to directly probe the LPMO reaction mechanism.

**Table 2.2.** Reduction potentials reported for LPMOs. Values marked with an \* were recorded at 50 °C. Those without were recorded at temperatures close to 25 °C (i.e.  $25 \pm 2$  °C). Note that, with the exception of reference [298], it would seem that those using redox titration as the method for determination of reduction potential use a literature value for the reduction potential of the redox dye *N,N,N',N'*-tetramethyl-*p*-phenylenediamine (TMP) at pH 8 of 273 mV vs SHE, whereas reference [298] reports the reduction potential of TMP to be 330 mV vs SHE. This means that the reduction potentials of the LPMOs reported in this table could actually be up to 57 mV higher than they have been reported to be.

LPMO family	LPMO name	pH	Reduction potential vs SHE (mV)	Measurement method
AA9	PaLPMO9H	5	326 <sup>327</sup>	Redox titration
AA9	NcLPMO9C	5.5	$224 \pm 3$ <sup>328</sup>	Redox titration
AA9	PaLPMOE	5	155 <sup>327</sup>	Redox titration
AA9	FoLPMO9	5	$\sim 272$ <sup>331</sup>	FTacV voltammetry
AA9	MtLPMO9	5	$\sim 322$ <sup>331</sup>	FTacV voltammetry
AA9	PcLPMO9D	5	$\sim 351^*$ <sup>332</sup>	FTacV voltammetry
AA9	LcLPMO9D	5	$\sim 412^*$ <sup>332</sup>	FTacV voltammetry
AA10	BaCBM33	5	275-370 <sup>298</sup>	Redox titration
AA10	CBP21	6	275 <sup>329</sup>	Redox titration
AA10	ScLPMO10B	5.5	251 <sup>330</sup>	Redox titration
AA10	CeIS2	5.5	242 <sup>330</sup>	Redox titration

Karantonis and co-workers successfully established direct electrochemical communication with LPMOs by immobilising them onto GC electrodes via simple adsorption and trapping them under a Nafion® film.<sup>331,332</sup> In these direct electrochemistry studies, interrogation via cyclic voltammetry was not feasible - the signals attributed to the redox activity of the LPMO copper centre were difficult to distinguish from the background capacitive current due to the low surface coverage of electroactively immobilised LPMO.<sup>331,332</sup> FTacV was instead used to determine the Cu<sup>(II/I)</sup> reduction potential, and as these reduction potentials were measured via a direct electrochemistry method they are likely to be among the most accurate values in **Table 2.2**, as they will not contain errors from the improper execution of the Aachmannan redox titration.<sup>329</sup> However, full simulation of the FTacV data to yield other important parameters, such as the electron transfer kinetics, were not performed.<sup>331,332</sup> A full rigorous electrochemical assay that probes the mechanism of action of LPMOs has not been reported,

even though doing so could substantially reduce the speculation regarding the reaction pathways in **Figure 2.3** and **Figure 2.4**. In this regard the method of Karantonis and co-workers suffers from a notable imitation: Nafion® films are poorly permeable to  $O_2$ <sup>334,335</sup> and would also be impermeable to oligosaccharides (some LPMOs can use soluble oligosaccharides as substrates).<sup>300</sup> This means that the usage of this system would be unsuitable for the study of LPMO electrochemistry in the presence of i)  $O_2$ , ii) oligosaccharide substrate, or iii)  $O_2$  and oligosaccharide substrate, and thus could not be used to fully elucidate the mechanisms of LPMOs. Interestingly however, Nafion® is highly permeable to  $H_2O_2$ ,<sup>336</sup> and thus this system could still be used to study the electrochemical response of LPMOs to  $H_2O_2$ .

Due to the limitations imposed by the usage of a Nafion® film, an alternative system for establishing direct electrochemical communication with LPMOs was desired. Previous attempts within the Parkin group at electroactive immobilisation of LPMOs had seen the usage of PGE, gold and GC electrodes,<sup>337,338</sup> but these approaches had either failed to yield signals attributable to the  $Cu^{(II/I)}$  redox couple altogether, or had only been successful in yielding tantalising glimpses of these signals with poor repeatability.<sup>337,338</sup> Nanotubes, drop-cast from a suspension onto GC electrode surfaces, have been successfully used to facilitate the electroactive immobilisation of a broad range of redox proteins via simple adsorption,<sup>74,81,82</sup> and it was hoped that usage of nanotube-functionalised electrode surfaces would enable the electroactive immobilisation of LPMOs without usage of a Nafion® membrane. If this were to be achieved, it would be theoretically possible to analyse the  $O_2$ ,  $H_2O_2$  and substrate-dependent behaviours of LPMOs using electrochemistry.

#### 2.1.4 Aims

Given the very small amount of electrochemical data on the redox activity of LPMOs, the aim of the work presented in this Chapter was to explore the feasibility of developing new film electrochemistry approaches for probing LPMO reactivity. Specifically, the work described shows how it has been possible to develop an electrochemical assay that satisfies the following criteria:

- 1) Achieve electroactive LPMO immobilisation to an electrode surface.
- 2) Identify Faradaic redox signals originating from the immobilised LPMO.
- 3) Illustrate the LPMO immobilised on the electrode surface is active.
- 4) Determine the formal potential of the LPMO redox signal over a range of pH values.
- 5) Fit experimental signals to simulated signals in order to extract thermodynamic parameters.
- 6) Determine parameters associated with the kinetics of electron transfer to the immobilised LPMO.

## 2.2 Results and Discussion

### 2.2.1 Preliminary analysis of an AA9 from *Aspergillus nidulans*: An6428-AA9

#### 2.2.1.1 Copper-loading and purification

An AA9 from *Aspergillus nidulans* (henceforth referred to as An6428-AA9) was supplied by Dr César Terrasan. This sample of An6428-AA9 required copper-loading and purification via size exclusion chromatography, which was carried out as described in **Section 8.3.3**. As shown in **Figure 2.5**, an SDS-PAGE gel confirmed that fractions containing An6428-AA9 were eluted from the column. Despite An6428-AA9 having a theoretical molecular weight of 22.5 kDa a clear protein band can be seen near the 31 kDa marker (**Figure 2.5**); this is because the enzyme is highly glycosylated, which not only adds mass to the protein but also affects how it runs in the gel, as the additional mass is not compensated with additional charge. The LPMO-containing fractions were pooled and concentrated, with the concentration of the sample being determined using UV-vis (**Figure 2.6**), using an  $\epsilon_{280}$  value of  $47180 \text{ M}^{-1}\text{cm}^{-1}$  (previously determined by Dr César Terrasan).

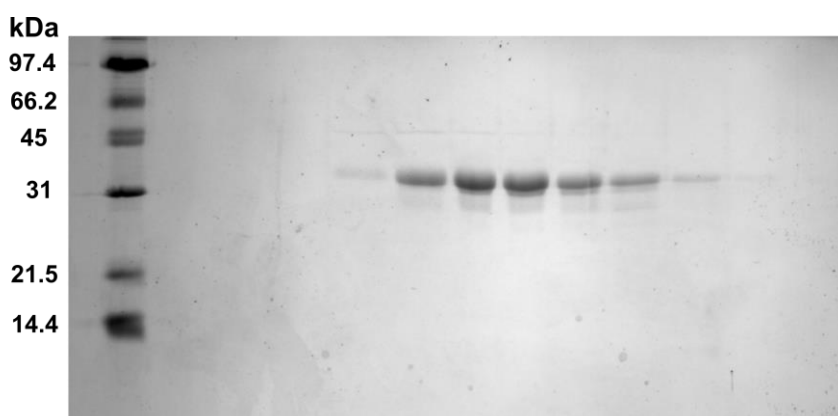


**Figure 2.5.** 15% SDS-PAGE gel illustrating the presence of purified An6428-AA9.

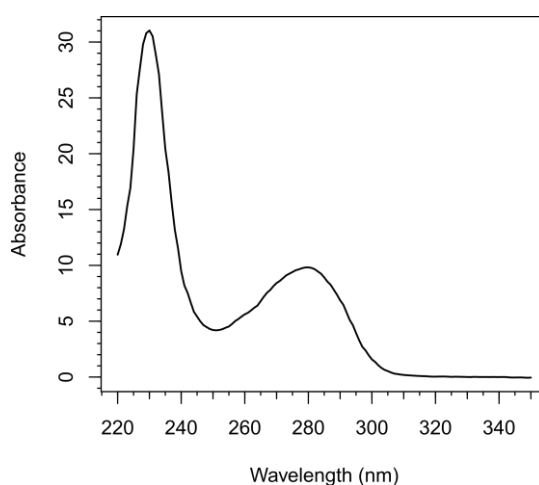


**Figure 2.6.** UV vis spectrum of An6428-AA9 at a concentration of  $208 \mu\text{M}$ , based on an  $\epsilon_{280}$  of  $47180 \text{ M}^{-1}\text{cm}^{-1}$ .

### 2.2.1.2 Structural analysis

There is currently no crystal structure available for *An6428-AA9*, but a high-resolution structure does exist for AA9 from *Lentinus similis* (*LsAA9*), and as aforementioned in **Section 2.1.1**, LPMOs share highly similar folds. Therefore, two different approaches were used to predict the 3D spatial location of residues in *An6428-AA9*. First, BLAST<sup>339</sup> and Needle<sup>340</sup> were used to generate sequence alignments of *An6428-AA9* and *LsAA9*, as shown in **Figure 2.7**. BLAST (which stands for “Basic Local Alignment Search Tool”)<sup>339</sup> identified two ranges in the *An6428-AA9* sequence that displayed significant local alignment with parts of the *LsAA9* sequence (**Figure 2.7**), although the aligned residues identified in Range 2 are already accounted for in Range 1, and thus Range 2 is unlikely to be relevant. BLAST did however fail to identify an important known area of homology – namely that of the *N*-terminal histidine residue. Needle, which outputs an optimal global alignment of two sequences,<sup>340</sup> was therefore used to detect homology in the *N*-terminal region of the proteins. Many of the aligned residues are proline and glycine residues, often neighbouring each other, as is common in looping regions of proteins.<sup>341</sup> Aromatic Tyr, Trp and Phe residues that reside in the hydrophobic core of *LsAA9* also align well with counterparts in *An6428-AA9*, as do key residues in the active site of *LsAA9*, such as His1 and His78 (which make up the *histidine brace*), and Tyr164 (the axial tyrosine). In order to provide a crude guide to the structure of *An6428-AA9* the image shown in the left panel of **Figure 2.8** was generated by highlighting the aligned residues of *An6428-AA9* and *LsAA9* (as identified using BLAST and Needle) on the *LsAA9* crystal structure. It is interesting to note however that the sequence alignment analyses in **Figure 2.7** indicate that the aromatic residues previously proposed to be part of a conserved long-range electron transfer pathway through AA9s (residues Trp5, Trp64 and Tyr65 in *LsAA9*)<sup>293</sup> are absent from *An6238-AA9*.

The structure of *An6428-AA9* was also predicted using Phyre2, which uses advanced remote homology detection methods to build 3D models of proteins.<sup>342</sup> As shown in the right-hand panel of **Figure 2.8**, this analysis predicts that the *An6428-AA9* structure has the highly conserved fold seen in all LPMOs. Comparison of the two panels of **Figure 2.8** also indicates that the conserved residues identified in the sequence alignment are predicted to be in similar locations.

## Chapter 2. Electrochemical interrogation of an AA9 LPMO

BLAST. Range 1: 28 to 220

Score	Expect	Method	Identities	Positives	Gaps
111 bits (278)	4e-35	Compositional matrix adjust	77/204 (38 %)	102/204 (50 %)	30/204 (14 %)
<i>An6428-AA9</i>	29	N G P V E D V T S L D I R C N K D A S T N G N A T E T L P V K A G E E I G F T V R T N I - - - - - G H P G F L L A	80		
<i>Ls AA9</i>	28	N N P V + + + T S D + C N D - - - - - N R V V P K S V P V N A G D T L T F E W Y H N T R D D D I I A S S H H G R I A V	85		
<i>An6428-AA9</i>	81	Y M A K A P G D A S D F D G D G Q V W F K I Y E D G P T V T D D G L T W P S D G A T N V N - - - - - F T I P S S L P D G D	136		
<i>Ls AA9</i>	85	Y I A P A A S N - - - - - G Q G N V W V K L F E D A Y N V T N S - - - - - T W A V D R L I T A H G Q H S V V V P H V A P - G D	136		
<i>An6428-AA9</i>	137	Y L L R V E H I A L H G A G T E - - - - - G G A Q F Y L S C G Q V S V T G G G N G D P A P L - V A F P G A Y D P T D P	189		
<i>Ls AA9</i>	137	Y L R E I A L H A + - - - - - G A Q F Y + S C Q + + + + - - - - - P P V F P G A Y + P	196		
<i>An6428-AA9</i>	190	G I L I N I Y W P V P T N Y T P P G P K V W S G	213		
<i>Ls AA9</i>	197	G I Q F N I Y T T P A T S Y V A P P S V W S G	220		

BLAST. Range 2: 19 to 30

Score	Expect	Method	Identities	Positives	Gaps
13.5 bits (23)	3.5	Compositional matrix adjust	6/12 (50 %)	6/12 (50 %)	0/12 (0 %)
<i>An6428-AA9</i>	194	N I Y W P V P T N Y T P	205		
<i>Ls AA9</i>	19	N I Y I R S P P N N N P	30		

Needle alignment: 1 to 31

Score	Matrix	Identity	Similarity	Gaps
20.5	EBLOSUM62	5/34 (26.5 %)	14/34 (41.2 %)	5/34 (14.7 %)
<i>An6428-AA9</i>	1	H Y V F P A L V Q D G A A T G D W K - - Y V R D W T G S Y G N G P V	32	
<i>Ls AA9</i>	1	H T L V W G V W V N G V D Q G D G R N I Y I R - - - S P P N N N P V	31	

**Figure 2.7.** BLAST and Needle sequence alignment analyses of *An6428-AA9* against *LsAA9*. Aligned residues from Range 1 of the BLAST analysis and those residues are highlighted in green, whereas those from Range 2 of the BLAST analysis are highlighted in yellow. BLAST analysis did not consider the first 32 residues of *An6428-AA9* to have significant similarities with the first 31 residues of *LsAA9*, but Needle analysis did find a similarity of 41.2%. Residues suggested to be aligned by Needle analysis are highlighted in orange. Residues Trp5, Trp64 and Tyr65 in *LsAA9* have been highlighted in red and appear to have no counterparts in *An6428-AA9*.

*An6428-AA9* is known to be *N*-glycosylated, and analysis of the *An6428-AA9* sequence using the NetNGlyc server (available at <http://www.cbs.dtu.dk/services/>) identified asparagine residues 51 and 125 as likely to bear *N*-glycosylation (see **Chapter 4, Section 4.2.2.1**). These glycosylation sites are highlighted in purple on the predicted *An6428-AA9* structure (**Figure 2.8, right**). The sequence alignments in **Figure 2.7** also made it possible to infer approximate loci where the glycosylation sites of *An6428-AA9* would reside in space based on the crystal structure of *LsAA9*, and these sites have also been highlighted in purple (**Figure 2.8 left**). Notably, in both cases these glycosylations appear to be at sites which are not proximal to the flat binding surface that interacts with crystalline cellulose, which makes sense as such a glycosylation would affect substrate binding.<sup>290</sup>

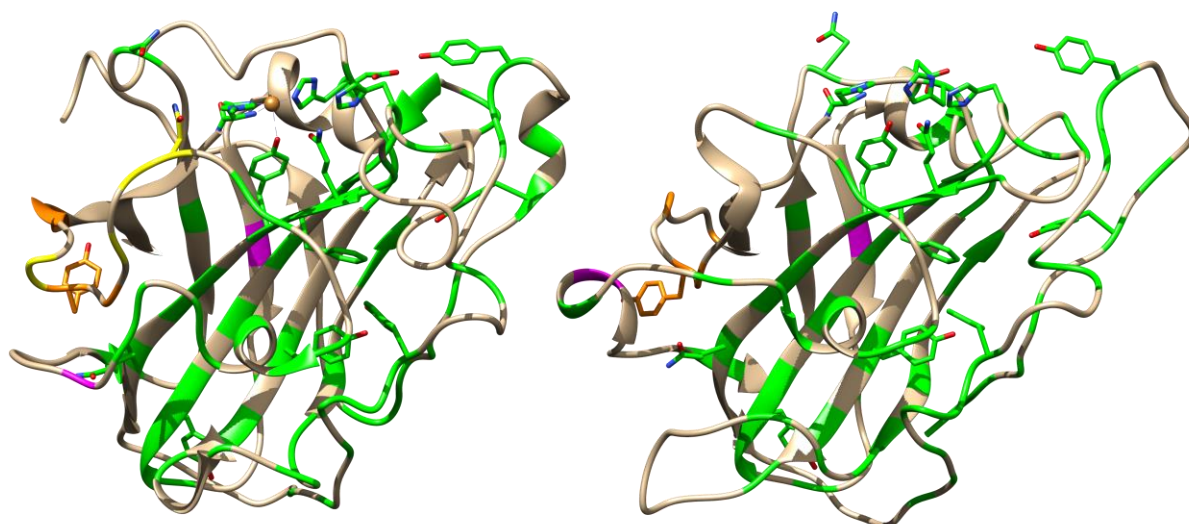


**Figure 2.8. Left)** The mapping of the aligned residues from *An6428-AA9* and *LsAA9* (identified using the sequence alignments in **Figure 2.7**) onto the crystal structure of *LsAA9* (PDB: 5N05).<sup>300</sup> Aligned residues from *An6428-AA9* **Figure 2.7** Range 1 are coloured green on the crystal structure of *LsAA9*, as is the *N*-terminal histidine residue. Residues aligned using Needle are coloured orange and locations corresponding to *An6428-AA9* sites predicted to be *N*-glycosylated are coloured purple. The sites coloured yellow are those that have been identified using **Figure 2.7** Range 2, and are likely not relevant, as the residues in question (*An6428-AA9* residues 194-205) are already accounted for by **Figure 2.7**, Range 1. **Right)** Predicted fold of *An6428-AA9* generated using Phyre2.<sup>342</sup> Residues identified as aligned with *LsAA9* by BLAST or Needle analysis are once again coloured green or orange, and predicted *N*-glycosylation sites are coloured purple.

### 2.2.1.3 Redox titration with *N,N,N',N'*-tetramethyl-*p*-phenylenediamine

An approximate reduction potential of *An6428-AA9* was determined using a variation of the method used by Achmannan<sup>329</sup> and many other LPMO researchers<sup>298,327-330</sup> (the theory underpinning this method is described in **Section 2.1.3**). As is described in **Section 8.2.4**, solutions of known TMP concentration (where TMP was in its reduced form  $\text{TMP}_{\text{red}}$ ) were mixed with *An6428-AA9* in oxygen-free pH 6 buffer at 20 °C in a  $\text{N}_2$ -filled glovebox, and the extent of resultant redox reaction was determined by measuring the absorbance from the TMP radical cation ( $\text{TMP}_{\text{ox}}$ ) at  $\lambda = 610$  nm (**Figure 2.9**). The experiment was performed at pH 6 and the reduction potential of TMP at pH 6 was determined via cyclic voltammetry to be 308 mV vs SHE at 20 °C (see **Appendix 3, Figure S1**). Dedicated measurement of the TMP reduction potential at pH 6 ensured that the calculation performed to determine the reduction potential of *An6428-AA9* did not contain the error associated with using the literature pH 8 TMP reduction potential<sup>333</sup> (which affects many of the entries in **Table 2.2**). Using the method described in **Section 8.2.4**, the reduction potential of *An6428-AA9* at pH 6 was determined to be  $330 \pm 30$  mV vs SHE at 20 °C. This is in agreement with the literature LPMO reduction potentials reported in **Table 2.2**, and while not an exact value, this does provide a voltage window within which any Faradaic signals observed in cyclic voltammetry could be regarded as putative *An6428-AA9* redox signals.

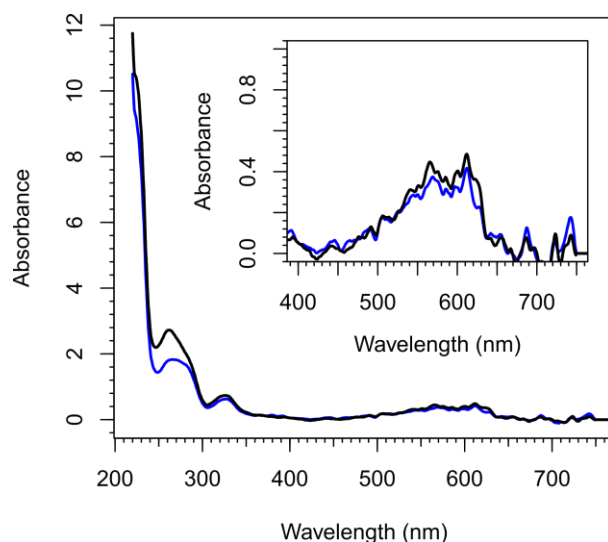


**Figure 2.9.** UV vis spectra of 35  $\mu\text{M}$  solutions of *An6428-AA9* + 300  $\mu\text{M}$  (black) or +200  $\mu\text{M}$  (blue) TMP. The concentration of oxidised TMP was determined based on an  $\epsilon_{610}$  of  $14000 \text{ M}^{-1}\text{cm}^{-1}$ .<sup>343</sup>

### 2.2.2 Electroactive immobilisation of *An6428-AA9*

The electroactive immobilisation of *An6428-AA9* was first achieved using inexpensive multi-walled carbon nanotubes (MWCNTs) purchased from Alfa Aesar (Sample A, **Table 2.3**, henceforth referred to as **MWCNT A**) drop-cast onto a GC electrode from a  $2 \text{ mg mL}^{-1}$  suspension in *N,N*-Dimethylformamide (DMF). GC surfaces functionalised with the drop-cast **MWCNT A** films but in the absence of LPMO (“Nanotubes” in **Figure 2.10**) displayed a greatly increased capacitance relative to unmodified GC surfaces (“GC” in **Figure 2.10**); this is attributed to the greatly increased surface area.<sup>344</sup> Importantly, these LPMO-free control experiments showed no notable redox reaction signals over the range of  $-0.02 \rightarrow 0.8 \text{ V}$  vs SHE in pH 7 buffer (“Nanotubes” in **Figure 2.10**, “MWCNT” traces in **Figure 2.11**).

**Table 2.3.** MWCNT samples sourced from several suppliers, and the information available regarding them.

Sample	Supplier	Outer diameter / nm	Inner diameter / nm	Length / $\mu\text{m}$	Preparation method	Purity
A	Alfa Aesar	$\leq 8$	2 – 5	0.5 – 2	Carbon arc (suspected)	Unspecified
B	Aldrich	6 – 13	Unspecified	2.5 – 20	Chemical vapor deposition	> 98% carbon basis
C	TCI	60 – 100	Unspecified	$\geq 5$	Unspecified	> 95% carbon (TPO)

Adsorption of *An6428-AA9* onto a **MWCNT A** surface was however accompanied by the appearance of an oxidative process in the initial few scans, with an onset potential of  $\sim 0.8 \text{ V}$  vs SHE (**Figure 2.11**). This oxidative process seemingly gives rise to several other redox signals, which increase in intensity

with successive scans until stabilising after about 7 scans (**Figure 2.11**). There are three readily discernible signals, the first of which appears at  $\sim 0.41$  V vs SHE, the second at  $\sim 0.28$  V vs SHE and the third at  $\sim 0.09$  V vs SHE (**Figure 2.10**). These signals were isolated and modelled using a specially written package of codes (see **Appendix 2**). These codes fit a baseline under these signals to estimate the background capacitive current (“Baseline” in **Figure 2.10**) and subtract this baseline from the experimental data to isolate the Faradaic signals (“Extracted signal” in **Figure 2.10**). The isolated Faradaic signals are then modelled as three overlapping Faradaic signals and the code package uses **Equation 7 (Section 1.4.1)** to simulate the signals in an attempt to reconstruct the “Extracted signal”. The output of this simulation are three individual Faradaic signals (“Simulated signal” 1, 2 and 3 in **Figure 2.10**). The values yielded for  $n_s$  and  $n_{app}$  (from **Equation 7, Section 1.4.1**) for each modelled signal were either unity or close to unity, and as such all the Faradaic signals would appear to arise from one-electron redox couples.

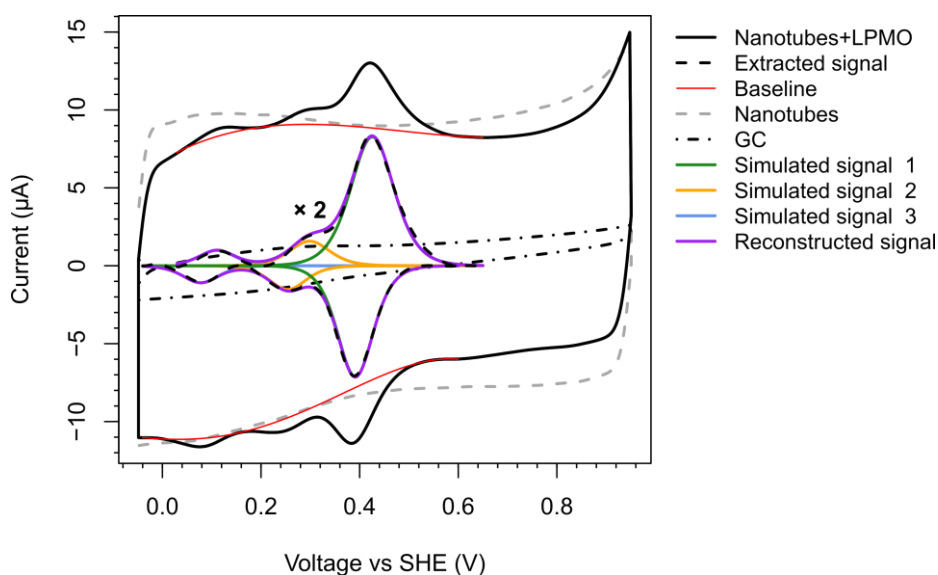


**Figure 2.10.** Cyclic voltammograms illustrating the absence of redox signals for unfunctionalised glassy carbon surfaces and GC surfaces functionalised with drop-cast nanotubes, and the presence of several redox signals upon that adsorption of *An6428-AA9* onto the nanotube functionalised electrodes. Scans recorded at  $33 \text{ mV s}^{-1}$  at 298 K under  $\text{N}_2$  atmosphere in pH 7 buffer (20 mM sodium phosphate, 20 mM sodium acetate, 500 mM  $\text{Na}_2\text{SO}_4$ ), using a glassy carbon working electrode, a platinum wire counter electrode and a saturated calomel reference electrode (saturated KCl). All scans commence at the most negative potential. Redox signals were isolated and simulated using the specialised code package described in **Appendix 2**, and the isolated signals are here replotted at  $2 \times$  their intensity.



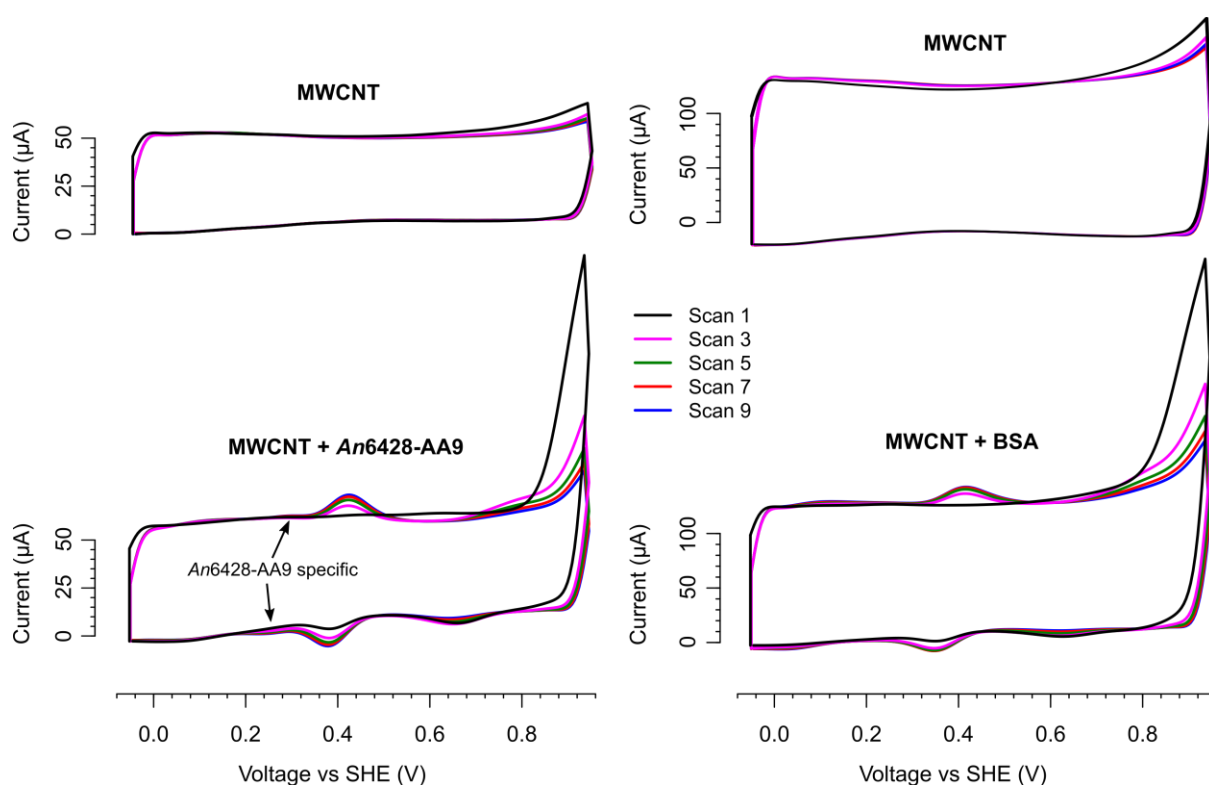


**Figure 2.11.** Cyclic voltammograms illustrating the appearance of an oxidative feature that onsets at  $\sim 0.8$  V vs SHE for GC electrodes functionalised with **MWCNT A** and then treated with protein. This oxidative feature decays in subsequent scans, whereas other redox signals become more intense with increasing scan number, before reaching a stable intensity. The pair of Faradaic signals centred at  $\sim 0.28$  V vs SHE only become visible for samples of MWCNTs treated with *An6428-AA9*. Scans recorded at  $113 \text{ mV s}^{-1}$  at 298 K under  $\text{N}_2$  atmosphere in pH 7 buffer (20 mM sodium phosphate, 20 mM sodium acetate, 500 mM  $\text{Na}_2\text{SO}_4$ ).

Unfortunately, control experiments revealed that the adsorption of any protein onto these MWCNT surfaces, including DsbA mutants (data not shown) and even the non-redox-active protein bovine serum albumin (BSA), gives rise to the oxidative process that commences at  $\sim 0.8$  V and is only visible in initial scans (**Figure 2.11**). Following this oxidation, only two of the reversible electron transfer signals within the  $-0.02 \rightarrow 0.8$  V range appear at pH 7: the pair of peaks centred at  $\sim 0.41$  V vs SHE and the pair of peaks centred at  $\sim 0.09$  V vs SHE (**Figure 2.11**, **Figure 2.12**). The largest of these signals (the one centred at  $\sim 0.41$  V vs SHE at pH 7) at first appears to be just within the range of the LPMO reduction potentials reported in the literature (**Table 2.2**), which makes this result appear like a false positive,<sup>332</sup> yet at pH 6 this signal shifts to  $\sim 0.45$  V vs SHE; outside the range of literature LPMO reduction potentials (see **Appendix 3**, **Figure S2**, **Table S1**). Notably however, the third signal observed in *An6428-AA9* experiments, i.e. the pair of oxidation and reduction peaks centred at  $\sim 0.28$  V vs SHE, only appears for MWCNT surfaces treated with the LPMO (**Figure 2.11**, **Figure 2.12**), and even more

encouragingly, at pH 6 this signal shifts to  $\sim 0.31$  V vs SHE (see **Appendix 3, Figure S2, Table S1**), placing it in excellent agreement with the AA9 reduction potentials previously reported in the literature (**Table 2.2**), and in excellent agreement with the TMP redox titration experiment, which suggested the reduction potential of An6428-AA9 was within the range of  $330 \pm 30$  mV vs SHE at pH 6 and at 20 °C.

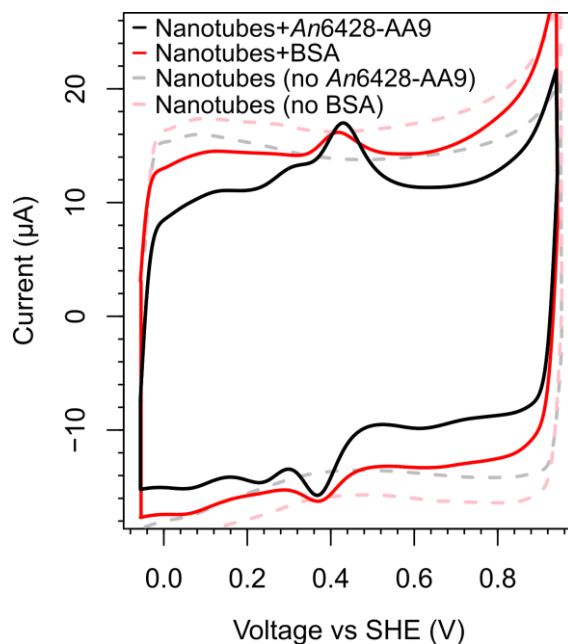


**Figure 2.12.** Cyclic voltammograms illustrating that a redox couple centred at  $\sim 0.28$  V vs SHE is only present for samples of nanotubes treated with An6428-AA9, whereas the redox couples centred at  $\sim 0.41$  V vs SHE and  $\sim 0.09$  V vs SHE becomes present when any protein adsorbs to the nanotubes and is subjected to the oxidation process at  $\sim 0.8$  V vs SHE, even non-redox-active proteins such as BSA. Scans recorded at  $33 \text{ mV s}^{-1}$  at 298 K under  $\text{N}_2$  atmosphere in pH 7 buffer (20 mM sodium phosphate, 20 mM sodium acetate, 500 mM  $\text{Na}_2\text{SO}_4$ ), using a glassy carbon working electrode, a platinum wire counter electrode and a calomel reference electrode (saturated KCl). Prior to recording these scans, the working electrode was held at 0.94 V vs SHE for 60 seconds, to allow the oxidative process to occur. All scans commence at the most negative potential.

### 2.2.3 The nature of the background signals

The origin of the oxidative process and the background signals that arise because of it, and the reason behind their dependence on the presence of an adsorbed protein film, remains a matter of speculation. Usage of MWCNT samples from other suppliers (**Section 2.2.2, Table 2.3**, samples **B** and **C**) resulted in the same signals arising, and yet again, only in the presence of a protein film (**Figure S3**). Such a phenomenon has not been reported in the literature, yet visually, the behaviour depicted in **Figure 2.11** has a striking resemblance to that depicted in **Figure 2.13** (reproduced with permission from ref [345]). Ref [345] describes the oxidation of a pyrene-functionalised molecule (1-Pyrenebutyric acid, PBA) into a radical cation species which subsequently reacts with the amine functionalities of an amine-functionalised nanotube surface via a second oxidative process. Together these two oxidative processes cause the irreversible oxidative feature in the first scans of **Figure 2.13 A** and **B**, and result in the formation of redox-active amino bridges; the amino bridges in-turn give rise to two new pairs of redox signals over subsequent scans (**Figure 2.13 B**). Ref [345] only gives limited details regarding the mechanism of the electro-oxidative pyrene-amino bridge forming reaction and gives even fewer details regarding the redox behaviour of the pyrene-amino bridges. However, **Figure 2.14 panel a** presents a proposed reaction mechanism for the electro-oxidative formation of amino bridges between amines and pyrene units, based on literature reaction mechanisms for electro-oxidative coupling in similar systems,<sup>346,347</sup> and **Figure 2.14 panel b** hypothesises that the nature of the redox couples accessible to a pyrene-amino bridge could be reminiscent of those of aniline,<sup>348</sup> as the pyrene-amino bridge species are essentially anilines with more extensive  $\pi$ -systems. **Figure 2.14 panel b** shows that two one-electron one-proton redox couples may be possible with a pyrene-amino bridge species (and theoretically a one-electron two-proton couple as well).

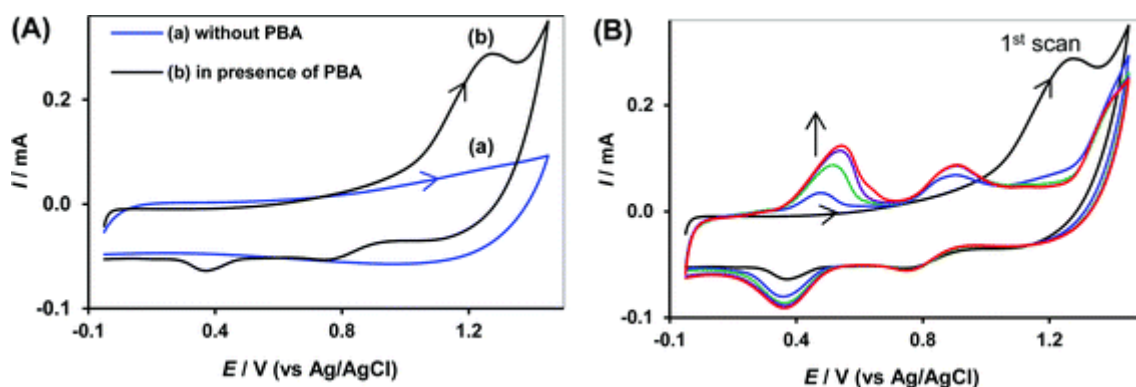


**Figure 2.13.** Reproduced from Ref. [345] with permission from The Royal Society of Chemistry (license number: 1096409-1). **(A)** Recorded CVs with scan rate of  $0.1 \text{ V s}^{-1}$  from the amino-CNTs-Gr-based electrode in 1 : 1 acetonitrile/DMF solution containing 1 mM PBA and 0.05 M tetraethylammonium hexafluorophosphate as supporting electrolyte, in the absence **(a)** and presence **(b)** of PBA. **(B)** Recorded cyclic voltammograms of GC/Gr/ $\text{NH}_2$ -CNTs modified electrode in acetonitrile/DMF solution containing 1 mM PBA and 0.05 M tetraethylammonium hexafluorophosphate during 6 successive cycles.

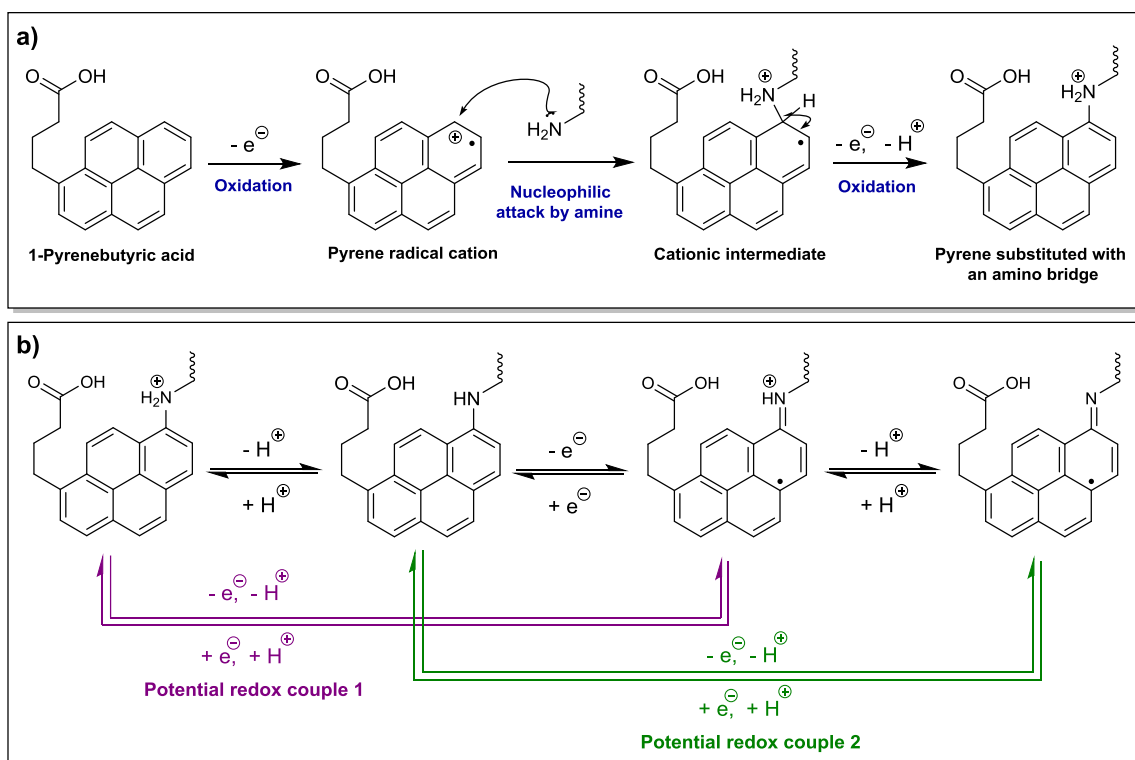


**Figure 2.14.** a) Proposed oxidative reaction pathway between 1-pyrenebutyric acid and a primary amine. Note that many regioisomeric products are possible, but only one is presented. b) Proposed redox behaviour of a pyrene compound substituted with an amino bridge, based on the redox behaviour of anilines.<sup>348</sup>

It could be theorised that, as opposed to an oxidised pyrene unit reacting with an amine-functionality on a nanotube surface to form redox-active amino bridges, an oxidised MWCNT surface might be capable of reacting with a protein's amine-functionalities. In the case of MWCNTs treated with *An6428-AA9*, these redox-active amino bridges may in turn facilitate direct electron transfer to the copper centre, causing the *An6428-AA9* specific signal to build-in alongside the signals theoretically attributable to the amino-bridges (**Figure 2.11**, **Figure 2.12**). With this hypothesis in mind however, it is still somewhat unclear why the irreversible oxidative feature in **Figure 2.11** is only observed in the presence of a protein film, although it could be proposed that the presence of the protein film somehow facilitates the oxidation of the MWCNT surface. Readers should note that ref [345] was only found at the time of writing, and thus experiments specifically designed to test the above hypotheses have not been conducted.

Other potential explanations for the background signals were investigated. Fullerene is listed as an impurity in the **MWCNT A (Table 2.3)**, but fullerenes only display redox activity at voltages lower than those covered by these experiments.<sup>349,350</sup> Very little information is available regarding the manufacturing method of **MWCNT A**, but other samples of nanotubes containing fullerenes sold by Alfa Aesar seem to be supplied as an "as-produced cathode deposit," where the nanotubes were

formed in the presence of a metal catalyst via a carbon arc method. As-produced cathode deposits sold by other vendors list not only fullerenes, but also carbon-coated metal nanoparticles and “amorphous carbon nanopowder” as impurities; if such species are present in the MWCNT samples they could be responsible for these strange redox signals. It is not clear why such species would only give signals in the presence of adsorbed protein, but it is possible that the rate of proton-coupled electron transfer processes, such as those of quinone-like organic species, become greatly enhanced in the presence of a proton acceptor/donor rich protein film.<sup>351</sup> The formal potential of the dominant background signal (the one centred at  $\sim 0.41$  V vs SHE at pH 7) varies strongly with pH, by  $-48$  mV per pH unit (**Figure 2.15, B**). This is in reasonable agreement with the theoretical relationship between standard reduction potential and pH ( $-59$  mV per pH unit) for redox processes described by **Equation 19**, where the number of protons transferred upon reduction is equal to the number of electrons.

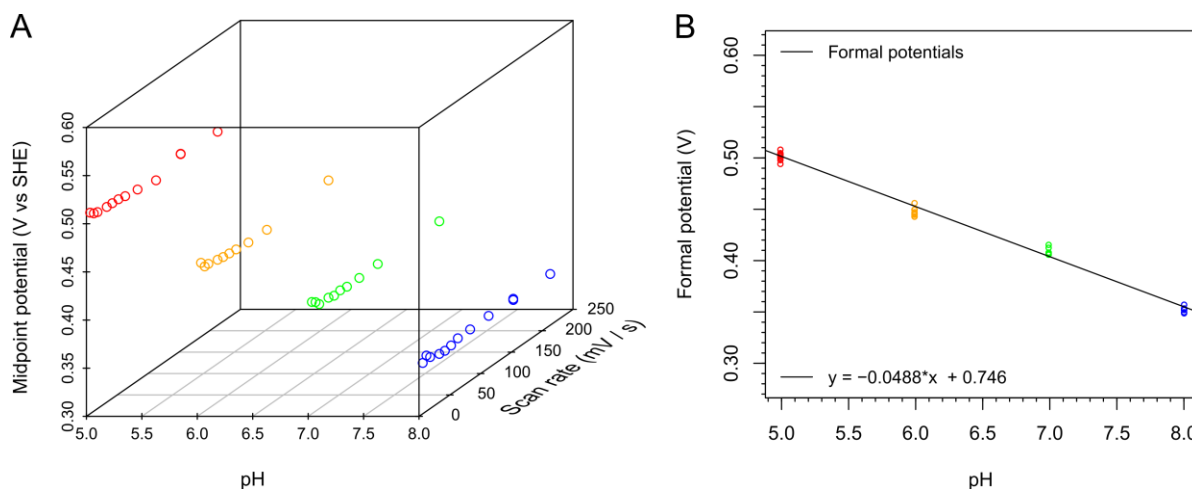


**Figure 2.15. A)** The midpoint potential of the dominant background redox couple is constant for scan rates  $< 200$   $\text{mV s}^{-1}$ , and thus reflects the formal potential of the redox couple for these scan rates. **B)** The relationship between formal potential and pH for the dominant background signal. Scans recorded at a range of scan rates at 298 K under  $\text{N}_2$  atmosphere in buffer (20 mM sodium phosphate, 20 mM sodium acetate, 500 mM  $\text{Na}_2\text{SO}_4$ ) at the appropriate pHs, using samples of **MWCNT A** treated with **An6428-AA9**.

A literature system details the electroactive immobilisation of horseradish peroxidase onto a graphite-epoxy electrode (GE) modified with multiwalled carbon nanotubes that had been previously oxidised using a  $\text{HNO}_3/\text{H}_2\text{SO}_4$  mixture.<sup>352,353</sup> The authors used this chemical oxidation step to introduce carboxylic acid surface functionalisation to the nanotubes, and also noted that these nanotubes

displayed a redox couple centred at 0.175 V vs SCE (0.416 V vs SHE) at pH 4, which they attributed to quinone-type species.<sup>352</sup> Extrapolating the relationship between the formal potential of the background signal and pH, the formal potential of the background signal observed in **Figure 2.12** would be expected to be around 0.55 V vs SHE at pH 4. The formal potential of a quinone-type redox couple is dependent on the nature of the quinone itself however, so this discrepancy could be due to the quinone species being generated via chemical oxidation being different to those generated via electrochemical oxidation, or different between different nanotube samples. Another account of similar signals comes from early nanotube electrochemical literature, which reports that SWCNTs functionalised with terminal carboxylic groups (via refluxing in HNO<sub>3</sub>)<sup>354</sup> show a redox couple for the reduction of carboxylic acids to alcohols/ oxidation of alcohols to carboxylic acids, centred at around 0.35 V vs SHE at pH 4, and around 0.17 V vs SHE at pH 7.<sup>355</sup>

Interestingly, the authors of the horseradish peroxidase study<sup>352</sup> speculate that the quinone species present on the chemically-oxidised nanotube surface help facilitate the immobilisation of the horseradish peroxidase via hydrogen bonding interactions with carboxylic acid groups.<sup>352</sup> Organic quinone-like species and pigments are known to be electron donors to LPMOs, and some LPMOs are known to interact with the phenolic-type species found in lignin. It could be hypothesised that the presence of quinones on the electrode surface may thus facilitate electroactive immobilisation of *An6428-AA9*. It is possible that presence of a protein film may facilitate the electrochemical oxidation of the nanotube surface by lowering the overpotential required to introduce a quinone-type species onto the nanotube surface, and once these quinones are present, they may in-turn facilitate a more electroactive mode of immobilisation for *An6428-AA9*.

To test this hypothesis a portion of **MWCNT A** was subjected to chemical oxidation using a mixture of HNO<sub>3</sub> and H<sub>2</sub>SO<sub>4</sub> (1:3 by volume) under sonication for 4 hours. After this time the mixture was placed on ice and slowly neutralised using NaOH. The nanotubes were pelleted via centrifugation, and salts were removed by repeatedly resuspending the nanotubes in deionised water before re-separating them via centrifugation. Interesting chemically oxidised nanotubes were cable of forming a stable suspension in water, whereas as-received **MWCNT A** is incapable of doing this; this could indicate that the chemical oxidation successfully introduced motifs cable of hydrogen-bonding, principally additional carboxylic acid groups, onto the nanotube surface. Treatment of MWCNTs with HNO<sub>3</sub>/H<sub>2</sub>O<sub>4</sub> mixtures for extended periods of time is also known to cause the nanotubes to become shortened, as extensive introduction of oxygen-containing groups onto the side walls of the nanotubes will eventually break them apart; and shorter nanotubes would also be more easily suspended. Attenuated total reflection infrared spectroscopy (ATR-IR) of the oxidised nanotubes was consistent with those reported in the literature, showing that upon treatment with the oxidising agent the

carbonyl band at  $\sim 1700\text{ cm}^{-1}$  subtly increases in intensity and displaces to a slightly higher frequency (**Figure 2.16, feature a**), and a subtle increase in the absorption at  $\sim 1200\text{ cm}^{-1}$  can be observed (**Figure 2.16, feature b**).<sup>353</sup> The displacing and increase in intensity of the carbonyl band is thought to be due to the introduction of carboxylic acid groups onto the nanotube side-walls, whereas the increase in intensity at  $\sim 1200\text{ cm}^{-1}$  is thought to be due to the appearance of new C-O groups at the open-ends of the nanotubes.<sup>353</sup>

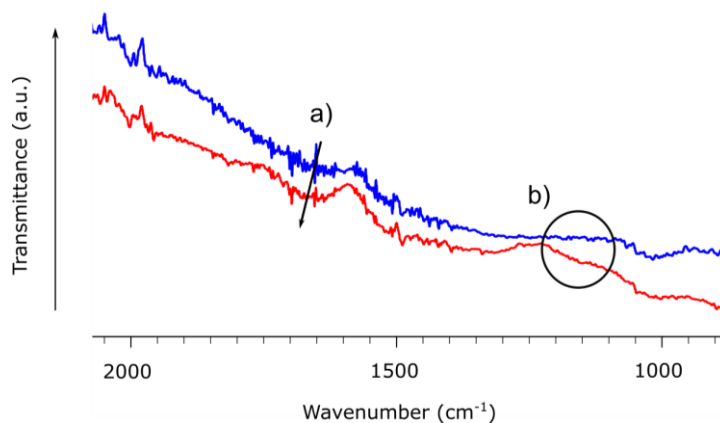


**Figure 2.16.** IR (ATR) spectrum of as-received **MWCNT A** (blue) and a sample of **MWCNT A** that had been subjected to chemical oxidation using a  $\text{H}_2\text{SO}_4/\text{HNO}_3$  mixture (red).

The sample of oxidised **MWCNT A** was drop-cast onto a glassy carbon electrode. Cyclic voltammetry revealed the appearance of a new redox couple, with a broad pair of peaks centred around 0.19 V vs SHE (**Figure 2.17 a**). This would appear to be consistent with the redox activity reported in ref [355] for carboxylic acids on nanotube surfaces. Although the formal potential of this couple is not an exact match for the redox couple observed at  $\sim 0.09\text{ V}$  vs SHE in **Figure 2.10** and **Figure 2.12**, it could be hypothesised that the signal at  $\sim 0.09\text{ V}$  vs SHE could originate from the redox activity of a lighter coverage of carboxylic acids, or perhaps from the carboxylic acids at the open ends of the nanotube (which are easier to introduce). As generation of carboxylic acids represents a more complete oxidation of the nanotube surface than the introduction of quinone species, the strength of  $\text{HNO}_3/\text{H}_2\text{SO}_4$  as an oxidising agent likely explains its preference for generation of carboxylic acids over quinones. Application of *An6428-AA9* as a film on the surface of the oxidised **MWCNT A** is once again accompanied by the oxidative feature at  $\sim 0.8\text{ V}$  vs SHE, that gives rise to a signal at  $\sim 0.41\text{ V}$  vs SHE in successive scans (**Figure 2.17, b**). However, comparison of **Figure 2.17** with **Figure 2.11** illustrates that the intensity of these signals is noticeably diminished for samples of chemically oxidised **MWCNT A** relative to samples of as-received **MWCNT A**, which could indicate that fewer sites remain on the chemically-oxidised **MWCNT A** surfaces that are eligible for oxidation to quinone-type species. Also of interest is that the peak at  $\sim 0.28\text{ V}$  vs SHE, suspected to be the *An6428-AA9* redox signal, is not clearly

visible (**Figure 2.17, c**), whereas it is under an analogous experiment that uses as-received **MWCNT A** (**Figure 2.17 d**). This would indicate that the sample of **MWCNT A** subjected to harsh chemical oxidation is less well suited to mediating electroactive immobilisation of *An6428-AA9*.

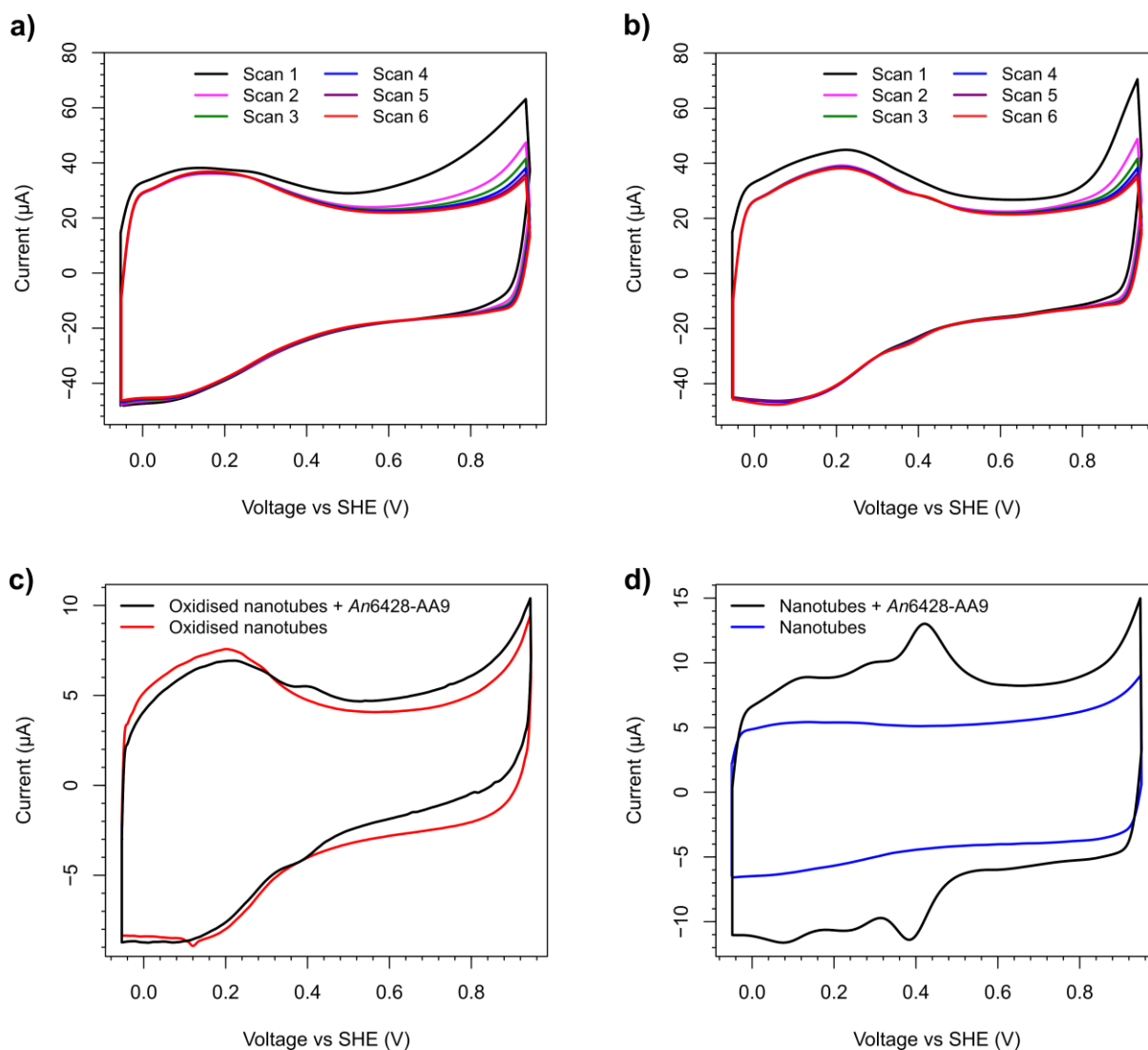


**Figure 2.17.** **a)** Cyclic voltammograms illustrating the absence of an oxidative feature that onsets at  $\sim 0.8$  V vs SHE for samples of chemically oxidised **MWCNT A** not treated with *An6428-AA9*. **b)** Cyclic voltammograms illustrating the presence of a small oxidative feature that onsets at  $\sim 0.8$  V vs SHE for samples of chemically oxidised **MWCNT A** treated with *An6428-AA9*. This oxidation feature decays in subsequent scans, while the feature at  $\sim 0.41$  V vs SHE becomes more intense with increasing scan number, before reaching a stable intensity. **c)** The feature at  $\sim 0.41$  V vs SHE is still dependent on the presence of adsorbed protein, while it is still visible and when using chemically oxidised **MWCNT A**, the signal at  $\sim 0.28$  V vs SHE, specific to *An6428-AA9*, is not. **d)** When samples of as-received **MWCNT A** are used, the signal at  $\sim 0.41$  V vs SHE is more intense and the signal at  $\sim 0.28$  V vs SHE, specific to *An6428-AA9*, is clearly visible. The cyclic voltammograms shown in **a)** and **b)** were recorded at  $113 \text{ mV s}^{-1}$ , while those shown in **c)** and **d)** were recorded at  $18 \text{ mV s}^{-1}$ . All cyclic voltammograms were recorded at 298 K under  $\text{N}_2$  atmosphere in pH 7 buffer (20 mM sodium phosphate, 20 mM sodium acetate, 500 mM  $\text{Na}_2\text{SO}_4$ ), using a glassy carbon working electrode, a platinum wire counter electrode and a calomel reference electrode (saturated KCl). All scans commence at the most negative potential.



A crude measure of the electron-transfer kinetics of the large “background” process centred at  $\sim 0.41$  V vs SHE at pH 7 was obtained courtesy of trumpet plot analysis. Trumpet plots were constructed for a range of pH values (see **Appendix 3, Figure S4**), but it was the datapoints residing beyond the irreversible limit in a large dataset collected at pH 7 which were easiest to fit to the linear models described in **Equation 9** and **Equation 10** (see **Section 1.4.1**). This is shown in **Figure 2.18**. This analysis yielded a value of  $k_0$  of  $\sim 3.6$  s $^{-1}$ . It should be noted that **Equation 7** (**Section 1.4.1**) can only be used to simulate redox signals within their reversible limit, and as such the peak voltage ( $E_p$ ) for the dominant background redox signal was approximated to simply be the maximum of the baseline-subtracted Faradaic current.

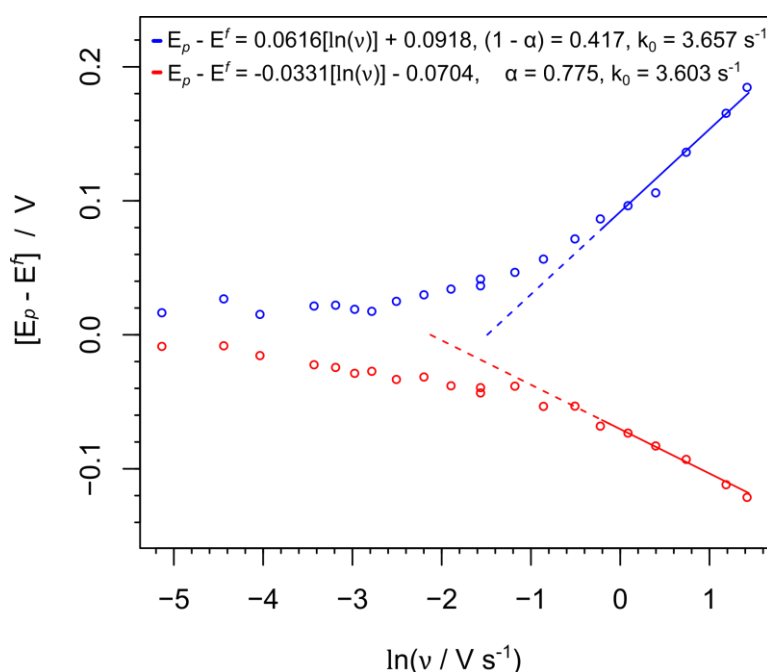


**Figure 2.18.** Trumpet plot showcasing the relationship between the natural logarithm of scan rate and the displacement of anodic (blue) and cathodic (red) peaks from the formal potential of the dominant background redox couple for **MWCNT A**-functionalised electrodes treated with *An6428-AA9*. Scans recorded at a range of scan rates at 298 K under  $\text{N}_2$  atmosphere in pH 7 buffer (20 mM sodium phosphate, 20 mM sodium acetate, 500 mM  $\text{Na}_2\text{SO}_4$ ).

The non-unity sum of the values of  $(1 - \alpha)$  and  $\alpha$  yielded from these linear regressions has an interesting implication. Studies based on surface-immobilised ferrocene-functionalised films have repeatedly found that the trumpet plots collected for these systems consistently yield non-unity sums of  $(1 - \alpha)$  and  $\alpha$ , due to a phenomenon related to imperfections in the structure of the film.<sup>257,258</sup> This is due to a disproportionate amount of charge being able to pass through defect points in the film which have ferrocene moieties in closer proximity to the underlying electrode surface, as lateral charge transfer between the ferrocene units allows the charge to be channelled to and from these points from across the whole film. This lateral charge transfer mechanism thus competes with the direct electron transfer of electrons between the electrode and the ferrocene units through the film.<sup>258</sup> It is fair to assume that the structure of drop-cast MWCNT films will be highly irregular, and thus the redox-active units on the MWCNTs in best electrical contact with the underlying electrode surface will behave akin in to the aforementioned defect ferrocene sites, with lateral charge transfer between the redox-active units allowing a disproportionate amount of charge to pass through them.

In order to gain even more information on the nature of the large “background” signal centred at  $\sim 0.41$  V vs SHE at pH 7, a dataset akin to that later described in **Section 3.2.3.1.2** was collected for **MWCNT A**-functionalised electrodes with adsorbed BSA films. This dataset has been sent to a collaborator for simulation, and no further information regarding these background-signals is available as-yet.

## 2.2.4 Electrochemical analysis of the putative An6428-AA9 redox couple.

### 2.2.4.1 Isolation and analysis

As detailed in **Appendix 2**, in spite of the non-ideal background electrode activity, the usage of a specially written package of codes allowed the putative An6428-AA9 signal to be isolated and fitted to the theoretical model described by **Equation 7 (Section 1.4.1)**. The results of this analysis (performed on the data in **Figure 2.10**) are tabulated in **Table 2.4**. The formal potential of this redox couple ( $E_{(O/R)}^f$ ) was determined to be 276 mV vs SHE at pH 7, and the shape of the signal is consistent with that expected for a one-electron redox couple ( $n_{app}$  is very close to unity). Due to the nature of the drop-cast MWCNT deposit, it was not practical to calculate/determine the electrode surface area, and accordingly for the purposes of signal fitting the electrode surface area was taken to be unity. This means that the coverages of the different electroactive species reported in **Table 2.4** are in fact indicative of the total molar quantity of these species present, rather than the molar quantity present per unit area.

**Table 2.4.** Parameters fitted to the baseline-subtracted signals in **Figure 2.10**, using **Equation 7 (Section 1.4.1)**, showing that the suspected *An6428-AA9* redox signal is characteristic of a 1 electron process. The exact surface area of the electrode cannot be easily determined due to the nature of the drop-cast MWCNT deposit. The surface area parameter of **Equation 7**,  $A$ , has thus been set to unity and rendered dimensionless. As such the coverages,  $\Gamma$ , in this table are indicative of the total molar quantity of electroactive species present, not the molar quantity present per unit area.

Parameter	Background 1	<i>An6428-AA9</i>	Background 2
$A$	1	1	1
$n_s$ cathodic	1	1	1
$n_s$ anodic	1	1	1
$n_{app}$ cathodic	1.05	1.03	1.06
$n_{app}$ anodic	0.87	0.94	1.05
Anodic peak potential / mV vs SHE	425	298	111
Cathodic peak potential / mV vs SHE	391	254	77
$E_{(O/R)}^f$ / V vs SHE	409	276	94
$\Gamma$ cathodic / pmol	109	24.0	16.6
$\Gamma$ anodic / pmol	153	27.1	15.2

The formal potential of the putative *An6428-AA9* signal is strongly dependant on pH, varying by -50 mV per pH unit (**Figure 2.19**). This is again in reasonable agreement with the -59 mV per pH unit that would be expected of redox transitions described by **Equation 19**, where the number of electrons transferred is during the redox couple is equal to the number of electrons transferred. The identity of the species that could be accepting a proton during the  $\text{Cu(II)} \rightarrow \text{Cu(I)}$  transition is however not yet clear, but a possible candidate could be the imidazole motif of histidine 147, which is a conserved residue between *LsAA9* and *An6428-AA9* (**Figure 2.7**), and is thus also likely to be in the secondary coordination sphere of the copper site of *An6428-AA9* (**Figure 2.20**). It has been suggested that histidine 147 may serve as a proton donor to a  $\text{Cu(II)}$ -superoxide species in *LsAA9*, and this step would have to occur after the reduction of the  $\text{Cu(I)}$  centre to  $\text{Cu(II)}$  (**Figure 2.3**).<sup>320</sup>

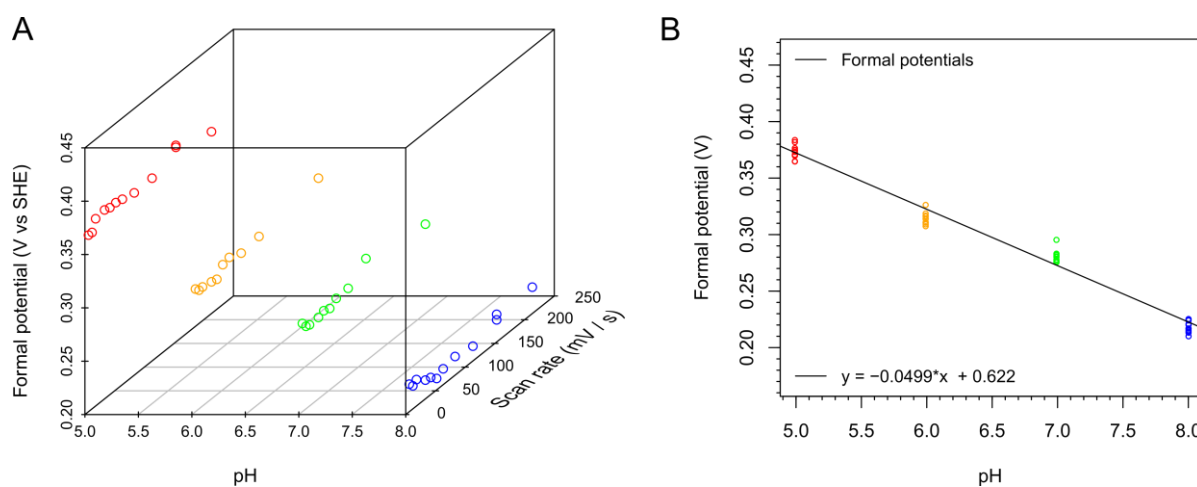


**Figure 2.19. A)** The midpoint potential of the putative *An6428-AA9* redox couple is constant for scan rates  $< 200 \text{ mV s}^{-1}$ , and thus reflects the formal potential of the redox couple for these scan rates. **B)** The relationship between formal potential and pH for the putative *An6428-AA9* redox couple. Scans recorded at a range of scan rates at 298 K under  $\text{N}_2$  atmosphere in buffer (20 mM sodium phosphate, 20 mM sodium acetate, 500 mM  $\text{Na}_2\text{SO}_4$ ) at the appropriate pHs, using GC electrodes drop-cast with **MWCNT A** and subsequently treated with *An6428-AA9*.

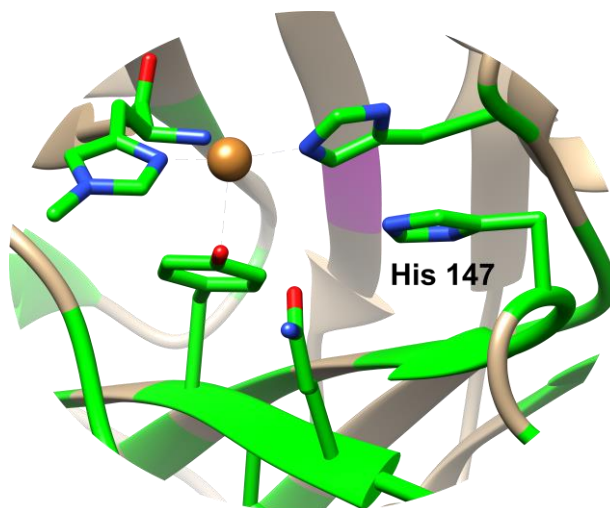


**Figure 2.20.** The mapping of the aligned residues from *An6428-AA9* and *LsAA9* (identified using the sequence alignments in **Figure 2.7**) onto the crystal structure of *LsAA9* (PDB: 5N05).<sup>300</sup> Aligned residues from *An6428-AA9* **Figure 2.7** are coloured green on the crystal structure of *LsAA9*.

Determination of the kinetics of electron transfer associated with the putative *An6428-AA9* signal is more difficult. FTaCV analysis of **MWCNT A**-functionalised electrodes treated with *An6428-AA9* is completely dominated by the redox signal at  $\sim 0.41$  V vs SHE, ruling out usage of this advanced technique for the determination of the rate constant for heterogeneous electron transfer ( $k_0$ ). Constructing a trumpet plot for the determination of an approximate value of the rate of  $k_0$  and  $\alpha$  also proved difficult to do with the putative *An6428-AA9* signal, as not only does the intensity of this signal decrease sharply with increasing scan rate, but it becomes increasingly hard to distinguish its contributions to the observed Faradaic signals from those of the dominant background signal, and beyond the irreversible limit of the redox couple, simulation of the signal using **Equation 7 (Section 1.4.1)** becomes inaccurate. As such, confidence in the trumpet plot constructed for the putative *An6428-AA9* signal and the values of  $\alpha$  and  $k_0$  it yields (**Figure 2.21**) is low.

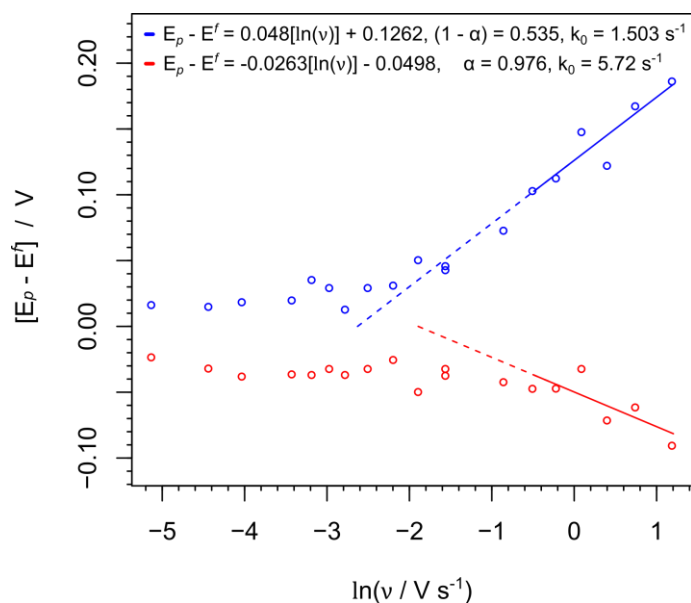


**Figure 2.21.** Trumpet plot showcasing the relationship between the natural logarithm of scan rate and the estimated displacement of anodic (blue) and cathodic (red) peaks from the formal potential of the putative *An6428-AA9* redox couple. Scans recorded at a range of scan rates at 298 K under  $N_2$  atmosphere in pH 7 buffer (20 mM sodium phosphate, 20 mM sodium acetate, 500 mM  $Na_2SO_4$ ).

### 2.2.5 Amperometric responses to $H_2O_2$ and oxygen

LPMOs are known to show peroxygenase activity, and as such *An6428-AA9* should be capable of catalysing  $H_2O_2$  reduction.<sup>356</sup> Amperometric experiments assaying the ability of the **MWCNT A**-functionalised electrode surfaces to catalytically reduce  $H_2O_2$  only showed catalytic current responses for nanotube films with adsorbed *An6428-AA9*, and not for nanotube films with adsorbed BSA (**Figure 2.22a**). The catalytic current was then isolated from the raw amperometry data (**Figure 2.22a**) by subtracting the background current (see **Section 8.2.4**, **Figure 8.6**). A correction was then applied to this isolated current which accounts for the slight but near-linear decrease observed in the catalytic current for a given  $[H_2O_2]$  with increasing time (see **Section 8.2.4**, **Figure 8.6**), which is likely due to a combination of a slowly decreasing capacitive current, protein desorption or possibly protein inactivation. The cathodic catalytic current ( $i_c$ ) for each value of  $[H_2O_2]$  was then determined, and **Equation 11** and **Equation 12** (see **Section 1.4.5**) were used to construct plots (**Figure 2.22b**) that enabled values for  $K_m^{app}$  and  $i_{max}$  to be determined (**Table 2.5**).

**Figure 2.22c**, and the standard errors reported in **Table 2.5**, illustrate that the values for  $K_m^{app}$  and  $i_{max}$  yielded by the first linear regression (**Figure 2.22b**, red) (**Table 2.5**) are not accurate, whereas those yielded by the second linear regression (**Figure 2.22b**, blue) (**Table 2.5**) and the non-linear regression (**Figure 2.22c**, green) (**Table 2.5**) can be used to closely simulate the experimental data.

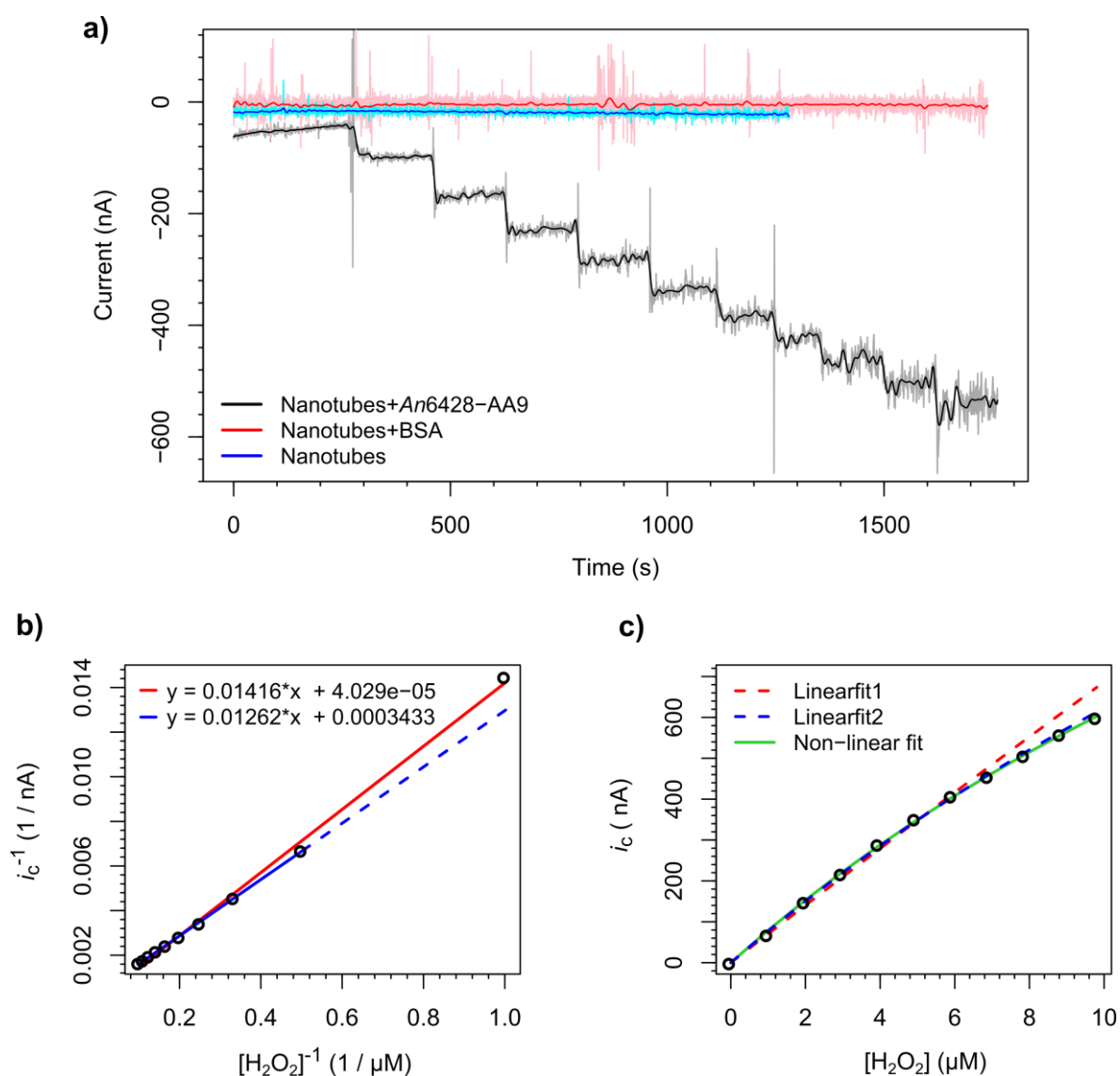


**Figure 2.22.** **a)** Amperometric experiments show that electrocatalytic  $\text{H}_2\text{O}_2$  reduction only occurs for samples of nanotubes (MWCNT A) drop cast onto a GC electrode and subsequently treated with An6428-AA9, and not for “plain” nanotubes or nanotubes treated with BSA. Amperometric traces were recorded by holding at a potential of 50 mV vs SHE, at 298 K under  $\text{N}_2$  atmosphere in pH 7 buffer (20 mM sodium phosphate, 20 mM sodium acetate, 500 mM  $\text{Na}_2\text{SO}_4$ ). Prior to recording these traces, 10 cyclic voltammograms (akin to those shown in **Figure 2.11**) were recorded, sweeping from -0.05  $\rightarrow$  0.95 V vs SHE at 113  $\text{mV s}^{-1}$ , thereby allowing the oxidative process that facilitates direct electron-transfer to An6428-AA9 to occur. **b)** Fitting of the cathodic currents to a Lineweaver–Burk equation (**Section 1.4.5, Equation 12**) gave two plausible linear fits, each yielding different values of  $K_m^{app}$  and  $i_{max}$ , which are tabulated in **Table 2.5**. **c)** The accuracy of these parameters was evaluated by using **Equation 11 (Section 1.4.5)** to simulate values of  $i_c$  and comparing the simulated dataset to the experimental dataset. Non-linear fitting of the experimental data to **Equation 11** was also used to yield values for  $K_m^{app}$  and  $i_{max}$ .

**Table 2.5.** Values of  $K_m^{app}$ ,  $i_{max}$  and  $k_{cat}$  yielded from the non-linear regression in **Figure 2.22c**.  $k_{cat}$  was calculated using **Equation 13**. The moles of An6428-AA9 enzyme present on the electrode surface ( $\Gamma \times A$  in **Equation 13**) was determined to be 12 → 18 pmol using baseline subtraction and simulation of the extracted signals (**Figure S5, Table S2**). The standard error is noted as “SE.”

Parameter	Linear fit 1	Linear fit 2	Non-linear fit
$K_m^{app} / \mu\text{M}$	351 (SE = 690)	36.8 (SE = 3.36)	29.8 (SE = 2.51)
$i_{max} / \mu\text{A}$	24.8 (SE = 48.5)	2.91 (SE = 0.24)	2.43 (SE = 0.16)
$k_{cat} / \text{s}^{-1}$	8.57 (SE = 1.68)	1.01 (SE = 0.22)	0.84 (SE = 0.18)

The values determined for  $K_m^{app}$  are in excellent agreement with those reported in the literature for NcLPMO9C (an AA9 LPMO from the fungus *Neurospora crassa*) catalysing  $\text{H}_2\text{O}_2$  reduction by 2,6-dimethoxyphenol (DMP), where DMP serves as a reducing agent that does not bind to NcLPMO9C.<sup>356</sup> The determined values for  $K_m^{app}$  are also within an order of magnitude of the earliest estimate of  $K_m^{app}$  for catalytic  $\text{H}_2\text{O}_2$  reduction by an LPMO,  $2.8 \pm 1.3 \mu\text{M}$  (which was derived for a chitin-active AA10).<sup>324</sup> The moles of enzyme present on the electrode surface was calculated to be 12 → 18 pmol via baseline subtraction and simulation of the extracted signals (See **Appendix 2, Figure S5, Table S2**), and **Equation 13** (see **Section 1.4.5**) was then used to determine the enzyme turnover number ( $k_{cat}$ ) for An6428-AA9 reducing  $\text{H}_2\text{O}_2$ . The most accurate simulation of the experimental data was afforded using the parameters yielded from the non-linear regression (**Figure 2.22c**, green) (**Table 2.5**), and thus the most likely value of  $k_{cat}$  is  $0.84 \text{ s}^{-1}$  (with a standard error of  $0.18 \text{ s}^{-1}$ ) (**Table 2.5**). A significant portion of the error in this value is derived from the uncertainty in quantity of An6428-AA9 present on the electrode surface (15 pmol, with a standard error of 3 pmol). A literature value of  $k_{cat}$  for LPMO catalysed  $\text{H}_2\text{O}_2$  reduction could not be found, nor could it be calculated using the literature values reported for the  $V_{max}$  of NcLPMO9C-catalysed  $\text{H}_2\text{O}_2$  reduction by DMP; the oxidation of DMP was shown to be the rate limiting step in the reaction.<sup>356</sup> Although only a crude measure of the rate of heterogeneous electron transfer  $k_0$ , **Figure 2.21** does suggest that  $k_0$  is greater than  $1 \text{ s}^{-1}$ , and thus it is likely that heterogeneous electron transfer between the electrode and An6428-AA9 is not the rate limiting step in the electrocatalytic reduction of  $\text{H}_2\text{O}_2$ , and that the  $k_{cat}$  values yielded are intrinsic to the An6428-AA9 itself.

LPMOs are known to generate  $\text{H}_2\text{O}_2$  in the presence of dioxygen and reducing agent,<sup>325</sup> but there does not appear to be any reported  $k_{cat}$  or  $K_m^{app}$  values in the literature for catalytic dioxygen reduction to  $\text{H}_2\text{O}_2$  by an LPMO.<sup>356</sup> An amperometric experiment was therefore conducted in an attempt to measure the ability of An6428-AA9 to catalytically reduce dioxygen. Mixtures of dinitrogen and dioxygen, of increasing dioxygen content, were successively bubbled through the electrolyte while the electrode potential was held at either 46 or 146 mV vs SHE. For both these applied potentials

however, the results remained the same; the plain MWCNT-functionalised GC electrode surfaces were superior dioxygen reduction catalysts compared to the MWCNT-functionalised GC electrodes treated with *An6428-AA9* (**Figure 2.23**, **Figure 2.24**), which unfortunately meant that determining  $k_{cat}$  or  $K_m^{app}$  for dioxygen reduction by *An6428-AA9* was not possible, although it did imply that *An6428-AA9* was indeed immobilised on the MWCNT surface!

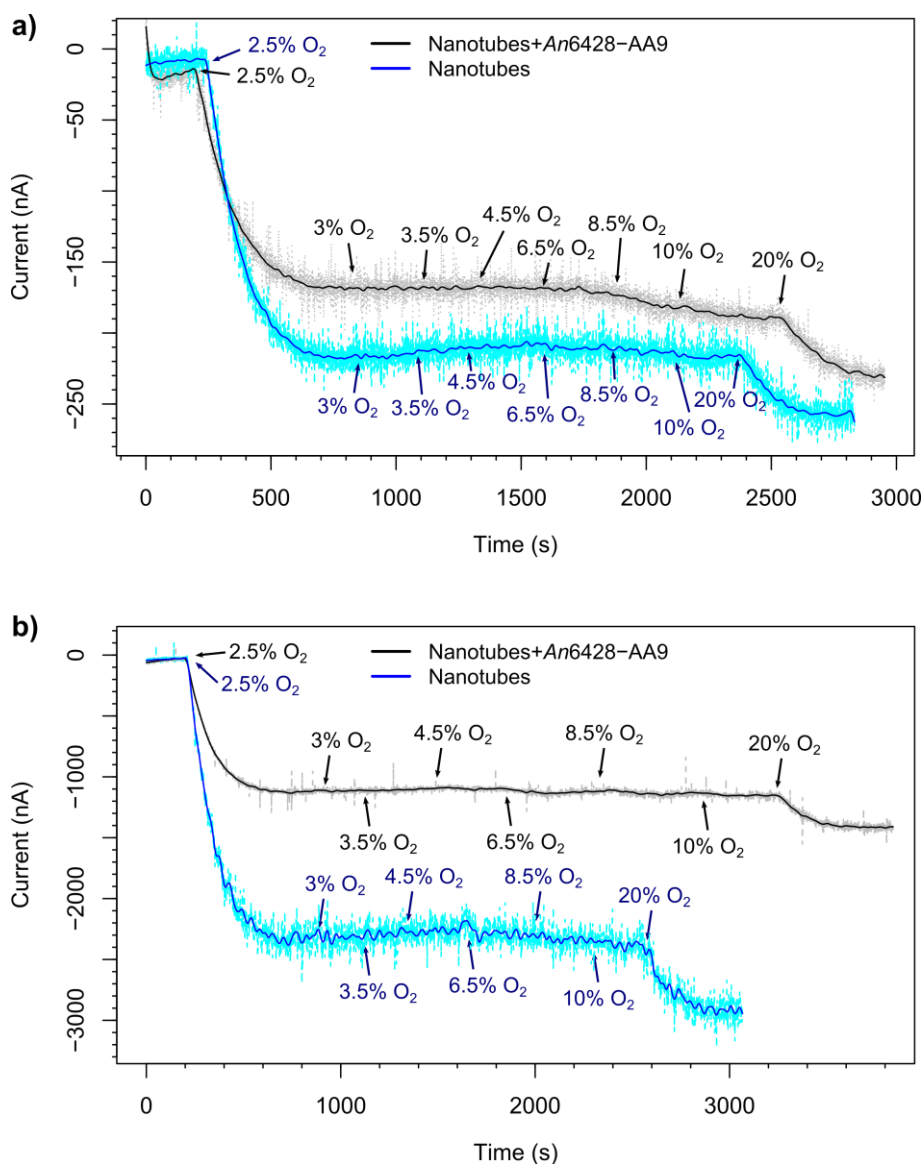


**Figure 2.23.** Amperometric experiments showing electrocatalytic  $O_2$  reduction by samples of nanotubes drop-cast onto a GC electrode. It can be seen that treatment of the drop-casted nanotubes (**MWCNT A**) with *An6428-AA9* does not improve their ability to function as an  $O_2$  electroreduction catalyst. **a)** Amperometric traces recorded by holding at a potential of 150 mV vs SHE, at 298 K under  $N_2$  atmosphere in pH 7 buffer (20 mM sodium phosphate, 20 mM sodium acetate, 500 mM  $Na_2SO_4$ ). **b)** Amperometric traces recorded by holding at a potential of 50 mV vs SHE, at 335 K under  $N_2$  atmosphere in pH 7 buffer (20 mM sodium phosphate, 20 mM sodium acetate, 500 mM  $Na_2SO_4$ ). Prior to recording these traces, 10 cyclic voltammograms (akin to those shown in **Figure 2.11**) were recorded, sweeping from  $-0.05 \rightarrow 0.95$  V vs SHE at  $113 \text{ mV s}^{-1}$ , thereby allowing the oxidative process that facilitates direct electron-transfer to *An6428-AA9* to occur.



This is not surprising; while conductive and semi-conductive carbon allotropes are commonly used as working electrodes in PFE due to their ability to facilitate redox protein adsorption, a notorious annoyance associated with their usage is their talent for electrocatalytic dioxygen reduction.<sup>357</sup> Indeed, this is one of the main reasons PFE is normally conducted under a nitrogen atmosphere. The poorer electrocatalytic response of the surfaces treated with *An6428-AA9* can be readily rationalized by considering that adsorbed *An6428-AA9* will partially block the MWCNT surface, or otherwise change its environment in such a way as to render it a poorer electroreduction catalyst. Whereas some copper redox-enzymes, such as bilirubin oxidase,<sup>208</sup> are highly efficient electrocatalysts of dioxygen reduction that give unmistakably strong current responses,<sup>208</sup> the loss of MWCNT electrocatalytic activity is clearly not offset by strong electrocatalytic activity from the immobilised *An6428-AA9*.

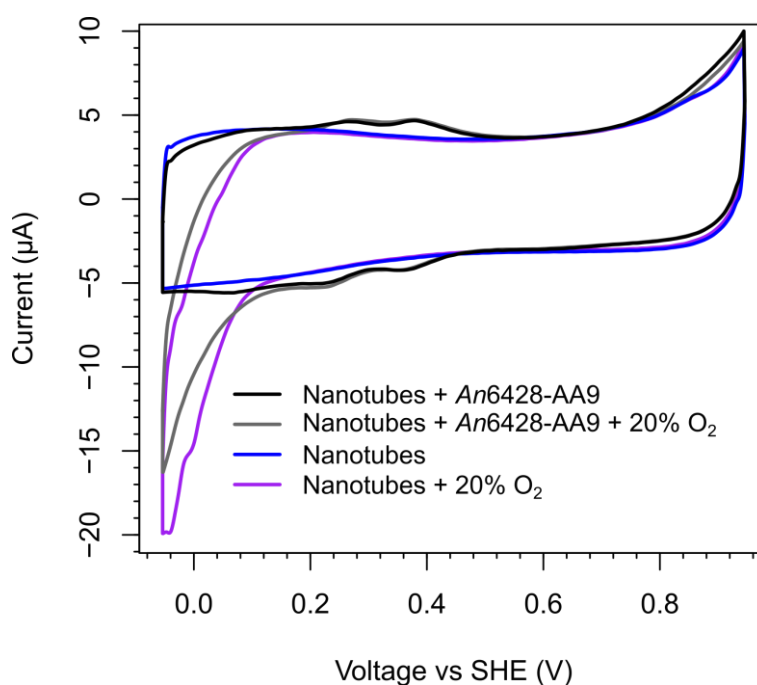


**Figure 2.24.** Cyclic voltammograms illustrating electrocatalytic  $O_2$  reduction by samples of nanotubes drop-cast onto a GC electrode. It can be seen that treatment of the drop-cast nanotubes (**MWCNT A**) with *An6428-AA9* does not improve their ability to function as an  $O_2$  electroreduction catalyst. Scans recorded at  $18 \text{ mV s}^{-1}$  at 335 K under either  $N_2$  or  $N_2 + 20\% O_2$  atmosphere in pH 7 buffer (20 mM sodium phosphate, 20 mM sodium acetate, 500 mM  $Na_2SO_4$ ), commencing at the most negative potential. Prior to recording these traces, 10 cyclic voltammograms (akin to those shown in **Figure 2.11**) were recorded, sweeping from  $-0.05 \rightarrow 0.95 \text{ V vs SHE}$  at  $113 \text{ mV s}^{-1}$ , thereby allowing the oxidative process that facilitates direct electron-transfer to *An6428-AA9* to occur.

### 2.3 Summary and conclusions

Electroactive immobilisation of the LPMO *An6428-AA9* was successfully achieved by adsorption onto MWCNTs, and the reduction potential of *An6428-AA9* was directly measured as 264 mV vs SHE at pH 7 at 25 °C. Only a single additional redox signal was observed for MWCNTs treated with *An6428-AA9*

compared to MWCNTs treated with BSA (or DsbA mutants), which suggests that only the copper centre of the An6428-AA9 was exchanging electrons with the underlying electrode surface, and that other residues, such as the active-site axial tyrosine residue, were not redox-active over the potential windows that were probed. The first reported amperometric assay of the rate of H<sub>2</sub>O<sub>2</sub> reduction by an LPMO was also conducted, and the catalytic current response almost perfectly followed Michaelis–Menten kinetics, allowing both the  $K_m^{app}$  and  $k_{cat}$  of this process to be determined as  $29.8 \pm 2.51 \mu\text{M}$  and  $0.84 \pm 0.18 \text{ s}^{-1}$  respectively. While no literature system reports a  $k_{cat}$  for H<sub>2</sub>O<sub>2</sub> reduction by an LPMO, a  $K_m^{app}$  of  $29.8 \pm 2.51 \mu\text{M}$  is in agreement or consistent with those reported in the literature.<sup>324,356</sup> This system remains far from ideal however, as large background signals originating from the carbon nanomaterial overlap with those originating from the An6428-AA9 itself. In addition, although LPMOs are known to be capable of dioxygen reduction even in the absence of substrate to H<sub>2</sub>O<sub>2</sub>,<sup>325</sup> the carbon nanomaterial is itself a good dioxygen reduction electro-catalyst, meaning amperometric measurement of the rate of dioxygen reduction by An6428-AA9 was not achieved. This is regrettable as the direct comparison of the behaviour of LPMOs in the presence of both oxygen and H<sub>2</sub>O<sub>2</sub> could have been used to gain valuable mechanistic insight, especially if the LPMO were capable of accepting soluble substrates while immobilised on the electrode surface.

It seems clear that the interactions facilitating the electroactive immobilisation of An6428-AA9 are complicated, and the conditions required to bring them into effect – i.e. applying a potential higher than 0.8 V vs SHE as an activation step - were only discovered by chance, and further investigation into the actual nature of the chemical processes involved (i.e. the possible formation of redox-active amino bridges) will be the subject of future research. It would be desirable to move to a system that could be far more easily understood and be specially chosen to showcase the properties of An6428-AA9 in the absence of background signals or background electrocatalytic activity. The development of a strategy that would allow for covalent site-selective crosslinking of An6428-AA9 to an electrode material that is a poor dioxygen reduction catalyst in such a manner that would still allow facile direct electron transfer would seem ideal. Site-selective ligation to An6428-AA9 could be achieved by either targeting the most-exposed tyrosine residue in the enzyme, which is on the binding face (**Figure 2.8**), or by incorporating non-canonical functional groups into the protein, such as azides, alkynes or aldehydes. While there are many established methods for performing selective ligations to tyrosine residues or non-canonical functional groups, a method that allows any site-selectively ligated protein to become immobilised onto any chosen electrode surface does not yet exist.

# Chapter 3

The functionalisation of electrode  
surfaces with amine moieties

## Chapter 3. The functionalisation of electrode surfaces with amine moieties

### 3.1 Introduction

#### 3.1.1 The utility of amine-functionalised surfaces

Methods that allow for the electroactive immobilisation of redox proteins onto electrode surfaces often seek to modify the electrode surface so that it can interact with the redox protein more favourably by non-covalent interactions, or covalently react with moieties on the protein itself. It was hypothesised that a versatile parent platform from which a multitude of different functionalisations could be developed via single-step functionalisations would be very useful. To this end, amines represent a useful functional group to introduce onto electrode surfaces, as they can be used to couple on more interesting functionalities via either amide bond formation, imine formation, reductive amination or alkylation (**Figure 3.1**). The ability to derivatise an electrode surface with amines and subsequently form amide bonds with carboxylic acid functionalised molecules seemed a particularly attractive prospect; many commercially available bio-orthogonally ligating/interacting probes have carboxylic acid motifs, and several existing literature methodologies describe the installation of amine-functionalised monolayers onto electrode surfaces for usage in amide coupling reactions.<sup>150,217,358</sup> Amines may also serve to change the electrostatics of the electrode surface, introducing positive charges at neutral pH which could interact favourably with proteins rich in negatively-charged carboxylate side chains.

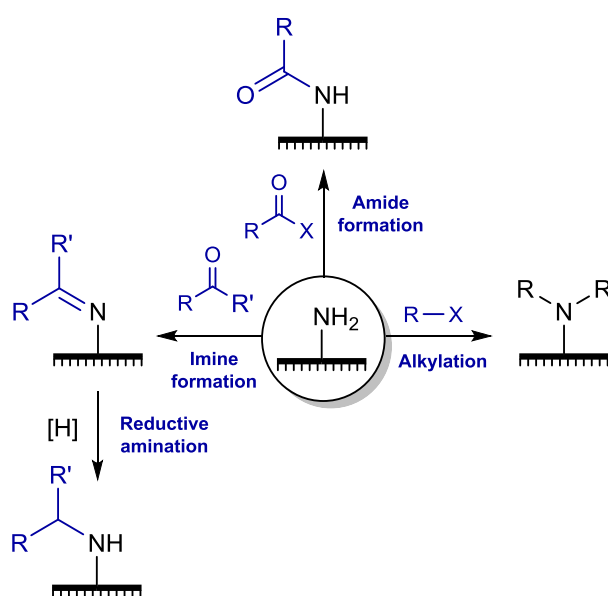


**Figure 3.1.** The usage of surface-confined amines for subsequent electrode derivatisation.

### 3.1.2 Common approaches for amine-functionalisation of electrode surfaces

Several families of approaches exist for the functionalisation of electrode surfaces with amines. The first involves the use of amine-terminated alkane-thiol self-assembled monolayers (SAMs, see **Section 1.3.2.1**).<sup>359,360</sup> While usage of alkane-thiol SAMs may be an easy and controllable way of achieving monolayer amine functionalisation, this approach can only be applied when using electrode surfaces made from a select few metals – i.e. metals which that do not form stable oxide layers, such as gold, palladium and mercury (see **Chapter 1**).<sup>127,128</sup>

Electrochemical oxidation of diamines or mono-protected diamines represents another approach.<sup>150,361,362</sup> In this method species such as ethylenediamine,<sup>362</sup> hexamethyldiamine<sup>361</sup> or mono-N-Boc-hexamethylenediamine<sup>150</sup> are subjected to a one-electron electrochemical oxidation, generating a nitrogen-centred radical cation which attacks the electrode surface, leading to bond formation between the surface and the nitrogen centre (**Figure 3.2**). In cases where non-protected diamines are used, it seems likely that double addition of the amine to the electrode surface will also occur. However, when a mono-protected diamine is used, controlled functionalisation of the surface as a monolayer of primary aliphatic amines can be achieved, even though an extra step is required to deprotect the terminal amine functionalities (**Figure 3.2**). This technique can also be applied in the preparation of mixed monolayers, by using different protecting groups on the mono-protected diamines which undergo deprotection under different conditions.<sup>150</sup> This technique can be applied both to semiconductors and metal surfaces, but requires a relatively harsh oxidative potential to be applied, ranging from + 1.5 V<sup>362</sup> to + 2.3 V<sup>150</sup> (vs SHE), depending on the diamine being used. These electrochemical oxidations are beyond the redox stability window of water, and as such are carried out in organic electrolyte solutions and use a non-aqueous reference electrode. Additionally, the highly oxidising potentials that would have to be used to use perform electrochemical grafting of amines would be incompatible with functional groups sensitive to oxidation, and while this would not represent a problem for the functionalisation of surfaces with amine groups, it could represent a problem if the technique were to later be applied to a more complicated molecule.

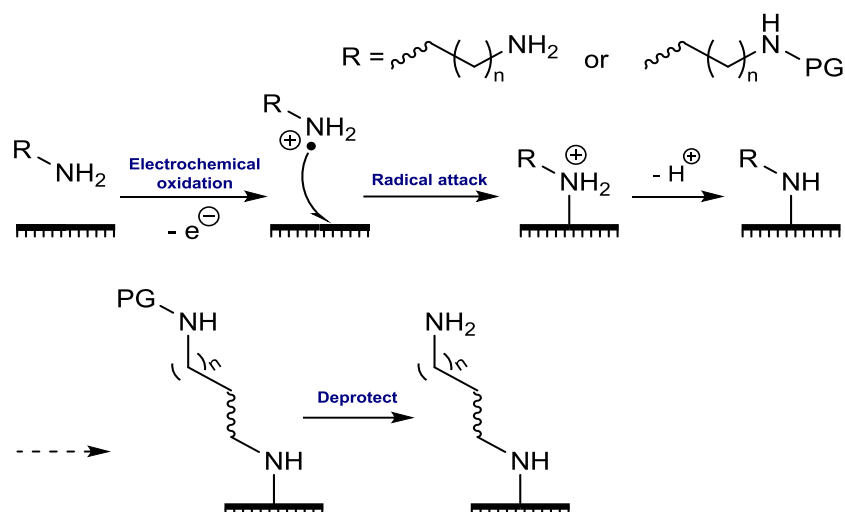


**Figure 3.2.** The electrochemical oxidation of diamines to yield amine functionalised electrode surfaces. Protecting groups are denoted as “PG.”

Introduction of functionality to electrode surfaces is also possible via carboxylic acid oxidation (Kolbe electrolysis, **Figure 3.3**),<sup>168</sup> and thus the oxidation of amino acid derivatives could hypothetically be used to achieve surface amine functionalisation. However, the potentials required to perform carboxylic acid oxidation are also relatively harsh; even when a relatively stable benzylic radical can be generated a potential of ca. + 1.3 V (vs SHE) has to be applied.<sup>363</sup> A protected amine group would thus have to be used in order to avoid simultaneous amine oxidation (**Figure 3.3**). The usage of a species such as 3-nitropropionic acid would hypothetically be suitable, as the nitro groups could be electrochemically reduced to amines after the oxidative grafting step (**Figure 3.4**). However, due to the harsh potentials that must be applied, the usage of carboxylic acid oxidation holds no real advantage over the usage of diamine oxidation. Reaction of a diamine with a carboxylic acid-functionalised surface is also possible,<sup>364</sup> and while several literature methods exist for the functionalisation of electrode surfaces with carboxylic acids, achieving amine functionalisation via this method would seem inefficient.

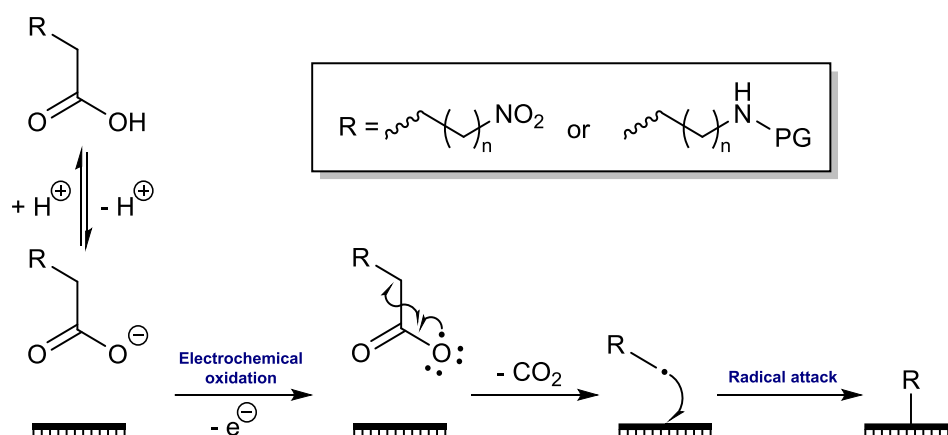


**Figure 3.3.** The potential usage of electrochemical oxidation of carboxylic acids to yield amine functionalised electrode surfaces. Protecting groups are denoted as “PG.”

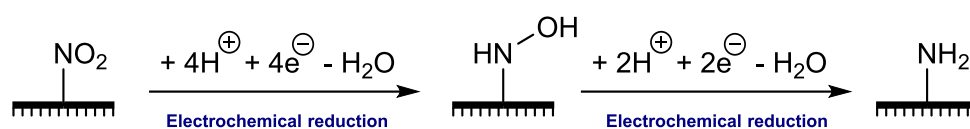


**Figure 3.4.** The electrochemical reduction of nitro groups to yield amine functionalities.

Aryl diazonium electro-grafting is a very flexible method that can be used to introduce a diverse range of functional groups to electrode surfaces. The flexibility of this approach is owed to its applicability to any conductive surface, and the procedure only requiring the application of mild reducing potentials (**Section 1.3.2.5.**). Diazonium electro-grafting can also be performed under an ambient atmosphere on the benchtop, an important practical consideration. Diazonium surface functionalisation approaches can even be applied to dielectric materials.<sup>162,365</sup> Diazonium electro-grafting was therefore the methodology explored in this Chapter.

### 3.1.3 Monolayer amine-functionalisation of electrode surfaces using diazonium chemistry

Diazonium electro-grafting commonly results in a thick multilayer coverage of grafted moieties on the electrode surface. This is a problem because the rate of electron transfer through electro-grafted diazonium films decreases exponentially with respect to film thickness.<sup>366</sup> As such, the functionalisation of the electrode surface with a monolayer would be preferable to functionalisation with a multilayer, allowing for faster electron transfer between immobilised molecules and the electrode surface. A monolayer-functionalised surface should also be more uniform, reducing the dispersion present in any immobilised sample.

Although the general practice of diazonium electro-grafting to electrode surfaces is introduced in **Section 1.3.2.5**, the usage of diazonium cations to introduce amine monolayers to electrode surfaces requires special considerations. Firstly, the synthesis of aryl diazonium salts typically involves the treatment of an aniline (also known as an aryl amine) with the electrophilic nitrosonium cation (**Figure 3.5**), and thus care has to be taken to avoid unwanted side reactions between the nitrosonium cation and the amine functionalities that are to be introduced onto the electrode surface. This is especially true when attempting to introduce aliphatic primary amines onto the electrode surface, as the reaction of aliphatic primary amines with the nitrosonium cation yields highly unstable aliphatic diazonium cations, which readily lose  $N_2$  and react via a myriad of undesired substitution, elimination, and carbocation rearrangement reactions (**Figure 3.6 panel a**).<sup>367</sup> Accidentally setting a reaction such as this in motion could result in an explosion. Secondary amines also react with nitrosonium cations to form highly carcinogenic *N*-nitrosamines (**Figure 3.6 panel b**),<sup>368,369</sup> and are especially unsuited for introduction onto electrode surfaces via diazonium electro-grafting as they perform more poorly in amide bond forming reactions than primary amines.

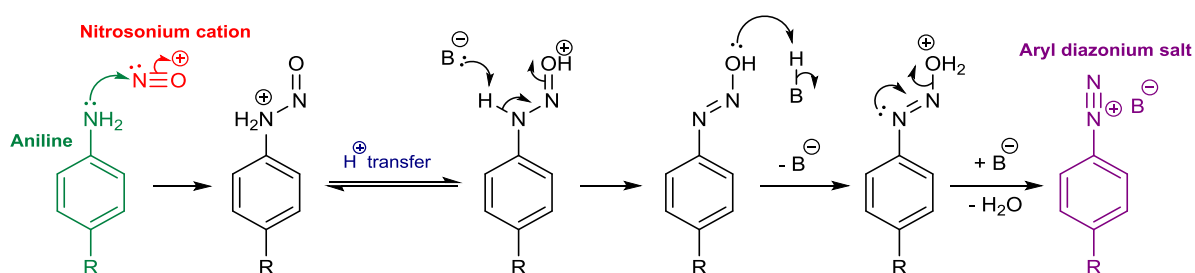


**Figure 3.5.** The diazotisation of an aniline via reaction with the nitrosonium cation. Bases are denoted “B”.

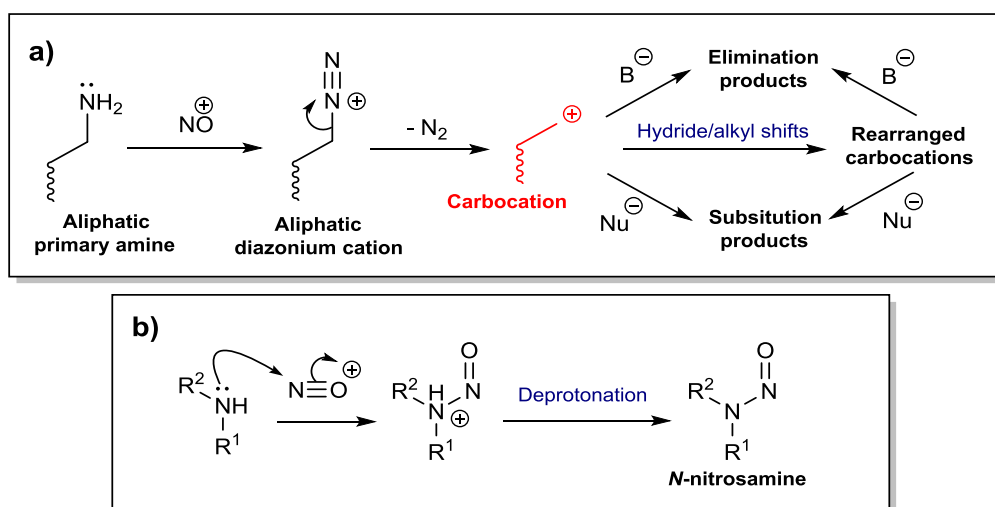


**Figure 3.6.** The reactions of **a)** aliphatic primary amines and **b)** secondary amines with the nitrosonium cation ( $NO^+$ ).



Literature approaches exist that circumnavigate the incompatibility of amine groups with the nitrosonium cation when using aryl diazonium cations to functionalise electrode surfaces with amine groups, and several of these approaches also facilitate the monolayer functionalisation of the electrode surfaces. The most popular approaches use 4-nitrobenzenediazonium cations - which are commercially available as 4-nitrobenzene diazonium tetrafluoroborate<sup>83,169,170,181-183,370-373</sup> (**Figure 3.6 a**) or can be prepared *in situ* via the diazotisation of 4-nitroaniline<sup>184,372,373</sup> - in the diazonium electro-grafting step, and then subsequently electrochemically reduce the electro-grafted nitrophenyl groups to anilines (see **Figure 3.4**).<sup>83,169,170,173,181-184,370-374</sup> The commercial availability of pure 4-nitrobenzene diazonium tetrafluoroborate also allows the diazonium electro-grafting to be performed under conditions compatible with the usage of species such as 2,2-diphenyl-1-picrylhydrazyl (DPPH, **Figure 3.6 a**), which can help facilitate monolayer functionalisation.<sup>169,170,173</sup> Literature diazonium electro-grafts performed in the presence of DPPH have been conducted in acetonitrile<sup>169,170,173</sup> (DPPH is insoluble in water), and a recent study suggests that acetonitrile is directly involved in the mechanism via which DPPH suppresses multilayer electro-grafting.<sup>173</sup>

DPPH is a radical species, and originally it was thought that DPPH functioned as a radical scavenger.<sup>169,170</sup> It was thought that while aryl radicals produced via the electrochemical reduction of aryl diazonium salts could attack and graft onto clean electrode surfaces very rapidly, the attack of aryl radicals on aryl functionalities already grafted to electrode surfaces was slow enough to allow them to be intercepted by DPPH (at appropriately high DPPH concentration) and undergo radical coupling.<sup>169,170</sup> Indeed, DPPH is capable of radical coupling with aryl radicals, as is evidenced by the isolation of a compound reported to be 2-[4-(4-nitro)phenyl]-2-phenyl-1-picrylhydrazine (shown on the right in **Figure 3.6 a**), which was obtained by the electrolysis of a solution containing DPPH and 4-nitrobenzene diazonium tetrafluoroborate.<sup>170,173</sup> As a point of intrigue however, upon closer examination it is difficult to justify the formation of this product when considering the resonance forms of DPPH. The <sup>1</sup>H-NMR data reported for this species describes 16 protons in 10 environments, but 2-[4-(4-nitro)phenyl]-2-phenyl-1-picrylhydrazine would only be expected to have 9 proton environments and the published <sup>1</sup>H-NMR spectrum appears to show additional aromatic signals to be present. I propose the possibility that an alternative regioisomer may be the product of the DPPH radical coupling reaction, 1-(4'-nitro-[1,1'-biphenyl]-3-yl)-1-phenyl-2-(2,4,6-trinitrophenyl)hydrazine (**Figure 3.6 b**), as the formation of this product can be justified by considering the resonance forms of DPPH and this product would be expected to have more aromatic proton environments. It has been reported in ref [170] that no radical-coupled product is obtained when comparable electrolysis is conducted using a DPPH analogue with bulky alkyl substituents at the 4-positions of the aromatic rings,<sup>173</sup> but it remains possible that it was not the occupancy of the 4-positions that prevented the

radical coupling reaction, but rather that steric hindrance from the bulky alkyl groups hindered coupling to the 3-positions.

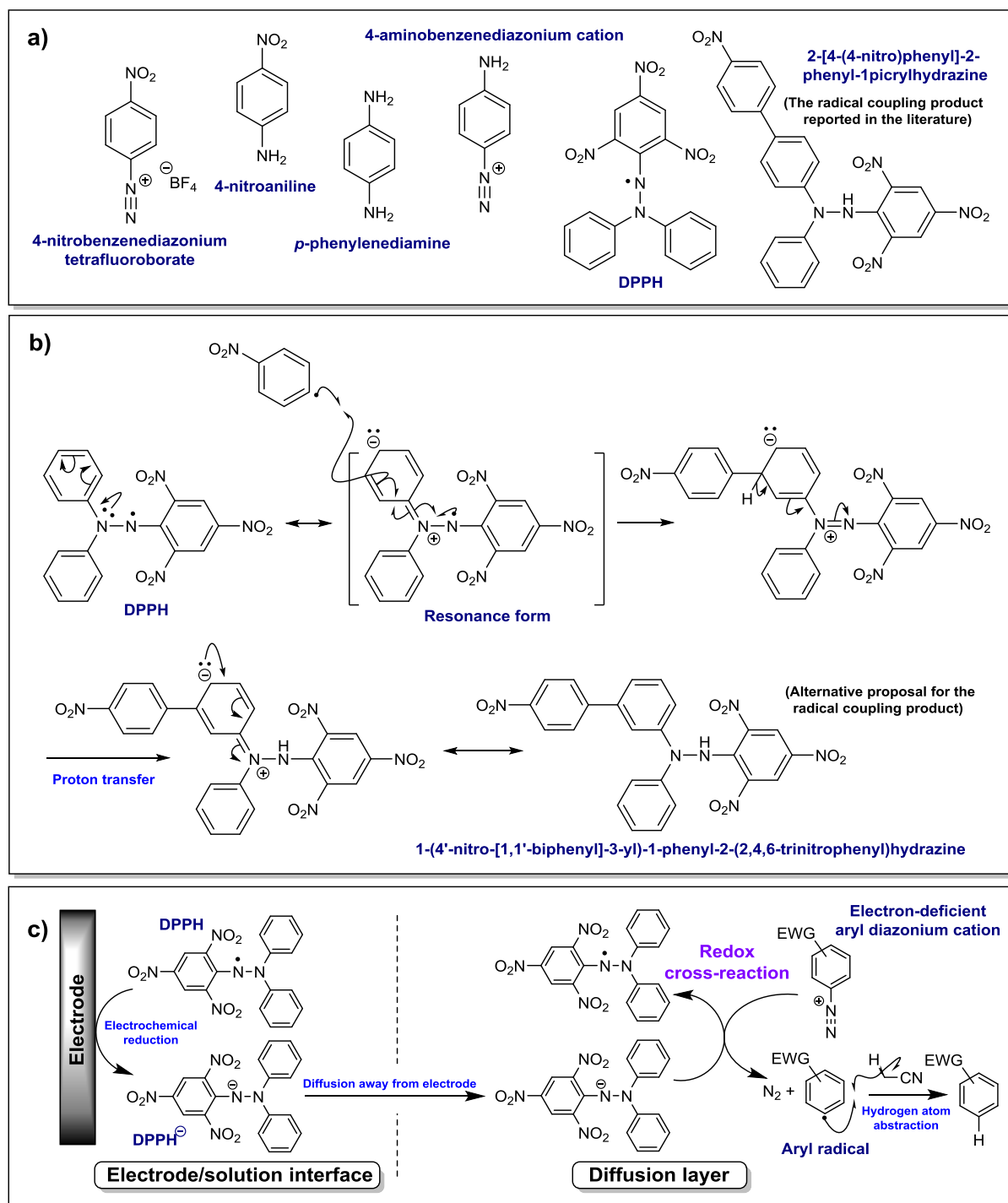


**Figure 3.7.** **a)** The structures of 4-nitrobenzene diazonium tetrafluoroborate, 4-nitroaniline, p-phenylenediamine, DPPH, and the reported radical scavenging product isolated during electro-grafting of 4-nitrobenzenediazonium in the presence of DPPH: 2-[4-(4-nitro)phenyl]-2-phenyl-1-picrylhydrazine.<sup>170</sup> **b)** Hypothetical mechanism to yield 1-(4'-nitro-[1,1'-biphenyl]-3-yl)-1-phenyl-2-(2,4,6-trinitrophenyl)hydrazine as the radical scavenging product produced during electro-grafting of 4-nitrobenzenediazonium in the presence of DPPH. **c)** Postulated mechanism via which redox cross-reactions between the DPPH anion and aryl diazonium cations limit multilayer electro-grafting, as described in ref [173].

Regardless of the nature of the coupling reaction between DPPH and aryl radicals, new evidence suggests that DPPH limits multilayer diazonium electro-grafting via redox cross-reactions rather than by radical scavenging.<sup>173</sup> The postulated mechanism for this process is shown in **Figure 3.6 c**.<sup>173</sup> The process begins with the reduction of DPPH into the DPPH anion (DPPH<sup>-</sup>, the most likely structure of which<sup>375</sup> is depicted in **Figure 3.6 c**) at the electrode surface/solution interface. DPPH<sup>-</sup> subsequently diffuses away from the electrode surface into the diffusion layer, whereafter it undergoes redox cross-reactions with aryl diazonium cations, regenerating DPPH and generating aryl radicals (**Figure 3.6 c**).<sup>173</sup> Having been generated at a distance from the electrode surface, the majority of aryl radicals will have abstracted a hydrogen atom from the acetonitrile solvent before they reach the electrode surface,<sup>173</sup> and thus the concentration of aryl radicals at the electrode surface is low, and therefore monolayer formation (which is thought to be a rapid process<sup>170</sup>) is favoured over multilayer formation (which is thought to occur more slowly<sup>170</sup>).<sup>173</sup>

It should be noted that DPPH cannot be used to enforce monolayer regimes in all diazonium electro-grafting processes however, as DPPH is only effective at arresting multilayer formation when performing electro-grafting with electron-deficient diazonium cations (i.e. those substituted with -M groups).<sup>169,371</sup> It has been suggested that this is due to multilayer formation being able to proceed via non-radical mechanisms (such as electrophilic aromatic substitution, which counts for the inclusion of azo linkages into many multilayer diazonium films) if strongly electron withdrawing substituents are not present.<sup>169,371</sup> However, in light of the new evidence that DPPH suppresses multilayer formation via redox cross-reactions,<sup>173</sup> another factor may also be at play. It could be suggested that the DPPH anion is not as effective at reducing electron-rich (i.e. harder to reduce) aryl diazonium species, as a lower difference in the reduction potentials of two species results in a lower kinetic rate constant for their redox cross-reaction (as described by Marcus theory),<sup>376</sup> and as such the arresting of multilayer formation via redox cross-reactions would be less effective when electron-rich diazonium cations are used. Indeed, ref [173] describes the usage of various electro-reducible molecules as agents to modulate the degree of electro-grafting of 4-nitrobenzene diazonium tetrafluoroborate, and reports that electro-reducible species with lower formal reduction potentials than DPPH are more effective than DPPH at inhibiting diazonium electro-grafting (as anions derived from difficult-to-reduce species are themselves more powerful reducing agents).<sup>173</sup> It remains to be seen if electro-reducible species with lower formal reduction potentials than DPPH are in any way effective at arresting multilayer film formation from electron-rich aryl diazonium cations.

The isolation and storage of pure diazonium salts can be inconvenient as diazonium salts are liable to decompose, and as such methods for the generation of diazonium cations *in situ* are often used.<sup>184,185</sup> The most common approach is to diazotise an aniline precursor via treatment with NaNO<sub>2</sub> in the presence of acid (which generates the nitrosonium cation *in situ*),<sup>184,185</sup> although an interesting variation of this *in situ* electro-grafting method is to electrochemically reduce a nitrophenyl precursor to an aniline (using the working electrode) in the presence of NaNO<sub>2</sub> and acid (**Section 1.3.2.5, Scheme 1.1**).<sup>163,377</sup> An interesting example of *in situ* diazonium electro-grafting being used for introducing aniline functionality onto electrode surfaces is the treatment of an excess of *p*-phenylenediamine (**Figure 3.7 a**) with a source of the nitrosonium cation, such that in the majority of cases only one aryl amine functional group becomes diazotized and the 4-aminobenzediazonium cation is generated *in situ* prior to performing electro-grafting.<sup>185</sup> However, while suitable for multilayer functionalisation of electrode surfaces,<sup>185</sup> achieving monolayer functionalisation using 4-aminobenzediazonium cation solutions could prove challenging as this diazonium cation does not offer an easy way to control the thickness of electro-grafted films. In addition, the usage of NaNO<sub>2</sub> as a diazotizing agent often necessitates aqueous conditions or water as a co-solvent, which causes compatibility issues with hydrophobic reagents which could be used to control the thickness of electro-grafted films, such as DPPH.

Attempts can be made to control electro-grafted film thickness by controlling the quantity of charge consumed during the electro-grafting step<sup>162</sup> via imposing strict control over the experimental conditions, i.e. the diazonium cation concentration, the duration of the electro-grafting procedure, and the potential applied across the working electrode,<sup>378</sup> as in general applying reducing potentials for shorter periods of time results in less diazonium electro-grafting and a thinner electro-grafted film. While this approach can indeed facilitate the formation of monolayers or even sub-monolayers, using such an approach requires optimisation for each different diazonium cation and electrode material used, and can be poorly reproducible.<sup>378</sup> A more advanced approach for enforcing monolayer regimes is the usage of specially-synthesised calix[4]arene-diazonium salts,<sup>378-381</sup> and are also several publications show that performing diazonium electro-grafting in ionic liquid solvents may help curb multilayer formation,<sup>371-374</sup> and the usage of certain ionic liquids may also allow for electro-grafting to be performed with diazonium cations generated *in situ*.<sup>372,373</sup>

Even though care must be taken to avoid reactions between aliphatic amines and nitrosonium cations, aliphatic amines are more nucleophilic than aryl amines and thus are better suited to amide bond coupling reactions.<sup>197,382</sup> As such, while the installation of aliphatic amine functionality onto electrode surfaces via diazonium electro-grafting may at first seem more challenging than installing aryl amine functionality, success in this endeavour may ultimately yield a platform more amenable to

subsequent derivatisation. Usage of diazonium cations functionalised with protected aliphatic amines has proven very useful in this regard, as the protecting groups not only prevent reaction of the aliphatic amines with nitrosonium cations, but can also help facilitate monolayer functionalisation due to sterically shielding the “root” aromatic group from attack<sup>197</sup> and/or by providing an additional aromatic system to which much of the multilayer film becomes anchored, application of deprotecting chemistry to remove the aromatic protecting group thereby strips the electrode of its thick inhomogeneous multilayer and instead leaving a thin, near-monolayer or monolayer coverage of amine moieties (**Figure 3.8**).<sup>171,197</sup> To this end a 2012 publication by Hauquier et al. details the usage of phthalimide protecting group chemistry to facilitate the formation of near-monolayers of 2-phenylethan-1-amine via diazonium electro-grafting,<sup>171</sup> and a 2015 publication by Downard and co-workers details the usage of Boc or Fmoc protecting group chemistry to install monolayers or near-monolayers of benzylamine functionality to electrode surfaces (**Figure 3.8**).<sup>197</sup> The Fmoc protecting group enforces a monolayer regime more strictly than the Boc group.<sup>197</sup> There is also literature precedent of the application of protecting group chemistry being used to ensure monolayer/near-monolayer electro-grafting regimes in the functionalisation of electrode surfaces with, aldehydes<sup>383</sup> thiols,<sup>384</sup> and carboxylic acids,<sup>385</sup> and thus the approaches of Downard and co-workers<sup>197</sup> and Hauquier et al.<sup>171</sup> represent robust stratagems.

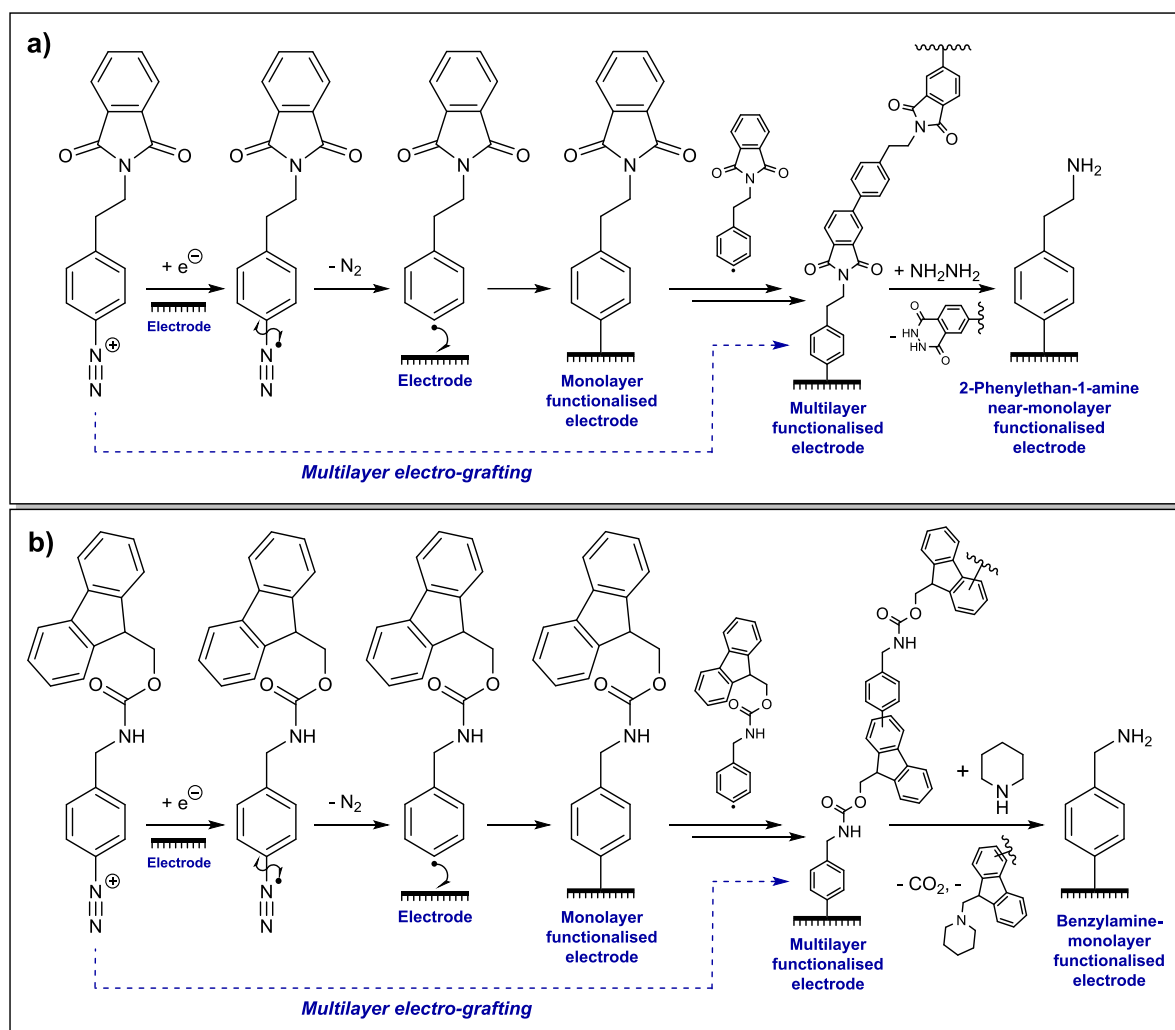


**Figure 3.8.** The methods of **a)** Hauquier et al<sup>171</sup> and **b)** Downard and co-workers<sup>197</sup> for introducing aliphatic amines onto electrode surfaces in near-monolayer or monolayer coverage, courtesy of the usage of protecting groups with aromatic-systems which, while grafted to, can be cleaved using deprotective chemistry.

The Results and Discussion section that follows (**Section 3.2**) is comprised of three subsections, the first (**Section 3.2.1**) describes the exploration of a variety of diazonium electro-grafting and amide-bond forming techniques that enabled the identification of the best methodologies upon which to base a diazonium electro-grafting enabled amine-functionalisation/amide bond coupling strategy. The second (**Section 3.2.2**) describes a versatile diazonium electro-grafting enabled amine-functionalisation/amide bond coupling strategy, and the third (**Section 3.2.3**) describes the applications of that methodology in the development of a new voltammetry method.

### 3.1.4 Aims

The optimal approach for surface amine functionalisation would preferably satisfy several criteria:

- 1) Directly deliver amine functionalities to the electrode surface.
- 2) Only require the application of relatively mild potentials.
- 3) Be applicable to a range of different conductive surfaces.
- 4) Functionalised electrode surfaces should not be passivated.
- 5) For convenience, the method should be compatible with the use of an aqueous reference electrode and be suitable for benchtop use.

A method to introduce amine groups to electrode surfaces by diazonium electro-grafting could hypothetically satisfy all these criteria. Additionally, due to the flexibility of diazonium electro-grafting, any experience gained from developing a diazonium electro-grafting-based system for amine functionalisation could prove useful in future projects.

## 3.2 Results and Discussion

### 3.2.1 Screening diazonium electro-reduction-based approaches relevant to the introduction of amine functionalities onto electrode surfaces

A broad variety of the diazonium electro-grafting strategies introduced in **Section 3.1** were initially investigated in order to become better versed in methods that could prove useful in the development a robust amine-based electrode-surface bioconjugation platform. In the interests of brevity, a summary of the different strategies, and a brief comment associated benefits and drawbacks of each strategy are reported overleaf in **Table 3.1**.

The electrochemical reduction of commercially available 4-nitrobenzene diazonium tetrafluoroborate (**Figure 3.7**) was performed in the absence and presence of 2 equivalents of DPPH (**Figure 3.7**), yielding GC electrode surfaces functionalised with nitrophenyl (NP) functionalities in both multilayer and monolayer coverage respectively (**Table 3.1**, use of DPPH). The subsequent electrochemical reduction of the NP functionalities to aniline (and phenylhydroxylamine) functionalities was then used to conveniently introduce aniline functionalities to the electrode surfaces (**Figure 3.4**, **Figure 3.9**).<sup>83,169,170,181-184,370-374</sup> As is expected, a larger reductive peak can be observed for the reduction of the NP functionalities for the electro-grafted multilayer than for the monolayer (**Figure 3.9**).<sup>169,170</sup>

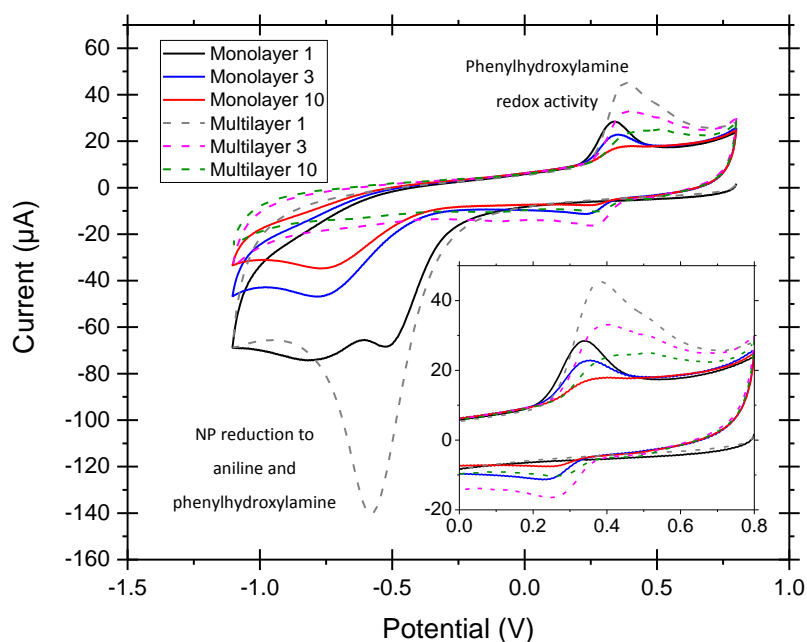
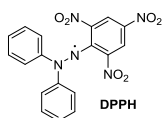


**Figure 3.9.** The electrochemical reduction of NP groups grafted onto a GC electrode as a multilayer or monolayer film. Solvent system: 1:5 water:acetonitrile + 1% 6.6 M HCl. Scans recorded at  $50 \text{ mV s}^{-1}$  under an ambient atmosphere at room temperature. Potentials are reported against the Ag/AgCl (3 M NaCl) reference electrode. Scans commence at the most positive potential.



**Table 3.1.** A brief guide to the different electrode functionalisation strategies investigated for the introduction of amine functionalities onto electrode surfaces.

Strategy	Benefits	Drawbacks	Characteristic electro-grafting CV
<i>In-situ</i> generation grafting	Quick and easy	Incompatible with unprotected amine groups.  Results in the build-up of pacifying multilayers.	
<i>In-situ</i> generation from a nitrophenyl precursor	Very little synthetic effort required. Easy  Can be used to nano-pattern surfaces using a scanning electrochemical microscopy tip. <sup>163</sup>	Incompatible with unprotected amine groups.  Results in the build-up of pacifying multilayers.	
Use of isolated diazonium salts	Issues associated with the reactivity of amine groups with the NO <sup>+</sup> cation can be circumvented.  Is compatible with the use of DPPH.	Results in the build-up of pacifying multilayers unless electro-reducible species such as DPPH are used.	
Use of DPPH	Can yield monolayer films. <sup>169,170</sup>	Cannot be used with aryl systems with +M groups and is most effective with -M groups. <sup>169</sup>  At present has to be used with isolated diazonium salts.	



Carboxylic acid-functionalised redox-active molecules were used in the screening of conditions for amide bond formation to the surface amines. This is common practice; if amide bond formation to the redox-active molecule is successful then surface-confined redox signals from that molecule should be visible, even after the electrode has been washed and transferred to an electrolyte solution that is free from the redox-active analyte.<sup>171,197</sup> However, forming amide bonds between the aniline-functionalised surfaces and the commercially available ferrocene carboxylic acid (**Figure 3.10**) proved difficult, despite being attempted under several conditions (**Table 3.2**).

**Table 3.2.** Conditions trialled in the attempted immobilisation of ferrocene carboxylic acid onto aniline functionalised electrode surfaces. Carbonyldiimidazole (CDI) and 2-(6-Chloro-1-H-benzotriazole-1-yl)-1,1,3,3-tetramethylammonium hexafluorophosphate (HCTU) are common carboxylic activating agents, and hydroxybenzotriazole (HOBt) is sometimes used as an additive in amide bond coupling reactions.

Conc of ferrocene carboxylic acid / mM	Coupling agent	Conc of coupling agent / mM	DIPEA conc / mM	Solvent	Pre-activation	Atmosphere
100	CDI	1.00	-	DMF	None	Ambient
27.0	HCTU	20.0	20.0	DCM	0 °C, 10 min	Argon
27.0	HCTU	26.5	54.0	DMF	0 °C, 10 min	Argon
100.0	HCTU	98.0	333	DMF	0 °C, 10 min	Argon
100	HCTU	196	666	DMF	0 °C, 60 min	Argon
200	HCTU+HOBt	200	666	DMF	0 °C, 60 min	Argon

The difficulty encountered when attempting immobilisation of ferrocene carboxylic acid was likely due to several factors, including the low reactivity of ferrocene carboxylic acid compared to most other carboxylic acids (due to the mesomeric effects of the cyclopentadienyl ligands) and a reduced reactivity of surface-immobilised aniline functionalities compared to solution-phase aniline. Downard and co-workers<sup>197</sup> have previously shown that the successful coupling of aniline-functionalised electrode surfaces to ferrocene carboxylic acid requires the activation of ferrocene carboxylic acid with oxalyl chloride to generate the corresponding acid chloride (ferrocenoyl chloride, **Figure 3.10**),<sup>197</sup> whereas the usage of the milder activating reagent [benzotriazol-1-yloxy(dimethylamino)methylidene]-dimethylazanium hexafluorophosphate (HBTU) was ineffective.<sup>197</sup> In the published study, ferrocenoyl chloride was capable of reacting with both the alcohol moieties found on unmodified glassy carbon electrode surfaces and the aniline moieties,<sup>197</sup> and as such the usage of an aniline/acid chloride system as a means of achieving controlled electrode functionalisation seemed undesirable.

There appears to be a broad literature consensus that despite the commercial availability of ferrocene carboxylic acid, more reactive carboxylic acid-functionalised derivatives of ferrocene are worth using as coupling partners for surface amine moieties; even when synthetic effort is required to obtain such derivatives. 3-(Ferrocenyl) propanoic acid, purified and delivered as its *N*-hydroxyphthalimide ester (**Figure 3.10**), represents one such example,<sup>171,386-388</sup> and (ferrocenyl)ethanoic acid represents another.<sup>197</sup> Due to the lack of conjugation between the carboxylic acid group and the cyclopentadienyl  $\pi$ -system, the reactivities of the carboxylic acid groups of these derivatives are not diminished by mesomeric effects. This effect is illustrated beautifully by Downard and co-workers,<sup>197</sup> who showed that (ferrocenyl)ethanoic acid can be efficiently coupled to aniline-functionalised electrode surfaces using HBTU, whereas ferrocene carboxylic acid cannot.<sup>197</sup>

Downard and co-workers also demonstrated that compared to aryl amine moieties, aliphatic amine functionalised electrode surfaces were superior coupling partners for carboxylic acid-functionalised ferrocene derivatives,<sup>197</sup> which is unsurprising as aliphatic amines are far more reactive nucleophiles than anilines.<sup>382</sup> The coupling of primary aliphatic amine-functionalised electrode surfaces to activated esters is also well documented in the literature,<sup>150,171,360,386</sup> and it was thus decided that the introduction of aliphatic amines onto an electrode surface would be preferable to the introduction of anilines, despite being a slightly more complicated endeavour, and that the coupling of aliphatic amines to activated esters represented the most controllable way of achieving further electrode derivatisation.

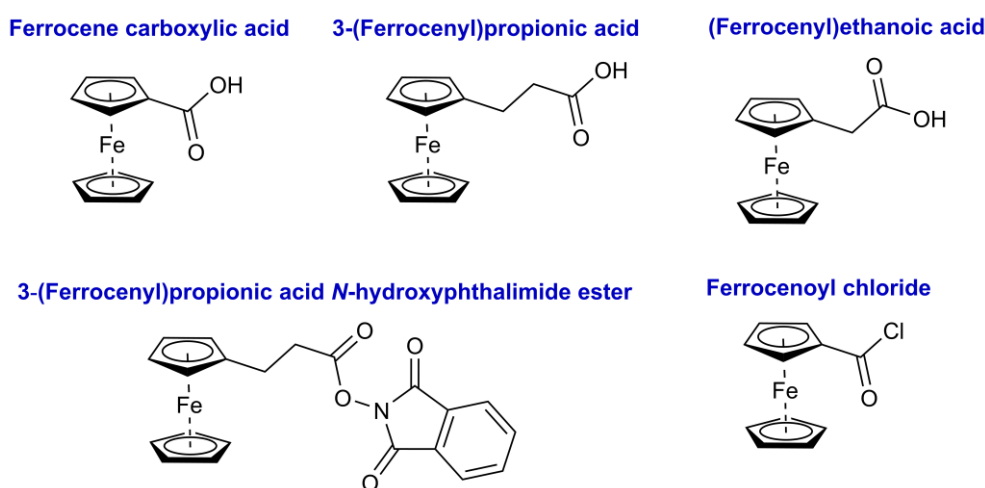


**Figure 3.10.** Carboxylic acid (or activated derivatives thereof) functionalised ferrocene compounds.

Electrode functionalisation with an aliphatic amine monolayer would not be achievable through the usage of diazonium electro-grafting in the presence of DPPH (**Table 3.1**), as the positive inductive effects of the alkyl group would allow access to non-radical grafting mechanisms (and/or would make redox cross-reaction with DPPH slower), allowing multilayer grafting to be achieved in spite of the action of DPPH.<sup>169</sup> A different strategy was thus required to ensure monolayer coverage with aliphatic amine functionalities, and fortunately the literature systems developed by Hauquier et al<sup>171</sup> and Downard and co-workers<sup>197</sup> (shown in **Figure 3.8**) were already well suited to meet the aims detailed in **Section 3.1.4**. The aliphatic amine functionalities introduced onto electrode surfaces using these systems can be subsequently coupled to activated esters, such as 3-(ferrocenyl) propanoic acid *N*-hydroxyphthalimide ester<sup>171</sup> or HBTU-activated (ferrocenyl)ethanoic acid (**Figure 3.11**). When considering these literature systems however, there would appear to be no necessity to use purified diazonium salts, as regardless of the origin of the diazonium salt that is being electrochemically reduced (*electro-grafted*), the subsequent removal of the amine protecting groups would always yield an aliphatic amine film in monolayer/near-monolayer coverage; any multilayers anchored to the protecting groups will become shed during the deprotection step. This presented an opportunity to simplify the literature systems so that near-monolayer coverages of amine functionalities could be installed onto electrode surfaces via the generation and electro-grafting of diazonium cations *in-situ*. The system selected for modification was that of Hauquier et al,<sup>171</sup> simply due to the shorter duration of the protecting group removal step (5 min)<sup>171</sup> compared to that of Downard and co-workers (120 min).<sup>197</sup>

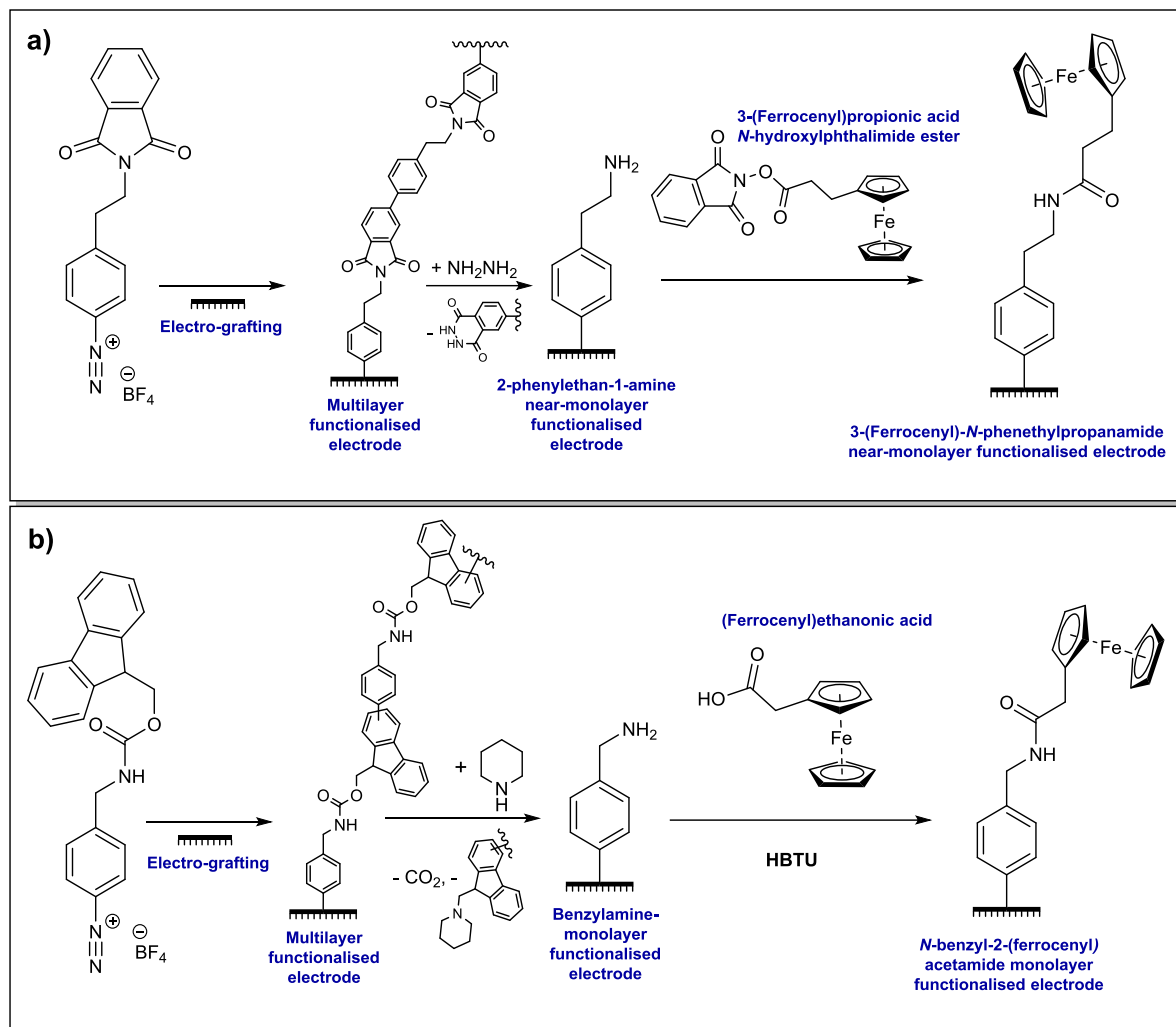
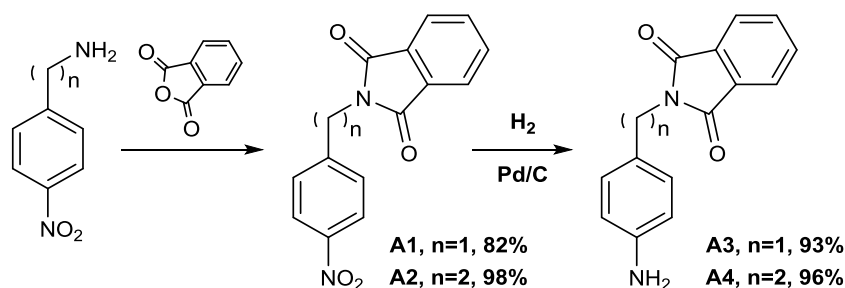


**Figure 3.11.** The methods of Hauquier et al,<sup>171</sup> and Downard and co-workers,<sup>197</sup> detailing the usage of a specially prepared and isolated diazonium cations bearing protected aliphatic amine groups for the introduction of aliphatic amine groups onto electrode surfaces, and the coupling of the aliphatic amines to a redox-active species via amide bond formation.

### 3.2.2 Development of a method for the introduction of reactive aliphatic amine functionalities onto electrode surfaces as near-monolayers

#### 3.2.2.1 The functionalisation of electrode surfaces with aliphatic amine near-monolayers.

Species **A1** and **A2** were both synthesised in one-step reactions from cheap commercially available precursors, crystallising in high yield and high purity upon cooling of the reaction mixture (**Scheme 3.1**). This represented a simpler synthesis than that documented in literature procedures.<sup>389</sup> Species **A3** and **A4** were subsequently synthesised via the hydrogenation of **A1** and **A2** (**Scheme 3.1**), and did not require any further purification.



**Scheme 3.1.** Synthesis of species **A1-A4**.

It is possible to perform diazonium electro-grafting of species **A1-A4**, using either the *nitro-grafting* or *in-situ generation grafting* approaches described in **Table 3.1**. Cyclic voltammograms for the *nitro-grafting* of **A1** and **A2** are shown below in **Figure 3.12**, and cyclic voltammograms for the *in-situ generated* diazonium electro-grafting of **A3** and **A4** are shown in **Figure 3.13**. **Figure 3.13** shows the characteristic irreversible broad reductive wave in the first scan and the passivation of the electrode surface in the subsequent scans, which is characteristic of diazonium electro-grafting.<sup>155,170-172,176,197</sup> The *in-situ* diazonium electro-grafting of species **A4** (**Figure 3.13, right**) shows two peaks within the reductive wave, a phenomenon that has been observed before in the literature when performing diazonium electro-grafting onto glassy carbon surfaces due to the occurrence of both surface-catalysed and uncatalysed electrochemical reduction mechanisms.<sup>390</sup>

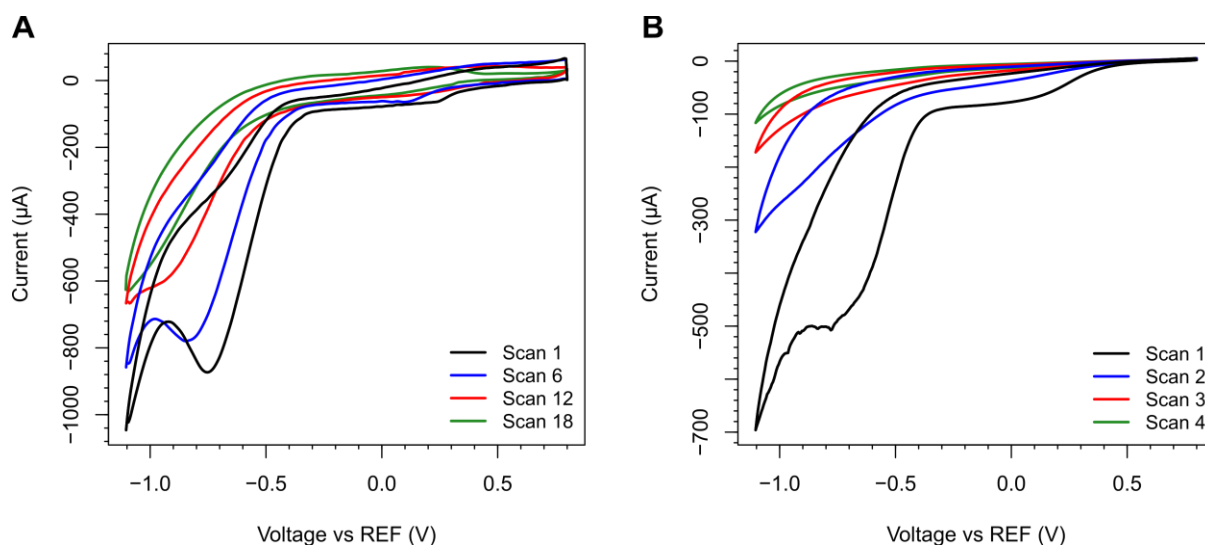


**Figure 3.12.** Nitro-grafting of species **A1** (A), and **A2** (B). Cyclic voltammograms were recorded using a 4 mM solution of the relevant nitro-phenyl compound in 1:5 water:acetonitrile + 0.1 M  $\text{Bu}_4\text{NPF}_6$  + 29 mM  $\text{NaNO}_2$  + 4% 6.6 M HCl at 0 °C, using a GC working electrode, a platinum wire counter electrode and a Ag/AgCl (3 M NaCl) reference electrode under an ambient atmosphere. Scan rate = 500  $\text{mV s}^{-1}$  in (A) and 50  $\text{mV s}^{-1}$  in (B). Scans commence at the most positive potential.

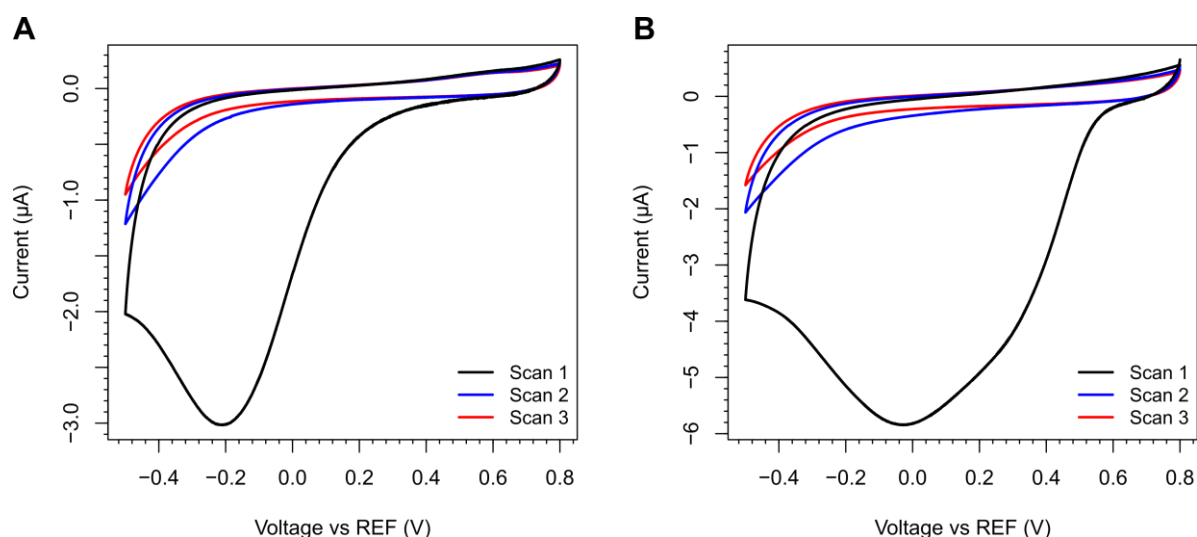


**Figure 3.13.** In-situ generation diazonium grafting of species **A3** (A), and **A4** (B). Cyclic voltammograms were recorded using a 1 mM solution of the *in-situ* generated diazonium salt in 1:5 water:acetonitrile + 0.1 M  $\text{Bu}_4\text{NPF}_6$  at 0 °C, using a GC working electrode, a platinum wire counter electrode and a Ag/AgCl (3 M NaCl) reference electrode under an ambient atmosphere. Scan rate = 20  $\text{mV s}^{-1}$ . Scans commence at the most positive potential.

As described by Hauquier et al,<sup>171</sup> the treatment of these passivated multilayer-functionalised electrodes with an ethanoic solution of hydrazine monohydrate at 80 °C removes the phthalimide groups, cleaving the multilayer and yielding surface-immobilised primary amine functionalities, presumably in near-monolayer coverage (**Figure 3.14**).<sup>171</sup> This modification process can be monitored via cyclic voltammetry using glassy carbon electrodes in various derivatisation states in aqueous ferricyanide solutions.

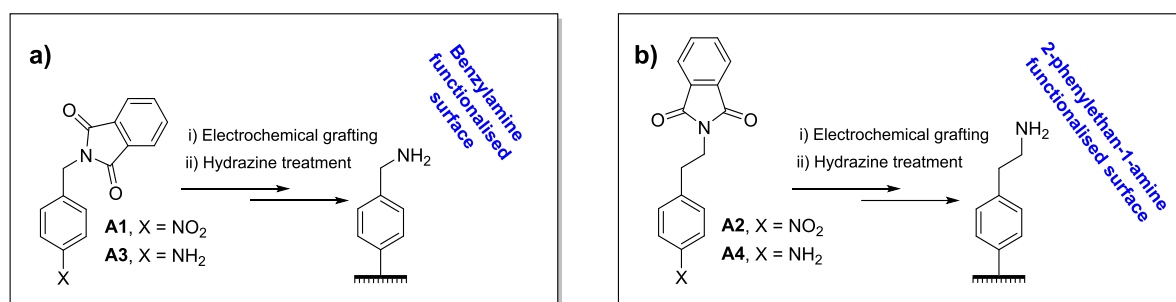


**Figure 3.14.** The functionalisation of GC electrode surfaces with, **a)** Benzylamine, **b)** 2-phenylethan-1-amine, functionalities using diazonium precursors, via either “nitro-grafting” or “*in-situ* generation” methods.

Cyclic voltammograms recorded of a 1 mM potassium ferricyanide ( $K_3[Fe(CN)_6]$ ) solution illustrate that a clean GC electrode surface is unpassivated towards the ferricyanide redox couple, clearly showing a pair of redox peaks of a shape typical of a solution-phase reversible/quasi-reversible redox couple (**Figure 3.15**). By contrast, electrodes electro-grafted with **A1-A4** are passivated towards the ferricyanide redox couple, as evidenced by the greatly reduced intensity of the Faradaic signals and the huge increase in the peak-to-peak separation (**Figure 3.15**, **Figure 3.16**). The passivation of the electrode surface towards the ferricyanide redox couple would be consistent with the formation of a non-polar multilayer on the electrode surface, disfavours the approach of the charged ferricyanide ions (**Figure 3.16**). After treatment with a solution of hydrazine monohydrate in ethanol at 80 °C, these electrodes become once-again unpassivated towards the ferricyanide redox couple (**Figure 3.15**, **Figure 3.16**), which is consistent with the removal of the thick multilayer to leave a near-monolayer of amines.<sup>171</sup> A subtler observation is that when using the surface functionalised with a near-monolayer of amines, the peak-to-peak separation of the  $Fe^{3+}/Fe^{2+}$  redox couple of ferricyanide is slightly smaller and the intensity of the signals is often greater (**Figure 3.15**). It is possible that the surface amine functionalities, which will carry positive charges at neutral pH, can interact with the  $[Fe(CN)_6]^{3-}/[Fe(CN)_6]^{4-}$  ions, drawing them closer to the electrode surface, increasing the local ferricyanide concentration; this will in turn increase the peak intensity and decrease the peak-to-peak separation (a phenomenon related to mass transport).<sup>247</sup>



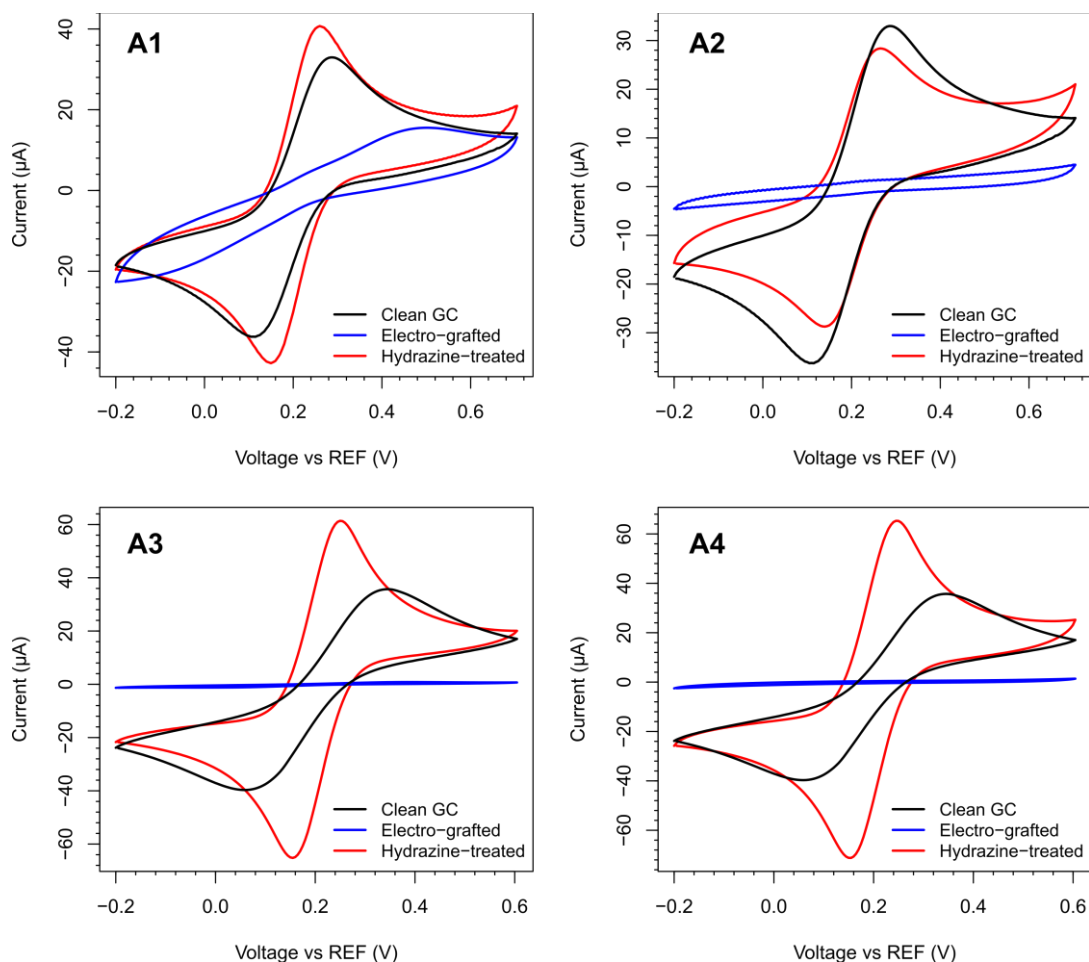


**Figure 3.15.** CVs of a 1 mM  $\text{K}_3\text{Fe}(\text{CN})_6$  + 0.1 M KCl solution recorded using clean GC electrodes (black), and electrodes functionalised with **A1-A4**, both before (blue) and after treatment with hydrazine (red). Scan rate =  $50 \text{ mV s}^{-1}$  for electrodes functionalised with **A1** and **A2**. Scan rate =  $500 \text{ mV s}^{-1}$  for electrodes functionalised with **A3** and **A4**. Potentials are reported vs an Ag/AgCl (3 M NaCl) reference electrode. Scans recorded at room temperature under an ambient atmosphere, and commence at the most negative potential.

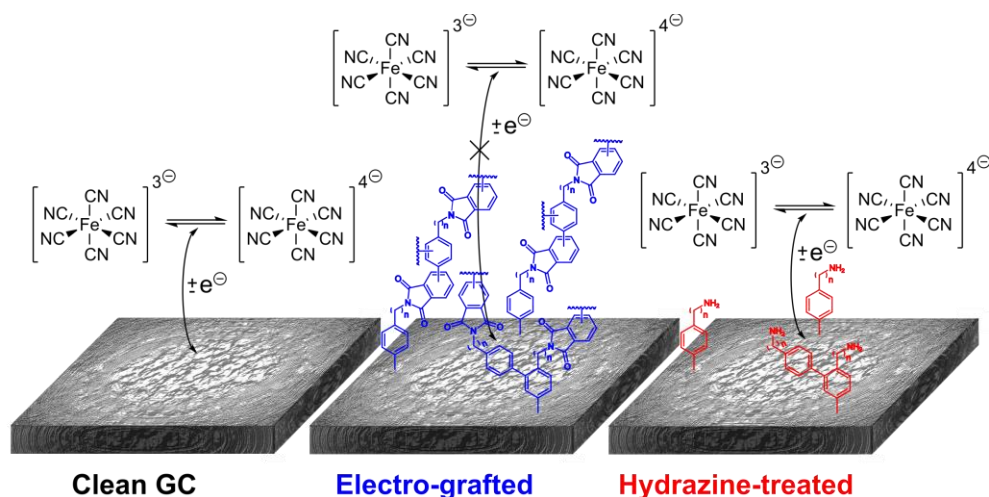
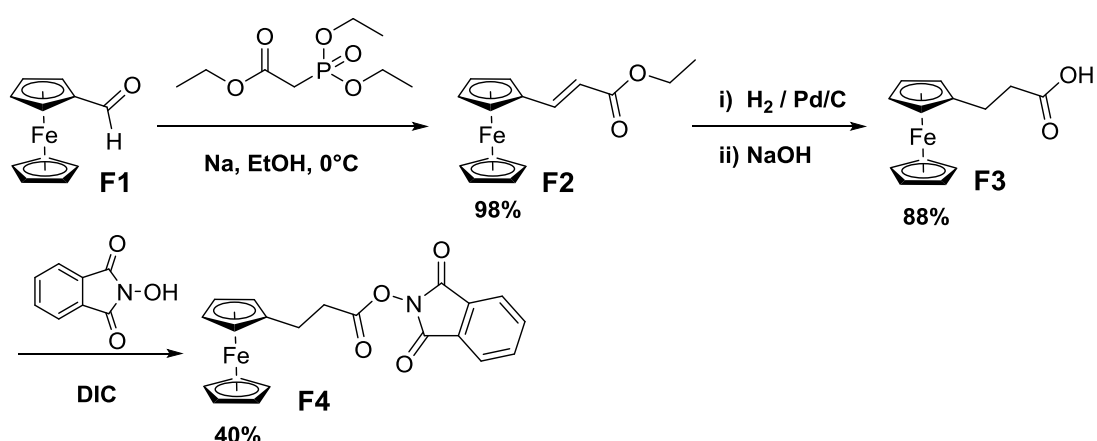


**Figure 3.16.** The  $\text{Fe}^{3+}/\text{Fe}^{2+}$  redox couple of ferricyanide is reversible on GC electrode surface, yet becomes hindered when electrode surfaces are functionalised with the phthalimide protected amine multilayers, presumably due to an interplay between physical obstruction by the contracted non-polar film and the lack of permeation of the charged ferricyanide anion through the non-polar film. Upon treatment of these functionalised electrode surfaces with hydrazine, the phthalimide protecting groups are cleaved, removing the pacifying multilayer, and leaving a near-monolayer coverage of amine functionalities. Once this has been conducted, the  $\text{Fe}^{3+}/\text{Fe}^{2+}$  redox couple of ferricyanide is once again reversible.

Although the preparation of species **A1** and **A2** requires fewer steps than the preparation of species **A3** and **A4**, on a practical note, both methodologies require the same number of components to be weighed out and the *nitro-grafting* methodology takes longer to yield functionalised electrode surfaces, due to the increased number of scans required to achieve full electrode passivation. As such, it was decided that *in-situ generation* diazonium electro-grafting using **A3/A4** represented the most suitable surface functionalisation technique.

### 3.2.2.2 Derivatisation of aliphatic amine-functionalised electrode surfaces via amide bond formation

To test the reactivity of the surface aliphatic amines, a redox-active moiety functionalised with an activated ester was required. 3-(Ferrocenyl) propanoic acid *N*-hydroxyphthalimide ester **F4** was synthesised as per a literature methodology (**Scheme 3.2**),<sup>171,386</sup> and the aliphatic amine-functionalised electrode surfaces were treated with a 10 mM solution of **F4** in DMF + 10 mM triethylamine, yielding either a *N*-(2-phenylethyl)propan-3-(ferrocenyl)-amide functionalised surface (**FSA**) or a *N*-(benzyl)propan-3-(ferrocenyl)-amide functionalised surface (**FSB**) (**Figure 3.17**). After this treatment, redox signals attributable to the  $\text{Fe}^{3+}/\text{Fe}^{2+}$  redox couple of ferrocene were readily apparent at  $\sim 0.43$  V (vs SHE), both for **FSA** (**Figure 3.18, left**) and **FSB** (**Figure 3.18, right**). Note that while **FSA** is detailed in a literature system,<sup>171</sup> the functionalisation of electrodes with **FSB** is not.



**Scheme 3.2.** The synthesis of 3-(ferrocenyl) propanoic acid *N*-hydroxyphthalimide hydroxyphthalimide ester, **F4**.

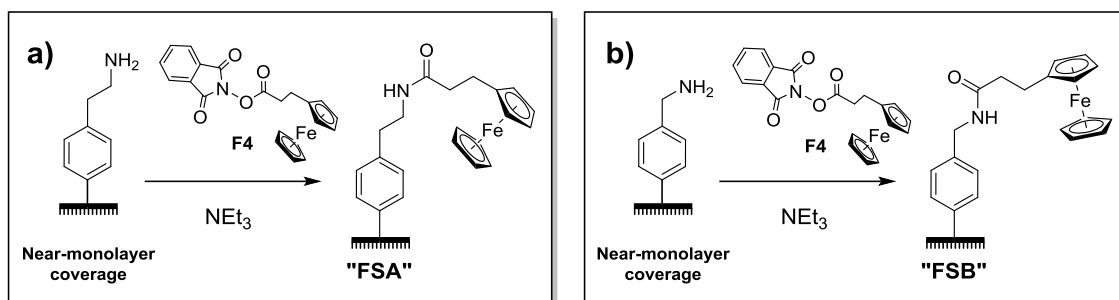


**Figure 3.17.** Coupling of ferrocene functionalities to surfaces functionalised with **a)** 2-phenylethan-1-amine functionalities **b)** benzylamine functionalities to yield **FSA** and **FSB** respectively.

For both **FSA** and **FSB**, the peak current of the redox signals was found to be proportional to scan rate (**Figure 3.18, bottom**), which is characteristic of surface-confined regimes.<sup>171,386</sup> The surface coverage of ferrocene moieties can be calculated using the integral of the redox signals (**see experimental**), and was found to vary between 20 → 160 pmol cm<sup>-2</sup>, with the higher surface coverages more often being achieved when using freshly-opened aliquots of **F4**. Hauquier et al. reported that 100-250 pmol cm<sup>-2</sup> of ferrocene moieties can be coupled to GC electrode surfaces when introducing **FSA** (using the method described in **Figure 3.11 a**)<sup>171</sup> and Downard and co-workers<sup>197</sup> reported that a coverage of 170 pmol cm<sup>-2</sup> of ferrocene moieties can be coupled to GC electrode surfaces using their similar system (shown in **Figure 3.11 b**).

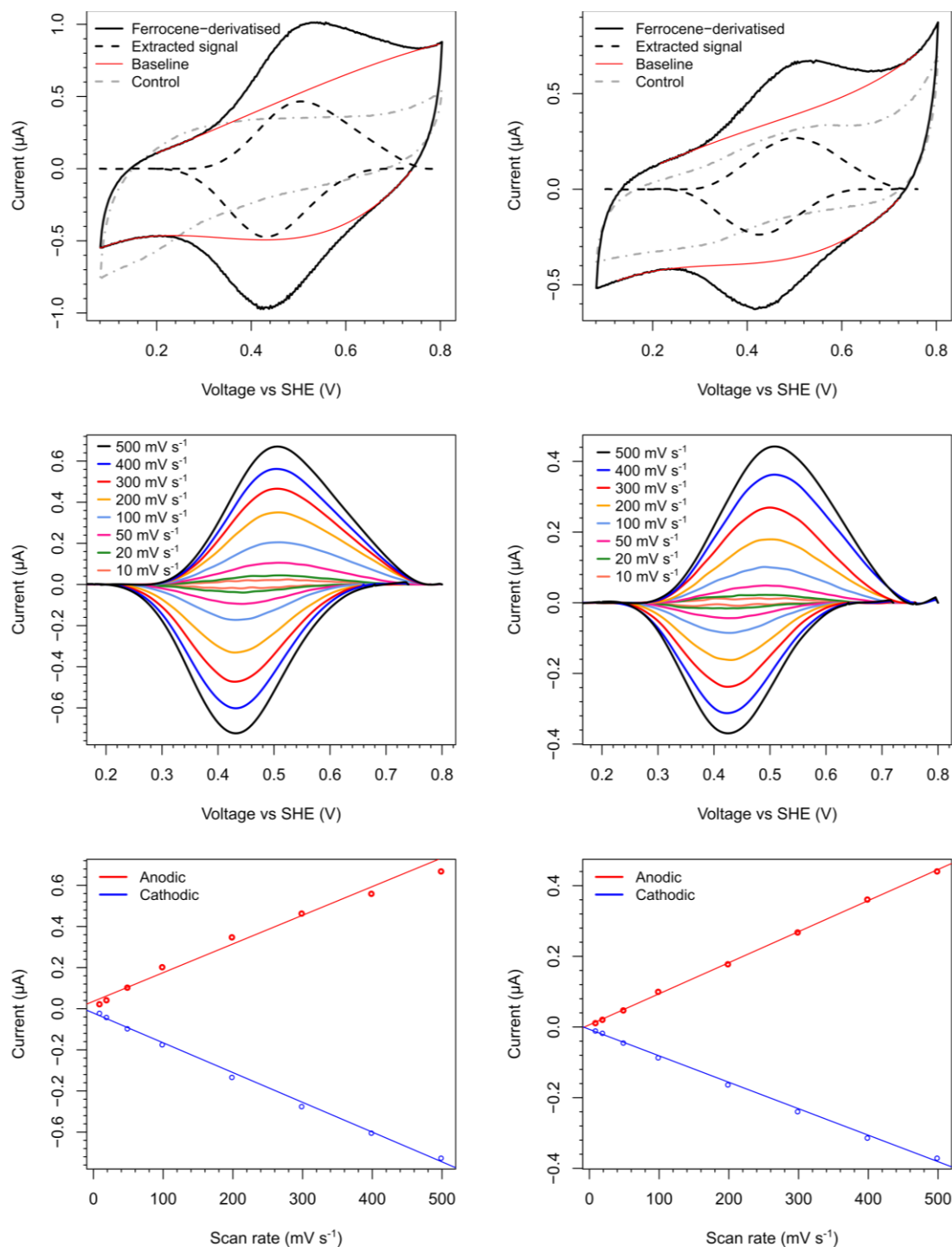


**Figure 3.18.** Top, CVs recorded at a scan rates of 300 mV s<sup>-1</sup> in pH 7.5 buffer (10 mM sodium phosphate, 140 mM NaCl) at 25 °C using GC working electrodes functionalised with FSA (left) and FSB (right), a platinum wire counter electrode and a SCE reference electrode under an N<sub>2</sub> atmosphere. Potentials are reported vs SHE, and scans commence at the most negative potential. Middle, extraction of the redox signals. Bottom, the peak intensity of the redox signals is directly proportional to scan rate, which is characteristic of the signals being from a surface-confined regime.<sup>171,386</sup> Note that the fitting of polynomials to fit the background capacitive current in the CVs presented was difficult due to the size of and broadness of the Faradaic signals, which occupying most of voltage window spanned by the CV. As such the size of the Faradaic signals have likely been underestimated in this figure.

### 3.2.3 Further applications of the near-monolayer amine-functionalisation system

The system detailed in **Section 3.2.2** for the functionalisation of electrode surfaces with aliphatic amine near-monolayers has found several applications within the Parkin group. The functionalisation of copper electrode surfaces with aliphatic amines of various lengths has been used by Mark Dowsett (a fellow PhD student) to tune the capacitance of electrode surfaces in such a way as to increase the efficiency of electrochemical CO<sub>2</sub> fixation.<sup>391</sup> **Chapter 5** describes the application of the chemistries explored in **Section 3.2.2** to the functionalisation of electrode surfaces with hydroxylamines - a functionality that can be used in bio-orthogonal oxime ligation to protein aldehydes. The context and usage of electrode surfaces functionalised with **FSB** as a model system for the development a new voltammetric technique in a recent publication<sup>265</sup> is described below.

#### 3.2.3.1 A model system for the development of Pure Sinusoidal Voltammetry

##### 3.2.3.1.1 The concept of Pure Sinusoidal Voltammetry

It had been postulated that a simpler voltammetric experiment which applies a high frequency sinusoid with an amplitude large enough to allow the sinusoid to span the redox window of interest (i.e. E1 to E2, **Figure 3.19**), but does not apply an underlying linear potential ramp, could be used to calculate some of the parameters required to accurately simulate an FTacV experiment in a computationally efficient manner. As such, if this ramp-free “Pure Sinusoidal Voltammetry” PSV experiment were to be conducted as a supplement to a conventional FTacV experiment, the multidimensional parameter space that would need to be explored during the simulation of the conventional FTacV experiment would be dramatically reduced. This would, in turn, reduce the computational effort required to extract information from an FTacV experiment. As computational simulation of FTacV experiments often takes several days to complete,<sup>265</sup> PSV could prove itself to be very useful, particularly in the analysis of enzyme film voltammetry data where the requirement for high frequency measurements adds a significant computational cost to data analysis.

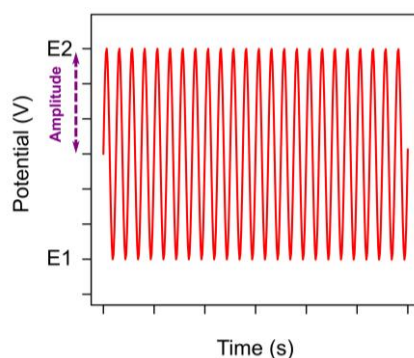


**Figure 3.19.** The waveform of a “pure sinusoidal voltammetry” (PSV) experiment.

### 3.2.3.1.2 The usage of the surface-confined ferrocenyl redox couple as a tool in the development of pure sinusoidal voltammetry

The development of PSV and the associated computational tools required for its analysis were highly desired, and it was realised that an electrode surface functionalised with a near-monolayer of ferrocenyl moieties represented an ideal model system of a surface-confined redox couple, upon which the new the voltammetric experiment and associated computational tools could be developed.

The system described in **Section 3.2.2** was therefore used to functionalise glassy carbon electrode surfaces with *N*-(benzyl)propan-3-(ferrocenyl)-amide (**FSB**). A large dataset was then collected; **FSB**-functionalised electrode surfaces were first subjected to a classic direct-current cyclic voltammetry experiment, followed by three FTacV experiments, then a second cyclic voltammetry experiment, then ten PSV experiments and a final cyclic voltammetry experiment (**Figure 3.20**). This dataset was sent to collaborators and computational tools have since been developed and published that can simulate and extract useful parameters from these PSV voltammograms.<sup>265</sup> **Figure 3.20** illustrates that the sequential experiments do not change the nature of the ferrocenyl couple under assay, as identical  $E^0$  values can be discerned from any of the sequential experiments.

## 3.3 Summary and conclusions

Multiple literature systems for the introduction of amine functionalities to electrode surfaces via diazonium electro-grafting were screened for their ability to deliver functionality as a monolayer or near-monolayer, and for the reactivity of the surface amine functionalities towards activated esters. A literature system for the introduction of aliphatic amines onto electrode surfaces via electrochemical reduction of a protected-amine functionalised diazonium cation was adapted and simplified without detrimentally affecting the reactivity and coverage of the aliphatic amines introduced to the electrode surface.

The resultant system is suitable for use on a range of conductive materials, ranging from carbon allotropes through to copper, and the amine-functionalised electrode surfaces are not passivated. The electrode-functionalisation steps can be carried out under an ambient atmosphere making the methodology suitable for performing in a fume-hood. This system has found several applications in other areas of the Parkin lab and represents a versatile platform from which further electrode derivatisation can be achieved.

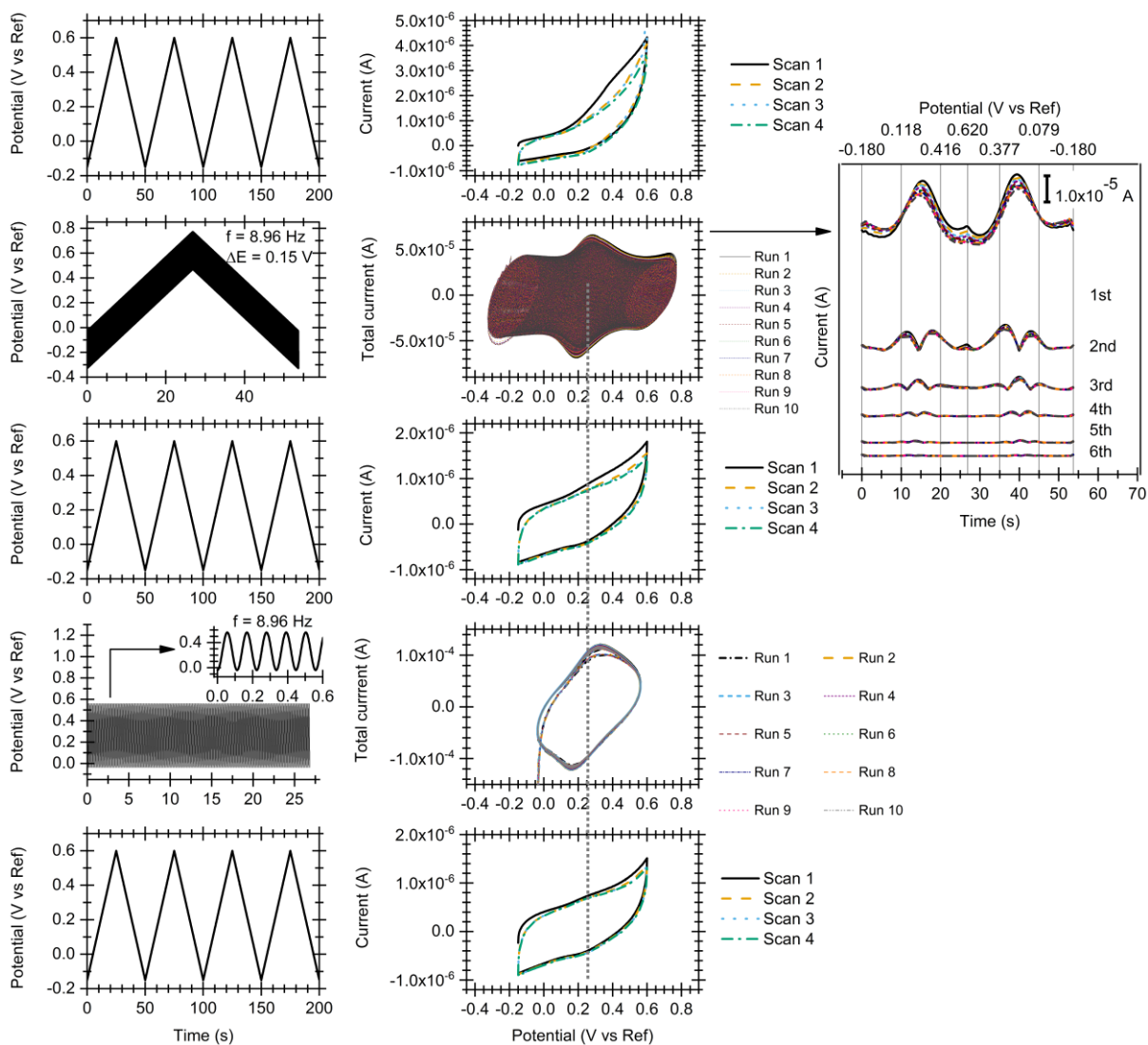


**Figure 3.20.** The assay of a glassy carbon electrode functionalised with **FSB** by cyclic voltammetry (top), FTacV (second from top), cyclic voltammetry (middle), PSV (second from bottom), and cyclic voltammetry (bottom). The applied potentials throughout the voltammetric experiments are shown on the left, whereas the resultant voltammograms (current plotted against applied potential) are shown on the right. The harmonic responses from the FTacV experiment are shown to the right of the FTacV voltammogram. Experiments performed in pH 7.4 buffer (100 mM sodium phosphate, 100 mM NaCl) at 25 °C under an  $N_2$  atmosphere, using a platinum wire counter electrode and a Ag/AgCl (3 M KCl) reference electrode. Cyclic voltammetry and FTacV experiments commenced from the most negative potential.

# Chapter 4

Introduction of aldehydes into proteins  
and solution-phase ligation



## Chapter 4. Introduction of aldehydes into proteins and solution-phase ligation

Part of following Chapter makes reference to my published work.<sup>392</sup>

### 4.1 Introduction

The ability to install bio-orthogonal handles into proteins that can undergo selective ligation is hugely beneficial when attempting to covalently crosslink redox proteins onto electrode surfaces in chosen orientations, (see **Chapter 1, Figure 1.13**).<sup>393</sup> Aldehydes are representative of such a bio-orthogonal handle, as there are a wealth of methods via which they can be installed into proteins and a series of well-developed strategies for bio-orthogonal ligation to them. These methods and strategies have been comprehensively reviewed by Spears et al.<sup>394</sup> Selected methods of aldehyde installation are depicted in **Figure 4.1** and several ligation strategies are depicted in **Figure 4.2**.

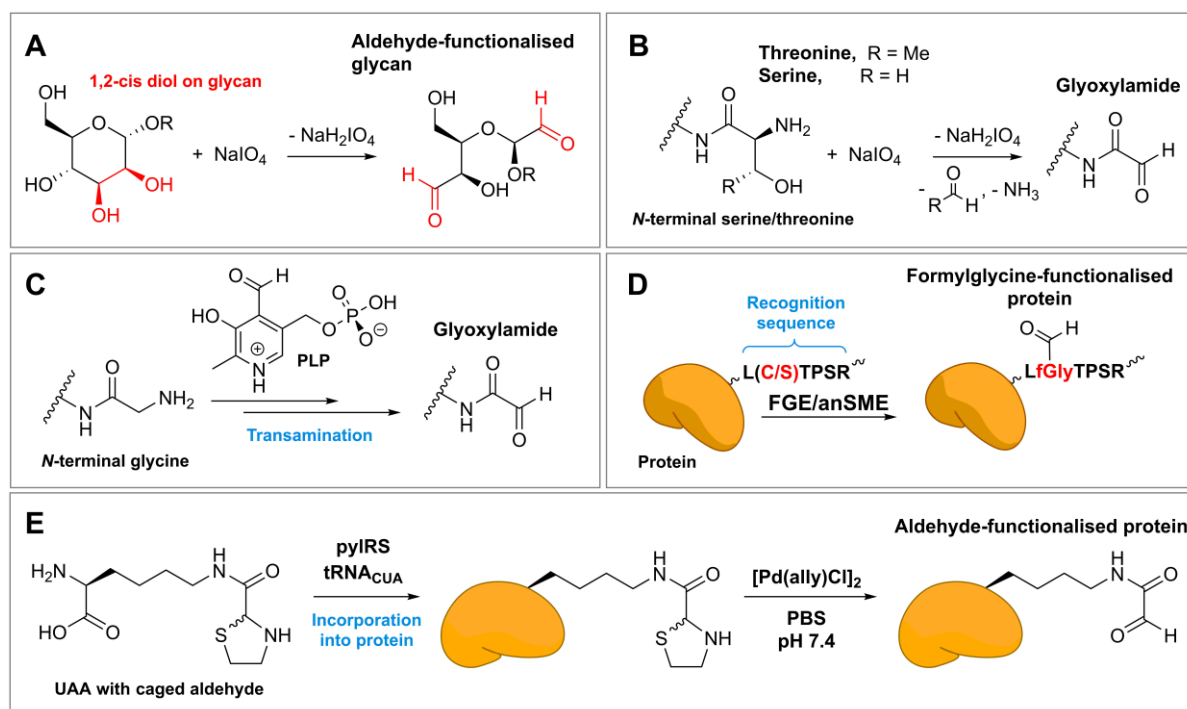


**Figure 4.1.** Summary of the variety of methods via which aldehyde motifs can be introduced into protein scaffolds. **(A)** The oxidation of a glycan presenting a cis-1,2 diol with sodium metaperiodate. **(B)** The oxidation of a 1,2-amino alcohol, such as *N*-terminal serine or threonine residues, with sodium metaperiodate. **(C)** Pyridoxal 5'-phosphate (PLP) mediated transamination of *N*-terminal glycine residues. **(D)** Post-translational modification of a pre-installed recognition sequence by formyl glycine generating enzyme (FGE), or an anaerobic sulfatase maturation enzyme (anSME). **(E)** Unnatural amino acid installation and manipulation using pyrrolysyl-tRNA synthetase (pyIRS) in conjunction with transfer RNA bearing the CUA anticodon (tRNA<sub>CUA</sub>).

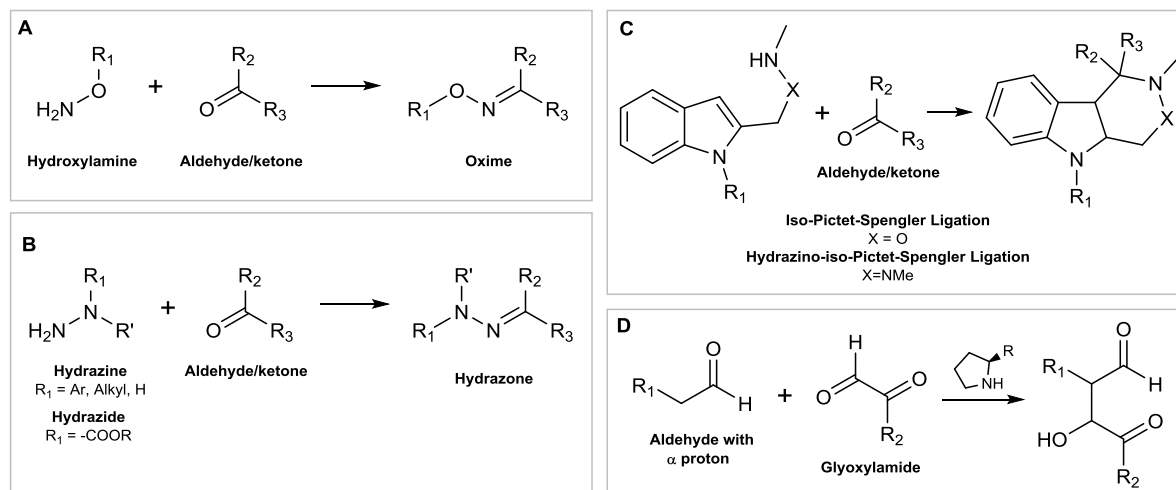


**Figure 4.2.** Selected methods of bio-orthogonal aldehyde ligation. **(A)** Oxime ligation.<sup>395</sup> **(B)** Hydrazone ligation.<sup>396</sup> **(C)** Iso-Pictet-Spengler-type ligations.<sup>397,398</sup> **(D)** Organocatalyst-mediated protein aldol ligation (OPAL).<sup>399</sup>

Installation of aldehydes at protein *N*-termini is relatively simple, requiring either an *N*-terminal serine or threonine residue or an *N*-terminal glycine (**Figure 4.1**, panels **B** and **C**). *N*-terminal serine or threonine residues can be subjected to oxidative cleavage using sodium metaperiodate ( $\text{NaIO}_4$ ) in a matter of minutes (min) at room temperature using as little as 1 equivalent of  $\text{NaIO}_4$ , owing to the high reactivity of 1,2-amino alcohols towards the periodate ion.<sup>394</sup> By contrast, the installation of an aldehyde using an *N*-terminal glycine residue can be achieved using pyridoxal 5'-phosphate (PLP) mediated transamination during an overnight reaction at 37 °C.<sup>394,399-401</sup> Periodate oxidation of *N*-terminal serine or threonine residues thus represents a far milder treatment than PLP-mediated transamination due to the short reaction time and lower temperature. However, the main limitation to both these approaches is that the aldehyde installation is shackled to the *N*-terminus. In the context of electroactive protein immobilisation via bio-orthogonal ligation, this means that if the *N*-terminus of the protein is out of quantum-tunnelling range (ca. 14 Å)<sup>45</sup> of a redox-active site or a long-range electron-transfer pathway then it is unlikely to make a suitable site via which to tether the protein to an electrode surface. In addition, it is not unusual for protein *N*-termini to form part of the active sites of redox proteins/enzymes;<sup>292</sup> this is presumably due to the unique chemical properties of protein *N*-termini, such as the lower pKa of the *N*-terminal amine or chelating effects arising from the *N*-terminal amine's proximity to side chain functionality, as is the case with LPMOs (see **Section 2.1.1**).<sup>268</sup>

The oxidative cleavage of *cis* 1,2-diols on the glycans of glycoproteins using  $\text{NaIO}_4$  represents another method of aldehyde installation (**Figure 4.1**, panel **A**).<sup>402-404</sup> The installation of aldehydes via this method can be performed in around 20 min at room temperature using an excess of sodium metaperiodate.<sup>404</sup> While not as mild a procedure as the installation of aldehydes via the comparable

oxidation of *N*-terminal serine or threonine residues, this method is still widely used in the preparation of labelled proteins and antibody-probe conjugates. Unfortunately, many glycoproteins have several sites of glycosylation and exist as several glycoforms,<sup>405,406</sup> leading to a range of products. In the context of serving as a tether to an electrode surface, ligation to oxidised glycan residues is thus unlikely to facilitate redox protein immobilisation in a controlled orientation. In addition, the length of the glycan serving as the tether could also mean that the redox-active site is not held close enough to the electrode surface to allow for facile direct electron transfer.

The installation of an aldehyde into a protein via unnatural amino acid mutagenesis (**Figure 4.1**, panel E) allows aldehydes to be potentially installed at any location within the protein, making unnatural amino acid mutagenesis an extremely powerful technique.<sup>230,407-409</sup> Unfortunately, while the usage of unnatural amino acid mutagenesis is highly amenable for proteins which are easily overexpressed, many redox proteins, such as hydrogenases, are assembled and matured using a complicated system of chaperones<sup>410</sup> and do not lend themselves well to overexpression in bacteria. This represents a practical limitation to the usage of unnatural amino acid mutagenesis; synthesising the requisite quantity of unnatural amino acid to prepare enough bacterial media to successfully generate high quantities of a basally-expressed aldehyde-functionalised protein would be financially unfeasible for most. In addition, while systems have been developed that allow unnatural amino acid mutagenesis to be performed in mammalian<sup>411,412</sup> and yeast<sup>413</sup> cells, and in plant<sup>414</sup> and insect<sup>415</sup> extracts, it remains far simpler to perform unnatural amino acid mutagenesis on proteins that correctly express in bacteria.<sup>408,409,416</sup>

#### 4.1.1 Aims

A series of methods for the introduction of aldehydes into proteins, and methods for the subsequent ligation of these aldehydes, are to be investigated in the hopes of identifying strategies potentially suited for covalent redox protein immobilisation. The aims are as follows:

- 1) Optimise several methods for the introduction of aldehydes into proteins.
- 2) Perform bio-orthogonal conjugation to the resultant protein aldehydes.
- 3) Critically assess the suitability of both the aldehyde installation strategy and the bio-orthogonal ligation strategy for potential usage in electroactive redox protein immobilisation.

## 4.2 Results and Discussion

### 4.2.1 Performing oxidative cleavage of *N*-terminal threonine/serine residues

#### 4.2.1.1 One-pot oxidation and derivatisation of the CTB *N*-terminus

The Cholera toxin (CT), secreted by *Vibrio cholerae* is estimated to cause up to 142,000 deaths per annum worldwide.<sup>417</sup> The CT protein complex is composed of two types of subunits: the nontoxic CT subunit B (CTB), which self-assembles to form a pentameric ring, and the toxic CT subunit A (CTA), which threads through the pore at the centre of the CTB pentamer and associates to form the complete CT complex.<sup>418,419</sup> This protein complex bears *N*-terminal threonine residues on the CTB subunits which have previously been exploited in chemical-modification strategies due to the medicinal interest in the action of CT.<sup>418,420</sup>

CTB is readily available from commercial suppliers but is also easy to prepare recombinantly. Although it is not a redox protein, the availability and literature precedent for the installation and labelling of aldehydes on CTB *N*-termini made it useful protein upon which to become familiarised with these techniques. A series of experiments were conducted using a batch of CTB prepared by Dr Tessa Keenan, and an educational experiment for undergraduates based on these experiments was later designed and published in which students perform a one-pot oxidation and derivatisation of the CTB *N*-terminus.<sup>392</sup>

Periodate oxidation of *N*-terminal threonine or serine residues (**Figure 4.1**, panel **B**) proceeds rapidly, yet given sufficient time periodate will also oxidise any amino acid.<sup>421-423</sup> Therefore, to minimize the occurrence of such side reactions (which could denature the protein), an excess of the free amino acid L-methionine can be added to the reaction solution. The oxidation of the *N*-terminal threonine of CTB was performed at pH 7 and at room temperature for 15 min in the presence of L-methionine, resulting in the installation of an *N*-terminal glyoxylamide-type aldehyde functionality (also referred to as a glyoxyl functionality) while not causing any observable protein degradation (**Figure 4.3**).<sup>421</sup> The average yield of this oxidation step was repeatedly predetermined by ESI-MS to be 90% (see **Figure 4.4**).

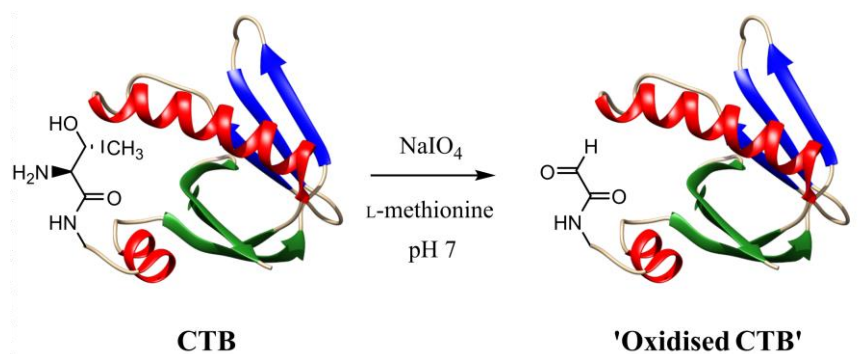


**Figure 4.3.** Oxidation of the *N*-terminal threonine residue of CTB using sodium metaperiodate to yield an exploitable aldehyde functionality. CTB structure from PDB: 1PZJ.<sup>424</sup>

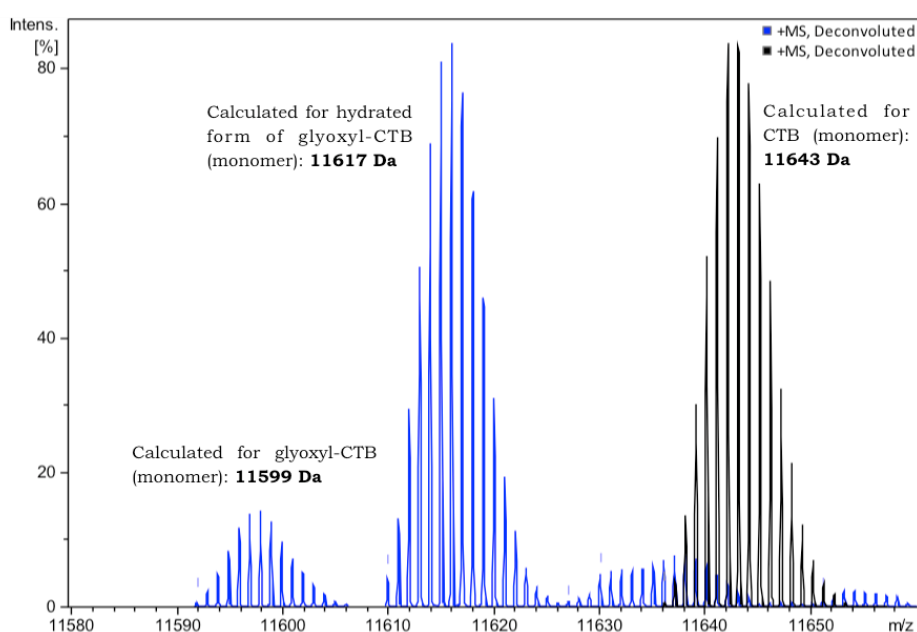


**Figure 4.4.** Deconvoluted mass spectrometric trace of CTB before (black) and after (blue) treatment with  $\text{NaIO}_4$ . The oxidised CTB can exist in two forms, both as the free aldehyde (“glyoxyl-CTB”, calculated mass 11599 Da) or as the hydrate of the aldehyde, a geminal diol (“hydrated glyoxyl-CTB”, calculated mass 11617 Da).

One of the challenges in developing an experiment suitable for undergraduates was finding a way to prove that ligation to a protein aldehyde had been achieved without using expensive equipment such as desalting columns or have the students using restricted instruments in the collection of mass spectra. To overcome these challenges we considered the use of 3-methyl-2-benzothiazolinone hydrazone (MBTH, **Figure 4.5**), which yields an azine upon reaction with aldehydes. Azines are chromophores, and upon the reaction of MBTH with an oxo-aldehyde (like that of a glyoxylamide) a new UV absorption peak can be observed with a  $\lambda_{\text{max}}$  of  $\sim 345 \text{ nm}$ ;<sup>425</sup> this wavelength is significantly greater than 280 nm, allowing the azine absorption to be distinguished from that of the canonical protein residues. In addition, the azine formed via the reaction of MBTH with a glyoxylamide has more

extensive conjugation and a more dominant azo-like resonance form than azines derived from an alkylic aldehydes such as acetaldehyde (see **Figure 4.5**, bottom), and thus selection of 345 nm as the probe wavelength will likely favour detection of the azines formed from the *N*-terminal glyoxylamides over those formed from the acetaldehyde biproduct released during the  $\text{NaIO}_4$  treatment.

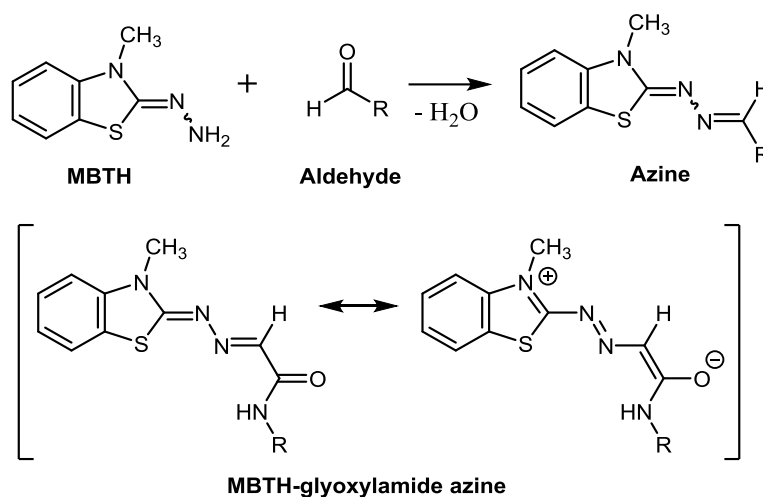


**Figure 4.5.** The reaction of MBTH with aldehydes to form azines (top), and the resonance of an azine formed via the reaction of an *N*-terminal glyoxylamide with MBTH (bottom). Note that the MBTH-glyoxylamide azine would likely be present as several stereoisomers.

The newly-introduced *N*-terminal glyoxylamide functionalities on CTB reacted efficiently with MBTH in the presence of aniline (which serves as a nucleophilic catalyst, accelerating the azine-forming reaction via transient aniline Schiff base formation)<sup>395</sup> within 20 min to afford the CTB–MBTH azine conjugate without the need for intermediate protein purification. The four students who trialled the experiment characterised and determined the yield of the CTB–MBTH azine product using HPLC-coupled UV–vis spectroscopy, setting the UV-unit to detect absorption at 345 nm and using a reverse-phase C-18 column. The students readily identified the CTB–MBTH azine adduct as a sharp peak on the chromatogram trace of the reaction solution (**Figure 4.7**). The stack-plot of student chromatograms in (**Figure 4.7**) demonstrates the robust and reproducible elution of the CTB–MBTH adduct at approximately 4 min, and shows that all four students were able to successfully perform the bioconjugation reaction. The students were able to use the area of this peak in conjunction with a calibration curve, constructed using samples of serine subjected to treatment with  $\text{NaIO}_4$  and aniline/MBTH solutions under conditions comparable to those used on the CTB samples, to estimate the total conversion of CTB into the CTB–MBTH analogue as 11%. It should be noted that this is likely an underestimate as the extinction coefficient of the CTB–MBTH azine at 345 nm is likely lower than that of the small molecule azine analogue.

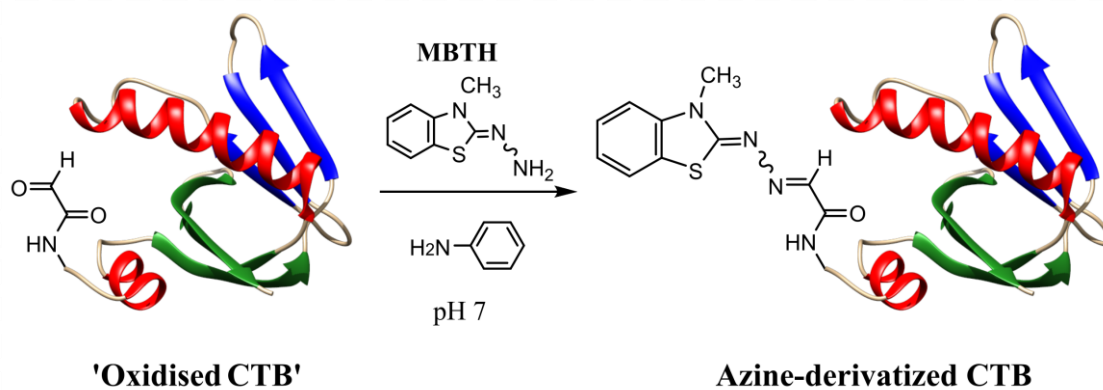


**Figure 4.6.** Formation of azine-derivatised CTB via the reaction of MBTH with the aldehyde functionality introduced at the N-terminus of CTB, at pH 7 in the presence of an aniline catalyst. CTB structure from PBD: 1PZJ.<sup>424</sup>

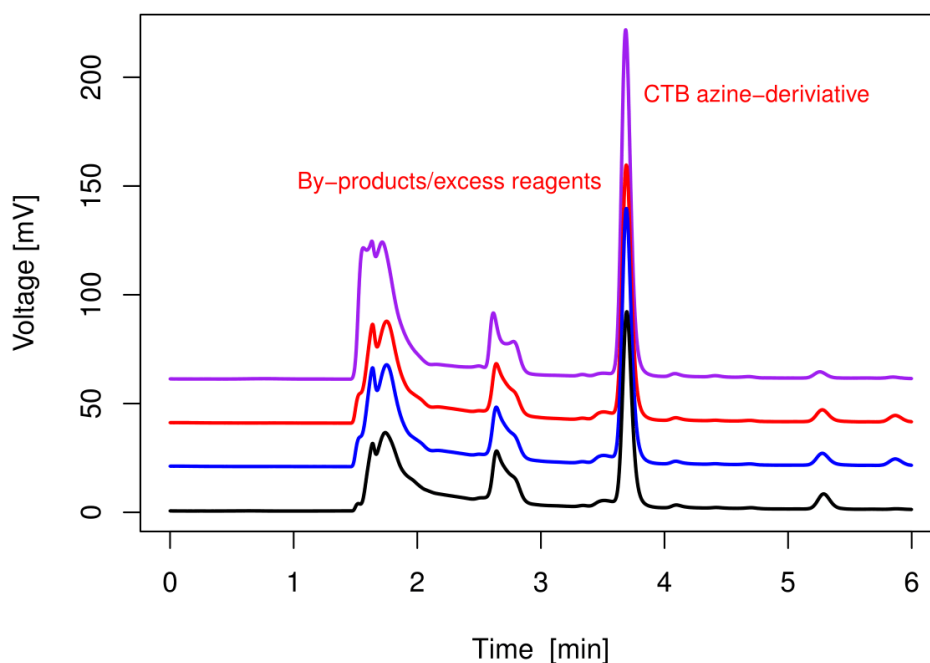


**Figure 4.7.** HPLC-coupled-UV-vis-spectroscopy-chromatogram stack-plot of student-acquired data, showing a consistent peak for the CTB-MBTH azine derivative.

All the steps of this experiment are summarised in **Figure 4.8**. This experiment serves as a useful experiment with introduces undergraduates to some of the techniques associated with protein handling and bioconjugation, while avoiding the use of expensive disposable lab consumables that are typically used in bioconjugation reactions, such as desalting columns and centrifugal protein concentrators.

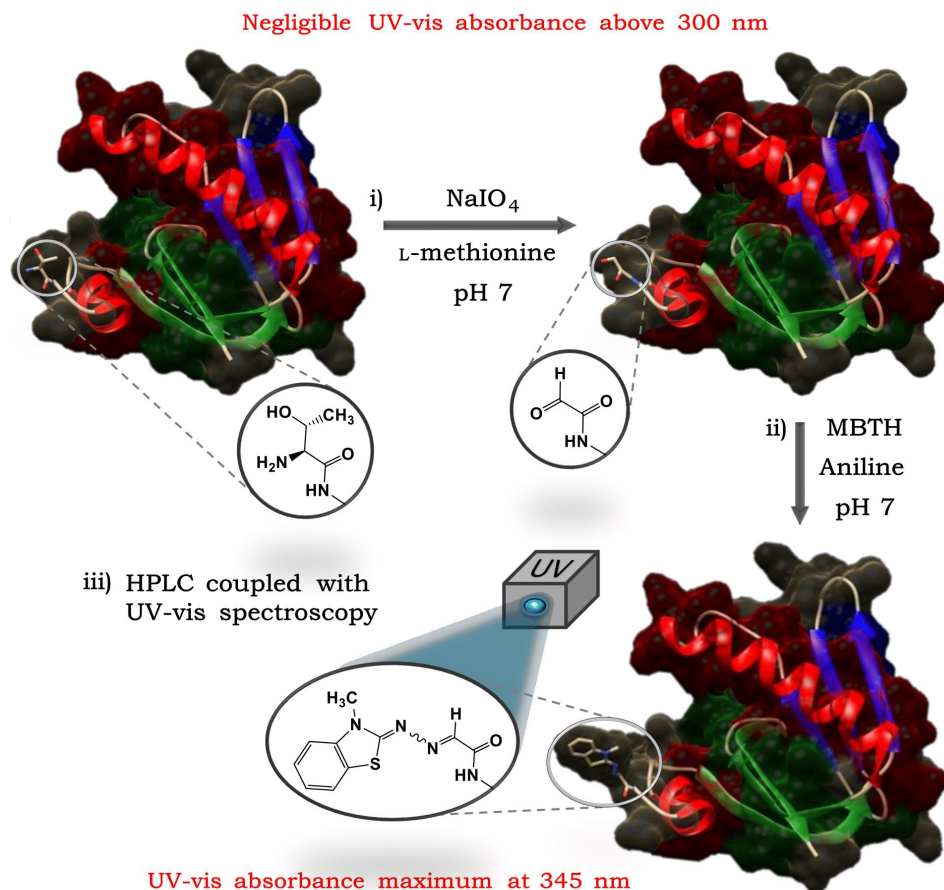


**Figure 4.8.** Preparation and detection of a CTB-MBTH adduct. The CTB-MBTH adduct can be distinguished from “untagged” proteins using a UV-vis-spectroscopy band with a maximum at 345 nm. A wavy bond line indicates the stereochemistry is unknown.

#### 4.2.1.2 Oxidation of the *N*-terminus of thioredoxin 1

Thioredoxins are small redox proteins that serve as antioxidants, facilitating the reduction of other proteins via the oxidation of the vicinal cysteines in the active site into a disulfide. Electrochemistry can be used to either oxidise vicinal cysteines into a disulfide or reduce disulfides into vicinal cysteines, depending on the applied potential.<sup>426</sup>

One of *E. coli*'s native thioredoxin proteins, thioredoxin 1 (TrxA), has an *N*-terminal serine residue and is commercially available.<sup>427</sup> In addition, the *N*-terminus of TrxA is relatively close to the redox-active site (ca. 15 Å) (**Figure 4.9**). Although it is commonly believed that rapid direct electron transfer between proteins and electrodes is dependent on an electron entry/exit site being within 14 Å of the electrode surface,<sup>45</sup> facile direct electron transfer to the TrxA active site could still be possible if TrxA were tethered to the electrode surface through the *N*-terminal residue, as the absolute orientation of immobilised TrxA could potentially bring the active site to within 14 Å of the electrode



surface. As such TrxA represented an interesting protein upon which to test the usage of aldehydes installed into redox proteins as tethers to electrode surfaces.

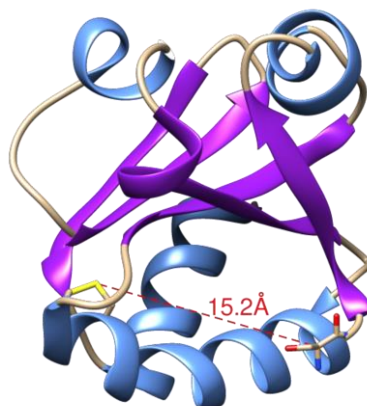


**Figure 4.9.** The structure of thioredoxin 1 from *E. coli*. Crystal structure PDB: 2TRX.<sup>428</sup> The 15.2 Å distance is taken between the sulfur atom of residue Cys35 and the backbone carbon atom of the *N*-terminal serine residue.

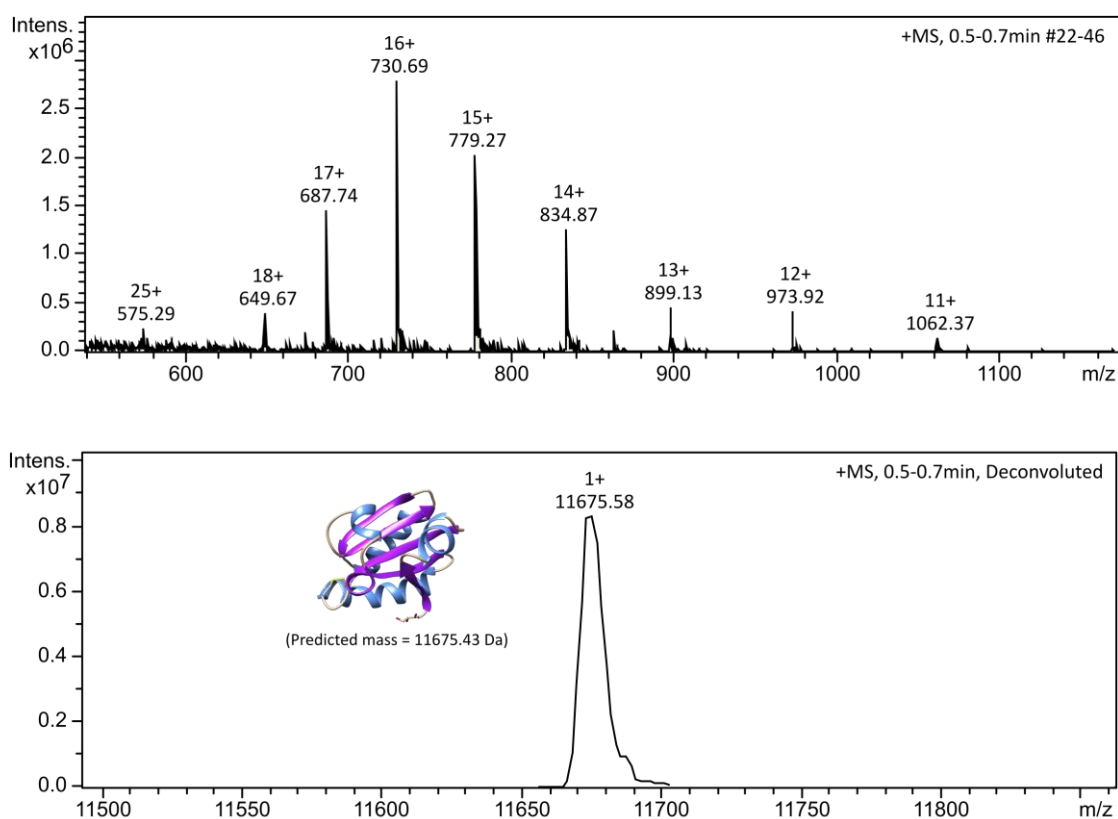


**Figure 4.10.** Protein mass spectrometry of unmodified TrxA. **Top)** Raw spectrometric data showing the TrxA charge-state ladder. **Bottom)** Deconvolution of the raw spectrometric data yields a single peak at  $m/z$  11675.58, which is in excellent agreement with the theoretical mass of unmodified TrxA (11675.43 Da).

Treatment of TrxA with  $\text{NaIO}_4$  at pH 7 (25 mM sodium phosphate buffer) at room temperature for 4 min converts the *N*-terminal serine to a glyoxylamide. This conversion can be readily observed upon comparison of the protein mass spectrums of unmodified TrxA (**Figure 4.10**) with that of  $\text{NaIO}_4$ -treated TrxA (**Figure 4.11**). The reactive nature of the aldehyde on the glyoxylamide-functionalised TrxA (Ald-TrxA) was verified via solution-phase oxime ligation and characterised by mass spectrometry (MS); the treatment of Ald-TrxA with *O*-benzylhydroxylamine in the presence of aniline (which serves as a nucleophilic catalyst)<sup>395</sup> at pH 4.5 yields the corresponding oxime product in 60% conversion within 4 hours (**Figure 4.12**). Furthermore, the complete conversion of unmodified TrxA into Ald-TrxA is evidenced by the lack of an unmodified TrxA peak in either of the mass spectrums presented in **Figure 4.11** or **Figure 4.12**.

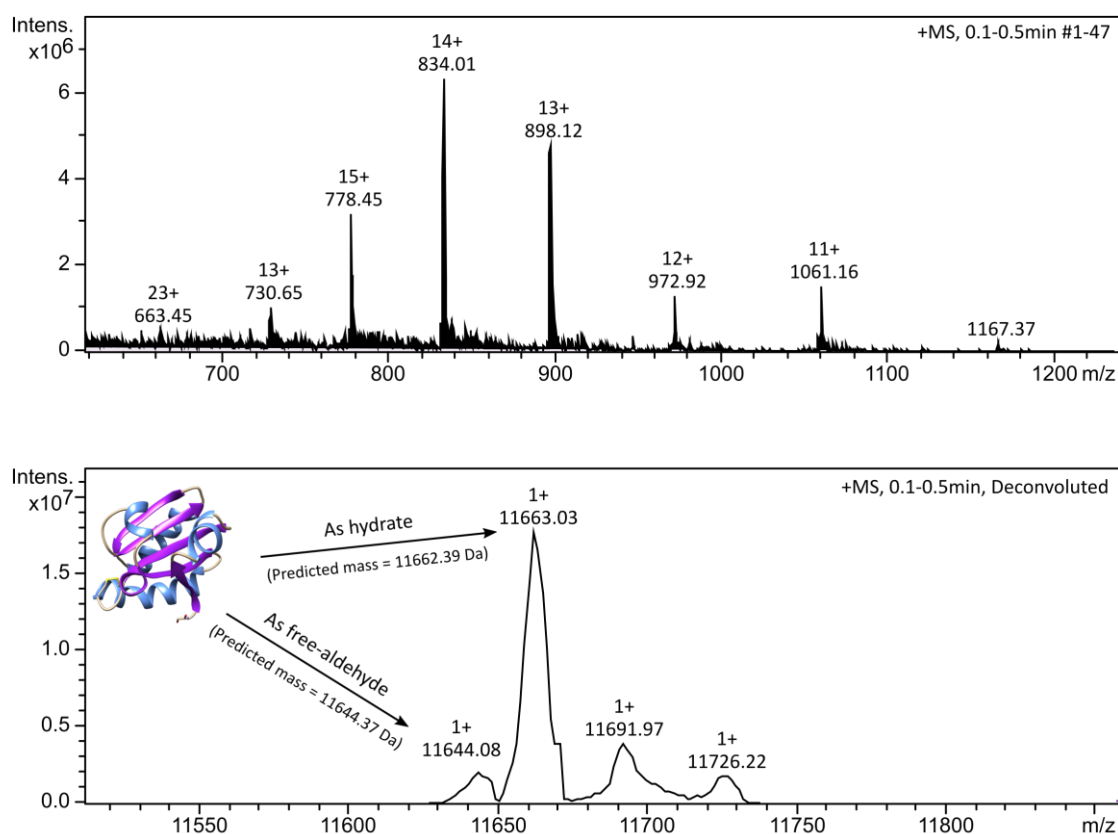


**Figure 4.11.** Mass spectrometric evidence of successful aldehyde introduction into TrxA after treatment with  $\text{NaIO}_4$ . **Top**) Raw spectrometric data showing Ald-TrxA charge-state ladders. **Bottom**) Deconvolution of the raw spectrometric data yields a strong peak in which is in excellent agreement with the theoretical mass of the hydrated form of Ald-TrxA (11662.39 Da) at an  $m/z$  of 11663.03, and three smaller peaks, one of which is in excellent agreement with the theoretical mass of Ald-TrxA in the free-aldehyde form (11644.37 Da), at an  $m/z$  of 11644.08.

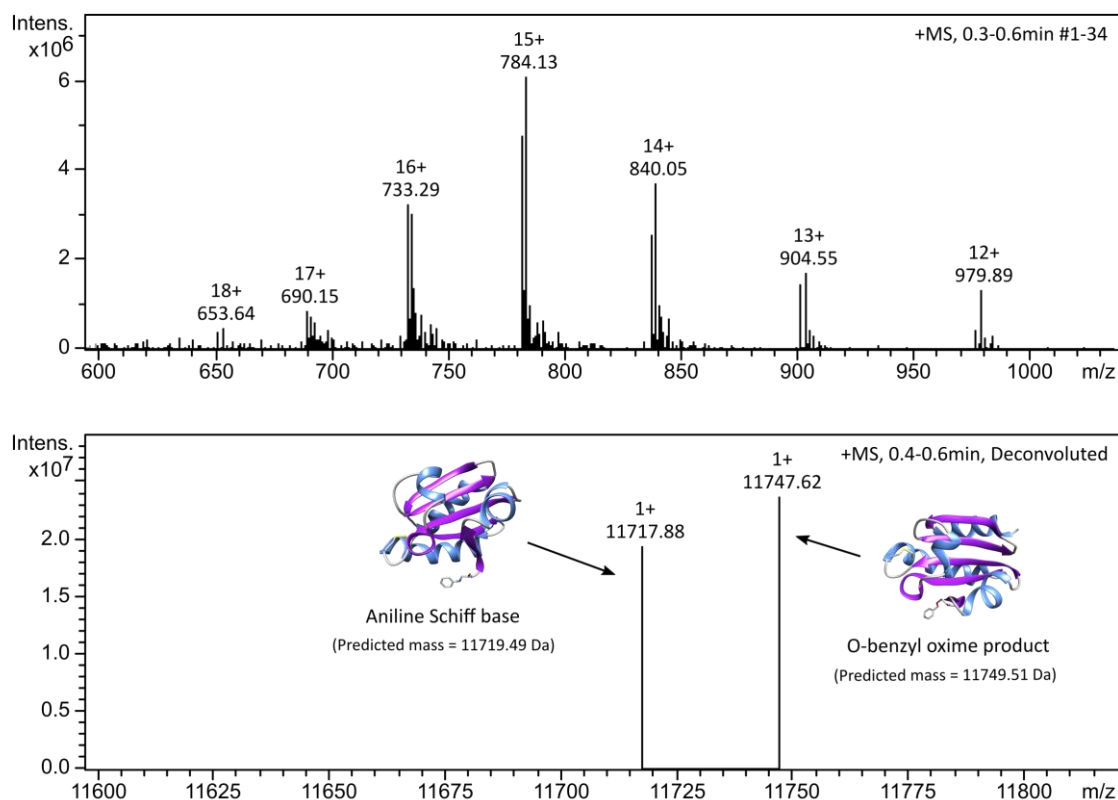


**Figure 4.12.** Mass spectrometry of a solution of Ald-TrxA treated with 10 equiv O-benzylhydroxylamine for 4 hours in a pH 4.5 buffer (100 mM sodium acetate + 100 mM aniline). **Top)** Raw spectrometric data showing charge-state ladders. **Bottom)** Deconvolution of the raw spectrometric data yields a pair strong peaks at m/z 11717.88 and 11747.62, which are in excellent agreement with the theoretical masses of the aniline Schiff base of Ald-TrxA (11719.49 Da) and the O-benzyl oxime adduct with Ald-TrxA (11749.51 Da).

#### 4.2.2 Performing oxidative cleavage on glycan 1,2-cis diols

Sialic acids and other monosaccharides which present 1,2-cis diols, such as mannose and galactose (**Figure 4.13**), are also susceptible to oxidation with NaIO<sub>4</sub>, allowing aldehydes to be installed onto glycoproteins under mild conditions (**Figure 4.1**, panel A).<sup>429</sup> Sialic acid is the most susceptible monosaccharide, with a working concentration of 1 mM NaIO<sub>4</sub> being sufficient to successfully oxidise the sialic acid residues in a 0.5 → 10 mg mL<sup>-1</sup> solution of glycoprotein.<sup>404,430,431</sup> Other monosaccharides that present 1,2-cis diols motifs, such as mannose, galactose and fucose can also be easily oxidised, yet require slightly more forceful conditions; oxidation of these residues in a 0.5 → 10 mg mL<sup>-1</sup> solution of glycoprotein requires a working NaIO<sub>4</sub> concentration of 10 mM.<sup>404,431,432</sup> Periodate oxidation using NaIO<sub>4</sub> can be performed at neutral pH but is more effective under slightly acidic conditions.<sup>404</sup> Buffers containing primary amines or sugars should also be avoided, as they can interfere with or complete in the periodate oxidation reaction.<sup>404</sup>

All glycoprotein *N*-glycans share a core structural motif rich in mannose residues ( $\text{Man}\alpha 1\text{--}6(\text{Man}\alpha 1\text{--}3)\text{Man}\beta 1\text{--}4\text{GlcNAc}\beta 1\text{--}4\text{GlcNAc}\beta 1\text{--Asn-X-Ser/Thr}$ ),<sup>429</sup> to which additional residues are appended to yield 3 classes of *N*-glycan: oligomannose *N*-glycans, which only have mannose residues are attached to the core; complex *N*-glycans, in which “antennae” beginning with *N*-acetylglucosamine (GlcNAc) residues extend off the core structure; and hybrid *N*-glycans, which only have mannose residues attached to the  $\text{Man}\alpha 1\text{--}6$  arm of the core, and have one or two antennae on the  $\text{Man}\alpha 1\text{--}3$  arm. An example of each type of *N*-glycan is shown overleaf in **Figure 4.14**.<sup>429,433</sup> As can be seen in **Figure 4.14**, most *N*-glycans can be expected to present residues susceptible to oxidation with  $\text{NaIO}_4$ .

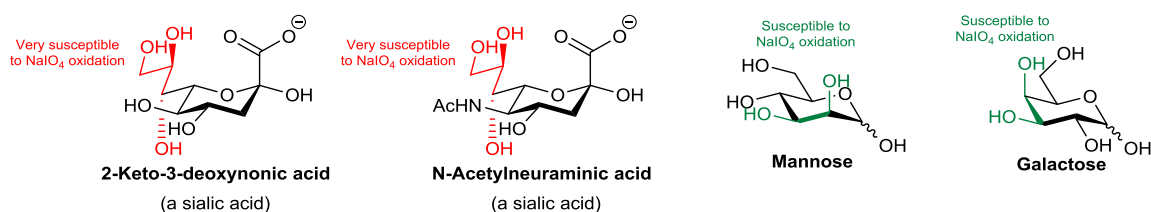


**Figure 4.13.** The structures of 2-keto-3-deoxyonic acid and *N*-acetylneuraminic acid, which are examples of sialic acids, and the structures of mannose and galactose. The *cis*-1,2-diol units in these sugars are marked, as are the susceptibility of these units to oxidation with  $\text{NaIO}_4$ .

Serine and threonine residues in proteins can also bear glycosylation: *O*-glycosylation. *O*-glycosylation is however far more variable than *N*-glycosylation, and *O*-glycan structure cannot be easily generalised across the different kingdoms of life.<sup>434</sup> As such, while *O*-glycosylation may indeed present sugars that are susceptible to periodate oxidation, such as *N*-acetylgalactosamine (GalNAc), mannose, or galactofuranose monosaccharides,<sup>434</sup> intentional manipulation of *O*-glycosylation is beyond the scope of this thesis.

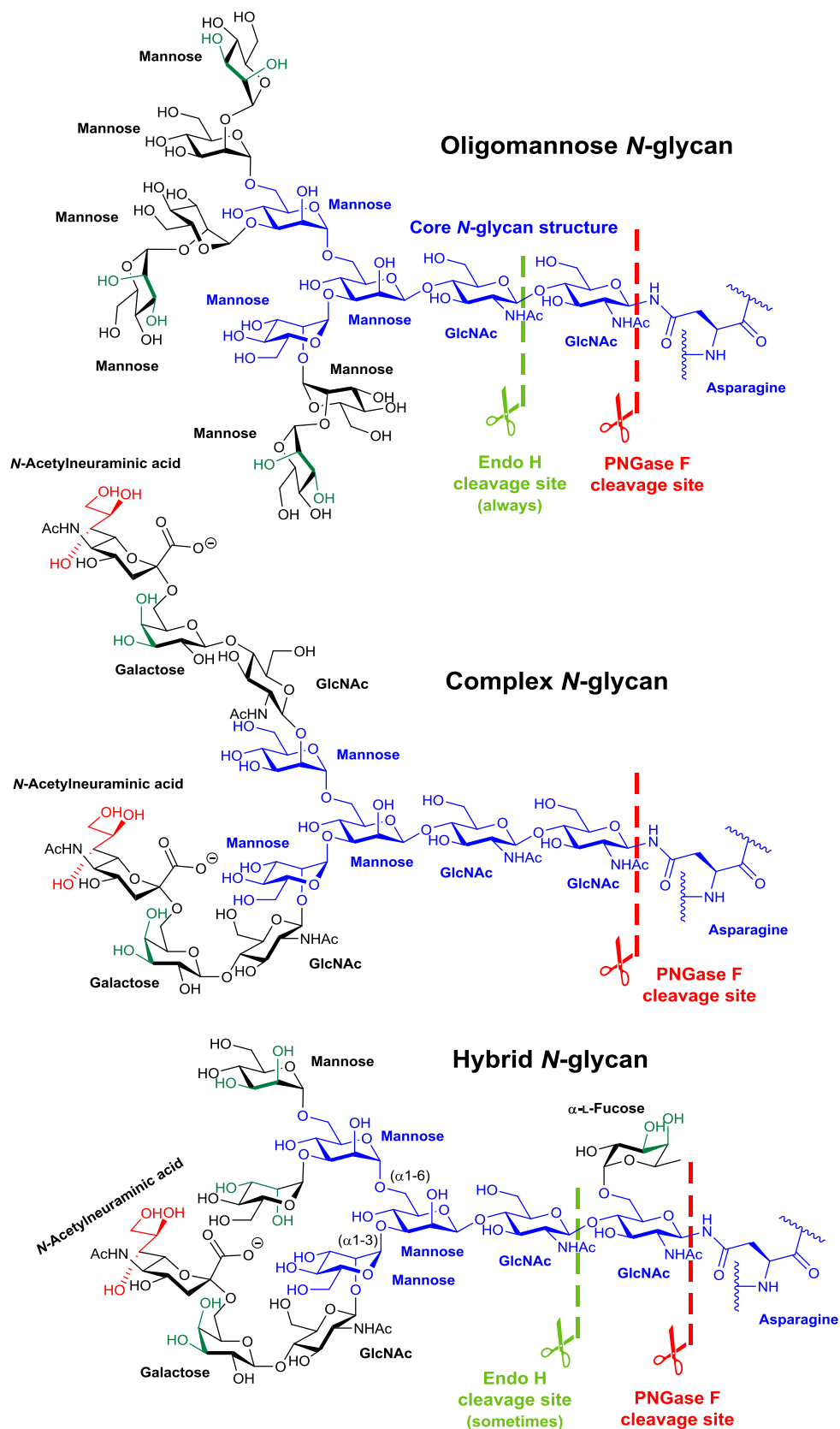


**Figure 4.14.** Example structures of oligomannose, complex and hybrid type *N*-glycans, and the sites at which the deglycosylating enzymes Endo H and PNGase F can cleave on each type of *N*-glycan.<sup>435,436</sup> Cis 1,2-diols susceptible to oxidative cleavage with 1 mM NaIO<sub>4</sub> are shown in red, whereas those susceptible to oxidative cleavage with 10 mM NaIO<sub>4</sub> are shown in dark green.

#### 4.2.2.1 Aldehyde-functionalisation and fluorescent labelling of the glycans on an AA9 LPMO

The sequence of An6428-AA9 - the glycosylated AA9 LPMO previously discussed in **Chapter 2** – was analysed using online tools to identify putative sites of glycosylation. Due to being expressed in a filamentous fungus, An6428-AA9 could bear both *N*- and *O*-glycosylation.<sup>290</sup>

The NetNGlyc server (available at <http://www.cbs.dtu.dk/services/>) detects the consensus sequence Asn-X-Ser/Thr/Cys (where X is any amino acid apart from proline)<sup>429,437</sup> within protein sequences to identify putative *N*-glycosylation sites. The NetNGlyc server was designed to identify *N*-linked glycosylation sites in human proteins, and while An6428-AA9 is fungal it was assumed that the NetNGlyc server could still prove useful as all *N*-glycans share the same structural core; which is presumably installed using the same enzymatic pathways and consensus sequences.<sup>429,437</sup> Analysis of the AsAA9 sequence using this tool identified two potential *N*-glycosylation sites: asparagine residues 51 and 125 (**Figure 4.15**).

Name:	Sequence	Length:	213
	HYVFPALVQDGAATGDWVKYVRDWTGSYGNPVEDVTSLDIRCNKDASTNGNATETLPVKAGEEIGFTVRTNIGHPGPLLA		80
	YMAKAPGDASDFDGDGQVWFKIYEDGPTVTDDGLTWPSDGATNVNFTIPSSLPDGDYLLRVEHIALHGAGTEGGAQFYLS		160
	CGQVSVTGGGNGDPAPLVAFPGAYDPTDPGILINIYWPVPTNYTPPGPKVWSG		
	.....N.....		80
	.....N.....		160
	.....		240

(Threshold=0.5)

SeqName	Position	Potential	Jury agreement	N-Glyc result
Sequence	51 NATE	0.7348	(9/9)	++
Sequence	125 NFTI	0.6639	(9/9)	++
Sequence	202 NYTP	0.1499	(9/9)	---

**Figure 4.15.** Output of the NetNGlyc server, identifying putative sites of *N*-glycosylation in An6428-AA9.

The NetOGlyc and DictyOGlyc servers (available at <http://www.cbs.dtu.dk/services/>) were designed to detect *O*-(*N*-acetylgalactosamine) glycosylation sites and *O*-( $\alpha$ )-(*N*-acetylglucosamine) glycosylation sites in animal (specifically mammalian) and Amoebozoa proteins respectively: proteins from different phyla of life to filamentous fungi. It was therefore not appropriate to analyse An6428-AA9 using these servers, as *O*-glycosylation in filamentous fungi begins with a mannose unit and there are no known consensus sequences for *O*-glycosylation in fungi.<sup>434</sup> It should be noted that despite this other authors, have previously used the NetOGlyc tool to identify *O*-glycosylation sites in AA9 LPMOs expressed in yeast.<sup>438</sup> It is however known that filamentous fungi *O*-glycosylation can terminate in galactofuranose residues,<sup>434</sup> which are highly susceptible to periodate oxidation, and there are

incidences of LPMO crystal structures that show *O*-glycosylation with single mannose units which are also susceptible to periodate oxidation.<sup>290</sup>

#### 4.2.2.2.1 Introduction of aldehyde functionalities via $\text{NaIO}_4$ treatment

To install an aldehyde handle into *An6428-AA9*, a 119  $\mu\text{M}$  sample was subjected to treatment with 10 mM  $\text{NaIO}_4$  in a pH 6.0 buffer (50 mM MES) for 20 min and then transferred into either a fresh pH 6.0 buffer (MES 50 mM) or a pH 4.5 buffer (200 mM sodium acetate) using a 10 kDa molecular weight cut-off centrifugal protein concentrator. Centrifugal protein concentrators were used in place of Sephadex G-25 desalting columns as it was unknown if the AA9 would show affinity for the dextran component of the G-25 resin. Electron paramagnetic resonance (EPR) spectroscopy (performed by Peter Lindley) was used to confirm that the LPMO had not become desaturated by the  $\text{NaIO}_4$  treatment (**Figure 4.16**).

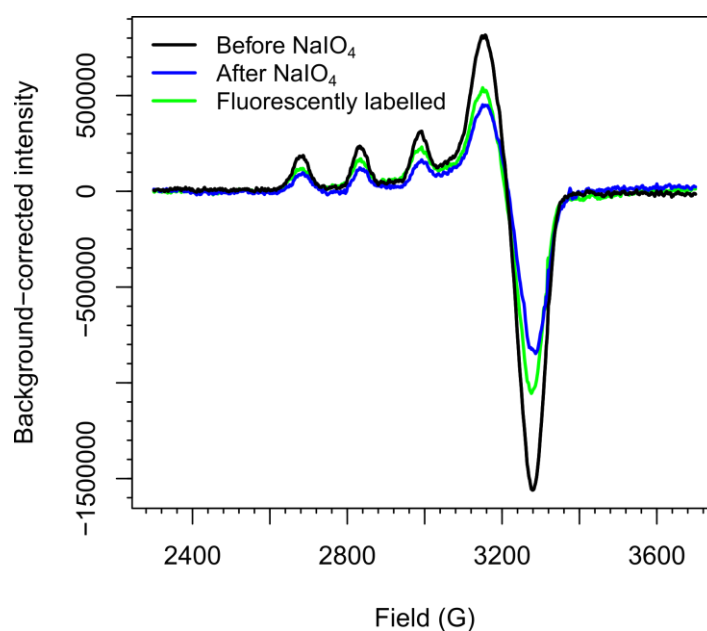
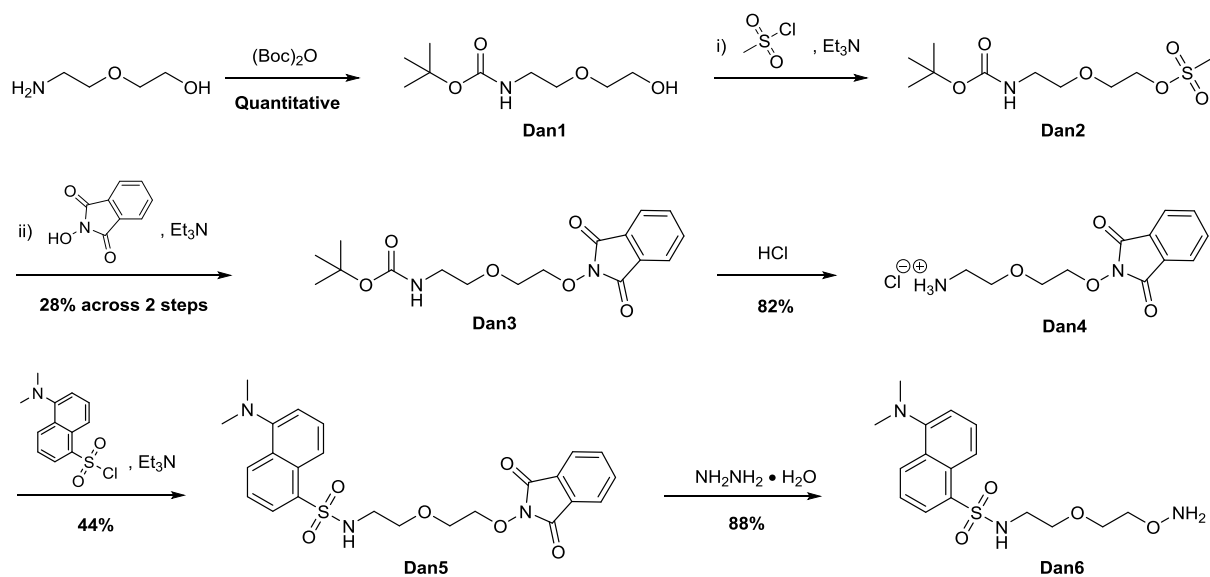


**Figure 4.16.** Continuous wave (cw) X-band EPR spectra collected for frozen solutions of *An6428-AA9* (ca. 0.1 mM) at pH 6.0 (20 mM sodium MES buffer) at 150 K. A sample of *An6428-AA9* was analysed at three different stages of derivatisation, firstly the underivatised protein was analysed (before treatment with  $\text{NaIO}_4$ , black), secondly the protein was analysed after treatment with  $\text{NaIO}_4$  (blue) and finally after treatment with  $\text{NaIO}_4$  and 100 equiv **Dan6**. Data collection was performed using a Bruker micro EMX spectrometer using a frequency of ca. 9.30 GHz, with modulation amplitude of 4 G, modulation frequency of 100 kHz and a microwave power of 10.02 mV. The data was intensity averaged over 3 scans.

## 4.2.2.2 Labelling of aldehyde-functionalised glycans using a dansylated hydroxylamine probe

A fluorescently-labelled aldehyde-reactive probe, dansylated hydroxylamine-functionalised probe **Dan6**, was synthesised in five-steps (**Scheme 4.1**). A series of ligation experiments were performed using both samples of *An6428-AA9* that had been treated with  $\text{NaIO}_4$  and samples of unmodified *An6428-AA9*, and analysis of these experiments was performed using sodium dodecyl sulfate–polyacrylamide gel electrophoresis (SDS-PAGE). The SDS-PAGE gel was run without dye to allow for detection of fluorescently tagged proteins (**Figure 4.17**, bottom), and then subjected to the standard procedure of staining with Coomassie dye to visualise the location of all proteins (**Figure 4.17**, top). The reaction conditions the different *An6428-AA9* samples were subjected to, and the location of these samples in the SDS-PAGE gel presented in **Figure 4.17**, are tabulated in **Table 4.1**. EPR was used to confirm that *An6428-AA9* did not become denatured after 1 hour at room temperature in a pH 4.5 buffer in the presence of 100 equiv of **Dan6** (**Figure 4.16**). Note that as a great excess of **Dan6** was used in the oxime ligation reactions it was not necessary to use a nucleophilic catalyst (such as aniline) to increase the rate of reaction.



**Scheme 4.1.** The synthesis of a dansylated hydroxylamine-functionalised probe (**Dan6**).



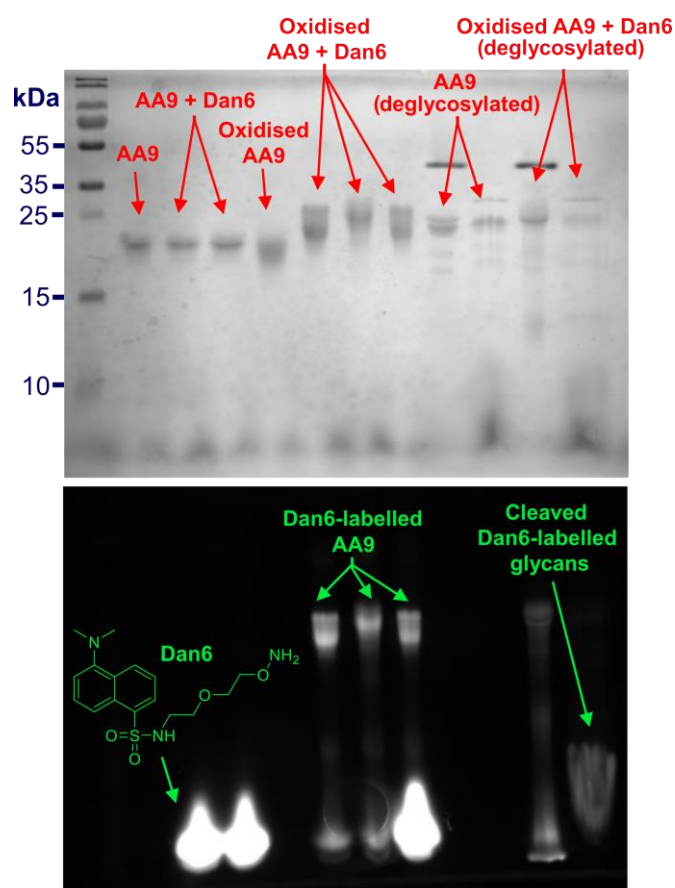


**Figure 4.17.** SDS-PAGE gel of samples of *An6428-AA9* glycoprotein (referred to here simply as “AA9”) subjected to a series of reaction conditions detailed in **Table 4.1**, including aldehyde introduction via *cis*-1,2-diol oxidative cleavage with  $\text{NaIO}_4$ , labelling of aldehydes with fluorescent hydroxylamine-functionalised probe **Dan6** and enzymatic deglycosylation. Prior to running on the SDS-PAGE gel, protein samples were boiled in a dye-free reducing buffer (2% SDS, 2 mM 2-mercaptoethanol, 4% glycerol, 40 mM Tris-HCl pH 6.8).

**Table 4.1.** The treatments the samples of *An6428-AA9* in **Figure 4.17** were subjected to.

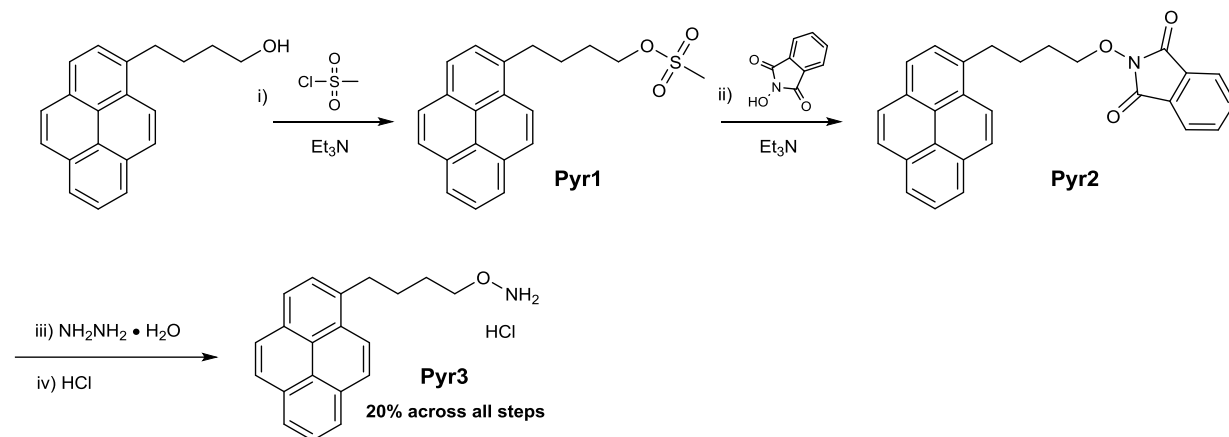
Gel Lane	Sample label in Figure	Treatment with $\text{NaIO}_4$	Dan6 reaction conditions	Enzyme used to perform deglycosylation
1	Ladder	N/A	N/A	N/A
2	AA9	<input checked="" type="checkbox"/>	N/A	N/A
3	AA9 + <b>Dan6</b>	<input checked="" type="checkbox"/>	pH 6, 100 equiv <b>Dan6</b>	N/A
4	AA9 + <b>Dan6</b>	<input checked="" type="checkbox"/>	pH 4.5, 100 equiv <b>Dan6</b>	N/A
5	Oxidised AA9	<input checked="" type="checkbox"/>	N/A	N/A
6	Oxidised AA9 + <b>Dan6</b>	<input checked="" type="checkbox"/>	pH 6, 100 equiv <b>Dan6</b>	N/A
7	Oxidised AA9 + <b>Dan6</b>	<input checked="" type="checkbox"/>	pH 4.5, 100 equiv <b>Dan6</b>	N/A
8	Oxidised AA9 + <b>Dan6</b>	<input checked="" type="checkbox"/>	pH 4.5, 100 equiv <b>Dan6</b> (repeated experiment)	N/A
9	AA9 (deglycosylated)	<input checked="" type="checkbox"/>	N/A	Endo H
10	AA9 (deglycosylated)	<input checked="" type="checkbox"/>	N/A	PNGase F
11	Oxidised AA9 + <b>Dan6</b> (deglycosylated)	<input checked="" type="checkbox"/>	pH 4.5, 100 equiv <b>Dan6</b>	Endo H
12	Oxidised AA9 + <b>Dan6</b> (deglycosylated)	<input checked="" type="checkbox"/>	pH 4.5, 100 equiv <b>Dan6</b>	PNGase F

As depicted in **Figure 4.17**, only samples of *An6428-AA9* that have been subjected to treatment with both  $\text{NaIO}_4$  and the fluorescent hydroxylamine-functionalised probe **Dan6** give rise to fluorescent bands in the SDS-PAGE gel. Evidence that the  $\text{NaIO}_4$  installs aldehyde functionality into the glycans of *An6428-AA9* is afforded by the loss of the fluorescence in the samples of LPMO that have subjected to deglycosylation with either of the deglycosylating enzymes Endo H or PNGase F, which act on *N*-glycans. The loss of fluorescence from the *An6428-AA9* band for the sample treated with PNGase F (**Figure 4.17**, lane 12) is more complete than that seen for the sample treated with Endo H (**Figure 4.17**, lane 11). This is likely due to the different substrate specificities of these enzymes; Endo H is a glycosidase which cleaves between the GlcNAc residues of the core *N*-glycan structure, but only on oligomannose and a limited number of hybrid *N*-glycans (**Figure 4.14**), whereas PNGase F is an amidase which cleaves all types of *N*-glycans between the GlcNAc and the asparagine residue, provided there is not an  $\alpha$ -(1,3)-linked core fucose residue (a problem typically only encountered with plant glycoproteins) (**Figure 4.14**).<sup>435,436</sup> As such it is possible that glycoforms of the fluorescently-labelled *An6428-AA9* with complex or hybrid *N*-glycans may not have lost all of their fluorescent labels upon treatment with Endo H, whereas all the *N*-glycans of the fluorescently-labelled *An6428-AA9* would be expected to lose their fluorescent labels upon treatment with PNGase F, regardless of glycoform. The near-total lack of fluorescence in the PNGase-F treated fluorescently labelled *An6428-AA9* sample (**Figure 4.17**, lane 12) would suggest that *An6428-AA9* does not present many *O*-glycans that are susceptible to periodate oxidation.

#### 4.2.2.2.3 Labelling of aldehyde-functionalised glycans using a pyrene-functionalised hydroxylamine probe

Pyrene motifs are fluorescent, and also have a strong affinity for the walls of carbon nanotubes due to  $\pi$ - $\pi$  stacking interactions.<sup>439,440</sup> Molecules with pyrene motifs are therefore commonly used in the literature to introduce desired functionalities to the surfaces of nanotubes,<sup>439-441</sup> and there are even incidences of pyrene-functionalised probes being used to functionalise carbon nanotubes with motifs that are subsequently used to ligate to a copper metallo-enzyme proteins in order to facilitate electroactive immobilisation of the enzyme onto the nanotubes (**Chapter 1, Figure 1.15**).<sup>235</sup> It was hoped that a similar strategy could prove useful in improving the electroactive immobilisation of *An6428-AA9* (discussed in **Chapter 2**), as it is possible that application of these pyrene-labelled conjugates to the MWCNT-functionalised GC electrode surfaces would yield *An6428-AA9* immobilised in such a way as to have superior electrical contact with the underlying electrode surface than *An6428-AA9* immobilised onto the MWCNTs via simple adsorption.

An aldehyde-reactive hydroxylamine probe functionalised with a pyrene motif, **Pyr3**, was synthesised in four-steps (**Scheme 4.2**). This probe was prepared as its hydrochloride salt as this aided initial dissolution of the probe into a stock solution.



**Scheme 4.2.** The synthesis of a pyrene-functionalised aldehyde-reactive hydroxylamine probe **Pyr3**.

The conjugation of **Pyr3** to An6428-AA9 was performed under identical conditions to that performed with **Dan6**. As with the experiments involving **Dan6**, SDS-PAGE gel analysis was used to confirm the successful conjugation of **Pyr3** to An6428-AA9 (**Figure 4.18**). The reaction conditions the different An6428-AA9 samples were subjected to, and the location of these samples in the SDS-PAGE gel presented in **Figure 4.18**, are tabulated in **Table 4.2**.

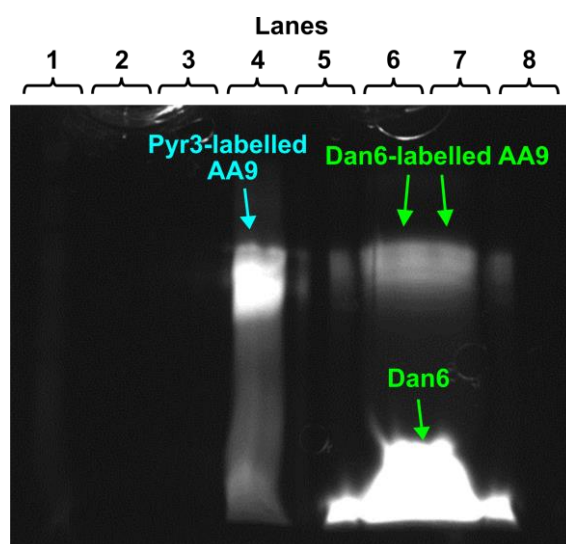


**Figure 4.18.** SDS-PAGE gel of samples of An6428-AA9 glycoprotein subjected to aldehyde introduction via cis-1,2-diol oxidative cleavage with  $\text{NaIO}_4$  and the labelling of these aldehydes with either dansylated or pyrene-functionalised fluorescent hydroxylamine probes, **Dan6** or **Pyr3**. Prior to running on the SDS-PAGE gel, protein samples were boiled in a dye-free reducing buffer (2% SDS, 2 mM 2-mercaptoethanol, 4% glycerol, 40 mM Tris-HCl pH 6.8).

**Table 4.2.** The treatments the samples of An6428-AA9 in **Figure 4.18** were subjected to.

Gel Lane	Occupancy	Treatment with NaIO <sub>4</sub>	Dan6 reaction conditions
1	Ladder	N/A	N/A
2	AA9	<input checked="" type="checkbox"/>	N/A
3	Oxidised AA9	<input checked="" type="checkbox"/>	N/A
4	Oxidised AA9 + <b>Pyr3</b>	<input checked="" type="checkbox"/>	pH 4.5, 100 equiv <b>Pyr3</b>
5	Space	N/A	N/A
6	Oxidised AA9 + <b>Dan6</b>	<input checked="" type="checkbox"/>	pH 4.5, 100 equiv <b>Dan6</b>
7	Oxidised AA9 + <b>Dan6</b>	<input checked="" type="checkbox"/>	pH 4.5, 100 equiv <b>Dan6</b>
8	Space	N/A	N/A

While it was hoped that **Pyr3**-An6428-AA9 conjugates could be used to build upon the electrochemical analysis of An6428-AA9 described in **Chapter 2**, this was not the case, and the electrochemical signal An6428-AA9 redox couple actually appeared to be comparable or weaker when these conjugates were used (data not shown).

### 4.2.3 Pyridoxal 5'-phosphate (PLP) mediated transamination of the N-terminal glycine residue of a c-type cytochrome

#### 4.2.3.1 Initial work with CjX183-D

During a piece of collaborative work with Dr Glyn Hemsworth (University of Leeds) and Dr Jessie Branch, the electrochemistry of a small c-type cytochrome from *Cellvibrio japonicus*, designated CjX183-D was investigated. Dr Glyn Hemsworth and Dr Jessie Branch suspected that reduced CjX183-D was acting as an electron donor to an AA9 LPMO they were analysing, but needed to definitively prove that the reduced CjX183-D itself, rather than the small molecule chemical reducing agents they were using to reduce the CjX183-D, was acting as the electron donor to the LPMO. To aid in this endeavour, an experiment was devised whereby CjX183-D was reduced electrochemically by holding the electrode potential at -0.4 V vs SHE in a 235  $\mu$ M solution of CjX183-D (pH 7, 150 mM NaCl, 50 mM Tris, 50 mM Na acetate, 50 mM Na phosphate, 50 mM Na MES) in the presence of a sub-stoichiometric quantity (0.01 equiv) of the redox-active species methyl viologen, which served a redox mediator between the CjX183-D and the high surface area carbon felt working electrode.

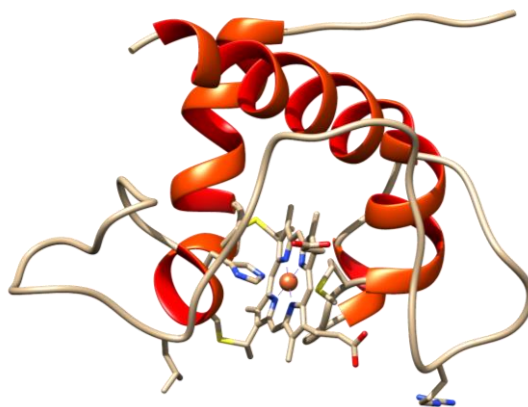


**Figure 4.19.** The structure of CjX183-D. Crystal structure yet to be published.

The function of methyl viologen as a redox mediator is clearly apparent in **Figure 4.20, left**, which shows catalytic reductive current in the presence of methyl viologen. The reduction of CjX183-D was determined to be complete via UV-vis (**Figure 4.20, right**), which shows the intense Soret band shift from 413 nm to 419 nm upon reduction. In addition to this shift in the Soret band, the broad absorption peak centred at  $\sim 530$  nm for the oxidised CjX183-D transforms into a two-pronged feature upon reduction; these  $\alpha$  and  $\beta$  peaks are typical of reduced c-type cytochromes.<sup>442</sup>

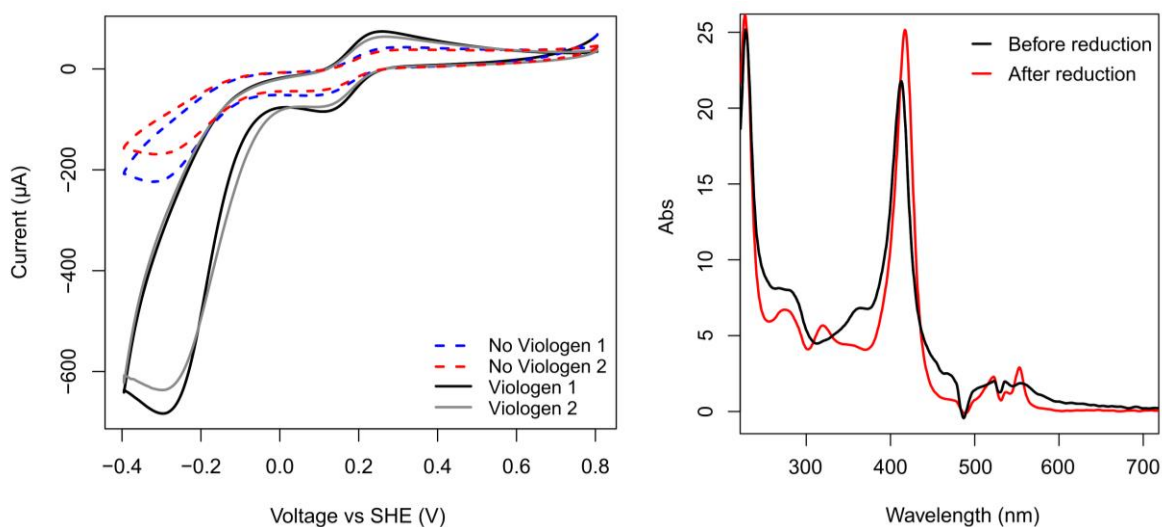


**Figure 4.20. (Left)** Cyclic voltammogram illustrating the mediation of CjX183-D electrochemical reduction by methyl viologen, showing a large catalytic reductive current in the presence of 0.01 equiv methyl viologen. **(Right)** UV-vis spectra illustrating the successful reduction of CjX183-D, due to the appearance of the two-pronged feature at  $\sim 540$  nm. CjX183-D solution was at a concentration of  $235 \mu\text{M}$  in pH 7 buffer (150 mM NaCl, and 50 mM each of Tris, acetate, phosphate and MES). The electrochemical experiment was conducted at  $0^\circ\text{C}$  at a scan rate of  $20 \text{ mV s}^{-1}$  under ambient atmosphere, using a Pt counter electrode, a Ag/AgCl (3 M NaCl) reference electrode and a carbon felt working electrode. All scans commenced from the most positive potential.

Reduced methyl viologen is unstable to oxidation by  $\text{O}_2$  in solution and is oxidised within seconds under ambient conditions - when the working electrode is held at a reducing potential in an aqueous methyl viologen solution under an ambient atmosphere the distinctive purple colour of reduced

methyl viologen vanishes as the molecules diffuse away from the electrode surface. In addition, and as soon as the electrode is switched off the whole solution loses its colour. Reduced CjX183-D does not reoxidise rapidly under ambient conditions. As only sub-stoichiometric quantities of methyl viologen were used, and can be expected to have been re-oxidised by ambient oxygen, the observation that the sample of electrochemically-reduced CjX183-D sample was able to supply electrons to the LPMO proved that the reduced CjX183-D was itself acting as the electron donor. This experiment is now reported in a manuscript recently submitted for publication.

The CjX183-D proved to be an amenable enzyme to study, as it is stable for months in the fridge and gives easily interpreted electrochemical signals, courtesy of its one-electron  $\text{Fe}^{2+}/\text{Fe}^{3+}$  redox couple, which could even be observed as a solution phase signal at  $\sim 200$  mV vs SHE in **Figure 4.20**. CjX183-D is also a small protein, at 11.2 kDa in size, and is thus amenable to characterisation via protein mass spectrometry. Interestingly, wild-type (WT) CjX183-D does not have any lysine residues, and thus a lysine mutant of this protein could easily and site-selectively be functionalised with NHS-ester armed probes,<sup>443</sup> provided the *N*-terminal amine could be rendered non-nucleophilic. Such a construct could later serve as a control system with which the conditions and potential problems associated with covalent immobilisation of redox proteins onto electrode surfaces in electroactive orientations could be explored, without having to invest time optimising more complicated bioconjugation strategies or synthesising more complicated probes. Producing a lysine mutant of CjX183-D was thus deemed to be a worthwhile venture.

The *N*-terminal residue of CjX183-D is a glycine residue, and the *N*-terminal amine could thus be removed via PLP-mediated transamination,<sup>400,401</sup> which replaces the *N*-terminal amine with a glyoxylamide-type aldehyde (**Figure 4.1**, panel **C**). It should be noted that this aldehyde would itself likely be too far from the redox-active centre of CjX183-D to serve as a viable tethering point for covalent electroactive immobilisation.

#### 4.2.3.2 Wild-type CjX183-D

##### 4.2.3.2.1 Preparation and purification of wild-type CjX183-D

The plasmids required to produce WT CjX183-D were kindly supplied by Dr Glyn Hemsworth. These plasmids were the construct for CjX183-D itself, designated CjX183D\_pCW, and PEC86, a plasmid which codes for the proteins of the complex multiprotein cytochrome *c* maturation (Ccm) system<sup>444</sup> in *E. coli* and allows them to be expressed constitutively.<sup>445</sup> Gram-negative bacteria typically only express the proteins of the Ccm system under anaerobic conditions,<sup>444,445</sup> but PEC86 not only increases the production of these proteins, but even allows them to be expressed under aerobic conditions,

greatly assisting in the overexpression of c-type cytochrome holoprotein.<sup>445</sup> The maps of both these plasmids are shown in **Appendix 3**.

Initially, the ability to remove the His<sub>6</sub> tag by inserting a TEV cleavage site was desired, and so the CjX183-D gene was sub-cloned into a commercial pET vector in such a manner to complete a TEV cleavage site (see **Appendix 4**). However, it was later found that the CjX183-D protein was not produced when using the new pET construct (when co-transformed with PEC86), and thus experiments continued using the original CjX183D\_pCW construct instead.

The CjX183D\_pCW plasmid construct codes for ampicillin resistance, whereas the PEC86 plasmid codes for chloramphenicol resistance. These plasmids were co-transformed into competent BL21 (DE3) *E. coli* via heat shock, and thereafter plated onto media containing both ampicillin and chloramphenicol. Colonies were thereafter selected and WT CjX183-D was successfully overexpressed under shake-flask conditions (see experimental), before being isolated and purified using nickel affinity chromatography, followed by size-exclusion chromatography (**Figure 4.21**).

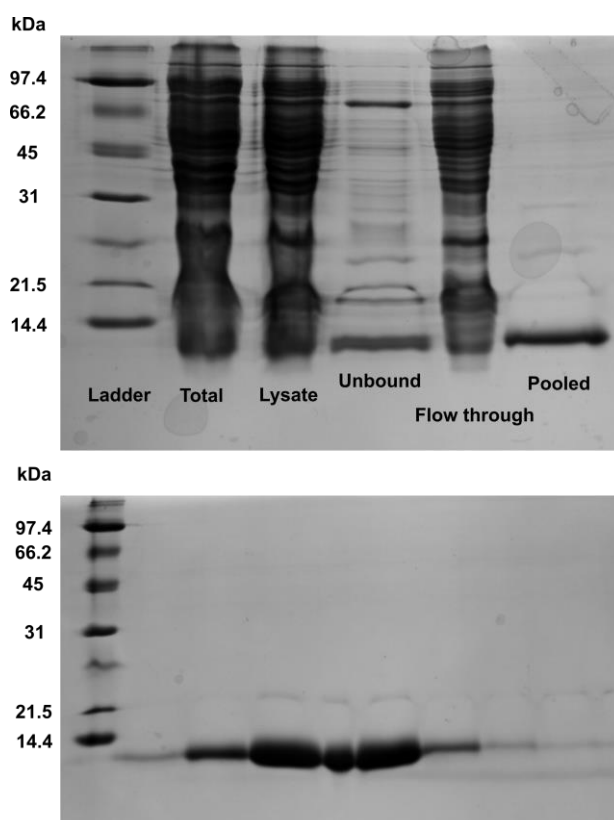


**Figure 4.21.** 15% SDS-PAGE gels illustrating the presence of WT CjX183-D. **Top)** 15% SDS-PAGE gel showing the purification of WT CjX183-D using Ni affinity chromatography. **Bottom)** 15% SDS-PAGE gel showing further purification of WT CjX183-D via size exclusion chromatography. CjX183-D has a theoretical molecular weight of 11.2 kDa, including the covalently attached c-type heme unit.

## 4.2.3.2.2 Electrochemistry of WT CjX183-D

The WT CjX183-D isolated was redox-active, showing a single well-defined redox couple when adsorbed to a pyrolytic graphite edge (PGE) electrode, which could easily be simulated (**Figure 4.22**, **Table 4.3**). This WT CjX183-D was subjected to a series of electrochemical experiments by Alice Hewson (an MChem student the Parkin lab), in order to collect a dataset akin to that described in **Section 3.2.3.1.2** for use by collaborators seeking to further develop pure sine wave voltammetry (see **Section 3.2.3.1.1**).

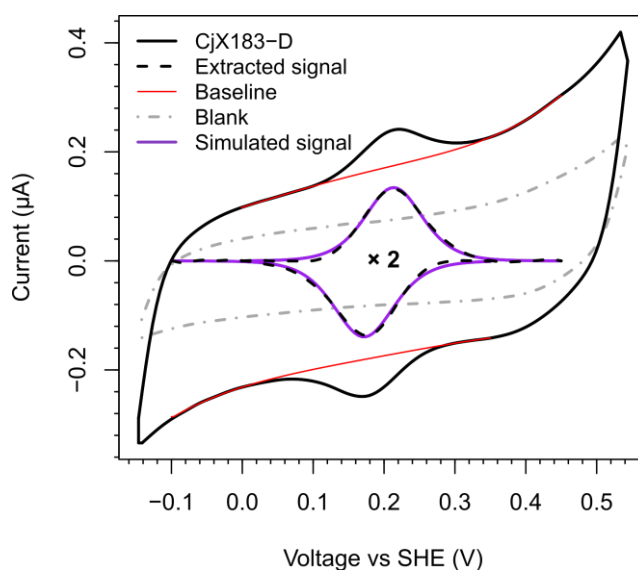


**Figure 4.22.** Cyclic voltammogram illustrating protein film voltammetry of WT CjX183-D in pH 7 buffer (50 mM phosphate, 150 mM NaCl). The electrochemical experiment was conducted at 5 °C at a scan rate of 30 mV s<sup>-1</sup> under a nitrogen atmosphere, using a Pt counter electrode, a calomel (sat KCl) reference electrode and a pyrolytic graphite edge working electrode. Scans commenced from the most negative potential.

**Table 4.3:** Parameters fitted to the baseline-subtracted signals in **Figure 4.22**, using **Equation 7**, showing that the CjX183-D redox signal is characteristic of a 1-electron process.

Parameter	Value
$A / \text{cm}^2$	0.03
$n_s$ cathodic	1
$n_s$ anodic	1
$n_{app}$ cathodic	0.835
$n_{app}$ anodic	0.872
Anodic peak potential / mV vs SHE	214
Cathodic peak potential / mV vs SHE	171
$E_{(O/R)}^f / \text{V vs SHE}$	193
$\Gamma$ cathodic / pmol cm <sup>-2</sup>	87
$\Gamma$ anodic / pmol cm <sup>-2</sup>	80



#### 4.2.3.2.3 Aldehyde introduction into WT CjX183-D

The purified WT CjX183-D yielded very clean protein mass spectrometric traces (**Figure 4.23**). The  $m/z$  of the protein in the deconvoluted spectrometric traces was however ca. 12  $m/z$  greater than would be expected of the theoretical mass of WT CjX183-D holo protein: 11226.14 Da. Due to the consistency of this discrepancy across all experiments, it is assumed to be the result of the calibration of the mass spectrometer.

PLP-mediated transamination (**Figure 4.1** panel C) of WT CjX183-D was performed by incubating CjX183-D at a concentration of ca. 40  $\mu\text{M}$  in pH 6.5 buffer (25 mM phosphate) in the presence of 10 mM PLP for 18 hours at 37  $^{\circ}\text{C}$ ; this method was based on literature procedures for the PLP-mediated transamination of myoglobin, which also has an *N*-terminal glycine.<sup>400,401</sup>

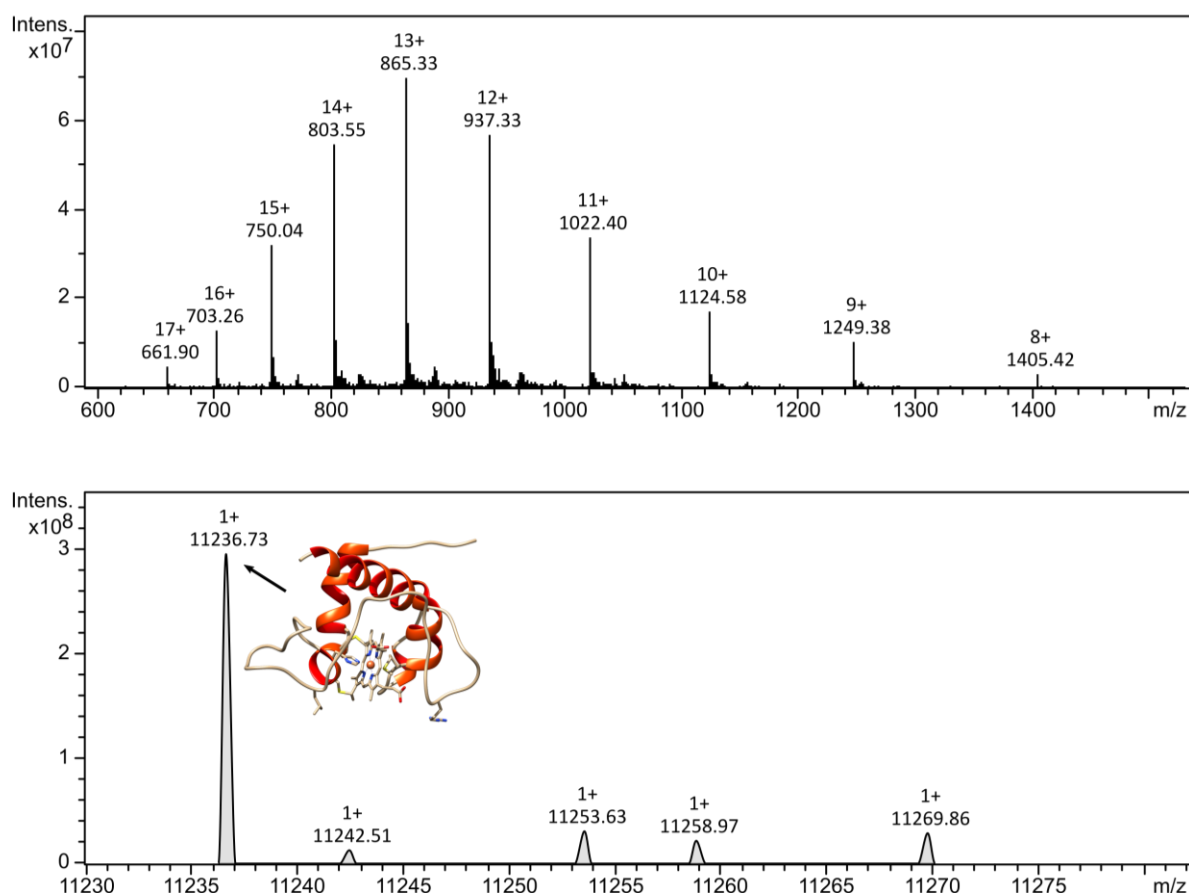


**Figure 4.23.** Positive ion mode ESI-LC/MS analysis of samples of WT CjX183-D. **Top)** The raw MS data showing the protein charge ladders. **Bottom)** Deconvoluted mass spectrum, showing a peak at  $m/z$  11236.73, which is +10.59 greater than the theoretical  $m/z$  of CjX183-D holo protein: 11226.14.

Clear confirmation of the presence of aldehyde functionality in PLP-treated CjX183-D was not possible via simple mass-spectrometry of PLP-treated CjX183-D, as successful aldehyde introduction into CjX183-D via PLP-mediated transamination would be expected to give a product that is only 1.03 Da lighter than unmodified CjX183-D. Some aldehyde would be expected to be in the hydrate form, and thus distinguishable from the unmodified CjX183-D by +17 Da, it would not be possible to get an accurate measure of conversion. Instead, PLP-treated CjX183-D was subjected to OPAL conditions<sup>399</sup> with phenylacetaldehyde (**Figure 4.24**). Mass spectrometry of this reaction clearly showed the corresponding OPAL product (**Figure 4.25**), whereas OPAL product was not observed for samples of CjX183-D subjected to OPAL conditions without previously being treated with PLP (**Figure 4.26**), providing clear evidence of the presence of aldehyde functionality in the PLP-treated CjX183-D. **Figure 4.25** also shows that the tandem PLP-mediated transamination-OPAL ligation does not go to completion, but a conversion of 93% is achieved.

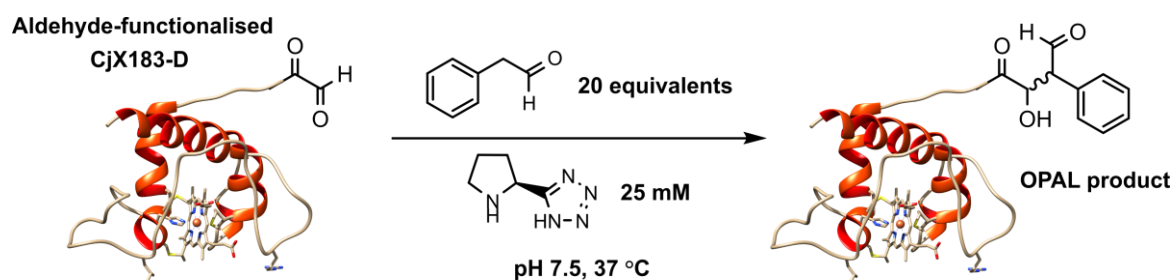


**Figure 4.24.** OPAL conjugation of phenylacetaldehyde to aldehyde-functionalised CjX183-D, using 20 equiv of phenylacetaldehyde and 25 mM (S)-5-(pyrrolidin-2-yl)-1H-tetrazole, at pH 7.5 for 1 hour at 37 °C.

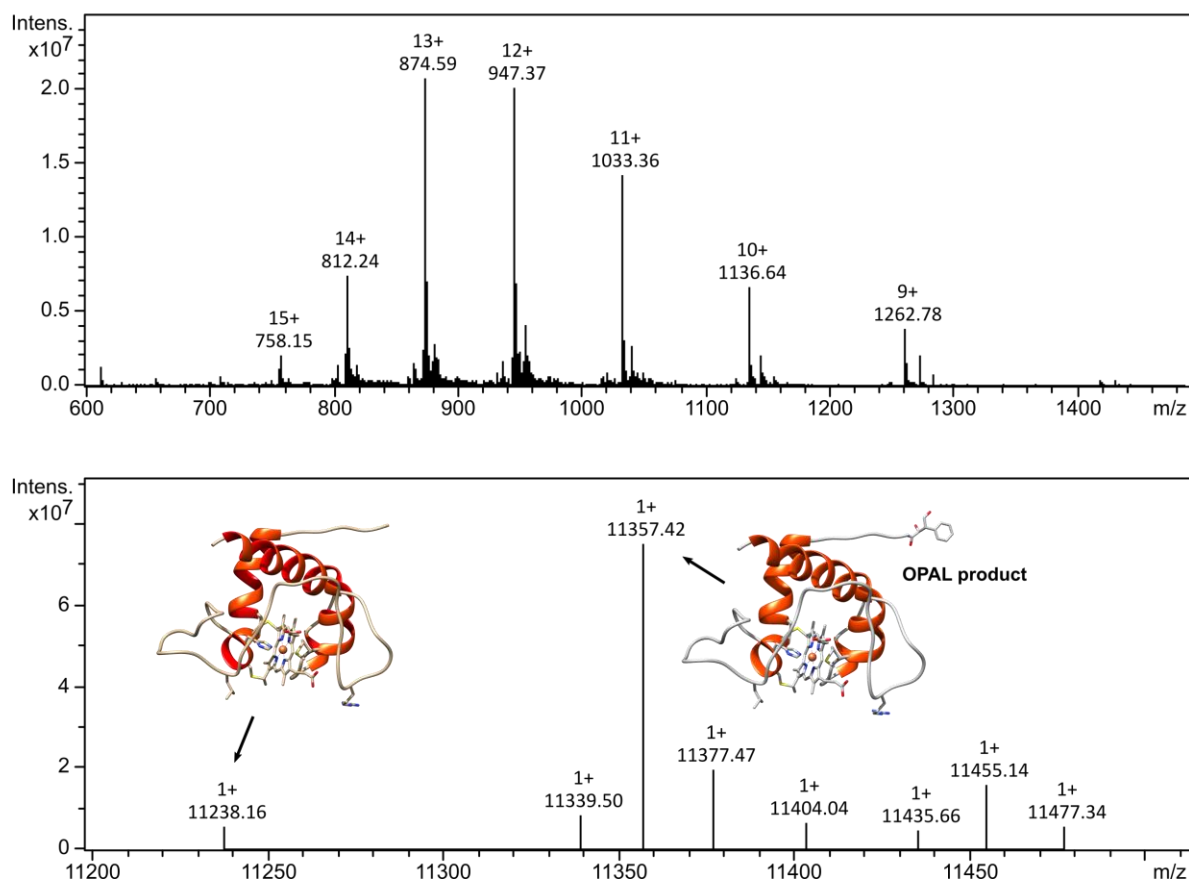


**Figure 4.25.** Positive ion mode ESI-LC/MS analysis of samples of WT CjX183-D that has been subjected to PLP-mediated transamination and OPAL to phenylacetaldehyde. **Top)** The raw MS data showing the protein charge ladders. **Bottom)** Deconvoluted mass spectrum, showing a peak at  $m/z$  11238.16, which is +12.02 greater than the theoretical  $m/z$  of CjX183-D holo protein: 11226.14. The OPAL product of glyoxylamide-functionalised CjX183-D to phenylacetaldehyde would be expected to give a peak with an  $m/z$  119.12 greater than that of WT CjX183-D, and the peak at  $m/z$  11357.42 is 119.26 greater than that at  $m/z$  11238.16.

Circular dichroism analysis of 19  $\mu$ M samples of CjX183-D and PLP-treated CjX183-D in pH 7 buffer (20 mM sodium phosphate) show CjX183-D remains folded, even after the PLP-transamination (**Figure 4.27**).

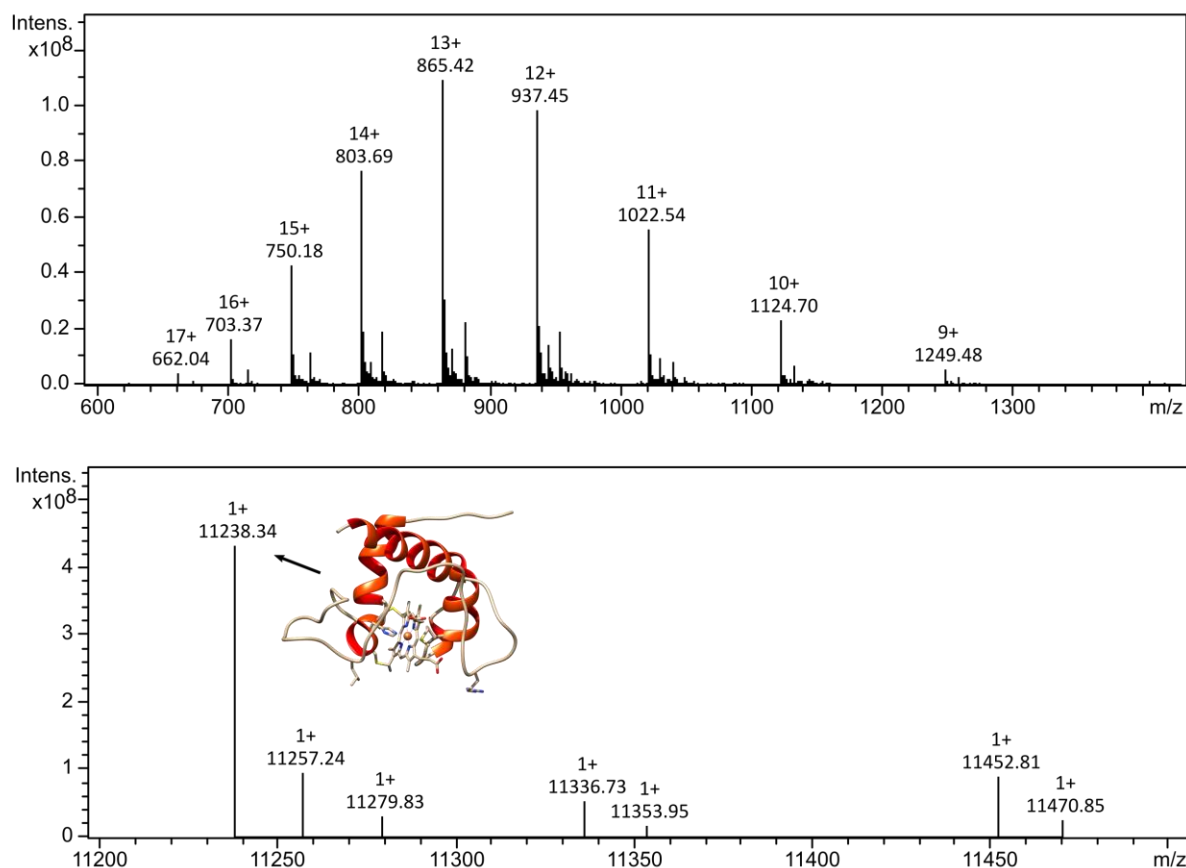


**Figure 4.26.** Positive ion mode ESI-LC/MS analysis of a sample of WT CjX183-D that has been subjected to OPAL conditions with phenylacetaldehyde, not to PLP-mediated transamination. **Top)** The raw MS data showing the protein charge ladders. **Bottom)** Deconvoluted mass spectrum, showing a peak at  $m/z$  11238.34, which is +12.2 greater than the theoretical  $m/z$  of CjX183-D holo protein: 11226.14. The OPAL product of glyoxylamide-functionalised CjX183-D to phenylacetaldehyde would be expected to give a peak with an  $m/z$  119.12 greater than that of WT CjX183-D, and no such peak is in evidence.

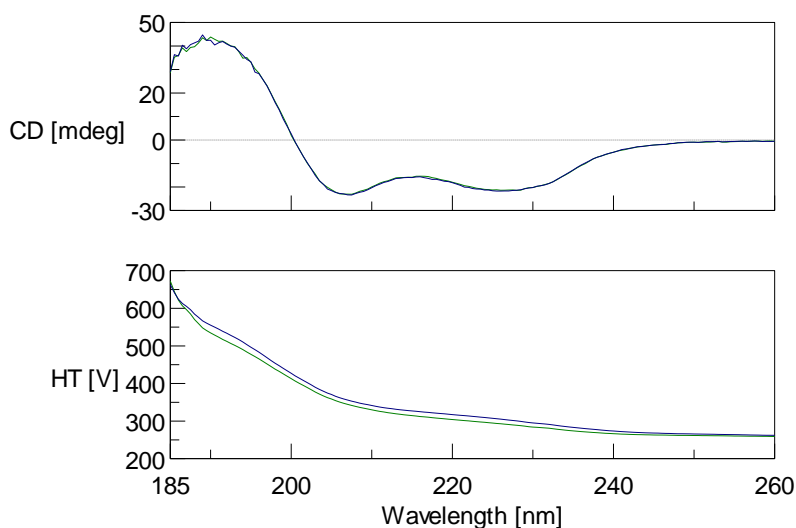


**Figure 4.27.** Circular dichroism of CjX813-D (green) and PLP-treated CjX183-D (blue), illustrating that the protein remains folded during PLP-mediated transamination. Dr Andrew Leech (from the Bioscience Technology Facility, University of York) is thanked for performing these Circular Dichroism experiments.

### 4.2.3.3 A lysine mutant of CjX183-D

#### 4.2.3.3.1 Preparation and purification of a lysine mutant of CjX183-D

A mutation was made to the original WT CjX183D\_pCW construct (**Appendix 4**) using a QuikChange site-directed mutagenesis kit (as detailed in **Appendix 5**), which yielded a plasmid that coded for a lysine mutant of CjX183-D, henceforth referred to as CjX183-D R51K (where arginine residue 51 has been replaced with a lysine residue). The sequence of both the WT CjX183-D and CjX183-D R51K genes are provided in **Appendix 6**.

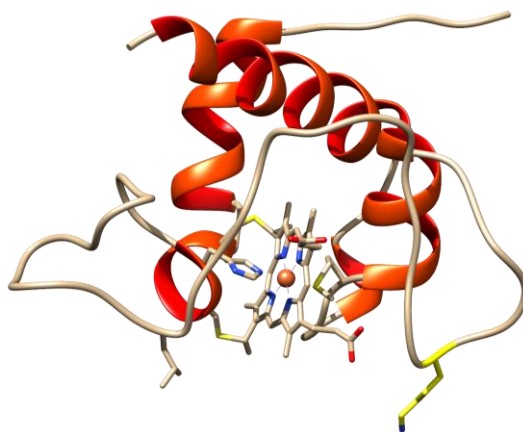


**Figure 4.28.** Depiction of the structure of CjX183-D R51K, based on the unpublished crystal structure of WT CjX183-D. The mutant lysine residue is highlighted in yellow.

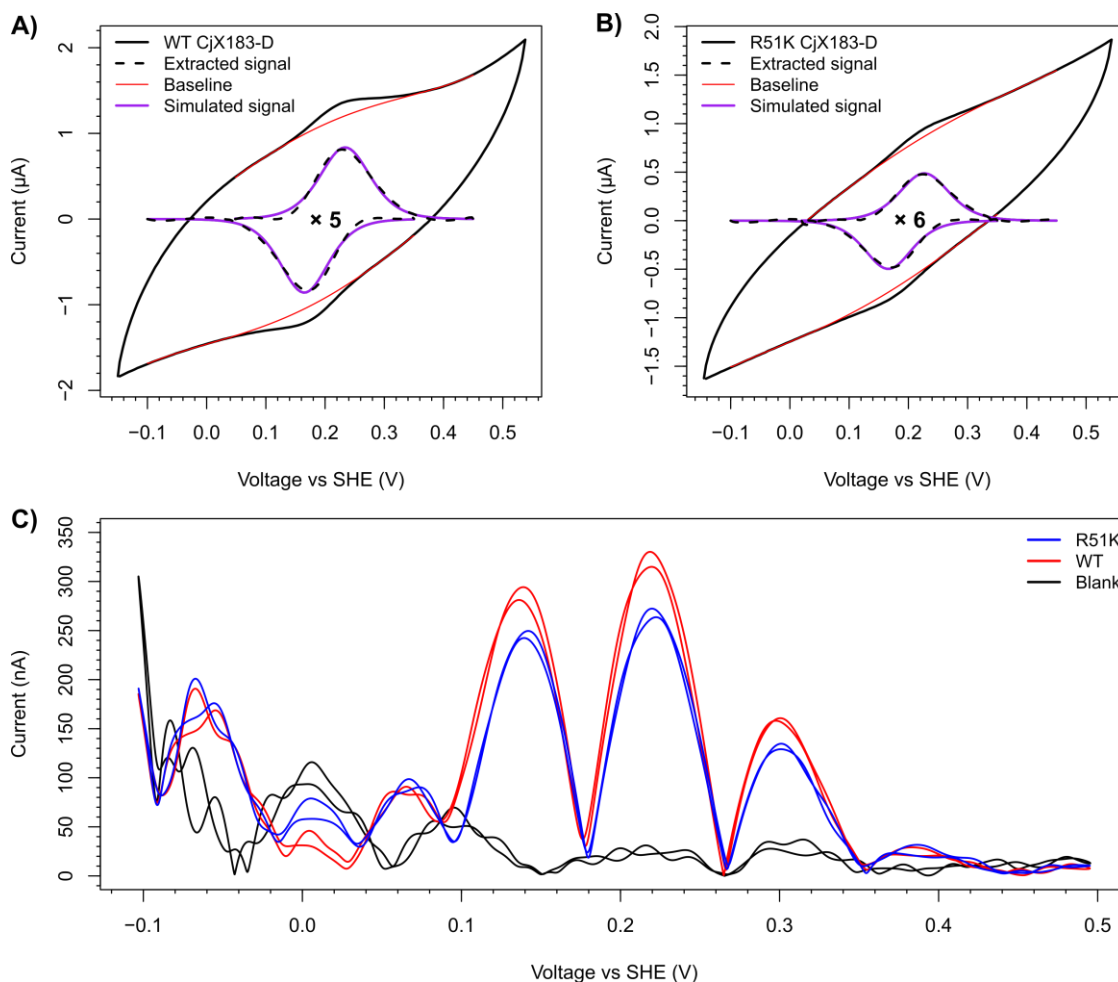
With the relevant mutation installed, CjX183-D R51K protein could be produced and purified in an identical manner to WT CjX183-D. The SDS-PAGE gels for this preparation and purification are shown in the Experimental (**Section 8.1.4.2**).

#### 4.2.3.3.2 Electrochemistry of CjX183-D R51K

The R51K mutant of CjX183-D was also redox-active, again showing a single well-defined redox couple when adsorbed to a pyrolytic graphite edge (PGE) electrode. The signals yielded from WT CjX183-D and CjX183-D R51K are too similar to be easily distinguished by cyclic voltammetry, (**Figure 4.29 A and B, Table 4.4**), and FTacV analysis would suggest that the formal potential of the two CjX183-D variants are comparable. There appears to be a discrepancy of as much as 20 mV between the formal potentials yielded from the cyclic voltammetry analysis ( $\sim 200$  mV vs SHE) and those suggested from visual inspection of the FTacV measurements ( $\sim 180$  mV vs SHE); this could be due to several factors, firstly, completely accurate interpretation of FTacV data requires computational simulation, and secondly, there may be inaccuracies in the cyclic voltammetry analysis, most likely derived from the fitting of the polynomials used to isolate the Faradaic signals from the background capacitive current (i.e. the “Baselines” in **Figure 4.29 A and Figure 4.29 B**).

**Table 4.4:** Parameters fitted to the baseline-subtracted signals in **Figure 4.29 A and B**, using **Equation 7**, showing that the CjX183-D redox signals are characteristic of a 1 electron process.

Parameter	WT CjX183-D	CjX183-D R51K
$A / \text{cm}^2$	0.03	0.03
$n_s$ cathodic	1	1
$n_s$ anodic	1	1
$n_{app}$ cathodic	0.875	0.899
$n_{app}$ anodic	0.841	0.858
Anodic peak potential / mV vs SHE	233	228
Cathodic peak potential / mV vs SHE	163	168
$E_{(O/R)}^f / \text{V vs SHE}$	200	198
$\Gamma$ cathodic / pmol $\text{cm}^{-2}$	209	97
$\Gamma$ anodic / pmol $\text{cm}^{-2}$	207	101

**Figure 4.29.** Protein film electrochemistry experiments of CjX183-D variants. **A)** Cyclic voltammogram illustrating protein film voltammetry of WT CjX183-D **B)** Cyclic voltammogram illustrating protein film voltammetry of R51K CjX183-D. **C)** Harmonic 6 of FTacV of R51K and WT CjX183-D. All experiments were performed in pH 7 buffer (50 mM phosphate, 150 mM NaCl) at 5 °C under a nitrogen atmosphere, using the same Pt counter electrode, calomel (sat KCl) reference electrode and pyrolytic graphite edge working electrode. Cyclic voltammograms were recorded at a scan rate of 30  $\text{mV s}^{-1}$ , FTacV experiments were recorded using a scan rate of 22.35  $\text{mV s}^{-1}$  at a frequency of 8.85 Hz. All scans commence from their most negative potential.

#### 4.2.3.3 Aldehyde introduction into CjX183-D R51K

The purified CjX183-D R51K also yielded very clean protein mass spectrometric traces (**Figure 4.30**), with the  $m/z$  of the major peak in the deconvoluted spectrometric traces being again ca. 12  $m/z$  greater than would be expected of the calculated mass of CjX183-D R51K holo protein: 11198.13 Da.

PLP-mediated transamination was performed in a manner identical to that established for the WT CjX183-D. PLP-treated CjX183-D R51K was then subjected to OPAL conditions with phenylacetaldehyde, again allowing the presence of aldehyde functionality to be inferred by the formation of the OPAL product (**Figure 4.31**). Once again, the OPAL product was not observed for samples of CjX183-D R51K subjected to OPAL conditions without previously being treated with PLP (**Figure 4.32**). **Figure 4.31** suggests that the PLP-mediated transamination of CjX183-D R51K proceeds with 95% conversion.

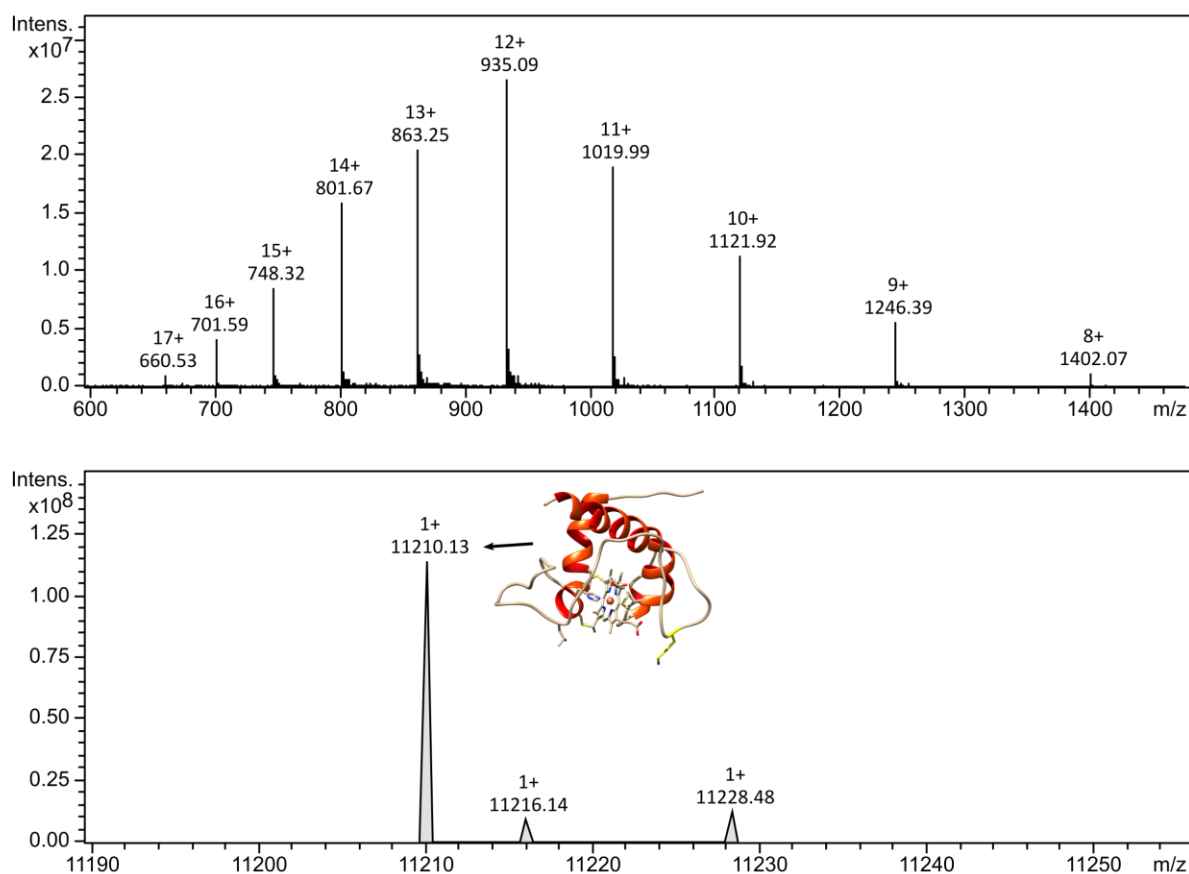


**Figure 4.30.** Positive ion mode ESI-LC/MS analysis of samples of CjX183-D R51K. **Top)** The raw MS data showing the protein charge ladders. **Bottom)** Deconvoluted mass spectrum, showing a peak at  $m/z$  11210.13, which is +12.00 greater than the theoretical  $m/z$  of CjX183-D R51K holo protein: 11198.13.

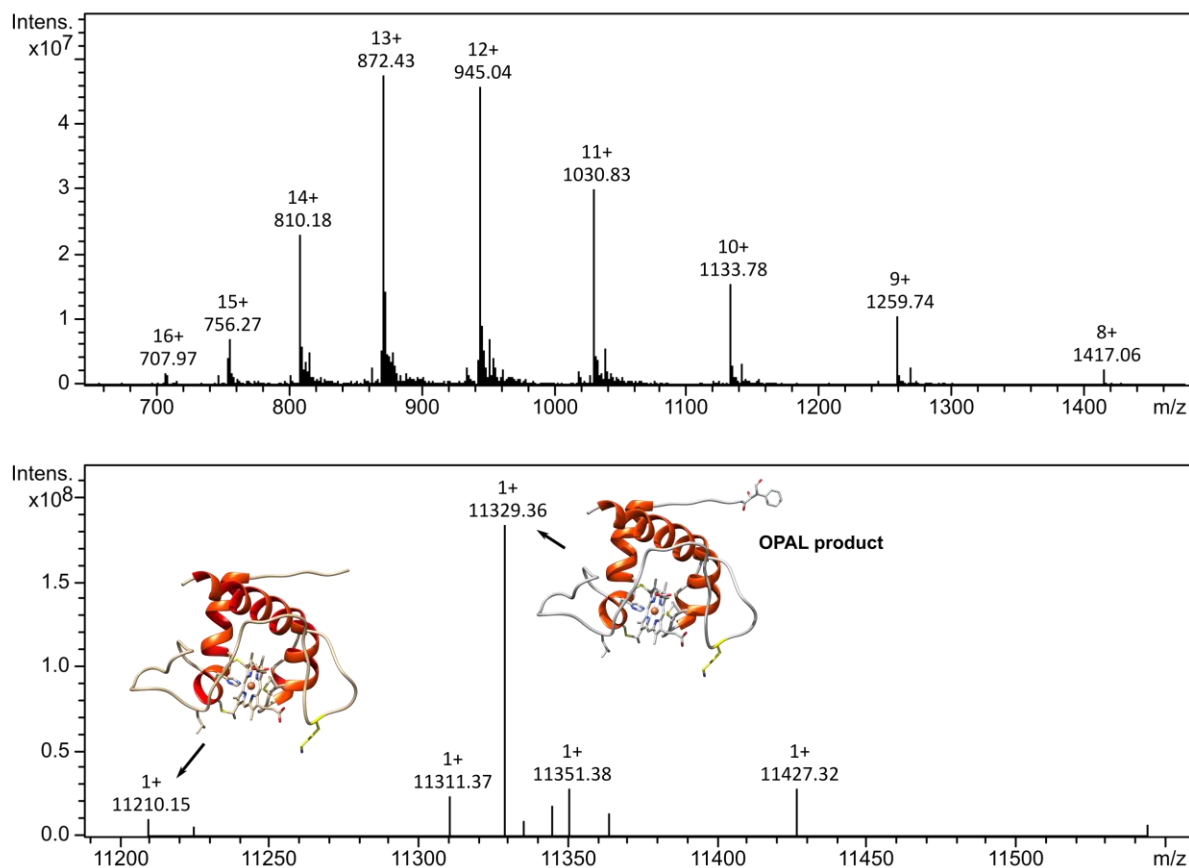


**Figure 4.31.** Positive ion mode ESI-LC/MS analysis of samples of CjX183-D R51K that has been subjected to PLP-mediated transamination and OPAL to phenylacetaldehyde. **Top)** The raw MS data showing the protein charge ladders. **Bottom)** Deconvoluted mass spectrum, showing a peak at  $m/z$  11210.15, which is +12.02 greater than the theoretical  $m/z$  of CjX183-D R51K holo protein: 11226.14. The OPAL product of glyoxylamide-functionalised CjX183-D R51K to phenylacetaldehyde would be expected to give a peak with an  $m/z$  119.12 greater than that of CjX183-D R51K, and the peak at  $m/z$  11329.36 is 119.21 greater than that at  $m/z$  11210.15.

Circular dichroism of 19  $\mu$ M samples of CjX183-D R51K and PLP-treated CjX183-D R51K in pH 7 buffer (20 mM sodium phosphate) show CjX183-D R51K remained folded, even after PLP-transamination (**Figure 4.33**). Comparison of the circular dichroism spectra of both WT CjX183-D and CjX183-D R51K, both before and after PLP-mediated transamination, (**Figure 4.34**) suggests that there are no meaningful differences in the overall fold of WT CjX183-D and CjX183-D R51K.



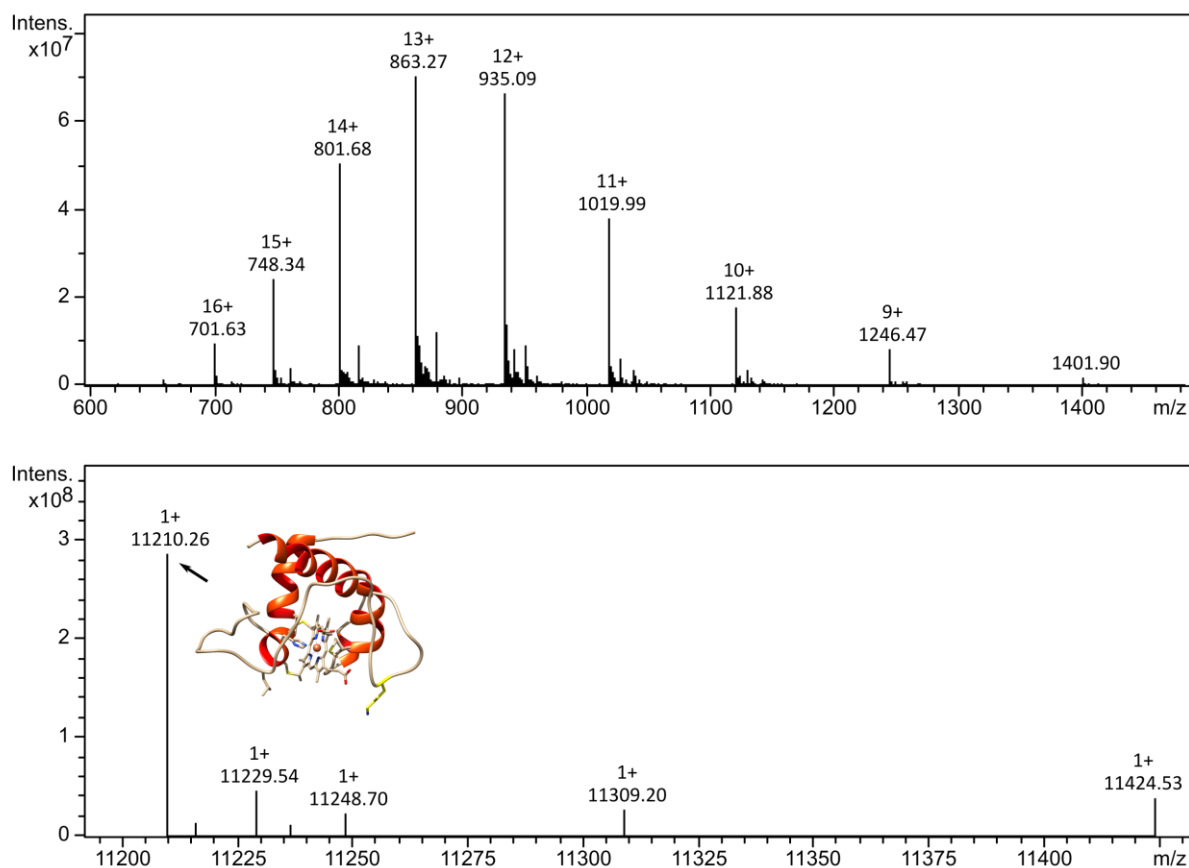


**Figure 4.32.** Positive ion mode ESI-LC/MS analysis of a sample of CjX183-D R51K that has been subjected to OPAL conditions with phenylacetaldehyde, not to PLP-mediated transamination. **Top)** The raw MS data showing the protein charge ladders. **Bottom)** Deconvoluted mass spectrum, showing a peak at  $m/z$  11210.26, which is +12.13 greater than the theoretical  $m/z$  of CjX183-D R51K holo protein: 11198.13. The OPAL product of glyoxylamide-functionalised CjX183-D R51K to phenylacetaldehyde would be expected to give a peak with an  $m/z$  119.12 greater than that of WT CjX183-D, and no such peak is in evidence.

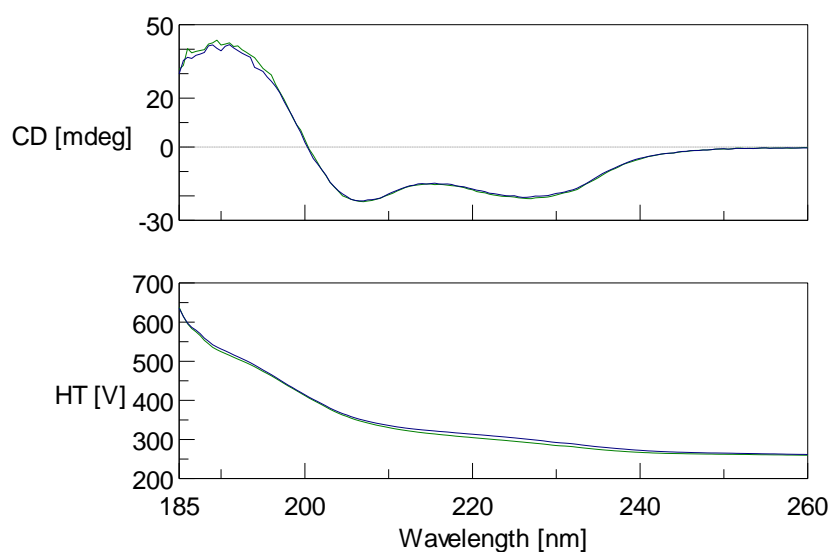


**Figure 4.33.** Circular dichroism of CjX813-D R51K (green) and PLP-treated CjX183-D R51K (blue), illustrating that the protein remains folded during PLP-mediated transamination. Dr Andrew Leech (from the Bioscience Technology Facility, University of York) is thanked for performing these Circular Dichroism experiments.

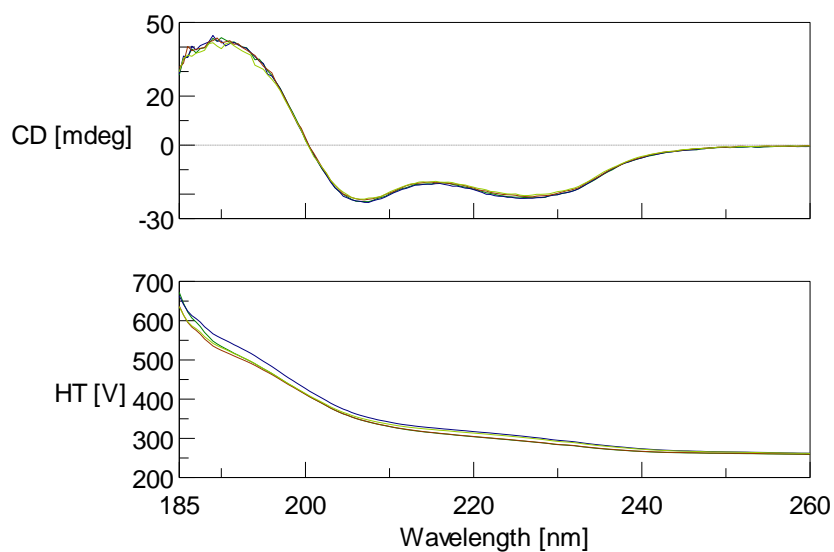
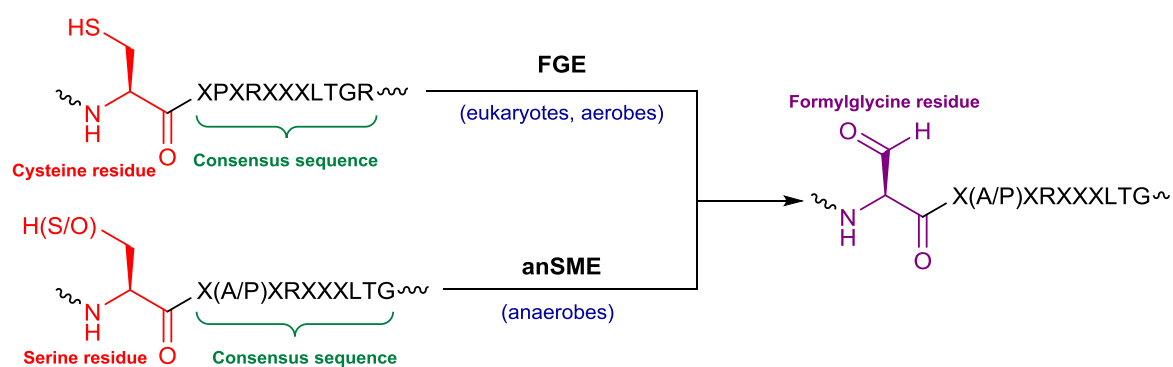


**Figure 4.34.** Circular dichroism overlays showing that the fold of the WT CjX813-D is essentially identical to that of CjX813-D R51K, both before and after PLP-mediated transamination. WT CjX813-D (dark green), CjX183\_D R51K (brown), PLP-treated WT CjX183-D (blue), PLP-treated CjX183-D R51K (light green). Dr Andrew Leech (from the Bioscience Technology Facility, University of York) is thanked for performing these Circular Dichroism experiments.

#### 4.2.4 Introduction of formylglycine residues into peptides and proteins

In both eukaryotes and prokaryotes, enzymes capable of introducing formylglycine (fGly) residues into proteins (**Figure 4.35**, **Scheme 4.3**) are essential for making post- or co-translational modifications to type I sulfatases<sup>446,447</sup> and some phosphonate monoester hydrolases/phosphodiesterases.<sup>448</sup> A fGly residue is generated by the selective oxidation of a cysteine or serine residue embedded within a conserved consensus sequence (C/S)XPXRXXXLTG (**Scheme 4.3**),<sup>447</sup> localised in the active site of type I sulfatases or close to the *N*-termini of certain phosphonate monoester hydrolases/phosphodiesterases.<sup>449</sup> This introduces an active-site aldehyde functionality, which when hydrated to a geminal diol serves as a nucleophile, allowing these enzymes to cleave sulfate/phosphonate esters.<sup>446,447,449</sup> In eukaryotes and aerobic microbes, cysteine predominates as the modification target, and formylglycine generating enzyme (FGE), a copper metalloenzyme, enzymatically oxidises this cysteine to formylglycine using molecular oxygen (**Figure 4.36**).<sup>450</sup> In anaerobic microbes both cysteine and serine can serve as the modification target (**Scheme 4.3**),<sup>447,451,452</sup> and these organisms use anaerobic sulfatase maturing enzymes (anSMEs) to perform the fGly incorporation.<sup>452-454</sup> anSMEs use an *S*-adenosyl-L-methionine co-substrate and successive electron transfers (tuned using three distinct [4Fe-4S] clusters) to perform dehydrogenase chemistry via a radical mechanism, all in the absence of oxygen (**Figure 4.37**).<sup>453,454</sup> Note that while anSMEs are enzymes that generate formylglycine, and thus are most certainly “formylglycine generating enzymes,” they are completely distinct from the previously mentioned copper-containing FGEs, and so will only be referred to as anSMEs in this thesis, to avoid any confusion.



**Scheme 4.3.** The oxidation of cysteine or serine residues by either FGE or anSME enzymes to yield formylglycine residues.

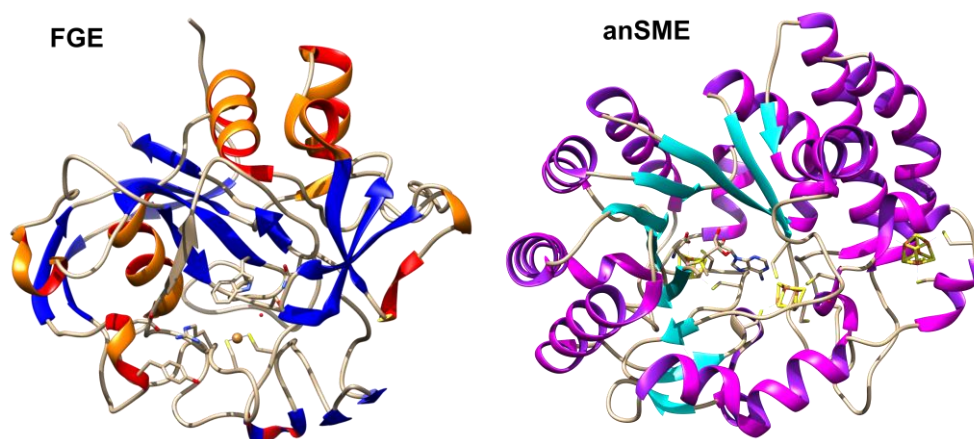


**Figure 4.35. Left)** Crystal structure of FGE from *Streptomyces coelicolor* (PDB code 6MUJ).<sup>450</sup> **Right)** Crystal structure of anSME from *Clostridium perfringens* (PDB code 4K36).<sup>453</sup>

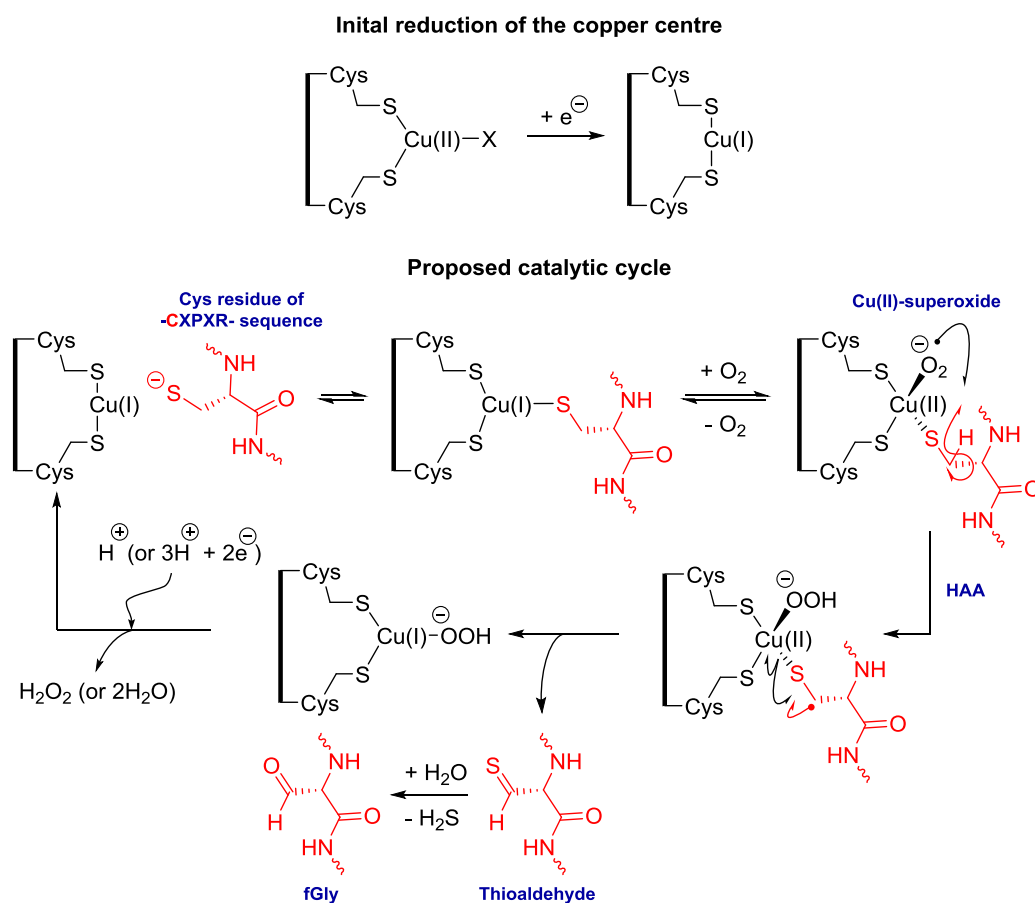


**Figure 4.36.** A proposed mechanism for fGly incorporation by FGE.<sup>450</sup>

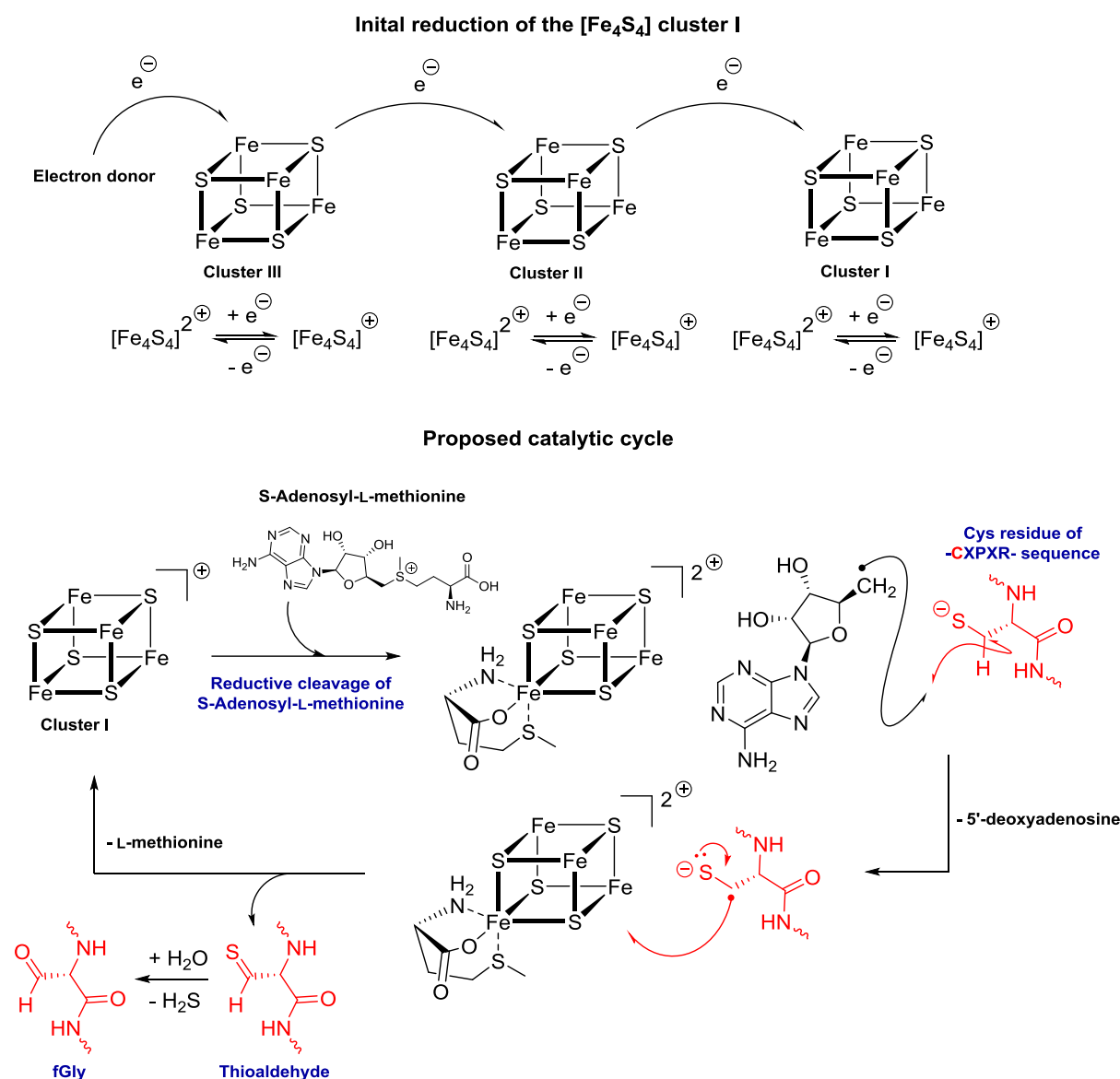


**Figure 4.37.** A proposed mechanism for fGly incorporation by anSME using a cysteine residue substrate. Note that it is thought that the same mechanism applies for anSME acting on a serine residue substrate.<sup>454</sup>

FGE from the prokaryote *Mycobacterium tuberculosis* (*Mt*-FGE) has been shown to recognise the abbreviated pentapeptide “core motif” consensus sequence of CXPXR (Figure 4.1, D).<sup>446,455</sup> Engineering protein mutants that feature this “core motif” and treating these proteins with (or co-expressing these proteins with) *Mt*-FGE thus represents a potentially powerful system for the incorporation of a bio-orthogonal aldehyde functionality into proteins in a site-specific manner.<sup>446,455</sup> The treatment of a CXPXR-labelled redox protein with FGE *in vitro* could hypothetically allow for aldehyde installation into complicated redox proteins which do not lend themselves well to overexpression, such as hydrogenases.

*Mt*-FGE had been previously produced by Julia Walton and was therefore available for use. The suitability of aldehyde introduction into CXPXR-labelled redox proteins via *in vitro* treatment with *Mt*-FGE as a method for installing bio-orthogonal handles amenable to ligation to electrode surfaces was thus to be investigated.

#### 4.2.4.1 Introduction of fGly into peptides

##### 4.2.4.1.1 Introduction of, and ligation to, fGly residues in a substrate peptide

A substrate peptide containing the CXPXR consensus sequence, ALCTPSRGSFLTGRG (**Figure 4.38**), was synthesised in 56% yield by MChem student Owen Jarman using solid phase peptide synthesis. The Positive ion mode electrospray ionisation liquid chromatography mass spectrometry (ESI-LC/MS) trace for this peptide showed it to be of a high purity (**Figure 4.39**) and showed two clear peaks at  $m/z$  762 and 508, which could be attributed to the  $[M+2H]^{2+}$  and  $[M+3H]^{3+}$  molecular ions respectively (**Figure 4.40, Table 4.5**).

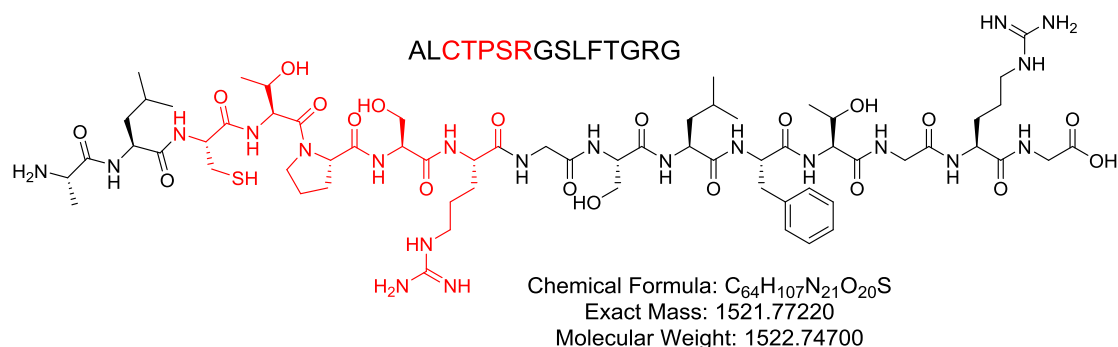


**Figure 4.38.** The structure of substrate peptide ALCTPSRGSFLTGRG.

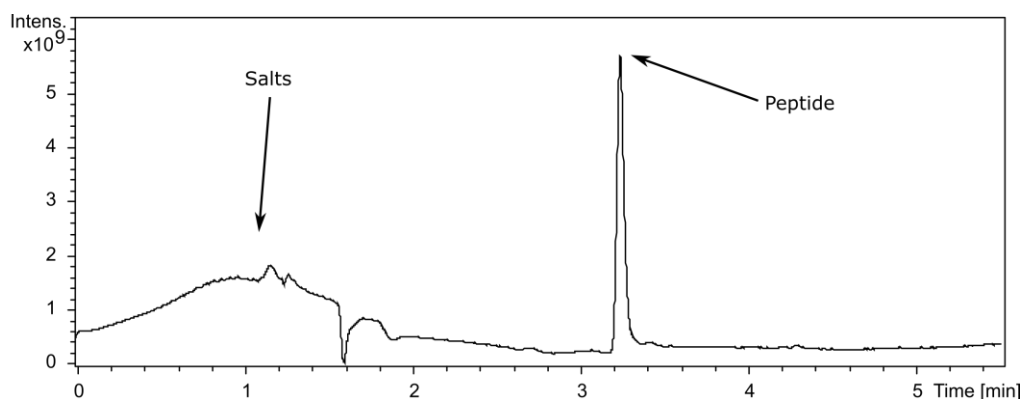


**Figure 4.39.** Positive ion mode ESI-LC/MS elution trace of substrate peptide ALCTPSRGSFLTGRG, monitoring the absorbance at 280 nm.

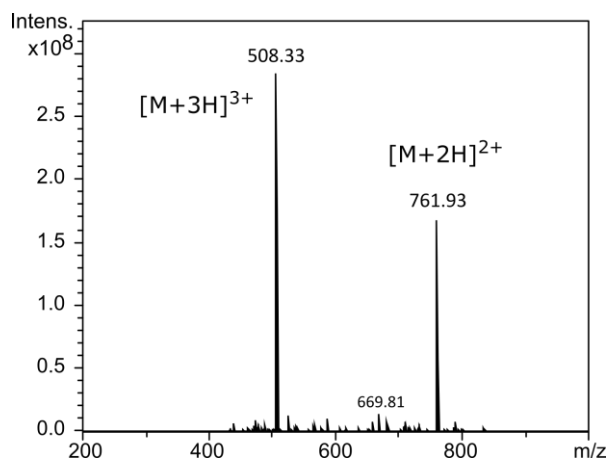


**Figure 4.40.** Mass spectrum of substrate peptide ALCTPSRGLFTGRG from positive ion mode ESI-LC/MS elution trace.

**Table 4.5.** The  $m/z$  values expected for the ALCTPSRGLFTGRG substrate peptide in a series of derivatisation states.

Peptide	$m/z$		
	$[M+H]^+$	$[M+2H]^{2+}$	$[M+3H]^{3+}$
Unmodified	1523	762	508
fGly functionalised	1505	753	502
fGly-hydrate functionalised	1523	762	508
fGly <i>O</i> -benzyl oxime functionalised	1610	805	537
<i>Iso</i> -Pictet Spengler functionalised	1735	868	579

The effect of several variables on the ability of purified *Mt*-FGE to introduce an fGly residue into the substrate peptide were investigated, including i) concentration of *Mt*-FGE (0.5–4.5  $\mu$ M), ii) reducing agent concentration and type (DTT,  $\beta$ -mercaptoethanol or sodium dithionite), iii) incubation time, iv) pH, v) pre-treatment of *Mt*-FGE with  $\text{CuSO}_4$ , and vi) the direct addition of  $\text{CuSO}_4$  to the reaction. Surprisingly, under many of the conditions trialled no peaks attributable to the fGly-labelled peptide could be detected via ESI-LC/MS, suggesting that conversion into fGly-labelled peptide did not occur under many conditions. Interestingly, pre-treatment of *Mt*-FGE with copper and direct addition of copper to the reaction did not result in greater conversion, which was surprising since recent reports have shown that the addition of copper to FGE (which is a copper metalloenzyme) can increasing its activity by as much 20-fold.<sup>448,456,457</sup>

The optimal conditions for the conversion of the substrate peptide by *Mt*-FGE were found to be pH 9 buffer (25 mM triethanolamine, 50 mM NaCl), 5 mM dithiothreitol, 500  $\mu$ M substrate peptide, 10  $\mu$ M FGE for 1–2 hours at 37  $^\circ\text{C}$ . ESI-LC/MS of substrate peptide, treated with *Mt*-FGE under the aforementioned conditions, yielded peaks at  $m/z$  753 and 502, attributable to the  $[M+2H]^{2+}$  and  $[M+3H]^{3+}$  molecular ions of the fGly-labelled peptide respectively (**Figure 4.41a black box, Table 4.5**).

Tandem mass spectrometry of the  $m/z$  502 peak served to further corroborate its assignment as the  $[M+3H]^{3+}$  peak of fGly-labelled peptide, as all peaks could be successfully assigned as fragments of the predicted fGly-peptide (**Figure 4.41**).

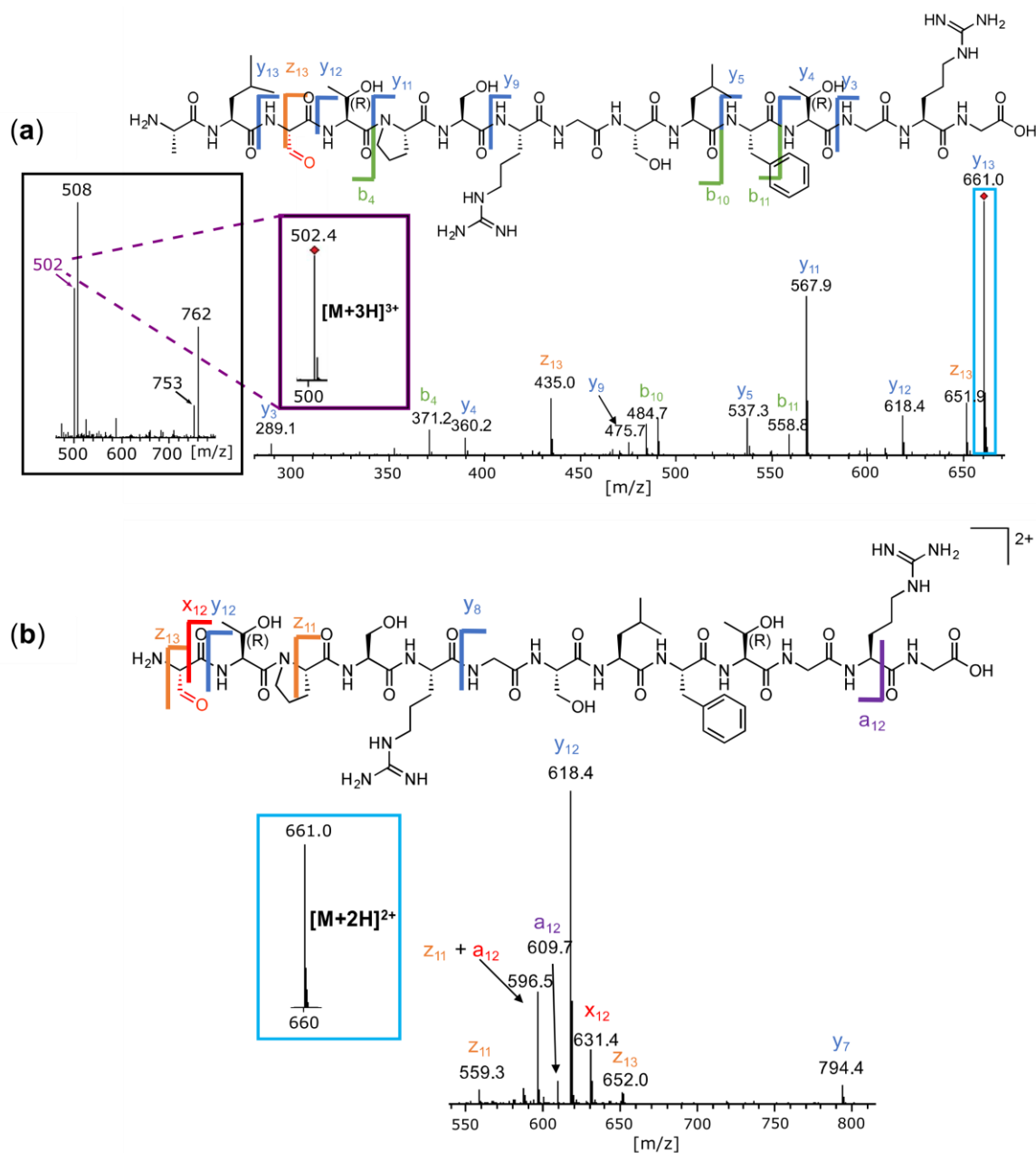


**Figure 4.41.** Tandem MS of fGly labelled peptide product ion peak at  $m/z$  502. The site of the fGly modification is highlighted in red. Peptide fragments are assigned according to standard peptide fragmentation nomenclature.<sup>458</sup> **(a)** The  $[M+3H]^{3+}$  product ion at  $m/z$  502.4 in the positive ion mode ESI-LC/MS trace of *Mt*-FGE-treated substrate peptide (shown in the black box) is fragmented and peaks assigned. Highlighted in the blue box is the most abundant fragment ion at  $m/z$  661.0, which is attributable to the  $[M+2H]^{2+}$  ion of the  $y_{13}$  peptide fragment, the structure of which is shown. **(b)** The  $[M+2H]^{2+}$  ion of the  $y_{13}$  peptide fragment was subjected to further fragmentation, and all peptide fragments identified were successfully assigned to the fGly-labelled peptide product. Figure adapted from the Advanced Research Project Dissertation of Owen Jarman.<sup>459</sup>



Positive ion mode ESI-LC/MS was to be used to assess conversion rates by comparing the intensities of the peaks for the product fGly-labelled peptide and the substrate peptide, operating under the assumption that both species have the same ionisation efficiency. However, it was realised that the mass of an fGly-residue in its hydrated form is hard to distinguish from that of a cysteine residue (**Figure 4.42**), and as such it is difficult to distinguish unmodified substrate peptide from fGly-functionalised peptide in its hydrated form (**Table 4.5**). Isotopic labelling of the sulfur of the cysteine residues was considered, but neither  $S^{34}$ - nor  $S^{36}$ -labelled cysteine are commercially available. Preparations of  $S^{34}$ -labelled cysteine have been reported,<sup>460</sup> but a simpler method to distinguish between unmodified substrate peptide and fGly/fGly-hydrate-functionalised peptide involved treating the reaction solutions with an excess of *O*-benzylhydroxylamine, labelling all the fGly residues as *O*-benzyl oximes prior to analysis via ESI-LC/MS (**Figure 4.42**). Reactions between *Mt*-FGE-treated substrate peptide and *O*-benzylhydroxylamine were performed in pH 4 buffer (100 mM sodium acetate, 150 mM NaCl) using 50  $\mu$ M of peptide and 500  $\mu$ M *O*-benzylhydroxylamine overnight at 37  $^{\circ}$ C. ESI-LC/MS of the reaction mixtures after this time showed all the peptide-associated peaks that had previously been observed to have disappeared, leaving only a single peak at  $m/z$  538. This peak is within 1  $m/z$  of that expected for the  $[M+3H]^{3+}$  peak for fGly *O*-benzyl oxime-functionalised peptide (**Table 4.5**). The disappearance of all other peptide-associated peaks suggested that the peaks at  $m/z$  762 and 508 in **Figure 4.41** are likely derived from fGly-hydrate functionalised peptide rather than “unmodified” cysteine-functionalised peptide, thus indicating that  $\sim$ 100% conversion of the substrate peptide is achieved under the optimal conditions identified above.

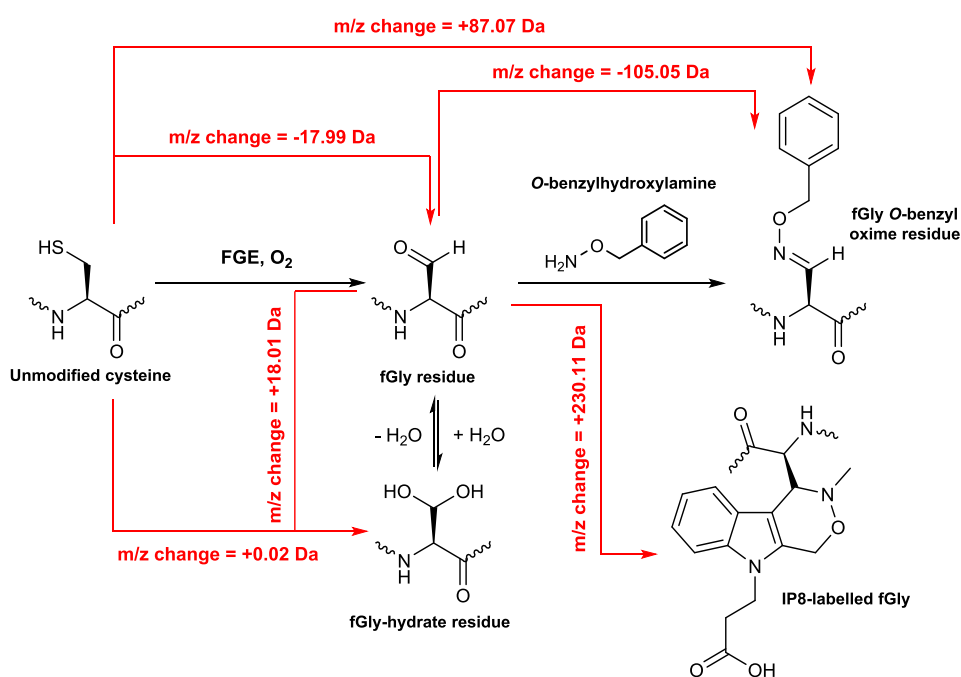


**Figure 4.42.** The mass differences between the different peptide/protein derivatisation states encountered in this Chapter.

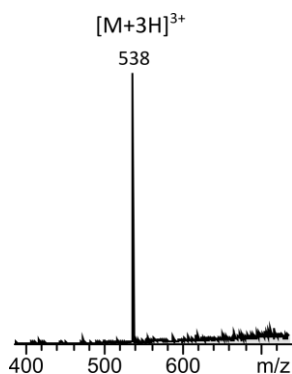
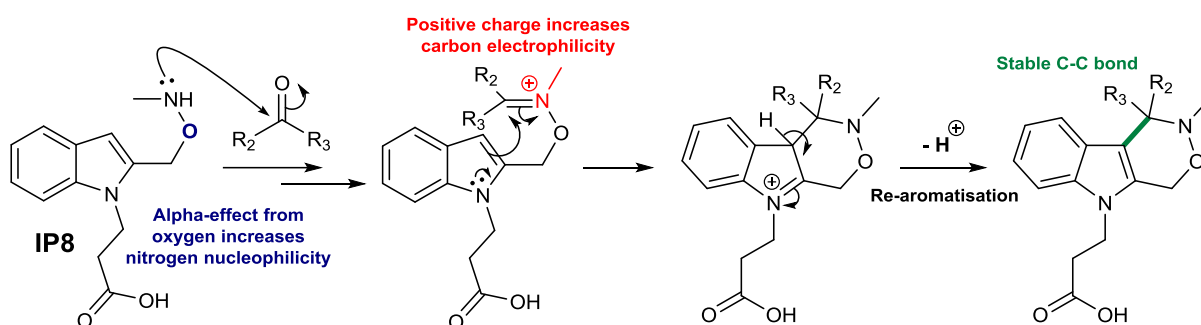


**Figure 4.43.** The mass spectroscopy peak attributed to fGly *O*-benzyl oxime functionalised peptide.

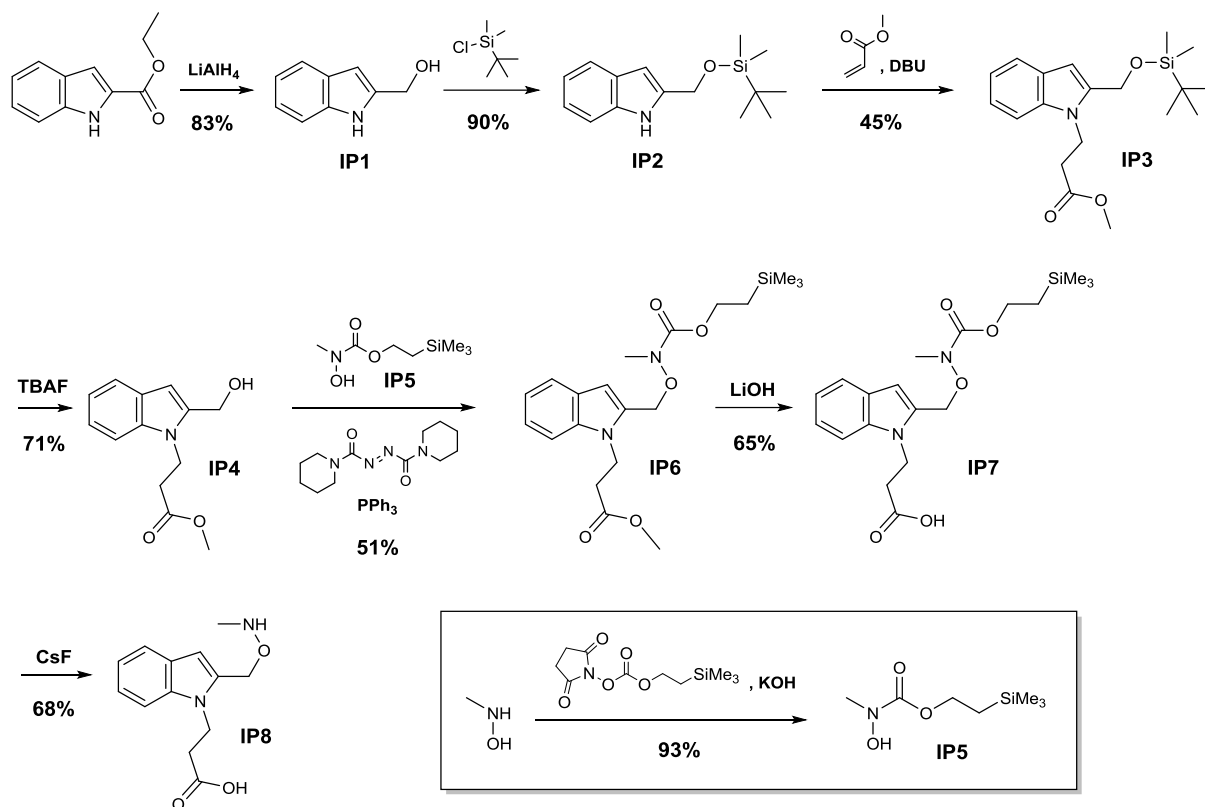
As well as allowing the percentage conversion of the substrate peptide into fGly functionalised peptide to be assessed, the successful reaction of the fGly residues with *O*-benzylhydroxylamine also clearly illustrates that fGly residues are capable of reacting with hydroxylamines under biologically relevant conditions. The ability of these fGly residues to react with another aldehyde-reactive probe in an *iso*-Pictet Spengler reaction was also investigated.

The *iso*-Pictet Spengler reaction involves the reaction between an aldehyde or ketone and an indole substituted at the 2-position with a short residue that terminating with an amine motif, and results in the formation of a stable C-C bond (**Scheme 4.4**). This gives *iso*-Pictet Spengler ligation a conceivable advantage over oxime ligation; oximes are hydrolytically unstable, with fGly-oximes having a half-life in serum of 18 h.<sup>461</sup> While this half-life provides a wholly appropriate time window within which to conduct protein film voltammetry experiments, a more stable ligation would be desirable for proteins immobilised as part of devices such as fuel cells.



**Scheme 4.4.** The *iso*-Pictet Spengler ligation of an aldehyde or ketone with IP8 to yield a product ligated by a stable C-C bond. The alpha-effect from the oxygen increases the nucleophilicity of the amine group, making nucleophilic attack of the amine group on the carbonyl carbon more favoured. The methylation on the amine nitrogen means the Schiff base formed between the amine group and the carbonyl compound carries a positive charge, increasing the electrophilicity of the Schiff base carbon, increasing the rate of C-C bond formation step.

An example of such an indole, optimised in its reactivity towards aldehydes and ketones courtesy of the *N*-methylhydroxylamine group, is 3-(2-(((methylamino)oxy)methyl)-1H-indol-1-yl)propanoic acid (**IP8**, **Scheme 4.4**). This species was synthesised by a somewhat lengthy 8-step literature synthesis<sup>397</sup> (**Scheme 4.5**, see experimental), and the propensity of **IP8** to ligate to fGly peptide residues was then investigated.



**Scheme 4.5.** The synthesis of *iso*-Pictet Spengler ligating probe **IP8**.

Reactions between *Mt*-FGE-treated substrate peptide and **IP8** were performed in pH 4 buffer (100 mM sodium acetate, 150 mM NaCl) using 50  $\mu$ M of peptide and 500  $\mu$ M **IP8** overnight at 37 °C. ESI-LC/MS of the reaction mixtures after this time showed a  $[M+3H]^{3+}$  product ion peak at  $m/z$  579, indicating successful ligation (**Figure 4.44**, **Table 4.5**). However, in contrast to the oxime ligation reaction, *iso*-Pictet Spengler ligation with **IP8** did not go to completion, as evidenced by the presence of the fGly-peptide peak at  $m/z$  502. The peak at  $m/z$  508 can once again be confirmed to be fGly-hydrate by treating the **IP8**-treated sample with excess *O*-benzylhydroxylamine, which causes both the  $m/z$  508 and 502 peaks to disappear and become replaced with a peak at  $m/z$  538, which can be assigned to fGly-*O*-benzyl oxime (**Figure 4.44**, **Table 4.5**).

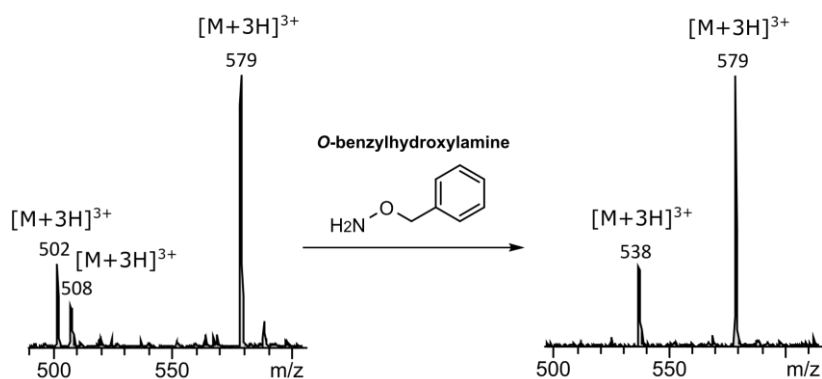


**Figure 4.44.** (Left) Mass spectroscopy of samples of *Mt*-FGE-treated peptide after exposure to IP8. (Right) Mass spectroscopy of samples of *Mt*-FGE-treated peptide that have been treated with IP8 and *O*-benzyl hydroxylamine sequentially.

Given the inferior performance of IP8 as a reagent for ligating to fGly residues, which was unable to achieve 100% conversion even when used in a 10-fold excess, reagents derived from IP8 were deemed insufficiently reactive to be useful as agents to covalently immobilise aldehyde-functionalised proteins onto electrode surfaces.

#### 4.2.4.1.2 Introduction and ligation of fGly residues in a ferrocene-labelled peptide

A peptide labelled with a ferrocene unit and bearing the FGE recognition sequence CTPSR, was synthesised using solid-phase peptide synthesis (Figure 4.45). This peptide was treated with *Mt*-FGE to yield “fGly-ferropeptide,” the fGly residue within which could be ligated to *O*-benzyl hydroxylamine (Figure 4.46). It was hoped that this ferrocene-labelled peptide could be used to screen conditions under which fGly-residues could be ligated to electrode surfaces, with the success of the ligation being evident due to the appearance of redox signals deriving from the ferrocene unit. In practice however both “Ferropeptide” and “fGly-Ferropeptide” adsorb strongly to electrode surfaces, regardless of the surface functionalisation, giving false positives in every instance. As such these ferrocene-labelled peptides did not prove useful.

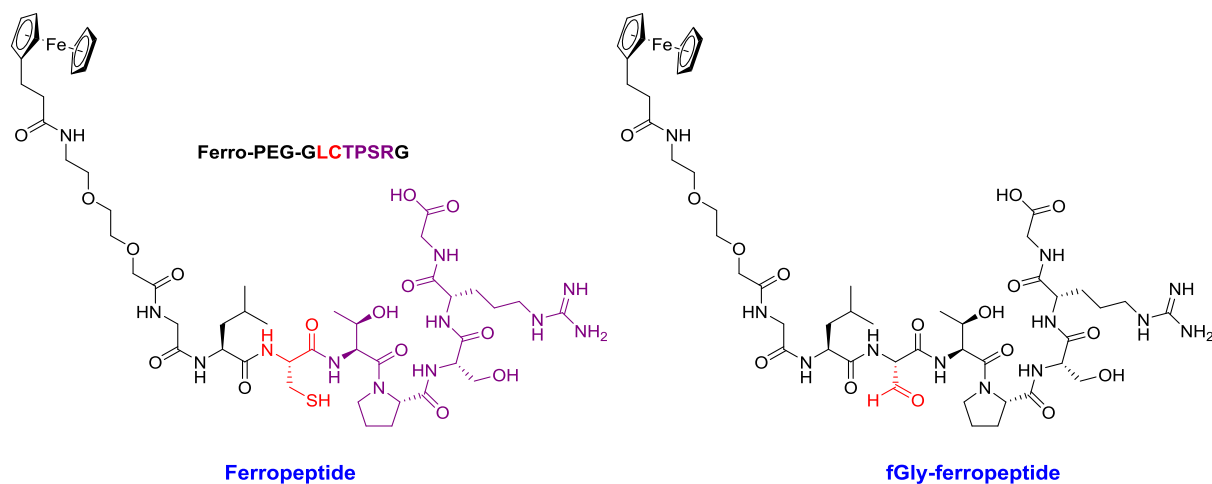


**Figure 4.45.** (Left) The structure of the ferrocene-labelled CTPSRG-containing peptide “Ferropeptide”, and (Right) the structure of “fGly-ferropeptide.”

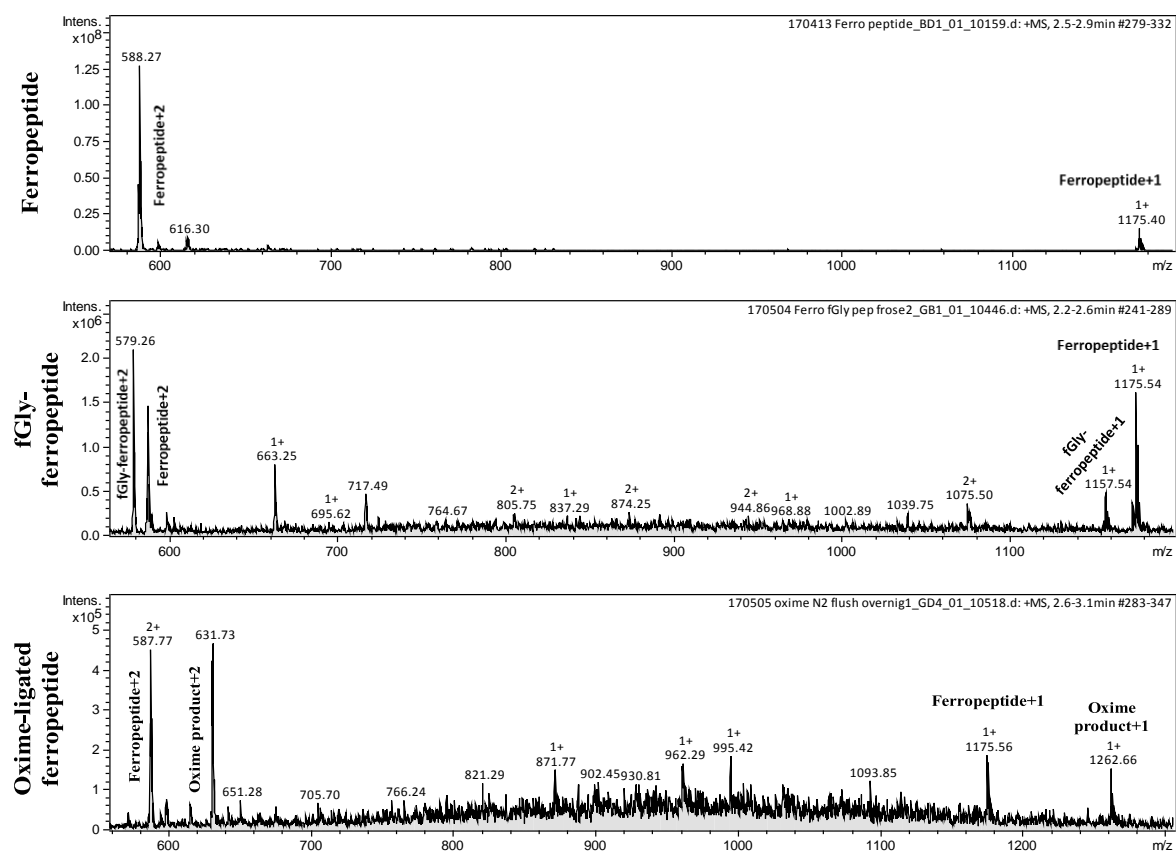


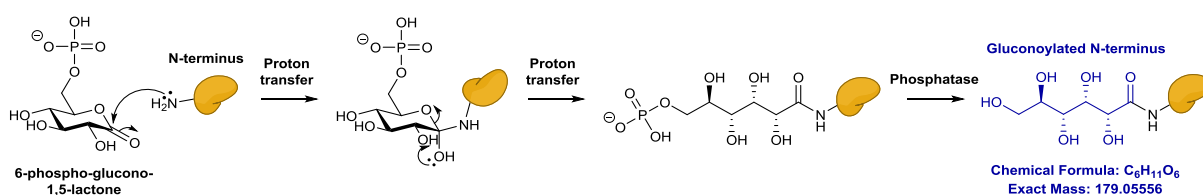
**Figure 4.46.** Positive ion mode ESI-LC/MS-spectra of samples of ferropeptide (**top**), FGE-treated ferropeptide (**middle**) and *Mt*-FGE-treated ferropeptide treated with *O*-benzylhydroxylamine (**bottom**).

#### 4.2.4.2 Introduction of fGly into a redox protein

DsbA is a bacterial thiol disulfide oxidoreductase which catalyses the formation of intrachain disulfide bonds for proteins in the bacteria's periplasm, and thus is an important bacterial virulence factor.<sup>462</sup> The interrogation of the electrochemistry of this redox protein could thus provide insights that could lead to the development of new antibacterial strategies. On a practical note, DsbA has a low molecular weight of around 26.5 kDa; a mass small enough to be readily monitored by protein mass spectrometry. DsbA from *M. tuberculosis* (hereafter referred to simply as DsbA) (PDB ID: 4K6X) represented an interesting model protein with which to investigate the process of generating fGly bio-orthogonal handles in proteins using FGE. Two different cysteine mutants of DsbA, DsbA<sub>C-term</sub> (which bears the CTPSRG FGE recognition sequence at the C-terminus) and DsbA<sub>middle</sub> (which bears the CTPSRG FGE recognition sequence at a more central location on the protein's surface) were prepared (Section 8.1.4.1) and treated with FGE *in vitro*.

##### 4.2.4.2.1 Preparation of DsbA mutants

pET151/D-TOPO plasmids bearing custom gene sequences for either DsbA<sub>C-term</sub> or DsbA<sub>middle</sub>, were ordered from Life Technologies (see Appendix 6 for gene sequences) and were transformed into *E. coli* BC21 (DE3) electrocompetent cells by electroporation. Both DsbA<sub>C-term</sub> and DsbA<sub>middle</sub> could be produced under shake-flask conditions and were purified using Ni-affinity chromatography (Section 8.1.4.1). Protein MS found DsbA<sub>C-term</sub> to have a mass of 26481 Da after deconvolution (Figure 5.2, top). This is within 3 Da of the calculated mass of 26478 Da, an acceptable error when performing deconvolution of protein charge state ladders. Likewise, mass spectrometric analysis found DsbA<sub>middle</sub> to have a deconvoluted mass of 25763 Da (Figure 5.2, bottom), which is in agreement with the calculated mass of 25763 Da. The +179 peak at 26660 Da in the deconvoluted mass spectrum of DsbA<sub>C-term</sub> (Figure 5.2, top) corresponds to a population of gluconoylated DsbA<sub>C-term</sub>. Gluconoylation is a post-translational *N*-terminal modification common for His<sub>6</sub>-tagged proteins overexpressed in *Escherichia coli* BL21 DE3 cells, and occurs as a result of the metabolite 6-phospho-glucono-1,5-lactone reacting spontaneously with a free protein *N*-terminus (Scheme 4.6).<sup>463,464</sup>



Scheme 4.6. The gluconoylation of protein *N*-termini.

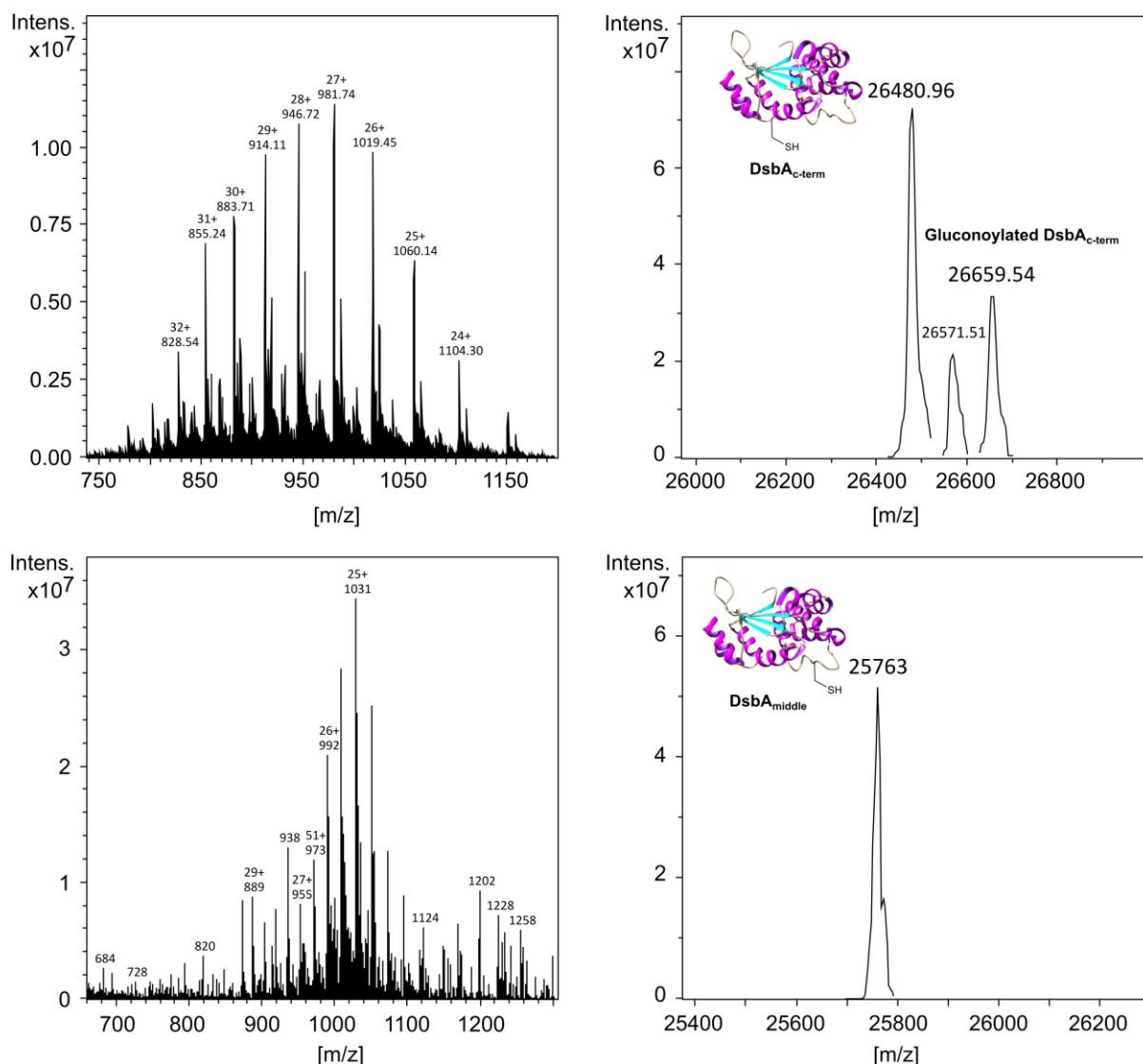


**Figure 4.47.** Positive ion mode ESI-LC/MS of samples of DsbA<sub>C-term</sub> (**top**), and DsbA<sub>middle</sub> (**bottom**). Raw MS data showing the protein charge ladders are shown on the left whereas deconvoluted spectra are shown on the right.

#### 4.2.4.2.2 Enzymatic introduction of fGly into DsbA mutants

Modification of the DsbA mutants by *Mt*-FGE was monitored by ESI-LC/MS. DsbA<sub>C-term</sub> was incubated with 0.2 equiv of *Mt*-FGE with at 37 °C overnight in pH 9 buffer (25 mM triethanolamine, 50 mM NaCl + 5 mM dithiothreitol). MS (**Figure 4.48**) showed that fGly-labelled DsbA<sub>C-term</sub> had formed as the deconvoluted protein mass had shifted by –18 Da (from 26481 Da to 26463 Da, compare **Figure 4.47 top** with **Figure 4.48**), which is a match for the expected –18 Da mass change (**Figure 4.42**). Interestingly a peak corresponding to unmodified DsbA<sub>C-term</sub> (i.e. within 3 Da of 26478 Da) was not observed; this not only suggests that the reaction had reached completion, but also that the vast majority of the fGly residues were not residing in the hydrated fGly-diol form. It could be postulated

that the protein fold creates a local environment for the fGly residue that favours the aldehyde form over the hydrated form. Once again, a smaller peak at +179 Da (26641 Da) can be observed which corresponds to the corresponding gluconoylated product (Gluconoylated fGly-labelled DsbA<sub>C-term</sub>) (**Figure 4.48**). Many studies using *Mt*-FGE *in vitro* have relied on using an excess of *Mt*-FGE modify large globular proteins,<sup>465</sup> whereas this work illustrates that *Mt*-FGE can be used in catalytic quantities to completely modify DsbA<sub>C-term</sub>.

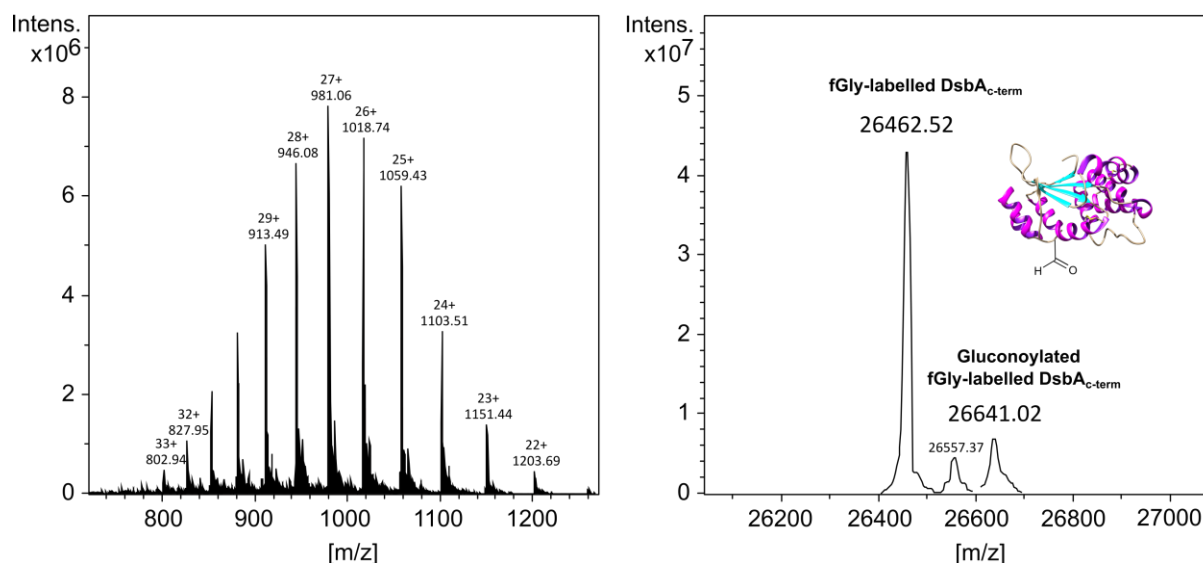


**Figure 4.48.** Positive ion mode ESI-LC/MS analysis of samples of *Mt*-FGE treated DsbA<sub>C-term</sub>. The raw MS data showing the protein charge ladders is shown on the left whereas the deconvoluted spectrum is shown on the right.

The fGly residue introduced into DsbA<sub>C-term</sub> was reacted with *O*-benzyl hydroxylamine under conditions analogous to that used on the substrate peptides (100 mM sodium acetate, 150 mM NaCl, pH 4, 50  $\mu$ M DsbA<sub>C-term</sub>, 5 mM *O*-benzyl hydroxylamine, 37 °C, 18 hours), yielding DsbA<sub>C-term</sub> fGly *O*-benzyl oxime. ESI-LC/MS analysis confirmed that this reaction proceeded to completion, with no peaks for DsbA<sub>C-term</sub> or fGly-labelled DsbA<sub>C-term</sub> being in evidence after deconvolution, only peaks at 26568.54 Da and 26746.56 Da (**Figure 4.49**), which are within 4 Da of the expected masses for DsbA<sub>C-term</sub> fGly *O*-benzyl oxime and the corresponding gluconoylated product (26565 Da and 26744 Da respectively).

DsbA<sub>middle</sub>, by contrast, did not undergo fGly incorporation upon treatment with *Mt*-FGE, despite several conditions being trialled. The most forceful condition involved using a 1:1 ratio of *Mt*-FGE to DsbA<sub>middle</sub> at 42 °C; these conditions were used by Bertozzi and co-workers to modify an internal site in an antibody,<sup>466</sup> yet still did not yield fGly-labelled DsbA<sub>middle</sub>. The successful reaction of the DsbA<sub>middle</sub> CTPSR cysteine residue with alkylating agent **Alk1** (**Scheme 4.7**) proved that the cysteine residue is accessible to solution phase ligation and thus that the CTPSR motif is not buried internally (**Figure 4.50**). It can be thus be hypothesised that the lack of success in enzymatic fGly incorporation



is due to the location of the CTPSR consensus sequence within a structurally defined, rigid region of the DsbA protein which is unable to enter the FGE active site.

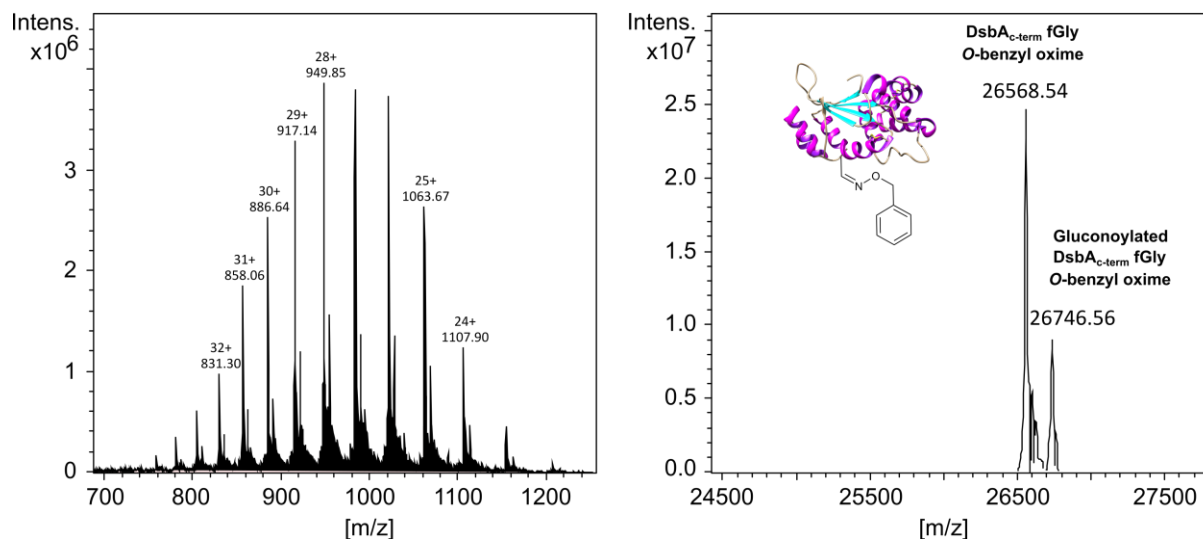
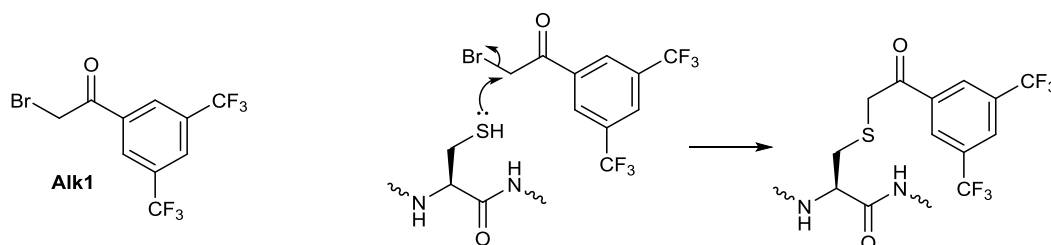


**Figure 4.49.** Positive ion mode ESI-LC/MS analysis of samples of fGly-labelled DsbA<sub>C-term</sub> treated with *O*-benzylhydroxylamine. The raw MS data showing the protein charge ladders is shown on the left whereas the deconvoluted spectrum is shown on the right.



**Scheme 4.7.** The structure of alkylating agent Alk1 and the mechanism of its reaction with cysteine residues.

F. Seebeck and co-workers have reported the engineering of FGE from *Thermomonospora curvata* (*Tc*FGE) to produce more active FGE enzymes.<sup>467</sup> F. Seebeck and co-workers first replaced all 4 cysteine residues outside the WT *Tc*FGE (*Tc*FGE<sub>WT</sub>) active site with alanine (for the three buried Cys residues 187, 231 and 298) or serine (for the surface-exposed Cys284) to yield a *Tc*FGE variant (*Tc*FGE<sub>4c</sub>) which surprisingly had a 7-fold increased activity relative to *Tc*FGE<sub>WT</sub>; the increased activity of which is primarily due to the Cys187Ala mutation.<sup>467</sup> Building on this work, F. Seebeck et al. mutated the highly-conserved (> 99% across bacterial and eukaryotic FGEs) Tyr273 residue of *Tc*FGE<sub>4c</sub> (the role of which still is not clear) to Phe, yielding the most active *Tc*FGE variant to date.<sup>467</sup> This variant, referred to as *Tc*FGE<sub>7</sub>, has a 40-fold increased catalytic efficiency for modifying peptides with the CTPSR consensus sequences relative to *Tc*FGE<sub>WT</sub>.<sup>467</sup> F. Seebeck and co-workers also report that *Tc*FGE<sub>7</sub> can be used to

introduce fGly functionality into an internal loop site in an GFP mutant, and it was hoped that *TcFGE*<sub>7</sub> might be capable of fGly incorporation into *DsbA*<sub>middle</sub>.<sup>467</sup>

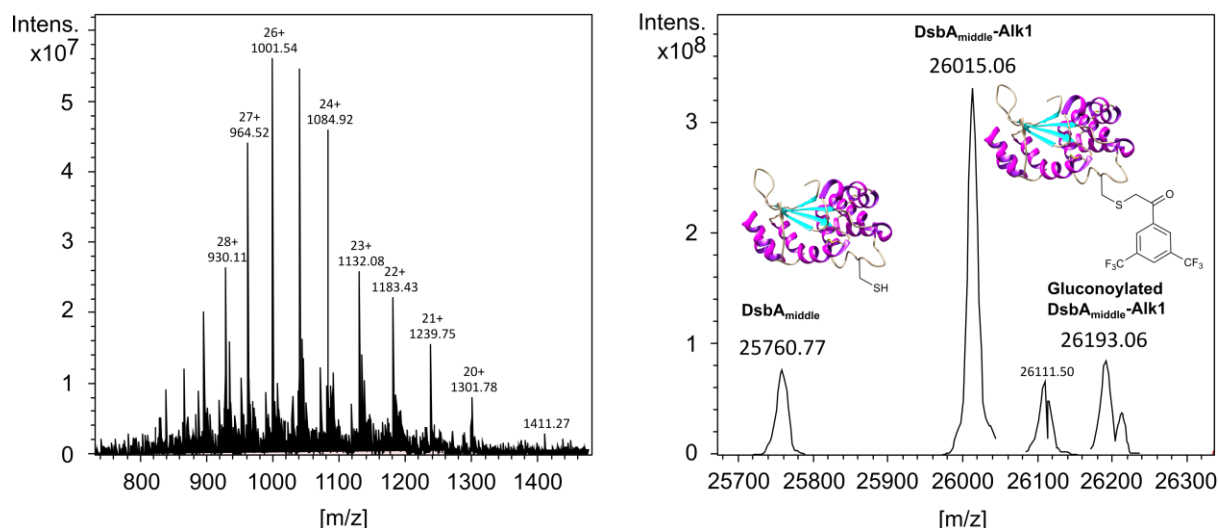


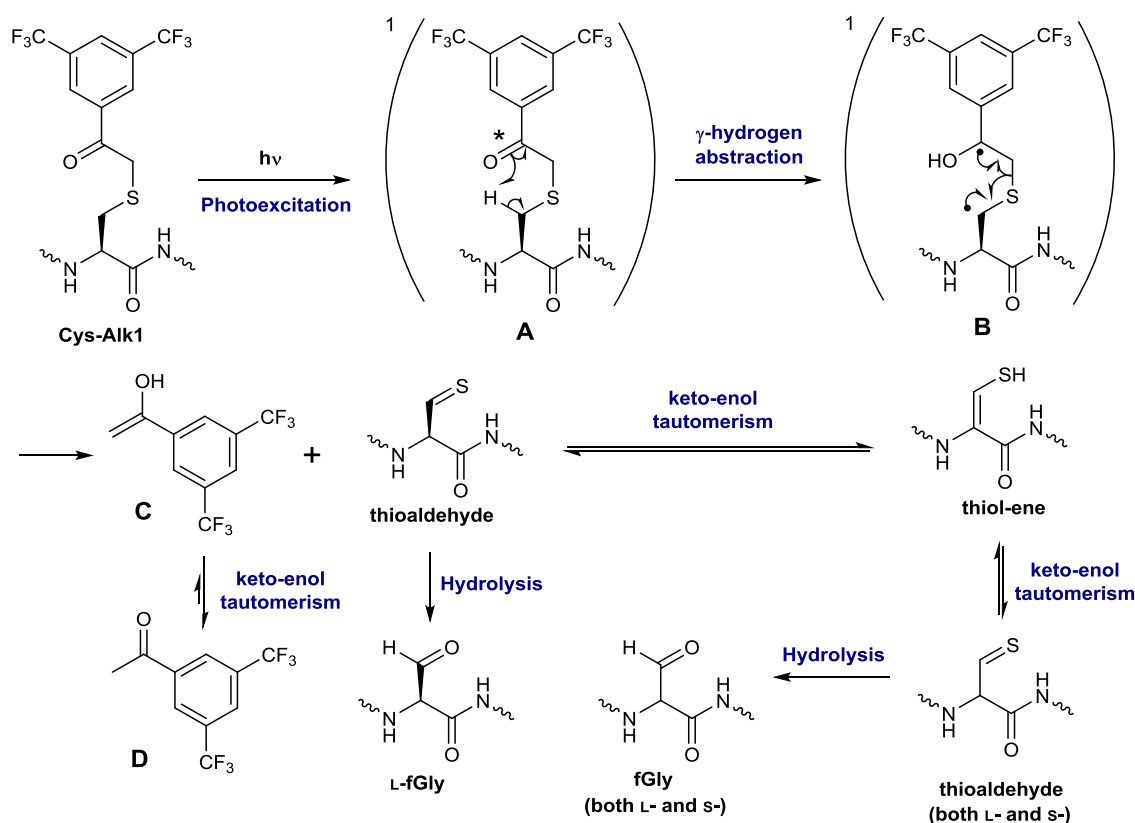
**Figure 4.50.** Positive ion mode ESI-LC/MS analysis of samples of *DsbA*<sub>middle</sub> treated with **Alk1**. The raw MS data showing the protein charge ladders is shown on the left whereas the deconvoluted spectrum is shown on the right.

*TcFGE*<sub>7</sub> was produced in-house by a member of the Parkin lab. The preparation was somewhat low yielding however and the *TcFGE*<sub>7</sub> isolated is suspected to be impure. The suspected impurity of the isolated *TcFGE*<sub>7</sub> comes from observations that treatment of *DsbA*<sub>c-term</sub> with *TcFGE*<sub>7</sub> *in vitro* resulted in only a 36% conversion to fGly-labelled *DsbA*<sub>c-term</sub>, whereas treatment with *Mt-FGE* resulted in 100% conversion. Treatment of *DsbA*<sub>middle</sub> with *TcFGE*<sub>7</sub> *in vitro* did once again fail to result in fGly incorporation. Although the *TcFGE*<sub>7</sub> was suspected to be impure, if it had any ability to modify *DsbA*<sub>middle</sub> some fGly-labelled *DsbA*<sub>middle</sub> would likely still be observed. It is noteworthy that in order to achieve fGly incorporation into the internal loop site of GFP, F. Seebeck et al, engineered an additional 12 residues into the loop,<sup>467</sup> causing the loop to become far larger and its fold to become more poorly defined; this would make it easier for the CTPSR consensus sequence to enter the FGE active site. The *DsbA*<sub>middle</sub> CTPSR consensus sequence by contrast, as mentioned earlier, is situated in a structurally well-defined region of the protein.

#### 4.2.4.2.3 Chemical introduction of fGly into *DsbA* mutants

Due to the limitations afflicting the *in vitro* enzymatic approach for fGly installation, a non-enzymatic method of fGly installation was investigated, in collaboration with Dr Eddie Myers (National University of Ireland, Galway) and his PhD student Lee-Ann Keane (National University of Ireland, Galway).

Cysteine residues alkylated using **Alk1** display interesting UV-activity.<sup>468</sup> This begins with photoexcitation of the carbonyl group of the aromatic ketone to generate a species with 1,2-biradical character (**Scheme 4.8**, species **A**), which subsequently undergoes Norrish Type II  $\gamma$ -hydrogen abstraction to yield a 1,4-biradical (**Scheme 4.8**, species **B**). This 1,4-biradical fragments to yield an enol (**Scheme 4.8**, species **C**) and a thioaldehyde, which equilibrate with several other species in aqueous solution (**Scheme 4.8**). Hydrolysis of thioaldehyde leads to the formation of fGly residues,<sup>450,456</sup> but the current data would suggest that this hydrolysis occurs slowly, presumably due to an interplay between the stability of the thioaldehyde species and the position of equilibrium between thioaldehyde and thiol-ene species.



**Scheme 4.8.** Photofragmentation of **Cys-Alk1** via a Norrish Type II reaction to yield thioaldehyde, thiol-ene and fGly.

DsbA<sub>middle</sub> was subjected to alkylation with **Alk1** and subsequently subjected to 1 hour of exposure to 365 nm UV radiation. ESI-LC/MS analysis (**Figure 4.51**) showed that the majority of the **Cys-Alk1** functionalisation (i.e. the peak at 26014 Da) had been removed, and the peak that could be assigned to DsbA<sub>middle</sub> in either the free cysteine or ene-thiol/thioaldehyde states (the peak at 25760 Da) had increased in intensity (**Figure 4.51**). While the masses of the ene-thiol/thioaldehyde and free cysteine states are too similar to be distinguished by LC/MS (due to the errors associated with charge

deconvolution), the growth of peak intensity of the 25760 Da peak at the expense of the 26014 Da peak is strong evidence of photodegradation (**Figure 4.51**). Interestingly, small signals can be discerned at 25740 Da and 25742 Da, which could conceivably be from fGly-labelled DsbA<sub>middle</sub> (which has a calculated mass of 25747 Da) (**Figure 4.51**).

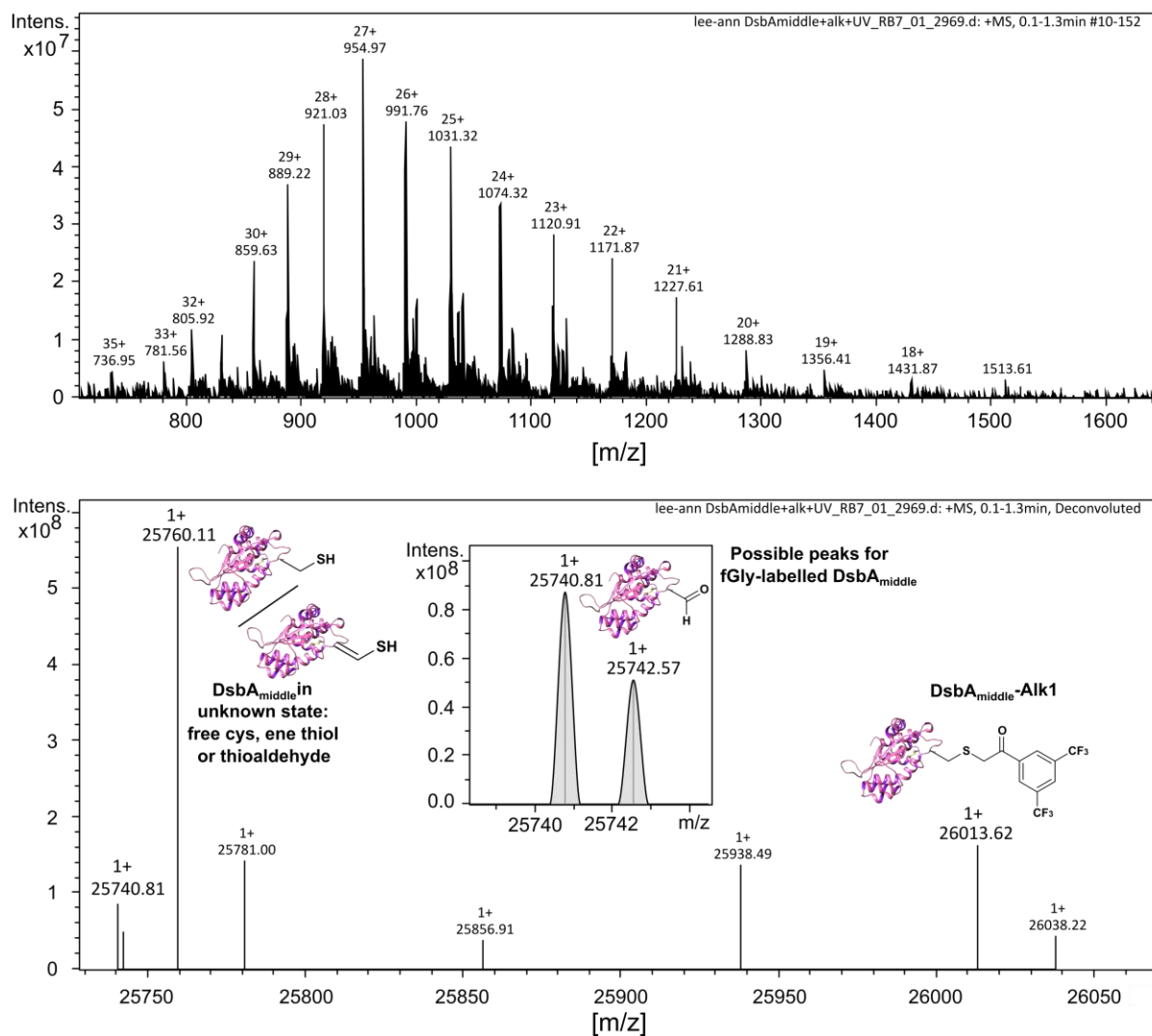


**Figure 4.51.** Positive ion mode ESI-LC/MS analysis of samples of DsbA<sub>middle</sub> treated with Alk1 and then subjected to 365 nm UV-irradiation for 1 hour. **Top)** The raw MS data showing the protein charge ladders. **Bottom)** Deconvoluted mass spectrum.

## 4.3 Summary and conclusions.

### 4.3.1 Critical assessment of aldehyde incorporation strategies

Several methods for the introduction of aldehydes into proteins have been identified and trialled on a series of proteins.

Of all these methods, arguably the most convenient, if applicable, is oxidative cleavage of 1,2 cis diols or 1,2 amino alcohols using  $\text{NaIO}_4$ , which can be achieved in a matter of min at neutral pH. Unfortunately, the price of this convenience is the aldehyde introduction is often restricted to the protein *N*-terminus (unless a special unnatural amino acid mutagenesis strategy is opted for) or onto glycans. These sites may not serve as choice tethering loci for electroactive redox protein immobilisation; either due to the distance of these sites from the redox centres of the proteins, the presence of several glycans, or several sites at which aldehydes may be introduced into the glycans, leading to a dispersity in the products. The *N*-terminus may also form part of the redox proteins active site, and thus may not always be available for bioconjugation.

PLP-mediated transamination likewise suffers from the same limitations of  $\text{NaIO}_4$  oxidation of *N*-terminal 1,2 amino alcohols; aldehyde introduction is restricted to the *N*-terminus. In addition to this limitation, the conditions for PLP-mediated transamination are somewhat harsher than those required for  $\text{NaIO}_4$  oxidation of 1,2 amino alcohols, requiring overnight incubation at 37 °C.

The introduction of fGly residues into proteins via the enzymatic action of FGE *in vitro* is likely to suffer from several limitations: the mutation of the target redox protein to bear the CXPXR consensus sequence could adversely affect the fold of the protein; the fold of the protein could prevent the CXPXR consensus sequence from fitting into the FGE active site, preventing enzymatic fGly introduction; and lastly, the treatment of a CXPXR-labelled redox protein with FGE *in vitro* represents an additional step during which some of the redox protein may become denatured. The preparation and handling of cysteine-labelled redox proteins has its own associated complications (such as the need to use reducing agents to prevent the formation of undesired disulfide bonds and the propensity of the mutant cysteine residues to partake in undesired ligation to cofactors), and thus a potential way to circumvent these complications would be to develop a system that uses a formylglycine generating enzyme that oxidise serine residues rather than cysteine residues (**Scheme 4.3**).

Additionally, there are a wealth of highly effective bioconjugation strategies that selectively and rapidly ligate to cysteine residues. The CXPXR motif contains a cysteine residue, and thus unless the redox protein contains several surface-exposed cysteine residues there is no obvious incentive to convert the CXPXR cysteine into an fGly residue for later use in an aldehyde-ligating reaction when

direct ligation to this cysteine could be achieved using a cysteine-ligating probe. A similar problem is encountered when considering the usage/development of reagents such as **Alk-1** to convert cysteine residues into formylglycine residues.

anSMEs such as AtsB could actually be more suited to *in vitro* use than FGE, as they are capable of oxidising either cysteine or serine residues to formylglycine,<sup>451,452</sup> and thus the complications associated with handling protein cysteine mutants could be circumvented. Recent publications have reported the usage of AtsB from *Methanosarcina mazei* for the introduction of fGly tags into proteins *in vitro*,<sup>451</sup> but the aforementioned problems associated with enzymatic action on a pre-folded protein would likely still restrict the sites at which fGly could be incorporated. anSME usage still requires the installation of a recognition sequence however,<sup>451</sup> a limitation it shares with usage of FGE.

The majority of the aforementioned limitations could be overcome if the action of FGE or anSME on the consensus sequence labelled protein occurred co-translationally, as modification of the target consensus sequence, prior to protein folding, would allow fGly to be introduced at sites inaccessible to enzymatic action when the protein is fully folded. The (C/S)XPXRXXXLTGR consensus sequence in sulfatases is located 50–80 amino acids away from the *N*-terminus, and is proof that FGE and anSME can introduce fGly into internal locations *in vivo*.<sup>469</sup> In addition, co-expression eliminates the need for an *in vitro* enzymatic treatment step, during which protein denaturation could occur. It is easier to culture *E. coli* under aerobic conditions than anaerobic, and thus the aerobic FGE enzymes would likely be more suited to *in vivo* usage under shake-flask conditions than anSMEs. Post-translational modification of the target CXPXR sequence would also eliminate the additional cysteine residue; this circumvents the complications associated with having mutant cysteine residues in redox proteins and also negates the potential advantage of using anSMEs to modify serine mutants.

Several studies that have used co-expression of CXPXR-labelled proteins with *Mt*FGE as a means to produce aldehyde-labelled proteins, illustrating the potential versatility of this approach.<sup>469-471</sup> However, several complications could be encountered when using this approach, including a variation in the percentage of CXPXR-label → fGly conversion between different protein substrates<sup>465,469-471</sup> and lower expression levels of and/or solubility issues with *Mt*FGE.<sup>465</sup> Other authors have also highlighted the possibility that cellular enzymes (such as aldehyde dehydrogenases)<sup>472,473</sup> may act upon the fGly aldehyde.<sup>465</sup> It seems that while there is great potential in the usage of FGE (or anSMEs) to label redox proteins with formylglycine, a simple universal method for achieving this, for now at least, remains frustratingly elusive.

### 4.3.2 Critical assessment of aldehyde ligation strategies

Several aldehyde ligation strategies have been screened in the previous Chapter: *iso*-Pictet Spengler ligation,<sup>397</sup> oxime ligation<sup>395</sup> and OPAL.<sup>399</sup> OPAL ligation is the fastest and mildest aldehyde ligation method, and does yield a C-C bond that would be unlikely to be affected by electrochemical oxidation or reduction. However, OPAL ligation is likely to be unsuitable for the ligation of protein aldehydes to electrode surfaces; there are many cases of successful immobilisation of redox proteins whereby imine formation occurs between protein lysine residues and aldehyde-functionalised electrode surfaces,<sup>174,176,177,191,199-201</sup> with the resultant imines being somewhat stabilised against hydrolysis due to the micro-environment afforded by the electrode surface. If an electrode surface were to be functionalised with OPAL probes, there is a good chance that these probes may form stable imines with the protein lysine residues, meaning that the OPAL reaction itself would not actually occur on a timescale that would make OPAL usage advantageous. The synthesis of an OPAL probe amenable to electrode surface immobilisation would also be far from simple.

*iso*-Pictet Spengler ligation would likely be unsuited to electrode-surface applications. While it does yield a stable C-C bond it is slow, and the conditions under which it is performed are no milder than those of the far simpler oxime ligation. The synthesis of *iso*-Pictet Spengler probes is also lengthy, and there is no literature precedent regarding what sort of conditions would be required to deprotect the surface-confined *iso*-Pictet Spengler moieties.

Oxime ligation is a long-established bioconjugation technique and has thus seen far more usage than either *iso*-Pictet Spengler ligation and OPAL ligation.<sup>395,474</sup> With the maturity of this technique come many advantages; the preparation of hydroxylamine probes is now relatively simple, and the usage of nucleophilic catalysis to both improve the sluggish reaction rate and allow the reaction to be performed under mild conditions is well documented.<sup>395,396</sup> The N=C bond formed during oxime ligation does eventually hydrolyse, but it will almost certainly remain intact long enough to allow an immobilised redox protein to be electrochemically interrogated. Although the N-O bond is susceptible to hydrogenation/reduction in chemical synthesis, it is electrochemically stable within the range of potentials relevant for most biological redox processes, meaning it is suitable for redox protein immobilisation.<sup>475</sup> Owing to its simplicity, it seemed that oxime ligation was the most obvious method via which to first attempt to immobilise a protein aldehyde.

# Chapter 5

Aldehyde-mediated protein-to-surface  
tethering via controlled diazonium  
electrode functionalisation using  
protected hydroxylamines



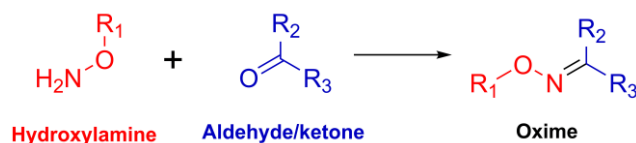
## Chapter 5. Aldehyde-mediated protein-to-surface tethering via controlled diazonium electrode functionalisation using protected hydroxylamines

The results in the following Chapter have formed the basis of my publication, “Aldehyde-mediated protein-to-surface tethering via controlled diazonium electrode functionalisation using protected hydroxylamines.”<sup>476</sup>

### 5.1 Introduction

There is an ever-growing chemical biology toolkit of methodologies for site-selective bio-orthogonal ligations to proteins.<sup>213,477,478</sup> However, a relatively small number of these methodologies have been converted into robust strategies for immobilizing proteins onto a wide range of solid substrates.<sup>393,479</sup> This is despite the need for protein immobilisation in industrial biocatalysis, medical diagnostics, tissue culturing, environmental sensing and biophysical characterisation.<sup>393,480,481</sup>

It is advantageous to design a protein-immobilisation strategy that targets aldehydes because there are a wide range of robust methodologies which will introduce these bio-orthogonal carbonyl functionalities into proteins, as is shown in **Chapter 4, Figure 4.1.**<sup>394,395,407,447</sup> Due to its ease and simplicity, oxime ligation between a hydroxylamine and an aldehyde or a ketone (**Scheme 5.1**)<sup>395</sup> is a widely used bio-orthogonal ligation strategy,<sup>395,474</sup> and has often been used to immobilise proteins onto non-conductive substrates,<sup>482,483</sup> yet has only seen limited usage in bioconjugation to conductive substrates.<sup>484</sup>



**Scheme 5.1.** The ligation of a hydroxylamine to an aldehyde or ketone to form an oxime.

By developing a procedure that enables the functionalisation of a wide range of solid substrates with hydroxylamine monolayers, the tethering of aldehyde-containing (bio)molecules to many solid-substrates via oxime bond formation would be enabled, and thus such a strategy would even have applications beyond electroactive protein immobilisation, such as in surface plasmon resonance (SPR)

detection of drug molecule binding,<sup>20,16</sup> the iterative synthesis of polypeptide conjugates,<sup>485</sup> or the assembly of DNA or RNA arrays, as nucleic acids are also readily aldehyde-functionalised.<sup>486,487</sup>

### 5.1.1 Aims

A method for the functionalisation of electrode surfaces with hydroxylamines for use in electroactive redox protein immobilisation would meet certain criteria:

- 1) Directly deliver hydroxylamine functionalities to the electrode surface.
- 2) The hydroxylamines should be capable of reacting with aldehydes.
- 3) Oxime ligation between a surface hydroxylamine and an aldehyde installed on a redox protein should facilitate electroactive immobilisation.

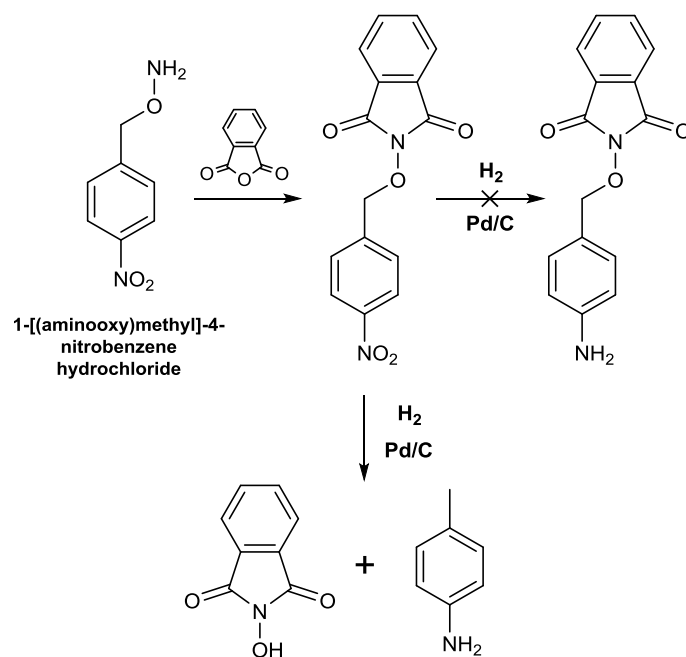
It was proposed that the phthalimide-protection/deprotection strategy detailed in **Chapter 3** would lend itself well to modification in such a way that would deliver a monolayer of hydroxylamines instead of aliphatic amines.

## 5.2 Results and Discussion

### 5.2.1 Development of a method for the introduction of hydroxylamine functionalities onto electrode surfaces as a near-monolayer

#### 5.2.1.1 The design and synthesis of a suitable aryl diazonium precursor

Despite the commercial availability of 1-[(aminooxy)methyl]-4-nitrobenzene hydrochloride (**Scheme 5.2**) a protected-hydroxylamine-functionalised aryl diazonium precursor cannot be synthesised in a manner analogous to that described in **Section 3.2.2 Scheme 3.1**, as the hydrogenation of a nitro group using a palladium on carbon catalyst would concurrently hydrogenate across the C-O bond of the benzyl ether motif (**Scheme 5.2**).<sup>488</sup> A nitro-graft could be attempted, removing the need for palladium-catalysed nitro group hydrogenation, but nitro-grafting is time consuming for the experimentalist. An alternative approach would be to generate a protected diazonium group prior to the formation of the N-O bond, and then deprotect the diazonium group immediately prior to performing electro-grafting.



**Scheme 5.2.** The incompatibility of the benzyl ether unit with palladium on carbon catalysed hydrogenation.

A suitable approach was to use aryl triazenes, which break down upon treatment with either Brønsted-Lowry or Lewis acids to yield diazonium cations.<sup>489-492</sup> In the absence of acids aryl triazenes have long shelf-lives and are stable enough to serve as protecting groups for diazonium cations, and the treatment of aryl triazenes with both Brønsted-Lowry acid and a Lewis acidic methylating agent has already been used to generate diazonium cations for use in electro-grafting.<sup>489-491</sup>

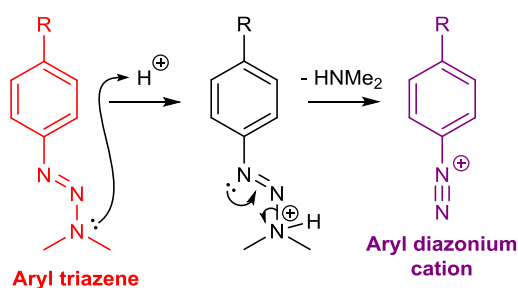
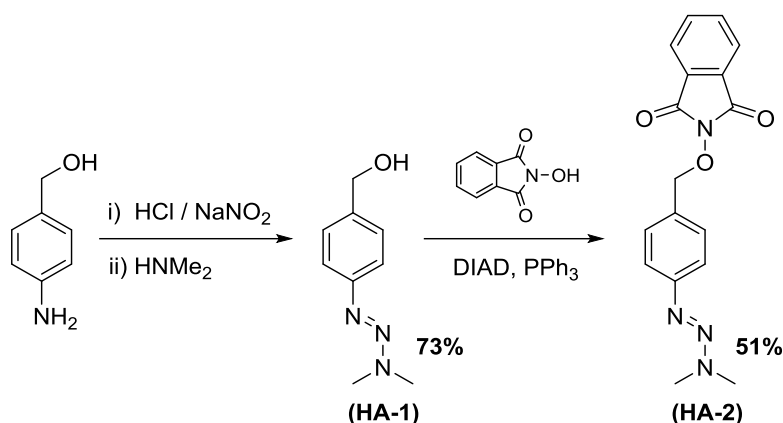


**Figure 5.1.** The generation of aryl diazonium cations from an aryl triazene precursor using a Brønsted-Lowry acid.

Species **HA-2** was obtained in two steps (**Scheme 5.3**). In the first reaction of the synthesis a commercially available (4-aminophenyl)methanol was diazotized and the resulting aryl diazonium reacted with dimethylamine to yield aryl triazene **HA-1**. The alcohol of triazene **HA-1** was then reacted with *N*-hydroxyphthalimide via a Mitsunobu reaction to yield aryl triazene **HA-2**. The propensity of

**HA-2** to form diazonium species upon protonation is evidenced by the presence of a species of  $m/z$  280.07 in the ESI-MS (**Figure 5.2**).



**Scheme 5.3:** The synthesis of aryl triazene **HA-2**.

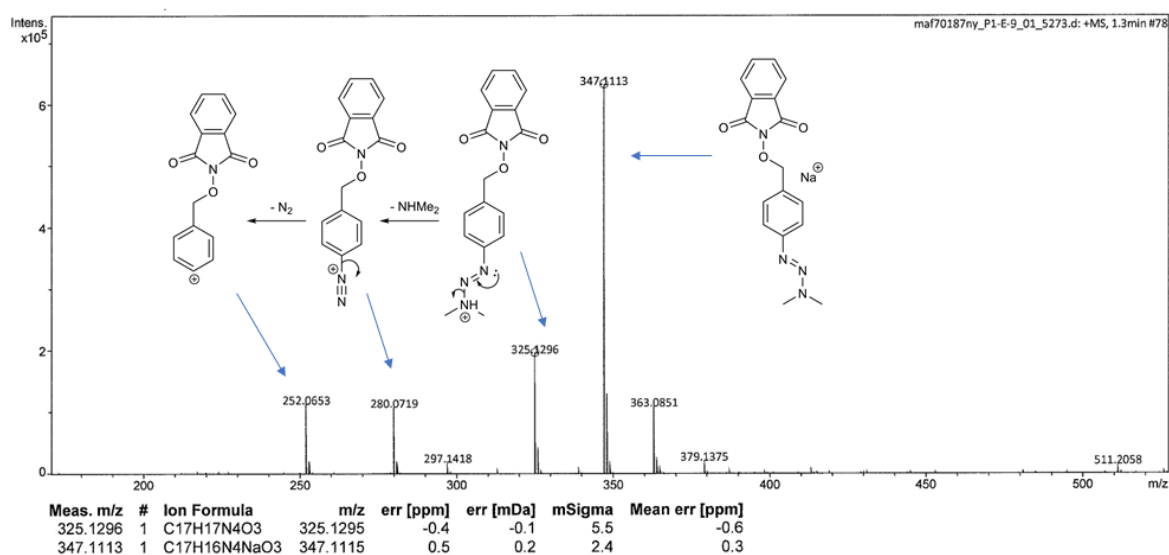


**Figure 5.2.** (ESI)HRMS spectrum of **HA-2**, illustrating its propensity to yield diazonium cations upon protonation.

### 5.2.1.2 The functionalisation of electrode surfaces with hydroxylamines

The acid-triggered *in situ* generation of diazonium species from triazene **HA-2** and the subsequent reductive electro-grafting process on a GC electrode was followed using cyclic voltammetry (**Figure 5.3**). The broad reductive wave (negative current) that is observed as the potential of the electrode is decreased from approximately +0.6 V to 0 V vs SHE in scan 1 is typical of diazonium reduction,<sup>162,365,493</sup> and the disappearance of this feature in subsequent scans indicates the formation of a thick multilayer (**Scheme 5.4**).<sup>171,494</sup>

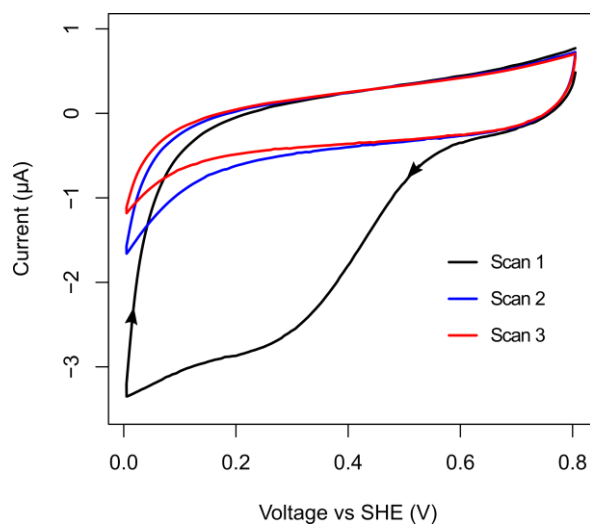
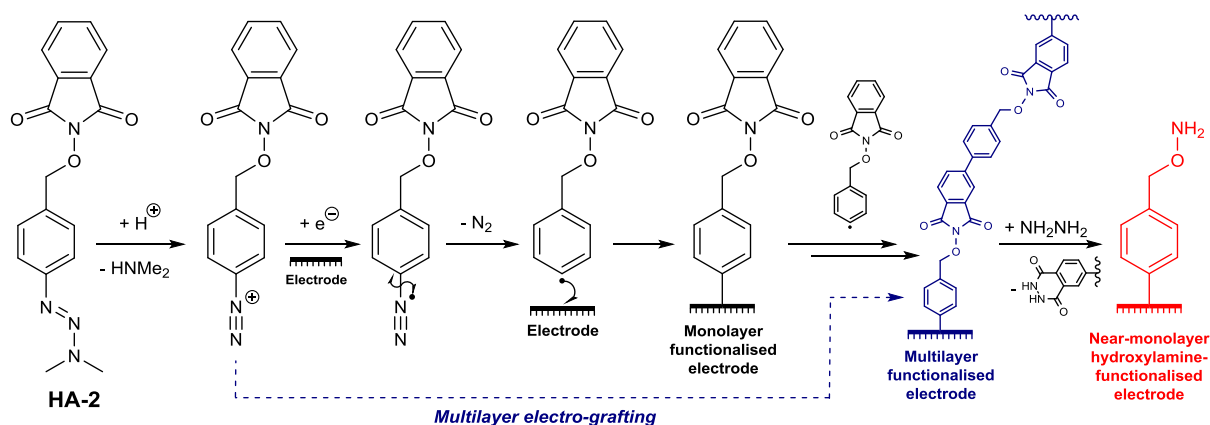


**Figure 5.3.** Cyclic voltammograms of a glassy carbon electrode during  $20 \text{ mV s}^{-1}$  electro-reductive modification scans with the aryl diazonium salt generated in situ from a  $1 \text{ mM}$  solution of **HA-2** in 1:5 v:v water:acetonitrile and  $0.1 \text{ M Bu}_4\text{NPF}_6$ ,  $0^\circ\text{C}$ . The scans commence at the most positive potential, then the voltage is lowered before being increased again.



**Scheme 5.4.** The use of aryl triazene **HA-2** in the diazonium electro-grafting based functionalisation of electrode surfaces with near-monolayers of hydroxylamines.

Diazonium electro-grafting using diazonium cations derived from aryl triazene **HA-2** can be performed on multiple electrode substrates. This is evidenced by **Figure 5.4**, which shows cyclic voltammograms characteristic of diazonium electro-grafting recorded using both boron-doped diamond (BDD) and gold electrodes, in which the substantial drop in reductive current which follows the first scan is again interpreted as evidence that a multilayer has formed on the electrode surface.<sup>171,494</sup>

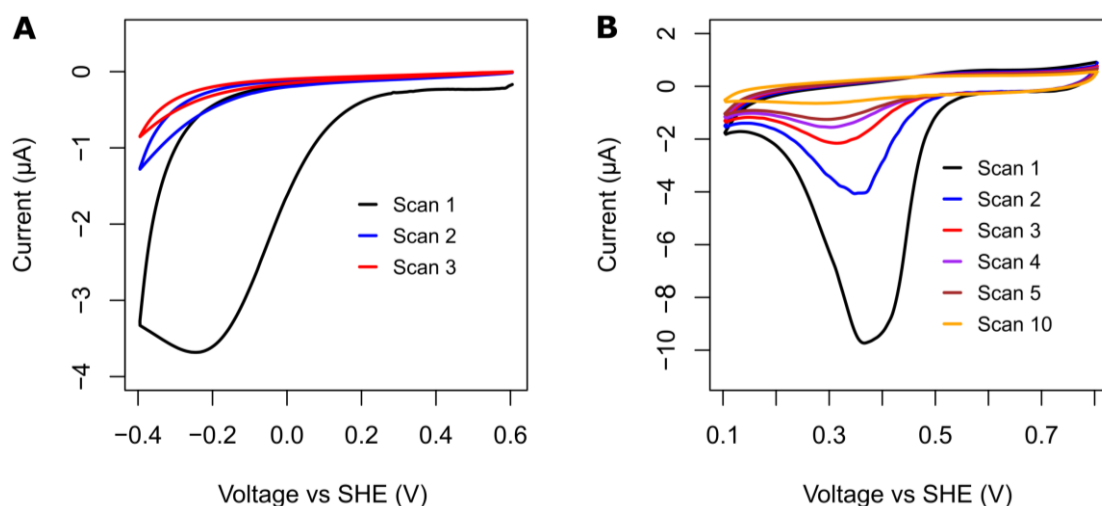


**Figure 5.4.** Cyclic voltammograms of a (A) BDD electrode and a (B) gold electrode during  $20 \text{ mV s}^{-1}$  electro-reductive modification scans with aryl diazonium salt generated *in situ* from a  $1 \text{ mM}$  solution of **HA-2** in 1:5 v:v water:acetonitrile and  $0.1 \text{ M Bu}_4\text{NPF}_6$ ,  $0^\circ \text{C}$ . The scans commence at the most positive potential.

As reported in **Chapter 3**, the treatment of multilayer electro-grafted surfaces with an ethanoic solution of hydrazine at  $80^\circ \text{C}$  removes the phthalimide groups,<sup>171</sup> and in this case leaves a near monolayer of hydroxylamines (**Scheme 5.4**). For this hydroxylamine system, the hydrazine also serves a secondary function, acting as a scavenger for trace carbonyl species and thus preventing the reaction of the resultant hydroxylamine-functionalised surface with contaminant carbonyl compounds such as ethanal or acetone.

### 5.2.1.3 Characterising derivatised electrode surfaces

#### 5.2.1.3.1 Response of derivatised electrode surfaces towards solution phase ferricyanide and electrochemical impedance spectroscopy

As shown in **Figure 5.5**, the electrode modification process can be monitored via the cyclic voltammetric response of GC electrodes in various derivatisation states towards the aqueous ferricyanide redox couple. Unmodified GC electrodes show the expected solution-voltammetry responses for reversible ferricyanide electrochemistry,<sup>494</sup> while electrode surfaces which have been subjected to multilayer electro-grafting (**Scheme 5.4**) display only a non-Faradaic (capacitive-only) voltammetric response to the same solution (**Figure 5.5**). GC electrodes which have been electro-grafted and subsequently treated with hydrazine (**Scheme 5.4**) show a return to the typical solution-phase redox couple voltammetric response (**Figure 5.5**). The inhibition of the redox chemistry upon multilayer electro-grafting is attributed to the formation of a thick multilayer that is impermeable to

the ferricyanide, whereas the fact that hydrazine-treatment restores the reversible solution voltammetry indicates that the deprotection of the phthalimide moiety strips the impermeable multilayer from the surface of the electrode. These results are analogous to those discussed in **Chapter 3, Section 3.2.2.1**.

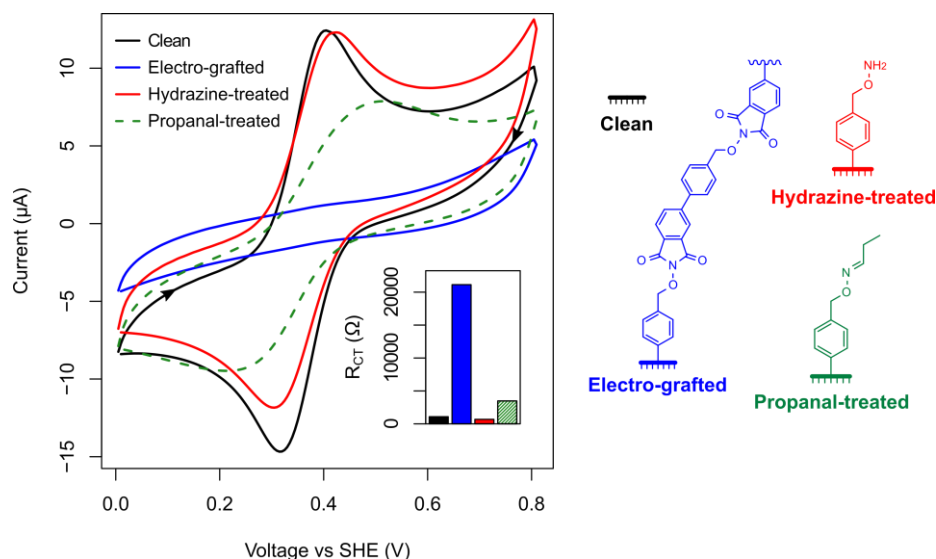


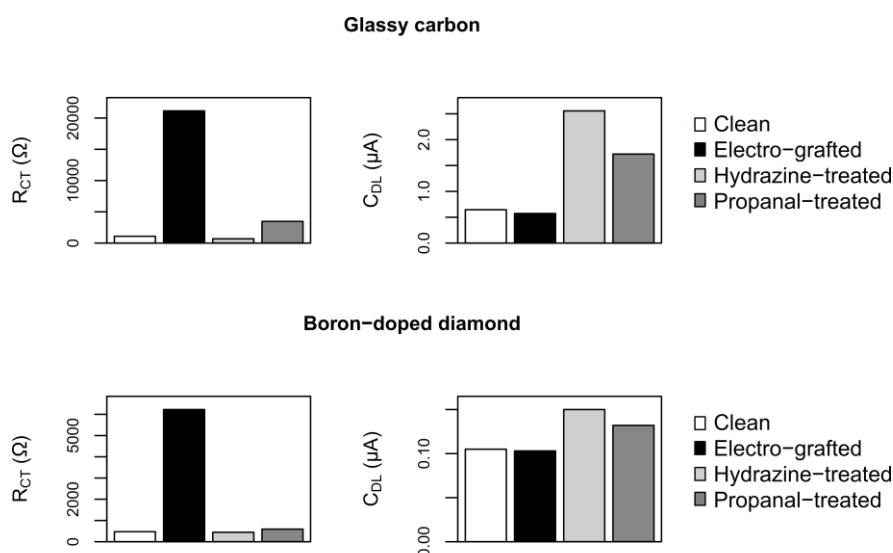
**Figure 5.5. (Main)** Cyclic voltammograms of GC electrodes from various stages in the modification process and after a “quench” reaction with propanal. All scans were measured at  $500 \text{ mV s}^{-1}$  in an aqueous solution of 1 mM potassium ferricyanide and 0.1 M NaCl. Scans commenced from the most negative potential. **(Inset)** The change in the resistance to charge transfer ( $R_{CT}$ ) determined from EIS experiments measured on the same electrodes and under the same experimental conditions.

Evidence that electro-grafting followed by hydrazine-treatment generates a hydroxylamine-functionalised surface is provided by reacting thus-modified GC electrodes with propanal; a simple aldehyde which would be expected to undergo facile ligation to a hydroxylamine-modified surface. Such treatment of the near-monolayer hydroxylamine functionalised electrode surface with propanal introduces short non-polar alkyl chains to the electrode surface, partially re-pacifying it towards the ferricyanide redox couple (**Figure 5.5**).

Electrochemical impedance spectroscopy (EIS) can also be carried out in solutions of ferricyanide, and likewise allows the changes in electrode derivatisation state to be tracked. The results of the EIS analysis of both GC and BDD electrode surfaces in a variety of derivatisation states are tabulated in **Table 5.1** and are plotted in **Figure 5.6**. Solution ferricyanide experiments were not conducted on gold because  $\text{CN}^-$  ions released by ferricyanide etch gold surfaces.<sup>495,496</sup>

**Table 5.1.** Electrochemical impedance spectroscopy analysis (kindly performed by Dr Mark Dowsett) of different electrodes at different stages in the modification process. Experiments were conducted in an aqueous solution of 1 mM ferricyanide and 0.1 M NaCl.

Electrode derivation state	$R_{sol} / \Omega$	$R_{CT} / \Omega$	$C_{DL} / \mu F$	$\Phi$	Warburg / $k\sigma$	$\chi^2 \times 10^{-3}$
Clean glassy carbon	159.4	1089	0.645	0.805	13.00	0.200
Electro-grafted glassy carbon	148.3	21140	0.572	0.796	16.91	6.300
Hydrazine-treated glassy carbon	160.4	686.0	2.556	0.763	13.18	0.100
Hydrazine-treated glassy carbon + propanal	167.9	3468	1.721	0.831	13.11	0.500
Clean boron-doped diamond	134.6	470.7	0.105	0.819	4.941	0.100
Electro-grafted boron-doped diamond	215.3	6226	0.103	0.952	5.285	0.003
Hydrazine-treated boron-doped diamond	237.5	444.1	0.150	0.861	4.845	0.096
Hydrazine-treated boron-doped diamond + propanal	206.7	592.6	0.132	0.840	4.823	0.100

**Figure 5.6.** Graphical summary of the resistance to charge transfer ( $R_{CT}$ ) and capacitance of the double layer ( $C_{DL}$ ) data from **Table 5.1**.

As shown in **Figure 5.6**, the changes to the resistance to charge transfer ( $R_{CT}$ ) values extracted from analysis of EIS data provide further evidence that the multilayer electro-grafting and hydrazine-treatment processes have profound effects on the surface chemistry of both GC and BDD electrodes. The high  $R_{CT}$  value of the multilayer electro-grafted surfaces is consistent with the notion that diazonium-modification forms an electrically insulated multilayer on the surface of the electrodes (note how the  $R_{CT}$  values and the cyclic voltammograms correlate in **Figure 5.5**).



The capacitance of the double layer ( $C_{DL}$ ) for the electrode surfaces also changes as a function of the electrode derivatisation state. Most notably, a notable increase in the capacitance of the electrode surface can be seen when moving from the electro-grafted multilayer state to the hydrazine-treated derivatisation state (**Figure 5.6**). It is possible that the hydroxylamine groups that are revealed upon hydrazine treatment could store charge via protonation. The  $pK_a$  of O-benzylhydroxylamine is 4.8,<sup>497</sup> but the local pH of an electrode surface or the  $pK_a$  of a surface-confined species may well be different to that of a corresponding species in solution. It is also possible that hydroxylamine functionalities simply facilitate the movement of charged ions in the proximity of the electrode surface far more effectively than the functionality present on the clean and multilayer electro-grafted electrode surfaces, thus increasing capacitance.

It should also be noted that although the same trends are seen in the  $R_{CT}$  and  $C_{DL}$  across the different derivatisation states of both GC and BDD electrodes, the absolute values for the  $R_{CT}$  are far higher in the multilayer functionalised state for the GC electrode, as is the spike in  $C_{DL}$  upon hydrazine treatment (**Figure 5.6, Table 5.1**). This would seem to be indicative of a less dense coverage of grafted moieties on the BDD electrode surface. This hypothesis would be supported by **Figure 5.7**, which shows only a slight passivation of BDD electrodes towards the ferricyanide redox couple after multilayer grafting, and only a slight improvement in the reversibility of the redox couple after subsequent hydrazine treatment. It is possible that the formation of a less dense electro-grafted film may be partly due to practical difficulties in polishing the BDD electrode surfaces prior to performing electro-grafting, as while the literature reports the formation of thick multilayers on BDD electrode surfaces via diazonium electro-grafting,<sup>498</sup> most of the BDD samples are freshly prepared via chemical vapor deposition as opposed to being a re-used existing sample that has simply been re-polished.<sup>498</sup>

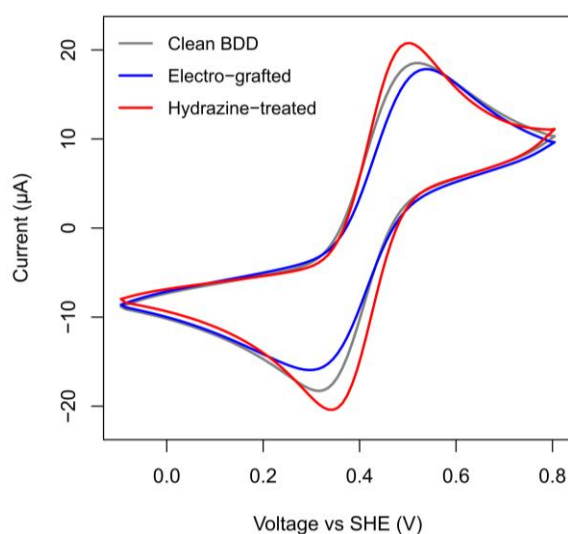


**Figure 5.7.** Cyclic voltammograms of ferricyanide in solution measured using a BDD electrode at various stages of surface modification. Scans measured at  $500 \text{ mV s}^{-1}$  in an aqueous solution of 1 mM ferricyanide and 0.1 M NaCl. Scans commenced from the most negative potential.

### 5.2.1.3.2 Atomic force microscopy

A gold-coated silicon wafer (99.999% Au, 1000 Å thickness) was cleaned using acidic piranha solution, subjected to multilayer electro-grafting with **HA-2** (**Figure 5.8**), and subsequently treated with an ethanolic solution of hydrazine monohydrate to yield a surface functionalised with a near-monolayer of hydroxylamines. The resultant surface was treated with propanal to yield a surface in the “propanal-treated” derivatisation state (see **Figure 5.5**). The surface topography of both a control, non-functionalised, piranha-cleaned gold surface and a surface in the “propanal-treated” derivatisation state were studied by atomic force microscopy (AFM) (**Figure 5.9**). A comparison of the AFM images shown in **Figure 5.9** with those recorded by Hauquier et al<sup>171</sup> (of their electro-grafted aliphatic amine system) shows that the “propanal-treated” AFM image in **Figure 5.9** more closely resembles a thin imperfect electro-grafted film than it does that a thick multilayer of phthalimide-protected moieties, which is of a far smoother topography.<sup>171</sup>

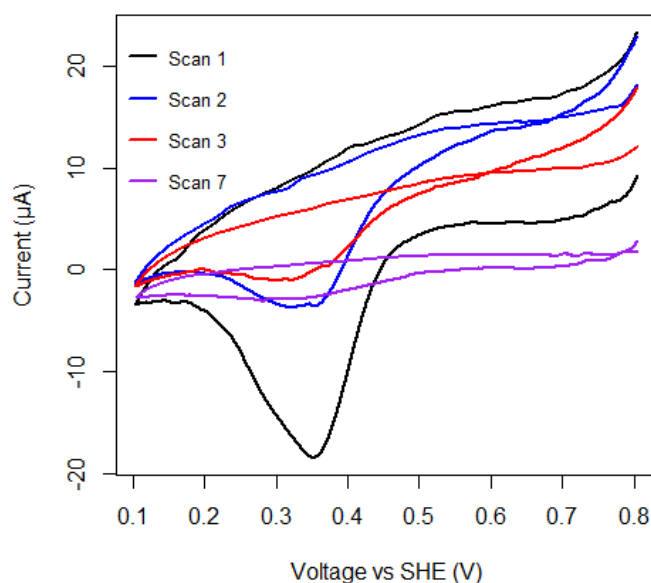


**Figure 5.8.** Cyclic voltammograms of 8 mm × 8 mm gold coated silicon wafer during 20 mV s<sup>-1</sup> electroreductive modification scans with aryl diazonium salt generated *in situ* from a 1 mM solution of **HA-2** in 1:5 v:v water:acetonitrile and 0.1 M Bu<sub>4</sub>NPF<sub>6</sub>, 0 °C. The scans commence at the most positive potential, then the voltage is lowered to the most reductive potential before being increased again. Note that the irregular shape of the cyclic voltammogram is due to the square shape leading to irregular mass-transfer.

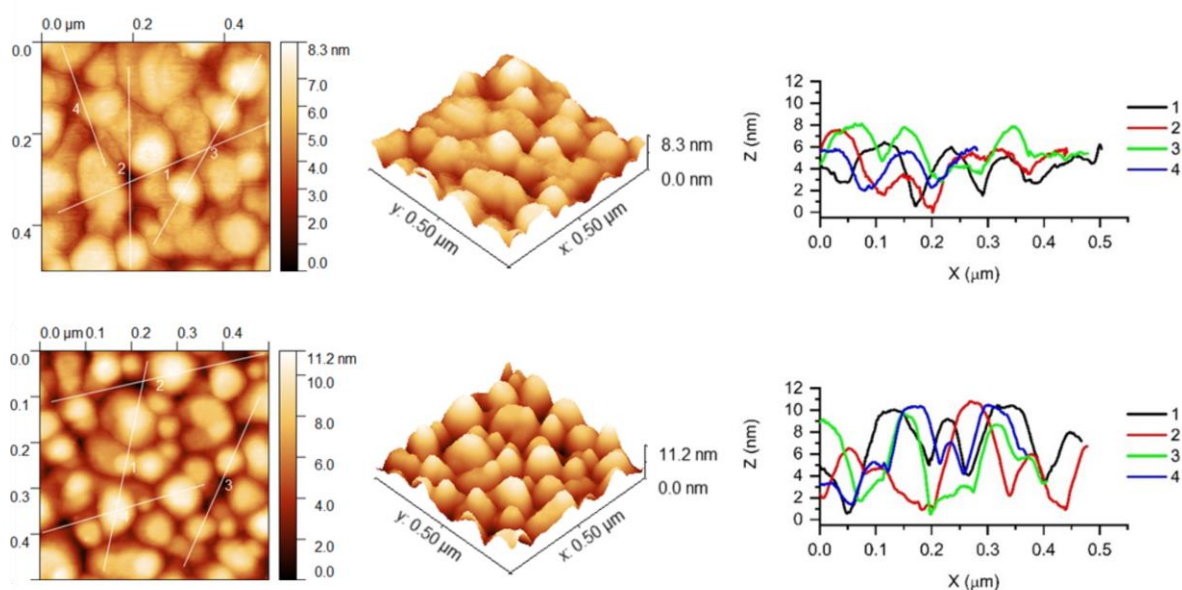


**Figure 5.9.** AFM analysis of **(Top)** an underivatized gold-coated silicon wafer and **(Bottom)** a gold-coated silicon wafer derivatised with a near-monolayer of propionaldehyde-*O*-benzylloxime functionality. AFM was performed with the assistance of Dr. S. P. Tear and Dr M. Dowsett.

### 5.2.1.3.3 X-ray photoelectron spectroscopy

The derivatisation state of gold electrode surfaces was also analysed via X-ray photoelectron spectroscopy (XPS). The standard voltammetric electro-grafting methodology for electro-grafting **HA-2** onto surfaces was applied to two gold-coated silicon wafers that had been cleaned using acidic piranha solution, and one of these surfaces was subsequently hydrazine-treated. XPS measurements were then made of the two modified gold surfaces and a control - a non-functionalised piranha-cleaned gold surface. The presence of a multilayer on the electro-grafted surface is indicated by comparing the survey spectra data for this surface relative to that for the control clean unmodified gold surface; the carbon-to-gold and oxygen-to-gold peak ratios both increase for the modified surface relative to the clean gold (**Figure 5.10A**). In detailed scans, the peak positions attributed to the different carbon and oxygen environments on the electro-grafted surface are expected based on the molecular structure of **HA-2**,<sup>499</sup> and the energy of the nitrogen peak is consistent with that observed for imide-type nitrogen atoms (**Figure 5.10B**).<sup>500</sup> Thus, the XPS data supports the structure of the “electro-grafted” surface shown in **Figure 5.5**.

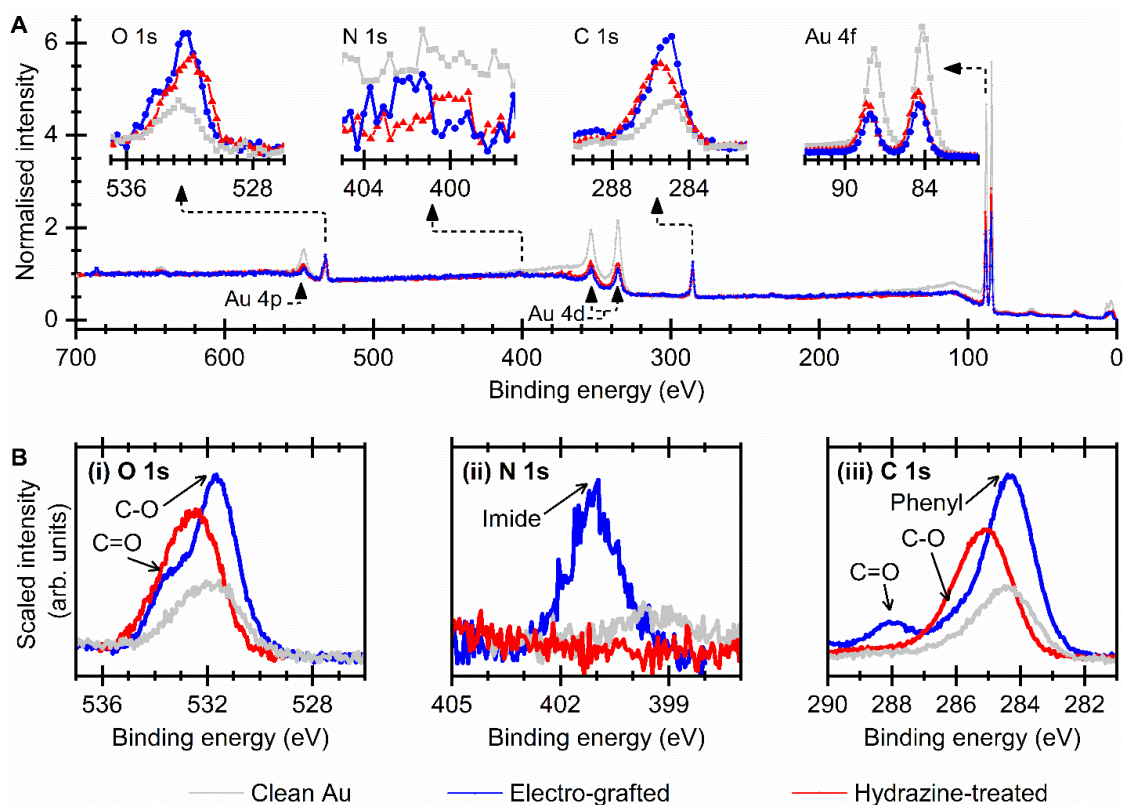
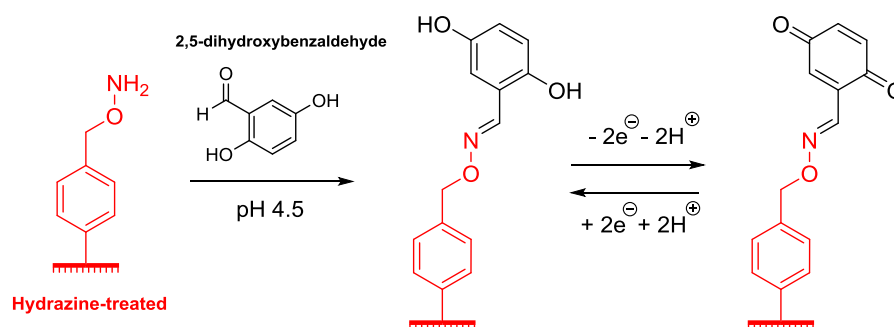


**Figure 5.10.** XPS of the surface of a gold-coated silicon wafer at different states of functionalisation. **(A)** Survey scans, each with the intensity normalized to the average count between 600 and 700 eV. **(B)** Detailed scans, for (i) and (iii) the relative intensities were scaled using the survey scan data while for (ii) data is scaled to the noise level. XPS data was recorded by Dr Andrew Pratt and Dr Phillip Bentley.

The notion that hydrazine deprotection of the phthalimide group strips a multilayer off “electro-grafted” gold surfaces is evidenced by the drop in the normalized intensity of the survey scan carbon and oxygen peaks following hydrazine-treatment (**Figure 5.10A**). With reference to the structures shown in **Figure 5.5**, the shift in the peak energies of the carbon and oxygen environments in the detailed scans of the “hydrazine-treated” case vs the clean control and “electro-grafted” cases (**Figure 5.10B**) is consistent with the hydrazine-treated surface being charged, an observation which is consistent with the sharp increase in capacitance observed upon the hydrazine-treatment of electro-grafted surfaces (**Table 5.1**, **Figure 5.6**). Therefore, although the population of nitrogen within the hydrazine-treated surface falls below the detection limit of the XPS survey, the presence of the hydroxylamine groups could be inferred from the charging of the monolayer surface.

### 5.2.1.4 Ligating hydroxylamine-functionalised electrode surfaces to aldehyde-functionalised redox-active molecules

It is possible to estimate the coverage of hydroxylamine functionalities on the hydrazine-treated electrode surfaces via oxime ligation to the redox-active species 2,5-dihydroxybenzaldehyde. Treatment of a hydroxylamine-functionalised GC electrode with a dilute 2,5-dihydroxybenzaldehyde solution (50  $\mu\text{M}$  in pH 4.5 100 mM sodium acetate + 150 mM NaCl), generates an electrode that shows surface-bound quinone redox signals (**Scheme 5.5** and **Figure 5.11**). These signals are comparable to data in the literature for surface-confined quinones.<sup>501-503</sup> Specifically, the broad nature of the oxidative peak and the shoulder present in the reductive peak are the result from the complicated square scheme that describes the variety of proton-coupled electron-transfer pathways via which the two-electron quinone redox chemistry can proceed.<sup>351,503</sup>



**Scheme 5.5.** The reaction of hydroxylamine ether functionalities on hydrazine-treated electrode surfaces with the aldehyde-functionalised redox-active probe 2,5-dihydroxybenzaldehyde yields surface-confined redox-active moieties.

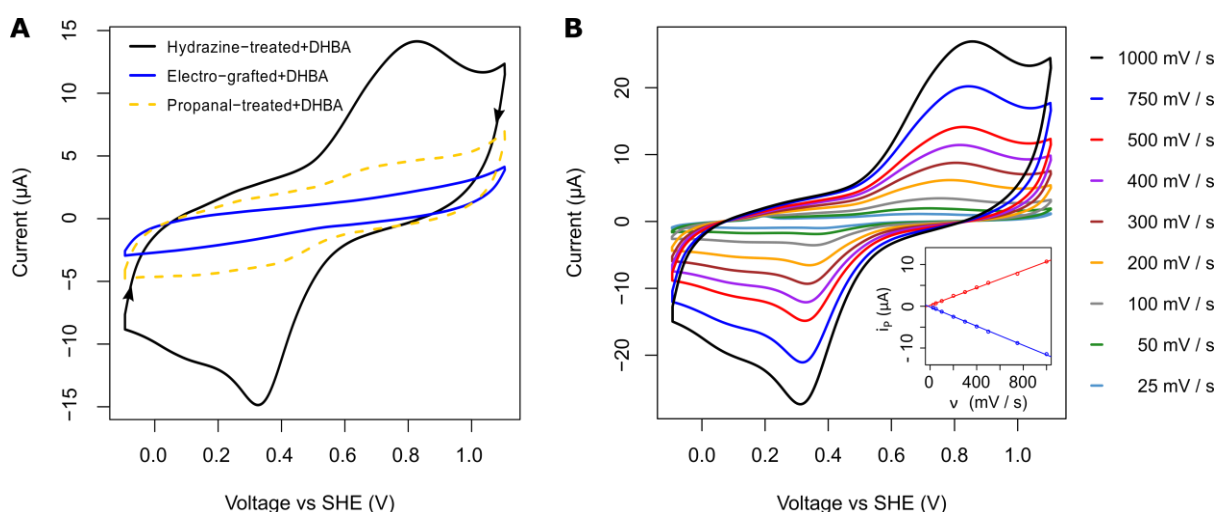


**Figure 5.11.** (A) Cyclic voltammograms of glassy carbon electrodes from various stages in the modification process and after a “quench” reaction with propanal that have been subsequently reacted with 2,5-dihydroxybenzaldehyde (DHBA). All scans were measured at 500  $\text{mV s}^{-1}$ , nitrogen, in aqueous pH 4.0 buffer solution (100 mM sodium acetate + 150 mM sodium sulfate). (B) Cyclic voltammograms of glassy carbon electrodes functionalised with DHBA via oxime ligation recorded at a variety of scan rates under nitrogen in aqueous pH 4.0 buffer solution (100 mM sodium acetate + 150 mM sodium sulfate). (B, inset) Analysis of the quinone-derived baseline-subtracted anodic (red) and cathodic (blue) peak currents shows a linear relationship to scan rate ( $v$ ).

The peak-current response scales linearly with scan rate in a manner that is indicative of surface confinement (**Figure 5.11B**).<sup>15,197,501-503</sup> The electroactive coverage of the redox-active quinone units, calculated via integration of the baseline-subtracted cathodic peaks (**Section 1.4.1, Equation 4**),<sup>249</sup> was found to be 150-170 pmol cm<sup>-2</sup>. This is in good agreement with the 100-250 pmol cm<sup>-2</sup> coverage of ferrocene units that has been reported when coupling activated ester ferrocene-derivatives to glassy carbon electrodes functionalised with monolayers of aliphatic amine functionalities.<sup>171,197</sup> The large separation in the potentials of peak oxidative and reductive current is expected based on literature data on surface-confined quinone species.<sup>501-503</sup> The potential window of the redox process also correlates well with both published data<sup>501-503</sup> and the solution-phase voltammetry of 2,5-dihydroxybenzaldehyde recorded under the same conditions as the data in **Figure 5.11** (see **Figure 5.12**).

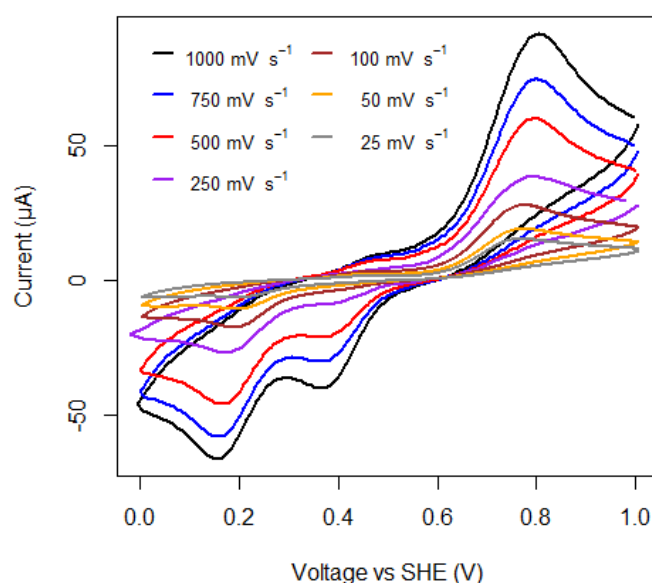
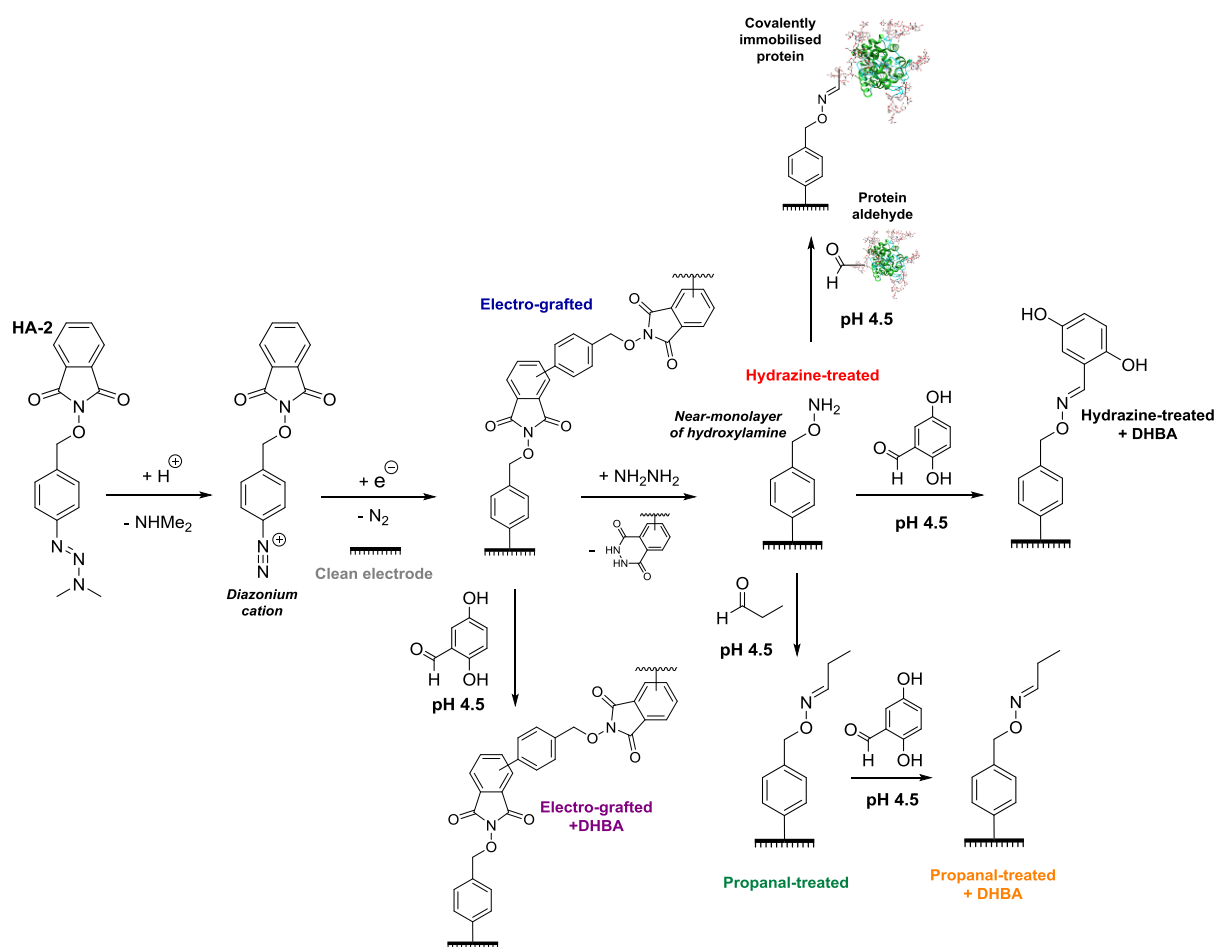


**Figure 5.12.** Solution phase cyclic voltammetry of 1 mM 2,5-dihydroxybenzaldehyde in a pH 4.0 buffer solution (100 mM sodium acetate, 150 mM NaCl) at a GC electrode under an N<sub>2</sub> atmosphere at 21 °C.

Hydrazine-treated glassy carbon electrodes that have been reacted with propanal prior to exposure to 2,5-dihydroxybenzaldehyde (**Scheme 5.6**) fail to show surface-bound quinone redox chemistry (**Figure 5.11**), which is consistent with the hydroxylamine electrode-functionalities being unavailable for reaction with 2,5-dihydroxybenzaldehyde due to quenching via oxime ligation to propanal. The reaction of hydrazine-treated electrodes with hydroquinone, rather than the aldehyde-containing derivative 2,5-dihydroxybenzaldehyde, also fails to yield surface-confined quinone redox signals (**Figure 5.13**). This shows that the presence of the aldehyde on 2,5-dihydroxybenzaldehyde is critical to the surface confinement of a quinone-containing molecule, and that the surface-confined redox chemistry is not observed due to simple adsorption. The proclivity of 2,5-dihydroxybenzaldehyde

towards oxime ligation with solution-phase hydroxylamine species has also been demonstrated (**Scheme 5.7**). It should be noted that while the solution-phase oxime ligation reactions in **Scheme 5.7** are performed with a 1:1 ratio hydroxylamine to 2,5-dihydroxybenzaldehyde, the solid-phase ligation has a great excess of 2,5-dihydroxybenzaldehyde to drive the reaction to completion.



**Scheme 5.6.** The decoration of conducting surfaces with a near-monolayer of hydroxylamines via the *in-situ* generation and electroreduction of phthalimide-protected hydroxylamine-functionalised diazonium cations and subsequent hydrazine treatment, and the immobilisation of selected aldehyde species onto the hydroxylamine-functionalised surface via oxime ligation.



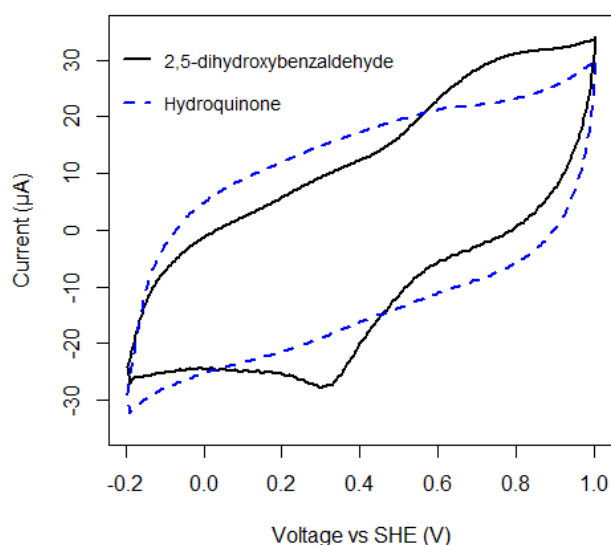
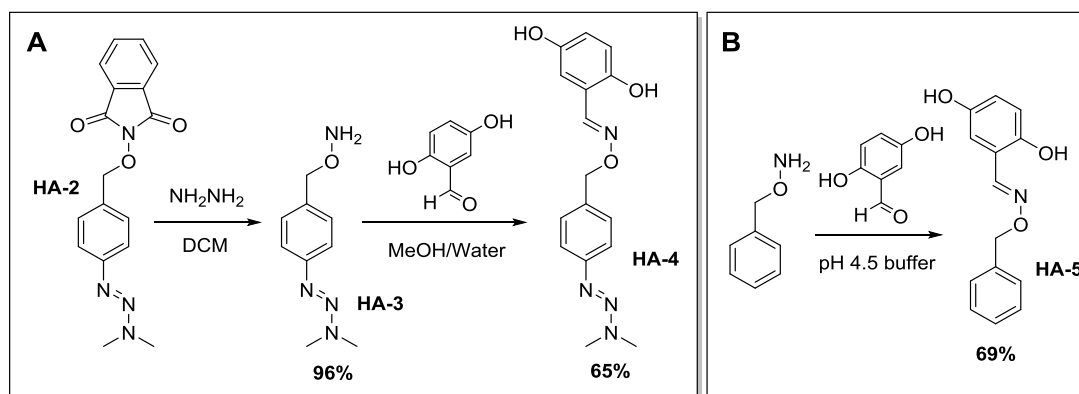


**Figure 5.13.** Cyclic voltammograms illustrating that signals from surface-confined quinone/hydroquinone redox chemistry do not appear when a hydroxylamine-modified electrode is incubated in hydroquinone. Scans recorded in pH 4.0 buffer (100 mM sodium acetate, 150 mM NaCl) at a modified glassy carbon electrode under a  $N_2$  atmosphere at room temperature (21 °C). Scan rate = 1000  $mV s^{-1}$ .



**Scheme 5.7.** Solution-phase analogue experiments to prove the phthalimide protecting group is cleaved from **HA-2** via hydrazine treatment (panel **A**), and that oxime bond formation is possible between 2,5-dihydroxybenzaldehyde and the revealed hydroxylamine functionalities (panels **A** and **B**).

To demonstrate that the hydroxylamine-surface functionalisation methodology can be applied to a wide range of different conducting materials, BDD and gold electrodes were likewise derivatised with hydroxylamines and treated with 2,5-dihydroxybenzaldehyde, which also resulted in surface-confined quinone redox couples (**Figure 5.14**) the signal intensities of which scale linearly with scan rate, as is typical of surface-confined redox processes (**Figure 5.15**).



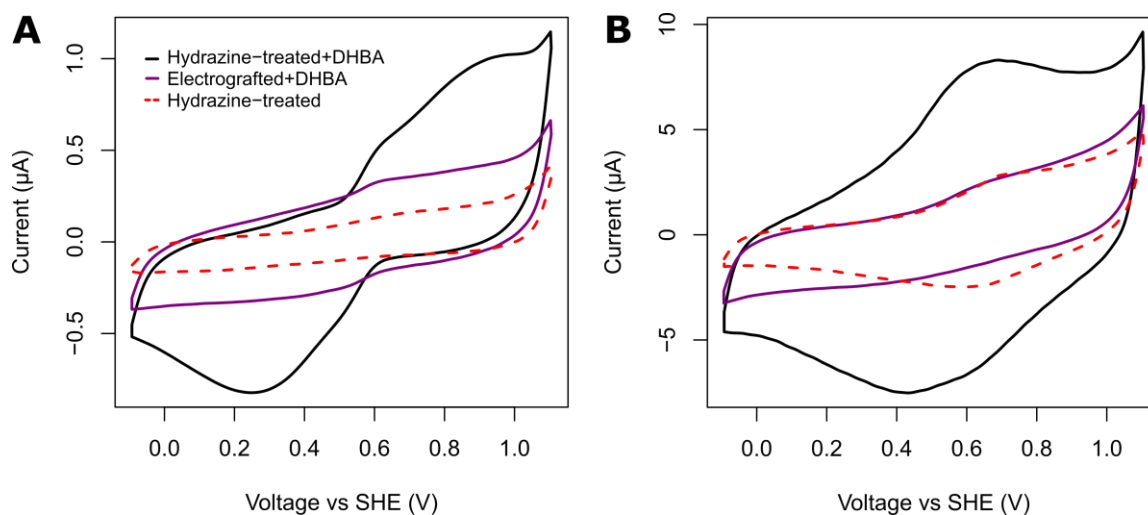


**Figure 5.14.** Cyclic voltammetry of a **(A)** BDD electrode and **(B)** gold electrode which have been electro-grafted with compound **HA-2**, and then **(black line)** hydrazine-treated prior to reaction with 2,5-dihydroxybenzaldehyde (DHBA), or **(blue line)** treated with DHBA while still in the electro-grafted state. **(Red dashed line)** Data from a control experiment where the hydrazine-treatment is not followed by DHBA reaction. The voltammograms shown were recorded at  $500 \text{ mV s}^{-1}$  at  $25 \text{ }^{\circ}\text{C}$  under  $\text{N}_2$  in an aqueous pH 4.0 buffer solution (100 mM sodium acetate + 150 mM  $\text{Na}_2\text{SO}_4$ ).

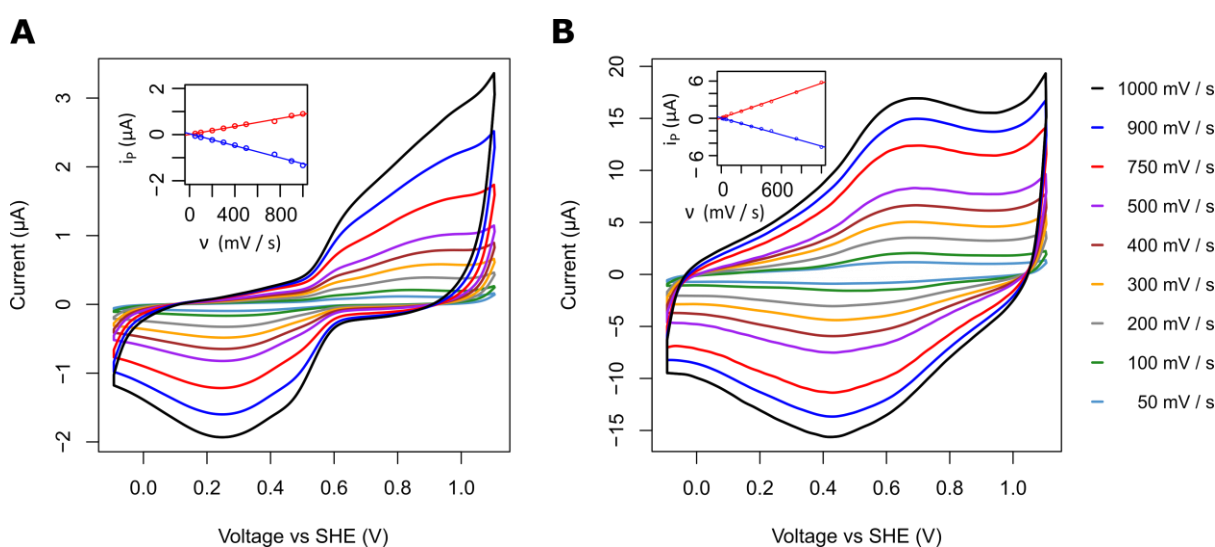


**Figure 5.15.** Cyclic voltammetry of a **(A)** BDD electrode and **(B)** gold electrode which have been electro-grafted with compound **HA-2**, and then hydrazine-treated prior to reaction with 2,5-dihydroxybenzaldehyde. **(Insets)** The magnitude of the baseline-subtracted (red) anodic and (blue) cathodic peak currents ( $i_p$ ) vs scan rate ( $v$ ). All voltammograms were recorded at the scan rates indicated in the legends in a pH 4 buffer solution (100 mM sodium acetate + 150 mM  $\text{Na}_2\text{SO}_4$ ) under  $\text{N}_2$  at  $25 \text{ }^{\circ}\text{C}$ .

On the gold electrodes, a quinone surface-coverage of approximately  $100 \text{ pmol cm}^{-2}$  is derived. This value can be compared to the GC value of surface-coverage of approximately  $160 \text{ pmol cm}^{-2}$ . According to the literature, achieving a lower surface density modification on a gold electrode relative to glassy carbon is to be expected, with previous studies indicating that the coverage of ferrocene units which could be coupled to a gold surface functionalised with a monolayer of aliphatic amine functionalities was 5 to 12.5 times lower than that achieved using similarly functionalised glassy

carbon electrodes.<sup>171</sup> This could be attributed to the fact that only the geometric surface area of the electrodes is accounted for in the calculations of surface coverage, while in reality electron microscopy<sup>504,505</sup> shows that gold electrodes<sup>504</sup> possess a far more planar surface, and thus lower 3D surface area, than glassy carbon.<sup>505</sup>

Integration of the peak area of baseline-subtracted quinone signals quantifies the surface coverage of hydroxylamine moieties on BDD electrodes as approximately 40 pmol cm<sup>-2</sup>. This is a lower coverage than reported for ferrocene-coated BDD electrodes generated via either Cu<sup>I</sup>-catalysed click reactions between diazonium electro-grafted phenyl azide and ethynylferrocene (250 pmol cm<sup>-2</sup>),<sup>506</sup> or photochemical immobilisation of vinylferrocene (450 pmol cm<sup>-2</sup>).<sup>507</sup> However, it can be noted that strict monolayer formation was not the objective of the modification strategies developed in these published examples, and practical difficulties associated with abrading the BDD electrodes prior to electrochemical derivatisation may have affected the coverage of electro-grafted moieties relative to the literature examples, which use samples of BDD freshly prepared via chemical-vapour deposition.

## 5.2.2 Immobilisation of horseradish peroxidase onto a hydroxylamine-functionalised electrode surface

### 5.2.2.1 Electrochemical assay.

Horseradish peroxidase (HRP) is a highly glycosylated enzyme,<sup>508-510</sup> the glycans of which display many cis 1,2-diol sites that are converted into aldehydes via periodate oxidation (**Figure 4.1, A**).<sup>508-510</sup> Gold electrodes in the hydrazine-treated, hydroxylamine-functionalised modification state were reacted with dilute solutions (50 μM) of either periodate oxidised (i.e. aldehyde-containing) horseradish peroxidase or native (i.e. aldehyde-free) horseradish peroxidase at pH 4.5. We conclude that the aldehyde-containing horseradish peroxidase is ligated to the modified electrode via oxime bond formation because subsequent cyclic voltammetry (at 25 °C under N<sub>2</sub> at pH 7.4) shows an intense reductive peak centred at approximately -0.15 V vs SHE and a broad oxidative peak centred around 0 V vs SHE (black line, **Figure 5.16**). The position of this signal correlates with that reported for other examples of immobilised horseradish peroxidase participating in direct-electron transfer with an underlying electrode surface, and is attributed to the Fe<sup>2+/3+</sup> redox couple of the heme.<sup>511,512</sup>

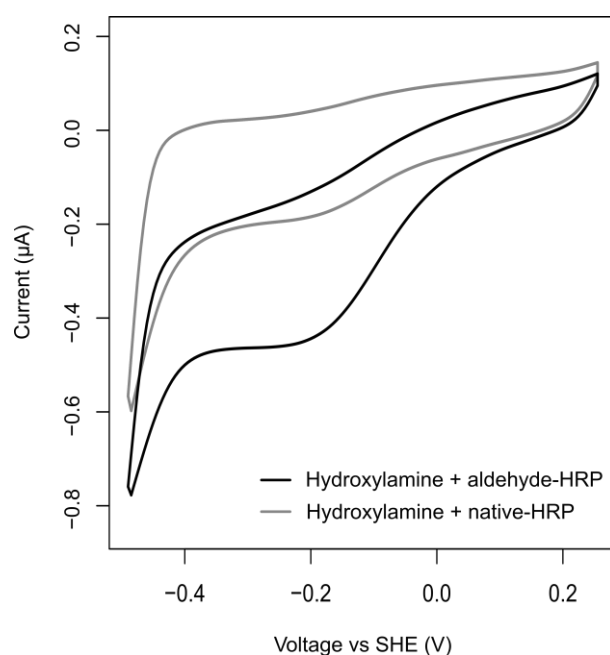


**Figure 5.16.** 30 mV s<sup>-1</sup> cyclic voltammograms showing that significant faradaic current attributable to horseradish peroxidase (HRP) is detected when the oxidised, aldehyde-containing enzyme is reacted with a hydrazine-treated gold electrode (black line), while far smaller redox peaks are observed when hydrazine-treated electrode surfaces are reacted with native (aldehyde-free) horseradish peroxidase (grey line). All experiments were conducted under nitrogen at 25 °C in (pH 7.4 100 mM sodium phosphate buffer solution).

Experiments using native horseradish peroxidase show that the Faradaic current originating from heme redox chemistry is approximately 4-fold smaller for a hydroxylamine-coated gold electrode reacted with the aldehyde-free native horseradish peroxidase (grey line, **Figure 5.16**). This is consistent with the native enzyme being unable to partake in oxime ligation to the electrode surface, resulting in poorer electroactive coverage. Additional control experiments (**Figure 5.17**) further confirm our assignment of the Faradaic signals to the redox activity of competent horseradish peroxidase immobilised on the electrode; this current is greatly diminished when boiled aldehyde-containing enzyme (i.e. denatured protein and free heme) is applied to a hydrazine-treated electrode, or native (aldehyde-free) horseradish peroxidase is applied to bare gold, or when a hydrazine-treated (i.e. hydroxylamine-functionalised) electrode surface is incubated with an enzyme-free buffer solution (**Figure 5.17**).

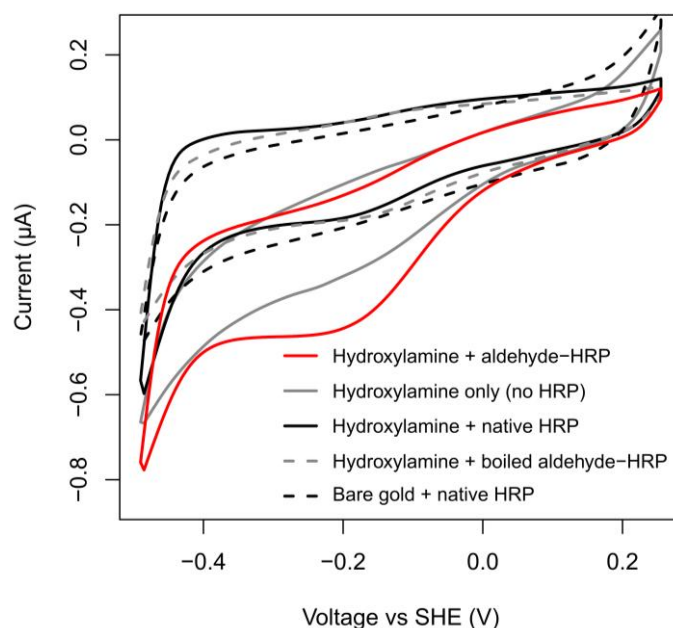


**Figure 5.17.** Cyclic voltammograms summarising the resultant responses of combining different electrode-surface derivatisation states with different HRP enzyme samples. All experiments were conducted under  $N_2$  at 25 °C in pH 7.4 0.1 M sodium phosphate buffer solution at a scan rate of  $30 \text{ mV s}^{-1}$ . Scans commence at the most positive potential.

Enzyme-free experiments using hydrazine-treated (i.e. hydroxylamine-functionalised) gold electrodes showed that these surfaces are highly effective at catalysing the electroreduction of  $H_2O_2$  (**Figure 5.18**). This unfortunately precluded the amperometric detection of the enzymatic activity of immobilised horseradish peroxidase.

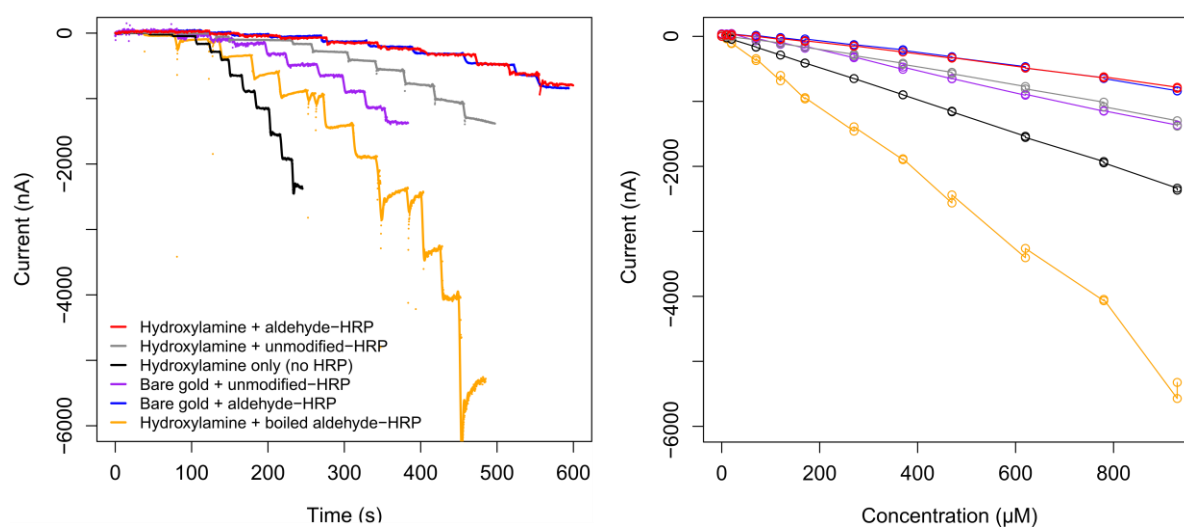


**Figure 5.18. (Left)** Amperometric plots showing that both clean gold and hydrazine-treated gold electrodes are highly effective at the electroreduction of  $H_2O_2$  in the absence of horseradish peroxidase. **(Right)** The current response of the derivatised electrode surfaces as a function of  $H_2O_2$  concentration. All experiments were conducted under  $N_2$  at 25 °C in pH 7.4 0.1 M phosphate buffer solution. Micromolar concentrations of  $H_2O_2$  were incrementally increased in the following series: 10, 20, 70, 120, 170, 270, 370, 470, 620, 780, 930.

### 5.2.2.2 Quartz crystal microbalance with dissipation monitoring

Further evidence for the immobilisation of aldehyde-containing horseradish peroxidase onto hydrazine-treated gold electrode surfaces was instead obtained via quartz crystal microbalance with dissipation monitoring (QCM-D), in collaboration with Dr Christopher Blanford (University of Manchester).

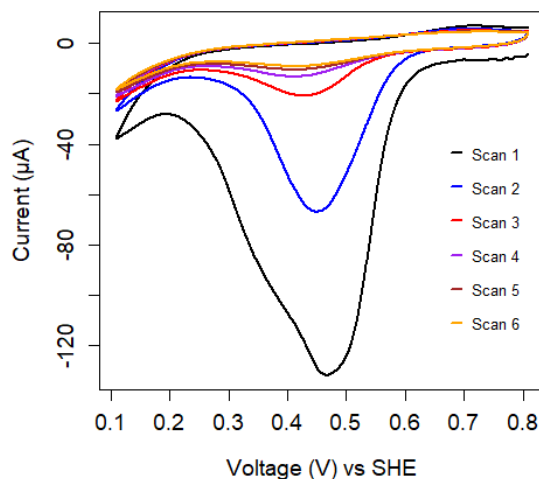


**Figure 5.19.** Cyclic voltammograms of QSX301 quartz crystal microbalance during  $20 \text{ mV s}^{-1}$  electroreductive modification scans with the aryl diazonium salt generated *in situ* from **HA-2** in 1:5 v:v water:acetonitrile and  $0.1 \text{ M Bu}_4\text{NPF}_6$ ,  $0 \text{ }^\circ\text{C}$ . The scans commence at the most positive potential.

A gold-coated quartz crystal microbalance (QCM) sensor was electro-grafted with **HA-2** (**Figure 5.19**) and washed successively in water and ethanol to remove any non-covalently attached organic material. This substrate was then temperature-equilibrated with  $50 \text{ }^\circ\text{C}$  ethanol in the QCM-D apparatus and data logging commenced after thermal equilibrium was reached (**Figure 5.20**). The experimental temperature may induce protein denaturation, but such conditions were required for the deprotective hydrazine-treatment step and to ensure that oxime ligation occurs over a timescale shorter than response drift from the QCM-D.

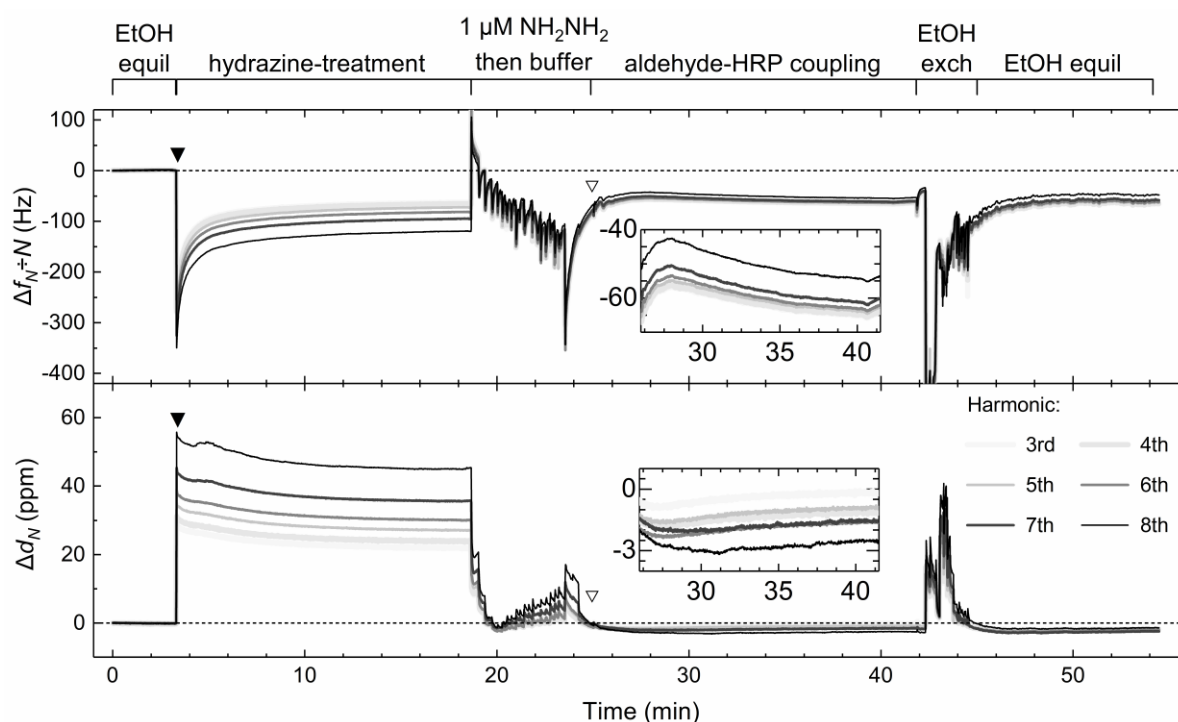


**Figure 5.20.** QCM-D results of frequency change ( $\Delta f$ ) and dissipation change ( $\Delta d$ ) against time for a gold-coated quartz crystal microbalance sensor electro-grafted with **HA-2** prior to the start of the experiment. Subsequent treatments are as indicated above the plot. The experiment was conducted at 50 °C. Values for  $\Delta f$  are divided by the harmonic number (Q-sense convention).

Upon the addition of hydrazine monohydrate ( $\blacktriangledown$ , **Figure 5.20**) the QCM-D showed an immediate decrease in  $\Delta f$  and a concomitant rise in  $\Delta d$  that is attributable to the change in solution viscosity.<sup>513</sup> The subsequent gradual increase in  $\Delta f$  is evidence of a decrease in the mass on the surface of the chip; this is attributed to hydrazine-deprotection of the phthalimide stripping multilayers from the electrode surface (**Scheme 5.6**).<sup>513,514</sup> The dissipation value,  $d$ , is strongly influenced by both the viscoelasticity of the adlayer and the density and viscosity of the bulk fluid above the film,<sup>515</sup> which complicates analysis of this region of the trace.

At approximately 18.5 min, the ethanolic solution of hydrazine was replaced with a 1  $\mu\text{M}$  aqueous solution of hydrazine, and at approximately 23.5 min this solution was exchanged with pH 4.5 buffer (**Figure 5.20**). Due to concerns regarding reaction of the hydrazine-treated surface with trace contaminant aldehyde and ketone species, a 35  $\mu\text{M}$  solution of horseradish peroxidase was added at approximately 25 min ( $\nabla$ , **Figure 5.20**), which was before full thermal equilibrium was reached. Enzyme ligation to the surface can be inferred from the steady drop in  $\Delta f$  between 28 and 40 min (**Figure 5.20**, inset), which is indicative of an increased adsorbed/attached mass on the QCM sensor;<sup>514,516</sup> the concomitant increases in  $\Delta d$ , is also attributed to formation of a protein film.<sup>514,516</sup> Using the equation  $\Delta m = C\Delta f$ , where  $C = -17.8 \text{ ng cm}^{-2} \text{ Hz}^{-1}$  for this system,<sup>513</sup> we estimate the mass change,  $\Delta m$ , to be 2  $\mu\text{g cm}^{-2}$  during protein ligation; this equates to a coverage of 50  $\text{pmol cm}^{-2}$ .

### 5.3 Summary and conclusions.

The concept of generating a near-monolayer of amine functionalities on a surface via the electro-grafting and subsequent deprotection of protected-amine containing diazonium salts could be applied to the generation of surfaces modified with a near-monolayer of hydroxylamine. This Chapter demonstrates the utility of such surfaces for immobilising aldehyde-containing molecules by making electrochemical measurements on both a surface-immobilised aldehyde-labelled hydroquinone and an aldehyde-labelled horseradish peroxidase, with immobilisation of target aldehyde species being achieved at dilute aldehyde concentrations (50  $\mu$ M) and mild pH (pH 4.5 100 mM sodium acetate + 150 mM NaCl). It is hoped that this methodology will find a broad range of applications; the ability to functionalise semi-conducting and conducting substrates with hydroxylamine monolayers could be useful in stabilizing small molecule catalysts in photochemistry and solar fuel applications.<sup>517</sup> The immobilisation of glycosylated enzymes, such as HRP, onto solid scaffolds can be utilized in the development of continuous flow biocatalysts reactors;<sup>481</sup> and hydroxylamine-decorated nanoparticles have already shown promise as drug delivery vehicles.<sup>518</sup> A recent publication has also described the usage of oxime ligation in the immobilisation of a laccase protein to an electrode surface, further illustrating the suitability of oxime ligation in redox protein immobilisation.<sup>475</sup>

However, this system described in the above Chapter is not without its limitations. Tethering a highly glycosylated protein via its glycans will likely result in the protein becoming tethered in a range of orientations. In addition, the long length of some glycans will cause some redox proteins immobilised via this method to be in poor electrical contact with the underlying electrode. Indeed, while this approach allowed for direct electrochemical communication with HRP, attempts to establish electroactive immobilisation of *An6428-AA9* (the glycoprotein discussed in **Chapter 2**) via this method were unsuccessful (data not shown). As such, a method that is more universally applicable and offers more control over immobilised protein orientation is still highly desired.

Interestingly, attempts to immobilise Ald-TrxA (the aldehyde functionalised thioredoxin 1 introduced in **Section 4.2.1.2**) were likewise unsuccessful (data not shown). This suggests that crosslinking to protein aldehydes installed into the peptide scaffold of the protein may be hindered due to steric factors, and indicates that there is likely a balance to be struck between the length of the tether linking the protein to the electrode and the steric availability of the reactive moieties partaking in the covalent crosslinking. In short, while shorter tethers would likely promote better electrochemical contact between the redox protein and the underlying electrode, they are likely to be more challenging to successfully form.

# Chapter 6

Usage of triazabutadienes  
as a photocaged source of  
diazonium cations in  
diazonium electro-grafting



## Chapter 6. Usage of triazabutadienes as a photocaged source of diazonium cations in diazonium electro-grafting

### 6.1 Introduction

As detailed in **Section 1.2**, the covalent immobilisation of redox proteins and enzymes onto electrode surfaces potentially offers several advantages over immobilisation via non-covalent interactions, such as increased device longevity, control over immobilised protein orientation and utility across different electrode substrates.<sup>393,476</sup> With all that stands to be gained from the covalent immobilisation of redox proteins, it is interesting that the literature has progressed little over the past 10 years. Most methodologies still broadly follow the same “*electrode-up*” approach – i.e. to first functionalise electrode surfaces with moieties capable of ligating to proteins, then subsequently treat the electrode surface with the protein in the hope that bioconjugation ensures (**Figure 6.1, i**).<sup>82,171,172,174,175,178-183,188-194,204,235</sup> Despite there being many examples of these “*electrode-up*” approaches in the literature, only a small portion of published PFE studies use protein that have been covalently crosslinked to the electrode; most studies still use redox proteins immobilised by adsorption.<sup>10-15</sup> This would suggest that very few of the currently reported methods for the covalent immobilisation of redox proteins in an electroactive manner are broadly applicable to different redox proteins, and/or these approaches are considered to be too inconvenient, too unreliable or too difficult by most experimentalists. The methodology utilised in **Chapter 5** exemplifies this well, as while the method could be used to successfully facilitate the electroactive immobilisation of the redox-enzyme enzyme horseradish peroxidase, it failed to facilitate the electroactive immobilisation of other redox-enzymes; namely thioredoxin 1 and An6428-AA9.

Indeed, when functionalising an electrode surface for use in an “*electrode-up*” approach several factors may have to be considered or controlled, such as the thickness and composition of the organic film grafted to the electrode surface, as was explored in detail in **Chapters 3** and **5**. Even when these variables are controlled, a great many of the more popular “*electrode-up*” approaches for the immobilisation of redox protein/enzymes onto electrodes surface – e.g. EDC/NHS coupling of protein lysine residues onto carboxylic acid functionalised alkane-thiol self-assembled monolayers<sup>189,192,193</sup> – only offer limited degrees of control over the orientation of immobilised protein. Consequently, many of these approaches are not reliably applicable to more challenging protein systems, wherein only particular protein orientations bring the redox-active sites of the protein within quantum tunnelling distance of the electrode surface.

Practical concerns regarding the characterisation of surface-ligated protein products also have to be addressed when considering “*electrode-up*” approaches. The presence of a covalently-tethered redox protein on an electrode surface is usually inferred via successful PFE of that protein, but if redox signals are not observed the experimentalist may have difficulty ascertaining what caused the experiment to fail - while the ligation to the target protein might have failed it is also possible that the protein may be tethered in a non-electroactive orientation. Conversely, “*electrode-up*” approaches may give false positives - if the chemical functionalisation of an electrode surface simply facilitates adsorption of the redox protein, an experimentalist may assume they have successfully covalently ligated to the protein. There may be a published incidence of this in which beautiful surface-confined electrochemical signals are reported from a WT horse-heart cytochrome c immobilised onto a maleimide-functionalised GC electrode,<sup>186</sup> yet both the cysteine residues present in this WT protein would be expected to be covalently bonded to the heme C cofactor as thioethers,<sup>519</sup> and therefore not amenable to maleimide ligation.

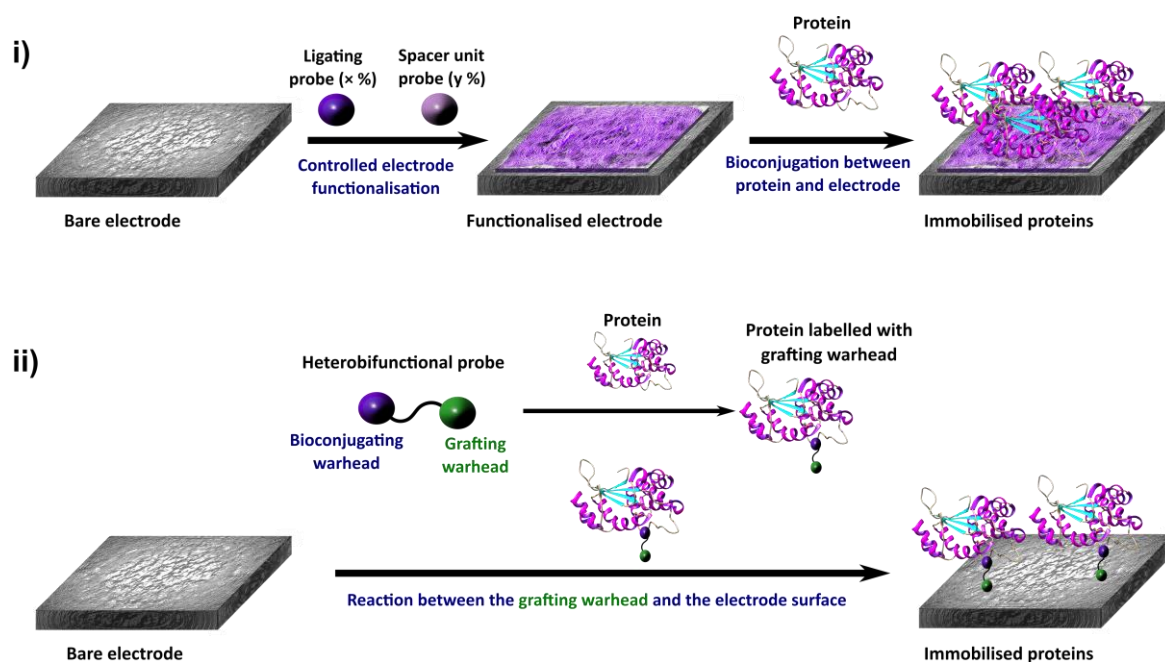


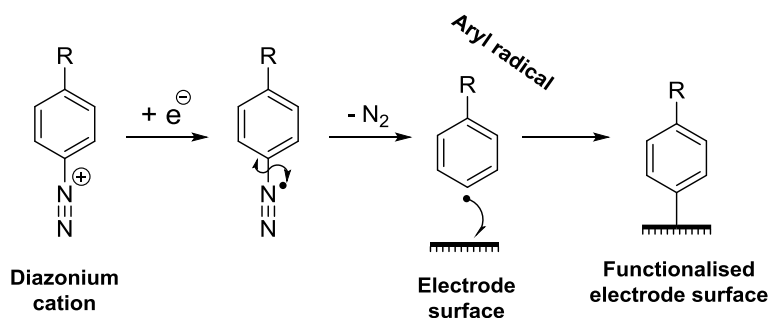
**Figure 6.1.** The steps involved in the covalent immobilisation of protein onto electrode surfaces via either **i)** “*electrode-up*” or **ii)** “*protein-down*” approaches.

Based on the earlier work presented, I concluded that there appears to be a need for a new method of covalently immobilising redox proteins that works in a fundamentally different way to those that already exist. An interesting premise would be to attempt a “*protein-down*” method of redox protein immobilisation, whereby chemical ligation between a heterobifunctional bio-orthogonal probe (one

end of which forms a covalent bond to the protein, the other end of which is to later be used in the formation of a covalent bond to an electrode surface) and the protein is done prior to the immobilisation of the protein onto the electrode surface. The ligation of a protein to such a heterobifunctional probe and the subsequent “*protein-down*” functionalisation of electrode surfaces (**Figure 6.1, ii**) would negate the need to control grafted film thickness and composition, as the steric bulk of the protein would enforce a monolayer regime. Additionally, the success of ligation of the target protein to the probe could be readily determined via methods such as mass spectrometry or fluorescent labelling.

### 6.1.1 Aryl-diazonium cation functionalisation of proteins could be used in a “*protein-down*” approach to redox protein immobilisation

As demonstrated in **Chapters 3** and **5**, attractive candidates for directly-immobilisable probes include probes that bear aryl diazonium functionalities, as these functionalities could be electrochemically reduced to produce aryl radicals which would rapidly form covalent bonds to essentially any conductive substrate; including carbon allotropes,<sup>154-156</sup> ITO,<sup>158</sup> silicon,<sup>157,520</sup> and a range of metals<sup>159</sup> (**Scheme 6.1**).



**Scheme 6.1:** The functionalisation of an electrode surface via the electrochemical reduction of an aryl diazonium salt.

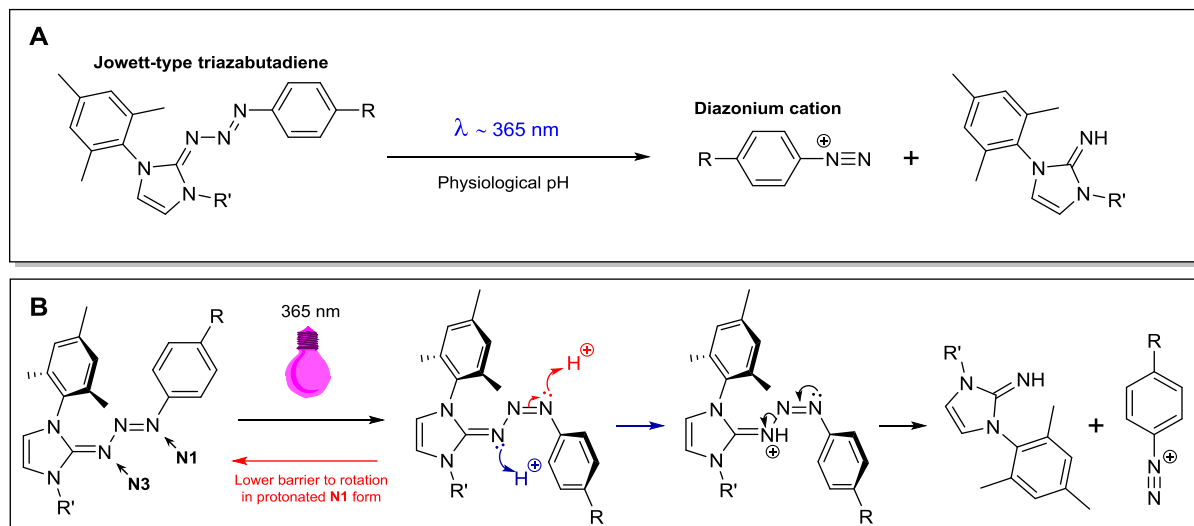
The first challenge is to find a practical method for installing diazonium functionalities into biomolecules. In terms of bio-electrochemical methodologies, there are only two examples of the use of aryl-diazonium based “*protein-down*” approaches for the immobilisation of redox proteins,<sup>512,521</sup> and both are limited by their use of harsh acidic conditions. In the first example electro-grafting was performed using a 2 mg mL<sup>-1</sup> solution of horseradish peroxidase (pre-labelled with 4-carboxybenzenediazonium cations via EDC/NHS coupling) in a 20 mM solution of HCl (which would be expected to have a pH of 1.7),<sup>512</sup> whereas the second example uses 10 mg mL<sup>-1</sup> of aminophenyl-

functionalised horseradish peroxidase in a 3.15 mM HCl + 3.15 mM NaNO<sub>2</sub> solution (which would be expected to have a pH of 2.5 and contains a reagent that would diazotize every amine residue present in the protein, not just the aminophenyl functionalities).<sup>521</sup> It should be noted that the diazotisation of the aliphatic amine residues of proteins would be expected to lead to a myriad of products as aliphatic diazonium cations are highly unstable (**Section 3.1.3, Figure 3.6**), and that the loss of all solvent-exposed lysine amine motifs, in addition to being exposed to low pH, would be expected to have detrimental effects on the folds of many proteins. As can be imagined, these methodologies would not be applicable to many proteins, and while the authors report that no denaturation or loss of enzymatic activity was observed<sup>512,521</sup> there are no circular dichroism data or solution-based assays to support this. In addition, the authors of one of these studies state that their diazonium-functionalised horseradish peroxidase is stable for over one week at 4 °C in water, retaining its ability to become immobilised onto electrode surfaces via electro-grafting and thereafter catalyse electrochemical H<sub>2</sub>O<sub>2</sub> reduction<sup>512</sup> - this would seem to be an extraordinarily very long lifespan for a diazonium species in aqueous solution, especially in the presence of tyrosine motifs (which can be selectively coupled to diazonium cations).<sup>522</sup>

There are several pieces of literature that report the functionalisation of antibodies with aryl diazonium motifs for use in the derivatisation of electrode surfaces via diazonium electro-grafting,<sup>523,524</sup> but the associated methodologies again use harsh conditions that would be incompatible with almost all proteins. In one example an antibody was labelled with 4-aminophenylacetic acid motifs using EDC/NHS coupling, and was then transferred into a 20 mM HCl + 20 mM NaNO<sub>2</sub> solution prior to performing electro-grafting;<sup>523</sup> this necessitates the antibody being subjected to a pH of 1.7 in the presence of a reagent which would not only have diazotised the aminophenyl groups, but also any exposed aliphatic amine groups. In another example an antibody was pre-labelled with 4-carboxybenzenediazonium cations using EDC/NHS coupling, whereafter electro-grafting was performed in a 5 mM HCl solution (i.e. at pH 2.3).<sup>524</sup> There would seem to be an underlying assumption that diazonium electro-grafting needs to be carried out under acidic conditions, yet this is not true – one relevant example is described in ref [491], where the electro-grafting of diazonium functionalised oligonucleotides was performed in pH 7.0 buffer (20 mM sodium phosphate, 150 M NaCl) without issue.<sup>491</sup> The consistency of the protein concentrations used in the diazonium electro-grafting methodologies also varies - one group performs electro-grafting of diazonium-labelled horseradish peroxidase using a 2 mg mL<sup>-1</sup> solution (~45 μM)<sup>512</sup> yet performs electro-grafting of diazonium-labelled IgG antibody using a 40 μg mL<sup>-1</sup> solution (~0.3 μM),<sup>524</sup> while another group performs electro-grafting of diazonium-labelled horseradish peroxidase using a 10 mg

mL<sup>-1</sup> solution (~225 μM),<sup>521</sup> and the electro-grafting of antibodies in a more recent publication uses a 5 mg mL<sup>-1</sup> solution (~33 μM).<sup>523</sup>

Moving away from the electrochemical literature, the utility of diazonium salts in bio-orthogonal “chemical biology” ligation reactions has long been recognised – in particular the ability of aryl diazonium cations to selectively label tyrosine residues,<sup>522,525,526</sup> or unnatural amino acids with more activated aromatic systems than tyrosine.<sup>527</sup> Compounds have thus been developed that can break down to yield aryl diazonium cations under physiologically relevant conditions (i.e. in aqueous conditions between the pH values of 4 and 10),<sup>491,527-532</sup> circumventing the need to expose biomolecules to the harsh conditions required to perform diazotisation reactions; biomolecules can instead be conjugated to one of these diazonium-releasing compounds, and the aryl diazonium cation functionalities can later be unveiled.<sup>491,527-532</sup> While many of these compounds break down gradually to yield aryl diazonium cations by acid-catalysed pathways (i.e. slowly protonating and subsequently breaking down),<sup>491,527-532</sup> the ability to “trigger” aryl diazonium cation formation/release at a chosen instance would be desirable when developing a methodology for the direct electro-grafting of aryl diazonium functionalised redox proteins onto electrode surfaces (ideally diazonium release could be “triggered” immediately prior to the electro-grafting step, thereby minimising the chances of side reactions with/degradation of the aryl diazonium cation motifs). To this end the light-activated triazabutadienes developed by Jowett and co-workers seemed particularly attractive.<sup>528-533</sup> These are species which, when exposed to long-wave UV irradiation ( $\lambda \sim 365$  nm), break down to yield aryl diazonium species in aqueous media at mild or even slightly basic pH (**Scheme 6.2 A**).<sup>528-533</sup> This behaviour arises due to optical isomerisation of the triazabutadiene from the E to the Z isomer (**Scheme 6.2 B**), which causes the conjugation between the triazabutadiene nitrogen atoms and the aryl system to become broken (due to the conformation of the Z isomer); this results in the electron density of these nitrogen atoms becoming more localised, and hence, the nitrogen atoms to become more basic.<sup>533</sup> Protonation of the most basic of these nitrogen atoms (**N1** in **Scheme 6.2 B**) simply facilitates conversion of the Z isomer back into the E isomer (**Scheme 6.2 B, red arrow**), but protonation of the second most basic nitrogen atom (**N3** in **Scheme 6.2 B**) leads to triazabutadiene breakdown and diazonium cation release (**Scheme 6.2 B, blue arrows**).



**Scheme 6.2.** The generation of diazonium salts under mild conditions via the irradiation of a light-activated triazabutadiene.

Previous works regarding the usage of light-activated triazabutadiene have focused either on performing bioconjugation reactions between proteins and diazonium species under neutral conditions,<sup>528,531</sup> or perhaps more interestingly, functionalising protein surfaces with diazonium moieties (via the non-site-selective coupling of an NHS-ester functionalised triazabutadiene probe to lysine residues on the surface of viral proteins) that are themselves used to react with other small molecule probes.<sup>529</sup> Currently, the only triazabutadiene reported in the literature that is suitable for performing bio-orthogonal conjugation is an alkyne-functionalised triazabutadiene, suitable for Cu-click chemistry with azides,<sup>531</sup> and even this triazabutadiene has not yet been reported to be appended to a protein site-specifically.

It should be noted that diazonium cations react with tyrosine residues.<sup>527,534</sup> However, while the highly electrophilic 4-nitrobenzenediazonium cation can be used to label tyrosine residues at physiological pH,<sup>527</sup> less electrophilic diazonium cations, such as the 4-carboxybenzenediazonium cation, only react rapidly with tyrosine residues at elevated pHs (such as at pH 9),<sup>527</sup> with no discernible reaction occurring within 30 min between 4-carboxybenzenediazonium cations (at a concentration of 0.5 mM) and tyrosine (at a concentration of 0.6 mM) in 100 mM phosphate buffer (pH 7) at room temperature.<sup>527</sup> As such, reaction with tyrosine residues is unlikely for diazonium cations released from triazabutadienes via UV-irradiation at 0 °C at near-neutral pH.

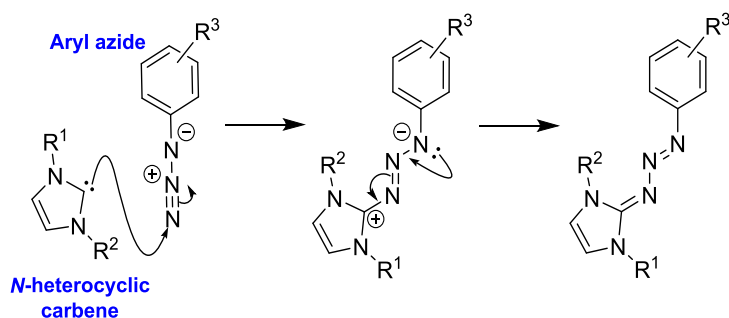
As such, the hypothesis explored in the Results and Discussion of this Chapter (**Section 6.2**) is that an amalgamation of two existing methodologies, i) the unveiling of diazonium cations on protein surfaces under neutral conditions using UV light, and ii) the direct electro-grafting of diazonium functionalised proteins onto electrode surfaces, could yield a widely applicable methodology via which

redox proteins could be electroactively immobilised onto electrode surfaces in a mild and controlled manner. However, the design and synthesis of triazabutadiene probes for this bespoke purpose first necessitates careful deliberations with regard to both the structure-function relationships of triazabutadienes and the restrictions imposed by the functional group intolerances of triazabutadienes (and their precursors) with commonly used bio-orthogonal ligating motifs. These considerations are evaluated below.

### 6.1.2 Considerations regarding the design and synthesis of triazabutadiene probes

Jowett and coworkers<sup>528-533</sup> prepare triazabutadienes via the reaction of a *N*-heterocyclic carbene (NHC) with an aryl azide. The mechanism of this reaction step has not been reported, but Khramov et al. report evidence in favour of nucleophilic attack of the NHC at the terminal nitrogen of an aryl azide.<sup>535</sup> A possible mechanism, not too dissimilar in nature to the Staudinger reaction, is shown in

**Scheme 6.3.**



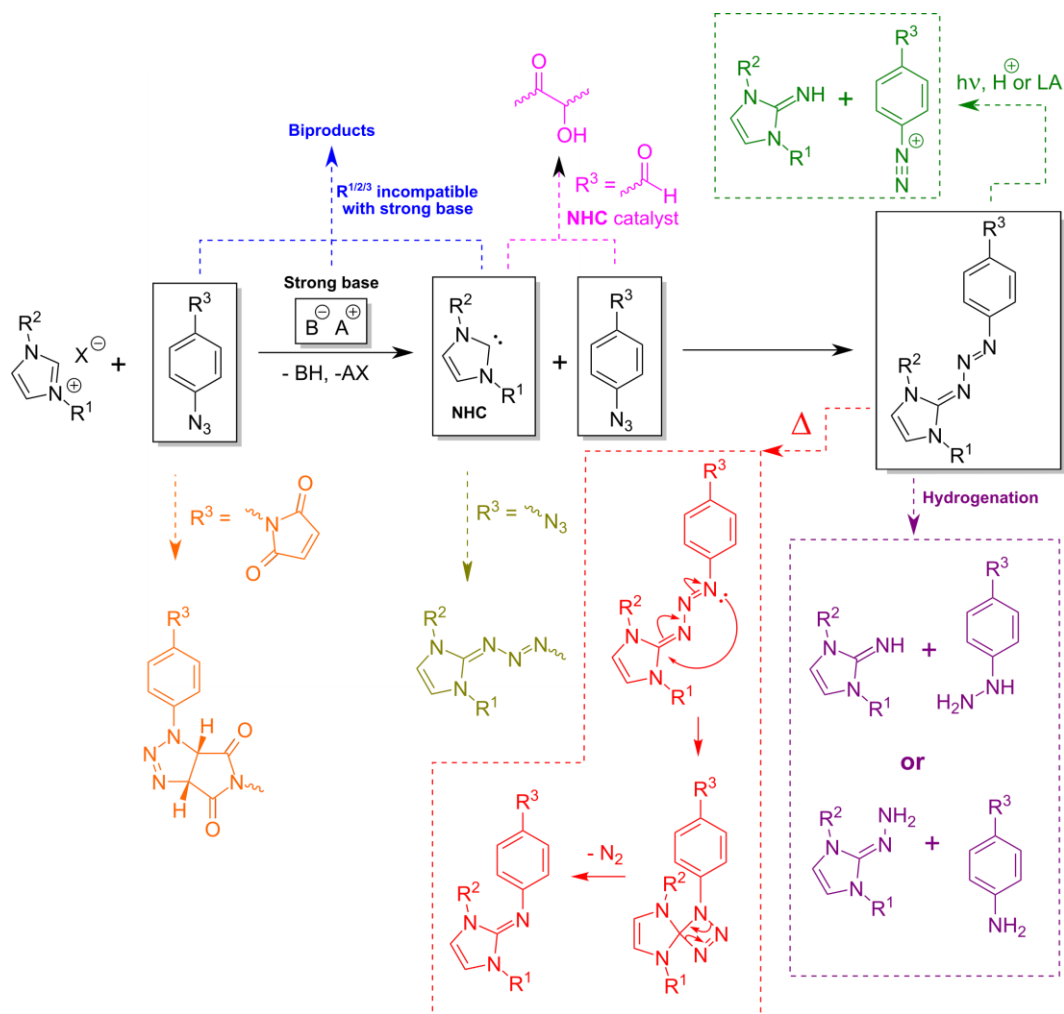
**Scheme 6.3.** Possible mechanism of reaction between *N*-heterocyclic carbenes and aryl azides to form triazabutadienes.

Designing triazabutadiene-functionalised heterobifunctional linkers is not as simple as it may seem. Great care has to be taken in order to avoid conditions that would degrade the triazabutadiene or the bio-orthogonally ligating motif. Triazabutadienes are firstly acid labile (**Scheme 6.4**, green),<sup>528-533</sup> and thus acid-cleaved protecting groups such as Boc or tert-butyl esters cannot usually be used once appended to a triazabutadiene. To complicate matters, triazabutadienes are synthesised under basic conditions - the NHC is generated by deprotonation of a salt precursor by a strong base in the presence of the aryl azide,<sup>529,531-533</sup> and thus usage of base-labile protecting groups would also be unsuitable (**Scheme 6.4**, blue). There is a published report detailing the installation of a protecting group onto triazabutadienes in order to increase acid stability,<sup>530</sup> but the removal of this group requires a basic hydrolysis step which some bio-orthogonally ligating motifs (such as maleimides) would not tolerate, so this strategy does not solve all the problems associated with triazabutadiene probe design. In

addition, the N-N bonds in a triazabutadiene are also likely to be unstable to hydrogenation (**Scheme 6.4**, purple), and triazabutadienes thermally decompose at high temperatures in a manner reminiscent of the Staudinger reaction, releasing nitrogen gas (**Scheme 6.4**, red).<sup>535</sup> This means that deprotection strategies based on hydrogenation (such as benzyl protection of amine groups) or applying heat (such as a retro-Diels Alder reaction liberating a maleimide motif from a furan) are also not likely to give a good yield of product. When protecting group chemistry represents a challenge in other syntheses, photochemically-cleaved protecting groups may be considered, but obviously this option is not viable when considering triazabutadiene-functionalised heterobifunctional linkers! The choice of deprotection strategy for a bio-orthogonally ligating motif appended to a triazabutadiene, would thus seemingly be limited to those based on treatment with nucleophiles; such as ester hydrolysis, treatment of silyl groups with F<sup>-</sup>, or phthalimide deprotection using hydrazine.

Due to the limitations associated with the protecting/deprotecting group strategies compatible with triazabutadienes, it may seem advantageous to pre-install the bio-orthogonally ligating motif onto the aryl azide unit prior to triazabutadiene formation. Unfortunately, this is rarely possible, as many bio-orthogonal probes would display cross-reactivity with either the NHC (i.e. azide probes would react to form triazabutadienes, as shown in **Scheme 6.4**, olive) or the aryl azide (maleimide motif undergo cycloaddition reactions with aryl azides,<sup>536</sup> as shown in **Scheme 6.4**, orange). NHCs are also very versatile catalysts, which could lead to unexpected reactivity from many other functional groups; for example an aldehyde motif pre-installed onto an aryl azide (which could later be used in OPAL conjugation to an aldehyde-functionalised protein) would likely partake in NHC-catalysed benzoin condensation (**Scheme 6.4**, pink),<sup>537</sup> whereas usage of unprotected alcohol (as either an aldehyde precursor or just to enhance the water-solubility of the triazabutadiene probe) would likely to lead to side-reactions due to the deprotonation of the alcohol, or even NHC-catalysed transesterification (if an ester is installed elsewhere on the probe).<sup>538</sup>





**Scheme 6.4.** The cross-reactivities and reaction condition incompatibilities that might be expected of triazabutadienes or triazabutadiene precursors with reference to common deprotection strategies and popular bio-orthogonally ligating motifs.<sup>535</sup>

To be suitable for the site-specific installation of diazonium cations onto proteins surfaces the triazabutadiene needs to remain intact during an initial bio-conjugation step. The stability of a triazabutadiene in aqueous solution is partially determined by the basicity of the nitrogen atoms – the less basic the nitrogen atoms the less likely the triazabutadiene will undergo acid-catalysed degradation.<sup>532</sup> The “classic” triazabutadienes that have been previously used in protein bioconjugation have a para carbonyl group (i.e.  $R^3$  in **Scheme 6.3** is a para carbonyl group); this -M group is important in stabilising the triazabutadiene as it reduces the basicity of the nitrogen atoms.<sup>532</sup> However, if a triazabutadiene is too stable the diazonium cations may be difficult to unveil at all; it has been demonstrated in the literature that usage of a para nitro group bestows such a degree of stabilisation that the triazabutadiene no longer functions properly as a photocaged source of diazonium cations.<sup>532</sup>

The Jowett triazabutadienes currently reported in the literature are of either one of two types.  $R^1 = R^2 = \text{Mes}$  or  $R^1 = (\text{CH}_2)_3\text{SO}_3\text{K}$ ,  $R^2 = \text{Mes}$  (using the numbering in **Scheme 6.3**). When comparing otherwise identical species, the  $R^1 = R^2 = \text{Mes}$  triazabutadienes persist for longer in buffered aqueous solution than their  $R^1 = (\text{CH}_2)_3\text{SO}_3\text{K}$ ,  $R^2 = \text{Mes}$  counterparts.<sup>529</sup> This shows that the identity of the groups bonded to the nitrogen atoms of the NHC ( $R^1$  and  $R^2$  in **Scheme 6.3**) also influences the stability of the triazabutadiene. If these groups are sterically bulky and hydrophobic then the N3 nitrogen atom (see **Scheme 6.2 B**) will be less likely to become protonated in aqueous solution.<sup>529</sup> However, the installation of a hydrophilic group on one of the nitrogen atoms of the NHC would increase the water-solubility of the triazabutadiene probe, which could hypothetically mean that more equivalents of the triazabutadiene probe could be used during a bioconjugation reaction, thereby allowing the bioconjugation to be performed more rapidly; this could help compensate for any shortening of the lifespan of the triazabutadiene probe.

### 6.1.3 Aims

In developing a method for the functionalisation of electrode surfaces with redox proteins via diazonium electro-grafting using UV-treated triazabutadienes several challenges need to be overcome.

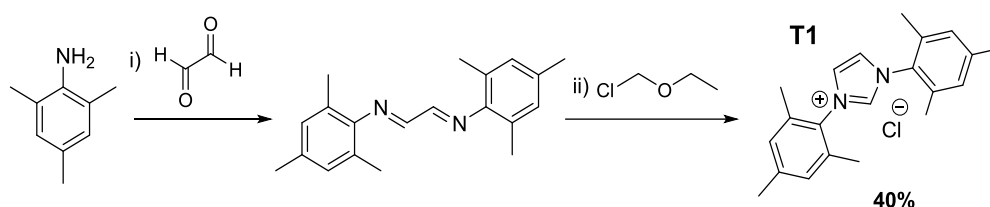
- 1) The ability of triazabutadienes to yield diazonium cations capable of undergoing diazonium electro-grafting at biologically relevant pHs needs to be demonstrated.
- 2) The longevity of triazabutadienes in buffered aqueous solution needs to be determined so that suitable bioconjugation methodologies can be identified.
- 3) Triazabutadienes functionalised with moieties capable of bioconjugation to redox proteins need to be designed and synthesised.
- 4) The bioconjugation of triazabutadiene probes to redox proteins needs to be performed and the resulting constructs characterised.
- 5) Conditions for the UV-degradation of the triazabutadiene motif need to be identified and the revealed diazonium cation must be confirmed to be viable to chemical modification.
- 6) Conditions for the direct electro-grafting of diazonium cation functionalised redox proteins should be screened.

## 6.2 Results and Discussion

### 6.2.1 The synthesis of different classes of triazabutadiene probes

#### 6.2.1.1 "Classic" triazabutadiene probes

In the literature, all the triazabutadiene probes used for bioconjugation to proteins have been of the  $R^1 = R^2 = \text{Mes}$  type (using the numbering in **Scheme 6.3**), and have been based on 1,3-dimesityl-1H-imidazol-3-ium chloride (**T1**). Although commercially available, **T1** was synthesised from 2,4,6-trimethylaniline, glyoxal and 1-(chloromethoxy)ethane via a two-step methodology (**Scheme 6.5**).



**Scheme 6.5.** The synthesis of **T1**.

Two of the most popular bioconjugation techniques are amide bond formation via reaction with *N*-hydroxysuccinimide-type activated esters and maleimide ligation (**Figure 6.2**). Two candidate probes, **T5** and **T8** (**Figure 6.3**), were initially identified/designed, based on the classic para carbonyl design. Probe **T5** is reported in the literature as being suitable for NHS coupling to protein amine residues (i.e. the  $\epsilon$ -amines of lysine residues and *N*-terminal amines),<sup>529</sup> whereas probe **T8** is a novel compound, suitable for maleimide ligation to protein cysteine functionalities.

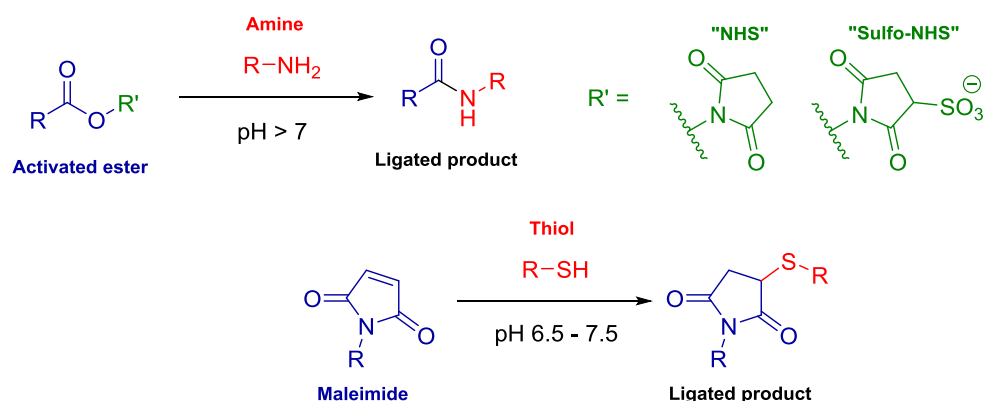


**Figure 6.2.** (Top) Amide bond formation between a *N*-hydroxysuccinimide-type activated ester and an amine. (Bottom) Maleimide ligation between a maleimide and a thiol.

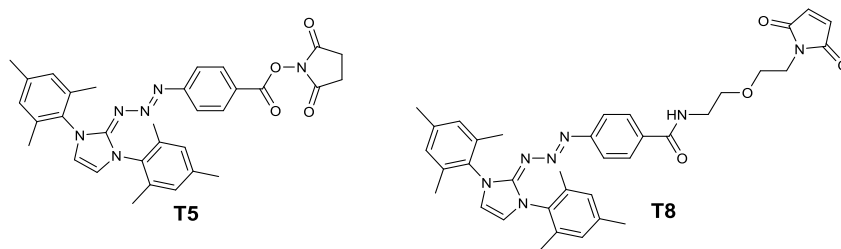
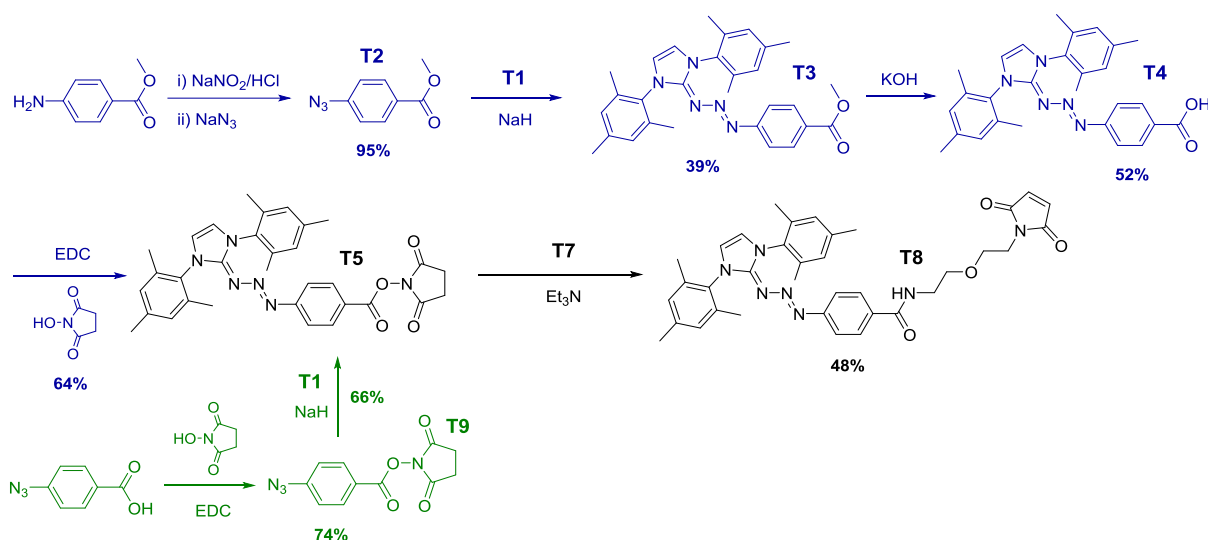
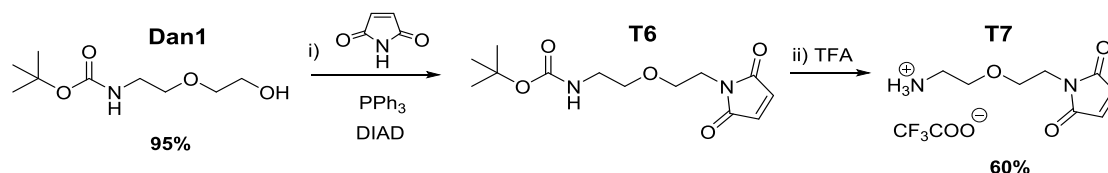


**Figure 6.3.** Candidate probes **T5** and **T8** for use in bioconjugation to lysine and cysteine tagged proteins respectively.

Triazabutadiene **T5** was initially synthesised in 4-steps (**Scheme 6.6**), using methodologies based on modified literature procedures.<sup>529</sup> This synthesis was later optimised such that **T5** could be obtained in 2-steps (**Scheme 6.6**). Triazabutadiene **T5** was then reacted with heterobifunctional linker **T7**, yielding **T8** (**Scheme 6.6** and **Scheme 6.7**).

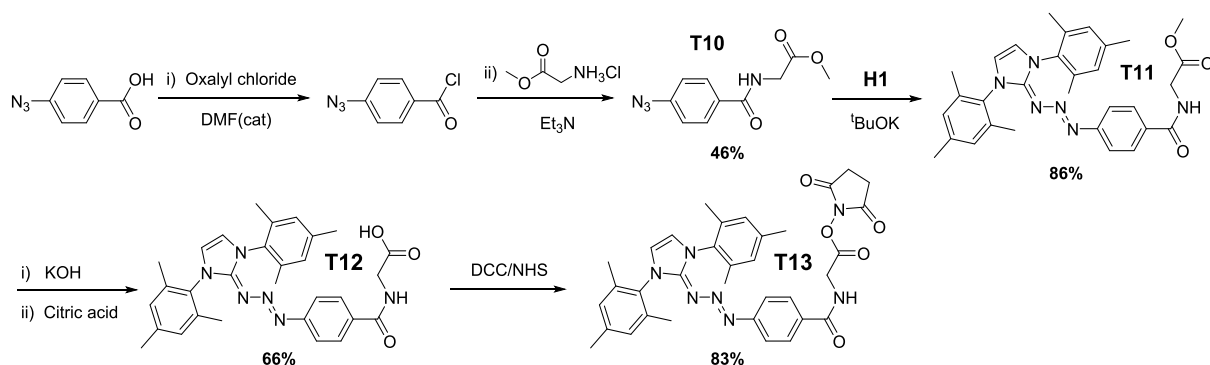


**Scheme 6.6.** The synthesis of initial candidate triazabutadiene probes **T5** and **T8**. The literature route for synthesising **T5** is shown in blue,<sup>529</sup> whereas the shortened synthesis is shown in green.

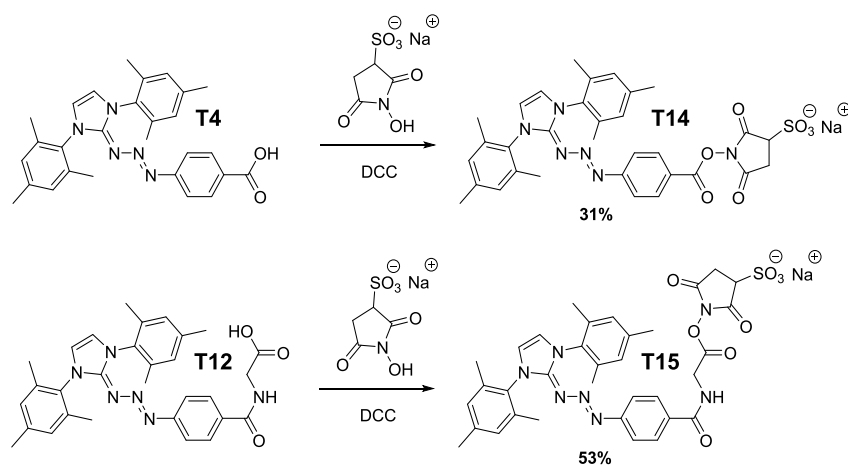


**Scheme 6.7.** The synthesis of the heterobifunctional maleimide and amine functionalised PEG-1 linker **T7**.

The reaction between **T5** and **T7** was relatively low yielding (**Scheme 6.6**); most likely as a consequence of the NHS ester being of diminished electrophilicity due to being in conjugation with a benzene ring substituted with a para +M group. It was anticipated that **T5** may not be the most effective probe for ligating to protein amine moieties, and thus novel compound probe **T13** was synthesised in 5-steps.



**Scheme 6.8.** The synthesis of a triazabutadiene probe **T13**, which bears a more reactive NHS ester than probe **T5**.



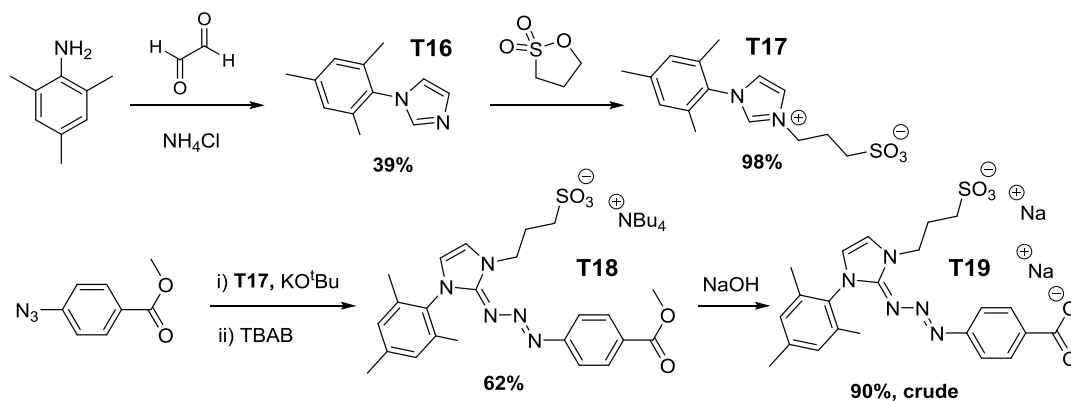
**Scheme 6.9.** The synthesis of water-soluble candidate triazabutadiene probes **T14** and **T15**.

Both probes **T5** and **T13** were however found to be almost completely insoluble in aqueous solution (even when the solution is made up to 10% v/v DMSO), and thus while NHS coupling to protein amine residues was attempted for several proteins (both the DsbA variants introduced in **Section 4.2.4.2** and CjX183-D R51K, which is introduced in **Section 4.2.3.3**), amide bond formation was not achieved for either **T5** or **T13** (even though the coupling of **T5** to protein amine residues has previously been described in the literature<sup>529</sup>). Novel **T1**-derived compounds of enhanced water solubility, **T14** and **T15**, were thus synthesised.

With several candidate probes synthesised, the suitability of **T1**-derived triazabutadienes for protein bio-conjugation and subsequent release of diazonium cations for use in electro-grafting was investigated (**Section 6.2.2.2**).

### 6.2.1.2 3-(1-mesityl-1H-imidazol-3-ium-3-yl)propane-1-sulfonate based triazabutadiene probes

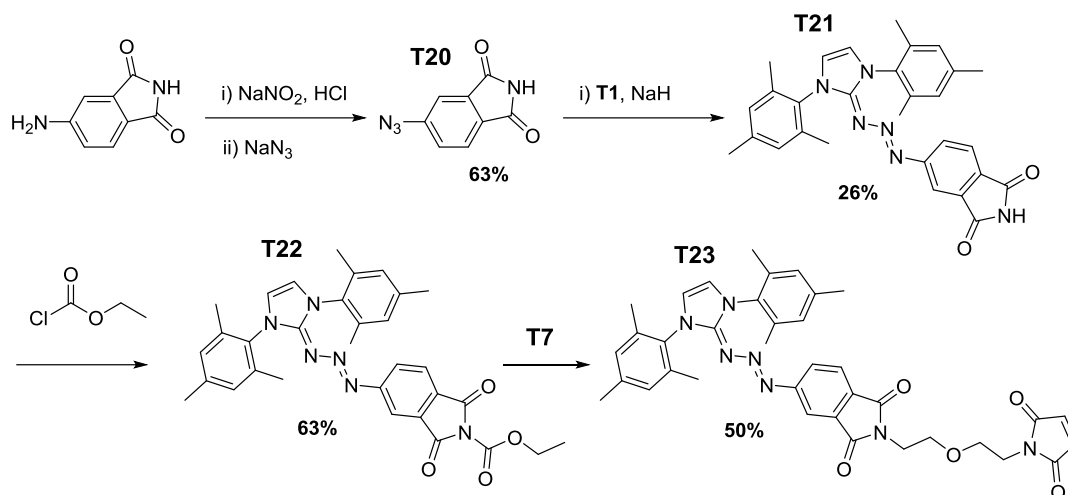
With the exception of **T14** and **T15**, the **T1**-derived triazabutadienes are poorly soluble in water. In an effort to address this, an alternative water-soluble NHC, 3-(1-mesityl-1H-imidazol-3-ium-3-yl)propane-1-sulfonate (**T17**), was used to construct several triazabutadienes of the  $R^1 = (\text{CH}_2)_3\text{SO}_3\text{K}$ ,  $R^2 = \text{Mes}$  type (using the numbering in **Scheme 6.3**). The only currently published example of a **T17**-derived triazabutadiene was synthesised using azidobenzene,<sup>533</sup> and thus did not a bare handle that enabled downstream derivatisation.<sup>533</sup> In a step forward with respect to the literature, a potentially more versatile **T17**-derived triazabutadiene (**T18**), bearing a methyl ester, was synthesised and isolated in good yield and purity. The ability to deprotect the methyl ester of **T18** to yield the free carboxylate (**T19**) was also demonstrated. Unfortunately, further derivatisation of this scaffold proved difficult, owing to practical difficulties associated with isolating and purifying such polar acid-labile compounds (i.e. the free carboxylate is a di-anion, and it is problematic to use an acid-wash in the workup of this species). The properties of these water-soluble **T17**-derived triazabutadienes with respect to release of diazonium cations for use in electro-grafting were however investigated (**Section 6.2.2.1**), to ascertain if future work into producing hetero-bifunctional linkers bearing these motifs would be a worthwhile venture, as synthesising such species is certainly possible.



**Scheme 6.10.** The synthesis of **T17**-derived triazabutadiene probes **T18** and **T19**.

### 6.2.1.3 Phthalimide-type triazabutadiene probes

In an effort to create a class of triazabutadienes of intermediate stability between those with a para carbonyl group and a para nitro group, triazabutadienes based on a phthalimide motif were synthesised (**T21-T23**). The ability of the maleimide functionalised probe **T23** to release diazonium cations upon exposure to UV light was then analysed.



**Scheme 6.11.** The synthesis of T1-derived phthalimide-type triazabutadiene probes.

## 6.2.2 UV-initiated diazonium release from different classes of triazabutadiene

### 6.2.2.1 UV-initiated diazonium release from 3-(1-mesityl-1H-imidazol-3-ium-3-yl)propane-1-sulfonate derived triazabutadiene probes

As triazabutadiene **T18** is a highly water-soluble species, analysing the rate at which it breaks down in the presence and absence of 365 nm UV irradiation in buffered aqueous solution was readily achievable. UV-vis spectra illustrate the complete disappearance of the triazabutadiene absorbance band within 5 min under irradiation by a 7 W 365 nm bulb in pH 7.4 buffer (which causes the solution to decolourise), and also show that the majority of the population of triazabutadiene **T18** can endure several hours in pH 7.4 buffer if kept in darkness (**Figure 6.4 a**, **Figure 6.4 c**). However, the majority of **T18** was shown to break down overnight at pH 7.4 at 4 °C, even in darkness (**Figure 6.5**). This would suggest that a heterobifunctional probe armed with a T17-derived triazabutadiene would be likely to remain intact long enough to perform bioconjugation reactions that reach completion in a matter of hours at neutral pH, but not long enough to perform bioconjugations that require harsher conditions or longer reaction times.

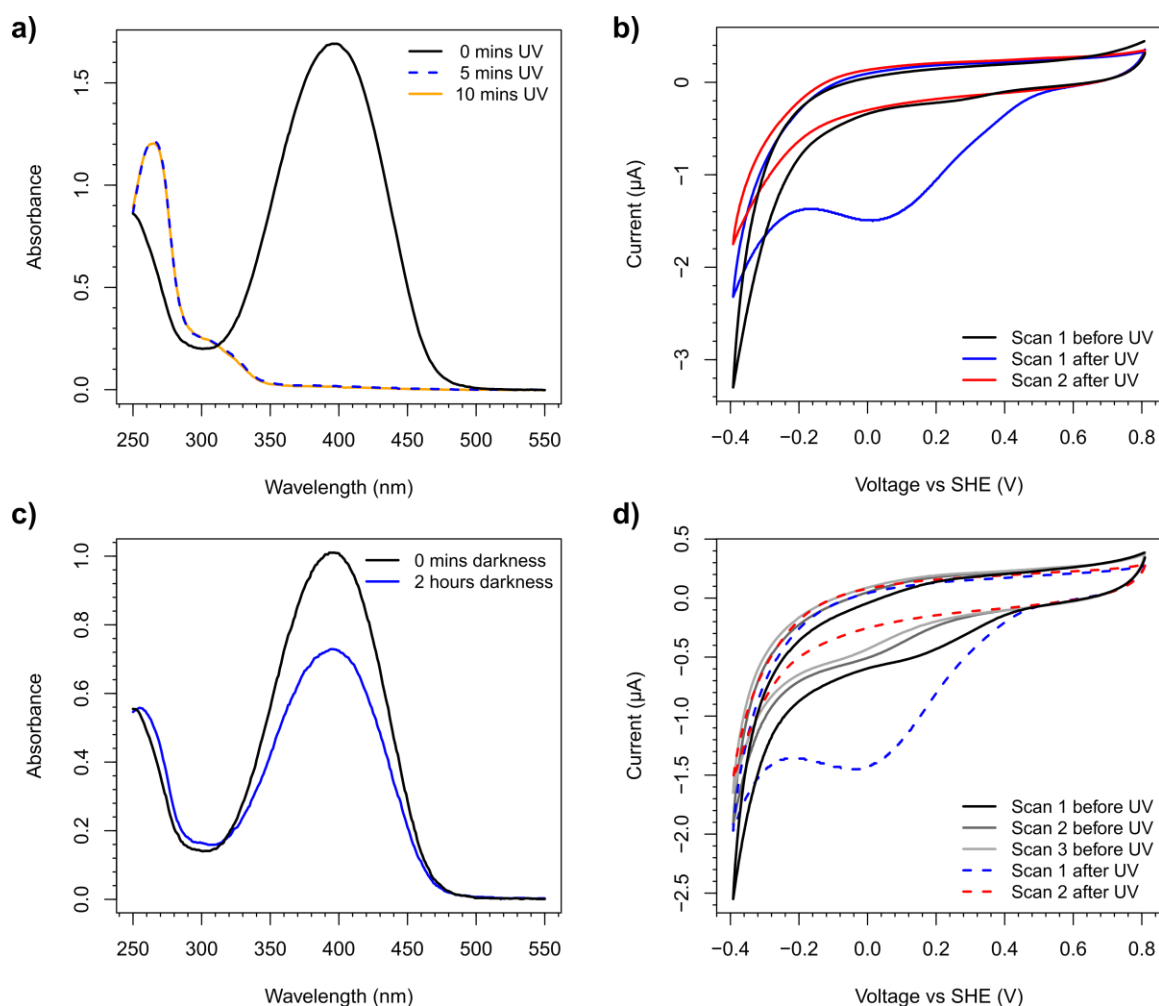


**Figure 6.4.** **a)** UV-vis spectra illustrating the degradation of a 50  $\mu\text{M}$  solution of **T18** in pH 7.4 buffer (sodium phosphate 100 mM) at 0  $^{\circ}\text{C}$  under exposure to UV irradiation from a 7 W 365 nm bulb. **b)** UV-initiated diazonium electro-grafting using a 1 mM solution of **T18** in pH 7.4 buffer at 0  $^{\circ}\text{C}$ . **c)** UV-vis spectra illustrating the degradation of a 50  $\mu\text{M}$  solution of **T18** in pH 7.4 buffer (100 mM sodium phosphate) at 4  $^{\circ}\text{C}$  in darkness. **d)** UV-initiated diazonium electro-grafting from a 1 mM solution of **T18** that has been incubated in pH 7.4 buffer (100 mM sodium phosphate) for 2 hours in darkness at 4  $^{\circ}\text{C}$ . Cyclic voltammograms were recorded at 0  $^{\circ}\text{C}$  in pH 7.4 buffer (100 mM sodium phosphate) under an ambient atmosphere at a scan rate of 20  $\text{mV s}^{-1}$  using a GC working electrode, a Ag/AgCl (3 M NaCl) reference electrode and a platinum wire counter electrode. The cyclic voltammograms commence at the most positive potential, then the voltage is lowered before being increased again. UV-vis spectra were recorded by undergraduate student Samuel Aron.

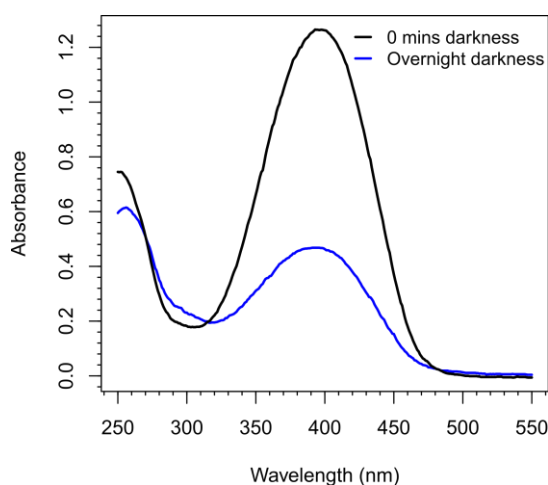


**Figure 6.5.** UV-vis spectra illustrating the degradation of a 50  $\mu\text{M}$  solution of **T18** in pH 7.4 buffer (100 mM sodium phosphate) at 4  $^{\circ}\text{C}$  in darkness overnight.



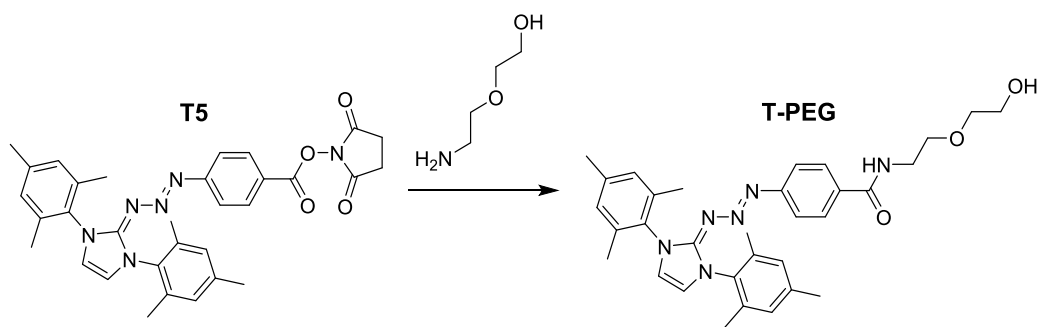
The high water-solubility of **T18** also allowed characteristic diazonium electro-grafting CVs to easily be recorded. It can readily be observed that if a sample of triazabutadiene **T18** is not treated with 365 nm UV irradiation prior to recording a CV, the reductive wave typical of diazonium electro-grafting is not observed (**Figure 6.4 b**). However, pre-treatment with 365 nm UV irradiation results in a CV characteristic of diazonium electro-grafting, with a broad reductive wave being in evidence in the first scan, this peak rapidly decreases in intensity over successive scans (**Figure 6.4 b**). The resemblance of **Figure 6.4 b** to **Figure 5.3** is truly quite striking, and it should be noted that **Figure 6.4 b** illustrates the first ever usage (to the knowledge of the author) of a triazabutadiene as a reagent for diazonium electro-grafting.

Evidence for the slow degradation of **T18** into free diazonium cations in solution, even in the absence of light, can be seen in the electrochemical data recorded for a sample of **T18** that has been incubated at 4 °C in darkness for 2 hours prior to interrogation (**Figure 6.4 d**). Even before treatment with UV, a small reductive wave typical of diazonium electro-grafting can be observed. This wave peaks at ever lower intensities and at ever lower potentials in successive scans, which is typical of electro-grafts performed with dilute solutions of diazonium cations, with the formation of a pacifying film on the electrode surface taking place over several scans. Once again, the validation that the majority of **T18** remains intact after 2 hours in darkness is provided by the return of a strong diazonium electro-reduction feature upon exposing the sample of **T18** to UV irradiation (**Figure 6.4 d**).

### 6.2.2.2 UV-initiated diazonium release from “Classic” triazabutadiene probes

#### 6.2.2.2.1 UV-initiated diazonium electro-grafting

**T5** is almost insoluble in aqueous solution, and while **T14** is water soluble, the UV-activity of the **T5/T14** species themselves is not as important as the UV-activity of the product of the reaction of **T5/T14** with an amine (as **T5/T14** are to be reacted with the  $\epsilon$ -amines of lysine residues or *N*-terminal amine residues). In light of this, **T-PEG** was prepared (**Scheme 6.12**), which is both more soluble in water than **T5**, and is the product of the reaction of **T5/T14** with a water-soluble primary amine.



**Scheme 6.12.** The synthesis of **T-PEG** from **T5**.

A 50 mM stock of **T-PEG** in DMSO was delivered to a pH 7.55 buffer solution (20 mM phosphate, 200 mM NaCl + 10% DMSO) such that the final concentration of **T-PEG** was 500  $\mu$ M. The solution was visibly green (**Figure 6.6**, left).

CVs of a blank buffer solution (pH 7.55, 20 mM phosphate, 200 mM NaCl + 10% DMSO) over the range of 0.6 V  $\rightarrow$  -0.6 V (vs SHE) at 0  $^{\circ}$ C using a boron-doped diamond (BDD) working electrode showed no redox activity aside from a reductive wave attributed to proton reduction, which can be observed at potential more negative than -0.1 V vs SHE (see “Blank 1” in **Figure 6.7**). CVs of the 500  $\mu$ M solution of **T-PEG** at 0  $^{\circ}$ C did not show any prominent Faradaic signals attributable to diazonium electro-grafting, although it did show a dampening of background electrode activity relative to the blank buffer (see “Before UV 1” in **Figure 6.7**), most likely due to adsorption of the sparingly soluble **T-PEG** to the electrode surface. However, after the solution/suspension of **T-PEG** was subjected to 4 min of UV irradiation at 0  $^{\circ}$ C using a 7 W 365 nm UV light bulb, the solution decolourised (**Figure 6.6**), and the CVs that were subsequently recorded clearly showed the characteristic irreversible reductive wave associated with diazonium electro-grafting (“After UV” 1-4 in **Figure 6.7**).

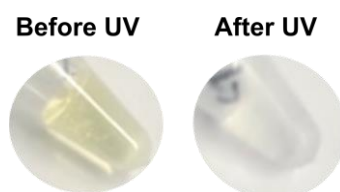


**Figure 6.6.** The decolourisation of a 500  $\mu$ M solution of **T-PEG** in pH 7.55 buffer (20 mM sodium phosphate, 200 mM NaCl + 10% DMSO) after irradiation from a 7 W 365 nm UV light bulb at 0  $^{\circ}$ C for 4 min.

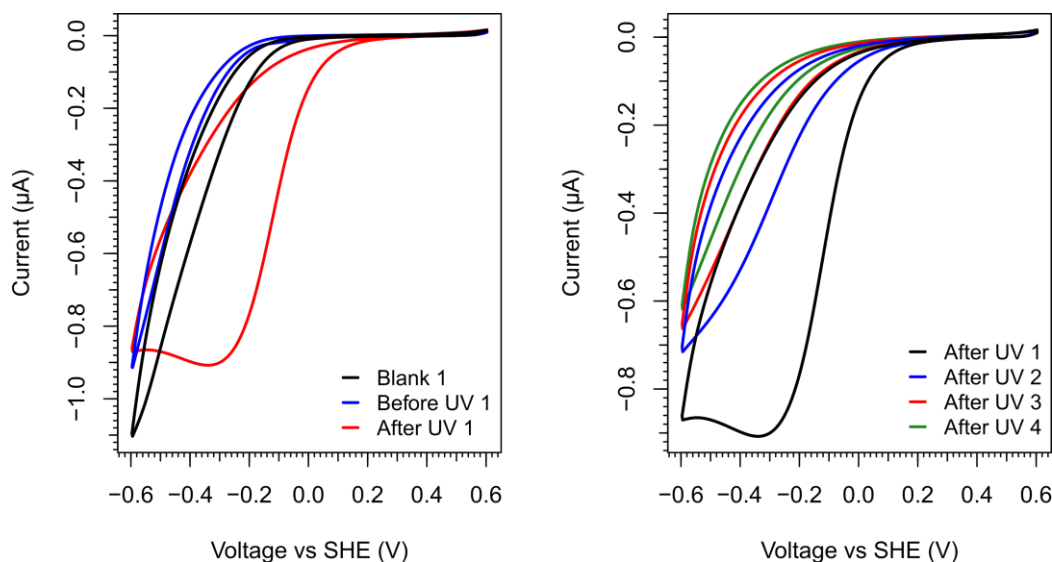


**Figure 6.7.** CVs illustrating UV-initiated diazonium electro-grafting of a 500  $\mu\text{M}$  solution of **T-PEG**, recorded at  $20 \text{ mV s}^{-1}$  in pH 7.55 buffer (20 mM sodium phosphate, 200 mM NaCl + 10% DMSO) buffer at  $0^\circ\text{C}$  on a BDD electrode. **Left)** Comparison of the CVs for a 500  $\mu\text{M}$  solution of **T-PEG** that has been exposed to 365 nm UV irradiation (After UV, 1) with a 1 mM solution of **T-PEG** that has been kept in darkness (Before UV, 1), and a blank solution of the pH 7.55 buffer (Blank 1), shows that diazonium electro-grafting is only observed after **T-PEG** has been exposed to UV irradiation. **Right)** The Diazonium electro-grafting observed for UV-irradiated **T-PEG** follows the typical trend of being a broad reductive wave that decays over subsequent scans.

Comparison of CVs recorded in a 1 mM potassium ferricyanide + 0.1 M NaCl solution using a clean BDD electrode with those recorded using the same electrode after UV-initiated diazonium electro-grafting from **T-PEG** showed that the BDD surface becomes passivated towards the ferricyanide redox couple after diazonium electro-grafting (**Figure 6.8**). This is consistent with the functionalisation of the surface with a pacifying multilayer film.

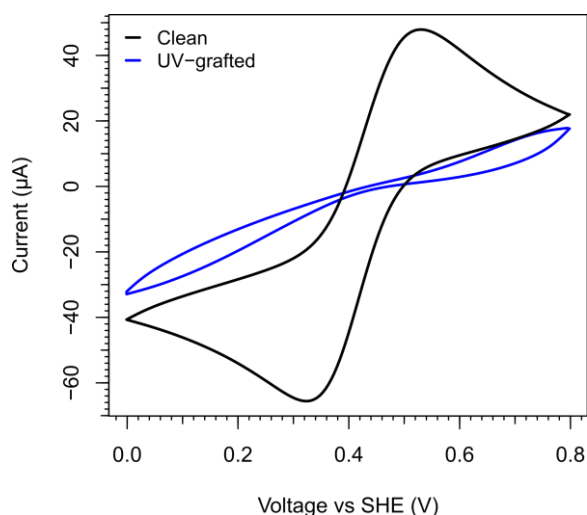


**Figure 6.8.** CVs recorded using either a clean BDD electrode (Clean) or a BDD electrode that has been subjected to UV-initiated diazonium electro-grafting with **T-PEG** (UV-grafted). Scans were recorded at  $500 \text{ mV s}^{-1}$  using a Ag/AgCl (3 M NaCl) reference electrode and a platinum-wire counter electrode in an aqueous solution of 1 mM potassium ferricyanide and 0.1 M NaCl at room temperature. Scans commenced from the most negative potential.

Comparable experiments were then conducted with the maleimide-functionalised triazabutadiene **T8**. A 25 mM stock of **T8** in DMSO was delivered to a pH 7.2 buffer solution (20 mM phosphate, 200 mM NaCl + 10% DMSO) such that the final concentration of **T8** would be 1 mM. **T8** was only partially soluble at this concentration, and some precipitate was observed.

CVs of the blank buffer solution (pH 7.2, 20 mM phosphate, 200 mM NaCl + 10% DMSO) over the range of 0.4 V  $\rightarrow$  -0.2 V (vs SHE) at 0 °C on GC working electrode showed no redox activity attributable to diazonium electro-grafting. CVs of the saturated solution/suspension of **T8** at 0 °C (before UV exposure) likewise did not show any prominent electrochemical signals attributable to diazonium electro-grafting, although it did show a significant dampening of background electrode activity relative to the blank buffer, most likely due to the adsorption of sparingly soluble **T8** to the electrode surface.

After the solution/suspension of **T8** had been subjected to 10 min of UV irradiation at 0 °C using a 7 W 365 nm UV light bulb, the precipitate had disappeared, likely due to the UV-degradation products being far more soluble than the triazabutadiene. The solution also underwent decolourisation. Cyclic voltammograms were then recorded, which clearly showed the characteristic irreversible reductive wave associated with diazonium electro-grafting (**Figure 6.9**).

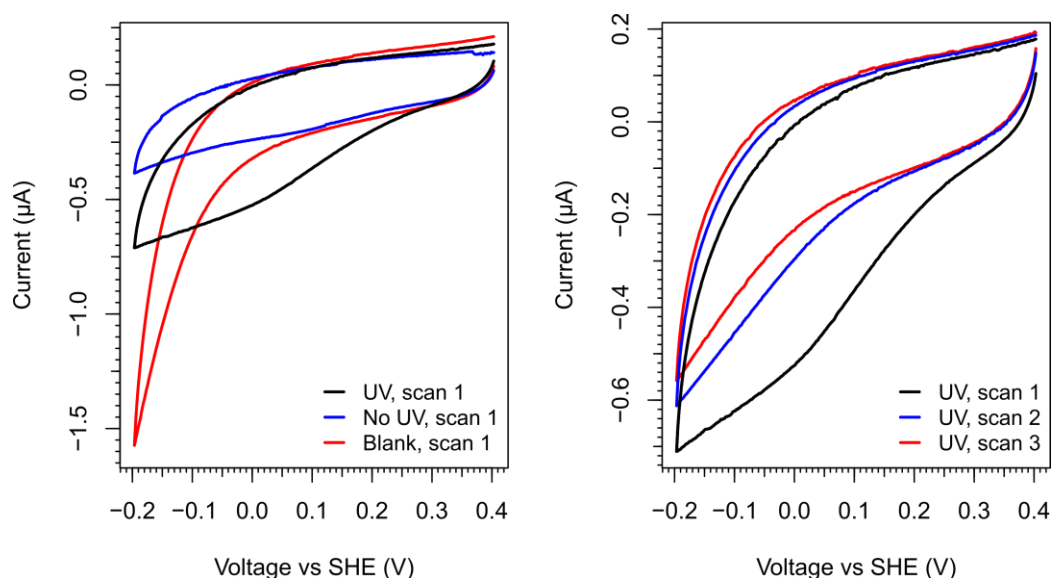


**Figure 6.9.** CVs illustrating UV-initiated diazonium electro-grafting of a saturated solution of **T8**, recorded at 20 mV s<sup>-1</sup> in pH 7.2 (20 mM phosphate, 200 mM NaCl + 10% DMSO) buffer at 0 °C on a GC working electrode. **Left)** Comparison of the CVs for a saturated solution of **T8** that has been exposed to 365 nm UV irradiation (UV, scan 1) with a saturated solution of **T8** that has been kept in darkness (No UV, scan 1), and a blank solution of the pH 7.2 buffer (Blank, scan 1), shows that strong diazonium electro-grafting is only observed after **T8** has been exposed to UV irradiation. **Right)** The Diazonium electro-grafting observed for UV-irradiated **T8** follows the typical trend of being a broad reductive wave that decays over subsequent scans.

### 6.2.2.2 Tracking photodegradation and diazonium cation reactivity

The reaction of diazonium cations with phenolic compounds yields azo-dyes. The reaction of diazonium cations with resorcinol species is especially rapid, due to a site being available for reaction that is both para and ortho to +M substituents.

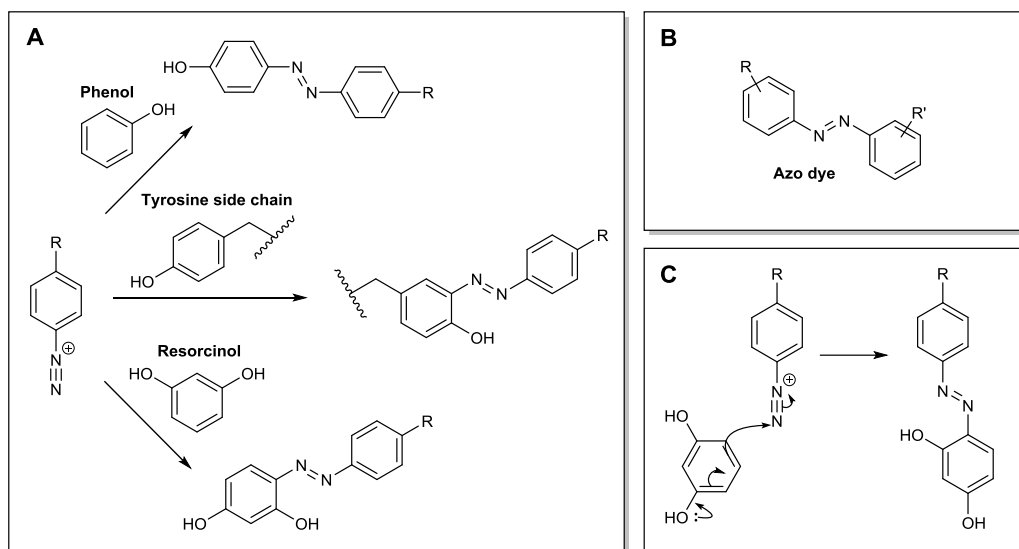
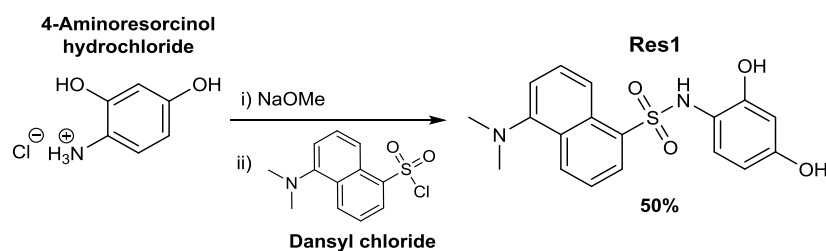


**Figure 6.10.** **A)** The reaction of diazonium cations with a variety of phenolic species to form azo-dyes. **B)** The general structure of an azo-dye. **C)** The mechanism of reaction of resorcinol with a diazonium cation.

**Res1** was synthesised in one-step from 4-aminoresorcinol hydrochloride and dansyl chloride. This species would be of later use in fluorescent labelling of diazonium-functionalised proteins, and due to the number of +M substituents on the resorcinol motif, it was hoped it would be highly reactive towards diazonium cations.



**Scheme 6.13.** The synthesis of **Res1**.

A 500  $\mu\text{M}$  solution of **T-PEG** in pH 7.55 buffer (20 mM phosphate, 200 mM NaCl + 10% DMSO) was prepared. To analyse the behaviour of **T-PEG** in response to UV radiation, a series of experiments were then conducted, with analysis being performed via UV vis spectroscopy (**Figure 6.11**). The conditions used in these experiments are tabulated in **Table 6.1**.

**Table 6.1.** The experimental conditions of the UV-vis interrogation of the UV-responsive behaviour of a 500  $\mu\text{M}$  solution of **T-PEG** in pH 7.55 buffer (20 mM phosphate, 200 mM NaCl + 10% DMSO). Samples were UV-irradiated at 0  $^{\circ}\text{C}$  using a 7 W 365 nm UV light bulb. Room temperature is denoted as rt.

Experiment	Conditions
1	<b>T-PEG</b> (no UV)
2	<b>T-PEG</b> (4 mins UV)
3	<b>T-PEG</b> + 2 equiv resorcinol (no UV, 20 min at rt)
4	<b>T-PEG</b> + 2 equiv resorcinol (4 mins UV, then 16 min at rt)
5	<b>T-PEG</b> + 2 equiv <b>Res1</b> (no UV, 20 min at rt)
6	<b>T-PEG</b> + 2 equiv <b>Res1</b> (4 mins UV, then 16 min at rt)

As can be seen in **Figure 6.11 A**, **T-PEG** undergoes the expected degradation when exposed to 365 nm irradiation, with the triazabutadiene-derived peak at  $\sim 400$  nm decreasing in intensity. However, if a sample of **T-PEG** is exposed to UV irradiation while in the presence of resorcinol, the diazonium cations released by **T-PEG** are attacked by the resorcinol to make an azo-dye, which has a strong UV-vis absorbance of its own, at a slightly longer wavelength than the absorbance of the triazabutadiene **Figure 6.11 B**. Unfortunately, UV-vis spectroscopy could not be used to discern whether **Res1** had reacted with diazonium cations to form an azo-dye, as the UV-vis absorbance of the dansyl unit dominates the UV-vis spectrum in the region at which an azo-dye peak would be expected **Figure 6.11 C**. An NMR experiment was therefore devised to discern the success of this reaction **Figure 6.12**.

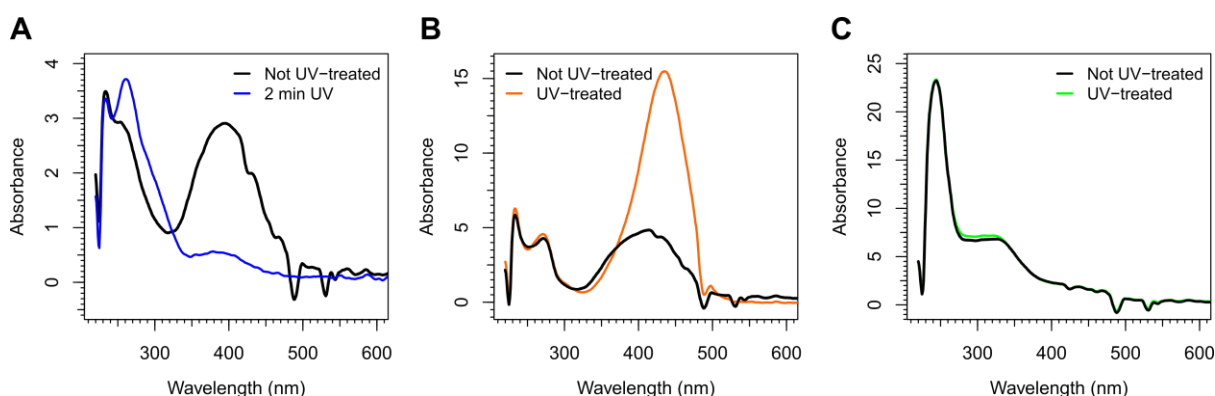


**Figure 6.11.** **A)** UV-vis spectra showing the UV-initiated degradation of a 500  $\mu\text{M}$  solution of **T-PEG** in pH 7.55 buffer (20 mM phosphate, 200 mM NaCl + 10% DMSO) in response to being subjected to UV-irradiation. **B)** UV vis spectra showing that when **T-PEG** is subjected to UV-irradiation in the presence of resorcinol, a new UV-peak will appear, attributable to the formation of an azo-dye. **C)** UV-vis spectra recorded before and after UV-initiated degradation of a 500  $\mu\text{M}$  solution of **T-PEG** in the presence of **Res1**. Experiments were conducted in pH 7.55 aqueous buffer using the conditions tabulated in **Table 6.1**; entries 1 and 2 correspond to plot **A**, conditions 3 and 4 correspond to plot **B** and entries 5 and 6 correspond to plot **C**.

**T-PEG** was dissolved in deuterated methanol and 10 equiv of formic acid were added. The NMR tube was then kept in the dark until  $^1\text{H}$ -NMR and COSY spectra were recorded. One equiv of **Res1** was then added and the tube again kept in the dark and another set of  $^1\text{H}$ -NMR and COSY spectra were

recorded, which showed no new signals attributable to species other than **T-PEG**, **Res1** or formic acid. The sample was then UV irradiated for 5 min using a 7 W 365 nm UV light bulb at 0 °C before being incubated at room temperature for 30 min.  $^1\text{H-NMR}$  and COSY spectra were again recorded, and new signals, likely corresponding to the azo-dye product, could be observed. The areas of the  $^1\text{H-NMR}$  spectra where the differences between the “Before UV” and “After UV” can be most easily discerned are shown in **Figure 6.12**. The signals that give the strongest evidence of the formation of an azo-dye product are new signals present in the “After UV” spectrum that show the spitting pattern of a 1,4-substituted benzene motif, H-4' and H-5', the chemical shifts of which are in good agreement with the chemical shifts of comparable protons in a structurally-similar literature azo-dye, 4-(2,4-dihydroxyphenylazo)benzoic acid<sup>539</sup> (which was derived from the reaction of the 4-carboxybenzenediazonium cation with resorcinol). Note that the  $^1\text{H-NMR}$  spectrum of a sample of **Res1** + formic acid does not undergo any changes after comparable UV exposure and incubation (data not shown).

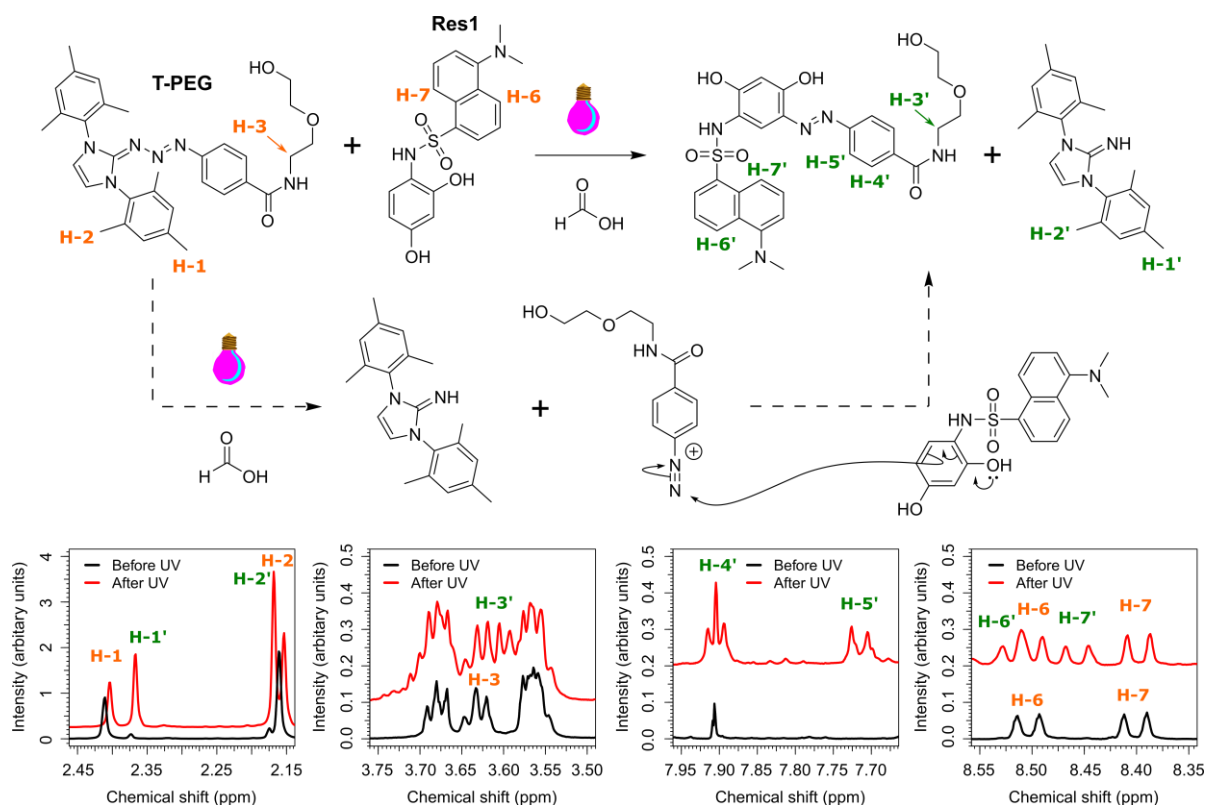


**Figure 6.12.** The UV-initiated reaction of **T-PEG** with **Res1** in the presence of formic acid, as evidenced by  $^1\text{H-NMR}$ .

A sample of **T-PEG** was also subjected to UV irradiation in the presence of formic acid but in the absence of **Res1**. This yielded diazonium cations that could be directly observed via  $^1\text{H-NMR}$ . This is illustrated in **Figure 6.13**, which clearly shows the appearance of new signals attributable to the diazonium cation between 8.8 and 8.3 ppm after UV exposure (for reference, literature  $^1\text{H-NMR}$  of 4-carboxybenzenediazonium tetrafluoroborate in  $\text{D}_2\text{O}$  shows two signals, one at 8.6 ppm and the other at 8.35 ppm<sup>540</sup>).

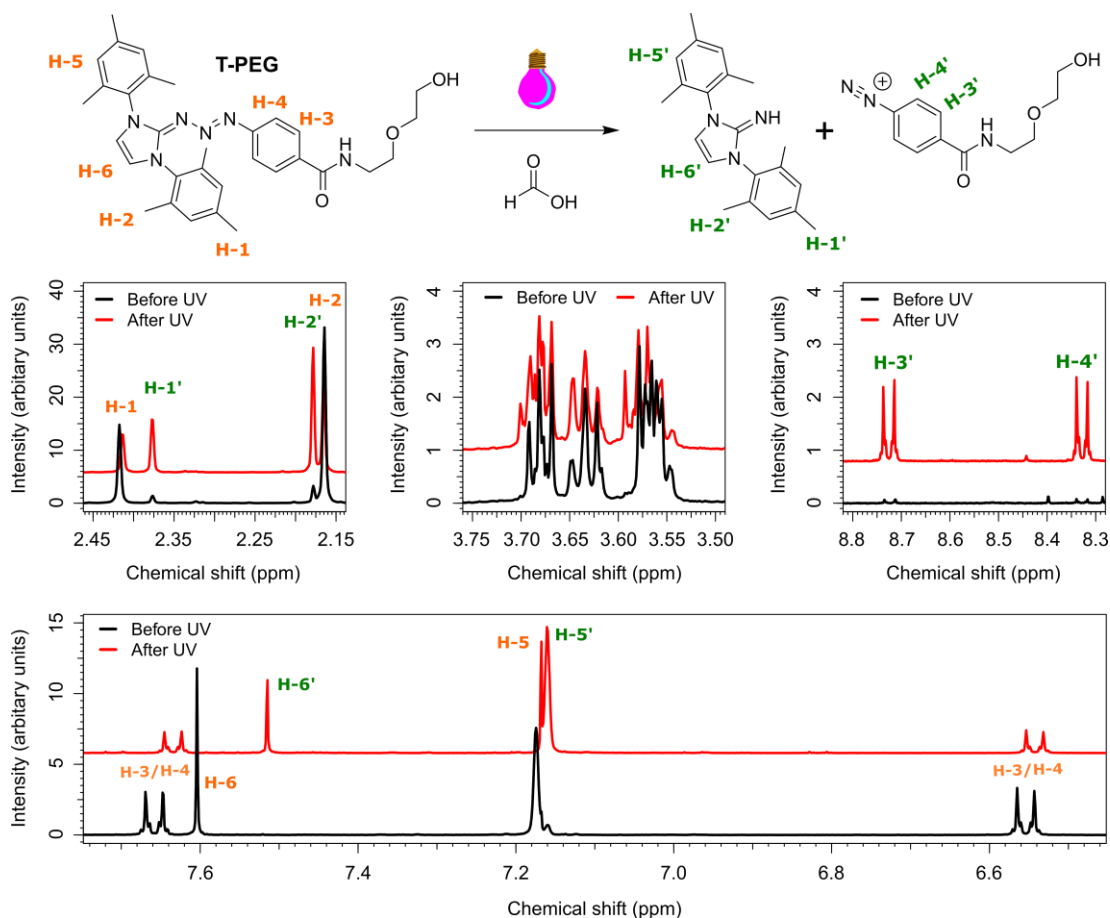


**Figure 6.13.** UV-initiated release of diazonium cations from **T-PEG** in the presence of formic acid, as evidenced by  $^1\text{H-NMR}$ .

Clean UV-vis spectra tracking the UV-initiated degradation of **T8** vs time could not be collected due to the presence of precipitated material. In addition, **T8**, being only sparingly soluble in water, did not give a strong UV response when precipitated material was removed by filtration (which was performed by pushing the solution through a 100  $\mu\text{L}$  Bevelled TipOne<sup>®</sup> Filter Tip).

The reaction of **T8** with cysteine forms **T8-cys** (**Figure 6.14**). **T8-Cys** is far more soluble than **T8** at neutral pH, presumably due to the zwitterionic cysteine motif. **T8** could thus be solubilised in aqueous buffer (pH 7.2, 20 mM sodium phosphate, 200 mM NaCl + 10% DMSO) at a high enough



concentrations to get a strong UV-vis spectrum, allowing the UV-initiated degradation of a 1 mM solution of **T8-Cys** to be monitored via UV-vis (**Figure 6.15**). As can be seen in **Figure 6.15**, **T8-Cys** undergoes complete degradation in response to UV light from a 7 W 365 nm UV light bulb within 4 min.  $^1\text{H-NMR}$  experiments, comparable to those conducted for **T-PEG**, were again used to illustrate that **T8** can be coupled to **Res1** after being exposed to 365 nm irradiation (**Figure 6.16**).

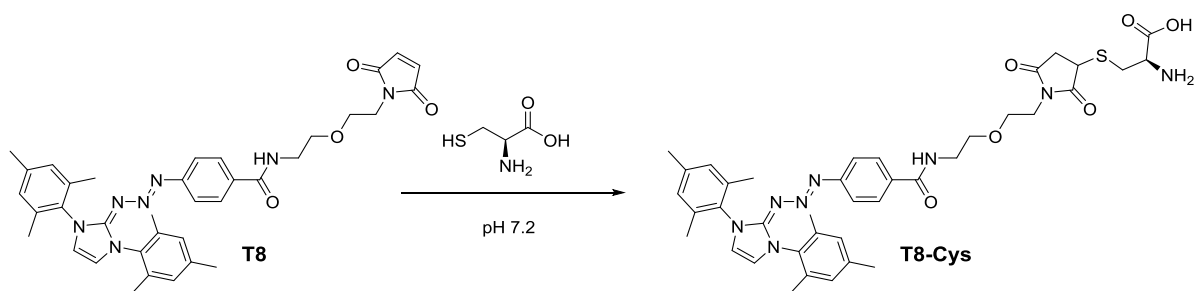


**Figure 6.14.** The reaction of **T8** with L-cysteine to form **T8-cys**.

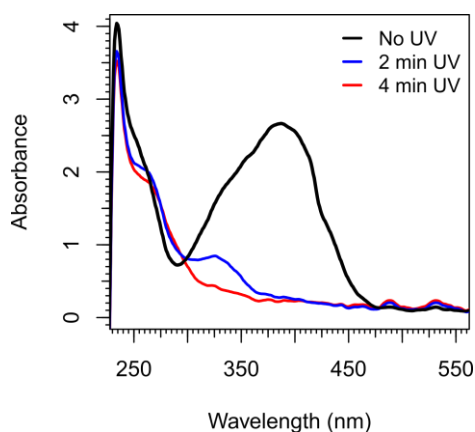


**Figure 6.15.** UV-vis spectra showing the UV-initiated degradation of a 1 mM solution of **T8-cys** in pH 7.2 aqueous buffer (20 mM sodium phosphate, 200 mM NaCl + 10% DMSO) over time.

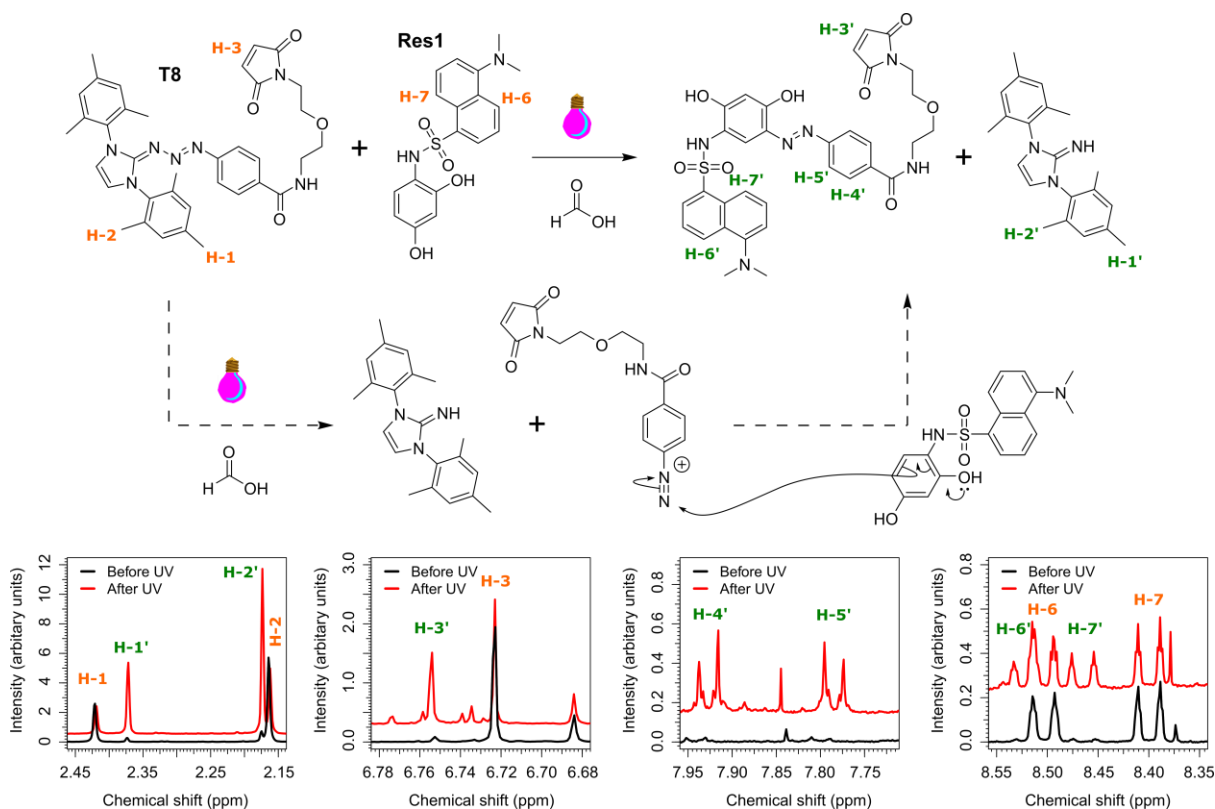


**Figure 6.16.** The UV-initiated reaction of **T8** with **Res1** in the presence of formic acid, as evidenced by  $^1\text{H-NMR}$ .

### 6.2.2.3 UV-initiated diazonium release from phthalimide-type triazabutadiene probes

Experiments were conducted to monitor the rate at which **T23** degrades under 365 nm UV irradiation. **T23** is very poorly soluble in aqueous solution. A solution of **T23** in DMSO was added to a solution of potassium thioacetate in DMSO to yield **T23-acetate** *in situ*, which would be of enhanced water solubility relative to **T23**, due to its ionic nature. The **T23-acetate** DMSO solution was then added into pH 7.4 buffer (20 mM sodium phosphate, 150 mM NaCl + 10% DMSO) such that the final concentration of **T23-acetate** would be 500  $\mu\text{M}$ . Precipitation of **T23-acetate** was however still observed, and filtration of the solution (by pushing the solution through a 100  $\mu\text{L}$  Bevelled TipOne<sup>®</sup> Filter Tip) removed almost all the **T23-acetate**, suggesting that the majority of the apparently-solubilised **T23-acetate** was actually present as a fine dispersion. It is thus readily apparent that the water-insoluble nature of **T23** would make it challenging to work with as a bio-orthogonal probe.

UV-vis spectra were recorded to monitor the UV-initiated degradation of the fine dispersion of **T23-acetate** in response to UV light from a 7 W 365 nm UV light bulb. Although the presence of precipitated material affected the quality of the obtained UV-vis spectra, it could be observed that minimal degradation of **T23** has occurred even after 7 min of UV exposure (**Figure 6.18**). This is in stark contrast with **Figure 6.11** and **Figure 6.15**, which show extensive degradation within two min, and full degradation within four min. Accordingly, UV-initiated diazonium electro-grafting experiments using **T23**, comparable to those in **Figure 6.9**, were unsuccessful (data not shown).

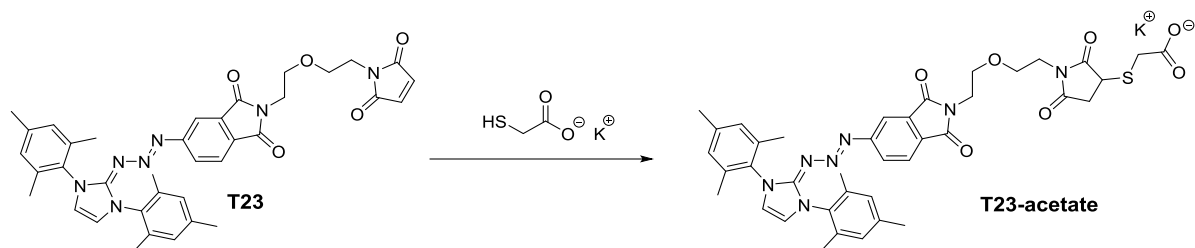


**Figure 6.17.** The reaction of **T23** with potassium thioacetate to form **T23-acetate**.

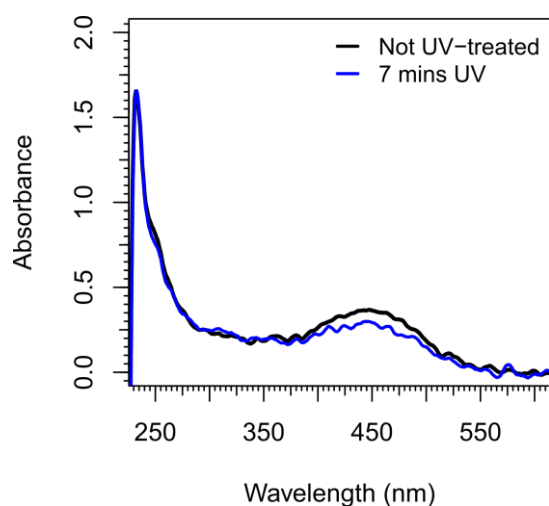


**Figure 6.18.** UV-vis spectra showing the UV-initiated degradation of a 500  $\mu\text{M}$  solution/dispersion of **T23-acetate** in pH 7.4 aqueous buffer (pH 7.2, 20 mM sodium phosphate, 200 mM NaCl + 20% DMSO) over time.

### 6.2.3 Reviewing the suitability of triazabutadiene scaffolds for usage in the diazonium electro-grafting of proteins

The “classic” triazabutadienes (where  $R^1$  and  $R^2 = \text{Mes}$  and  $R^3$  is a para carbonyl group in **Scheme 6.3**) and the “phthalimide type” (where  $R^1$  and  $R^2 = \text{Mes}$  and  $R^3$  represents para and meta carbonyl groups in **Scheme 6.3**) are synthetically easy to synthesise and handle, but with the exception of **T14** and **T15** suffer from poor water solubility. By contrast, the triazabutadienes based on the **T17** NHC, where  $R^1 = (\text{CH}_2)_3\text{SO}_3\text{K}$  and  $R^2 = \text{Mes}$  (using the numbering in **Scheme 6.3**), are highly water soluble yet are more challenging to obtain and isolate synthetically. Both the “classic” and the **T17**-based triazabutadiene scaffolds are suitable for the facile release of diazonium cations, whereas the “phthalimide type” triazabutadiene scaffold of **T23** is not. It should also be noted that diazonium cations released from phthalimide-type triazabutadiene scaffolds would be more reactive than diazonium cations that just bear a para-carbonyl group (due to being more electron-deficient), and while this would mean that phthalimide-type diazonium cations would be more easily reduced it would also mean that they would be more likely to partake in side reactions with tyrosine residues. Considering these observations, it is apparent that the phthalimide-type triazabutadiene scaffold of **T23** is unsuitable for developing a protein diazonium electro-grafting methodology.

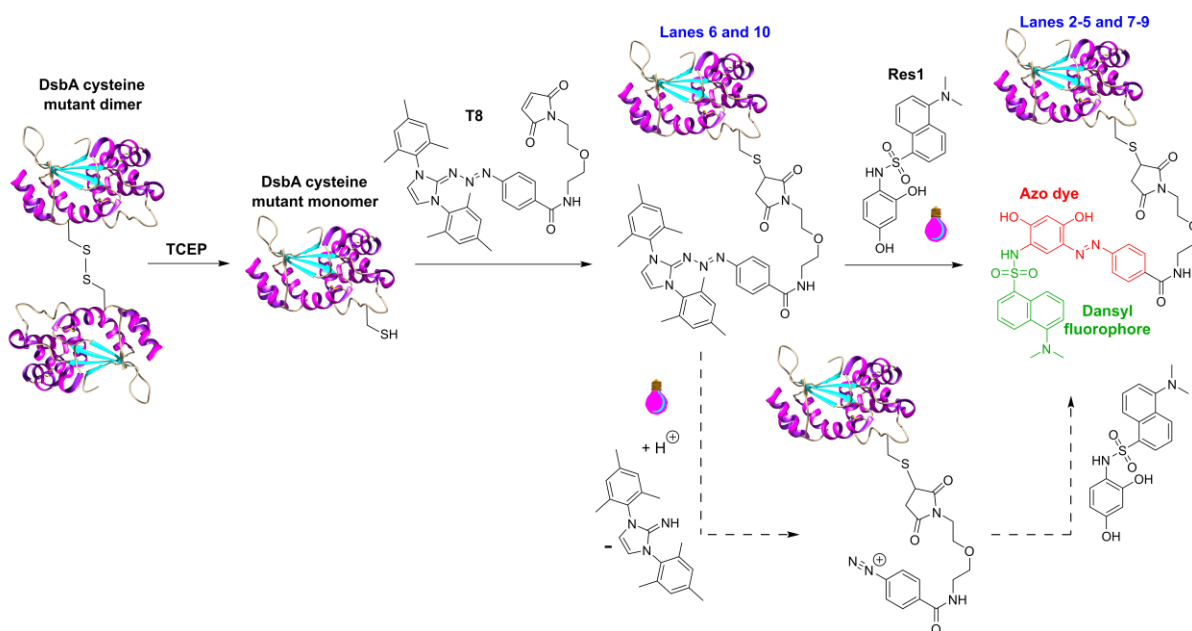
The **T17**-derived triazabutadienes would be expected to degrade in aqueous solution faster than their **T1**-derived counterparts,<sup>529</sup> but this may not be an issue if using facile bioconjugation ligation techniques, and excess equivs of the highly water soluble **T17**-derived species could be easily delivered. Another factor to be considered is that appending a hydrophobic **T1**-derived triazabutadiene to a protein would likely have an adverse effect on the protein’s solubility, whereas appending an ionic **T17**-derived triazabutadiene would not. However, since the **T1**-derived triazabutadienes are more convenient to synthesise and isolate they were chosen for usage in the protein bioconjugation experiments detailed hereafter.

## 6.2.4 Bioconjugation of triazabutadiene probes to redox proteins

With the synthesis of triazabutadienes probes hypothetically capable of bioconjugation to proteins being successful, and the ability of these triazabutadienes to release diazonium cations suitable for diazonium electro-grafting verified, further development of the methodology for the direct electro-grafting of diazonium cation functionalised proteins necessitated that conditions needed to be found under which these triazabutadienes could, i) be appended to redox proteins at a location that could serve as a suitable tethering site to an electrode surface, and ii) later be photodegraded to unveil diazonium cations on the surface of the protein. To this end experiments were performed with cysteine variants of the redox protein DsbA (first introduced in **Section 4.2.4.2**) and variants of the CjX183-D protein (first introduced in **Section 4.2.3**).

### 6.2.4.1 The usage of **T8** in maleimide ligation to DsbA mutants

120  $\mu$ M solutions of two different DsbA cysteine mutants, DsbA<sub>c-term</sub> and DsbA<sub>middle</sub> (see **Section 4.2.4.2**) in pH 7.2 buffer (20 mM sodium phosphate, 200 mM NaCl) in the presence of excess tris(2-carboxyethyl)phosphine (TCEP) were prepared and incubated in the dark for 20 min (in order to reduce all interprotein disulfide bonds). After this time, the protein solutions were split to give four samples of each protein, and suitable volumes of a DMSO stock solutions of **T8** were added, such that either 1 or 10 equiv of **T8** were delivered to each sample and the total concentration of DMSO in the reaction solution reached 10% (v/v). The reaction was allowed to proceed at room temperature in the dark for 30 min, after which time the reaction solutions were exchanged into pH 7.55 phosphate buffer (20 mM phosphate, 200 mM NaCl + 5% DMSO) using PD MiniTrap™ G-25 desalting columns. To these solutions were added either 0 or 10 equiv of **Res1**. The solutions were then exposed to the radiation from a 7 W 365 nm UV light bulb for 5 min at 0 °C, and were subsequently incubated at room temperature for 30 min. These reaction steps are shown in **Scheme 6.14**.



**Scheme 6.14.** The functionalisation of DsbA cysteine mutants with **T8** and further derivatisation with **Res1**.

A non-reducing dye-free buffer was then added to each of the samples, and the samples were run on a 15% polyacrylamide SDS-PAGE gel **Figure 6.19**. The identity of the samples run in each lane of the gel are tabulated in **Table 6.2**. The lanes that contain species with both the fluorescent dansyl and azo-dye motifs (**Figure 6.19**, lanes 2-5 and 7-9) show protein bands that are visible both under visible light and via fluorescence. The fluorescence is not as strong as would normally be expected of the dansyl unit due to the broad-spectrum fluorescence quenching abilities of the azo-dye motifs.<sup>541-543</sup>

**Table 6.2.** The identities of the samples ran in the 15% polyacrylamide SDS-PAGE gel presented in **Figure 6.19**. All samples were exposed to UV light for 5 min at 0 °C using a 7 W 365 nm UV light bulb.

Lane	Sample
1	Ladder
2	DsbA <sub>C-term</sub> + 1 equiv <b>T8</b> + 10 equiv <b>Res1</b>
3	DsbA <sub>C-term</sub> + 1 equiv <b>T8</b> + 10 equiv <b>Res1</b>
4	DsbA <sub>C-term</sub> + 10 equiv <b>T8</b> + 10 equiv <b>Res1</b>
5	DsbA <sub>C-term</sub> + 10 equiv <b>T8</b> + 10 equiv <b>Res1</b>
6	DsbA <sub>C-term</sub> + 10 equiv <b>T8</b>
7	DsbA <sub>middle</sub> + 1 equiv <b>T8</b> + 10 equiv <b>Res1</b>
8	DsbA <sub>middle</sub> + 10 equiv <b>T8</b> + 10 equiv <b>Res1</b>
9	DsbA <sub>middle</sub> + 10 equiv <b>T8</b> + 10 equiv <b>Res1</b>
10	DsbA <sub>middle</sub> + 10 equiv <b>T8</b>

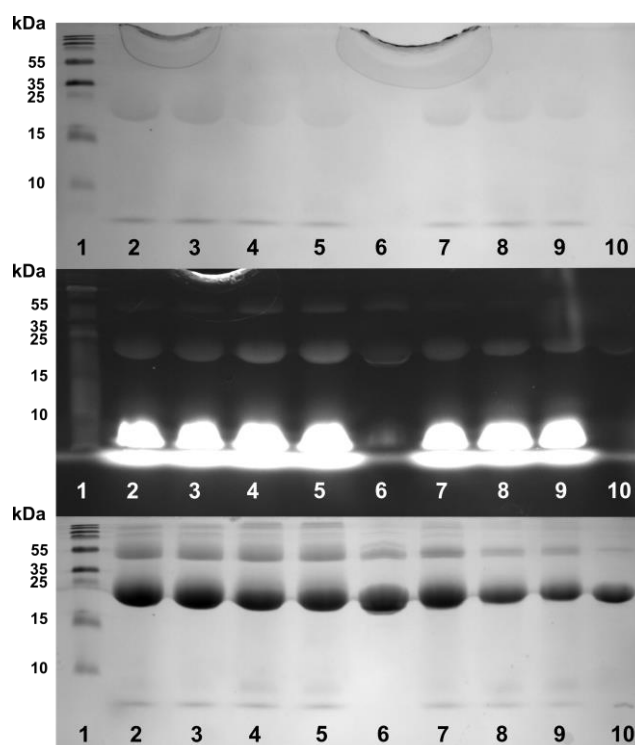
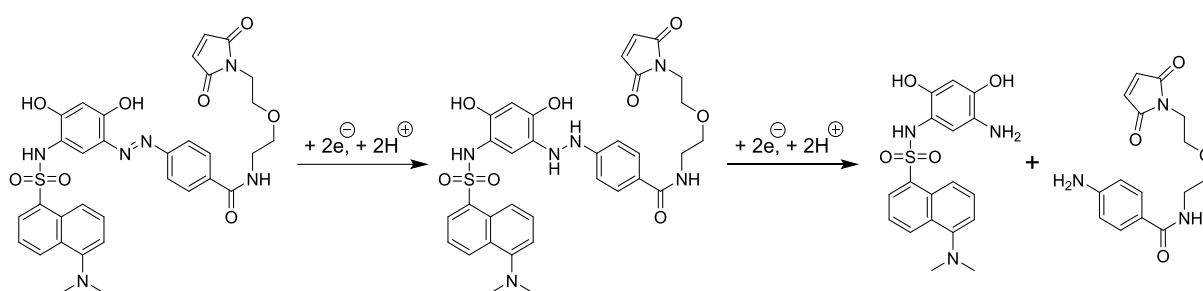


**Figure 6.19.** 15% polyacrylamide SDS-PAGE gel of showing DsbA cysteine mutants labelled with **T8** or **T8-Res1** azo-dye photographed under visible light (**top**), mid wave fluorescence (**middle**), and visible light after staining with Coomassie dye (**bottom**). Prior to running on the SDS-PAGE gel, protein samples were mixed with a 5 × concentrated buffer that was both dye and reducing-agent free (10% SDS, 20% glycerol, 200 mM Tris-HCl pH 6.8). The samples were not boiled prior to being run on the gel.

The lanes that contain DsbA samples that have been treated with **T8** but not with **Res1** and UV (lanes 6 and 10, **Figure 6.19**) only weakly fluoresce. Pre-staining, these lanes do show bands under visible light either. All lanes contain DsbA protein (which has a theoretical mass of 26 kDa), and thus all lanes show visible bands post-Coomassie staining at around 25 kDa (**Figure 6.19**). It can also be observed that while DsbA dimer is present in all lanes, higher order DsbA aggregates seem to be more prevalent in the lanes treated with UV (**Figure 6.19**, lanes 2-5 and 7-10), which could indicate that the diazonium cations revealed on the DsbA surface are reacting with tyrosine residues on other DsbA proteins. It can also be observed that the higher order DsbA aggregates seem to be more prevalent in the DsbA<sub>c-term</sub> samples, which would be expected due to the mutant cysteine in DsbA<sub>c-term</sub> being more sterically available than that in DsbA<sub>middle</sub>.

The proteins band at ~25 kDa in lanes 2-5 and 7-9 were excised from the gel and submitted to the Bioscience Technology Facility at University of York for digestion experiments with Trypsin and endoproteinase AspN, both of which should yield peptides that provide sequence coverage over all the cysteine residues in the proteins. The results from these experiments are tabulated in **Table 6.3** and **Table 6.4** (overleaf). Peptide fragments bearing the intended azo-dye label on the mutant cysteine residues could not be found via ESI LC/MS, possibly due to the reductive nature of some of

the steps used in preparation of the samples for digestion experiments which could cause the breakdown of the azo-dye motif, possibly into several species (**Scheme 6.15**). It could, however, still be discerned that the mutant surface-exposed cysteine residues in both DsbA<sub>c-term</sub> and DsbA<sub>middle</sub> were being targeted by **T8** over the internal active-site and structural disulfide cysteine residues, as peaks corresponding to the masses of peptide fragments containing the structural and active-site cysteine residues could be all be found (**Table 6.3** and **Table 6.4**), whereas in all but one experiment (**Table 6.3** DsbA<sub>c-term</sub>, 10 equivalents of **T8**, Trypsin digestion) no peaks could be found that corresponded to peptide fragments containing the free mutated cysteine residues (**Table 6.3** and **Table 6.4**). As such, by virtue of the absence of this sequence coverage, the preference of **T8** to ligate to the mutant cysteine residues was indicated.



**Scheme 6.15.** The reduction of a Res1 azo-dye into anilines, via a hydrazine.

**Table 6.3.** The results of the digestion experiments conducted on the DsbA<sub>c-term</sub> samples in the 15% polyacrylamide SDS-PAGE gel in **Figure 6.19**. The sequence covered by detected peptide fragments is coloured black, whereas sequences that were undetected are coloured red. Mutant cysteine residues are highlighted yellow.

DsbA <sub>c-term</sub> 1 equiv of T8: Trypsin digestion					
1	SRDDKKDGVA	GPGDAVRVTS	SKLVTQPGTS	NPKAVVSFYE	DFLCPACGIF
51	ERGFPGPTVSK	LVDIGAVAAD	YTMVAILDSA	SNQHYSSRAA	AAAYCVADES
101	IEAFRRFHAA	LFSKDIQPAE	LGKDFPDNAR	LIELAREAGV	VGKVPDCINS
151	GKYIEKVDGL	AAAVNVHATP	TVRVNGTEYE	WSTPAALVAK	IKEIVGDVPG
201	IDSAAATATS	LCTPSR			
DsbA <sub>c-term</sub> 1 equiv of T8: Asp-N digestion					
1	SRDDKKDGVA	GPGDAVRVTS	SKLVTQPGTS	NPKAVVSFYE	DFLCPACGIF
51	ERGFPGPTVSK	LVDIGAVAAD	YTMVAILDSA	SNQHYSSRAA	AAAYCVADES
101	IEAFRRFHAA	LFSKDIQPAE	LGKDFPDNAR	LIELAREAGV	VGKVPDCINS
151	GKYIEKVDGL	AAAVNVHATP	TVRVNGTEYE	WSTPAALVAK	IKEIVGDVPG
201	IDSAAATATS	LCTPSR			
DsbA <sub>c-term</sub> 10 equiv of T8: Trypsin digestion					
1	SRDDKKDGVA	GPGDAVRVTS	SKLVTQPGTS	NPKAVVSFYE	DFLCPACGIF
51	ERGFPGPTVSK	LVDIGAVAAD	YTMVAILDSA	SNQHYSSRAA	AAAYCVADES
101	IEAFRRFHAA	LFSKDIQPAE	LGKDFPDNAR	LIELAREAGV	VGKVPDCINS
151	GKYIEKVDGL	AAAVNVHATP	TVRVNGTEYE	WSTPAALVAK	IKEIVGDVPG
201	IDSAAATATS	LCTPSR			
DsbA <sub>c-term</sub> 10 equiv of T8: Asp-N digestion					
1	SRDDKKDGVA	GPGDAVRVTS	SKLVTQPGTS	NPKAVVSFYE	DFLCPACGIF
51	ERGFPGPTVSK	LVDIGAVAAD	YTMVAILDSA	SNQHYSSRAA	AAAYCVADES
101	IEAFRRFHAA	LFSKDIQPAE	LGKDFPDNAR	LIELAREAGV	VGKVPDCINS
151	GKYIEKVDGL	AAAVNVHATP	TVRVNGTEYE	WSTPAALVAK	IKEIVGDVPG
201	IDSAAATATS	LCTPSR			



**Table 6.4.** The results of the digestion experiments conducted on the DsbA<sub>middle</sub> samples in the 15% polyacrylamide SDS-PAGE gel in **Figure 6.19**. The sequence covered by detected peptide fragments is coloured black, whereas sequences that were undetected are coloured red. Mutant cysteine residues are highlighted yellow.

DsbA <sub>middle</sub> 1 equiv of T8: Trypsin digestion						
1	SRDDK	KDGVA	GPGDAVRVTS	SKLVTQPGTS	NPKAVVSFYE	DFLCPACGIF
51	ERGF	GPTVSK	LVDIGAVAAD	YTMVAILDSA	SNQHYSSRAA	AAAYCVADES
101	IEAFRRFHAA	LFSK	DIQLCT	PSRDFPDNAR	LIELAREAGV	VGKVPDCINS
151	GKYIEKVDGL	AAAVNVHATP	TVRVNGTEYE	WSTPAALVAK	IKEIVGDVPG	
201	IDSAAATATS					
DsbA <sub>middle</sub> 1 equiv of T8: Asp-N digestion						
1	SRDDK	KDGVA	GPGDAVRVTS	SKLVTQPGTS	NPKAVVSFYE	DFLCPACGIF
51	ERGF	GPTVSK	LVDIGAVAAD	YTMVAILDSA	SNQHYSSRAA	AAAYCVADES
101	IEAFRRFHAA	LFSK	DIQLCT	PSRDFPDNAR	LIELAREAGV	VGKVPDCINS
151	GKYIEKVDGL	AAAVNVHATP	TVRVNGTEYE	WSTPAALVAK	IKEIVGDVPG	
201	IDSAAATATS					
DsbA <sub>middle</sub> 10 equiv of T8: Trypsin digestion						
1	SRDDK	KDGVA	GPGDAVRVTS	SKLVTQPGTS	NPKAVVSFYE	DFLCPACGIF
51	ERGF	GPTVSK	LVDIGAVAAD	YTMVAILDSA	SNQHYSSRAA	AAAYCVADES
101	IEAFRRFHAA	LFSK	DIQLCT	PSRDFPDNAR	LIELAREAGV	VGKVPDCINS
151	GKYIEKVDGL	AAAVNVHATP	TVRVNGTEYE	WSTPAALVAK	IKEIVGDVPG	
201	IDSAAATATS					
DsbA <sub>middle</sub> 10 equiv of T8: Asp-N digestion						
1	SRDDK	KDGVA	GPGDAVRVTS	SKLVTQPGTS	NPKAVVSFYE	DFLCPACGIF
51	ERGF	GPTVSK	LVDIGAVAAD	YTMVAILDSA	SNQHYSSRAA	AAAYCVADES
101	IEAFRRFHAA	LFSK	DIQLCT	PSRDFPDNAR	LIELAREAGV	VGKVPDCINS
151	GKYIEKVDGL	AAAVNVHATP	TVRVNGTEYE	WSTPAALVAK	IKEIVGDVPG	
201	IDSAAATATS					

While the Trypsin/Asp-N digestion experiments indicate that the mutant surface-exposed cysteine residues in either of the DsbA mutants could be selectively targeted, DsbA<sub>middle</sub> was identified as the preferable protein with which to continue experiments, as the mutant cysteine residue is in closer proximity of the active site disulfide relative to that of the DsbA<sub>c-term</sub> mutant (**Figure 6.20**).

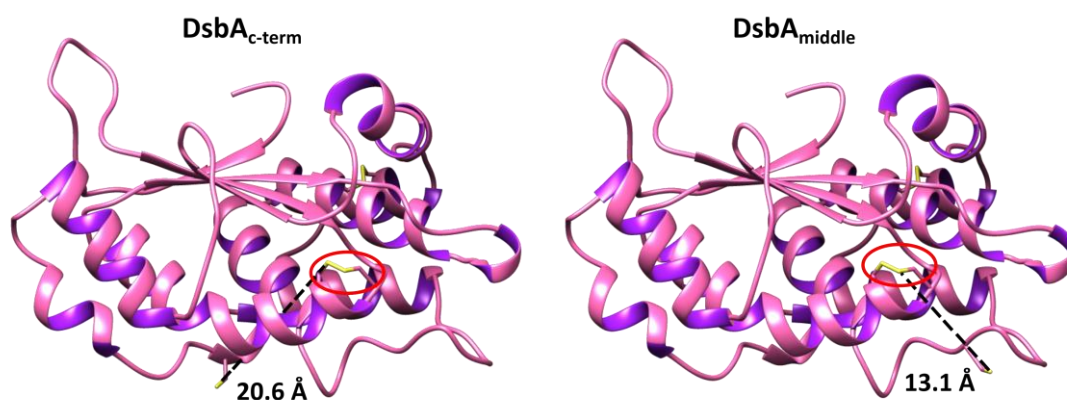
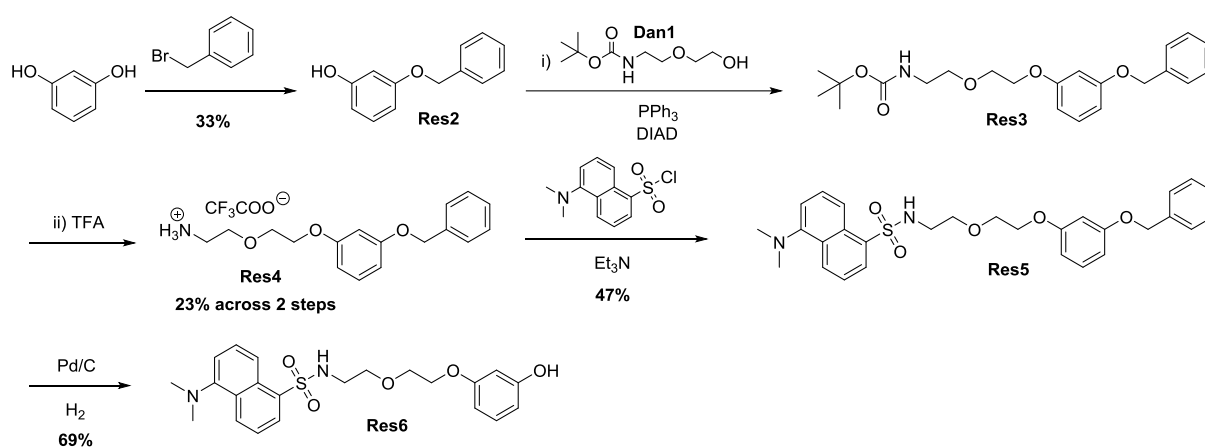


**Figure 6.20.** Models of DsbA<sub>c-term</sub> and DsbA<sub>middle</sub> based on the crystal structure of WT DsbA (PDB ID: 4K6X). The active site disulfide is circled, and the distances between the mutant cysteine residues and the active site disulfide are marked.

Suspecting that both the triazabutadiene and the azo-dye motifs could be susceptible to the reducing nature of TCEP, a second round of experiments were conducted on DsbA<sub>middle</sub>, firstly without TCEP altogether (*no TCEP*), and secondly with the removal of TCEP prior to the addition of **T8** (*TCEP-removed*). A second dansylated resorcinol probe **Res6** was synthesised (**Scheme 6.16**) in the hope that its azo-dye product may not be as efficient at quenching fluorescence than the azo-dye product of **Res1**. **Res1**, **Res6** and resorcinol were used to react with unveiled diazonium functionalities, with excess equivalents of **T8** being removed prior to the introduction of the resorcinol probes using a PD MiniTrap™ G-25 desalting column.



**Scheme 6.16.** The synthesis of **Res6** via intermediate species **Res2-5**.

The 15% polyacrylamide SDS-PAGE gel run in the analysis of the *no TCEP* experiments is shown in **Figure 6.21**. The occupancies of the lanes in this gel are tabulated in **Table 6.5**. In contrasting **Figure 6.19** with **Figure 6.21** it can be seen that the absence of TCEP increases the amount of DsbA<sub>middle</sub> dimer observed (at proximately 55 kDa) and also greatly reduces the efficiency of labelling with **T8** + **Res1** and **T8** + **Res6**. This is to be expected as most of the surface-exposed mutant cysteine residues will be unavailable to maleimide ligation due to inter-protein disulfide bonds. Note that in **Figure 6.21** the samples had been exchanged into fresh buffer using spin-traps prior to running on the gel, resulting in a lower intensity fluorescence from washed-off free fluorescent probes than observed in **Figure 6.19**.

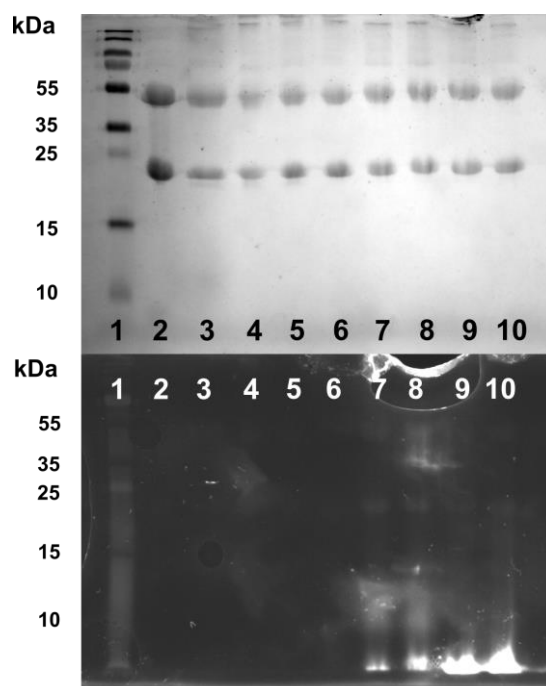


**Figure 6.21.** 15% polyacrylamide SDS-PAGE gel of DsbA<sub>middle</sub> (no TCEP) samples subjected to the various treatments without using TCEP under mid wave fluorescence (**bottom**), and visible light after staining with Coomassie dye (**top**). No staining from azo-dyes was observed under visible light. Prior to running on the SDS-PAGE gel, protein samples were mixed with a 5 × concentrated buffer that was both dye and reducing-agent free (10% SDS, 20% glycerol, 200 mM Tris-HCl pH 6.8). The samples were not boiled prior to being run on the gel.

**Table 6.5.** The identities of the DsbA<sub>middle</sub> (no TCEP) samples ran in the 15% polyacrylamide SDS-PAGE gel shown in **Figure 6.21**. UV treated samples were exposed to UV light for 5 min at 0 °C using a 7 W 365 nm UV light bulb.

Lane	Sample
1	Ladder
2	DsbA <sub>middle</sub>
3	DsbA <sub>middle</sub> + 10 equiv <b>T8</b> (no UV)
4	DsbA <sub>middle</sub> + 10 equiv <b>T8</b> (with UV)
5	DsbA <sub>middle</sub> + 10 equiv <b>T8</b> + 10 equiv resorcinol (no UV)
6	DsbA <sub>middle</sub> + 10 equiv <b>T8</b> + 10 equiv resorcinol (with UV)
7	DsbA <sub>middle</sub> + 10 equiv <b>T8</b> + 10 equiv <b>Res1</b> (no UV)
8	DsbA <sub>middle</sub> + 10 equiv <b>T8</b> + 10 equiv <b>Res1</b> (with UV)
9	DsbA <sub>middle</sub> + 10 equiv <b>T8</b> + 10 equiv <b>Res6</b> (no UV)
10	DsbA <sub>middle</sub> + 10 equiv <b>T8</b> + 10 equiv <b>Res6</b> (with UV)

The 15% polyacrylamide SDS-PAGE gel run in the analysis of the *TCEP-removed* experiments is shown in **Figure 6.22**. The occupancies of the lanes in this gel are tabulated in **Table 6.6**.

**Table 6.6.** The identities of the DsbA<sub>middle</sub> (TCEP-removed) samples ran in the 15% polyacrylamide SDS-PAGE gel shown in **Figure 6.22**. UV treated samples were exposed to UV light for 5 min at 0 °C using a 7 W 365 nm UV light bulb.

Lane	Sample
1	Ladder
2	DsbA <sub>middle</sub>
3	DsbA <sub>middle</sub> + 5 equiv <b>T8</b> (no UV)
4	DsbA <sub>middle</sub> + 5 equiv <b>T8</b> (with UV)
5	DsbA <sub>middle</sub> + 5 equiv <b>T8</b> + 10 equiv resorcinol (no UV)
6	DsbA <sub>middle</sub> + 5 equiv <b>T8</b> + 10 equiv resorcinol (with UV)
7	DsbA <sub>middle</sub> + 5 equiv <b>T8</b> + 10 equiv <b>Res1</b> (no UV)
8	DsbA <sub>middle</sub> + 5 equiv <b>T8</b> + 10 equiv <b>Res1</b> (with UV)
9	DsbA <sub>middle</sub> + 5 equiv <b>T8</b> + 10 equiv <b>Res6</b> (no UV)
10	DsbA <sub>middle</sub> + 5 equiv <b>T8</b> + 10 equiv <b>Res6</b> (with UV)

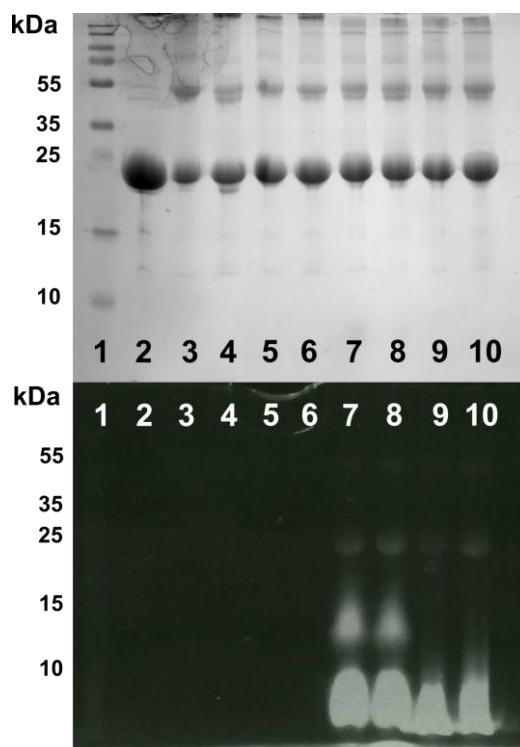


**Figure 6.22.** 15% polyacrylamide SDS-PAGE gel of DsbA<sub>middle</sub> (TCEP-removed) samples subjected to the various treatments without using TCEP under mid wave fluorescence (**bottom**), and visible light after staining with Coomassie dye (**top**). No staining from azo-dyes was observed under visible light. Prior to running on the SDS-PAGE gel, protein samples were mixed with a 5 × concentrated buffer that was both dye and reducing-agent free (10% SDS, 20% glycerol, 200 mM Tris-HCl pH 6.8). The samples were not boiled prior to being run on the gel.

It can be seen by contrasting **Figure 6.21** with **Figure 6.22** that the pre-treatment of DsbA<sub>middle</sub> with TCEP decreased the amount of DsbA<sub>middle</sub> dimer observed and greatly increased the efficiency of labelling with **T8** + **Res1** and **T8** + **Res6**, despite fewer equivalents of **T8** being used in this set of experiments (5 equivalents vs 10). Note that in **Figure 6.22** the samples had not been exchanged into fresh buffer using spin-traps prior to running on the gel, resulting in a greater intensity of fluorescence in the washed-off free fluorescent probes. In **Figure 6.22** a macromolecular fluorescent species of a lower mass than the DsbA<sub>middle</sub> can be observed in lanes 7 and 8, and the identity of this species is unclear, mayhap an aggregate of **Res1**. There is only a subtle difference in the intensity of the fluorescence in the non-UV irradiated and UV-irradiated bands for DsbA<sub>middle</sub> samples treated with **Res1** (lanes 7 and 8 respectively, **Figure 6.22**), but there is a more pronounced difference in the intensity of the fluorescence in the non-UV irradiated and UV-irradiated bands for DsbA<sub>middle</sub> samples treated with **Res6** (lanes 9 and 10 respectively, **Figure 6.22**), perhaps indicating that **Res6** is not as efficient as **Res1** at coupling to aryl diazonium cations.

The presence of **T8** on the surface of DsbA<sub>middle</sub> can also be detected using UV-vis spectroscopy. As shown in **Figure 6.23**, DsbA<sub>middle</sub>, (pre-treated with TCEP and then exchanged into a fresh pH 7.55 phosphate buffer solution) shows no absorbance in 300-500 nm window. Once treated with 5 equivalents of **T8** for half an hour, and then once again exchanged into fresh pH 7.55 phosphate buffer using a PD MiniTrap™ G-25 desalting column to remove free **T8**, a new broad absorption band is observed at about 385 nm (**Figure 6.23**). If this sample is subjected to UV irradiation for 2 min the intensity of the 385 nm absorption band approximately halves (**Figure 6.23**), which is consistent with the UV-irradiation causing photoisomerisation of the triazabutadiene unit of **T8** and triggering diazonium release. Diazonium release can also be inferred by performing the same UV-irradiation experiment in the presence of 10 equivalents of resorcinol, which itself has no discernible UV-vis absorption between 300-500 nm (**Figure 6.23**), yet upon azo-dye formation gives rise to a new broad absorption band at about 435 nm (**Figure 6.23**).

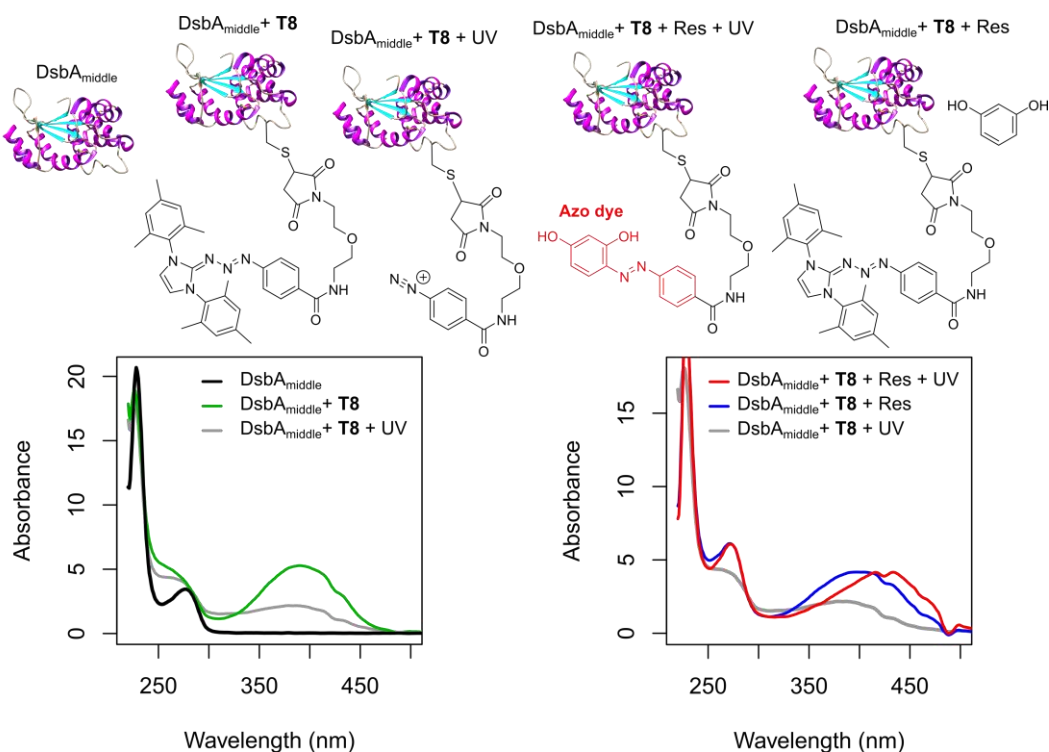


**Figure 6.23.** (Left) UV-vis experiments showing the presence of **T8** on the surface of  $\text{DsbA}_{\text{middle}}$  and the breakdown of the triazabutadiene motif under UV irradiation. (Right) When a sample of  $\text{DsbA}_{\text{middle}}$  labelled with **T8** is subjected to UV-irradiation in the presence of resorcinol, a new absorption band attributable to an azo-dye is observed. UV-treated samples were exposed to UV light for 2 min at 0 °C using a 7 W 365 nm UV light bulb.

The presence of this azo-dye species can also be confirmed via mass spectrometry (**Figure 6.24**). Although the charge state ladder for this sample is admittedly rather messy, the target mass expected of the azo-dye product has clearly been found (**Figure 6.24**). Also notable is the absence of un-ligated  $\text{DsbA}_{\text{middle}}$ , which has an expected mass of 25761 Da. Other  $\text{DsbA}_{\text{middle}}$  derived species also appear to be present, although they may simply be artefacts of the deconvolution. One such species appears to have a mass consistent with a phenyl hydrazine derivative (**Figure 6.24**), which is a hypothesised reduction product of a triazabutadiene (**Scheme 6.4**). Reduction of aryl diazonium cations using reducing agents such as  $\text{SnCl}_2$  can be used to generate phenyl hydrazines,<sup>544</sup> and as such it is possible that reduction of a diazonium cation, perhaps by TCEP, could give rise to this species, although this is far from certain. The peak at 26184 Da is either an artefact of deconvolution or could be attributable to an oxidised azo-dye derivative (**Figure 6.24**).

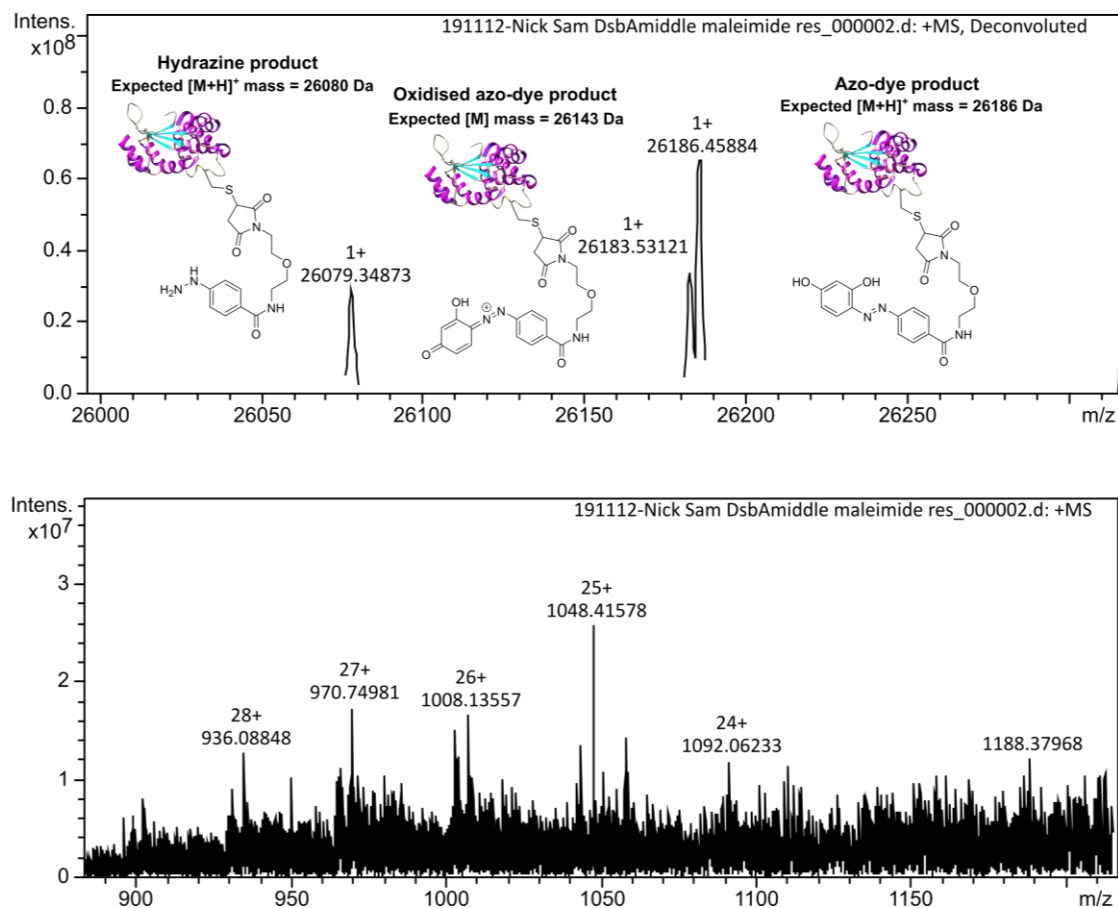


**Figure 6.24.** (Top) Deconvoluted protein ESI mass spectrum obtained on a Bruker Solarix XR 9.4 T instrument for a sample of TCEP-treated DsbA<sub>middle</sub> ligated to **T8**, exposed to UV irradiation for 5 min at 0 °C using a 7 W 365 nm UV light bulb in the presence of resorcinol, then incubated at rt for 30 min. (Bottom) The raw protein ESI mass spectrum.

#### 6.2.4.2 The usage of T14 for amide bond formation to CjX183-D

As detailed in **Section 4.2.3**, CjX183-D is a small c-type cytochrome with no naturally occurring lysine residues and an *N*-terminal glycine residue. This presented a tantalising opportunity with respect to using an easy-to-handle and characterise redox protein to develop a direct diazonium electro-grafting methodology which with to immobilise redox proteins onto electrode surfaces in specific orientations.

A lysine mutant of this protein CjX183-D R51K (see **Section 4.2.3.3**) was designed and produced in which the lysine residue is located at a site which should be suitable for crosslinking to electrode surfaces, due to this site being proximal to the heme redox centre ( $\sim 12$  Å from the Fe centre) yet not being part of the active site coordination sphere (**Figure 6.25**). As detailed in **Section 4.2.3**, the *N*-terminal glycine residue can be converted to a glyoxylamide-type aldehyde using PLP-mediated transamination, meaning that the only amine present in PLP-treated CjX183-D R51K is the

$\epsilon$ -amine of the mutant lysine residue. This allows activated-ester functionalised triazabutadiene probes, such as **T14**, to be conjugated to PLP-treated CjX183-D R51K site-selectively. This constitutes an ideal test system, whereby a simple bioconjugation technique can be used on a simple redox protein so that the focus of experimental optimisation can ultimately be on finding conditions for direct diazonium electro-grafting from triazabutadiene-labelled proteins.

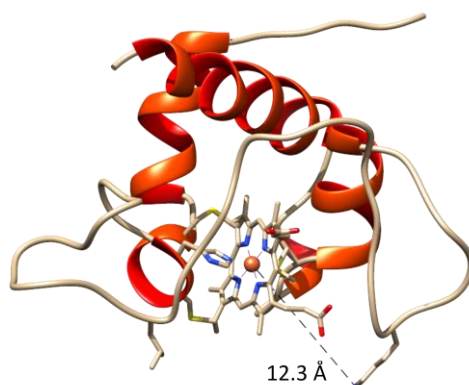


**Figure 6.25.** A depiction of the structure of CjX183-D R51K, based on the unpublished crystal structure of WT CjX183-D. The distance between the  $\epsilon$ -amine of the mutant lysine residue and the Fe centre is shown in black.

Reactions between CjX183-D variants (WT CjX183-D, PLP-treated WT CjX183-D, CjX183-D R51K and PLP-treated CjX183-D R51K) and the activated ester functionalised triazabutadiene probes **T5**, **T13**, **T14** and **T15** were conducted, but ultimately it was found that only **T14** yielded triazabutadiene-CjX183-D conjugate derived products (**Figure 6.26**). The failure of **T5** and **T13** in this regard can easily be accounted for by the insolubility of these species in aqueous solution. The failure of **T15** is somewhat more vexing, but could perhaps be due to the more reactive nature of the **T15** sulfo-NHS ester (relative to the **T14** sulfo-NHS ester) making it prone to hydrolysis during storage. The expected additional masses of **T14**-derived CjX183-D conjugates are shown in **Figure 6.27**.

**T14** should only be capable of amide bond formation to WT CjX183-D at a single site - the *N*-terminal glycine residue. This single-site ligation was verified via the incubation of WT CjX183-D with 15 equiv of **T14** for 1 hour, followed by buffer exchange, the addition of 15 equiv **Res6**, treatment with 365 nm UV irradiation, and overnight incubation at room temperature (**Figure 6.27**). The samples were then exchanged into HPLC grade water and analysed via MS, which yielded only a single protein species after deconvolution, with a mass consistent with that expected for WT CjX183-D conjugated to an azo-dye derived from **Res6** and a diazonium cation released from **T14** (**Figure 6.28**).



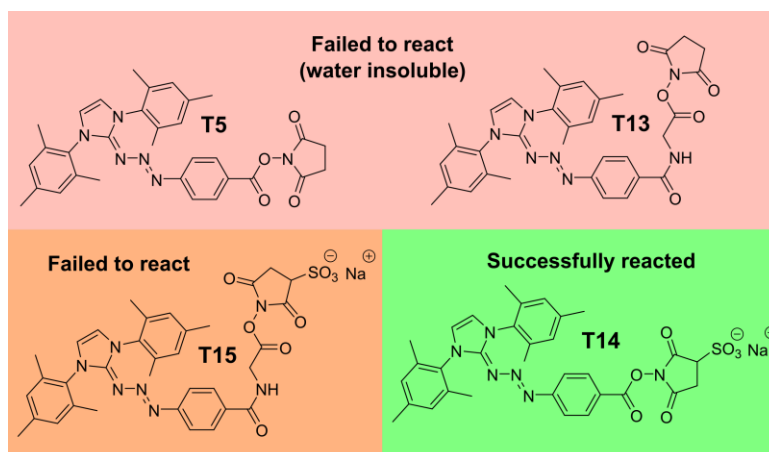


**Figure 6.26.** The structure of activated ester functionalised triazabutadiene probes **T5**, **T13**, **T14** and **T15**, and their ability to react with CjX183-D variants.

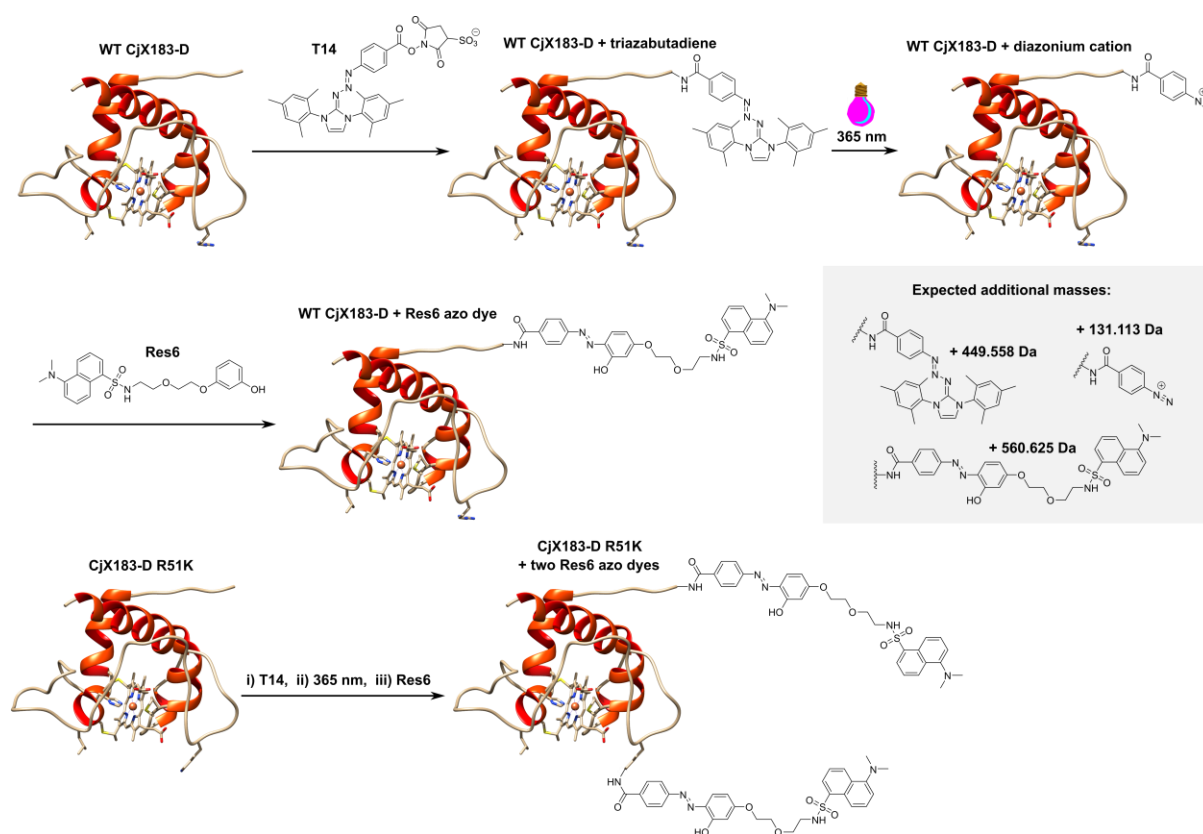


**Figure 6.27.** The functionalisation of CjX183-D variants with **T14** and further derivatisation with **Res6**. WT CjX183-D is only expected to become conjugated to a single **Res6** azo-dye motif as the only amine present is the *N*-terminal glycine residue, whereas CjX183-D R51K is expected to become conjugated to two **Res6** azo-dye motifs as it contains a mutant lysine residue.

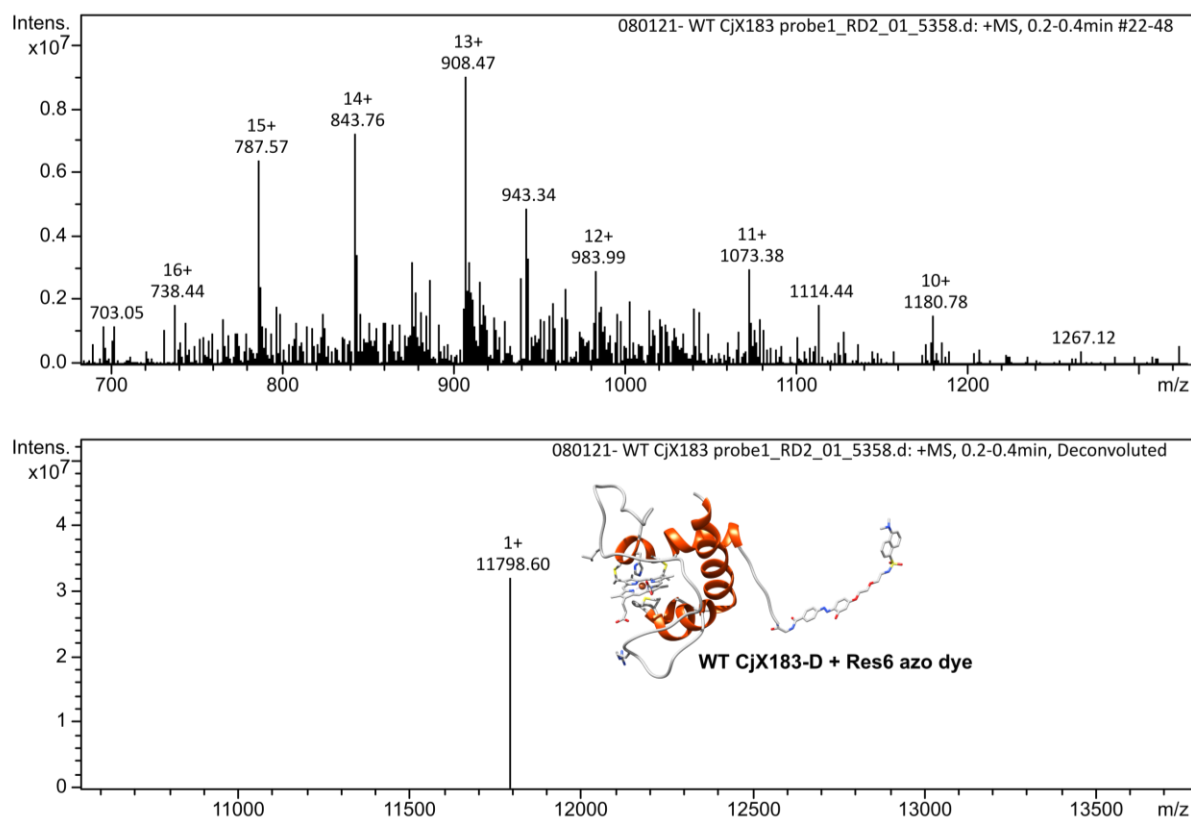


**Figure 6.28.** Positive ion mode ESI-LC/MS analysis of a sample of WT CjX183-D treated with **T14**, **Res6** and 365 nm UV irradiation sequentially. **Top**) The raw MS data showing the protein charge ladders. **Bottom**) Deconvoluted mass spectrum, showing a peak at  $m/z$  11798.60. This is 561.87 greater than the  $m/z$  observed for unmodified WT CjX183-D, which was 11236.73 (**Section 4.2.3**, **Figure 4.23**). The theoretical additional mass for the addition of the **Res6** azo-dye motif is 560.63 Da. UV exposure was conducted for 4 min at 0 °C using a 7 W 365 nm UV light bulb.

CjX183-D R51K, by contrast, is shown to be capable of reacting with **T14** at two locations; these should be the *N*-terminal glycine residue and the  $\epsilon$ -amine of the mutant lysine residue. Comparable treatment of CjX183-D R51K with **T14**, **Res6**, and finally 365 nm UV irradiation before overnight incubation at room temperature (**Figure 6.27**) and analysis via MS, yielded only a single protein species after deconvolution, the mass of which was consistent with that expected for CjX183-D R51K + two **Res6** azo-dye motifs (**Figure 6.29**).

The reaction of these CjX183-D variants with **T14** and **Res6** went to completion, as evidenced by the absence of peaks for unmodified WT CjX183-D or CjX183-D R51K in **Figure 6.28** and **Figure 6.29**. However, it is uncertain as to whether reaction completion between **T14** and the protein amine residues occurred strictly within the intended one-hour time period, as difficulties were encountered when trying to fully remove excess **T14** prior to the addition of **Res6**, which could have allowed a population of **T14** to continue to react with CjX183-D amine residues overnight. In addition, any diazonium cations released from **T14** but unconjugated to CjX183-D would also have become

conjugated to **Res6**, and these resultant azo-dyes would hypothetically still be capable of becoming conjugated to the CjX183-D variant (provided the NHS ester had not become hydrolysed).

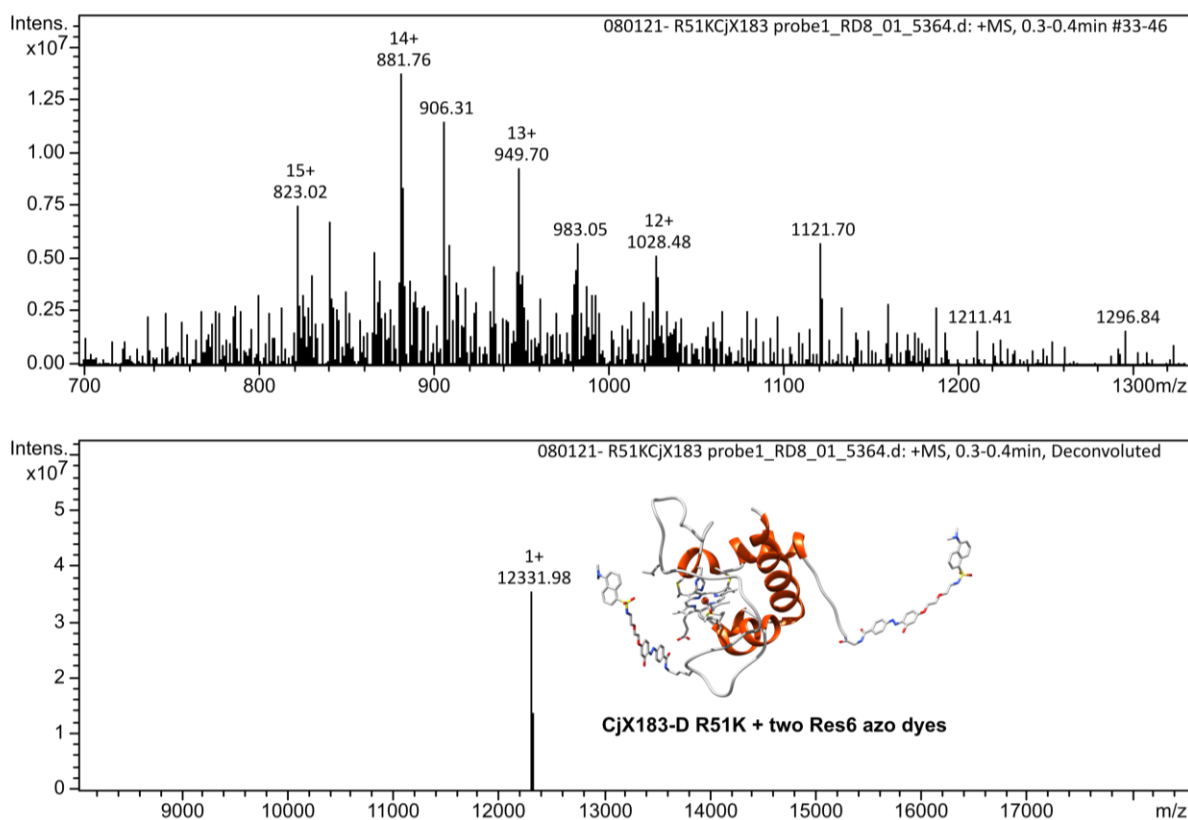


**Figure 6.29.** Positive ion mode ESI-LC/MS analysis of a sample of CjX183-D R51K treated with **T14**, **Res6** and 365 nm UV irradiation sequentially. **Top)** The raw MS data showing the protein charge ladders. **Bottom)** Deconvoluted mass spectrum, showing a peak at m/z 12331.98. This is 1121.85 greater than the m/z observed for unmodified CjX183-D R51K, which was 11210.13 (**Section 4.2.3**, **Figure 4.30**). The theoretical additional mass for the addition of two **Res6** azo-dye motifs is 1121.25 Da. UV exposure was conducted for 4 min at 0 °C using a 7 W 365 nm UV light bulb.

CjX183-D R51K, singly conjugated to a triazabutadiene via its mutant lysine residue, is the desired conjugate for usage in diazonium electro-grafting. To find optimal conditions for synthesising this conjugate a series of reaction conditions were trialed using PLP-treated samples of CjX183-D R51K (in which the only amine present is the  $\epsilon$ -amine of the mutant lysine residue, see **Section 4.2.3.3**) and **T14**. These reaction conditions are tabulated in **Table 6.7**. Reactions incubated at pH 8 were found to give higher conversions than those conducted at pH 7.5; this is to be expected as at higher pH lysine residues are less likely to be protonated and thus perform better as nucleophiles. Interestingly, incubation at 37 °C resulted in both di- and tri- addition of **T14** to CjX183-D (data not shown). Some di-addition of **T14** can likely be accounted for by a small population of the PLP-treated CjX183-D retaining a glycine residue. The third ligation might be attributable to the fact that while NHS (and sulfo-NHS) esters preferably react with amine groups, reaction of these esters with tyrosine and serine/threonine residues is also known.<sup>545</sup> Most protocols for NHS ester/protein couplings specify

conducting the coupling reaction at  $rt^{431,546}$  or at  $4\text{ }^{\circ}\text{C}/\text{on ice}^{431}$  and it is unsurprising that usage of elevated temperatures decreases the selectivity of NHS ester conjugation. The optimal conditions were thus identified as those in **Table 6.7 Entry 2**, under which CjX183-D only reacted once with **T14**, as verified by LC-MS (**Figure 6.30**).

**Table 6.7.** The reaction conditions trialed to find optimal conditions for the coupling of **T14** to PLP-treated CjX183-D R51K. Reactions were performed in pH 7.5 (25 mM sodium phosphate buffer + 10% DMSO), or pH 8 (25 mM sodium phosphate buffer, titrated from pH 7.5 to pH 8 using saturated  $\text{NaHCO}_3$ , + 10% DMSO) buffer. Reactions were incubated in darkness.

Entry	pH	[PLP-treated CjX183-D]	Equiv of T14	Temperature	Incubation time
1	7.5	50 $\mu\text{M}$	20	Room temperature	1 hour
2	8	50 $\mu\text{M}$	20	Room temperature	1 hour
3	7.5	50 $\mu\text{M}$	20	37 $^{\circ}\text{C}$	1 hour
4	7.5	50 $\mu\text{M}$	20	37 $^{\circ}\text{C}$	2 hours
5	8	50 $\mu\text{M}$	20	37 $^{\circ}\text{C}$	2 hours
6	8	50 $\mu\text{M}$	20	37 $^{\circ}\text{C}$	1 hour

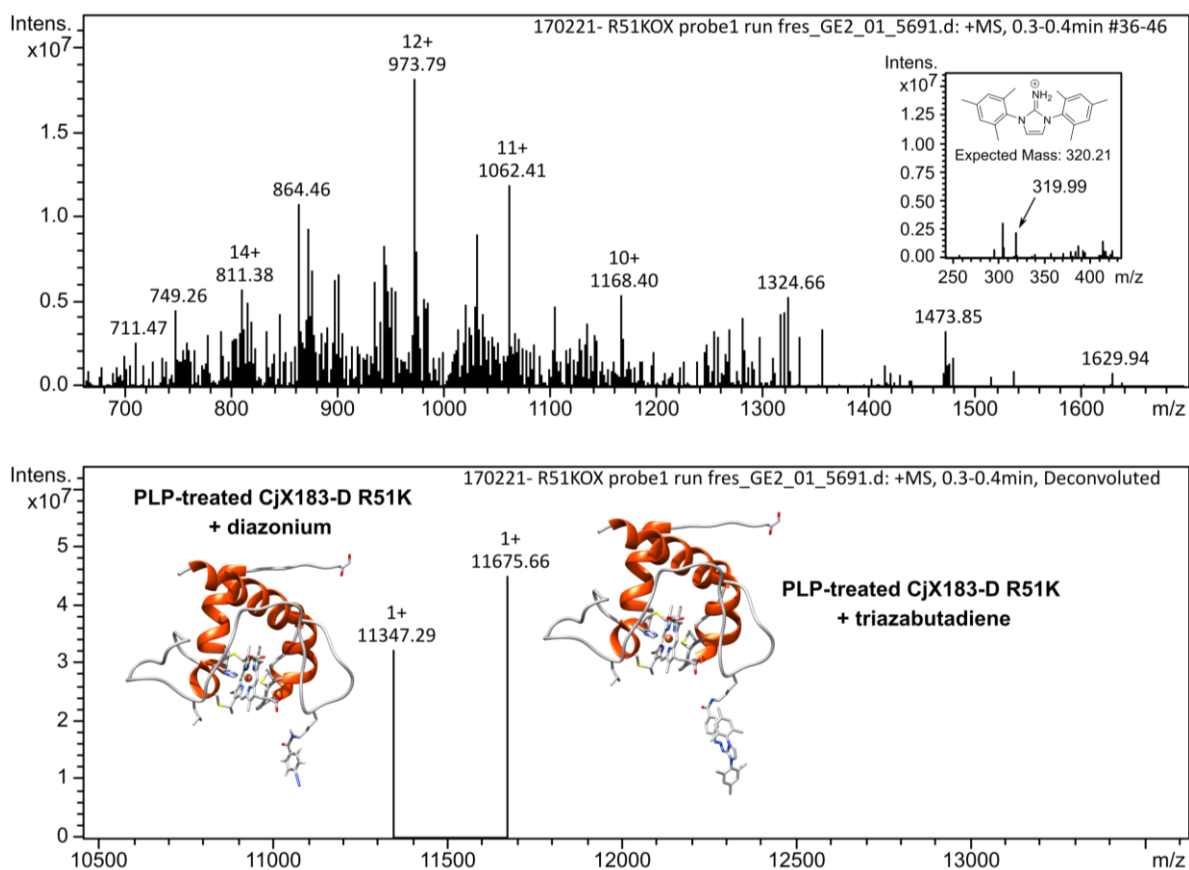


**Figure 6.30.** Positive ion mode ESI-LC/MS analysis of a sample of PLP-treated CjX183-D R51K reacted with **T14** using the conditions described in **Table 6.7 Entry 2** and purified using a His SpinTrap<sup>TM</sup>. **Bottom)** Deconvoluted mass spectrum. A peak would be expected at +467.56  $m/z$  relative to CjX183-D R51K for protein labelled with the intact triazabutadiene probe and with an *N*-terminal glyoxylamide in a hydrated form (at  $m/z$  11677.71 if accounting for the +12 Da systematic error) and at +149.11  $m/z$  for the free diazonium (at  $m/z$  11359.26 if accounting for the +12 Da systematic error, and at  $m/z$  11347.26 if using the theoretical mass of the protein).

Purification of CjX183-D-triazabutadiene conjugates prior to usage in diazonium electro-grafting is essential, as if unconjugated triazabutadienes remain free in solution the diazonium cations from these species would out-compete the diazonium cation-labelled proteins during electro-grafting. Performing such a purification was however complicated by the ability of excess **T14** to co-elute with CjX183-D when using G-25 resins to conduct buffer exchanges; one hypothesis is that the bipolar nature of **T14** allows it to form colloidal dispersions in aqueous solution, thus increasing the speed at which it travels through size exclusion chromatography resins. Purification via nickel affinity chromatography using a His SpinTrap™ (Cytiva) (followed by buffer exchange into pH 7.5 25 mM sodium phosphate to remove imidazole) did however prove successful (**Figure 6.31**), and it is the LC-MS data of the thus purified PLP-treated CjX183-D R51K-triazabutadiene conjugate that is presented in **Figure 6.30**.

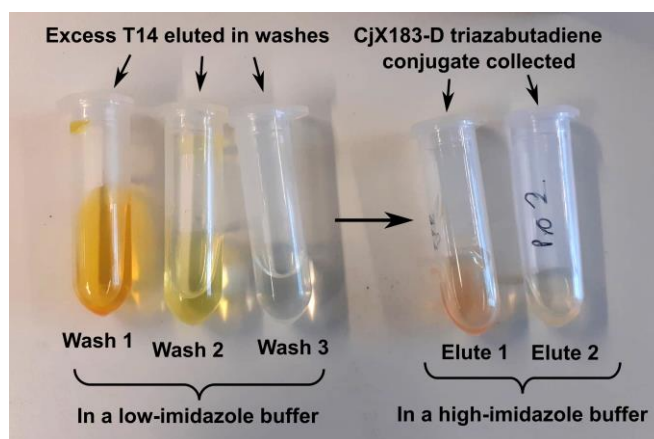


**Figure 6.31.** Purification of a PLP-treated CjX183-D R51K-triazabutadiene conjugate using a His SpinTrap™. As can be seen, excess **T14** can be removed by washing with a low-imidazole buffer (25 mM sodium phosphate, titrated from pH 7.5 to pH 8 with saturated NaHCO<sub>3</sub>, + 30 mM imidazole) while the CjX183-D conjugate is retained on the Ni-affinity resin, and the CjX183-D can later be eluted using a high-imidazole buffer (25 mM sodium phosphate, titrated from pH 7.5 to pH 8 with saturated NaHCO<sub>3</sub>, + 800 mM imidazole).

It can be observed in **Figure 6.30** that some of the triazabutadiene motifs appended to the protein have degraded into diazonium cations (giving rise to the peak at  $m/z$  11347 in **Figure 6.30**), which is not surprising due to the presence of formic acid in the LC mobile phase. A small amount of the biproduct of triazabutadiene breakdown can also be observed as a peak at  $m/z$  320 (**Figure 6.30**). However, the fact that light is needed to initiate diazonium formation in the majority of the sample was confirmed by the treatment of the purified PLP-treated CjX183-D R51K-triazabutadiene conjugate with 365 nm UV irradiation prior to analysis by LC-MS (**Figure 6.32**). This resulted in the complete loss of the triazabutadiene peak (which was at  $m/z$  11676 in **Figure 6.30**), but the peak for the diazonium-labelled conjugate could still be observed at  $m/z$  11347, as could a peak for an aryl cation-labelled conjugate at  $m/z$  11330 (see **Figure 6.32**). Note that observing aryl cations is a common occurrence when conducting MS on diazonium species as N<sub>2</sub> is an excellent leaving group. The peak for the

biproduc of triazabutadiene breakdown (at  $m/z$  320) is also notably more intense in **Figure 6.32** than it is in **Figure 6.30**. UV treatment of the purified PLP-treated CjX183-D R51K-triazabutadiene conjugate also caused a change in its UV-vis spectrum, whereas UV treatment of an unlabelled CjX183-D R51K sample did not (**Figure 6.33**).

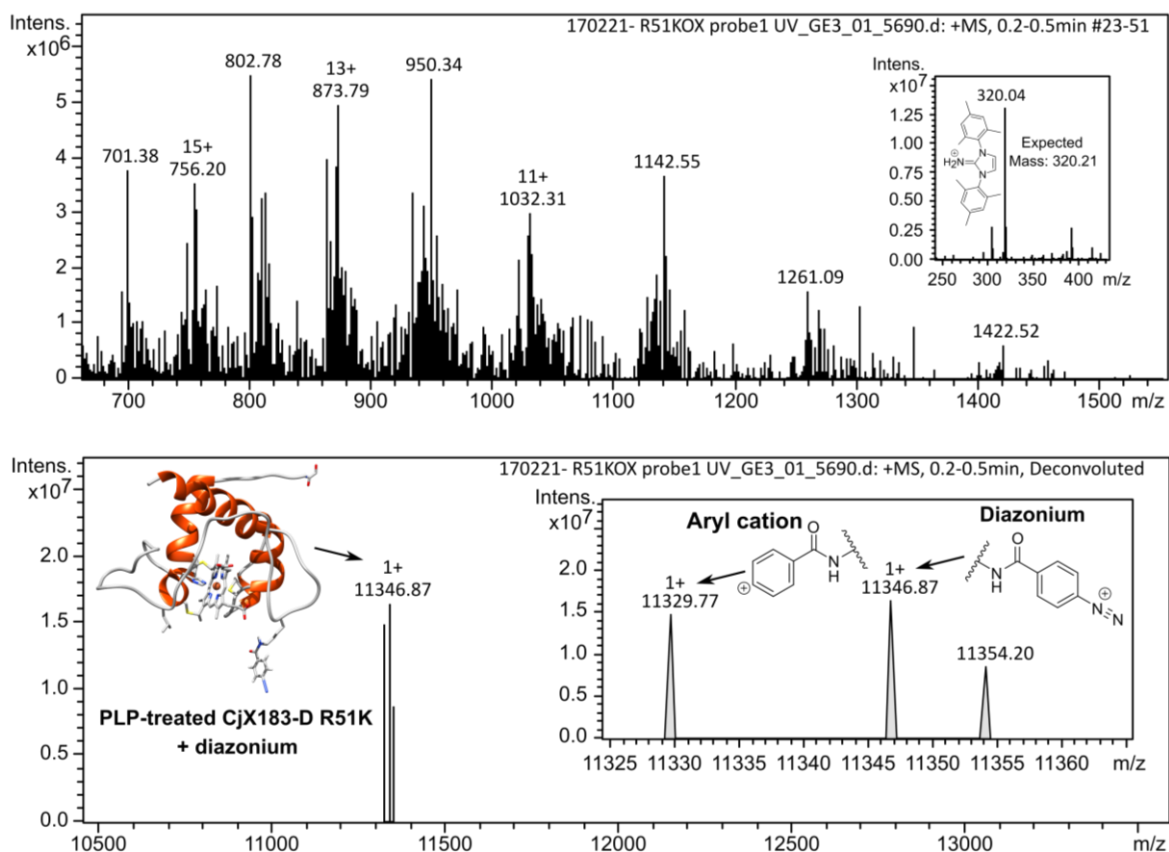


**Figure 6.32.** Positive ion mode ESI-LC/MS analysis of a sample of PLP-treated CjX183-D R51K reacted with **T14** using the conditions described in **Table 6.7 Entry 2**, purified using a His SpinTrap™, and then treated with 365 nm UV irradiation from a 7 W 365 nm UV light bulb at 0 °C for 3 min. **Bottom**) Deconvoluted mass spectrum. A peak would be expected at +149.11  $m/z$  for protein labelled with the free diazonium and with an *N*-terminal glyoxylamide in a hydrated form (at  $m/z$  11359.26 if accounting for the +12 Da systematic error, and at  $m/z$  11347.26 if using the theoretical mass of the protein). A peak would be expected at +103.10  $m/z$  relative to CjX183-D R51K for a carbocation probe at ( $m/z$  11331.25 when accounting for the +12 Da systematic error).

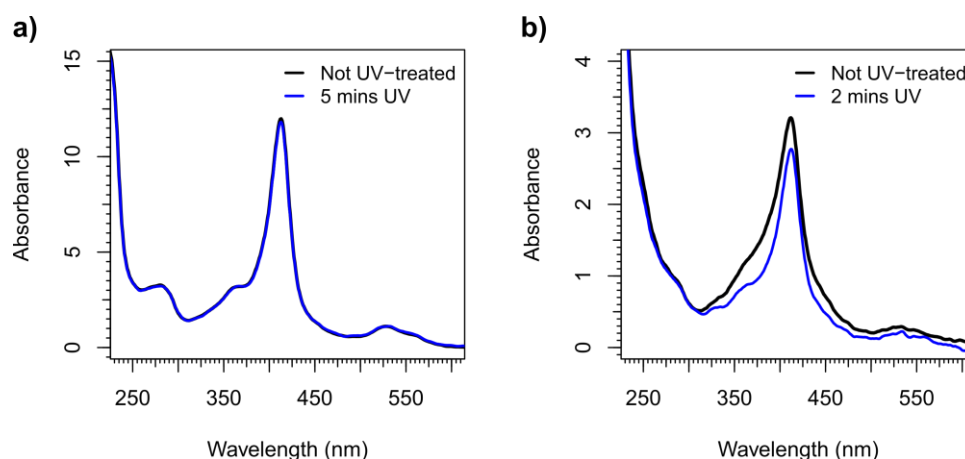


**Figure 6.33.** **a)** UV-vis experiments showing that the UV-vis spectrum of CjX183-D R51K does not change after exposure to UV-radiation for a short period of time. **b)** UV-vis experiments showing that the UV-vis spectrum of triazabutadiene-labelled CjX183-D R51K changes after exposure to UV-radiation for a short period of time, with the visible absorption peak at 410 nm becoming slimmer in profile due to the loss of the underlying broad triazabutadiene absorbance band. UV-treated samples exposed to UV light for the specified time 0 °C using a 7 W 365 nm UV light bulb.

## 6.2.5 Preliminary attempts at diazonium electro-grafting using triazabutadiene-labelled proteins

### 6.2.5.1 Attempted usage of DsbA<sub>middle</sub> + T8 in direct electro-grafting to electrode surfaces

A sample of DsbA<sub>middle</sub> labelled with T8 was exchanged into pH 7.2 buffer (20 mM sodium phosphate, 200 mM NaCl) using a PD MiniTrap™ G-25 desalting column and concentrated to about 700 μM.

Both a BDD and a GC electrode were freshly polished, and a CV, an FTacV experiment and an impedance experiment were recorded at 25 °C over the range of 0.2 → -0.6 V vs SHE in pH 7.2 buffer (20 mM phosphate, 200 mM NaCl); a redox window which should encompass the reduction potential of DsbA (which has been reported as -89 mV or -124 mV vs SHE).<sup>547</sup> The buffer was then taken and subjected to UV irradiation for 4 min, with care being taken to ensure that the electrode surface was not exposed to any radiation (as the exposure of BDD surfaces to UV irradiation caused the appearance of redox signals, presumably due to a photovoltaic effect<sup>548</sup>). The electrode was then re-immersed in the buffer and an amperometric trace was recorded, holding at -0.56 V vs SHE for 10 min. After this time the electro-grafting buffer was replaced with fresh (i.e. not UV-treated) buffer and a

CV, an FTacV experiment and an impedance experiment were recorded. The process was then repeated with a 700  $\mu\text{M}$  sample of **T8**-labelled DsbA<sub>middle</sub> (in pH 7.2, 20 mM phosphate, 200 mM NaCl buffer). The CVs for both the control and the DsbA<sub>middle</sub> experiments are shown in **Figure 6.34**. The third harmonics of the FTacV experiments for both the control and the DsbA<sub>middle</sub> experiments are shown in **Figure 6.35**. There would appear to be a faint signal in evidence at approximately -0.05 V vs SHE in **Figure 6.34 bottom left**, which could conceivably be from DsbA<sub>middle</sub>. However, this signal was not in evidence in the FTacV data, suggesting that if this signal is present, it is from a slow electron transfer process.

For both GC and BDD electrodes, the FTacV data (**Figure 6.35**) shows a profound dampening of Faradaic signals to occur after an amperometric experiment with **T8**-labelled DsbA<sub>middle</sub> is performed, which could indicate that DsbA<sub>middle</sub> is coating the electrode surface and smothering the background electrode activity of the electrode. The absence of redox signals derived from DsbA<sub>middle</sub> is not easily explained, but could be due to the DsbA<sub>middle</sub> becoming immobilised in an orientation that does not facilitate direct electron transfer, or could be due to the DsbA<sub>middle</sub> being redox inactive (perhaps the incorporation of a mutant cysteine residue in a thiol disulfide oxidoreductase causes unseen problems, such as the transient formation of unintended intra-chain disulfides, causing misfolding) or only capable of slow direct electron transfer. The active site disulfide of DsbA is indeed known to be more stable when DsbA is misfolded.<sup>549</sup> To test the redox activity of the DsbA<sub>middle</sub> mutant, FTacV of DsbA<sub>middle</sub> was attempted with a PGE electrode in the hope that some DsbA<sub>middle</sub> would adsorb in an electroactive orientation, and the highly sensitive FTacV technique would be able to detect Faradaic signals from this population. The results of this experiment are shown in **Figure 6.36**. Note that the DsbA<sub>middle</sub> sample applied to the PGE electrode surface had been pre-treated with TCEP and the TCEP had been removed prior to application to the PGE electrode surface.



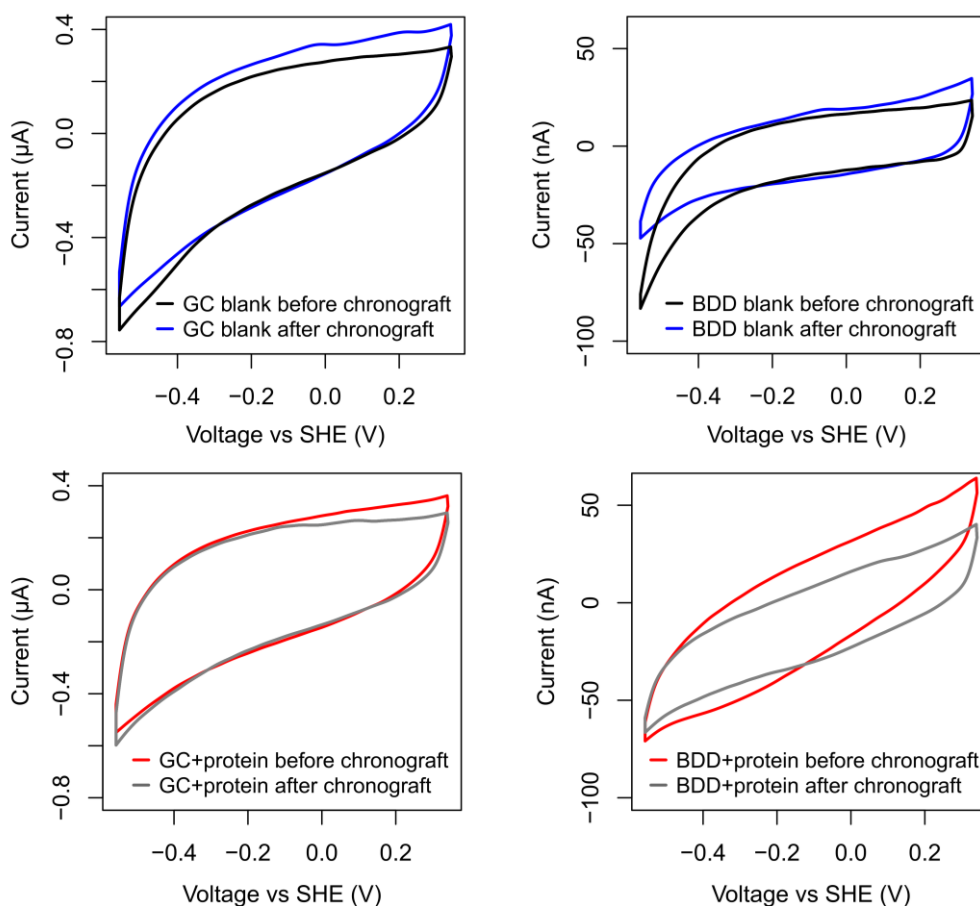


**Figure 6.34.** (Top) Cyclic voltammograms recorded at  $25 \text{ mV s}^{-1}$  in a pH 7.2 (20 mM phosphate, 200 mM NaCl) buffer solution at  $25 \text{ }^\circ\text{C}$  using a GC electrode (Left) and a BDD electrode (Right) both before and after performing an amperometric experiment holding at  $-0.56 \text{ V vs SHE}$  for 10 min. (Bottom) Cyclic voltammograms recorded at  $25 \text{ mV s}^{-1}$  in a  $700 \text{ }\mu\text{M}$  solution of **T8**-labelled  $\text{DsbA}_{\text{middle}}$  (exposed to UV light for 3 min at  $0 \text{ }^\circ\text{C}$  using a 7 W 365 nm UV light bulb) in pH 7.2 (20 mM phosphate, 200 mM NaCl) buffer solution at  $25 \text{ }^\circ\text{C}$  using a GC electrode (Left) and a BDD electrode (Right), both before and after performing an amperometric experiment holding at  $-0.56 \text{ V vs SHE}$  for 10 min.

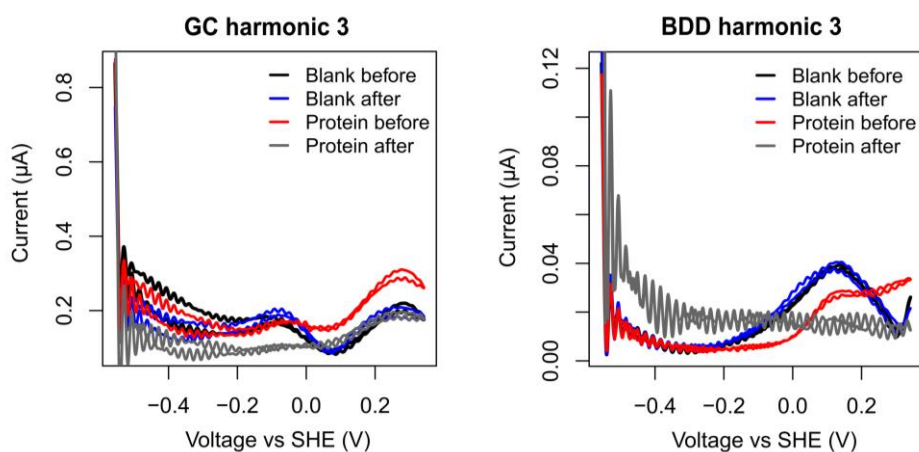


**Figure 6.35.** The third harmonic for the FTacV experiments recorded at  $16.76 \text{ mV s}^{-1}$  with an applied sinusoidal waveform with a frequency of 8.9 Hz and an amplitude of 150 mV in a pH 7.2 (20 mM sodium phosphate, 200 mM NaCl) buffer solution at  $25 \text{ }^\circ\text{C}$  using a GC electrode (left) and a BDD electrode (right) both before and after performing an amperometric experiment holding at  $-0.56 \text{ V vs SHE}$  for 10 min for both control and  $\text{DsbA}_{\text{middle}} + \text{T8}$  experiments.

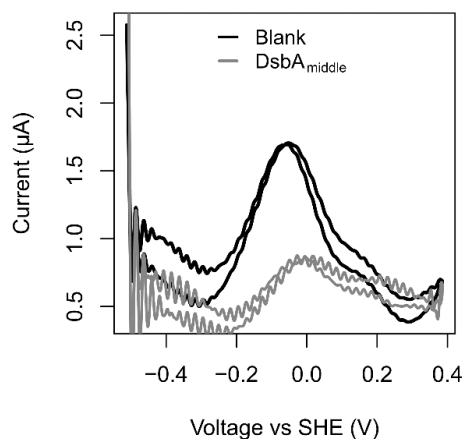


**Figure 6.36.** The third harmonic of an FTacV experiment recorded at  $16.76 \text{ mV s}^{-1}$  with an applied sinusoidal waveform with a frequency of 8.9 Hz and an amplitude of 150 mV in a pH 7.2 (20 mM phosphate, 200 mM NaCl) buffer solution at 25 °C using PGE electrode both before and after applying a film of DsbA<sub>middle</sub> (as a 10  $\mu\text{L}$  droplet of a 120  $\mu\text{M}$  solution, which was allowed to adsorb for 5 min).

**Figure 6.36** shows a similar trend to that shown in **Figure 6.35**, in that the only effect the presence of DsbA<sub>middle</sub> seems to have is a dampening effect on the background electrode activity. No discernible redox signals can be seen beyond harmonic 4 when DsbA<sub>middle</sub> is applied to the PGE electrode (data not shown), whereas in the absence of DsbA<sub>middle</sub> background electrode activity can still be seen. This is in stark contrast with the FTacV obtained by previous members of the Parkin lab for a different active-site disulfide containing redox protein, HypD, which gave strong and clear disulfide-derived Faradaic signals even at high harmonics (and was electroactively immobilised via simple adsorption on a PGE electrode).<sup>264,550</sup> Redox signals from DsbA observable via PFV have only been reported once in the literature (and in this instance a PGE electrode was also used), and the authors do report experiencing difficulty when trying to obtain these signals.<sup>426</sup> All other reduction potentials reported for DsbA have been determined using redox titration. This would perhaps indicate that while DsbA may be an interesting protein with which to eventually showcase the power of the direct diazonium electro-grafting of redox proteins to electrode surfaces in chosen orientations, its poorly characterised PFE makes it a non-ideal protein for use in the initial development of the direct diazonium electro-grafting of redox proteins methodology.

### 6.2.5.2 Attempted usage of triazabutadiene-labelled CjX183-D R51K in direct electro-grafting to electrode surfaces

A series of PLP-treated CjX183-D R51K samples were prepared, either unlabelled or labelled with a triazabutadiene on the mutant lysine via reaction with **T14**, as is described in **Section 6.2.4.1**. These samples were subjected to a series of conditions/treatments in an effort to immobilise the proteins onto a PGE electrode. These conditions/treatments are tabulated in **Table 6.8**, including an attempt at direct diazonium electro-grafting using a sample of triazabutadiene-labelled PLP-treated CjX183-D R51K. Note that the CVs recorded during the electro-grafting process for this conjugate did not show the broad reductive wave typically associated with diazonium electro-grafting (see **Appendix 3, Figure S6**). However, the reductive current that would be recorded from a 20  $\mu\text{M}$  solution of a diazonium cation functionalised protein would be minimal, as the solution is not only dilute, but the protein would also be expected to diffuse slowly, leading to a slow rate of electro-reduction and a correspondingly low current. The only feature that distinguishes the electro-grafting CVs of the CjX183-D conjugate from that of a blank solution is the Faradaic signal from the  $\text{Fe}^{(\text{III/II})}$  redox couple of CjX183-D (see **Appendix 3, Figure S6**).

**Table 6.8.** The treatments the samples of CjX183-D R51K used in electrode-immobilisation experiments were subjected to. All CjX183-D R51K samples (including the R51K control) were treated with PLP to convert the *N*-terminal glycine residue to a glyoxylamide, ensuring that triazabutadiene labels were site-selectively introduced onto the mutant lysine residue. Samples treated with UV were exposed to UV light for 3 min at 0 °C using a 7 W 365 nm UV light bulb. Protein samples were in pH 7.5 buffer (25 mM sodium phosphate + 150 mM NaCl). Electro-grafting was performed using a solution of triazabutadiene-labelled protein (25  $\mu\text{M}$ ) in pH 7.5 buffer (25 mM sodium phosphate + 150 mM NaCl) by recording 12 CVs at 50  $\text{mV s}^{-1}$  at 22 °C, using a PGE working electrode cycling between +0.5 and -0.5 V vs SHE under an  $\text{N}_2$  atmosphere using a leak free Ag/AgCl reference electrode (see **Appendix 3, Figure S6**).

Sample name	Triazabutadiene-label	Concentration of protein solution	UV-treatment	Application method
R51K control	<input checked="" type="checkbox"/>	50 $\mu\text{M}$	4 min of irradiation	10 $\mu\text{L}$ droplet, evaporated onto PGE to form a film
No UV, drop-cast	<input checked="" type="checkbox"/>	25 $\mu\text{M}$	None	10 $\mu\text{L}$ droplet, evaporated onto PGE to form a film
UV, drop-cast	<input checked="" type="checkbox"/>	25 $\mu\text{M}$	4 min of irradiation	10 $\mu\text{L}$ droplet, evaporated onto PGE to form a film
UV, electro-grafted	<input checked="" type="checkbox"/>	25 $\mu\text{M}$	4 min of irradiation	Electro-grafted

After immobilisation of the CjX183-D R51K samples onto the electrode, CVs were recorded in triplicate every 5 min over a 20-hour period. A representative CV for each entry in **Table 6.8** is shown in **Figure 6.37**. An automated code (modified from that described in **Appendix 2** to automatically use parameters suitable for the extraction of the Faradaic signals from CjX183-D R51K) was used to isolate

the cathodic peaks from these CVs, and to subsequently use **Equation 4 (Section 1.4.1)** to calculate the electrode coverage of immobilised CjX183-D R51K at each time increment. Plots of electrode coverage vs time could then be constructed for each entry in **Table 6.8**, and these plots are shown in **Figure 6.38**.

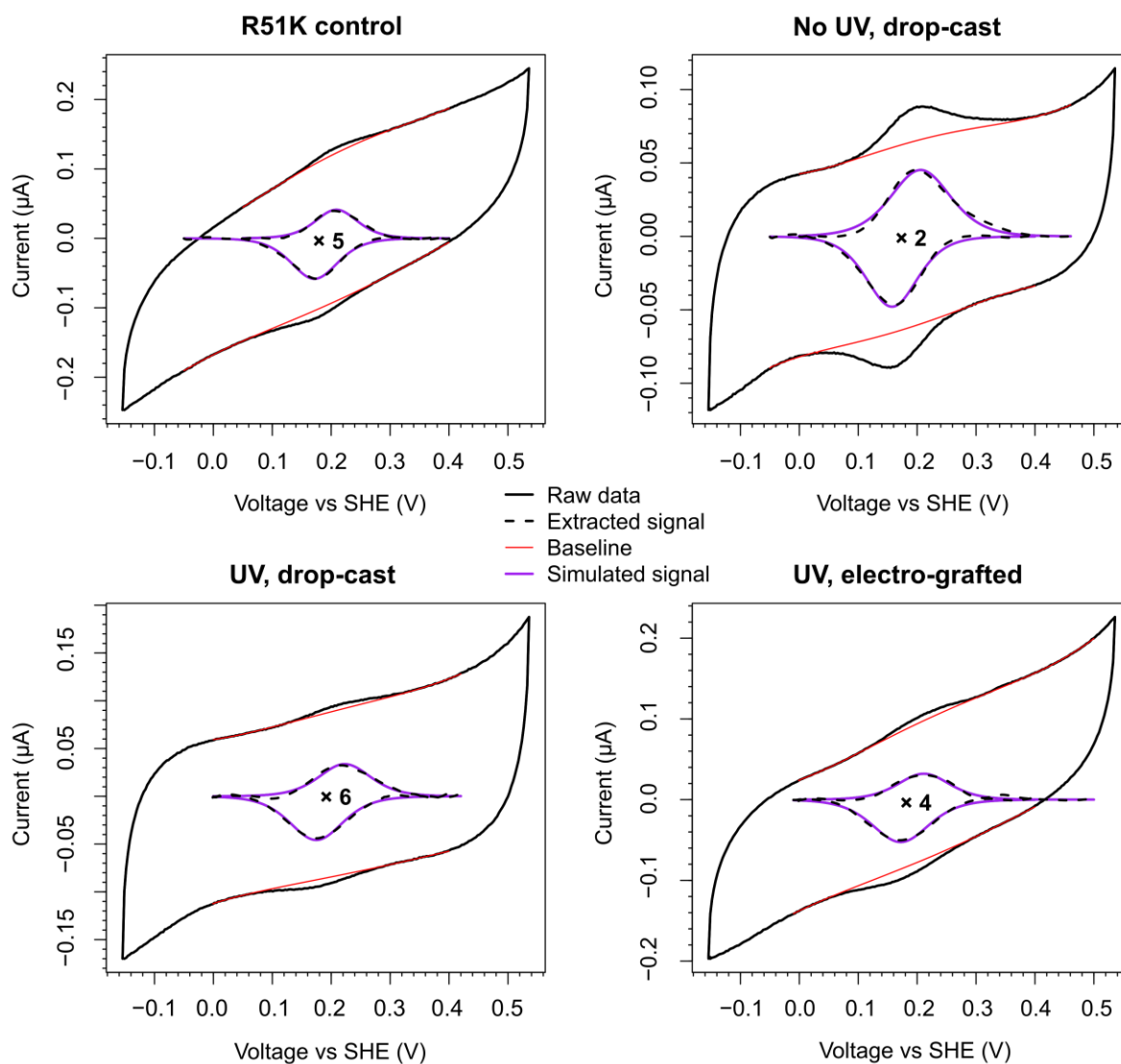


**Figure 6.37.** Representative CVs recorded for the samples of CjX183-D R51K described in **Table 6.8** after 23.7 min on the electrode. CVs were recorded in pH 7 buffer (50 mM phosphate, 150 mM NaCl). The electrochemical experiment was conducted at 5 °C at a scan rate of 30 mV s<sup>-1</sup> under a nitrogen atmosphere, using a Pt counter electrode, a calomel (sat KCl) reference electrode and a PGE working electrode. Scans commenced from the most negative potential.

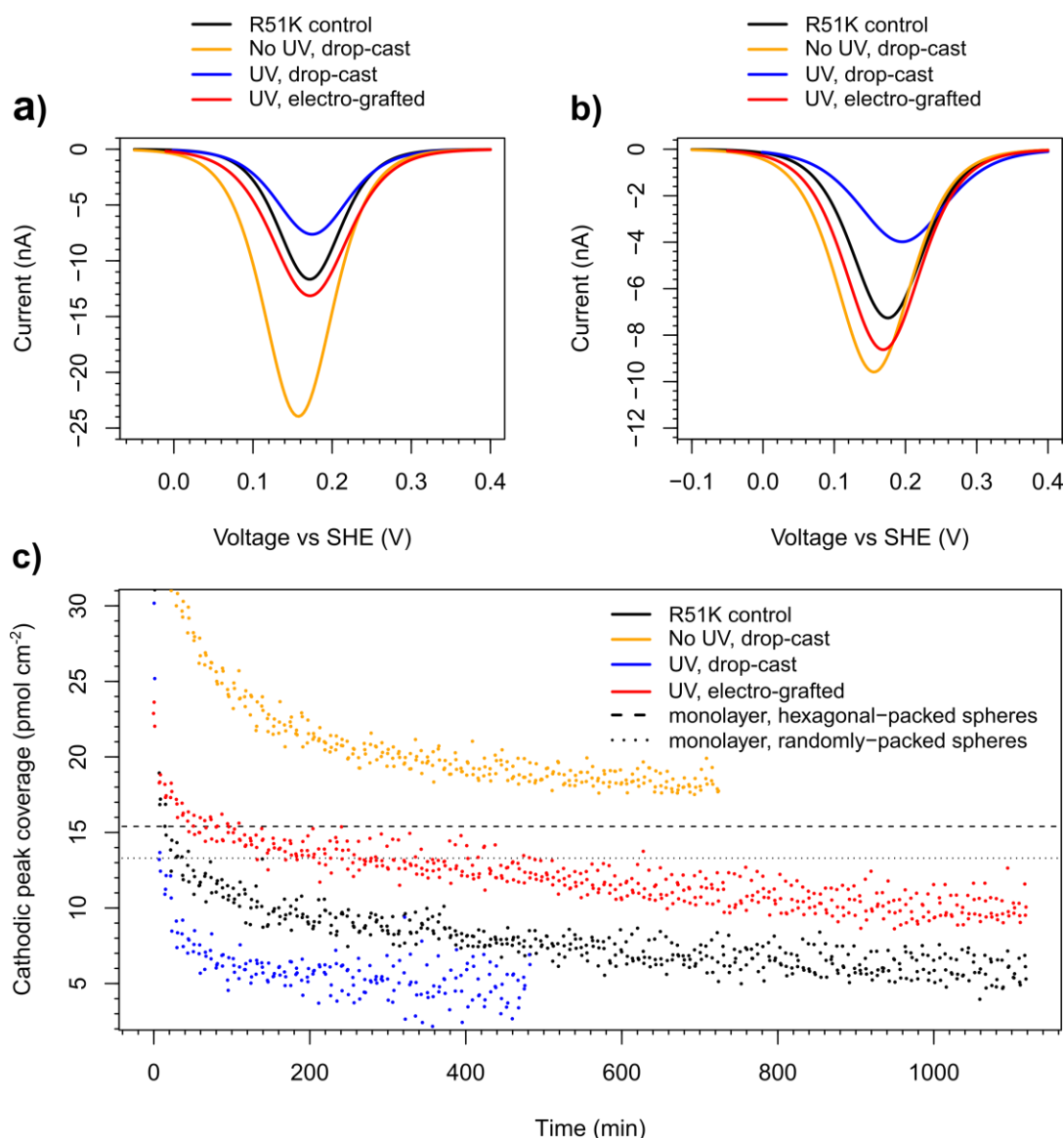


**Figure 6.38.** For each of the electrode-immobilisation experiments described in **Table 6.8**, **a)** The fitted cathodic signals derived from CjX183-D R51K after desorption of protein has been allowed to occur for 3 min. **b)** The fitted cathodic signals derived from CjX183-D R51K after desorption of protein has been allowed to occur for 31 min. **c)** Plots of electrode coverage of CjX183-D R51K against time after electrode tip immersion. The CVs from which these data were extracted were recorded in triplicate every 5 min, under a nitrogen atmosphere in pH 7 buffer (50 mM phosphate, 150 mM NaCl) at 5 °C at a scan rate of 30 mV s<sup>-1</sup> using a Pt counter electrode, a calomel (sat KCl) reference electrode and a PGE working electrode. Scans commenced from the most negative potential.

In a surprising result, **Figure 6.38** shows that the best strategy for CjX183-D R51K immobilisation on a PGE electrode is to label the mutant lysine residue with a triazabutadiene, but then to simply drop-cast the conjugate onto the electrode surface without first using UV-light to reveal diazonium cations and without applying an electro-grafting step (**Table 6.8**, **Figure 6.38**, “No UV, drop-cast”); using this methodology results in a greatest and longest-lasting electroactive coverage of CjX183-D. It could be suggested that the appending of the hydrophobic triazabutadiene unit onto CjX183-D R51K lowers the

solubility of the protein, and that the hydrophobic and aromatic-rich triazabutadiene unit would likely interact favourably with exposed  $\pi$ -systems on the PGE electrode surface. It should be noted that the electroactive coverage maintained using this technique seemingly exceeds the theoretical maximum monolayer coverage estimate for CjX183-D (assuming CjX183-D to be spherical and hexagonally packed on an planar surface of a 2 mm diameter disk electrode), but PGE electrode surfaces are not truly planar and actually have a rough topology (**Section 1.3.1, Figure 1.6**), and thus calculating a theoretical maximum monolayer coverage in this manner will likely give an underestimate. Equally, CjX183-D is not spherical, so may be capable of a more efficient packing than that of spheres.

The second most successful immobilisation strategy is for the UV-treated and electro-grafted sample of triazabutadiene-labelled PLP-treated CjX183-D R51K (**Table 6.8, Figure 6.38, “UV, electro-grafted”**). Use of the “UV, electro-grafted” resulted in a greater coverage of protein than simply drop-casting PLP-treated CjX183-D R51K onto the electrode surface (**Table 6.8, Figure 6.38, “R51K control”**), even though the “UV, electro-grafted” sample was only half the concentration of the “R51K control” sample. The importance of using electro-grafting in addition to UV-treatment in the “UV, electro-grafted” method is verified by the poor performance of the triazabutadiene-labelled PLP-treated CjX183-D R51K sample subjected to UV-treatment but simply drop-cast onto the electrode surface (**Table 6.8, Figure 6.38, “UV, drop-cast”**), which gave the poorest coverage of CjX183-D.

### 6.3 Summary and conclusions

The development of a methodology for the direct electro-grafting of diazonium-cation labelled redox proteins using triazabutadienes is showing great promise. The suitability of diazonium cations released from triazabutadiene-precursors for usage in diazonium electro-grafting has been demonstrated (a literature first), with solutions of diazonium cations released from UV-irradiated triazabutadienes being shown to yield CVs with characteristic broad reductive waves that decay over subsequent scans (**Section 6.2.2**). The most suitable triazabutadiene scaffolds for this application are either those in which  $R^1$  and  $R^2 = \text{Mes}$  and  $R^3$  is a para carbonyl group, or where  $R^1 = (\text{CH}_2)_3\text{SO}_3\text{K}$ ,  $R^2 = \text{Mes}$  and  $R^3$  is a para carbonyl group (using the numbering in **Scheme 6.3**), due to the ability of these scaffolds to rapidly release diazonium cations upon exposure to 365 nm UV irradiation. Of these two triazabutadiene scaffolds, the  $R^1 = R^2 = \text{Mes}$  class was easier to synthesise and were thus investigated more extensively, even though the  $R^1 = (\text{CH}_2)_3\text{SO}_3\text{K}$ ,  $R^2 = \text{Mes}$  class is far more water soluble (**Section 6.2.1**), and investigation of the usage of this more soluble class of triazabutadiene warrants future research.

A synthesis has been developed for a maleimide-functionalised triazabutadiene (**T8**, **Section 6.2.1.1**), which is suitable for site-selection bioconjugation to mutant cysteine residues installed at desired sites in redox proteins via site-directed mutagenesis. While a synthesis has been reported for alkyne-functionalised triazabutadienes, which are suitable for Cu-click chemistry with azides,<sup>531</sup> **T8** is the first reported triazabutadiene that can selectively target cysteine residues. The precursor to this maleimide-functionalised triazabutadiene probe is an NHS-ester functionalised triazabutadiene (**T5**, **Section 6.2.1.1**), which itself can be derivatised with any primary amine-functionalised molecule; this means other bio-orthogonally ligating warheads can be installed onto the triazabutadiene with ease. I report a two-step synthesis of **T5**, whereas the currently published literature synthesis is four steps.<sup>529</sup> A synthesis has also been developed for a sulfo-NHS ester functionalised triazabutadiene (**T14**, **Section 6.2.1.1**), suitable for reaction with protein lysine residues and *N*-terminal glycine residues, which is more water soluble than its literature counterpart, **T5**, and thus a superior reagent for performing bioconjugation reactions.

The ability to install triazabutadienes site-specifically onto redox proteins has been demonstrated for several redox proteins – two cysteine mutants of DsbA (**Section 6.2.4.1**) and a lysine mutant of CjX183-D (**Section 6.2.4.2**) – and has been validated using MS and UV-vis spectroscopy. The ability to site-specifically install triazabutadienes onto proteins also represents a literature first. The ability to unveil diazonium cations suitable for reaction with diazonium-selective probes has been demonstrated, and has been characterised via fluorescent labelling (and SDS-PAGE gel analysis), MS and UV-vis spectroscopy (**Section 6.2.4**). Initial attempts have been made to perform diazonium electro-grafting using UV-treated triazabutadiene-labelled redox proteins at mild pH (**Section 6.2.5**), but these experiments are still in their early stages and a method for the direct diazonium electro-grafting of redox proteins at mild pH requires further development and optimisation. Surface-characterisation techniques such as AFM will also be needed to validate the success of diazonium electro-grafting, as these techniques will be able to determine the orientation of the immobilised proteins, which should be dictated by the site of diazonium cation installation.

# Chapter 7

## Conclusion and future perspectives



## Chapter 7. Conclusion and future perspectives

In conclusion, the works presented within this thesis have led to the development of a several methodologies which add to the literature regarding the electrochemical behaviour of AA9 proteins (**Chapter 2**), surface functionalisation methods (**Chapters 3, 5 and 6**) and protein bioconjugation techniques (**Chapters 4, 5 and 6**). A summary of the findings of each Chapter and future research ideas can be found below.

In **Chapter 2**, the electroactive immobilisation of an LPMO *An6428-AA9* was successfully achieved by adsorption onto MWCNTs, and the reversible  $\text{Cu}^{2+/1+}$  reduction potential of *An6428-AA9* was directly measured as 264 mV vs SHE at pH 7.0 at 25 °C. The first reported amperometric assay of the rate of  $\text{H}_2\text{O}_2$  reduction by an LPMO was also conducted, with the catalytic current response almost perfectly following Michaelis–Menten kinetics.

However, further PFE assay of LPMOs is required to further elucidate their mechanisms of action. In theory, voltammetry measurements could be used to obtain thermodynamic information through the measurement of  $\text{Cu}^{2+/1+}$  reduction potentials in a number of different enzymes and enzyme single-site variants, which could serve as input for computational models. Other insights could also be gained through voltammetric measurements, such as whether any amino acid residues in the active-site (i.e. axial tyrosine residues) or in postulated long range electron transfer pathways<sup>293</sup> are redox-active. Catalytic amperometric experiments could be used to assess the sensitivity of LPMOs to inactivation by hydrogen peroxide, and potentially find the rates at which they reduce  $\text{H}_2\text{O}_2$  and  $\text{O}_2$ . However, this is not currently possible because the MWCNT system used in **Chapter 2** to immobilise the LPMO is in-itself a good  $\text{O}_2$  reduction electro-catalyst. A potential remedy would be to immobilise the LPMOs onto different electrode surfaces, and to achieve this, one could seek to immobilise the LPMO via a conserved tyrosine, thought to be involved in substrate binding, that is solvent-exposed on the flat binding face of many AA9 LPMOs (**Figure 7.1**).<sup>270</sup> An advantage of such a strategy is that this residue could be targeted selectively (it is the most solvent-exposed tyrosine in the crystal structure of *LsAA9*) using 4-nitrobenzene diazonium tetrafluoroborate to yield an azo-dye, which could then be reduced using a reagent such as sodium dithionite ( $\text{Na}_2\text{S}_2\text{O}_4$ )<sup>543</sup> to yield a 3-amino-L-tyrosine residue. The LPMO could then be immobilised using a Diels-Alder reaction using a methodology similar to that described in ref [237] (**Figure 7.1 a**) (the application of the method in ref [237] on myoglobin is shown in **Section 1.3.4.3** in **Figure 1.16**), or perhaps via oxidative coupling to an monolayer-aniline functionalised electrode (such as that obtained in **Section 3.2.1**) via the rapid and chemoselective oxidative coupling of anilines to aminophenols (**Figure 7.1 b**).<sup>551</sup> It would be hoped that the immobilised orientation would be electro-active, as the copper co-factor of LPMOs is located

in the centre of the flat binding face, and tethering via the binding face tyrosine residue would result in the binding face being orientated towards the electrode surface. This could enable comparative studies of the copper redox chemistry of different LPMOs and allow the impact of different active-site on LPMO copper chemistries to be assessed (via comparative studies of LPMO active-site mutants). A limitation of such a short surface tether is that it would probably block substrate binding, which would mean that collecting data that is complementary to certain EPR studies, which have probed active site changes upon substrate binding,<sup>271,552</sup> would be difficult.

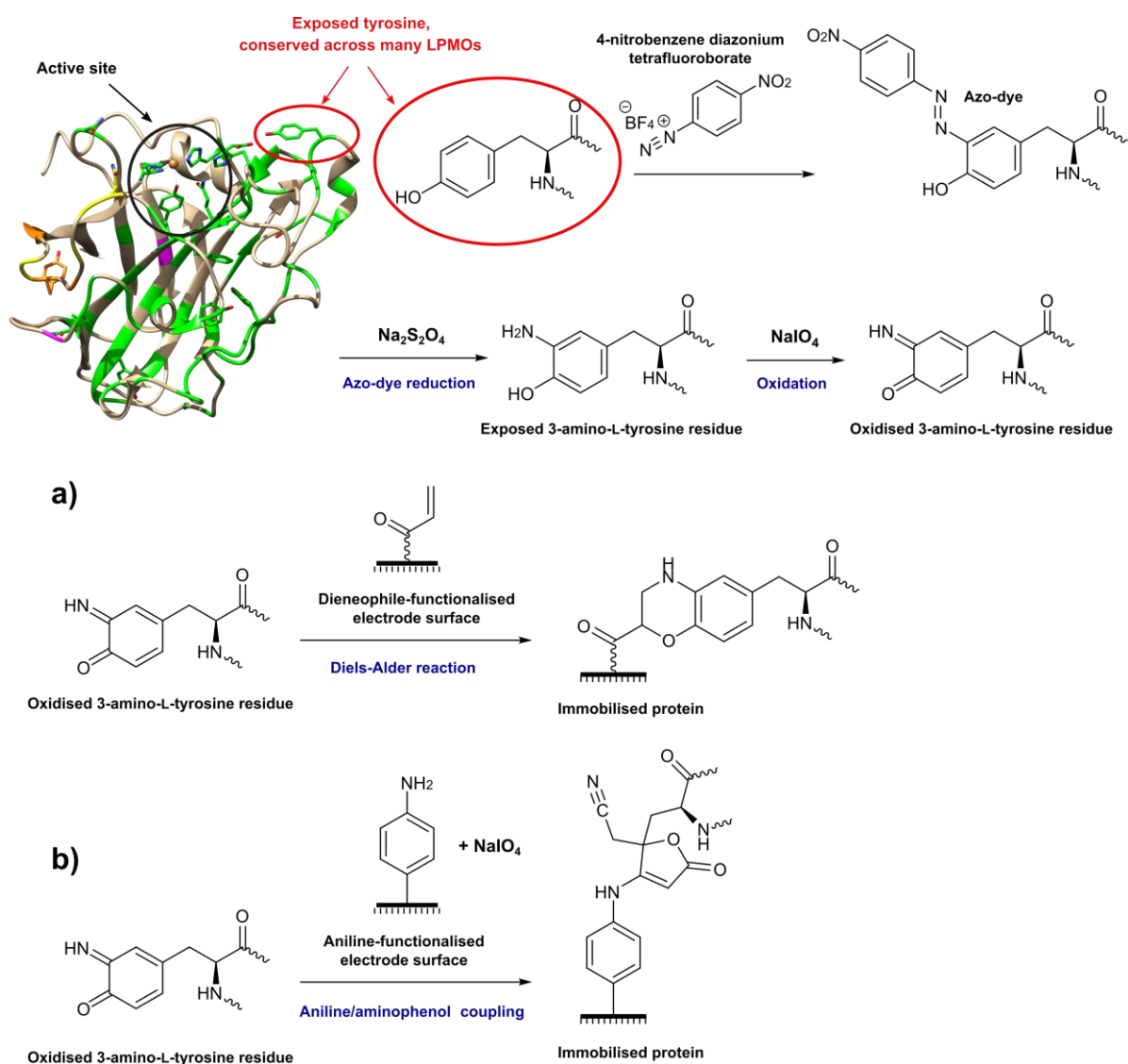


**Figure 7.1.** A potential method for the orientation-specific covalent immobilisation of LPMOs via the targeting of a solvent-exposed tyrosine residue commonly found on the LPMO binding face in the vicinity of the active site. Once a 3-amino-L-tyrosine residue has been installed, crosslinking to the residue could be achieved via **a)** a Diels-Alder reaction or **b)** oxidative coupling to an aminophenol. The LPMO depicted in this figure is *LsAA9* (PDB: 5N05),<sup>300</sup> and is coloured as described in the caption of **Figure 2.8**.

Instead, another interesting application of selective-targeting of the solvent-exposed tyrosine residues of AA9s would be to use this residue, and the mutant lysine residue in CjX183-D R51K (Section 4.2.3.2.3), to prepare crosslinked AA9-CjX183-D constructs (a hypothetical approach is shown in Figure 7.2). The preparation of this construct, where an AA9 is shackled to a physiological redox partner (see Section 4.2.3.1), could result in the AA9 behaving in a manner more reflective of its true behaviour *in vivo*. In addition, CjX183-D adsorbs onto PGE electrode surfaces with ease, and so performing PFE of an AA9-CjX183-D construct may be easier than performing PFE of an AA9 on its own, and even if direct electron transfer between the electrode and the AA9 copper centre is still not possible, the CjX183-D may still be able to mediate the electron transfer, which may still allow the catalytic responses of the AA9 to H<sub>2</sub>O<sub>2</sub> and O<sub>2</sub> to be directly measured and compared, while also hopefully increasing substrate accessibility to the LPMO active site.

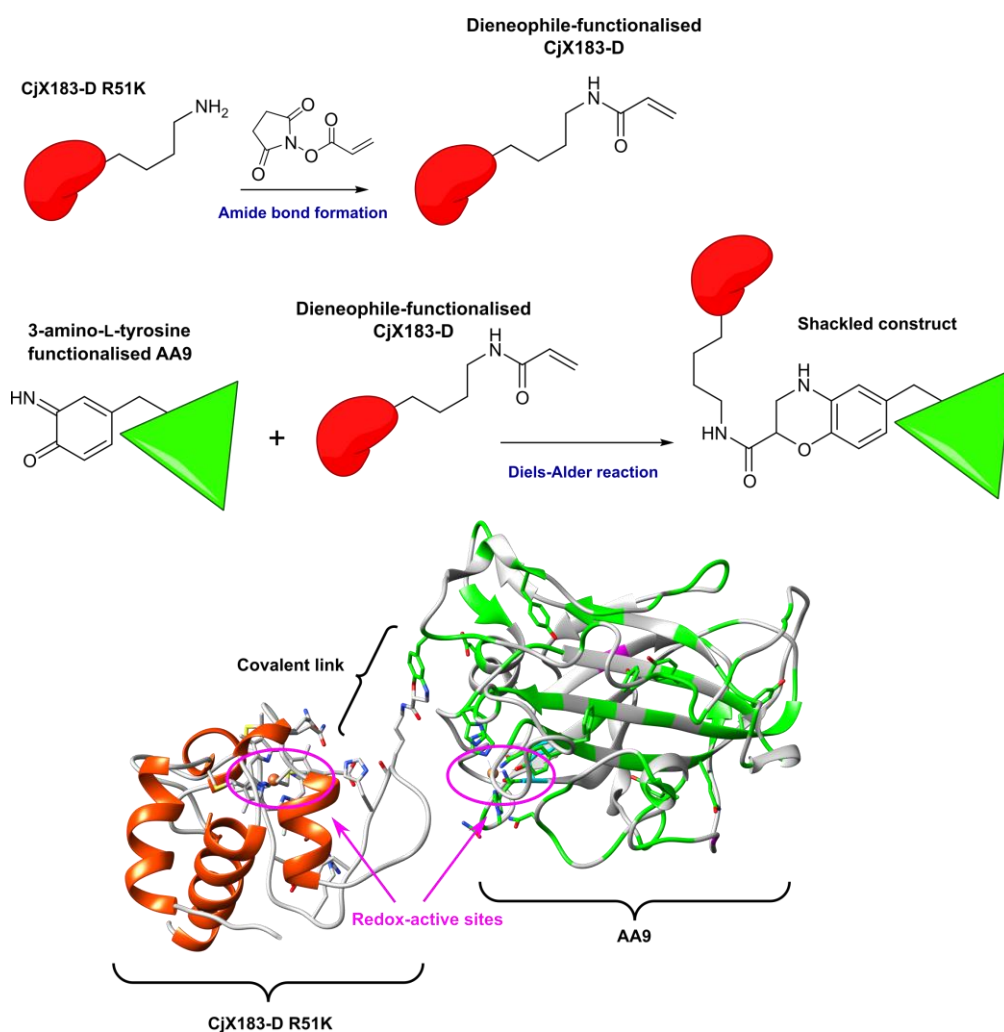


**Figure 7.2.** A potential method for the preparation of a fused construct of CjX183-D and an AA9, via forming a covalent linkage between the mutant lysine residue of CjX183-D R51K and the solvent exposed tyrosine residue located on the binding face of many AA9 LPMOs. The fused CjX183-D-AA9 construct proposed in this figure was made by fusing the crystal structures of CjX183-D (unpublished) and LsAA9 (PDB: 5N05),<sup>300</sup> and is only intended to be an illustration. LsAA9 is coloured as described in the caption of Figure 2.8.

As detailed above, it would be highly desirable to directly measure and compare the rates at which LPMOs turn over polysaccharide substrates using either  $\text{H}_2\text{O}_2$  or  $\text{O}_2$  as co-substrates. However, the delivery of soluble oligosaccharides to the active-sites of electroactively-immobilised LPMOs is likely to prove challenging; not only because (i), as above, electroactively-immobilised LPMOs are likely to be immobilised in such a way the Cu-centre is proximal to the electrode surface (thus constricting access to the active-site), but also because (ii) only a few LPMOs have been shown to bind to soluble oligosaccharide substrates,<sup>300</sup> and higher order polysaccharide polymers are insoluble and slow to diffuse. However, conductive electrode materials comprised of chitin/chitosan carbon nanomaterial composites<sup>87,88,256,553</sup> could prove interesting in this regard, as the presence of chitin/chitosan on the electrode may not only help facilitate binding of LPMOs (especially chitin-active LPMOs) to the electrode, but it may also be possible for the LPMO to use the chitin/chitosan as a substrate while receiving electrons from the electrode surface (although of course, this would have a destructive effect on the substrate which could lead to complications such as desorption). In the presence of this surface-confined substrate, direct electrochemical communication between an LPMO and an electrode might allow a comparative study between  $\text{O}_2$  co-substrate /  $\text{H}_2\text{O}_2$  co-substrate LPMO catalytic cycles to be conducted, and the nature of the electron transfers involved in these catalytic cycles to be assessed.

The suspected formation of “amino-bridges” between MWCNTs and protein lysine residues discussed in **Section 2.2.3** also warrants further investigation. While the appearance of additional redox signals that do not originate from the redox protein under assay is often an annoyance in PFV measurements, these amino bridges could hypothetically act as redox mediators between the electrode surface and the redox centres of the protein active site, so could actually serve to establish electrochemical communication between electrodes and proteins with difficult-to-access redox-active sites. Redox enzymes in which electrons are delivered to the redox-active site via these “amino-bridges” would still be capable of performing redox catalysis (as is likely the case for the  $\text{H}_2\text{O}_2$ -reducing *An6428-AA9* enzyme in **Section 2.2.5**) and thus immobilisation of proteins onto MWCNTs via oxidative coupling through “amino-bridge” formation could be a very useful methodology for the preparation of biosensors. Indeed, briefly applying an oxidising potential across an electrode surface would represent a very mild and simple method of achieving covalent immobilisation of proteins onto nanotube or pyrene-functionalised surfaces. Several variations of this idea can also be proposed (see **Figure 7.3**); firstly, the installation of pyrene motifs onto both the electrode surface and the protein could be used to direct the protein to become adsorbed to the electrode in a chosen orientation, and the subsequent application of an oxidising potential could be used to cross-link the electrode-confined pyrene motif to either a proximal protein lysine residue (**Figure 7.3 i**), or the protein-confined pyrene

motif (**Figure 7.3 ii**), thereby facilitating orientation-selective redox protein immobilisation via covalent bond formation. In another variation, a pyrene motif could be site-selectively appended to a protein via bioconjugation, and the application of an oxidising potential could be used to electro-oxidatively couple the protein onto an amine-functionalised electrode surface (such as the amine-functionalised electrode surfaces prepared in **Chapter 3**) (**Figure 7.3 iii**). Using these premises, it may even be possible to graft arrays of proteins (either redox enzymes or other important biosensing proteins, such as antibodies) onto surfaces via microelectrochemical patterning using scanning electrochemical microscopy (SECM), where the microscopy tip could be used to apply oxidising potentials in a tip-generation/sample-collection mode.<sup>554</sup>

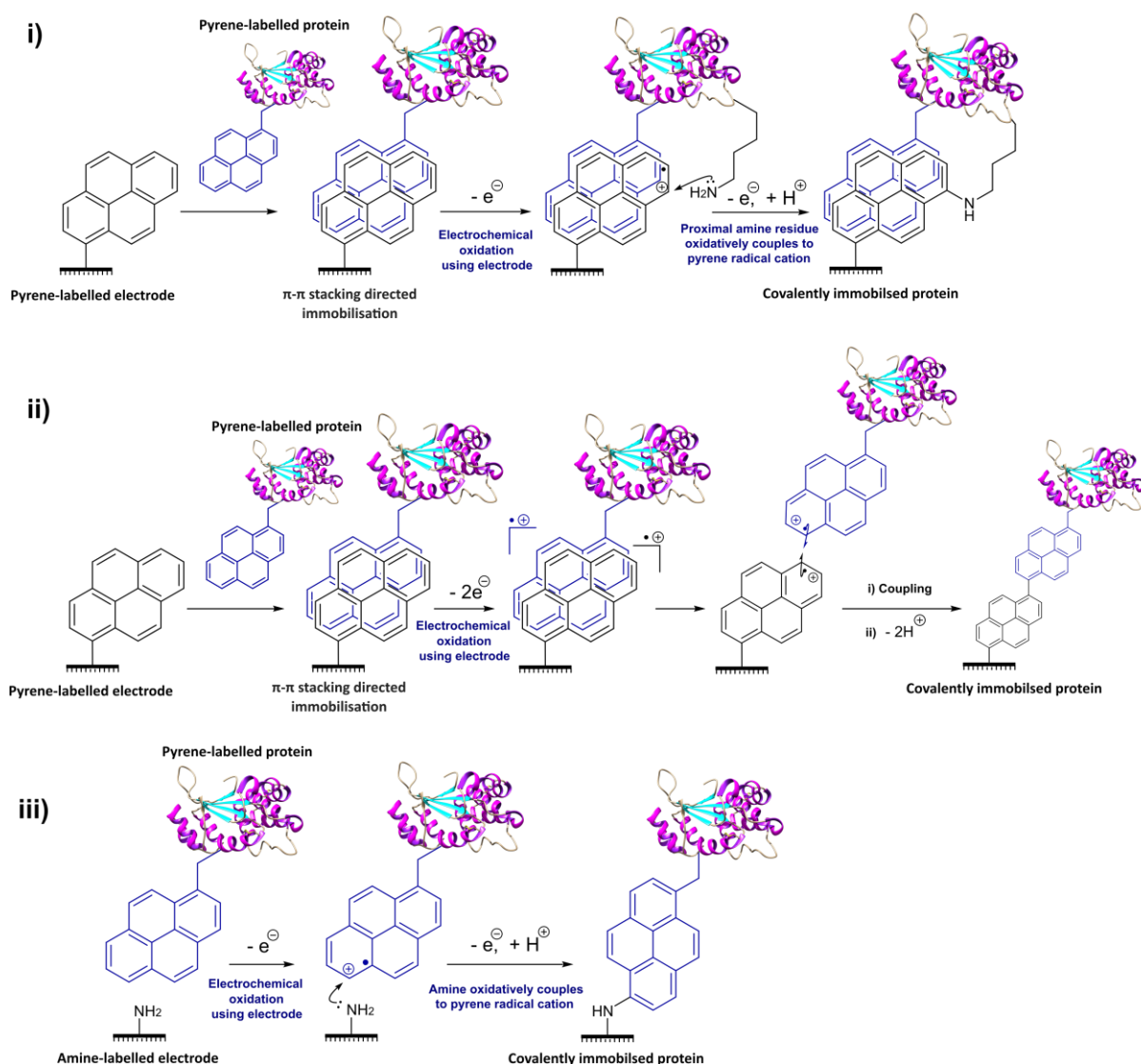


**Figure 7.3.** Potential approaches whereby oxidative amine-pyrene<sup>345</sup> or pyrene-pyrene<sup>555</sup> coupling reactions could be used to facilitate the immobilisation of proteins in specific orientations via covalent bond formation. **i)** Usage of a pyrene-functionalised electrode to direct the orientation in which a pyrene-functionalised protein adsorbs to an electrode via  $\pi$ - $\pi$  stacking, and subsequent electro-oxidative coupling of the electrode-confined pyrene motif to a proximal protein amine residue. **ii)** Usage of a pyrene-functionalised electrode to direct the orientation in which a pyrene-functionalised protein adsorbs to an electrode via  $\pi$ - $\pi$  stacking, and subsequent electro-oxidative coupling of the pyrene motifs. **iii)** Electro-oxidative coupling of a pyrene-functionalised protein to an amine-functionalised electrode surface.

**Chapter 3** describes adaptations of published methods for achieving the monolayer functionalisation of electrode surfaces with amine moieties. Electrode surfaces functionalised with aliphatic primary amines proved to be a versatile platform from which to perform further electrode derivatisation can be achieved, and the coupling of these amine moieties to redox-active molecules served as a useful model system in the development of a new voltammetric technique.

**Chapter 4** described a variety of methods via which proteins can be functionalised with bio-orthogonal aldehyde groups which are the subject of subsequent ligation reactions. Critical assessment of the benefits and drawbacks of each aldehyde introduction and ligation technique allowed for the identification of the techniques that were most suited for redox-protein immobilisation via bio-orthogonal conjugation in **Chapter 5**.

**Chapter 5** further developed and applied the chemistries and techniques explored in Chapters **3** and **4**, leading to the development of an immobilisation methodology whereby redox proteins/enzymes could be immobilised by performing oxime ligation between an electrode surface and an aldehyde-functionalised protein. However, the resultant method was limited in its utility, as the only confirmed case of electroactive protein immobilisation was being obtained for the glycoprotein horseradish peroxidase, via the installation of aldehyde functionalities into its glycans (**Section 5.2.2**). It could be proposed that the limitations of the aforementioned immobilisation methodology at least in part stem from the steric difficulties associated with performing bio-conjugation reactions between macromolecular biomolecules and surfaces, and these steric difficulties likely afflict many of the currently published protein immobilisation methodologies that also seek to form covalent bonds between electrodes and proteins.

In an effort to address the issues encountered in **Chapter 5**, **Chapter 6** describes the proof-of-concept development of a new method of covalently-immobilising redox proteins that is distinct in its approach; instead of performing electrode functionalisations prior to performing bio-conjugation, bioconjugation is performed prior to electrode functionalisation. It is hoped that this will be made possible via the usage of triazabutadienes as a photochemically-caged source of diazonium cations (which are highly effective agents for electrode derivatisation procedures). The usage of triazabutadienes to release diazonium cations that are suitable for diazonium electro-grafting has been demonstrated (**Section 6.2.2**), as has the ability to site-selectively append triazabutadiene motifs onto the surfaces of redox proteins (**Section 6.2.4**). However, initial attempts to perform electro-grafting using triazabutadiene/diazonium cation functionalised redox proteins have not yet yielded definitive results, and the conditions under which these electro-grafting experiments are conducted require both optimisation and trialling across multiple electrode substrates. Further experiments

should seek to further elucidate whether covalent bond formation is being achieved via these triazabutadiene/diazonium cation functionalised redox protein electro-grafting experiments, using techniques such as AFM to probe immobilised protein orientation as a function of the site of triazabutadiene installation.

Currently-published methods for the electro-grafting of diazonium-functionalised proteins to electrode surfaces are limited by the very harsh conditions required to diazotise aniline residues that have been pre-installed onto the protein (i.e. the usage of a HCl/NaNO<sub>2</sub> reagent), very harsh pH (i.e. pH 1.7), and the non-site selective installation of diazonium cations onto the protein surface.<sup>523,524</sup> It is my hope that future development of a triazabutadiene-facilitated protein diazonium electro-grafting methodology will enable orientation-specific covalent electroactive immobilisation of redox proteins to be achieved across multiple conduct substrates via UV-initiated diazonium electro-grafting at pH 7. The UV-initiated electro-grafting of diazonium cations from triazabutadiene precursors could also have interesting future applications in the photopatterning of surfaces, both for triazabutadiene-labelled biomolecules or small molecules, which could be useful in the fabrication of biosensors or novel materials.

# Chapter 8

## Experimental procedures and characterisation



## Chapter 8. Experimental procedures and characterisation

### 8.1 Non-chapter specific experimental procedures/information

#### 8.1.1 Spectroscopic and spectrometric instruments and standard practices

$^1\text{H-NMR}$  (400 MHz) and  $^{13}\text{C-NMR}$  (100 MHz) experiments were conducted using a JEOL 400 instrument at The University York Centre for Magnetic Resonance. Where NMR is reported, multiplicities are given as singlet (s), doublet (d), triplet (t), quartet (q), pentet (p) or multiplet (m). The prefix of “br” indicates a broad signal (i.e. “br s” denotes a broad singlet), and compounded multiplicities are noted appropriately (i.e. “dd” denotes a double doublet, and “dt” denotes a double triplet). In some cases, multiplets may be marked as  $m^{\text{AA'BB'}}$  in order to denote the AA'BB' splitting that is typical of 1,4-disubstituted aromatics. All NMR chemical shifts ( $\delta$ ) were recorded in ppm and coupling constants ( $J$ ) are reported in Hz. ACDLABS 12.0 NMR Processor Academic Edition was primarily used for processing the spectral data.

FTIR spectra were recorded from  $4000 - 400 \text{ cm}^{-1}$  using a PerkinElmer ATR Two FTIR instrument. Unless otherwise stated, UV-vis spectra were recorded using a nanodrop spectrophotometer (DeNovix). ESI-MS experiments used for the characterisation of small molecules were conducted using a Bruker micrOTOF mass spectrometer coupled to an Agilent 1200 series LC system. More details regarding the ESI-LC/MS analysis of peptides and proteins can be found below.

##### 8.1.1.1 ESI-LC/MS of peptides and proteins

Peptide LC-MS analysis was performed on a Dionex UltiMate<sup>®</sup> 3000 Ci Rapid Separation LC system equipped with an UltiMate<sup>®</sup> 3000 photodiode array detector probing at 250-400 nm using a Waters Symmetry C18 3.5  $\mu\text{m}$  column,  $2 \times 60 \text{ mm}$ , coupled to a HCT ultra ETD II (Bruker Daltonics) ion trap spectrometer, using Chromeleon<sup>®</sup> 6.80 SR12 software (ThermoScientific), Compass 1.3 for esquire HCT Build 581.3, esquireControl version 6.2, Build 62.24 software (Bruker Daltonics), and Bruker compass HyStar 3.2-SR2, HyStar version 3.2, Build 44 software (Bruker Daltonics) at The University York Centre of Excellence in Mass Spectrometry (CoEMS). Data analysis was performed using ESI Compass 1.3 DataAnalysis, Version 4.4 software (Bruker Daltonics). Unless otherwise stated in the caption of the relevant Figure, protein LC-MS analysis was conducted in an analogous manner, but without the usage of a column. All peptide/protein mass spectrometry was conducted in positive ion mode unless stated otherwise.

**Analysis of peptide samples:** As stated above peptide samples were analysed using a Symmetry C18 5  $\mu\text{m}$  3.0 x 150 mm reverse-phase column (Waters). Water + 0.1% formic acid by volume (solvent A) and acetonitrile + 0.1% formic acid (solvent B) were used as a mobile phase at a flow rate of 500  $\mu\text{L min}^{-1}$  at room temperature. A multi-step gradient of 7.5 min was programmed as follows: 90% A for 0.5 min, followed by a linear gradient to 95% B over 4.5 min, followed by 95% B for an additional 0.5 min. A linear gradient to 95% A was used to equilibrate the column. Under these conditions all substrate peptides typically eluted between 2.0-4.0 min.

**Analysis of protein samples:** As mentioned above protein samples were analysed without the use of a column. Analysis was performed at room temperature. HPLC-grade water with 0.1% (v/v) formic acid (solvent A) and acetonitrile with 0.1% (v/v) formic acid (solvent B) were used as the mobile phase at a 1:1 ratio over the course of 3 min as follows: 50  $\mu\text{L min}^{-1}$  to 250  $\mu\text{L min}^{-1}$  for 1 min, 250  $\mu\text{L min}^{-1}$  for 1 min, followed by 1000  $\mu\text{L min}^{-1}$  for 1 min. Under these conditions, all proteins typically eluted between 0.1-1.5 min.

Typically, prior to analysis via LC/MS, protein samples would be exchanged into HPLC grade water using an appropriate method (i.e. using dialysis, a centrifugal protein concentrator, a PD MiniTrap™ G-25 desalting column, or a PD SpinTrap™ G-25 desalting column) and diluted into a 50% (v/v) HPLC grade water/acetonitrile, 1% formic acid solution such that the protein concentration was  $\sim 20 \mu\text{M}$ . Where buffer exchange into HPLC grade water was not possible/practical, the protein solution was diluted straight into to the 50% (v/v) HPLC grade water/acetonitrile, 1% formic acid solution. Where, after exchange into HPLC grade water, samples of protein were relatively dilute, the MS sample was prepared by diluting the sample 1:1 with an acetonitrile + 2% formic acid solution.

Specific protein samples may have been analysed via a column-free method using a solariX XR FTMS 9.4T (Bruker) instrument, using ftms Control, ftmsControl 2.1.0 Build: 98 software (Bruker Daltonics). The usage of this instrument instead of the HCT ultra ETD II instrument is specified in the captions of the relevant figures.

### **8.1.2 Sodium dodecyl sulfate polyacrylamide gel electrophoresis (SDS-PAGE) analysis of proteins**

SDS-PAGE was often used for the analysis of protein expression, purification, or bio-conjugation experiments. The percentage of acrylamide used in the preparation of the SDS-PAGE gel is noted in

the captions of the relevant figures. SDS-PAGE gels were poured in-house using a specialised kit. The recipe used to prepare these gels is tabulated in **Table 8.1**.

**Table 8.1.** The composition of SDS-PAGE gels of varying acrylamide percentages. The resolving buffer is (1.5 M Tris-HCl, 0.4% SDS, pH 8.8). TEMED stands for Tetramethylethylenediamine.

<b>% Acrylamide</b>	<b>10</b>	<b>12</b>	<b>15</b>
H <sub>2</sub> O / mL	4	3.2	2.4
Resolving buffer / mL	2.5	2.5	2.5
30% acrylamide stock / mL	3.3	4.2	5
20% ammonium persulfate solution / $\mu$ L	50	50	50
TEMED / $\mu$ L	10	10	10

Once the gel had set a stacking gel was allowed to get on top of the main gel, with a comb inserted to create sample lanes. The recipe for preparing the stacking gel is tabulated in **Table 8.2**.

**Table 8.2.** The composition of SDS-PAGE gels of varying acrylamide percentages. The stacking buffer is (0.5 M Tris-HCl, 0.4% SDS, pH 6.8).

<b>Component</b>	<b>Quantity</b>
H <sub>2</sub> O	3.2 mL
Stacking buffer	1.3 mL
30% acrylamide stock	0.5 mL
20% ammonium persulfate solution	12.5 $\mu$ L
TEMED	8 $\mu$ L

Once the SDS-PAGE gels were fully prepared, complete with stacker gel and sample lanes, the SDS-PAGE gels were ready to be loaded with samples. Unless otherwise stated, samples were mixed with a 5  $\times$  concentrated reducing buffer (10% SDS, 10 mM 2-mercaptoethanol, 20% glycerol, 200 mM Tris-HCl pH 6.8, 0.05% bromophenol blue) and boiled for 5 min prior to running on the SDS-PAGE gel. The molecular weight markers used were either PageRuler Plus Prestained Protein Ladder (ThermoScientific) or SDS-PAGE Molecular Weight Standards, Low Range (Bio-Rad). Each gel was run at 200 V for 30-80 min in SDS running buffer (25 mM Tris, 192 mM Gly, not pH adjusted). In cases where concentrations could be easily determined, typically  $\sim$  2  $\mu$ g of purified protein was loaded into each gel lane when conducting SDS-PAGE analyses.

After being run, SDS-PAGE gels were fixed via gel emersion in a fixing solution (40% water, 50% MeOH, 10% AcOH) which was gently rocked for 60 minutes. For experiments in which the SDS-PAGE gel was subsequently stained with Coomassie stain, the fixed gels were then immersed in a solution of 0.1% Coomassie Brilliant Blue R-250 (in 40% water, 50% MeOH, 10% AcOH), and the solution brought to the

boil in a microwave, before being gently rocked at room temperature for a further 20 min. The Coomassie stained gels would then be destained via emersion in a detaining solution (50% water, 40% MeOH, 10% AcOH), which was periodically replaced with dye-free destaining solution as the destaining process progressed. Images of the resulting gels were captured and analysed using a Syngene G:BOX Chemi XRQ equipped with a Synoptics 4.0 MP camera, with GeneSys software (Version 1.5.7.0). Note that for experiments where fluorescently-labelled proteins were used, imaging of fluorescence was performed after fixing the SDS-PAGE gel in fixing solution, but prior to Coomassie staining.

### 8.1.3 Bradford Assay and protein extinction coefficients

Standards of bovine serum albumin (BSA) were prepared between 0 and 1000  $\mu\text{g mL}^{-1}$  by diluting stock BSA into the relevant protein storage buffer for DsbA<sub>c-term</sub>, DsbA<sub>middle</sub>, Mt-FGE or TcFGE<sub>7</sub>. Each standard/sample (10  $\mu\text{L}$ ) was mixed with 50% (v/v) Bradford reagent (Thermo Scientific) in water (1 mL). The absorbance at 595 nm was measured for each standard and protein sample using a DeNovix spectrophotometer. The protein concentration was determined from a linear standard curve produced from the standards. Where desired, the Beer-Lambert Law molar extinction coefficients at 280 nm ( $\epsilon_{280}$ ) for these proteins could be calculated (**Table 8.3**). The  $\epsilon_{280}$  of DsbA<sub>middle</sub> was taken to be the same as that determined for DsbA<sub>c-term</sub>.

**Table 8.3.** Molar extinction coefficients at 280 nm for the non-commercially available proteins discussed in this thesis.

Protein	$\epsilon_{280}$
DsbA <sub>c-term</sub> / DsbA <sub>middle</sub>	16700 mol <sup>-1</sup> dm <sup>3</sup> cm <sup>-1</sup>
Mt-FGE	77900 mol <sup>-1</sup> dm <sup>3</sup> cm <sup>-1</sup>
TcFGE <sub>7</sub>	78000 mol <sup>-1</sup> dm <sup>3</sup> cm <sup>-1</sup>

The molar extinction coefficients of the heme in CjX183-D proteins were previously determined by the research group of Dr Glyn Hemsworth (University of Leeds) to be as follows (**Table 8.4**). Note that under ambient conditions the CjX183-D proteins can be expected to be in their oxidised state.

**Table 8.4.** Molar extinction coefficients (at wavelengths of 410 nm and 550 nm) for the heme in CjX183-D proteins in different redox states.

Redox state of CjX183-D	Extinction coefficient
Oxidised (i.e. Fe <sup>3+</sup> in heme)	$\epsilon_{410} = 106000 \text{ mol}^{-1} \text{ dm}^3 \text{ cm}^{-1}$
Reduced (i.e. Fe <sup>2+</sup> in heme)	$\epsilon_{550} = 27500 \text{ mol}^{-1} \text{ dm}^3 \text{ cm}^{-1}$

### 8.1.4 Protein preparations

All protein purifications via Nickel-affinity chromatograph using a HisTrap HP column (GE Healthcare) were performed on an AKTA Start, (GE Healthcare). Purifications via size-exclusion chromatography using Superdex S75 gel filtration columns were performed on an AKTA Explorer (GE Healthcare).

#### 8.1.4.1 Preparation of DsbA mutants

##### Transformation of DsbA mutant plasmids into B121 DE3 competent cells and preparation of glycerol stocks

pET151/D-TOPO plasmids bearing custom gene sequences for either DsbA<sub>c-term</sub> or DsbA<sub>middle</sub>, were ordered from LifeTechnologies. The gene sequences of are found in **Appendix 6**. 2  $\mu\text{L}$  of either the DsbA<sub>c-term</sub> or DsbA<sub>middle</sub> plasmid (concentration 100 ng  $\mu\text{L}^{-1}$ ) were added to B121 DE3 electrocompetent cells (50  $\mu\text{L}$ ) on ice, and the cells were then left on ice for 10 min. These cells were then pipetted into the electroporation cuvette, electroporated (at 2.5 kV, on the “Gene Pulse” function), and resuspend in SOC (1 mL, preheated to 37 °C). The resultant solution was then incubated at 37 °C, 240 rpm for 1 hour, before being subjected to centrifugation (1000 g for 2 min). 950  $\mu\text{L}$  of supernatant was removed, and the cells resuspended in the remaining 50  $\mu\text{L}$ . The cells were then plated onto LB-Amp agar and the plate incubated at 37 °C overnight.

2 mL of LB + Amp was inoculated with a single colony from the plate, and incubated at 37 °C, 180 rpm overnight. The cells were pelleted by centrifugation (1000 g for 2 min), and 1.5 mL of the supernatant removed. The cells were resuspended in the remaining 500  $\mu\text{L}$ , and 50% glycerol (750  $\mu\text{L}$ ) was added, pipetting the solution several times to ensure mixing. The resulting solution was flash frozen using liquid N<sub>2</sub> and the resultant glycerol stock stored at -80 °C.

##### Preparation of DsbA<sub>c-term</sub>

B121 DE3 cells transformed with the DsbA<sub>c-term</sub> plasmid were plated from glycerol stocks onto LB-Amp agar and grown at 37 °C overnight. A starter culture of 25 mL LB-Amp was inoculated with a single colony and incubated at 37 °C, 180 rpm. After 5 h the starter culture was added to 2  $\times$  750 mL LB-Amp and grown aerobically at 37 °C, 180 rpm. At OD<sub>600</sub> = 0.8 the incubation temperature was reduced to 16 °C and expression of DsbA<sub>c-term</sub> induced 30 min later by addition of IPTG (0.5 mM). After 16 h, cells were centrifuged (5000 g, 30 min, 5 °C) and the resultant pellet re-suspended in 50 mL buffer C (pH 8.0, 20 mM Tris, 150 mM NaCl, 10% glycerol, 20 mM imidazole) containing half a protease inhibitor tablet (Thermo Scientific) and DNase I (10  $\mu\text{g mL}^{-1}$ ). Cells were lysed by sonication (30 s pulses, 20 microns). Lysate was centrifuged (20000 g, 40 min, 5 °C) and supernatant loaded on a HisTrap HP

column (GE Healthcare) equilibrated with buffer C. After washing with buffer C, DsbA<sub>c-term</sub> was eluted with a linear gradient of buffer D (pH 8.0, 20 mM Tris, 150 mM NaCl, 10% glycerol, 200 mM imidazole) over 8 column volumes. DsbA<sub>c-term</sub>-containing fractions were identified by 12% SDS-PAGE and dialysed overnight in storage buffer (pH 8.0, 20 mM HEPES, 150 mM NaCl, 10% glycerol). Purified DsbA<sub>c-term</sub> was then concentrated using 10 kDa molecular weight cut-off centrifugal protein concentrators to the desired concentration (in this case the DsbA<sub>c-term</sub> concentration was determined to be 230  $\mu$ M via Bradford assay), frozen using liquid N<sub>2</sub>, aliquoted, and stored at -80 °C.

#### Preparation of DsbA<sub>middle</sub>

B121 DE3 cells transformed with the DsbA<sub>middle</sub> plasmid were plated from glycerol stocks onto LB-Amp agar and grown at 37 °C overnight. A starter culture of 25 mL LB-Amp was inoculated with a single colony and incubated at 37 °C, 180 rpm. Three two-litre conical flasks were filled with 600 mL of LB-Amp and 600  $\mu$ L of the starter culture was added to each. The flasks were incubated at 37 °C, 180 rpm, until OD<sub>600</sub> = 0.8. The flasks were then allowed to cool on the bench top for 10 min, after which time IPTG was added such that the concentration in the flasks is 0.5 mM. The flasks were incubated at 16 °C overnight. The cells were then centrifuged (6000 g, 20 min, 4 °C), and the supernatant removed. The cell pellet was resuspended in 25 mL of lysis buffer (pH 8.0, 20 mM Tris, 150 mM NaCl, 10% glycerol), using the lysis buffer to wash out the centrifuge flasks. At this point the suspended cells can be frozen at -80 °C if required.

To the 25 mL of suspended cells was added another 25 mL of lysis buffer, yielding 50 mL of cell solution. A protease inhibitor tablet (Thermo Scientific) was then added, as was 20  $\mu$ L of Benzonase (2.5 U  $\mu$ L<sup>-1</sup>). The solution was sonicated in bursts of 30 seconds (with 30 second cooling times between bursts) on ice until centrifugation of samples of the cell solution showed the presence of nuclear debris (a black dot). The lysed cell solution was then subjected to centrifugation (30750 g, 4 °C, 30 min). The supernatant was isolated, and imidazole added such that that imidazole concentration reached 20 mM.

The supernatant was then loaded on a HisTrap HP column (GE Healthcare) equilibrated with equilibration buffer (pH 8.0, 20 mM Tris, 150 mM NaCl, 10% glycerol, 20 mM imidazole). After washing with equilibration buffer (pH 8.0, 20 mM Tris, 150 mM NaCl, 10% glycerol, 20 mM imidazole), DsbA<sub>middle</sub> was eluted with a linear gradient of elution buffer (pH 8.0, 20 mM Tris, 150 mM NaCl, 10% glycerol, 200 mM imidazole) over 8 column volumes. DsbA<sub>middle</sub>-containing fractions were identified by 12% SDS-PAGE (**Figure 8.1**) and dialysed overnight in storage buffer (pH 8.0, 20 mM HEPES, 150 mM NaCl, 10% glycerol). Purified DsbA<sub>middle</sub> was then concentrated using 10 kDa molecular weight cut-

off centrifugal protein concentrators to the desired concentration, frozen using liquid N<sub>2</sub>, aliquoted, and stored at -80 °C.



**Figure 8.1.** 12% SDS-PAGE analysis of the purification of DsbA<sub>middle</sub> via nickel affinity chromatography. T = total, I = insoluble, L = load, ft = flow-through.

#### 8.1.4.2 Preparation of CjX183-D variants

##### Co-transformation of CjX183-D plasmids and PEC86 into B121 DE3 competent cells and preparation of glycerol stocks

1  $\mu\text{L}$  of either the CjX183D\_pCW or CjX183D-R51K\_pCW plasmids (concentration 50 ng  $\mu\text{L}^{-1}$ ) and 1  $\mu\text{L}$  of the PEC86 plasmid (concentration 50 ng  $\mu\text{L}^{-1}$ ) was added to B121 DE3 chemically competent cells (50  $\mu\text{L}$ ) in a sterile 15 mL falcon tube on ice, and the cells were then left on ice for 30 min. These cells were then heat shocked at 42 °C for 45 seconds before being placed back on ice for 2 min. 200  $\mu\text{L}$  of room temperature SOC media was added and the cells were incubated at then 37 °C at 200 rpm. The cells were then plated onto LB agar (which contained 100  $\mu\text{g}/\text{mL}$  Ampicillin and 35  $\mu\text{g}/\text{mL}$  Chloramphenicol: Amp and ChloroAmp), and the plates incubated overnight at 37 °C. Individual colonies were then selected (successful co-transformation can result in colonies that appear to be a slightly red/orange colour) and transferred into 5 mL 2 $\times$ YT (which contained 100  $\mu\text{g}/\text{mL}$  Ampicillin and 35  $\mu\text{g}/\text{mL}$  Chloramphenicol). The inoculated 2 $\times$ YT was incubated at 37 °C, 180 rpm overnight. 2 mL of the overnight culture was then taken, the cells were pelleted by centrifugation (1000 g for 2 min), and 1.5 mL of the supernatant was removed. The cells can be red/pink in colour. The cells were resuspended in the remaining 500  $\mu\text{L}$ , and 50% glycerol (750  $\mu\text{L}$ ) was added, pipetting the solution several times to ensure mixing. The resulting solution was flash frozen using liquid N<sub>2</sub> and the resultant glycerol stock stored at -80 °C.

**Preparation of CjX183-D protein variants**

B121 DE3 cells co-transformed with either the CjX183D\_pCW or CjX183D-R51K\_pCW plasmid and PEC86 were plated from glycerol stocks onto LB-Amp+ChoroAmp agar and grown at 37 °C overnight. A single colony was then selected and grown in 5 mL of 2×YT (with Amp and ChloroAmp) at 37 °C and 200 rpm throughout the day. This culture was then transferred into 100 mL 2×YT (with Amp and ChloroAmp) and incubated overnight at 37 °C and 200 rpm. After this time, as a preliminary test to confirm that both the desired plasmids are in these cells, a portion of these cells were pelleted via centrifugation, and were red/pink in colour.

10 mL of the overnight culture was then used to inoculate 1000 mL of 2×YT (with Amp and ChloroAmp) in a non-baffled conical flask, and the conical flask was incubated at 37 °C and 180 rpm until  $OD_{600} = 0.6$ . The culture was then cooled to 16 °C and shaken at 150 rpm before inducing using a 1 mM concentration of IPTG (delivered via the addition of 1 mL of a 1 M IPTG solution). Cultures were then incubated at 16 °C and 150 rpm overnight.

Cells were harvested via centrifugation (6000 g, 4 °C, 20 min) and the supernatant removed. The cells were pink in colour (**Figure 8.2 a**). The cell pellet was resuspended in 25 mL of lysis buffer (20 mM Tris, 150 mM NaCl, 10% glycerol, pH 8.0), using the lysis buffer to wash out the centrifuge flasks. At this point the suspended cells can be frozen at -80 °C if required.

To the 25 mL of suspended cells was added another 25 mL of lysis buffer, yielding 50 mL of cell solution. A protease inhibitor tablet (Thermo Scientific) was then added, as was 20 µL of Benzonase (2.5 U µL<sup>-1</sup>). The solution was sonicated in bursts of 30 seconds (with 30 second cooling times between bursts) on ice until centrifugation of samples of the cell solution showed the presence of nuclear debris (a black dot). The lysed cell solution was then subjected to centrifugation (30750 g, 4 °C, 30 min). The supernatant was isolated, and imidazole added such that that imidazole concentration reached 30 mM.

The supernatant (**Figure 8.2 b**) was then loaded on a HisTrap HP column (GE Healthcare) equilibrated with equilibration buffer (pH 8.0, 20 mM Tris, 200 mM NaCl, 30 mM imidazole). After washing with equilibration buffer (pH 8.0, 20 mM Tris, 200 mM NaCl, 30 mM imidazole), the CjX183-D variant was eluted with a linear gradient of elution buffer (pH 8.0, 20 mM Tris, 200 mM NaCl, 300 mM imidazole) over 10 column volumes. The presence of CjX183-D holo-protein on the HisTrap HP column is clearly visible (**Figure 8.2 c**). The CjX183-D variant-containing fractions were identified by 15% SDS-PAGE (**Figure 8.3**) (but these fractions were also red!) and dialysed overnight into storage buffer (pH 8.0, 20 mM Tris, 200 mM NaCl). The CjX183-D variant solution was then concentrated to 2 mL using 3 kDa molecular weight cut-off centrifugal protein concentrators and purified using a HiLoad



Superdex® S75 column (GE Healthcare) equilibrated with storage buffer (pH 8.0, 20 mM Tris, 200 mM NaCl) (**Figure 8.2 d**). A 2000  $\mu\text{L}$  injection loop was used and the column was run at a flow rate of  $1 \text{ mL min}^{-1}$ , collecting fractions after  $\frac{1}{3}$  of a column volume had been passed. Fractions containing the purified CjX183-D variant were identified by 15% SDS-PAGE (**Figure 8.4**) (these fractions were also red, **Figure 8.2 e**), concentrated using 3 kDa molecular weight cut-off centrifugal protein concentrators to the desired concentration, frozen using liquid  $\text{N}_2$ , aliquoted, and stored at  $-80 \text{ }^\circ\text{C}$ .



**Figure 8.2.** The appearance of pellets/solutions encountered throughout the preparation of CjX183-D variants. **a)** The cell pellet of CjX183-D holo-protein containing cells. **b)** The CjX183-D holo-protein containing supernatant of the cell lysate. **c)** CjX183-D holo-protein being retained on a HisTrap HP column. **d)** CjX183-D holo-protein travelling through a HiLoad Superdex® S75 column. **e)** Purified CjX183-D holo protein.

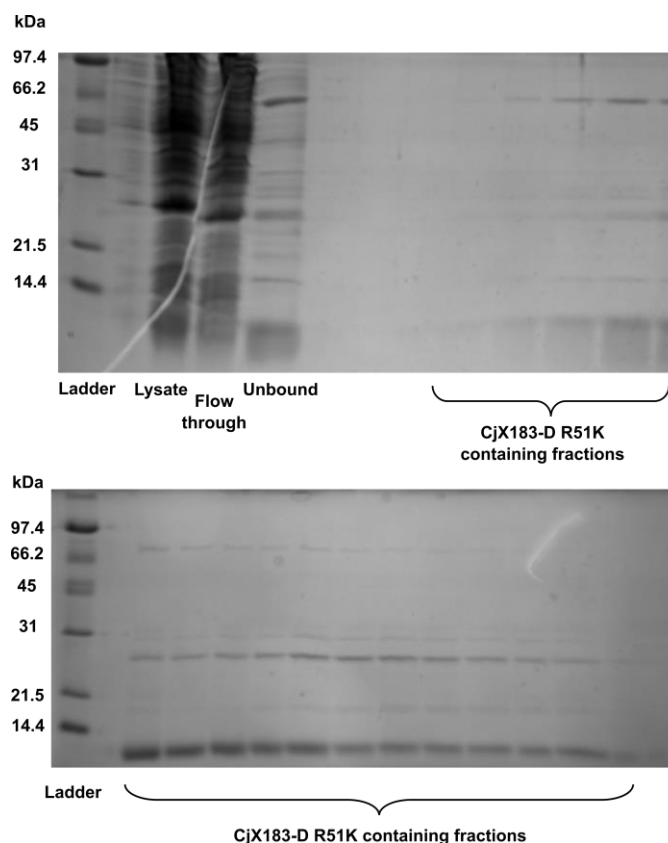


**Figure 8.3.** 15% SDS-PAGE gel showing the purification of CjX183-D R51K using Ni-affinity chromatography. CjX183-D R51K has a theoretical molecular weight of 11.2 kDa, including the covalently attached c-type heme unit.

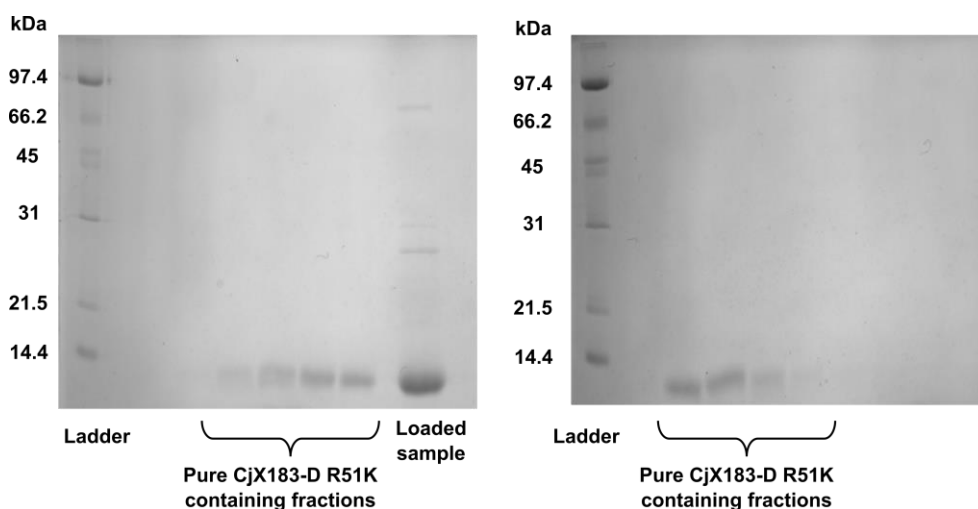


**Figure 8.4.** 15% SDS-PAGE gel showing the purification of CjX183-D R51K via size-exclusion chromatography. CjX183-D R51K has a theoretical molecular weight of 11.2 kDa, including the covalently attached c-type heme unit.

## 8.1.5 Electrochemical apparatus and standard electrochemical practice

### 8.1.5.1 Electrochemical cells and electrode setup

Experiments were conducted in all-glass electrochemical cells (constructed in-house by University of York Department of Chemistry Glass Workshop) which support a three-electrode setup (**Figure 8.5**). The three-electrode setup consists of a working electrode, a Pt wire counter electrode, and a reference electrode - either a Ag/AgCl (3 M NaCl) electrode, a saturated calomel electrode (SCE), or a leak-free Ag/AgCl electrode. The SCE was purchased from Scientific Laboratory Supplies (SLS) and the Ag/AgCl (3 M NaCl) and leak-free Ag/AgCl electrodes were purchased from Alvatek. The Pt wire counter electrode was made in-house from wire of 1 mm diameter, purchased from Sigma-Aldrich.

When in use the Ag/AgCl (3 M NaCl) reference electrode was commonly housed in a Luggin capillary (which was filled with 3 M NaCl), which interfaces with the electrolyte solution under assay (**Figure 8.5A**). As a practical note, it was found that usage of a Luggin capillary is not suitable for FTacV or PSV experiments, presumably due to the Luggin capillary somewhat restricting the electrical contact between the reference electrode and the electrolyte solution under assay, making it difficult for the potentiostat to apply rapid changes/oscillations in the applied electrode potential. As such, all FTacV experiments were performed using the SCE electrode, which was able to directly interface with the electrolyte solution under assay due to its length and frit (**Figure 8.5**). Note that the leak-free Ag/AgCl electrode was also unsuitable for FTacV experiments.

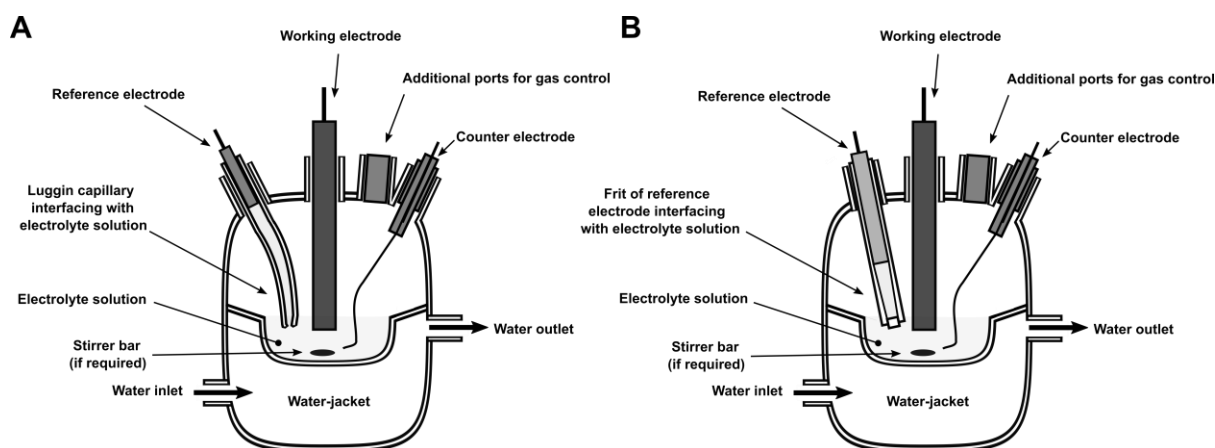


**Figure 8.5.** Setup of water-jacketed electrochemical cells supporting a three-electrode setup. The atmosphere inside the cells can also be controlled. **A)** Usage of a reference electrode that interfaces with the electrolyte under assay via a Luggin capillary, as is appropriate for dCV, impedance and chronoamperometry/ampereometry experiments. **B)** Usage of a reference electrode which interfaces directly with electrolyte solution under assay, as is appropriate for dCV, impedance, chronoamperometry/ampereometry, PSV and FTacV experiments.

The interior temperature of the electrochemical cells could be controlled using a water-jacket and a thermostatted water circulator (Grant) (**Figure 8.5**). With the exception of experiments stated to have been conducted under an ambient atmosphere (which were conducted in a fume hood), experiments were conducted in a glovebox (in-house design and construction) which itself is under an  $N_2$  atmosphere ( $O_2 \leq 40$  ppm), yet the atmospheric composition inside the cells can be further controlled via the connection of the cell to the house gas-lines, using a mass flow controller (Sierra Instruments) to control and monitor the rate of influx of different gases. In these experiments a bubbler (filled with paraffin oil or water) was connected to the gas outlet of the cell to provide visual confirmation of the movement of gases through the cell. The working electrode was not rotated in any experiments, but for chronoamperometry/ampereometry experiments the electrolyte solution was stirred using a magnetic stirrer bar and a battery-powered stirrer plate.

#### 8.1.5.2 Working Electrodes

3 mm diameter disk working electrodes were either purchased from BASI (GC electrodes used in **Chapter 3**), eDAQ (GC electrodes used in **Chapters 5** and **6** and gold electrodes), Windsor Scientific (BDD electrodes) or OrigaLys (GC “OrigaTip” electrodes, used in **Chapter 2**). 2 mm diameter PGE working electrodes were constructed in house.

#### 8.1.5.3 Potentiostats

An EmStat<sup>3</sup> potentiostat (PalmSens) with PSTrace 4.4 for Windows software was used for all electrochemical experiments conducted under an ambient atmosphere. Experiments conducted in

the glovebox utilised a CompactStat potentiostat (Ivium technologies) with IviumSoft software for Windows.

Custom-made instrumentation was used to perform FTacV and PSV experiments (and any impedance experiments collected as part of FTacV/PSV data packages sent to collaborators for use in the calculation of uncompensated resistance values), and this instrumentation has been described elsewhere.<sup>556,557</sup> The custom-made instrumentation was operated using specially written software, named “pot.”

#### 8.1.5.4 Standard electrochemical practice

Potentials are reported either versus the SHE reference electrode or, where this is not possible (such as when a large unknown junction potential is likely to exist between the reference electrode and the electrolyte solution under assay), vs the reference electrode used in the experiment. Potentials given relative to the SHE electrode were calculated using the following relationship:  $E(V \text{ vs SHE}) = E(V \text{ vs REF}) + C(V)$  where  $C$  was calculated by recording a cyclic voltammogram in a standard ferricyanide solution and comparing the midpoint potential to the literature value.<sup>558</sup>  $C$  was typically  $\sim 205$  mV for Ag/AgCl (3M NaCl) reference electrodes and  $\sim 241$  mV for the SCE reference electrode. As the reference electrodes were housed in Luggin capillaries, or were otherwise of such length that only a small portion is in contact with the thermostatted electrolyte solution, it is a fair approximation to assume that the reference electrodes were maintained at room temperature.

The conditions under which electrochemistry experiments were conducted can be found in the captions of the relevant figures. Cyclic voltammograms and FTacV experiments were obtained by cycling between the limiting potentials shown in the relevant figure, and commence at either the most positive or negative potential (as indicated in the captions of the relevant figures). Impedance measurements were often taken before and after FTacV and PSV experiments, as simulation of these experiments requires a value for the uncompensated resistance. Impedance was measured at potentials devoid of Faradaic current, and an uncompensated resistance value could be obtained from these measurements using a simple RC circuit model (pre-set impedance waveforms and RC circuit model fittings are provided as part of the “pot” software).

Prior to performing electrochemical experiments, the working electrodes were freshly mechanically abraded/polished and sometimes subjected to other chemical/electrochemical cleaning methods. These procedures are often unique to the working electrode being used or the experiment being performed, and thus details of working electrode cleaning methods used can be found in the

Experimental Sections specific for individual Chapters, as can more detailed information regarding specific electrochemistry experiments.

## 8.2 Experimental procedures for Chapter 2

### 8.2.1 Materials

**MWCNT A** was purchased from Alfa Aesar. **MWCNT B** was purchased from Aldrich and **MWCNT C** was purchased from TCI. Details of the specifications of these nanotube samples can be found in **Table 2.3** (see **Section 2.2.2**). *N,N,N',N'*-tetramethyl-p-phenylenediamine (TMP) was purchased from Sigma-Aldrich.

### 8.2.2 Chemical oxidation of MWCNT A

5 mg of **MWCNT A** was added into 6.5 mL of a 1:3 volume concentrated solution of  $\text{HNO}_3/\text{H}_2\text{SO}_4$  at room temperature. The sample was then subjected to sonication for 4 hours, during which time the mixture became homogenous. The mixture was then diluted into Milli-Q water (30 mL) and neutralized using NaOH until the pH of the solution reached pH 2. The oxidised MWCNTs were then deposited by centrifuging and the supernatant discarded. Excess acid and salts were removed from the oxidised MWCNTs by repeatedly resuspending the oxidised MWCNT deposit in fresh Milli-Q water and re-depositing them by centrifuging. After washing out excess acids and salts the oxidised MWCNTs were again re-suspended in fresh Milli-Q water before being flash-frozen and lyophilized, yielding 3.3 mg of oxidised MWCNTs.

### 8.2.3 Copper-loading and purification of An6428-AA9

A partially purified (i.e. already subjected to ion-exchange and hydrophobic-interaction chromatographies) sample of An6428-AA9 was supplied by Dr César Terrasan at an estimated concentration of 1.6 mM in pH 6.0 50 mM Na MES buffer. The sample bore a reddish colour due to the presence of pigments from *Aspergillus nidulans* that had been carried through the first few purification steps, and required treatment with copper to guarantee that the An6428-AA9 would all be present as holo-protein.

**Copper-loading:** The partially purified sample of An6428-AA9 was treated with 2 equivalents of  $\text{CuSO}_4$  under mild conditions so as not to prompt precipitation. 100  $\mu\text{L}$  of the partially-purified An6428-AA9 sample was diluted to 1.25 mL with pH 6.0 50 mM Na MES buffer. This resultant solution was then

kept on ice while 1.25 mL of a 256  $\mu\text{M}$   $\text{CuSO}_4$  solution (also in pH 6.0 50 mM Na MES buffer) was added to it in 50-100  $\mu\text{L}$  instalments over the course of 10 min. The resultant solution was then incubated at 4  $^\circ\text{C}$  in the dark overnight.

Prior to purification via size exclusion chromatography the sample of copper-treated *An6428-AA9* was concentrated to a volume of 200  $\mu\text{L}$  using 10 kD molecular weight cut-off centrifugal protein concentrators. These cut-offs were also used to simultaneously remove excess  $\text{CuSO}_4$  by repeatedly adding fresh pH 6.0 50 mM Na MES buffer and reconcentrating.

**Size-exclusion:** A Superdex 75 10/300 (GE Healthcare) column was equilibrated in 50 mM Na MES buffer pH 6.0. The *An6428-AA9* sample was loaded onto the column using a 200  $\mu\text{L}$  injection loop and the column was run at a flow rate of 1  $\text{mL min}^{-1}$ , collecting fractions after  $\frac{1}{3}$  of a column volume had been passed. Eluted fractions were analysed using SDS-PAGE and those presenting the purified enzyme were then pooled and concentrated to 208  $\mu\text{M}$ . The concentration of the sample was determined using UV-vis spectroscopy, based on an  $\epsilon_{280}$  of 47180  $\text{M}^{-1}\text{cm}^{-1}$  (as had been previously determined by César Terrasan).

## 8.2.4 Electrochemical experiments/procedures/electrode modification

### Redox titration with *N,N,N',N'*-tetramethyl-*p*-phenylenediamine

An approximate reduction potential of *An6428-AA9* was determined using a variation of the method used by Aachmannan, the theory of which is described in **Section 2.1.3**.<sup>329</sup>

Solutions (20  $\mu\text{L}$ ) of TMP in its reduced form ( $\text{TMP}_{\text{red}}$ ) at either 300  $\mu\text{M}$  or 200  $\mu\text{M}$  concentration in oxygen-free pH 6.0 buffer (20 mM sodium MES) buffer were mixed with 20  $\mu\text{L}$  of 70  $\mu\text{M}$  *An6428-AA9* in oxygen-free pH 6.0 buffer (20 mM sodium MES) at 20  $^\circ\text{C}$  in a  $\text{N}_2$ -filled glovebox (oxygen concentration 60 ppm). The extent of reaction was determined by measuring the absorbance from the TMP radical cation ( $\text{TMP}_{\text{ox}}$ ) formed upon *An6428-AA9* reduction by  $\text{TMP}_{\text{red}}$  at  $\lambda = 610$  nm (**Section 2.2.3, Equation 16, Figure 2.9**) using an extinction coefficient of 14.0  $\text{mM}^{-1}\text{cm}^{-1}$ .<sup>343</sup> As such,  $[\text{TMP}_{\text{ox}}] = [\text{Cu(I)-An6428-AA9}]$  and  $[\text{TMP}_{\text{red}}] = [\text{TMP}_{\text{total}}] - [\text{TMP}_{\text{ox}}] = [\text{Cu(II)-An6428-AA9}]$ , and with these concentrations known, the equilibrium constant of the reaction can be calculated (**Section 2.1.3, Equation 16**), and thus so can  $\Delta_r G^\theta$ , and by extension,  $E_{\text{TMP}+\text{LPMO}}^\theta$  (using **Equation 17** in **Section 2.1.3**). The reduction potential of TMP at pH 6 was determined by cyclic voltammetry to be 308 mV vs SHE at 20  $^\circ\text{C}$  (see **Appendix 3, Figure S1**), and addition of the standard reduction potential of TMP

( $E_{TMP}^{\theta}$ ) to the standard cell potential of the TMP+LPMO redox reaction,  $E_{TMP+LPMO}^{\theta}$ , gives the LPMO- $\text{Cu}^{(II/I)}$  reduction potential,  $E_{LPMO-Cu^{(II/I)}}^{\theta}$  (as shown by **Equation 18** in **Section 2.1.3**). Using this method, the reduction potential of An6428-AA9 at pH 6 was determined to be  $330 \pm 30$  mV vs SHE at 20 °C.

### Electrochemical cell setup

All experiments were performed at 25 °C using the electrochemical cell setup described in **Section 8.1.5**.

### Cleaning of GC electrode surfaces

OrigaTip GC electrode surfaces were freshly abraded prior to use via mechanical polishing for 1–2 min using nylon polishing pads (Buehler) impregnated with 1  $\mu\text{m}$  RS PRO Blue Diamond Paste (RS Components Ltd.). The electrodes were then rinsed with Milli-Q water, sonicated in Milli-Q water for 5 min and finally sonicated in ethanol for 5 min before being allowed to dry.

### Drop-casting MWCNTs onto GC electrode surfaces

Samples of MWCNTs (see **Table 2.3**) were suspended in DMF at a concentration of 2  $\text{mg mL}^{-1}$  via sonication for 20 min. A 7  $\mu\text{L}$  droplet of the MWCNT suspension was then applied to the GC electrode surface and the DMF was allowed to evaporate. This left a drop-cast MWCNT film.

### Adsorption of protein onto drop-cast MWCNT films

Proteins (either An6428-AA9, BSA, DsbC<sub>term</sub> or DsbA<sub>middle</sub>) were adsorbed onto drop-cast MWCNT films by pipetting a 7  $\mu\text{L}$  droplet of  $\sim 100$   $\mu\text{M}$  protein solution (in pH 6.0 50 mM Na MES buffer) and allowing this to dry for  $\sim 15$  min, until the protein droplet becomes a slick on the MWCNT films surface. A good indicator of the quality of drop-cast MWCNT films is whether the protein solution initially sits as a bead-like droplet on top the MWCNT film, due to hydrophobic repulsion.

### Oxidative pre-treatment via cyclic voltammetry

Prior to many electrochemical experiments involving An6428-AA9, 10 cyclic voltammograms (akin to those shown in **Figure 2.11**) were recorded, sweeping from  $-0.05 \rightarrow 0.95$  V vs SHE at 113  $\text{mV s}^{-1}$ , thereby allowing the oxidative process that facilitates direct electron-transfer to An6428-AA9 to occur.

### Amperometric determination of peroxygenase activity

Prior to recording amperometric traces, 10 cyclic voltammograms (akin to those shown in **Figure 2.11**) were recorded, sweeping from  $-0.05 \rightarrow 0.95$  V vs SHE at  $113 \text{ mV s}^{-1}$ , thereby allowing the oxidative process that facilitates direct electron-transfer to An6428-AA9 to occur.

Amperometric traces were recorded by holding at a potential of 50 mV vs SHE, at 298 K under  $\text{N}_2$  atmosphere in pH 7 buffer (20 mM sodium phosphate, 20 mM sodium acetate, 500 mM  $\text{Na}_2\text{SO}_4$ ). A stirrer-bar was used during these experiments, as described in **Section 8.1.5**.

The volume of the electrolyte solution was 50 mL, and  $\text{H}_2\text{O}_2$  was added to this solution 10 successive 100  $\mu\text{L}$  instalments of a 500  $\mu\text{M}$   $\text{H}_2\text{O}_2$ , varying the  $\text{H}_2\text{O}_2$  concentration of the electrolyte solution over the range of  $0 \rightarrow 10 \mu\text{M}$ .

Raw amperometry data was first filtered using a specially-written code that rejected current spikes arising due to noise, identifying outlying datapoints based on how much they differ from the rolling median average of a selection of datapoints either side of the datapoint being screened, and then applies a smoothing spline. The data was then zeroed, and a correction applied to counteract the near-linear diminishing of the isolated current over time (approximating to a loss of around  $0.074 \text{ nA s}^{-1}$ ). Datapoints were then taken from the “flat” portions of the step-like amperometric trace. All the above steps are shown in **Figure 8.6**.



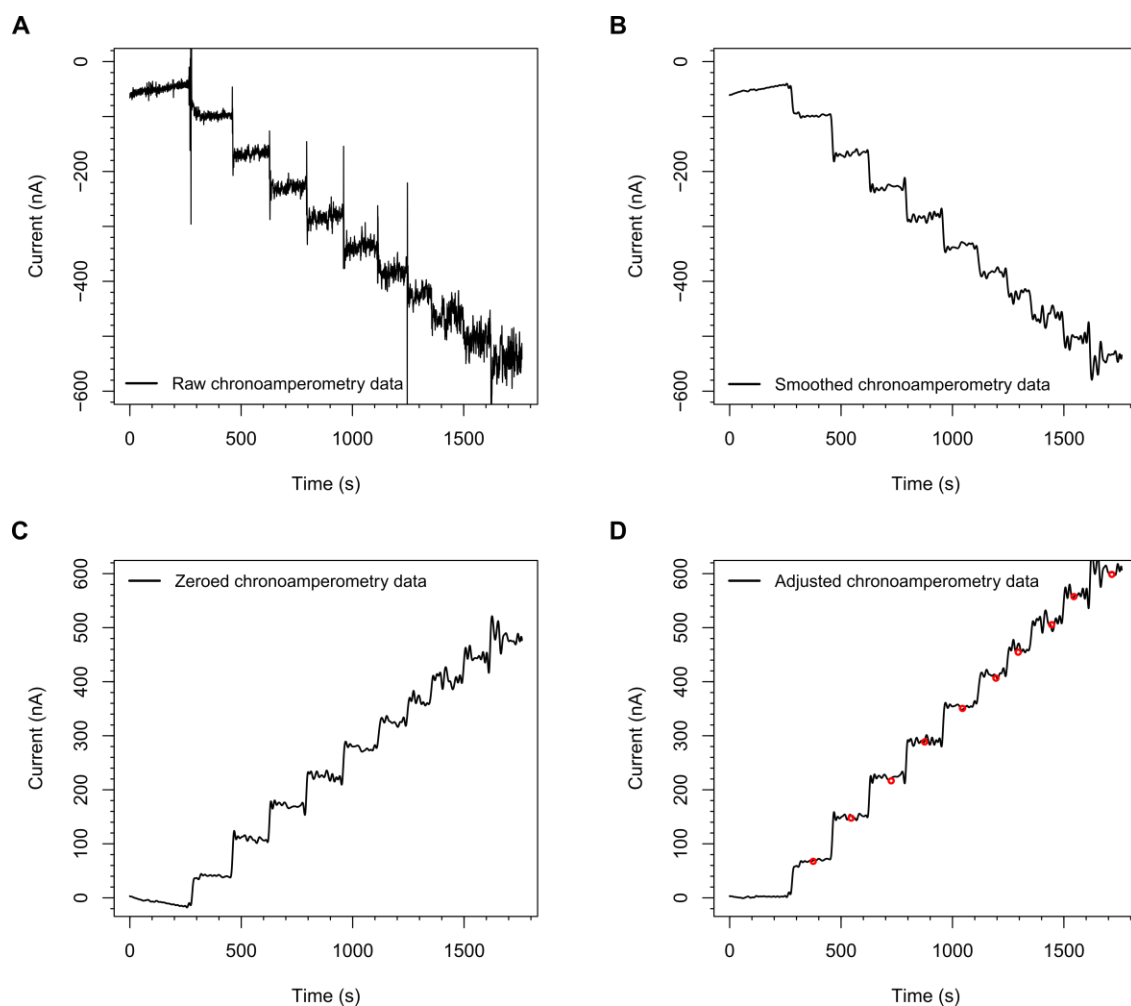


**Figure 8.6.** **A)** Raw amperometric data showing electrocatalytic  $\text{H}_2\text{O}_2$  reduction by  $\text{An6428-AA9}$ . **B)** Amperometric data that has been subjected to noise filtering and smoothing. **C)** Amperometric data that has been zeroed and the cathodic current treated as positive, in order to isolate just the catalytic current. **D)** Isolated cathodic catalytic current that has been subjected to a correction factor that accounts for the pseudo first-order desorption/deactivation of  $\text{An6428-AA9}$ . The datapoints used for the Michaelis-Menten kinetics analyses are shown in red.

### Amperometric determination of oxygen reduction activity

Prior to recording amperometric traces, 10 cyclic voltammograms (akin to those shown in **Figure 2.11**) were recorded, sweeping from -0.05  $\rightarrow$  0.95 V vs SHE at 113 mV s<sup>-1</sup>, thereby allowing the oxidative process that facilitates direct electron-transfer to An6428-AA9 to occur.

Mixtures of nitrogen and oxygen were bubbled through the electrolyte solution at a flow rate of 100 mL min<sup>-1</sup>. A stirrer bar was used to improve the rate of mass transport, and the composition of the gas mixture and the flow rate were controlled using the mass flow controllers (see **Section 8.1.5**).

Amperometric traces were recorded by holding at potentials of either i) 150 mV or ii) 50 mV vs SHE, at i) 298 K or ii) 335 K under N<sub>2</sub> atmosphere in pH 7 buffer (20 mM sodium phosphate, 20 mM sodium acetate, 500 mM Na<sub>2</sub>SO<sub>4</sub>). The composition of the nitrogen/gas mixture was changed stepwise throughout the experiment over the range of 0%  $\rightarrow$  20% oxygen.

## 8.3 Experimental procedures for Chapter 3

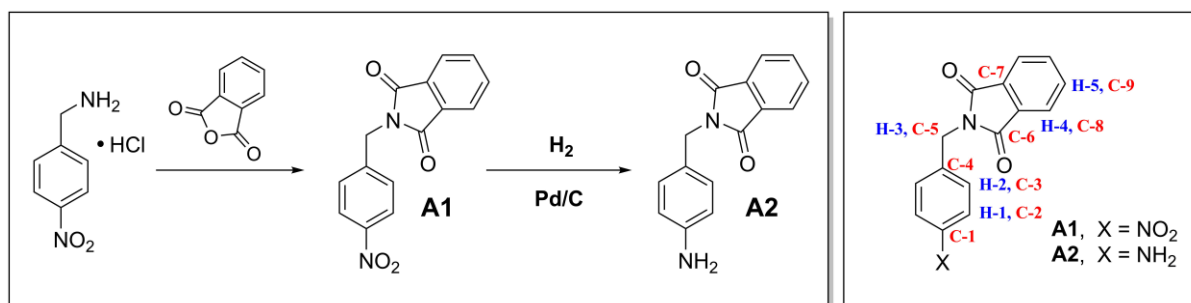
### 8.3.1 Materials

4-Nitrobenzylamine hydrochloride and ferrocene carboxaldehyde were purchased from Alfa aesar, phthalic anhydride, *N*-hydroxyphthalimide, triethyl phosphonoacetate, and palladium on activated carbon (10 wt% palladium) were purchased from Sigma Aldrich.

### 8.3.2 Synthetic procedures/molecular characterisations

#### 8.3.2.1 Protected aliphatic amine functionalised aryl diazonium precursors

**Scheme 8.1** summarizes the methodology used to synthesize 2-(4-aminobenzyl)isoindoline-1,3-dione from commercially available 4-nitrobenzylamine hydrochloride via the intermediate 2-(4-nitrobenzyl)isoindoline-1,3-dione, henceforth referred to as “**A1**”.



**Scheme 8.1.** (Left) The synthesis of 2-(4-aminobenzyl)isoindoline-1,3-dione (**A2**) via intermediate 2-(4-nitrobenzyl)isoindoline-1,3-dione (**A1**), and (right) the numbering of hydrogen and carbon environments in species **A1** and **A2**.

### 2-(4-nitrobenzyl)isoindoline-1,3-dione (**A1**)

4-nitrobenzylamine hydrochloride (0.500 g, 2.65 mmol) and phthalic anhydride (0.392 g, 2.65 mmol, 1 eq) were dissolved in glacial acetic acid (6 mL) and the solution refluxed, with stirring, for 18 h. The reaction solution was concentrated *in vacuo* to ca. 3 mL then cooled to 0 °C. The crystals of product were collected by filtration, washed with ice-cold water and dried *in vacuo*, yielding **A1** as off-white crystals, 0.613 g (81.9%). The product was characterised by NMR and MS, as summarized below.

**$^1\text{H-NMR}$  of **A1**** (400 MHz,  $\text{CDCl}_3$ , **Figure 8.7**):  $\delta_{\text{H}}$  8.19 (m<sup>AA'BB'</sup>, 2H, H-1), 7.88 (m, 2H, H-4), 7.76 (m, 2H, H-5), 7.59 (m<sup>AA'BB'</sup>, 2H, H-2), 4.94 (s, 2H, H-3)

**$^{13}\text{C-NMR}$  of **A1**** (100 MHz,  $\text{CDCl}_3$ , **Figure 8.8**):  $\delta_{\text{C}}$  167.69 (C-6), 147.74 (C-1), 143.19 (C-4), 134.26 (C-9), 131.74 (C-7), 129.27 (C-3), 123.88 (C-2), 123.53 (C-8), 40.77 (C-5)

**(ESI)HRMS of **A1**** (**Figure 8.9**): Found  $[\text{M}+\text{Na}]^+$  305.0526,  $\text{C}_{15}\text{H}_{10}\text{N}_2\text{NaO}_4$  requires 305.0533

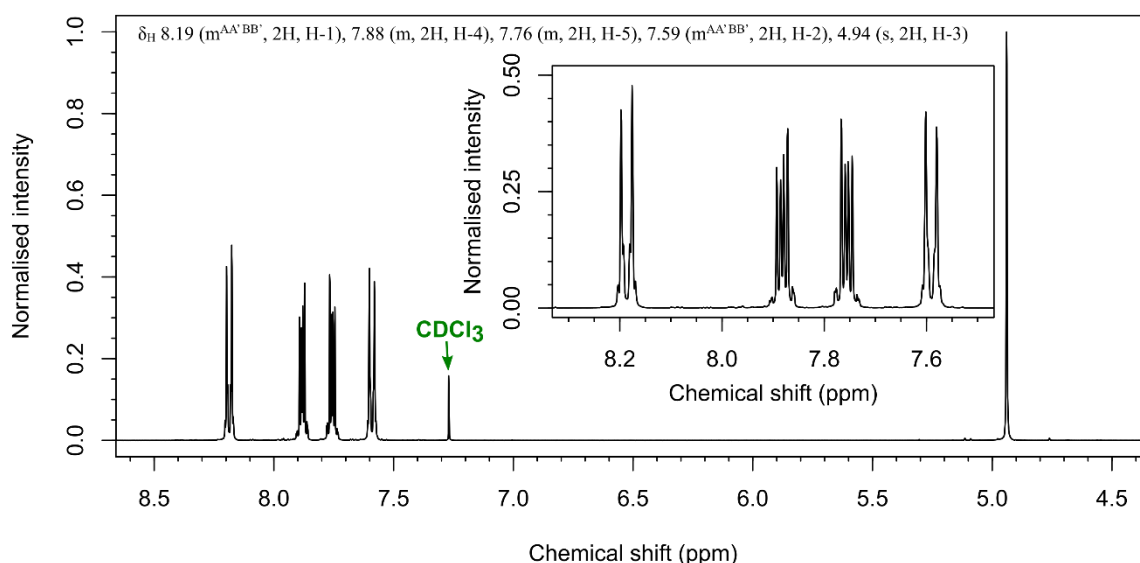


**Figure 8.7.**  $^1\text{H-NMR}$  spectrum of **A1**.

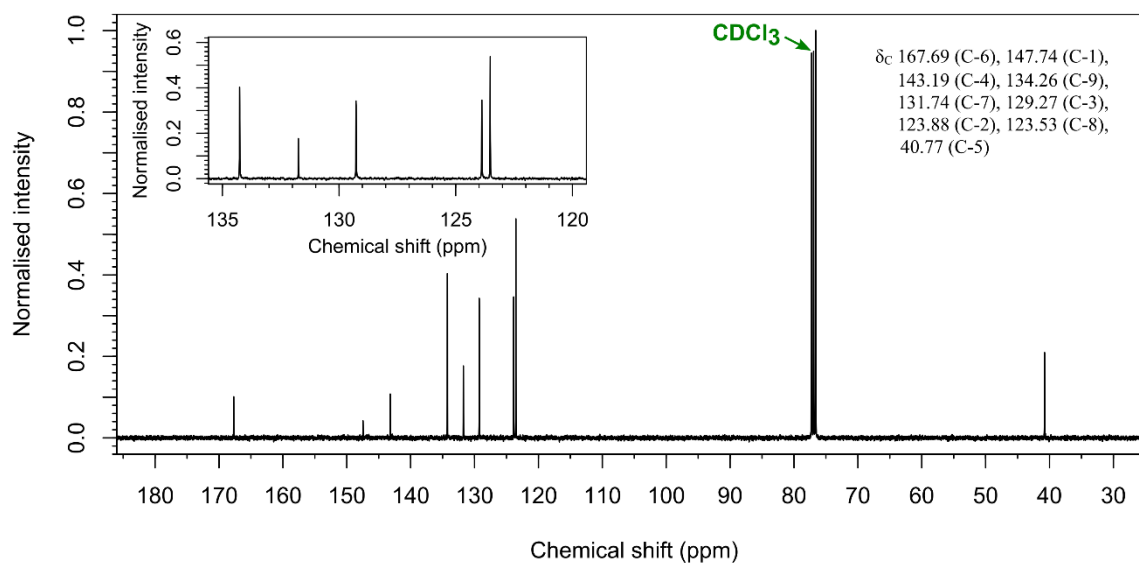
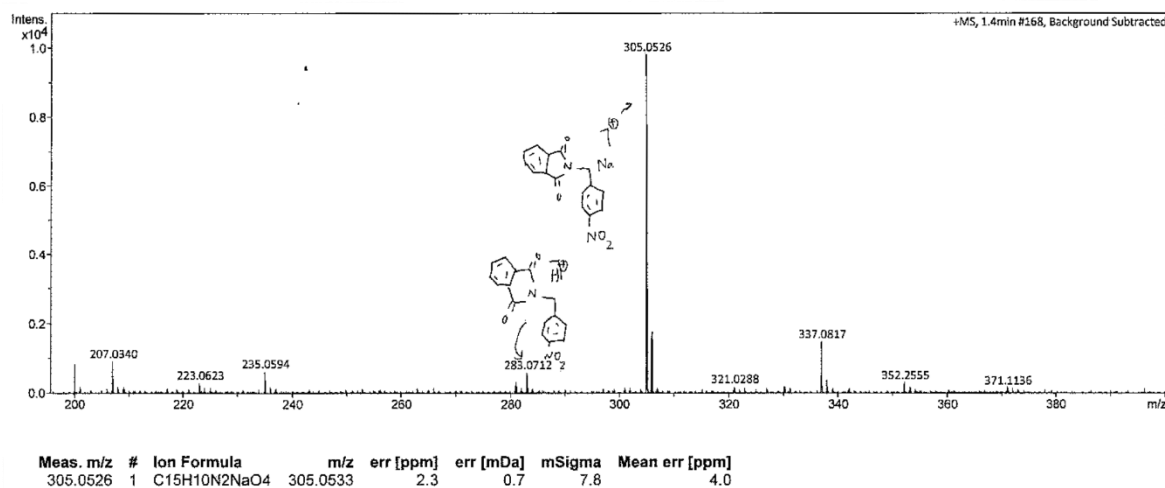
Figure 8.8.  $^{13}\text{C}$ -NMR spectrum of A1.

Figure 8.9. (ESI)HRMS spectrum of A1.

### 2-(4-aminobenzyl)isoindoline-1,3-dione (A2)

To make 2-(4-aminobenzyl)isoindoline-1,3-dione (**A2** in **Scheme 8.1**), **A1** (0.191 g, 0.675 mmol) and a spatula-end of 10% Pd/C were placed in a round bottom flask and the flask was placed under argon. Methanol (6.25 mL) and ethyl acetate (10 mL) were then added, and the system placed under 1 atm of hydrogen. The reaction progress was monitored by TLC and was found to be complete (by the presence of a single purple spot with ninhydrin stain) after 1 h. The Pd/C carbon was removed via filtration and the filtrate concentrated *in vacuo* to yield 2-(4-aminobenzyl)isoindoline-1,3-dione as a green solid (0.158 g, 92.6%). The product was characterised by NMR and MS, as summarized below.

$^1\text{H}$ -NMR (400 MHz,  $\text{CDCl}_3$ , **Figure 8.10**):  $\delta_{\text{H}}$  7.83 ( $m^{\text{AA'BB}}$ , 2H, H-4), 7.69 (m, 2H, H-5), 7.27 ( $m^{\text{AA'BB}}$ , 2H, H-2), 6.62 (m, 2H, H-1), 4.74 (s, 2H, H-3).

$^{13}\text{C-NMR}$  (100 MHz,  $\text{CDCl}_3$ , **Figure 8.11**):  $\delta_{\text{C}}$  168.11 (C-6), 146.01 (C-1), 133.08 (C-9), 132.15 (C-7), 130.09 (C-3), 126.41 (C-4), 123.18 (C-8), 114.19 (C-2), 41.15 (C-5).

(ESI)HRMS (**Figure 8.13**): Found  $[\text{M}+\text{H}]^+$  253.0975,  $\text{C}_{15}\text{H}_{13}\text{N}_2\text{O}_2$  requires 253.0975.

IR (ATR) (**Figure 8.13**) ( $\nu_{\text{max}}/\text{cm}^{-1}$ ): 3449 (N-H stretch), 3364 (N-H stretch), 2923 (C-H alkyl), 1694 (C=O), 1634 (N-H bend), 1510 (C=C aromatic), 1290 (C-N stretch, aromatic), 1280 (C-N stretch, aromatic), 1068 (C-H bend, aromatic), 715 (C-H bend, aromatic).

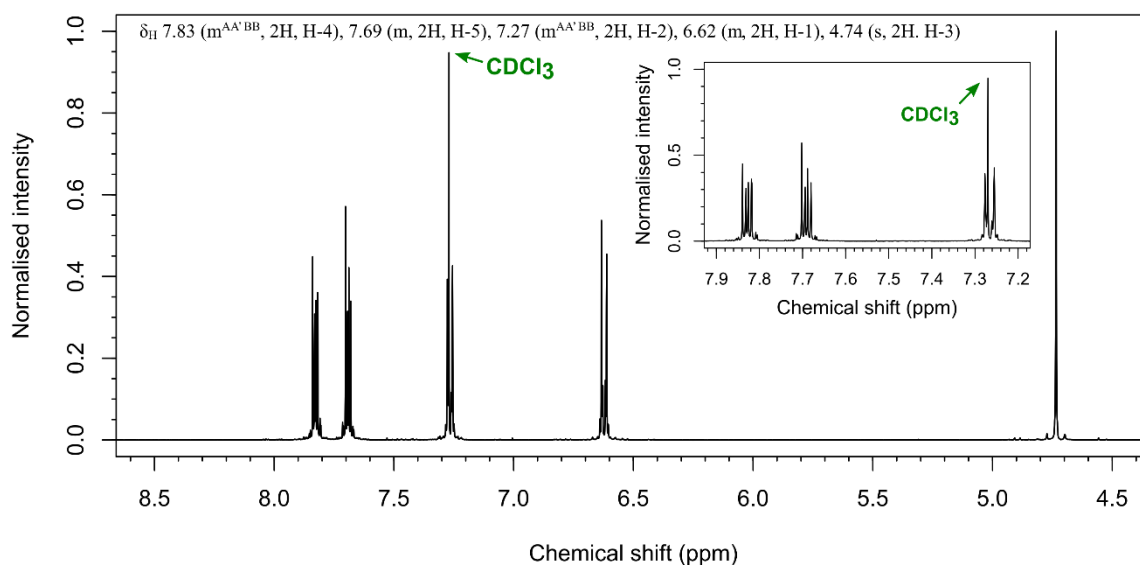


**Figure 8.10.**  $^1\text{H-NMR}$  spectrum of A2.

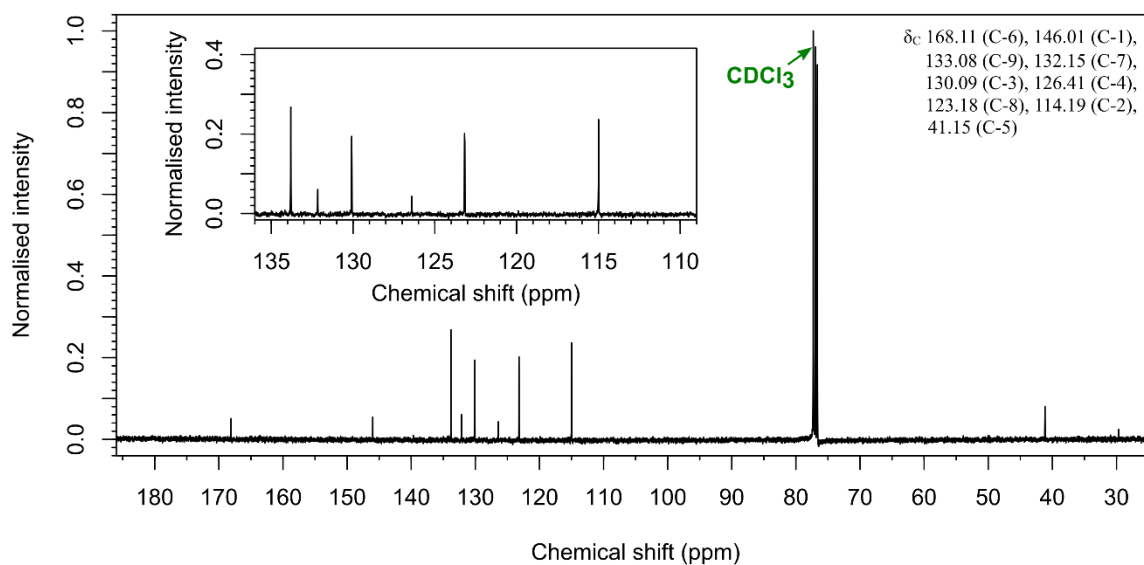


**Figure 8.11.**  $^{13}\text{C-NMR}$  spectrum of A1.

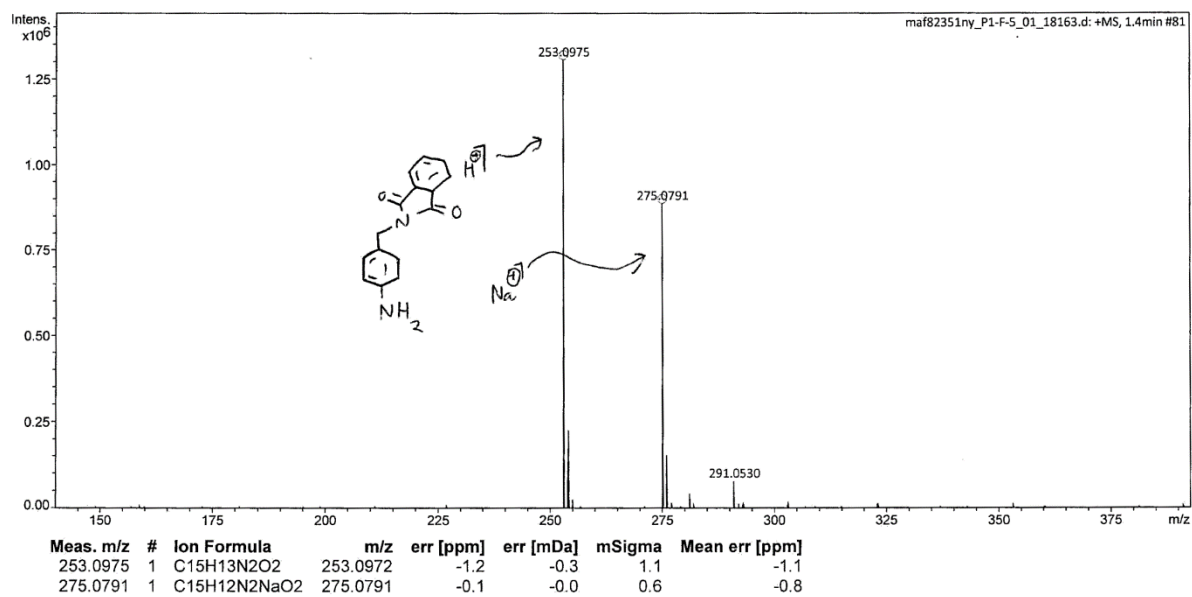


Figure 8.12. (ESI)HRMS spectrum of A2.

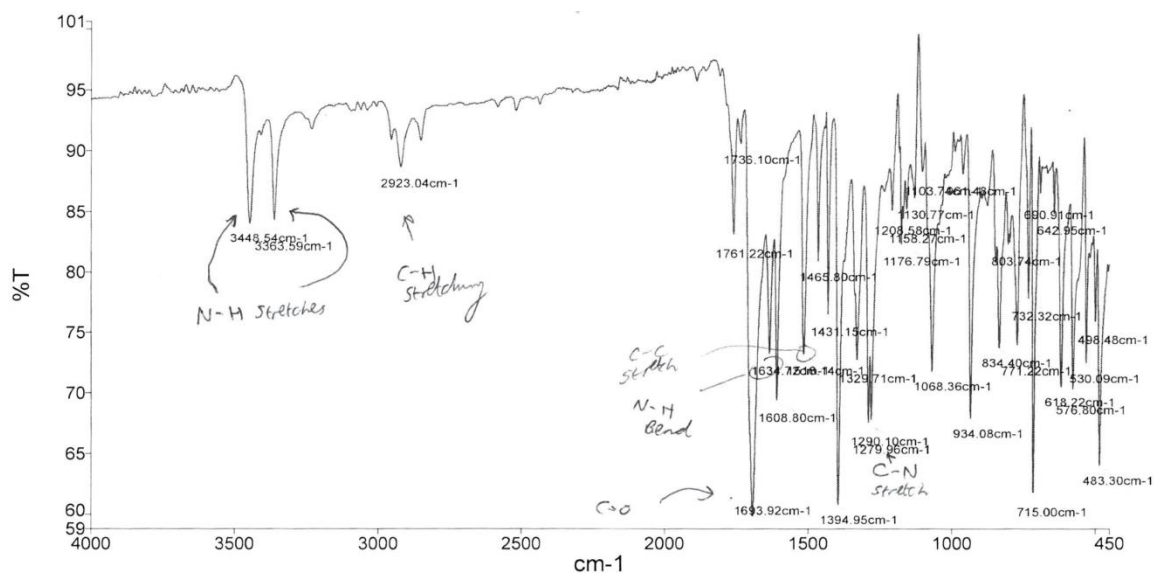
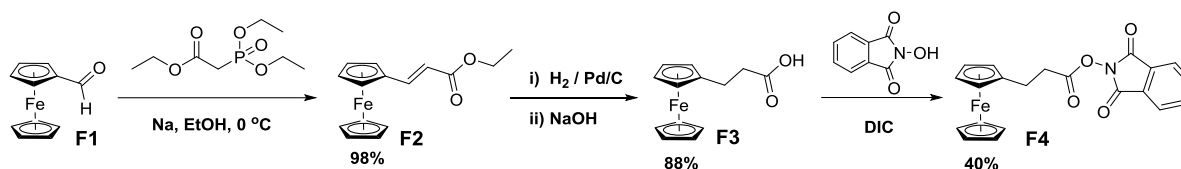


Figure 8.13. IR (ATR) spectrum of A2.

## 8.3.2.2 Ferrocene derivatives

**Scheme 8.2** summarizes the methodology used to synthesize 3-(ferrocenyl) propanoic acid *N*-hydroxyphthalimide ester (**F4**) from commercially available ferrocenecarboxaldehyde (**F1**), via intermediates 1-[(2-ethoxycarbonyl)ethenyl]ferrocene (**F2**) and ferrocene propanoic acid (**F3**). Detailed protocols for each reaction step are provided below.



**Scheme 8.2.** The synthesis of 3-(ferrocenyl) propanoic acid *N*-hydroxyphthalimide ester (**F4**) from ferrocenecarboxaldehyde (**F1**), via intermediates 1-[(2-ethoxycarbonyl)ethenyl]ferrocene (**F2**) and ferrocene propanoic acid (**F3**).

1-[(2-Ethoxycarbonyl)ethenyl]ferrocene (**F2**)

**F2** was synthesized as per a previously published procedure.<sup>388</sup> Triethyl phosphonoacetate (0.930 g, 0.823 mL, 4.67 mmol) was added dropwise to a solution of sodium (0.11 g, 6.67 mmol) in ethanol (46 mL) at 0 °C. A solution of **F1** (1.00 g, 4.67 mmol) in ethanol (20 mL) was then added dropwise to the reaction solution at 0 °C. The resultant mixture was stirred at room temperature for 1 h and then concentrated under reduced pressure. The crude product was purified by flash column chromatography (SiO<sub>2</sub>, hexane → ethyl acetate), giving **F2** as red crystals in quantitative yield. <sup>1</sup>H-NMR analysis was consistent with the literature.<sup>388</sup>

<sup>1</sup>H-NMR of **F2** (400 MHz, CDCl<sub>3</sub>): 7.57 (d, *J* = 15.57 Hz, 1H), 6.04 (d, *J* = 15.57 Hz, 1H), 4.49 (dd, *J* = 1.83, 1.83 Hz, 2H), 4.41 (dd, *J* = 1.83, 1.83 Hz, 2H), 4.23 (q, *J* = 7.33 Hz, 2H), 4.17 (s, 5H), 1.34 (t, *J* = 7.33 Hz, 3H).

Ferrocene propanoic acid (**F3**)

**F3** as synthesized as per previously published procedures.<sup>387,388</sup> **F2** (1.32 g, 4.67 mmol) and 10% Pd/C (0.13 g) were placed under argon and dissolved, with stirring, in ethyl acetate (60 mL). After 30 min. de-gassing under argon the atmosphere was replaced with H<sub>2</sub> (1 atm). The reaction mixture was stirred vigorously for 24 h, whereupon the Pd/C was removed via filtration. The filtrate was concentrated *in vacuo*, yielding 1.20g of an orange solid. This residue was dissolved in a basic ethanol solution (0.34 g NaOH in 21 mL ethanol) and the resultant solution stirred under reflux for 1 h. The reaction solution was concentrated *in vacuo*, whereupon water (40 mL) was added. The aqueous solution was extracted using diethyl ether (2 × 30 mL) and was then acidified with 2 M HCl until its pH was 4-5. The acidified

solution was then further extracted with diethyl ether (2 × 30 mL). The organic extracts were combined, dried over MgSO<sub>4</sub> and concentrated *in vacuo* to yield **F3** as an orange solid: (1.06 g, 88.3%). The characterisation data was consistent with that in the literature.<sup>387,388</sup>

**<sup>1</sup>H-NMR of F3** (400 MHz, CDCl<sub>3</sub>): δ<sub>H</sub> 4.15 (s, 5H), 4.12 (s, 2H), 4.10 (s, 2H), 2.73-2.58 (m, 4H).

**<sup>13</sup>C-NMR of F3** (100 MHz, CDCl<sub>3</sub>): δ<sub>C</sub> 178.92, 87.31, 68.65, 67.98, 67.50, 35.29, 24.52.

**(ESI)HRMS of F3:** Found [M+H]<sup>+</sup> 258.0343, C<sub>13</sub>H<sub>14</sub>FeO<sub>2</sub> requires 258.0338.

### **3-(Ferrocenyl) propanoic acid *N*-hydroxyphthalimide ester (F4)**

**F4** was synthesized as per a previously published procedure.<sup>387</sup> **F3** (50.0 mg, 0.194 mmol) and *N*-hydroxyphthalimide (40.0 mg, 0.245 mmol) were placed under argon and dissolved in anhydrous DCM (2 mL). DIC (40 μL, 0.260 mmol) was added and the reaction solution stirred under argon for 16 h. Water (4 mL) was added, then the organic layer was extracted and washed with brine (3 × 10 mL). The organic layer was dried over MgSO<sub>4</sub> and concentrated *in vacuo* to yield a crude residue which was purified by flash column chromatography (SiO<sub>2</sub>, DCM). This yielded **F4** as an orange solid: (33.6 mg, 43.0%). The characterisation data was consistent with that in the literature.<sup>387</sup>

**<sup>1</sup>H-NMR of F4** (400 MHz, CDCl<sub>3</sub>): δ<sub>H</sub> 7.91 (m, 2H), 7.81 (m, 2H), 4.20-4.10 (m, 9H), 2.92 (m, 2H), 2.83 (m, 2H).

**<sup>13</sup>C-NMR of F4** (100 MHz, CDCl<sub>3</sub>): δ<sub>C</sub> 169.04, 161.94, 134.76, 128.88, 123.98, 86.25, 68.57, 67.97, 67.62, 32.60, 24.69.

**(ESI)HRMS of F4:** Found [M+Na]<sup>+</sup> 426.0401, C<sub>21</sub>H<sub>17</sub>FeNNaO<sub>4</sub> requires 426.0399.

**IR (ATR) of F4** (ν<sub>max</sub>/cm<sup>-1</sup>): 1785 (C=O), 1737 (C=O), 1188 (C-O, ester), 1070 (C-H bend, aromatic), 692 (C-H bend aromatic).



### 8.3.3 Electrochemical experiments/procedures/electrode modification

#### Electrochemical cell setup

All experiments were performed under the conditions reported in the relevant figure captions using the electrochemical cell setup described in **Section 8.1.5**. The parameters used to record cyclic voltammograms can likewise be found in the relevant figure captions. The potentials reported for the experiments performed in 1:5 v/v water/acetonitrile + 0.1 M tetrabutylammonium hexafluorophosphate ( $\text{Bu}_4\text{NPF}_6$ ) electrolyte do not account for any junction potential that may exist between the Ag/AgCl (3 M NaCl) reference electrode and the mixed solvent electrolyte. All experiments that were conducted under a nitrogen atmosphere were carried out in a nitrogen-filled glovebox of dioxygen  $\leq 40$  ppm; otherwise, experiments were performed in air. An EmStat3 potentiostat (PalmSens) with PSTrace 5.5 for Windows software was used for the diazonium electrografting experiments. The electrochemical assays of surface confined ferrocene species were conducted using a CompactStat potentiostat (Ivium technologies) with IviumSoft software for Windows.

#### Cleaning of GC electrode surfaces

Prior to electrochemical derivatisation, the GC disk electrodes (purchased from eDAQ) were cleaned using the following procedures. GC electrode surfaces were mechanically polished for 1–2 min using 1–5  $\mu\text{m}$  alumina slurry impregnated onto a WhiteFelt polishing pad (Buehler). Electrodes were then rinsed with Milli-Q water and sonicated in acetonitrile for 5 min.

#### PSV, FTacV, and impedance experimental parameters

The parameters used in the PSV experiments for the **FSB** dataset (described in **Section 3.2.3.1.2**) are shown below in **Figure 8.14**. Note that the start, max and end potentials are used in conjunction with the Rate parameter to determine the length of the experiment (and hence how many cycles of the sinusoid are recorded). The “No DC Scan” option has to be ticked in order for the PSV to run correctly. The amplitude of the applied sinusoid cannot exceed 300 mV. The parameters below define an experiment that applies a 300 mV amplitude sinusoid on top of a potential of 260 mV, and thus covers a voltage window of - 40 mV vs REF to 560 mV vs REF. Note that only one “Multi frequency” has non-zero amplitude.

Single Frequency CV

<b>Scan control</b> Rate (mV/s): 10.36    Direction (a/c): a Scans: <input type="text"/> <input checked="" type="checkbox"/> No DC Scan	<b>Potentials</b> Start (mV): 260.00    Max (mV): 300.00 End (mV): 62.00    Min (mV): 62.00
<b>Data Control</b> Data points: 1048576	<b>Pre waveform control</b> Initial (mV): 0.00    Initial (ms): 0.00 Pre (mV): 260.00    Pre (ms): 5000.00
<b>Perturbation control</b> Freq (Hz): 0.04    Amp (mV): 0.00 Type: Multi    n(1-max): 1 User E(t) file: <input type="text"/> <input type="button" value="Browse"/>	<b>Post waveform control</b> Post (mV): 0.00    Post (ms): 0.00
<input type="button" value="Apply"/> <input type="button" value="Save As"/> <input type="button" value="OK"/> <input type="button" value="Cancel"/>	
<b>Multi frequency</b> Frequency 1 (Hz): 8.94    Amplitude 1 (mV): 300.00    Phase 1 (deg): 270.00 Frequency 2 (Hz): 0.60    Amplitude 2 (mV): 0.00    Phase 2 (deg): 0.00	

Figure 8.14. Parameters used to record the PSV experiments in the FSB dataset.

The parameters used in the FTacV experiments for the FSB dataset (described in Section 3.2.3.1.2) are shown below in Figure 8.15.

Single Frequency CV

<b>Scan control</b> Rate (mV/s): 29.80    Direction (a/c): a Scans: <input type="text"/> <input type="checkbox"/> No DC Scan	<b>Potentials</b> Start (mV): -180.00    Max (mV): 620.00 End (mV): -180.00    Min (mV): -180.00
<b>Data Control</b> Data points: 2097152	<b>Pre waveform control</b> Initial (mV): -180.00    Initial (ms): 5.00 Pre (mV): 0.00    Pre (ms): 0.00
<b>Perturbation control</b> Freq (Hz): 8.88    Amp (mV): 150.00 Type: Sine    n(1-max): 1 User E(t) file: <input type="text"/> <input type="button" value="Browse"/>	<b>Post waveform control</b> Post (mV): 0.00    Post (ms): 0.00
<input type="button" value="Apply"/> <input type="button" value="Save As"/> <input type="button" value="OK"/> <input type="button" value="Cancel"/>	

Figure 8.15. Parameters used to record the FTacV experiments in the FSB dataset.

Impedance readings in the FSB dataset (described in Section 3.2.3.1.2) were recorded using the “18kHz many data points” predefined waveform in the “pot” software.

### 8.3.3.1 Functionalisation of glassy carbon electrode surfaces with amines

#### Monolayer aniline-functionalisation of electrode surfaces

To 990  $\mu\text{L}$  of a dry acetonitrile + 0.1 M  $\text{Bu}_4\text{NPF}_6$  solvent system at 0  $^\circ\text{C}$  under a stream of argon was added 10  $\mu\text{L}$  of a 100 mM stock of 4-nitrobenzenediazonium tetrafluoroborate in acetonitrile. 20  $\mu\text{L}$  of a 100 mM stock of 2,2-diphenyl-1-picrylhydrazyl in acetonitrile was then added and the resultant solution briefly agitated. Electrochemical grafting experiments were then conducted to yield electrodes functionalised with a monolayer of nitrophenyl moieties by cycling between the potentials shown in the relevant figure (see **Section 3.2.1, Table 3.1**) at a scan rate of 50  $\text{mV s}^{-1}$ . After electrochemical grafting, the electrode surfaces were rinsed with Milli-Q water, sonicated in acetonitrile for 5 min, and then rinsed again with Milli-Q water before being allowed to dry under an ambient atmosphere.

Nitrophenyl moieties were electrochemically reduced to aniline moieties by cycling between the potentials shown in **Section 3.2.1, Figure 3.9** at 50  $\text{mV s}^{-1}$  in a 1:5 water:acetonitrile + 1% 6.6 M HCl solvent system at room temperature until the Faradaic signal corresponding to nitro-reduction disappeared. After electrochemical grafting, the electrode surfaces were rinsed with Milli-Q water, sonicated in acetonitrile for 5 min, and then rinsed again with Milli-Q water before being allowed to dry under an ambient atmosphere.

#### Nitro-grafting of A1/A2

To 1 mL of a 4.4 mM solution of **A1/A2** in a 1:5 v/v water/ acetonitrile + 0.1 M  $\text{Bu}_4\text{NPF}_6$  solvent system at 0  $^\circ\text{C}$  was added 40  $\mu\text{L}$  of 6.6 M HCl, followed by 10  $\mu\text{L}$  of a 2.9 M stock solution of  $\text{NaNO}_2$  in water. The resultant solution was briefly shaken and electrochemical grafting experiments were then conducted to yield an electro-grafted surface (**Section 3.2.2.1, Figure 3.16**) by cycling between the potentials shown in the relevant figures (**Section 3.2.2.1, Figure 3.12, A and B**) at a scan rate of either 50  $\text{mV s}^{-1}$  or 500  $\text{mV s}^{-1}$  at 0  $^\circ\text{C}$  until electrode passivation was observed. After electrochemical grafting, the electrode surfaces were rinsed with Milli-Q water, sonicated in acetonitrile for 5 min, and then rinsed again with Milli-Q water before being allowed to dry under an ambient atmosphere.

#### In-situ diazonium electro-grafting of A3/A4

A 5  $\mu\text{L}$  portion of a 6.6 M hydrochloric acid solution was added to 975  $\mu\text{L}$  a 1:5 v/v water/acetonitrile + 0.1 M  $\text{Bu}_4\text{NPF}_6$  solvent system at 0  $^\circ\text{C}$ . To this solution was added 10  $\mu\text{L}$  of a 100 mM stock solution of **A3** or **A4** in a 1:5 v/v water/ acetonitrile + 0.1 M  $\text{Bu}_4\text{NPF}_6$  solvent system. 10  $\mu\text{L}$  of a 400 mM stock

solution of  $\text{NaNO}_2$  in water was then added at  $0\text{ }^\circ\text{C}$ , triggering the formation of diazonium cations via diazotisation of the aniline moieties. The resultant solution was briefly shaken and then kept at/below  $0\text{ }^\circ\text{C}$  for 30 mins or more, yielding a solution of a maximum diazonium salt concentration of 1 mM. Electrochemical grafting experiments to yield an electro-grafted surface (**Section 3.2.2.1, Figure 3.16**) were then carried out by cycling three times between the potentials shown in the relevant figures (**Section 3.2.2.1, Figure 3.13, A and B**) at a scan rate of  $20\text{ mV s}^{-1}$  at  $0\text{ }^\circ\text{C}$ , using the diazonium solution as the electrolyte. After electrochemical grafting, the electrode surfaces were rinsed with Milli-Q water, sonicated in acetonitrile for 5 min, and then rinsed again with Milli-Q water before being allowed to dry under an ambient atmosphere.

#### **Hydrazine-deprotection of A1 $\rightarrow$ A4 electro-grafted electrode surfaces**

The hydrazine deprotection step conducted on electro-grafted electrode surfaces to yield either i) benzylamine or ii) 2-phenylethan-1-amine functionalised electrodes (**Section 3.2.2.1, Figure 3.14**) was carried out by adding 155  $\mu\text{L}$  of hydrazine monohydrate to 2 mL of ethanol and heating the resultant solution to  $80\text{ }^\circ\text{C}$ . The electro-grafted electrodes were then placed into this solution for 5 min, with the intention of yielding the benzylamine or 2-phenylethan-1-amine near-monolayer “hydrazine-treated” surface depicted in **Figure 3.16**. Upon removal from this solution, the electrodes were sonicated in acetonitrile for 5 min, before being allowed to dry under an ambient atmosphere.

#### **8.3.3.2 Functionalisation of glassy carbon electrode surfaces with ferrocene moieties**

Benzylamine or 2-phenylethan-1-amine functionalised electrodes (**Section 3.2.2.1, Figure 3.14**) were immersed in a 10 mM solution of 3-(ferrocenyl) propanoic acid *N*-hydroxyphthalimide ester (**F4**) in DMF + 10 mM triethylamine. Amide bond formation, covalently linking ferrocene to the electrode surface, was left to proceed for 24 h at room temperature under  $\text{N}_2$  in the dark, yielding **FSA** (derived from 2-phenylethan-1-amine functionalised electrodes) or **FSB** (derived from benzylamine functionalised electrodes) (see **Section 3.2.2.2, Figure 3.17**). Prior to usage in electrochemical experiments these electrodes were sonicated in acetonitrile for 5 min to remove non-covalently attached species, before being allowed to dry under a nitrogen atmosphere.

## 8.4 Experimental procedures for Chapter 4

### 8.4.1 Oxidative cleavage of *N*-terminal threonine/serine residues

#### CTB oxidation and labelling:

Experimental methods regarding the usage of CTB can be found in the experimental and supporting information of reference [392], Yates, N. D. J. et al. Chemical Bioconjugation of Proteins in an Undergraduate Lab: One-Pot Oxidation and Derivatization of the N-Terminus. *Journal of Chemical Education* **96**, 1245-1249, doi:10.1021/acs.jchemed.8b00787 (2019).

#### Thioredoxin 1 oxidation:

To 100  $\mu\text{L}$  of a 88  $\mu\text{M}$  (1 mg mL<sup>-1</sup>) stock of thioredoxin 1 from *Escherichia coli* (pH 7, 25 mM phosphate buffer) was added 1  $\mu\text{L}$  of a 66 mM stock of L-methionine and 1  $\mu\text{L}$  of a 33 mM stock of NaIO<sub>4</sub>. The resulting solution was incubated in the dark for 4 min at room temperature before being exchanged into a pH 4.5 100 mM sodium acetate buffer containing 100 mM aniline using a PD Spintrap™ G-25 column.

#### Solution phase oxime ligation to thioredoxin 1:

To 20  $\mu\text{L}$  of a 85  $\mu\text{M}$  solution of thioredoxin 1 from *Escherichia coli* (pH 4.5, 100 mM sodium acetate buffer, 100 mM aniline) was added 17 nM *o*-benzylhydroxylamine (10 equiv) in 20  $\mu\text{L}$  of a 10% solution of DMSO in pH 4.5 100 mM sodium acetate buffer). The reaction solution was allowed to react at room temperature for 4 hours before a sample was taken for mass spectrometric analysis.

### 8.4.2 Oxidative cleavage of glycan cis-diols

#### Aldehyde installation via oxidative cleavage of An6428-AA9 glycan 1,2-cis diols

To 125  $\mu\text{L}$  of an An6428-AA9 solution of ca. 100  $\mu\text{M}$  concentration (based on an extinction coefficient of 47180 M<sup>-1</sup> cm<sup>-1</sup>) in pH 6.0 50 mM Na MES buffer was added 5  $\mu\text{L}$  of a 262  $\mu\text{M}$  solution of NaIO<sub>4</sub> in water, yielding a solution with a final NaIO<sub>4</sub> concentration of 10 mM. The resultant solution was incubated in the dark for 30 min at room temperature. After this time a 10 kD molecular weight cut-off centrifugal protein concentrator was used with successive instalments of fresh pH 6.0 50 mM Na MES buffer to remove the NaIO<sub>4</sub>.

Note that a 262  $\mu\text{M}$  solution of NaIO<sub>4</sub> can be prepared by dissolving 5.6 mg NaIO<sub>4</sub> in 100  $\mu\text{L}$  of water.

#### Labelling of *An6428-AA9* glycan aldehydes

To a 100  $\mu\text{M}$  solution of  $\text{NaIO}_4$ -treated *An6428-AA9* in either pH 6.0 (50 mM Na MES) or pH 4.5 (200 mM sodium acetate) buffer was added 100 equivalents of **Dan6** or **Pyr3** (delivered in an equal volume of the relevant buffer: either pH 6.0 50 mM Na MES or pH 4.5 200 mM sodium acetate). The resultant solutions were incubated for 1 hour at room temperature, after which time the *An6428-AA9* was exchanged into fresh pH 6.0 50 mM Na MES buffer using PD SpinTrap™ G-25 columns, and re-concentrated back to ca. 100  $\mu\text{M}$  using 10 kD molecular weight cut-off centrifugal protein concentrators. Samples were then analysed using a 15% SDS page gel, visualising fluorescence before Coomassie staining.

#### De-glycosylation of *An6428-AA9*

**Using Endo H:** The following approach is adapted from the New England BioLabs Endo H/Endo H<sub>f</sub> protocol,<sup>559</sup> and was performed using the New England BioLabs Endo H kit.<sup>560</sup>

To 8  $\mu\text{L}$  of a 100  $\mu\text{M}$  solution of *An6428-AA9* (which had been subjected to any of the treatments detailed in **Table 4.1**) was added 1  $\mu\text{L}$  of 10  $\times$  Glycoprotein Denaturing Buffer (5% SDS, 400 mM DTT) and 1  $\mu\text{L}$  of water. The resultant solution was incubated at 100  $^\circ\text{C}$  for 10 min, denaturing the protein. After this time, the solution was allowed to cool back to room temperature. 2  $\mu\text{L}$  of 10  $\times$  GlycoBuffer 3 (500 mM sodium acetate, pH 6.0 at 25  $^\circ\text{C}$ ), 5  $\mu\text{L}$  Endo H solution and 3  $\mu\text{L}$   $\text{H}_2\text{O}$  were added, and the resultant solution incubated at 37  $^\circ\text{C}$  for 1 hour. Samples were then analysed using a 15% SDS page gel, visualising fluorescence before Coomassie staining.

**Using PNGase F:** The following approach is adapted from the New England BioLabs PNGase F denaturing conditions protocol,<sup>561</sup> and uses the New England BioLabs PNGase F kit.<sup>562</sup>

To 8  $\mu\text{L}$  of a 100  $\mu\text{M}$  solution of *An6428-AA9* (which had been subjected to any of the treatments detailed in **Table 4.1**) was added 1  $\mu\text{L}$  of 10  $\times$  Glycoprotein Denaturing Buffer (5% SDS, 400 mM DTT) and 1  $\mu\text{L}$  of water. The resultant solution was incubated at 100  $^\circ\text{C}$  for 10 min, denaturing the protein. The solution was then chilled on ice until cool and subsequently centrifuged for 10 seconds to remove insoluble material.

2  $\mu\text{L}$  of 10  $\times$  GlycoBuffer 2 (50 mM sodium phosphate pH 7.5 at 25  $^\circ\text{C}$ ), 2  $\mu\text{L}$  of 10% NP-40 (a detergent) and 6  $\mu\text{L}$   $\text{H}_2\text{O}$  were then added, followed by 1  $\mu\text{L}$  of PNGase F solution, pipetting the solution such that good mixing is ensured. The resultant solution was then incubated at 37  $^\circ\text{C}$  for 1 hour. Samples were then analysed using a 15% SDS page gel, visualising fluorescence before Coomassie staining.

### 8.4.3 Pyridoxal 5'-phosphate mediated transamination of *N*-terminal glycine residues

#### Transamination of the *N*-terminal glycine residue of CjX183-D

PLP-mediated transamination of both WT CjX183 or CjX183-D R51K was performed by incubating the CjX183-D protein at a concentration of ca. 40  $\mu\text{M}$  in pH 6.5 buffer (25 mM sodium phosphate) in the presence of 10 mM PLP for at least 18 hours at 37 °C. This was achieved by mixing CjX183-D solutions of ca. 80  $\mu\text{M}$  concentration with an equal volume of a 20 mM PLP solution (also in pH 6.5 25 mM sodium phosphate buffer).

After incubation, PLP was removed by buffer exchanging the CjX183-D into a buffer of choice using a PD MiniTrap™ G-25 desalting column. The CjX183-D sample was then re-concentrated using 3 kD molecular weight cut-off centrifugal protein concentrators, which simultaneously served to remove residual PLP. Prior to analysis by positive ion mode ESI-LC/MS, a 10  $\mu\text{L}$  sample of reaction mixture was added to 40  $\mu\text{L}$  50% (v/v) water/acetonitrile, 1% formic acid.

The 20 mM PLP stock solution can be prepared by dissolving 5.3 mg PLP monohydrate in 1 mL of pH 6.5 buffer (25 mM sodium phosphate). Upon dissolution, this PLP stock solution will be excessively acidic, so prior to usage 24  $\mu\text{L}$  of 1 M NaOH should be added, and the near-neutrality of the resultant solution should be verified using pH paper.

Note that the above method was based on literature procedures for the PLP-mediated transamination of myoglobin, which also has an *N*-terminal glycine, and is likely to work for *N*-terminal glycine bearing proteins with final concentrations between 10 to 500  $\mu\text{M}$ .<sup>400,401</sup>

#### Organocatalyst-mediated protein aldol ligation to aldehyde-functionalised CjX183-D

To 20  $\mu\text{L}$  of PLP-treated CjX183-D (either WT or R51K) of ca. 50  $\mu\text{M}$  concentration of in pH 7.5 (25 mM sodium phosphate buffer) was added 1  $\mu\text{L}$  of a solution of (*S*)-5-(pyrrolidin-2-yl)-1*H*-tetrazole (the organocatalyst) in DMSO (550 mM, 76 mg mL<sup>-1</sup>), followed by 1  $\mu\text{L}$  of a solution of phenylacetaldehyde (20 mM, 2.4 mg mL<sup>-1</sup>). The resultant solution was incubated at 37 °C for 1 hour, after which time 3 kDa molecular weight cut-off molecular weight cut-off centrifugal protein concentrators were used to exchange the CjX183-D into HPLC-grade water. Prior to analysis by positive ion mode ESI-LC/MS, a 10  $\mu\text{L}$  sample of reaction mixture was added to 40  $\mu\text{L}$  50% (v/v) water/acetonitrile, 1% formic acid.

#### 8.4.4 Formylglycine installation

##### Introduction of fGly into ALCTPSRGSFLTGRG peptide using *Mt*-FGE

This methodology is from the work of Owen Jarman.<sup>459</sup>

*Mt*-FGE was buffer exchanged into conversion buffer (25 mM triethanolamine (TEAM), 50 mM NaCl, 5 mM dithiothreitol (DTT), pH 9.0) using a PD SpinTrap™ G-25 column (GE Healthcare) before concentrating using a 10 kDa centrifugal protein concentrator. ALCTPSRGSFLTGRG peptide (500 μM) was incubated with *Mt*-FGE (10 μM, 0.02 eqiv.) in a total volume of 100 μL for 6.5 h at 37 °C in conversion buffer (25 mM triethanolamine (TEAM), 50 mM NaCl, 5 mM dithiothreitol (DTT), pH 9.0). Reaction was initiated by addition of peptide and vortexing for 3 s. After 1-2 hours, the sample was flash frozen with N<sub>2</sub> and stored at -80 °C. Prior to analysis by ESI-LC/MS, a 5 μL sample of reaction mixture was added to 45 μL 50% (v/v) water/acetonitrile, 1% formic acid.

##### Introduction of fGly into ALCTPSRGSFLTGRG peptide using *Tc*FGE<sub>7</sub>

This methodology is from the work of Ben Jansco.<sup>563</sup>

Prior to all reactions, *Tc*FGE<sub>7</sub> was buffer exchanged into conversion buffer (25 mM triethanolamine (TEAM), 50 mM NaCl, 5 mM dithiothreitol (DTT), pH 9.0) using a PD SpinTrap™ G-25 column (GE Healthcare) before using a 10 kDa centrifugal protein concentrator. Bradford assay was used to determine the concentration of the *Tc*FGE<sub>7</sub> concentrate before making up reactions. Substrate peptide (500 μM) was incubated with *Tc*FGE<sub>7</sub> (10 μM, 0.02 eq.) in a total volume of 100 μL for 1-2 h at 37 °C in conversion buffer. Reaction was initiated by addition of peptide and vortexing for 3 s. Prior to analysis by ESI-LC/MS, a 20 μL sample of reaction mixture was quenched with 2 μL 1 M HCl and 2.5 μL of acetonitrile + 1% formic acid (v/v), and made up to 40 μL with 50% (v/v) water/acetonitrile, 1% formic acid).

##### Oxime ligation of fGly-modified ALCTPSRGSFLTGRG peptide

This methodology is from the works of Owen Jarman<sup>459</sup> and Ben Jansco.<sup>563</sup>

ALCTPSRGSFLTGRG peptide (500 μM) was incubated with *Mt*-FGE (10 μM) or *Tc*FGE<sub>7</sub> (10 μM) in a total volume of 100 μL for 3 h at 37 °C in conversion buffer (25 mM TEAM, 50 mM NaCl, 5 mM DTT, pH 9.0). The FGE-peptide reaction mixture (20 μL), was diluted into 80 μL pH 4.0 ligation buffer (100 mM sodium acetate, 150 mM NaCl, pH 4.0). To the diluted *Mt*-FGE-peptide mixture (20 μL, 500 μM) was added 4 μL *o*-benzylhydroxylamine (5 mM stock in ligation buffer) and made up to 40 μL with ligation buffer to a final concentration of 50 μM peptide and 500 μM *o*-benzylhydroxylamine. The



reaction was incubated at 37 °C overnight. Prior to analysis via positive ion mode ESI-LC/MS, a 5 µl sample of reaction mixture was added to 45 µL of 50% (v/v) water/acetonitrile, 1% formic acid.

#### ***Iso*-Pictet–Spengler ligation of fGly-modified ALCTPSRGSFLTGRG peptide**

This methodology is from the work of Owen Jarman.<sup>459</sup>

ALCTPSRGSFLTGRG peptide (500 µM) was incubated with *Mt*-FGE (50 µM) in a total volume of 100 µL for 3 h at 37 °C in conversion buffer (25 mM TEAM, 50 mM NaCl, 5 mM DTT, pH 9.0). The FGE-peptide reaction mixture (20 µL), was diluted into 80 µL pH 4.0 ligation buffer (100 mM sodium acetate, 150 mM NaCl, pH 4.0). To the diluted FGE-peptide mixture (20 µL, 500 µM) was added 4 µL of a 5 mM stock of IP8 in DMSO. After overnight incubation, a subsequent oxime ligation on the *iso*-Pictet-Spengler ligated peptide reaction mixture was performed by addition of 4 µL *o*-benzylhydroxylamine (5 mM stock in ligation buffer) to the reaction mixture (20 µL) to a final concentration of 0.8 µM *o*-benzylhydroxylamine. Reaction was incubated at 37 °C overnight and monitored by positive ion mode ESI-LC/MS.

#### **Introduction of fGly into ferropeptide using *Mt*-FGE**

*Mt*-FGE was buffer exchanged into conversion buffer using a PD SpinTrap G-25 column (GE Healthcare). Ferropeptide (500 µM) was incubated with FGE (µM, 0.02 equiv.) in a total volume of 100 µL for 6.5 h at 37 °C in conversion buffer (25 mM triethanolamine (TEAM), 50 mM NaCl, 5 mM dithiothreitol (DTT), pH 9.0). Reaction was initiated by addition of peptide and vortexing for 3 s. After 6.5 hours, the sample was flash frozen with N<sub>2</sub> and stored at -80 °C. Prior to analysis via LC-MS, a 5 µl sample of reaction mixture was added to 45 µL 50% (v/v) water/acetonitrile, 1% formic acid.

#### **Solution phase oxime ligation of fGly-ferropeptide**

Ferropeptide (500 µM) was incubated with *Mt*-FGE as detailed above. 20 µL of this reaction mixture, containing modified fGly-ferropeptide, was diluted with 80 µL ligation buffer (100 mM sodium acetate, 150 mM NaCl, pH 4.0). 4 µL of a 5 mM *o*-benzylhydroxylamide stock was then added to 20 µL of the diluted fGly-ferropeptide solution, and the resultant solution made up to 40 µL with ligation buffer to a final concentration of 50 µM peptide and 500 µM *o*-benzylhydroxylamine. The resulting solution was de-gassed via N<sub>2</sub> bubbling, and was incubated at 37 °C overnight under N<sub>2</sub>. Prior to analysis via LC-MS, a 5 µl sample of reaction mixture was added to 45 µL 50% (v/v) water/acetonitrile, 1% formic acid.

#### **Analysis of peptide experiments via LC-MS**

Peptide samples were analysed as described in **Section 8.1.1**. Under these conditions ALCTPSRGSFLTGRG-based peptides typically eluted at ~3.2 min, whereas ferropeptide-based peptides typically eluted at ~2.5 min.

**Tandem mass spectroscopy of ALCTPSRGSFLTGRG peptide.** Modified ALCTPSRGSFLTGRG peptide samples (fGly, oxime-ligated and *iso*-Pictet–Spengler ligated) were analysed by tandem mass spectroscopy. Base peaks of the  $[M+3H]^{3+}$  product ions were selected and fragmented. The major fragment ion was then subjected to further fragmentation. Mass spectra were assigned according to standard peptide fragmentation nomenclature.<sup>458</sup>

#### **Modification of DsbA<sub>c-term</sub> by Mt-FGE**

DsbA<sub>c-term</sub> and Mt-FGE were buffer exchanged into conversion buffer (25 mM TEAM, 150 mM NaCl, 5 mM DTT, pH 9.0) using a PD SpinTrap G-25 column (GE Healthcare). Multiple 50 µL reactions were prepared to a final concentration of 48 µM DsbA<sub>c-term</sub> and 10 µM Mt-FGE. Reaction was incubated at 37 °C for 20 h yielding fGly-DsbA<sub>c-term</sub>. Prior to MS analysis, 150 µL of reaction mixture was buffer exchanged into water using a SpinTrap and was diluted 1:1 with 50% (v/v) HPLC grade water/acetonitrile, 1% formic acid.

#### **Modification of DsbA<sub>c-term</sub> by TcFGE<sub>7</sub>**

This methodology is from the work of Ben Jansco.<sup>563</sup>

DsbA<sub>c-term</sub> and TcFGE<sub>7</sub> were buffer exchanged into conversion buffer (25 mM TEAM, 150 mM NaCl, 5 mM DTT, pH 9.0) using a PD SpinTrap G-25 column (GE Healthcare). Multiple 50 µL reactions were prepared to a final concentration of 50 µM DsbA<sub>c-term</sub> and 10 µM TcFGE<sub>7</sub>. Reaction was incubated at 37 °C for 20 h yielding fGly-DsbA<sub>c-term</sub> in 36% conversion. Prior to MS analysis, 150 µL of reaction mixture was buffer exchanged into water using a SpinTrap and was diluted 1:1 with 50% (v/v) HPLC grade water/acetonitrile, 1% formic acid.

#### **fGly-labelled DsbA<sub>c-term</sub> oxime ligation**

DsbA<sub>c-term</sub> was modified either using Mt-FGE or TcFGE<sub>7</sub> as described above. Reaction mixture containing fGly-DsbA<sub>c-term</sub> (150 µL) was buffer exchanged using PD SpinTrap G-25 into ligation buffer (100 mM sodium acetate, 150 mM NaCl, pH 4.0), yielding 150 µL of fGly-DsbA<sub>c-term</sub> solution. Ligation commenced upon addition of 1.5 µL of *o*-benzylhydroxylamine stock (500 mM in ligation buffer)

resulting in a final concentration of 5 mM *o*-benzylhydroxylamine in the reaction solution. The solution was incubated at 37 °C for 20 h. Prior to MS analysis, 150 µL of reaction mixture was buffer exchanged into water using a SpinTrap and was diluted 1:1 with 50% (v/v) HPLC grade water/acetonitrile, 1% formic acid.

#### **Attempted modification of DsbA<sub>middle</sub> by FGE enzymes**

Modification of DsbA<sub>middle</sub> using *Mt*-FGE or *Tc*FGE<sub>7</sub> and subsequent oxime ligation was attempted using the same conditions described above for DsbA<sub>c-term</sub>, but were unsuccessful, showing no products to be present besides unmodified DsbA<sub>middle</sub>. More forcing fGly installation conditions were trialled as well, using a 1:1 ratio of DsbA<sub>middle</sub> to *Mt*-FGE and a temperature of 42 °C, but fGly-DsbA<sub>middle</sub> was still not observed.

#### **Modification of DsbA<sub>middle</sub> by Alk1**

To 0.5 mL of a 130 µM solution of DsbA<sub>middle</sub> in pH 8.0 buffer (20 mM HEPES, 150 mM NaCl, 10% glycerol) was added Tris(2-carboxyethyl)phosphine (TCEP) (100 equiv), via the delivery of 57 µL of a 100 mM TCEP hydrochloride stock solution (which had been pre-neutralised using an NaOH solution). The resultant solution was incubated in the dark for 20 min, then exchanged into pH 9 buffer (20 mM sodium phosphate, 200 mM NaCl) using a PD MiniTrap™ G-25 desalting column. This yielded 1 mL of a 60 µM DsbA<sub>middle</sub> solution (as determined via UV-vis). TCEP (1 equiv) was added (via the delivery of 0.6 µL of the 100 mM TCEP hydrochloride stock), followed by 1-(3,5-bis(trifluoromethyl)phenyl)-2-bromoethan-1-one (**Alk1**) (5 equiv, delivered via the addition of 31 µL of a 10 mM stock of **Alk1** in DMSO). The resultant solution was incubated overnight at room temperature before being concentrated to a volume of 0.5 mL (using 3 kDa molecular weight cut-off centrifugal protein concentrators) and exchanged into pH 7.2 buffer (20 mM sodium phosphate, 200 mM NaCl) using a PD MiniTrap™ G-25 desalting column. A sample was then taken and dialysed into HPLC-grade water prior to analysis via MS.

The remaining solution of **Alk1**-labelled DsbA<sub>middle</sub> in pH 7.2 buffer was then exposed to UV light for 1 hour at room temperature using a 7 W 365 nm UV light bulb. A sample was then taken and dialysed into HPLC-grade water prior to analysis via MS.

#### **Analysis of DsbA samples via MS**

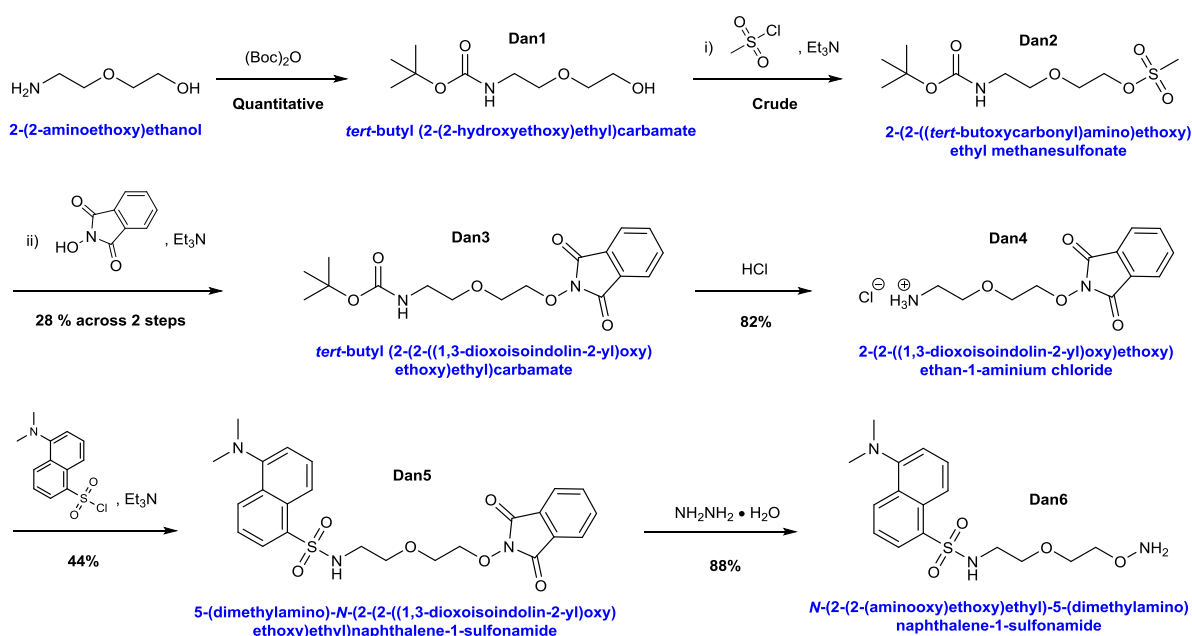
DsbA samples were analysed without a column using ESI-MS. Water + 0.1% formic acid by volume (solvent A) and acetonitrile + 0.1% formic acid (solvent B) were used as a mobile phase at a constant

mixture of 50% at room temperature. A multi-step flow rate was programmed as followed: flow rate increased to 250  $\mu\text{L}/\text{min}$  over 1 min, followed by a constant flow rate of 250  $\mu\text{L min}^{-1}$  for 1.5 min, followed by an increase to 1000  $\mu\text{L min}^{-1}$  over 0.5 min. Raw data of protein charge ladders were then deconvoluted using ESI Compass 1.3 DataAnalysis Version 4.1 software.

## 8.4.5 Synthesis of aldehyde-ligating probes

### 8.4.5.1 Synthesis of Dan6

**Scheme 8.3** summarizes the synthesis methodology used to generate the fluorescently-labelled hydroxylamine probe **Dan6** from commercially available 2-(2-aminoethoxy)ethanol via five intermediate species. Detailed protocols for the preparation of each species are provided below.



**Scheme 8.3.** The synthesis of the dansylated hydroxylamine-functionalised probe **Dan6** via intermediate species **Dan1**→**6**.

#### *tert*-butyl (2-(2-hydroxyethoxy)ethyl)carbamate (Dan1)

To a solution of 2-(2-aminoethoxy)ethanol (1.05 g, 10 mmol) in DCM (20 mL) at room temperature was added di-*tert*-butyl decarbonate (2.18 g, 10 mmol). The resultant solution was stirred overnight at room temperature, after which time it was concentrated *in vacuo*, and purified via flash column chromatography ( $\text{SiO}_2$ , hexane  $\rightarrow$  ethyl acetate), yielding *tert*-butyl (2-(2-hydroxyethoxy)ethyl)carbamate as a colourless oil in quantitative yield.  $^1\text{H-NMR}$  was in agreement with that reported in the literature.<sup>564</sup>

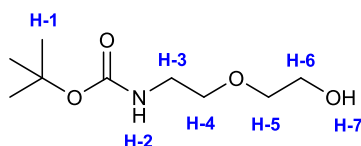


Figure 8.16. The structure and labelling of chemical environments of **Dan1**.

$^1\text{H-NMR}$  (400 MHz,  $\text{CDCl}_3$ ):  $\delta_{\text{H}}$  3.74 (t,  $J = 4.85$  Hz, 2H), 3.60-3.52 (m, 4H), 3.32 (t,  $J = 5.50$  Hz), 1.44 (s, 9H).

### 2-(2-((*tert*-butoxycarbonyl)amino)ethoxy)ethyl methanesulfonate (**Dan2**)

To a solution of **Dan1** (1.31 g, 6.38 mmol) in DCM (20 mL) at 0 °C was added triethylamine (1.34 mL, 9.57 mmol, 1.50 equivs). To the resultant solution was added methane sulfonyl chloride (0.60 mL, 7.75 mmol, 1.21 equivs) dropwise. The resultant solution was then placed under a nitrogen atmosphere and allowed was stirred at room temperature for 3 hours. After this time the solution was transferred to a separating funnel and washed with water (1 × 20 mL) and brine (1 × 20 mL), prior to being dried over  $\text{MgSO}_4$  and concentrated *in vacuo* to yield **Dan2** as a brown residue that was used crude (1.49 g,  $\leq 82\%$ ).

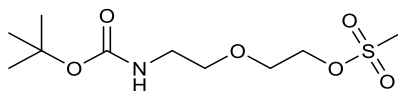


Figure 8.17. The structure of **Dan2**.

### *tert*-butyl 2-(2-((1,3-dioxoisindolin-2-yl)oxy)ethoxy)ethyl carbamate (**Dan3**)

To a solution of crude **Dan2** (0.745 g,  $\leq 2.62$  mmol) in DMF (10 mL) at room temperature was added *N*-hydroxyphthalimide (0.470 g, 2.88 mmol) and triethylamine (0.67 mL, 4.8 mmol). The resultant solution was refluxed overnight, after which time the solution was concentrated *in vacuo*. The crude residue was then re-dissolved in DCM (30 mL), and transferred to a separating funnel. The solution was washed with an aqueous 10% citric acid solution (2 × 20 mL), saturated  $\text{NaHCO}_3$  (aq) (1 × 20 mL), and brine (1 × 20 mL), then dried over  $\text{MgSO}_4$  and concentrated *in vacuo*. The crude residue was then purified via flash column chromatography ( $\text{SiO}_2$ , hexane  $\rightarrow$  ethyl acetate) to yield **Dan3** as an olive-green coloured oil (0.253 g, 28% across two steps).

$^1\text{H-NMR}$  (400 MHz,  $\text{CDCl}_3$ , **Figure 8.19**):  $\delta_{\text{H}}$  7.85 (m, 2H, H-7), 7.76 (m, 2H, H-8), 5.10 (apparent br s, 1H, H-2), 4.39-4.34 (m, 2H, H-6), 3.83 (m, 2H, H-5), 3.55 (t,  $J = 5.04$  Hz, 2H, H-4), 3.25 (br dt,  $J = 10.07$ , 5.04 Hz, 2H, H-3), 1.44 (s, 9H, H-1).

$^{13}\text{C-NMR}$  (100 MHz,  $\text{CDCl}_3$ , **Figure 8.20**):  $\delta_c$  163.49 (C-8), 155.97 (C-3), 134.51 (C-11), 128.81 (C-9), 123.52 (C-10), 79.10 (C-2), 77.14 (C-7) 70.54 (C-5), 68.85 (C-6), 40.22 (C-4), 28.37 (C-1).

(ESI)HRMS (**Figure 8.21**): Found  $[\text{M}+\text{Na}]^+$  373.1369,  $\text{C}_{17}\text{H}_{22}\text{N}_2\text{NaO}_6$  requires 373.1370.

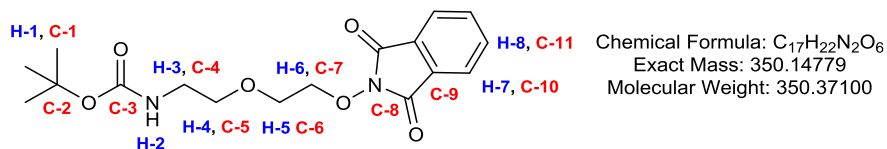


**Figure 8.18.** The structure and labelling of chemical environments of **Dan3**.

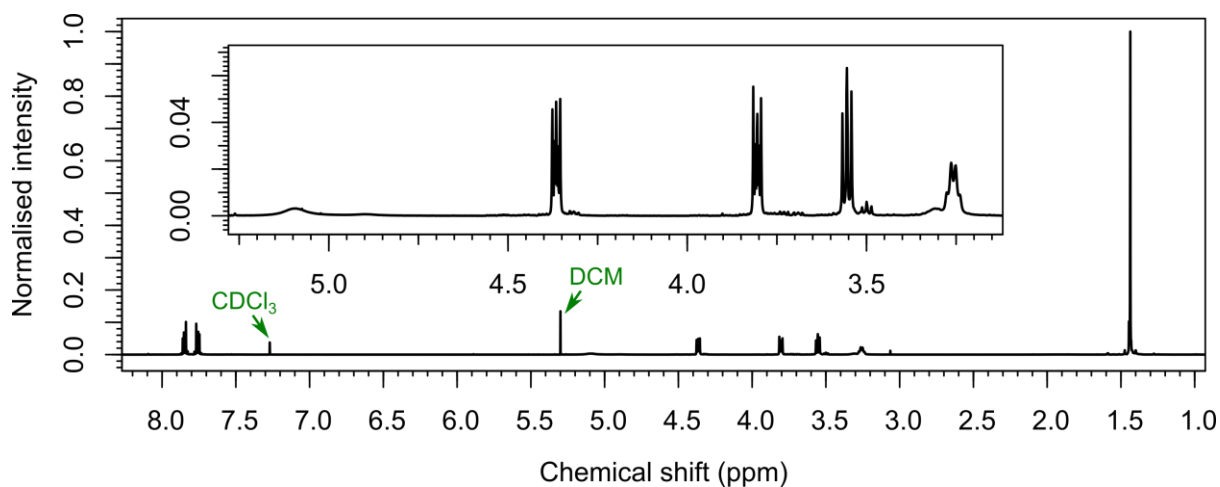


**Figure 8.19.**  $^1\text{H-NMR}$  spectrum of **Dan3**.

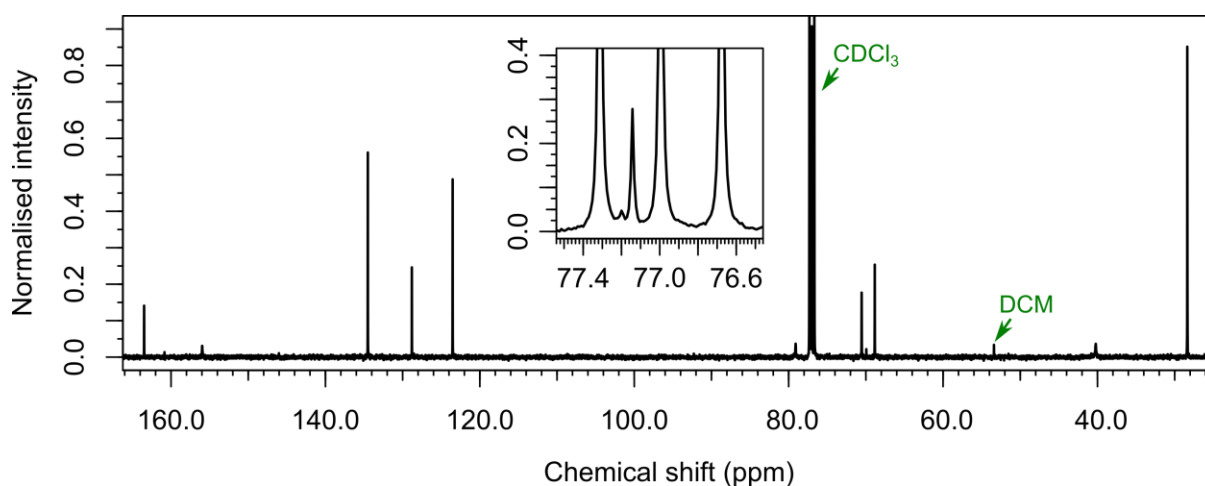


**Figure 8.20.**  $^{13}\text{C-NMR}$  spectrum of **Dan3**.

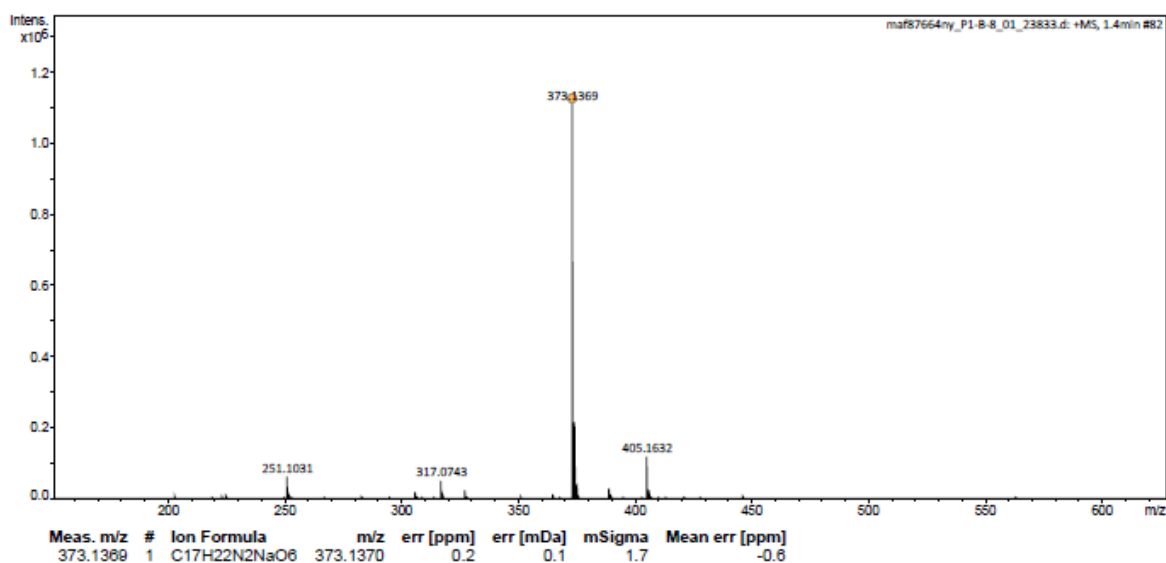


Figure 8.21. ESI-LC/MS spectrum of Dan3.

#### 2-(2-((1,3-dioxisoindolin-2-yl)oxy)ethoxy)ethan-1-amium chloride (Dan4)

To **Dan3** (0.169 g, 0.483 mmol) was dissolved in a 2 M solution of HCl in diethyl ether, and the resultant solution stirred for 48 hours at room temperature, during which time **Dan4** precipitated. Solvents were then removed *in vacuo*, and the resultant residue dissolved in the minimum volume of DMF. The DMF solution was then added drop-by-drop into 30 mL of diethyl ether at room temperature, causing pure **Dan4** to precipitate as a fine powder. **Dan4** was isolated by centrifugation, and DMF was removed by resuspending **Dan4** in fresh diethyl ether, before isolating once again by centrifugation. This yielded **Dan4** as a pale brown solid (0.113 g, 82%).

<sup>1</sup>H-NMR (400 MHz, methanol-d<sub>4</sub>, **Figure 8.23**): δ<sub>H</sub> 7.92-7.79 (m, 4H, H-6,7), 4.40-4.35 (m, 2H, H-5), 3.88-3.82 (m, 2H, H-4), 3.22-3.12 (m, 2H, H-2).

<sup>13</sup>C-NMR (100 MHz, methanol-d<sub>4</sub>, **Figure 8.24**): δ<sub>C</sub> 165.41 (C-5), 136.29 (C-8 (rotamer), 136.08 (C-8 rotamer), 130.40 (C-6), 124.75 (C-7 rotamer), 124.52 (C-7 rotamer), 78.77 (C-2), 69.86 (C-4) 68.10 (C-3), 40.80 (C-1). The carbon signals for C-4, C-3 and C-1 also seem to have smaller satellite signals, presumed to be due to rotamers.

(ESI)HRMS: Found [M-Cl]<sup>+</sup> 251.1034, C<sub>12</sub>H<sub>15</sub>N<sub>2</sub>O<sub>4</sub> requires 251.1026.

IR (ATR) (**Figure 8.26**) (u<sub>max</sub>/cm<sup>-1</sup>): 3000-2700 (N-H stretch, amine salt), 1721 (C=O stretching), 696 (C-H bend aromatic).

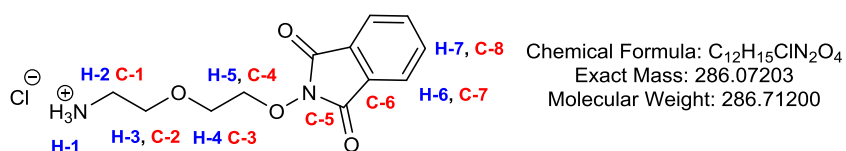


Figure 8.22. The structure and labelling of chemical environments of **Dan4**.

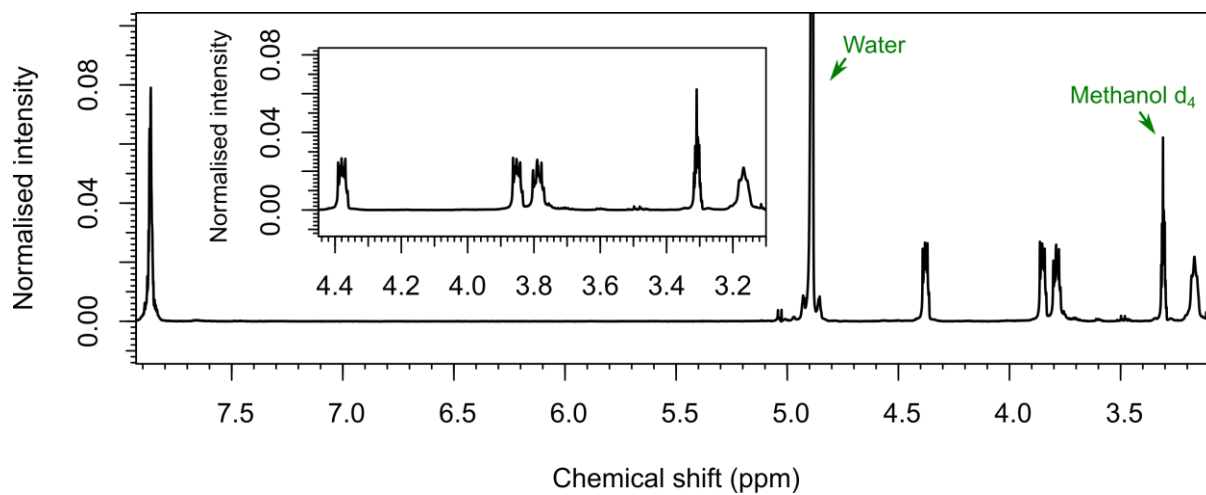


Figure 8.23.  $^1\text{H-NMR}$  spectrum of **Dan4**.

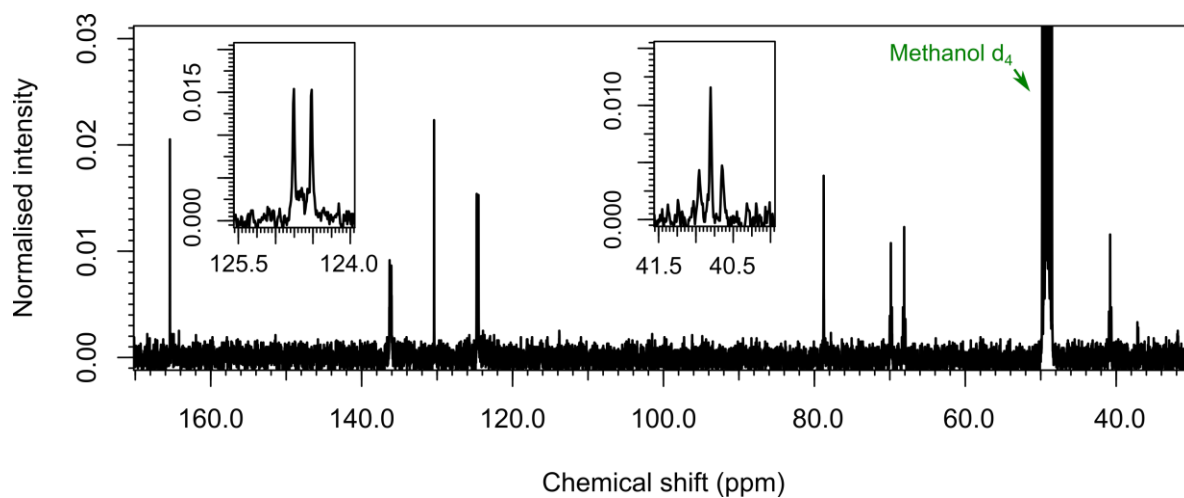


Figure 8.24.  $^{13}\text{C-NMR}$  spectrum of **Dan4**, showing the unexpected twinning (or even tripling) of certain signals.



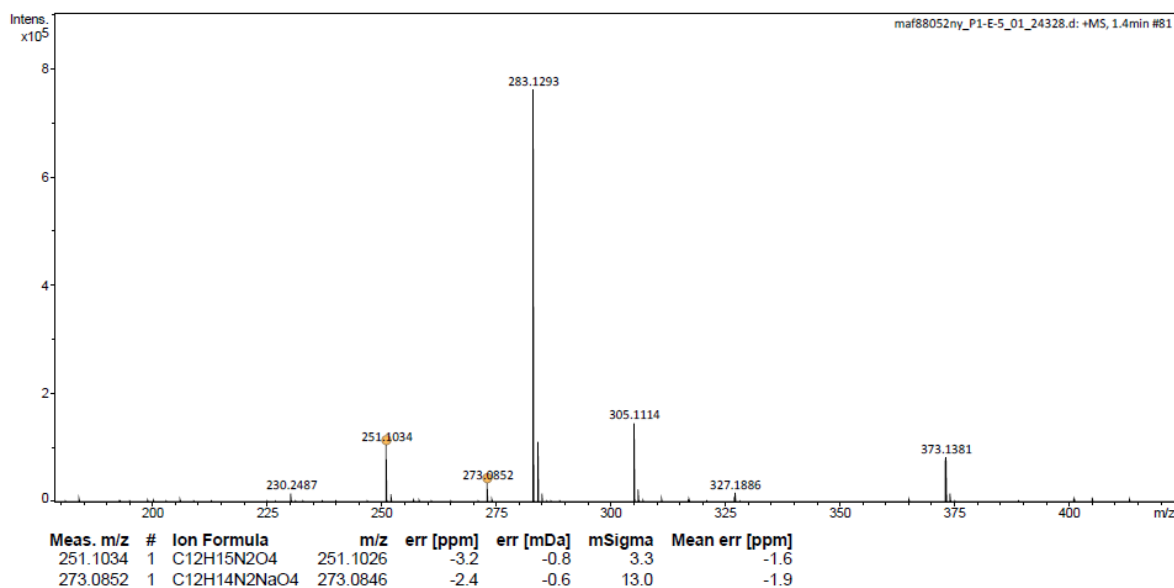


Figure 8.25. ESI-LC/MS spectrum of Dan4.

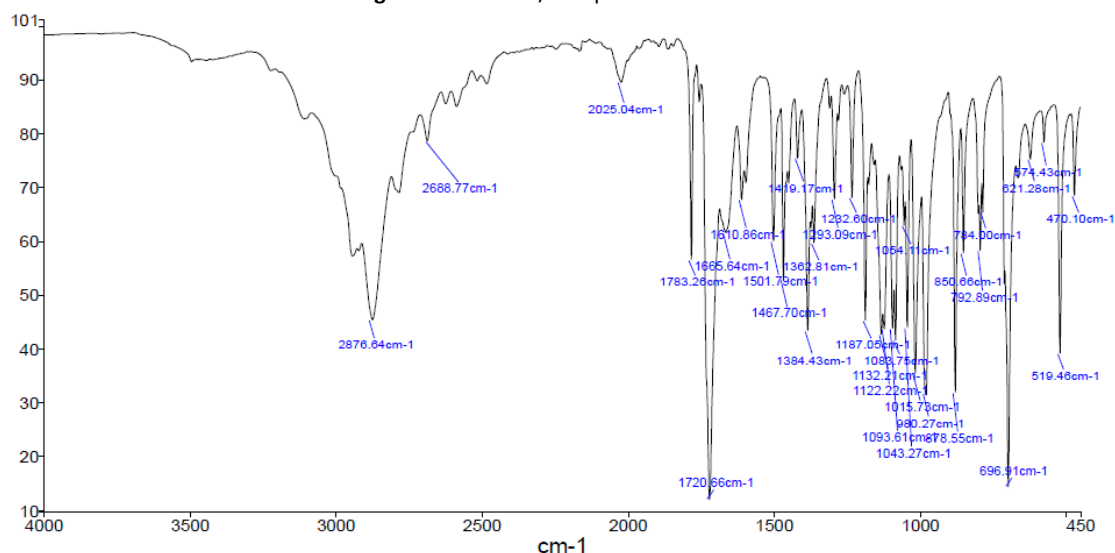


Figure 8.26. IR (ATR) spectrum of Dan4.

#### 5-(dimethylamino)-N-(2-(2-((1,3-dioxisoindolin-2-yl)oxy)ethoxy)ethyl)naphthalene-1-sulfonamide (Dan5)

To a solution of **Dan4** (70.0 mg, 0.259 mmol) dissolved in DMF (4 mL) at 0 °C was added triethylamine (78.5 mg, 110  $\mu$ L, 0.776 mmol), followed by dansyl chloride (0.135 g, 0.5 mmol). The resultant solution was subsequently stirred overnight at room temperature. The reaction solution was then concentrated *in vacuo*, re-suspended in DCM (30 mL) and transferred to a separating funnel before being washed with water (2  $\times$  30 mL) sat NaHCO<sub>3</sub> (aq) (30 mL) and brine (30 mL). The organic extraction was then dried over MgSO<sub>4</sub>, dry-loaded onto silica, and purified via flash column chromatography (hexane  $\rightarrow$  ethyl acetate), yielding **Dan5** as a green oil (55.7 mg, 0.115 mmol, 44%).

**$^1\text{H-NMR}$**  (400 MHz,  $\text{CDCl}_3$ , **Figure 8.28**):  $\delta_{\text{H}}$  8.53 (d,  $J = 8.23$  Hz, 1H, H-7), 8.24 (dd,  $J = 7.32, 1.37$  Hz, 1H, H-5), 7.87-7.81 (m, 2H, H-13), 7.78-7.71 (m, 2H, H-14), 7.58-7.48 (m, 2H, H-3,6), 7.19 (d,  $J = 7.32$  Hz, 1H, H-2), 5.70 (br t,  $J = 5.49$  Hz, 1H, H-8), 4.32-4.18 (m, 2H, H-12), 3.55-3.50 (m, 2H, H-11), 3.40 (t,  $J = 5.03$  Hz, 2H, H-10), 3.09 (dt,  $J = 5.49, 5.03$  Hz, 2H, H-9), 2.89 (s, 6H, H-1).

**$^{13}\text{C-NMR}$**  (100 MHz,  $\text{CDCl}_3$ , **Figure 8.29**):  $\delta_{\text{C}}$  163.40 (C-16), 135.57 (C-2), 153.50 (C-7), 134.44 (C-19), 129.97 (C-10), 129.53 (C-6), 129.42 (C-11), 129.09 (C-4), 128.45 (C-8), 128.05 (C-17), 123.46 (C-18), 123.01 (C-9), 119.02 (C-5), 115.00 (C-3), 76.90 (C-15), 69.32 (C-13), 68.30 (C-14), 45.22 (C-1), 42.67 (C-12).

**(ESI)HRMS** (**Figure 8.30**): Found  $[\text{M}+\text{Na}]^+$  506.1363,  $\text{C}_{24}\text{H}_{25}\text{N}_3\text{NaO}_6\text{S}$  requires 506.1356.

**IR (ATR)** (**Figure 8.31**) ( $\text{umax}/\text{cm}^{-1}$ ): 2958 (C-H alkyl), 2895 (C-H alkyl), 1731 (C=O stretch), 1705 (C=O stretch), 1395 (S=O stretch, sulfonamide), 1024 (C-H aromatic), 878 (C-H bend aromatic), 788 (C-H bend aromatic).

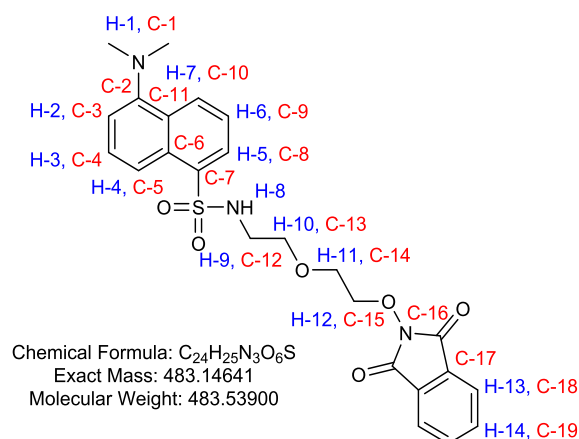


**Figure 8.27.** The structure and labelling of chemical environments of **Dan5**.

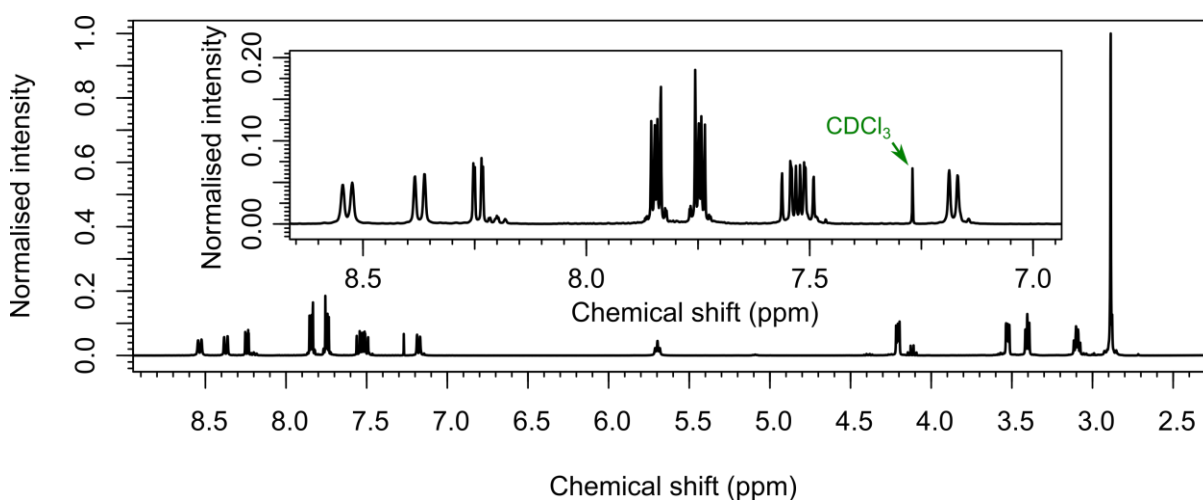


**Figure 8.28.**  $^1\text{H-NMR}$  spectrum of **Dan5**.

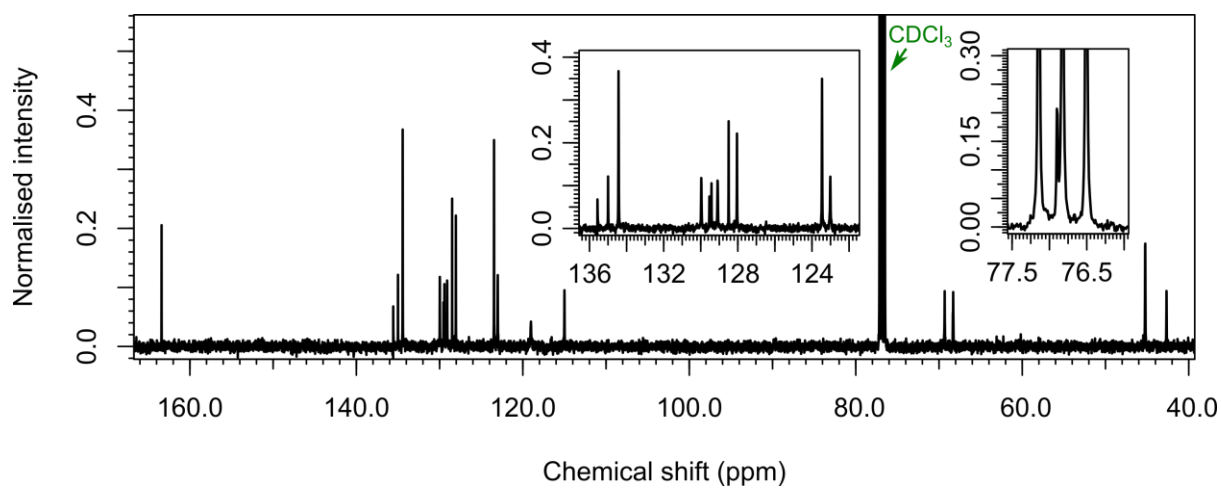
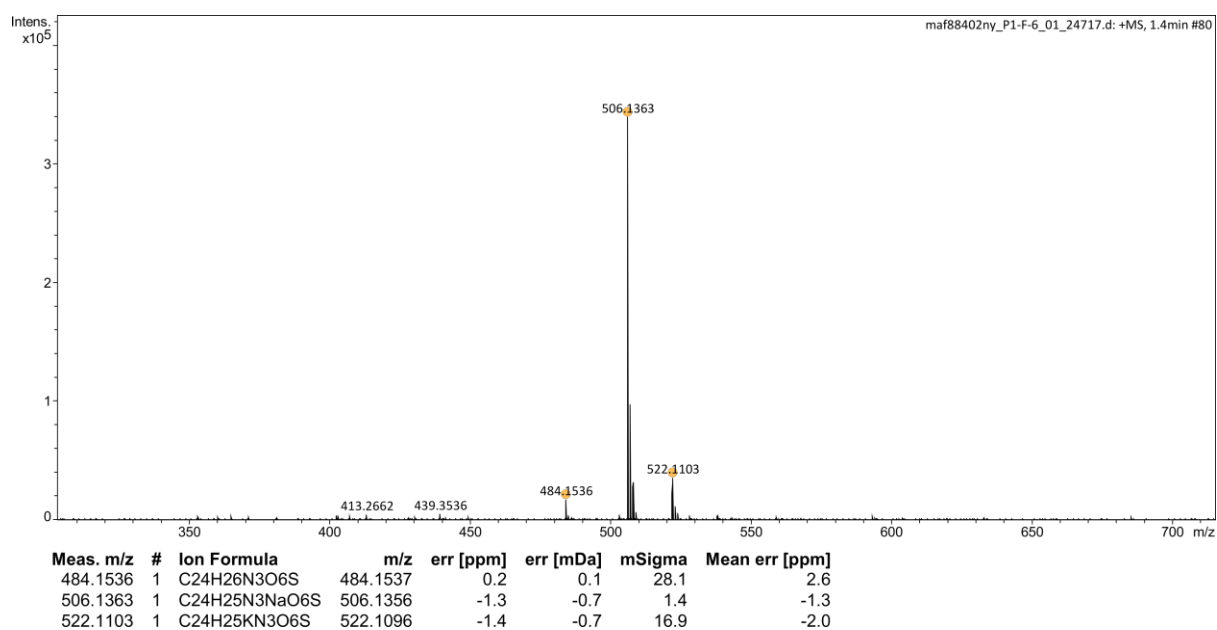
Figure 8.29.  $^{13}\text{C}$ -NMR spectrum of Dan5.

Figure 8.30. ESI-LC/MS spectrum of Dan5.

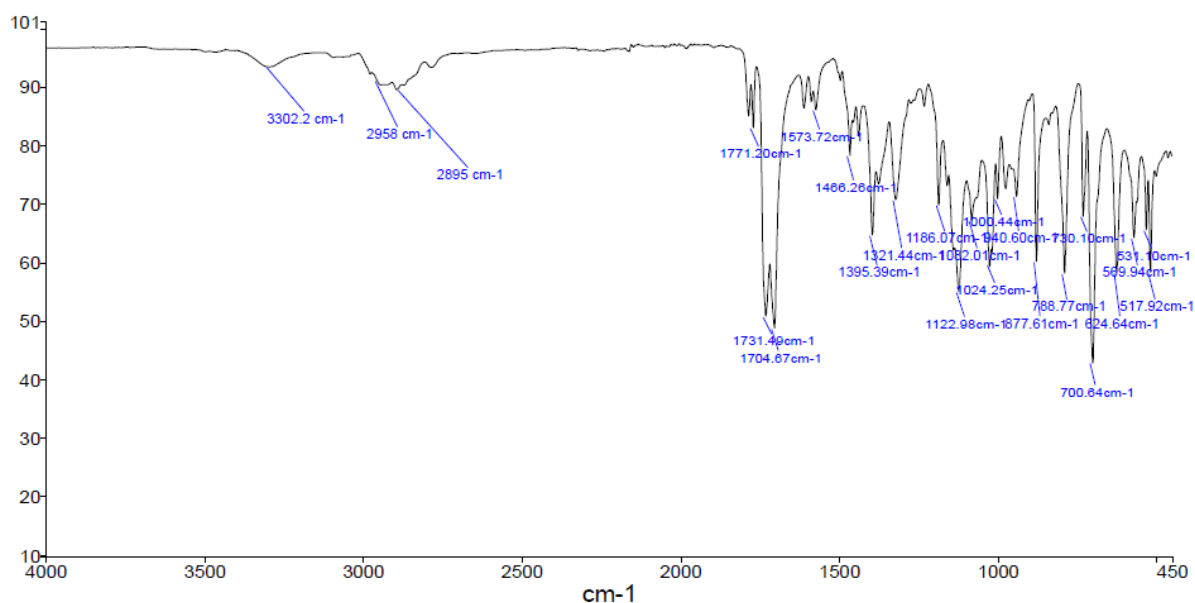


Figure 8.31. IR (ATR) spectrum of Dan5.

***N*-(2-(2-(aminooxy)ethoxy)ethyl)-5-(dimethylamino)naphthalene-1-sulfonamide (Dan6)**

To a solution of **Dan5** (45 mg, 0.093 mmol) dissolved in the minimum volume of DCM was added hydrazine monohydrate (85  $\mu$ L, 5.2 mg, 0.10 mmol) The resultant solution was stirred at room temperature for 4 hours, whereafter a precipitate formed. The precipitate was removed via filtration and the filtrate purified via flash column chromatography (hexane  $\rightarrow$  ethyl acetate) to yield **Dan6** as a pale green residue (29 mg, 0.082 mmol, 88%).

**$^1\text{H-NMR}$**  (400 MHz,  $\text{CDCl}_3$ , **Figure 8.33**):  $\delta_{\text{H}}$  8.56 (d,  $J = 8.70$  Hz, 1H, H-7), 8.35 (d,  $J = 8.70$  Hz, 1H, H-4), 8.26 (d,  $J = 7.33$  Hz, 1H, H-5), 7.61 (dd,  $J = 8.70, 7.73$  Hz, H-3), 7.53 (dd,  $J = 8.70, 7.79$  Hz, H-6), 7.22 (d,  $J = 7.79$  Hz, 1H, H-2), 5.85 (br t,  $J = 5.04$  Hz, 1H, H-8), 3.77 (m, 2H, H-12), 3.34-3.35 (m, 4H, H-10,11), 3.18-3.11 (m, 2H, H-9) 2.91 (s, 6H, H-1).

**$^{13}\text{C-NMR}$**  (100 MHz,  $\text{CDCl}_3$ , **Figure 8.34**):  $\delta_{\text{C}}$  152.18 (C-2), 135.15 (C-7), 130.27 (C-10), 129.76 (C-6), 129.59 (C-11), 129.33 (C-4), 128.37 (C-8), 123.28 (C-9), 119.15 (C-5), 115.31 (C-3), 77.19 (C-15), 69.68 (C-13), 69.40 (C-14), 45.45 (C-1), 42.95 (C-12).

**(ESI)HRMS (Figure 8.35)**: Found  $[\text{M}+\text{H}]^+$  354.1486,  $\text{C}_{16}\text{H}_{24}\text{N}_3\text{O}_4\text{S}$  requires 354.1482.

**IR (ATR) (Figure 8.36)** ( $\text{umax}/\text{cm}^{-1}$ ): 3307 (N-H stretch), 2946 (C-H alkyl), 2869 (C-H alkyl), 1710 (N-H bend, hydroxylamine), 1353 (S=O stretch, sulfonamide), 1314 (C-N stretch, aromatic amine), 1140 (C-O stretch), 1091 (C-H aromatic), 790 (C-H bend aromatic).

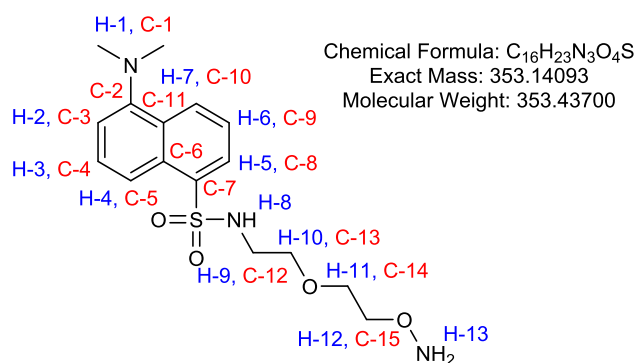


Figure 8.32. The structure and labelling of chemical environments of Dan6.

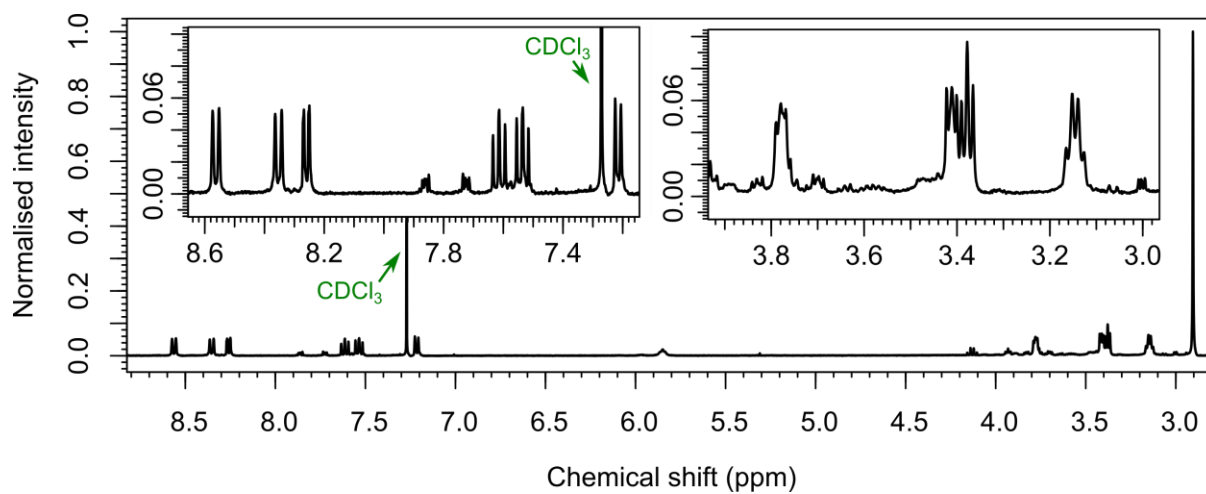


Figure 8.33.  $^1\text{H-NMR}$  spectrum of Dan6.

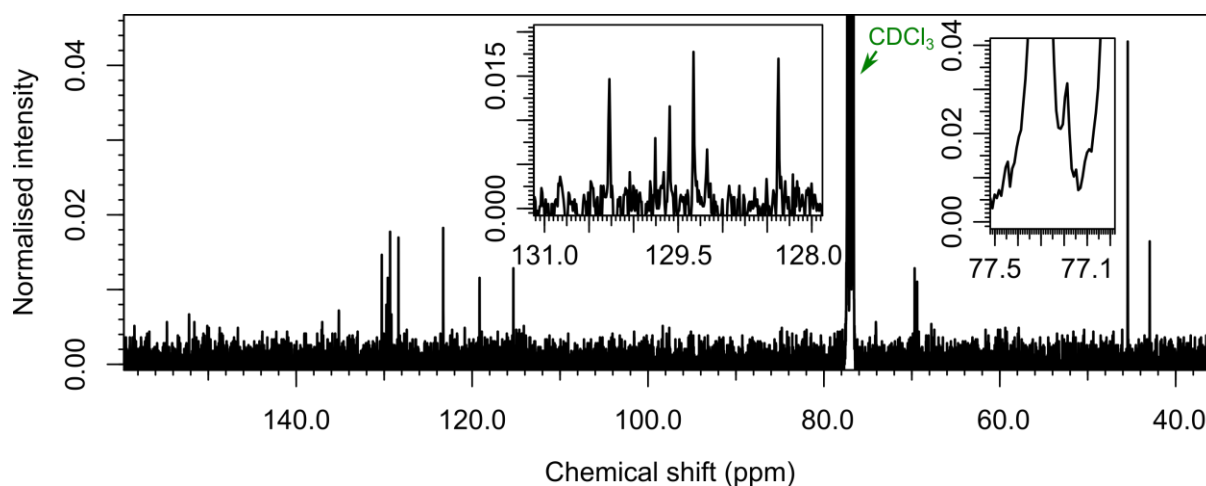


Figure 8.34.  $^{13}\text{C-NMR}$  spectrum of Dan6.

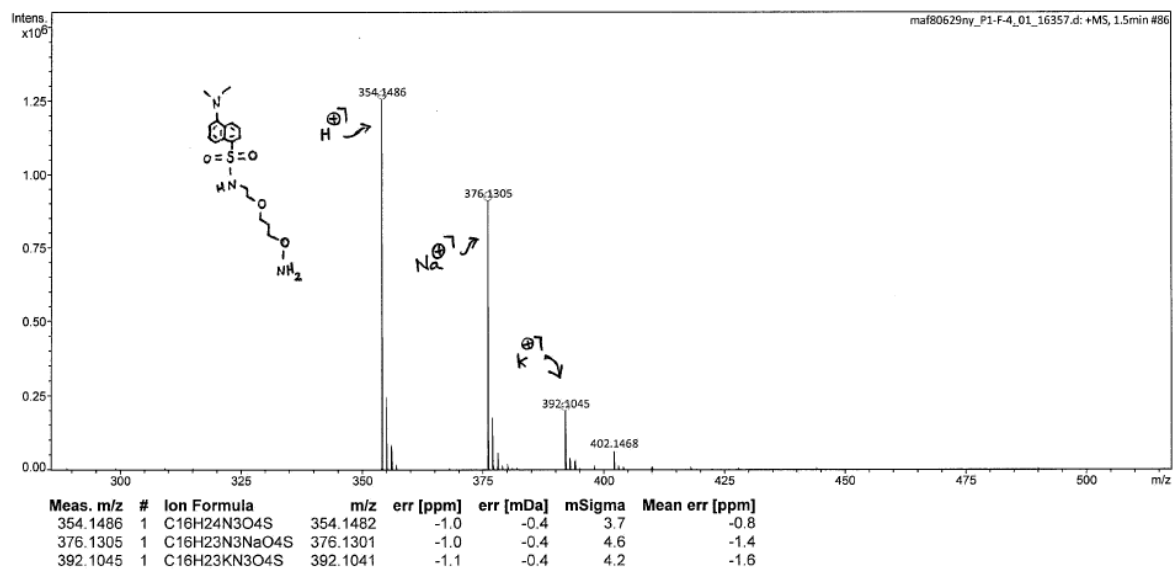


Figure 8.35. ESI-LC/MS spectrum of Dan6.

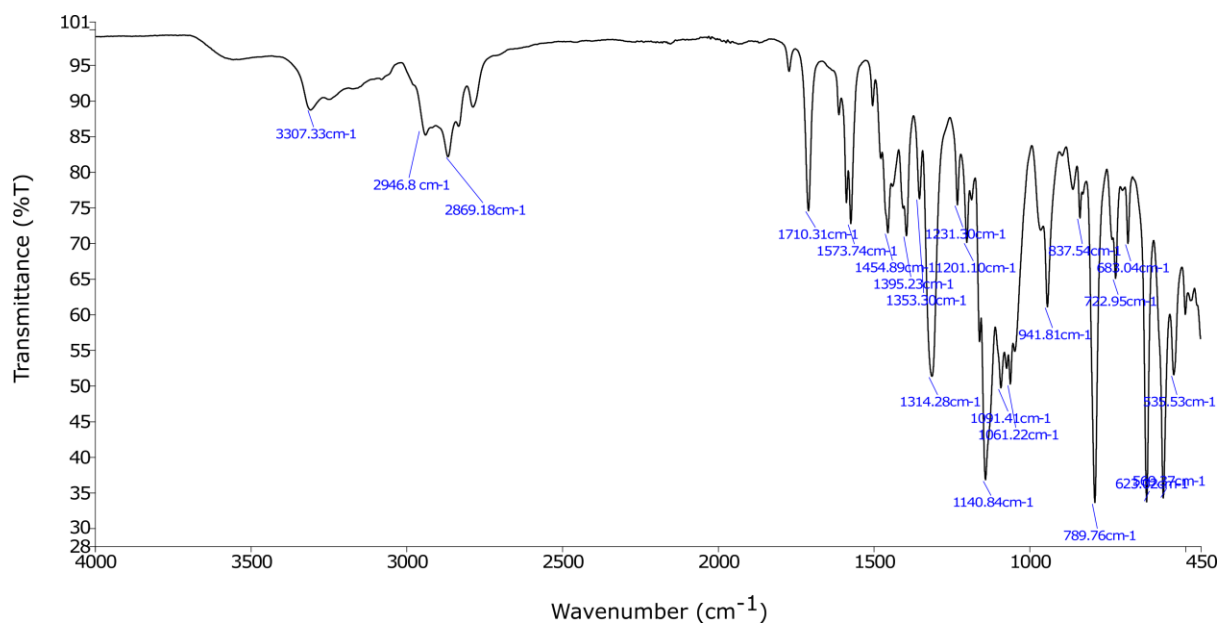
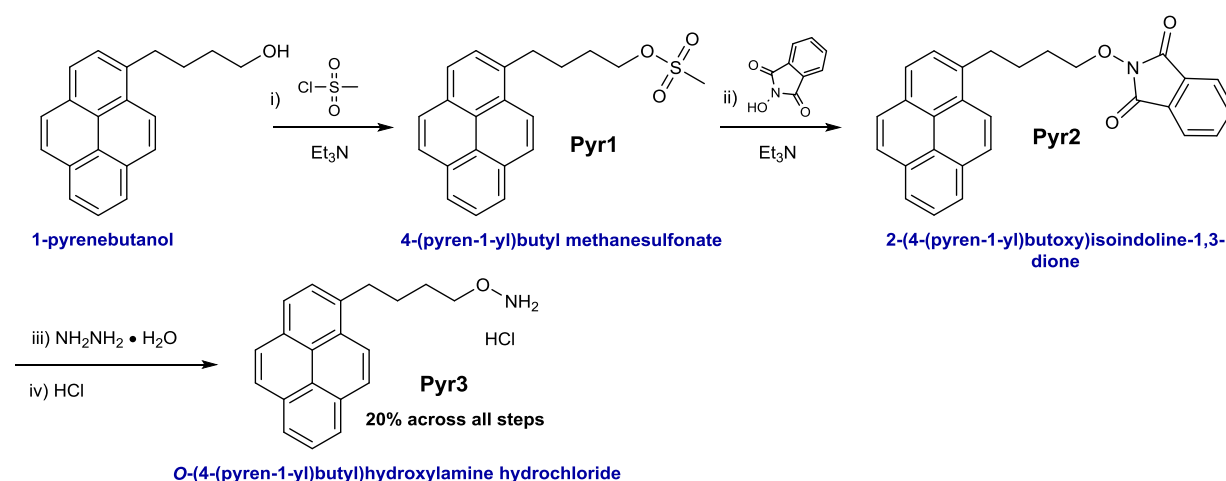


Figure 8.36. IR (ATR) spectrum of Dan6.

## 8.4.5.2 Synthesis of Pyr3

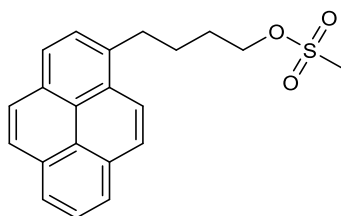
**Scheme 8.4** summarizes the synthesis methodology used to generate the pyrene-labelled hydroxylamine probe **Pyr3** from commercially available 1-pyrenebutanol. Detailed protocols for the preparation of each species are provided below.



**Scheme 8.4.** The synthesis of a pyrene-functionalised aldehyde-reactive hydroxylamine probe **Pyr3**.

4-(pyren-1-yl)butyl methanesulfonate (**Pyr1**)

A flask charged with 1-pyrenebutanol (0.274 g, 1.00 mmol) was placed under a nitrogen atmosphere. Anhydrous DCE (6 mL) and triethylamine (0.76 mL, 5.5 mmol) were then added with stirring. Methanesulfonyl chloride (0.12 mL, 1.5 mmol) was then added dropwise and the resultant solution stirred for 2 hours at room temperature. After this time the reaction solution was transferred to a separating funnel and washed with 1 M aqueous HCl (20 mL), water (2 × 20 mL) and brine (20 mL), dried over  $\text{MgSO}_4$  and concentrated *in vacuo*. This yielded **Pyr1** as a crude light brown residue which was immediately used in the next reaction step.



Chemical Formula:  $\text{C}_{21}\text{H}_{20}\text{O}_3\text{S}$   
Exact Mass: 352.11332  
Molecular Weight: 352.44800

**Figure 8.37.** Structure of **Pyr1**.

**2-(4-(pyren-1-yl)butoxy)isoindoline-1,3-dione (Pyr2)**

To the crude sample of **Pyr1** ( $\leq 1.00$  mmol) was added 2 mL of DMF, and the resultant solution stirred at room temperature. *N*-hydroxyphthalimide (0.326 g, 2 mmol) was then added, followed by triethylamine (0.29 mL, 2.1 mmol). The resultant deep red solution was stirred overnight at 50 °C. After this time DCM was added (100 mL) and the resultant solution was transferred to a separating funnel, where it was washed with water (100 mL), NaHCO<sub>3</sub> (2 × 100 mL), 1 M HCl (100 mL) and brine (100 mL). The organic extraction was then dried over MgSO<sub>4</sub> and concentrated *in vacuo*. The resulting crude residue was partly purified via flash column chromatography, yielding a sample of 2-(4-(pyren-1-yl)butoxy)isoindoline-1,3-dione (0.268 g,  $< 0.638$  mmol,  $< 64\%$ ) seemingly contaminated with an unknown phthalimide-functionalised compound (known due to proton NMR). This crude product was then used immediately in the next reaction step.

<sup>1</sup>H-NMR (400 MHz, CDCl<sub>3</sub> **Figure 8.39**):  $\delta_{\text{H}}$  8.35 (d,  $J = 9.62$  Hz, 1H, H-1), 8.20-8.10 (m, 4H, H-2,3,5,8), 8.07-8.02 (m, 2H, H-6,7) 8.00 (dd,  $J = 7.79, 7.33$  Hz, 1H, H-4), 7.91 (d,  $J = 7.79$  Hz, 1H, H-4), 7.85-7.81 (m, 2H, H-14), 7.76-7.73 (m, 2H, H-15), 4.30 (t,  $J = 6.41$  Hz, 2H, H-13), 3.46 (t,  $J = 7.79$  Hz, 2H, H-10), 2.14-2.06 (m, 2H, H-11) 2.04-1.93 (m, 2H, H-12).

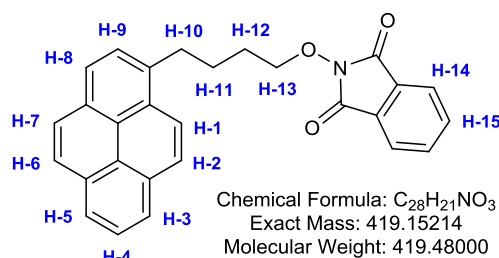


**Figure 8.38.** Structure of **Pyr2**.

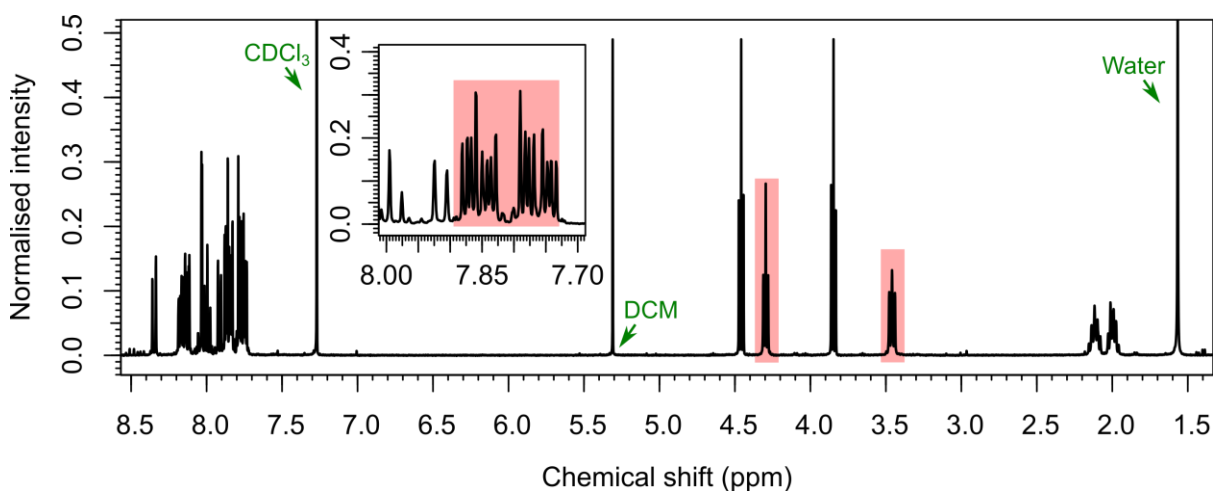


**Figure 8.39.** Crude <sup>1</sup>H-NMR spectrum of **Pyr2**. Regions that contain contributions from species other than **Pyr2** are highlighted.



**O-(4-(pyren-1-yl)butyl)hydroxylamine hydrochloride (Pyr3)**

The crude sample of 2-(4-(pyren-1-yl)butoxy)isoindoline-1,3-dione (assumed to contain a maximum of 0.638 mmol) was dissolved in DCM (10 mL) and hydrazine monohydrate (100  $\mu$ L, 1.71 mmol) was added. The resultant solution was stirred for 1 hour, whereupon a white precipitate formed. This precipitate was removed via filtration and the filtrate washed with water (2  $\times$  20 mL), NaHCO<sub>3</sub> (20 mL) and brine (20 mL). The organic extract was dried over MgSO<sub>4</sub> and concentrated *in vacuo* to yield a crude yellow oily residue, which was purified by flash column chromatography (SiO<sub>2</sub>, hexane  $\rightarrow$  ethyl acetate) to yield a yellow oil (0.074 g, maximum 0.25 mmol). This yellow oil was dissolved in DCM (4 mL) and HCl (2 M in diethyl ether, 0.13 mL, 0.26 mmol) was added, whereupon **Pyr3** precipitated. **Pyr3** was isolated by filtration and dried to yield a yellow solid (0.065 g, 0.20 mmol, 20% across all previous steps).

**<sup>1</sup>H-NMR** (400 MHz, Methanol-d<sub>4</sub> (**Figure 8.41**)):  $\delta_{\text{H}}$  8.33 (d,  $J$  = 9.16 Hz, 1H, H-1), 8.22-8.17 (m, 2H, H-3,5), 8.17-8.13 (m, 2H, H-2,8), 8.07-8.04 (m, 2H, H-6,7) 8.01 (dd,  $J$  = 7.79, 7.33 Hz, 1H, H-4), 7.91 (d,  $J$  = 7.79 Hz, 1H, H-4), 4.09 (t,  $J$  = 6.41 Hz, 2H, H-13), 3.43 (t,  $J$  = 7.79 Hz, 2H, H-10), 2.03-1.93 (m, 2H, H-11) 1.92-1.81 (m, 2H, H-12).

**<sup>13</sup>C-NMR** (100 MHz, Methanol-d<sub>4</sub> (**Figure 8.42**)):  $\delta_{\text{C}}$  137.59 (C-16), 133.02, 132.46, 131.56, 130.02, 128.70 (C-15), 128.64, 128.56, 127.91, 127.23, 126.44, 126.49, 126.20, 126.10, 126.01, 124.48 (C-4), 76.39 (C-20), 34.00 (C-17), 29.22 (C-19), 28.89 (C-18).

**(ESI)HRMS** (**Figure 8.43**): Found [M-Cl]<sup>+</sup> 290.1539, C<sub>20</sub>H<sub>20</sub>NO requires 290.1539.

**IR (ATR)** (**Figure 8.44**) ( $\nu_{\text{max}}/\text{cm}^{-1}$ ): 2893 (C-H stretch), 2683 (C-H stretch), 1578 (aromatic C-H bend overtone), 843 (C-H bend aromatic).

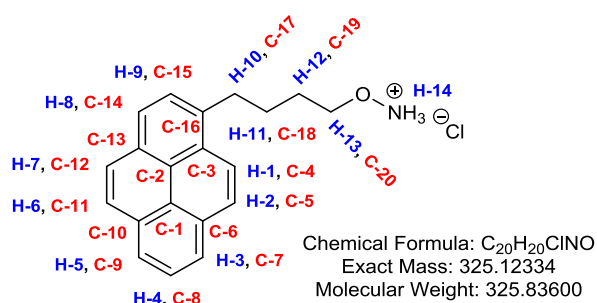


**Figure 8.40.** Structure and labelling of chemical environments of **Pyr3**.

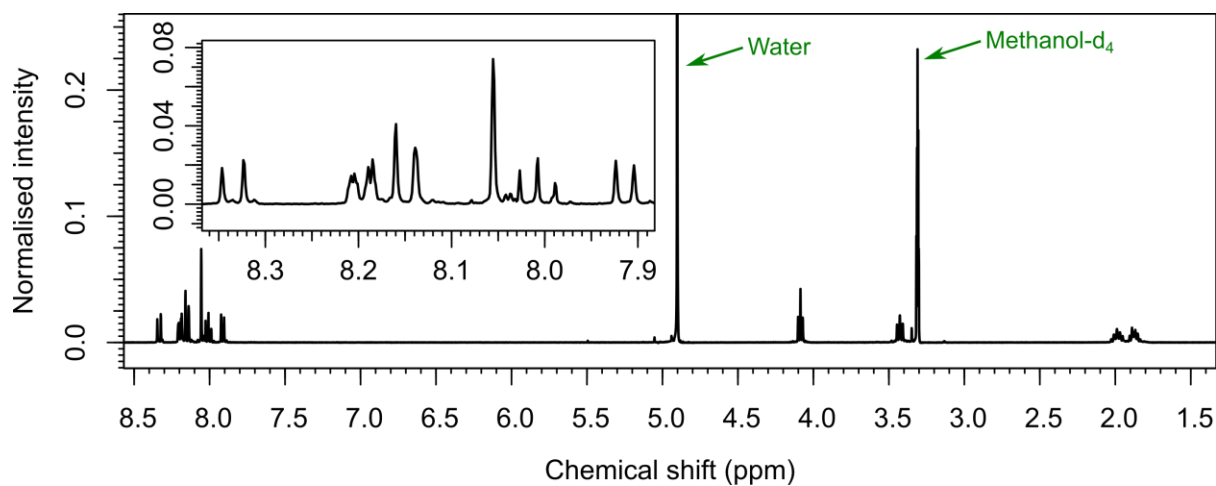
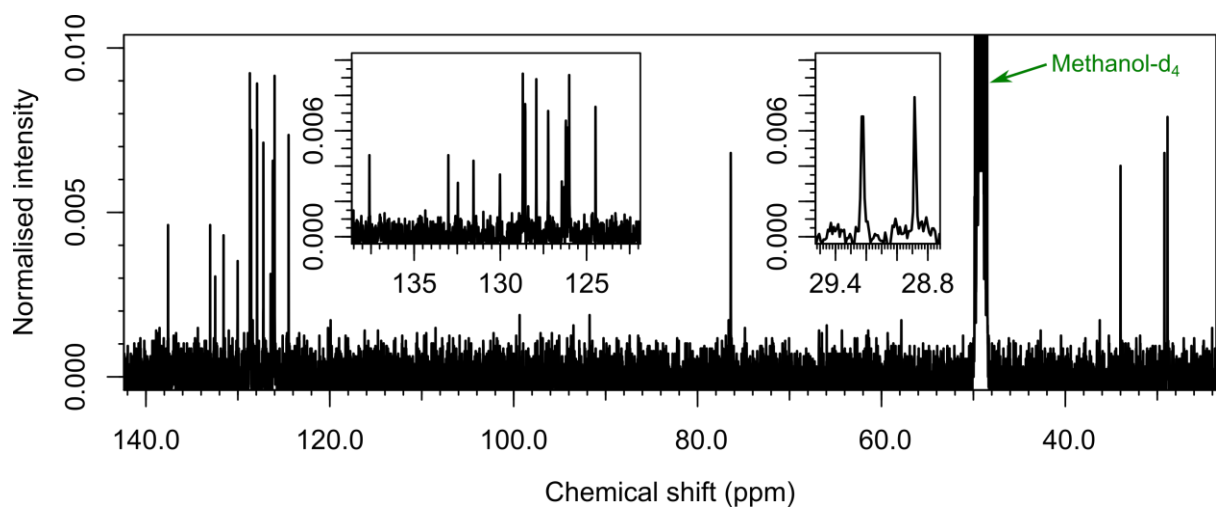
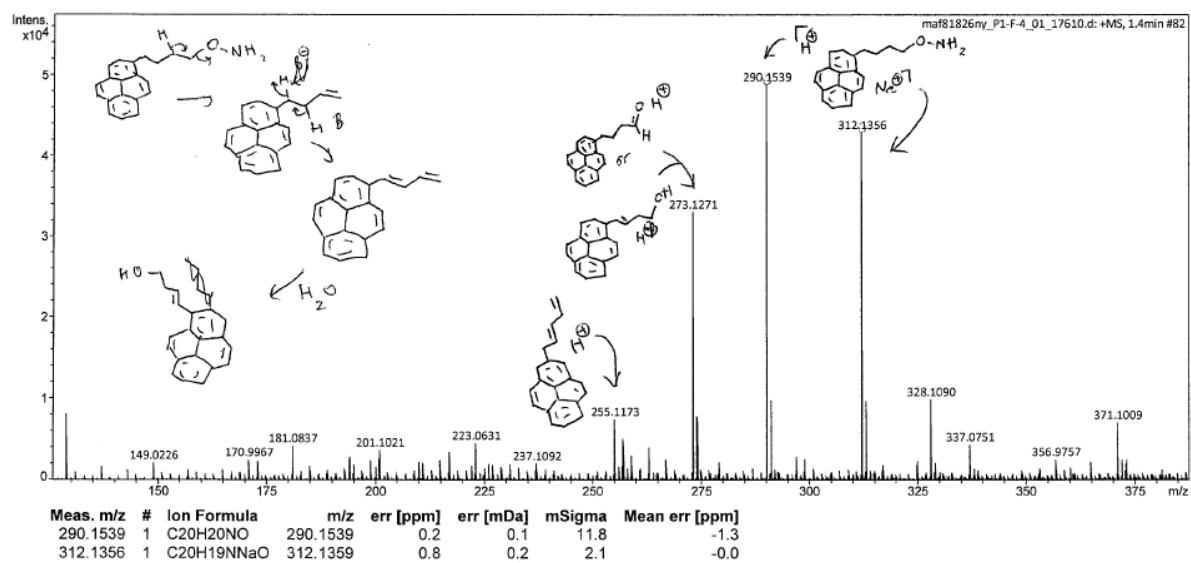
Figure 8.41.  $^1\text{H}$ -NMR spectrum of Pyr3.Figure 8.42.  $^{13}\text{C}$ -NMR spectrum of Pyr3.

Figure 8.43. ESI-LC/MS spectrum of Pyr3.

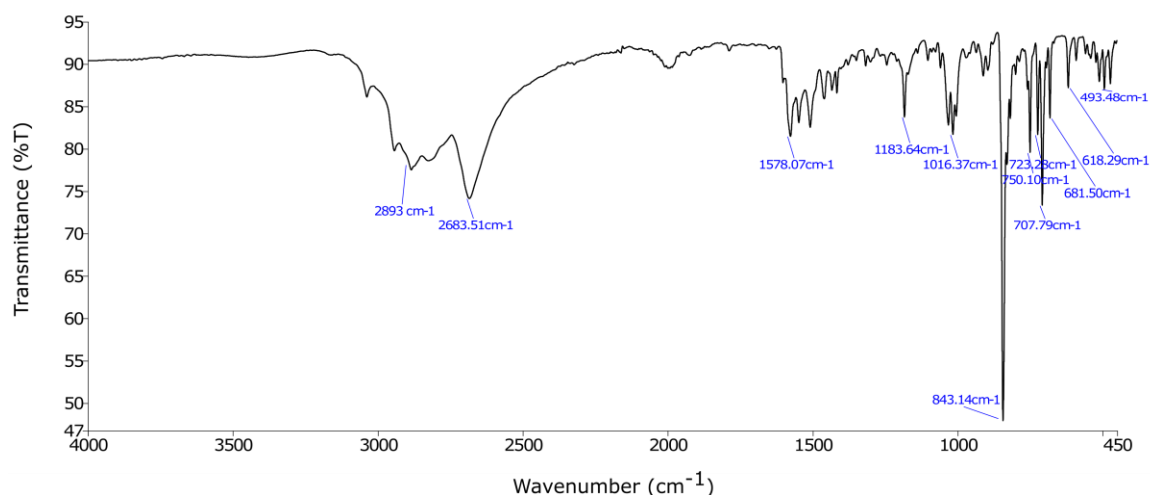
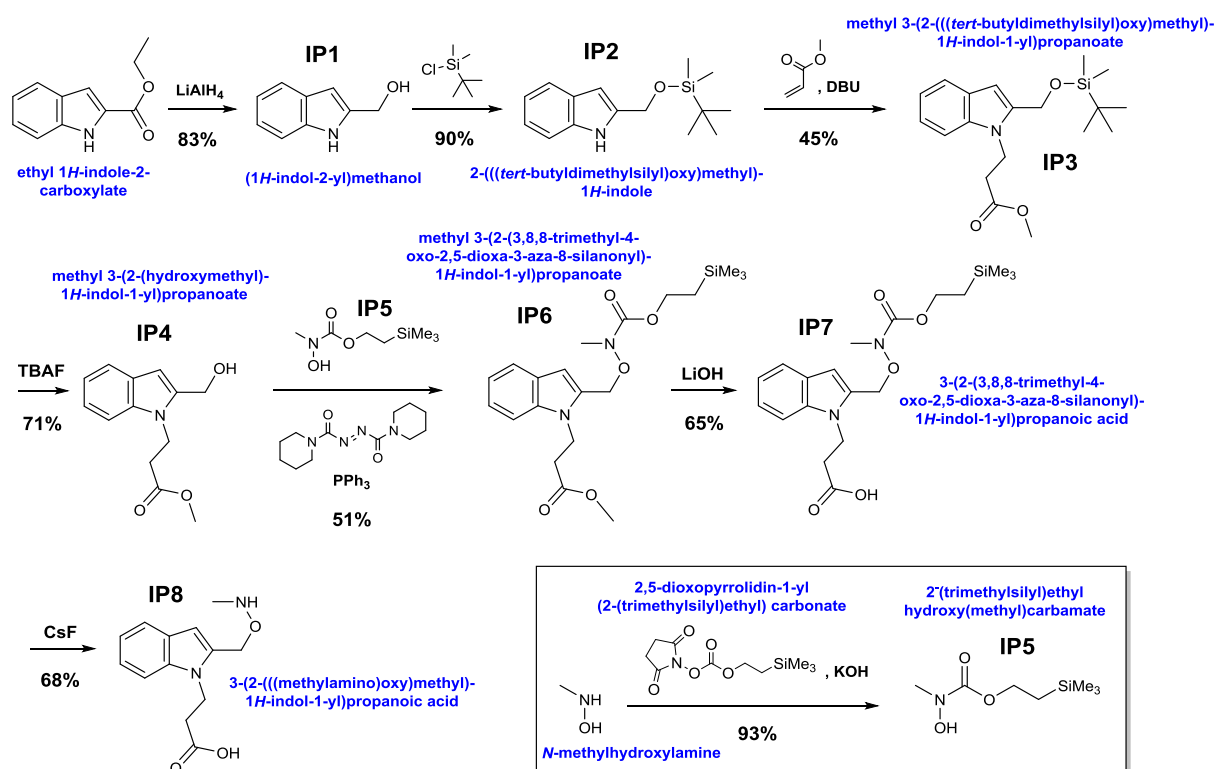


Figure 8.44. IR (ATR) spectrum of Pyr3.

### 8.4.5.3 Synthesis of IP8

Scheme 8.5 summarizes the synthesis methodology used to generate the *iso*-Pictet Spengler ligating probe **IP8** from commercially available ethyl 1*H*-indole-2-carboxylate via six intermediate species. Detailed protocols for the preparation of each species are provided below. Steps onwards from the synthesis of 2-(((tert-butyl)dimethylsilyloxy)methyl)-1*H*-indole are based on a literature synthesis.<sup>397</sup>

Scheme 8.5. The synthesis of *iso*-Pictet Spengler ligating probe **IP8**.

**(1*H*-indol-2-yl)methanol (IP1)**

Under an N<sub>2</sub> atmosphere, ethyl 1*H*-indole-2-carboxylate (5.00 g, 26.4 mmol) was dissolved in anhydrous THF (20 mL), and the resultant solution cooled to 0 °C. Lithium aluminium hydride solution (1 M in THF) was then added dropwise (26.8 mL, 26.8 mmol, 1.02 eq.) and the resultant solution stirred at 0 °C for 3.5 hours. The reaction was then quenched via the addition of water (5.3 mL), followed by the addition of 2 M NaOH (6.6 mL), then the addition of water (16 mL). The mixture was then stirred at rt for 15 min, and the precipitate removed via gravity filtration, and washed with THF. The filtrate was then dried using MgSO<sub>4</sub> concentrated, yielding (1*H*-indol-2-yl)methanol as a pale yellow solid (3.21 g, 83%). The NMR is consistent with that in the literature.<sup>565</sup>

<sup>1</sup>H-NMR (400 MHz, CDCl<sub>3</sub>): δ<sub>H</sub> 8.44 (br s, 1H, H-1), 7.60 (dd, *J* = 7.79, 0.92 Hz, 1H, H-5), 7.33 (dd, *J* = 8.24, 1.37 Hz, 1H, H-2), 7.20 (ddd, *J* = 8.24, 6.87, 1.37 Hz, 1H, H-3), 7.12 (ddd, *J* = 7.79, 6.87, 0.92 Hz, 1H, H-4), 6.41 (s, 1H, H-5), 4.79 (s, 2H, H-7).

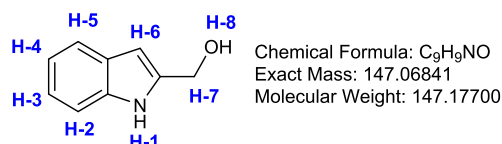


**Figure 8.45.** Structure and labelling of chemical environments in **IP1**.

**2-(((*tert*-butyldimethylsilyl)oxy)methyl)-1*H*-indole (IP2)**

Under an N<sub>2</sub> atmosphere, **IP1** (3.21 g, 21.8 mmol), imidazole (4.39 g, 64.3 mmol, 3.00 eq.) and *tert*-butyldimethylsilylchloride (3.58 g, 23.7 mmol, 1.10 eq.) were dissolved in anhydrous DCM (80 mL). After 16 h, the solution was concentrated to a crude orange residue. This crude residue was then re-dissolved in Et<sub>2</sub>O (100 mL), washed with 5% (v/v) aqueous AcOH (3 × 100 mL), and brine (50 mL), then dried over MgSO<sub>4</sub> and concentrated to give **IP2** as an orange oil (5.11 g, 90% yield). The NMR was consistent with that reported in the literature.<sup>397</sup>

<sup>1</sup>H-NMR (400 MHz, CDCl<sub>3</sub>): δ<sub>H</sub> 8.30 (br s, 1H, H-1), 7.57 (dd, *J* = 7.79, 0.92 Hz, 1H, H-5), 7.38 (dd, *J* = 8.24, 0.92 Hz, 1H, H-2), 7.17 (ddd, *J* = 8.24, 6.87, 0.92 Hz, 1H, H-3), 7.09 (ddd, *J* = 7.79, 6.87, 0.92 Hz, 1H, H-4), 6.32 (m, 1H, H-6), 4.89 (s, 2H, H-7), 0.95 (s, 9H, H-9), 0.12 (s, 6H, H-8).

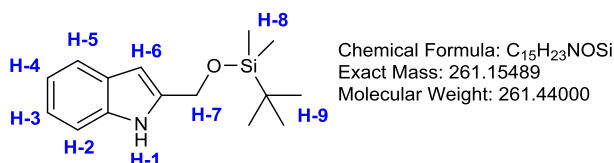


**Figure 8.46.** Structure and labelling of chemical environments of **IP2**.

**Methyl 3-(2-(((*tert*-butyldimethylsilyloxy)methyl)-1*H*-indol-1-yl)propanoate (IP3)**

Under an N<sub>2</sub> atmosphere, **IP2** (5.11 g, 19.5 mmol) and methyl acrylate (8.80 mL, 97.7 mmol, 5.00 eq.) were dissolved in anhydrous MeCN (46 mL). 1,8-diazabicyclo[5.4.0]undec-7-ene (DBU; 1.47 mL, 9.80 mmol, 0.50 eq.). The resulting solution was brought to reflux, and refluxed for 18 h, at which time the solution was cooled and concentrated to an orange oil which was purified by silica gel chromatography (9:1 hexanes:EtOAc, R<sub>f</sub> = 0.4) to yield **IP3** as an orange oil (3.05 g, 8.77 mmol, 45%). The NMR was consistent with that reported in the literature.<sup>397</sup>

<sup>1</sup>H-NMR (400 MHz, CDCl<sub>3</sub>): δ<sub>H</sub> 7.59 (dd, *J* = 7.79, 0.92 Hz, 1H, H-4), 7.35 (dd, *J* = 8.24, 0.92 Hz, 1H, H-1), 7.22 (ddd, *J* = 8.24, 6.87, 0.92 Hz, 1H, H-2), 7.11 (ddd, *J* = 7.79, 6.87, 0.92 Hz, 1H, H-3), 6.40 (s, 1H, H-5), 4.85 (s, 2H, H-6), 4.53 (t, *J* = 7.79 Hz, 2H, H-9), 3.70 (s, 3H, H-11), 2.88 (t, *J* = 7.79 Hz, 2H, H-10), 0.92 (s, 9H, H-8), 0.11 (s, 6H, H-7).

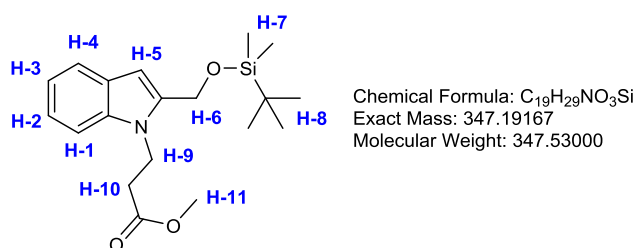


**Figure 8.47.** Structure and labelling of chemical environments of **IP3**.

**Methyl 3-(2-(hydroxymethyl)-1*H*-indol-1-yl)propanoate (IP4)**

Under an N<sub>2</sub> atmosphere, **IP3** (3.05 g, 8.77 mmol) was dissolved in tetrahydrofuran (47.5 mL) at 0 °C was added tetrabutylammonium fluoride (1.0 M in THF, 9.30 mL, 9.30 mmol, 1.06 eq.). After 15 min, the reaction mixture was diluted with diethyl ether (47.5 mL) and washed with NaHCO<sub>3</sub> (sat. aq., 3 x 50 mL), and concentrated to a pale green oil. The oil was purified by silica gel chromatography (2:1 hexanes:EtOAc, R<sub>f</sub> = 0.25) to yield **IP4** as a pale yellow oil (1.45 g, 71%). The NMR was consistent with that reported in the literature.<sup>397</sup>

<sup>1</sup>H-NMR (400 MHz, CDCl<sub>3</sub>): δ<sub>H</sub> 7.60 (d, *J* = 7.79 Hz, 1H, H-4), 7.35 (d, *J* = 8.24 Hz, 1H, H-1), 7.24 (dd, *J* = 8.24, 6.87 Hz, 1H, H-2), 7.12 (dd, *J* = 7.79, 6.87 Hz, 1H, H-3), 6.47 (s, 1H, H-5), 4.83 (s, 2H, H-6), 4.55 (t, *J* = 7.33 Hz, 2H, H-8), 3.67 (s, 3H, H-10), 2.91 (t, *J* = 7.33 Hz, 2H, H-9).

(ESI)HRMS: Found [M+H]<sup>+</sup> 234.1126, C<sub>13</sub>H<sub>16</sub>NO<sub>3</sub> requires 234.1125.

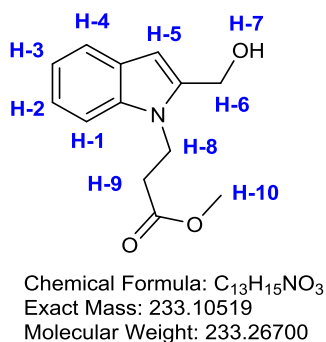


Figure 8.48. Structure and labelling of chemical environments of IP4.

### 2-(trimethylsilyl)ethyl hydroxy(methyl)carbamate (IP5)

To *N*-methylhydroxylamine hydrochloride (338 mg, 4.05 mmol, 1.05 eq.) was added KOH (0.1 M solution in MeOH, 41 mL, 4.1 mmol, 1.01 equiv), resulting in the formation of a white precipitate. After 5 min, *N*-[2-(trimethylsilyl)ethoxycarbonyloxy]succinimide (1.00 g, 3.86 mmol) was added. After 4 h, the solution was concentrated *in vacuo* and the residue was suspended in ethyl acetate (41 mL). The organic solution was washed with sodium bicarbonate (saturated aqueous solution, 3 x 20 mL) and brine (20 mL), dried over MgSO<sub>4</sub>, and then concentrated to a colourless oil (0.72 g, 93%), which was used crude.

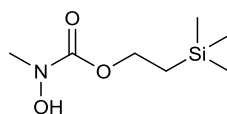


Figure 8.49. Structure of IP5.

### Methyl 3-(2-(3,8,8-trimethyl-4-oxo-2,5-dioxo-3-aza-8-silanonyl)-1H-indol-1-yl)propanoate (IP6)

To an oven-dried flask charged with IP4 (700 mg, 3.00 mmol), IP5 (718 mg, 4.05 mmol, 1.26 equiv), and tributylphosphine (896  $\mu$ L, 3.75 mmol, 1.26 equiv) was added anhydrous toluene (86 mL) followed by 1,1'-(azodicarbonyl)dipiperidine (939 mg, 3.71 mmol, 1.23 equiv). A thick white precipitate formed over the next hour, after which time diethyl ether (143 mL) was added and the solution was filtered through Celite. The filtrate was concentrated to a yellow oil and then purified by silica gel chromatography (4:1 hexanes:EtOAc, R<sub>f</sub> = 0.3) to IP6 as a yellow oil (622 mg, 1.53 mmol, 51%). The NMR was consistent with that reported in the literature.<sup>397</sup>

<sup>1</sup>H-NMR (400 MHz, CDCl<sub>3</sub>):  $\delta$ <sub>H</sub> 7.60 (d, *J* = 7.79 Hz, 1H, H-4), 7.37 (d, *J* = 8.24 Hz, 1H, H-1), 7.25 (m, 1H, H-2), 7.12 (m, 1H, H-3), 6.58 (s, 1H, H-5), 5.05 (s, 2H, H-6), 4.63 (t, *J* = 7.33 Hz, 2H, H-11), 4.26-4.19 (m, 2H, H-8), 3.67 (s, 3H, H-13), 3.09 (s, 3H, H-7), 2.88 (t, *J* = 7.33 Hz, 2H, H-12), 1.03-0.96 (m, 2H, H-9), 0.06 (s, 9H, H-10).

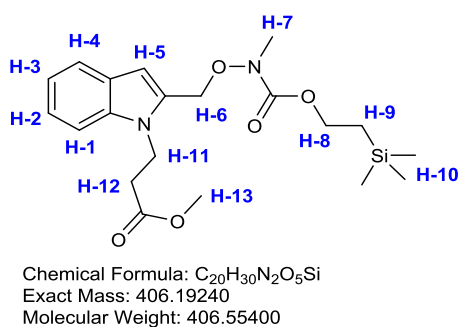


Figure 8.50. Structure and labelling of chemical environments of IP6.

### 3-(2-(3,8,8-trimethyl-4-oxo-2,5-dioxo-3-aza-8-silanonyl)-1H-indol-1-yl)propanoic acid (IP7)

IP6 (622 mg, 1.53 mmol) was dissolved in dioxane (12 mL), whereupon LiOH (0.5 M aqueous solution, 6.11 mL, 3.06 mmol, 2.00 equiv) was added. The reaction was allowed to proceed, with stirring, for 2 hours, after which time the reaction was quenched via the addition of AcOH (5% v/v aqueous, 17 mL). The product was extracted using EtOAc (3 × 17 mL), the organic extracts washed with brine, dried over MgSO<sub>4</sub> and concentrated *in vacuo*. The crude residue was purified via by silica gel chromatography (2:1 hexanes:EtOAc + 2% AcOH, R<sub>f</sub> = 0.4) to yield IP7 as a tan solid (389 mg, 0.991 mmol, 65%). The NMR was consistent with that reported in the literature.<sup>397</sup>

<sup>1</sup>H-NMR (400 MHz, CDCl<sub>3</sub>): δ<sub>H</sub> 7.61 (d, *J* = 7.79 Hz, 1H, H-4), 7.37 (m, 1H, H-1), 7.26 (m, 1H, H-2), 7.13 (m, 1H, H-3), 6.59 (s, 1H, H-5), 5.05 (s, 2H, H-6), 4.64 (t, *J* = 7.33 Hz, 2H, H-11), 4.26-4.19 (m, 2H, H-8), 3.12 (s, 3H, H-7), 2.95 (t, *J* = 7.33 Hz, 2H, H-12), 1.03-0.96 (m, 2H, H-9), 0.06 (s, 9H, H-10).

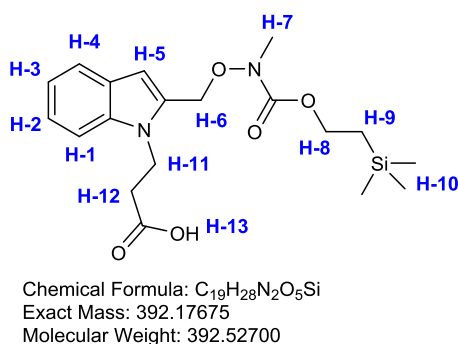


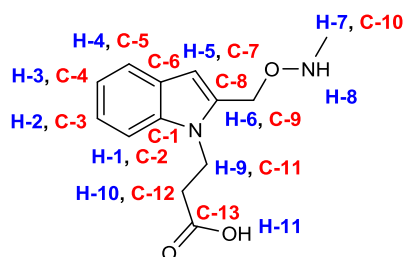
Figure 8.51. Structure and labelling of chemical environments of IP7.

**3-(2-(((methylamino)oxy)methyl)-1H-indol-1-yl)propanoic acid (IP8)**

To a flask charged with **IP7** (188 mg, 479  $\mu\text{mol}$ ) and CsF (423 mg, 2.79 mmol, 5.81 equiv) was added DMF (8.8 mL, anhydrous). After 20 h,  $\text{H}_2\text{O}$  (5.3 mL) was added, resulting in the evolution of a gas. The solution was then concentrated and purified by silica gel chromatography (5% AcOH, 3% MeOH in  $\text{CH}_2\text{Cl}_2$ ,  $R_f = 0.25$ ) affording **IP8** as a yellow solid (81 mg, 0.33 mmol, 68%). The NMR was consistent with that reported in the literature.<sup>397</sup>

**$^1\text{H-NMR}$**  (400 MHz,  $\text{CDCl}_3$ ):  $\delta_{\text{H}}$  8.71 (br s, 1H, H-8), 7.61 (d,  $J = 7.79$  Hz, 1H, H-4), 7.61 (d,  $J = 8.24$  Hz, 1H, H-1), 7.24 (ddd,  $J = 8.24, 6.87, 1.37$  Hz, 1H, H-2), 7.12 (ddd,  $J = 7.79, 6.87, 0.92$  Hz, 1H, H-3), 6.56 (s, 1H, H-5), 4.93 (s, 2H, H-6), 4.53 (t,  $J = 7.33$  Hz, 2H, H-9), 2.89 (t,  $J = 7.33$  Hz, 2H, H-10), 2.75 (s, 3H, H-7).

**$^{13}\text{C-NMR}$**  (100 MHz,  $\text{CDCl}_3$ ):  $\delta_{\text{C}}$  177.52 (C-13), 137.13 (C-1/8), 134.53 (C-1/8), 127.58 (C-6), 122.51 (C-4), 121.29 (C-5), 120.01 (C-3), 109.38 (C-2), 104.45 (C-7), 67.17 (C-9), 39.14 (C-11), 38.81 (C-10), 34.79 (C-12).



Chemical Formula:  $\text{C}_{13}\text{H}_{16}\text{N}_2\text{O}_3$   
Exact Mass: 248.11609  
Molecular Weight: 248.28200

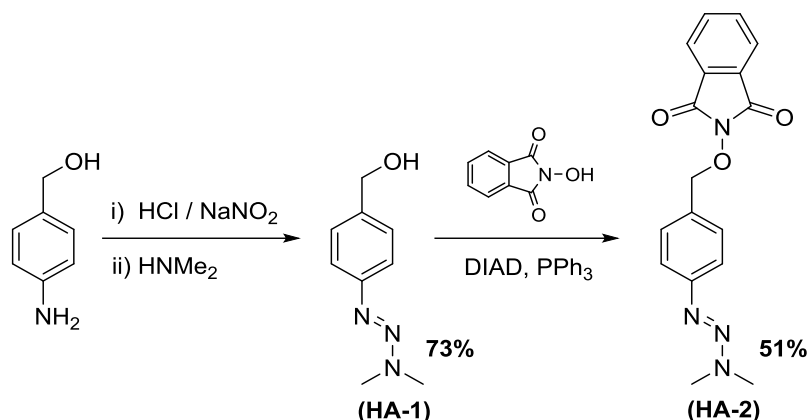
**Figure 8.52.** Structure and labelling of chemical environments of **IP8**.



## 8.5 Experimental procedures for Chapter 5

### 8.5.1 Synthesis of protected hydroxylamine-functionalised aryl diazonium precursors

**Scheme 8.6** summarises the synthesis methodology used to generate the protected hydroxylamine ether (**HA-2**) from commercially available 4-aminophenyl methanol via an intermediate (**HA-1**). Detailed protocols for each reaction step are provided below.



**Scheme 8.6.** The synthesis of a protected hydroxylamine ether (**HA-2**) species for the controlled functionalisation of electrode surfaces.

#### (E)-(4-(3,3-dimethyltriaz-1-en-1-yl)phenyl)methanol (**HA-1**)

Compound **HA-1** in **Scheme 8.6**, (E)-(4-(3,3-dimethyltriaz-1-en-1-yl)phenyl)methanol, was synthesized as described previously, and the characterisation data is in agreement with that of the literature.<sup>490</sup> To a stirred solution of 4-aminophenyl methanol (10 mmol) in 13% HCl (20.2 mL) at 0 °C was added a NaNO<sub>2</sub> solution (0.71 g in 6 mL distilled water) dropwise. The resultant solution was stirred at 0 °C for 5 min. This solution was subsequently added dropwise to 20 mL of 40% aqueous dimethylamine at 0 °C with stirring. The resultant mixture was further stirred at 0 °C for 15 min before being allowed to warm to room temperature. The product was extracted with DCM (2 × 20 mL), and the organic layers combined and washed with distilled water (4 × 20 mL), before being dried over MgSO<sub>4</sub>, concentrated *in vacuo*, and the resultant brown residue was purified via flash column chromatography (10:1 DCM:EtOAc, r.f. 0.2) to yield a yellow solid (1.31 g, 73%).

<sup>1</sup>H-NMR (400 MHz, CDCl<sub>3</sub>, **Figure 8.53**): δ<sub>H</sub> 7.42 (m<sup>AA'BB'</sup>, 2H, H-4), 7.33 (m<sup>AA'BB'</sup>, 2H, H-3), 4.67 (s, 2H, H-2), 3.35 (br s, 6H, H-5).

<sup>13</sup>C-NMR (100 MHz, CDCl<sub>3</sub>, **Figure 8.54**): δ<sub>C</sub> 150.55 (C-5), 137.88 (C-2), 127.84 (C-3), 120.66 (C-4), 65.30 (C-1).

(ESI)HRMS (Figure 8.55): Found  $[M+H]^+$  180.1132,  $C_{10}H_{13}N_3O$  requires 180.1131.

IR (ATR) (Figure 8.56) ( $\nu_{max}/cm^{-1}$ ): 3300 (O-H stretch), 2902 (C-H alkyl), 1731 (C=O), 1446 (C=C aromatic), 1386 (N=N stretch), 1327 (O-H bend), 1281 (C-O stretch), 1073 (C-H aromatic), 818 (C-H bend aromatic).

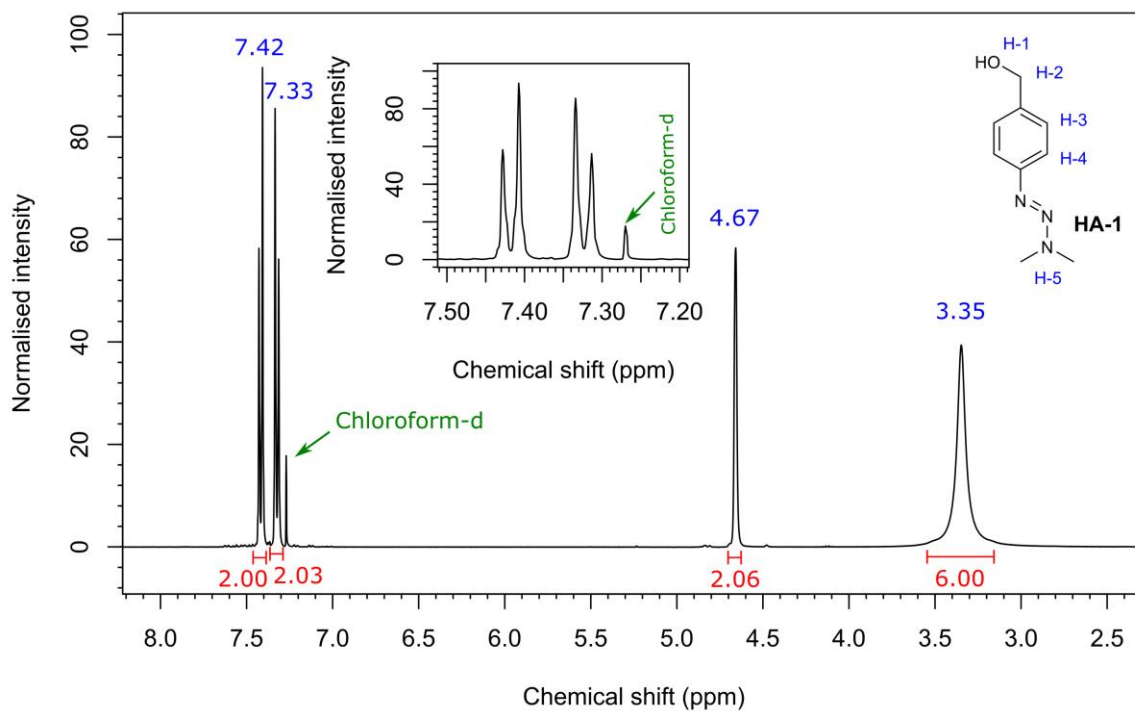


Figure 8.53.  $^1H$ -NMR spectrum of HA-1.

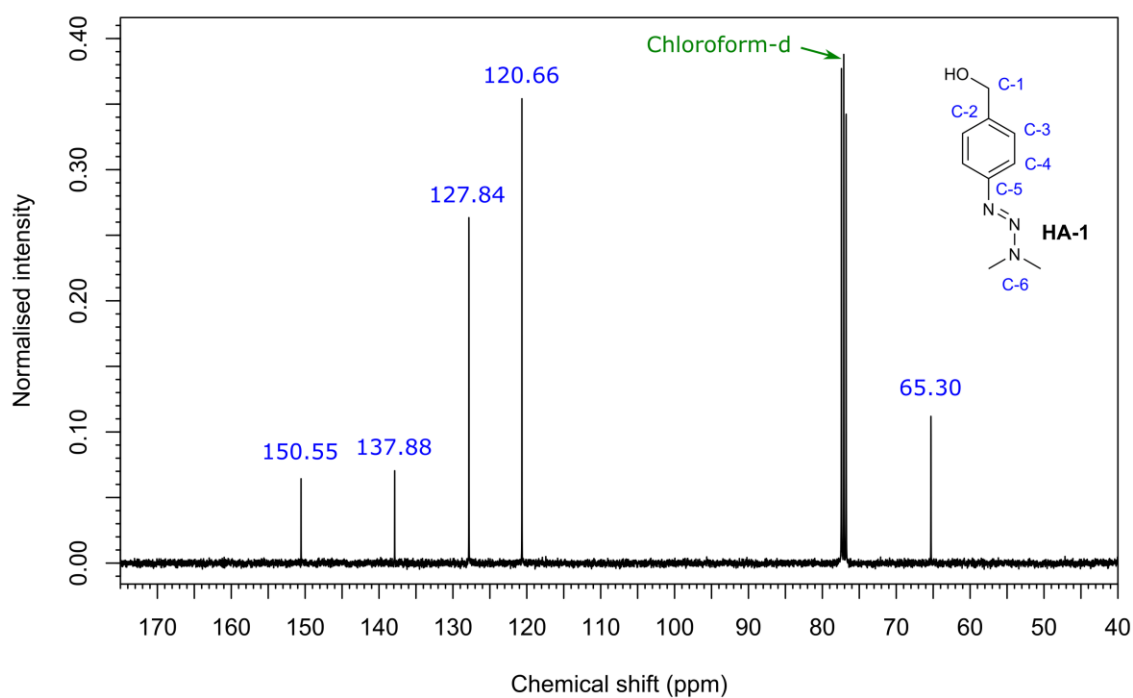


Figure 8.54.  $^{13}C$ -NMR spectrum of HA-1.

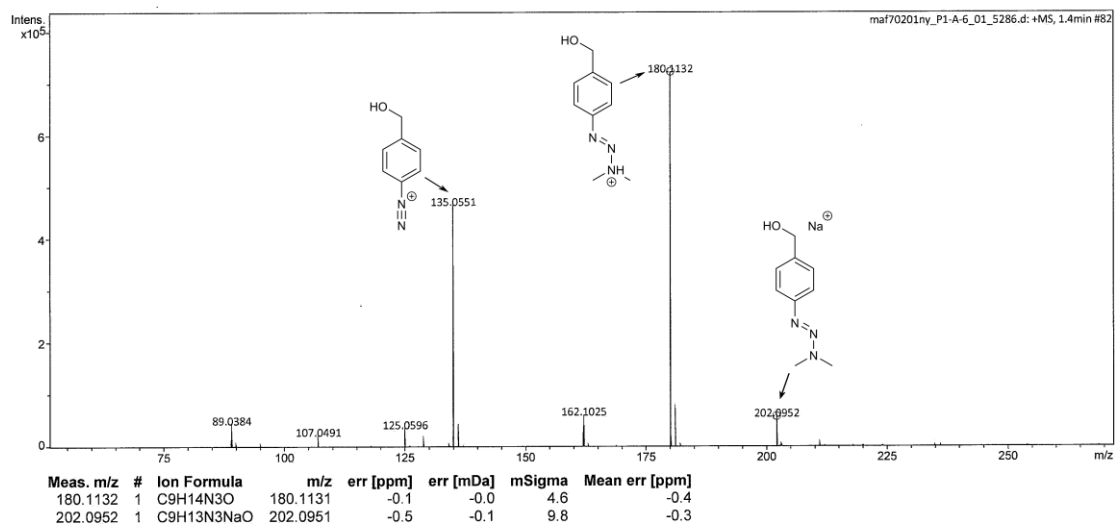


Figure 8.55. (ESI)HRMS spectrum of HA-1, illustrating its propensity to yield diazonium species upon protonation.

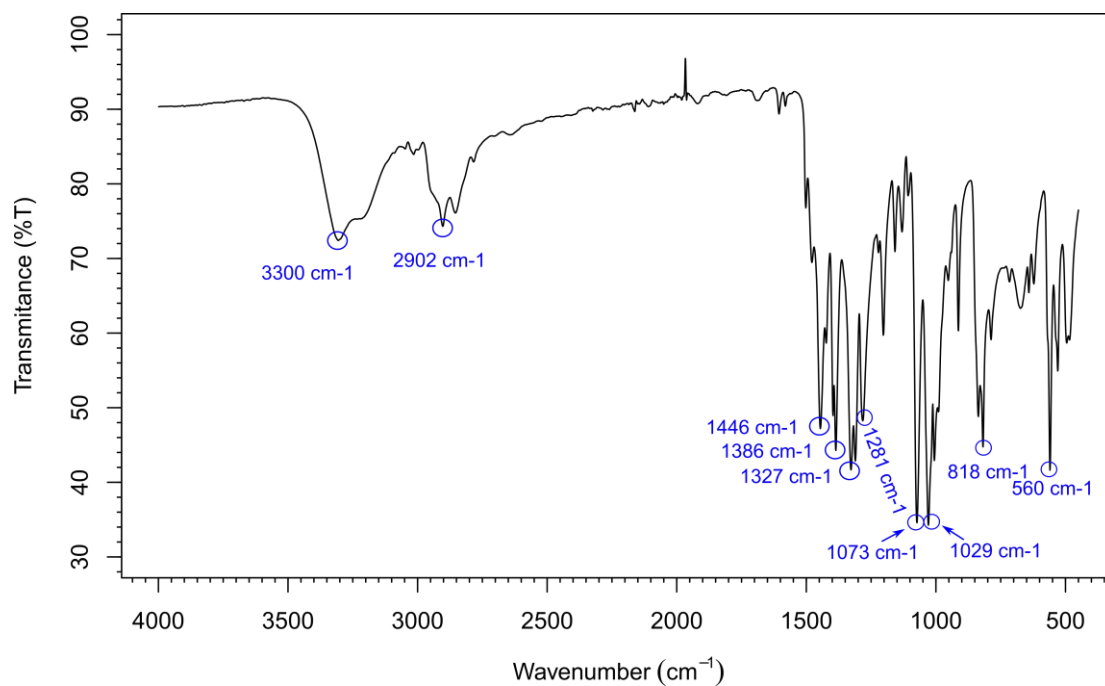


Figure 8.56. IR (ATR) spectrum of HA-1.

**(E)-2-((4-(3,3-dimethyltriaz-1-en-1-yl)benzyl)oxy)isoindoline-1,3-dione (HA-2)**

(E)-4-(3,3-dimethyltriaz-1-en-1-yl)phenyl)methanol (**HA-1** in **Scheme 8.6**) (0.905 g, 5.91 mmol) *N*-hydroxyphthalimide (1.05 g, 6.44 mmol, 1.09 equiv) and triphenylphosphine (1.70 g, 6.44 mmol, 1.09 equiv) were dissolved in 45 mL of anhydrous THF under an N<sub>2</sub> atmosphere. The resultant solution was then cooled to 0 °C, whereupon diisopropyl azodicarboxylate (1.29 mL, 6.50 mmol, 1.1 equiv) was added dropwise. The reaction solution was then allowed to warm to room temperature and was stirred overnight. Water (50 mL) and DCM (50 mL) were then added, and the organic phase collected. The aqueous phase was washed with DCM (50 mL) and the organic phases were combined, dried over MgSO<sub>4</sub> and concentrated *in vacuo*, affording an orange residue. The residue was purified via flash column chromatography (DCM, r.f. 0.3) to yield the product as an off-white solid, which was further purified via recrystallisation from EtOAc/hexane to yield off-white crystals (0.976 g, 51%).

**<sup>1</sup>H-NMR** (400 MHz, CDCl<sub>3</sub>, **Figure 8.57**): δ<sub>H</sub> 7.81 (m, 2H, H-2), 7.73 (m, 2H, H-1), 7.49 (m<sup>AA'BB'</sup>, 2H, H-5), 7.42 (m<sup>AA'BB'</sup>, 2H, H-4), 5.21 (s, 2H, H-3), 3.35 (s, 6H, H-6).

**<sup>13</sup>C-NMR** (100 MHz, CDCl<sub>3</sub>, **Figure 8.58**): δ<sub>C</sub> 163.45 (C-4), 151.59 (C-9), 134.25 (C-1), 130.73 (C-7), 130.24 (C-3), 128.78 (C-6), 123.36 (C-2), 120.44 (C-8), 79.54 (C-5), (C-10 not observed due to rotation).

**(ESI)HRMS** (**Figure 8.59**): Found [M+H]<sup>+</sup> 347.1113, C<sub>17</sub>H<sub>16</sub>N<sub>4</sub>NaO<sub>3</sub> requires 347.1115.

**IR (ATR)** (**Figure 8.60**) (u<sub>max</sub>/cm<sup>-1</sup>): 2903 (C-H alkyl), 1731 (C=O), 1453 (C=C aromatic), 1392 (N=N stretch), 1138 (C-O), 1072 (C-H aromatic), 698 (C-H bend aromatic).

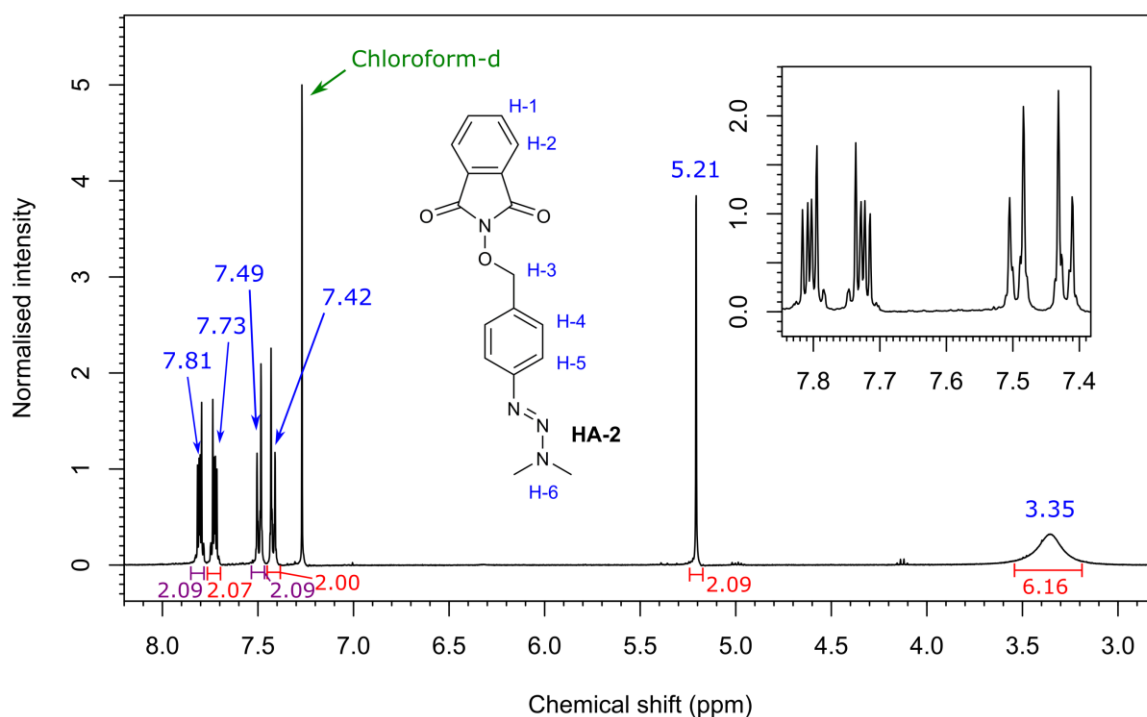


**Figure 8.57.** <sup>1</sup>H-NMR spectrum of **HA-2**.

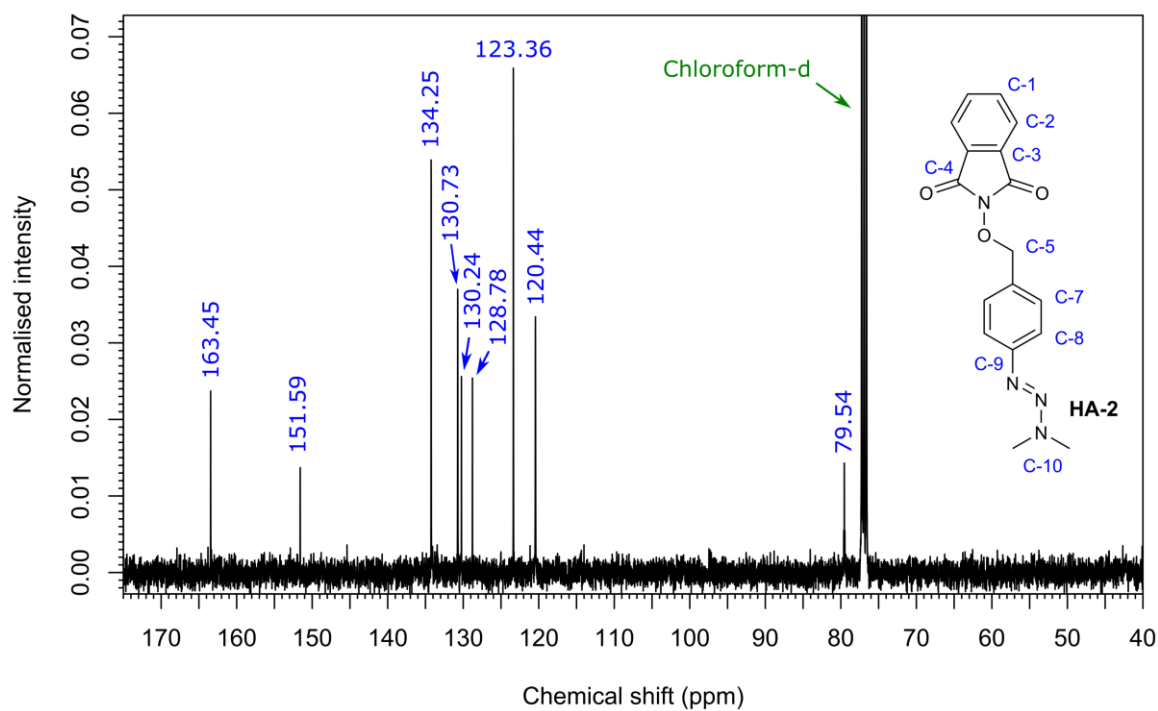
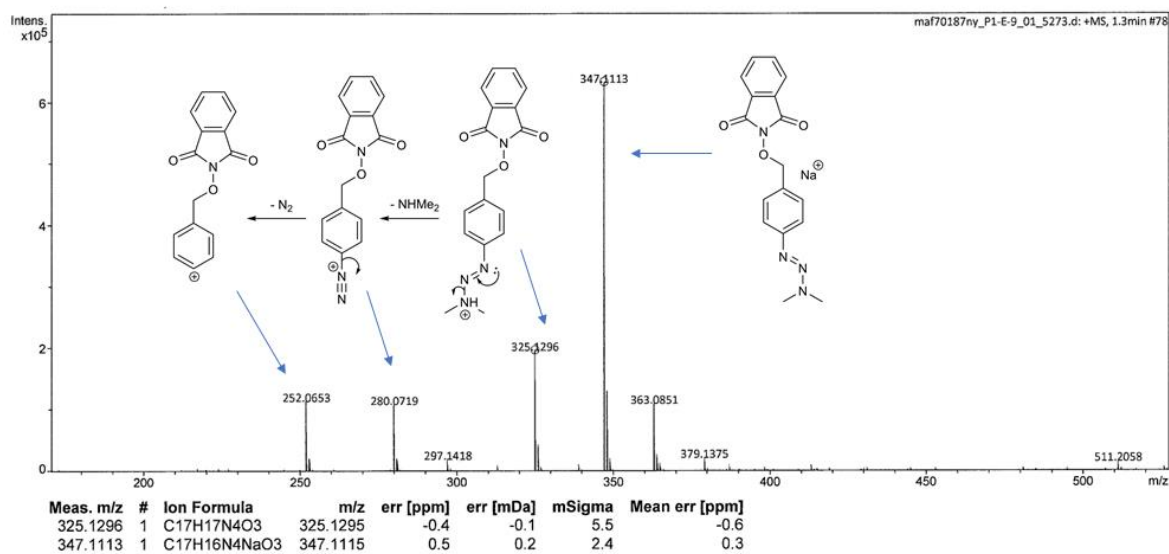
Figure 8.58.  $^{13}\text{C}$ -NMR spectrum of HA-2.

Figure 8.59. (ESI)HRMS spectrum of HA-2, illustrating its propensity to yield diazonium species upon protonation.

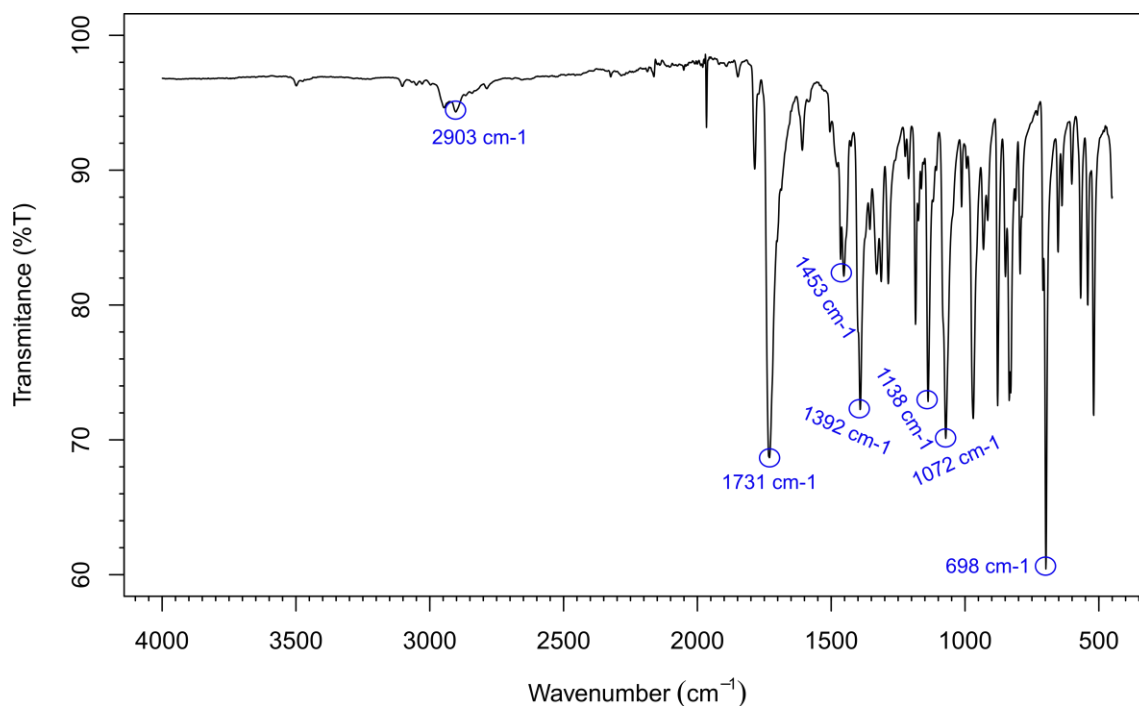
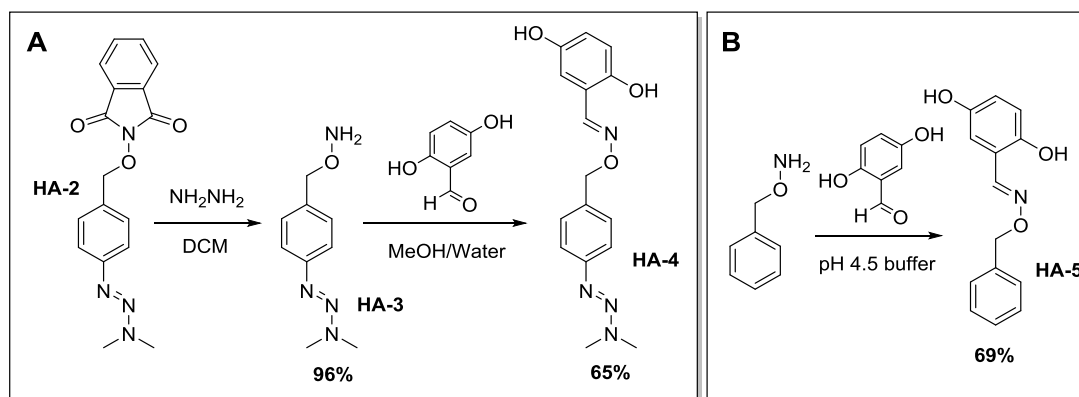


Figure 8.60. IR (ATR) spectrum of HA-2.

### 8.5.2 Solution analogues of the electrode-surface reactions

To confirm that hydrazine treatment of HA-2 would reveal free hydroxylamine functionalities and that oxime bond formation would result from reacting 2,5-dihydroxybenzaldehyde with organic hydroxylamines in solution, the control reactions summarized in **Scheme 8.7** were carried out. These reactions yielded products that could be characterised using NMR, ESI-MS and IR (ATR) to confirm the structures.



**Scheme 8.7.** Solution-phase analogue experiments to prove the phthalimide protecting group is cleaved from HA-2 via hydrazine treatment (panel A), and that oxime bond formation is possible between 2,5-dihydroxybenzaldehyde and the revealed hydroxylamine functionalities (panels A and B).

**(E)-O-(4-(3,3-dimethyltriaz-1-en-1-yl)benzyl)hydroxylamine (HA-3)**

To a round bottom flask containing **HA-2** (0.253 g, 0.781 mmol) dissolved in DCM (25 mL) was added hydrazine monohydrate (75.7  $\mu$ L, 1.56 mmol). The resultant solution was stirred at room temperature for 18 hours, whereupon the reaction solution was washed with 2 M NaOH (3  $\times$  20 mL), then brine (20 mL). The organic layer was then dried over MgSO<sub>4</sub> and concentrated in vacuo to yield **HA-3** as a yellow oil (0.145g, 96%), see **Scheme 8.7**.

**<sup>1</sup>H-NMR** (400 MHz, CDCl<sub>3</sub>, **Figure 8.61**):  $\delta_{\text{H}}$  7.45-7.40 (m<sup>AA'BB'</sup>, 2H, H-4), 7.36-7.30 (m<sup>AA'BB'</sup>, 2H, H-3), 5.37 (br s, 2H, H-1), 4.68 (s, 2H, H-2), 3.35 (s, 6H, H-5).

**<sup>13</sup>C-NMR** (100 MHz, CDCl<sub>3</sub>, **Figure 8.62**):  $\delta_{\text{C}}$  150.63 (C-5), 133.92 (C-2), 129.06 (C-3), 120.35 (C-4), 77.73 (C-1), (C-6 not observed due to rotation).

**(ESI)HRMS** (**Figure 8.63**): Found [M+H]<sup>+</sup> 195.1239, C<sub>9</sub>H<sub>15</sub>N<sub>4</sub>O requires 195.1240.

**IR (ATR)** (**Figure 8.64**) ( $\nu_{\text{max}}$ /cm<sup>-1</sup>): 3309 (N-H stretch), 2907 (C-H stretch alkyl), 1445 (C=C stretch aromatic), 1386 (N=N stretch), 1282 (C-O stretch), 1082 (C-H aromatic), 822 (C-H bend aromatic).

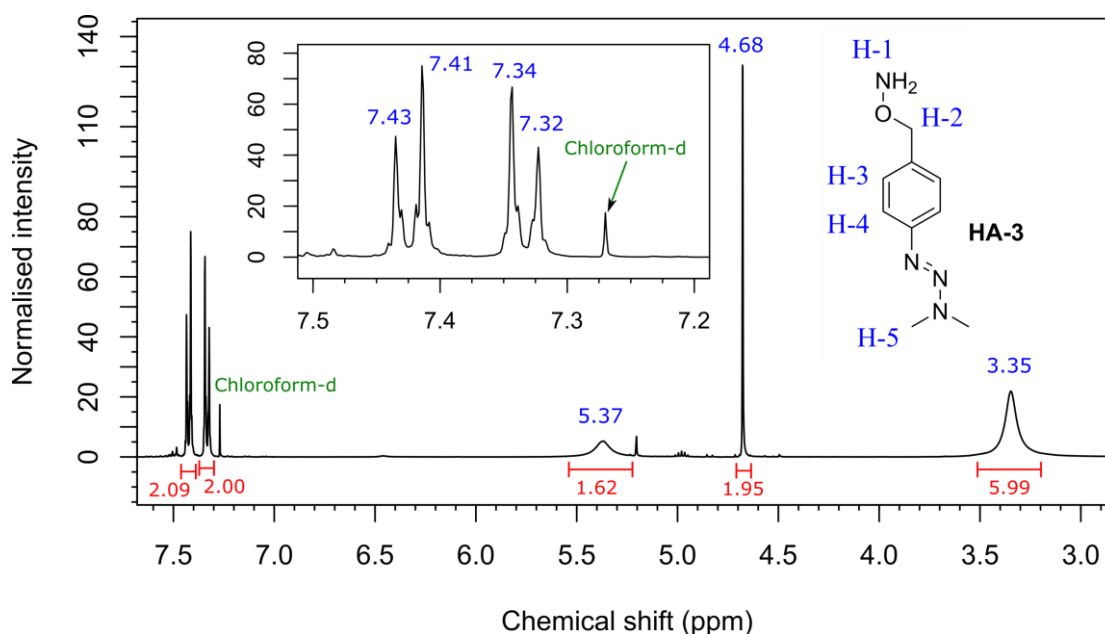


**Figure 8.61.** <sup>1</sup>H-NMR spectrum of **HA-3**.

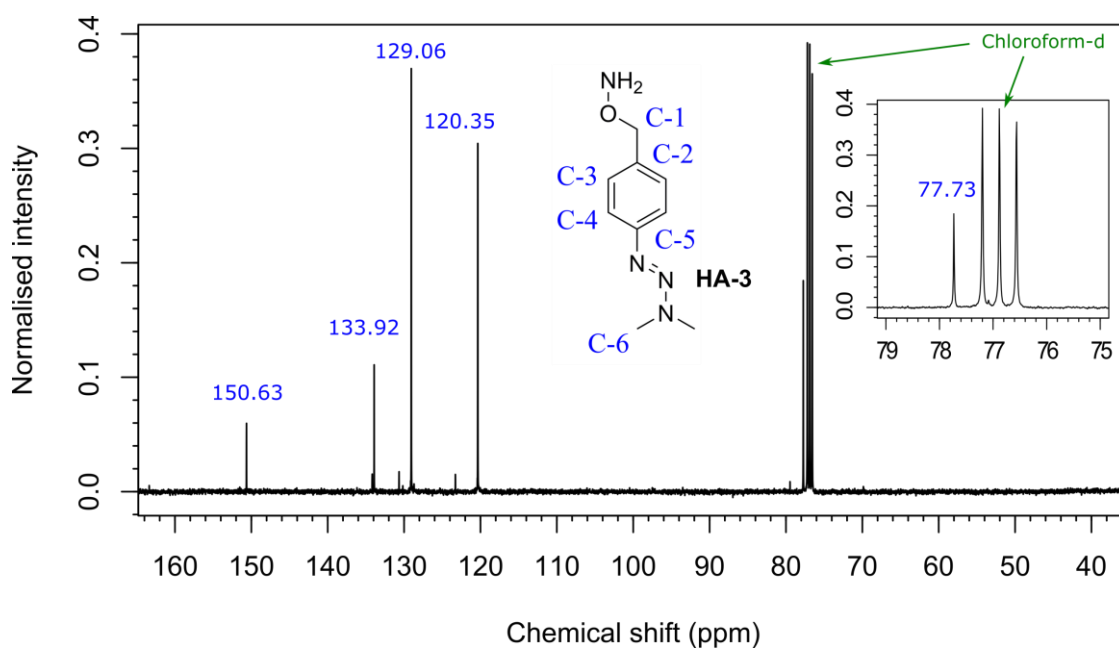
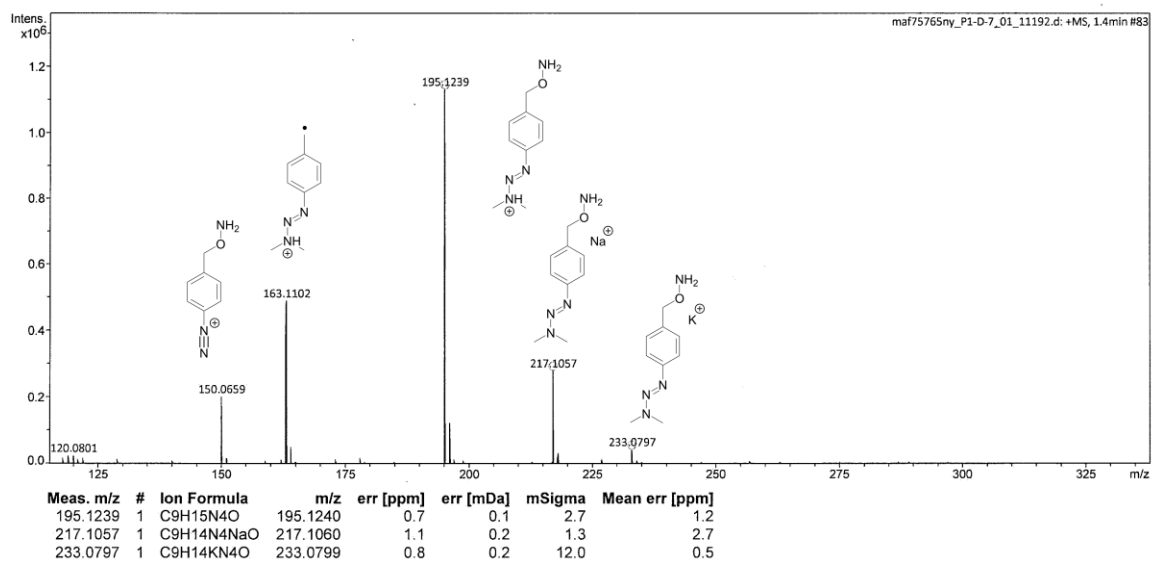
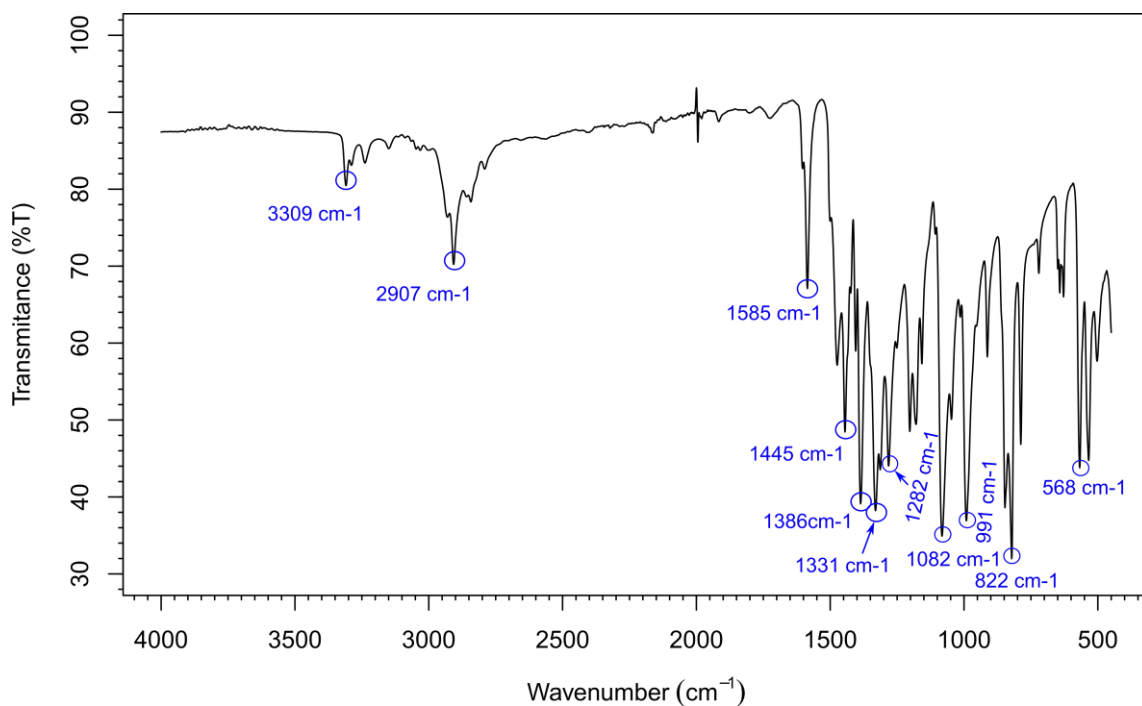
Figure 8.62:  $^{13}\text{C}$ -NMR spectrum of HA-3.

Figure 8.63. (ESI)HRMS of HA-3, illustrating its propensity to yield diazonium species upon protonation.





**Figure 8.64.** IR (ATR) spectrum of **HA-3**.

**(E)-2,5-dihydroxybenzaldehyde O-(4-((E)-3,3-dimethyltriaz-1-en-1-yl)benzyl) oxime (HA-4)**

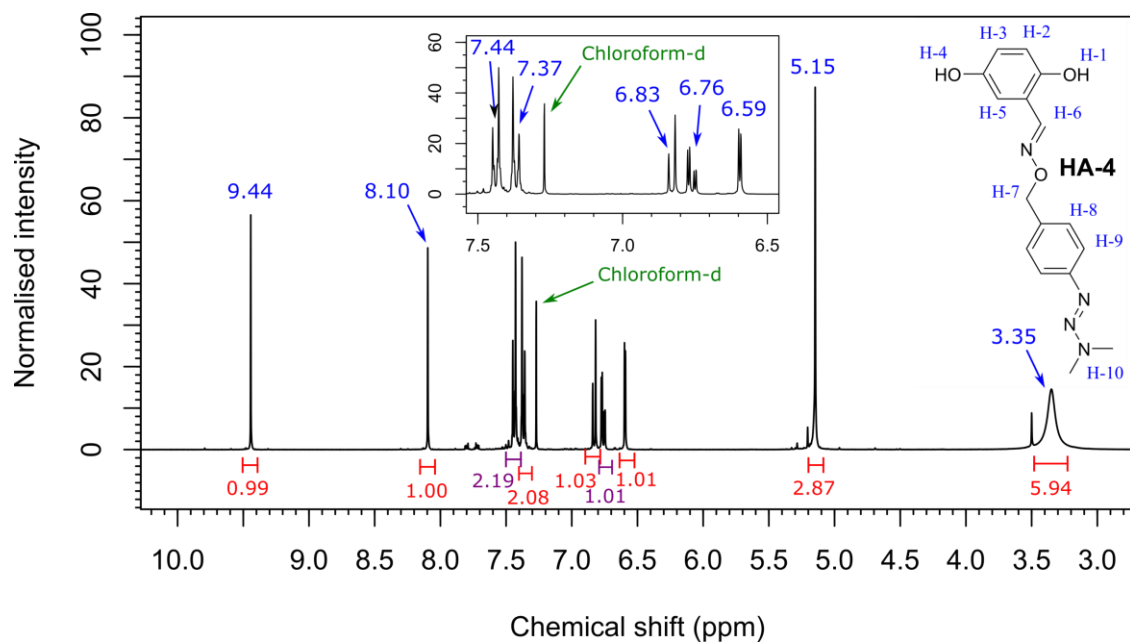
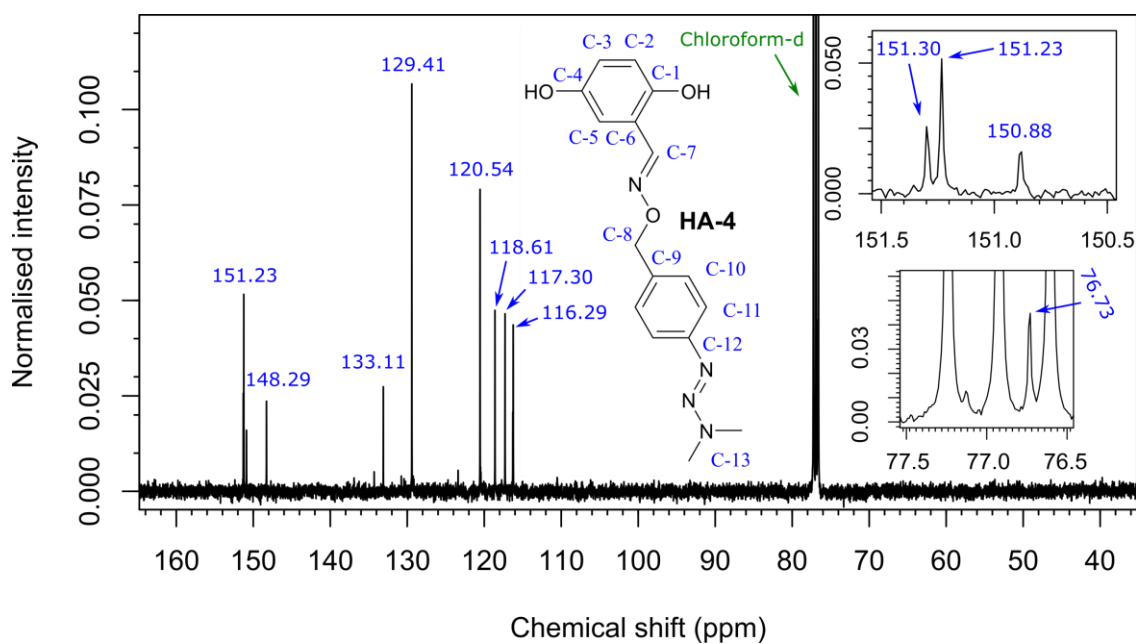
To a sample vial containing a solution of **HA-3** (39.4 mg, 0.203 mmol) in MeOH (1 mL) was added 2,5-dihydroxybenzaldehyde (28.0 mg, 0.203 mmol) in deionized water (5 mL). The mixture was vortexed vigorously, whereupon a precipitate formed. After 20 min the precipitate was isolated via filtration and washed with water, yielding **HA-4** as an off-white solid (41.2 mg, 65%).

**<sup>1</sup>H-NMR** (400 MHz, CDCl<sub>3</sub>, **Figure 8.65**):  $\delta_{\text{H}}$  9.44 (s, 1H, H-1), 8.10 (s, 1H, H-6), 7.47-7.42 (m<sup>AA'BB'</sup>, 2H, H-9), 7.39-7.35 (m<sup>AA'BB'</sup>, 2H, H-8), 6.83 (d,  $J = 8.70$  Hz, 1H, H-2), 6.76 (dd,  $J = 8.70, 2.75$  Hz, 1H, H-3), 6.59 (d,  $J = 2.75$  Hz, 1H, H-5), 5.15 (s, 2H, H-7), 3.35 (br s, 6H, H-10), (H-4 not observed due to exchange).

**<sup>13</sup>C-NMR** (100 MHz, CDCl<sub>3</sub>, **Figure 8.66**)  $\delta_{\text{C}}$  151.30 (C-4), 151.23 (C-7), 150.88 (C-1), 148.29 (C-12), 133.11 (C-9), 129.41 (C-10), 120.54 (C-11), 118.61 (C-2), 117.30 (C-3), 116.29 (C-6), 116.24 (C-5), 76.73 (C-8), (C-13 not observed due to rotation).

**(ESI)HRMS** (**Figure 8.67**): Found  $[M+Na]^+$  337.1278, C<sub>16</sub>H<sub>18</sub>N<sub>4</sub>O<sub>3</sub>Na requires 337.1278.

**IR (ATR)** (**Figure 8.68**) ( $\nu_{\text{max}}/\text{cm}^{-1}$ ): 3150 (O-H stretch), 2932 (C-H stretch alkyl), 1469 (C=C stretch aromatic), 1385 (N=N stretch), 1349, (O-H bend), 1254 (C-O stretch), 665 (C-H bend aromatic).

Figure 8.65.  $^1\text{H}$ -NMR spectrum of HA-4.Figure 8.66.  $^{13}\text{C}$ -NMR spectrum of HA-4.

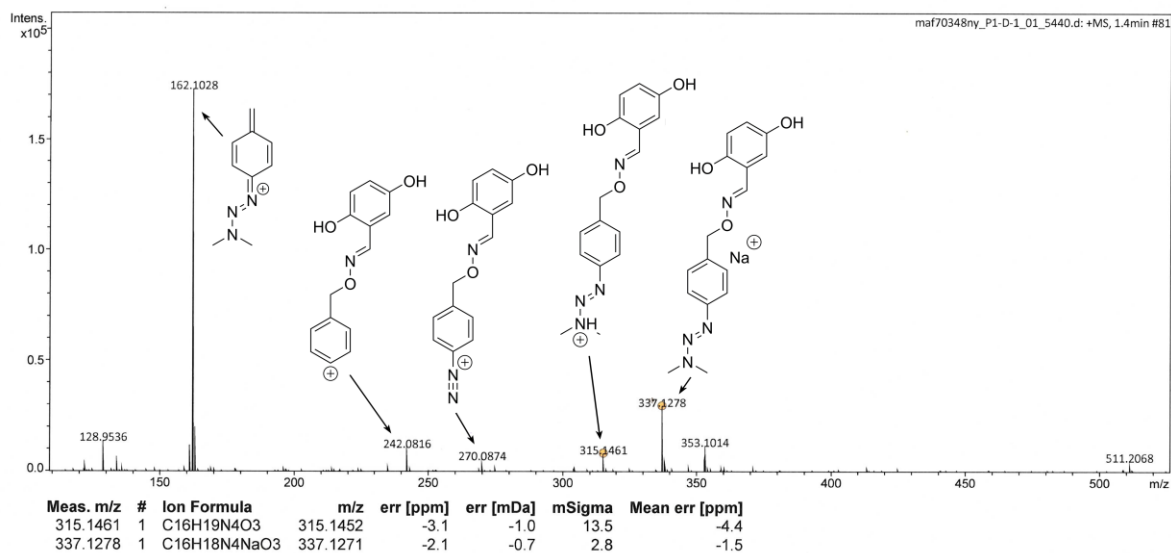


Figure 8.67. (ESI)HRMS of HA-4, illustrating its propensity to yield diazonium species upon protonation.

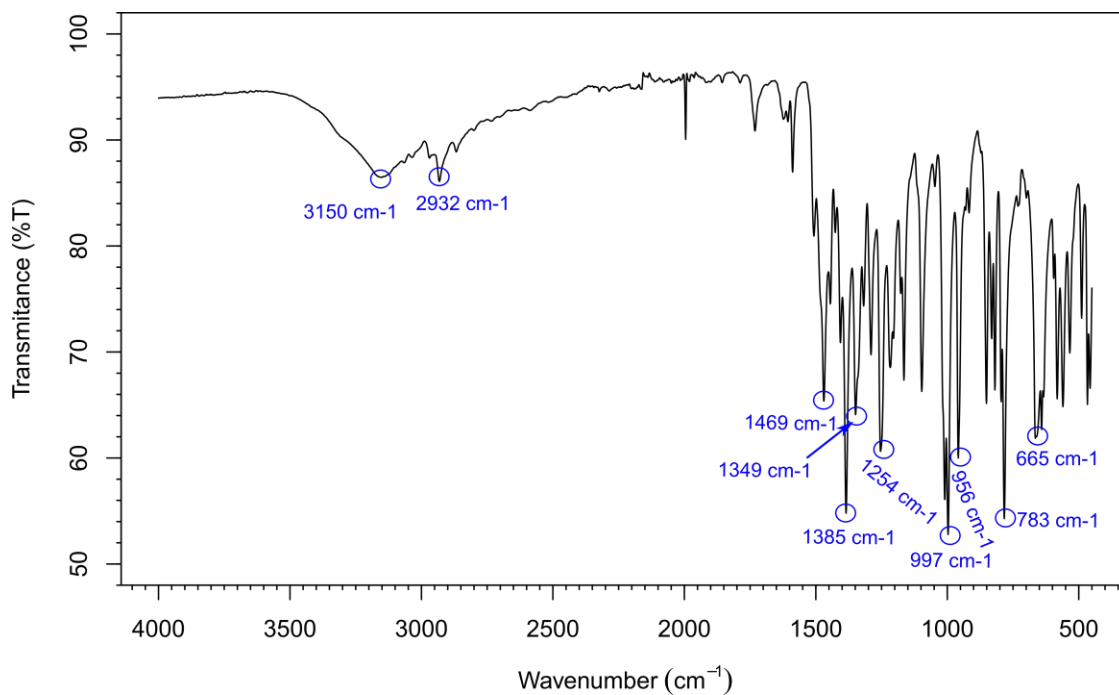


Figure 8.68. IR (ATR) spectrum of HA-4.

**(E)-2,5-dihydroxybenzaldehyde O-benzyl oxime (HA-5)**

To a stirred solution of 2,5-dihydroxybenzaldehyde (10.0 mg, 0.0724 mmol) in aqueous buffer (100 mM sodium acetate, 150 mM NaCl, pH 4.5, 2mL) was added o-benzylhydroxylamine (11.6 mg, 11  $\mu$ L). Within seconds a white precipitate formed, and the reaction solution decolorized from green to colourless. The white precipitate was filtered off within 2 min and left to dry. This yielded **HA-5** as a white solid (12.1 mg, 69%), see **Scheme 8.7**. The actual yield is likely higher than this (no extraction was performed on the filtrate and some solid would be left on the filter paper).

**<sup>1</sup>H-NMR** (400 MHz, CDCl<sub>3</sub>, **Figure 8.69**)  $\delta_{\text{H}}$  9.39 (s, 1H, H-Quin-1), 8.13 (s, 1H, H-Ox), 7.44-7.32 (m, 5H, H-Ar), 6.85 (d,  $J = 9.16$  Hz, 1H, H-Quin-2), 6.78 (dd,  $J = 9.16, 2.75$  Hz, 1H, H-Quin-3), 6.63 (d,  $J = 2.75$  Hz, 1H, H-Quin-5), 4.50 (br s, 1H, H-Quin-4).

**<sup>13</sup>C-NMR** (100 MHz, CDCl<sub>3</sub>, **Figure 8.70**)  $\delta_{\text{C}}$  151.54 (C-Quin-1/4), 151.36 (C-Ox), 148.17 (C-Quin-1/4), 136.39 (C-Ar-1), 128.60 (C-Ar-3, C-Ar-4), 128.40 (C-Ar-2), 118.71 (C-Quin-2), 117.46 (C-Quin-3), 116.31 (C-Quin-5, C-Quin-6), 76.91 (C-Alk).

**(ESI)HRMS** (**Figure 8.71**): Found  $[M+H]^+$  244.096, C<sub>14</sub>H<sub>14</sub>NO<sub>3</sub> requires 244.0968.

**IR (ATR)** (**Figure 8.72**) ( $\nu_{\text{max}}/\text{cm}^{-1}$ ): 3292 (O-H stretch), 3015 (C-H stretch alkyl), 1492 (C=C stretch aromatic), 1358 (O-H bend), 1260 (C-O stretch), 697 (C-H bend aromatic).

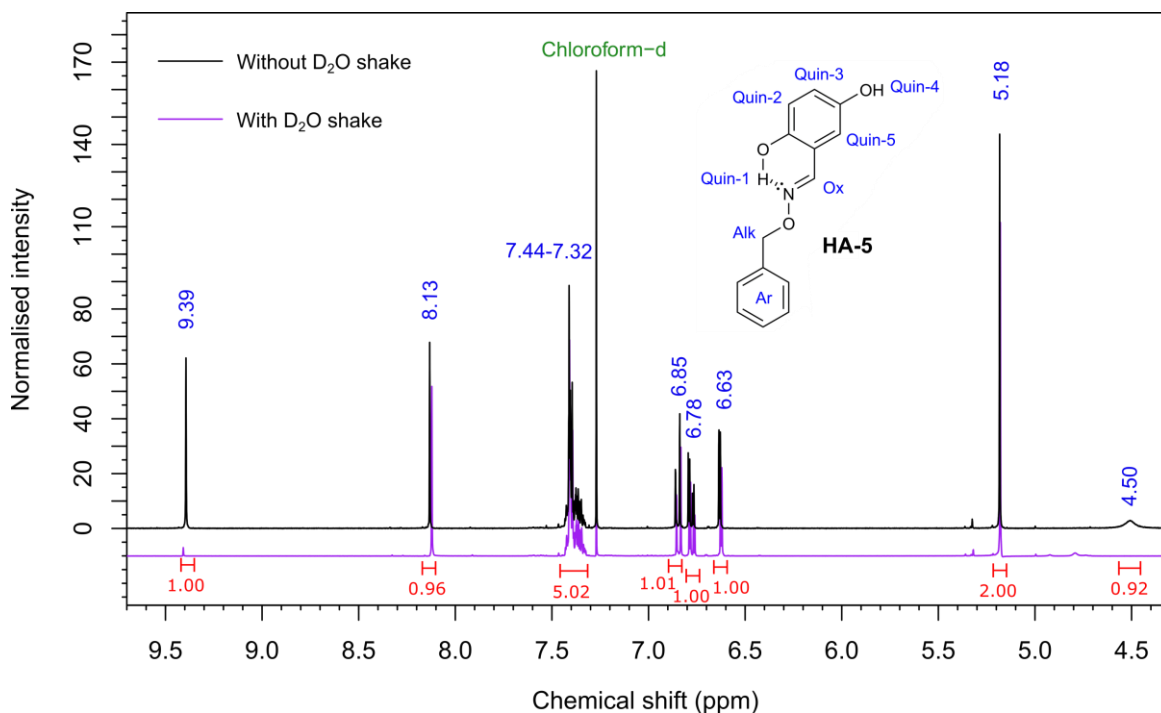


**Figure 8.69:** <sup>1</sup>H-NMR spectrum of (E)-2,5-dihydroxybenzaldehyde O-benzyl oxime, **HA-5**.

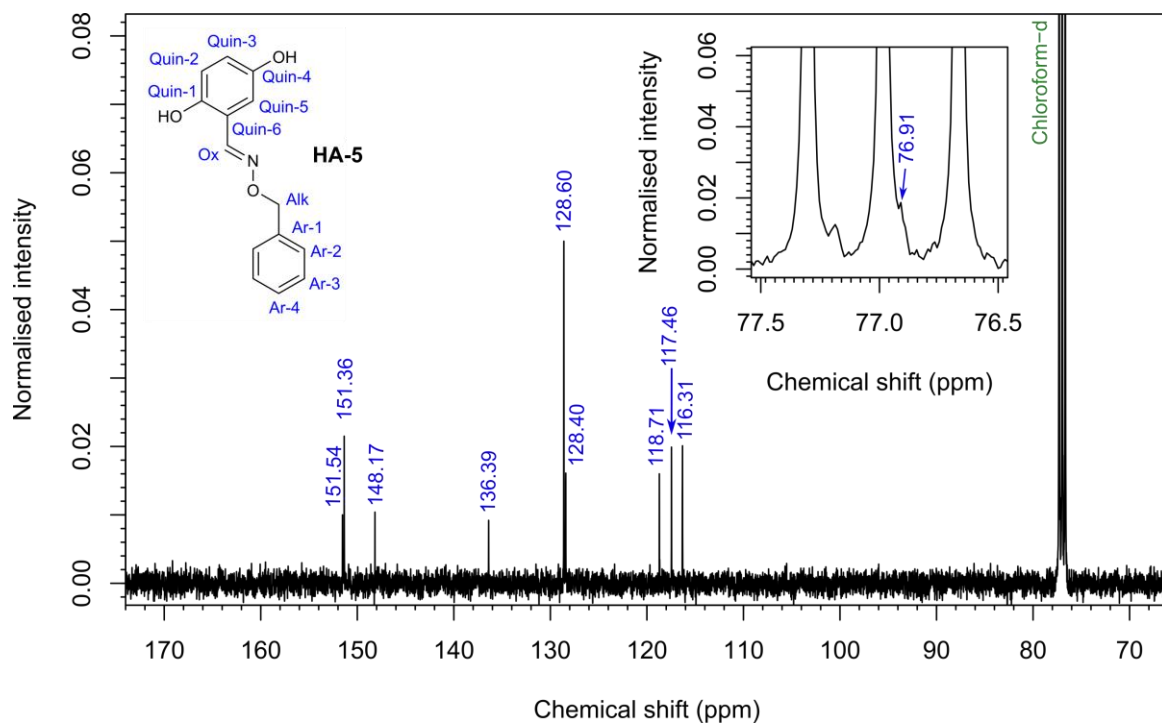


Figure 8.70:  $^{13}\text{C}$ -NMR spectrum of (E)-2,5-dihydroxybenzaldehyde O-benzyl oxime, HA-5.

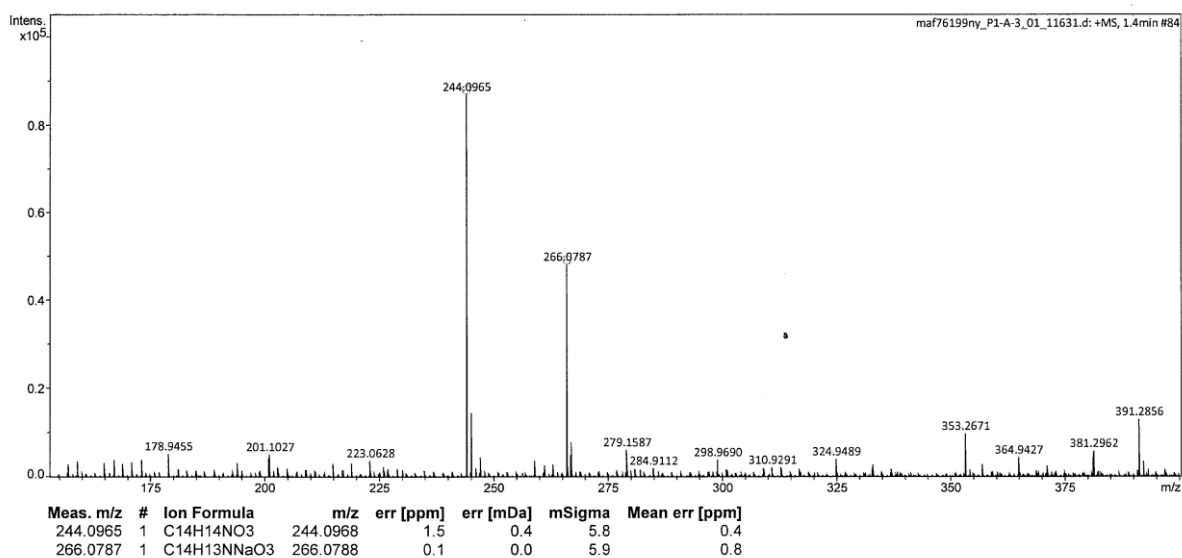


Figure 8.71: (ESI)HRMS of HA-5, showing both protonated ( $m/z = 244.0964$ ) and sodiated ( $m/z = 266.0787$ ) ions.

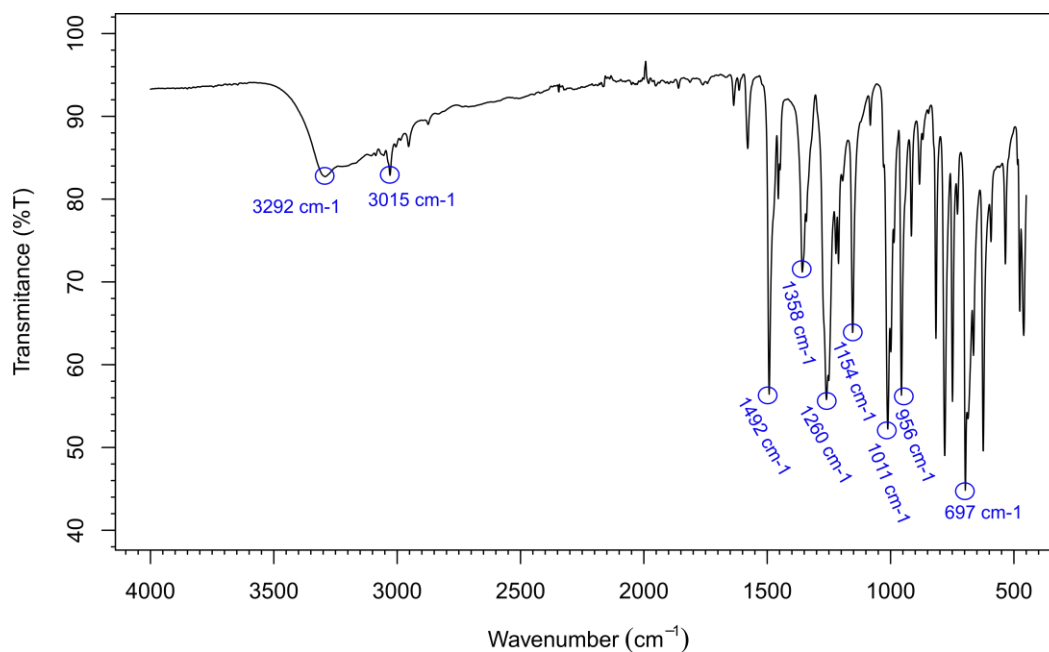


Figure 8.72. IR (ATR) spectrum of HA-5.

### 8.5.3 Functionalisation of electrode surfaces with hydroxyl amines via diazonium electro-grafting

#### Electrochemical Setup

Electrochemical experiments were conducted using the electrochemical cell setup described in **Section 8.1.5**. The disk working electrodes (3 mm diameter) used in the cyclic voltammetry and EIS electrochemical surface-analysis experiments were either purchased from eDAQ (glassy carbon and gold electrodes) or Windsor Scientific (boron-doped diamond electrodes). All potentials were converted to versus the standard hydrogen electrode using the correction factor of  $E \text{ (V vs SHE)} = E \text{ (V vs ref)} + 0.205$ , which was experimentally determined using the ferricyanide redox couple as calibration. The potentials reported for the experiments performed in 1:5 v/v water/acetonitrile + 0.1 M tetrabutylammonium hexafluorophosphate ( $\text{Bu}_4\text{NPF}_6$ ) electrolyte do not account for any junction potential that may exist between the Ag/AgCl (3 M NaCl) reference electrode and the mixed solvent electrolyte. All experiments that were conducted under a nitrogen atmosphere were carried out in a nitrogen-filled glovebox of dioxygen  $\leq 40$  ppm; otherwise, experiments were performed in air. An EmStat3 potentiostat (PalmSens) with PSTrace 5.5 for Windows software was used for the diazonium electro-grafting experiments. The electrochemical assays of surface confined quinone species were conducted using a CompactStat potentiostat (Ivium technologies) with IviumSoft software for

Windows. The electrochemical impedance spectroscopy experiments were carried out using a Plamsens4 potentiostat.

#### Cleaning of electrode surfaces

Glassy carbon electrode surfaces were mechanically polished for 1–2 min using 1–5  $\mu\text{m}$  alumina slurry impregnated onto a WhiteFelt polishing pad (Buehler). Electrodes were then rinsed with Milli-Q water and sonicated in acetonitrile for 5 min.

Gold electrodes were polished for approximately 1 min using nylon polishing pads (Buehler) impregnated with 1  $\mu\text{m}$  RS PRO Blue Diamond Paste (RS Components Ltd.) and then for approximately 1 min with a 1/10  $\mu\text{m}$  RS PRO Gray Diamond Paste (RS Components Ltd.). This was followed by polishing for approximately 1 min using 1–5  $\mu\text{m}$  alumina slurry impregnated onto a WhiteFelt polishing pad, and then rinsing and sonication for 1 min in Milli-Q water. Electrochemical polishing was then performed by recording 50 cyclic voltammograms from 0.35 to 1.81 V vs SHE in 0.5 M  $\text{H}_2\text{SO}_4$  at 100  $\text{mV s}^{-1}$ , after which the electrodes were rinsed with Milli-Q water and immersed in Milli-Q water until used.

Boron-doped diamond electrodes were polished for 1–2 min using nylon polishing pads (Buehler) impregnated with 1  $\mu\text{m}$  RS PRO Blue Diamond Paste (RS Components Ltd.) and for approximately 1 min using a 1/10  $\mu\text{m}$  RS PRO Gray Diamond Paste (RS Components Ltd.). The electrodes were then rinsed with Milli-Q water and sonicated in acetonitrile for 5 min.

#### Hydroxylamine-functionalisation of disk electrodes

Once the disk electrodes were cleaned, they were hydroxylamine functionalised using the following procedure for *in situ* diazonium cation generation and electro-grafting, and subsequent hydrazine deprotection. A 2  $\mu\text{L}$  portion of a 6.6 M hydrochloric acid solution was added to 100  $\mu\text{L}$  of a 15 mM solution of **2** in a 1:5 v/v water/acetonitrile + 0.1 M  $\text{Bu}_4\text{NPF}_6$  solvent system at 0  $^\circ\text{C}$ , triggering the formation of diazonium cations via protonation of the triazene moiety.<sup>490,491</sup> A 65  $\mu\text{L}$  portion of this solution was added to 935  $\mu\text{L}$  of 1:5 v/v water/acetonitrile + 0.1 M  $\text{Bu}_4\text{NPF}_6$  at 0  $^\circ\text{C}$ , yielding a solution of a 1 mM maximum diazonium salt concentration. Electrochemical grafting experiments to yield an electro-grafted surface (**Scheme 5.4**) were carried out by cycling between the potentials shown in the relevant figures (**Figure 5.3**, **Figure 5.4**) at a scan rate of 20  $\text{mV s}^{-1}$  and 0  $^\circ\text{C}$ . After electrochemical grafting, the electrode surfaces were cleaned by sonication in acetonitrile for 2 min and then rinsed with Milli-Q water before being allowed to dry in air. The hydrazine deprotection step (**Scheme 5.4**) was carried out by adding 155  $\mu\text{L}$  of hydrazine monohydrate to 2 mL of ethanol and heating the

resultant solution to 80 °C. The electro-grafted electrodes were then placed into this solution for either 5 min (glassy carbon and boron-doped diamond electrodes) or 10 min (gold electrodes) with the intention of yielding the hydroxylamine near-monolayer “hydrazine-treated” surface depicted in **Scheme 5.4** and **Figure 5.5**. The electrodes were then allowed to cool for 30 s in a 10 µM ice-cold solution of (aminoxy)acetic acid hemihydrochloride, a solution designed to prevent cross-contamination of the hydroxylamine surfaces with trace carbonyl species. Prior to treatment of the surfaces with target aldehyde species, the electrodes were rinsed briefly in ice-cold water and dried under a stream of argon.

#### **Reaction of hydroxylamine-functionalised disk electrodes with aldehyde-containing species**

To investigate propanal binding to hydroxylamine-functionalised glassy carbon surfaces, modified disk electrodes were placed in aqueous pH 4.5 buffer solution (100 mM sodium acetate + 150 mM NaCl) spiked with 5% v/v propanal for 1 h at room temperature, after which the electrodes were rinsed with Milli-Q water and air-dried before electrochemical testing, *vide infra*.

To investigate 2,5-dihydroxybenzaldehyde binding to hydroxylamine-functionalised glassy carbon, boron-doped diamond, and gold disk electrodes, thus-modified disk electrodes were placed in a 50 µM solution of 2,5-dihydroxybenzaldehyde in aqueous pH 4.5 buffer solution (100 mM sodium acetate + 150 mM NaCl). The reaction was left overnight at room temperature, after which the electrodes were rinsed with Milli-Q water and sonicated with acetonitrile for 30 s prior to cyclic voltammetric interrogation at 25 °C in aqueous pH 4.0 buffer solution (100 mM sodium acetate + 150 mM sodium sulfate).

#### **Surface-immobilisation of oxidised (aldehyde-functionalised) horseradish peroxidase**

Oxidised horseradish peroxidase (EZ-Link Plus Activated Peroxidase) was purchased from Thermo Scientific. For the electrode-protein ligation experiment, hydroxylamine-functionalised 3 mm gold disk electrodes were treated with a 50 µM solution of oxidised horseradish peroxidase in aqueous pH 4.5 buffer solution (100 mM sodium acetate + 150 mM NaCl). The reaction was left to proceed overnight at room temperature, after which the electrodes were rinsed with aqueous pH 7.4 100 mM sodium phosphate buffer solution prior to electrochemical analysis. Control experiments were performed by carrying out the same procedure but using non-oxidised, native horseradish peroxidase (peroxidase from horseradish, Type I, Sigma Aldrich). The concentration of the horseradish peroxidase solutions was determined using the extinction coefficient  $\epsilon = 100 \text{ mM cm}^{-1}$  at 403 nm.<sup>566</sup>



**Attempted immobilisation of thioredoxin 1**

10  $\mu\text{L}$  of an 85  $\mu\text{M}$  solution of aldehyde-functionalised thioredoxin 1 from *Escherichia coli* (in pH 4.5, 100 mM sodium acetate, 150 mM NaCl buffer) was pipetted onto hydroxylamine-functionalised electrode surfaces and the resultant reaction allowed to proceed for 4 hours at room temperature and overnight at 4  $^{\circ}\text{C}$ , after which the electrodes were rinsed with aqueous pH 7.4 100 mM sodium phosphate buffer solution prior to electrochemical analysis. However, no signals could be observed from thioredoxin 1. The addition of several aniline-based nucleophilic catalysts (**Figure 8.73**) to the aldehyde-functionalised thioredoxin 1 reaction solution was also trialled (at 100 mM or saturated concentrations of aniline catalyst), in the hopes that they would promote oxime ligation to the hydroxylamine-functionalised electrode surface. Yet again no signals were observed from thioredoxin 1. Control experiments showed that these aniline catalysts, even in the absence of other redox-active species, would cause Faradaic signals to be observed on GC electrode surfaces after overnight incubation, and thus could give rise to false positives. The aniline catalyst that was least prone to causing the appearance of these unknown Faradaic signals is the one in the box in **Figure 8.73**.

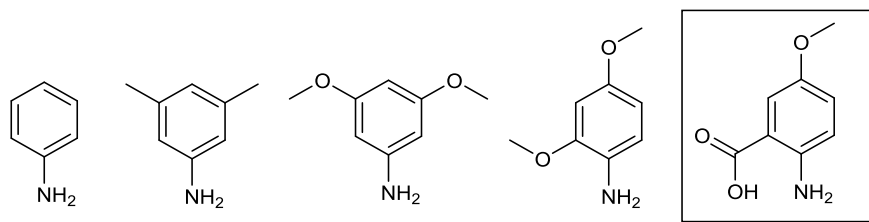


**Figure 8.73.** Aniline catalysts that were used in attempts to facilitate oxime ligation between aldehyde functionalized thioredoxin 1 and hydroxylamine-functionalised GC electrode surfaces.

**X-ray Photoelectron Spectroscopy**

The X-ray photoelectron spectroscopy (XPS) experiments were conducted using a monochromated Al  $K\alpha$  source at 1486.6 eV (XM1000, Scienta Omicron GmbH) in an ultrahigh vacuum system with a base pressure below  $2 \times 10^{-10}$  mbar. X-rays were incident at  $22.5^{\circ}$  to the sample normal and at  $45^{\circ}$  to the hemispherical energy analyser (EA 125, Scienta Omicron GmbH) used to detect emitted photoelectrons. An input aperture diameter of 6 mm was used for all scans.

To prepare the samples for XPS analysis, gold-coated silicon wafer (99.999% (Au), layer thickness 1000  $\text{\AA}$ , 99.99% (Ti adhesion layer)) was purchased from Sigma-Aldrich and cut into 8 mm  $\times$  8mm squares. A solution of acidic piranha (**Caution:** Piranha solution reacts violently with organic matter and should be handled with extreme care!) was prepared by adding 1 part of 30% hydrogen peroxide to 3 parts of concentrated sulfuric acid. The solution was used while hot to clean the 8 mm

× 8 mm samples, which were only removed after the reaction had ceased. The gold substrates were then rinsed with water and dried under a stream of argon prior to electrochemical grafting (**Figure 5.8**). Any subsequent hydrazine treatment was carried out as described for disk electrodes.

Survey scans on the three surfaces tested were measured from a binding energy of 700 to 0 eV in −0.3 eV steps and with a dwell time of 0.5 s. To allow comparison of relevant peaks, these scans were normalized to the average count measured between 600 and 700 eV. High resolution core level spectra were measured over the range of the O 1s, N 1s, and C 1s peaks of interest with −0.05 eV steps and a 1 s dwell time; typically, five separate scans were obtained and then averaged. For the O 1s and C 1s peaks, the data were normalized to the relative weights observed in the survey spectra. The N 1s data were scaled to give a consistent noise level.

#### **Quartz Crystal Microbalance with Dissipation Monitoring**

A Qsense E1 quartz crystal microbalance with dissipation monitoring (QCM-D) was used to quantify mass changes associated with the deprotection of the grafted layer and subsequent protein coupling. A QSX301 quartz crystal microbalance chip purchased from QSense ( $f_o = (4.95 \pm 0.05)$  MHz) was used as the solid substrate and cleaned with a solution of basic piranha that was prepared by adding 1 part of 30% hydrogen peroxide to 3 parts of ammonium hydroxide solution. **Caution:** Piranha solution reacts violently with organic matter and should be handled with extreme care! The resultant solution was then heated to 60 °C and used for cleaning while hot. Once reaction between the piranha solution and the gold surface ceased, the gold chip was subjected to UV/ozone treatment prior to electrochemical grafting. Cyclic voltammograms of the electro-grafting procedure are shown in **Figure 5.19**. Postgrafting, the chip was rinsed in water and then ethanol. After loading into the QCM-D instrument, the electro-grafted surface was temperature-equilibrated with 50 °C ethanol in a custom-built open-topped static chamber attached to a standard QSense base. The frequency and dissipation responses from odd harmonics from 3 to 13 were probed in sequence with a time resolution of approximately 0.8 s. After thermal equilibrium was reached, hydrazine monohydrate was added such that a 7% v/v solution of hydrazine in ethanol was obtained. After deprotection had been observed via an increase in  $\Delta f$ , the hydrazine ethanol solution was replaced with a solution of 1 μM hydrazine monohydrate in distilled water. This solution was then exchanged with aqueous pH 4.5 buffer solution (100 mM sodium acetate + 150 mM NaCl); then a 35 μM solution of horseradish peroxidase in the same buffer was added, and the response in  $\Delta f$  was observed. Finally, the solution of horseradish peroxidase was exchanged for ethanol.

#### **Electrochemical impedance spectroscopy**

This procedure was performed by fellow PhD student Dr Mark Dowsett. A Palmsens4 potentiostat was used to apply an AC voltage input at +0.197 V vs Ag/AgCl in a solution of 1 mM potassium ferricyanide in 0.1 M NaCl(aq) with an oscillation amplitude of 5 mV and current ranges of 10 mA – 1 nA. A pre-equilibration time of 30 s was used before frequencies were scanned in the range 1 MHz to 0.1 Hz at 15 points per decade. All frequency cycles were recorded for a minimum of 10 s to obtain at least one full waveform. The full electrochemical set-up, excluding the potentiostat, was placed inside a custom-built Faraday cage. All experimental traces were routinely analyzed from 100 kHz – 0.1 Hz and fitted to the circuits in **Figure 8.74** using PSTrace 5.5 and the built-in circuit fitting program. These circuits were used to account for typical resistances from the solution (R1) and of charge transfer (R2). The charge stored (Q1) was modelled using a CPE to allow for an inhomogeneous surface. Charge stored in  $\mu\text{F}$  was obtained by accounting for the capacitance exponent.<sup>567</sup> Finally a Warburg element was used to account for diffusion of solution species to the electrode with varying fields of diffusion. It is likely that circuit (b) could have been used for all analysis, though EIS spectra modelled using (a) did not scan to a low enough frequency as this was not of interest.<sup>568</sup>

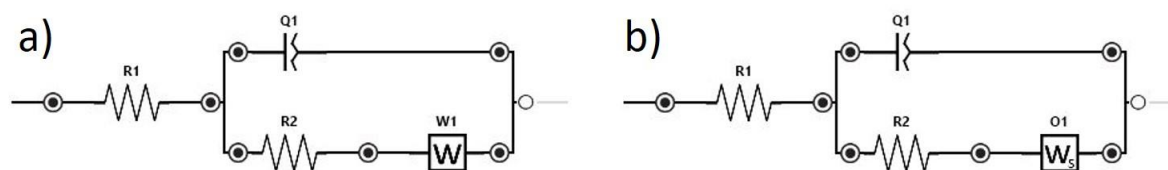


**Figure 8.74.** Theoretical circuits for fittings of oxime ligation processes to a glassy carbon electrode (a) and a boron-doped diamond electrode (b). R1: solution resistance ( $R_{sol}$ ), Q1: constant phase element to quantify capacitance (CDL) whilst allowing for surface inhomogeneity ( $\phi$ ), R2: charge transfer resistance (RCT), W1 Warburg element for diffusion, O1 Warburg short for finite-length diffusion with a transmissive boundary.

## 8.6 Experimental procedures for Chapter 6

### 8.6.1 Synthetic procedures/molecular characterisations

#### 8.6.1.1 Synthesis of triazabutadienes

##### 1,3-dimesityl-1H-imidazol-3-ium chloride (T1)

Although commercially available, **T1** could be synthesised easily and cheaply.

To a stirred solution of 37% aqueous glyoxal (5.2 mL) and formic acid (0.134 mL) in methanol (70 mL) was added 2,4,6-trimethylaniline (13 mL, 92.6 mmol). The resultant solution was stirred for 3 hours, after which time the di-imine precipitate was removed by filtration and washed with cold methanol before being dried *in vacuo*. The di-imine precipitate (8.80 g, 30 mmol) was then dissolved in anhydrous THF (75 mL) under an N<sub>2</sub> atmosphere and heated to 40 °C. Chloromethyl ethyl ether (3 mL) was added dropwise and the resultant solution stirred at 40 °C for 18 hours. Diethyl ether (75 mL) was then added and product collected by filtration. The product was first washed with diethyl ether, then with acetone and dried *in vacuo*, yielding a grey powder (6.33 g, 40% across 2 steps). The <sup>1</sup>H-NMR matched that of the literature.<sup>569</sup>

<sup>1</sup>H-NMR (400 MHz, CDCl<sub>3</sub>) δ<sub>H</sub> 11.02 (t, *J* = 1.53 Hz, 1H), 7.58 (d, *J* = 1.53 Hz, 2H), 7.05 (s, 4H), 2.35 (s, 6H), 2.20 (s, 12H).

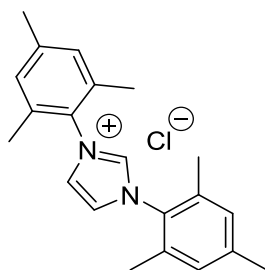


Figure 8.75. The structure of **T1**.

##### Methyl 4-azidobenzoate (T2)

To a solution of methyl 4-aminobenzoate (1.06 g, 7.00 mmol) in water (40 mL), 4.2 M hydrochloric acid (12 mL) was added, then cooled to 0 °C. NaNO<sub>2</sub> (0.531 g, 7.70 mmol, 1.1 equiv) was dissolved in water (10 mL) and added to the reaction mixture, which was stirred for 20 minutes at 0 °C. NaN<sub>3</sub> (0.546 g, 8.4 mmol, 1.2 equiv) was added and the reaction mixture stirred for 4 hours at room temperature. The resultant mixture was transferred to a separating funnel, and extracting the organic layer each

time, the resultant solution was washed with diethyl ether (3 x 40 mL), sodium bicarbonate (100 mL), water (100 mL) and brine (100mL). The organic layer was then dried over  $\text{MgSO}_4$  and concentrated *in vacuo* to yield **T2** as a yellow powder (1.27 g, 95%).  $^1\text{H-NMR}$  was in agreement with that of the literature.<sup>570</sup>

$^1\text{H-NMR}$  (400 MHz,  $\text{CDCl}_3$ ):  $\delta_{\text{H}}$  8.04 (m, 2H), 7.08 (m, 2H), 3.92 (s, 1H).

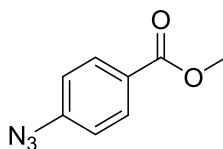


Figure 8.76. The structure of **T2**.

#### Methyl (E)-4-((1,3-dimesityl-1,3-dihydro-2H-imidazol-2-ylidene)triaz-1-en-1-yl)benzoate (**T3**)

To a solution of **T2** (68 mg, 0.383 mmol) and **T1** (130 mg, 0.383 mmol) dissolved in the minimum volume of anhydrous DMSO was added potassium *tert*-butoxide (43 mg, 0.383 mmol). The resultant solution was stirred overnight in the dark under  $\text{N}_2$ , after which time DCM was added (40 mL), and the resultant solution was transferred to a separating funnel. DMSO was removed via washing with water (3 x 40 mL) and the organic extraction was then dried over  $\text{MgSO}_4$  and concentrated *in vacuo*. The crude residue was then purified via flash column chromatography (hexane  $\rightarrow$  ethyl acetate to yield a yellow/orange foamy solid (72 mg, 39 %). The characterisations were in agreement with those of the literature.<sup>529</sup>

$^1\text{H-NMR}$  (400 MHz,  $\text{CDCl}_3$ , **Figure 8.78**):  $\delta_{\text{H}}$  7.70 (m<sup>AA'BB'</sup>, 2H, H-6), 7.01 (s, 4H, H-2), 6.64 (s, 2H, H-4), 6.58 (m<sup>AA'BB'</sup>, 2H, H-5), 3.86 (s, 3H, H-7), 2.38 (s, 6H, H-1), 2.16 (s, 12H, H-3).

$^{13}\text{C-NMR}$  (100 MHz,  $\text{CDCl}_3$ , **Figure 8.79**):  $\delta_{\text{C}}$  167.17 (C-13), 155.19 (C-8), 151.44 (C-6/9), 138.84 (C-6/9), 134.81 (C-11/10), 133.77 (C-2), 129.68 (C-5), 129.28 (C-3), 126.17 (C-12), 120.79 (C-5), 117.16 (C-7), 51.71 (C-14), 21.01 (C-5), 17.82 (C-1).

(ESI)HRMS (**Figure 8.80**): Found  $[\text{M}+\text{H}]^+$  482.2554,  $\text{C}_{29}\text{H}_{32}\text{N}_5\text{O}_2$  requires 482.2551.

IR (ATR) (**Figure 8.81**) ( $\text{umax}/\text{cm}^{-1}$ ): 3058 (C-H stretch, aromatic), 2858 (C-H stretch, alkyl), 1705 (C=O stretching), 1525 (C-C stretch, aromatic), 1358 (C-N stretching), 1176 (C-N stretching), 853 (C-H bend, aromatic), 773 (C-H bend, aromatic).

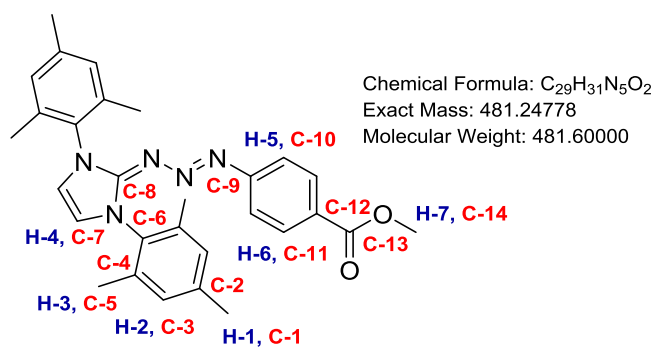
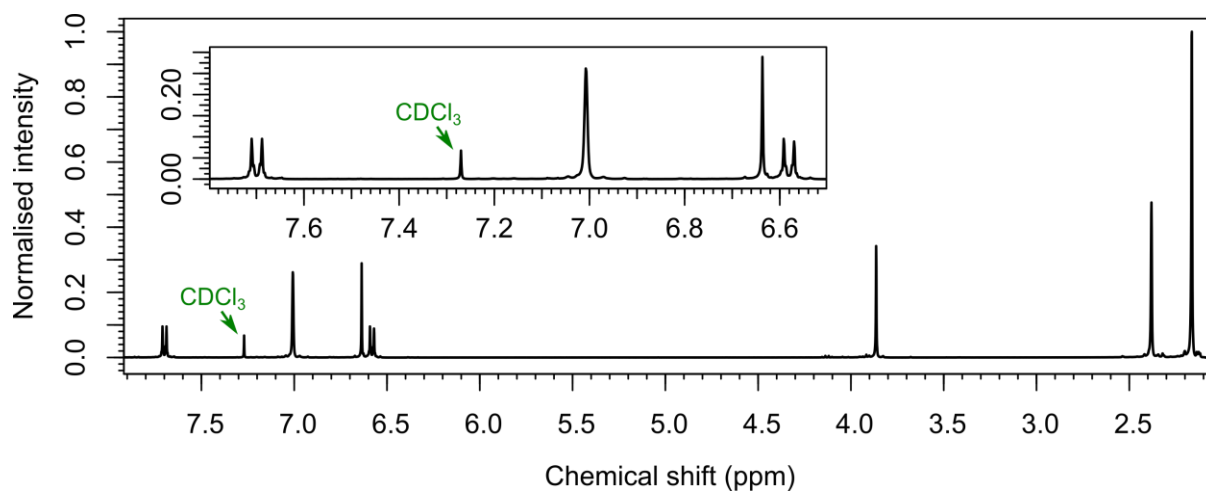
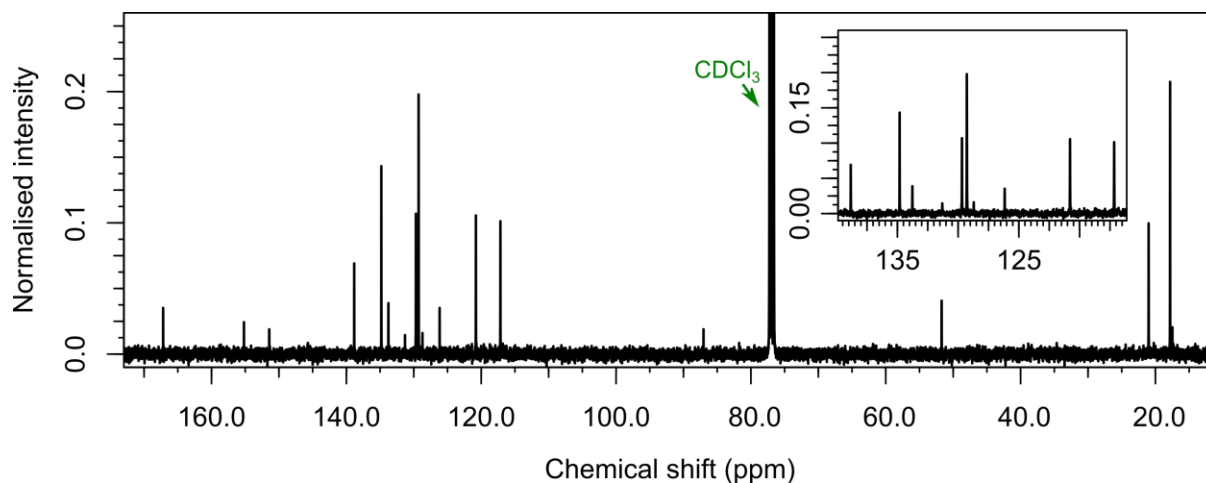
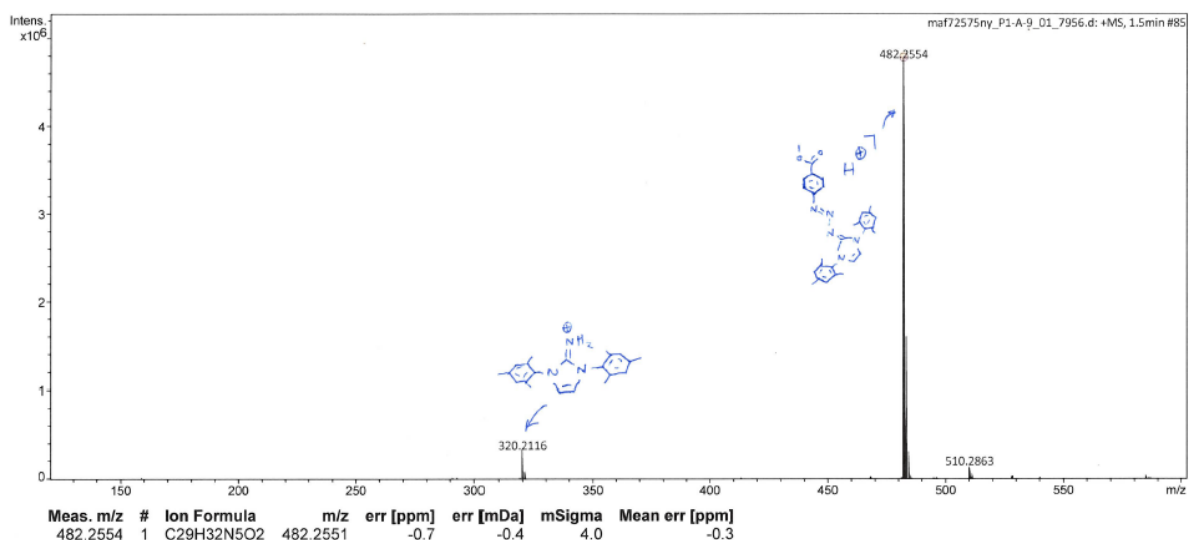
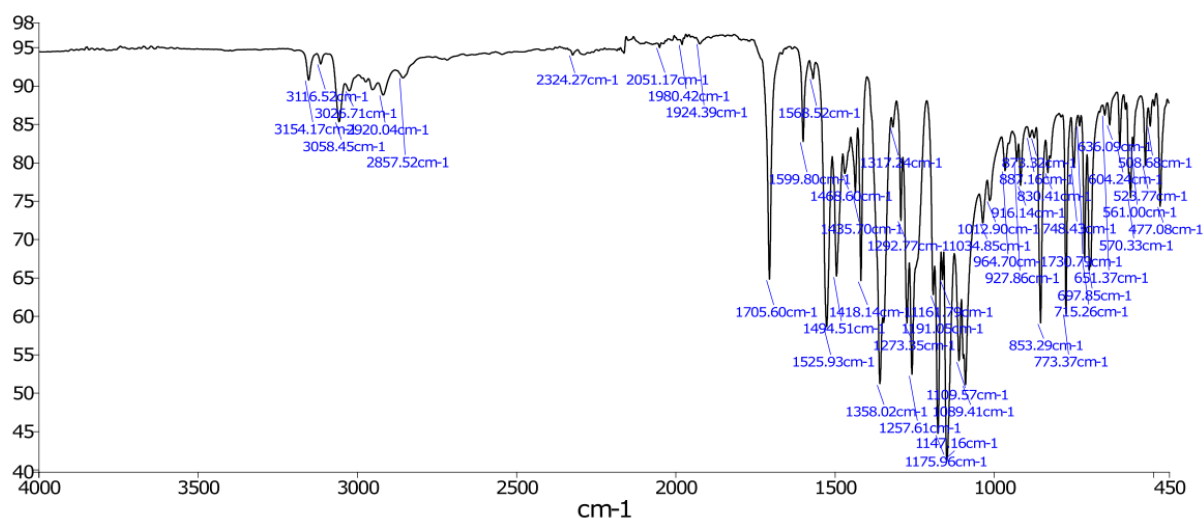


Figure 8.77. The structure of T3.

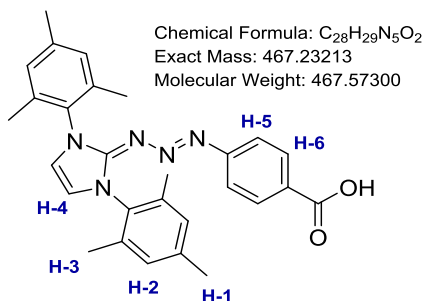
Figure 8.78.  $^1\text{H-NMR}$  spectrum of T3.Figure 8.79.  $^{13}\text{C-NMR}$  spectrum of T3.

Figure 8.80. ESI-LC/MS spectrum of **T3**.Figure 8.81. IR (ATR) spectrum of **T3**.**(E)-4-((1,3-dimesityl-1,3-dihydro-2H-imidazol-2-ylidene)triaz-1-en-1-yl)benzoic acid (**T4**)**

To a stirred methanolic solution of **T3** (0.890 g, 1.80 mmol in 50 mL methanol) was added KOH (1.76 g 31.4 mmol). The resulting solution was then refluxed at 80 °C until TLC showed the reaction to be complete (2.5 hours). The reaction solution was then poured into ethyl acetate and washed with water. The organic layer was then dried over MgSO<sub>4</sub> and concentrated *in vacuo* to yield **T4** as a bright yellow residue (0.678 g, 79%). This residue was partially purified by flash column chromatography (10:1 DCM:methanol, r.f. 0.3) to yield a yellow solid (0.441 g, 52%).

$^1\text{H-NMR}$  (400 MHz,  $\text{CDCl}_3$ , **Figure 8.83**):  $\delta_{\text{H}}$  7.75 (m<sup>AA'BB'</sup>, 2H, H-6), 7.01 (s, 4H, H-2), 6.65 (s, 2H, H-4), 6.59 (m<sup>AA'BB'</sup>, 2H, H-5), 2.38 (s, 6H, H-1), 2.17 (s, 12H, H-3).

(ESI)HRMS (**Figure 8.84**): Found  $[\text{M}+\text{H}]^+$  468.2397,  $\text{C}_{28}\text{H}_{29}\text{N}_5\text{O}_2$  requires 468.2394.



**Figure 8.82.** The structure of T4.

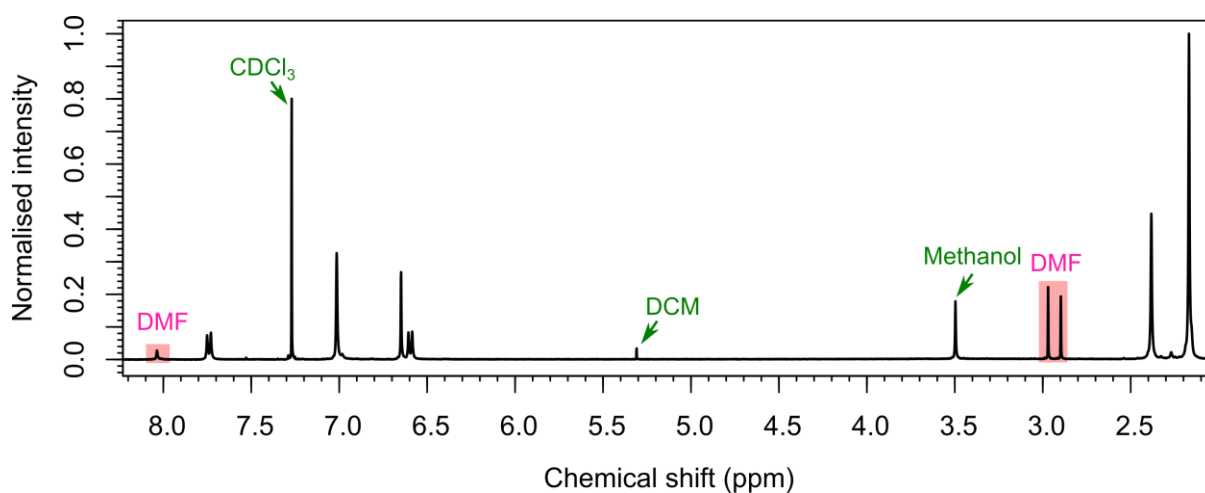


**Figure 8.83.**  $^1\text{H-NMR}$  spectrum of T4.

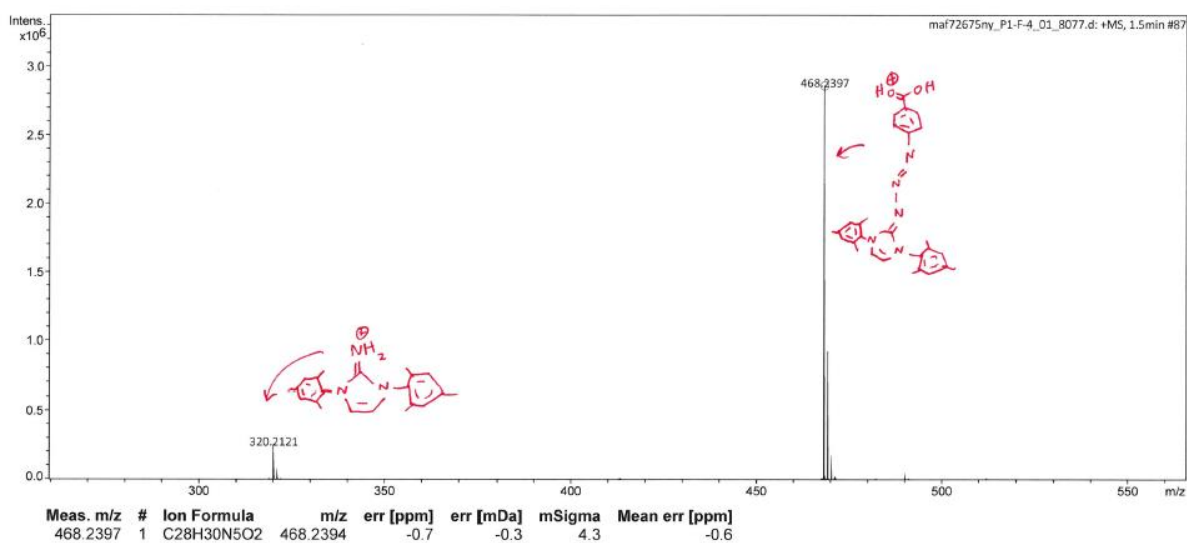


**Figure 8.84.** ESI-LC/MS spectrum of T4.



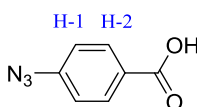
**4-azidobenzoic acid**

Although commercially available, 4-aminobenzoic acid could also be easily and cheaply prepared.

To a suspension of 4-aminobenzoic acid, pre-ground in a mortar and pestle, (5.00 g, 36.3 mmol) in 3 M H<sub>2</sub>SO<sub>4</sub>, kept below to -5 °C using an acetone/ice bath, was added NaNO<sub>2</sub> (3.06 g, 44.4 mmol, dissolved in 5 mL water) dropwise, keeping the temperature of the reaction below -5 °C. The resultant solution was then stirred at -5 °C for 30 min, whereupon the solution became homogeneous. EtOAc (10 mL) was then added, and a solution of NaN<sub>3</sub> (3.66 g, 54.5 mmol, in 10 mL water) was added dropwise to the reaction mixture under continuous stirring. The result solution was allowed to stir for a further 30 min while warming to room temperature. EtOAc and water were added, the EtOAc layer separated and washed a further time with water, then with brine, then dried over MgSO<sub>4</sub>. Concentration *in vacuo* yielded 4-azidobenzoic acid as a yellow solid (5.01 g, 92%). The <sup>1</sup>H-NMR was indistinguishable from that of commercially-sourced 4-azidobenzoic acid.

<sup>1</sup>H-NMR (400 MHz, CDCl<sub>3</sub>): δ<sub>H</sub> 8.06-7.99 (m<sup>AA'BB'</sup>, 2H, H-2), 7.16-7.10 (m<sup>AA'BB'</sup>, 2H, H-1).

(ESI)HRMS: Found [M-H]<sup>-</sup>: 162.0309, C<sub>7</sub>H<sub>4</sub>N<sub>3</sub>O<sub>2</sub> requires 162.0309.



Chemical Formula: C<sub>7</sub>H<sub>5</sub>N<sub>3</sub>O<sub>2</sub>  
Exact Mass: 163.03818  
Molecular Weight: 163.13600

**Figure 8.85.** The structure of 4-azidobenzoic acid.

**2,5-dioxopyrrolidin-1-yl 4-azidobenzoate (T9)**

To a solution of 4-azidobenzoic acid (1.00 g, 6.13 mmol) and *N*-hydroxysuccinimide (0.848 g, 7.37 mmol) in DMF (20 mL) was added 1-ethyl-3-(3-dimethylaminopropyl)carbodiimide hydrochloride (1.40 g, 7.30 mmol). The resultant solution was allowed to stir overnight at room temperature, after which time the DMF was removed *in vacuo*, and the resultant residue dissolved in 150 mL ethyl acetate, and washed thrice with 100 mL water. The organic layer was then washed with saturated NaHCO<sub>3</sub>(aq) solution, dried over MgSO<sub>4</sub> and concentrated *in vacuo*. The crude residue was then dissolved in the minimum volume of warm EtOAc, and precipitation induced using hexane and cooling in an ice bath. The precipitated product was isolated by filtration and allowed to dry, yielding a pale-yellow powder (1.18 g, 4.53 mmol, 74%). Characterisations matched those of the literature.<sup>571</sup>

$^1\text{H-NMR}$  (400 MHz,  $\text{CDCl}_3$ , **Figure 8.87**):  $\delta_{\text{H}}$  8.12 ( $m^{\text{AA}'\text{BB}}$ , 2H, H-2), 7.13 ( $m^{\text{AA}'\text{BB}}$ , 2H, H-1), 2.91 (s, 4H, H-3).

$^{13}\text{C-NMR}$  (100 MHz,  $\text{CDCl}_3$ , **Figure 8.88**):  $\delta_{\text{C}}$  169.14 (C-5), 160.91 (C-5), 146.78 (C-1), 132.33 (C-3), 121.08 (C-4), 119.14 (C-2), 25.50 (C-7).

**IR (ATR)** (**Figure 8.89**) ( $\mu\text{max}/\text{cm}^{-1}$ ): 2127 (N=N=N stretch, azide), 2095 (N=N=N stretch, azide), 1727 (C=O stretching), 1597 (C-C stretch, aromatic), 1175 (C-N stretching), 850 (C-H bend, aromatic), 753 (C-H bend, aromatic).

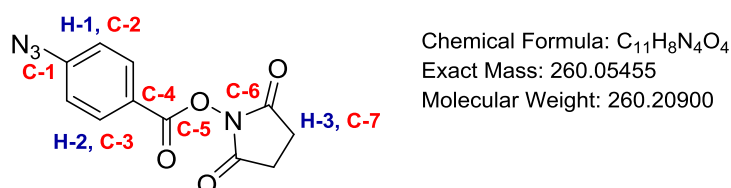


**Figure 8.86.** The structure of T9.

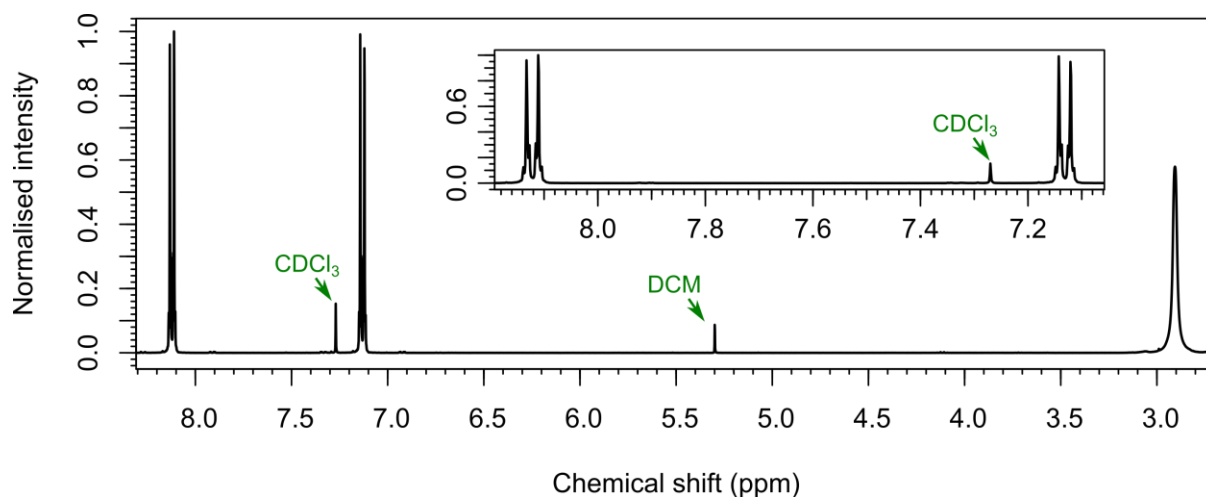


**Figure 8.87.**  $^1\text{H-NMR}$  spectrum of T9.

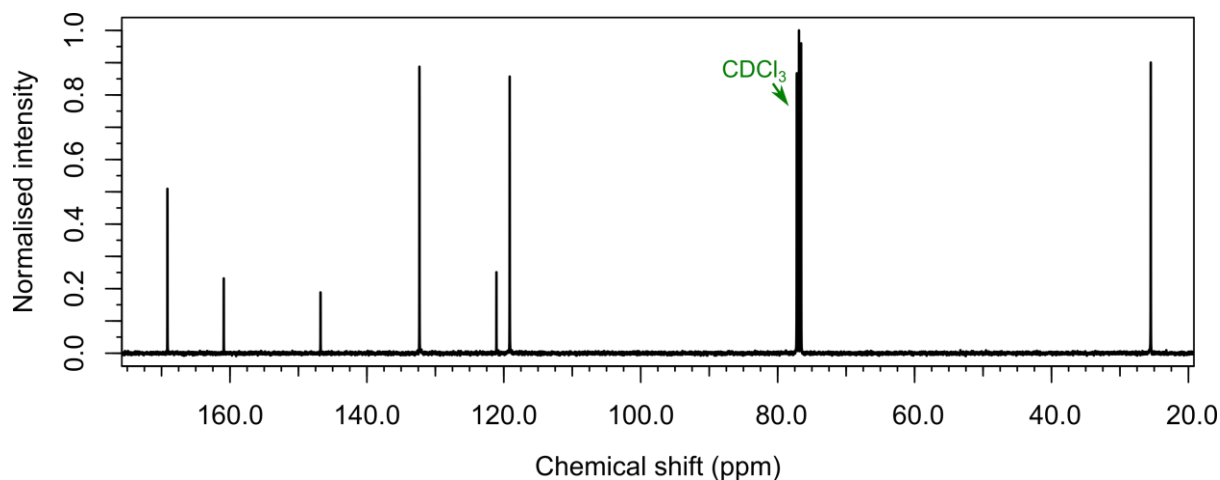


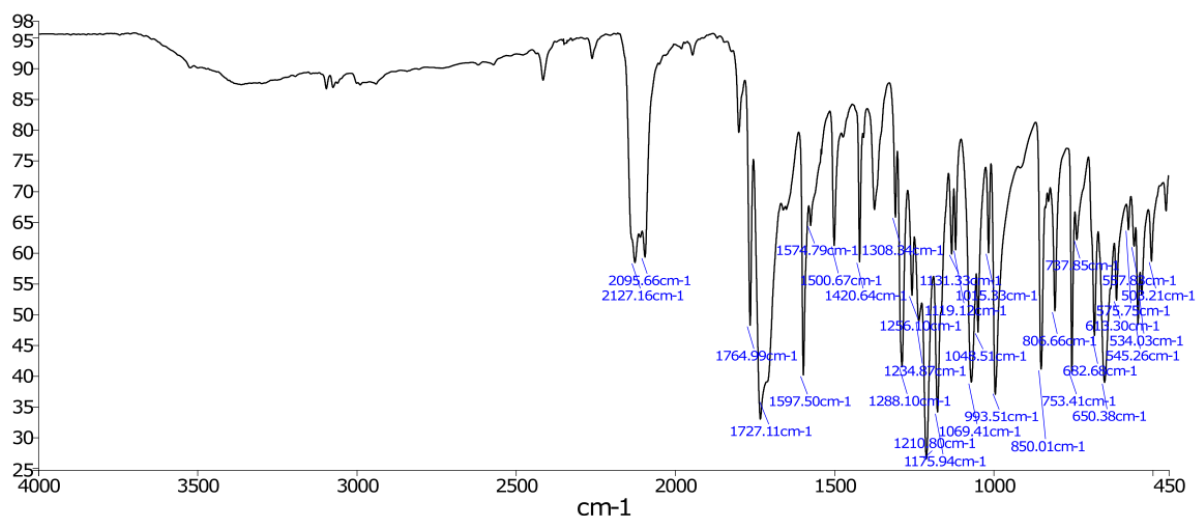
Figure 8.88.  $^{13}\text{C}$ -NMR spectrum of T9.

Figure 8.89. IR (ATR) spectrum of T9.

### 2,5-dioxopyrrolidin-1-yl (E)-4-((1,3-dimesityl-1,3-dihydro-2H-imidazol-2-ylidene)triaz-1-en-1-yl)benzoate (T5)

To a solution of 2,5-dioxopyrrolidin-1-yl 4-azidobenzoate (0.250 g, 0.961 mmol), in 10 mL dry THF at 0 °C was added 1,3-dimesitylimidazolium chloride (0.326 g, 0.961 mmol), and the resultant solution stirred at 0 °C for 5 min. To this solution, 44.5 mg NaH (0.961 mmol, 60% in mineral oil) and 11 mg of potassium tert-butoxide (0.0961 mmol) were added, and the reaction further stirred for 18 h, gradually warming from ice to room temperature. The reaction was then diluted with DCM and washed with brine. DCM fractions were combined and dried using  $\text{MgSO}_4$ . The product was then purified by flash column chromatography (automatic, hexane  $\rightarrow$  ethyl acetate) yielding a yellow/orange foamy solid (0.349 g, 64%).  $^1\text{H}$ -NMR spectral characterisation was consistent with that reported in the literature.<sup>529</sup>

$^1\text{H}$ -NMR (400 MHz,  $\text{CDCl}_3$ , Figure 8.91):  $\delta_{\text{H}}$  7.78 (m<sup>AA'BB'</sup>, 2H, H-6), 7.02 (s, 4H, H-2), 6.67 (s, 2H, H-4), 6.61 (m<sup>AA'BB'</sup>, 2H, H-5), 2.89 (m, 4H, H-7), 2.38 (s, 6H, H-1), 2.16 (s, 12H, H-3).

$^{13}\text{C}$ -NMR (100 MHz,  $\text{CDCl}_3$ , Figure 8.92):  $\delta_{\text{C}}$  169.35 (C-14), 161.71 (C-13), 156.71 (C-8), 151.09 (C-9), 138.93 (C-6), 134.64 (C-4), 133.50 (C-12), 130.82 (C-11), 129.27 (C-3), 120.95 (C-10), 120.26 (C-2), 117.45 (C-7), 25.50 (C-15), 20.93 (C-1), 17.73 (C-5).

(ESI)HRMS (Figure 8.93): Found  $[\text{M}+\text{H}]^+$  565.2562,  $\text{C}_{32}\text{H}_{33}\text{N}_6\text{O}_4$  requires 565.2558.

**IR (ATR) (Figure 8.94)** ( $\nu_{\max}/\text{cm}^{-1}$ ): 2921 (C-H stretch, alkyl), 1760 (C=O stretching), 1736 (C=O stretching), 1597 (C-C stretch, aromatic), 1523 (C-C stretch, aromatic), 1352 (C-N stretching), 1183 (C-O stretch, ester), 1141 (C-N stretching), 855 (C-H bend, aromatic).

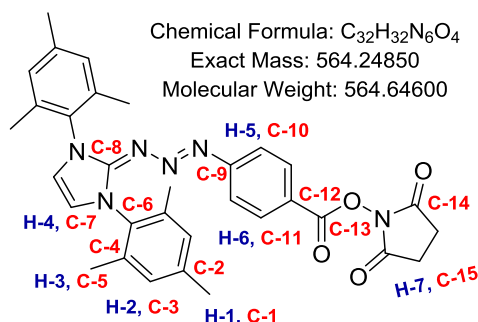


**Figure 8.90.** The structure and labelling of chemical environments in **T5**.

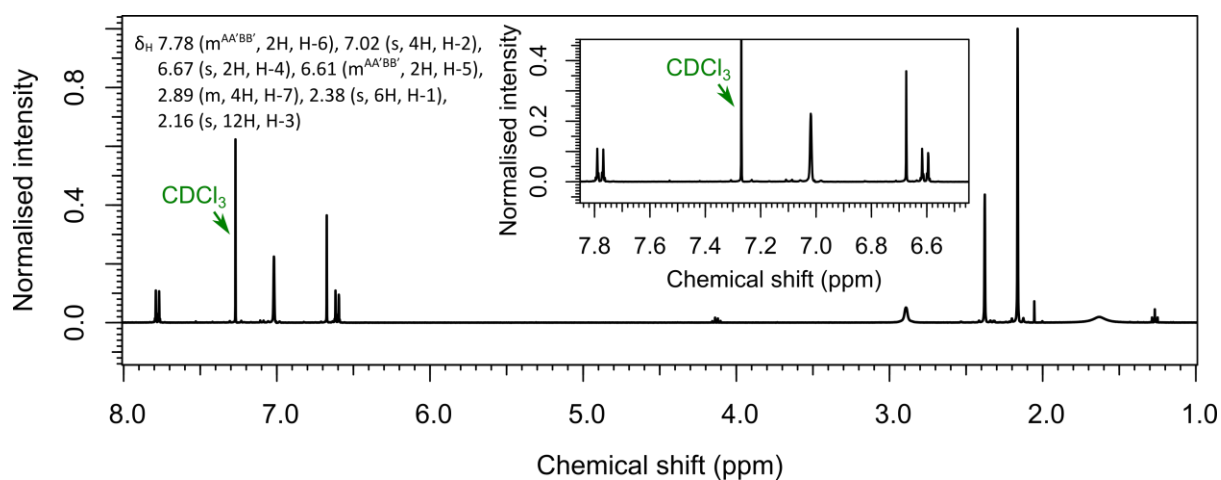


**Figure 8.91.**  $^1\text{H}$ -NMR spectrum of **T5**.

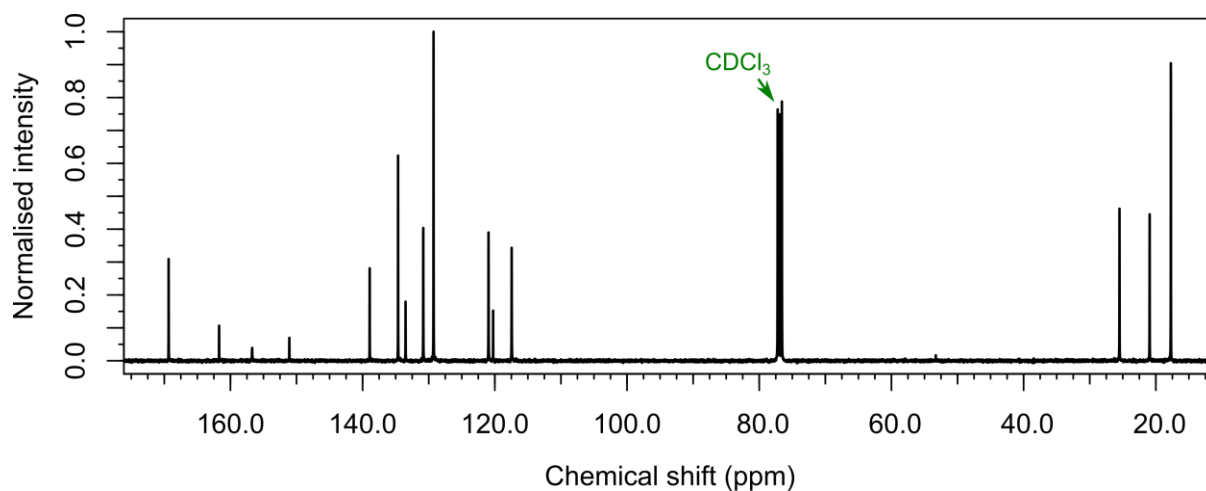


**Figure 8.92.**  $^{13}\text{C}$ -NMR spectrum of **T5**.

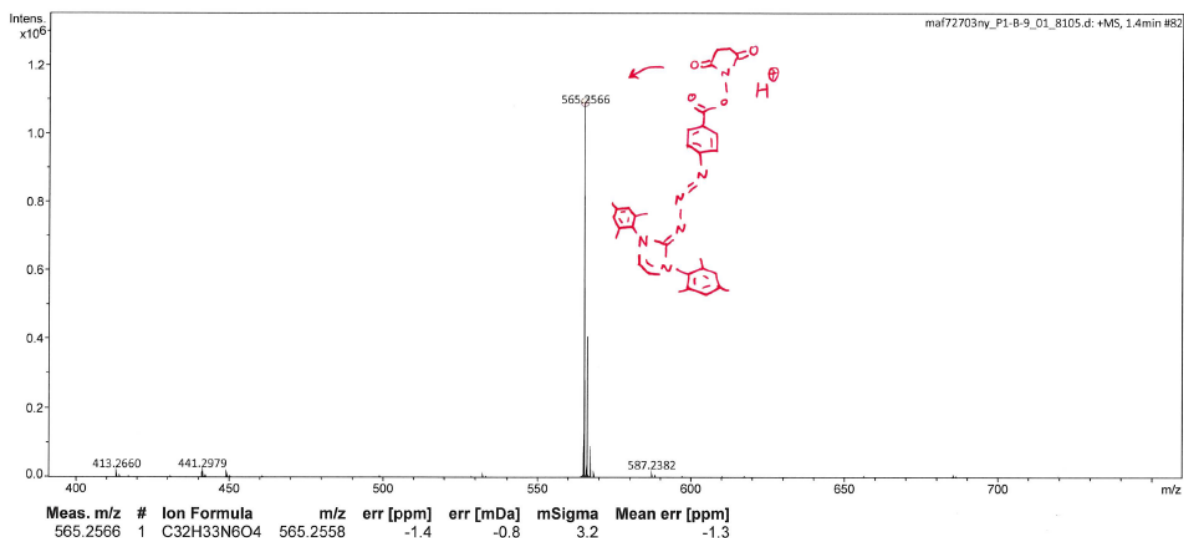


Figure 8.93. ESI-LC/MS spectrum of T5.

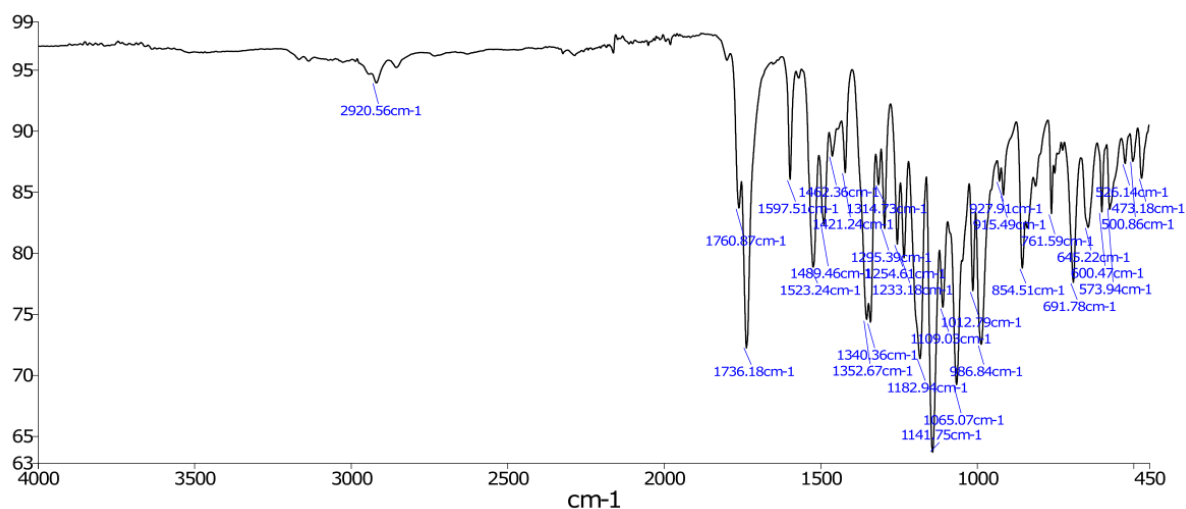


Figure 8.94. IR (ATR) spectrum of T5.

#### 1-(2-(2-aminoethoxy)ethyl)-1H-pyrrole-2,5-dione 2,2,2-trifluoroacetate (T7), via T6

*Tert*-butyl (2-(2-hydroxyethoxy)ethyl)carbamate (**Dan1**, see **Section 8.4.5**) (0.513 g, 2.50 mmol), maleimide (0.268 g, 2.75 mmol, 1.1 equiv) and triphenylphosphine (0.72 g, 2.75 mmol, 1.1 equiv) were dissolved in 25 mL of anhydrous THF under an N<sub>2</sub> atmosphere with stirring. The resultant solution was cooled to 0 °C, and diisopropyl azodicarboxylate (0.6 mL, 3.00 mmol, 1.2 equiv) was then added dropwise over a 10-min period. The reaction solution was then stirred overnight at room temperature. Water (25 mL) and DCM (25 mL) were then added, and the organic phase collected. The aqueous

phase was washed with DCM (25 mL) and the organic phases combined, dried over  $\text{MgSO}_4$  and concentrated to a small volume *in vacuo* and diethyl ether was added. This was followed by hexane until a permanent yellow milky colouration was observed. The resultant solution was left in the fridge over the weekend, precipitating crystals of triphenylphosphine oxide, which were subsequently removed by filtration. The eluate was concentrated *in vacuo* to yield a crude yellow residue, which was itself redissolved in DCM and purified via flash column chromatography ( $\text{SiO}_2$ , 1:1 hexane:ethyl acetate). *Tert*-butyl (2-(2-(2,5-dioxo-2,5-dihydro-1H-pyrrol-1-yl)ethoxy)ethyl)carbamate (**T6**) only faintly appeared on TLC plates, and only when using ninhydrin stain), and was found (via HRMS (**Figure 8.99**) and  $^1\text{H-NMR}$  (**Figure 8.100**)) in the fractions of r.f values of approximately 0.5, and co-eluted with diisopropyl hydrazine-1,2-dicarboxylate. As such, **T6** was used crude. Boc deprotection of **T6** to yield **T7** was performed by dissolving the crude **T6** in DCM (40 mL), then slowly adding TFA (10 mL). The resultant solution was stirred for 2 hours before being concentrated *in vacuo*. The resultant residue was then purified by flash column chromatography ( $\text{SiO}_2$ , 10% MeOH in DCM + 1 % acetic acid. R.f. 0.1) to yield **T7** as a yellow oil (0.45 g, 60% across 2 steps).

$^1\text{H-NMR}$  (400 MHz, methanol- $d_4$ , **Figure 8.96**):  $\delta_{\text{H}}$  6.85 (s, 2H, H-1), 3.76-3.62 (m, 6H, H-2/3/4/5), 3.08 (t,  $J = 5.04$  Hz, 2H, H-2/5).

$^{13}\text{C-NMR}$  (100 MHz, methanol- $d_4$ , **Figure 8.97**):  $\delta_{\text{C}}$  172.77 (C-1), 135.66 (C-2), 69.52 (C-4), 67.34 (C-5) 40.74 (C-3/6), 37.92 (C-3/6).

$^{19}\text{F-NMR}$  (376 MHz, methanol- $d_4$ ):  $\delta_{\text{F}}$  -76.83 (s)

(ESI)HRMS (**Figure 8.98**): Found  $[\text{M}-\text{C}_2\text{O}_2\text{F}_3]^+$  185.0915,  $\text{C}_8\text{H}_{13}\text{N}_2\text{O}_3$  requires 185.0921.

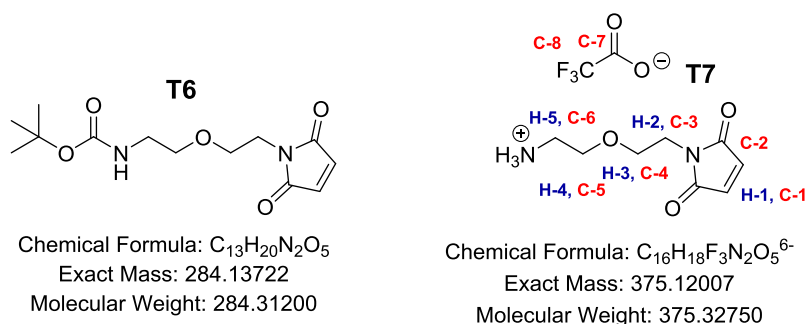


**Figure 8.95.** The structures of **T6** and **T7**.

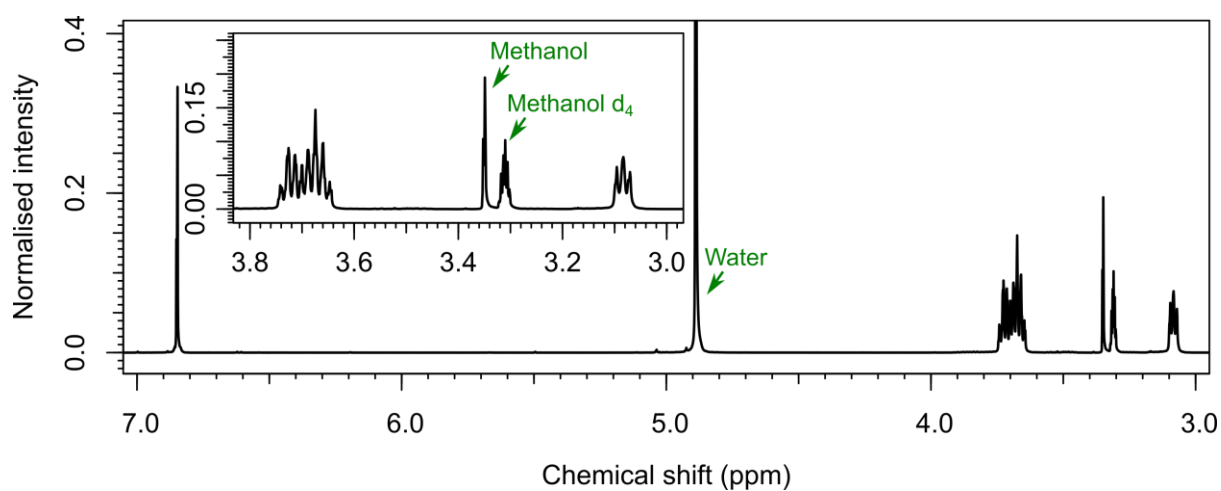
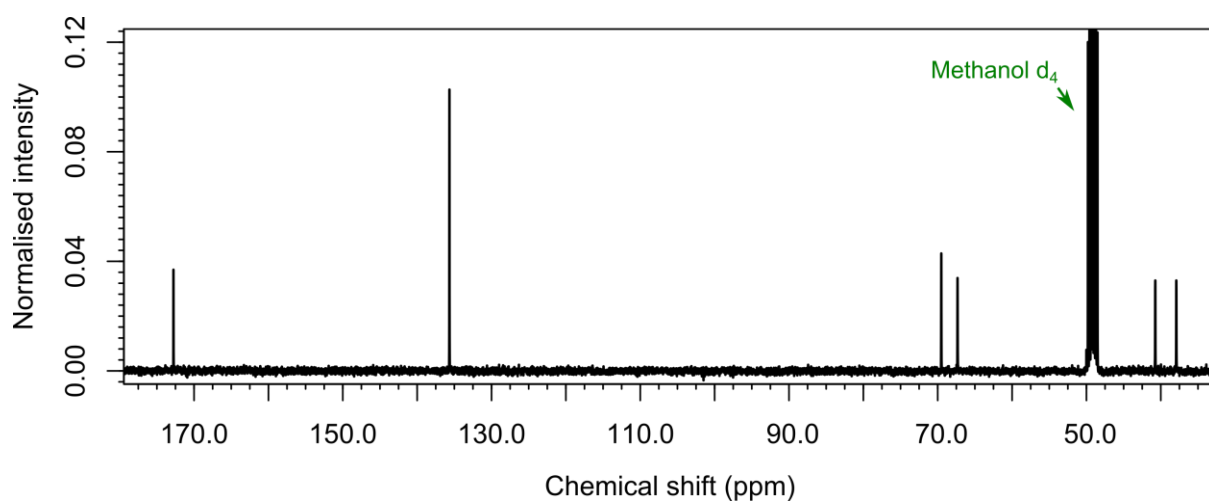
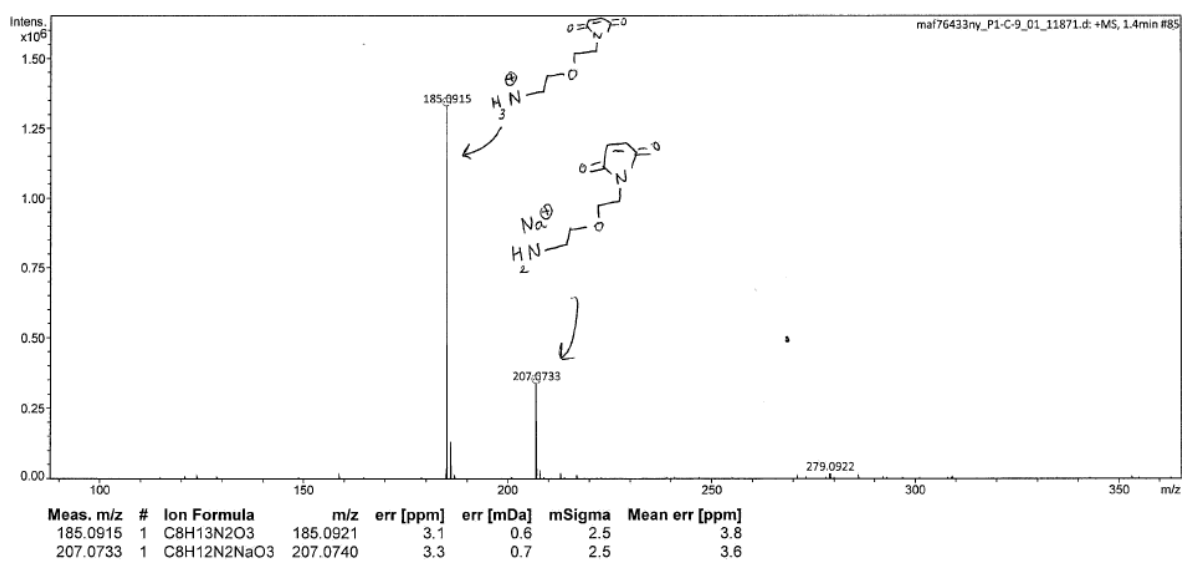
Figure 8.96.  $^1\text{H-NMR}$  spectrum of T7.Figure 8.97.  $^{13}\text{C-NMR}$  spectrum of T7.

Figure 8.98. ESI-LC/MS spectrum of T7.

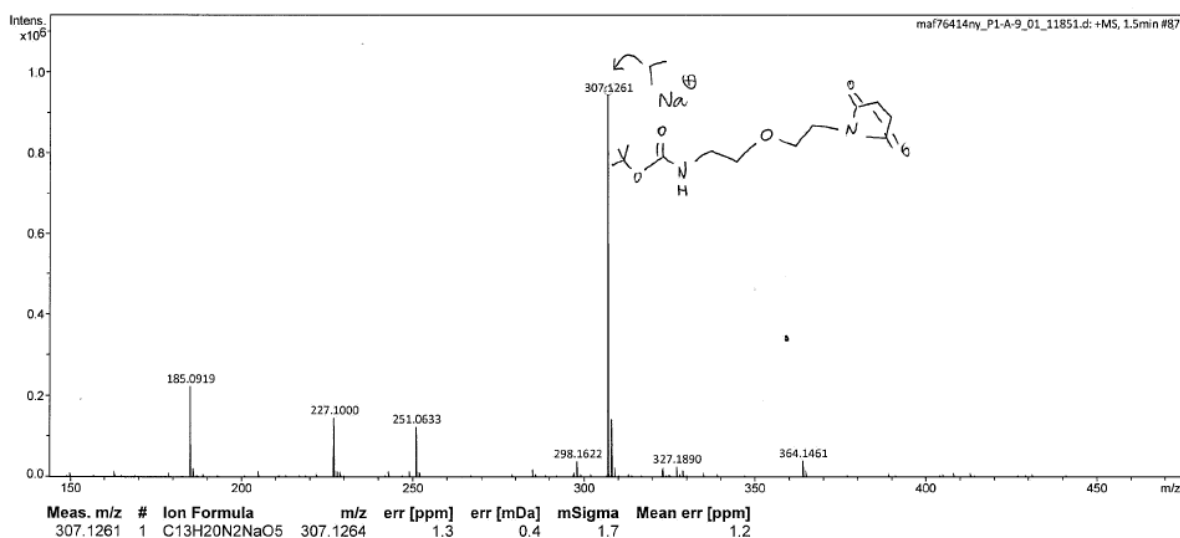
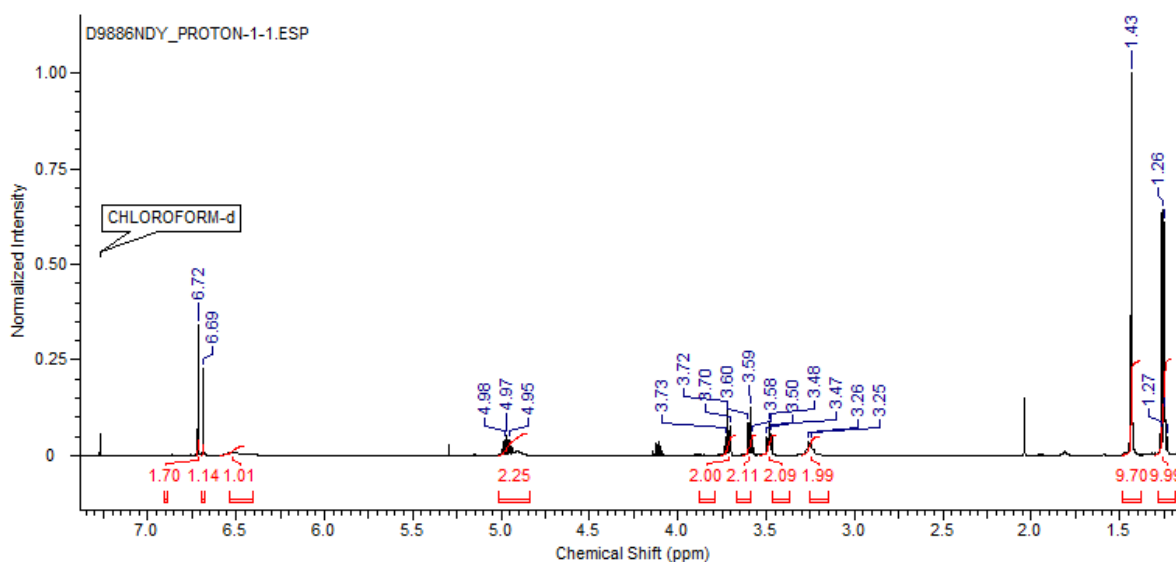


Figure 8.99. ESI-LC/MS spectrum of T6.

Figure 8.100. <sup>1</sup>H-NMR spectrum of T6.

**(E)-4-((1,3-dimesityl-1,3-dihydro-2H-imidazol-2-ylidene)triaz-1-en-1-yl)-N-(2-(2-(2,5-dioxo-2,5-dihydro-1H-pyrrol-1-yl)ethoxy)ethyl)benzamide (T8)**

To **T5** (0.131 g, 0.231 mmol), dissolved in the minimum volume of THF and stirred, was added **T7** (0.104 g, 0.346 mmol), followed by triethylamine (96  $\mu$ L, 0.693 mmol). The resultant solution was stirred overnight at room temperature in the dark. The reaction mixture was then concentrated in vacuo, dissolved in DCM (30 mL), washed once with water (20 mL) and once with brine (20 mL), and dried over MgSO<sub>4</sub>. The DCM was then removed in vacuo and the product purified via flash column chromatography (hexane  $\rightarrow$  ethyl acetate, r.f. = 0.45 in ethyl acetate) to yield **T8** as a yellow/orange foamy solid (70 mg, 48%).



**$^1\text{H-NMR}$**  (400 MHz,  $\text{CDCl}_3$ , **Figure 8.102**):  $\delta_{\text{H}}$  7.49 ( $m^{\text{AA}'\text{BB}'}$ , 2H, H-6), 7.01 (s, 4H, H-2), 6.63 (s, 2H, H-4), 6.60 ( $m^{\text{AA}'\text{BB}'}$ , 2H, H-5), 6.54 (s, 2H, H-12), 6.48 (br t,  $J = 5.04$  Hz, 1H, H-7), 3.73 (t,  $J = 5.50$  Hz, 2H, H-11), 3.61 (t,  $J = 5.50$  Hz, 2H, H-10), 3.60-3.55 (m, 4H, H-8,9), 2.38 (s, 6H, H-1), 2.17 (s, 12H, H-3).

**$^{13}\text{C-NMR}$**  (100 MHz,  $\text{CDCl}_3$ , **Figure 8.103**):  $\delta_{\text{C}}$  170.70 (C-17), 167.25 (C-12), 138.92, 134.83 (C-4), 133.99 (C-18), 133.76 (could be 2 almost-perfectly overlapping peaks), 130.59, 129.32 (C-3), 127.16 (C-10), 120.84 (C-9), 117.21 (C-7), 69.33 (C-13), 68.15 (C-15), 39.51 (C-13), 37.26 (C-16), 21.06 (C-1), 17.86 (C-5).

**(ESI)HRMS** (**Figure 8.104**): Found  $[\text{M}+\text{H}]^+$  634.3125,  $\text{C}_{36}\text{H}_{40}\text{N}_7\text{O}_4$  requires 634.3136.

**IR (ATR)** (**Figure 8.105**) ( $\mu\text{max}/\text{cm}^{-1}$ ): 2923 (C-H stretch, alkyl), 1705 (C=O stretching), 1637 (C=C stretch, conjugated alkene), 1526 (C-C stretch, aromatic), 1361 (C-N stretching), 1148 (C-N stretching), 855 (C-H bend, aromatic), 694 (C-H bend, aromatic).

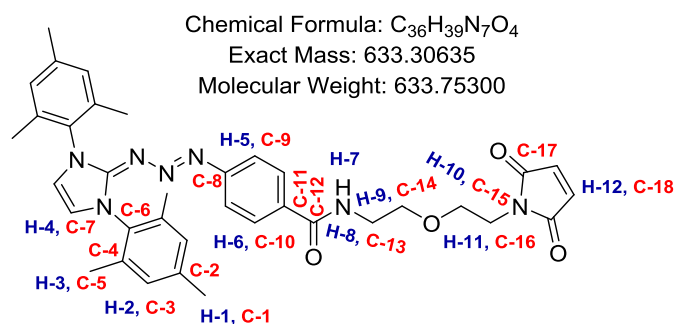


**Figure 8.101.** The structure and labelling of chemical environments in **T8**.

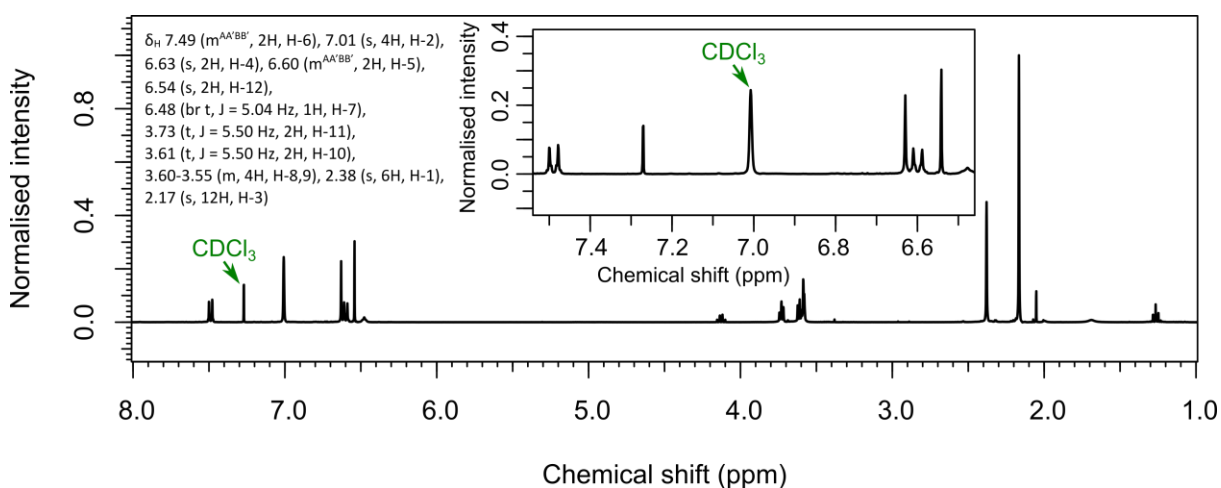


**Figure 8.102.**  $^1\text{H-NMR}$  spectrum of **T8**.

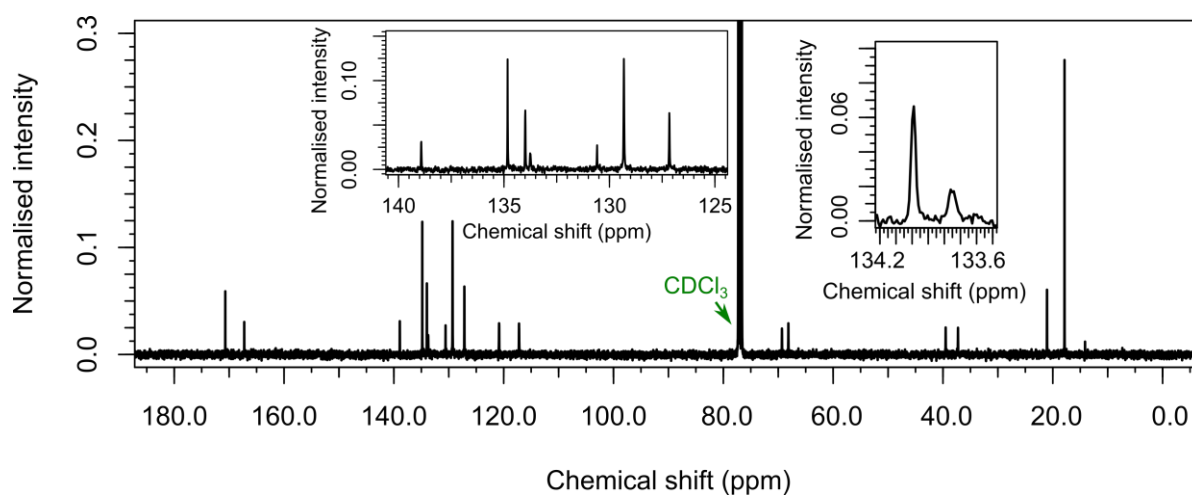
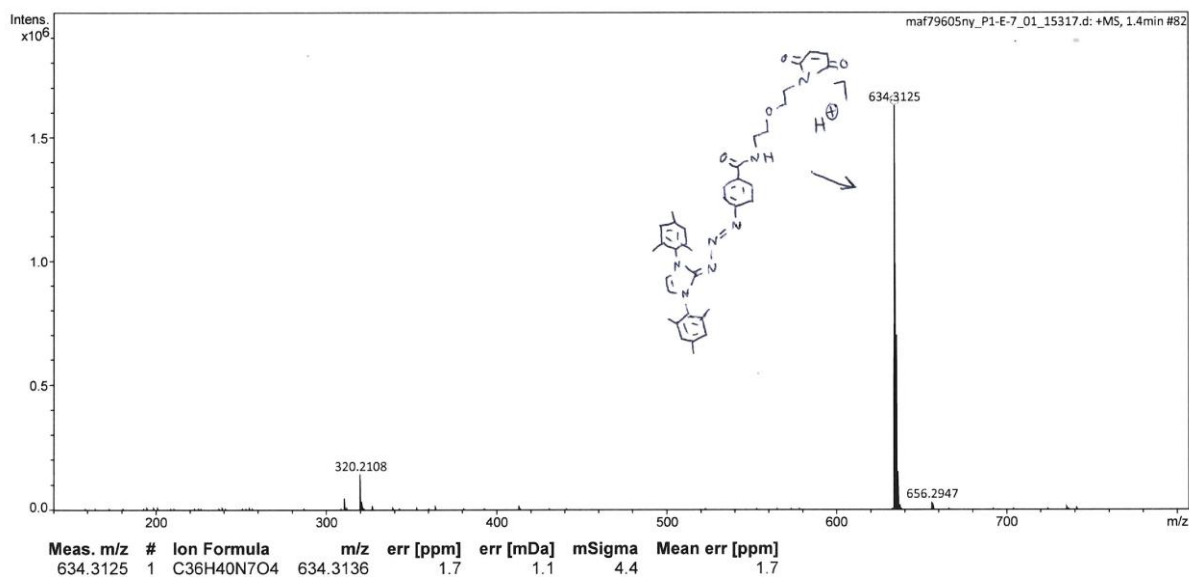
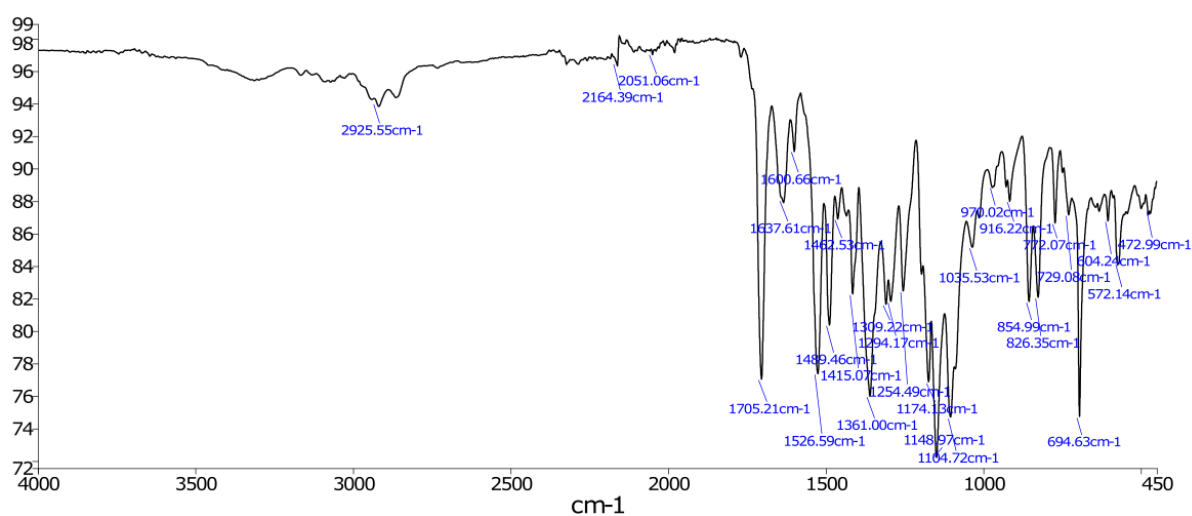
Figure 8.103.  $^{13}\text{C}$ -NMR spectrum T8.Figure 8.104. (ESI)HRMS of T8, showing its protonated molecular ion (theoretical  $m/z = 634.3136$ ).

Figure 8.105. IR (ATR) spectrum of T8.

**(E)-4-((1,3-dimesityl-1,3-dihydro-2H-imidazol-2-ylidene)triaz-1-en-1-yl)-N-(2-(2-hydroxyethoxy)ethyl)benzamide (T-PEG)**

**T5** (25 mg, 44  $\mu$ M) was dissolved in 2 mL of DCM. To this solution was added three equivalents of 2-(2-aminoethoxy)ethanol. The resulting solution was then stirred overnight in the dark at room temperature. DCM (10 mL) was added and the solution was transferred to a separating funnel, washed once with 1 M HCl (5 mL) and washed once with saturated NaHCO<sub>3</sub> solution (10 mL). The organic layer was then dried over MgSO<sub>4</sub> and concentrated *in vacuo* to yield **T-PEG**.

**<sup>1</sup>H-NMR** (400 MHz, CDCl<sub>3</sub>, **Figure 8.107**):  $\delta_{\text{H}}$  7.45 (m<sup>AA'BB'</sup>, 2H, H-6), 6.99 (s, 4H, H-2), 6.71 (m, 1H, H-7), 6.62 (s, 2H, H-4), 6.55 (m<sup>AA'BB'</sup>, 2H, H-5), 3.70 (t,  $J = 4.12$  Hz, 2H, H-11), 3.64-3.58 (m, 4H, H-8,9), 3.55 (t,  $J = 4.12$  Hz, 2H, H-10), 2.36 (s, 6H, H-1), 2.15 (s, 12H, H-3).

**<sup>13</sup>C-NMR** (100 MHz, CDCl<sub>3</sub>, **Figure 8.108**):  $\delta_{\text{C}}$  167.53 (C-12), 153.83, 151.4, 138.83, 134.83 (C-4), 133.77, 130.60, 129.27 (C-3), 127.05 (C-10), 120.92 (C-9), 117.12 (C-7), 72.12 (C-15), 69.86 (C-14), 61.52 (C-16), 39.56 (C-13), 21.02 (C-1), 17.83 (C-5).

**(ESI)HRMS** (**Figure 8.109**): Found [M+H]<sup>+</sup> 555.3095, C<sub>32</sub>H<sub>39</sub>N<sub>6</sub>O<sub>3</sub> requires 555.3078.

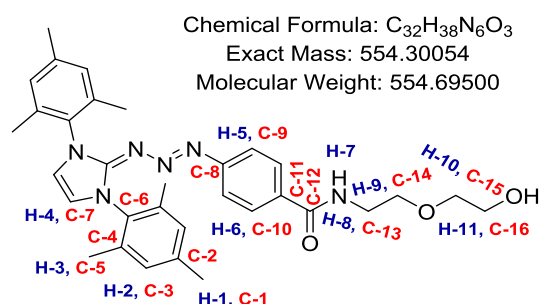


**Figure 8.106.** The structure and labelling of chemical environments in **T-PEG**.

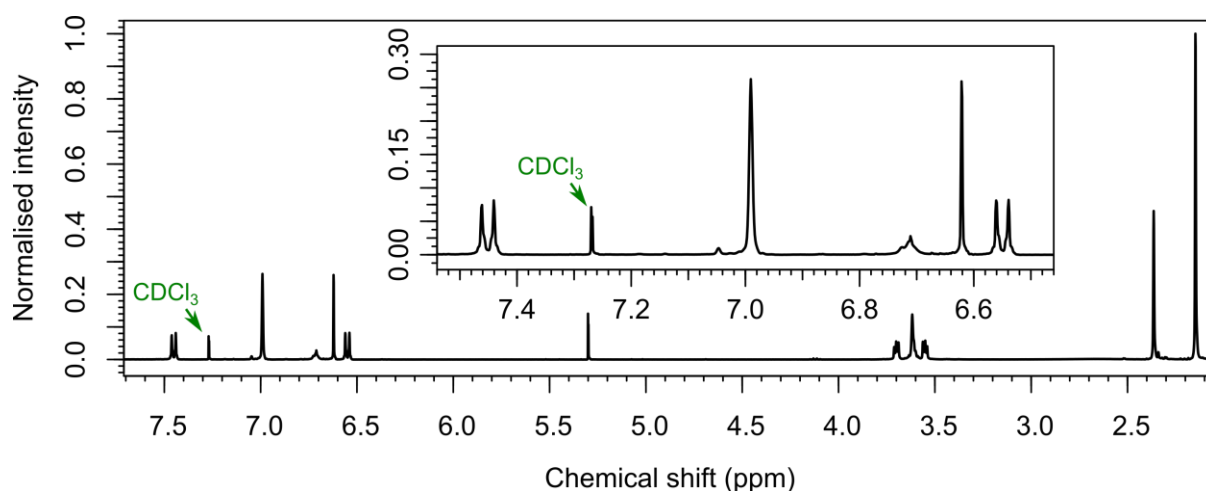


**Figure 8.107.** <sup>1</sup>H-NMR spectrum of **T-PEG**.

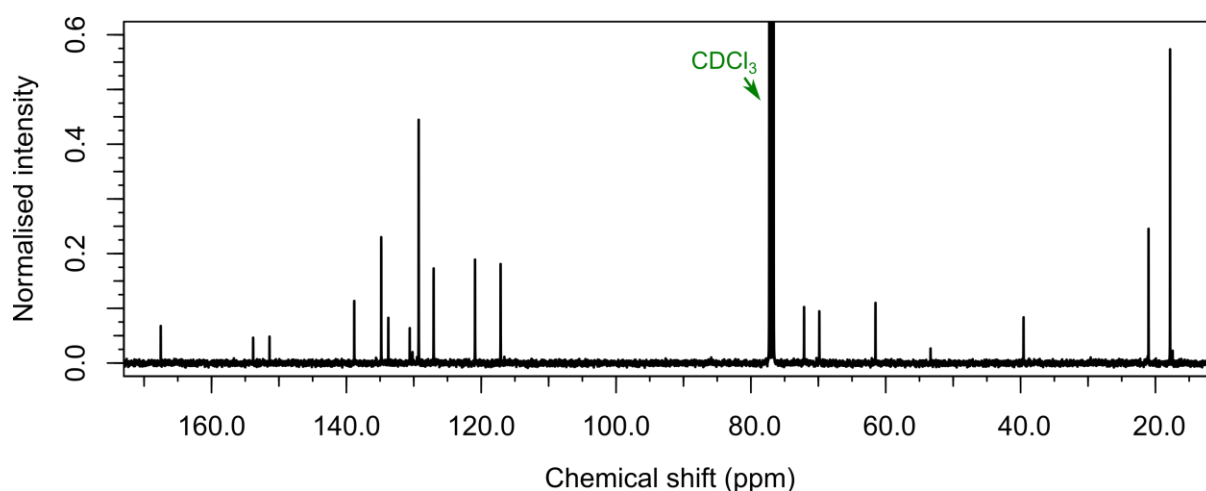
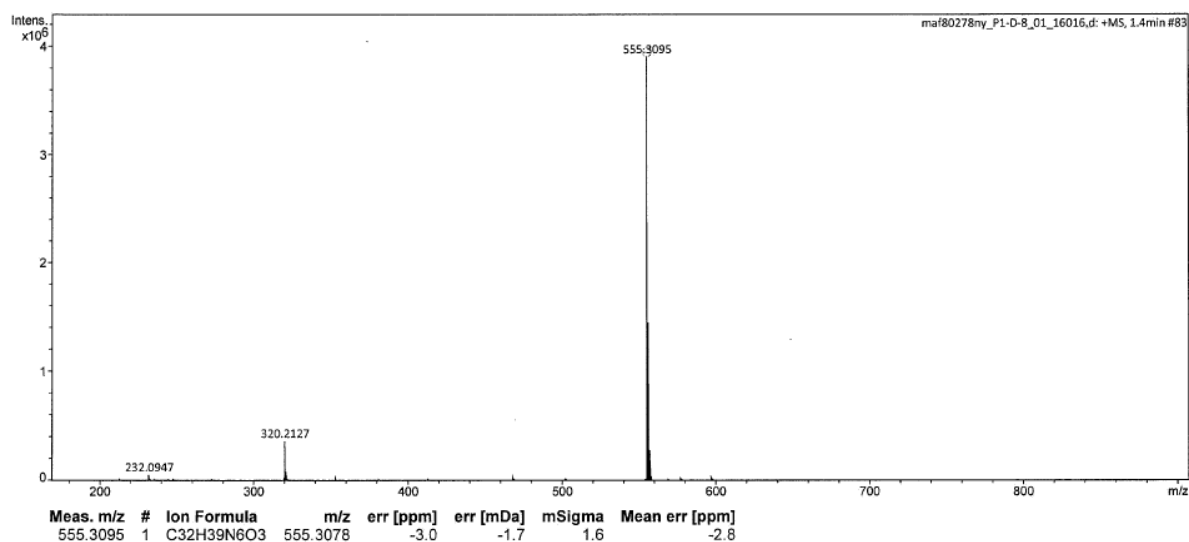
Figure 8.108.  $^{13}\text{C}$ -NMR spectrum of T-PEG.

Figure 8.109. ESI-LC/MS spectrum of T-PEG.

### Methyl (4-azidobenzoyl)glycinate (T10)

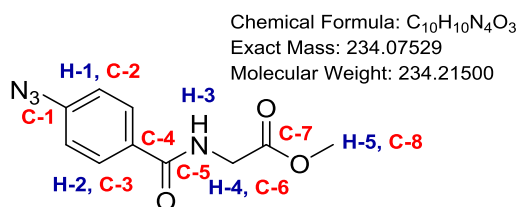
To a stirred solution of 4-azidobenzoic acid (0.200 g, 1.23 mmol) in DCM (1.7 mL) at 0 °C was added a drop of *N,N*-diisopropylethylamine. Oxalyl chloride (0.54 mL, 6.15 mmol, 5 equiv) was subsequently added dropwise. The reaction solution was then allowed to warm to room temperature and stirred at room temperature for 2 hours. Volatiles were subsequently removed *in vacuo* and the resultant residue of the crude acid chloride as re-dissolved in DCM and added dropwise to a stirred solution of methyl glycinate hydrochloride (0.155 g, 1.23 mmol, 1 eq) and triethylamine (0.343 mL, 2.46 mmol) in

THF (20 mL). The resultant solution was stirred for 18 hours at room temperature. EtOAc (50 mL) was then added, and the resultant solution washed with 1 M HCl (2 × 30 mL), and saturated NaHCO<sub>3</sub> (2 × 30 mL), followed by brine (30 mL). The organic extraction was then dried over MgSO<sub>4</sub> and concentrated to yield a crude yellow residue which was purified by flash column chromatography (SiO<sub>2</sub>, Hexane → EtOAc) yielding **T10** as a pale yellow solid (0.130 g, 0.553 mmol, 46%).

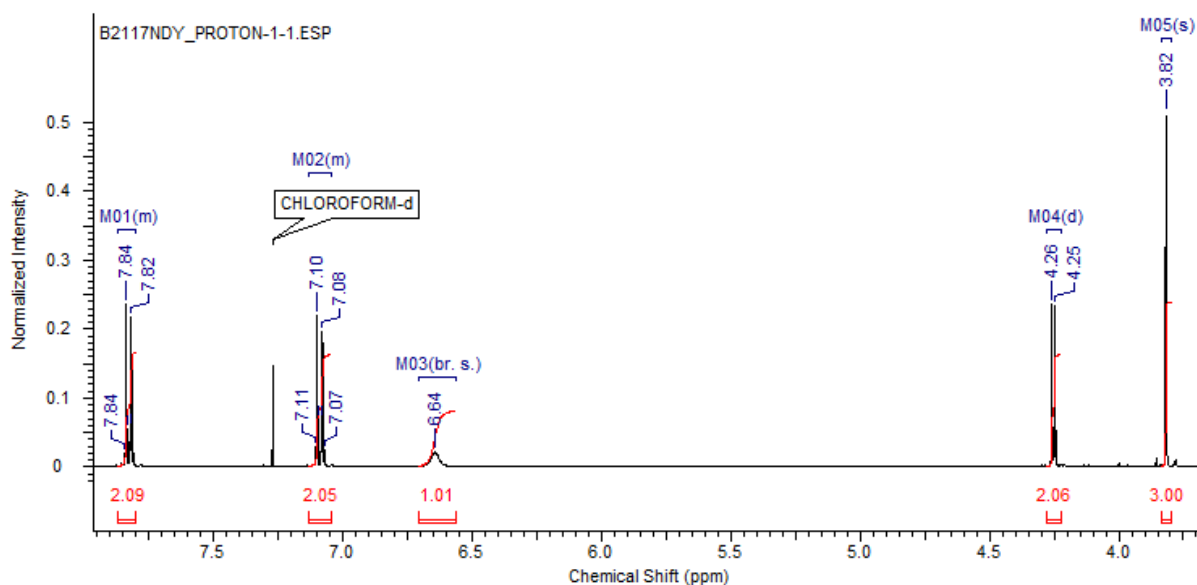
<sup>1</sup>H-NMR (400 MHz, CDCl<sub>3</sub>, **Figure 8.111**): δ<sub>H</sub> 7.83 (m<sup>AA'BB'</sup>, 2H, H-2), 7.09 (m<sup>AA'BB'</sup>, 2H, H-1), 6.65 (br t, *J* = 5.04 Hz, 1H, H-3), 4.25 (d, *J* = 5.04 Hz, 1H, H-4), 3.82 (s, 3H, H-5).

<sup>13</sup>C-NMR (100 MHz, CDCl<sub>3</sub>, **Figure 8.112**): δ<sub>C</sub> 170.51 (C-7), 166.34 (C-5), 143.69 (C-1), 130.02 (C-4), 128.85 (C-3), 119.04 (C-2), 52.54 (C-8), 41.71 (C-6).

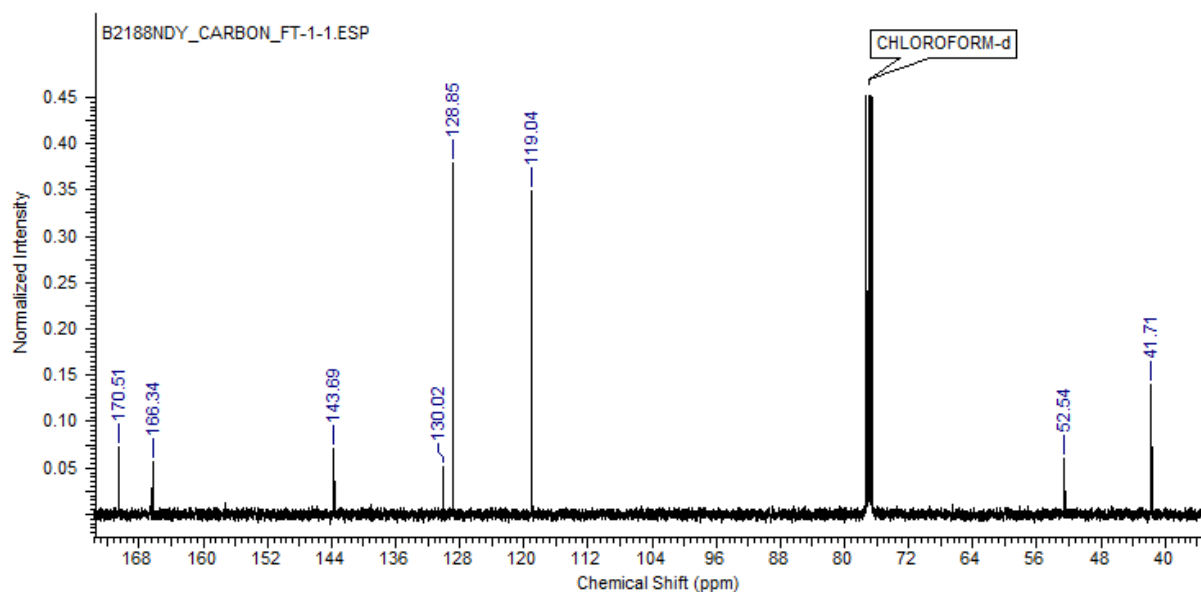
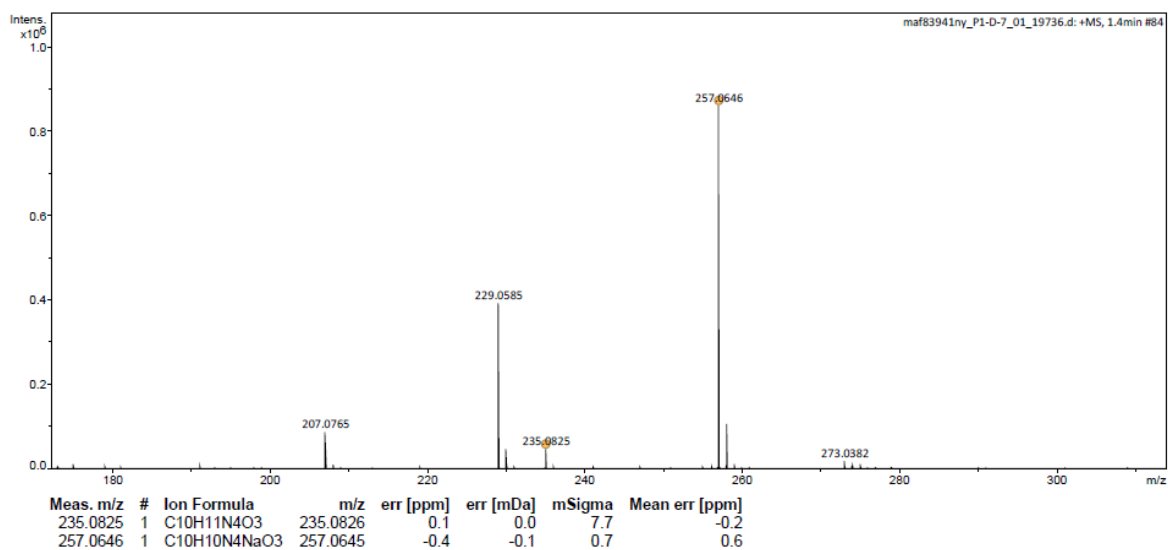
(ESI)HRMS (**Figure 8.113**): Found [M+Na]<sup>+</sup> 257.0646, C<sub>10</sub>H<sub>10</sub>N<sub>4</sub>NaO<sub>3</sub> requires 257.0645.



**Figure 8.110.** The structure of **T10**.



**Figure 8.111.** <sup>1</sup>H-NMR spectrum of **T10**.

Figure 8.112.  $^{13}\text{C}$ -NMR spectrum of **T10**.Figure 8.113. ESI-LC/MS spectrum of **T10**.

### Methyl (E)-4-((1,3-dimesityl-1,3-dihydro-2H-imidazol-2-ylidene)triaz-1-en-1-yl)benzoyl)glycinate (**T11**)

To a solution of **T10** (47.0 mg, 0.200 mmol) and **T1** (68.0 mg, 0.200 mmol) dissolved in the minimum volume of anhydrous DMSO was added potassium *tert*-butoxide (23.0 mg, 0.206 mmol) dissolved in the minimum volume of anhydrous DMSO. The resultant solution was stirred overnight in the dark under  $\text{N}_2$ , after which time DCM was added (30 mL), and the resultant solution was transferred to a separating funnel. DMSO was removed via washing with water ( $3 \times 30$  mL) and the organic extraction

was then washed with brine (30 mL), dried over  $\text{MgSO}_4$  and concentrated *in vacuo*. The crude residue was then purified via flash column chromatography (hexane  $\rightarrow$  ethyl acetate to yield a yellow/orange foamy solid (93 mg, 86%).

$^1\text{H-NMR}$  (400 MHz,  $\text{CDCl}_3$ , **Figure 8.115**):  $\delta_{\text{H}}$  7.48 (m<sup>AA'BB'</sup>, 2H, H-6), 7.00 (s, 4H, H-2), 6.63 (s, 2H, H-4), 6.61-6.56 (m, 3H, H-5, H-7), 4.21 (d,  $J = 5.04$  Hz, 2H, H-8), 3.79 (s, 3H, H-9), 2.37 (s, 6H, H-1), 2.16 (s, 12H, H-3).

$^{13}\text{C-NMR}$  (100 MHz,  $\text{CDCl}_3$ , **Figure 8.116**):  $\delta_{\text{C}}$  170.56 (C-15), 167.32 (C-13), 154.35 (C-8), 151.45 (C-9), 138.83 (C-6), 134.85 (C-4), 133.80 (C-12), 129.69 (C-2), 129.29 (C-3), 127.12 (C-11), 121.06 (C-10), 117.14 (C-7), 52.33 (C-16), 41.61 (C-13), 21.04 (C-5), 17.84 (C-1).

(ESI)HRMS (**Figure 8.117**): Found  $[\text{M}+\text{H}]^+$  539.2765,  $\text{C}_{31}\text{H}_{35}\text{N}_6\text{O}_4$  requires 539.2775.

IR (ATR) (**Figure 8.118**) ( $\nu_{\text{max}}/\text{cm}^{-1}$ ): 3325 (N-H stretch), 2933 (C-H alkyl), 2116 (unknown), 1747 (C=O), 1641 (C=O), 1632 (N-H bend), 1525 (C=C aromatic), 1490 (C=C aromatic), 1360 (C-N stretch), 1149, 852 (C-H bend aromatic).

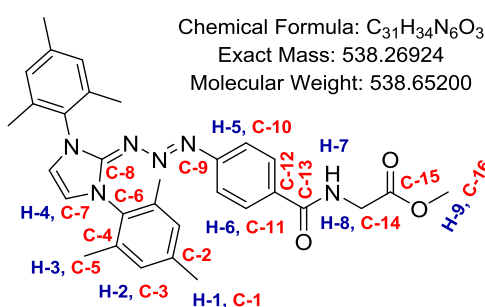


**Figure 8.114.** The structure of T11.

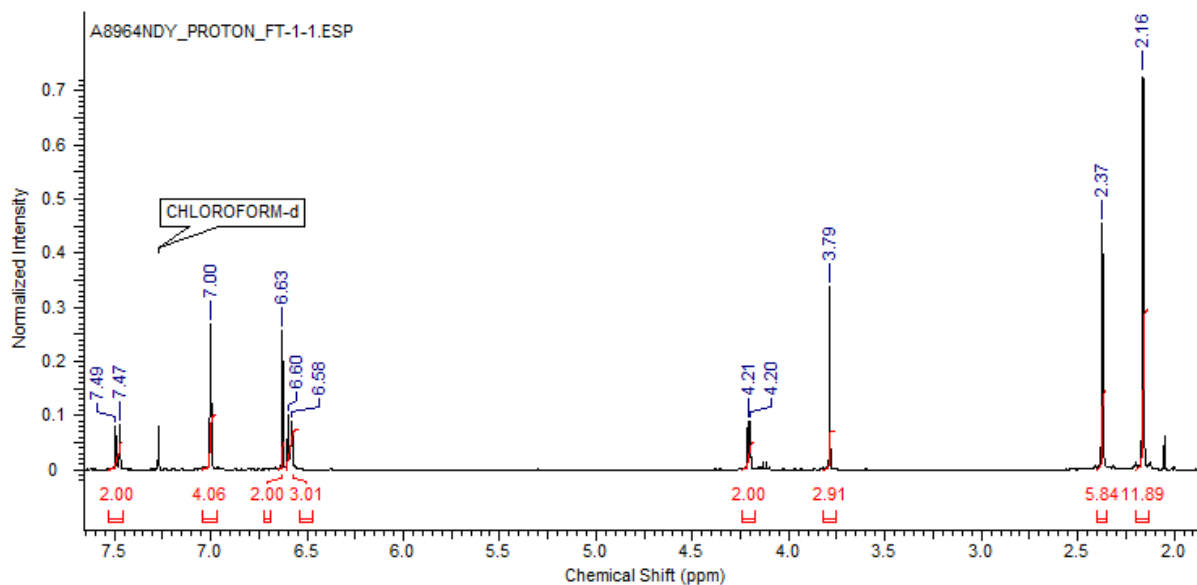


**Figure 8.115.**  $^1\text{H-NMR}$  spectrum of T11.

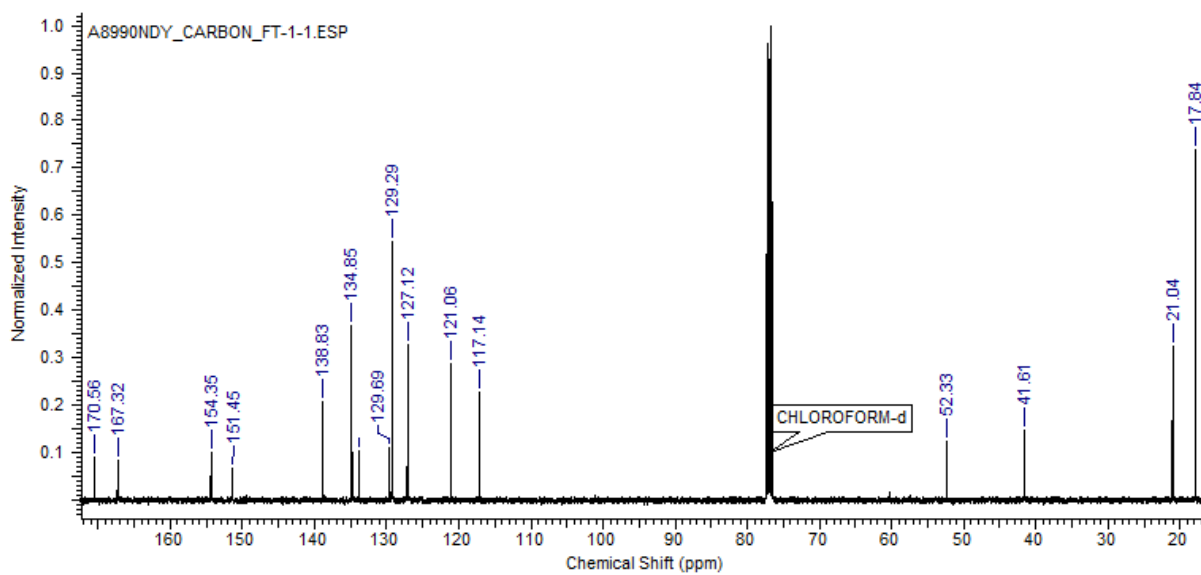
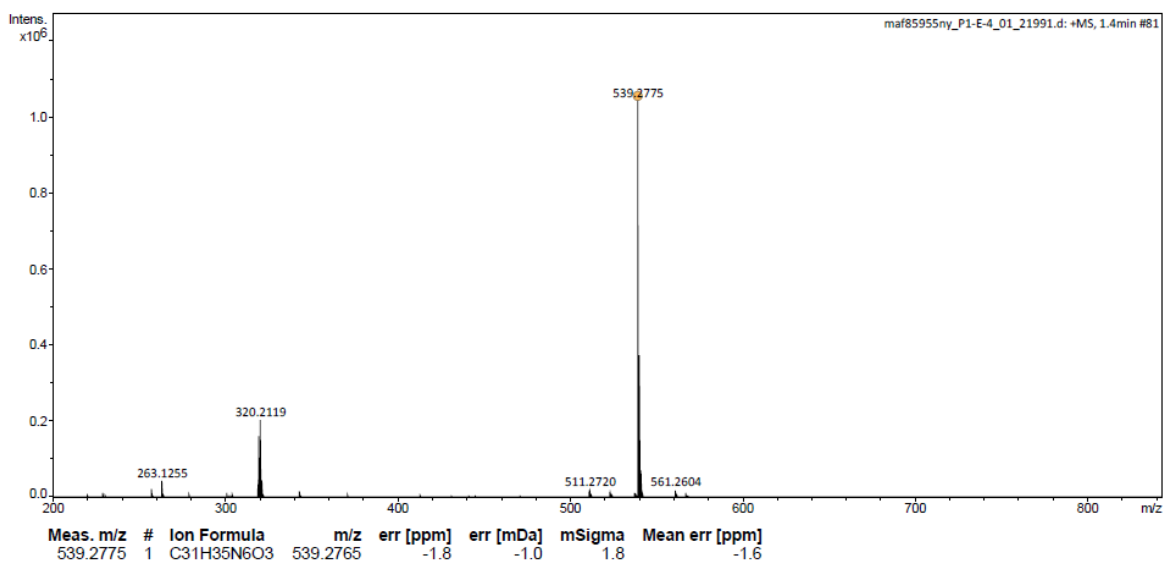
Figure 8.116.  $^{13}\text{C}$ -NMR spectrum of T11.

Figure 8.117. ESI-LC/MS spectrum of T11.



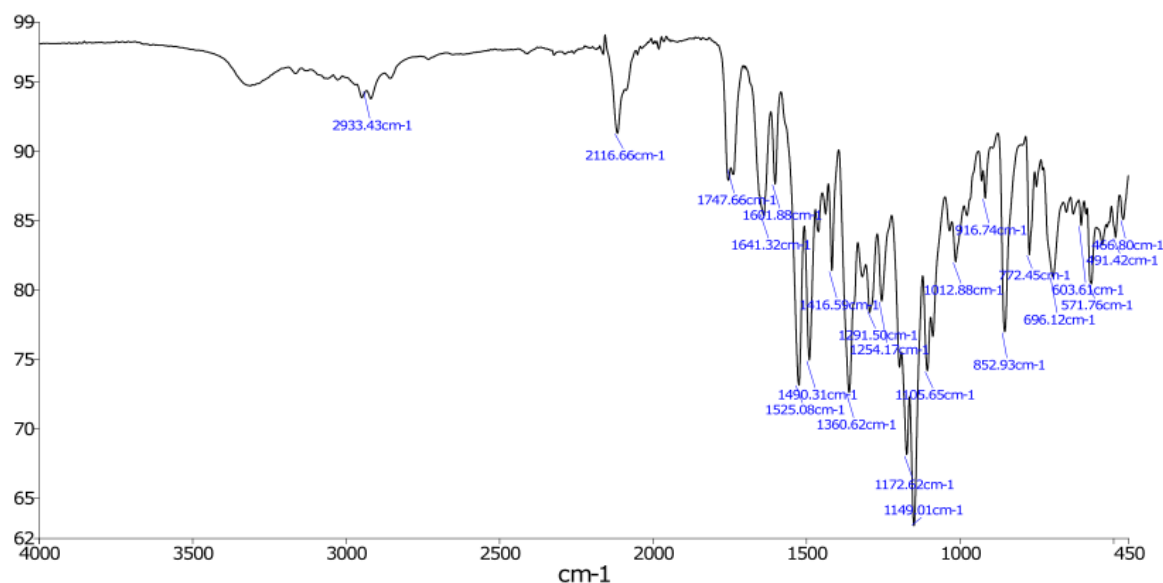


Figure 8.118. IR (ATR) spectrum of **T11**.

**E)-4-((1,3-dimesityl-1,3-dihydro-2H-imidazol-2-ylidene)triaz-1-en-1-yl)benzoyl)glycine (**T12**)**

To a stirred methanolic solution of KOH (0.362 g, 6.46 mmol, in 12 mL MeOH) was added **T11** (0.193 g, 0.358 mmol). The resulting solution was then refluxed at 80 °C until TLC showed the reaction to be complete (20 min). Citric acid (0.413 g, 2.15 mmol), dissolved in the minimum volume of MeOH, was added dropwise, causing the formation of a precipitate. EtOAc (30 mL) was then added, and precipitates were removed via filtration. The filtrate was then concentrated *in vacuo* onto silica, and dry-loaded onto a silica column. Purification via flash column chromatography (DCM → 40% MeOH) yielded a yellow solid (0.110 g, 66%), which was difficult to fully characterise owing to its instability in solution. The product was thus used crude.

<sup>1</sup>H-NMR (400 MHz, CDCl<sub>3</sub>, **Figure 8.120**): δ<sub>H</sub> 7.54-7.44 (m, 2H, H-6), 6.96 (s, 4H, H-2), 6.62 (s, 2H, H-4), 6.59-6.51 (m, 2H, H-5), 3.94 (br s, 2H, H-8), 2.29 (s, 6H, H-1), 2.14 (s, 12H, H-3).

(ESI)HRMS (**Figure 8.121**): Found [M+H]<sup>+</sup> 525.2609, C<sub>30</sub>H<sub>33</sub>N<sub>6</sub>O<sub>3</sub> requires 525.2622.

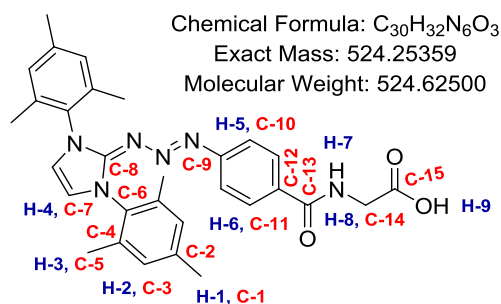


Figure 8.119. The structure of **T12**.

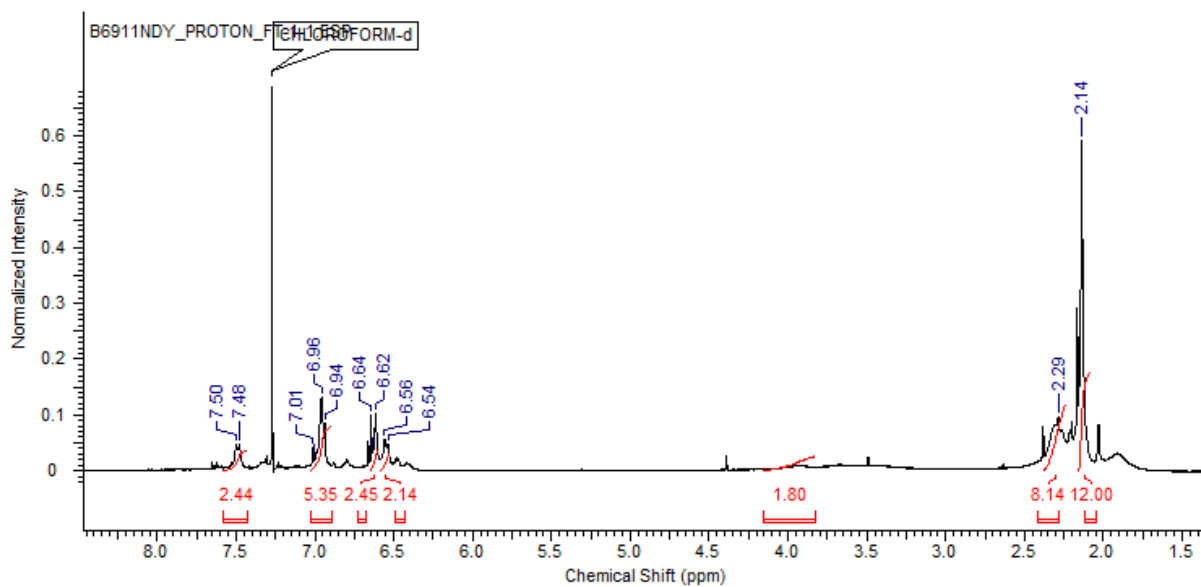
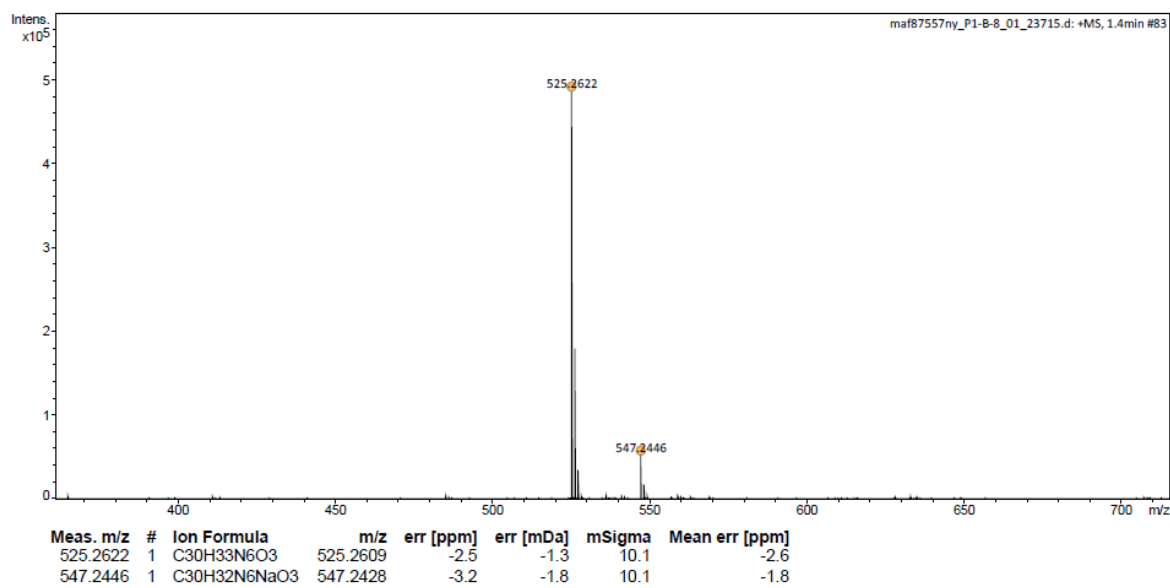
Figure 8.120.  $^1\text{H-NMR}$  spectrum of T12.

Figure 8.121. ESI-LC/MS spectrum of T12.

**2,5-dioxopyrrolidin-1-yl (E)-4-((1,3-dimesityl-1,3-dihydro-2H-imidazol-2-ylidene)triaz-1-en-1-yl)benzoyl)glycinate (T13)**

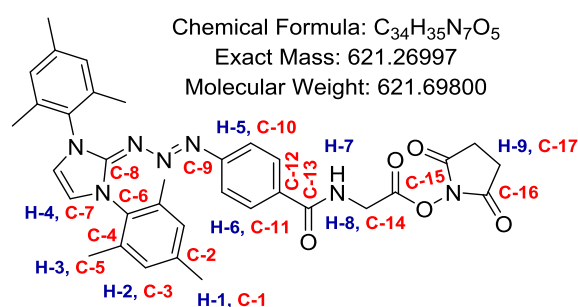
To a stirred solution of **T12** (0.103 g, 0.197 mmol), in DCM (5 mL) was added *N*-hydroxysuccinimide (23 mg, 0.217 mmol). *N,N'*-dicyclohexylcarbodiimide (40.0 mg, 0.194 mmol) was then added, and the resultant solution was stirred in the dark overnight at room temperature. The reaction solution was then filtered through a plug of cotton wool inside a Pasteur pipette to remove DCU urea, before being further allowed to concentrate under a stream of N<sub>2</sub>. The resultant solution was then diluted with MeCN, and allowed to sit at -20 °C for 2 hours. Precipitated DCU was again removed by filtering through a plug of cotton wool inside a Pasteur pipette. The resultant filtrate was then concentrated *in vacuo* to yield **T13** as a deep orange solid that was used without further purification (0.102 g, 0.164 mmol, 83% (crude)).

**<sup>1</sup>H-NMR** (400 MHz, CDCl<sub>3</sub>, **Figure 8.123**): δ<sub>H</sub> 7.48 (m<sup>AA'BB'</sup>, 2H, H-6), 7.00 (s, 4H, H-2), 6.64 (s, 2H, H-4), 6.62-6.56 (m, 3H, H-5,7), 4.57 (d, *J* = 5.50 Hz, 2.85 (m, 4H, H-9), 2.37 (s, 6H, H-1), 2.15 (s, 12H, H-3).

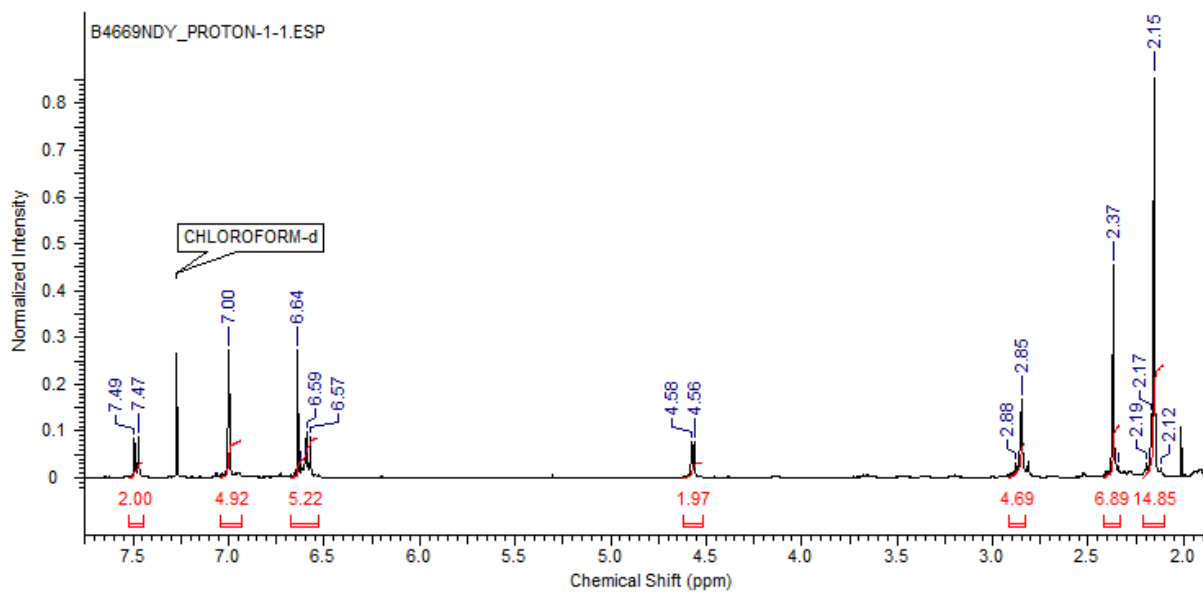
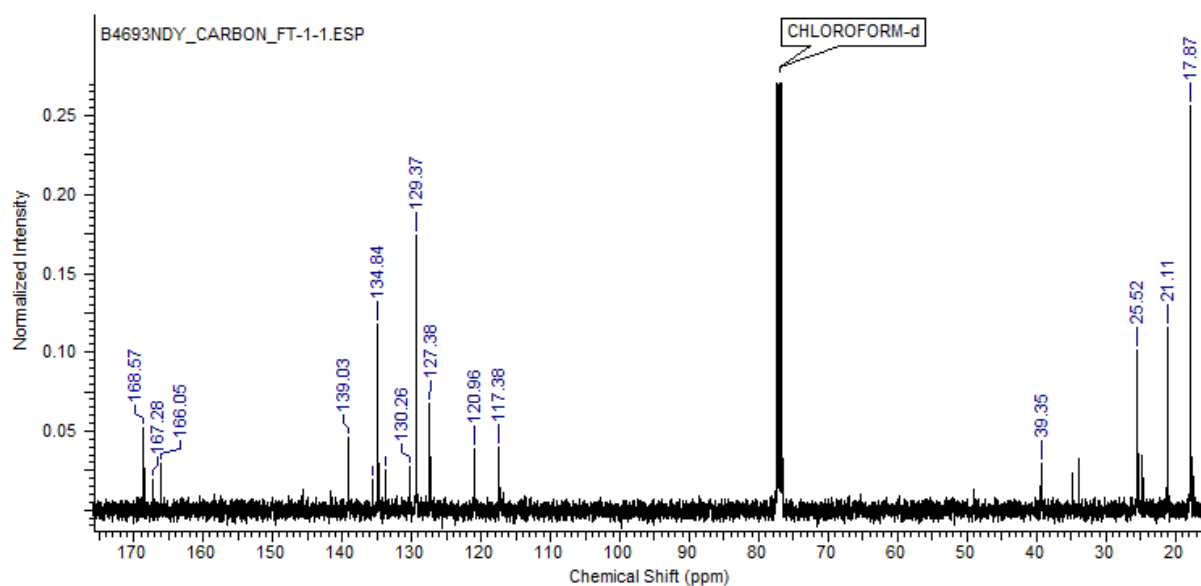
**<sup>13</sup>C-NMR** (100 MHz, CDCl<sub>3</sub>, **Figure 8.124**): δ<sub>C</sub> 169.57 (C-16), 167.28 (C-14), 166.05 (C-13), 139.03 (C-6), 135.67, 134.84 (C-4), 133.69 (C-12) 130.26, 129.37 (C-3), 127.38 (C-11), 120.96 (C-10), 117.38 (C-7), 39.35 (C-14), 25.52 (C-17), 21.11 (C-1), 17.87 (C-5).

**(ESI)HRMS** (**Figure 8.125**): Found [M+H]<sup>+</sup> 622.2779, C<sub>34</sub>H<sub>36</sub>N<sub>7</sub>O<sub>5</sub> requires 622.2772.

**IR (ATR)** (**Figure 8.126**) (ν<sub>max</sub>/cm<sup>-1</sup>): 2929 (C-H stretch, alkyl), 2115 (unknown), 1737 (C=O stretching), 1525 (C-C stretch, aromatic), 1361 (C-N stretching), 1149 (C-N stretching), 855 (C-H bend, aromatic).



**Figure 8.122.** The structure of **T13**.

Figure 8.123. <sup>1</sup>H-NMR spectrum of T13.Figure 8.124. <sup>13</sup>C-NMR spectrum of T13.

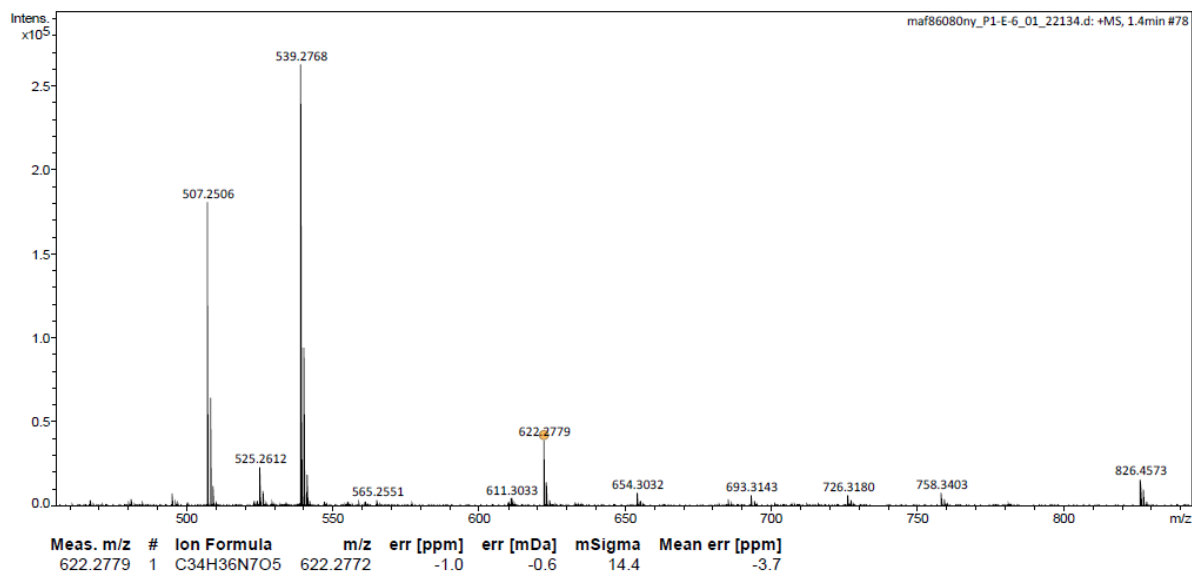


Figure 8.125. ESI-LC/MS spectrum of T13.

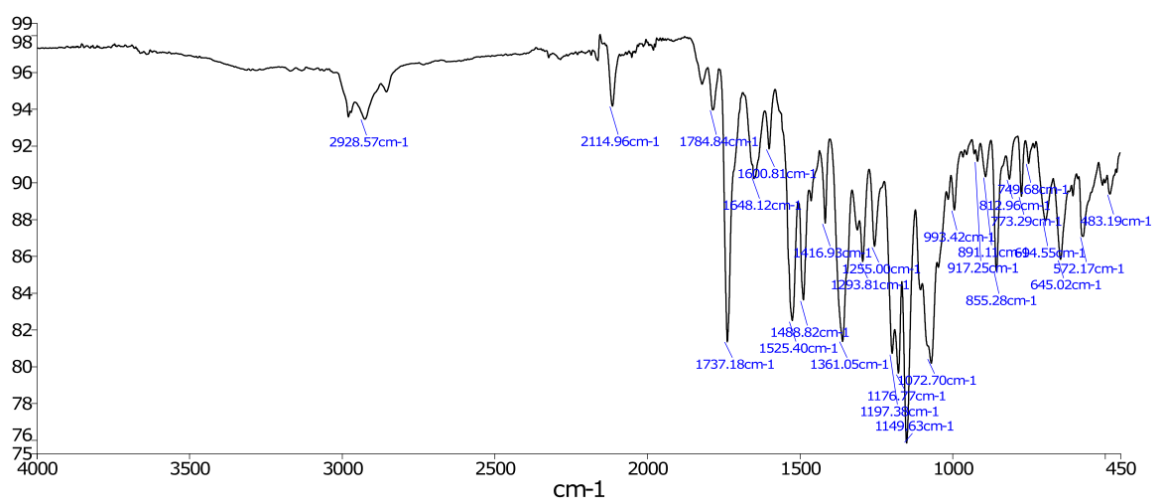


Figure 8.126. IR (ATR) spectrum of T13.

**Sodium (E)-1-((4-((1,3-dimesityl-1,3-dihydro-2H-imidazol-2-ylidene)triaz-1-en-1-yl)benzoyl)oxy)-2,5-dioxopyrrolidine-3-sulfonate (T14)**

To a stirred solution of **T14** (51.8 mg, 0.111 mmol) in anhydrous DMF (1.1 mL) was added *N*-hydroxysulfosuccinimide sodium salt (24.1 mg, 0.111 mmol). *N,N'*-dicyclohexylcarbodiimide (37.6 mg, 0.183 mmol) was then added, and the resultant solution was stirred in the dark overnight at room temperature. The reaction solution was then cooled to 4 °C and filtered through a plug of cotton wool inside a Pasteur pipette (to remove DCU urea), into diethyl ether (17 mL), whereupon a mixture of **T14** and *N*-hydroxysulfosuccinimide sodium salt precipitated. The precipitate was pelleted by centrifugation and the supernatant removed. The precipitate was then resuspended in diethyl ether (30 mL) before once again being pelleted by centrifugation and isolated from the supernatant. This re-suspension/centrifugation step was repeated thrice. The isolated precipitate was dried *in vacuo* in darkness, yielding a crude sample of **T14** + *N*-hydroxysulfosuccinimide sodium salt (33.6 mg), which was found to be 66% **T14** by mass (via the comparison of the extinction coefficients of samples of **T14** with that of **T5** in DMSO). As such, the above synthesis yielded 22.1 mg of **T14** (31%). Further purification was not deemed practical.

**<sup>1</sup>H-NMR** (400 MHz, DMSO-*d*<sub>6</sub>, **Figure 8.128**): δ<sub>H</sub> 7.68 (m<sup>AA'BB'</sup>, 2H, H-6), 7.38 (s, 2H, H-4), 7.13 (s, 4H, H-2), 6.46 (m<sup>AA'BB'</sup>, 2H, H-5), 4.06-3.94 (m, 1H, H-7), 3.24-3.15 (m, 1H, H-8), 2.94-2.87 (m, 1H, H-9), 2.35 (s, 6H, H-1), 2.07 (s, 12H, H-3).

**(ESI)HRMS** (**Figure 8.129**): Found [M-Na]<sup>-</sup> 643.1977, C<sub>32</sub>H<sub>31</sub>N<sub>6</sub>O<sub>7</sub>S requires 643.1980.

**IR (ATR)** (**Figure 8.130**) (u<sub>max</sub>/cm<sup>-1</sup>): 2973 (C-H stretch, alkyl), 1739 (C=O stretching), 1708 (C=O stretching), 1601 (C-C stretch, aromatic), 1358 (S=O stretch, sulfonate), 1192 (S=O stretch, sulfonate), 854 (C-H bend, aromatic), 779 (C-H bend, aromatic).

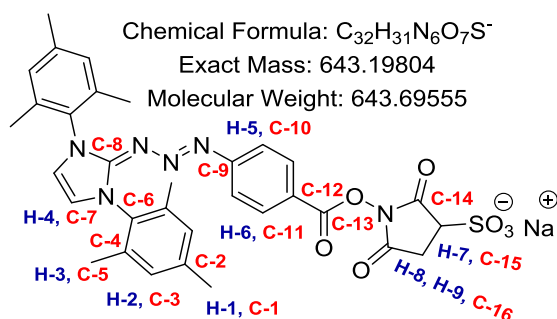


**Figure 8.127.** The structure of **T14**.

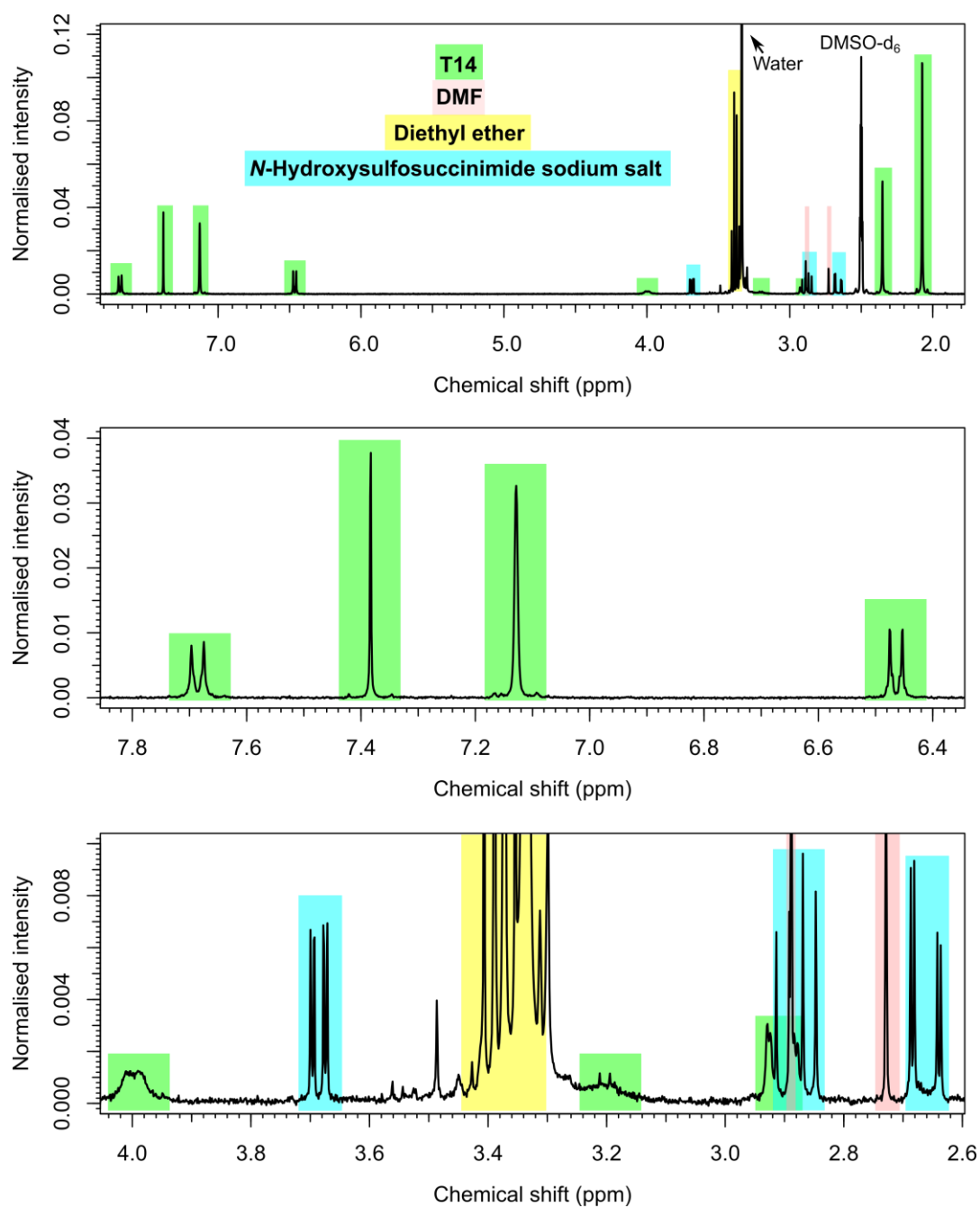


Figure 8.128.  $^1\text{H-NMR}$  spectrum of a crude sample of T14.

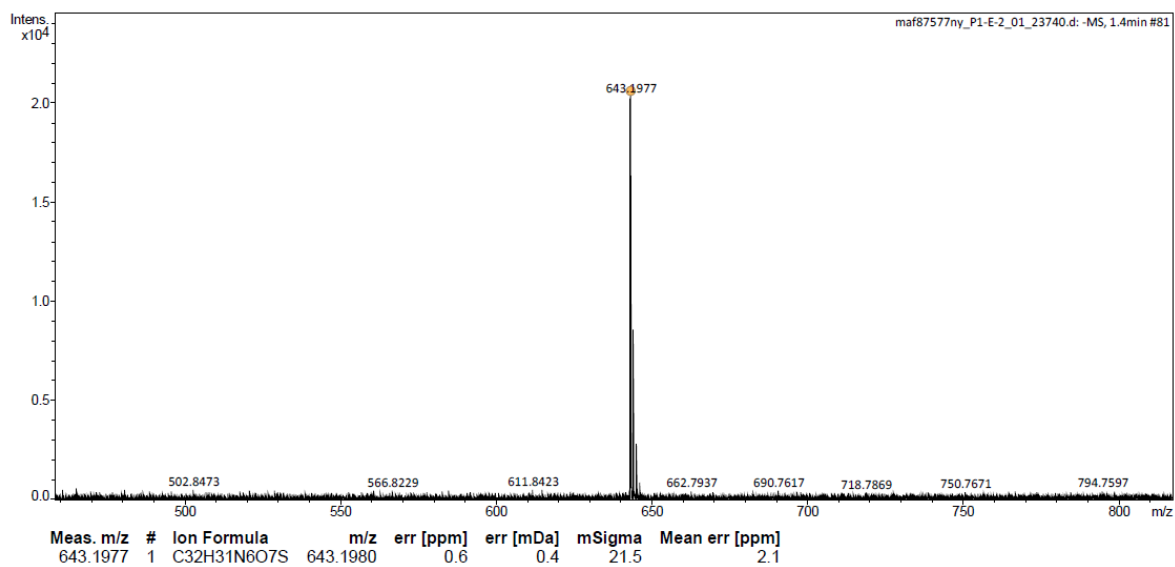


Figure 8.129. ESI-LC/MS spectrum of T14.

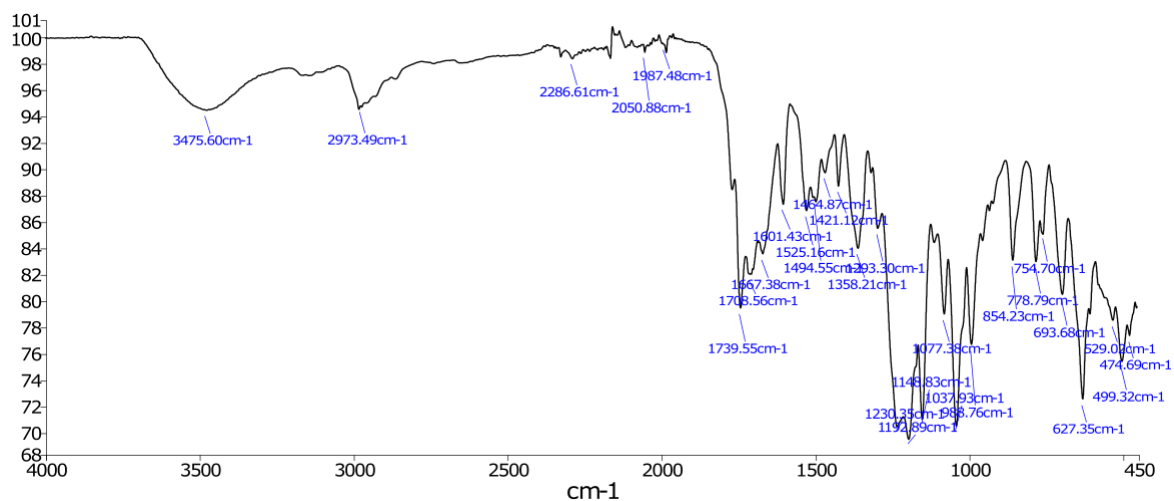


Figure 8.130. IR (ATR) spectrum of a crude sample of T14.



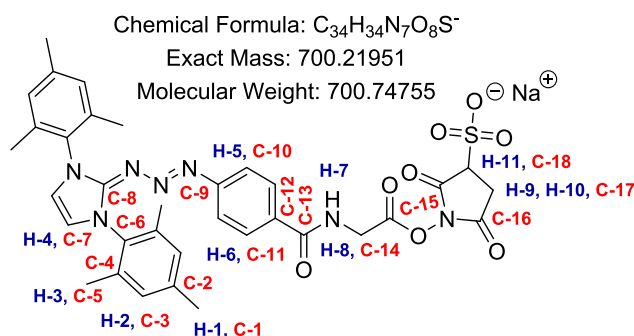
**Sodium (E)-1-(((4-((1,3-dimesityl-1,3-dihydro-2H-imidazol-2-ylidene)triaz-1-en-1-yl)benzoyl)glycyl)oxy)-2,5-dioxopyrrolidine-3-sulfonate (T15)**

To a stirred solution of **T12** (0.100 g, 0.191 mmol) in anhydrous DMF (2 mL) was added *N*-hydroxysulfosuccinimide sodium salt (45.5 mg, 0.191 mmol). *N,N'*-dicyclohexylcarbodiimide (65.0 mg, 0.316 mmol) was then added, and the resultant solution was stirred in the dark overnight at room temperature. The reaction solution was then cooled to 4 °C and filtered through a plug of cotton wool inside a Pasteur pipette (to remove DCU urea), into diethyl ether (25 mL), whereupon a mixture of **T15** and *N*-hydroxysulfosuccinimide sodium salt precipitated. The precipitate was pelleted by centrifugation and the supernatant removed. The precipitate was then resuspended in diethyl ether (30 mL) before once again being pelleted by centrifugation and isolated from the supernatant. This re-suspension/centrifugation step was repeated thrice. The isolated precipitate was dried *in vacuo* in darkness, yielding a crude sample of **T14** + *N*-hydroxysulfosuccinimide sodium salt (85.0 mg), which was found to be 86% **T14** by mass (via the comparison of the extinction coefficients of samples of **T15** with that of **T13** in DMSO). As such, the above synthesis yielded 73.1 mg of **T15** (53%). Further purification was not deemed practical, and characterisation was complicated by the degradation of **T15** NMR samples (presumably as a consequence of its photosensitivity). The NMR data reported below is proposed based on the the crude spectrum (**Figure 8.132**).

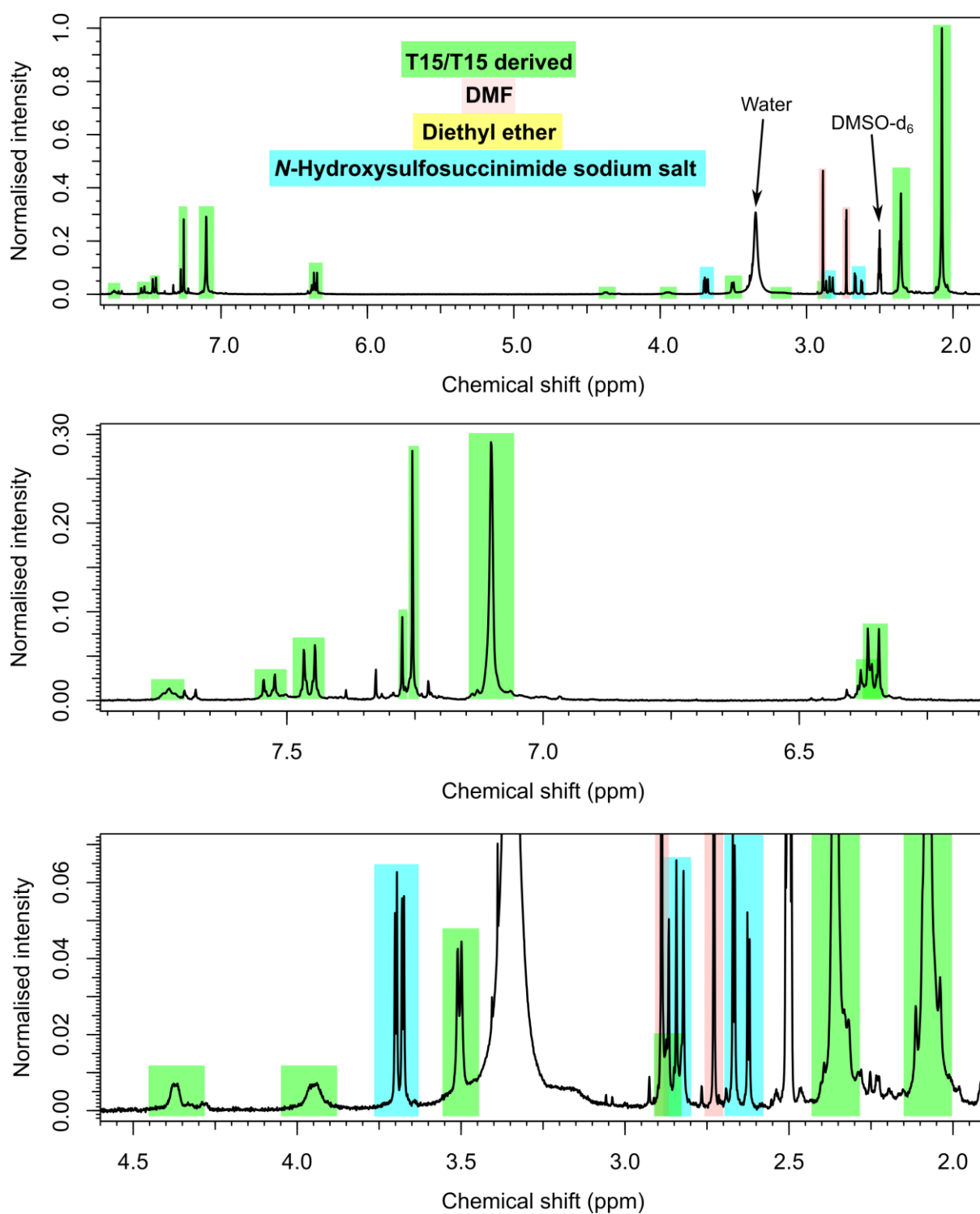
**<sup>1</sup>H-NMR** (400 MHz, DMSO-*d*<sub>6</sub>, **Figure 8.132**): δ<sub>H</sub> 7.63, (br t, *J* = 4.48 Hz, H-7), 7.46 (m<sup>AA'BB'</sup>, 2H, H-6), 7.26 (s, 2H, H-4), 7.10 (s, 4H, H-2), 6.35 (m<sup>AA'BB'</sup>, 2H, H-5), 3.99-3.90 (m, 1H, H-11), 3.50 (d, *J* = 4.48 Hz, H-8), 3.24-3.11 (m, 1H, H-10), 2.90-2.84 (m, 1H, H-9), 2.36 (s, 6H, H-1), 2.08 (s, 12H, H-3).

**(ESI)HRMS** (**Figure 8.133**): Found [M+H]<sup>+</sup> 724.2167, C<sub>34</sub>H<sub>35</sub>N<sub>7</sub>NaO<sub>8</sub>S requires 724.2160.

**IR (ATR)** (**Figure 8.134**) (u<sub>max</sub>/cm<sup>-1</sup>): 2958 (C-H stretch, alkyl), 1740 (C=O stretching), 1649 (C=O stretching), 1602 (C-C stretch, aromatic), 1365 (S=O stretch, sulfonate), 1196 (S=O stretch, sulfonate), 856 (C-H bend, aromatic), 774 (C-H bend, aromatic).



**Figure 8.131.** The structure of **T15**.

Figure 8.132.  $^1\text{H-NMR}$  spectrum of a crude sample of T15.

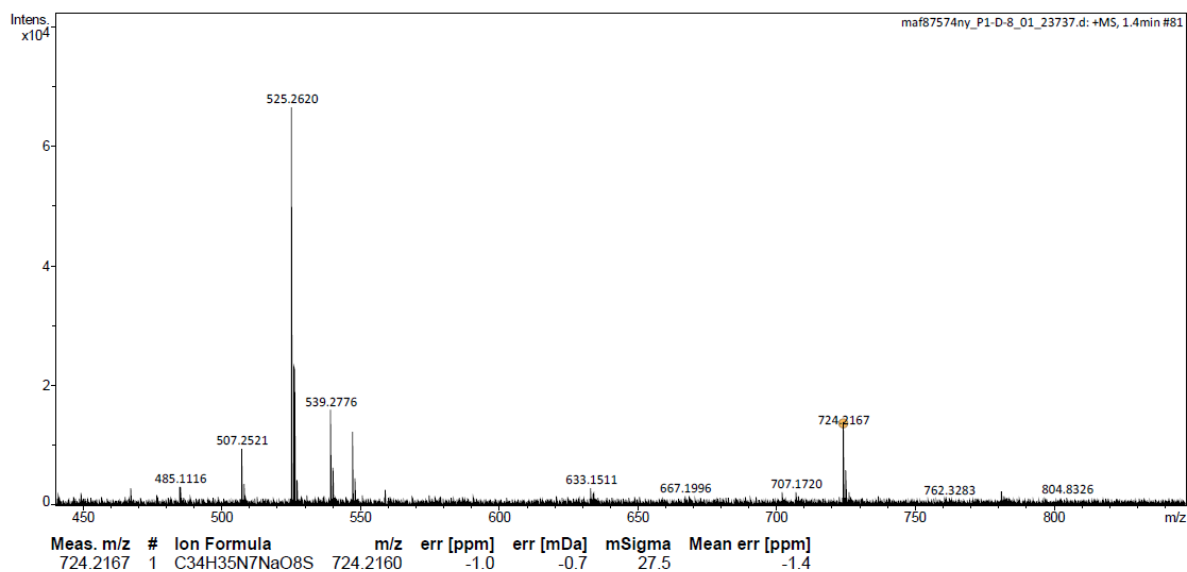


Figure 8.133. ESI-LC/MS spectrum of T15.

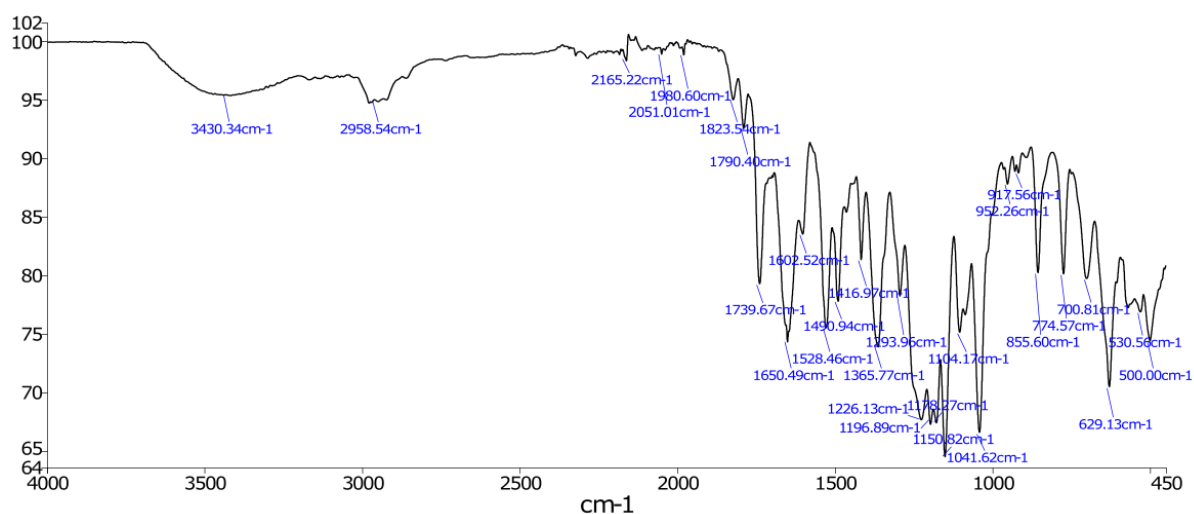


Figure 8.134. IR (ATR) spectrum of a crude sample of T15.

**1-mesityl-1H-imidazole (T16)**

This synthesis was adapted from refs [572,573].

A stirred solution of 37% aqueous glyoxal (4.6 mL) and 37% aqueous formaldehyde (3 mL) in glacial acetic acid (10 mL) was heated to 70 °C whereupon a solution of 2,4,6-trimethylaniline (5.39 g, 40.0 mmol), water (2 mL), and ammonium acetate (3.08 g, 40.0 mmol) in glacial acetic acid (10 mL) was added dropwise. The resultant solution was stirred at 70 °C for 18 hours, after which time the solution was cooled to room temperature and added to a solution of NaHCO<sub>3</sub> (29.4 g) in water (300 mL). The product was then removed by filtration, dried *in vacuo* and purified by flash column chromatography (20:1 DCM:methanol) to yield **T16** as a light brown microcrystalline solid (2.88 g, 39%).

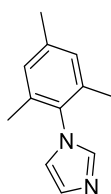


Figure 8.135. The structure of **T16**.

**3-(1-mesityl-1H-imidazol-3-ium-3-yl)propane-1-sulfonate (T17)**

To a stirred solution of **T16** (1.00 g, 5.37 mmol) in dry toluene (30 mL) was added 1,3-propanesultone (1.00 g, 8.19 mmol, 1.52 equiv). The resultant solution was refluxed overnight after which time the solution was allowed to cool to room temperature. The product was then collected by filtration and washed with diethyl ether before being dried *in vacuo*. This yielded **T17** as a light grey powder (1.62 g, 98%). <sup>1</sup>H-NMR was in agreement with that of the literature.<sup>574,575</sup>

<sup>1</sup>H-NMR (400 MHz, D<sub>2</sub>O, **Figure 8.137**): δ<sub>H</sub> 8.94 (m, 1H), 7.75 (m, 1H), 7.52 (m, 1H), 7.08 (s, 2H), 4.45 (t, *J* = 7.33 Hz, 2H), 2.89 (t, *J* = 7.79 Hz, 2H), 2.36 (tt, *J* = 7.79, 7.33 Hz), 2.27 (s, 3H), 1.97 (s, 6H).

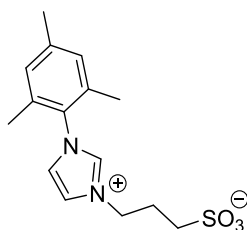


Figure 8.136. The structure of **T17**.

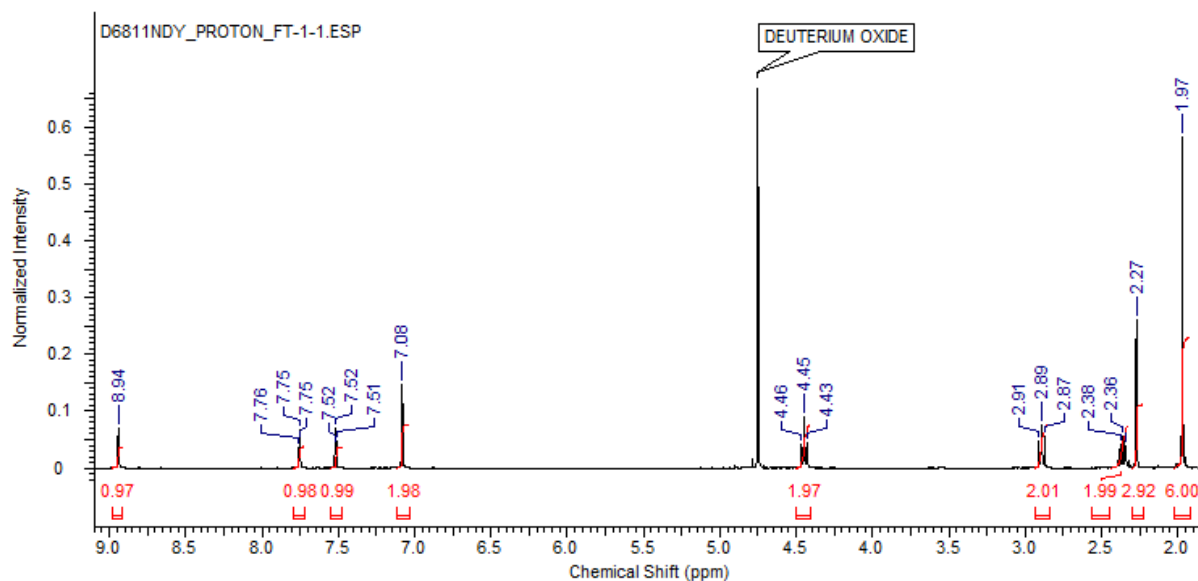


Figure 8.137.  $^1\text{H-NMR}$  spectrum of **T17**.

**Tetrabutylammonium 3-((Z)-3-mesityl-2-((E)-(4-(methoxycarbonyl)phenyl)triaz-2-en-1-ylidene)-2,3-dihydro-1H-imidazol-1-yl)propane-1-sulfonate (T18)**

To a mixture of **T17** (0.569 g, 1.8 mmol) and methyl **T2** (0.325 g, 1.8 mmol) under nitrogen was added 20 mL of anhydrous DMSO, followed by potassium tert-butoxide (0.252 g, 2.2 mmol). The resultant solution was stirred at room temperature overnight, under nitrogen and in the dark. To the resultant solution, tetrabutyl ammonium bromide (0.590 g, 1.8 mmol) was added. The solution was stirred for 5 minutes, then DCM (200 mL) was added. The resultant solution was transferred to a separating funnel and was washed with water (3  $\times$  100 mL). The organic layer was dried over  $\text{MgSO}_4$  and the filtrate concentrated *in vacuo* to yield **T18** as an orange foam (0.810 g, 62%).

$^1\text{H-NMR}$  (400 MHz,  $\text{CDCl}_3$ , **Figure 8.139**):  $\delta_{\text{H}}$  7.72-7.66 (m<sup>AA'BB'</sup>, 2H, H-10), 7.19 (d,  $J = 3.05$  Hz, 1H, H-4/5), 6.96 (s, 2H, H-2), 6.63-6.57 (m<sup>AA'BB'</sup>, 2H, H-9), 6.32 (d,  $J = 3.05$  Hz, 1H, H-4/5), 4.38 (t,  $J = 6.87$  Hz, 2H, H-6), 3.84 (s, 3H, H-11), 3.33-3.23 (m, 8H, H-12), 2.86 (t,  $J = 6.87$  Hz, 2H, H-8), 2.44-2.34 (m, 5H, H-1, H-7), 1.98 (s, 6H, H-3), 1.70-1.58 (m, 8H, H-13), 1.43 (qt,  $J = 7.63, 7.63$  Hz, 8H, H-14), 0.99 (t,  $J = 7.63$  Hz, 12H, H-15).

$^{13}\text{C-NMR}$  (100 MHz,  $\text{CDCl}_3$ , **Figure 8.140**):  $\delta_{\text{C}}$  167.19 (C-17), 155.52, 150.74, 138.25, 135.64, 134.20, 129.72 (C-3), 129.11 (C-15), 125.70, 120.51 (C-14), 117.60 (C-7/8), 116.27 (C-7/8), 56.68 (C-19), 51.67 (C-18), 47.33 (C-11), 44.41 (C-9), 40.86 (C-10), 23.89 (C-20), 20.98 (C-1), 19.62 (C-21), 17.78 (C-5), 13.58 (C-22).

(ESI)HRMS (**Figure 8.141**): Found  $[\text{M}+\text{Na}+\text{H}]^+$  508.1606,  $\text{C}_{23}\text{H}_{27}\text{N}_5\text{NaO}_5\text{S}$  requires 508.1625.

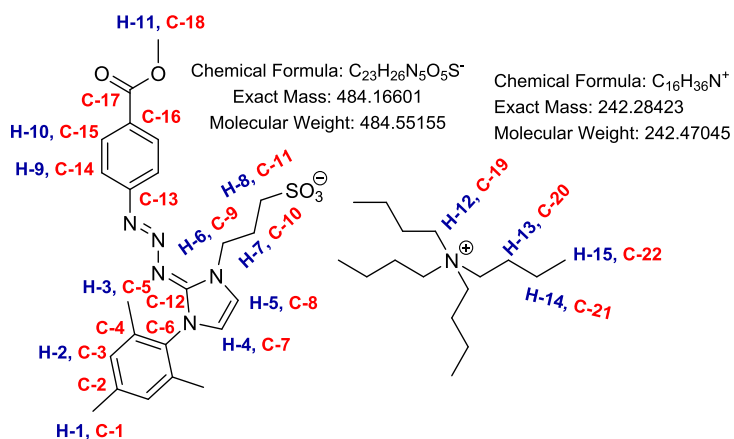
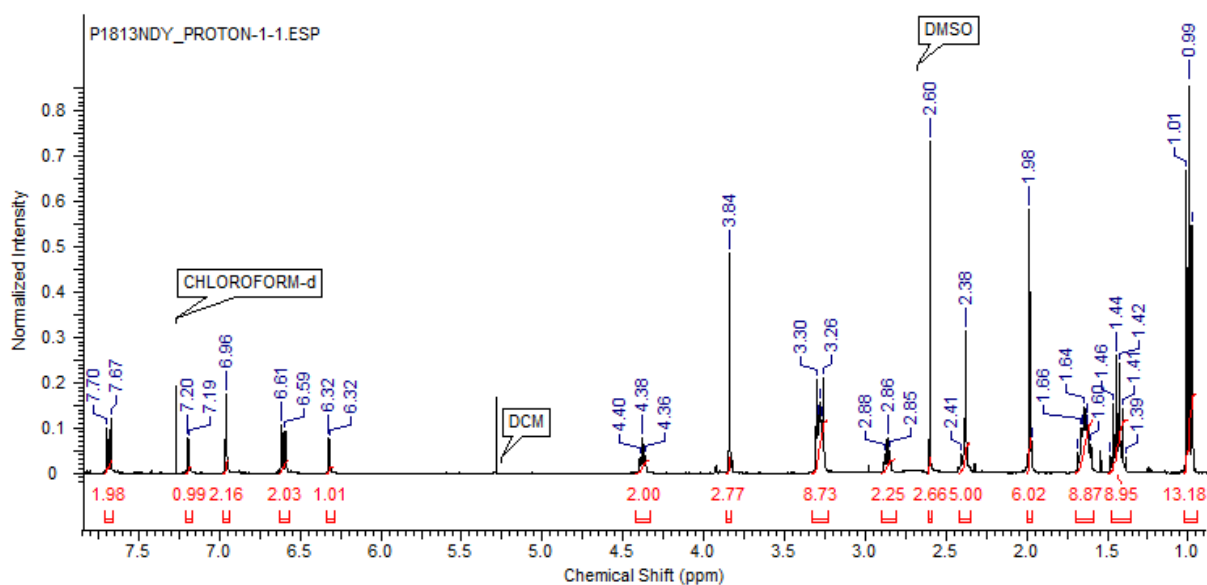
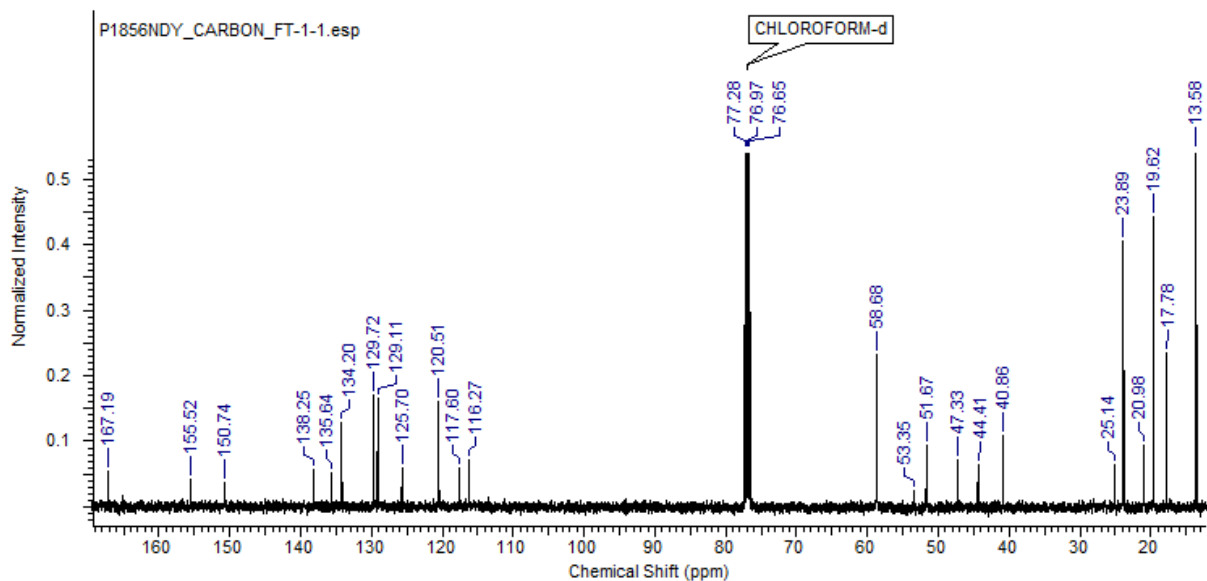


Figure 8.138. The structure of T18.

Figure 8.139.  $^1H$ -NMR spectrum of T18.Figure 8.140.  $^{13}C$ -NMR spectrum of T18.

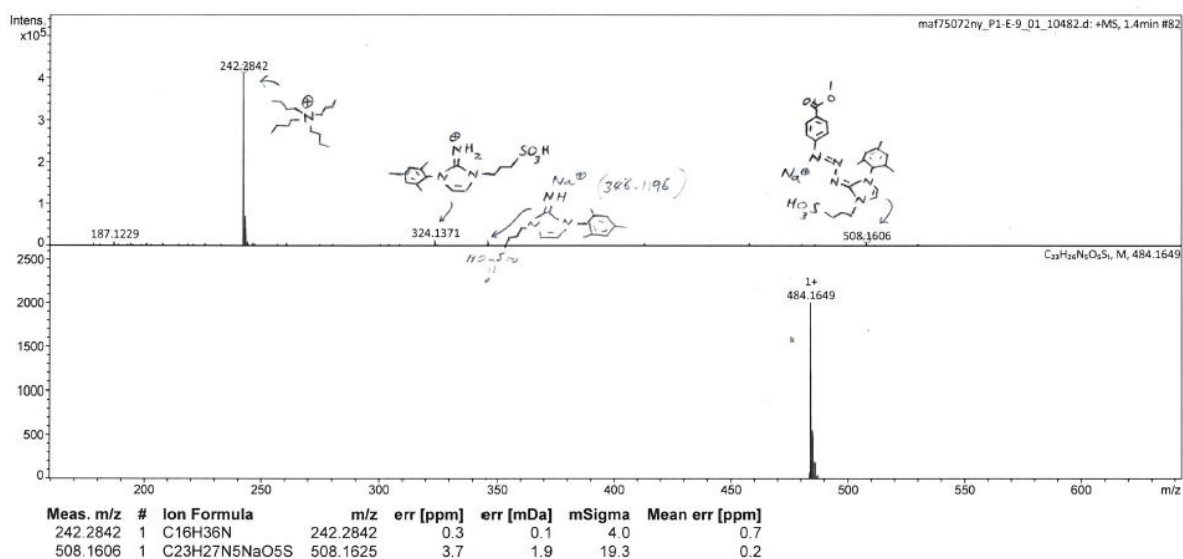


Figure 8.141. ESI-LC/MS spectrum of T18.

#### Sodium 4-((E)-((E)-1-mesityl-3-(3-sulfonatopropyl)-1,3-dihydro-2H-imidazol-2-ylidene)triaz-1-en-1-yl)benzoate (T19)

To a stirred methanolic solution of methyl of T18 (0.202 g, 0.280 mmol in 2.5 mL DCM) was added 0.280 mL of a 3 N methanolic solution of NaOH (0.84 mmol). The resulting solution was gently agitated (using a rotating peptide synthesiser) at room temperature in the dark overnight, whereupon crude T19 precipitated as an orange solid (0.130 g, 90%). Note that NaOH is likely to have co-precipitated with T19.

<sup>1</sup>H-NMR (400 MHz, methanol-d<sub>4</sub>, Figure 8.143): δ<sub>H</sub> 7.68 (m<sup>AA'BB'</sup>, 2H, H-10), 7.19 (d, *J* = 2.29 Hz, 1H, H-4/5), 7.06 (s, 2H, H-2), 6.72 (d, *J* = 2.29 Hz, 1H, H-4/5), 6.50 (m<sup>AA'BB'</sup>, 2H, H-9), 4.27 (t, *J* = 6.87 Hz, 2H, H-6), 2.91 (t, *J* = 6.87 Hz, 2H, H-8), 2.42 (s, 3H, H-1), 2.34 (tt, *J* = 6.87, 6.87 Hz, 2H, H-7), 2.03 (s, 6H, H-3).

(ESI)HRMS (Figure 8.144): Found [M+H]<sup>-</sup> 508.1606, C<sub>23</sub>H<sub>27</sub>N<sub>5</sub>NaO<sub>5</sub>S requires 508.1625.

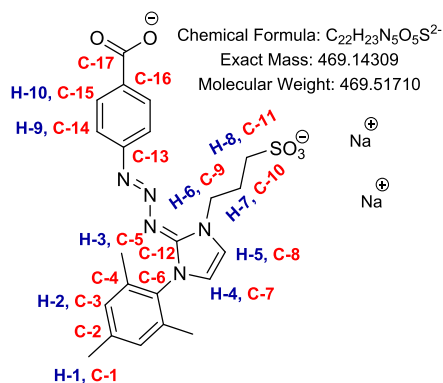


Figure 8.142. The structure of T19.

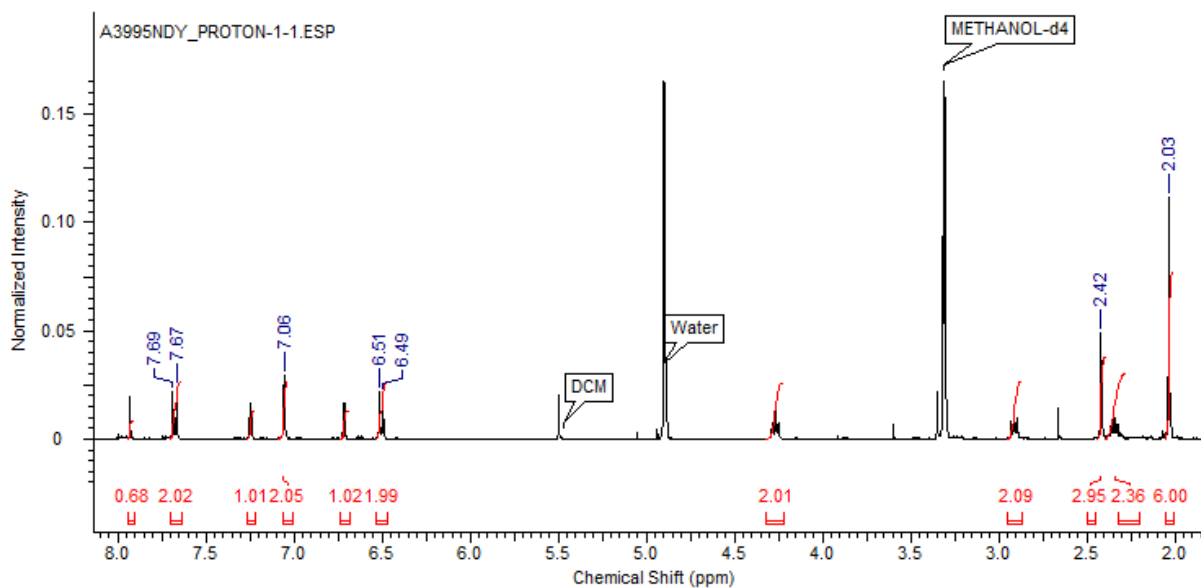
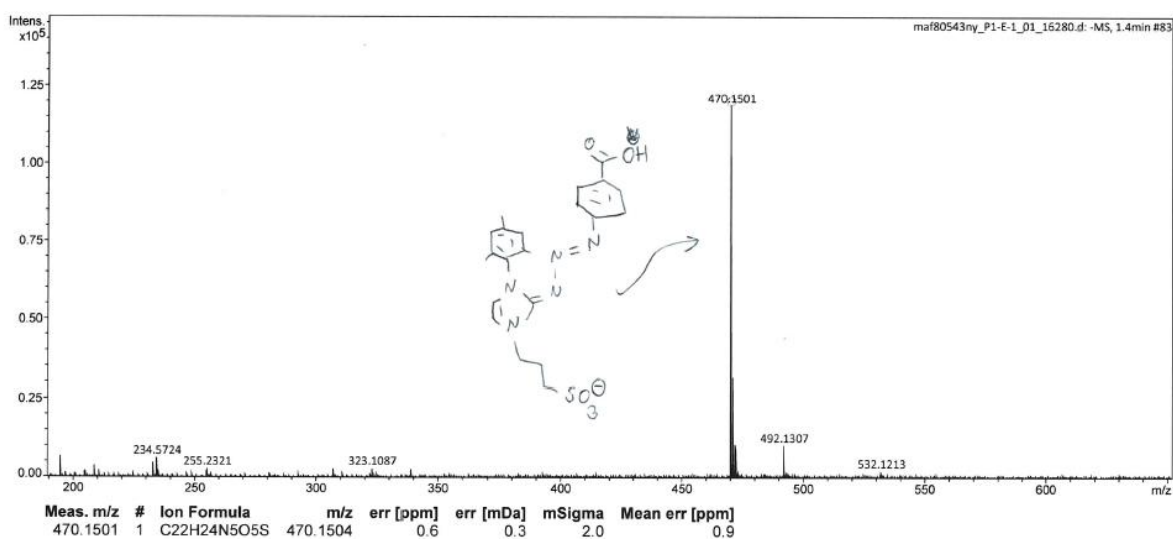
Figure 8.143.  $^1\text{H}$ -NMR spectrum of T19.

Figure 8.144. ESI-LC/MS spectrum of T19.



**4-Azidophthalimide (T20)**

This method is a adaption of a literature procedure.<sup>576</sup>

To a stirred solution of 4-aminophthalimide (0.810 g, 5.00 mmol) in concentrated HCl (7 mL) was added water (20 mL) (**CAUTION:** adding concentrated acid to water is highly exothermic). A solution of NaNO<sub>2</sub> (0.379 g, 5.50 mmol) in water (1.5 mL) was then added dropwise at 0 °C. The mixture was then stirred for 30 min, after which time a solution of NaN<sub>3</sub> (0.357 g, 5.50 mmol) in water (2 mL) was added dropwise at 0 °C, and the resultant mixture stirred for 30 min, whereupon **T20** precipitated. **T20** was isolated via filtration (using a sinter funnel), and washed successively with water (5 mL), concentrated HCl (10 mL), and water (10 mL), and recrystallised from hot ethanol, yielding 0.58 g of crude **T20** (<63%).

**<sup>1</sup>H-NMR** (400 MHz, CDCl<sub>3</sub>, **Figure 8.146**): δ<sub>H</sub> 8.12 (s, 1H, H-4), 6.84 (d, *J* = 9.16 Hz, 1H, H-3), 6.77 (dd, *J* = 9.16, 2.75 Hz, H1, H-2), 6.62 (d, *J* = 2.75 Hz, H1, H-1).

**(ESI)HRMS** (**Figure 8.147**): Found [M+Na]<sup>+</sup> 211.0231, C<sub>8</sub>H<sub>4</sub>N<sub>4</sub>NaO<sub>2</sub> requires 211.0226.

**IR (ATR)** (**Figure 8.148**) (ν<sub>max</sub>/cm<sup>-1</sup>): 3211 (N-H stretch, imide), 2127 (N=N=N stretch, azide), 1749 (C=O stretching), 1709 (C=O stretching), 892 (C-H bend, aromatic), 743 (C-H bend, aromatic).

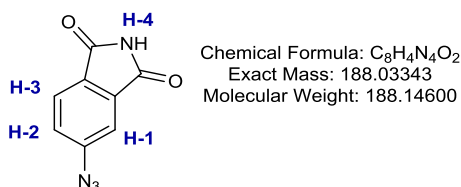


**Figure 8.145.** The structure of **T20**.

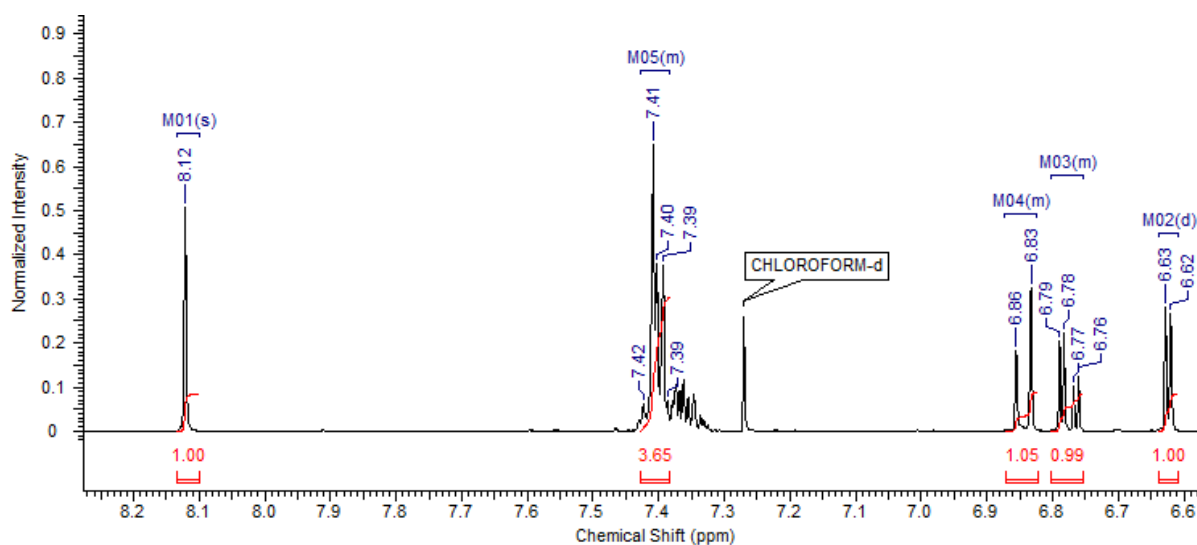


**Figure 8.146.** <sup>1</sup>H-NMR spectrum of **T20**.

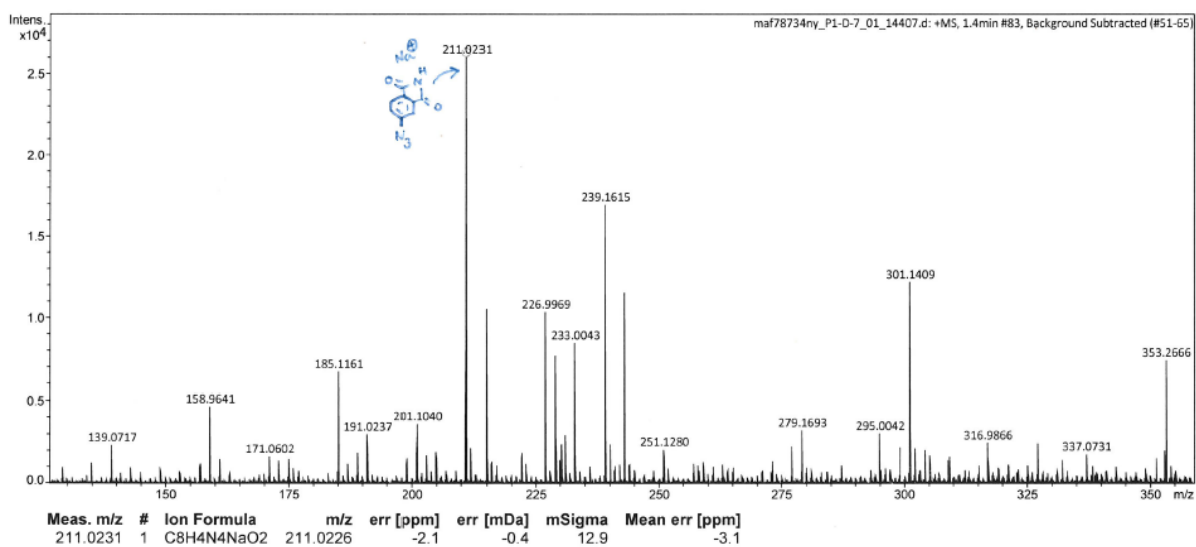


Figure 8.147. ESI-LC/MS spectrum of T20.

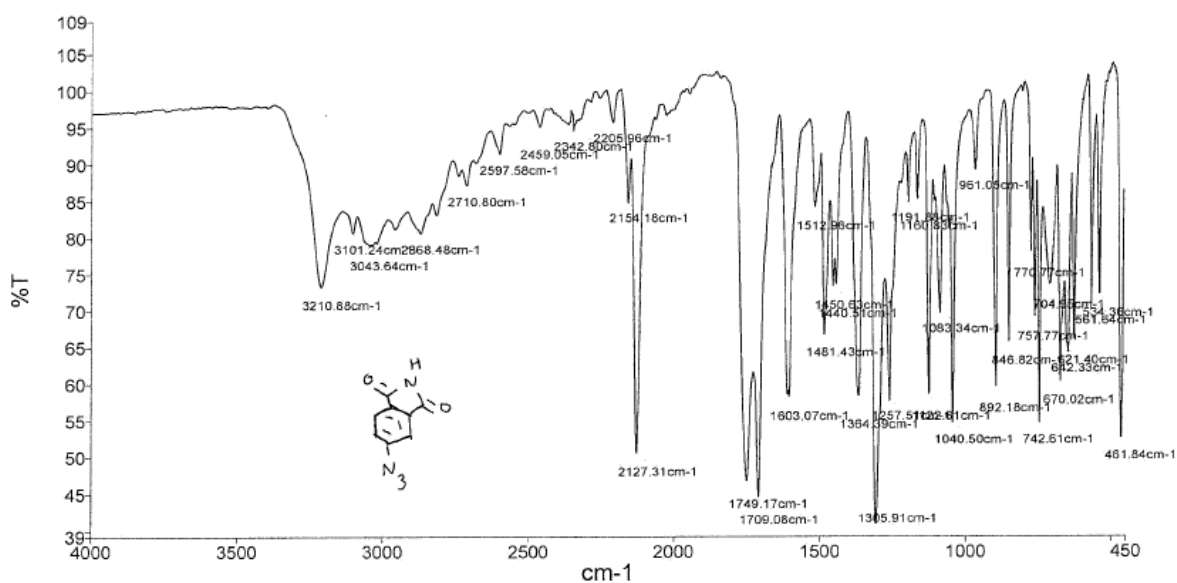


Figure 8.148. IR (ATR) spectrum of a crude sample of T20.

**(E)-5-((1,3-dimesityl-1,3-dihydro-2H-imidazol-2-ylidene)triaz-1-en-1-yl)isoindoline-1,3-dione (T21)**

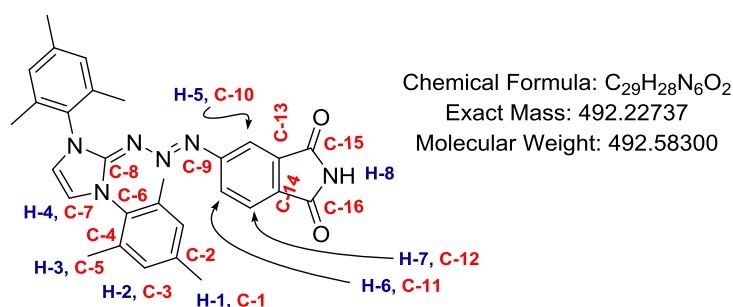
To a solution **T20** (0.360 g, 1.92 mmol), in dry THF (22.5 mL), at 0 °C was added **T1** (0.651 g, 1.917 mmol), and the resultant solution stirred at 0 °C for 20 min. To this solution, NaH (0.247 g, 4.92 mmol, 60% in mineral oil) was added, and the reaction further stirred for 18 h, gradually warming from 0 °C to room temperature. The reaction was then quenched via the addition of water (50 mL), and transferred to a separating funnel. 3 mL of 1 M HCl was added to 50 mL portion of water, and the acidified water was also added to the separating funnel and the organic layer extracted. The aqueous layer was washed with DCM (3 × 50 mL). All organic extractions were combined and dried over MgSO<sub>4</sub>. Concentration in vacuo yielded an orange solid. This residue was purified by flash column chromatography (SiO<sub>2</sub> 2:1 hexane:ethyl acetate → 1:1 hexane:ethyl acetate), yielding an orange solid (0.250 g, 26%).

**<sup>1</sup>H-NMR** (400 MHz, CDCl<sub>3</sub>, **Figure 8.150**): δ<sub>H</sub> 7.50 (d, *J* = 7.79 Hz, 1H, H-7), 7.31 (s, 1H, H-8), 7.04 (s, 4H, H-2), 7.00 (d, *J* = 1.83 Hz, 1H, H-5), 6.97 (dd, *J* = 7.79, 1.83 Hz, 1H, H-6), 6.70 (s, 2H, H-4), 2.36 (s, 6H, H-1), 2.18 (s, 12H, H-3).

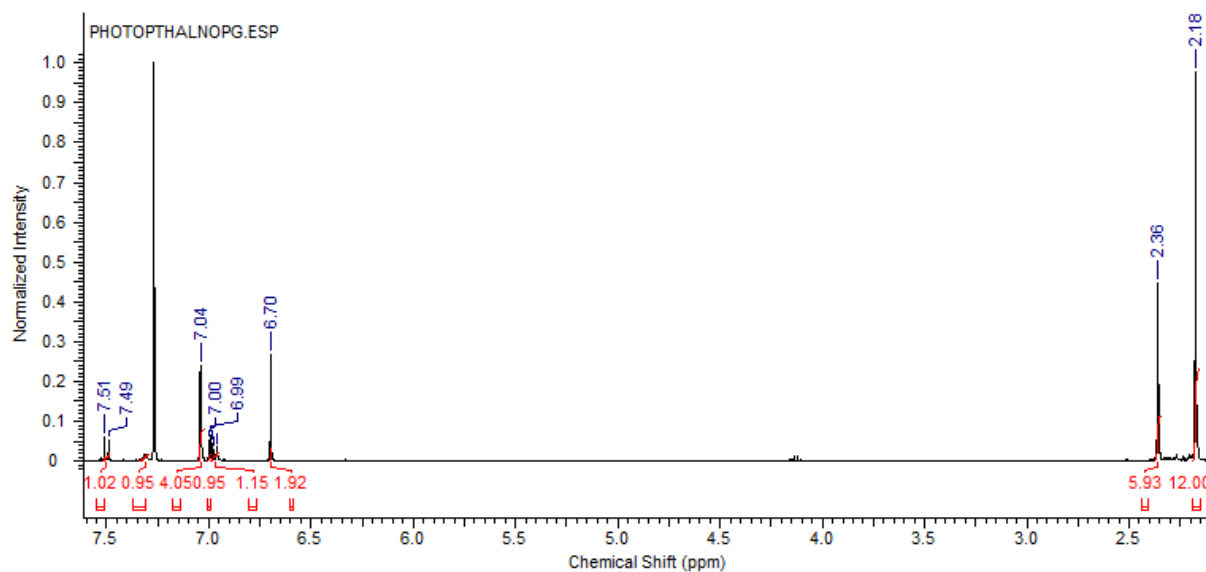
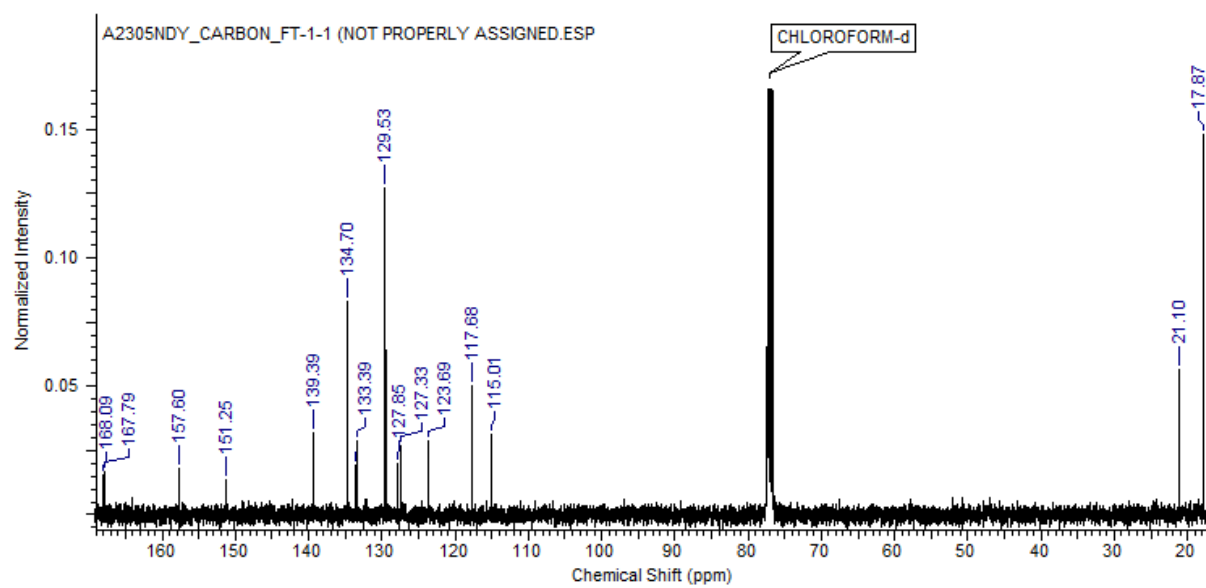
**<sup>13</sup>C-NMR** (100 MHz, CDCl<sub>3</sub>, **Figure 8.151**): δ<sub>C</sub> 168.09 (C-15/16), 167.79 (C-15/16), 157.60, 151.25, 139.39, 134.70, 133.55 (C-13/14), 133.39 (C-13/14) 129.53 (C-3), 127.85, 127.33, 123.69, 117.68 (C-7), 115.01, 21.10 (C-1), 17.87 (C-5).

**(ESI)HRMS** (**Figure 8.152**): Found [M+H]<sup>+</sup> 493.2347, C<sub>29</sub>H<sub>29</sub>N<sub>6</sub>O<sub>2</sub> requires 493.2347.

**IR (ATR)** (**Figure 8.153**) (umax/cm<sup>-1</sup>): 3217 (N-H stretch, imide), 2917 (C-H stretch, alkyl), 1713 (C=O stretching), 1607 (C-C stretch, aromatic), 1336 (C-N stretching), 1159 (C-N stretching), 851 (C-H bend, aromatic), 753 (C-H bend, aromatic).



**Figure 8.149.** The structure of **T21**.

Figure 8.150. <sup>1</sup>H-NMR spectrum of T21.Figure 8.151. <sup>13</sup>C-NMR spectrum of T21.

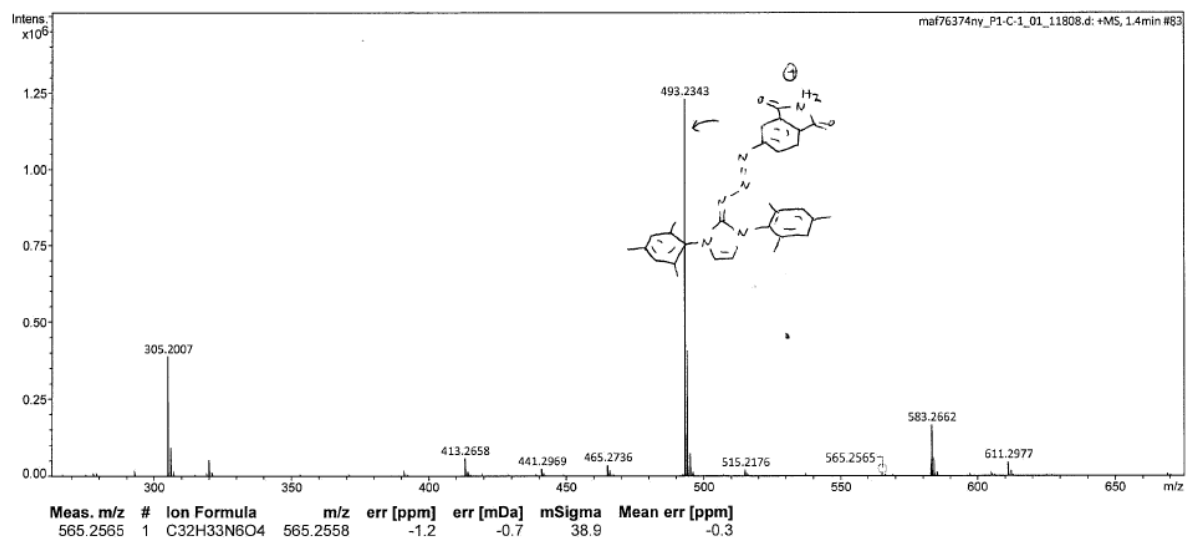


Figure 8.152. ESI-LC/MS spectrum of T21.

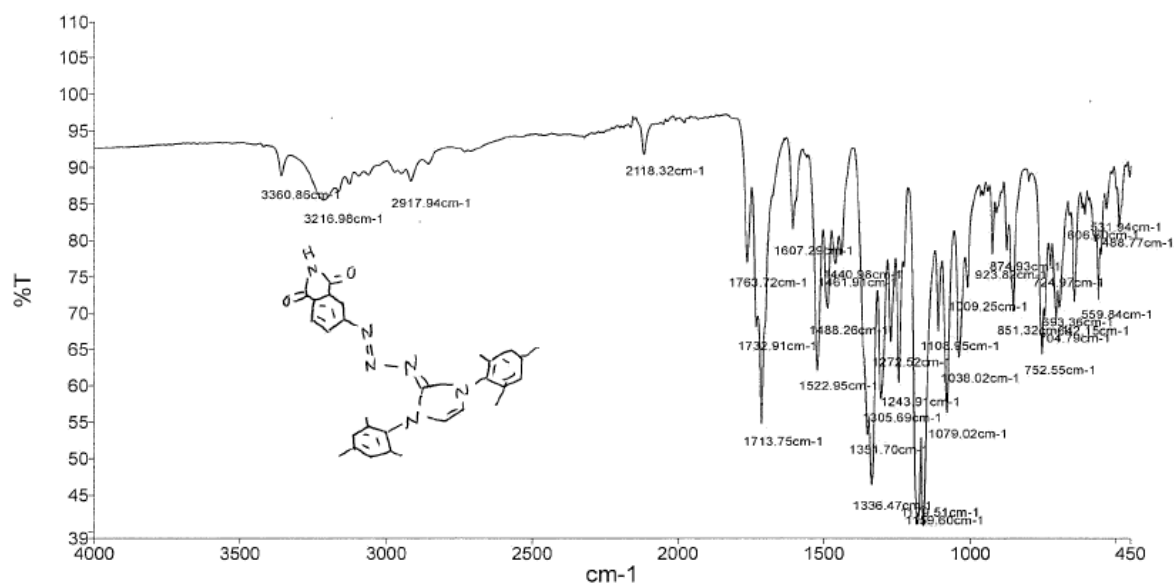


Figure 8.153. IR (ATR) spectrum of T21.

**Ethyl (E)-5-((1,3-dimesityl-1,3-dihydro-2H-imidazol-2-ylidene)triaz-1-en-1-yl)-1,3-dioxoisindoline-2-carboxylate (T22)**

To a solution of **T21** (0.148 g, 0.300 mmol) in anhydrous DMF (0.5 mL) at room temperature was added triethylamine (56  $\mu$ L, 0.40 mmol). The temperature of the reaction mixture was then lowered to 0  $^{\circ}$ C, and ethylchloroformate (35  $\mu$ L, 0.40 mmol) was added in three instalments. The reaction mixture was then stirred at room temperature for 3 hours, before being poured into ice-cold water. **T22** precipitated as a bright-orange solid, was isolated via filtration, washed with cold water and allowed to dry in darkness to yield **T22** (0.106 g, 0.188 mmol, 63%).

**$^1$ H-NMR** (400 MHz,  $\text{CDCl}_3$ , **Figure 8.155**):  $\delta_{\text{H}}$  7.60 (d,  $J = 8.24$  Hz, 1H, H-7), 7.09 (dd,  $J = 8.24$ , 1.83 Hz, 1H, H-6), 7.05 (s, 4H, H-2), 7.02 (d,  $J = 1.83$  Hz, 1H, H-5), 6.72 (s, 2H, H-4), 4.47 (q,  $J = 6.87$  Hz, 2H, H-8), 2.36 (s, 6H, H-1), 2.18 (s, 12H, H-3), 1.44 (t,  $J = 6.87$  Hz, 2H, H-9).

**$^{13}$ C-NMR** (100 MHz,  $\text{CDCl}_3$ , **Figure 8.156**):  $\delta_{\text{C}}$  163.93 (C-15/16), 163.89 (C-15/16), 158.55, 151.15, 148.82 (C-17), 139.51, 134.64, 133.25 (C-13/14), 132.10 (C-13/14) 129.57 (C-3), 128.82, 124.66, 117.86 (C-7), 114.95, 99.88, 63.69 (C-18), 21.11 (C-1), 17.85 (C-5), 14.11 (C-19).

**(ESI)HRMS** (**Figure 8.157**): Found  $[\text{M}+\text{H}]^+$  565.2568,  $\text{C}_{32}\text{H}_{32}\text{N}_6\text{O}_4$  requires 565.2558.

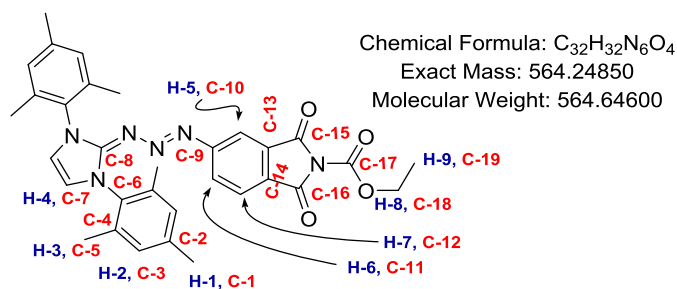


**Figure 8.154.** The structure of **T22**.

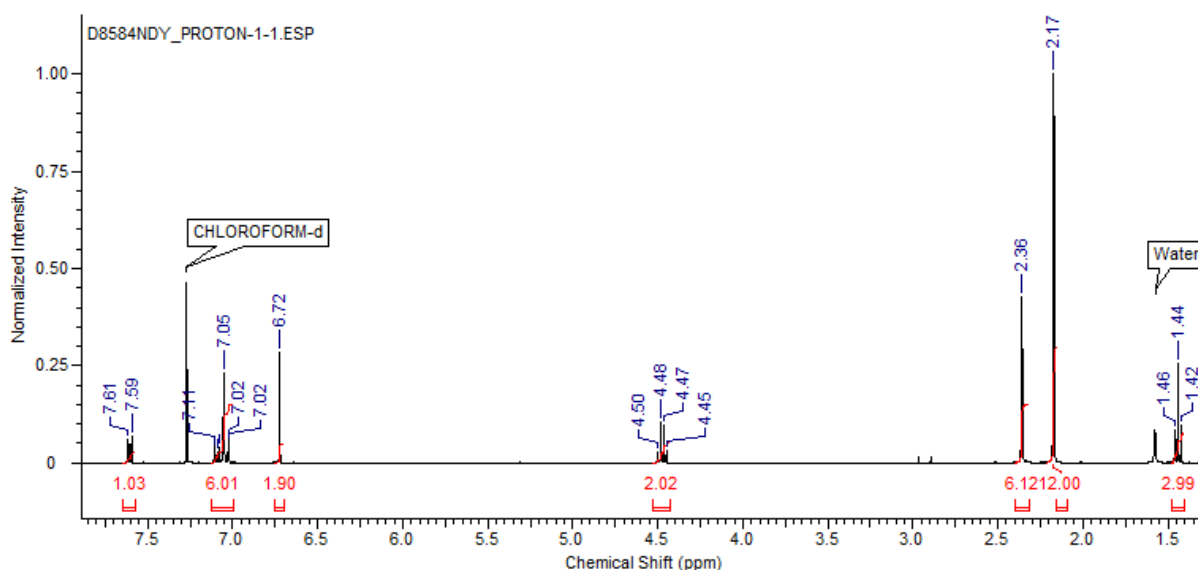


**Figure 8.155.**  $^1\text{H-NMR}$  spectrum of **T22**.

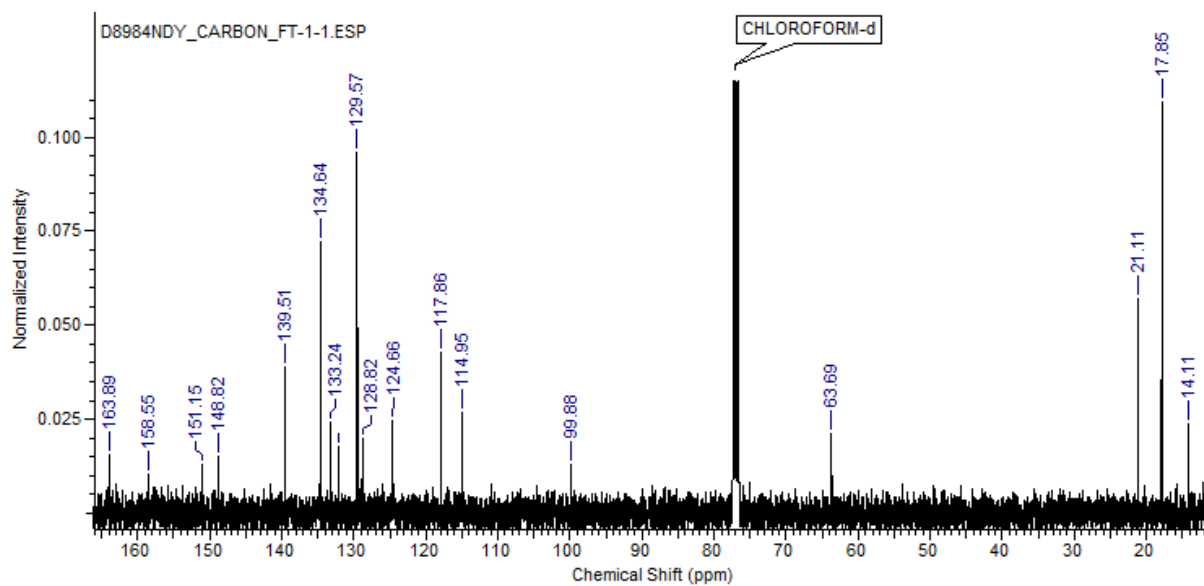
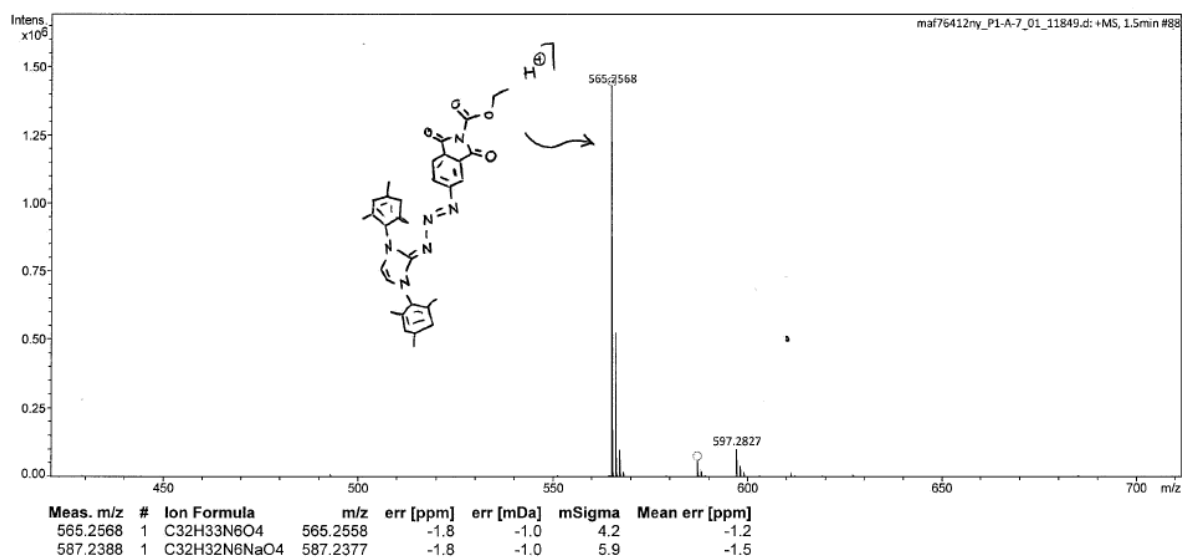
Figure 8.156.  $^{13}\text{C}$ -NMR spectrum of T22.

Figure 8.157. ESI-LC/MS spectrum of T22.

**(E)-5-((1,3-dimesityl-1,3-dihydro-2H-imidazol-2-ylidene)triaz-1-en-1-yl)-2-(2-(2-(2,5-dioxo-2,5-dihydro-1H-pyrrol-1-yl)ethoxy)ethyl)isoindoline-1,3-dione (T23)**

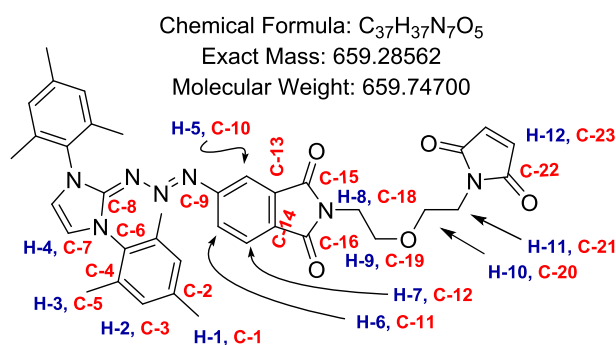
To a solution of **T22** (0.106 g, 0.188 mmol) in anhydrous THF (1 mL) was added a solution of **T7** (60.0 mg, 0.200 mmol, 1.07 equiv) and triethylamine (52  $\mu$ L, 0.376 mmol, 2.00 equiv) in THF (1 mL) at 0 °C. The resultant solution was stirred overnight at room temperature in darkness. After this time the reaction mixture was concentrated *in vacuo* and purified via flash column chromatography (SiO<sub>2</sub> 1:1 hexane:ethyl acetate, **T23** r.f. = 0.2), yielding **T23** (62 mg, 50%).

**<sup>1</sup>H-NMR** (400 MHz, CDCl<sub>3</sub>, **Figure 8.159**):  $\delta_{\text{H}}$  7.46 (d,  $J$  = 7.63 Hz, 1H, H-7), 7.04 (s, 4H, H-2), 7.00 (d,  $J$  = 1.53 Hz, 1H, H-5), 6.89 (dd,  $J$  = 7.63, 1.53 Hz, 1H, H-6), 6.69 (s, 2H, H-4), 6.52 (s, 2H, H-12), 3.79 (t,  $J$  = 6.10 Hz, 2H, H-11), 3.70-3.58 (m, 6H, H-8,9,10), 2.36 (s, 6H, H-1), 2.18 (s, 12H, H-3).

**<sup>13</sup>C-NMR** (100 MHz, CDCl<sub>3</sub>, **Figure 8.160**):  $\delta_{\text{C}}$  170.50 (C-22), 168.31 (C-15,16), 157.16, 139.36, 134.71 (C-23), 133.86, 133.43 (C-13/C-14), 132.95 (C-13/14), 129.53 (C-3), 126.63, 123.34, 117.62 (C-7), 115.04, 67.54 (C-18/21), 67.24 (C-18/21), 37.07 (C-19/20), 36.97 (C-19/20), 21.10 (C-1), 17.88 (C-5).

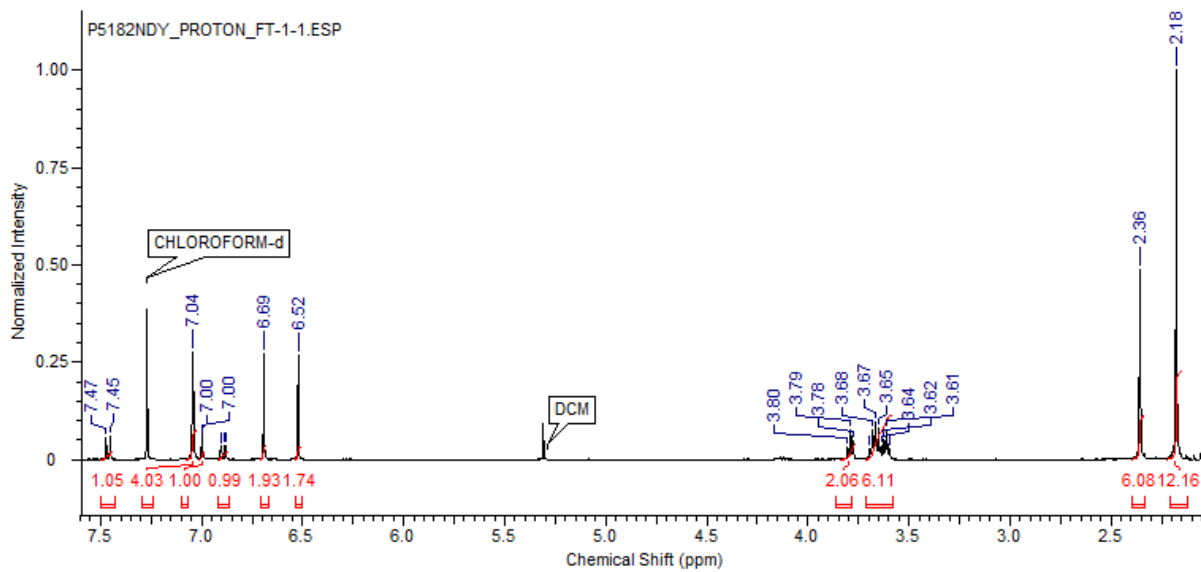
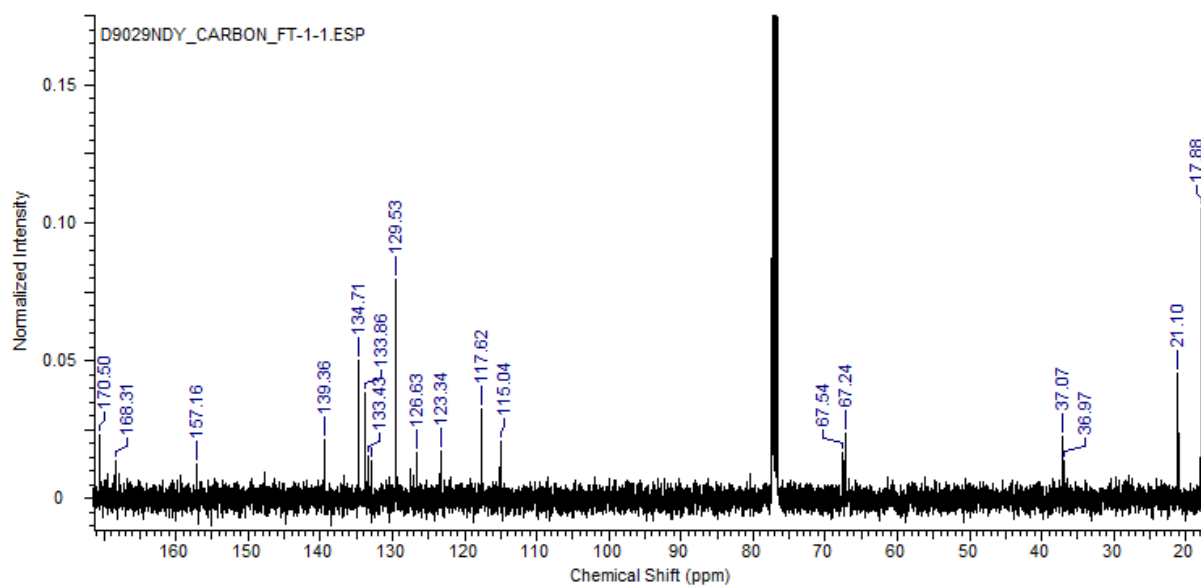
**(ESI)HRMS** (**Figure 8.161**): Found  $[M+H]^+$  660.2934, C<sub>37</sub>H<sub>38</sub>N<sub>7</sub>O<sub>5</sub> requires 660.2929.

**IR (ATR)** (**Figure 8.162**) ( $\nu_{\text{max}}/\text{cm}^{-1}$ ): 2921 (C-H stretch, alkyl), 1704 (C=O stretching), 1522 (C-C stretch, aromatic), 1358 (C-N stretching), 1158 (C-N stretching), 851 (C-H bend, aromatic), 751 (C-H bend, aromatic).



**Figure 8.158.** The structure of **T23**.



Figure 8.159. <sup>1</sup>H-NMR spectrum of T23.Figure 8.160. <sup>13</sup>C-NMR spectrum of T23.

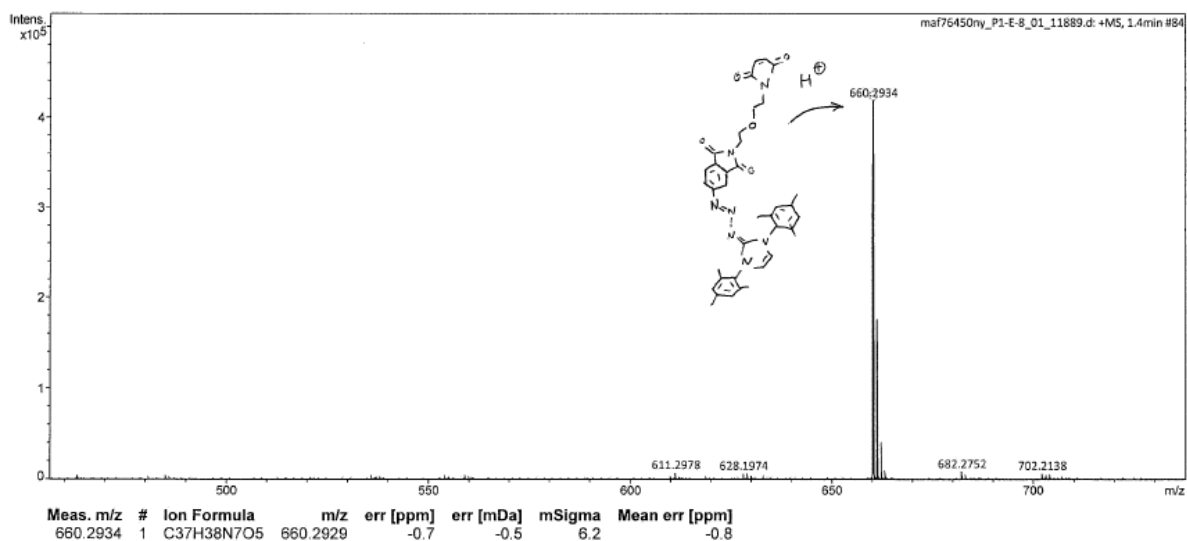


Figure 8.161. ESI-LC/MS spectrum of T23.

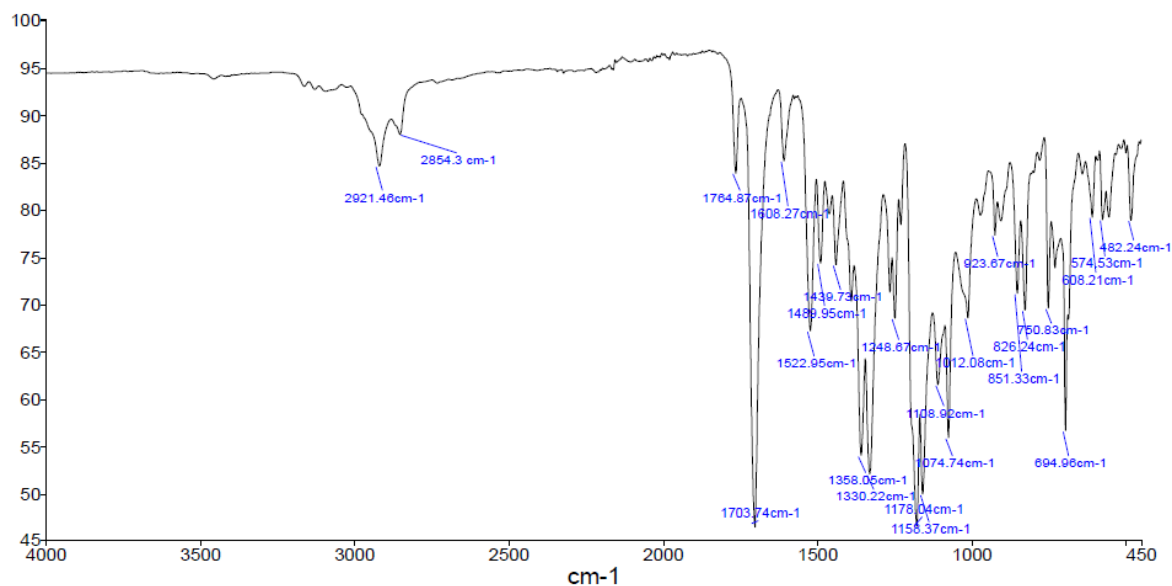


Figure 8.162. IR (ATR) spectrum of T23.

### 8.6.1.2 Synthesis of resorcinol probes

#### *N*-(2,4-dihydroxyphenyl)-5-(dimethylamino)naphthalene-1-sulfonamide (Res1)

Dansyl chloride (0.150 g, 0.556 mmol) was dissolved in the minimum volume of dry THF under N<sub>2</sub>. 4-aminoresorcinol hydrochloride (0.162 g, 1.00 mmol) was suspended in MeOH (1 mL), and sodium methoxide (54 mg, 1 mmol) was added, resulting in a purple solution. The methanolic solution of 4-aminoresorcinol was then added dropwise to the dansyl chloride solution at room temperature, and the resultant solution was stirred under N<sub>2</sub> at 60 °C for 2 hours. After this time, saturated NaHCO<sub>3</sub> was added to the reaction solution (10 mL). DCM (50 mL) was added, and the organic layer extracted, dried over MgSO<sub>4</sub> and concentrated *in vacuo* to yield a crude brown residue. This residue was then purified by flash column chromatography (automated column, hexane → ethyl acetate), yielding a dull orange solid (90 mg, 0.25 mmol, 50%).

<sup>1</sup>H-NMR (400 MHz, CDCl<sub>3</sub>, **Figure 8.164**): δ<sub>H</sub> 8.54 (d, *J* = 8.24 Hz, 1H, H-7), 8.34 (*J* = 8.70 Hz, 1H, H-4), 8.04 (dd, *J* = 7.33, 1.37 Hz, 1H, H-5), 7.64 (ddd, *J* = 8.70, 7.33, 1.37 Hz, 1H, H-3), 7.42 (ddd, *J* = 8.24, 7.33, 1.37 Hz, 1H, H-6), 7.24 (d, *J* = 7.33 Hz, 1H, H-2), 6.66 (s, 1H, H-12), 6.37 (d, *J* = 2.75 Hz, 1H, H-11/13), 6.27 (s, 1H, H-11/13), 6.05 (dd, *J* = 8.70, 1.37 Hz, 1H, H-9), 5.95 (ddd, *J* = 8.70, 3.21, 2.75 Hz, 1H, H-10), 4.98 (s, 1H, H-8), 2.92 (d, *J* = 1.37 Hz, 6H, H-1).

(ESI)HRMS (**Figure 8.165**): Found [M+Na]<sup>+</sup> 381.0878, C<sub>18</sub>H<sub>18</sub>N<sub>2</sub>NaO<sub>4</sub>S requires 381.0879.

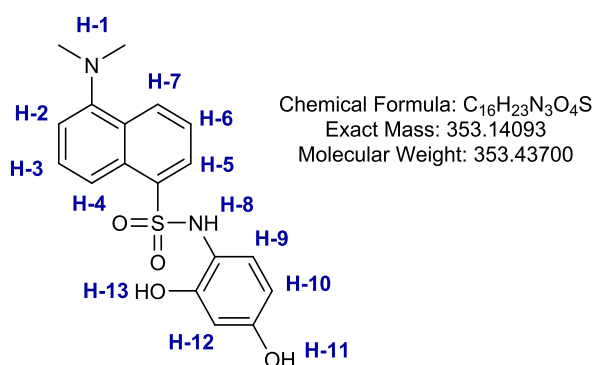


**Figure 8.163.** The structure of T23.

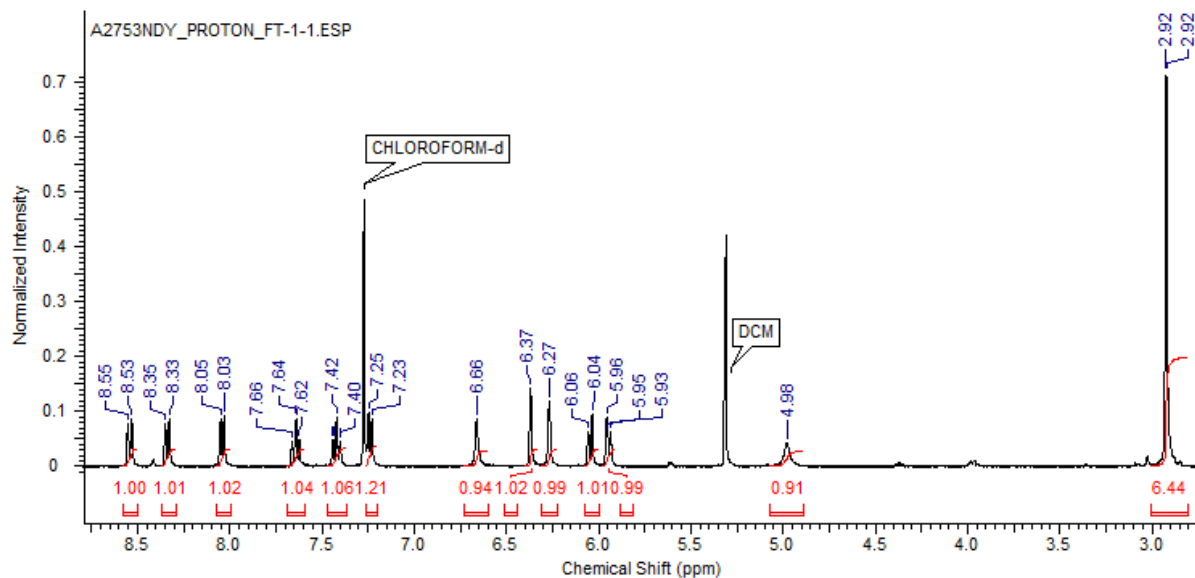
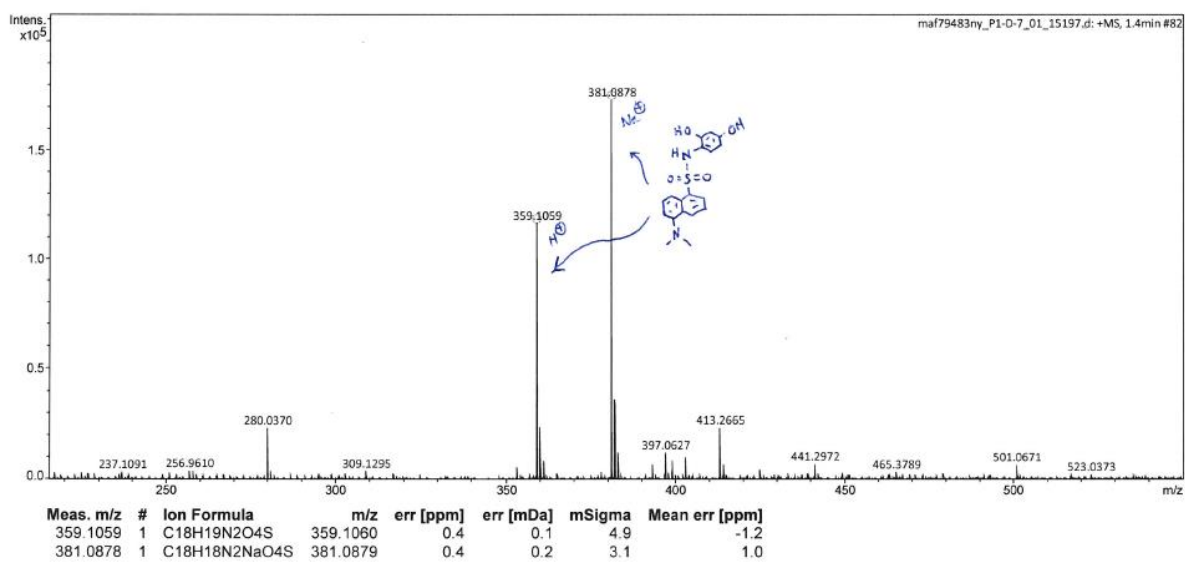
Figure 8.164.  $^1\text{H}$ -NMR spectrum of Res1.

Figure 8.165. ESI-LC/MS spectrum of Res1.

**3-(benzyloxy)phenol (Res2)**

Resorcinol (2.00 g, 18.2 mmol) was dissolved in acetone (25 mL) with stirring. To this solution was added potassium carbonate (3.85 g, 27.9 mmol), followed by benzyl bromide (2.38 g, 13.9 mmol). The resultant solution was refluxed overnight at 80 °C. After this time, water (100 mL) was added, and the product was extracted using ethyl acetate (3 × 100 mL). The organic extractions were then washed with brine (100 mL), dried over MgSO<sub>4</sub> and concentrated *in vacuo* to yield a crude residue which was purified via flash column chromatography (automated column, hexane → ethyl acetate), yielding **Res2** as a colourless oil (1.19 g, 33%). The proton NMR is consistent with that reported in the literature.<sup>577</sup>

**<sup>1</sup>H-NMR** (400 MHz, CDCl<sub>3</sub>, **Figure 8.167**): δ<sub>H</sub> 7.43-7.38 (m, 2H, H-8), 7.38-7.32 (m, 2H, H-9), 7.31-7.25 (m, 1H, H-10), 7.05 (dd, *J* = 8.24, 8.24 Hz, 1H, H-2), 6.46 (ddd, *J* = 8.24, 2.29, 0.92 Hz, 1H, H-1/3), 6.43 (dd, *J* = 2.29, 2.29 Hz, 1H, H-6), 6.38 (ddd, *J* = 8.24, 2.29, 0.92 Hz, 1H, H-1/3), 5.00 (s, 2H, H-7).

**(ESI)HRMS** (**Figure 8.168**): Found [M-H]<sup>-</sup> 199.0766, C<sub>13</sub>H<sub>12</sub>O<sub>2</sub> requires 199.0765.

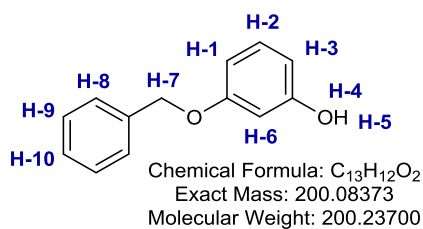


**Figure 8.166.** The structure of **Res2**.

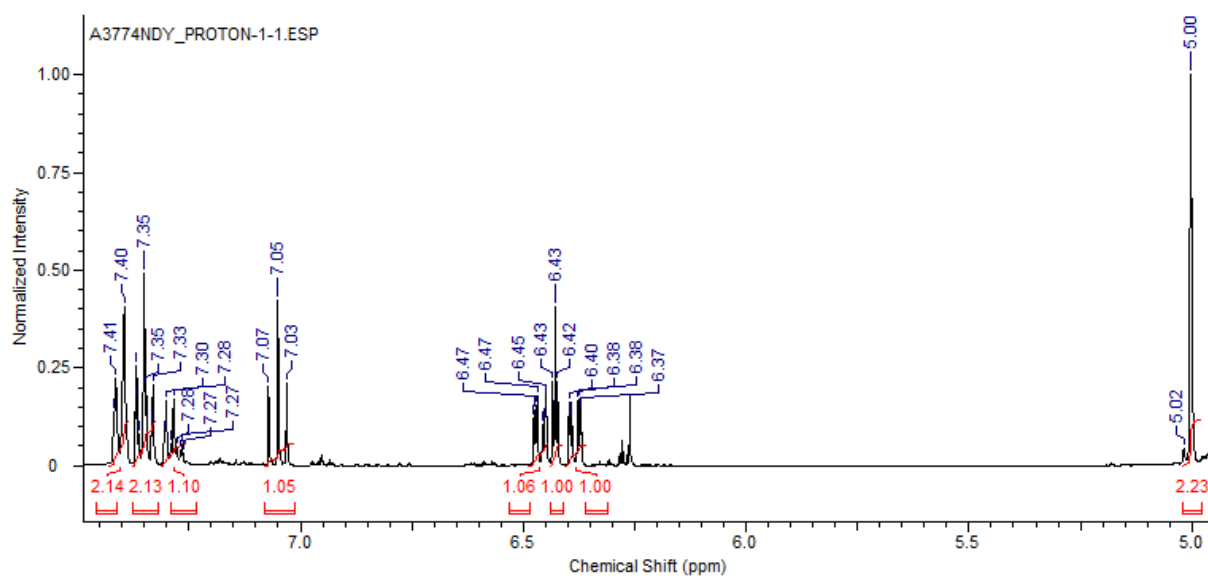


**Figure 8.167.** <sup>1</sup>H-NMR spectrum of **Res2**.

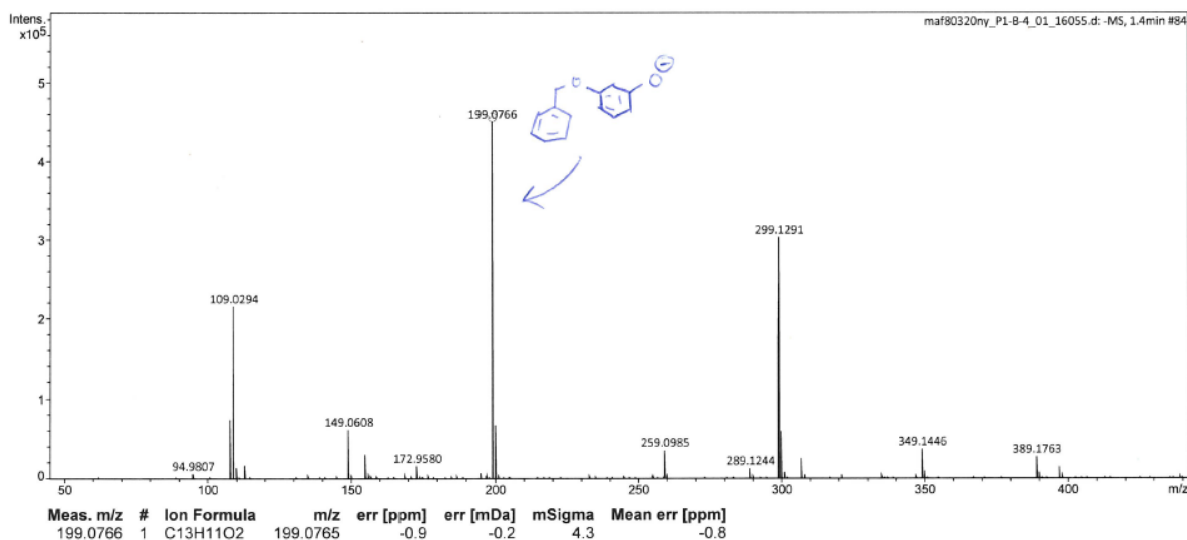


Figure 8.168. ESI-LC/MS spectrum of Res2.

#### **Tert-butyl (2-(2-(3-(benzyloxy)phenoxy)ethoxy)ethyl)carbamate (Res4) (via Res3)**

**Dan1** (see Section 8.4.5.1) (0.616 g, 3.00 mmol) and triphenylphosphine (0.925 g, 3.30 mmol, 1.1 equiv) were dissolved in the minimum volume of anhydrous DCM under N<sub>2</sub>, and the resultant solution was cooled to 0 °C. Diisopropyl azodicarboxylate (0.65 mL, 3.31 mmol, 1.1 equiv) was then added dropwise. The resultant solution was then allowed to warm to room temperature, and was stirred at room temperature for 48 hours. The reaction solution was then concentrated *in vacuo*. **Res3** was partially purified via flash column chromatography (SiO<sub>2</sub>, hexane → ethyl acetate), but did co-elute with diisopropyl hydrazine-1,2-dicarboxylate (Figure 8.172). As such, **Res3** was used crude. Boc deprotection of **Res3** to yield **Res4** was performed by dissolving the crude **Res3** in a 4:1 DCM:TFA solution (50 mL). The resultant solution was stirred for 2 hours before being concentrated *in vacuo*. The resultant residue was then purified by flash column chromatography (SiO<sub>2</sub>, DCM → 10% MeOH in DCM) to yield **Res4** (0.305 g, 23% across 2 steps).

<sup>1</sup>H-NMR (400 MHz, CDCl<sub>3</sub>, Figure 8.170): δ<sub>H</sub> 8.04 (br s, 3H, H-10), 7.50-7.23 (m, 5H, H-12,13,14), 7.31-7.14 (dd, *J* = 8.24, 8.24 Hz, 2H, H-2), 6.59 (dd, *J* = 8.24, 2.29 Hz, 1H, H-1/3), 6.54 (dd, *J* = 2.29, 1.83 Hz, 1H, H-4), 6.49 (dd, *J* = 8.24, 1.83 Hz, 1H, H-1/3), 5.02 (s, 2H, H-11), 4.07-4.02 (m, 2H, H-5), 4.80-3.75 (m, 2H, H-6), 3.74-3.70 (m, 2H, H-7), 3.17-3.05 (m, 2H, H-8).

<sup>13</sup>C-NMR (100 MHz, CDCl<sub>3</sub>, Figure 8.171): δ<sub>C</sub> 159.95 (C-4/11), 159.50 (C4/11), 136.78 (C-13), 130.02, 128.53, 127.94, 127.45, 107.63 (C-1/3), 106.98 (C-1/3), 101.94 (C-5), 69.91, 69.52, 67.16, 66.60, 39.45 (C-9).

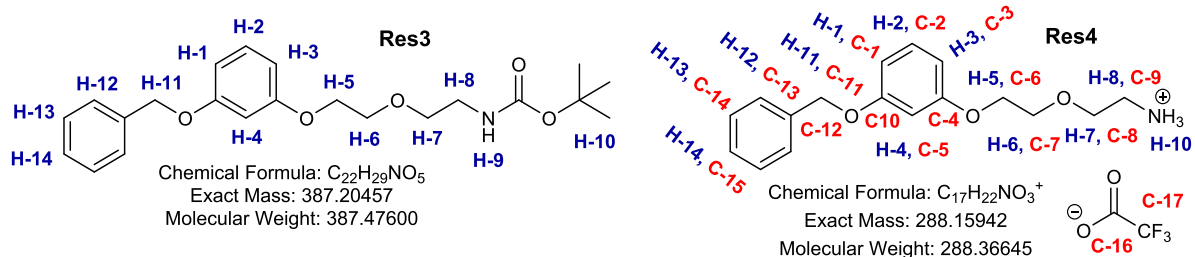


Figure 8.169. The structures of Res3 and Res4.

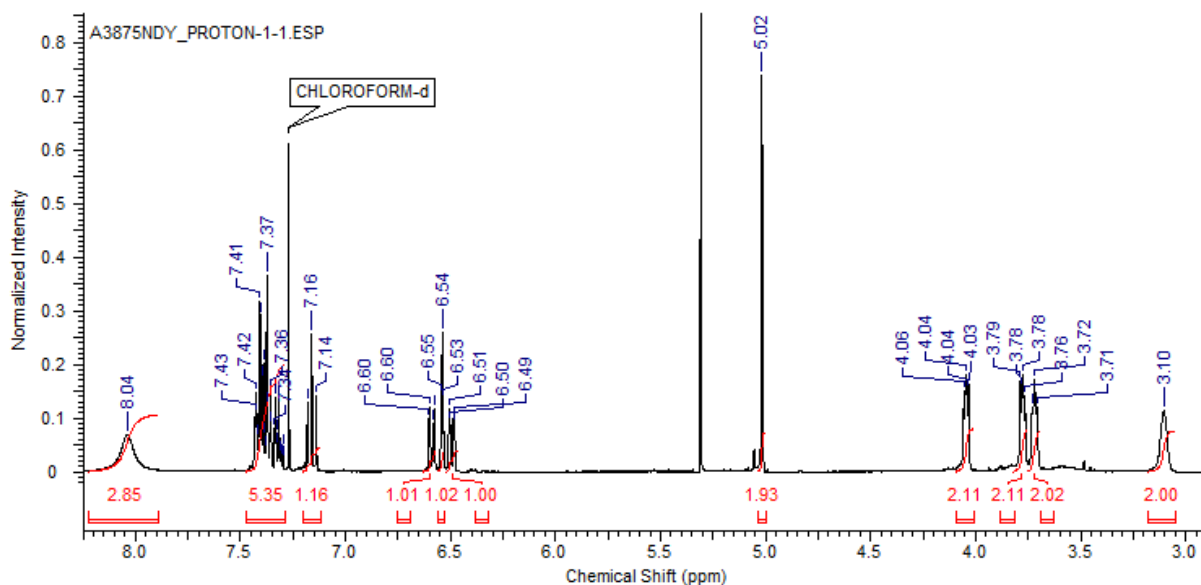


Figure 8.170.  $^1H$ -NMR spectrum of Res4.

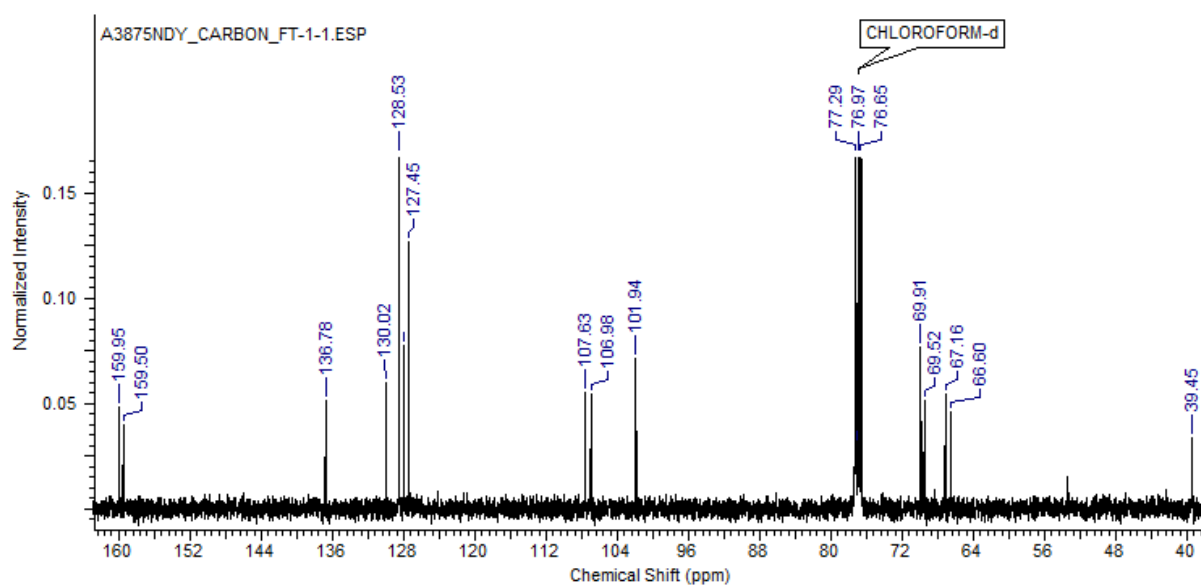


Figure 8.171.  $^{13}C$ -NMR spectrum of Res4.

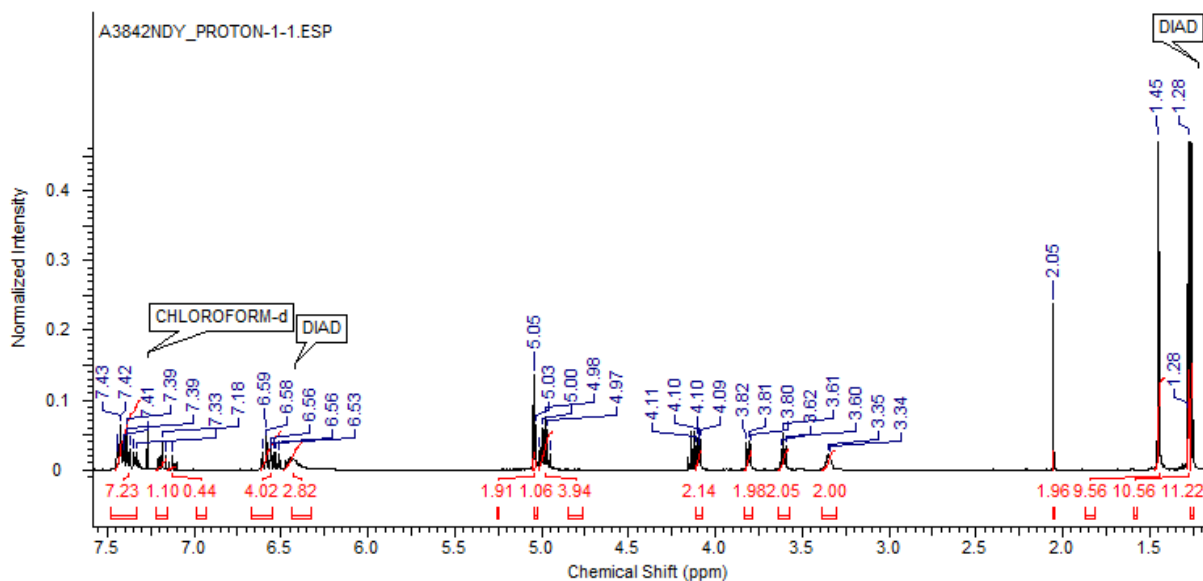


Figure 8.172.  $^1\text{H-NMR}$  spectrum of a crude sample of Res3.

#### N-(2-(2-(3-(benzyloxy)phenoxy)ethoxy)ethyl)-5-(dimethylamino)naphthalene-1-sulfonamide (Res5)

To a stirred solution of Res4 (0.305 g, 0.759 mmol) dissolved in DCM (30 mL) at 0 °C was added triethylamine (0.154 g, 0.212 mL, 1.52 mmol, 2 equiv), followed by dansyl chloride (0.205 g, 0.759 mmol, 1 equiv). The resultant solution was then allowed to warm to room temperature and was stirred for 18 hours. The solution was then transferred to a separating funnel and washed successively with water (50 mL) and brine (50 mL). The organic extraction was then dried over  $\text{MgSO}_4$ , and concentrated *in vacuo* to yield a crude residue which was purified by flash column chromatography ( $\text{SiO}_2$ , hexane  $\rightarrow$  ethyl acetate) to yield Res5 as a bright green oil (0.186 g, 47%).

$^1\text{H-NMR}$  (400 MHz,  $\text{CDCl}_3$ , Figure 8.174):  $\delta_{\text{H}}$  8.63-8.52 (m, 1H, H-11), 8.37-8.20 (m, 2H, H-9,15), 7.60-7.29 (m, 7H, H-10,14,17,18,19), 7.23-7.11 (m, 2H, H-4,13), 6.62 (dd,  $J = 8.24, 2.29$  Hz, 1H, H-1/3), 6.56 (dd,  $J = 2.29, 2.29$  Hz, 1H, H-4), 6.50 (dd,  $J = 8.24, 2.29$  Hz, 1H, H-1/3), 5.26 (t,  $J = 5.95$  Hz, 1H, H-9) 5.06 (s, 2H, H-16), 3.91 (t,  $J = 4.58$  Hz, 2H, H-5), 3.53 (t,  $J = 4.58$  Hz, 2H, H-6), 3.43 (t,  $J = 5.04$  Hz, 2H, H-7), 3.13 (dt,  $J = 5.95, 5.04$  Hz, 2H, H-6) 2.90 (s, 6H, H-12).

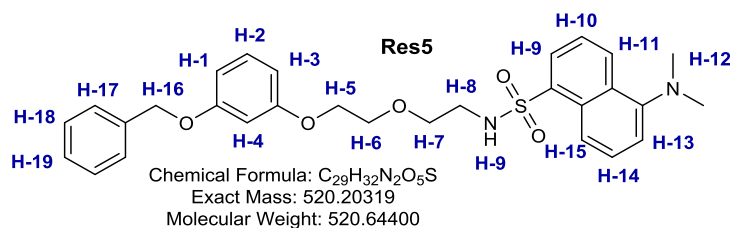
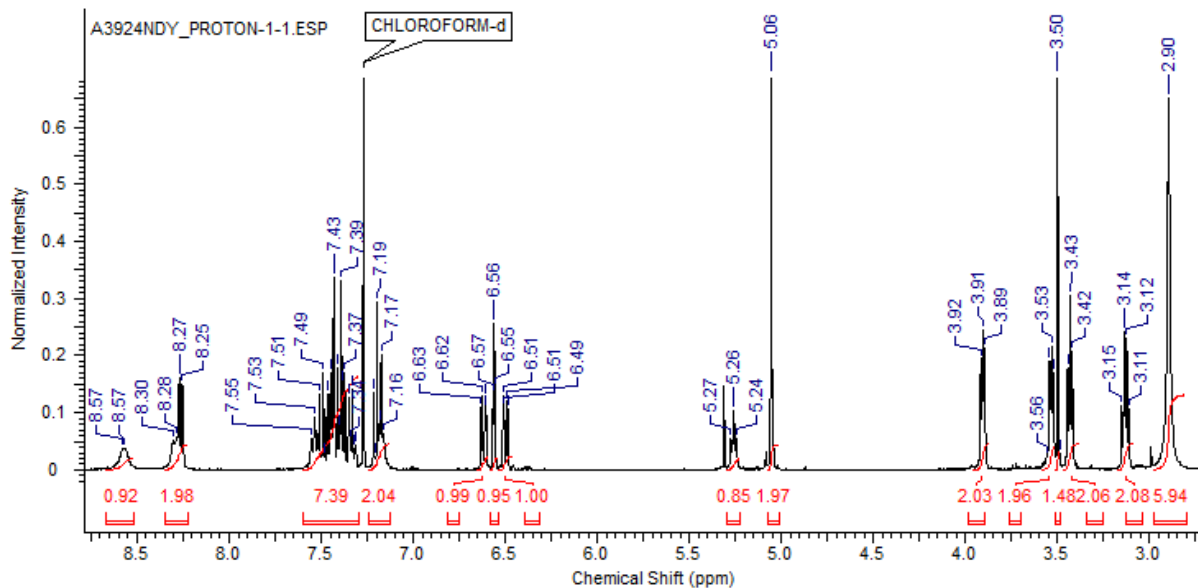


Figure 8.173. The structure of Res5.



Figure 8.174.  $^1\text{H}$ -NMR spectrum of Res5.

#### 5-(dimethylamino)-N-(2-(2-(3-hydroxyphenoxy)ethoxy)ethyl)naphthalene-1-sulfonamide (Res6)

To a stirred solution of Res5 (0.186 g, 0.356 mmol) in methanol (30 mL) was added a spatula-end of 10% Pd/C. The system was then placed under  $\text{N}_2$ , then placed under 1 atm of hydrogen and stirred overnight at room temperature. The Pd/C carbon was removed via filtration and the filtrate concentrated *in vacuo*. Purification of the crude residue via flash column chromatography ( $\text{SiO}_2$ , hexane  $\rightarrow$  ethyl acetate) yielded Res6 as a tacky pale green oil (0.105 g, 0.245 mmol, 69 %).

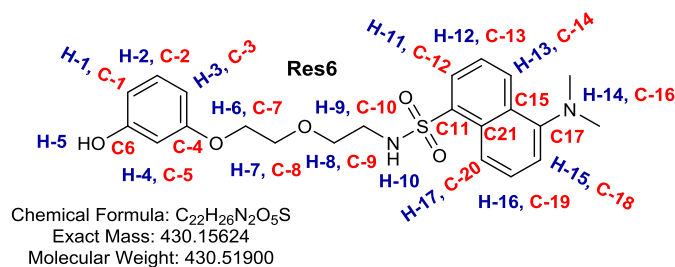


Figure 8.175. The structure of Res6.

$^1\text{H}$ -NMR (400 MHz,  $\text{CDCl}_3$ , Figure 8.176):  $\delta_{\text{H}}$  8.64-8.52 (m, 1H, H-13), 8.36-8.28 (m, 1H, H-11/17), 8.26 (d,  $J = 7.32$  Hz, 1H, H-11/17), 7.54 (d,  $J = 8.23$  Hz, H-12/16), 7.50 (d,  $J = 8.23$  Hz, H-12/16), 7.25-7.18 (m, 1H, H-15), 7.12 (dd,  $J = 8.23, 8.23$  Hz, 1H, H-2) 6.48 (dd,  $J = 7.78, 2.29$  Hz, 1H, H-1/3), 6.42 (dd,  $J = 8.23, 2.29$  Hz, 1H, H-1/3), 6.30 (dd,  $J = 2.29, 2.29$  Hz, 1H, H-4), 5.90 (br s, 1H, H-5), 5.32 (t,  $J = 5.95$  Hz, 1H, H-10), 3.78 (t,  $J = 5.03$  Hz, 2H, H-6), 3.50 (t,  $J = 5.03$  Hz, 2H, H-7), 3.40 (t,  $J = 5.03$  Hz, 2H, H-8), 3.15 (dt,  $J = 5.95, 5.03$  Hz, 2H, H-9) 2.93 (s, 6H, H-14).

**$^{13}\text{C-NMR}$**  (100 MHz,  $\text{CDCl}_3$ , **Figure 8.177**):  $\delta_{\text{C}}$  159.57 (C-4), 156.89 (C-6), 135.69, 130.07 (C-2), 129.47, 108.31 (C-1/3), 106.72 (C-1/3), 102.11 (C-5), 69.33, 69.03, 66.91, 45.46 (C-16), 43.05 (C-10). More signals are expected.

**(ESI)HRMS** (**Figure 8.178**): Found  $[\text{M}+\text{Na}]^+$  453.1463,  $\text{C}_{22}\text{H}_{26}\text{N}_2\text{NaO}_5\text{S}$  requires 453.1455.

**IR (ATR)** (**Figure 8.179**) ( $\text{u}_{\text{max}}/\text{cm}^{-1}$ ): 3297 (N-H/OH stretch), 2950 (C-H alkyl), 2873 (C-H alkyl), 1710 (N-H bend, hydroxylamine), 1310 (S=O stretch, sulfonamide), 1136 (C-O stretch, ether), 1075 (C-H aromatic), 789 (C-H bend aromatic).

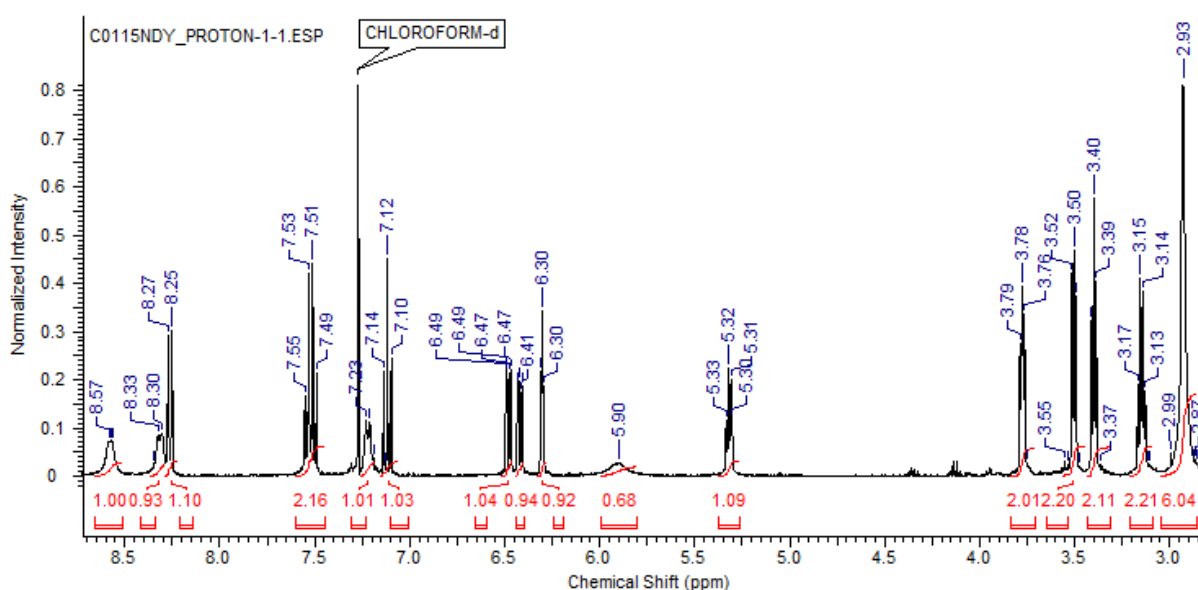


Figure 8.176.  $^1\text{H-NMR}$  spectrum of Res6.

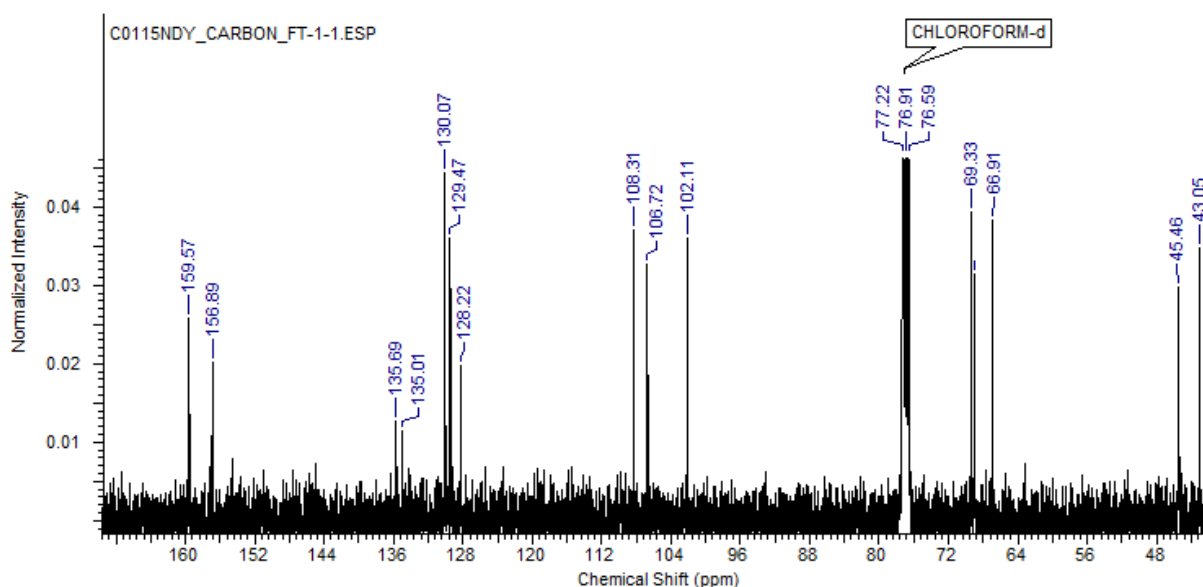


Figure 8.177.  $^{13}\text{C-NMR}$  spectrum of Res6. A higher number of scans will be needed to fully reveal some of the peaks for tertiary environments.

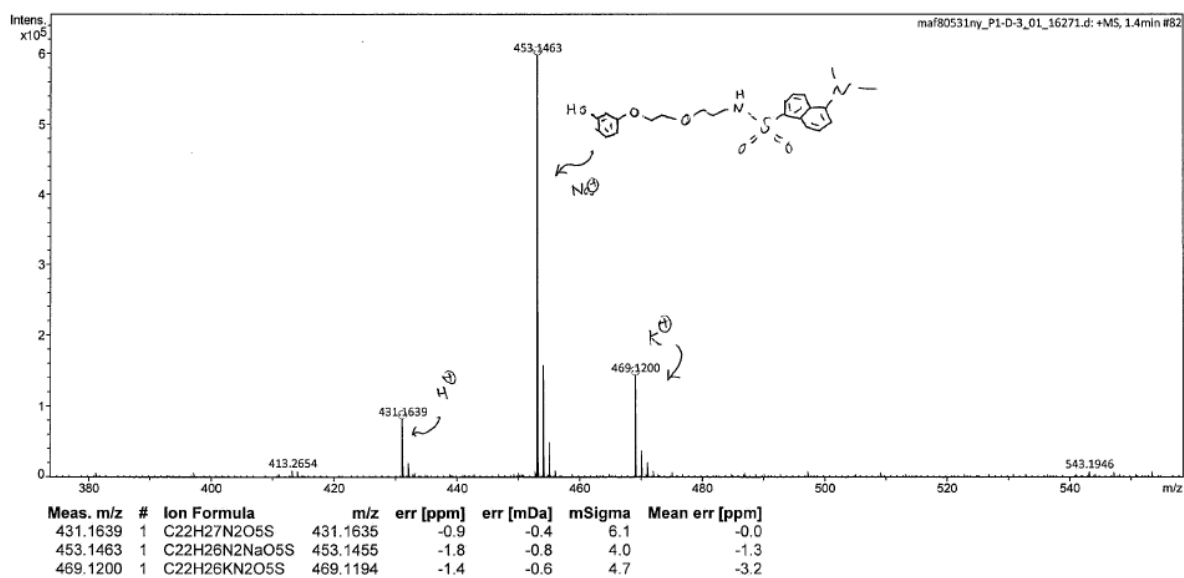


Figure 8.178. ESI-LC/MS spectrum of Res6.

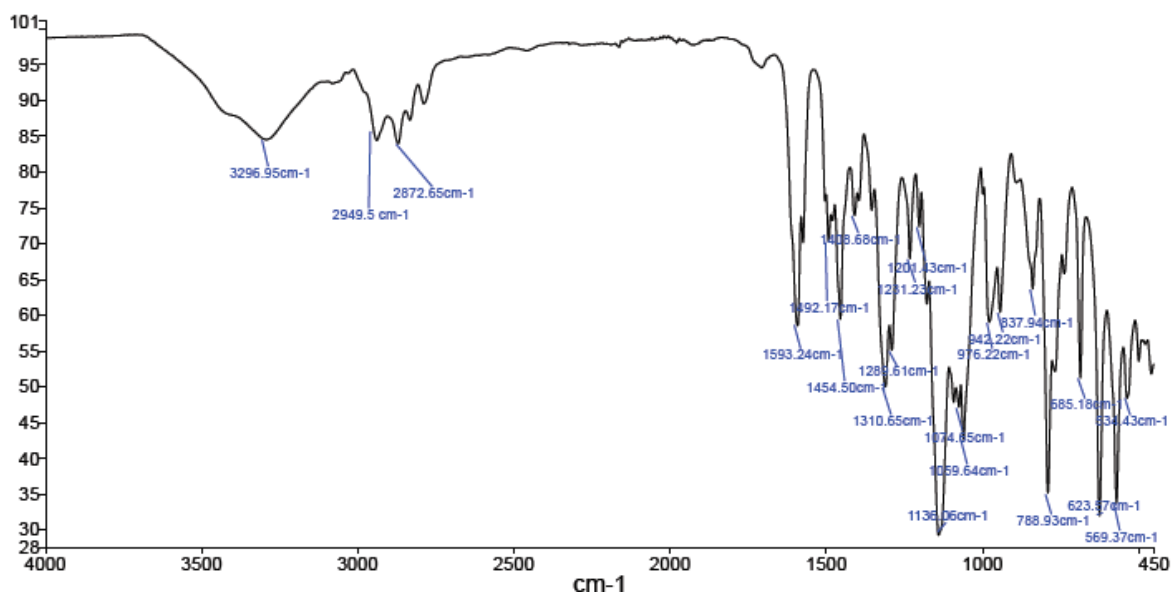


Figure 8.179. IR (ATR) spectrum of Res6.

## 8.6.2 UV-initiated diazonium release from different classes of triazabutadiene

### 8.6.2.1 Tracking triazabutadiene degradation/diazonium cation reactivity via UV-vis spectrometry

Triazabutadiene solutions were prepared as described in the captions / accompanying text of the relevant figures (**Figure 6.4** for **T18**, **Figure 6.11** for **T-PEG**, **Figure 6.15** for **T8-cys** and **Figure 6.18** for **T23-acetate**) and subjected to UV irradiation from a 7 W 365 nm bulb at 0 °C for the periods of time specified in the captions of the relevant Figures prior to analysis using a nanodrop spectrophotometer (DeNovix). The concentrations of any additional reagents that may have been added to react with released diazonium cations, and the conditions under which these reactions were performed, are reported in the relevant tables (i.e. **Table 6.1** for **T-PEG**).

### 8.6.2.2 Tracking triazabutadiene degradation/diazonium cation reactivity using <sup>1</sup>H-NMR

Triazabutadiene reaction solutions were prepared as described in the tables below.

**Table 8.5.** The composition of the triazabutadiene reaction solution analysed using <sup>1</sup>H-NMR in **Figure 6.16**

Component	Quantity	Quantity / $\mu$ moles
<b>T8</b>	3.6 mg	5.7
Formic acid (26.5 M)	2.2 $\mu$ L	58
<b>Res1</b>	2 mg	5.6
Deuterated methanol	To suitable volume in NMR tube	-

**Table 8.6.** The composition of the triazabutadiene reaction solution analysed using  $^1\text{H-NMR}$  in **Figure 6.12**.

Component	Quantity	Quantity / $\mu\text{moles}$
<b>T-PEG</b>	5 mg	9.0
Formic acid (26.5 M)	3.4 $\mu\text{L}$	90
<b>Res1</b>	3.2 mg	8.9
Deuterated methanol	To suitable volume in NMR tube	-

**Table 8.7.** The composition of the triazabutadiene reaction solution analysed using  $^1\text{H-NMR}$  in **Figure 6.13**

Component	Quantity	Quantity / $\mu\text{moles}$
<b>T-PEG</b>	5 mg	9.0
Formic acid (26.5 M)	3.4 $\mu\text{L}$	90
Deuterated methanol	To suitable volume in NMR tube	-

The methods via which the experiments were performed were as follows:

Reaction solutions comprising of triazabutadiene (**T-PEG** or **T8**) and formic acid were transferred into an NMR tube and the tube was kept in the dark until  $^1\text{H-NMR}$  and COSY spectra could be recorded. The specified quantities of **Res1** (i.e. 0 or 1 equiv) were then delivered to the reaction solutions by quickly pipetting the reaction solutions from the NMR tubes into sample vials containing **Res1**, pipetting upwards and downwards several times to rapidly dissolve **Res1**. The resulting solutions were then transferred back into their respective NMR tubes, and additional deuterated methanol was added to these tubes if required. The NMR tubes were then, again, kept in the dark until another set of  $^1\text{H-NMR}$  and COSY spectra could be recorded. The samples were then UV irradiated for 5 min using a 7 W 365 nm UV light bulb at 0 °C before being incubated at room temperature for 30 min (with the exception of the sample in **Figure 6.13**, which was kept on ice until a final set of  $^1\text{H-NMR}$  and COSY spectra could be recorded). A final set of  $^1\text{H-NMR}$  and COSY spectra were then recorded.

Control experiments were also performed in which these solutions were prepared without triazabutadiene (i.e. without **T8** or **T-PEG**) to illustrate that **Res1** did not photodegrade in response to the UV-irradiation treatment.

### 8.6.3 Bio-conjugation of triazabutadienes to redox proteins

#### 8.6.3.1 The usage of **T8** in maleimide ligation to DsbA mutants and subsequent ligation to resorcinol probes

Two DsbA mutants, DsbA<sub>c-term</sub> and DsbA<sub>middle</sub> (see **Section 4.2.4.2**), were exchanged into pH 7.2 buffer (20 mM sodium phosphate, 200 mM NaCl) using a PD SpinTrap™ G-25 column and concentrated to 120 μM using a 10 kDa centrifugal protein concentrator. Tris(2-carboxyethyl)phosphine (TCEP) (100 equiv), was added by delivering a suitable volume of a 100 mM TCEP hydrochloride stock solution (which had been pre-neutralised using an NaOH solution), and the resultant solution was left at room temperature in the dark for 20 min. After this time, the protein solutions were split to give four samples of each protein, and suitable volumes of a 25 mM stock of **T8** were added, such that either 1 or 10 equiv of **T8** were delivered to each sample. The concentration of DMSO was then made up to 10% through the addition of additional DMSO. The reaction was allowed to proceed at room temperature in the dark for 30 min, after which time the reaction solutions were exchanged into pH 7.55 phosphate buffer (20 mM phosphate, 200 mM NaCl + 5% DMSO) using PD MiniTrap™ G-25 desalting columns. This yielded samples of DsbA labelled with an intact **T8** moiety.

To these solutions were added either 0 or 10 equiv of **Res1** from a suitably concentrated DMSO stock. The solutions were then exposed to UV light for 5 min at 0 °C using a 7 W 365 nm UV light bulb before being incubated at room temperature for 30 min. These reaction steps are shown in **Scheme 6.14**, and the samples were analysed using a 15% polyacrylamide SDS-PAGE gel and LC-MS. Bands from the 15% SDS-PAGE gel were also excised and submitted to the Bioscience Technology Facility at University of York for digestion experiments with Trypsin and endoproteinase AspN, which were kindly performed by Dr Adam A. Dowle and Dr Chris J. Taylor. When preparing samples to run on the SDS-PAGE gel, the DsbA samples were mixed in a 4:1 ratio with a 5 × concentrated buffer that was both dye and reducing-agent free (10% SDS, 20% glycerol, 200 mM Tris-HCl pH 6.8). The samples were not boiled prior to being run on the gel.

These reaction steps were then repeated (only for DsbA<sub>middle</sub> samples) with variations in how TCEP was used. A set of experiments were performed in which no TCEP was used (*no TCEP*), and a set of experiments were performed in which TCEP was removed using a PD MiniTrap™ G-25 desalting column (with the resultant solution being reconcentrated back to 120 μM using a 10 kDa centrifugal protein concentrator) prior to the splitting of the samples and the addition of **T8** (*TCEP-removed*). Excess equivalents of **T8** were removed prior to the introduction of resorcinol probes using a PD MiniTrap™ G-25 desalting column (with the resultant solution being reconcentrated back to ~ 120 μM using a centrifugal protein concentrator). In addition, a broader range of resorcinol-functionalised

probes were used to react with diazonium functionalities in these experiments; 0 or 10 equiv of either **Res1**, **Res6** or resorcinol were delivered after excess **T8** had been removed. These experiments were analysed using a 15% polyacrylamide SDS-PAGE gel. When preparing samples to run on the SDS-PAGE gel, the DsbA samples were mixed in a 4:1 ratio with a 5 × concentrated buffer that was both dye and reducing-agent free (10% SDS, 20% glycerol, 200 mM Tris-HCl pH 6.8). The samples were not boiled prior to being run on the gel.

### 8.6.3.2 The usage of **T14** in amide bond formation ligation to CjX183-D

#### 8.6.3.2.1 The functionalisation of CjX183-D variants with **T14** and further derivatisation with **Res6**

The chemical steps of the following methodology are illustrated in **Figure 6.27**. To 100 µL of a 50 µM solution of either WT CjX183-D or CjX183-D R51K in pH 7.5 buffer (25 mM sodium phosphate) was added 15 equiv of **T14** (via the delivery of 5 µL of a 15 mM stock of **T14** in anhydrous DMSO). The resultant solution was then incubated at room temperature in the dark for 1 hour before the labelled CjX183-D was buffer exchanged into fresh pH 7.5 buffer (25 mM sodium phosphate) using 3 kDa molecular weight cut-off centrifugal protein concentrators (to remove the majority of the excess **T14**) and concentrated back to a volume of ~ 100 µL. To the resultant solution was added 15 equiv **Res6** (via the delivery of 5 µL of a 15 mM stock of **Res6** in DMSO). The sample was then subjected to 4 min of UV irradiation at 0 °C using a 7 W 365 nm UV light bulb, after which the sample was incubated overnight at room temperature. The samples were then exchanged into HPLC grade water and analysed via MS.

#### 8.6.3.2.2 Screening conditions for the labelling the lysine residue of CjX183-D R51K with **T14**

**Table 6.7** tabulates the different conditions screened in this trial. PLP-treated CjX183-D R51K (i.e. CjX183-D R51K in which the *N*-terminal glycine residue has been converted to a glyoxylamide) was prepared as described in **Section 8.4.3**. To 100 µL of a 50 µM solution of PLP-treated CjX183-D R51K in pH 7.5 buffer (25 mM sodium phosphate) or pH 8 buffer (prepared via the titration of a pH 7.5 25 mM sodium phosphate to pH 8 using a saturated NaHCO<sub>3</sub> solution) was added 20 equiv of **T14** (via the delivery of 6.7 µL of a 15 mM stock of **T14** in anhydrous DMSO). Reactions were then incubated in the dark for either 1 or 2 hours, either at room temperature or at 37 °C. After reaction completion, samples were exchanged into HPLC-grade water using PD SpinTrap™ G-25 columns, whereafter samples were analysed via MS.

### 8.6.3.2.3 Preparation and purification of triazabutadiene-labelled CjX183-D R51K

PLP-treated CjX183-D R51K (i.e. CjX183-D R51K in which the *N*-terminal glycine residue has been converted to a glyoxylamide) was prepared as described in **Section 8.4.3**. To 520  $\mu\text{L}$  of a 50  $\mu\text{M}$  solution of PLP-treated CjX183-D R51K in pH 8 buffer (prepared via the titration of a pH 7.5 25 mM sodium phosphate to pH 8 using a saturated  $\text{NaHCO}_3$  solution) was added 20 equiv of **T14** (via the delivery of 35  $\mu\text{L}$  of a 15 mM stock of **T14** in anhydrous DMSO). The resultant solution was then incubated in the dark for 1 hour, after which time imidazole was added such that the imidazole concentration reached 30 mM (this was achieved via the addition of 17  $\mu\text{L}$  of a 1 M solution of imidazole in the aforementioned pH 8 buffer), and triazabutadiene-labelled CjX183-D R51K was purified via nickel affinity chromatography using a His SpinTrap<sup>TM</sup> (Cytiva), followed by buffer exchange into a pH 7.5 buffer (25 mM sodium phosphate) using a PD MiniTrap<sup>TM</sup> G-25 desalting column, in order to remove imidazole. The triazabutadiene-labelled CjX183-D R51K was then concentrated back to  $\sim 500 \mu\text{L}$ . Two samples were taken for analysis via MS, and the remaining solution was aliquoted into 50  $\mu\text{L}$  or 100  $\mu\text{L}$  portions. These aliquots were then frozen using liquid  $\text{N}_2$  and stored in darkness at  $-80 \text{ }^\circ\text{C}$ .

Note that the purification using the His SpinTrap<sup>TM</sup> was performed using the methodology detailed in the a His SpinTrap<sup>TM</sup> (Cytiva) manual. The binding buffer was the pH 8 buffer described above + 30 mM imidazole, and the elution buffer was the pH 8 buffer described above + 800 mM imidazole.

## 8.6.4 Electrochemical experiments/procedures/electrode modification

### Electrochemical cell setup

With the exception of the attempted electro-grafting of **T8**-labelled DsbA<sub>middle</sub> via amperometry, and the attempted electro-grafting of triazabutadiene-labelled PLP-treated CjX183-D R51K via cyclic voltammetry (shown in **Figure S6**), the electrochemical experiments were conducted using the electrochemical cell setup described in **Section 8.1.5**.

The attempted electro-grafts using triazabutadiene-labelled redox proteins were performed using the electrochemical cell setup depicted below in **Figure 8.180**. A leak-free Ag/AgCl reference electrode was used when FTacV was not required, and a Ag/AgCl (3M NaCl) reference electrode, not housed in a Luggin capillary, was used for experiments where FTacV was required. The working electrode, platinum wire counter electrode and reference electrodes interface with each other and the electro-grafting solutions courtesy of the application of the electro-grafting solution as a droplet on top of the inverted working electrode. The working electrodes used in the amperometry electro-



grafting of T8-labelled DsbA<sub>middle</sub> were either GC or BDD electrodes (for details regarding these electrodes see **Section 8.1.5.2**). A PGE working electrode was used in the electro-grafting of triazabutadiene-labelled PLP-treated CjX183-D R51K via cyclic voltammetry (**Figure S6**).

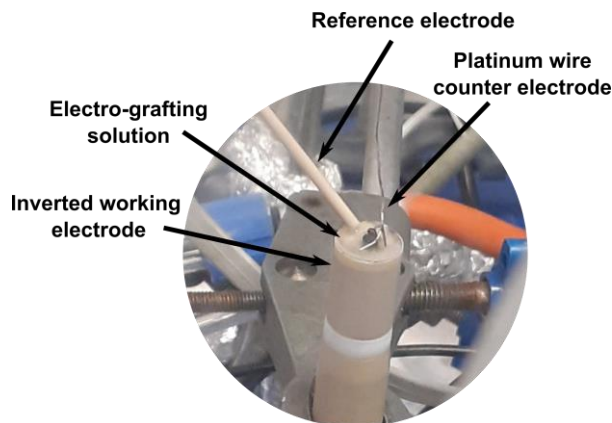


**Figure 8.180.** The electrochemical cell setup used for the attempted electro-grafting of triazabutadiene-labelled redox proteins.

#### Cleaning of electrode surfaces

Prior to electrochemical derivatisation, the GC disk electrodes (purchased from eDAQ) were cleaned using the following procedures. GC electrode surfaces were mechanically polished for 1–2 min using 1–5  $\mu\text{m}$  alumina slurry impregnated onto a WhiteFelt polishing pad (Buehler). Electrodes were then rinsed with Milli-Q water and sonicated in acetonitrile for 5 min.

Boron-doped diamond electrodes were polished for 1–2 min using nylon polishing pads (Buehler) impregnated with 1  $\mu\text{m}$  RS PRO Blue Diamond Paste (RS Components Ltd.) and for approximately 1 min using a 1/10  $\mu\text{m}$  RS PRO Gray Diamond Paste (RS Components Ltd.). The electrodes were then rinsed with Milli-Q water and sonicated in acetonitrile for 5 min.

PGE electrodes were freshly abraded with emery paper prior to use, leaving a streak of graphite on the paper.

#### General electrochemical experimental methods

The parameters used to record cyclic voltammograms can be found in the relevant figure captions, as can the conditions under which these experiments were performed. When samples were subjected to exposure to UV-irradiation, care was taken to not expose the electrode surface to the UV-irradiation (i.e. samples were irradiated in a separate vessel, then transferred into the electrochemical cell setups afterwards).

### 8.6.4.1 Specialised electrochemical experiment methods

#### Electro-grafting of T8-labelled DsbA<sub>middle</sub> using amperometry

The method, conditions and parameters used for the electro-grafting via amperometry experiments (which were attempted for T8-labelled DsbA<sub>middle</sub>) are as follows. Both a BDD and a GC electrode were freshly polished, and a CV, an FTacV experiment and an impedance experiment were recorded at 25 °C over the range of 0.2 → -0.6 V vs SHE in either a blank pH 7.2 buffer (20 mM phosphate, 200 mM NaCl) or a 700 μM T8-labelled DsbA<sub>middle</sub> solution (in pH 7.2, 20 mM phosphate, 200 mM NaCl buffer). The blank buffer / T8-labelled DsbA<sub>middle</sub> solution was then taken and subjected to UV irradiation for 4 min at 0 °C using a 7 W 365 nm UV light bulb. The UV-treated solution was then reapplied to the surface of the inverted working electrode as a droplet (with care being made to make sure that all the electrodes interface with the droplet). Amperometric traces were then recorded, holding at -0.56 V vs SHE for 10 min. After this time the electro-grafting solution was replaced with blank pH 7.2 buffer (regardless of whether T8-labelled DsbA<sub>middle</sub> or a blank electro-grafting solution had been used in the previous steps) and a CV, an FTacV experiment and an impedance experiment were recorded. The parameters used in the FTacV experiments are shown below in **Figure 8.181**. Impedance readings were recorded using the “18kHz many data points” predefined waveform in the “pot” software.

Single Frequency CV

<b>Scan control</b> Rate (mV/s): 16.76    Direction (a/c): a Scans: 1 <input type="checkbox"/> No DC Scan	<b>Potentials</b> Start (mV): -700.00    Max (mV): 200.00 End (mV): -700.00    Min (mV): -700.00
<b>Data Control</b> Data points: 4194304	<b>Pre waveform control</b> Initial (mV): -700.00    Initial (ms): 5.00 Pre (mV): 0.00    Pre (ms): 0.00
<b>Perturbation control</b> Freq (Hz): 8.92    Amp (mV): 150.00 Type: Sine    n(1-max): 1 User E(t) file: <input type="text"/> <input type="button" value="Browse"/>	<b>Post waveform control</b> Post (mV): 0.00    Post (ms): 0.00
<input type="button" value="Apply"/> <input type="button" value="Save As"/> <input type="button" value="OK"/> <input type="button" value="Cancel"/>	

**Figure 8.181.** Parameters used to record the FTacV experiments involving DsbA<sub>middle</sub>. The potentials are vs the Ag/AgCl (3M NaCl) reference electrode.

**Electro-grafting/immobilisation experiments using triazabutadiene-labelled PLP-treated CjX183-D R51K**

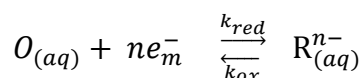
PLP-treated CjX183-D R51K samples were prepared as described in **Section 8.4.3**. Samples of purified triazabutadiene-labelled PLP-treated CjX183-D R51K were prepared as described in **Section 8.6.3.2.3**. These samples were subjected to a series of conditions/treatments, and these are reported in **Table 6.8**. Note that NaCl was added to the protein samples via the addition of an appropriate volume of a 6 M NaCl solution, such that the NaCl concentration of protein solutions reached 150 mM; after this NaCl addition, the buffer the proteins were in was pH 7.5 buffer (25 mM sodium phosphate + 150 mM NaCl). Electro-grafting was performed using the conditions reported in the caption of **Table 6.8**, using the setup depicted in **Figure 8.180**, with a leak-free Ag/AgCl reference electrode, an inverted PGE working electrode and a platinum wire counter electrode.

## Appendix 1. The connection of electrochemistry to thermodynamics

### The connection of electrochemistry to thermodynamics

Consider the redox couple defined in **Reaction 1**. Once an electrode is introduced to a solution of  $O_{(aq)}$  and/or  $R_{(aq)}^{n-}$ , the system will move towards its electrochemical equilibrium, with charge moving between species in solution and the electrode surface. Once electrochemical equilibrium has been established there is no further net movement of charge.<sup>247</sup>

#### Reaction 1



$O_{(aq)}$  = oxidised species of the solution phase redox couple

$e_m^-$  = an electron. The (m) denotes that the electron comes from the electrode.

$n$  = number of electrons transferred in redox couple.

$R_{(aq)}^{n-}$  = reduced species of the solution phase redox couple.

$k_{red}$  = rate constant for the reduction of  $O_{(aq)}$ .

$k_{ox}$  = rate constant for the oxidation of  $R_{(aq)}^{n-}$ .

Electrochemical equilibrium differs from chemical equilibrium in that while chemical equilibrium represents a balance between the chemical potentials of the reactants and products, electrochemical equilibrium represents a balance between the electrochemical potentials of the reactants and products. The electrochemical potential ( $\bar{\mu}_j$ ) of a species is defined according to **Equation 20**.<sup>247</sup>

$$\bar{\mu}_j = \mu_j + Z_j F \Phi_{phase} \quad \text{Equation 20}$$

$\bar{\mu}_j$  = electrochemical potential of species j / J mol<sup>-1</sup>.

$\mu_j$  = chemical potential of species j / J mol<sup>-1</sup>.

$Z_j$  = charge on species j / multiples of the elementary charge  $e$ .

$F$  = the Faraday constant / C mol<sup>-1</sup>.

$\Phi_{phase}$  = potential of the phase species j is in / J C<sup>-1</sup>.

where

$$\mu_j = \mu_j^0 + RT \ln([j]\gamma_j)$$

$\mu_j$  = chemical potential of species j / J mol<sup>-1</sup>.

$\mu_j^0$  = standard chemical potential of species j / J mol<sup>-1</sup>.

$R$  = gas constant / J mol<sup>-1</sup> K<sup>-1</sup>.

$T$  = temperature / K.

$[j]$  = concentration of species j / mol dm<sup>-3</sup>.

$\gamma_j$  = activity coefficient of species j (dimensionless).

At electrochemical equilibrium a balance between the electrochemical potentials of all the species in the redox couple defined in **Reaction 1** will have been reached, as described by **Equation 21**.<sup>247</sup> Note that the equation below can be applied to species immobilised on the electrode surface as well:  $\bar{\mu}_{O(aq)}$  and  $\bar{\mu}_{R(aq)}^{n-}$  would just instead be used as terms for the electrochemical potential oxidised/reduced species on the surface of the electrode.

$$\bar{\mu}_{O(aq)} + n\bar{\mu}_{e_m^-} = \bar{\mu}_{R(aq)}^{n-} \quad \text{Equation 21}$$

$\bar{\mu}_{O(aq)}$  = electrochemical potential oxidised species in solution / J mol<sup>-1</sup>.

$\bar{\mu}_{e_m^-}$  = electrochemical potential of the electrons from the electrode / J mol<sup>-1</sup>.

$\bar{\mu}_{R(aq)}^{n-}$  = electrochemical potential of the reduced species in solution / J mol<sup>-1</sup>.

$n$  = the number of electrons transferred in the redox couple.

Expanding **Equation 21** using **Equation 20** yields the following equation,

$$\mu_{O(aq)}^0 + n\mu_{e_m^-} + RT \ln([O_{(aq)}]\gamma_{O(aq)}) - \mu_{R(aq)}^{0n-} - RT \ln([R_{(aq)}^{n-}]\gamma_{R(aq)}) = nF(\phi_m - \phi_s)$$

$\mu_{O(aq)}^0$  = standard chemical potential oxidised species in solution / J mol<sup>-1</sup>.

$n$  = the number of electrons transferred in the redox couple.

$\mu_{e_m^-}$  = chemical potential of the electrons from the electrode / J mol<sup>-1</sup>.

$R$  = gas constant / J mol<sup>-1</sup> K<sup>-1</sup>.

$T$  = temperature / K.

$[O_{(aq)}]$  = concentration of oxidised species in solution / mol dm<sup>-3</sup>.

$\gamma_{O(aq)}$  = activity coefficient of oxidised species in solution (dimensionless).

$\mu_{R(aq)}^{0n-}$  = standard chemical potential of the reduced species in solution / J mol<sup>-1</sup>.

$[R_{(aq)}^{n-}]$  = concentration of reduced species in solution / mol dm<sup>-3</sup>.

$\gamma_{R(aq)}^{n-}$  = activity coefficient of reduced species in solution (dimensionless).

$F$  = the Faraday constant / C mol<sup>-1</sup>.

$\phi_m$  = potential of the electrode / J C<sup>-1</sup>.

$\phi_s$  = potential of the solution / J C<sup>-1</sup>.

This simplifies to **Equation 22**,

$$\frac{-\Delta\mu_{(O/R)}^0}{nF} - \frac{RT}{nF} \ln\left(\frac{[R_{(aq)}^{n-}]\gamma_R}{[O_{(aq)}]\gamma_O}\right) = \phi_m - \phi_s \quad \text{Equation 22}$$

Where

$$\Delta\mu_{(O/R)}^0 = \mu_{R_{(aq)}^{n-}}^0 - \mu_{O_{(aq)}}^0 - n\mu_{e_m^-}$$

$\Delta\mu_{(O/R)}^0$  = standard change in the chemical potentials of the redox couple / J mol<sup>-1</sup>.

$\mu_{O_{(aq)}}^0$  = standard chemical potential oxidised species in solution / J mol<sup>-1</sup>.

$\mu_{e_m^-}$  = chemical potential of the electrons from the electrode / J mol<sup>-1</sup>.

$\mu_{R_{(aq)}^{n-}}^0$  = standard chemical potential of the reduced species in solution / J mol<sup>-1</sup>.

As can be seen from the equation above, once the system has moved to its electrochemical equilibrium a net charge separation will have developed between the electrode and the solution at the electrode/solution interface: a potential difference ( $\phi_m - \phi_s$ ) known as an electrode potential, as defined in **Equation 23**.<sup>247</sup>

$$E_{(O/R)} = \phi_m - \phi_s \quad \text{Equation 23}$$

$E_{(O/R)}$  = The electrode potential for the O/R redox couple / J C<sup>-1</sup>.

$\phi_m$  = potential of the electrode / J C<sup>-1</sup>.

$\phi_s$  = potential of the solution / J C<sup>-1</sup>.

To allow a potential difference to be measured, a tiny test current has to be allowed to flow between two points, passing through a digital voltmeter. This necessitates the introduction of (as a minimum) a second electrode, to complete an external circuit. The measured potential difference will be the difference between the electrode potentials of the electrodes (i.e. the difference between the  $\phi_m - \phi_s$  values for both of the electrode/solution interfaces). If the electrode potential of one of the electrodes is constant that electrode can be used as a reference electrode. The electrode interacting with the redox couple of interest ( $O_{(aq)}$  and  $R_{(aq)}^{n-}$ ) is referred to as the working electrode. The measured potential difference is now referred to as an electrode potential, and can be expressed by **Equation 24**.<sup>247</sup>

$$\begin{aligned} E_{measured} &= (\phi_m - \phi_s)_{working} - (\phi_m - \phi_s)_{Reference} \\ &= E_{working} - E_{Reference} \end{aligned} \quad \text{Equation 24}$$

$E_{measured}$  = potential difference measured / J C<sup>-1</sup>.

$E_{working}$  = electrode potential of the working electrode / J C<sup>-1</sup>.

$E_{Reference}$  = electrode potential of the reference electrode / J C<sup>-1</sup>.

$(\phi_m - \phi_s)_{working}$  = potential difference across the working electrode / J C<sup>-1</sup>.

$(\phi_m - \phi_s)_{Reference}$  = potential difference across the reference electrode / J C<sup>-1</sup>.

By taking the reference electrode as the standard hydrogen electrode (SHE), for which the electrode potential is conventionally defined as 0 V, the  $E_{Reference}$  term can be omitted, and thus

$$E_{\text{measured vs SHE}} = E_{\text{working}} = (\phi_m - \phi_s)_{\text{working}}$$

The amount of Gibbs energy lost from a reaction system is equal to the maximum amount of useful work that can be performed with that energy, as described by **Equation 25**.<sup>248</sup>

$$w = -\Delta_r G \quad \text{Equation 25}$$

$w$  = maximum work done / J.

$\Delta_r G$  = Gibbs free energy change of reaction / J.

In the context of electrochemical systems, this work is electrical work, as potential difference is the energy available per unit of charge ( $\text{J C}^{-1}$ ) and thus provides electrons with the energy to move. It stands to reason that the amount of electrical work that can be done is equal to the amount of energy available to each electron, and thus we arrive at **Equation 26**, which tells us that  $\Delta_r G = -nFE$ .<sup>248</sup>

$$w = nFE = -\Delta_r G \quad \text{Equation 26}$$

$w$  = maximum work done / J.

$\Delta_r G$  = Gibbs free energy change of reaction / J.

$F$  = the Faraday constant /  $\text{C mol}^{-1}$ .

$n$  = the number of electrons transferred in the redox couple.

$E$  = electrode potential /  $\text{J C}^{-1}$ .

This allows **Equation 22** to be expressed as **Equation 27**, which is perhaps the most famous equation in electrochemistry, the *Nernst equation*.<sup>247,248</sup>

$$E = E_{f(O/R)} - \left(\frac{RT}{nF}\right) \ln \left(\frac{[R_{(aq)}^{n-}]}{[O_{(aq)}]}\right) \quad \text{Equation 27}$$

$E$  = electrode potential /  $\text{J C}^{-1}$ .

$E_{f(O/R)}$  = formal potential of the redox couple /  $\text{J C}^{-1}$ .

$R$  = gas constant /  $\text{J mol}^{-1} \text{K}^{-1}$ .

$T$  = temperature / K.

$n$  = the number of electrons transferred in the redox couple.

$F$  = the Faraday constant /  $\text{C mol}^{-1}$ .

$[O_{(aq)}]$  = concentration of oxidised species in solution /  $\text{mol dm}^{-3}$ .

$[R_{(aq)}^{n-}]$  = concentration of reduced species in solution /  $\text{mol dm}^{-3}$ .

The formal potential ( $E_{f(O/R)}$ ) is defined by **Equation 28**. Note that  $-\frac{\Delta\mu_{(O/R)}^0}{nF} = -\frac{\Delta G_{(O/R)}^0}{nF} = E_{(O/R)}^0$ , as is outlined in **Equation 26**.<sup>247</sup>

$$E_{f(O/R)} = E_{(O/R)}^0 - \left(\frac{RT}{nF}\right) \ln \left(\frac{\gamma_{R(aq)}^{n-}}{\gamma_{O(aq)}}\right) \quad \text{Equation 28}$$

$E_{f(O/R)}$  = formal potential of the redox couple / J C<sup>-1</sup>.

$E_{(O/R)}^0$  = standard potential of the redox couple / J C<sup>-1</sup>.

$\gamma_{O(aq)}$  = activity coefficient of oxidised species in solution (dimensionless).

$\gamma_{R(aq)}^{n-}$  = activity coefficient of reduced species in solution (dimensionless).

$R$  = gas constant / J mol<sup>-1</sup> K<sup>-1</sup>.

$T$  = temperature / K.

$n$  = the number of electrons transferred in the redox couple.

$F$  = the Faraday constant / C mol<sup>-1</sup>.

Both  $E_{f(O/R)}$  and  $E_{(O/R)}^0$  depend on temperature and pressure, but  $E_{f(O/R)}$  will also depend on solution composition (i.e. electrolyte concentrations) as this can influence ion activities. As such,  $E_{f(O/R)}$  loses the thermodynamic generality of  $E_{(O/R)}^0$ , but when near-ideal behaviour is being exhibited the  $\ln \left(\frac{\gamma_{R(aq)}^{n-}}{\gamma_{O(aq)}}\right)$  term in **Equation 28** tends to zero (as both  $\gamma_{R(aq)}^{n-}$  and  $\gamma_{O(aq)} = 1$  for an ideal system) making  $E_{f(O/R)}$  approximate very well to  $E_{(O/R)}^0$ .<sup>247</sup>

As explained earlier, the immersion of the working electrode into a solution containing a redox couple will cause electrons to flow until an electrode potential has been established that reflects the position of electrochemical equilibrium of the redox process. Electrode potential, like other thermodynamic parameters, is a state function, and therefore the application of an electrode potential across the electrode/solution interface solicits a shift in the position of the electrochemical equilibrium of the solution-phase redox couple until it reflects the applied electrode potential. The shift in this position of electrochemical equilibrium in response to the applied potential necessitates the movement of charge (current) through the electrode. This current is recorded as signals that can inform the experimentalist about the properties of the system under assay. This is the basis of all voltammetric techniques.  $E_{f(O/R)}$  can be directly measured using voltammetric techniques, and due to the relationship between electrode potential and Gibbs energy (**Equation 26**), this allows the standard Gibbs energy change associated with a redox couple ( $\Delta G_{(O/R)}^0$ ) to be determined.



## Appendix 2. Specially written code package

The code package has been published online,<sup>578</sup> and is available for download.

### Using the code package

The code package is written in Rscript, and requires the user to have first downloaded R and the App RStudio to work. Several R libraries may also need to be downloaded, but RStudio will give an error message detailing which library is missing in this case.

The code package consists of a “Background codes” folder, and two Rscript files: “Bulk analysis platform no blanks.R” and “Bulk analysis platform.R”. One of these Rscripts can be used to produce a simulated plot of with a piece of data and match it up with the corresponding control experiments, whereas the other can be used to just produce the simulated plot. These Rscripts function like Apps, reading in data from elsewhere, and using the codes stored in “Background codes” folder to process that data.

It is easiest to have the data to be processed reside in the same directory as these Rscripts, but be systematically organised in their own folders. In the example below, all the LPMO data is stored in the “LPMO” folder, all the experiments performed with blank nanotube samples are stored in the “Nanotube blank” folder, and all the experiments performed using a unmodified glassy carbon electrode surface are stored in the “GC blank folder”.

This PC > Documents > A better system of organised files > Thesis > Code package for appendix

Name	Date modified	Type	Size
Background codes	29/01/2021 10:12	File folder	
GC blank	29/01/2021 10:31	File folder	
LPMO	29/01/2021 10:32	File folder	
Nanotube blank	29/01/2021 10:32	File folder	
Bulk analysis platform no blanks.R	06/09/2020 10:04	R File	2 KB
Bulk analysis platform.R	24/08/2020 10:42	R File	2 KB

All the data stored in the folders should have a systematic name. For example, the example piece of data stored in the “GC blank” folder is named “1 Example GC Blank 33\_4”. This denotes that this

experiment was experiment number 1 of the Example GC Blank dataset, was recorded at a scan rate of  $33 \text{ mV s}^{-1}$  and is scan 4 of the resultant cyclic voltammogram.

This PC > Documents > A better system of organised files > Thesis > Code package for appendix > GC blank

Name	Date modified	Type	Size
1 Example GC Blank 33_4	11/08/2020 08:54	File	68 KB

The LPMO and nanotube blank datasets are comparably named.

This PC > Documents > A better system of organised files > Thesis > Code package for appendix > LPMO

Name	Date modified	Type	Size
1 Example LPMO 33_4	11/08/2020 08:42	File	68 KB

This PC > Documents > A better system of organised files > Thesis > Code package for appendix > Nanotube blank

Name	Date modified	Type	Size
1 Example Nano blank 33_4	11/08/2020 08:50	File	68 KB

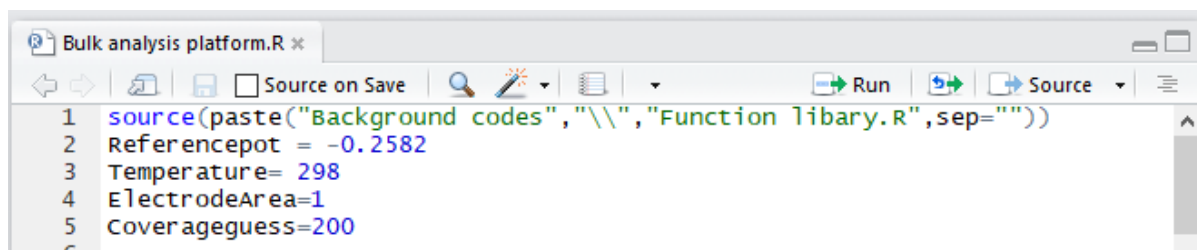
When processing real datasets, there could be more than one file in folder. Many different scan rates could be used, and there would be many different experiment numbers, but naming all the files systematically in this way allows the Rscript to find and read in each file automatically.

Here we'll be using the "Bulk analysis platform.R" Rscript, as we have blank experiments to pair up with the LPMO dataset.

This PC > Documents > A better system of organised files > Thesis > Code package for appendix

Name	Date modified	Type	Size
Background codes	29/01/2021 10:12	File folder	
GC blank	29/01/2021 10:31	File folder	
LPMO	29/01/2021 10:32	File folder	
Nanotube blank	29/01/2021 10:32	File folder	
Bulk analysis platform no blanks.R	06/09/2020 10:04	R File	2 KB
Bulk analysis platform.R	24/08/2020 10:42	R File	2 KB

Once opened in RStudio, in the first few lines of code can be seen parameters such as the reference electrode potential. This is set by the user. Here the reference electrode potential is - 0.2582 V vs SHE (i.e. to express potential vs SHE, a value of 0.2582 V needs to be added onto the voltage of the raw data). The surface area of the electrode (in  $\text{cm}^{-2}$ ) can also be set here by the user, as can the temperature (in K) at which the experiment was conducted.

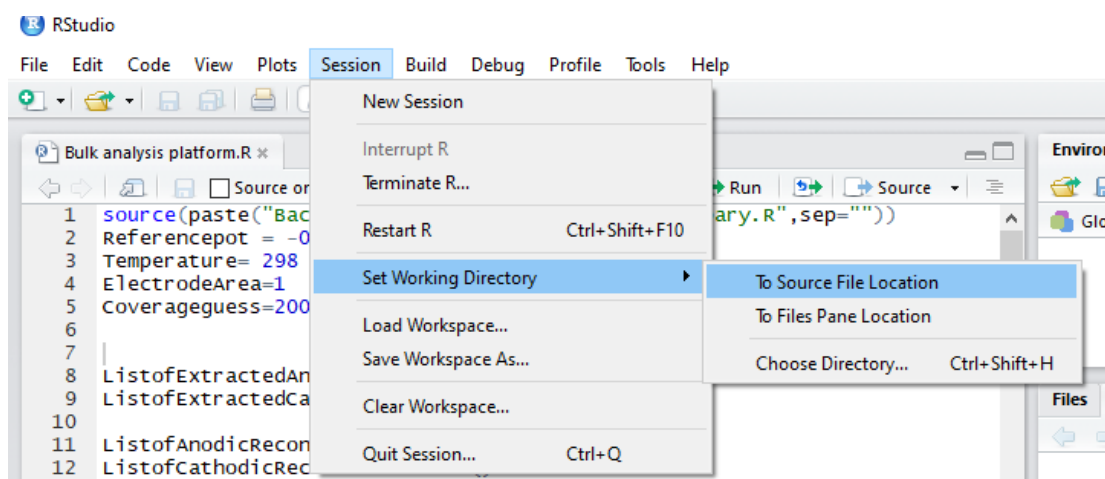


```

1 source(paste("Background codes", "\\ ", "Function library.R", sep=""))
2 Referencepot = -0.2582
3 Temperature= 298
4 ElectrodeArea=1
5 Coverageguess=200
6

```

The working directory should be set to the Source File Location.



Line 22 contains a vector of all the scan rates used in the datasets to be read in.

```

22 scanrates=c(113, 83, 63, 52, 213, 431, 1111, 2133, 4217, 815, 313, 153, 3333, 153, 1515)

```

As our example dataset only contains a single scan rate, 33  $\text{mV s}^{-1}$ , our vector could just be

```

22 scanrates=c(33)

```

As mentioned earlier, the systematic naming of data allows datasets to be recognised and read in automatically. To enable this, the lines of code that assemble the expected systematic names need to be modified to match the naming convention. In our case it can be done as follows:

```

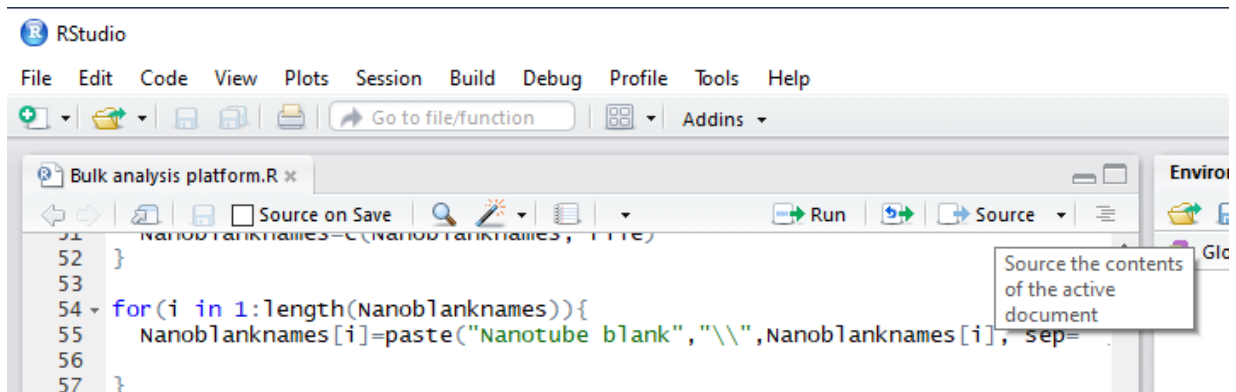
24 for(i in 1:length(Scanrates)){
25   file=paste(i, " Example LPMO ",Scanrates[i],"_4", sep="")
26   Filenames=c(Filenames, file)
27 }
28
29 for(i in 1:length(Filenames)){
30   Filenames[i]=paste("LPMO","\\",Filenames[i], sep="")
31 }
32 }

38 for(i in 1:length(Scanrates)){
39   file=paste(i, " Example GC blank ",Scanrates[i],"_4", sep="")
40   GCblanknames=c(GCblanknames, file)
41 }
42
43 for(i in 1:length(GCblanknames)){
44   GCblanknames[i]=paste("GC blank","\\",GCblanknames[i], sep="")
45 }
46 }

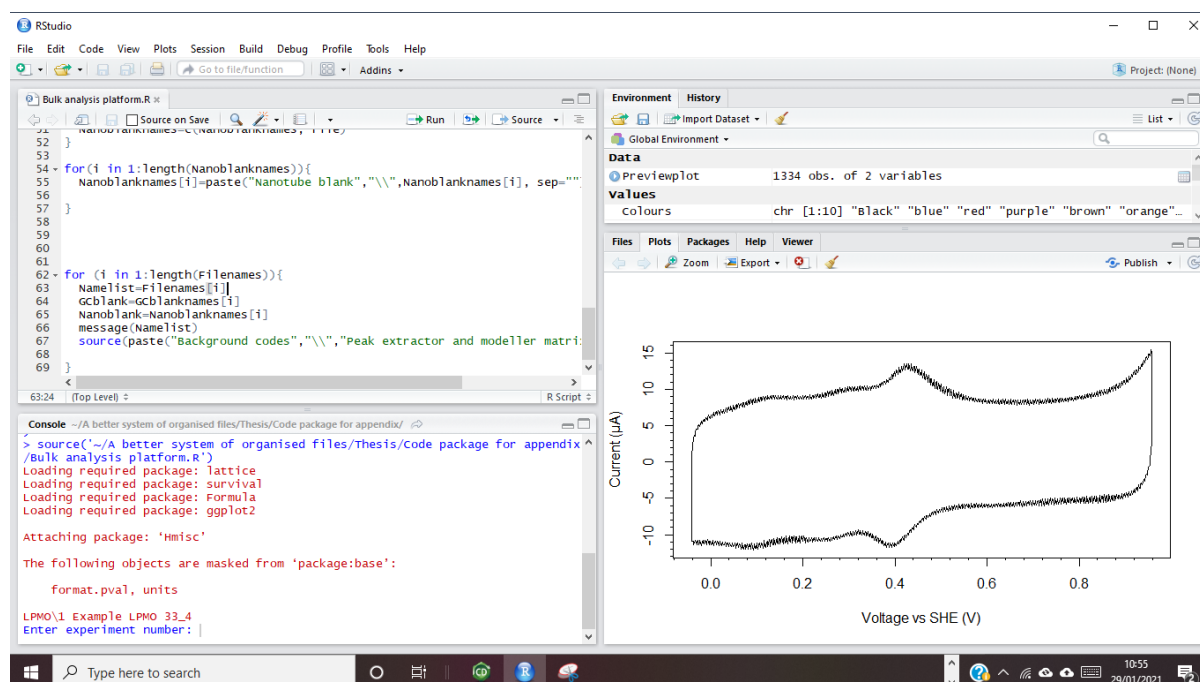
49 for(i in 1:length(Scanrates)){
50   file=paste(i, " Example Nano blank ",Scanrates[i],"_4", sep="")
51   Nanoblanknames=c(Nanoblanknames, file)
52 }
53
54 for(i in 1:length(Nanoblanknames)){
55   Nanoblanknames[i]=paste("Nanotube blank","\\",Nanoblanknames[i], sep="")
56 }
57 }

```

The RScript is now ready to be Sourced:



The first dataset will be read in, causing a plot to appear.



The name of the dataset is messaged to the user. The experiment number, scan rate and the number of redox couples to be extracted are then entered:

```

Console ~/A better system of organised files/Thesis/code package for appendix/
Loading required package: lattice
Loading required package: survival
Loading required package: Formula
Loading required package: ggplot2

Attaching package: 'Hmisc'

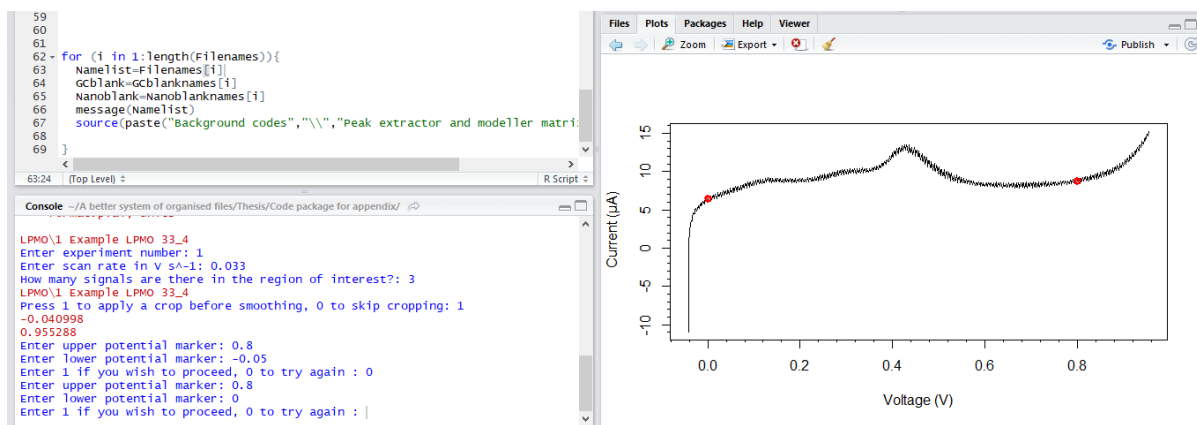
The following objects are masked from 'package:base':
  format.pval, units

LPMO\1 Example LPMO 33_4
Enter experiment number: 1
Enter scan rate in V s-1: 0.033
How many signals are there in the region of interest?: 3|

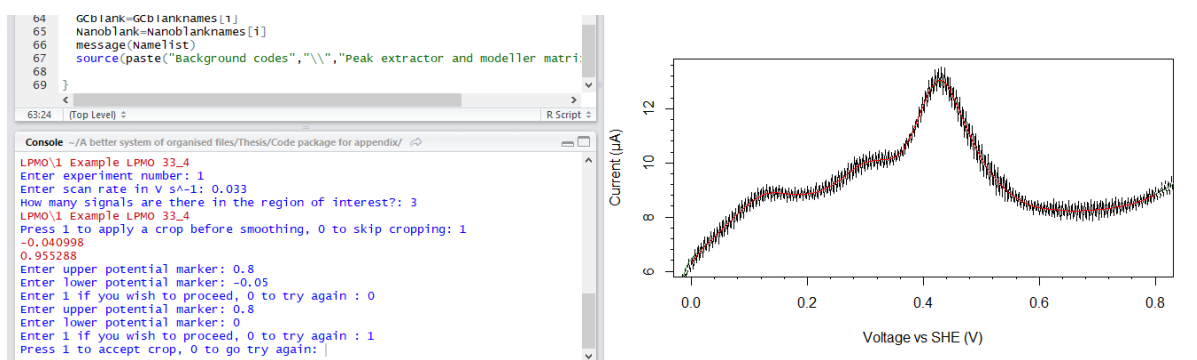
```

The forward scan of the cyclic voltammogram is then displayed, and the user is offered options for cropping the plot (to eliminate the extremities where capacitive background current behaves strangely).

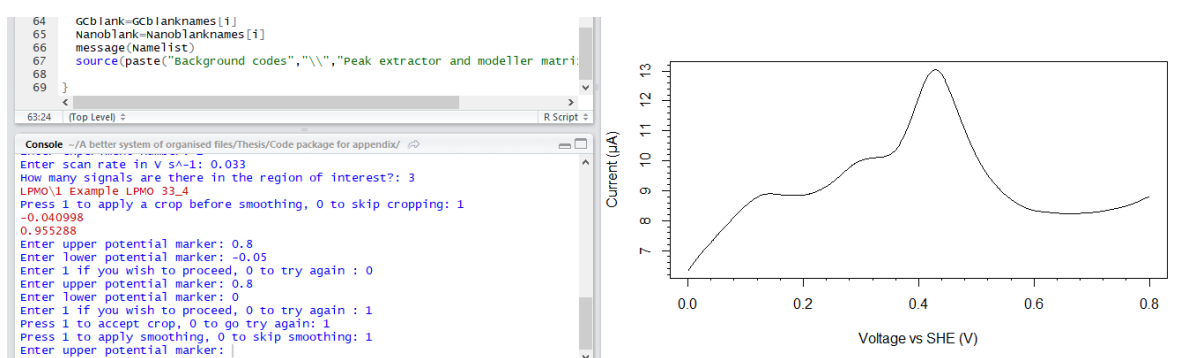
## Appendix 2



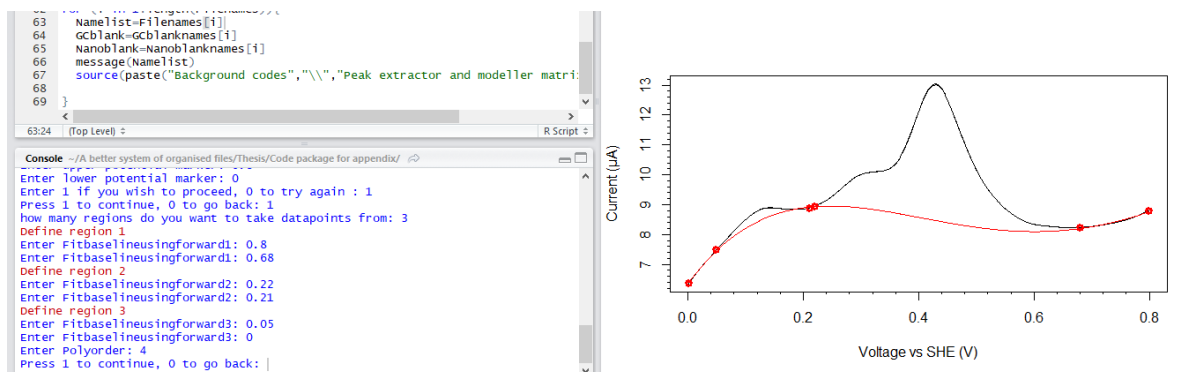
If cropping has been chosen, the cropped plot will appear.



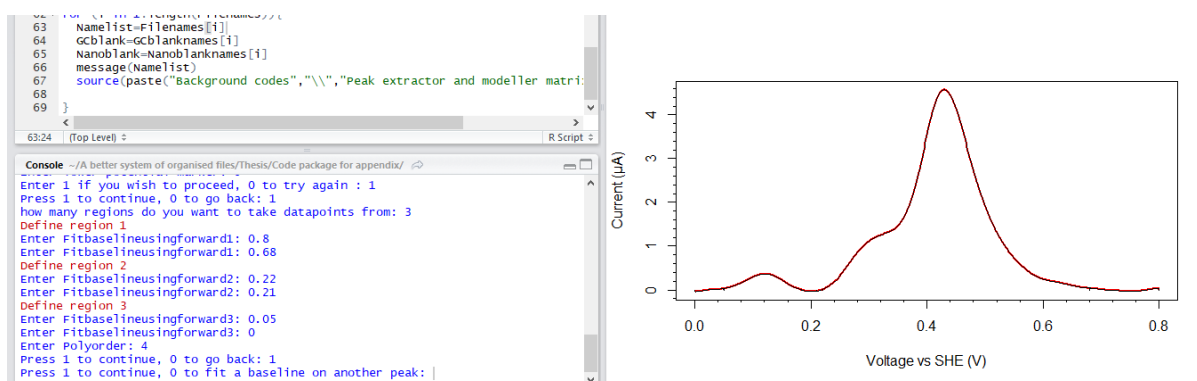
The user can then choose whether or not to smooth the dataset (which is good for removing random noise).



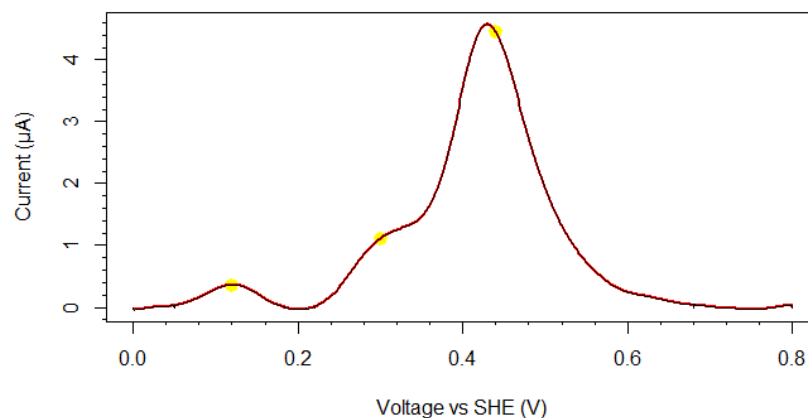
The user is then offered a series of options for fitting polynomials to isolate the redox signals from the background capacitive current.



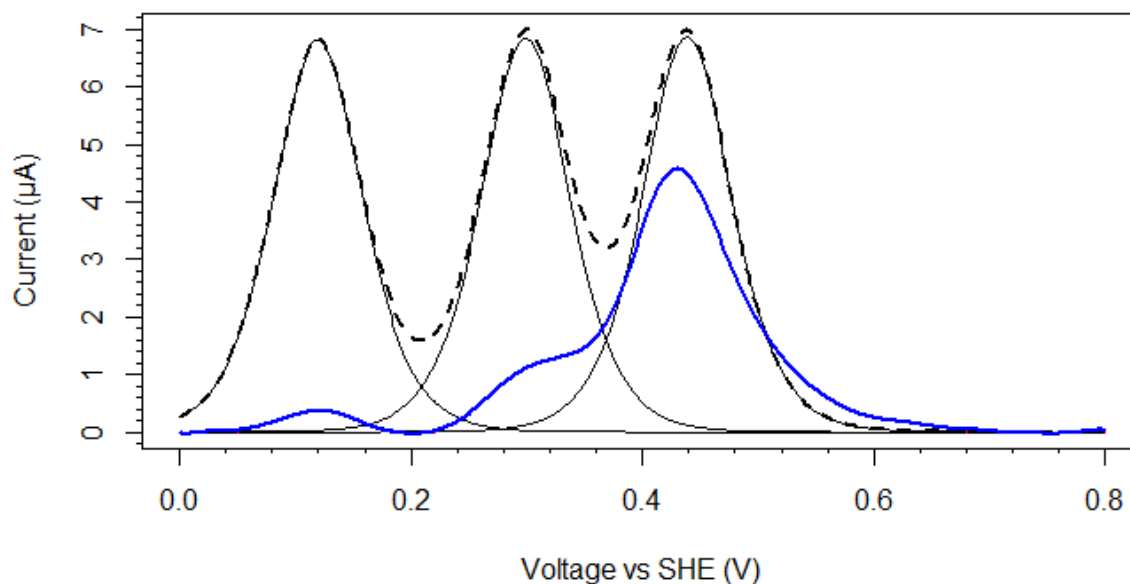
Once this has been done the isolated redox signals will appear. The user has an option here to try and fit a polynomial baseline elsewhere, in order to isolate any redox signals not found within the range of their original polynomial. Any signals isolated using this second polynomial will then be displayed along with those isolated with the first polynomial. In this case all the redox signals could be isolated using a single polynomial, so fitting another is not necessary.



Approximate locations of the peak maxima are then entered by the user, and these locations are highlighted in yellow on the plot. The user is offered the option to try again or continue.



Once starting locations for the peak maxima have been marked, simulated peaks will appear centred around these marked locations. The size of these peaks is based on the integral of the isolated redox signals – when only one signal is isolated the simulated peak will be a reasonable match for the isolated signal, but here the simulated peaks are too large, as the integral upon which they are based is for 3 signals.



The user does however have the option to scale these peaks so that they match the isolated signals a little better. This crude fit serves as the starting point for the optimisation process.

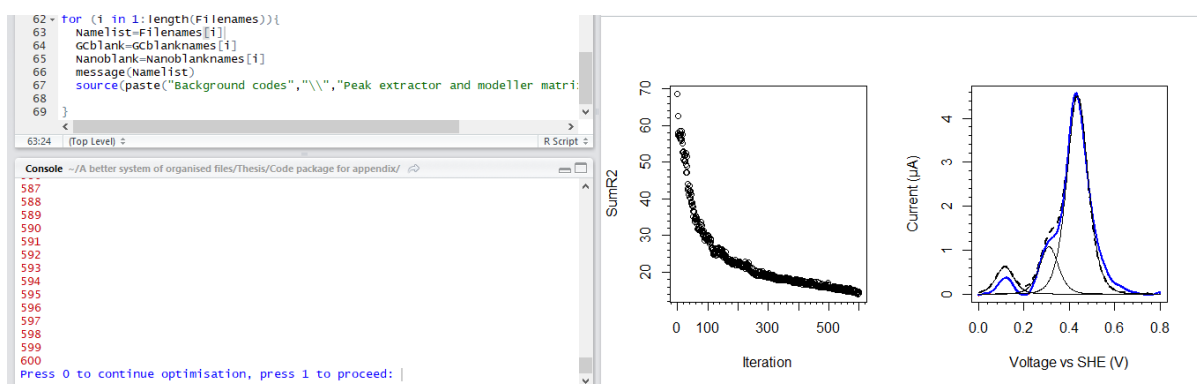


```

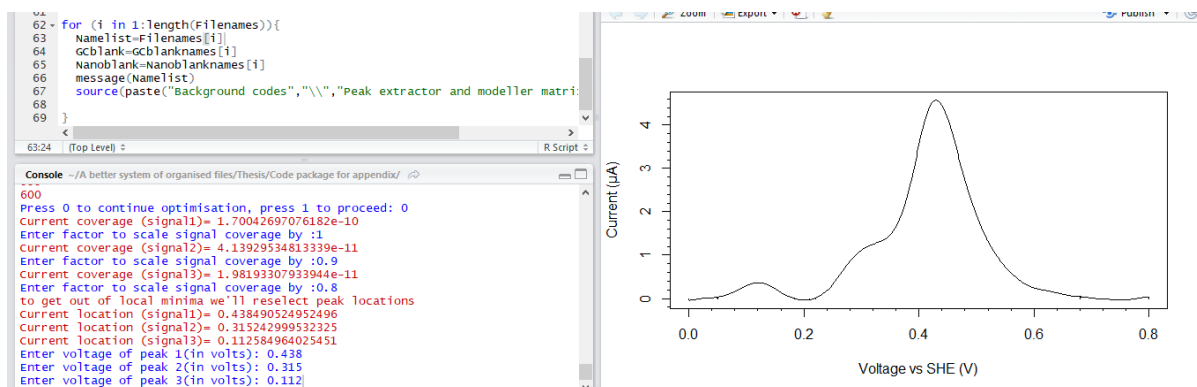
Current coverage (signal1)= 2.22083711725258e-10
Enter factor to scale signal coverage by :0.8
Current coverage (signal2)= 2.20608072444692e-10
Enter factor to scale signal coverage by :0.2
Current coverage (signal3)= 2.20608072444692e-10
Enter factor to scale signal coverage by :0.1

```

The optimisation undergoes 600 iterations, modifying the input variables randomly and slightly each time, accepting results that give a better fit and then randomly modifying the variables associated with that result. This causes the fit to gradually get better over subsequent iterations, tending towards a minimum residual<sup>2</sup> (Sum R<sup>2</sup>) value. As can be seen in the example below, the initial round of optimisation had not reached a minimum. The option to continue the optimisation was therefore selected.

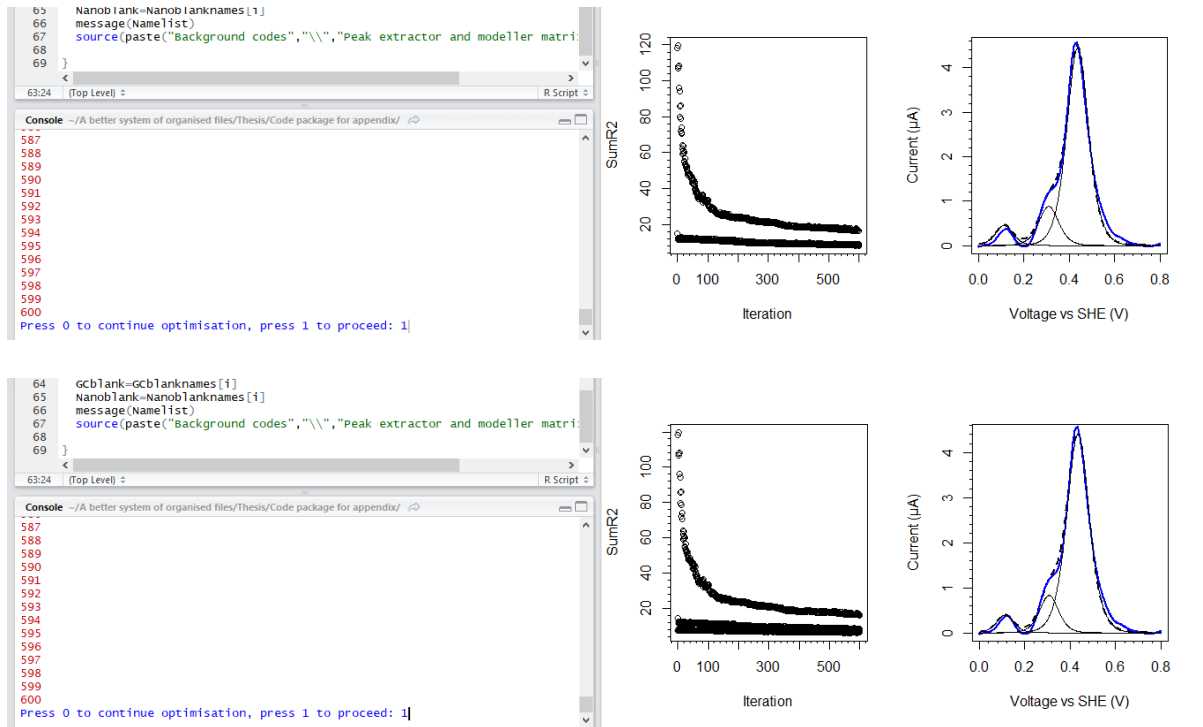


The location of the peaks can be re-specified in order to escape any local minima accidentally reached during the random optimisation process (such as two small simulated peaks combining to simulate one large signal). Options to adjust the scaling are also available if one peak is clearly too large or small.

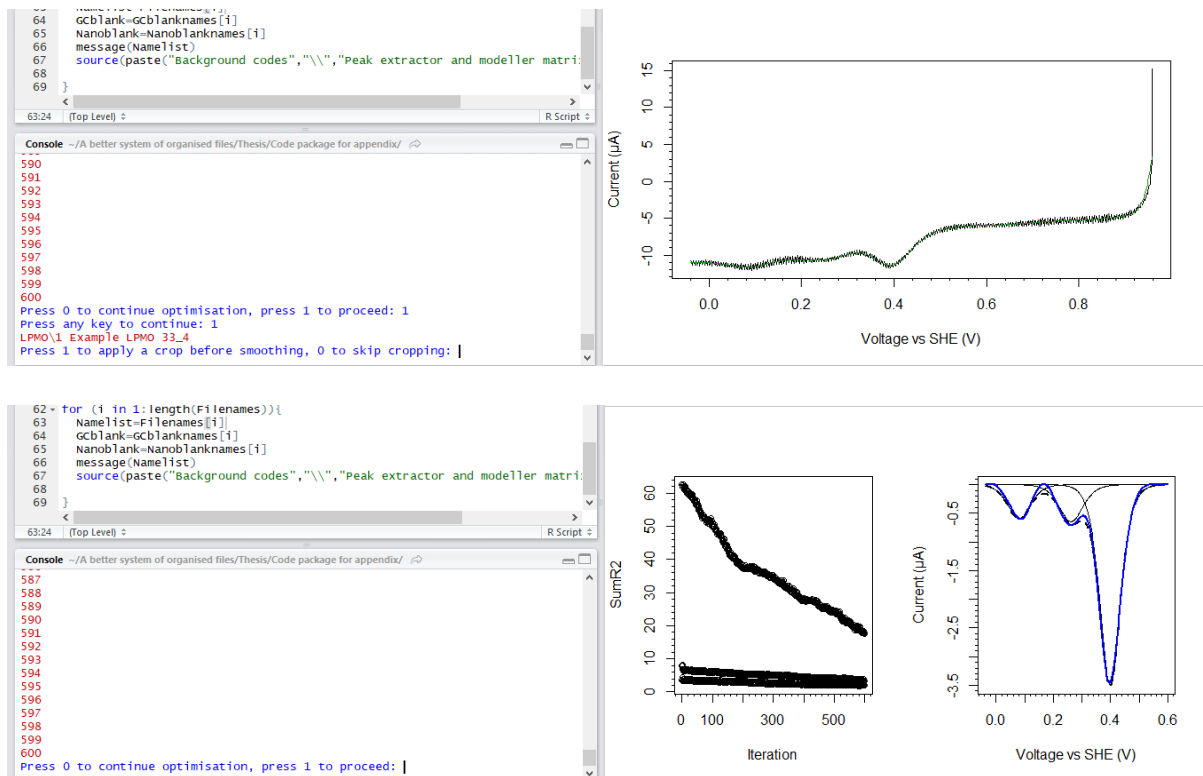


In the example below, the optimisation process was then ran again, twice. As can be seen below, the quality of the fits after the second and third rounds of optimisation are much improved.

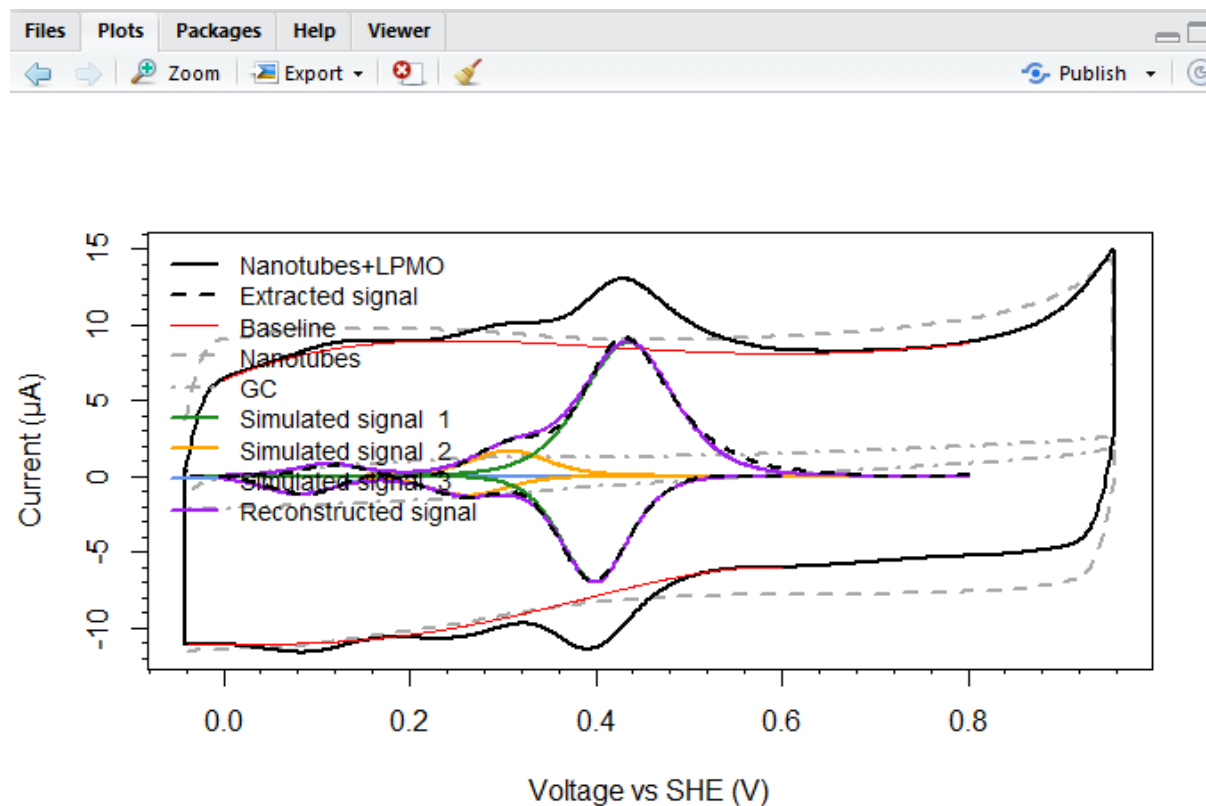
## Appendix 2



Once the user is satisfied with the simulation, the results can be accepted. The process then repeats for the reverse scan of the cyclic voltammogram:



Once the redox peaks in the reverse scan are satisfactorily simulated, the user can proceed to generate output files. The user specifies a name for the output files and has the option to apply smoothing to the output graph and modify the scaling of the extracted signals. A graph will then be generated.



When the user is happy with the appearance of the graph, they can accept the graph.

```
Console ~/A better system of organised files/Thesis/Code package for appendix/
594
595
596
597
598
599
600
Press 0 to continue optimisation, press 1 to proceed: 1
Press any key to continue: 1
Enter shorthand name for file: Example LPMO 33
Press 1 if you want to smooth the main plot, 0 to skip this: 1
LPMO\1 Example LPMO 33_4
LPMO\1 Example LPMO 33_4
Enter scale factor for extracted peaks?: 2
Press 1 to accept the graph, 0 to re-apply a scale factor: |
```

A new folder will have appeared in the directory with the datasets, with the name specified earlier by the user.

This PC > Documents > A better system of organised files > Thesis > Code package for appendix

Name	Date modified	Type	Size
Background codes	29/01/2021 10:12	File folder	
Example LPMO 33	29/01/2021 11:25	File folder	
GC blank	29/01/2021 10:48	File folder	
LPMO	29/01/2021 10:48	File folder	
Nanotube blank	29/01/2021 10:49	File folder	
Bulk analysis platform no blanks.R	06/09/2020 10:04	R File	2 KB
Bulk analysis platform.R	29/01/2021 10:54	R File	2 KB

Inside that folder are the outputted files, including xy datasets for all the simulated peaks, a csv file containing all the parameters used to simulate the redox signals, and a high quality pdf file of the graph.

This PC > Documents > A better system of organised files > Thesis > Code package for appendix > Example LPMO 33

Name	Date modified	Type	Size
Example LPMO 33 .pdf	29/01/2021 11:25	Adobe Acrobat D...	59 KB
Example LPMO 33 Extractedsignalbackw...	29/01/2021 11:23	Microsoft Excel C...	15 KB
Example LPMO 33 Extractedsignalforwar...	29/01/2021 11:23	Microsoft Excel C...	18 KB
Example LPMO 33 Signal 1 SimulatedAn...	29/01/2021 11:23	Microsoft Excel C...	19 KB
Example LPMO 33 Signal 1 SimulatedCat...	29/01/2021 11:23	Microsoft Excel C...	16 KB
Example LPMO 33 Signal 2 SimulatedAn...	29/01/2021 11:23	Microsoft Excel C...	19 KB
Example LPMO 33 Signal 2 SimulatedCat...	29/01/2021 11:23	Microsoft Excel C...	16 KB
Example LPMO 33 Signal 3 Baselinetoplo...	29/01/2021 11:23	Microsoft Excel C...	18 KB
Example LPMO 33 Signal 3 Baselinetoplo...	29/01/2021 11:23	Microsoft Excel C...	15 KB
Example LPMO 33 Signal 3 SimulatedAn...	29/01/2021 11:23	Microsoft Excel C...	20 KB
Example LPMO 33 Signal 3 SimulatedCat...	29/01/2021 11:23	Microsoft Excel C...	16 KB
Extraparameters.csv	29/01/2021 11:23	Microsoft Excel C...	1 KB
Fittedparameters.csv	29/01/2021 11:23	Microsoft Excel C...	1 KB
Example LPMO 33.RData	29/01/2021 11:23	R Workspace	402 KB

**Common problems**

**Reading in data.** If xy data is not reading in correctly, it is worth checking the “Process” function in the “Function library.R” file found in the “Background codes” folder. The processing function currently found there was written to take xy data generated using the “Export dataset as ASCII” function in IviumSoft software for windows (the data that was exported was originally recorded using a CompactStat potentiostat (Ivium technologies). If xy data has been generated in a different way, it may have a slightly different format regarding columns and row names, and the “Process” function will need to be modified accordingly to accommodate this.
























**Separating the cyclic voltammogram into two halves.** This code package has been written to process cyclic voltammograms that start and finish at their most negative potential. If the cyclic voltammogram being processed starts and finishes at its most positive potential, the contents of the “Chopf” and “Chopb” functions should be swapped in “Function library.R”. If the cyclic voltammogram starts and finishes at neither the most positive or most negative potential, the “Chopf” and “Chopb” functions will have to be suitably re-written in order to still split the cyclic voltammogram into anodic and cathodic sweeps.

## Advanced usage

The code has been set up above to simulate n=1 redox couples. It can be set to simulate n=2 (or more) redox couples quite easily however.

Inside the “Background codes” folder are the codes that actually make the “Bulk analysis platforms” work.

This PC > Documents > A better system of organised files > Thesis > Code package for appendix > Background codes

Name	Date modified	Type	Size
 Anodic peak modeller matrix new.R	07/08/2020 14:29	R File	2 KB
 Anodic peak modeller matrix rough.R	14/07/2020 13:04	R File	2 KB
 Anodic peak modeller matrix.R	14/07/2020 13:39	R File	2 KB
 Baseline plotter1 matrix backup.R	06/08/2020 11:58	R File	8 KB
 Baseline plotter1 matrix.R	07/08/2020 14:10	R File	7 KB
 Baseline plotter2 matrix.R	07/08/2020 13:50	R File	7 KB
 Cathodic peak modeller matrix new.R	07/08/2020 15:03	R File	2 KB
 Cathodic peak modeller matrix.R	14/07/2020 12:00	R File	2 KB
 Extrapeakextractbackward.R	07/08/2020 14:06	R File	5 KB
 Extrapeakextractforward.R	07/08/2020 11:58	R File	5 KB
 fitbaselineusingbackward matrix multipl...	04/08/2020 14:45	R File	2 KB
 fitbaselineusingbackward matrix.R	14/07/2020 11:16	R File	1 KB
 fitbaselineusingforward matrix alternativ...	16/07/2020 15:53	R File	1 KB
 fitbaselineusingforward matrix multiple.R	04/08/2020 13:01	R File	2 KB
 fitbaselineusingforward matrix.R	14/07/2020 09:40	R File	1 KB
 Function library.R	29/01/2021 10:12	R File	22 KB
 markersforward.R	10/07/2020 11:38	R File	1 KB
 Peak extractor and modeller matrix new ...	13/08/2020 13:16	R File	15 KB
 Peak extractor and modeller matrix new.R	11/08/2020 10:03	R File	15 KB
 Plot creator matrix no blank.R	13/08/2020 13:31	R File	8 KB
 Plot creator matrix.R	19/08/2020 13:30	R File	10 KB
 Plot points on backward scan matrix.R	05/08/2020 11:27	R File	1 KB
 Plot points on forward scan matrix.R	05/08/2020 11:27	R File	1 KB

If “Peak extractor and modeller matrix new.R” (or the “no blanks” version) is opened, a few lines of code can be found as comments (i.e. inactivated using a #). These lines, if activated, should allow the user to specify the n value for each redox couple the next time the “Bulk analysis platform” is used.

```

46 ParameterinputAnod=as.data.frame(ParameterinputAnod)
47 ParameterinputCath=as.data.frame(ParameterinputCath)
48
49 #for(i in 1:length(Numsig)){
50 # message(paste("Signal ", i))
51 #nforcouple=as.numeric(readline(prompt="n=?: "))
52 #ParameterinputAnod[1,i]=nforcouple
53 #parameterinputCath[1,i]=nforcouple
54 #}
55 #These hashed-out lines above would have to be used to simulate
56 #n=2 electrode redox processes
57
58 ParameterinputAnod[4,]=Coverageguess*(10^-12)
59 ParameterinputCath[4,]=Coverageguess*(10^-12)
60

```

Inside both the “Cathodic peak modeller matrix new.R”, and it’s anodic counterpart, are lines of code that set limits on how low the  $n_{app}$  value can go. When  $n = 1$ , a constraint on  $n_{app}$  preventing it from falling lower than 0.7 seems reasonable. If  $n = 2$  (or higher), a new constraint may be necessary. This could be specified by the user in a way chosen by them. An example is shown below, which could constrain  $n_{app}$  so that it has to be greater than  $0.7*n$ .

```

variablevector=variablevector+(variablevector*Randomnumbervector/300)

if(variablevector[2] < 0.7){
  variablevector[2] = 0.8
}
#the above means that the CathodicAppElectrons cannot fall below 0.7
#and it resets it to 0.8. If n=2 for the redox process this constraint
#could be modified so that CathodicAppElectrons couldn't fall below
#0.7*NumelectronsCathodic or something else appropriate
#to do this could write
|
#if(variablevector[2] < 0.7*ParameterinputCath[1,1]){
#  variablevector[2] = 0.8*ParameterinputCath[1,1]
#}

```

Should changes to the plotted graph be desired, changes can be made in the “Plot creator matrix” scripts.

## Appendix 3. Supplementary Figures and Tables

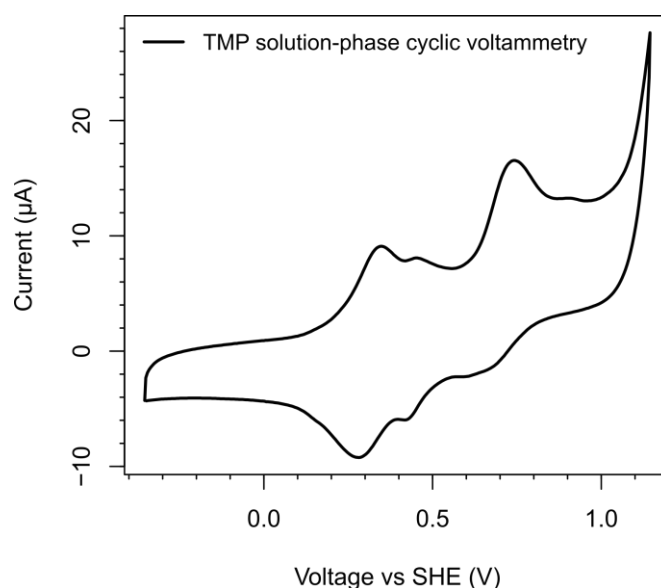


**Figure S1.** Cyclic voltammetry of *N,N,N',N'*-tetramethyl-*p*-phenylenediamine (TMP) at a concentration of 1 mM in pH 6 buffer (30 mM Na MES, 100 mM NaCl) at 293 K using a glassy carbon working electrode, a platinum wire counter electrode and a calomel reference electrode (saturated KCl). Scans recorded under a nitrogen atmosphere at a scan rate of 50 mV s<sup>-1</sup>.

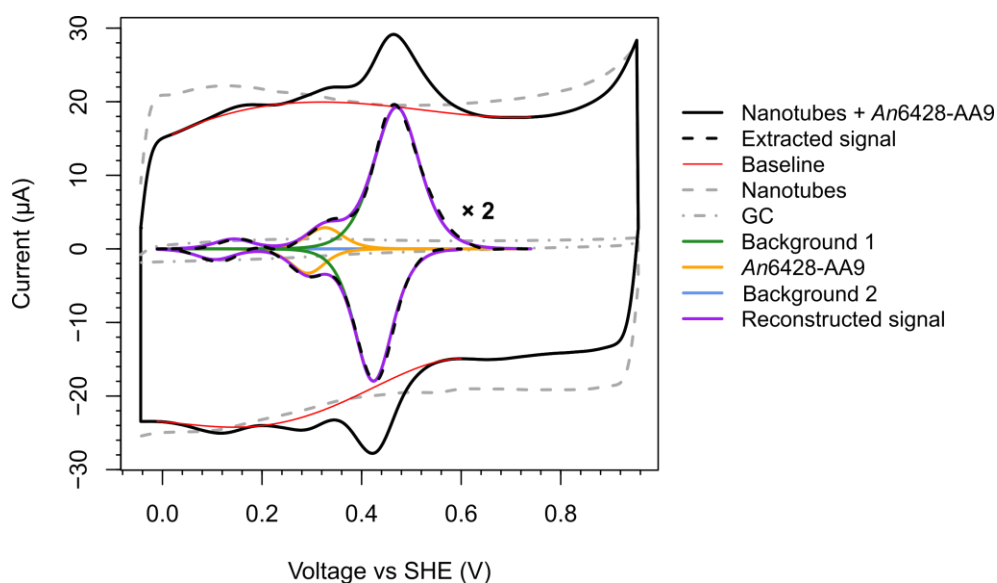


**Figure S2.** Cyclic voltammograms illustrating the absence of redox signals for unfunctionalized glassy carbon surfaces and GC surfaces functionalised with drop-cast nanotubes, and the presence of several redox signals upon that adsorption of An6428-AA9 onto the nanotube functionalised electrodes. Scans recorded at 33 mV s<sup>-1</sup> at 298 K under N<sub>2</sub> atmosphere in pH 6 buffer (20 mM sodium phosphate, 20 mM sodium acetate, 500 mM Na<sub>2</sub>SO<sub>4</sub>), using a glassy carbon working electrode, a platinum wire counter electrode and a saturated calomel reference electrode (saturated KCl). Redox signals were isolated and simulated using the specialised code package described in **Appendix 2**. Extracted signals are shown at twice their intensity.



**Table S1.** Parameters fitted to the baseline-subtracted signals in **Figure S2**, using **Equation 7**, showing that the suspected An6428-AA9 redox signal is characteristic of a 1 electron process. The exact surface area of the electrode cannot be easily determined due to the nature of the drop-cast MWCNT deposit. The surface area,  $A$ , has thus been set to unity, and the coverages,  $\Gamma$ , are therefore indicative of the total molar quantity of species present, not the molar quantity present per unit area.

Parameter	Background 1	An6428-AA9	Background 2
$A / \text{cm}^2$	1	1	1
$n_s$ cathodic	1	1	1
$n_s$ anodic	1	1	1
$n_{app}$ cathodic	1.01	1.12	1.00
$n_{app}$ anodic	0.83	1.04	1.00
Anodic peak potential / mV vs SHE	470	327	143
Cathodic peak potential / mV vs SHE	424	292	106
$E_{(O/R)}^f / \text{V vs SHE}$	448	310	125
$\Gamma$ cathodic / pmol $\text{cm}^{-2}$	288	47.3	23.4
$\Gamma$ anodic / pmol $\text{cm}^{-2}$	375	44.6	21.6

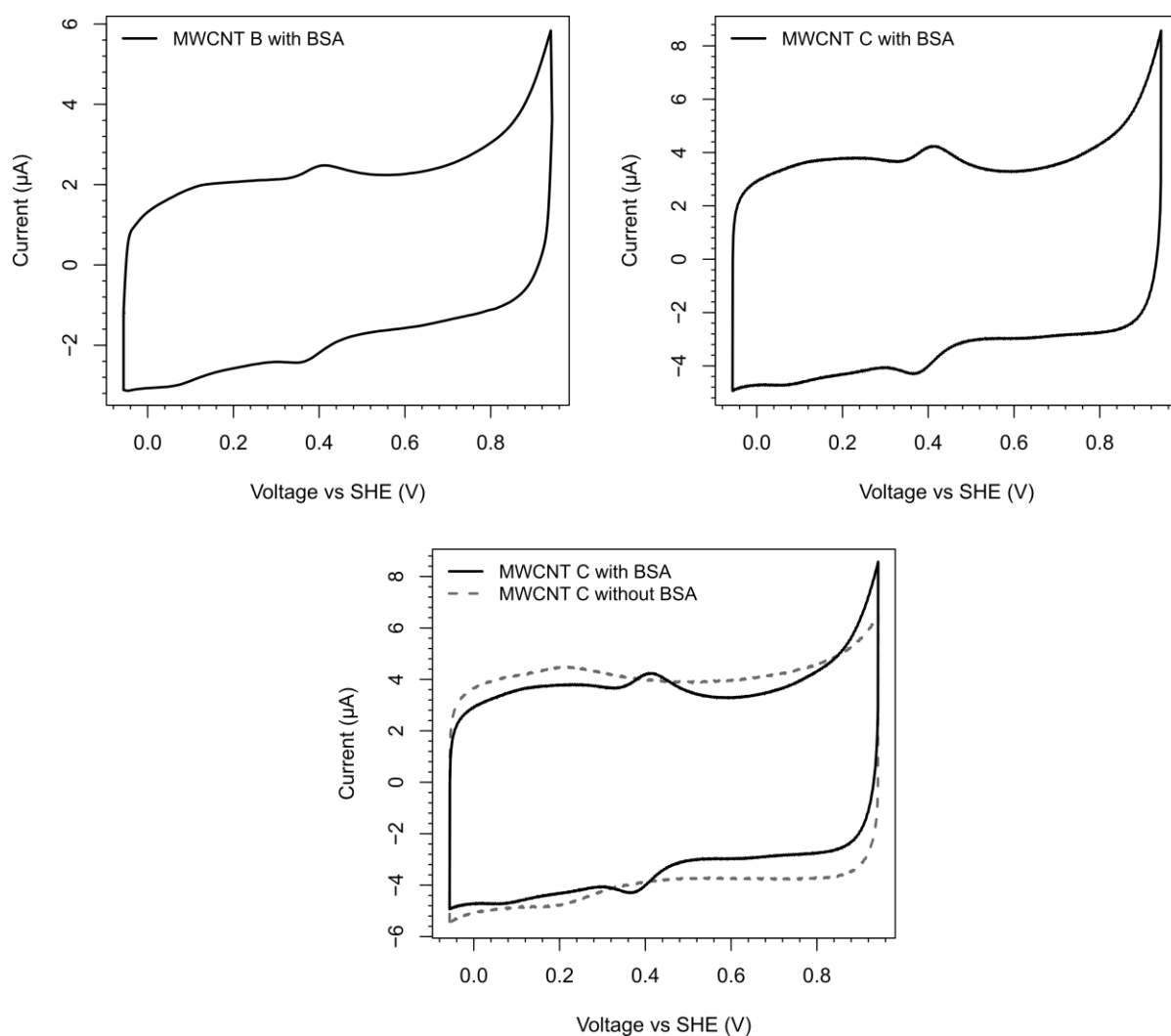


**Figure S3.** Cyclic voltammograms showing two redox couples are present for samples of **MWCNT B** and **MWCNT C** (see table **Table 2.3**) treated with BSA, even though BSA is not redox-active. This illustrates that the phenomenon of background redox signals, dependent on the presence of a protein-film (but independent of the identity of that protein) is not restricted to **MWCNT A**. **MWCNT C** does seem to show some background redox activity even in the absence of a protein film, perhaps due to a carboxylic acid or quinone-type redox couple. Scans recorded at  $33 \text{ mV s}^{-1}$  at 298 K under  $\text{N}_2$  atmosphere in pH 7 buffer (20 mM sodium phosphate, 20 mM sodium acetate, 500 mM  $\text{Na}_2\text{SO}_4$ ), using a glassy carbon working electrode, a platinum wire counter electrode and a calomel reference electrode (saturated KCl).

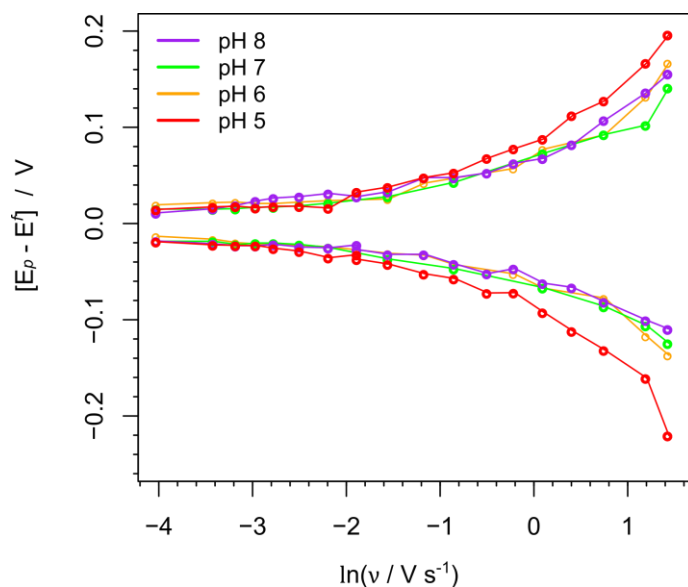


**Figure S4.** Trumpet plot showcasing the relationship between the natural logarithm of scan rate and the displacement of anodic peaks ( $E_p - E_f > 0$ ) and cathodic peaks ( $E_p - E_f < 0$ ) from the formal potential of the dominant background redox couple for **MWCNT A**-functionalised electrodes treated with *An6428-AA9*. Scans recorded at a range of scan rates at 298 K under  $N_2$  atmosphere at a range of pHs. Buffer conditions: pH 5-8, 20 mM sodium phosphate, 20 mM sodium acetate, 500 mM  $Na_2SO_4$ ).

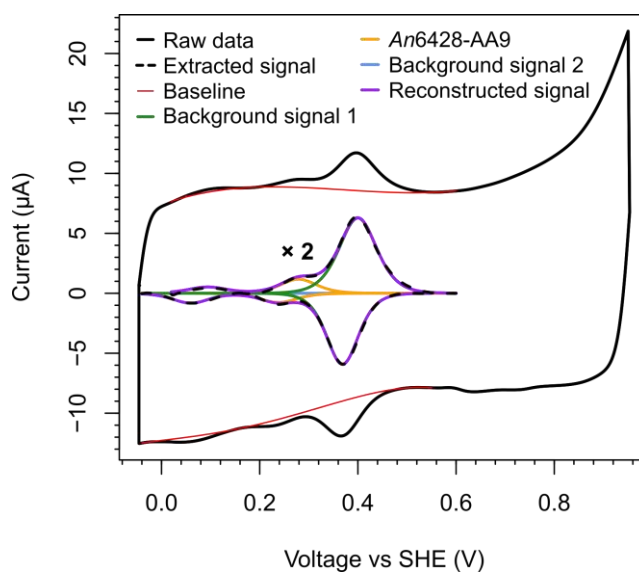


**Figure S5.** The fitting of simulated signals to cyclic voltammograms recorded for the electrode surface (GC working electrode, functionalised with drop-cast **MWCNT A** and subsequently treated with *An6428-AA9*) used for amperometry experiments with  $H_2O_2$ . Scans recorded at  $33 \text{ mV s}^{-1}$  at 298 K under  $N_2$  atmosphere in pH 7 buffer (20 mM sodium phosphate, 20 mM sodium acetate, 500 mM  $Na_2SO_4$ ), using a platinum wire counter electrode and a saturated calomel reference electrode (saturated KCl). Redox signals were isolated and simulated using the specialised code packaged described in **Appendix 2**. Extracted signals are shown at twice their intensity.

**Table S2.** Parameters fitted to the baseline-subtracted signals in **Figure S5**, using **Equation 7**, showing that the suspected An6428-AA9 redox signal is characteristic of a 1 electron process. The exact surface area of the electrode cannot be easily determined due to the nature of the drop-cast MWCNT deposit. The surface area,  $A$ , has thus been set to unity, and the coverages,  $\Gamma$ , are therefore indicative of the total molar quantity of species present, not the molar quantity present per unit area.

Parameter	Background 1	An6428-AA9	Background 2
$A / \text{cm}^2$	1	1	1
$n_s$ cathodic	1	1	1
$n_s$ anodic	1	1	1
$n_{app}$ cathodic	1.18	1.02	1.04
$n_{app}$ anodic	1.00	1.03	0.96
Anodic peak potential / mV vs SHE	400	279	111
Cathodic peak potential / mV vs SHE	368	254	59
$E_{(O/R)}^f / \text{V vs SHE}$	385	259	94
$\Gamma$ cathodic / pmol $\text{cm}^{-2}$	81.2	12.2	12.7
$\Gamma$ anodic / pmol $\text{cm}^{-2}$	101	18.2	8.8

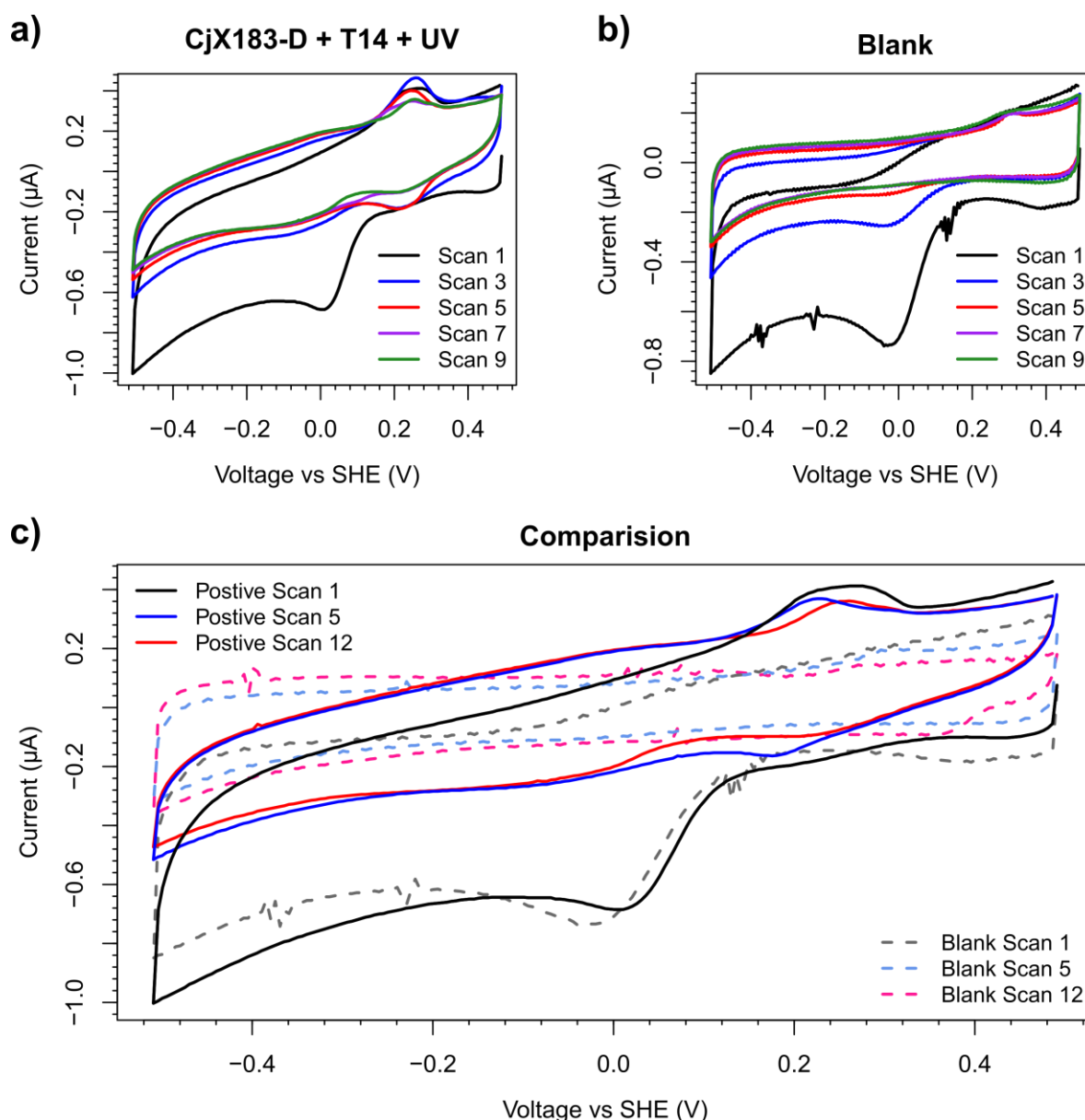


**Figure S6.** **a)** CVs showing the electro-grafting of a 25  $\mu\text{M}$  solution of diazonium-labelled CjX183-D R51K (CjX183-D R51K labelled with **T14** and treated with irradiation from a 7 W 365 nm UV light bulb for 5 minutes at 0  $^{\circ}\text{C}$  prior to electro-grafting) in pH 7.5 buffer (25 mM sodium phosphate + 150 mM NaCl). **b)** CVs showing comparable scans recorded using a blank solution of pH 7.5 buffer (25 mM sodium phosphate + 150 mM NaCl). **c)** Overlays of scans recorded in both the blank and diazonium-labelled CjX183-D R51K solutions. Scans were recorded at 50  $\text{mV s}^{-1}$  at 22  $^{\circ}\text{C}$  under an  $\text{N}_2$  atmosphere using a leak free Ag/AgCl reference electrode, a platinum wire counter electrode and a PGE working electrode.

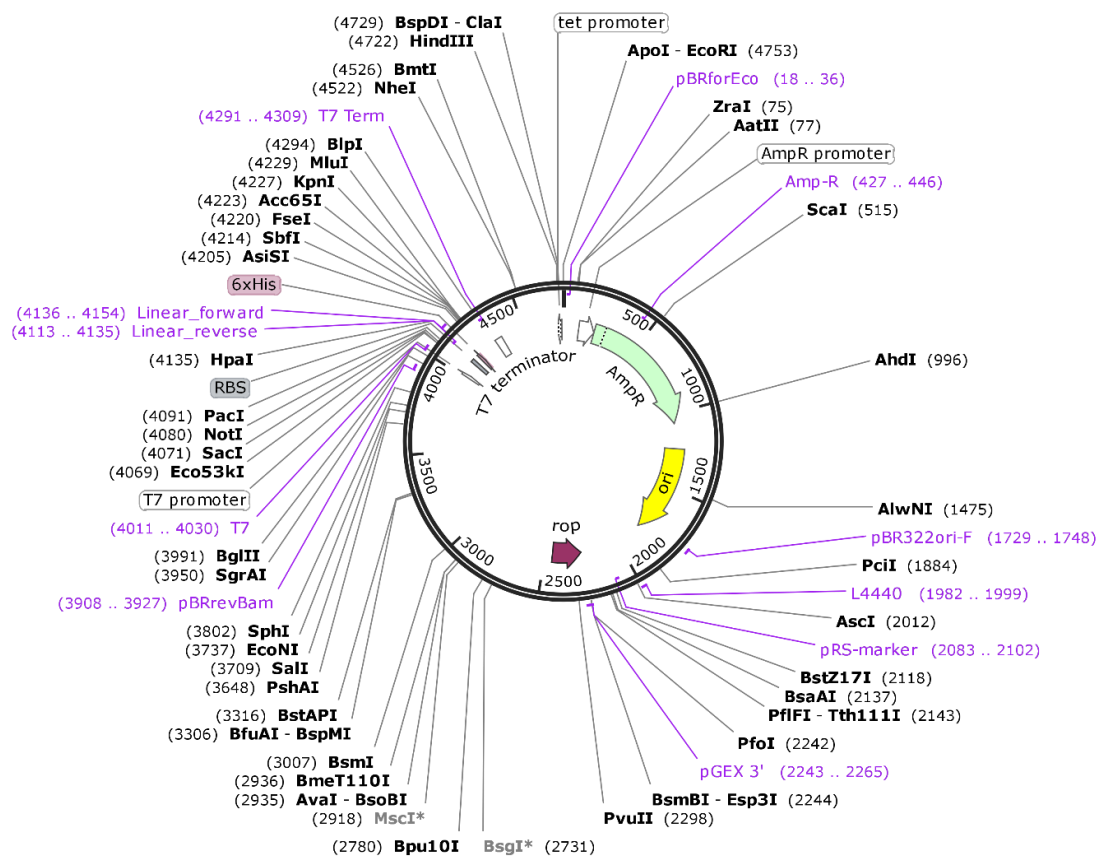
It is curious that the intensity of the  $\text{Fe}^{(\text{III/II})}$  redox couple of CjX183-D R51K in **Figure S6 a** and **c** appears to decrease in intensity over successive scans, which may indicate that over successive scans the electrode surface may be becoming increasingly passivated towards the solution-phase  $\text{Fe}^{(\text{III/II})}$  redox couple of CjX183-D R51K. It is likely that solution-phase CjX183-D R51K transiently becomes associated adsorbed to the electrode surface before exchanging electrons with the electrode, and thus the covalent immobilisation of CjX183-D R51K could actually partly pacify the electrode surface towards the solution-phase CjX183-D R51K  $\text{Fe}^{(\text{III/II})}$  redox couple.

## Appendix 4. Experimentation with creating a CjX183-D-TEV-HIS<sub>6</sub>\_pET construct

Dr Alison Parkin suspects that a His<sub>6</sub> tag can help facilitate adsorption of proteins onto electrode surfaces, and thus when designing a methodology for controlled immobilisation of proteins in a orientation-specific manner onto electrode surfaces may be advantageous to use a protein without a His<sub>6</sub> tag.

### Commercially available PET vector

The commercially available Addgene plasmid #48285 codes for a His<sub>6</sub> tag and an incomplete TEV cleavage site, which can be completed when inserting the gene of interest. Usage of this PET vector thus allows a protein to be produced with a TEV cleavage site preceding a His<sub>6</sub> tag at the protein C-terminus. The His<sub>6</sub> tag could thus be cleaved from such a protein after it has served its purpose (i.e. after nickel affinity chromatography has been performed), by treating the protein with TEV protease.



pET C-terminal TEV His<sub>6</sub> cloning vector with BioBrick polycistronic restriction sites (9Bc)  
4755 bp

Figure S7. Plasmid map of Addgene plasmid #48285.

Addgene plasmid #48285 was purchased, arriving as a bacterial stab. Upon arrival a pipette tip was used to streak the bacterial stab onto an LB agar + ampicillin (0.1 mg mL<sup>-1</sup>) plate, and was incubated at 37 °C overnight, yielding single colonies. Four single colonies were then selected and grown up for minipreps in 5 mL LB + ampicillin at 37 °C overnight with shaking. For three colonies, the cells were pelleted via centrifuging and the plasmid extracted using a QIAprep Spin Miniprep Kit. For the fourth colony the cells were used to make a glycerol stock.

The extracted plasmid was then linearised using PCR. The primers used for this linearisation are shown below (see **Table S3**), as is the locus at which these primers linearise the plasmid – at the HpaI restriction site (see **Figure S8**).

**Table S3.** The primers used to linearise Addgene plasmid #48285.

Oligo Name	Sequence (5' → 3')	Length (bp)	GC%	T <sub>m</sub> (Å °C)	Gene Specific T <sub>m</sub> (Å °C)
Oligo 1 (Destination Vector) Forward	AACCTCTACTTCCAATCCG	19	47	56.3	56.3
Oligo 2 (Destination Vector) Reverse	AACTATATCTCCTTCTTAAAGTT	23	26	52.4	52.4

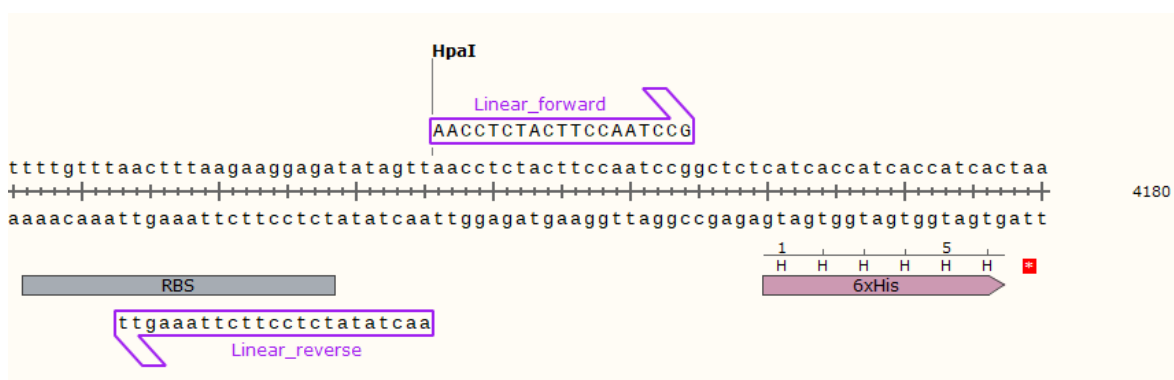


**Figure S8.** The location within Addgene plasmid #48285 that the primers in **Table S3** served to linearise.

A New England Biolabs Q5<sup>®</sup> High-Fidelity PCR Kit was used to carry out the PCR. The setup of the PCR experiment and the conditions under which the PCR was performed are shown in **Table S4** and **Table S5**.

#### Appendix 4. Experimentation with creating a CjX183-D-TEV-HIS<sub>6</sub>-pET construct

**Table S4.** The setup of the PCR experiment used to linearise Addgene plasmid #48285. dNTP stands for deoxynucleoside triphosphate.

Reaction component	Quantity
Q5 polymerase	1.5 $\mu$ L
10mM dNTPs	3 $\mu$ L
10 $\mu$ M forward primer	7.5 $\mu$ L
10 $\mu$ M reverse primer	7.5 $\mu$ L
Plasmid DNA (1 ng $\mu$ L <sup>-1</sup> )	3 $\mu$ L
5 $\times$ Q5 buffer	30 $\mu$ L
Autoclaved MQ water	97.5 $\mu$ L

The PCR conditions were as follows:

**Table S5.** The conditions used in the linearisation of Addgene plasmid #48285 by PCR.

Step	Temperature / °C	Time / s
Initial denaturation	98	120
Denaturation	98	10
Annealing	56	30
Extension	72	150
Final extension	72	600
Hold	4	-

**35 cycles**

The linearised plasmid product of the PCR was purified using a 0.8% agarose gel, excising the band containing the desired product and using a QIAquick Gel Extraction Kit to isolate the DNA from the gel.



### The CjX183D\_pCW construct

Below is the plasmid map for the CjX183D\_pCW plasmid gifted by Dr Glyn Hemsworth. It contains the gene for the c-type cytochrome CjX183-D, but with a non-cleavable His<sub>6</sub> tag.

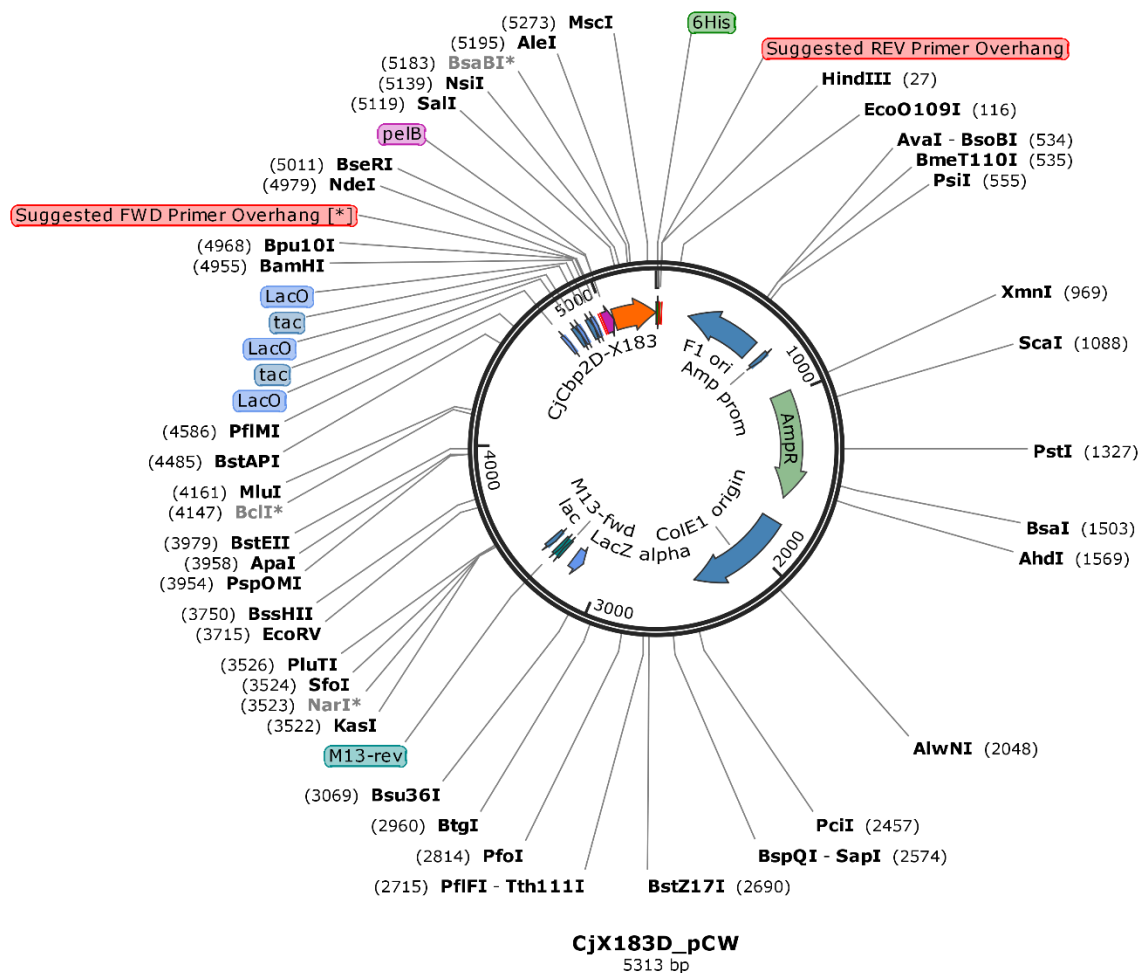


Figure S9. Plasmid map of CjX183D\_pCW.

A fragment containing the gene for the CjX183-D protein was isolated from the CjX183D\_pCW plasmid using PCR. The primers used to clone-out this fragment are shown below (Table S6), as are the locations at which they anneal with CjX183D\_pCW (Figure S10). As can be seen, it is not sufficient to just isolate the DNA that directly codes for the CjX183-D protein; the *pelB* leader sequence that precludes this coding DNA has to be isolated as well.

## Appendix 4. Experimentation with creating a CjX183-D-TEV-HIS<sub>6</sub>-pET construct

**Table S6.** The primers used to clone-out the pelB-CjX183-D fragment from CjX183D\_pCW.

Oligo Name	Sequence (5' → 3')	Length (bp)	GC%	T <sub>m</sub> (Å °C)	Gene Specific T <sub>m</sub> (Å °C)
Oligo 3 (Insert 1) Forward	GAAGGAGATATAGTTCATGAAATACCTGCTGCCGACC	37	46	70	64
Oligo 4 (Insert 1) Reverse	TTGGAAGTAGAGGTTCTCCAGGTGCGGATAAAGG	35	51	72.5	62.5



**Figure S10.** The location within CjX183D\_pCW that the primers in **Table S6** anneal.

These primers not only facilitate the isolation of the pelB-CjX183-D fragment from the CjX183D\_pCW construct, but also add additional nucleobases to the sequence. These additional nucleobases will later complete the TEV cleavage sequence once the pelB-CjX183-D fragment is inserted into Addgene plasmid #48285, and also add an additional 15 base pairs on either side of the pelB-CjX183-D fragment that are homologous to the ends of linearised Addgene plasmid #48285. It is this homology that allows In-Fusion® cloning to be used to insert the pelB-CjX183-D fragment into the linearised Addgene plasmid #48285.

An In-Fusion® HD Cloning Plus kit was purchased, and the CloneAmp HiFi PCR Premix was used to carry out the amplification and isolation of the pelB-CjX183-D fragment by PCR. The setup of the PCR experiment and the conditions under which the PCR was performed are shown in **Table S4** and **Table S5**.

**Table S7.** The setup of the PCR experiment used to linearise Addgene plasmid #48285. CloneAmp is a premix that contains a DNA polymerase, dNTPs and buffer, all at 2 × working concentration.

Reaction component	Quantity
CloneAmp	37.5 µL
10 µM forward primer	1.5 µL
10 µM reverse primer	1.5 µL
Plasmid DNA (1 ng µL <sup>-1</sup> )	3 µL
Autoclaved MQ water	31.5 µL

The PCR conditions were as follows:

**Table S8.** The PCR conditions used for amplification and isolation of the pelB-CjX183-D fragment.

Step	Temperature / °C	Time / s
Initial denaturation	98	120
Denaturation	98	10
Annealing	57	10
Extension	72	10
Final extension	72	600
Hold	4	-

**35 cycles**

The linearised plasmid product of the PCR was purified using a 0.9% agarose gel, excising the band containing the desired product and using a QIAquick Gel Extraction Kit to isolate the DNA from the gel.

### Making the CjX183-D-TEV-HIS<sub>6</sub>\_pET construct

The In-Fusion<sup>®</sup> HD Cloning kit was used to insert the pelB-CjX183-D fragment into the linearised Addgene plasmid #48285. The set-up of the reaction is tabulated below.

**Table S9.** In-Fusion<sup>®</sup> reaction setup.

Reaction component	Quantity required	Volume added (µL)
pelB-CjX183-D fragment (57 ng µL <sup>-1</sup> )	23.2 ng	0.4
Linearised Addgene plasmid #48285 (24 ng µL <sup>-1</sup> )	150 ng	6.4
5 × HD enzyme premix	2 µL	2
Autoclaved MQ water	to 10 µL	1.2

The reaction was then incubated for 15 min at 50 °C, then placed on ice. The reaction mixture was then transformed into Stellar Competent Cells, as detailed in the In-Fusion® HD Cloning Kit User Manual.

These Stellar Cells were then used to clone the CjX183-D-TEV-HIS<sub>6</sub>\_pET construct. The construct was then isolated using an QIAprep Spin Miniprep Kit. Sequencing of the construct using LightRun Tubes (Eurofins Genomics) showed it to have the desired sequence.

## Appendix 5. Preparation of the CjX183D-R51K\_pCW construct

A QuickChange Site-Directed Mutagenesis Kit (Agilent Technologies) was used to prepare the CjX183-D R51K\_pCW plasmid (which codes for the CjX183-D R51K protein) from the CjX183-D\_pCW plasmid (which codes for the WT CjX183-D protein), using the method contained in the QuickChange Site-Directed Mutagenesis Kit instruction manual. The primers used to create this mutation are shown below in **Table S10** and **Figure S11**. The composition of the QuickChange PCR reaction mixture is tabulated in **Table S11**. The cycling parameters used for the PCR are tabulated in **Table S12**.

**Table S10.** The primers used for QuickChange Site-Directed Mutagenesis.

Oligo Name	Sequence (5' → 3')	Length (bp)	GC%	T <sub>m</sub> (°C)
R51Kforward	TGCACGGTCTCTGGGTATCCTTGCTGTGGCGATAGAGATC	39	56.4	69.2
R51Kreverse	GATCTCTATCGCCACAGCAAGGATACCCAGGACCGTGCA	39	56.4	69.2



**Figure S11.** The site of mutation in the CjX183-D gene targeted by the primers in **Table S10**.

**Table S11.** QuickChange Site-Directed Mutagenesis reaction setup.

Reaction component	Quantity
Reaction buffer (× 10)	5 µL
CjX183-D_pCW (the dsDNA template)	35 ng
R51Kforward	125 ng
R51Kreverse	125 ng
dNTP mix	1 µL
<i>PfuTurbo</i> DNA polymerase (2.5 U / µL)	1 µL
Double-distilled water	to 50 µL

## Appendix 5. Preparation of the CjX183D-R51K\_pCW construct

**Table S12.** The PCR conditions used for QuickChange Site-Directed Mutagenesis.

Step	Temperature / °C	Time / s	
Initial denaturation	95	30	
Denaturation	95	30	<b>16 cycles</b>
Annealing	55	60	
Extension	68	319	

Following temperature cycling, the reaction mixture was placed on ice for 2 minutes, to cool the reaction to  $\leq 37$  °C. The reaction mixture was then transformed into XL1-Blue Supercompetent Cells and the cells plated (onto LB-Amp agar) as detailed in the QuickChange Site-Directed Mutagenesis Kit instruction manual. Colonies were selected and plasmids were harvested using a QIAprep Spin Miniprep Kit.

Sequencing of the CjX183-D R51K\_pCW construct was conducted using LightRun Tubes (Eurofins Genomics), using the primers tabulated in **Table S13**, and showed the construct to have the desired sequence.

**Table S13.** The primers used to sequence the CjX183-D R51K\_pCW construct.

Oligo Name	Sequence (5' → 3')	Length (bp)	GC%	T <sub>m</sub> (°C)
CjX183D_pCW_SEQ_FOR	GGAAACAGGATCAGCTTAC	19	47.4	50.4
CjX183D_pCW_SEQ_REV	CCTTTCGTCTTCAAGCAGAT	20	45.0	52.7

## Appendix 6. Gene/amino acid sequences, theoretical isoelectric points and molecular weights of proteins

### WT CjX183-D

Gene sequence with **pelB leader**, without his tag:

```
atgaaatacctgctgccgaccgctgctgctggtctgctgctcctcgctgcccagccggcgatggcdGG  
TTATCTGGTTGGCGATGCAACACGCGGTGCAAACCTGTGGAATACCCAAACCTGCGTGGCTTGTACAG  
GTGTCGACGGTGAGCGCAATGCATCCGGTACGCCAGCATTGACCCCGCTCAATCCAAACCGCGATCTC  
TATCGCCACAGCCGTGATACCCAGGACCGTGCACTGAGAGACTTCATTTCCATGTGGATGCCGCAAGG  
TAATGAAGGCAGTTGTACTGGCCAGTGCGCCGCTGATATTGAAGCCTTTATCCGCACCTGG
```

Amino acid Sequence without pelB leader, with His<sub>6</sub> tag:

```
GYLVGDATRGANLWNTQTCVACHGVDGERNASGTPALTPLNPNRDLYRHSRDTQDRALRDFISMWMPQ  
GNEGSTGQCAADIEAFIRTWHHHHHH
```

Theoretical pI/Mw: 6.45 / 10623.67 Da.

Theoretical Mw +heme: 11226.14 Da

### CjX183-D R51K

Gene acid sequence with **pelB leader**, without his tag. **Lysine mutation:**

```
atgaaatacctgctgccgaccgctgctgctggtctgctgctcctcgctgcccagccggcgatggcdGG  
TTATCTGGTTGGCGATGCAACACGCGGTGCAAACCTGTGGAATACCCAAACCTGCGTGGCTTGTACAG  
GTGTCGACGGTGAGCGCAATGCATCCGGTACGCCAGCATTGACCCCGCTCAATCCAAACCGCGATCTC  
TATCGCCACAGCAAGGATAACCCAGGACCGTGCACTGAGAGACTTCATTTCCATGTGGATGCCGCAAGG  
TAATGAAGGCAGTTGTACTGGCCAGTGCGCCGCTGATATTGAAGCCTTTATCCGCACCTGG
```

Amino acid sequence without pelB leader, with His<sub>6</sub> tag. **Lysine mutation:**

```
GYLVGDATRGANLWNTQTCVACHGVDGERNASGTPALTPLNPNRDLYRHSKDTQDRALRDFISMWMPQ  
GNEGSTGQCAADIEAFIRTWHHHHHH
```

Theoretical pI/Mw: 6.45 / 10595.66 Da

Theoretical Mw +heme: 11198.13 Da

### DsbA<sub>c-term</sub>

Construct amino acid sequence with His<sub>6</sub> tag, Tev cleavage site, and mutant FGE recognition sequence:

MHHHHHGGKPIPNPLLGLDSTENLYFQGIDPFSTRDDKKDGVAGPGDAVRVTSSKLVTPGTSNPKAV  
VSFYEDFLCPACGIFERGFPTVSKLVDIGAVAADYTMVAI LDSASNQHYSSRAAAAAYCVADESIEA  
FRRFHAALFSKDIQPAELGKDFPDNARLIELAREAGVVGKVPDCINSGKYIEKVDGLAAAVNVHATPT  
VRVNGTEYEWSTPAALVAKIKEIVGDVPGIDSAAATATSLCTPSRG

Theoretical pI/Mw: 5.68 / 26477.81 Da

### DsbA<sub>middle</sub>

Construct amino acid sequence with His<sub>6</sub> tag, Tev cleavage site, and mutant FGE recognition sequence:

MHHHHHGGKPIPNPLLGLDSTENLYFQGIDPFSTRDDKKDGVAGPGDAVRVTSSKLVTPGTSNPKAV  
VSFYEDFLCPACGIFERGFPTVSKLVDIGAVAADYTMVAI LDSASNQHYSSRAAAAAYCVADESIEA  
FRRFHAALFSKDIQPAELCTPSRDNARLIELAREAGVVGKVPDCINSGKYIEKVDGLAAAVNVHATPT  
VRVNGTEYEWSTPAALVAKIKEIVGDVPGIDSAAATATS

Theoretical pI/Mw: 5.68 / 25762.99 Da

### Mt-FGE

Construct amino acid sequence with His<sub>6</sub> tag:

MGSSHHHHHSSGLVPRGSHMLTELVDLPGGSFMRMGSTRFYPEEAPIHTVTVRAFAVERHPVTNAQFA  
EFVSATGYVTVAEQPLDPGLYPGVDAADLCPGAMVFCPTAGPVDLRDWRQWDDWVPGACWRHPFGRDS  
DIADRAGHPVVQVAYPDAVAYARWAGRRLPTEAEWEYAARGGTTATYAWGDQEKPGMLMANTWQGRF  
PYRNDGALGWVGTSPVGRFPANGFGLLDMIGNVWEWTTTEFYPHHRIDPPSTACCAPVKLATAADPTI  
SOTLKGGSHLCAPEYCHRYRPAARSPQSQDTATTHIGFRCVADPVSG

Theoretical pI/Mw: 6.22 / 34907.07

### TcFGE<sub>7</sub>

Construct amino acid sequence with His<sub>6</sub> tag:

SSSHHHHHSSGLVPRGSVAIPGGTFRMETGGEDPDAFPEDGE GPVRTVRLSPFLIDRYAVSNRQFAA  
FVKATGYVTDAERYGWSFVFHAAHVAPGTPVMETDAVVPEAPWWWAVPGAYWKAPEGPGSSITDRPNHP  
VVHVSWNDAYATWAGKRLPTEAEWEMETAARGGLDQARYPWGNELTPRGRHRANIWQGTFFVHDTG  
EDGYTGTA PVNAFAPNGYGLYNVAGNVWEWAADWWSADWHATESPATRIDPRGPETGTARVTKGGSFL  
CHESFCNRYRVAARTSNTPDSSAAHTGFRAAADPL

Theoretical pI/Mw: 5.89 / 33458.73



---

## References

- 1 Liu, J. *et al.* Metalloproteins Containing Cytochrome, Iron–Sulfur, or Copper Redox Centers. *Chemical Reviews* **114**, 4366-4469, doi:10.1021/cr400479b (2014).
- 2 Prabhulkar, S., Tian, H., Wang, X., Zhu, J.-J. & Li, C.-Z. Engineered Proteins: Redox Properties and Their Applications. *Antioxidants & Redox Signaling* **17**, 1796-1822, doi:10.1089/ars.2011.4001 (2012).
- 3 Datta, S. *et al.* Structure of a quinohemoprotein amine dehydrogenase with an uncommon redox cofactor and highly unusual crosslinking. *Proceedings of the National Academy of Sciences* **98**, 14268, doi:10.1073/pnas.241429098 (2001).
- 4 Nauser, T., Steinmann, D. & Koppenol, W. H. Why do proteins use selenocysteine instead of cysteine? *Amino Acids* **42**, 39-44, doi:10.1007/s00726-010-0602-7 (2012).
- 5 McLendon, G. in *Congress Proceedings* Ch. 75-80, (Elsevier Inc., 1992).
- 6 Saen-Oon, S., Lucas, M. F. & Guallar, V. Electron transfer in proteins: theory, applications and future perspectives. *Physical Chemistry Chemical Physics* **15**, 15271-15285, doi:10.1039/C3CP50484K (2013).
- 7 Hosseinzadeh, P. *et al.* Design of a single protein that spans the entire 2-V range of physiological redox potentials. *Proceedings of the National Academy of Sciences* **113**, 262-267, doi:10.1073/pnas.1515897112 (2016).
- 8 Marshall, N. M. *et al.* Rationally tuning the reduction potential of a single cupredoxin beyond the natural range. *Nature* **462**, 113-116, doi:10.1038/nature08551 (2009).
- 9 Williams, R. J. P. & Fraústo da Silva, J. J. R. *Bringing Chemistry to Life: From Matter to Man*. 1 edn, (Oxford University Press, 1999).
- 10 Léger, C. & Bertrand, P. Direct electrochemistry of redox enzymes as a tool for mechanistic studies. *Chemical Reviews* **108**, 2379-2438, doi:10.1021/cr0680742 (2008).
- 11 Blanford, C. F. The birth of protein electrochemistry. *Chemical Communications* **49**, 11130, doi:10.1039/c3cc46060f (2013).
- 12 Armstrong, F. A. *et al.* Dynamic electrochemical investigations of hydrogen oxidation and production by enzymes and implications for future technology. *Chemical Society Reviews* **38**, 36-51, doi:10.1039/B801144N (2009).
- 13 Armstrong, F. A. *et al.* Guiding Principles of Hydrogenase Catalysis Instigated and Clarified by Protein Film Electrochemistry. *Accounts of Chemical Research* **49**, 884-892, doi:10.1021/acs.accounts.6b00027 (2016).
- 14 Gates, A. J. *et al.* The relationship between redox enzyme activity and electrochemical potential—cellular and mechanistic implications from protein film electrochemistry. *Physical Chemistry Chemical Physics* **13**, 7720-7720, doi:10.1039/c0cp02887h (2011).
- 15 Armstrong, F. A., Heering, H. A. & Hirst, J. Reactions of complex metalloproteins studied by protein-film voltammetry. *Chemical Society Reviews* **26**, 169-179, doi:10.1039/cs9972600169 (1997).
- 16 Phan, A. D., Hoang, T. X., Nghiem, T. H. L. & Woods, L. M. Surface plasmon resonances of protein-conjugated gold nanoparticles on graphitic substrates. *Applied Physics Letters* **103**, 163702-163702, doi:10.1063/1.4826514 (2013).
- 17 Schasfoort, R. B. M. in *Handbook of Surface Plasmon Resonance (2)* 1-26 (The Royal Society of Chemistry, 2017).
- 18 Patching, S. G. Surface plasmon resonance spectroscopy for characterisation of membrane protein–ligand interactions and its potential for drug discovery. *Biochimica et Biophysica Acta (BBA) - Biomembranes* **1838**, 43-55, doi:10.1016/j.bbamem.2013.04.028 (2014).

- 19 Capelli, D. *et al.* Surface Plasmon Resonance as a Tool for Ligand Binding Investigation of Engineered GPR17 Receptor, a G Protein Coupled Receptor Involved in Myelination. *Frontiers in Chemistry* **7**, 910 (2020).
- 20 Douzi, B. (eds Laure Journet & Eric Cascales) 257-275 (Springer New York, 2017).
- 21 Dixon, M. C. Quartz crystal microbalance with dissipation monitoring: enabling real-time characterization of biological materials and their interactions. *Journal of Biomolecular Techniques* **19**, 151-158 (2008).
- 22 Hampitak, P. *et al.* Protein interactions and conformations on graphene-based materials mapped using a quartz-crystal microbalance with dissipation monitoring (QCM-D). *Carbon* **165**, 317-327, doi:10.1016/j.carbon.2020.04.093 (2020).
- 23 Nielsen, S. B. & Otzen, D. E. in *Lipid-Protein Interactions. Methods in Molecular Biology* Vol. 2003 (ed J Kleinschmidt) (Humana, 2019).
- 24 Spicer, C. D., Jumeaux, C., Gupta, B. & Stevens, M. M. Peptide and protein nanoparticle conjugates: versatile platforms for biomedical applications. *Chemical Society Reviews* **47**, 3574-3620, doi:10.1039/C7CS00877E (2018).
- 25 Spicer, C. D. Hydrogel scaffolds for tissue engineering: the importance of polymer choice. *Polymer Chemistry* **11**, 184-219, doi:10.1039/C9PY01021A (2020).
- 26 Pompe, T., Salchert, K., Alberti, K., Zandstra, P. & Werner, C. Immobilization of growth factors on solid supports for the modulation of stem cell fate. *Nature Protocols* **5**, 1042-1050, doi:10.1038/nprot.2010.70 (2010).
- 27 Lowndes, M., Rotherham, M., Price, J. C., El Haj, A. J. & Habib, S. J. Immobilized WNT Proteins Act as a Stem Cell Niche for Tissue Engineering. *Stem Cell Reports* **7**, 126-137, doi:10.1016/j.stemcr.2016.06.004 (2016).
- 28 Alberti, K. *et al.* Functional immobilization of signaling proteins enables control of stem cell fate. *Nature Methods* **5**, 645-650, doi:10.1038/nmeth.1222 (2008).
- 29 Adamson, H. *et al.* Retuning the Catalytic Bias and Overpotential of a [NiFe]-Hydrogenase via a Single Amino Acid Exchange at the Electron Entry/Exit Site. *Journal of the American Chemical Society* **139**, 10677-10686, doi:10.1021/jacs.7b03611 (2017).
- 30 Rollin, J. A. *et al.* High-yield hydrogen production from biomass by in vitro metabolic engineering: Mixed sugars coutilization and kinetic modeling. *Proceedings of the National Academy of Sciences* **112**, 4964-4969, doi:10.1073/pnas.1417719112 (2015).
- 31 Lubitz, W., Ogata, H., Rüdiger, O. & Reijerse, E. Hydrogenases. *Chemical Reviews* **114**, 4081-4148, doi:10.1021/cr4005814 (2014).
- 32 Ragsdale, S. W. Nickel-based enzyme systems. *Journal of Biological Chemistry* **284**, 18571-18575, doi:10.1074/jbc.R900020200 (2009).
- 33 Frandsen, K. E. H. *et al.* The molecular basis of polysaccharide cleavage by lytic polysaccharide monoxygenases. *Nature Chemical Biology* **12**, 298-303, doi:10.1038/nchembio.2029 (2016).
- 34 Yu, Y., Hu, C., Xia, L. & Wang, J. Artificial Metalloenzyme Design with Unnatural Amino Acids and Non-Native Cofactors. *ACS Catalysis*, acscatal.7b03754-acscatal.03757b03754, doi:10.1021/acscatal.7b03754 (2018).
- 35 Wieszczycka, K. & Staszak, K. Artificial metalloenzymes as catalysts in non-natural compounds synthesis. *Coordination Chemistry Reviews* **351**, 160-171, doi:10.1016/j.ccr.2017.06.012 (2017).
- 36 Reda, T., Plugge, C. M., Abram, N. J. & Hirst, J. Reversible interconversion of carbon dioxide and formate by an electroactive enzyme. *Proceedings of the National Academy of Sciences* **105**, 10654-10658, doi:10.1073/pnas.0801290105 (2008).
- 37 Can, M., Armstrong, F. A. & Ragsdale, S. W. Structure, Function, and Mechanism of the Nickel Metalloenzymes, CO Dehydrogenase, and Acetyl-CoA Synthase. *Chemical Reviews* **114**, 4149-4174, doi:10.1021/cr400461p (2014).
- 38 Moehlenbrock, M. J. & Minteer, S. D. in *Enzyme Stabilization and Immobilization: Methods and Protocols* Vol. 1504 (ed Shelley D. Minteer) 1-7 (Springer New York, 2017).

- 39 King, P. W. Designing interfaces of hydrogenase-nanomaterial hybrids for efficient solar conversion. *Biochimica et Biophysica Acta (BBA) - Bioenergetics* **1827**, 949-952, doi:10.1016/j.bbabi.2013.03.006 (2013).
- 40 Bachmeier, A. & Armstrong, F. Solar-driven proton and carbon dioxide reduction to fuels — lessons from metalloenzymes. *Current Opinion in Chemical Biology* **25**, 141-151, doi:10.1016/j.cbpa.2015.01.001 (2015).
- 41 Siritanaratkul, B. *et al.* Transfer of photosynthetic NADP<sup>+</sup>/NADPH recycling activity to a porous metal oxide for highly specific, electrochemically-driven organic synthesis. *Chemical Science* **8**, 4579-4586, doi:10.1039/C7SC00850C (2017).
- 42 Bishop, G. W. & Rusling, J. F. in *Nanoelectrochemistry* (eds M. Mirkin & S. Amemiya) 469-512 (CRC press, 2015).
- 43 Cass, A. E. G. *et al.* Ferrocene-mediated enzyme electrode for amperometric determination of glucose. *Analytical Chemistry* **56**, 667-671, doi:10.1021/ac00268a018 (1984).
- 44 Grabarczyk, D. B. *et al.* Structural basis for specificity and promiscuity in a carrier protein/enzyme system from the sulfur cycle. *Proceedings of the National Academy of Sciences* **112**, E7166-E7175, doi:10.1073/pnas.1506386112 (2015).
- 45 Page, C. C., Moser, C. C., Chen, X. & Dutton, P. L. Natural engineering principles of electron tunnelling in biological oxidation-reduction. *Nature* **402**, 47-52, doi:10.1038/46972 (1999).
- 46 Léger, C. in *Practical Approaches to Biological Inorganic Chemistry* (ed Ricardo Louro) 179-216 (Elsevier, 2013).
- 47 Winkler, J. R., Nocera, D. G., Yocom, K. M., Bordignon, E. & Gray, H. B. Electron-Transfer Kinetics of Pentaammineruthenium(III)(histidine-33)-Ferricytochrome c. Measurement of the Rate of Intramolecular Electron Transfer between Redox Centers Separated by 15 Å in a Protein. *Journal of the American Chemical Society* **104**, 5798-5800, doi:10.1021/ja00385a047 (1982).
- 48 Winkler, J. R. & Gray, H. B. Long-range electron tunneling. *Journal of the American Chemical Society* **136**, 2930-2939, doi:10.1021/ja500215j (2014).
- 49 Léger, C., Jones, A. K., Albracht, S. P. J. & Armstrong, F. A. Effect of a dispersion of interfacial electron transfer rates on steady state catalytic electron transport in [NiFe]-hydrogenase and other enzymes. *The Journal of Physical Chemistry B* **106**, 13058-13063, doi:10.1021/jp0265687 (2002).
- 50 Scouten, W. H., Luong, J. H. T. & Stephen Brown, R. Enzyme or protein immobilization techniques for applications in biosensor design. *Trends in Biotechnology* **13**, 178-185, doi:10.1016/S0167-7799(00)88935-0 (1995).
- 51 Nöll, T. & Nöll, G. Strategies for “wiring” redox-active proteins to electrodes and applications in biosensors, biofuel cells, and nanotechnology. *Chemical Society Reviews* **40**, 3564-3564, doi:10.1039/c1cs15030h (2011).
- 52 Palecek, E., Tkac, J., Bartosik, M., Ostatna, V. & Palec, J. Electrochemistry of Nonconjugated Proteins and Glycoproteins. Toward Sensors for Biomedicine and Glycomics. *Chemical Reviews* **115**, 2045-2108, doi:10.1021/cr500279h (2015).
- 53 Plumeré, N. *et al.* A redox hydrogel protects hydrogenase from high-potential deactivation and oxygen damage. *Nature Chemistry* **6**, 822-827, doi:10.1038/nchem.2022 (2014).
- 54 McCreery, R. L. Advanced carbon electrode materials for molecular electrochemistry. *Chemical Reviews* **108**, 2646-2687, doi:10.1021/cr068076m (2008).
- 55 Banks, C. E. & Compton, R. G. New electrodes for old : from carbon nanotubes to edge plane pyrolytic graphite { . *Analyst* **131**, 15-21, doi:10.1039/b512688f (2006).
- 56 Hirst, J. Elucidating the mechanisms of coupled electron transfer and catalytic reactions by protein film voltammetry. *Biochimica et Biophysica Acta (BBA) - Bioenergetics* **1757**, 225-239, doi:10.1016/j.bbabi.2006.04.002 (2006).
- 57 Jeuken, L. J. C. in *Biophotoelectrochemistry: From Bioelectrochemistry to Biophotovoltaics* (ed Lars J. C. Jeuken) 43-73 (Springer International Publishing, 2016).

- 58 Armstrong, F. A. in *Bioinorganic Chemistry. Structure and Bonding* Vol. 72 137-221 (Springer, Berlin, Heidelberg, 1990).
- 59 Armstrong, F. A., Allen, H., Hill, O., Oliver, B. N. & Whitford, D. Direct electrochemistry of the photosynthetic blue copper protein plastocyanin. Electrostatic promotion of rapid charge transfer at an edge-oriented pyrolytic graphite electrode. *Journal of the American Chemical Society* **107**, 1473-1476, doi:10.1021/ja00292a004 (1985).
- 60 Bachmeier, A. S. J. L. in *Metalloenzymes as Inspirational Electrocatalysts for Artificial Photosynthesis* Ch. 4, 157-176 (Springer, 2016).
- 61 Hexter, S. V., Grey, F., Happe, T., Climent, V. & Armstrong, F. A. Electrocatalytic mechanism of reversible hydrogen cycling by enzymes and distinctions between the major classes of hydrogenases. *Proceedings of the National Academy of Sciences* **109**, 11516 LP-11521 (2012).
- 62 Armstrong, F. A. *et al.* Fast voltammetric studies of the kinetics and energetics of coupled electron-transfer reactions in proteins. *Faraday discussions*, 191-203; discussion 257-268, doi:10.1039/b002290j (2000).
- 63 Morris, G. P. *et al.* Theoretical analysis of the relative significance of thermodynamic and kinetic dispersion in the dc and ac voltammetry of surface-confined molecules. *Langmuir* **31**, 4996-5004, doi:10.1021/la5042635 (2015).
- 64 Patel, A. N., Tan, S. Y., Miller, T. S., MacPherson, J. V. & Unwin, P. R. Comparison and reappraisal of carbon electrodes for the voltammetric detection of dopamine. *Analytical Chemistry* **85**, 11755-11764, doi:10.1021/ac401969q (2013).
- 65 Kalimuthu, P., Ringel, P., Kruse, T. & Bernhardt, P. V. Direct electrochemistry of nitrate reductase from the fungus *Neurospora crassa*. *Biochimica et Biophysica Acta (BBA) - Bioenergetics* **1857**, 1506-1513, doi:10.1016/j.bbabi.2016.04.001 (2016).
- 66 Huong Le, T. X., Bechelany, M. & Cretin, M. Carbon felt based-electrodes for energy and environmental applications: A review. *Carbon* **122**, 564-591, doi:10.1016/j.carbon.2017.06.078 (2017).
- 67 Hambourger, M. *et al.* [FeFe]-hydrogenase-catalyzed H<sub>2</sub> production in a photoelectrochemical biofuel cell. *Journal of the American Chemical Society* **130**, 2015-2022, doi:10.1021/ja077691k (2008).
- 68 Mazurenko, I., de Poulpique, A. & Lojou, E. Recent developments in high surface area bioelectrodes for enzymatic fuel cells. *Current Opinion in Electrochemistry* **5**, 74-84, doi:10.1016/j.coelec.2017.07.001 (2017).
- 69 *Electrochemistry of Carbon Electrodes*. (Wiley-VCH Verlag GmbH & Co. KGaA, 2015).
- 70 Downard, A. J. & Roddick, A. D. Protein Adsorption at Glassy Carbon Electrodes : The Effect of Covalently Bound Surface Groups. *Electroanalysis* **7**, 376-378 (1995).
- 71 Liu, G., Paddon-Row, M. N. & Justin Gooding, J. A molecular wire modified glassy carbon electrode for achieving direct electron transfer to native glucose oxidase. *Electrochemistry Communications* **9**, 2218-2223, doi:10.1016/j.elecom.2007.06.016 (2007).
- 72 Chen, H. & Dong, S. Direct electrochemistry and electrocatalysis of horseradish peroxidase immobilized in sol-gel-derived ceramic-carbon nanotube nanocomposite film. *Biosensors and Bioelectronics* **22**, 1811-1815, doi:10.1016/j.bios.2006.08.013 (2007).
- 73 Wang, J., Li, M., Shi, Z., Li, N. & Gu, Z. Direct electrochemistry of cytochrome c at a glassy carbon electrode modified with single-wall carbon nanotubes. *Analytical Chemistry* **74**, 1993-1997, doi:10.1021/ac010978u (2002).
- 74 Yin, Y., Lü, Y., Wu, P. & Cai, C. Direct Electrochemistry of Redox Proteins and Enzymes Promoted by Carbon Nanotubes. *Sensors* **5**, 220-234, doi:10.3390/s5040220 (2005).
- 75 Ma, G. X., Lu, T. H. & Xia, Y. Y. Direct electrochemistry and bioelectrocatalysis of hemoglobin immobilized on carbon black. *Bioelectrochemistry* **71**, 180-185, doi:10.1016/j.bioelechem.2007.04.002 (2007).

- 76 Zhu, L. *et al.* Direct electrochemistry behavior of Cytochrome c on silicon dioxide nanoparticles-modified electrode. *Science in China, Series B: Chemistry* **50**, 304-307, doi:10.1007/s11426-007-0078-9 (2007).
- 77 Wang, J. Carbon-nanotube based electrochemical biosensors: A review. *Electroanalysis* **17**, 7-14, doi:10.1002/elan.200403113 (2005).
- 78 Tasis, D., Tagmatarchis, N., Bianco, A. & Prato, M. Chemistry of Carbon Nanotubes. *Chemical Reviews* **106**, 1105-1136, doi:10.1021/cr050569o (2006).
- 79 Kihara, T. *et al.* Direct electron transfer to hydrogenase for catalytic hydrogen production using a single-walled carbon nanotube forest. *International Journal of Hydrogen Energy* **36**, 7523-7529, doi:10.1016/j.ijhydene.2011.03.135 (2011).
- 80 Punbusayakul, N. Carbon nanotubes architectures in electroanalysis. *Procedia Engineering* **32**, 683-689, doi:10.1016/j.proeng.2012.01.1327 (2012).
- 81 Gao, C., Guo, Z., Liu, J.-H. & Huang, X.-J. The new age of carbon nanotubes: An updated review of functionalized carbon nanotubes in electrochemical sensors. *Nanoscale* **4**, 1948-1948, doi:10.1039/c2nr11757f (2012).
- 82 Zhao, Y.-D., Zhang, W.-D., Chen, H. & Luo, Q.-M. Direct Electron Transfer of Glucose Oxidase Molecules Adsorbed onto Carbon Nanotube Powder Microelectrode. *Analytical Sciences* **18**, 939-941, doi:10.2116/analsci.18.939 (2002).
- 83 Wang, J. & Carlisle, J. A. Covalent immobilization of glucose oxidase on conducting ultrananocrystalline diamond thin films. *Diamond and Related Materials* **15**, 279-284, doi:10.1016/j.diamond.2005.09.017 (2006).
- 84 Hata, K. *et al.* Water-assisted highly efficient synthesis of impurity-free single-walled carbon nanotubes - SOM. *Science* **306**, 1362-1364, doi:10.1126/science.1104962 (2004).
- 85 Yu, X., Chattopadhyay, D., Galeska, I., Papadimitrakopoulos, F. & Rusling, J. F. Peroxidase activity of enzymes bound to the ends of single-wall carbon nanotube forest electrodes. *Electrochemistry Communications* **5**, 408-411, doi:10.1016/S1388-2481(03)00076-6 (2003).
- 86 Wu, P. *et al.* Direct electrochemistry of glucose oxidase assembled on graphene and application to glucose detection. *Electrochimica Acta* **55**, 8606-8614, doi:10.1016/j.electacta.2010.07.079 (2010).
- 87 Kang, X. *et al.* Glucose Oxidase-graphene-chitosan modified electrode for direct electrochemistry and glucose sensing. *Biosensors and Bioelectronics* **25**, 901-905, doi:10.1016/j.bios.2009.09.004 (2009).
- 88 Xu, H., Dai, H. & Chen, G. Direct electrochemistry and electrocatalysis of hemoglobin protein entrapped in graphene and chitosan composite film. *Talanta* **81**, 334-338, doi:10.1016/j.talanta.2009.12.006 (2010).
- 89 Zhou, Y. *et al.* Direct electrochemistry of sarcosine oxidase on graphene, chitosan and silver nanoparticles modified glassy carbon electrode and its biosensing for hydrogen peroxide. *Electrochimica Acta* **71**, 294-301, doi:10.1016/j.electacta.2012.04.014 (2012).
- 90 Wu, J. F., Xu, M. Q. & Zhao, G. C. Graphene-based modified electrode for the direct electron transfer of Cytochrome c and biosensing. *Electrochemistry Communications* **12**, 175-177, doi:10.1016/j.elecom.2009.11.020 (2010).
- 91 Shao, Y. *et al.* Graphene based electrochemical sensors and biosensors: A review. *Electroanalysis* **22**, 1027-1036, doi:10.1002/elan.200900571 (2010).
- 92 Kontani, R., Tsujimura, S. & Kano, K. Air diffusion biocathode with CueO as electrocatalyst adsorbed on carbon particle-modified electrodes. *Bioelectrochemistry* **76**, 10-13, doi:10.1016/j.bioelechem.2009.02.009 (2009).
- 93 Tominaga, M., Otani, M., Kishikawa, M. & Taniguchi, I. UV-Ozone Treatments Improved Carbon Black Surface for Direct Electron-transfer Reactions with Bilirubin Oxidase under Aerobic Conditions. *Chemistry Letters* **35**, 1174-1175, doi:10.1246/cl.2006.1174 (2006).
- 94 Minteer, S. D., Atanassov, P., Luckarift, H. R. & Johnson, G. R. New materials for biological fuel cells. *Materials Today* **15**, 166-173, doi:10.1016/S1369-7021(12)70070-6 (2012).

- 95 Kamitaka, Y., Tsujimura, S., Setoyama, N., Kajino, T. & Kano, K. Fructose/dioxygen biofuel cell based on direct electron transfer-type bioelectrocatalysis. *Physical Chemistry Chemical Physics* **9**, 1793-1793, doi:10.1039/b617650j (2007).
- 96 Duca, M., Weeks, J. R., Fedor, J. G., Weiner, J. H. & Vincent, K. A. Combining Noble Metals and Enzymes for Relay Cascade Electrocatalysis of Nitrate Reduction to Ammonia at Neutral pH. *ChemElectroChem* **2**, 1086-1089, doi:10.1002/celec.201500166 (2015).
- 97 Reisner, E., Powell, D. J., Cavazza, C., Fontecilla-camps, J. C. & Armstrong, F. A. Visible Light-Driven H<sub>2</sub> Production by Hydrogenases Attached to Dye-Sensitized TiO<sub>2</sub> Nanoparticles. *Journal of the American Chemical Society* **131**, 18457-18466 (2009).
- 98 Mersch, D. *et al.* Wiring of Photosystem II to Hydrogenase for Photoelectrochemical Water Splitting. *Journal of the American Chemical Society* **137**, 8541-8549, doi:10.1021/jacs.5b03737 (2015).
- 99 Chaudhary, Y. S. *et al.* Visible light-driven CO<sub>2</sub> reduction by enzyme coupled CdS nanocrystals. *Chemical Communications* **48**, 58-60, doi:10.1039/C1CC16107E (2012).
- 100 Liu, Y. *et al.* Macroporous indium tin oxide electrode layers as conducting substrates for immobilization of bulky electroactive guests. *Electrochimica Acta* **140**, 108-115, doi:10.1016/j.electacta.2014.05.046 (2014).
- 101 Topoglidis, E., Discher, B. M., Moser, C. C., Dutton, P. L. & Durrant, J. R. Functionalizing Nanocrystalline Metal Oxide Electrodes with Robust Synthetic Redox Proteins. *ChemBioChem* **4**, 1332-1339, doi:10.1002/cbic.200300707 (2003).
- 102 Topoglidis, E. *et al.* Immobilization and electrochemistry of negatively charged proteins on modified nanocrystalline metal oxide electrodes. *Electroanalysis* **17**, 1035-1041, doi:10.1002/elan.200403211 (2005).
- 103 Fourmond, V. & Léger, C. in *Biophotoelectrochemistry: From Bioelectrochemistry to Biophotovoltaics* (ed Lars J. C. Jeuken) Ch. 1, 1-41 (Springer International Publishing, 2016).
- 104 Morra, S., Valetti, F., Sadeghi, S. J. & King, P. W. Direct electrochemistry of an [FeFe]-hydrogenase on a TiO<sub>2</sub> Electrode. *Chemical Communications* **47**, 10566-10568, doi:10.1039/c1cc14535e (2011).
- 105 Morra, S. *et al.* Hydrogen production at high Faradaic efficiency by a bio-electrode based on TiO<sub>2</sub> adsorption of a new [FeFe]-hydrogenase from *Clostridium perfringens*. *Bioelectrochemistry* **106**, 258-262, doi:10.1016/j.bioelechem.2015.08.001 (2015).
- 106 Goldet, G. *et al.* Electrochemical kinetic investigations of the reactions of [FeFe]-hydrogenases with carbon monoxide and oxygen: Comparing the importance of gas tunnels and active-site electronic/redox effects. *Journal of the American Chemical Society* **131**, 14979-14989, doi:10.1021/ja905388j (2009).
- 107 Parkin, A., Cavazza, C., Fontecilla-Camps, J. C. & Armstrong, F. A. Electrochemical Investigations of the Interconversions between Catalytic and Inhibited States of the [FeFe]-Hydrogenase from *Desulfovibrio desulfuricans*. *Journal of the American Chemical Society* **128**, 16808-16815, doi:10.1021/ja064425i (2006).
- 108 Ciornii, D. *et al.* Bioelectronic Circuit on a 3D Electrode Architecture: Enzymatic Catalysis Interconnected with Photosystem i. *Journal of the American Chemical Society* **139**, 16478-16481, doi:10.1021/jacs.7b10161 (2017).
- 109 Topoglidis, E., Campbell, C. J., Cass, A. E. G. & Durrant, J. R. Factors that affect protein adsorption on nanostructured titania films. A novel spectroelectrochemical application to sensing. *Langmuir* **17**, 7899-7906, doi:10.1021/la010309b (2001).
- 110 Svetlitchnyi, V., Peschel, C. & Acker, G. Two Membrane-Associated NiFeS-Carbon Monoxide Dehydrogenases from the Anaerobic Carbon-Monoxide-Utilizing Eubacterium *Carboxydotherrmus hydrogenoformans*. *Journal of Bacteriology* **183**, 5134-5144, doi:10.1128/JB.183.17.5134 (2001).

- 111 Reisner, E., Fontecilla-Camps, J. C. & Armstrong, F. A. Catalytic electrochemistry of a [NiFeSe]-hydrogenase on TiO<sub>2</sub> and demonstration of its suitability for visible-light driven H<sub>2</sub> production. *Chemical Communications*, 550-552, doi:10.1039/B817371K (2009).
- 112 Woolerton, T. W. *et al.* Efficient and clean photo-reduction of CO<sub>2</sub> to CO by enzyme-modified TiO<sub>2</sub> nanoparticles using visible light. *Journal of the American Chemical Society* **132**, 2132-2133, doi:10.1021/ja910091z.Efficient (2010).
- 113 Braun, R. S. M. & Shulten, K. S. Genetically Engineered Gold-Binding Polypeptides : Structure Prediction and Molecular Dynamics. *Journal of Biomaterials Science* **13**, 747-758, doi:10.1163/156856202760197384 (2002).
- 114 Wadu-Mesthrige, K., Amro, N. A. & Liu, G. Y. Immobilization of proteins on self-assembled monolayers. *Scanning* **22**, 380-388, doi:10.1002/sca.4950220607 (2000).
- 115 Song, S., Clark, R. A., Bowden, E. F. & Tarlov, M. J. Characterization of cytochrome c/alkanethiolate structures prepared by self-assembly on gold. *The Journal of Physical Chemistry* **97**, 6564-6572, doi:10.1021/j100126a037 (1993).
- 116 Jeuken, L. J. C. & Armstrong, F. A. Electrochemical origin of hysteresis in the electron-transfer reactions of adsorbed proteins: Contrasting behavior of the "Blue" copper protein, azurin, adsorbed on pyrolytic graphite and modified gold electrodes. *The Journal of Physical Chemistry B* **105**, 5271-5282, doi:10.1021/jp004283t (2001).
- 117 Khoshtariya, D. E., Dolidze, T. D., Tretyakova, T., Waldeck, D. H. & van Eldik, R. Electron transfer with azurin at Au-SAM junctions in contact with a protic ionic melt: impact of glassy dynamics. *Physical Chemistry Chemical Physics* **15**, 16515-16526, doi:10.1039/C3CP51896E (2013).
- 118 Khoshtariya, D. E., Dolidze, T. D., Shushanyan, M. & van Eldik, R. Long-Range Electron Transfer with Myoglobin Immobilized at Au/Mixed-SAM Junctions: Mechanistic Impact of the Strong Protein Confinement. *The Journal of Physical Chemistry B* **118**, 692-706, doi:10.1021/jp4101569 (2014).
- 119 Leopold, M. C. & Bowden, E. F. Influence of Gold Substrate Topography on the Voltammetry of Cytochrome c Adsorbed on Carboxylic Acid Terminated Self-Assembled Monolayers. *Langmuir* **18**, 2239-2245, doi:10.1021/la011456c (2002).
- 120 Bossertdt, M., Gajovic-Eichelman, N. & Scheller, F. W. Modulation of direct electron transfer of cytochrome c by use of a molecularly imprinted thin film. *Analytical and Bioanalytical Chemistry* **405**, 6437-6444, doi:10.1007/s00216-013-7009-8 (2013).
- 121 Qiang Feng, Z., Imabayashi, S., Kakiuchi, T. & Niki, K. Long-range electron-transfer reaction rates to cytochrome c across long- and short-chain alkanethiol self-assembled monolayers: Electroreflectance studies. *Journal of the Chemical Society, Faraday Transactions* **93**, 1367-1370, doi:10.1039/A605567B (1997).
- 122 Mondal, P. C. & Fontanesi, C. Electrochemistry of Metalloproteins Attached through Functional Self-Assembled Monolayers on Gold and Ferromagnetic Electrodes. *ChemPhysChem* **19**, 60-66, doi:10.1002/cphc.201701018 (2018).
- 123 Nahir, T. M. & Bowden, E. F. The distribution of standard rate constants for electron transfer between thiol-modified gold electrodes and adsorbed cytochrome c. *Journal of Electroanalytical Chemistry* **410**, 9-13, doi:10.1016/0022-0728(96)04551-2 (1996).
- 124 Sigma-Aldrich, Technical Bulletin AL-266: Preparing Self-Assembled Monolayers (SAMs), a Step-by-Step Guide for Solution-Based Self-Assembly, [https://www.sigmaaldrich.com/insite\\_al\\_techbull\\_al266](https://www.sigmaaldrich.com/insite_al_techbull_al266) (Accessed 1st December 2017).
- 125 Love, J. C., Estroff, L. A., Kriebel, J. K., Nuzzo, R. G. & Whitesides, G. M. Self-assembled monolayers of thiolates on metals as a form of nanotechnology. *Chemical Reviews* **105**, 1103-1169, doi:10.1021/cr0300789 (2005).
- 126 Gooding, J. J. & Ciampi, S. The molecular level modification of surfaces: from self-assembled monolayers to complex molecular assemblies. *Chemical Society Reviews* **40**, 2704-2718, doi:10.1039/C0CS00139B (2011).

- 127 Finklea, H. O. in *Encyclopedia of Analytical Chemistry* (eds Meyers, R.A., H.S. White, & R.M. Crooks) 2-4 (John Wiley & Sons, Ltd, 2006).
- 128 Sezer, M. *et al.* Redox properties and catalytic activity of surface-bound human sulfite oxidase studied by a combined surface enhanced resonance Raman spectroscopic and electrochemical approach. *Physical Chemistry Chemical Physics* **12**, 7894-7903, doi:10.1039/B927226G (2010).
- 129 Laibinis, P. E. *et al.* Comparison of the structures and wetting properties of self-assembled monolayers of n-alkanethiols on the coinage metal surfaces, copper, silver, and gold. *Journal of the American Chemical Society* **113**, 7152-7167, doi:10.1021/ja00019a011 (1991).
- 130 Love, J. C. *et al.* Formation and Structure of Self-Assembled Monolayers of Alkanethiolates on Palladium. *Journal of the American Chemical Society* **125**, 2597-2609, doi:10.1021/ja028692+ (2003).
- 131 Schuhmann, W. Amperometric enzyme biosensors based on optimised electron-transfer pathways and non-manual immobilisation procedures. *Reviews in Molecular Biotechnology* **82**, 425-441, doi:10.1016/S1389-0352(01)00058-7 (2002).
- 132 Chi, Q., Zhang, J., Andersen, J. E. T. & Ulstrup, J. Ordered assembly and controlled electron transfer of the blue copper protein azurin at gold (111) single-crystal substrates. *The Journal of Physical Chemistry B* **105**, 4669-4679, doi:10.1021/jp0105589 (2001).
- 133 Frasconi, M., Mazzei, F. & Ferri, T. Protein immobilization at gold-thiol surfaces and potential for biosensing. *Analytical and Bioanalytical Chemistry* **398**, 1545-1564, doi:10.1007/s00216-010-3708-6 (2010).
- 134 Salverda, J. M. *et al.* Fluorescent cyclic voltammetry of immobilized azurin: Direct observation of thermodynamic and kinetic heterogeneity. *Angewandte Chemie International Edition* **49**, 5776-5779, doi:10.1002/anie.201001298 (2010).
- 135 Patil, A. V. & Davis, J. J. Visualizing and tuning thermodynamic dispersion in metalloprotein monolayers. *Journal of the American Chemical Society* **132**, 16938-16944, doi:10.1021/ja1065448 (2010).
- 136 Krassen, H. *et al.* Immobilization of the [FeFe]-hydrogenase CrHydA1 on a gold electrode: Design of a catalytic surface for the production of molecular hydrogen. *Journal of Biotechnology* **142**, 3-9, doi:10.1016/j.jbiotec.2009.01.018 (2009).
- 137 Sato, Y. & Mizutani, F. Electrochemical responses of cytochrome c on a gold electrode modified with mixed monolayers of 3-mercaptopropionic acid and n-alkanethiol. *Journal of Electroanalytical Chemistry* **438**, 99-104 (1997).
- 138 Imabayashi, S. I., Mita, T. & Kakiuchi, T. Effect of the electrostatic interaction on the redox reaction of positively charged cytochrome c adsorbed on the negatively charged surfaces of acid-terminated alkanethiol monolayers on a Au(111) electrode. *Langmuir* **21**, 1470-1474, doi:10.1021/la047992x (2005).
- 139 Fojta, M. *Electrochemistry of Nucleic Acids and Proteins – Towards Electrochemical Sensors for Genomics and Proteomics*. Vol. 1 (2005).
- 140 Tanimura, R. *et al.* Active Carboxylic Acid-Terminated Alkanethiol Self-Assembled Monolayers on Gold Bead Electrodes for Immobilization of Cytochromes c. *Electrochemical and Solid-State Letters* **5**, E67-E70 (2002).
- 141 Glenn, J. D. H. & Bowden, E. F. Diffusionless Electrochemistry of Cytochrome b5 Adsorbed on a Multilayer Film Electrode. *Chemistry Letters* **25**, 399-400, doi:10.1246/cl.1996.399 (1996).
- 142 Frey, B. L., Jordan, C. E., Kornguth, S. & Corn, R. M. Control of the Specific Adsorption of Proteins onto Gold Surfaces with Poly(L-lysine) Monolayers. *Analytical Chemistry* **67**, 4452-4457, doi:10.1021/ac00120a003 (1995).
- 143 Mizutani, F., Sato, Y., Yabuki, S. & Hirata, Y. Enzyme Ultra-thin Layer Electrode Prepared by the Co-adsorption of Poly-L-lysine and Glucose Oxidase onto a Mercaptopropionic Acid-Modified Gold Surface. *Chemistry Letters* **25**, 251-252, doi:10.1246/cl.1996.251 (1996).



- 144 Barker, P. D., Butler, J. L., de Oliveira, P., Hill, H. A. O. & Hunt, N. I. Direct electrochemical studies of cytochromes b562. *Inorganica Chimica Acta* **252**, 71-77, doi:10.1016/S0020-1693(96)05299-1 (1996).
- 145 Kazlauskaitė, J., Hill, H. A. O., Wilkins, P. C. & Dalton, H. Direct Electrochemistry of the Hydroxylase of Soluble Methane Monooxygenase from *Methylococcus Capsulatus* (Bath). *European Journal of Biochemistry* **241**, 552-556, doi:10.1111/j.1432-1033.1996.00552.x (1996).
- 146 Arnold, S., Feng, Z. Q., Kakiuchi, T., Knoll, W. & Niki, K. Investigation of the electrode reaction of cytochrome c through mixed self-assembled monolayers of alkanethiols on gold(111) surfaces. *Journal of Electroanalytical Chemistry* **438**, 91-97, doi:10.1016/S0022-0728(96)05065-6 (1997).
- 147 Jeuken, L. J. C. *et al.* Redox Enzymes in Tethered Membranes. *Journal of the American Chemical Society* **128**, 1711-1716, doi:10.1021/ja056972u (2006).
- 148 Radu, V., Frielingsdorf, S., Evans, S. D., Lenz, O. & Jeuken, L. J. C. Enhanced Oxygen-Tolerance of the Full Heterotrimeric Membrane-Bound [NiFe]-Hydrogenase of *Ralstonia eutropha*. *Journal of the American Chemical Society* **136**, 8512-8515, doi:10.1021/ja503138p (2014).
- 149 Radu, V., Frielingsdorf, S., Lenz, O. & Jeuken, L. J. Reactivation from the Ni-B state in [NiFe] hydrogenase of *Ralstonia eutropha* is controlled by reduction of the superoxidised proximal cluster. *Chemical Communications* **52**, 2632-2635, doi:10.1039/c5cc10382g (2016).
- 150 Wright, E. J., Sosna, M., Bloodworth, S., Kilburn, J. D. & Bartlett, P. N. Design of maleimide-functionalised electrodes for covalent attachment of proteins through free surface cysteine groups. *Chemistry – A European Journal* **20**, 5550-5554, doi:10.1002/chem.201400246 (2014).
- 151 Laibinis, P. E., Fox, M. A., Folkers, J. P. & Whitesides, G. M. Comparisons of self-assembled monolayers on silver and gold: mixed monolayers derived from HS(CH<sub>2</sub>)<sub>21</sub>X and HS(CH<sub>2</sub>)<sub>10</sub>Y (X, Y = CH<sub>3</sub>, CH<sub>2</sub>OH) have similar properties. *Langmuir* **7**, 3167-3173 (1991).
- 152 Armstrong, F. A. *et al.* Fast, long-range electron-transfer reactions of a 'blue' copper protein coupled non-covalently to an electrode through a stilbenyl thiolate monolayer. *Chemical Communications*, 316-317, doi:10.1039/B312936E (2004).
- 153 Krassen, H. *et al.* Tailor-Made Modification of a Gold Surface for the Chemical Binding of a High-Activity [FeFe] Hydrogenase. *European Journal of Inorganic Chemistry* **2011**, 1138-1146, doi:10.1002/ejic.201001190 (2011).
- 154 Downard, A. J. Electrochemically Assisted Covalent Modification of Carbon Electrodes. *Electroanalysis* **12**, 1085-1096, doi:10.1002/1521-4109(200010)12:14<1085::AID-ELAN1085>3.0.CO;2-A (2000).
- 155 Pinson, J. & Podvorica, F. Attachment of organic layers to conductive or semiconductive surfaces by reduction of diazonium salts. *Chemical Society Reviews* **34**, 429-439, doi:10.1039/B406228K (2005).
- 156 Sinitskii, A. *et al.* Kinetics of Diazonium Functionalization of Chemically Converted Graphene Nanoribbons. *ACS Nano* **4**, 1949-1954, doi:10.1021/nn901899j (2010).
- 157 He, T. *et al.* Controlled Modulation of Conductance in Silicon Devices by Molecular Monolayers. *Journal of the American Chemical Society* **128**, 14537-14541, doi:10.1021/ja063571l (2006).
- 158 Maldonado, S. *et al.* Surface Modification of Indium Tin Oxide via Electrochemical Reduction of Aryldiazonium Cations. *Langmuir* **22**, 2884-2891, doi:10.1021/la052696l (2006).
- 159 Bernard, M.-C. *et al.* Organic Layers Bonded to Industrial, Coinage, and Noble Metals through Electrochemical Reduction of Aryldiazonium Salts. *Chemistry of Materials* **15**, 3450-3462, doi:10.1021/cm034167d (2003).
- 160 Saby, C., Ortiz, B., Champagne, G. Y. & Bélanger, D. Electrochemical Modification of Glassy Carbon Electrode Using Aromatic Diazonium Salts. 1. Blocking Effect of 4-Nitrophenyl and 4-Carboxyphenyl Groups. *Langmuir* **13**, 6805-6813, doi:10.1021/la961033o (1997).

- 161 Pinson, J. in *Aryl Diazonium Salts: New Coupling Agents in Polymer and Surface Science* (ed Mohamed Mehdi Chehimi) Ch. 1, 1-4 (Wiley-VCH Verlag GmbH & Co. KGaA, 2012).
- 162 Chehimi, M. M. *Aryl Diazonium Salts: New Coupling Agents in Polymer and Surface Science*. 1 edn, (Wiley-VCH Verlag GmbH & Co, 2012).
- 163 Cougnon, C., Gohier, F., Bélanger, D. & Mauzeroll, J. In Situ Formation of Diazonium Salts from Nitro Precursors for Scanning Electrochemical Microscopy Patterning of Surfaces. *Angewandte Chemie International Edition* **48**, 4006-4008, doi:10.1002/anie.200900498 (2009).
- 164 Delamar, M., Hitmi, R., Pinson, J. & Savéant, J. Covalent Modification of Carbon Surfaces by Grafting of Functionalized Aryl Radicals Produced from Electrochemical Reduction of Diazonium Salts. *Journal of the American Chemical Society* **114**, 5883-5884, doi:10.1021/ja00040a074 (1992).
- 165 Allongue, P. *et al.* Covalent Modification of Carbon Surfaces by Aryl Radicals Generated from the Electrochemical Reduction of Diazonium Salts. *Journal of the American Chemical Society* **119**, 201-207, doi:10.1021/ja963354s (1997).
- 166 Delamar, M. *et al.* Modification of carbon fiber surfaces by electrochemical reduction of aryl diazonium salts: Application to carbon epoxy composites. *Carbon* **35**, 801-807, doi:10.1016/S0008-6223(97)00010-9 (1997).
- 167 Liu, G., Böcking, T. & Gooding, J. J. Diazonium salts: Stable monolayers on gold electrodes for sensing applications. *Journal of Electroanalytical Chemistry* **600**, 335-344, doi:10.1016/j.jelechem.2006.09.012 (2007).
- 168 Randriamahazaka, H. & Ghilane, J. Electrografting and Controlled Surface Functionalization of Carbon Based Surfaces for Electroanalysis. *Electroanalysis* **28**, 13-26, doi:10.1002/elan.201500527 (2016).
- 169 Menanteau, T., Dias, M., Levillain, E., Downard, A. J. & Breton, T. Electrografting via Diazonium Chemistry: The Key Role of the Aryl Substituent in the Layer Growth Mechanism. *The Journal of Physical Chemistry C* **120**, 4423-4429, doi:10.1021/acs.jpcc.5b12565 (2016).
- 170 Menanteau, T., Levillain, E. & Breton, T. Electrografting via diazonium chemistry: From multilayer to monolayer using radical scavenger. *Chemistry of Materials* **25**, 2905-2909, doi:10.1021/cm401512c (2013).
- 171 Hauquier, F., Debou, N., Palacin, S. & Joussetme, B. Amino functionalized thin films prepared from Gabriel synthesis applied on electrografted diazonium salts. *Journal of Electroanalytical Chemistry* **677-680**, 127-132, doi:10.1016/j.jelechem.2012.05.016 (2012).
- 172 Combellas, C., Kanoufi, F., Pinson, J. & Podvorica, F. I. Sterically Hindered Diazonium Salts for the Grafting of a Monolayer on Metals. *Journal of the American Chemical Society* **130**, 8576-8577, doi:10.1021/ja8018912 (2008).
- 173 López, I., Cesbron, M., Levillain, E. & Breton, T. Diazonium Grafting Control through a Redox Cross-Reaction: Elucidation of the Mechanism Involved when using 2,2-Diphenylpicrylhydrazyl as an Inhibitor. *ChemElectroChem* **5**, 1197-1202, doi:10.1002/celec.201701331 (2018).
- 174 Vakurov, A., Simpson, C. E., Daly, C. L., Gibson, T. D. & Millner, P. A. Acetylcholinesterase-based biosensor electrodes for organophosphate pesticide detection: I. Modification of carbon surface for immobilization of acetylcholinesterase. *Biosensors and Bioelectronics* **20**, 1118-1125, doi:10.1016/j.bios.2004.03.039 (2004).
- 175 Alonso-Lomillo, M. A., Yardimci, C., Domínguez-Renedo, O. & Arcos-Martínez, M. J. CYP450 2B4 covalently attached to carbon and gold screen printed electrodes by diazonium salt and thiols monolayers. *Analytica Chimica Acta* **633**, 51-56, doi:10.1016/j.aca.2008.11.033 (2009).
- 176 Cortina-Puig, M., Muñoz-Berbel, X., Calas-Blanchard, C. & Marty, J. L. Diazonium-functionalized tyrosinase-based biosensor for the detection of tea polyphenols. *Microchimica Acta* **171**, 187-193, doi:10.1007/s00604-010-0425-y (2010).

- 177 Radi, A.-E., Muñoz-Berbel, X., Cortina-Puig, M. & Marty, J.-L. A Third-Generation Hydrogen Peroxide Biosensor Based on Horseradish Peroxidase Covalently Immobilized on Electrografted Organic Film on Screen-Printed Carbon Electrode. *Electroanalysis* **21**, 1624-1629, doi:10.1002/elan.200904587 (2009).
- 178 Liu, M., Qi, Y. & Zhao, G. Carboxyphenyl Covalent Immobilization of Heme Proteins and its Favorable Biocompatible Electrochemical and Electrocatalytic Characteristics. *Electroanalysis* **20**, 900-906, doi:10.1002/elan.200704114 (2008).
- 179 Bourdillon, C. *et al.* Immobilization of glucose oxidase on a carbon surface derivatized by electrochemical reduction of diazonium salts. *Journal of Electroanalytical Chemistry* **336**, 113-123, doi:10.1016/0022-0728(92)80266-7 (1992).
- 180 Yang, X., Hall, S. B. & Ngim Tan, S. Electrochemical Reduction of a Conjugated Cinnamic Acid Diazonium Salt as an Immobilization Matrix for Glucose Biosensor. *Electroanalysis* **15**, 885-891, doi:10.1002/elan.200390110 (2003).
- 181 Zhou, Y. & Zhi, J. Development of an amperometric biosensor based on covalent immobilization of tyrosinase on a boron-doped diamond electrode. *Electrochemistry Communications* **8**, 1811-1816, doi:10.1016/j.elecom.2006.08.022 (2006).
- 182 Alonso-Lomillo, M. A., Domínguez-Renedo, O., Hernández-Martín, A. & Arcos-Martínez, M. J. Horseradish peroxidase covalent grafting onto screen-printed carbon electrodes for levetiracetam chronoamperometric determination. *Analytical Biochemistry* **395**, 86-90, doi:10.1016/j.ab.2009.08.004 (2009).
- 183 Asturias-Arribas, L., Asunción Alonso-Lomillo, M., Domínguez-Renedo, O. & Julia Arcos-Martínez, M. Cytochrome P450 2D6 based electrochemical sensor for the determination of codeine. *Talanta* **129**, 315-319, doi:10.1016/j.talanta.2014.05.053 (2014).
- 184 Radi, A.-E., Muñoz-Berbel, X., Cortina-Puig, M. & Marty, J.-L. Novel Protocol for Covalent Immobilization of Horseradish Peroxidase on Gold Electrode Surface. *Electroanalysis* **21**, 696-700, doi:10.1002/elan.200804466 (2009).
- 185 Flavel, B. S., Gross, A. J., Garrett, D. J., Nock, V. & Downard, A. J. A simple approach to patterned protein immobilization on silicon via electrografting from diazonium salt solutions. *ACS Applied Materials & Interfaces* **2**, 1184-1190, doi:10.1021/am100020a (2010).
- 186 Harper, J. C., Polsky, R., Wheeler, D. R. & Brozik, S. M. Maleimide-Activated Aryl Diazonium Salts for Electrode Surface Functionalization with Biological and Redox-Active Molecules. *Langmuir* **24**, 2206-2211, doi:10.1021/la702613e (2008).
- 187 Singh, K., McArdle, T., Sullivan, P. R. & Blanford, C. F. Sources of activity loss in the fuel cell enzyme bilirubin oxidase. *Energy & Environmental Science* **6**, 2460-2464, doi:10.1039/C3EE00043E (2013).
- 188 Samanta, D. & Sarkar, A. Immobilization of bio-macromolecules on self-assembled monolayers: methods and sensor applications. *Chemical Society Reviews* **40**, 2567-2592, doi:10.1039/C0CS00056F (2011).
- 189 Collinson, M., Bowden, E. F. & Tarlov, M. J. Voltammetry of covalently immobilized cytochrome c on self-assembled monolayer electrodes. *Langmuir* **8**, 1247-1250, doi:10.1021/la00041a004 (1992).
- 190 Ducker, R. E., Montague, M. T. & Leggett, G. J. A comparative investigation of methods for protein immobilization on self-assembled monolayers using glutaraldehyde, carbodiimide, and anhydride reagents. *Biointerphases* **3**, 59-65, doi:10.1116/1.2976451 (2008).
- 191 Karimi Shervedani, R. & Samiei Ferooshani, M. Comparative Electrochemical Behavior of Proteins; Cytochrome c, Agaricus Bisporus Laccase, and Glucose Oxidase, Immobilized onto Gold-Thiol Self-Assembled Monolayer via Electrostatic, Covalent, and Covalent Coordinate Bond Methods. *Electrochimica Acta* **187**, 646-654, doi:10.1016/j.electacta.2015.11.080 (2016).

- 192 Davis, K. L. *et al.* Electron-Transfer Kinetics of Covalently Attached Cytochrome *c*/SAM/Au Electrode Assemblies. *The Journal of Physical Chemistry C* **112**, 6571-6576, doi:10.1021/jp711834t (2008).
- 193 Ge, B. & Lisdat, F. Superoxide sensor based on cytochrome *c* immobilized on mixed-thiol SAM with a new calibration method. *Analytica Chimica Acta* **454**, 53-64, doi:10.1016/S0003-2670(01)01545-8 (2002).
- 194 Sohn, Y.-s. & Lee, Y. K. Site-directed immobilization of antibody using EDC-NHS-activated protein A on a bimetallic-based surface plasmon resonance chip. *Journal of Biomedical Optics* **19**, 1-7, doi:10.1117/1 (2014).
- 195 Krishnan, S. & Armstrong, F. A. Order-of-magnitude enhancement of an enzymatic hydrogen-air fuel cell based on pyrenyl carbon nanostructures. *Chemical Science* **3**, 1015-1023, doi:10.1039/C2SC01103D (2012).
- 196 Griveau, S., Mercier, D., Vautrin-UI, C. & Chaussé, A. Electrochemical grafting by reduction of 4-aminoethylbenzenediazonium salt: Application to the immobilization of (bio)molecules. *Electrochemistry Communications* **9**, 2768-2773, doi:10.1016/j.elecom.2007.09.004 (2007).
- 197 Lee, L., Leroux, Y. R., Hapiot, P. & Downard, A. J. Amine-terminated monolayers on carbon: Preparation, characterization, and coupling reactions. *Langmuir* **31**, 5071-5077, doi:10.1021/acs.langmuir.5b00730 (2015).
- 198 Lalaoui, N. *et al.* Direct Electron Transfer between a Site-Specific Pyrene-Modified Laccase and Carbon Nanotube/Gold Nanoparticle Supramolecular Assemblies for Bioelectrocatalytic Dioxxygen Reduction. *ACS Catalysis* **6**, 1894-1900, doi:10.1021/acscatal.5b02442 (2016).
- 199 Vakurov, A., Simpson, C. E., Daly, C. L., Gibson, T. D. & Millner, P. A. Acetylcholinesterase-based biosensor electrodes for organophosphate pesticide detection: II. Immobilization and stabilization of acetylcholinesterase. *Biosensors and Bioelectronics* **20**, 2324-2329, doi:10.1016/j.bios.2004.07.022 (2005).
- 200 Sun, Y., Yan, F., Yang, W. & Sun, C. Multilayered construction of glucose oxidase and silica nanoparticles on Au electrodes based on layer-by-layer covalent attachment. *Biomaterials* **27**, 4042-4049, doi:10.1016/j.biomaterials.2006.03.014 (2006).
- 201 Wang, H., Castner, D. G., Ratner, B. D. & Jiang, S. Probing the Orientation of Surface-Immobilized Immunoglobulin G by Time-of-Flight Secondary Ion Mass Spectrometry. *Langmuir* **20**, 1877-1887, doi:10.1021/la035376f (2004).
- 202 Hong, Q. *et al.* Immobilisation of proteins at silicon surfaces using undecenylaldehyde: demonstration of the retention of protein functionality and detection strategies. *Analyst* **134**, 593-601, doi:10.1039/B813328J (2009).
- 203 Onoda, A., Inoue, N., Campidelli, S. & Hayashi, T. Cofactor-specific covalent anchoring of cytochrome *b* 562 on a single-walled carbon nanotube by click chemistry. *RSC Advances* **6**, 65936-65940, doi:10.1039/C6RA14195A (2016).
- 204 Stan, R. C., Kros, A., Appel, J. & Sanghamitra, N. J. M. Probing the Active Site of an Azurin Mutant Hot-Wired to Gold Electrodes. *The Journal of Physical Chemistry C* **120**, 7639-7645, doi:10.1021/acs.jpcc.6b01159 (2016).
- 205 Berg, J. M., Tymoczko, J. L. & Stryer, L. *Biochemistry*. 5 edn, (W. H. Freeman and Company, 2002).
- 206 Blanford, C. F., Foster, C. E., Heath, R. S. & Armstrong, F. A. Efficient electrocatalytic oxygen reduction by the 'blue' copper oxidase, laccase, directly attached to chemically modified carbons. *Faraday Discussions* **140**, 319-335, doi:10.1039/B808939F (2009).
- 207 Blanford, C. F., Heath, R. S. & Armstrong, F. A. A stable electrode for high-potential, electrocatalytic O<sub>2</sub> reduction based on rational attachment of a blue copper oxidase to a graphite surface. *Chemical Communications*, 1710-1712, doi:10.1039/B703114A (2007).
- 208 dos Santos, L., Climent, V., Blanford, C. F. & Armstrong, F. A. Mechanistic studies of the 'blue' Cu enzyme, bilirubin oxidase, as a highly efficient electrocatalyst for the oxygen reduction

- reaction. *Physical Chemistry Chemical Physics* **12**, 13962-13974, doi:10.1039/C0CP00018C (2010).
- 209 Wait, A. F., Parkin, A., Morley, G. M., dos Santos, L. & Armstrong, F. A. Characteristics of Enzyme-Based Hydrogen Fuel Cells Using an Oxygen-Tolerant Hydrogenase as the Anodic Catalyst. *The Journal of Physical Chemistry C* **114**, 12003-12009, doi:10.1021/jp102616m (2010).
- 210 O'Brien, E. *et al.* The [4Fe4S] cluster of human DNA primase functions as a redox switch using DNA charge transport. *Science* **355**, doi:10.1126/science.aan2396 (2017).
- 211 Chalker, J. M., Bernardes, G. J. L., Lin, Y. A. & Davis, B. G. Chemical Modification of Proteins at Cysteine: Opportunities in Chemistry and Biology. *Chemistry – An Asian Journal* **4**, 630-640, doi:10.1002/asia.200800427 (2009).
- 212 Chalker, J. M. *et al.* Methods for converting cysteine to dehydroalanine on peptides and proteins. *Chemical Science* **2**, 1666-1676, doi:10.1039/C1SC00185J (2011).
- 213 Spicer, C. D. & Davis, B. G. Selective chemical protein modification. *Nature Communications* **5**, 4740, doi:10.1038/ncomms5740 (2014).
- 214 Chalker, J. M., Bernardes, G. J. L. & Davis, B. G. A "Tag-and-Modify" Approach to Site-Selective Protein Modification. *Accounts of Chemical Research* **44**, 730-741, doi:10.1021/ar200056q (2011).
- 215 Marino, S. M. & Gladyshev, V. N. Analysis and functional prediction of reactive cysteine residues. *Journal of Biological Chemistry* **287**, 4419-4425, doi:10.1074/jbc.R111.275578 (2012).
- 216 van der Felt, C. *et al.* Electron-transfer rates govern product distribution in electrochemically-driven P450-catalyzed dioxygen reduction. *Journal of Inorganic Biochemistry* **105**, 1350-1353, doi:10.1016/j.jinorgbio.2011.03.006 (2011).
- 217 Al-Lolage, F. A., Meneghello, M., Ma, S., Ludwig, R. & Bartlett, P. N. A Flexible Method for the Stable, Covalent Immobilization of Enzymes at Electrode Surfaces. *ChemElectroChem* **4**, 1528-1534, doi:10.1002/celec.201700135 (2017).
- 218 Lo, K. K.-W., Wong, L.-L. & Hill, H. A. O. Surface-modified mutants of cytochrome P450cam: enzymatic properties and electrochemistry. *FEBS Letters* **451**, 342-346, doi:10.1016/S0014-5793(99)00611-0 (1999).
- 219 van Vught, R., Pieters, R. J. & Breukink, E. Site-Specific Functionalization of Proteins and their Applications to Therapeutic Antibodies. *Computational and Structural Biotechnology Journal* **9**, e201402001, doi:10.5936/csbj.201402001 (2014).
- 220 Evans, R. M. *et al.* Principles of Sustained Enzymatic Hydrogen Oxidation in the Presence of Oxygen – The Crucial Influence of High Potential Fe–S Clusters in the Electron Relay of [NiFe]-Hydrogenases. *Journal of the American Chemical Society* **135**, 2694-2707, doi:10.1021/ja311055d (2013).
- 221 Kim, Y. *et al.* Efficient Site-Specific Labeling of Proteins via Cysteines. *Bioconjugate Chemistry* **19**, 786-791, doi:10.1021/bc7002499 (2008).
- 222 Della Pia, E. A., Macdonald, J. E., Elliott, M. & Jones, D. D. Direct Binding of a Redox Protein for Single-Molecule Electron Transfer Measurements. *Small* **8**, 2341-2344, doi:10.1002/sml.201102416 (2012).
- 223 Plumere, N. & Nowaczyk, M. M. in *Biophotoelectrochemistry: From Bioelectrochemistry to Biophotovoltaics* (ed Lars J. C. Jeuken) Ch. 4, 111-136 (Springer International Publishing, 2016).
- 224 Nair, D. P. *et al.* The Thiol-Michael Addition Click Reaction: A Powerful and Widely Used Tool in Materials Chemistry. *Chemistry of Materials* **26**, 724-744, doi:10.1021/cm402180t (2014).
- 225 Zimmermann, J. L., Nicolaus, T., Neuert, G. & Blank, K. Thiol-based, site-specific and covalent immobilization of biomolecules for single-molecule experiments. *Nature Protocols* **5**, 975-985, doi:10.1038/nprot.2010.49 (2010).

- 226 Hoyle, C. E. & Bowman, C. N. Thiol-ene click chemistry. *Angewandte Chemie International Edition* **49**, 1540-1573, doi:10.1002/anie.200903924 (2010).
- 227 Zhang, L. *et al.* Immobilization of Cysteine-Tagged Proteins on Electrode Surfaces by Thiol–Ene Click Chemistry. *ACS Applied Materials & Interfaces* **8**, 17591-17598, doi:10.1021/acsami.6b02364 (2016).
- 228 Houseman, B. T., Gawalt, E. S. & Mrksich, M. Maleimide-Functionalized Self-Assembled Monolayers for the Preparation of Peptide and Carbohydrate Biochips. *Langmuir* **19**, 1522-1531, doi:10.1021/la0262304 (2003).
- 229 Wals, K. & Ovaa, H. Unnatural amino acid incorporation in *E. coli*: current and future applications in the design of therapeutic proteins. *Frontiers in Chemistry* **2**, 15-15, doi:10.3389/fchem.2014.00015 (2014).
- 230 Brabham, R. & Fascione, M. A. Pyrrolysine Amber Stop-Codon Suppression: Development and Applications. *ChemBioChem* **18**, 1973-1983, doi:10.1002/cbic.201700148 (2017).
- 231 Lang, K. & Chin, J. W. Cellular Incorporation of Unnatural Amino Acids and Bioorthogonal Labeling of Proteins. *Chemical Reviews* **114**, 4764-4806, doi:10.1021/cr400355w (2014).
- 232 Wang, F., Robbins, S., Guo, J., Shen, W. & Schultz, P. G. Genetic Incorporation of Unnatural Amino Acids into Proteins in *Mycobacterium tuberculosis*. *PLOS ONE* **5**, e9354, doi:10.1371/journal.pone.0009354 (2010).
- 233 Ryu, Y. & Schultz, P. G. Efficient incorporation of unnatural amino acids into proteins in *Escherichia coli*. *Nature Methods* **3**, 263-265, doi:10.1038/nmeth864 (2006).
- 234 Tookmanian, E. M., Fenlon, E. E. & Brewer, S. H. Synthesis and protein incorporation of azido-modified unnatural amino acids. *RSC Advances* **5**, 1274-1281, doi:10.1039/C4RA14244F (2015).
- 235 Guan, D., Kurra, Y., Liu, W. & Chen, Z. A click chemistry approach to site-specific immobilization of a small laccase enables efficient direct electron transfer in a biocathode. *Chemical Communications* **51**, 2522-2525, doi:10.1039/C4CC09179E (2015).
- 236 Amir, L. *et al.* Surface Display of a Redox Enzyme and its Site-Specific Wiring to Gold Electrodes. *Journal of the American Chemical Society* **135**, 70-73, doi:10.1021/ja310556n (2013).
- 237 Ray, S. *et al.* Implications of active site orientation in myoglobin for direct electron transfer and electrocatalysis based on monolayer and multilayer covalent immobilization on gold electrodes. *Electrochimica Acta* **99**, 85-93, doi:10.1016/j.electacta.2013.03.080 (2013).
- 238 Juan-Colás, J. *et al.* The electrophotonic silicon biosensor. *Nature Communications* **7**, 12769, doi:10.1038/ncomms12769 (2016).
- 239 Jewett, J. C. & Bertozzi, C. R. Cu-free click cycloaddition reactions in chemical biology. *Chemical Society Reviews* **39**, 1272-1279, doi:10.1039/B901970G (2010).
- 240 Moses, J. E. & Moorhouse, A. D. The growing applications of click chemistry. *Chemical Society Reviews* **36**, 1249-1262, doi:10.1039/B613014N (2007).
- 241 Bard, A. J. & Faulkner, L. R. *Electrochemical Methods: Fundamentals and Applications*. 2 edn, (Wiley, 2001).
- 242 Adamson, H. *et al.* Electrochemical evidence that pyranopterin redox chemistry controls the catalysis of YedY, a mononuclear Mo enzyme. *Proceedings of the National Academy of Sciences* **112**, 14506-14511, doi:10.1073/pnas.1516869112 (2015).
- 243 Butt, J. in *Encyclopedia of Applied Electrochemistry* (eds Gerhard Kreysa, Ken-ichiro Ota, & Robert F. Savinell) 2103-2109 (Springer New York, 2014).
- 244 Randviir, E. P. A cross examination of electron transfer rate constants for carbon screen-printed electrodes using Electrochemical Impedance Spectroscopy and cyclic voltammetry. *Electrochimica Acta* **286**, 179-186, doi:10.1016/j.electacta.2018.08.021 (2018).
- 245 Léger, C. in *Practical Approaches to Biological Inorganic Chemistry* (eds Robert Crichton & Ricardo Louro) 179-216 (Elsevier, 2013).
- 246 Oldham, K. B., Myland, J. C. & Bond, A. M. *Electrode Reactions*. 1 edn, 125-144 (John Wiley & Sons, Ltd, 2012).

- 247 Compton, R. G. & Banks, C. E. *Understanding Voltammetry*. 2nd edn, (Imperial College Press, 2011).
- 248 Atkins, P. & de Paula, J. *Physical Chemistry*. (W. H. Freeman, 2007).
- 249 Heering, H. A., Weiner, J. H. & Armstrong, F. A. Direct Detection and Measurement of Electron Relays in a Multicentered Enzyme: Voltammetry of Electrode-Surface Films of *E. coli* Fumarate Reductase, an Iron–Sulfur Flavoprotein. *Journal of the American Chemical Society* **119**, 11628-11638, doi:10.1021/ja9723242 (1997).
- 250 Atkins, P. *Shriver and Atkins' inorganic chemistry*. (Oxford University Press, USA, 2010).
- 251 Fisher, A. C. *Electrode Dynamics*. (Oxford University Press, 1996).
- 252 Brett, C. M. A. & Brett, A. M. O. *Electroanalysis*. (Oxford University Press, 1998).
- 253 Stuve, E. M. in *Encyclopedia of Applied Electrochemistry* (eds Gerhard Kreysa, Ken-ichiro Ota, & Robert F. Savinell) 1445-1453 (Springer New York, 2014).
- 254 Adesokan, B. J. *et al.* Experimentation and numerical modeling of cyclic voltammetry for electrochemical micro-sized sensors under the influence of electrolyte flow. *Journal of Electroanalytical Chemistry* **763**, 141-148, doi:10.1016/j.jelechem.2015.12.029 (2016).
- 255 Laviron, E. General expression of the linear potential sweep voltammogram in the case of diffusionless electrochemical systems. *Journal of Electroanalytical Chemistry and Interfacial Electrochemistry* **101**, 19-28, doi:10.1016/S0022-0728(79)80075-3 (1979).
- 256 Kang, Z. *et al.* Direct electrochemistry and bioelectrocatalysis of glucose oxidase in CS/CNC film and its application in glucose biosensing and biofuel cells. *RSC Advances* **7**, 4572-4579, doi:10.1039/c6ra26636c (2017).
- 257 Hanna, C. M., Sanborn, C. D., Ardo, S. & Yang, J. Y. Interfacial Electron Transfer of Ferrocene Immobilized onto Indium Tin Oxide through Covalent and Noncovalent Interactions. *ACS Applied Materials & Interfaces* **10**, 13211-13217, doi:10.1021/acsami.8b01219 (2018).
- 258 Hong, H. G. & Mallouk, T. E. Electrochemical measurements of electron transfer rates through zirconium 1,2-ethanediylbis(phosphonate) multilayer films on gold electrodes. *Langmuir* **7**, 2362-2369, doi:10.1021/la00058a065 (1991).
- 259 Kasa, T. & Solomon, T. Cyclic Voltammetric and Electrochemical Simulation Studies on the Electro-Oxidation of Catechol in the Presence of 4, 4'-bipyridine. *American Journal of Physical Chemistry* **5**, 45-55, doi:doi: 10.11648/j.ajpc.20160503.11 (2016).
- 260 Mirceski, V., Laborda, E., Guziejewski, D. & Compton, R. G. New Approach to Electrode Kinetic Measurements in Square-Wave Voltammetry: Amplitude-Based Quasireversible Maximum. *Analytical Chemistry* **85**, 5586-5594, doi:10.1021/ac4008573 (2013).
- 261 Gulaboski, R., Mirceski, V. & Lovric, M. Square-wave protein-film voltammetry: new insights in the enzymatic electrode processes coupled with chemical reactions. *Journal of Solid State Electrochemistry* **23**, 2493-2506, doi:10.1007/s10008-019-04320-7 (2019).
- 262 Lubner, C. E. *et al.* Mechanistic insights into energy conservation by flavin-based electron bifurcation. *Nature Chemical Biology* **13**, 655-659, doi:10.1038/nchembio.2348 (2017).
- 263 <https://creativecommons.org/licenses/by/3.0/> (Accessed January 2021).
- 264 Adamson, H., Bond, A. M. & Parkin, A. Probing biological redox chemistry with large amplitude Fourier transformed ac voltammetry. *Chemical Communications* **53**, 9519-9533, doi:10.1039/C7CC03870D (2017).
- 265 Using Purely Sinusoidal Voltammetry for Rapid Parameterization of Surface-Confined Electrochemistry. doi:10.26434/chemrxiv.12919367.v1 (2020).
- 266 Oliveira, B. L., Guo, Z. & Bernardes, G. J. L. Inverse electron demand Diels–Alder reactions in chemical biology. *Chemical Society Reviews* **46**, 4895-4950, doi:10.1039/C7CS00184C (2017).
- 267 Ramil, C. P. & Lin, Q. Bioorthogonal chemistry: strategies and recent developments. *Chemical Communications* **49**, 11007-11022, doi:10.1039/C3CC44272A (2013).
- 268 Hemsworth, G. R., Johnston, E. M., Davies, G. J. & Walton, P. H. Lytic Polysaccharide Monoxygenases in Biomass Conversion. *Trends Biotechnol* **33**, 747-761, doi:10.1016/j.tibtech.2015.09.006 (2015).

- 269 Frandsen, K. E. H. *et al.* Insights into an unusual Auxiliary Activity 9 family member lacking the histidine brace motif of lytic polysaccharide monooxygenases. *Journal of Biological Chemistry* **294**, 17117-17130, doi:10.1074/jbc.RA119.009223 (2019).
- 270 Zhou, X. & Zhu, H. Current understanding of substrate specificity and regioselectivity of LPMOs. *Bioresources and Bioprocessing* **7**, doi:10.1186/s40643-020-0300-6 (2020).
- 271 Simmons, T. J. *et al.* Structural and electronic determinants of lytic polysaccharide monooxygenase reactivity on polysaccharide substrates. *Nature Communications* **8**, 1064, doi:10.1038/s41467-017-01247-3 (2017).
- 272 Vaaje-Kolstad, G. *et al.* An Oxidative Enzyme Boosting the Enzymatic Conversion of Recalcitrant Polysaccharides. *Science* **330**, 219, doi:10.1126/science.1192231 (2010).
- 273 Harris, P. V. *et al.* Stimulation of Lignocellulosic Biomass Hydrolysis by Proteins of Glycoside Hydrolase Family 61: Structure and Function of a Large, Enigmatic Family. *Biochemistry* **49**, 3305-3316, doi:10.1021/bi100009p (2010).
- 274 Levasseur, A., Drula, E., Lombard, V., Coutinho, P. M. & Henrissat, B. Expansion of the enzymatic repertoire of the CAZy database to integrate auxiliary redox enzymes. *Biotechnology for Biofuels* **6**, 41, doi:10.1186/1754-6834-6-41 (2013).
- 275 Rossi, B. R. *et al.* Cellulose nanofibers production using a set of recombinant enzymes. *Carbohydrate Polymers* **256**, 117510, doi:10.1016/j.carbpol.2020.117510 (2021).
- 276 Koskela, S. *et al.* Lytic polysaccharide monooxygenase (LPMO) mediated production of ultra-fine cellulose nanofibres from delignified softwood fibres. *Green Chemistry* **21**, 5924-5933, doi:10.1039/c9gc02808k (2019).
- 277 Agostoni, M., Hangasky, J. A. & Marletta, M. A. Physiological and Molecular Understanding of Bacterial Polysaccharide Monooxygenases. *Microbiology and Molecular Biology Reviews* **81**, e00015-00017, doi:10.1128/MMBR.00015-17 (2017).
- 278 Paspaliari, D. K., Loose, J. S. M., Larsen, M. H. & Vaaje-Kolstad, G. *Listeria monocytogenes* has a functional chitinolytic system and an active lytic polysaccharide monooxygenase. *The FEBS Journal* **282**, 921-936, doi:10.1111/febs.13191 (2015).
- 279 Askarian, F. *et al.* The lytic polysaccharide monooxygenase CbpD promotes *Pseudomonas aeruginosa* virulence in systemic infection. *Nature Communications* **12**, 1230, doi:10.1038/s41467-021-21473-0 (2021).
- 280 Munzone, A. *et al.* Characterization of a bacterial copper-dependent lytic polysaccharide monooxygenase with an unusual second coordination sphere. *The FEBS Journal* **287**, 3298-3314, doi:10.1111/febs.15203 (2020).
- 281 Jagadeeswaran, G., Veale, L. & Mort, A. J. Do Lytic Polysaccharide Monooxygenases Aid in Plant Pathogenesis and Herbivory? *Trends in Plant Science* **26**, 142-155, doi:10.1016/j.tplants.2020.09.013 (2021).
- 282 Sabbadin, F. *et al.* An ancient family of lytic polysaccharide monooxygenases with roles in arthropod development and biomass digestion. *Nature Communications* **9**, 756, doi:10.1038/s41467-018-03142-x (2018).
- 283 Fowler, C. A. *et al.* Discovery, activity and characterisation of an AA10 lytic polysaccharide oxygenase from the shipworm symbiont *Teredinibacter turnerae*. *Biotechnology for Biofuels* **12**, 232, doi:10.1186/s13068-019-1573-x (2019).
- 284 Hemsworth, G. R., Henrissat, B., Davies, G. J. & Walton, P. H. Discovery and characterization of a new family of lytic polysaccharide monooxygenases. *Nature Chemical Biology* **10**, 122-126, doi:10.1038/nchembio.1417 (2014).
- 285 Lo Leggio, L. *et al.* Structure and boosting activity of a starch-degrading lytic polysaccharide monooxygenase. *Nature Communications* **6**, 5961, doi:10.1038/ncomms6961 (2015).
- 286 CAZy database, <http://www.cazy.org/Auxiliary-Activities.html> (Accessed 25th March 2020).
- 287 Chiu, E. *et al.* Structural basis for the enhancement of virulence by viral spindles and their in vivo crystallization. *Proceedings of the National Academy of Sciences* **112**, 3973, doi:10.1073/pnas.1418798112 (2015).



- 288 Filiatrault-Chastel, C. *et al.* AA16, a new lytic polysaccharide monooxygenase family identified in fungal secretomes. *Biotechnology for Biofuels* **12**, 55, doi:10.1186/s13068-019-1394-y (2019).
- 289 Johansen, K. S. Lytic Polysaccharide Monooxygenases: The Microbial Power Tool for Lignocellulose Degradation. *Trends in Plant Science* **21**, 926-936, doi:10.1016/j.tplants.2016.07.012 (2016).
- 290 Meier, K. K. *et al.* Oxygen Activation by Cu LPMOs in Recalcitrant Carbohydrate Polysaccharide Conversion to Monomer Sugars. *Chemical Reviews* **118**, 2593-2635, doi:10.1021/acs.chemrev.7b00421 (2018).
- 291 Petrović, D. M. *et al.* Methylation of the N-terminal histidine protects a lytic polysaccharide monooxygenase from auto-oxidative inactivation. *Protein Science* **27**, 1636-1650, doi:10.1002/pro.3451 (2018).
- 292 Tandrup, T., Frandsen, K. E. H., Johansen, K. S., Berrin, J. G. & Lo Leggio, L. Recent insights into lytic polysaccharide monooxygenases (LPMOs). *Biochemical Society Transactions* **46**, 1431-1447, doi:10.1042/BST20170549 (2018).
- 293 Paradisi, A. *et al.* Formation of a Copper(II)-Tyrosyl Complex at the Active Site of Lytic Polysaccharide Monooxygenases Following Oxidation by H<sub>2</sub>O<sub>2</sub>. *Journal of the American Chemical Society* **141**, 18585-18599, doi:10.1021/jacs.9b09833 (2019).
- 294 Forsberg, Z. *et al.* Comparative Study of Two Chitin-Active and Two Cellulose-Active AA10-Type Lytic Polysaccharide Monooxygenases. *Biochemistry* **53**, 1647-1656, doi:10.1021/bi5000433 (2014).
- 295 McEvoy, A., Creutzberg, J., Singh, R. K., Bjerrum, M. J. & Hedegård, E. D. The role of the active site tyrosine in the mechanism of lytic polysaccharide monooxygenase. *Chemical Science* **12**, 352-362, doi:10.1039/d0sc05262k (2021).
- 296 Jones, S. M., Transue, W. J., Meier, K. K., Kelemen, B. & Solomon, E. I. Kinetic analysis of amino acid radicals formed in H<sub>2</sub>O<sub>2</sub>-driven CuI LPMO reoxidation implicates dominant homolytic reactivity. *Proceedings of the National Academy of Sciences* **117**, 11916, doi:10.1073/pnas.1922499117 (2020).
- 297 Frandsen, K. E. H. & Lo Leggio, L. Lytic polysaccharide monooxygenases: a crystallographer's view on a new class of biomass-degrading enzymes. *IUCrJ* **3**, 448-467, doi:10.1107/S2052252516014147 (2016).
- 298 Hemsworth, G. R. *et al.* The Copper Active Site of CBM33 Polysaccharide Oxygenases. *Journal of the American Chemical Society* **135**, 6069-6077, doi:10.1021/ja402106e (2013).
- 299 Walton, P. H. & Davies, G. J. On the catalytic mechanisms of lytic polysaccharide monooxygenases. *Current Opinion in Chemical Biology* **31**, 195-207, doi:10.1016/j.cbpa.2016.04.001 (2016).
- 300 Frandsen, K. E. H., Poulsen, J.-C. N., Tandrup, T. & Lo Leggio, L. Unliganded and substrate bound structures of the celooligosaccharide active lytic polysaccharide monooxygenase LsAA9A at low pH. *Carbohydrate Research* **448**, 187-190, doi:10.1016/j.carres.2017.03.010 (2017).
- 301 Concia, A. L. *et al.* in *Bioinspired Chemistry Vol. Volume 5 Series on Chemistry, Energy and the Environment* 185-263 (WORLD SCIENTIFIC, 2018).
- 302 Couturier, M. *et al.* Lytic xylan oxidases from wood-decay fungi unlock biomass degradation. *Nature Chemical Biology* **14**, 306-310, doi:10.1038/nchembio.2558 (2018).
- 303 Forsberg, Z. *et al.* Polysaccharide degradation by lytic polysaccharide monooxygenases. *Current Opinion in Structural Biology* **59**, 54-64, doi:10.1016/j.sbi.2019.02.015 (2019).
- 304 Harris, P. V., Xu, F., Kreef, N. E., Kang, C. & Fukuyama, S. New enzyme insights drive advances in commercial ethanol production. *Current Opinion in Chemical Biology* **19**, 162-170, doi:10.1016/j.cbpa.2014.02.015 (2014).
- 305 Sanhueza, C., Carvajal, G., Soto-Aguilar, J., Lienqueo, M. E. & Salazar, O. The effect of a lytic polysaccharide monooxygenase and a xylanase from *Gloeophyllum trabeum* on the enzymatic

- hydrolysis of lignocellulosic residues using a commercial cellulase. *Enzyme and Microbial Technology* **113**, 75-82, doi:10.1016/j.enzmictec.2017.11.007 (2018).
- 306 Quist, D. A., Diaz, D. E., Liu, J. J. & Karlin, K. D. Activation of dioxygen by copper metalloproteins and insights from model complexes. *JBIC Journal of Biological Inorganic Chemistry* **22**, 253-288, doi:10.1007/s00775-016-1415-2 (2017).
- 307 Liu, I. P.-C., Chen, P. P. Y. & Chan, S. I. Models for the trinuclear copper(II) cluster in the particulate methane monooxygenase from methanotrophic bacteria: Synthesis, spectroscopic and theoretical characterization of trinuclear copper(II) complexes. *Comptes Rendus Chimie* **15**, 214-224, doi:10.1016/j.crci.2011.11.014 (2012).
- 308 Chan, S. I. *et al.* Redox Potentiometry Studies of Particulate Methane Monooxygenase: Support for a Trinuclear Copper Cluster Active Site. *Angewandte Chemie International Edition* **46**, 1992-1994, doi:10.1002/anie.200604647 (2007).
- 309 Blain, I., Slama, P., Giorgi, M., Tron, T. & Réglie, M. Copper-containing monooxygenases: enzymatic and biomimetic studies of the O-atom transfer catalysis. *Reviews in Molecular Biotechnology* **90**, 95-112, doi:10.1016/S1389-0352(01)00068-X (2002).
- 310 Cowley, R. E., Tian, L. & Solomon, E. I. Mechanism of O<sub>2</sub> activation and substrate hydroxylation in noncoupled binuclear copper monooxygenases. *Proceedings of the National Academy of Sciences* **113**, 12035-12040, doi:10.1073/pnas.1614807113 (2016).
- 311 Sygmond, C. *et al.* Characterization of the two *Neurospora crassa* cellobiose dehydrogenases and their connection to oxidative cellulose degradation. *Applied and Environmental Microbiology* **78**, 6161-6171, doi:10.1128/AEM.01503-12 (2012).
- 312 Li, X., Beeson, William T., Phillips, Christopher M., Marletta, Michael A. & Cate, Jamie H. D. Structural Basis for Substrate Targeting and Catalysis by Fungal Polysaccharide Monooxygenases. *Structure* **20**, 1051-1061, doi:10.1016/j.str.2012.04.002 (2012).
- 313 Courtade, G. *et al.* Interactions of a fungal lytic polysaccharide monooxygenase with  $\beta$ -glucan substrates and cellobiose dehydrogenase. *Proceedings of the National Academy of Sciences* **113**, 5922-5927, doi:10.1073/pnas.1602566113 (2016).
- 314 Tan, T. C. *et al.* Structural basis for cellobiose dehydrogenase action during oxidative cellulose degradation. *Nature Communications* **6**, 7542, doi:10.1038/ncomms8542 (2015).
- 315 Chen, P. & Solomon, E. I. Oxygen Activation by the Noncoupled Binuclear Copper Site in Peptidylglycine  $\alpha$ -Hydroxylating Monooxygenase. Reaction Mechanism and Role of the Noncoupled Nature of the Active Site. *Journal of the American Chemical Society* **126**, 4991-5000, doi:10.1021/ja031564g (2004).
- 316 Kim, S., Stahlberg, J., Sandgren, M., Paton, R. S. & Beckham, G. T. Quantum mechanical calculations suggest that lytic polysaccharide monooxygenases use a copper-oxyl, oxygen-rebound mechanism. *Proceedings of the National Academy of Sciences* **111**, 149-154, doi:10.1073/pnas.1316609111 (2014).
- 317 Dhar, D. & Tolman, W. B. Hydrogen atom abstraction from hydrocarbons by a copper(III)-hydroxide complex. *Journal of the American Chemical Society* **137**, 1322-1329, doi:10.1021/ja512014z (2015).
- 318 Dhar, D., Yee, G. M., Markle, T. F., Mayer, J. M. & Tolman, W. B. Reactivity of the copper(III)-hydroxide unit with phenols. *Chemical Science* **8**, 1075-1085, doi:10.1039/c6sc03039d (2017).
- 319 Kjaergaard, C. H. *et al.* Spectroscopic and computational insight into the activation of O<sub>2</sub> by the mononuclear Cu center in polysaccharide monooxygenases. *Proceedings of the National Academy of Sciences* **111**, 8797-8802, doi:10.1073/pnas.1408115111 (2014).
- 320 Hedegard, E. D. & Ryde, U. Molecular mechanism of lytic polysaccharide monooxygenases. *Chemical Science* **9**, 3866-3880, doi:10.1039/c8sc00426a (2018).
- 321 Bissaro, B. *et al.* Molecular mechanism of the chitinolytic peroxygenase reaction. *Proceedings of the National Academy of Sciences* **117**, 1504-1513, doi:10.1073/pnas.1904889117 (2020).

- 322 Wang, B. *et al.* QM/MM Studies into the H<sub>2</sub>O<sub>2</sub>-Dependent Activity of Lytic Polysaccharide Monooxygenases: Evidence for the Formation of a Caged Hydroxyl Radical Intermediate. *ACS Catalysis* **8**, 1346-1351, doi:10.1021/acscatal.7b03888 (2018).
- 323 Bissaro, B. *et al.* Oxidative cleavage of polysaccharides by monocopper enzymes depends on H<sub>2</sub>O<sub>2</sub>. *Nature Chemical Biology* **13**, 1123-1128, doi:10.1038/nchembio.2470 (2017).
- 324 Kuusk, S. *et al.* Kinetics of H<sub>2</sub>O<sub>2</sub>-driven degradation of chitin by a bacterial lytic polysaccharide monooxygenase. *Journal of Biological Chemistry* **293**, 523-531, doi:10.1074/jbc.M117.817593 (2018).
- 325 Caldararu, O., Oksanen, E., Ryde, U. & Hedegard, E. D. Mechanism of hydrogen peroxide formation by lytic polysaccharide monooxygenase. *Chemical Science* **10**, 576-586, doi:10.1039/c8sc03980a (2019).
- 326 Hangasky, J. A., Iavarone, A. T. & Marletta, M. A. Reactivity of O<sub>2</sub> versus H<sub>2</sub>O<sub>2</sub> with polysaccharide monooxygenases. *Proceedings of the National Academy of Sciences* **115**, 4915-4920, doi:10.1073/pnas.1801153115 (2018).
- 327 Garajova, S. *et al.* Single-domain flavoenzymes trigger lytic polysaccharide monooxygenases for oxidative degradation of cellulose. *Scientific Reports* **6**, 28276, doi:10.1038/srep28276 (2016).
- 328 Borisova, A. S. *et al.* Structural and Functional Characterization of a Lytic Polysaccharide Monooxygenase with Broad Substrate Specificity. *Journal of Biological Chemistry* **290**, 22955-22969 (2015).
- 329 Aachmann, F. L., Sorlie, M., Skjak-Braek, G., Eijsink, V. G. & Vaaje-Kolstad, G. NMR structure of a lytic polysaccharide monooxygenase provides insight into copper binding, protein dynamics, and substrate interactions. *Proceedings of the National Academy of Sciences* **109**, 18779-18784, doi:10.1073/pnas.1208822109 (2012).
- 330 Forsberg, Z. *et al.* Structural and functional characterization of a conserved pair of bacterial cellulose-oxidizing lytic polysaccharide monooxygenases. *Proceedings of the National Academy of Sciences* **111**, 8446-8451, doi:10.1073/pnas.1402771111 (2014).
- 331 Zouraris, D., Dimarogona, M., Karnaouri, A., Topakas, E. & Karantonis, A. Direct electron transfer of lytic polysaccharide monooxygenases (LPMOs) and determination of their formal potentials by large amplitude Fourier transform alternating current cyclic voltammetry. *Bioelectrochemistry* **124**, 149-155, doi:10.1016/j.bioelechem.2018.07.009 (2018).
- 332 Muraleedharan, M. N. *et al.* Effect of lignin fractions isolated from different biomass sources on cellulose oxidation by fungal lytic polysaccharide monooxygenases. *Biotechnology for Biofuels* **11**, 296, doi:10.1186/s13068-018-1294-6 (2018).
- 333 Liu, Y., Seefeldt, L. C. & Parker, V. D. Entropies of Redox Reactions between Proteins and Mediators: The Temperature Dependence of Reversible Electrode Potentials in Aqueous Buffers. *Analytical Biochemistry* **250**, 196-202, doi:10.1006/abio.1997.2222 (1997).
- 334 Jablonski, A., Kulesza, P. J. & Lewera, A. Oxygen permeation through Nafion 117 membrane and its impact on efficiency of polymer membrane ethanol fuel cell. *Journal of Power Sources* **196**, 4714-4718, doi:10.1016/j.jpowsour.2011.01.045 (2011).
- 335 Broka, K. & Ekdunge, P. Oxygen and hydrogen permeation properties and water uptake of Nafion® 117 membrane and recast film for PEM fuel cell. *Journal of Applied Electrochemistry* **27**, 117-123, doi:10.1023/A:1018469520562 (1997).
- 336 Tjell, A. Ø. & Almdal, K. Diffusion rate of hydrogen peroxide through water-swelled polyurethane membranes. *Sensing and Bio-Sensing Research* **21**, 35-39, doi:10.1016/j.sbsr.2018.10.001 (2018).
- 337 Brooke, E. *Direct and Mediated Electrochemistry of Two Lytic Polysaccharide Mono-Oxygenases, TaAA9 and BaAA10* MChem thesis, The University of York, (2015).
- 338 Yates, N. *Electrode Functionalisation and the Direct Electrochemistry of an AA9 Lytic Polysaccharide Monooxygenase* MChem thesis, The University of York, (2016).

- 339 NCBI, Align Sequences Protein BLAST, <https://blast.ncbi.nlm.nih.gov/Blast.cgi> (Accessed 2020).
- 340 EMBL-EBI, EMBOSS Needle Pairwise Sequence Alignment, [https://www.ebi.ac.uk/Tools/psa/emboss\\_needle/](https://www.ebi.ac.uk/Tools/psa/emboss_needle/) (Accessed 2020).
- 341 Krieger, F., Möglich, A. & Kiefhaber, T. Effect of Proline and Glycine Residues on Dynamics and Barriers of Loop Formation in Polypeptide Chains. *Journal of the American Chemical Society* **127**, 3346-3352, doi:10.1021/ja042798i (2005).
- 342 Kelley, L. A., Mezulis, S., Yates, C. M., Wass, M. N. & Sternberg, M. J. E. The Phyre2 web portal for protein modeling, prediction and analysis. *Nature Protocols* **10**, 845-858, doi:10.1038/nprot.2015.053 (2015).
- 343 Sørlie, M., Seefeldt, L. C. & Parker, V. D. Use of Stopped-Flow Spectrophotometry to Establish Midpoint Potentials for Redox Proteins. *Analytical Biochemistry* **287**, 118-125, doi:10.1006/abio.2000.4826 (2000).
- 344 Pumera, M. Electrochemical properties of double wall carbon nanotube electrodes. *Nanoscale Research Letters* **2**, 87, doi:10.1007/s11671-006-9035-3 (2007).
- 345 Navaee, A. & Salimi, A. Graphene-supported pyrene-functionalized amino-carbon nanotube: a novel hybrid architecture of laccase immobilization as effective bioelectrocatalyst for oxygen reduction reaction. *Journal of Materials Chemistry A* **3**, 7623-7630, doi:10.1039/c4ta06867j (2015).
- 346 Workentin, M. S., Johnston, L. J., Wayner, D. D. M. & Parker, V. D. Reactivity of Aromatic Radical Cations. Rate Constants for Reactions of 9-Phenyl- and 9,10-Diphenylanthracene Radical Cations with Acyclic Amines. *Journal of the American Chemical Society* **116**, 8279-8287, doi:10.1021/ja00097a038 (1994).
- 347 de Robillard, G., Makni, O., Cattey, H., Andrieu, J. & Devillers, C. H. Towards sustainable synthesis of pyren-1-yl azoliums via electrochemical oxidative C–N coupling. *Green Chemistry* **17**, 4669-4679, doi:10.1039/C5GC01142F (2015).
- 348 Cases, F., Huerta, F., Garcés, P., Morallón, E. & Vázquez, J. L. Voltammetric and in situ FTIRS study of the electrochemical oxidation of aniline from aqueous solutions buffered at pH 5. *Journal of Electroanalytical Chemistry* **501**, 186-192, doi:10.1016/S0022-0728(00)00526-X (2001).
- 349 Sun, N. *et al.* Electrochemistry of fullerene peapod modified electrodes. *Electrochemistry Communications* **7**, 1148-1152, doi:10.1016/j.elecom.2005.08.020 (2005).
- 350 Goryunkov, A. A., Ovchinnikova, N. S., Trushkov, I. V. & Yurovskaya, M. A. Synthesis, structures and reactivity of polyhalo[60]fullerenes. *Russian Chemical Reviews* **76**, 289-312, doi:10.1070/RC2007v076n04ABEH003668 (2007).
- 351 Cobb, S. J., Ayres, Z. J., Newton, M. E. & Macpherson, J. V. Deconvoluting Surface-Bound Quinone Proton Coupled Electron Transfer in Unbuffered Solutions: Toward a Universal Voltammetric pH Electrode. *Journal of the American Chemical Society* **141**, 1035-1044, doi:10.1021/jacs.8b11518 (2019).
- 352 Cahuantzi-Muñoz, S. L. *et al.* Electrochemical Biosensor for Sensitive Quantification of Glyphosate in Maize Kernels. *Electroanalysis* **31**, 927-935, doi:10.1002/elan.201800759 (2019).
- 353 Goyanes, S. *et al.* Carboxylation treatment of multiwalled carbon nanotubes monitored by infrared and ultraviolet spectroscopies and scanning probe microscopy. *Diamond and Related Materials* **16**, 412-417, doi:10.1016/j.diamond.2006.08.021 (2007).
- 354 Li Bo, L. Y.-F. S. H. I. Z.-J. G. U. Z.-N. Chemical Modification of Single-wall Carbon Nanotube. *Chemical Journal of Chinese Universities* **21**, 1633-1635 (2000).
- 355 Luo, H., Shi, Z., Li, N., Gu, Z. & Zhuang, Q. Investigation of the Electrochemical and Electrocatalytic Behavior of Single-Wall Carbon Nanotube Film on a Glassy Carbon Electrode. *Analytical Chemistry* **73**, 915-920, doi:10.1021/ac000967l (2001).

- 356 Breslmayr, E. *et al.* A fast and sensitive activity assay for lytic polysaccharide monoxygenase. *Biotechnology for Biofuels* **11**, 79, doi:10.1186/s13068-018-1063-6 (2018).
- 357 Gara, M. & Compton, R. G. Activity of carbon electrodes towards oxygen reduction in acid: A comparative study. *New Journal of Chemistry* **35**, 2647-2652, doi:10.1039/C1NJ20612E (2011).
- 358 Nicosia, C. & Huskens, J. Reactive self-assembled monolayers: from surface functionalization to gradient formation. *Materials Horizons* **1**, 32-45, doi:10.1039/c3mh00046j (2014).
- 359 Ge, C., Miao, W., Ji, M. & Gu, N. Glutaraldehyde-modified electrode for nonlabeling voltammetric detection of p16 INK4A gene. *Analytical and Bioanalytical Chemistry* **383**, 651-659, doi:10.1007/s00216-005-0032-7 (2005).
- 360 Brockman, J. M., Frutos, A. G. & Corn, R. M. A Multistep Chemical Modification Procedure To Create DNA Arrays on Gold Surfaces for the Study of Protein–DNA Interactions with Surface Plasmon Resonance Imaging. *Journal of the American Chemical Society* **121**, 8044-8051, doi:10.1021/ja991608e (1999).
- 361 Hayat, A., Haider, W., Rolland, M. & Marty, J. L. Electrochemical grafting of long spacer arms of hexamethyldiamine on a screen printed carbon electrode surface: application in target induced ochratoxin A electrochemical aptasensor. *Analyst* **138**, 2951-2957, doi:10.1039/c3an00158j (2013).
- 362 Kumar, R., Bhuvana, T., Mishra, G. & Sharma, A. A polyaniline wrapped aminated graphene composite on nickel foam as three-dimensional electrodes for enzymatic microfuel cells. *RSC Advances* **6**, 73496-73505, doi:10.1039/c6ra08195a (2016).
- 363 Hazimeh, H. *et al.* Radical Chemistry from Diazonium-Terminated Surfaces. *Chemistry of Materials* **25**, 605-612, doi:10.1021/cm3039015 (2013).
- 364 Tran, Q. T., de Sanoit, J., Pierre, S., Arnault, J.-C. & Bergonzo, P. Diamond electrodes for trace alpha pollutant sequestration via covalent grafting of nitrilotriacetic acid (NTA) ligand. *Electrochimica Acta* **136**, 430-434, doi:10.1016/j.electacta.2014.05.087 (2014).
- 365 Mahouche-Chergui, S., Gam-Derouich, S., Mangeney, C. & Chehimi, M. M. Aryl diazonium salts: a new class of coupling agents for bonding polymers, biomacromolecules and nanoparticles to surfaces. *Chemical Society Reviews* **40**, 4143-4166, doi:10.1039/C0CS00179A (2011).
- 366 Lillethorup, M., Torbensen, K., Ceccato, M., Pedersen, S. U. & Daasbjerg, K. Electron Transport through a Diazonium-Based Initiator Layer to Covalently Attached Polymer Brushes of Ferrocenylmethyl Methacrylate. *Langmuir* **29**, 13595-13604, doi:10.1021/la402535u (2013).
- 367 Kouklovsky, C. in *Comprehensive Organic Functional Group Transformations II* (eds Alan R. Katritzky & Richard J. K. Taylor) 231-285 (Elsevier, 2005).
- 368 Beard, J. C. & Swager, T. M. An Organic Chemist's Guide to N-Nitrosamines: Their Structure, Reactivity, and Role as Contaminants. *The Journal of Organic Chemistry* **86**, 2037-2057, doi:10.1021/acs.joc.0c02774 (2021).
- 369 Chaudhary, P., Gupta, S., Muniyappan, N., Sabiah, S. & Kandasamy, J. An efficient synthesis of N-nitrosamines under solvent, metal and acid free conditions using tert-butyl nitrite. *Green Chemistry* **18**, 2323-2330, doi:10.1039/C5GC02880A (2016).
- 370 Ghilane, J., Martin, P., Fontaine, O., Lacroix, J.-C. & Randriamahazaka, H. Modification of carbon electrode in ionic liquid through the reduction of phenyl diazonium salt. Electrochemical evidence in ionic liquid. *Electrochemistry Communications* **10**, 1060-1063, doi:10.1016/j.elecom.2008.05.017 (2008).
- 371 Breton, T. & Downard, A. J. Controlling Grafting from Aryldiazonium Salts: A Review of Methods for the Preparation of Monolayers. *Australian Journal of Chemistry* **70**, 960-972 (2017).
- 372 Carvalho Padilha, J., Noël, J.-M., Bergamini, J.-F., Rault-Berthelot, J. & Lagrost, C. Functionalization of Carbon Materials by Reduction of Diazonium Cations Produced in Situ in

- a Brønstedt Acidic Ionic Liquid. *ChemElectroChem* **3**, 572-580, doi:10.1002/celec.201500434 (2016).
- 373 Shul, G., Ruiz, C. A. C., Rochefort, D., Brooksby, P. A. & Bélanger, D. Electrochemical functionalization of glassy carbon electrode by reduction of diazonium cations in protic ionic liquid. *Electrochimica Acta* **106**, 378-385, doi:10.1016/j.electacta.2013.05.082 (2013).
- 374 Fontaine, O., Ghilane, J., Martin, P., Lacroix, J.-C. & Randriamahazaka, H. Ionic Liquid Viscosity Effects on the Functionalization of Electrode Material through the Electroreduction of Diazonium. *Langmuir* **26**, 18542-18549, doi:10.1021/la103000u (2010).
- 375 Ionita, P. Synthesis and spectral comparison of electronic and molecular properties of some hydrazines and hydrazyl free radicals. *Arkivoc* **2019**, doi:10.24820/ark.5550190.p011.119 (2020).
- 376 Marcus, R. A. Chemical and Electrochemical Electron-Transfer Theory. *Annual Review of Physical Chemistry* **15**, 155-196, doi:10.1146/annurev.pc.15.100164.001103 (1964).
- 377 Bouden, S., Trippé-Allard, G., Ghilane, J. & Randriamahazaka, H. Electrochemical immobilization of redox active molecule based ionic liquid. *Electrochemistry Communications* **58**, 65-68, doi:10.1016/j.elecom.2015.06.010 (2015).
- 378 Mattiuzzi, A. *et al.* Strategies for the Formation of Monolayers From Diazonium Salts: Unconventional Grafting Media, Unconventional Building Blocks. *Frontiers in Chemistry* **8**, 559, doi:10.3389/fchem.2020.00559 (2020).
- 379 Mattiuzzi, A. *et al.* Electrografting of calix[4]arene-diazonium salts to form versatile robust platforms for spatially controlled surface functionalization. *Nature Communications* **3**, 1130, doi:10.1038/ncomms2121 (2012).
- 380 Malytskyi, V. *et al.* Synthesis of a Calix[4]arene-Monodiazonium Salt for Surface Modification. *European Journal of Organic Chemistry* **2018**, 6590-6595, doi:10.1002/ejoc.201801253 (2018).
- 381 Troian-Gautier, L., Mattiuzzi, A., Reinaud, O., Lagrost, C. & Jabin, I. Use of calixarenes bearing diazonium groups for the development of robust monolayers with unique tailored properties. *Organic & Biomolecular Chemistry* **18**, 3624-3637, doi:10.1039/D0OB00070A (2020).
- 382 Clayden, J., Greeves, N. & Warren, S. *Organic Chemistry*. 2nd edn, (Oxford University Press, 2012).
- 383 Malmos, K. *et al.* Using a Hydrazone-Protected Benzenediazonium Salt to Introduce a Near-Monolayer of Benzaldehyde on Glassy Carbon Surfaces. *Journal of the American Chemical Society* **131**, 4928-4936, doi:10.1021/ja809816x (2009).
- 384 Nielsen, L. T. *et al.* Electrochemical Approach for Constructing a Monolayer of Thiophenolates from Grafted Multilayers of Diaryl Disulfides. *Journal of the American Chemical Society* **129**, 1888-1889, doi:10.1021/ja0682430 (2007).
- 385 Lee, L. *et al.* Covalently Anchored Carboxyphenyl Monolayer via Aryldiazonium Ion Grafting: A Well-Defined Reactive Tether Layer for On-Surface Chemistry. *Langmuir* **30**, 7104-7111, doi:10.1021/la5013632 (2014).
- 386 Goff, A. L. *et al.* Facile and tunable functionalization of carbon nanotube electrodes with ferrocene by covalent coupling and  $\pi$ -stacking interactions and their relevance to glucose biosensing. *Journal of Electroanalytical Chemistry* **641**, 57-63, doi:10.1016/j.jelechem.2010.01.014 (2010).
- 387 Brisset, H. *et al.* Electrosynthesis of a functional conducting polymer incorporating ferrocene unit from an EDOT-based bithiophenic precursor. *Journal of Electroanalytical Chemistry* **603**, 149-154, doi:10.1016/j.jelechem.2007.01.017 (2007).
- 388 Navarro, A.-E. *et al.* Automated synthesis of new ferrocenyl-modified oligonucleotides: study of their properties in solution. *Nucleic Acids Res* **32**, 5310-5319, doi:10.1093/nar/gkh874 (2004).
- 389 Moloney, G. P. *et al.* A Novel Series of 2,5-Substituted Tryptamine Derivatives as Vascular 5HT<sub>1B/1D</sub> Receptor Antagonists. *Journal of Medicinal Chemistry* **40**, 2347-2362, doi:10.1021/jm9605849 (1997).

- 390 Lee, L., Brooksby, P. A., Hapiot, P. & Downard, A. J. Electrografting of 4-Nitrobenzenediazonium Ion at Carbon Electrodes: Catalyzed and Uncatalyzed Reduction Processes. *Langmuir*, doi:10.1021/acs.langmuir.5b03233 (2016).
- 391 Dowsett, M. *Electrochemical carbon dioxide capture via mineralisation or reduction* PhD thesis, University of York, (2020).
- 392 Yates, N. D. J. *et al.* Chemical Bioconjugation of Proteins in an Undergraduate Lab: One-Pot Oxidation and Derivatization of the N-Terminus. *Journal of Chemical Education* **96**, 1245-1249, doi:10.1021/acs.jchemed.8b00787 (2019).
- 393 Yates, N. D. J., Fascione, M. A. & Parkin, A. Methodologies for “Wiring” Redox Proteins/Enzymes to Electrode Surfaces. *Chemistry – A European Journal* **24**, 12164-12182, doi:10.1002/chem.201800750 (2018).
- 394 Spears, R. J. & Fascione, M. A. Site-selective incorporation and ligation of protein aldehydes. *Organic & Biomolecular Chemistry* **14**, 7622-7638, doi:10.1039/C6OB00778C (2016).
- 395 Agten, S. M., Dawson, P. E. & Hackeng, T. M. Oxime conjugation in protein chemistry: from carbonyl incorporation to nucleophilic catalysis. *Journal of Peptide Science* **22**, 271-279, doi:10.1002/psc.2874 (2016).
- 396 Larsen, D. *et al.* Exceptionally rapid oxime and hydrazone formation promoted by catalytic amine buffers with low toxicity. *Chemical Science* **9**, 5252-5259, doi:10.1039/c8sc01082j (2018).
- 397 Agarwal, P., van der Weijden, J., Sletten, E. M., Rabuka, D. & Bertozzi, C. R. A Pictet-Spengler ligation for protein chemical modification. *Proceedings of the National Academy of Sciences* **110**, 46, doi:10.1073/pnas.1213186110 (2013).
- 398 Agarwal, P. *et al.* Hydrazino-Pictet-Spengler Ligation as a Biocompatible Method for the Generation of Stable Protein Conjugates. *Bioconjugate Chemistry* **24**, 846-851, doi:10.1021/bc400042a (2013).
- 399 Spears, R. J. *et al.* Site-selective C–C modification of proteins at neutral pH using organocatalyst-mediated cross aldol ligations. *Chemical Science* **9**, 5585-5593, doi:10.1039/C8SC01617H (2018).
- 400 Gilmore, J. M., Scheck, R. A., Esser-Kahn, A. P., Joshi, N. S. & Francis, M. B. N-Terminal Protein Modification through a Biomimetic Transamination Reaction. *Angewandte Chemie International Edition* **45**, 5307-5311, doi:10.1002/anie.200600368 (2006).
- 401 Witus, L. S. & Francis, M. Site-Specific Protein Bioconjugation via a Pyridoxal 5'-Phosphate-Mediated N-Terminal Transamination Reaction. *Current Protocols in Chemical Biology* **2**, 125-134, doi:10.1002/9780470559277.ch100018 (2010).
- 402 Murachi, T., Yasuda, Y. & Takahashi, N. Periodate oxidation of carbohydrate moiety of stem bromelain without much alteration in enzymic activity. *Biochemistry* **10**, 2624-2630, doi:10.1021/bi00789a032 (1971).
- 403 Nakamura, S., Hayashi, S. & Koga, K. Effect of periodate oxidation on the structure and properties of glucose oxidase. *Biochimica et Biophysica Acta (BBA) - Enzymology* **445**, 294-308, doi:10.1016/0005-2744(76)90084-X (1976).
- 404 G-Biosciences, Sodium metaperiodate protocol, [https://www.gbiosciences.com/image/pdfs/protocol/BKC-12\\_protocol.pdf](https://www.gbiosciences.com/image/pdfs/protocol/BKC-12_protocol.pdf) (Accessed 2020).
- 405 Quaranta, A. *et al.* N-Glycosylation profiling of intact target proteins by high-resolution mass spectrometry (MS) and glycan analysis using ion mobility-MS/MS. *Analyst* **145**, 1737-1748, doi:10.1039/c9an02081k (2020).
- 406 Ucakurk, E. Analysis of glycoforms on the glycosylation site and the glycans in monoclonal antibody biopharmaceuticals. *Journal of Separation Science* **35**, 341-350, doi:10.1002/jssc.201100684 (2012).
- 407 Brabham, R. L. *et al.* Palladium-unleashed proteins: gentle aldehyde decaging for site-selective protein modification. *Chemical Communications* **54**, 1501-1504, doi:10.1039/C7CC07740H (2018).

- 408 Willis, J. C. W. & Chin, J. W. Mutually orthogonal pyrrolysyl-tRNA synthetase/tRNA pairs. *Nature Chemistry* **10**, 831-837, doi:10.1038/s41557-018-0052-5 (2018).
- 409 Saleh, A. M., Wilding, K. M., Calve, S., Bundy, B. C. & Kinzer-Ursem, T. L. Non-canonical amino acid labeling in proteomics and biotechnology. *Journal of Biological Engineering* **13**, 43, doi:10.1186/s13036-019-0166-3 (2019).
- 410 Schubert, T., Lenz, O., Krause, E., Volkmer, R. & Friedrich, B. Chaperones specific for the membrane-bound [NiFe]-hydrogenase interact with the Tat signal peptide of the small subunit precursor in *Ralstonia eutropha* H16. *Molecular Microbiology* **66**, 453-467, doi:10.1111/j.1365-2958.2007.05933.x (2007).
- 411 Chatterjee, A., Xiao, H., Bollong, M., Ai, H.-W. & Schultz, P. G. Efficient viral delivery system for unnatural amino acid mutagenesis in mammalian cells. *Proceedings of the National Academy of Sciences* **110**, 11803, doi:10.1073/pnas.1309584110 (2013).
- 412 Oller-Salvia, B., Kym, G. & Chin, J. W. Rapid and Efficient Generation of Stable Antibody-Drug Conjugates via an Encoded Cyclopropene and an Inverse-Electron-Demand Diels-Alder Reaction. *Angewandte Chemie International Edition* **57**, 2831-2834, doi:10.1002/anie.201712370 (2018).
- 413 Wang, Q. & Wang, L. in *Unnatural Amino Acids: Methods and Protocols* (eds Loredano Pollegioni & Stefano Servi) 199-213 (Humana Press, 2012).
- 414 Ogawa, A., Namba, Y. & Gakumasawa, M. Rational optimization of amber suppressor tRNAs toward efficient incorporation of a non-natural amino acid into protein in a eukaryotic wheat germ extract. *Organic & Biomolecular Chemistry* **14**, 2671-2678, doi:10.1039/c5ob02533h (2016).
- 415 Taki, M., Tokuda, Y., Ohtsuki, T. & Sisido, M. Design of carrier tRNAs and selection of four-base codons for efficient incorporation of various nonnatural amino acids into proteins in *Spodoptera frugiperda* 21 (Sf21) insect cell-free translation system. *Journal of Bioscience and Bioengineering* **102**, 511-517, doi:10.1263/jbb.102.511 (2006).
- 416 Chin, J. W. Expanding and reprogramming the genetic code. *Nature* **550**, 53-60, doi:10.1038/nature24031 (2017).
- 417 Ali, M. *et al.* The global burden of cholera. *Bull World Health Organ* **90**, 209-218A, doi:10.2471/BLT.11.093427 (2012).
- 418 Branson, T. R. *et al.* A Protein-Based Pentavalent Inhibitor of the Cholera Toxin B-Subunit. *Angewandte Chemie International Edition* **53**, 8323-8327, doi:10.1002/anie.201404397 (2014).
- 419 Bharati, K. & Ganguly, N. Cholera toxin: A paradigm of a multifunctional protein. *Indian Journal of Medical Research* **133**, 179-187 (2011).
- 420 Chen, J., Zeng, W., Offord, R. & Rose, K. A Novel Method for the Rational Construction of Well-Defined Immunogens: The Use of Oximation To Conjugate Cholera Toxin B Subunit to a Peptide-Polyoxime Complex. *Bioconjugate Chemistry* **14**, 614-618, doi:10.1021/bc025651u (2003).
- 421 Geoghegan, K. F. & Stroh, J. G. Site-directed conjugation of nonpeptide groups to peptides and proteins via periodate oxidation of a 2-amino alcohol. Application to modification at N-terminal serine. *Bioconjugate Chemistry* **3**, 138-146, doi:10.1021/bc00014a008 (1992).
- 422 Mikolajczyk, S. D. *et al.* High yield, site-specific coupling of N-terminally modified beta-lactamase to a proteolytically derived single-sulfhydryl murine Fab'. *Bioconjugate Chemistry* **5**, 636-646, doi:10.1021/bc00030a020 (1994).
- 423 Clamp, J. R. & Hough, L. The Periodate Oxidation of Amino Acids with Reference to Studies on Glycoproteins. *Biochem J* **94**, 17-24, doi:10.1042/bj0940017 (1965).
- 424 Mitchell, D. D., Pickens, J. C., Korotkov, K., Fan, E. & Hol, W. G. J. 3,5-Substituted phenyl galactosides as leads in designing effective cholera toxin antagonists: synthesis and crystallographic studies. *Bioorganic & Medicinal Chemistry* **12**, 907-920, doi:10.1016/j.bmc.2003.12.019 (2004).



- 425 Soda, K. A Spectrophotometric Microdetermination of Keto Acids with 3-Methyl-2-benzothiazolone Hydrazone. *Agricultural and Biological Chemistry* **31**, 1054-1060, doi:10.1080/00021369.1967.10858916 (1967).
- 426 Bewley, K. D. *et al.* Rheostat Re-Wired: Alternative Hypotheses for the Control of Thioredoxin Reduction Potentials. *PLOS ONE* **10**, e0122466, doi:10.1371/journal.pone.0122466 (2015).
- 427 Sigma-Aldrich, Thioredoxin from Escherichia coli, <https://www.sigmaaldrich.com/catalog/product/sigma/t0910?lang=en&region=GB> (Accessed 10th December 2020).
- 428 Katti, S. K., LeMaster, D. M. & Eklund, H. Crystal structure of thioredoxin from Escherichia coli at 1.68 Å resolution. *Journal of Molecular Biology* **212**, 167-184, doi:10.1016/0022-2836(90)90313-B (1990).
- 429 Stanley, P., Schachter, H. & Taniguchi, N. in *Essentials of Glycobiology* (eds A Varki, RD Cummings, & JD Esko) Ch. 8, (Cold Spring Harbor Laboratory Press, 2009).
- 430 Hounsell, E. F., Davies, M. J. & Smith, K. D. in *The Protein Protocols Handbook* (ed John M. Walker) 1215-1217 (Humana Press, 2009).
- 431 ThermoFisher Scientific, Carbonyl-reactive Crosslinker Chemistry, <https://www.thermofisher.com/uk/en/home/life-science/protein-biology/protein-biology-learning-center/protein-biology-resource-library/pierce-protein-methods/carbonyl-reactive-crosslinker-chemistry.html> (Accessed 2020).
- 432 Kirkeby, S. Binding of fluorescently labeled cholera toxin subunit B to glycolipids in the human submandibular gland and inhibition of binding by periodate oxidation and by galactose. *Biotechnic & Histochemistry* **91**, 1-8, doi:10.3109/10520295.2015.1065000 (2016).
- 433 Doering, T. L., Cummings, R. D. & Aebi, M. in *Essentials of Glycobiology [Internet]. 3rd edition* (eds A Varki, RD Cummings, & JD Esko) Ch. 23, (Cold Spring Harbor Laboratory Press, 2017).
- 434 Goto, M. Protein O-Glycosylation in Fungi: Diverse Structures and Multiple Functions. *Bioscience, Biotechnology, and Biochemistry* **71**, 1415-1427, doi:10.1271/bbb.70080 (2014).
- 435 Promega. PNGase F, <https://www.promega.co.uk/products/mass-spectrometry/glycosidases/pngase-f/?catNum=V4831> (Accessed 2020).
- 436 Promega, Endo H, <https://www.promega.co.uk/products/mass-spectrometry/glycosidases/endoglycosidase-h/?catNum=V4871> (Accessed 2020).
- 437 Medzihradszky, K. F. in *Post-translational Modifications of Proteins: Tools for Functional Proteomics* (ed Christoph Kannicht) 293-316 (Humana Press, 2008).
- 438 Liu, B., Olson, Å., Wu, M., Broberg, A. & Sandgren, M. Biochemical studies of two lytic polysaccharide monooxygenases from the white-rot fungus *Heterobasidion irregulare* and their roles in lignocellulose degradation. *PLOS ONE* **12**, e0189479, doi:10.1371/journal.pone.0189479 (2017).
- 439 Petrov, P., Stassin, F., Pagnouille, C. & Jérôme\*, R. Noncovalent functionalization of multi-walled carbon nanotubes by pyrene containing polymers. *Chemical Communications*, 2904-2905, doi:10.1039/B307751A (2003).
- 440 Chen, R. J., Zhang, Y., Wang, D. & Dai, H. Noncovalent Sidewall Functionalization of Single-Walled Carbon Nanotubes for Protein Immobilization. *Journal of the American Chemical Society* **123**, 3838-3839, doi:10.1021/ja010172b (2001).
- 441 Yang, Q., Shuai, L., Zhou, J., Lu, F. & Pan, X. Functionalization of Multiwalled Carbon Nanotubes by Pyrene-Labeled Hydroxypropyl Cellulose. *The Journal of Physical Chemistry B* **112**, 12934-12939, doi:10.1021/jp805424f (2008).
- 442 Rodríguez-Roldán, V. *et al.* A comparative kinetic analysis of the reactivity of plant, horse, and human respiratory cytochrome c towards cytochrome c oxidase. *Biochemical and Biophysical Research Communications* **346**, 1108-1113, doi:10.1016/j.bbrc.2006.06.022 (2006).
- 443 Nanda, J. S. & Lorsch, J. R. in *Methods in Enzymology* Vol. 536 (ed Jon Lorsch) 87-94 (Academic Press, 2014).

- 444 Stevens, J. M. *et al.* Cytochrome c biogenesis System I. *The FEBS Journal* **278**, 4170-4178, doi:10.1111/j.1742-4658.2011.08376.x (2011).
- 445 Arslan, E., Schulz, H., Zufferey, R., Künzler, P. & Thöny-Meyer, L. Overproduction of the Bradyrhizobium japonicum c-type cytochrome subunits of the cbb3 oxidase in Escherichia coli. *Biochemical and Biophysical Research Communications* **251**, 744-747, doi:<https://doi.org/10.1006/bbrc.1998.9549> (1998).
- 446 Carlson, B. L. *et al.* Function and structure of a prokaryotic formylglycine-generating enzyme. *Journal of Biological Chemistry* **283**, 20117-20125, doi:10.1074/jbc.M800217200 (2008).
- 447 Appel, M. J. & Bertozzi, C. R. Formylglycine, a post-translationally generated residue with unique catalytic capabilities and biotechnology applications. *ACS Chemical Biology* **10**, 72–84, doi:10.1021/cb500897w (2015).
- 448 Knop, M., Engi, P., Lemnar, R. & Seebeck, F. P. In Vitro Reconstitution of Formylglycine-Generating Enzymes Requires Copper(I). *ChemBioChem* **16**, 2147-2150, doi:10.1002/cbic.201500322 (2015).
- 449 Jonas, S., van Loo, B., Hyvönen, M. & Hollfelder, F. A New Member of the Alkaline Phosphatase Superfamily with a Formylglycine Nucleophile: Structural and Kinetic Characterisation of a Phosphonate Monoester Hydrolase/Phosphodiesterase from Rhizobium leguminosarum. *Journal of Molecular Biology* **384**, 120-136, doi:10.1016/j.jmb.2008.08.072 (2008).
- 450 Appel, M. J. *et al.* Formylglycine-generating enzyme binds substrate directly at a mononuclear Cu(I) center to initiate O<sub>2</sub> activation. *Proceedings of the National Academy of Sciences* **116**, 5370, doi:10.1073/pnas.1818274116 (2019).
- 451 Kruger, T. *et al.* Conversion of Serine-Type Aldehyde Tags by the Radical SAM Protein AtsB from Methanosarcina mazei. *ChemBioChem* **20**, 2074-2078, doi:10.1002/cbic.201900322 (2019).
- 452 Grove, T. L., Lee, K.-H., St. Clair, J., Krebs, C. & Booker, S. J. In Vitro Characterization of AtsB, a Radical SAM Formylglycine-Generating Enzyme That Contains Three [4Fe-4S] Clusters. *Biochemistry* **47**, 7523-7538, doi:10.1021/bi8004297 (2008).
- 453 Goldman, P. J. *et al.* X-ray structure of an AdoMet radical activase reveals an anaerobic solution for formylglycine posttranslational modification. *Proceedings of the National Academy of Sciences* **110**, 8519, doi:10.1073/pnas.1302417110 (2013).
- 454 Benjdia, A. *et al.* Anaerobic sulfatase-maturing enzyme—a mechanistic link with glycy radical-activating enzymes? *The FEBS journal* **277**, 1906-1920, doi:10.1111/j.1742-4658.2010.07613.x (2010).
- 455 Rabuka, D., Rush, J. S., deHart, G. W., Wu, P. & Bertozzi, C. R. Site-specific chemical protein conjugation using genetically encoded aldehyde tags. *Nature Protocols* **7**, 1052-1067, doi:10.1038/nprot.2012.045 (2012).
- 456 Holder, P. G. *et al.* Reconstitution of Formylglycine-generating Enzyme with Copper(II) for Aldehyde Tag Conversion. *Journal of Biological Chemistry* **290**, 15730-15745, doi:10.1074/jbc.M115.652669 (2015).
- 457 Knop, M., Dang, T. Q., Jeschke, G. & Seebeck, F. P. Copper is a Cofactor of the Formylglycine-Generating Enzyme. *ChemBioChem* **18**, 161-165, doi:10.1002/cbic.201600359 (2017).
- 458 Roepstorff, P. & Fohlman, J. Proposal for a common nomenclature for sequence ions in mass spectra of peptides. *Biomedical Mass Spectrometry*, doi:10.1002/bms.1200111109 (1984).
- 459 Jarman, O. *Harnessing formylglycine-generating enzyme for the site-selective covalent modification of proteins* MChem thesis, The University of York, (2017).
- 460 Ono, K. *et al.* Synthesis of l-cysteine derivatives containing stable sulfur isotopes and application of this synthesis to reactive sulfur metabolome. *Free Radical Biology & Medicine* **106**, 69-79, doi:10.1016/j.freeradbiomed.2017.02.023 (2017).
- 461 Kudirka, R. *et al.* Generating site-specifically modified proteins via a versatile and stable nucleophilic carbon ligation. *Chemistry & Biology* **22**, 293-298, doi:10.1016/j.chembiol.2014.11.019 (2015).

- 462 Bocian-Ostrzycka, K. M., Grzeszczuk, M. J., Banas, A. M. & Jagusztyn-Krynicka, E. K. Bacterial thiol oxidoreductases - from basic research to new antibacterial strategies. *Applied Microbiology & Biotechnology* **101**, 3977-3989, doi:10.1007/s00253-017-8291-8 (2017).
- 463 Schweida, D. *et al.* The NMR signature of gluconoylation: a frequent N-terminal modification of isotope-labeled proteins. *Journal of Biomolecular NMR* **73**, 71-79, doi:10.1007/s10858-019-00228-6 (2019).
- 464 Aon, J. C. *et al.* Suppressing posttranslational gluconoylation of heterologous proteins by metabolic engineering of *Escherichia coli*. *Applied and Environmental Microbiology* **74**, 950-958, doi:10.1128/AEM.01790-07 (2008).
- 465 Liu, J. *et al.* An Efficient Site-Specific Method for Irreversible Covalent Labeling of Proteins with a Fluorophore. *Scientific Reports* **5**, doi:10.1038/srep16883 (2015).
- 466 Smith, E. L. *et al.* Chemoenzymatic Fc Glycosylation via Engineered Aldehyde Tags. *Bioconjugate Chemistry* **25**, 788-795, doi:10.1021/bc500061s (2014).
- 467 Knop, M., Lemnar, R. & Seebeck, F. P. Mutation of Conserved Residues Increases in Vitro Activity of the Formylglycine-Generating Enzyme. *ChemBioChem* **18**, 1755-1761, doi:10.1002/cbic.201700174 (2017).
- 468 Keane, L.-A. *Small-molecule-based crosslinking and bioconjugation of biomolecules* PhD thesis, NUI Galway, (2020).
- 469 Shi, X. *et al.* Quantitative fluorescence labeling of aldehyde-tagged proteins for single-molecule imaging. *Nature Methods* **9**, 499-503, doi:10.1038/nmeth.1954 (2012).
- 470 Carrico, I. S., Carlson, B. L. & Bertozzi, C. R. Introducing genetically encoded aldehydes into proteins. *Nature Chemical Biology*, doi:10.1038/nchembio878 (2007).
- 471 Wu, P. *et al.* Site-specific chemical modification of recombinant proteins produced in mammalian cells by using the genetically encoded aldehyde tag. *Proceedings of the National Academy of Sciences* **106**, 3000, doi:10.1073/pnas.0807820106 (2009).
- 472 Vasiliou, V., Pappa, A. & Petersen, D. R. Role of aldehyde dehydrogenases in endogenous and xenobiotic metabolism. *Chemico-Biological Interactions* **129**, 1-19, doi:10.1016/S0009-2797(00)00211-8 (2000).
- 473 Jackson, B. *et al.* Update on the aldehyde dehydrogenase gene (ALDH) superfamily. *Human Genomics* **5**, 283, doi:10.1186/1479-7364-5-4-283 (2011).
- 474 Ulrich, S., Boturyn, D., Marra, A., Renaudet, O. & Dumy, P. Oxime Ligation: A Chemoselective Click-Type Reaction for Accessing Multifunctional Biomolecular Constructs. *Chemistry – A European Journal* **20**, 34-41, doi:10.1002/chem.201302426 (2014).
- 475 Gentil, S. *et al.* Clicked Bifunctional Dendrimeric and Cyclopeptidic Addressable Redox Scaffolds for the Functionalization of Carbon Nanotubes with Redox Molecules and Enzymes. *Langmuir*, doi:10.1021/acs.langmuir.0c02095 (2021).
- 476 Yates, N. D. *et al.* Aldehyde-Mediated Protein-to-Surface Tethering via Controlled Diazonium Electrode Functionalization Using Protected Hydroxylamines. *Langmuir* **36**, 5654-5664, doi:10.1021/acs.langmuir.9b01254 (2020).
- 477 Boutureira, O. & Bernardes, G. J. L. Advances in Chemical Protein Modification. *Chemical Reviews* **115**, 2174-2195, doi:10.1021/cr500399p (2015).
- 478 Zhang, Y., Park, K.-Y., Suazo, K. F. & Distefano, M. D. Recent progress in enzymatic protein labelling techniques and their applications. *Chemical Society Reviews* **47**, 9106-9136, doi:10.1039/C8CS00537K (2018).
- 479 Meldal, M. & Schoffelen, S. Recent advances in covalent, site-specific protein immobilization. *F1000Research* **5**, doi:10.12688/f1000research.9002.1 (2016).
- 480 Algar, W. R., Dawson, P. & Medintz, I. L. *Chemoselective and Bioorthogonal Ligation Reactions: Concepts and Applications*. (Wiley, 2017).
- 481 Britton, J., Majumdar, S. & Weiss, G. A. Continuous flow biocatalysis. *Chemical Society Reviews* **47**, 5891-5918, doi:10.1039/C7CS00906B (2018).

- 482 Christman, K. L., Broyer, R. M., Tolstyka, Z. P. & Maynard, H. D. Site-specific protein immobilization through N-terminal oxime linkages. *Journal of Materials Chemistry* **17**, 2021-2021, doi:10.1039/b618002g (2007).
- 483 Lempens, E. H. M., Helms, B. A., Merckx, M. & Meijer, E. W. Efficient and Chemoselective Surface Immobilization of Proteins by Using Aniline-Catalyzed Oxime Chemistry. *ChemBioChem* **10**, 658-662, doi:10.1002/cbic.200900028 (2009).
- 484 Park, S. & Yousaf, M. N. An Interfacial Oxime Reaction To Immobilize Ligands and Cells in Patterns and Gradients to Photoactive Surfaces. *Langmuir* **24**, 6201-6207, doi:10.1021/la8005663 (2008).
- 485 Decostaire, I. E., Lelievre, D., Aucagne, V. & Delmas, A. F. Solid phase oxime ligations for the iterative synthesis of polypeptide conjugates. *Organic & Biomolecular Chemistry* **12**, 5536-5543, doi:10.1039/c4ob00760c (2014).
- 486 Pfander, S., Fiammengo, R., Kirin, S. I., Metzler-Nolte, N. & Jaschke, A. Reversible site-specific tagging of enzymatically synthesized RNAs using aldehyde-hydrazine chemistry and protease-cleavable linkers. *Nucleic Acids Res* **35**, e25, doi:10.1093/nar/gkl1110 (2007).
- 487 Proudnikov, D. & Mirzabekov, A. Chemical Methods of DNA and RNA Fluorescent Labeling. *Nucleic Acids Res* **24**, 4535-4542, doi:10.1093/nar/24.22.4535 (1996).
- 488 Soom, N. A. & Thiemann, T. Hydrogenation of Alkenes with NaBH<sub>4</sub>, CH<sub>3</sub>CO<sub>2</sub>H, Pd/C in the Presence of O- and N-Benzyl Functions. *International Journal of Organic Chemistry* **06**, 1-11, doi:10.4236/ijoc.2016.61001 (2016).
- 489 Hudson, J. L., Jian, H., Leonard, A. D., Stephenson, J. J. & Tour, J. M. Triazenes as a stable diazonium source for use in functionalizing carbon nanotubes in aqueous suspensions. *Chemistry of Materials* **18**, 2766-2770, doi:10.1021/cm060020l (2006).
- 490 Kongsfelt, M. *et al.* Combining Aryltriazenes and Electrogenerated Acids To Create Well-Defined Aryl-Tethered Films and Patterns on Surfaces. *Journal of the American Chemical Society* **133**, 3788-3791, doi:10.1021/ja111731d (2011).
- 491 Hansen, M. N. *et al.* Synthesis and Application of a Triazene-Ferrocene Modifier for Immobilization and Characterization of Oligonucleotides at Electrodes. *The Journal of Organic Chemistry* **75**, 2474-2481, doi:10.1021/jo9024368 (2010).
- 492 Landman, I. R. *et al.* Bronsted and Lewis acid adducts of triazenes. *Dalton Transactions* **49**, 2317-2322, doi:10.1039/d0dt00049c (2020).
- 493 Bélanger, D. & Pinson, J. Electrografting: a powerful method for surface modification. *Chemical Society Reviews* **40**, 3995-4048, doi:10.1039/C0CS00149J (2011).
- 494 Liu, G., Liu, J., Böcking, T., Eggers, P. K. & Gooding, J. J. The modification of glassy carbon and gold electrodes with aryl diazonium salt: The impact of the electrode materials on the rate of heterogeneous electron transfer. *Chemical Physics* **319**, 136-146, doi:10.1016/j.chemphys.2005.03.033 (2005).
- 495 Lazar, J., Schnelting, C., Slavcheva, E. & Schnakenberg, U. Hampering of the Stability of Gold Electrodes by Ferri-/Ferrocyanide Redox Couple Electrolytes during Electrochemical Impedance Spectroscopy. *Analytical Chemistry* **88**, 682-687, doi:10.1021/acs.analchem.5b02367 (2016).
- 496 Vogt, S., Su, Q., Gutiérrez-Sánchez, C. & Nöll, G. Critical View on Electrochemical Impedance Spectroscopy Using the Ferri/Ferrocyanide Redox Couple at Gold Electrodes. *Analytical Chemistry* **88**, 4383-4390, doi:10.1021/acs.analchem.5b04814 (2016).
- 497 Marquis, B. J., Louks, H. P., Bose, C., Wolfe, R. R. & Singh, S. P. A New Derivatization Reagent for HPLC-MS Analysis of Biological Organic Acids. *Chromatographia* **80**, 1723-1732, doi:10.1007/s10337-017-3421-0 (2017).
- 498 Raymakers, J., Haenen, K. & Maes, W. Diamond surface functionalization: from gemstone to photoelectrochemical applications. *Journal of Materials Chemistry C* **7**, 10134-10165, doi:10.1039/C9TC03381E (2019).

- 499 Beamson, G. & Briggs, D. *High Resolution XPS of Organic Polymers : The Scienta ESCA300 Database*. (John Wiley and Sons Ltd, 1992).
- 500 Gengenbach, T. R., Chatelier, R. C. & Griesser, H. J. Correlation of the Nitrogen 1s and Oxygen 1s XPS Binding Energies with Compositional Changes During Oxidation of Ethylene Diamine Plasma Polymers. *Surface and Interface Analysis* **24**, 611-619, doi:10.1002/(SICI)1096-9918(19960916)24:9<611::AID-SIA169>3.0.CO;2-7 (1996).
- 501 Petrangolini, P., Alessandrini, A., Berti, L. & Facci, P. An electrochemical scanning tunneling microscopy study of 2-(6-mercaptoalkyl)hydroquinone molecules on Au(111). *Journal of the American Chemical Society* **132**, 7445–7453, doi:10.1021/ja101666q (2010).
- 502 Trammell, S. A. *et al.* Heterogeneous electron transfer of quinone–hydroquinone in alkaline solutions at gold electrode surfaces: Comparison of saturated and unsaturated bridges. *Journal of Electroanalytical Chemistry* **606**, 33-38, doi:10.1016/j.jelechem.2007.04.008 (2007).
- 503 Tse, E. C. *et al.* Proton transfer dynamics dictate quinone speciation at lipid-modified electrodes. *Physical Chemistry Chemical Physics* **19**, 7086-7093, doi:10.1039/c6cp07586j (2017).
- 504 Pillay, J., Agboola, B. O. & Ozoemena, K. I. Electrochemistry of 2-dimethylaminoethanethiol SAM on gold electrode: Interaction with SWCNT-poly(m-aminobenzene sulphonic acid), electric field-induced protonation–deprotonation, and surface pKa. *Electrochemistry Communications* **11**, 1292-1296, doi:10.1016/j.elecom.2009.04.028 (2009).
- 505 Mayer, P. & Holze, R. Electrocatalysis of redox reactions by metal nanoparticles on graphite electrodes. *Journal of Solid State Electrochemistry* **5**, 402-411, doi:10.1007/s100080000169 (2001).
- 506 Yeap, W. S. *et al.* Boron-Doped Diamond Functionalization by an Electrografting/Alkyne–Azide Click Chemistry Sequence. *ChemElectroChem* **1**, 1145-1154, doi:10.1002/celc.201402068 (2014).
- 507 Kondo, T. *et al.* Photochemical Modification of a Boron-doped Diamond Electrode Surface with Vinylferrocene. *The Journal of Physical Chemistry C* **112**, 11887-11892, doi:10.1021/jp802875c (2008).
- 508 Wisdom, G. B. in *The Protein Protocols Handbook* (ed John M. Walker) 273-274 (Humana Press, 1996).
- 509 Baker, M. R. *et al.* Site-Specific N-Glycosylation Characterization of Windmill Palm Tree Peroxidase Using Novel Tools for Analysis of Plant Glycopeptide Mass Spectrometry Data. *Journal of Proteome Research* **15**, 2026-2038, doi:10.1021/acs.jproteome.6b00205 (2016).
- 510 Capone, S. *et al.* Glyco-variant library of the versatile enzyme horseradish peroxidase. *Glycobiology* **24**, 852-863, doi:10.1093/glycob/cwu047 (2014).
- 511 Nicolini, J. V., Ferraz, H. C. & de Resende, N. S. Immobilization of horseradish peroxidase on titanate nanowires for biosensing application. *Journal of Applied Electrochemistry* **46**, 17-25, doi:10.1007/s10800-015-0907-z (2016).
- 512 Polsky, R. *et al.* Diazonium-Functionalized Horseradish Peroxidase Immobilized via Addressable Electrodeposition: Direct Electron Transfer and Electrochemical Detection. *Langmuir* **23**, 364-366, doi:10.1021/la062916a (2007).
- 513 Singh, K. & Blanford, C. F. Electrochemical Quartz Crystal Microbalance with Dissipation Monitoring: A Technique to Optimize Enzyme Use in Bioelectrocatalysis. *ChemCatChem* **6**, 921-929, doi:10.1002/cctc.201300900 (2014).
- 514 McArdle, T., McNamara, T. P., Fei, F., Singh, K. & Blanford, C. F. Optimizing the Mass-Specific Activity of Bilirubin Oxidase Adlayers through Combined Electrochemical Quartz Crystal Microbalance and Dual Polarization Interferometry Analyses. *ACS Applied Materials & Interfaces* **7**, 25270-25280, doi:10.1021/acsami.5b07290 (2015).
- 515 McNamara, T. P. & Blanford, C. F. A sensitivity metric and software to guide the analysis of soft films measured by a quartz crystal microbalance. *Analyst* **141**, 2911-2919, doi:10.1039/C6AN00143B (2016).

- 516 Nelson, G. W. *et al.* Surface Characterization and in situ Protein Adsorption Studies on Carbene-Modified Polymers. *Langmuir* **31**, 11086-11096, doi:10.1021/acs.langmuir.5b01644 (2015).
- 517 Zhang, B. & Sun, L. Artificial photosynthesis: opportunities and challenges of molecular catalysts. *Chemical Society Reviews* **48**, 2216-2264, doi:10.1039/C8CS00897C (2019).
- 518 Ferris, D. P. *et al.* Oxime Ligation on the Surface of Mesoporous Silica Nanoparticles. *Organic Letters* **17**, 2146-2149, doi:10.1021/acs.orglett.5b00740 (2015).
- 519 Bushnell, G. W., Louie, G. V. & Brayer, G. D. High-resolution three-dimensional structure of horse heart cytochrome c. *Journal of Molecular Biology* **214**, 585-595, doi:10.1016/0022-2836(90)90200-6 (1990).
- 520 Stewart, M. P. *et al.* Direct Covalent Grafting of Conjugated Molecules onto Si, GaAs, and Pd Surfaces from Aryldiazonium Salts. *Journal of the American Chemical Society* **126**, 370-378, doi:10.1021/ja0383120 (2004).
- 521 Corgier, B. P., Laurent, A., Perriat, P., Blum, L. J. & Marquette, C. A. A Versatile Method for Direct and Covalent Immobilization of DNA and Proteins on Biochips. *Angewandte Chemie International Edition* **46**, 4108-4110, doi:10.1002/anie.200605010 (2007).
- 522 Leier, S., Richter, S., Bergmann, R., Wuest, M. & Wuest, F. Radiometal-Containing Aryl Diazonium Salts for Chemoselective Bioconjugation of Tyrosine Residues. *ACS Omega* **4**, 22101-22107, doi:10.1021/acsomega.9b03248 (2019).
- 523 Chrouda, A. *et al.* Electrically addressable deposition of diazonium-functionalized antibodies on boron-doped diamond microcells for the detection of ochratoxin A. *Analytical Methods* **7**, 2444-2451, doi:10.1039/C4AY02899F (2015).
- 524 Polsky, R. *et al.* Electrically addressable diazonium-functionalized antibodies for multianalyte electrochemical sensor applications. *Biosensors and Bioelectronics* **23**, 757-764, doi:10.1016/j.bios.2007.08.013 (2008).
- 525 Gavriilyuk, J., Ban, H., Nagano, M., Hakamata, W. & Barbas, C. F. Formylbenzene Diazonium Hexafluorophosphate Reagent for Tyrosine-Selective Modification of Proteins and the Introduction of a Bioorthogonal Aldehyde. *Bioconjugate Chemistry* **23**, 2321-2328, doi:10.1021/bc300410p (2012).
- 526 Murphy, A. R., St John, P. & Kaplan, D. L. Modification of silk fibroin using diazonium coupling chemistry and the effects on hMSC proliferation and differentiation. *Biomaterials* **29**, 2829-2838, doi:10.1016/j.biomaterials.2008.03.039 (2008).
- 527 Addy, P. S., Erickson, S. B., Italia, J. S. & Chatterjee, A. A Chemoselective Rapid Azo-Coupling Reaction (CRACR) for Unclickable Bioconjugation. *Journal of the American Chemical Society* **139**, 11670-11673, doi:10.1021/jacs.7b05125 (2017).
- 528 Shadmehr, M., Davis, G. J., Mehari, B. T., Jensen, S. M. & Jewett, J. C. Coumarin Triazabutadienes for Fluorescent Labeling of Proteins. *ChemBioChem* **19**, 2550-2552, doi:10.1002/cbic.201800599 (2018).
- 529 Jensen, S. M., Kimani, F. W. & Jewett, J. C. Light-Activated Triazabutadienes for the Modification of a Viral Surface. *ChemBioChem* **17**, 2216-2219, doi:10.1002/cbic.201600508 (2016).
- 530 Guzman, L. E., Kimani, F. W. & Jewett, J. C. Protecting Triazabutadienes To Afford Acid Resistance. *ChemBioChem* **17**, 2220-2222, doi:10.1002/cbic.201600517 (2016).
- 531 Cornali, B. M., Kimani, F. W. & Jewett, J. C. Cu-Click Compatible Triazabutadienes To Expand the Scope of Aryl Diazonium Ion Chemistry. *Organic Letters* **18**, 4948-4950, doi:10.1021/acs.orglett.6b02420 (2016).
- 532 Kimani, F. W. & Jewett, J. C. Water-soluble triazabutadienes that release diazonium species upon protonation under physiologically relevant conditions. *Angewandte Chemie International Edition* **54**, 4051-4054, doi:10.1002/anie.201411277 (2015).
- 533 He, J., Kimani, F. W. & Jewett, J. C. A Photobasic Functional Group. *Journal of the American Chemical Society* **137**, 9764-9767, doi:10.1021/jacs.5b04367 (2015).

- 534 Hooker, J. M., Kovacs, E. W. & Francis, M. B. Interior Surface Modification of Bacteriophage MS2. *Journal of the American Chemical Society* **126**, 3718-3719, doi:10.1021/ja031790q (2004).
- 535 Khramov, D. M. & Bielawski, C. W. Donor-Acceptor Triazenes: Synthesis, Characterization, and Study of Their Electronic and Thermal Properties. *The Journal of Organic Chemistry* **72**, 9407-9417, doi:10.1021/jo070789x (2007).
- 536 Sinclair, A. J., del Amo, V. & Philp, D. Structure-reactivity relationships in a recognition mediated [3+2] dipolar cycloaddition reaction. *Organic & Biomolecular Chemistry* **7**, 3308-3318, doi:10.1039/b908072d (2009).
- 537 Breslow, R. On the Mechanism of Thiamine Action. IV.1 Evidence from Studies on Model Systems. *Journal of the American Chemical Society* **80**, 3719-3726, doi:10.1021/ja01547a064 (1958).
- 538 Grasa, G. A., Güveli, T., Singh, R. & Nolan, S. P. Efficient Transesterification/Acylation Reactions Mediated by N-Heterocyclic Carbene Catalysts. *The Journal of Organic Chemistry* **68**, 2812-2819, doi:10.1021/jo0267551 (2003).
- 539 Roy, M., Roy, S., Singh, K. S., Kalita, J. & Singh, S. S. Synthesis, characterisation and anti-diabetic activities of triorganotin(IV) azo-carboxylates derived from amino benzoic acids and resorcinol: Crystal structure and topological study of a 48 membered macrocyclic-tetrameric trimethyltin(IV) complex. *Inorganica Chimica Acta* **439**, 164-172, doi:10.1016/j.ica.2015.10.012 (2016).
- 540 Patouret, R. & Kamenecka, T. M. Synthesis of 2-aryl-2H-tetrazoles via a regioselective [3+2] cycloaddition reaction. *Tetrahedron Letters* **57**, 1597-1599, doi:10.1016/j.tetlet.2016.02.102 (2016).
- 541 Hofstetter, O., Hofstetter, H., Miron, T. & Wilchek, M. The conversion of azo-quenchers to fluorophores. *Analytical Biochemistry* **585**, 113400, doi:10.1016/j.ab.2019.113400 (2019).
- 542 Laikhter, A., Behlke, M., Walder, J., Roberts, K. & Yong, Y. FLUORESCENCE QUENCHING AZO DYES, THEIR METHODS OF PREPARATION AND USE. WO/2005/049849 (2005).
- 543 Addy, P. S., Zheng, Y., Italia, J. S. & Chatterjee, A. A "Quencherogenic" Chemoselective Protein Labeling Strategy. *ChemBioChem* **20**, 1659-1663, doi:10.1002/cbic.201800817 (2019).
- 544 Marinozzi, M., Marcelli, G., Carotti, A. & Natalini, B. One-pot, telescoped synthesis of N-aryl-5-aminopyrazoles from anilines in environmentally benign conditions. *RSC Advances* **4**, doi:10.1039/c3ra47541g (2014).
- 545 Mädler, S., Bich, C., Touboul, D. & Zenobi, R. Chemical cross-linking with NHS esters: a systematic study on amino acid reactivities. *Journal of Mass Spectrometry* **44**, 694-706, doi:10.1002/jms.1544 (2009).
- 546 Lumiprobe, Antibody labeling protocol, <https://www.lumiprobe.com/manual/antibody-labeling-kits> (Accessed 18th March 2021).
- 547 Wunderlich, M. & Glockshuber, R. Redox properties of protein disulfide isomerase (dsba) from *Escherichia coli*. *Protein Science* **2**, 717-726, doi:10.1002/pro.5560020503 (1993).
- 548 Prince, M. B. in *Applied Solid State Physics* (eds W. Low & M. Schieber) 223-234 (Springer US, 1970).
- 549 Zapun, A., Bardwell, J. C. A. & Creighton, T. E. The reactive and destabilizing disulfide bond of DsbA, a protein required for protein disulfide bond formation in vivo. *Biochemistry* **32**, 5083-5092, doi:10.1021/bi00070a016 (1993).
- 550 Adamson, H. *et al.* Analysis of HypD Disulfide Redox Chemistry via Optimization of Fourier Transformed ac Voltammetric Data. *Analytical Chemistry* **89**, 1565-1573, doi:10.1021/acs.analchem.6b03589 (2017).
- 551 Behrens, C. R. *et al.* Rapid chemoselective bioconjugation through oxidative coupling of anilines and aminophenols. *Journal of the American Chemical Society* **133**, 16398-16401, doi:10.1021/ja2033298 (2011).



- 552 Courtade, G. *et al.* Mechanistic basis of substrate-O<sub>2</sub> coupling within a chitin-active lytic polysaccharide monooxygenase: An integrated NMR/EPR study. *Proceedings of the National Academy of Sciences* **117**, 19178-19189, doi:10.1073/pnas.2004277117 (2020).
- 553 Kolodziej, A., Fic, K. & Frackowiak, E. Towards sustainable power sources: chitin-bound carbon electrodes for electrochemical capacitors. *Journal of Materials Chemistry A* **3**, 22923-22930, doi:10.1039/c5ta06750b (2015).
- 554 Wittstock, G., Burchardt, M., Pust, S. E., Shen, Y. & Zhao, C. Scanning Electrochemical Microscopy for Direct Imaging of Reaction Rates. *Angewandte Chemie International Edition* **46**, 1584-1617, doi:10.1002/anie.200602750 (2007).
- 555 Bachman, J. C. *et al.* Electrochemical polymerization of pyrene derivatives on functionalized carbon nanotubes for pseudocapacitive electrodes. *Nature Communications* **6**, 7040, doi:10.1038/ncomms8040 (2015).
- 556 Bond, A. M. *et al.* An integrated instrumental and theoretical approach to quantitative electrode kinetic studies based on large amplitude Fourier transformed a.c. voltammetry: A mini review. *Electrochemistry Communications* **57**, 78-83, doi:10.1016/j.elecom.2015.04.017 (2015).
- 557 Bond, A. M., Duffy, N. W., Guo, S.-X., Zheng, J. & Elton, D. Changing the Look of Voltammetry. *Analytical Chemistry* **77**, 186 A-195 A, doi:10.1021/ac053370k (2005).
- 558 O'Reilly, J. E. Oxidation-reduction potential of the ferro-ferricyanide system in buffer solutions. *Biochimica et Biophysica Acta (BBA) - Bioenergetics* **292**, 509-515, doi:10.1016/0005-2728(73)90001-7 (1973).
- 559 New England BioLabs, Endo H/Endo Hf Protocol, <https://international.neb.com/protocols/2012/10/18/endo-hf-protocol#:~:text=Hf%20Protocol-,Endo%20H%2FEndo%20Hf%20Protocol,%C2%B0C%20for%2010%20minutes> (Accessed 13th January 2021).
- 560 New England BioLabs, Product: Endo H, <https://international.neb.com/products/p0702-endo-h#Product%20Information> (Accessed 2020).
- 561 New England BioLabs, PNGase F protocol, <https://international.neb.com/protocols/2014/07/31/pngase-f-protocol> (Accessed 2021).
- 562 New England BioLabs, Product: PNG F, <https://international.neb.com/products/p0704-pngase-f#Product%20Information> (Accessed 13th January 2021).
- 563 Jancso, B. *MChem dissertation: Ben Jancso* MChem thesis, The University of York, (2018).
- 564 Gustafson, J. L. *et al.* Small-Molecule-Mediated Degradation of the Androgen Receptor through Hydrophobic Tagging. *Angewandte Chemie International Edition* **54**, 9659-9662, doi:10.1002/anie.201503720 (2015).
- 565 Mora-Radó, H. *et al.* Synthetic and Mechanistic Investigation of an Oxime Ether Electrocyclization Approach to Heteroaromatic Boronic Acid Derivatives. *Chemistry – A European Journal* **24**, 9530-9534, doi:10.1002/chem.201802350 (2018).
- 566 Delincée, H. & Radola, B. J. Fractionation of Horseradish Peroxidase by Preparative Isoelectric Focusing, Gel Chromatography and Ion-Exchange Chromatography. *European Journal of Biochemistry* **52**, 321-330, doi:doi:10.1111/j.1432-1033.1975.tb04000.x (1975).
- 567 Kerner, Z. & Pajkossy, T. On the origin of capacitance dispersion of rough electrodes. *Electrochimica Acta* **46**, 207-211, doi:10.1016/S0013-4686(00)00574-0 (2000).
- 568 Lasia, A. *Electrochemical Impedance Spectroscopy and its Applications*. 1 edn, XIII, 367 (Springer-Verlag, 2014).
- 569 Klein, T. & Kickelbick, G. Aluminum nanoparticle preparation via catalytic decomposition of alane adducts – influence of reaction parameters on nanoparticle size, morphology and reactivity. *Dalton Transactions* **49**, 9820-9834, doi:10.1039/D0DT01820A (2020).



- 570 Bou-Hamdan, F. R., Lévesque, F., O'Brien, A. G. & Seeberger, P. H. Continuous flow photolysis of aryl azides: Preparation of 3H-azepinones. *Beilstein J Org Chem* **7**, 1124-1129, doi:10.3762/bjoc.7.129 (2011).
- 571 Bunchuay, T., Docker, A., Martinez-Martinez, A. J. & Beer, P. D. A Potent Halogen-Bonding Donor Motif for Anion Recognition and Anion Template Mechanical Bond Synthesis. *Angewandte Chemie International Edition* **58**, 13823-13827, doi:10.1002/anie.201907625 (2019).
- 572 Occhipinti, G., Jensen, V. R., Törnroos, K. W., Frøystein, N. Å. & Bjørsvik, H.-R. Synthesis of a new bidentate NHC–Ag(I) complex and its unanticipated reaction with the Hoveyda–Grubbs first generation catalyst. *Tetrahedron* **65**, 7186-7194, doi:10.1016/j.tet.2009.05.095 (2009).
- 573 Ruddlesden, A. J., Mewis, R. E., Green, G. G. R., Whitwood, A. C. & Duckett, S. B. Catalytic Transfer of Magnetism Using a Neutral Iridium Phenoxide Complex. *Organometallics* **34**, 2997-3006, doi:10.1021/acs.organomet.5b00311 (2015).
- 574 Asensio, J. M. *et al.* Synthesis of Water-Soluble Palladium Nanoparticles Stabilized by Sulfonated N-Heterocyclic Carbenes. *Chemistry – A European Journal* **23**, 13435-13444, doi:10.1002/chem.201702204 (2017).
- 575 Strassner, T. & Ahrens, S. Salts Comprising Aryl-Alkyl-Substituted Imidazolium and Triazolium Cations and the Use Thereof. US2011105761 (2009).
- 576 Kálái, T., Rozsnyai, B., Jerkovich, G. & Hideg, K. Crosslinking 2,5-Dihydro-1H-pyrrol-1-yloxy Spin-Label Reagents Bifunctionalized with Azidophthalimidyl and Methylthiosulfonyloxy Groups. *ChemInform* **26** (1995).
- 577 Cervi, A. *et al.* Gold(I)-Catalyzed Intramolecular Hydroarylation of Phenol-Derived Propiolates and Certain Related Ethers as a Route to Selectively Functionalized Coumarins and 2H-Chromenes. *The Journal of Organic Chemistry* **86**, 178-198, doi:10.1021/acs.joc.0c02011 (2021).
- 578 Nicholas Yates, [nyates-york/Surface-confined-cyclic-voltammetry-analyser, https://zenodo.org/badge/latestdoi/334178834](https://zenodo.org/badge/latestdoi/334178834), doi:10.5281/zenodo.4479317 (Accessed 2021).